ICENTE'19

SELCUK UNIVERSITY FACULTY OF TECHNOLOGY

INTERNATIONAL CONFERENCE ON ENGINEERING TECHNOLOGIES

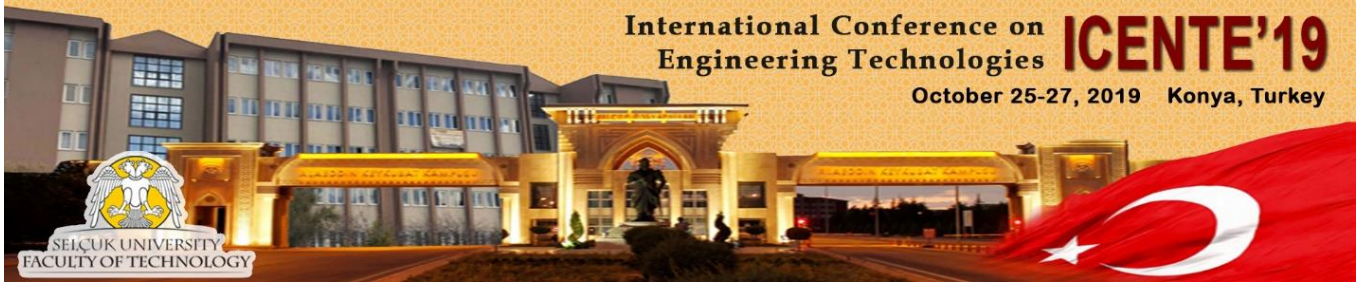## October 25-27, 2019

Konya/TURKEY

PROCEEDINGS

International Conference on Engineering Technologies

3th International Conference, ICENTE
Konya, Turkey, October 25-27, 2019

Proceedings

Editors
Ismail SARITAS
Mehmet CUNKAS
Fatih BASCIFTCI

International Conference on Engineering Technologies

3th International Conference, ICENTE
Konya, Turkey, October 25-27, 2019

Proceedings

Editors
Ismail SARITAS
Mehmet CUNKAS
Fatih BASCIFTCI

E-ISBN: 978-605-68537-9-1

www.snbt.com.tr

SN Bilgi Teknolojileri

Kürden Mh. Temizciler Sk. No:5/3 Meram / KONYA
Tel: 0.332 323 07 39
October – 2019

EDITORS   :

Prof. Dr. Ismail SARITAS
Selcuk University, Turkey
Depertmant of Electrical and Electronics Engineering, Faculty of Technology
Alaeddin Keykubat Campus 42031 Konya, Turkey
isaritas@selcuk.edu.tr

Prof. Dr. Mehmet CUNKAS
Selcuk University, Turkey
Depertmant of Electrical and Electronics Engineering, Faculty of Technology
Alaeddin Keykubat Campus 42031 Konya, Turkey
mcunkas@selcuk.edu.tr

Prof. Dr. Fatih BASCIFTCI
Selcuk University, Turkey
Depertmant of Computer Engineering, Faculty of Technology
Alaeddin Keykubat Campus 42031 Konya, Turkey
basciftci@selcuk.edu.tr

ASSISTANT EDITORS   :

Ilker Ali OZKAN
Selcuk University, Turkey
Depertmant of Computer Engineering, Faculty of Technology
Alaeddin Keykubat Campus 42031 Konya, Turkey
ilkerozkan@selcuk.edu.tr

Murat KOKLU
Selcuk University, Turkey
Depertmant of Computer Engineering, Faculty of Technology
Alaeddin Keykubat Campus 42031 Konya, Turkey
mkoklu@selcuk.edu.tr

PREFACE

International Conference on Engineering Technologies (ICENTE'19) was organized in Konya, Turkey on 25-27 October 2019.

The main objective of ICENTE'19 is to present the latest research and results of scientists related to Electrical and Electronics, Biomedical, Computer, Civil, Mechanical, Mechatronics, Metallurgical and Materials Engineering fields. This conference provides opportunities for the delegates from different areas in order to exchange new ideas and application experiences, to establish business or research relations and to find global partners face to face for future collaborations.

All paper submissions have been double blind and peer reviewed and evaluated based on originality, technical and/or research content/depth, correctness, relevance to conference, contributions, and readability. Selected papers presented in the conference will be published in the Journal of Selcuk Technic if their content matches with the topics of the journal.

At this conference, there are 203 paper submissions. Each paper proposal was evaluated by two reviewers. And finally, 123 papers were presented at the conference from 8 different countries (Albania, Azerbaijan, Bulgaria, Crotia, Iraq, Macedonia, Latvia, Turkey).

In particular, we would like to thank Prof. Dr. Mustafa SAHIN, Rector of Selcuk University; Prof. Dr. Prof. Dr. Jurgis Porins, Riga Technical University (RTU); Prof. Dr. Tzvetomir Vassilev, University of Ruse; Journal of Selcuk Technic. They have made a crucial contribution towards the success of this conference. Our thanks also go to the colleagues in our conference office.

<div align="right">

Ismail SARITAS – Mehmet CUNKAS – Fatih BASCIFTCI
Editors

</div>

PROGRAMME COMMITTEES

HONORARY CHAIR   :
  Mustafa Sahin, Rector of Selcuk University, Turkey

GENERAL CHAIRS   :
  Ismail Saritas, Selcuk University, Turkey
  Mehmet Cunkas, Selcuk University - Turkey
  Fatih Basciftci, Selcuk University – Turkey

CO-CHAIRS   :
  Necmettin Tarakcioglu, Selcuk University, Turkey
  Alla Anohina Naumeca, Riga Technical University, Latvia
  Silyan Sibinov Arsov, Rousse University, Bulgaria
  Murat Ciniviz, Selcuk University, Turkey

SECTION EDITORS :
  Mehmet Cunkas, Selcuk University, Turkey
  Fatih Basciftci, Selcuk University, Turkey
  Ibrahim Uyanik, Selcuk University, Turkey
  Mustafa Altin, Konya Technical University, Turkey
  Adem Golcuk, Selcuk University, Turkey
  Ali Yasar, Selcuk University, Turkey
  Murat Ciniviz, Selcuk University, Turkey

INTERNATIONAL ADVISORY BOARD   :
  Adem Alpaslan Altun, Selcuk University, Turkey
  Ahmet Fenercioglu, Gaziosmanpasa University, Turkey
  Ahmet Yonetken, Afyon Kocatepe University, Turkey
  Ahmet Afsin Kulaksiz, Selcuk University, Turkey
  Alexander Sudnitson, Tallinn University of Technology, Estonia
  Alina Ivan Dramogir, Gheorghe Asachitechnical University of Iasi, Romania
  Alla Anohina Naumeca, Riga Technical University, Latvia
  Almoataz Youssef Abdelaziz, Ain Shams University, Egypt
  Amar Ramdane Cherif, University of Versailles, France
  Anca Loana Andreescu, Academy of Economic Studies, Bulgaria
  Anne Villems, University of Tartu, Estonia
  Antonella Reitano, University of Calabria, Italy
  Antonio Mendes, Universidade De Coimbra, Portugal
  Arif Gok, Amasya Teknoloji Faculty, Turkey
  Aristomenis Antoniadis, Technical University of Crete, Greece
  Artan Luma, South East European University, Macedonia
  Asrun Matthiasdottir, Reykjavik University, Israel
  Bahattin Karakaya, Istanbul University, Turkey
  Biagio Lenzitti, University of Palermo, Italy
  Binod Kumar, Jspm Jayawant Institute of Computer Applications Pune, India
  Boris Akanaev, Kazak National University, Kazakhstan
  Dimitris Dranidis, Sheffield University, Greece
  Domenico Tegolo, Universita Degli Studi Di Palermo, Italy
  Eisha Akanksha, Mvj College of Engineering, India
  Elinda Kajo Mece, Polytechnic University of Tirana, Romania
  Engin Ozdemir, Kocaeli University, Turkey
  Erdal Bekiroglu, Abant Izzet Baysal University, Turkey

Erdinc Kocer, Selcuk University, Turkey
Erol Turkes, Kirklareli University, Turkey
Ertugrul Durak, Suleyman Demirel University, Turkey
Gabriel Luna Sandoval, Sonora State University, Mexico
Hakan Isik, Selcuk University, Turkey
Hamit Saruhan, Duzce University, Turkey
Hamza Bensouilah, Laboratoire de Mecanique et Structures, Algeria
Hasan Gokkaya, Karabuk University, Turkey
Hayri Arabaci, Selcuk University, Turkey
Heinz Dietrich Wuttke, Ilmenau University of Technology, Germany
Howard Duncan, Dublin City University, Ireland
Hulusi Karaca, Selcuk University, Turkey
Humar Kahramanli, Selcuk University, Turkey
Huse Fatkic, University of Sarajevo, Bosnia and Herzegovina
Ibrahim Uyanik, Selcuk University, Turkey
Ihsan Korkut, Gazi University, Turkey
Ilker Ali Ozkan, Selcuk University, Turkey
Ivan Jelinek, Czech Technical University, Czech Republic
Jaharah A Ghani, National University of Malaysia, Malaysia
Jan Vom Brocke, University of Liechtenstein, Liechtenstein
Janis Grundspenkis, Riga Technical University, Latvia
Janusz Jablonowski, Warsaw University, Poland
Jiri Srba, Aalborg University, Denmark
Kadir Gok, Manisa Celal Bayar University, Turkey
Karl Jones, Liverpool John Moores University, United Kingdom
Laurentiu Cristian Deaconu, University of Pitesti, Romania
Luca Lombardi, University of Pavia, Italy
M Ugras Cuma, Cukurova University, Turkey
Mahdi Shahbakhti, Michigan Technology University, United States
Mahmut Sami Donduren, Konya Technical University, Turkey
Majida Ali Abed Meshari, Tikrit University, Iraq
Marco Porta, University of Pavia, Italy
Mehmet Akbaba, Karabuk University, Turkey
Mehmet Kamanli, Konya Technical University, Turkey
Mehmet Akif Sahman, Selcuk University, Turkey
Mehmet Cengiz Kayacan, Suleyman Demirel University, Turkey
Mehmet Turan Demirci, Selcuk University, Turkey
Mirjana Ivanovic, University of Novi Sad, Serbia
Miroslav Neslusan, University of Zilina, Slovakia
Muciz Ozcan, Necmettin Erbakan University, Turkey
Muhammad Zia Ur Rehman, National Defence University, Pakistan
Mumtaz Mutluer, Necmettin Erbakan University, Turkey
Murat Koklu, Selcuk University, Turkey
Musa Hakan Arslan, Konya Technical University, Turkey
Mustafa Altin, Konya Technical University, Turkey
Mustafa Tolga Cogurcu, Konya Technical University, Turkey
Natasa Hoic Bozic, Universityof Rijeka, Croatia
Nihat Yildirim, Gaziantep University, Turkey
Nikolaos Blasis, Technical University of Crete, Greece
Novruz Allahverdi, Tob Karatay University, Turkey
Osman Nuri Celik, Konya Technical University, Turkey
Pantha Ghosal, University of Technology Sydney, Australia
Pino Caballero Gil, University of La Laguna, Spain

Saadetdin Herdem, Selcuk University, Turkey
Sakir Tasdemir, Selcuk University, Turkey
Shahabuddin Memon, University of Sindh, Pakistan
Silyan Sibinov Arsov, Rousse University, Bulgaria
Spiridon Cretu, Gheorghe Asachitechnical University of Iasi, Romania
Stavros Christodoulakis, Technical University of Crete, Greece
Stavros Nikolopoulos, University of Ioannina, Greece
Tahir Sag, Selcuk University, Turkey
Tatjana Dulinskiene, Kaunas University of Technology, Latvia
Temel Kayikcioglu, Karadeniz Technical University, Turkey
Thomas Engel, University of Luxembourg, Luxembourg
Tugce Demirdelen, Adana Science Technology University, Turkey
Ulku Sultan Keskin, Konya Technical University, Turkey
Ulvi Seker, Gazi University, Turkey
Virginio Cantoni, University of Pavia, Italy
Yuri Pavlov, Bulgarian Academy of Sciences, Bulgaria
Zarifa Jabrayilova, Institute of Information Technology Anas, Azerbaijan

ORGANIZING COMMITTEE   :

Alla Anohina Naumeca, Riga Technical University, Latvia
Silyan Sibinov Arsov, Rousse University, Bulgaria
Angel Smrikarov, Rousse University, Bulgaria
Lilia Georgieva, Heriot Watt University, United Kingdom
Ismail Saritas, Selcuk University, Turkey
Fatih Basciftci, Selcuk University, Turkey
Mehmet Cunkas, Selcuk University, Turkey
Ibrahim Uyanik, Selcuk University, Turkey
Polyxeni Arapi, Technical University of Greece, Greece
Murat Ciniviz, Selcuk University, Turkey
Adem Golcuk, Selcuk University, Turkey
Ali Yasar, Selcuk University, Turkey
Ayhan Erol, Afyon Kocatepe University, Turkey
Mustafa Altin, Konya Technical University, Turkey

TECHNICAL COMMITTEE :

Ilker Ali Ozkan, Selcuk University, Turkey
Murat Koklu, Selcuk University, Turkey
Esra Kaya, Selcuk University, Turkey
Burak Tezcan, Selcuk University, Turkey

CONTENTS

Feature Selection from Electroencephalogram Signals by Means of Using Principal Component Analysis

S. YILDIRIM[1] and H.E. KOCER[2]

[1] Konya Technical University, Konya/Turkey, semayildirim@selcuk.edu.tr
[2] Selcuk University, Konya/Turkey, ekocer@selcuk.edu.tr

Abstract - The aim of this study is to determine the success of the feature vector (FV) that was obtained by a variety of feature extraction methods and the success of the eigenvalues that were obtained by Principal Component Analysis (PCA). EEG signals (EEGs) that were collected retrospectively from Selcuk University Faculty of Medicine Hospital were used in this study. Feature vector was obtained from 30 epilepsy patients and 30 normal via statistical methods and discrete wavelet transform (DWT). Dimensions of these feature vectors were reduced via Principal Component Analysis (PCA) method. Four eigenvectors with the highest relationship that include 71, 52, 33 and 15 according to PCA correlation matrix were included in the study. The performances of the eigenvectors were calculated and compared using an Artificial Neural Network (ANN). Performance evaluation of the used ANN algorithm were carried out by performing Receiver Operation Characteristic (ROC) analysis. Experimental results have shown that eigenvector 3 (EV3) including 33 features is more successful than the other feature vector and eigenvectors with 93.67% training and 88.30% test. Furthermore, the performance of all eigenvectors was observed to be higher than the performance of the feature vector. As a consequence, the use of more meaningful eigenvectors improves the classification performance instead of high-dimensional feature vectors.

Keywords - Electroencephalogram, Discrete Wavelet Transforms, Principal Component Analysis, Artificial Neural Network, epilepsy.

I. INTRODUCTION

Epilepsy is a common neurological disorder that is characterized by occurrence of recurrent seizures [1]. There are a lot of methods to automatically classify the seizures on EEGs without spending long hours for visual control [2]. The major steps of these methods are the feature extraction/selection and the classification that constitute a pattern recognition process. Feature extraction/selection plays an important role in classifying systems such as neural networks. It significantly contributes to the performance of the classifier and reduces data size without losing its distinguishing power. It has been noticed that the accuracy of classification entirely depends on the selection features to be applied on the EEG time series [3]–[5]. Therefore, the aim of this study is;

- To determine the success on the classification of the different eigenvectors,
- To identify the superiority of the feature vectors and eigenvectors.

In that context, some features were extracted by using different feature extracting methods. While, the statistical features including minimum, maximum, mean, median, interquartile range, standard deviation, range, variance, kurtosis and skewness were extracted by using statistical functions, power of sub-bands in time domain was decomposed by using DWT. PCA feature selection method was utilized in order to reduce the feature vector size. The rest of this paper is organized as follows: data selection, feature extraction/selection, classifiers are introduced in Section 2. The experimental results and discussion for the classification of epileptic and normal EEGs are given in Section 3. Finally, Section 4 gives the conclusions and future work.

II. MATERIALS AND METHODS

A. Data Acquisition

We collected the EEG data that was recorded in the Department of Neurology. It is used with decision of Selcuk University Faculty of Medicine Hospital (Non-Invasive Clinical Research Ethics Committee No. 2014/423). EEGs of 60 subjects (30 epilepsies, 30 normal) that were collected between 2012 and 2015 were used in the study. All of the EEGs were obtained from routine EEG recording and all subjects were awake. The mean age of 30 epilepsy patients was 38 (14 males, 16 female) and mean age of 30 normal patients was 46 (14 males, 16 female). EEG signals were recorded with 18 channels and 200 sampling frequency. An epoch (page) contains 3000 (200 x 15) sampling because every epoch is 15 seconds.

Recording times is different from each other due to the fact that the situation of each subject in recording time is different. Moreover, dataset showing epileptic activity that is determined by specialists are selected. This dataset was created EEGs that include various waves such as sharp wave, spike, spike and slow wave, multiple spike and slow wave complex. In this study, we just used 5 epochs that are both epileptic and normal patients and the length of each epoch was composed of 3000 samples. 300 segment data for 60 subjects were obtained as a result of calculations and adjustments. Whereas a value of 1 is given for 150 epileptic data, a value of 0 is given for 150 normal data in order to classify.

B. Feature Extraction

1. Discrete Wavelet Transform

Wavelet Transform (WT) for time-scale analysis is a powerful method for the signals that provide a unified framework for different techniques [6], [7]. DWT is a series

of WT that have been successful in many works for pre-analysis of the epileptic seizures detection unlike FFT, because EEGs is non-stationary [6]. DWT analyzes the signal at different frequency bands, with different resolutions by decomposing the signal into a coarse approximation and detailed information. Selection of suitable wavelet and the number of levels of decomposition are very important in the analysis of signals using DWT. The wavelet function selected was Daubechies Wavelet with order 4, which was also proven to be the best suitable wavelet function for epileptic EEGs analysis [8].

2. *Statistical Features*

It is known that the number of feature has a direct impact on the success of classification. Therefore, the number of feature must be a number that describes the used database in the best way. Therefore, some statistical features were used in the study as well as the features obtained from the power of the sub-band in the time domain by using DWT. In accordance with this purpose, 10 features that include minimum, maximum, mean, median, interquartile range, standard deviation, range, variance, kurtosis, skewness of every channel were extracted from each EEG channel data as they were the most representative values to describe the original signals. Thus, as a result of obtaining the power of 72 sub-bands and 180 statistical features by the feature extraction method, 252 feature spaces were obtained. Since the number of example in the study is 300, (5 epochs of 60 patient) database that consists of a matrix of 300 x 252 was obtained. All feature vectors were computed by the usage of the Matlab (Version 7.11, R2010b) software package because the features were required to be determined to achieve results faster and more accurately.

C. *Dimension Reduction by Principal Component Analysis*

Selection of the proposed model inputs is very important because it will affect the performance of classifier [9]. Meanwhile, it is very crucial that the number of inputs in the system which is classifier method must have been selected very carefully. In that context, if the number of inputs is selected unnecessarily high, performance of the system might decrease because of difficulty of the calculation of the network. On the other hand, if the number of inputs is selected unnecessarily low, the system may not give the result accurately and confidently. As a consequence, selection of the number of inputs was very significant for these systems [10].

PCA is mathematically defined as an orthogonal linear transformation that transforms the data to a new coordinate system such that the greatest variance by some projection of the data comes to lie on the first coordinate (called the first principal component), the second greatest variance on the second coordinate, and so on [11]. PCA can be used for dimensionality reduction in a dataset while retaining those characteristics of the dataset that contribute most to its variance, by keeping lower-order principal component and

ignoring higher-order one. Such low-order components often contain the 'most important' aspects of the data, but this is not necessarily the case, depending on the application. PCA has the distinction of being the optimal linear transformation for keeping the subspace that has largest variance. This advantage, however, comes at the price of greater computational requirement if compared, for example, to the discrete cosine transform. Unlike other linear transforms, the PCA does not have a fixed set of basis vectors. Its basis vectors depend on the data set [12].

D. *Artificial Neural Network (ANN)*

ANN consists of three layers that include input, hidden and output layers. The aim of hidden layer is process and transmits from the input information to the output layer [13], [14], [15]. The input is processed and relayed from one layer to the other, until the final result is computed. As shown in Figure 1, a feedforward backpropagation ANN was used for classification. In addition, the hyperbolic tangent sigmoid transfer function was used in the entire neuron units has been shown in Figure 2.
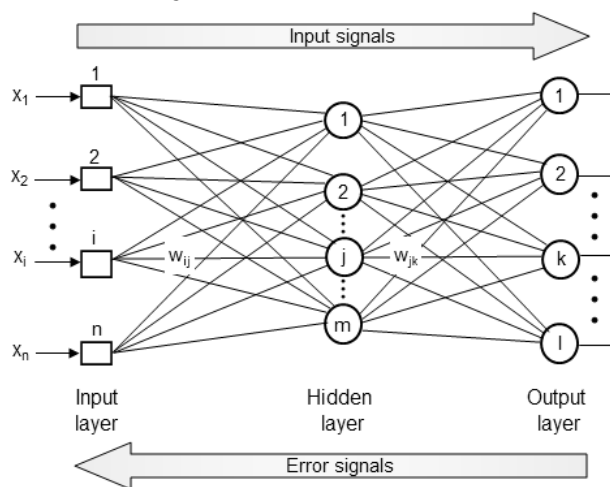
Figure 1: The general structure of feedforward backpropagation neural network.
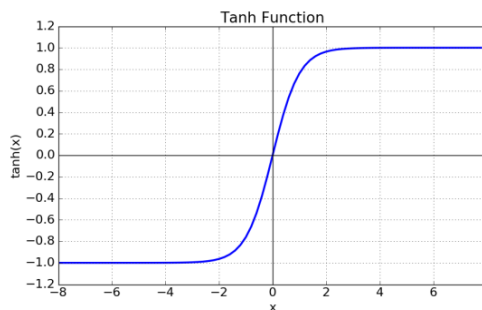
Figure 2: The hyperbolic tangent sigmoid transfer function

.

III. RESULTS AND DISCUSSION

In this study, we used 5 epochs for each record that was taken from Selcuk University Faculty of Medicine Hospital, the Department of Neurology in view of the different recording times. 3000 (200 x 15) samples for each patient were obtained since the fact that 1 second includes 200 sampling frequency and each epoch includes 15 seconds. Therefore, 300 x 3000 dataset were obtained for 30 epilepsies and 30 normal patients.

The number of decomposition levels is chosen based on the dominant frequency components of the signal. The levels are chosen such that those parts of the signal that correlate well with the frequencies required for classification of the signal are retained in the wavelet coefficients [16]. The results of the studies in literature have demonstrated that the WT is the most promising method to extract features from the EEG signals [13], [17], [18]. Therefore, in this study, DWT was applied for time-frequency analysis of EEG signals for the classification using wavelet coefficients. EEG signals were decomposed into sub-bands using DWT.

The value of 1 for the output of epilepsy patients and the value of 0 for the out of normal patients is given in the dataset. 252 feature vectors were obtained by performing statistical features including min, max, mean, median, iqr, range, std, var, kurtosis, skewness were extracted and sub-band features were decomposed fifth-level packet decomposition using DWT via Matlab software. Prior to reducing the size of this feature vector by applying PCA, 252 (180 statistical features, 72 the power of the sub-band by DWT) properties were obtained using different feature extraction methods.

The number of the feature vectors has a direct impact on both the performance and speed of the classifier. Speed of the classifier substantially decreases in the classification that is performed by using 252 features obtained in this study, while the success of classification reduces. Hence, PCA is used for dimension reduction of the features from all data set by the variances in the PCA space. We found out that the eight eigenvalues of the PCA contain 97 % (the ones under 1000) of the information of the eigenspace (PCA space) and 252 dimension can be expressed using only 33 dimensions. Therefore, the classifier does not receive redundant information through this approach.

According to sorting of eigenvalues, the impact on classification is observed by using the first meaningful eigenvectors. In that context, 71, 52, 33 and 15 neurons have been choosing for new features by means of using latent vector. Eigenvectors and the number of the attributes that were obtained according to correlation matrix are given in Figure 3.

ANN is used to compare the performance of feature vector and eigenvectors. While hyperbolic tangent sigmoid transfer function is used for activation function of all neurons in the network, the backpropagation algorithm, which is based on searching an error surface using gradient descent for points with minimum error, is relatively easy to implement. Classification algorithm is carried out by changing some of the parameters such as hidden layer neurons number and so on. Different neuron numbers for

the hidden layer were tested and 10 was found to be most suitable number. The optimum values that were used in the classification performing by ANN in this study are given in the Table 1.
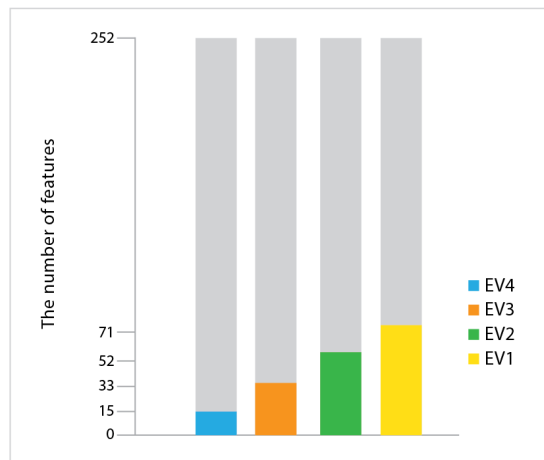
Figure 3: The chart of eigenvectors after applying PCA to FV.

Table 1: Training parameters for ANN.

Parameters	Values
Error tolerance	0.001
Transfer function	Tangent sigmoid
Maximum epoch	500/1000
Input neurons	252/71/52/33/15
Output neuron	1
Hidden neurons	10
Bias	1

In order to identify the correctness of the diagnosis, the concepts of sensitivity (SEN) and specificity (SPE) were utilized. The definitions of these concepts were given by the statements below, where TP (true positive), TN (true negative), FP (false positive), FN (false negative) stand for diagnosing illness when the patient is ill, diagnosing healthy person as healthy, diagnosing healthy person as ill and lastly diagnosing ill patient as healthy, respectively [19];

$$Sensitivity = TP/(TP+FN) x100\% \qquad (1)$$

$$Specificity = TN/(TN+FP) x100\% \qquad (2)$$

$$Accuracy = (Sensitivity + Specificity)/2 x100\% \qquad (3)$$

We evaluated true positive, true negative, false positive and false negative values as shown in confusion matrix of all feature vectors in Table 2. While columns represent predictions, row represent true classes in confusion matrix, every condition is shown by using code number, like in 0 and 1 as normal and epilepsy. The number of correct predictions in the classification after training for FV is the lowest with 115 and 133. On the other hand, the highest number of correct predictions for EV3 was obtained with 135 and 146 as shown in Table 2 d). At the same time, EV3 is highly successful than FV and the other EV. On the contrary, we calculated separately sensitivity and specificity values that are statistical measures of the performance of a binary classification test.

Table 2: (a) The Confusion matrix of FV. (b) The Confusion matrix of EV1. (c) The Confusion matrix of EV2. (d) The Confusion matrix of EV3. (e) The Confusion matrix of EV4.

(a)

FV	True condition 1	0	
Predicted condition 1	115	17	132
0	35	133	168
	150	150	300

SEN = 0.767
SPE = 0.887

(b)

EV1	True condition 1	0	
Predicted condition 1	134	13	147
0	16	137	153
	150	150	300

SEN = 0.893
SPE = 0.913

(c)

EV2	True condition 1	0	
Predicted condition 1	132	8	140
0	18	142	160
	150	150	300

SEN = 0.880
SPE = 0.947

(d)

EV3	True condition 1	0	
Predicted condition 1	135	4	139
0	15	146	161
	150	150	300

SEN = 0.900
SPE = 0.973

(e)

EV4	True condition 1	0	
Predicted condition 1	112	8	120
0	38	142	180
	150	150	300

SEN = 0.747
SPE = 0.947

The performance of the training and testing of all feature vectors is given in Table 3. There is no doubt that EV3 is the highest achievement than the other feature vectors with 93.67% of the training success and 88.30% of the test success.

Table 3: The performance of training and test for all features.

	FV	EV1	EV2	EV3	EV4
Training	82.67%	90.33%	91.33%	**93.67%**	84.67%
Test	76.70%	85.00%	86.70%	**88.30%**	83.30%

The performance of training and testing is given in Table 3. It is obvious that FV includes 252 features being the lowest with 82.67% training and 76.70% testing than the other EV. Furthermore, while classification accuracy increases from EV1 to EV3, the classification accuracy decreases after EV3. In other words, increasing classification accuracy was observed to decrease the number of features while the classification accuracy decreases fewer features than 33 features. As a result, the highest classification success can be obtained with the number 33 or close to 33. The classification successes of the training and tests of the Artificial Neural Network are given in Figure 4 (a) and (b), respectively. In the graph (a), where the number of features and classification success is shown, the success of the EV vector with 252 features and the success of the EV4 vector with 15 features are very close to each other, but are lower than the success of other eigenvectors. On the other hand, when the number of features was 53 and 71, the success rate increased. However, the highest success value was obtained with FV3 which contains 33 properties. When

the test graph was examined, it was observed that all feature vectors were more successful than the diminished PV with PCA. Classification was performed by using different values of training, test and validation for each dataset. 75% for training, 20% for test and 5% for validation were reserved on the dataset. The number of samples for training, test and validation and the value of Mean Square Error (MSE) that shows mean square difference between output and target in the classification results in Table 4. As it is known to all approaching the value 0 of the MSE shows the minimum error and the highest success. The lowest MSE value was obtained for EV3 in this study as seen in Table 4. In a different manner, the lowest MSE value for the test was found to be EV2. However, there is a small difference of 0.0199 among the test values of EV2 and EV3. In this case, we can easily reach a conclusion that EV3 has the small MSE value for both training and testing.

Receiver operating characteristics (ROC) graphs are useful for organizing the classifiers and visualizing their performance. ROC graphs are commonly used in medical decision making, and in recent years they have been used increasingly in machine learning and data mining research. Although ROC graphs are apparently simple, there are some common misconceptions and pitfalls when using them in practice [20]. By the help of these calculated values, the ROC curve has been drawn. After such a curve is drawn, the Area Under Curve (AUC) may be calculated. Higher values of the 'area under the ROC curve' (AUC) measures indicate better classifier performance [21].
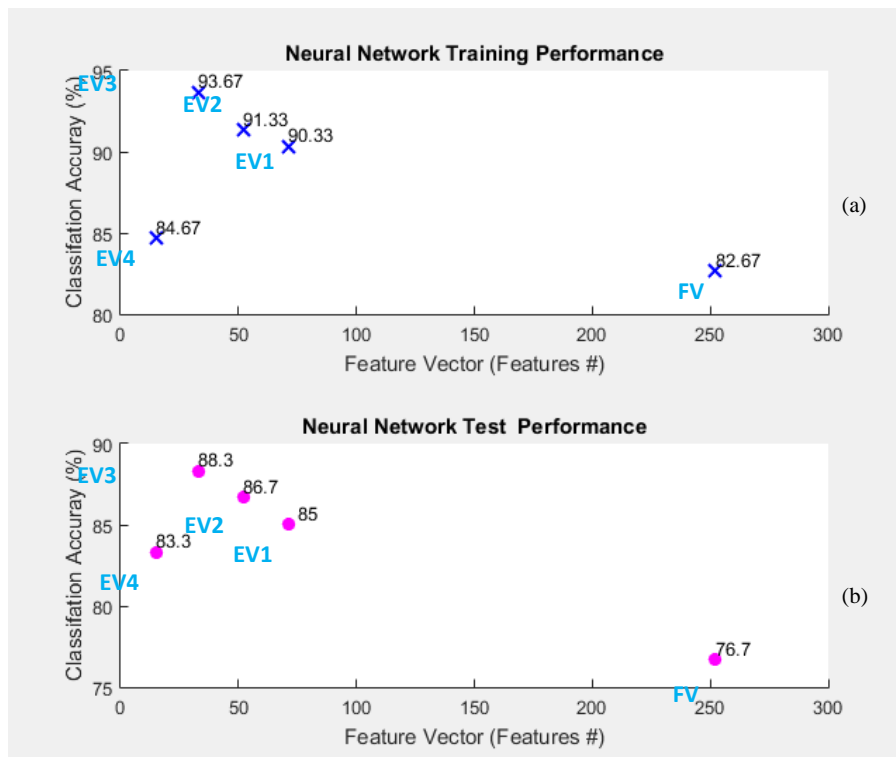
Figure 4: The performances of Neural Network for all feature vectors. (a) Training Performance. (b) Test Performance.

Table 4. MSE values and the number of samples of training, test and validation.

	Training	Validation	Test
Samples	**225**	**15**	**60**
MSE FV	1.27428E-01	1.12298E-01	1.48544E-01
MSE EV1	6.36103E-02	7.20272E-02	1.17063E-01
MSE EV2	7.00467E-02	3.18929E-02	9.28362E-02
MSE EV3	**4.73113E-02**	**6.69442E-02**	**9.48262E-02**
MSE EV4	1.11837E-01	2.07771E-01	1.26806E-01

There is no doubt that the success of classifier is directly affected by the number of input values and the appropriate features. The aim of this study is to find the optimal number of features and features from EEG data that were collected retrospectively. The success and performances of feature vector and eigenvectors were tested, eigenvector that provides the highest success was determined. The high number feature reduced both speed and the success of the classifier. On the other hand, a high success could not be achieved with a small number of features. In this study, EV3 was found to be appropriate eigenvector from EEGs that include epileptic activities and normal signals as shown in Figure 5. The success of the EV3 can be detected using different classifiers and classification of different datasets.

Figure 5: ROC graph of NN classifier for EV3. (a) Training ROC. (b) Test ROC.

IV. CONCLUSIONS

Automated detection of EEGs is very important for determining of normal and epileptic activities preictal, interictal and ictal. We tried to identify the most appropriate features on EEGs of epilepsy and normal patients. Initially, 252 features were extracted from the sub-bands obtained after the decomposition through the DWT and statistical methods. Principle component analysis was used for dimension reduction of EEG data in the study. High dimensional data and spatial redundancy reduced by PCA recognizing first few principle components. Therefore, excessive information was not received to classifiers through this reduction algorithm [22].　ANN algorithm was performed for detecting the best eigenvector.

As is known, PCA is a method that gives the most relevant and relevant features in matrices with a large number of properties. With this method, the number of property vectors obtained by using different property extraction methods was reduced and the success of the classification vectors obtained was tested with ANN, which is one of the best classification methods. There is no doubt that the PCA method has greatly increased the success of data with such a large number of features.

V. ACKNOWLEDGMENT

REFERENCES

[1] N. V Thakor and S. Tong, "Advances in quantitative electroencephalogram analysis methods," *Annu. Rev. Biomed. Eng.*, vol. 6, pp. 453–495, 2004.

[2] S. Altunay, Z. Telatar, and O. Erogul, "Expert Systems with Applications Epileptic EEG detection using the linear prediction error energy," *Expert Syst. Appl.*, vol. 37, no. 8, pp. 5661–5665, 2010.

[3] N. Kannathal, M. L. Choo, U. R. Acharya, and P. K. Sadasivan, "Entropies for detection of epilepsy in EEG," *Comput. Methods Programs Biomed.*, vol. 80, no. 3, pp. 187–194, 2005.

[4] V. P. Nigam and D. Graupe, "A neural-network-based detection of epilepsy," *Neurol. Res.*, 2013.

[5] S. P. Kumar, N. Sriraam, P. G. Benakop, and B. C. Jinaga, "Entropies based detection of epileptic seizures with artificial neural network classifiers," *Expert Syst. Appl.*, vol. 37, no. 4, pp. 3284–3291, 2010.

[6] H. Adeli, Z. Zhou, and N. Dadmehr, "Analysis of EEG records in an epileptic patient using wavelet transform," *J. Neurosci. Methods*, vol. 123, no. 1, pp. 69–87, 2003.

[7] O. A. Rosso, M. T. Martin, and A. Plastino, "Brain electrical activity analysis using wavelet-based informational tools," *Phys. A Stat. Mech. its Appl.*, vol. 313, no. 3, pp. 587–608, 2002.

[8] A. Subasi, "EEG signal classification using wavelet feature extraction and a mixture of expert model," *Expert Syst. Appl.*, vol. 32, no. 4, pp. 1084–1093, May 2007.

[9] I. Güler and E. D. Übeyli, "Adaptive neuro-fuzzy inference system for classification of EEG signals using wavelet coefficients," *J. Neurosci. Methods*, vol. 148, no. 2, pp. 113–121, 2005.

[10] P. Berg and M. Scherg, "A multiple source approach to the correction of eye artifacts," *Electroencephalogr. Clin. Neurophysiol.*, vol. 90, no. 3, pp. 229–241, 1994.

[11] I. T. Jolliffe, "Principal component analysis for special types of data," *Princ. Compon. Anal.*, pp. 338–372, 2002.

[12] V. G. Ivancevic and T. T. Ivancevic, *Computational mind: a complex dynamics perspective*, vol. 60. Springer, 2007.

[13] N. Hazarika, J. Z. Chen, A. C. Tsoi, and A. Sergejew, "Classification of EEG signals using the wavelet transform," in *Digital Signal Processing Proceedings, 1997. DSP 97., 1997 13th International Conference on*, 1997, vol. 1, pp. 89–92.

[14] S. N. Oğulata, C. Şahin, and R. Erol, "Neural network-based computer-aided diagnosis in classification of primary generalized epilepsy by EEG signals," *J. Med. Syst.*, vol. 33, no. 2, pp. 107–112, 2009.

[15] a Subasi, "Epileptic seizure detection using dynamic wavelet network," *Expert Syst. Appl.*, vol. 29, no. 2, pp. 343–355, Aug. 2005.

[16] E. D. Übeyli, "Statistics over features: EEG signals analysis," *Comput. Biol. Med.*, vol. 39, no. 8, pp. 733–741, 2009.

[17] M. K. Kiymik, M. Akin, and A. Subasi, "Automatic recognition of alertness level by using wavelet transform and artificial neural network," *J. Neurosci. Methods*, vol. 139, no. 2, pp. 231–240, 2004.

[18] Y. U. Khan and J. Gotman, "Wavelet based automatic seizure detection in intracerebral electroencephalogram," *Clin. Neurophysiol.*, vol. 114, no. 5, pp. 898–908, 2003.

[19] C. E. Metz, "Basic principles of ROC analysis," in *Seminars in nuclear medicine*, 1978, vol. 8, no. 4, pp. 283–298.

[20] T. Fawcett, "An introduction to ROC analysis," *Pattern Recognit. Lett.*, vol. 27, no. 8, pp. 861–874, 2006.

[21] S. Mitra and G. Indiveri, "Spike-based synaptic plasticity and classification on VLSI," *The Neuromorphic Engineer*, vol. 10.2417, no. 1200904.1636, Citeseer, pp. 1–3, 2009.

[22] M. S. Bascil, A. Y. Tesneli, and F. Temurtas, "Multi-channel EEG signal feature extraction and pattern recognition on horizontal mental imagination task of 1-D cursor movement for brain computer interface," *Australas. Phys. Eng. Sci. Med.*, vol. 38, no. 2, pp. 229–239, 2015.

Fracture Toughness as a Key Aspect of Bone Fracture Resistance

M.ÜNAL

Karamanoglu Mehmetbey University, Karaman/Turkey, mustafaunal@kmu.edu.tr

Abstract – **Bone fractures are among the biggest health concerns in the world. Understanding the factors leading to bone fracture is the essential step to develop new strategies for dealing with this costly and deadly health problem. Studies published in recent years highlighted that all bone fractures are not only associated with low bone strength. In fact, fracture toughness, which is the material property focusing of resistance of the material to sudden and unstable growth of cracks, is an emerging field in bone research to better understand bone fragility associated with diseases and aging. Fracture toughness may be more closely associated with hip fractures and atypical femoral fractures which are two of the most common of bone fractures seen in the clinics. In this study, the possible association between fracture toughness and bone fractures was discussed in light of recently emerged studies.**

Keywords – **bone biomechanics, mechanical properties, fracture toughness, bone fracture**

I. INTRODUCTION

Bone tissue is mainly composed of mineral, collagen, and water [1]. The unique hierarchical arrangement of these three main components at different scales provides bone a superior resistance to fracture (Figure 1) [1]. However, aging and diseases-related numerous changes in bone tissue and structure make the bone more brittle and vulnerable to fracture. Such alterations in bone matrix and structure cause mainly bone fractures-associated with less traumatic or non-traumatic fractures such as falling from a standing distance. Such non-traumatic bone fractures, in fact, affect millions of people around the world and result in huge medical costs of more than $50 billion annually [2-4]. More critically, the mortality rate among elderly people because of bone fractures and subsequent complications is very high with 30% following the year of fracture [2-4]. In order to prevent these bone fractures, the mechanisms that cause bone fractures should be elucidated firstly, and then strategies to stop or reverse these mechanisms should be revealed. The mechanisms that cause bone fracture can be viewed from different perspectives such as molecular mechanisms or biomechanical mechanisms. From a biomechanical perspective, bone fractures are, in fact, a mechanical event that occurs when a bone is overloaded then it can bear. The biomechanical source of the resistance of bone to fracture is related to the bone mass or bone mineral density (BMD), the structural/morphological properties of the bone, and the material properties of bone tissue [1].
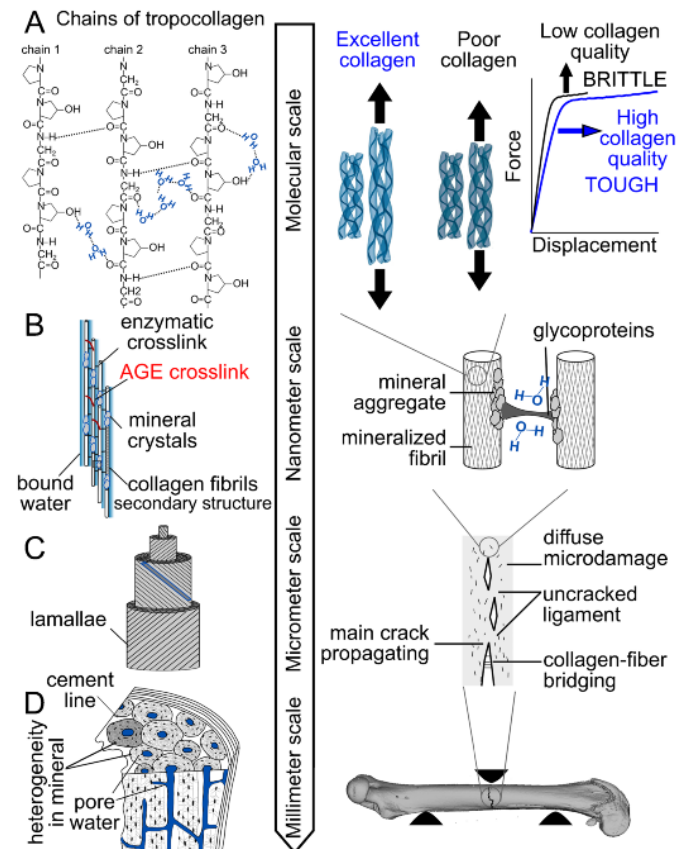
Figure 1: Bone fracture resistance or fracture toughness is not only associated with a single toughening mechanism. Changes in (A) collagen structure, (B) enzymatic and non-enzymatic modifications, (C) overall alterations in hydration and collagen structure, and (D) porosity are closely related to fracture toughness of bone. This figure is reused from [1].

BMD measured by double energy x-ray absorptiometry (DEXA) is currently used as the gold standard for the diagnosis of osteoporosis as well as the risk assessment of bone fracture. Although previous studies have shown that BMD is closely related to bone density and bone structural/morphological features [5], the relationship between BMD and bone material properties is limited. The material properties of bone are generally supposed to refer only strength of the bone, especially among researches with a non-engineering background. In fact, bone strength is the value of

the maximum stress that bone specimens can withstand without breaking under a high amount of constant load during mechanical tests such as tensile, compression or bending tests. Since bone strength is easily obtained experimentally and its interpretation is relatively easy, bone strength is frequently used as an indicator of bone material quality by the researchers working in the field of bone research. However, researchers who do not have an engineering background have the misconception that deterioration of bone strength is the only cause of bone mechanical failure. Indeed, bone fractures in the clinic cannot be explained solely with the deterioration of the strength of the bone. Recent years have revealed that the fracture toughness of the bone is at least as important as the bone strength [6-10]. The aim of this critical review is to briefly introduce fracture toughness, which causes mechanical deficiency of bone, and to discuss its possible association with bone fractures.

II. Brief Description of Fracture Toughness

Unlike the yield strength that evaluates a material's internal resistance to irreversible (plastic) deformation, fracture toughness is a measure of the resistance of a material to sudden and unstable growth of preexisting micro-cracks at the stress concentration. Stress concentrations (or so-called stress amplifiers) are the areas in which stress is increased due to sharp edges, large holes, the region of sudden shape changes, rapid changes in material properties, or pre-existing cracks. Such stress concentrated areas, which are abundant in bone naturally, are the main source of crack initiation. In order to prevent fracture, several toughening mechanisms such as uncoiling of the collagen molecules, collagen-fiber bridging, un-cracked ligament etc. (Figure 1) exist in the bone to increase the required energy for a crack growth, thereby increasing fracture toughness of bone [6-10]. However, age and diseases-related alterations in bone matrix and structure may also damage these toughening mechanisms, resulting in lower fracture toughness. Therefore, measuring the fracture toughness of bone has become one of the important aspects of bone biomechanics during the past decade [6-10].

The fracture toughness, which is calculated as the stress intensity at the tip of the primary crack leading to rapid unstable cracks, is generally confused with material`s toughness. The toughness of the material is the amount of energy absorbed by a material before breaking and it is not necessarily to be a surrogate measure of fracture toughness. In materials with low fracture toughness, such as glass and ceramics, the crack grows smoothly and rapidly and the material completely breaks down during the fracture event. On the other hand, in the case of polyethylene-type plastics with relatively high fracture toughness than glass and ceramic, the crack grows more slowly and does not shatter when the breaking event occurs. Similarly, crack growth is more torturous in the healthy bone due to the aforementioned toughening mechanisms (Figure 1) whereas a micro-crack can easily and suddenly grow into a huge size in unhealthy bone.

III. Possible Association of Fracture Toughness with Clinical Bone Fracture

Bone fractures can be caused by a single high impact load such as a fall from the standing height when walking, as well as by the loads that the bones are subjected to during the daily activities [11]. Therefore, looking at the possible load regime of bone exposed during the daily life could provide insight into understanding the possible relationship of material properties to bone fractures. Human bones can be exposed to large loads once or more a year as a result of falling from standing height, as mostly occurring among the elderly people, with the exception of car accidents or high trauma loads such as falling from a high place [12]. On the other hand, human bones can be subjected to moderate loads that occur during the lifting of something less than body weight several times a week as a part of daily life activities. As a result of walking and other activities in the daily life, the bones are also exposed to low loads daily. Such variety of loads regimes can cause both a traumatic bone fracture due to the exceeding bone`s yield strength and non-traumatic fracture due to the lower fracture toughness depending on bone quality.

Hip fractures are one of the most common types of osteoporosis-related bone fractures. Approximately 90% of hip fractures occur due to falls from a standing height [12, 13]. From this point of view, considering hip fracture as a result of single high load exposure may simply lead to the conclusion that the hip fractures are directly related to the insufficiency of bone strength. Although this can be true to some extent, recent studies also highlighted the possibility of involving micro-cracks in fracture event. In such perspective, micro-cracks at the stress concentration areas such as the Haversian canals and cement line may occur during the previous fall that did not result in a fracture or during other activities that the bones were exposed to moderate loads. Such micro-cracks in the stress concentration areas may then cause sudden and rapid growth in cracks which turn into bone fracture during the last falls or other activities [13, 14]. Therefore, it can be concluded that hip fractures can be considered as a form of fracture that occurs with involving both insufficiencies of bone strength and fracture toughness.

Atypical femur fractures, which are caused by long-term use of drugs that inhibit bone resorption, usually occur with a rapid and sudden transverse growth of a single crack after feeling bone pain related to the accumulation of damage into the bone [15, 16]. In terms of a biomechanical perspective, these fractures are emerged by uncontrolled crack growth during a single medium load following damage accumulation (i.e., micro-cracks accumulation) in the bone when the bone has lower fracture toughness [17]. Therefore, atypical femur fractures are mostly considered as a form of bone fracture that occurs due to the insufficiency of fracture toughness.

IV. Conclusion

Many studies have been established the correlation between bone strength and BMD [18, 19], which is currently used as the gold standard in the diagnosis of osteoporosis as well as in

assessing bone fracture risk. However, the relationship between BMD and fracture toughness has been reported to be weak [9, 20]. As also discussed in the previous studies [11, 13, 15, 17], every bone fracture-associated with aging and diseases is not a form of fracture occurring as a result of decreasing in bone strength. On the other hand, numerous animal studies on understanding the mechanisms leading to bone fractures or studies testing a new form of drugs/treatment often examine the structural properties of bone and BMD. Such studies do not mostly report mechanical properties of bone or only report the strength of whole bone. Since not all bone fractures are caused by the same failure mechanism (e.g., insufficiency of bone strength), the studies that exclude the examination of material/mechanical properties only provide us limited understanding on the causes of bone fractures. Focusing on solely changes in BMD, architectural structure or rarely bone strength may result in an incomplete conclusion. Therefore, focusing on fracture toughness along with bone strength can help us to better understand the causes of bone fractures and to develop new forms of diagnosis and treatment. In this respect, considering the possible relationships discussed above with respect to the bone fractures, it would be useful to report fracture toughness of bone. Such studies can be further ensured that the relationship of fracture toughness with clinical bone fractures is experimentally proved.

REFERENCES

[1] Unal, M., Creecy, A., and Nyman, J. S., "The Role of Matrix Composition in the Mechanical Behavior of Bone," *Curr Osteoporos Rep,* 16(3): 205-215, 2018.

[2] Johnell, O. and Kanis, J., "An estimate of the worldwide prevalence and disability associated with osteoporotic fractures," *Osteoporosis International,* 17(12): 1726-1733, 2006.

[3] Dyer, S. M., Crotty, M., Fairhall, N., Magaziner, J., Beaupre, L. A., Cameron, I. D., and Sherrington, C., "A critical review of the long-term disability outcomes following hip fracture," *BMC geriatrics,* 16(1): 158, 2016.

[4] Burge, R., Dawson Hughes, B., Solomon, D. H., Wong, J. B., King, A., and Tosteson, A., "Incidence and Economic Burden of Osteoporosis‐Related Fractures in the United States, 2005‐2025," *Journal of Bone and Mineral Research,* 22(3): 465-475, 2007.

[5] Wachter, N., Krischak, G., Mentzel, M., Sarkar, M., Ebinger, T., Kinzl, L., Claes, L., and Augat, P., "Correlation of bone mineral density with strength and microstructural parameters of cortical bone in vitro," *Bone,* 31(1): 90-95, 2002.

[6] Zimmermann, E. A., Busse, B., and Ritchie, R. O., "The fracture mechanics of human bone: influence of disease and treatment," *BoneKEy Reports,* 42015.

[7] Nyman, J. S. and Makowski, A. J., "The contribution of the extracellular matrix to the fracture resistance of bone," *Curr Osteoporos Rep,* 10(2): 169-177, 2012.

[8] Seref-Ferlengez, Z., Kennedy, O. D., and Schaffler, M. B., "Bone microdamage, remodeling and bone fragility: how much damage is too much damage?," *BoneKEy Reports,* 42015.

[9] Unal, M., Uppuganti, S., Timur, S., Mahadevan-Jansen, A., Akkus, O., and Nyman, J. S., "Assessing matrix quality by Raman spectroscopy helps predict fracture toughness of human cortical bone," *Scientific Reports,* 9(1): 7195, 2019.

[10] Burr, D. B., "Stress concentrations and bone microdamage: John Currey's contributions to understanding the initiation and arrest of cracks in bone," *Bone,* 127 517-525, 2019.

[11] Hernandez, C. J. and van der Meulen, M. C., "Understanding bone strength is not enough," *Journal of Bone and Mineral Research,* 32(6): 1157-1162, 2017.

[12] Masud, T. and Morris, R. O., "Epidemiology of falls," *Age Ageing,* 30(suppl_4): 3-7, 2001.

[13] Anderson, D. E., Bruno, A. G., and Bouxsein, M. L., "Biomechanics of hip and vertebral fractures," in *Osteoporosis*, ed: Elsevier, 2013, pp. 497-516.

[14] Reeve, J. and Loveridge, N., "The fragile elderly hip: mechanisms associated with age-related loss of strength and toughness," *Bone,* 61 138-148, 2014.

[15] Shane, E., Burr, D., Ebeling, P. R., Abrahamsen, B., Adler, R. A., Brown, T. D., Cheung, A. M., Cosman, F., Curtis, J. R., and Dell, R., "Atypical subtrochanteric and diaphyseal femoral fractures: report of a task force of the American Society for Bone and Mineral Research," *Journal of Bone and Mineral Research,* 25(11): 2267-2294, 2010.

[16] Schilcher, J., Sandberg, O., Isaksson, H., and Aspenberg, P., "Histology of 8 atypical femoral fractures: remodeling but no healing," *Acta Orthopaedica,* 85(3): 280-286, 2014.

[17] Ettinger, B., Burr, D., and Ritchie, R., "Proposed pathogenesis for atypical femoral fractures: lessons from materials research," *Bone,* 55(2): 495-500, 2013.

[18] Carter, D. R. and Hayes, W. C., "Bone compressive strength: the influence of density and strain rate," *Science,* 194(4270): 1174-1176, 1976.

[19] Kopperdahl, D. L., Morgan, E. F., and Keaveny, T. M., "Quantitative computed tomography estimates of the mechanical properties of human vertebral trabecular bone," *Journal of orthopaedic research,* 20(4): 801-805, 2002.

[20] Wang, X. D., Masilamani, N., Mabrey, J., Alder, M., and Agrawal, C., "Changes in the fracture toughness of bone may not be reflected in its mineral density, porosity, and tensile properties," *Bone,* 23(1): 67-72, 1998.

Blood glucose control algorithms and explanation of insulin and carbohydrate mechanisms for Type 1 Diabetes Mellitus

N. ÇANKAYA[1] and Ö. AYDOĞDU[2]

[1]Necmettin Erbakan University, Konya/Turkey, ncankaya@erbakan.edu.tr
[2]Konya Technical University, Konya/Turkey, oaydogdu@ktun.edu.tr

Abstract - **There are approximately 50 million Type 1 Diabetes Mellitus (T1DM) patients in the world. All of these patients need external insulin injection. Because this disease is an autoimmune disease, the best treatment foreseen in the short and medium term is insulin supplementation. With proper insulin administration, T1DM patients can lead a near-normal life. Artificial pancreas is the most accurate way to administer correct insulin. Therefore, artificial pancreas studies are gaining speed. Artificial pancreas systems deliver insulin with a closed-loop control system according to blood glucose value from continuous glucose monitoring system and food intake. In use of artificial pancreas; it is very important to model carbohydrate and insulin mechanism correctly, to determine metabolic parameters of the patients and to develop an algorithm suitable for the regulation of blood glucose. It is one of the most important parameters for good blood glucose management that a thorough understanding of insulin and carbohydrate mechanisms for patients, relatives and physicians. But, the mechanisms of insulin and carbohydrates involve differential equations. Therefore, they are not easy to understand for people who do not have a certain level of mathematical knowledge. T1DM patients, their parents or physicians do not have to know high mathematics and often do not. Therefore, the mathematical models used are far from these people. However, the fact that both patients and physicians know and actively use these models increases the effectiveness of blood glucose management. In this study, in order to provide an easy understanding of the mechanism of insulin and carbohydrate, these mechanisms were exemplified on PIMF function which was a MATLAB function. Through this model; the mechanism of insulin and its effect on blood glucose, carbohydrate mechanism and its effect on blood glucose were explained. In addition, the correct overlap of these two mechanisms was expressed mathematically. Hypoglycemia and hyperglycemia status estimation related to the change in blood glucose value were explained. Insulin and carbohydrate mechanisms have been tried to be expressed in a simple way for physicians, patients and their relatives to use without having to know high mathematics.**

Keywords – **carbohydrate, insulin, mathematical models, T1DM.**

I. INTRODUCTION

A healthy person's pre-meal blood glucose (BG) value is between 80-100 mg/dL and after-meal blood glucose is below 140 mg / dl. The BG value is regulated by the pancreas. There is no insulin production in T1DM patients. For this reason, the amount of insulin taken for each nutrient must be calculated and given externally. Insulin is given by multiple injections four times a day or is given by subcutaneous and continuous injection using a pump. The subject of this study was T1DM patients using pumps. The nutrients taken increase the BG value. The effects of each food group on metabolism are different. Carbohydrate (CHO) is basically the main element that increases the BG value. Therefore, the CHO quantity of the diet taken should be known. Also; fats, fibers, protein and conditions in which metabolism is involved are effective in the system. For T1DM, predetermination of some values is required. The parameter that indicates how many grams of CHO a unit of insulin corresponds to is called carbohydrate-insulin ratio (CIR). The parameter that indicates how many mg/dL BG of a unit of insulin causes a decrease is called insulin correction factor (ICF). The amount of CHO, protein, fat and fiber in foods should be known as weight. Once this information has been determined, there are three steps in calculating the insulin requirement for a nutrient. These are to determine the total amount of insulin for food taken, the amount of insulin to be given to normalize the BG value and the amount of insulin currently active in the body [1-7].

The CHO mechanism is the basic dynamic that raises the BG value. It refers to the increase in BG per unit time. In other words, the integral of the CHO mechanism gives an increase in BG value. In other words, the derivative of the increase in BG value refers to the mechanism of that food. BG value is integral of CHO mechanism. The insulin mechanism is the basic dynamic that decreases BG value. Refers to the decrease in BG per unit time. In other words, the integral of the insulin mechanism gives a decrease in BG value. In other words, the derivative of the decrease in BG value refers to the insulin mechanism. The sum of the integrals of insulin and CHO mechanisms taken over a given period gives the current value of BG value. Insulin and CHO mechanisms have their own characteristics. These curves vary slightly from person to person. Other physical conditions also create differences in the functioning of these mechanisms. In fact, these mechanisms are systems of theoretically complex differential equations. However, these models require high knowledge of mathematics to understand and interpret. Therefore, the feature that is very useful for patients and physicians is not

used sufficiently due to lack of knowledge of mathematics [8-16].

In this study, insulin and carbohydrate mechanisms were tried to be explained in a language that physicians, patients and parents could easily understood. The necessity of overlapping these two mechanisms was expressed on the mathematical model. Difficulties in making this overlap were explained. The role and function of intelligent control algorithms in this overlap process were explained.

II. MATERIAL AND METHODS

In this study, the method used by Çankaya and Aydoğdu (2019) [1] was taken as reference and the findings of this study [1] were used to explain the mechanisms. The referenced insulin and glucose values were collected from previous literature [17-41]. This study was performed using MATLAB by creating a scenario file as an in silico work. The created in silico patient parameters were given in Table 1 [1].

Table 1: In silico patient scenario values for the study [1].

Variables	Values
Age (year)	8
Length (cm)	135
Weight (kg)	22
Total daily insulin (unit)	13.2
Total daily bolus insulin (unit)	8.58
Total daily basal insulin (unit)	4.62
Pre meal blood glucose(mg/dL)	100
Target blood glucose value (mg/dL)	100
Insulin effect type	Fast
Glycemic index type CHO	medium
Dinner time	22:00
CIR value for dinner time	9.5
Total CHO effect time (minute)	100
Total insulin effect time (minute)	150

The CIR values in this scenario were given in Figure 1 [1]. The CIR value is different every hour of the day. It gets its lowest value in the morning.
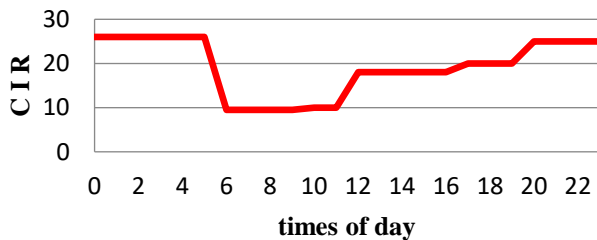
Figure 1: CHO and Insulin Ratio (CIR) for times of day [1].

Insulin and CHO mechanisms have been identified with the PINF function to make the study more understandable. PIMF

is Pi-shaped curve membership function. pimf(X, PARAMS) returns a matrix that is the Pi-shaped membership function evaluated at

$$X. \; PARAMS = [a \; b \; c \; d] \qquad (1)$$

X.PARAMS in (2) is a 4-element vector that determines the break points of this membership function. The parameters a and d specify the "feet" of the curve, while b and c specify its "shoulders". The equations of PIMF were given in (2). CHO mechanism was selected as pimf(x,[0,32,32,65]) and insulin mechanism was selected as pimf(x,[-5,50,50,150]).

$$f(x;a,b,c,d) = \begin{cases} 0, & x \le a \\ 2\left(\dfrac{x-a}{b-a}\right)^2, & a \le x \le \dfrac{a+b}{2} \\ 1-2\left(\dfrac{x-b}{b-a}\right)^2, & \dfrac{a+b}{2} \le x \le b \\ 1, & b \le x \le c \\ 1-2\left(\dfrac{x-c}{d-c}\right)^2, & c \le x \le \dfrac{c+d}{2} \\ 2\left(\dfrac{x-d}{d-c}\right)^2, & \dfrac{c+d}{2} \le x \le d \\ 0, & x \ge d \end{cases} \qquad (2)$$

III. RESULTS AND DISCUSSION

The graphs obtained [1] were expressed in a way that physicians, patients and their relatives can understand without requiring high mathematical knowledge.

The carbohydrate mechanism curve (Figure 2) shows how much it acts at which moment during the duration of the action. For any moment, it indicates the increase in BG per unit time.
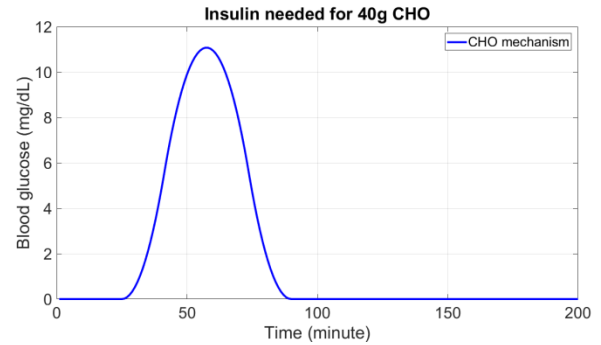
Figure 2: CHO mechanism [1].

The integral of the CHO mechanism curve (Fig. 3), the area under the curve, shows the total increase in BG in the selected time period.
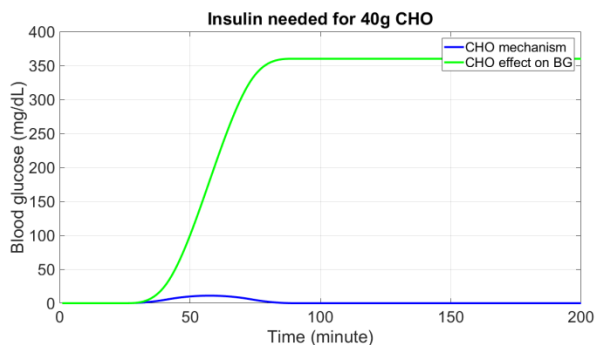
Figure 3: CHO mechanism and its effect on BG [1].

Figure 4 shows the CHO mechanism curve, the change caused by the CHO mechanism and the instantaneous values of BG.

Figure 4: CHO mechanism, its effect on BG and BG value [1].

The insulin mechanism curve (Figure 5) shows how much it acts at what time during the duration of the action. For any moment, it indicates the decrease in BG per unit time.

Figure 5: Insulin mechanism [1].

The integral of the insulin mechanism curve (Fig. 6), the area under the curve, shows the total decrease in BG in the selected time period. This graph shows how much insulin will decrease the BG value over time. The BG value can be calculated from this curve at any time.

Figure 6: Insulin mechanism and its effect on BG [1].

Figure 7 shows the insulin mechanism curve, the change caused by the insulin mechanism and the instantaneous values of BG.

Figure 7: Insulin mechanism, its effect on BG and BG value [1].

The curves in Figure 8, the effects of all dynamics alone and together on BG were given. In this graph, the waiting time after insulin injection to food intake was 20 minutes. It was observed that BG value was within acceptable limits. The waiting time was determined correctly.

Figure 8: All dynamics after insulin injection and food intake [1].

In Figure 9, the insulin mechanism was late. For this reason, BG value was out of range and hyperglycemia occurred. The reason for this was the early start of the meal. The waiting time given in this graph was 2 minutes. However, such a graph may also occur due to the difficulties associated with insulin absorption.
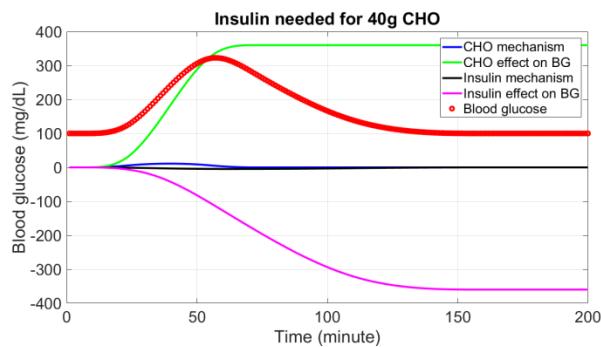
Figure 9: Early food intake (late insulin effect) [1].

In Figure 10, the insulin mechanism was activated before the CHO mechanism. For this reason, BG value was out of range and hypoglycemia occurred. The reason for this was the late start of the meal. The waiting time given in this graph is 29 minutes. However, such a graph may also occur due to the high fat and fiber content of the food taken.
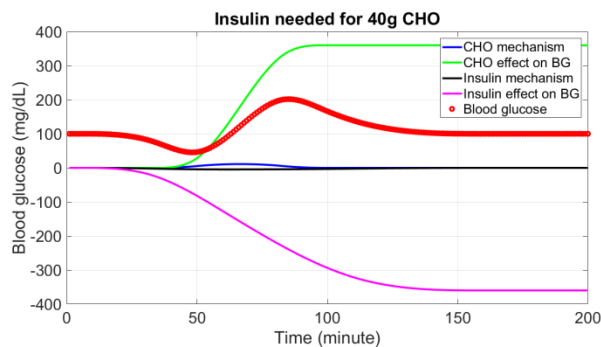
Figure 10: Late food intake (early insulin effect) [1].

As can be seen from these curves, it is not possible to fully overlap insulin and CHO mechanisms. For some nutrients, a more suitable overlap may be provided. For some food groups, this situation gets worse. In this case, diet should be established according to the insulin mechanism. Or much more advanced artificial pancreatic algorithms should be developed. With these algorithms, the insulin injection style can be changed. In this way, the insulin mechanism is likened to the diet mechanism. Of course, doing both will yield more successful results.

IV. CONCLUSION

In this study, insulin and CHO mechanisms and their effects on BG value were tried to be expressed in a way that physicians, patients and parents could understood. The mechanisms of insulin and CHO were expressed by the PIMF function in MATLAB to facilitate understanding of the subject. Insulin and CHO mechanisms do not fully coincide due to their characteristic properties. Therefore, further and sophisticated applications like improved control algorithms are needed to keep BG value within normal limits.

REFERENCES

[1] N. Çankaya and Ö. Aydoğdu, "Determining the optimum waiting time for starting the meal after insulin injection in type 1 diabetes mellitus patients by using artificial intelligence." International Conference on Computer Technologies and Applications in Food and Agriculture ICCTAFA 2019, July 11-12, Konya, pp. 115-124, 2019

[2] A. Schiffrin and M. Belmonte, "Multiple daily self-glucose monitoring: its essential role in long-term glucose control in insulin-dependent diabetic patients treated with pump and multiple subcutaneous injections." Diabetes Care, vol. 5, no. 5, pp. 479–484, 1982.

[3] D. C. Klonoff, "The current status of bolus calculator decision-support software." J Diabetes Sci Technol, vol. 6, no. 5, pp. 990–994, Sep 2012.

[4] T. M. Gross, D. Kayne, A. King, C. Rother and S. Juth, "A bolus calculator is an effective means of controlling postprandial glycemia in patients on insulin pump therapy." Diabetes Technol Ther, vol. 5, no. 3, pp. 365–369, 2003.

[5] B. Shashaj, E. Busetto and N. Sulli, "Benefits of a bolus calculator in pre- and postprandial glycaemic control and meal flexibility of paediatric patients using continuous subcutaneous insulin infusion (csii)." Diabet Med, vol. 25, no. 9, pp. 1036–1042, Sep 2008.

[6] G. Lepore, A. R. Dodesini, I. Nosari, C. Scaranna, A. Corsi and R. Trevisan, "Bolus calculator improves long-term metabolic control and reduces glucose variability in pump-treated patients with type 1 diabetes." Nutr Metab Cardiovasc Dis, vol. 22, no. 8, pp. e15–e16, Aug 2012.

[7] K. Barnard, C. Parkin, A. Young A and M. Ashraf, "Use of an automated bolus calculator reduces fear of hypoglycemia and improves confidence in dosage accuracy in patients with type 1 diabetes mellitus treated with multiple daily insulin injections." J Diabetes Sci Technol, vol. 6, no. 1, pp. 144–149, Jan 2012.

[8] A. M. Albisser, "Analysis: toward algorithms in diabetes selfmanagement," Diabetes Technol. Ther., vol. 5, no. 3, pp. 371–373, 2003.

[9] C. L. Owens, H. Zisser, L. Jovanovic, B. Srinivasan, D. Bonvin and F. J. Doyle, "Run-to-run control of blood glucose concentrations for people with type 1 diabetes mellitus," IEEE Trans. Biomed. Eng., vol. 53, no. 6, pp. 996–1005, 2006.

[10] P. Herrero, P. Pesl, J. Bondia, M. Reddy, N. Oliver, P. Georgiou and C. Toumazou, "Method for automatic adjustment of an insulin bolus calculator: In silico robustness evaluation under intra-day variability," Computer Methods and Programs in Biomedicine, p. (in press), 2015.

[11] H. Zisser, L. Robinson, W. Bevier, E. Dassau, C. Ellingsen, F. J. Doyle III and L. Jovanovic, "Bolus calculator: a review of four "smart" insulin pumps." Diabetes Temchnol Ther, vol. 10, no. 6, pp. 441–444, 2008.

[12] P. Herrero, P. Pesl, M. Reddy, N. Oliver, P. Georgiou and C. Toumazou, "Advanced insulin bolus advisor based on run-to-run control and casebased reasoning." IEEE J Biomed Health Inform, Jun 2014.

[13] J. Kolodner, "Case-based Reasoning". Morgan Kaufmann Publishers In., 1993.

[14] A. Aamodt and E. Plaza, "Case-based reasoning: foundational issues, methodological variations, and system approaches," AI Communications, vol. 7, no. 1, pp. 39–59, 1994.

[15] T.W. Liao, Z. Zhang and C.R. Mount, "Similarity measures for retrieval in case-based reasoning systems," Applied Artificial Intelligence, vol. 12, no. 4, pp. 267–288, 1998.

[16] C.C. Palerm, H. Zisser, W. C. Bevier, L. Jovanovi˘c and F. J. Doyle III. "Prandial insulin dosing using run-to-run control: application of clinical data and medical expertise to define a suitable performance metric," Diabetes Care, vol. 30, no. 5, pp. 1131–1136, 2007.

[17] R. Visentin, M. Schiavon, C. Giegerich, T. Klabunde, C. Dalla Man and C. Cobelli, "Incorporating Long-Acting Insulin Glargine into the UVA/Padova Type 1 Diabetes Simulator for In Silico Testing of MDI Therapies. IEEE Trans Biomed Eng. 2019 Feb 6. doi: 10.1109/TBME.2019.2897851.

[18] D. Shi, E. Dassau and F. J. Doyle III, " Multivariate learning framework for long-term adaptation in the artificial pancreas." Bioeng Transl Med. 2018 Nov 12;4(1):61-74.

[19] J. Xie and Q. Wang, "A Data-Driven Personalized Model of Glucose Dynamics Taking Account of the Effects of Physical Activity for Type 1 Diabetes: An In Silico Study." J Biomech Eng. 2019 Jan 1;141(1). doi: 10.1115/1.4041522.

[20] R. Visentin, M. Schiavon, C. Giegerich, T. Klabunde, C. Dalla Man and C. Cobelli, "Long-acting Insulin in Diabetes Therapy: In Silico Clinical Trials with the UVA/Padova Type 1 Diabetes Simulator." Conf Proc IEEE Eng Med Biol Soc. 2018 Jul;2018:4905-4908. doi: 10.1109/EMBC.2018.85132.

[21] M. Schiavon, G. Acciaroli, M. Vettoretti, A. Giaretta and R. Visentin, "A Model of Acetaminophen Pharmacokinetics and its Effect on Continuous Glucose Monitoring Sensor Measurements." Conf Proc IEEE Eng Med Biol Soc. 2018 Jul;2018:159-162. doi: 10.1109/EMBC.2018.8512257.

[22] G. Cappon, M. Vettoretti, F. Marturano, A. Facchinetti and G. Sparacino, "Optimal Insulin Bolus Dosing in Type 1 Diabetes Management: Neural Network Approach Exploiting CGM Sensor Information." Conf Proc IEEE Eng Med Biol Soc. 2018 Jul;2018:1-4. doi: 10.1109/EMBC.2018.8512250.

[23] G. Cappon, M. Vettoretti, F. Marturano, A. Facchinetti and G. Sparacino, "A Neural-Network-Based Approach to Personalize Insulin Bolus Calculation Using Continuous Glucose Monitoring." J Diabetes Sci Technol. 2018 Mar;12(2):265-272

[24] R. Visentin, E. Campos-Náñez, M. Schiavon, D. Lv, M. Vettoretti, M. Breton, B. P. Kovatchev, C. Dalla Man and C. Cobelli, "The UVA/Padova Type 1 Diabetes Simulator Goes From Single Meal to Single Day." J Diabetes Sci Technol. 2018 Feb 1:1932296818757747. doi: 10.1177/1932296818757747

[25] G. M. Steil, " Best Use of Models to Advance the Artificial Pancreas." Diabetes Technol Ther. 2018 Feb 15. doi: 10.1089/dia.2017.0420.

[26] P. Herrero, J. Bondia, O. Adewuyi, P. Pesl, M. El-Sharkawy, M. Reddy, C. Toumazou, N. Oliver, P. Georgiou. "Enhancing automatic closed-loop glucose control in type 1 diabetes with an adaptive meal bolus calculator – in silico evaluation under intra-day variability." Comput Methods Programs Biomed. 2017 Jul;146:125-131.

[27] M. D. Breton, R. Hinzmann, E. Campos-Nañez, S. Riddle, M. Schoemaker and G. Schmelzeisen-Redeker , "Analysis of the Accuracy and Performance of a Continuous Glucose Monitoring Sensor Prototype: An In-Silico Study Using the UVA/PADOVA Type 1 Diabetes Simulator". J Diabetes Sci Technol. 2017 May;11(3):545-552./1932296817710474.

[28] E. Campos-Náñez, K. Fortwaengler and M. D. Breton, "Clinical Impact of Blood Glucose Monitoring Accuracy: An In-Silico Study." J Diabetes Sci Technol. 2017 May 1:1932296817710474. doi: 10.1177/1932296817710474.

[29] M. Viceconti, C. Cobelli, T. Haddad, A. Himes, B. Kovatchev and M. Palmer, "In silico assessment of biomedical products: The conundrum of rare but not so rare events in two case studies." Proc Inst Mech Eng H. 2017 May;231(5):455-466.

[30] C. Toffanin, R. Visentin, M. Messori, F. Di Palma, L. Magni and C. Cobelli, "Towards a Run-to-Run Adaptive Artificial Pancreas: In Silico Results." IEEE Trans Biomed Eng. 2017 Jan 11. doi: 10.1109/TBME.2017.2652062

[31] M. Vettoretti, A. Facchinetti, G. Sparacino and C. Cobelli, " Predicting Insulin Treatment Scenarios with the Net Effect Method: Domain of Validity." Diabetes Technol Ther. 2016 Nov;18(11):694-704.

[32] E. Daskalaki, P. Diem and S. G. Mougiakakou, " Model-Free Machine Learning in Biomedicine: Feasibility Study in Type 1 Diabetes." PLoS One. 2016 Jul 21;11(7):e0158722. doi: 10.1371/journal.pone.0158722. eCollection 2016.

[33] M. Messori, C. Toffanin, S. Del Favero, G. De Nicolao, C. Cobelli and L. Magni, "Model individualization for artificial pancreas." Comput Methods Programs Biomed. 2016 Jul 5. pii: S0169-2607(15)30443-0. doi: 10.1016/j.cmpb.2016.06.006.

[34] R. Visentin, C. Giegerich, R. Jäger, R. Dahmen, A. Boss, M. Grant, C. Dalla Man, C. Cobelli and T. Klabunde, " Improving Efficacy of Inhaled Technosphere Insulin (Afrezza) by Postmeal Dosing: In-silico Clinical Trial with the University of Virginia/Padova Type 1 Diabetes Simulator." Diabetes Technol Ther. 2016 Jun 22.

[35] P. Colmegna, R. Sanchez-Pena, R. Gondhalekar, E. Dassau and F. Doyle, " Switched LPV Glucose Control in Type 1 Diabetes". IEEE Trans Biomed Eng. 2015 Oct 5.

[36] S. Zavitsanou, A. Mantalaris, M. C. Georgiadis and E. N. Pistikopoulos, "In Silico Closed-Loop Control Validation Studies for Optimal Insulin Delivery in Type 1 Diabetes". IEEE Trans Biomed Eng. 2015 Oct;62(10):2369-78. doi: 10.1109/TBME.2015.2427991. Epub 2015 Apr 29.

[37] P. Herrero, P. Pesl, M. Reddy, N. Oliver, P. Georgiou, and C. Toumazou, "Advanced Insulin Bolus Advisor Based on Run-To-Run Control and Case-Based Reasoning". IEEE J Biomed Health Inform. 2015 May;19(3):1087-96.

[38] C. Zhao and C. Yu, "Rapid model identification for online subcutaneous glucose concentration prediction for new subjects with type I diabetes". Comput Methods Programs Biomed. 2015 Apr;119(1):1-8. doi: 10.1016/j.cmpb.2015.02.003. Epub 2015 Feb 16.

[39] P. Herrero, P. Pesl, J. Bondia, M. Reddy, N. Oliver, P. Georgiou and C. Toumazou, "Method for automatic adjustment of an insulin bolus calculator: in silico robustness evaluation under intra-day variability". IEEE Trans Biomed Eng. 2015 May;62(5):1333-44. doi: 10.1109/TBME.2014.2387293. Epub 2015 Jan 1.

[40] R. Hu and C. Li, "An Improved PID Algorithm Based on Insulin-on-Board Estimate for Blood Glucose Control with Type 1 Diabetes". Comput Math Methods Med. 2015;2015:281589. doi: 10.1155/2015/281589. Epub 2015 Oct 5.

[41] R. Visentin, C. Dalla Man, Y. C. Kudva, A. Basu and C. Cobelli, "Circadian variability of insulin sensitivity: physiological input for in silico artificial pancreas". Diabetes Technol Ther. 2015 Jan;17(1):1-7. doi: 10.1089/dia.2014.0192.

Biomedical Applications of Collagen

Gülsüm Tiraş[1], Ahmet Erharman[1], and Esma Eryılmaz[1]*

*Corresponding author: Email: eeryilmaz@selcuk.edu.tr

[1]Selcuk University, Konya/Turkey, Faculty of Technology, Department of Biomedical Engineering

Abstract - **Collagen is one of the most common biomaterials. It is perfectly biologically compatible and safe, because of its variety of properties such as biodegradability, poor antigenicity, and self-aggregation. Collagen has also ability of forming extra-strength fibers with cross-linking between molecules. Collagens are used in many different forms such as sponges, mini-pellets, shields, gel formulation as well as in many drug delivery systems including skin replacement, artificial blood vessels, bone substitutes and valves. Thus, we discussed, in this article, different applications of collagen in biomedical sciences. These properties make collagens a primary source for medical applications.**

Keywords – **Collagen, drug delivery, biomedical**

I. INTRODUCTION

In human body, collagen is one of the most abundant protein. They are classified according to their structure and the common types are called as fibril-forming collagens which are type I, type II, type III, type V, and type XI. Among them type I is mostly found in body tissue [1]. There are 28 different types of collagen [2]. Collagen synthesis occurs in fibroblast cells, which are the basic cells of connective tissue. In addition, collagen synthesis occurs not only inside the cell but also outside the cell [3].

Due to the fact that collagens are highly biocompatible and safe, they are regarded as very useful. They play important roles in certain biological functions of the body such as differentiation, cell binding, reconstruction, proliferation, and staying alive. They are also crucial for forming scaffold of cells, basement membranes [4].

As collagens are biodegradable and weakly antigenic, they are mainly used as a resource for medical applications. Collagens are used as many drug delivery systems which are sponges, pellets, shields, gel formulation as well as used skin replacement, artificial blood vessels, bone substitutes, and valves [1].

Table 1: Collagen types and properties

Fibril-forming collagens	Type I, II, III, V, XI
	The most abundant type of collagen is type I which is generally found in connective tissue
Type I	such as skin, bone, dermis, ligament, cornea and tendon. Type I collagen is heterotrimer since it has two identical α_1 (I)-chains and one α_2 (I)-chain [1, 5-8].
Type II	Found in cartilage, embryonic epithelial mesenchymal transitions, corneal epithelium, notochord, nucleus pulposus of intervertebral discs, and vitreous body. Consisted of three α_1 (II)-chains forming homotrimeric. Type I and type II show similar properties such as size and biomechanical properties [1, 9-13].
Type III	Generally found in skin, vessel wall, intestines and reticular fibres. Type III collagen is homotrimeric, has three α_1 (III)-chains. Type I and type III are found in body tissue mostly together [1, 14-17].
Type V	Type V is mostly found with type I collagen found in bone, lung, cornea, fetal membranes [18-20].
Type XI	Generally type XI and type II collagens coexist in vitreous body, intervertebral disc, and cartilage [1, 4].

FACIT (Fibril-associated collagens with interrupted triple helices)	Type IX, XII, XIV, XIX, XX, XXI
Type IX	Found in cartilage, vitreous humor and cornea with type II collagen. Type IX has not only three triple-helical domains but also three non-helical domains [4, 21].
Type XII	Type XII is found in tendon, perichondrium and, ligament correlated to type I collagen fibrils [1, 15, 22].
Type XIV	Type XIV is found in skin, dermis, tendon, vessel wall, placenta, lungs and liver, correlated to type I collagen fibrils [21, 23, 24].
Type XIX	Found in human rhabdomyosarcoma. Type XIX collagen has five triple-helical domains [1, 23].
Type XX	Type XX is found in fibrils such as corneal epithelium, embryonic skin, sternal cartilage, and tendon. It is associated with type I

	collagen fibril, similar with type XII and type XIV collagen in terms of structure [1, 24].
Type XXI	Type XXI is found in blood vessels walls of stomach, kidney, heart, placenta and muscle. The structure of it is α_1 triple helix. [4, 25, 26].
Network-forming collagens	Type IV, VIII, X
Type IV	Also named basement membrane collagens. Type IV is the basic constituent of basement membrane [1, 4].
Type VIII	Also named Hexagonal network-forming collagens. Found in mostly endothelium. Type VIII collagen has a short chain collagen structure [27]. The structure of type VIII is similar to the type X, since it contains both triple helix and carboxyl-terminal non-triple helix domains [28].
Type X	Also named Hexagonal network-forming collagens. Type X, found in hypertrophic cartilage, is a short chain collagen. Type X similar to type VIII in terms of polymeric structure [2, 23].
Multiplexin collagens	Type XV, XVI, XVIII
Type XV	Type XV belongs to class of basement membrane collagen. Found in fibroblasts, smooth muscle cells, kidney, and pancreas. Type XV can act in the control of angiogenesis [1, 4].
Type XVI	Also named Fibril-associated collagens with interrupted triple helices (FACIT). Found in amnion, keratinocytes, and fibroblasts [1, 4, 23].
Type XVIII	Type XVIII belongs to class of basement membrane collagen. Found in liver, lungs, and vascularized tissues [1, 4].
Transmembrane collagens	Type XIII, XVII
Type XIII	Type XIII has a single transmembrane N-terminal domain and found in epidermis, hair follicle, endomysium, intestine, chondrocytes, lungs, and liver [1, 4].
Type XVII	Found in dermal-epidermal junctions [1].
Microfibrillar collagens	Type VI
Type VI	Also named Beaded filament-forming collagen [4]. Found in intervertebral disc, cartilage, lungs, vessel wall, dermis, and placenta. Type VI has a short triple-helical domain [1, 23].
Anchoring fibril-	Type VII

forming collagens	
Type VII	Type VII has filaments that anchoring the epithelial basement membrane to fibril tissue [23]. Found in dermal–epidermal junction; oral mucosa, cervix, and skin [1].

II. BIOMEDICAL APPLICATIONS OF COLLAGEN

A. Shields

Collagen corneal shields were originally designed for bandage contact lenses [29]. Theoretical, experimental, and clinical studies have shown that collagen shields are effective in drug system [30]. As a matter of fact that collagen molecules of the human eye is very similar to porcine sclera tissue, collagen corneal shield can be produced from porcine sclera tissue [29]. The reason for using shields in collagen based drug delivery systems are ease of application to ocular surface under traumatic corneal conditions [29, 30].

Drug transfer through collagen shields depends on the loading of the drug and subsequent release by the shield [31]. After drugs were added to collagen shield which is served as a reservoir, the drugs interact with tears, and they begin to dissolve. In view of the fact that friction force between the cornea and the eyelid is significantly reduced, it was seen that the duration of effect of the cornea increased upon with addition of drug [32].

B. Sponges

Collagen sponges are used in places requiring the use of biological wound dressings which are pressure sores, leg ulcers, and donor sites. They are also used in the treatment of severe burn and wounds [33]. As the name suggests, collagen sponges prevent tissue leakage. They provide as smooth adhesion on wound, thereby protecting the wound site from mechanical damage and bacterial infection [34, 35]. As a result, in experiments used collagen sponge implantation showed a rapid healing in burns, dermal and epidermal wounds [36, 37].

C. Hydrogel-collagen

Hydrogels have lots of properties such as easy production, self-application, low antigenicity, and biodegradability. These properties have allowed the widespread use of hydrogels as a drug delivery system and gene delivery carriers. The hydrogels are generally used with polymers or injectable gels in clinical applications.

A hydrogel matrix can be successfully generated from collagen and a glycopolymer. The optical properties of the obtained composite hydrogels can be equivalent or superior to that of human cornea. Because of the biocompatibility and suturability of composite hydrogel, composite hydrogel can be used in corneal lamellar keratoplasty [38].

D. Pellet/tablet

Mini pellets are used as one of the drug delivery method. Mini pellets with a diameter of 1 mm and a length of 1 cm have an

area large enough to carry drugs that are small enough to be injected into the body [29]. Collagen-based pellets have not only been used as drug delivery systems, but also many studies have shown that they can be also used as gene delivery carrier. Atelocollagen which is a low immunogenic collagen derivative, in pellet form has been used for gene transfer. Atelocollagen is allowed products to circulate within the system for a long time, also facilitating the use of vectors in somatic gene therapy [39].

E. Collagen as skin replacement

Collagen - based regeneration templates are natural polymers used as a means of transporting drug carriers for diabetes-induced wounds and burn wounds [29, 40]. Diluted type 1 collagen is suitable for collagen-based implants because of high biocompatibility and mechanical change properties [41]. The healing effect can be increased by applying various modifications to the collagen-based implant [42]. These modifications can occur by the combination of collagen with fibrin, glycosaminoglycan and biotin [29]. Studies have found that the skin membrane, made from a combination of collagen and glycosaminoglycan, is suitable for human epidermal cells. These findings suggest that collagen combinations can be used for skin substitution [43].

F. Collagen as bioengineered tissues

Collagen forms of wound dressings used for the treatment of wounds and burns which are biocompatible can used in skin replacement. This applications have pioneered studies in the field of bioengineering [44]. Collagen is hemostatic. This feature is an important factor in tissue repair because it increases platelet formation and allows platelets to stick and accumulate [45]. Owing to the fact that biodegradable collagen structure scaffolds have large surface area, they used for heart valves, blood vessels and cell transport process [46, 47]. Tissue graft containing collagen can be produced from small intestine, ureter or bladder [48]. The low antigenicity property of collagen and its ability to adapt to tissues enables it to be used in surgical repairs [49]. Studies have shown that from collagen-based materials developable biomaterials can be produced.

G. Collagen in Nanotechnology

Aqueous collagen solutions allow us to produce non-woven nets by electrospinning. Electrospinned aqueous solutions of collagen has two major advantages: high surface area and high porosity. Electrospinning also has an advantage, which is thin multi-layer scaffolding allows us to produce. This advantage provides high strength [50].

Nanofibers derived from collagen via electrospinning process were used for production of wound dressing. Because of the fact that the collagen nanofibers have high strength, high surface, and a wide range of pore size distributions, they significantly contribute to cell growth, proliferation and binding. Therefore, these properties of the collagen nanofibers allow for the use in wound dressing [51].

Type I collagen nanofibers is prepared by electrospin device and mesenchymal stem cells are clinged on type I collagen nanofibers. Firstly, just mesenchymal stem cells were evaluated in terms of morphology, growth, adhesion, cell motility, and osteogenic differentiation by scanning electron microscope. Likewise, mesenchymal stem cells clinged on type I collagen nanofibers were evaluated. In accordance with these findings the type I collagen has been observed to have a positive effect on growth, viability, adhesion, motility. If low numbers of cells for cell therapy, this method can be suitable in terms of proliferation of cells [52].

By using biomimetic synthesis, bone scaffolding material (nano-hydroxyapatite / collagen / Polylactic acid composite) has been developed which shows some properties of natural bone and has high mechanical strength and shaping ability. This scaffold helps to repair bone defects in the clinical setting. The porous microstructure of the scaffold is similar to spongy bone. It provides actively using in cell culture and implant experiments [53].

H. Collagen as bone implant

Collagen is abundant in the extracellular matrix of bone. Owing to the fact that collagens have perfect features such as vascular growth, growth factor, mineral deposition, which features provide appropriate places to bone regeneration, they can be used in bone implant applications [54].

III. CONCLUDING REMARKS

Collagen is the most abundant protein in the human body. It is constitute a quarter of the total amount of protein. Collagen is found in many tissues such as skin, bone, ligament, tendon, and cornea. There are 28 different types of collagen. The most abundant of these are fibril-forming collagens which are type I, type II, type III, type V, type XI. Collagen can be forms fibers which have extra strength and stability, because collagens have self-aggregation and cross-linking. It is often preferred in biomedical applications because of its biocompatible, safe, biodegradable and poor antigenicity properties. The study of collagen use in drug delivery systems and tissue engineering may play an important role in the diagnosis and treatment of diseases. Considering the applications mentioned in this paper, it is expected that useful studies on applications of collagens in biomedical field will be carried out in the future.

REFERENCES

1. Gelse, K., E. Pöschl, and T.J.A.d.d.r. Aigner, *Collagens—structure, function, and biosynthesis.* 2003. **55**(12): p. 1531-1546.
2. Ricard-Blum, S.J.C.S.H.p.i.b., *The collagen family.* 2011. **3**(1): p. a004978.
3. Wu, M. and J.S. Crane, *Biochemistry, Collagen Synthesis.* 2018.
4. Yang, C., et al., *The application of recombinant human collagen in tissue engineering.* 2004. **18**(2): p. 103-119.

5. Olsen, D.R., et al., *Production of human type I collagen in yeast reveals unexpected new insights into the molecular assembly of collagen trimers.* 2001. **276**(26): p. 24038-24043.

6. Toman, P.D., et al., *Production of recombinant human type I procollagen homotrimer in the mammary gland of transgenic mice.* 1999. **8**(6): p. 415-427.

7. Fleischmajer, R., et al., *Dermal collagen fibrils are hybrids of type I and type III collagen molecules.* 1990. **105**(1-3): p. 162-169.

8. Niyibizi, C. and D.R.J.C.t.r. Eyre, *Bone type V collagen: chain composition and location of a trypsin cleavage site.* 1989. **20**(1-4): p. 247-250.

9. Eyre, D.J.A.R. and Therapy, *Articular cartilage and changes in arthritis: collagen of articular cartilage.* 2001. **4**(1): p. 30.

10. Fernandes, R.J., T.M. Schmid, and D.R.J.e.j.o.b. Eyre, *Assembly of collagen types II, IX and XI into nascent hetero-fibrils by a rat chondrocyte cell line.* 2003. **270**(15): p. 3243-3250.

11. Fertala, A., et al., *Synthesis of recombinant human procollagen II in a stably transfected tumour cell line (HT1080).* 1994. **298**(1): p. 31-37.

12. Fertala, A., et al., *Collagen II Containing a Cys Substitution for Arg-α1− 519: Abnormal Interactions of the Mutated Molecules with Collagen IX.* 2001. **40**(48): p. 14422-14428.

13. Bruckner, P., M.J.M.r. van der Rest, and technique, *Structure and function of cartilage collagens.* 1994. **28**(5): p. 378-384.

14. Vaughan, P.R., et al., *Production of recombinant hydroxylated human type III collagen fragment in Saccharomyces cerevisiae.* 1998. **17**(6): p. 511-518.

15. Mazzorana, M., et al., *Involvement of Prolyl 4-Hydroxylase in the Assembly of Trimeric Minicollagen XII STUDY IN A BACULOVIRUS EXPRESSION SYSTEM.* 1996. **271**(46): p. 29003-29008.

16. Myllyharju, J., et al., *Expression of recombinant human type I-III collagens in the yeast Pichia pastoris.* 2000, Portland Press Limited.

17. Vuorela, A., et al., *Assembly of human prolyl 4-hydroxylase and type III collagen in the yeast Pichia pastoris: formation of a stable enzyme tetramer requires coexpression with collagen and assembly of a stable collagen requires coexpression with prolyl 4-hydroxylase.* 1997. **16**(22): p. 6702-6712.

18. Chanut-Delalande, H., et al., *Control of heterotypic fibril formation by collagen V is determined by chain stoichiometry.* 2001. **276**(26): p. 24352-24359.

19. Niyibizi, C. and D.R.J.E.j.o.b. Eyre, *Structural Characteristics of Cross-Linking Sites in type V Collagen of Bone: Chain Specificities and Heterotypic Links to Type I Collagen.* 1994. **224**(3): p. 943-950.

20. Birk, D.E., et al., *Collagen type I and type V are present in the same fibril in the avian corneal stroma.* 1988. **106**(3): p. 999-1008.

21. Von der Mark, K., *Structure, biosynthesis and gene regulation of collagens in cartilage and bone*, in *Dynamics of Bone and Cartilage Metabolism. Principles and Clinical Applications*. 2006, Academic Press/Elsevier Burlington, MA. p. 3-40.

22. Cheng, E.L., et al., *Expression of type XII collagen and hemidesmosome-associated proteins in keratoconus corneas.* 2001. **22**(5): p. 333-340.

23. Ricard-Blum, S., B. Dublet, and M. van der Rest, *Unconventional Collagens: Types 6, 7, 8, 9, 10, 12, 14, 16, and 19.* 2000: Oxford University Press on Demand.

24. Koch, M., et al., *Collagen XXIV, a vertebrate fibrillar collagen with structural features of invertebrate collagens selective expression in developing cornea and bone.* 2003. **278**(44): p. 43236-43244.

25. Fitzgerald, J. and J.F.J.F.l. Bateman, *A new FACIT of the collagen family: COL21A1.* 2001. **505**(2): p. 275-280.

26. Tuckwell, D.J.M.b., *Identification and analysis of collagen α1 (XXI), a novel member of the FACIT collagen family.* 2002. **21**(1): p. 63-66.

27. Yamaguchi, N., R. Mayne, and Y.J.J.o.B.C. Ninomiya, *The alpha 1 (VIII) collagen gene is homologous to the alpha 1 (X) collagen gene and contains a large exon encoding the entire triple helical and carboxyl-terminal non-triple helical domains of the alpha 1 (VIII) polypeptide.* 1991. **266**(7): p. 4508-4513.

28. Sawada, H., H. Konomi, and K.J.T.J.o.c.b. Hirosawa, *Characterization of the collagen in the hexagonal lattice of Descemet's membrane: its relation to type VIII collagen.* 1990. **110**(1): p. 219-227.

29. Lee, C.H., A. Singla, and Y.J.I.j.o.p. Lee, *Biomedical applications of collagen.* 2001. **221**(1-2): p. 1-22.

30. Willoughby, C., M. Batterbury, and S.J.S.o.o. Kaye, *Collagen corneal shields.* 2002. **47**(2): p. 174-182.

31. Leaders, F., et al., *New polymers in drug delivery.* 1973. **5**(5): p. 513-6 passim.

32. Kaufman, H.E.J.J.o.C. and R. Surgery, *Collagen shield symposium.* 1988. **14**(5): p. 487-488.

33. Geesin, J.C., et al., *Development of a skin model based on insoluble fibrillar collagen.* 1996. **33**(1): p. 1-8.

34. Yannas, I.V.J.A.C.I.E.i.E., *Biologically active analogues of the extracellular matrix: artificial skin and nerves.* 1990. **29**(1): p. 20-35.

35. Pachence, J.J.M.D.D.I., *Collagen: its place in the medical device industry.* 1987. **9**: p. 49-55.

36. Marks, M.G., C. Doillon, and F.H.J.J.o.b.m.r. Silvert, *Effects of fibroblasts and basic fibroblast growth factor on facilitation of dermal wound healing by type I collagen matrices.* 1991. **25**(5): p. 683-696.

37. Royce, P.M., et al., *The enhancement of cellular infiltration and vascularisation of a collagenous dermal implant in the rat by platelet-derived growth factor BB.* 1995. **10**(1): p. 42-52.

38. Deng, C., et al., *Collagen and glycopolymer based hydrogel for potential corneal application.* 2010. **6**(1): p. 187-194.

39. Ochiya, T., et al., *New delivery system for plasmid DNA in vivo using atelocollagen as a carrier material: the Minipellet.* 1999. **5**(6): p. 707.

40. Meena, C., S. Mengi, and S. Deshpande. *Biomedical and industrial applications of collagen*. in *Proceedings of the Indian Academy of Sciences-Chemical Sciences*. 1999. Springer.

41. Panduranga Rao, K.J.J.o.B.S., Polymer Edition, *Recent developments of collagen-based materials for medical applications and drug delivery systems.* 1996. **7**(7): p. 623-645.

42. Koide, M., et al., *A new type of biomaterial for artificial skin: Dehydrothermally cross-linked composites of fibrillar and denatured collagens.* 1993. **27**(1): p. 79-87.

43. Boyce, S.T., D.J. Christianson, and J.F.J.J.o.b.m.r. Hansbrough, *Structure of a collagen-GAG dermal skin substitute optimized for cultured human epidermal keratinocytes.* 1988. **22**(10): p. 939-957.

44. Auger, F.A., et al., *Tissue-engineered human skin substitutes developed from collagen-populated hydrated gels: clinical and fundamental applications.* 1998. **36**(6): p. 801-812.

45. Miyata, T., T. Taira, and Y.J.C.m. Noishiki, *Collagen engineering for biomaterial use.* 1992. **9**(3-4): p. 139-148.

46. Kuzuya, M. and J.L.J.E.c.r. Kinsella, *Induction of endothelial cell differentiation in vitro by fibroblast-derived soluble factors.* 1994. **215**(2): p. 310-318.

47. Chevallay, B., et al., *Collagen-based biomaterials as 3D scaffold for cell cultures: applications for tissue engineering and gene therapy.* 2000. **38**(2): p. 211-218.

48. Clarke, K.M., et al., *Intestine submucosa and polypropylene mesh for abdominal wall repair in dogs.* 1996. **60**(1): p. 107-114.

49. Van der Laan, J., et al., *TFE-plasma polymerized dermal sheep collagen for the repair of abdominal wall defects.* 1991. **14**(10): p. 661-666.

50. Buttafoco, L., et al., *Electrospinning of collagen and elastin for tissue engineering applications.* 2006. **27**(5): p. 724-734.

51. Rho, K.S., et al., *Electrospinning of collagen nanofibers: effects on the behavior of normal human keratinocytes and early-stage wound healing.* 2006. **27**(8): p. 1452-1461.

52. Shih, Y.R.V., et al., *Growth of mesenchymal stem cells on electrospun type I collagen nanofibers.* 2006. **24**(11): p. 2391-2397.

53. Liao, S., et al., *Hierarchically biomimetic bone scaffold materials: nano-HA/collagen/PLA composite.* 2004. **69**(2): p. 158-165.

54. Giannoudis, P.V., H. Dinopoulos, and E.J.I. Tsiridis, *Bone substitutes: an update.* 2005. **36**(3): p. S20-S27.

Semi-Automatic Cardiac Vector and Angle Calculator Development

A.IŞIK[1] and MF. AKŞAHİN[2]

[1] Baskent University, Ankara/Turkey, isik_atakan@gmail.com
[2]Baskent University, Ankara/Turkey, maksahin@hotmail.com

Abstract - **One of the important diagnostic data in ECG is determining Heart axial vector. This vector can help doctors to diagnose a disease or to state the heart's medical condition from electrical signals. However, determine these vectors have some difficulties like drawing and calculating QRS or any other important regions like S-T on the ECG paper. This is also a very long process. Besides during the process, there is a high possibility to make mistakes by human hand. To shorten this process and at the same time to avoid the mistakes by human hand during the measuring and calculating heart vectors, we approached via image processing techniques and designed a Python-based Graphical User Interface. The program was designed manually calibrating-globally usable. We aim to make this process short and more reliable. This program can measure the distance between two dots that the user has determined on ECG papers and according to data program can calculate the aVf, aVl, aVr and Lead 1 deviations' heart axis and their angle. Thus, the user can measure any region on these deviations mathematically and calculating the heart vectors from these deviations. We analyze ECG Papers from real patients by the program and by hand. As a result, the recorded data are correlated with high accuracy.**

Keywords - **ECG, GUI, Biomedical, Image Processing, Cardiac Axes**

I. INTRODUCTION

Basically ECG is a routine test to diagnose many heart diseases. The test showed us electrical signals that the heart produces and the ECG records these signals from the electrodes on the patient's surface skin. One of the most important data that can be calculated from ECG signals is the cardiac vector. The cardiac axis is the net or means direction the electricity takes during ventricular depolarization [1]. The concept of cardiac vector describing the electrical activity of the heart and the three cardinal bipolar limbs lead vectors (lead I, lead II & lead III) forming an equilateral triangle with heart at the center of the homogeneous volume spherical conductor which was firstly described by Einthoven [2]. In classical ECG analysis, many deviations are used to collect data and calculating heart vectors. In literature, there are 6 cardiac axes. Basically Lead 1, 2, 3 axis and aVf, aVl, aVr axis that is distributed from basic axis. This shows all six leads' view of the heart [3]. If we are looking at the heart to the front side, the Lead 1 axis is intersected heart's middle point horizontally. Lead 2 has a 60-degree angle to down from lead 1 and lead 3 has a

120-degree angle. The distributed axis aVf is intersected heart's middle point vertically. aVl axis has a 30-degree angle to the right side from aVf and aVr has a 30-degree angle to the left side from aVf. So we have 6 axes that intersected in one point but directed different points in particular angles. From here we can demonstrate this axis' in X-Y plan and express the axis as trigonometric equations. Determining the cardiac axis is an important component of 12-lead ECG interpretation and can help to confirm the presence of various cardiac conditions [4].

Calculating heart vectors is not only about the axis. Before the vector calculation, we need to measure the QRS-T region of a specific deviation signal. After the maximum and the minimum value measurement of specific QRS-T value, the user can enter the values for related deviations and calculates the heart vector or angle.

Several methods can be used to calculate the cardiac axis, though occasionally it can prove extremely difficult to determine [5]. In this study, we develop software that make easy to calculating heart vector using image processing techniques on ECG papers.

II. MATERİAL AND METHOD

We aim the making calculating heart vectors faster and more reliable in the study. In this manner, we developed the software prototype that can measure the distance in the regions of the ECG and we use these distance on calculating the heart vectors. Principle of the calculating is analytical geometry. Each heart axis can be mathematically expressed as an equation on the XY plane. So using this we develop the software which is manually calibrating and globally usable.

A. Graphical User Interface(GUI) and Image Loading

We use python 2.7 and openCV library for design and coding our GUI. Our GUI has one large image panel and several buttons and a textbox for measurement. The image panel's resolution is 1280*720 pixels. It is great to see the images detail without losing any detail. Image names must be all Latina characters and must not contain any special characters for loading. So we renamed the ECG paper images like 1.jpg, 2.jpg, etc. The software window has been given in figure 1. We can load an image from file then start a measurement.
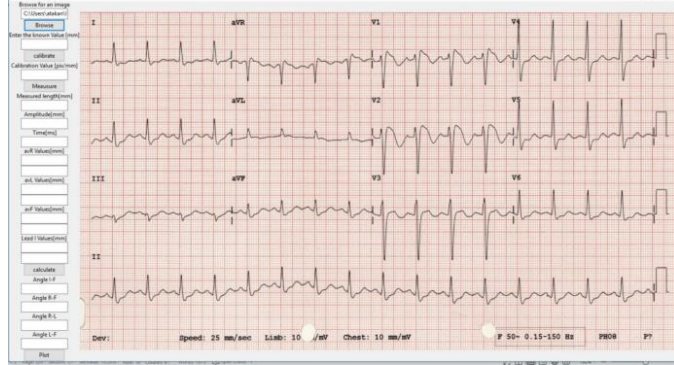
Figure 1. ECG analyzes GUI

B. Distance Measurement

In the study first, we must measure the distance between the selected 2 dots. For this purpose, we design the algorithm that saves the pixel coordinate on the computer screen when the left mouse clicks and then draw a line to the second point that occurs when right mouse click. After saving the coordinates we can measure the pixel length of the line using the formula of the distance between two points. Measuring screen has been shown in figure 5. Formula has been given on equation 1 [8].

$$d(A,B)^2 = (x_2 - x_1)^2 + (y_2 - y_1)^2 \quad (1)$$

C. Calibration

After the measurement of the distance of two points, we face a problem. The problem is the distance that we calculate is not metric but is a pixel value. For converting pixel to metric we must know the real distance of the line that we draw on the ECG paper photo. Generally, ECG papers print on the graph paper and have information about the mm(millimeter)/mV(millivolt). So if we draw the line on ECG paper we can see the real distance using the graph papers spacing. And we can create a calibration factor. Calibration Factor equation has been given on equation 2. We use a calibration image for testing calibration algorithm.

$$Cf = Rd / Pd \quad (2)$$

Where CF is calibration factor, Rd is real distance and Pd is pixel distance.

Figure 2. Calibration Screen

D. ECG Measurement

After the creating calibration factor, we can draw a new line on ECG. We select any 2 points and measure the length of line. Also using the coordinates of points that the algorithm saves before the measurement we can measure the distance on the X plane and Y plane separately. X plane represents the time vector on ECG and Y plane represents the amplitude of the ECG signal. ECG has many signals of different deviations. So we can measure any deviations and any pulses amplitude or time difference. For minimizing the mistake on the point selection after the selection, a new window will show up and we can zoom in the image and control the points and line.Zoomed image has been shown in figure 4. Also, we can save or move the image in this window. In this study, The ECG is analyzed for only aVF, aVL, aVR and lead 1 axis. The heart axis figure has been given in figure 4 [10].
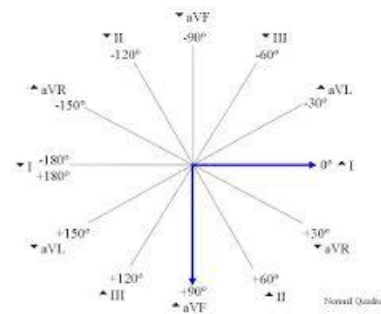
Figure 3. Cardiac Axis Plane

As seen in figure 3 above we can simply express lead 1 and aVF axis as an equation. Lead 1 intersects origin horizontally and aVF intersects the origin vertically. So we can calculate the slopes of the other axis using the angles between the x=0 and y=0 lines shown in equation 3.

$$x = 0; y = 0; y = 2 * x / \sqrt{3}; y = -2 * x / \sqrt{3} \qquad (3)$$

The equations are evaluated in the software and written software can calculate each coordinate from the measured value of the related axis.

Software user must enter the value of the axis vector by 2 different numbers after measurement of the related axis. Firstly the highest voltage of the pulse is determined from the origin and secondly, the lowest voltage value is determined from the origin. Then using the determined values of the related axis, the algorithm calculates the perpendicular line of the related axis and the coordinate of intersection point on the axis plane. Software makes subtraction of highest positive value and lowest negative value as a default operation. If we want summation, we can multiply the lowest negative distance with -1 by entering this value in the textbox. After all values entered, the calculate button will calculate the planar angles between the particular axis and we can see these angle values on the screen. Calculating screen has been shown in figure 6. Calculating is a bunch of simple mathematical process. Firstly, algorithm takes the values of the axis and calculates the axis vector. Then create intersection lines that are perpendicular to the axis values to all axes. Finally, the angle between the vector and x=0 line is calculated and as a result, the algorithm calculates the heart vector's angle between any specific axis. We used the corrected formulas of the previous study [6]. Process order and using equations has been given in equation 4 [8].

$$y = mx + n; m_1 = -\frac{1}{m_2}; \tan(\alpha) = |m_2 - m_1| / |1 + m_2 * m_1| \qquad (4)$$
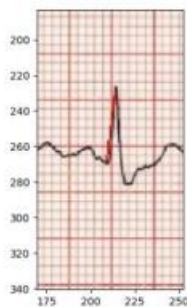
Figure 4. Zoomed Measured Region
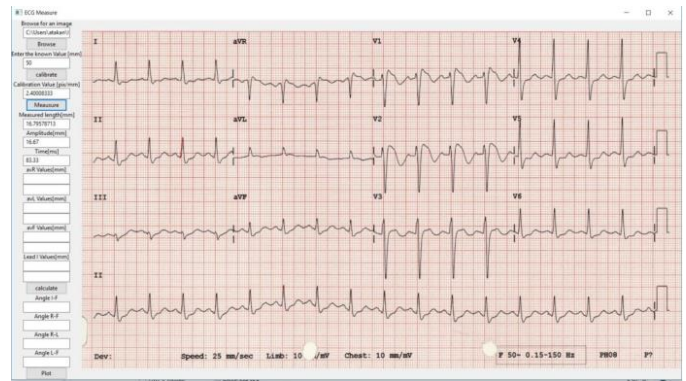
Figure 5. Measuring Screen
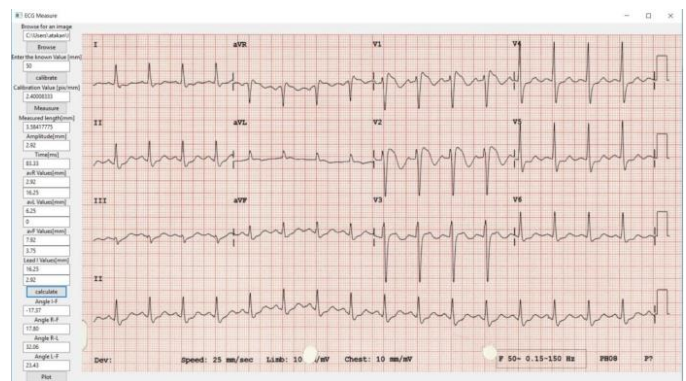
Figure 6. Calculation Screen

E. Plotting Axial Plane

After all this process we know the angles and we can plot the axial plane which has heart axes such as aVF, aVL,aVR, lead 1 and perpendicular intersection to these axis' vector values that we measure and enter by using the software. Plotting screen has been shown in figure 7.
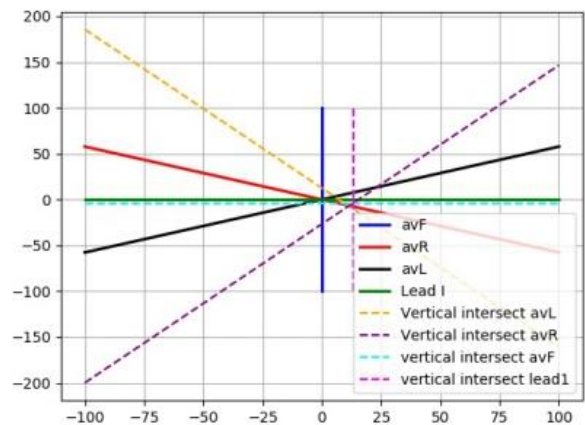
Figure 7. Plotting Screen

III. RESULT AND CONCLUSİON

We used 8 different clinical ECG sheets to compare our algorithm working correctly. 8 different ECG sheets have been measured 4 different scorers via hand and then we compare results with our software results. As you can see in table 1, our software calculated the heart planar angle correctly. Paper images have been collected from reference [9].

Table 1 . aVR, aVL, aVF positive and negative values measured by hand and by software

	aVR Pos and Neg Values		aVL Pos and Neg Values		aVF Pos and Neg Values	
	Doctor Measurements	Software Measurements	Doctor Measurements	Software Measurements	Doctor Measurements	Software Measurements
ECG Paper 1	1mm-4mm	0.672mm-3.23mm	1mm-2mm	1.11mm-2.26mm	5mm-2mm	4.14mm-1.11mm
ECG Paper 2	4mm-11mm	1.78mm-9.58mm	11mm-4mm	8.66mm-2mm	4mm-5mm	3.55mm-3.1mm
ECG Paper 3	0mm-10mm	0.89mm-9.32mm	11mm-1mm	7.22mm-2mm	3mm-1mm	1.78mm-0.67mm
ECG Paper 4	1mm-5mm	0.89mm-4mm	3mm-4mm	1.55mm-2.89	7mm-0mm	5.33mm-0mm
ECG Paper 5	3mm-12mm	2mm-9.10mm	5mm-0mm	4.22m-0mm	6mm-3mm	4.22mm-2mm
ECG Paper 6	1mm-10mm	0.67mm-7.10mm	7mm-1mm	4mm-0.67mm	3mm-1mm	2.22mm-0mm
ECG Paper 7	2mm-23mm	3.11mm-13.33	3mm-6mm	2.46mm-3.16mm	21mm-2mm	11.41mm-2.36mm
ECG Paper 8	0.5mm-9.5mm	0.71mm-6.67mm	5mm-1.5mm	3.33mm-0.95mm	5mm-0.5mm	3.10mm-0.48mm

REFERENCES

[1] Hampton, J. (2003). The ECG Made Easy E-Book. Elsevier Health Sciences.

[2] Jaakko Malmivuo, Robert Plonsey Bioelectromagnetism - Principles and Applications of Bioelectric and Biomagnetis Fields, Chapter: 15, Oxford University Press, 1995; 277-289.

[3] Morris F, Edhouse J, Brady WJ, Camm J (2003) ABC of Clinical Electrocardiography. BMJ Books, London

[4] Daviesis, A. (2007). Calculating cardiac axis on a 12-lead ECG. British Journal of Cardiac Nursing, 2(11), 513-517.

[5] Meek, S., & Morris, F. (2002). Introduction. I—Leads, rate, rhythm, and cardiac axis. Bmj, 324(7334), 415-418.

[6] Novosel, D., Noll, G., & Lüscher, T. F. (1999). Corrected formula for the calculation of the electrical heart axis. Croatian medical journal, 40, 77-79.

[7] Kors, J. A., de Bruyne, M. C., Hoes, A. W., van Herpen, G., Hofman, A., van Bemmel, J. H., & Grobbee, D. E. (1998). T axis as an indicator of risk of cardiac events in elderly people. The Lancet, 352(9128), 601-605.

[8] https://www.superprof.co.uk/resources/academic/maths/geometry/line/analytic-geometry-formulas.html

[9] https://lifeinthefastlane.com/table/ecg-database/

[10] http://ems12lead.com/2008/10/11/axis-determination-part-vi/

Analysing Resting-State Functional MRI Using Dynamic Causal Modeling in Schizophrenia

G.ÖZMEN[1] and B. YILMAZ[2]

[1] Selcuk University, Konya/Turkey, gozmen@selcuk.edu.tr
[2]Konya Food and Agriculture University, Konya/Turkey, burak.yilmaz@gidatarim.edu.tr

Abstract - **Schizophrenia is one of the most important psychiatric diseases which affect daily life negatively and cause disruption in emotion and behavior. Functional MRI studies have shown that there are differences between schizophrenia patients and healthy individuals. In this study, the effective brain connectivity of a schizophrenic patient and a healthy person of the same age were analyzed with functional MRI. Spatial preprocessing steps were applied to the resting-state data used for this purpose and dynamic causal modeling analysis was performed. At the analysis stage, effective connectivity between the medial prefrontal cortex, posterior cingulate cortex, right inferior parietal lobe and left parietal inferior lobe were investigated. According to the analysis, it was observed that effective connectivity was increased between the medial prefrontal cortex and right inferior parietal lobe regions in a schizophrenic patient.**

Keywords – fMRI, DCM, Resting-State, Schizophrenia

I. INTRODUCTION

Schizophrenia is a mental disorder that affects a person's thinking, speech, and behavior, causing genderless to lose contact with reality. The diagnosis of schizophrenia is made by a psychiatrist who evaluates clinical findings such as schizophrenia symptoms test, examination, and diagnostic tests [1]. In recent years, with the increasing popularity of neuroimaging techniques, functional MR imaging (fMRI) has been used to examine biomarkers of schizophrenia [2]. Functional MR is a noninvasive technique for monitoring brain activations [3] . In an fMRI experiment, three-dimensional MR images are recorded while the subject is performing some tasks on the MR device and the changes in the measured signals between these images are determined [4]. fMRI is generally used to determine neurological losses after surgical interventions. It is also preferred to reveal the basics of cognitive indicators in the brain and to examine the connectivity of regions that interact with each other in the brain. There are differences in brain activations in diseases such as mild traumatic brain injury, Alzheimer's, depression, schizophrenia compared to healthy individuals. This is important for the development of methods to assist physicians in diagnosing the disease [5]. Brain functions can be significantly understood by a task or stimulus-based fMRI. In addition, a method called resting-state fMRI (rs-fMRI) has been used to demonstrate the brain functions when it is not under any task.

With rs-fMRI, functional connectivity of structurally unconnected regions can be examined. [6]. Functional connectivity is defined as the correlation between distant brain regions. Researchers have shown by functional connectivity analysis that functional integration in patients with schizophrenia is impaired [7]. Moreover, another method in which the connectivity in the brain is examined is effective connectivity. [8] have proposed that "effective connectivity should be understood as the experiment- and time-dependent, simplest possible circuit diagram that would replicate the observed timing relationships between the recorded neurons". That is, effective connectivity emerges as a result of causal interaction between neurons in the nervous system [9]. Friston et al. (2011) have mentioned that effective connectivity is activity dependent and based on an interaction or a coupling model. At this point, it can be said that there are differences between functional connectivity and effective connectivity. Functional connectivity is expressed by measurements of statistical dependencies such as correlation coherence or transfer entropy, while effective connectivity is expressed by parameters that attempt to explain observable dependencies such as functional connectivity [10] . Effective connectivity analysis uses Dynamic Causal Modeling (DCM) to estimate the coupling between brain areas and how this coupling is affected by changes. DCM is a model that works with the estimation of problems arising from experimental inputs as well as incorporating nonlinear and dynamic aspects of neuronal interactions [11]. DCM analysis is performed under SPM toolbox which based on Matlab. With DCM analysis, the connectivity between the main components of the Default Mode Network (DMN) can be analyzed [12].

In the literature, there are many studies in which fMRI is used in schizophrenia. These are generally divided into two groups as classification and connectivity analysis. In the classification of schizophrenia, resting-state data are widely used [4, 13-16] and the disease is classified above 90% accuracy [17]. In addition, there are studies examining the interaction between DMN regions of the brain in connectivity analysis. For example; Schlösser et al. (2003); showed that there were differences in connectivity strengths in a cortical-subcortical-cerebellar network between schizophrenic patients treated with typical and atypical antipsychotics and healthy controls [18].

Deserno et al. (2012); mentioned the disordered prefrontal parietal effective connectivity in schizophrenia using DCM and they showed the decreased WM-dependent modulation of effective connectivity from dlPFC to PCC is reduced in patients [19]. Kirino et al. (2017) used EEG and resting-state fMRI data in their study, and demonstrated that functional connectivity between the right posterior temporal gyrus and the medial prefrontal cortex was stronger in patients with schizophrenia than healthy subjects [20]. In this study, effective connectivity between medial prefrontal cortex, posterior cingulate cortex, right inferior parietal lobe and left parietal inferior lobe in DMN regions were investigated. For this purpose, rs- fMR images of a schizophrenic patient and healthy person were analyzed with DCM.

II. MATERIAL AND METHOD

A. Used Data

Resting-state functional MRI data for schizophrenia and control subjects were obtained from http://fcon_1000.projects.nitrc.org/indi/retro/cobre.html. which was archived by the Center for Biomedical Research Excellence (Cobre). A multi-echo MPRAGE data were acquired on a 3·0-T Siemens Trio scanner with the following parameters: TR (repetition time) =1.64, TE (echo times) = 3.5, voxel size =1x1x1 mm, total scan time = 6 min. Moreover Resting State data was collected with single-shot full k-space echo-planar imaging (EPI) with TR: 2 s, TE: 29 ms, matrix size: 64x64, 32 slices, voxel size: 3x3x4 mm3) [21].

B. Pre-processing:

The preprocessing stage consists of data transformation, re-alignment, slice-timing, co-registration, normalization and smoothing. These processes are performed before dynamic causal modeling. The data is processed and the parameters which are used in the analysis are generated. For this purpose, firstly, resting-state data with .nii extension obtained from Cobre database were rearranged and 150 fMR images were obtained. Preprocessing steps were applied to these 150 fMR and T1 Anatomic volumes using SPM12 (http://www.fil.ion.ucl.ac.uk/spm). For this purpose, the fMR images were re-aligned to a reference volume in order to correct the movements caused by MRI. After realignment, the aligned images are averaged and used for co-registration. At the same time, motion regression used in DCM analysis is produced. Exact timing is an important procedure for functional MRI data analysis. Data sets are generally measured using repeated 2D imaging methods. A transient cross-sectional shift occurs when 2D images are sequenced. To eliminate the timing difference between the slices, the slice-timing correction is used. With slice-timing, each slice was temporarily aligned to a reference slice depending on the appropriate sampling method. The recorded 3D structural and functional images do not match with each other depending on the inconsistent cross-sectional orientation and voxel

resolution of the different MR contrasts. This causes problems when it is desired to show the brain regions in which the activation occurs. The 3D structural and functional images do not match with each other depending on the inconsistent cross-sectional orientation and voxel resolution of the different MR contrasts. This causes problems when it is desired to show the brain regions in which the activation occurs. Functional-structural co-registration was applied to the data by matching the functional and structural images. In another step, high-resolution T1 images were normalized to a T1-weighted standard brain template. This process is applied to standardize different brain sizes. Finally, spatial smoothing was applied to eliminate noise in the images. For this analysis, images were smoothed with a Gaussian kernel with FWHM = 9 mm.

C. Effective Connectivity Analysis

DCM, or spectral DCM (spDCM), is used to estimate the effective connectivity between coupled neurons that cause functional connectivity. In this study, SPM12 based DCM was used to investigate the effective connectivity between DMN regions [22]. DMN is a brain system that is active when dreaming or thinking about the future. The DMN regions include the medial prefrontal cortex (mPFC), a part of the posterior cingulate cortex (PCC), and a portion of the inferior parietal lobe and superior frontal regions. In order to determine the effective connectivity that occurs between these regions, time series are obtained by using the General Linear Model (GLM) from resting-state data. Also, time series are obtained from white matter and CSF for use as confounds. For this purpose, the volume of Interest (VOI) for each region is created. The objective of the VOI analysis is to calculate the distribution of pixel values in bounded tissue structures. SPM calculates the first principle component of the time series from all the voxels contained in the sphere. VOI's are created for the regions where connectivity analysis is performed (PCC ([0 -52 26]), mPFC ([3 54 -2]), LIPC ([-50 -63 32]) and RIPC ([48 -69 35])). In this study, after estimating the time series, DCM was constructed and a fully connected system including PCC, mPFC and bilateral IPC was modeled. Figure 1 shows the coordinates and voxel numbers of these regions.

Name	Voxels	Location (mm)		Name	Voxels	Location (mm)
(A)				(B)		
LIPC	254	-50 -63 32		LIPC	256	-50 -63 32
PCC	257	0 -52 26		PCC	257	0 -52 26
RIPC	213	48 -63 35		RIPC	117	48 -63 35
mPFC	256	3 54 -2		mPFC	253	3 54 -2
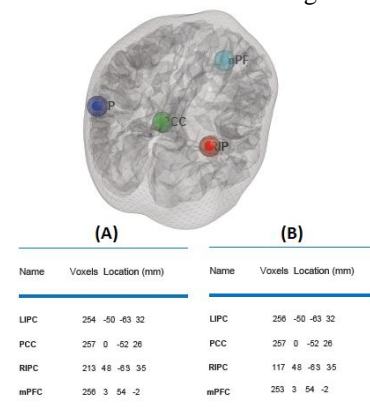
Figure1. The coordinates and voxel numbers of PCC, mPFC,LIPC ve RIPC A) Patient B) Control

III.   RESULTS

Head motion parameters and smoothed resting-state fMR images which are obtained with preprocessing steps   were used in DCM analysis. Figure 2 shows the check-registration process of the smoothed fMR image and the T1-weighted MR image. Images show that the lateral ventricular edges coincide.
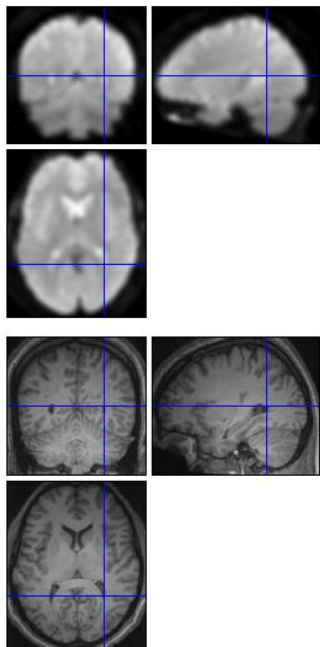
Figure 2. Smoothed fMR image and the T1-weighted MR image

After preprocessing time series were calculated by GLM in order to apply DCM to fMRI. Firstly, the time series extracted from white matter and csf were then used as confounds in model estimation. In order to built the DCM model, VOI's were created in PCC, mPFC, LIPC and RIPC regions and time series were obtained from these regions too. Figure 3 presents the time series obtained from the DMN regions for the patient and healthy subject.
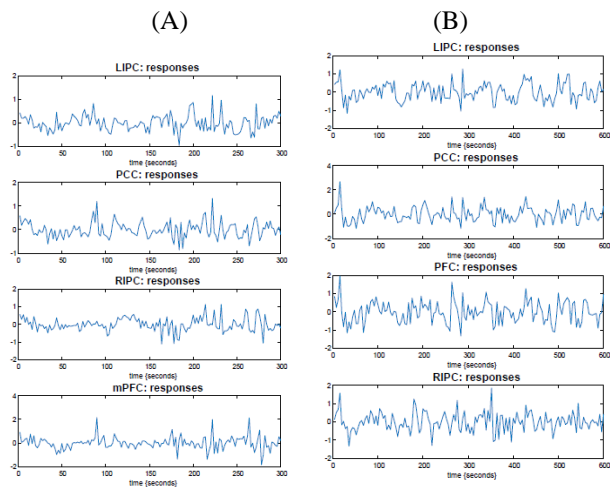
Figure 3. Time series of DMN regions of (A) schizophrenia patient and (B) control

A fully-connected system comprising PCC, mPFC and bilateral IPC is modelled by building DCM. The results are shown in the Figure 4 .
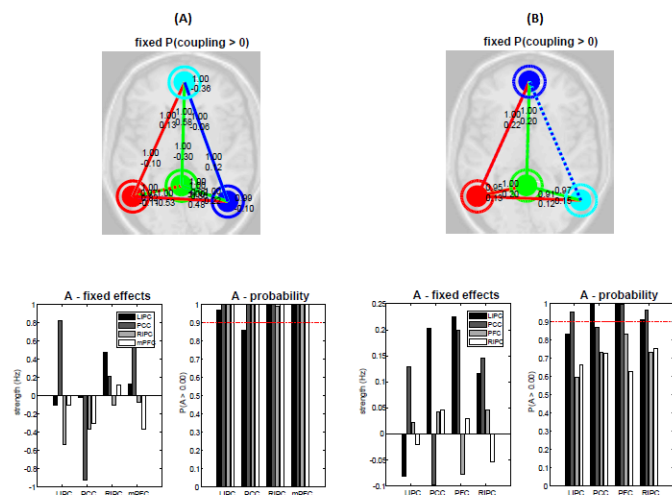
FIGURE 4. Estimated the fix effects and the probabilities (A) Patient (B) Control

Figure 4 shows the difference between a patient (A) and healthy person (B). The graphs below Figure 4 show the weights with a power exceeding 0.1 Hz and a probability greater than 0.95 with a bold line. The lines between the DMN regions indicate the weight of the connections, and the bold lines represent the increase in connectivity and the dashed lines represent the decrease. The fixed effects and probabilities values in Figure 5 are given in Tables 1 and 2.

Table 1. Fixed effects for patient

	mPFC	PCC	LIPC	RIPC
mPFC	-0.36	0.58	0.13	-0.06
PCC	-0.3	-0.92		-0.36
LIP	-0.10	0.82	-0.11	-0.53
RIP	0.12	0.22	0.48	-0.10

Table 2. Fixed effects for control

	mPFC	PCC	LIPC	RIPC
mPFC	-	0.2	0.22	-
PCC	-	-	0.2	-
LIP	-	0.13	-	-
RIP	-	0.15	0.12	-

In Table 1, when the patient's weight strength is examined, it is seen that all regions except PCC have effective connectivity with themselves and others. There is one-way connectivity between PCC-LIPC. In addition, Table 2 shows the weight strength of a healthy person. According to Table 2, the weight strengths of all regions with themselves are less than 0.1 Hz. Also, probabilities have lower values compared to the patient. It is also understood from the dashed lines that there is a decreased effective connectivity between the RIPC and the mPFC regions. For the schizophrenic patient, there is increasing connectivity between these two regions.

IV. DISCUSSION

In this study, functional MRI data of a patient and healthy person were analyzed. Increasing the number of subjects will increase the reliability of the results. In addition, the features of RIPC and mPFC regions are thought to provide valuable information in the classification of schizophrenic patients and healthy individuals.

REFERENCES

[1]　R. M. Murray, E. O'Callaghan, D. J. Castle, and S. W. Lewis, "A neurodevelopmental approach to the classification of schizophrenia," *Schizophrenia Bulletin,* vol. 18, no. 2, pp. 319-332, 1992.

[2]　H. Yang, J. Liu, J. Sui, G. Pearlson, and V. D. Calhoun, "A hybrid machine learning method for fusing fMRI and genetic data: combining both improves classification of schizophrenia," *Frontiers in human neuroscience,* vol. 4, p. 192, 2010.

[3]　K. Kwong, "Functional magnetic resonance imaging with echo planar imaging," in *Functional MRI*: Springer, 1996, pp. 73-90.

[4]　W. Gore Ranjana and D. Dharmadhikari Dipa, "Classification Of Schizophrenic And Controls Using Fmri Data."

[5]　J. Ford *et al.*, "Patient Classification of fMRI Activation Maps," Berlin, Heidelberg, 2003: Springer Berlin Heidelberg, in Medical Image Computing and Computer-Assisted Intervention - MICCAI 2003, pp. 58-65.

[6]　M. H. Lee, C. D. Smyser, and J. S. Shimony, "Resting-state fMRI: a review of methods and clinical applications," *American Journal of neuroradiology,* vol. 34, no. 10, pp. 1866-1872, 2013.

[7]　K. J. Friston and C. D. Frith, "Schizophrenia: a disconnection syndrome," *Clin Neurosci,* vol. 3, no. 2, pp. 89-97, 1995.

[8]　M. Erb and A. Aertsen, "Dynamics of activity in biology-oriented neural network models: stability at low firing rates," in *Information processing in the cortex*: Springer, 1992, pp. 201-223.

[9]　K. E. Stephan and K. J. Friston, "Analyzing effective connectivity with functional magnetic resonance imaging," *Wiley Interdisciplinary Reviews: Cognitive Science,* vol. 1, no. 3, pp. 446-459, 2010.

[10]　K. J. Friston, "Functional and effective connectivity: a review," *Brain connectivity,* vol. 1, no. 1, pp. 13-36, 2011.

[11]　K. J. Friston, L. Harrison, and W. Penny, "Dynamic causal modelling," *Neuroimage,* vol. 19, no. 4, pp. 1273-1302, 2003.

[12]　S. Esménio *et al.*, "Using resting-state DMN effective connectivity to characterize the neurofunctional architecture of empathy," *Scientific reports,* vol. 9, no. 1, p. 2603, 2019.

[13]　M. S. Cetin *et al.*, "Multimodal classification of schizophrenia patients with MEG and fMRI data using static and dynamic connectivity measures," *Frontiers in neuroscience,* vol. 10, p. 466, 2016.

[14]　M. R. Arbabshirani, E. Castro, and V. D. Calhoun, "Accurate classification of schizophrenia patients based on novel resting-state fMRI features," in *2014 36th Annual International Conference of the IEEE Engineering in Medicine and Biology Society*, 2014: IEEE, pp. 6691-6694.

[15]　M. R. Arbabshirani, K. Kiehl, G. Pearlson, and V. D. Calhoun, "Classification of schizophrenia patients based on resting-state functional network connectivity," *Frontiers in neuroscience,* vol. 7, p. 133, 2013.

[16]　X. L. Cai *et al.*, "Generalizability of machine learning for classification of schizophrenia based on resting-state functional MRI data," *Human Brain Mapping,* 2019.

[17]　D. Chyzhyk, A. Savio, and M. Graña, "Computer aided diagnosis of schizophrenia on resting state fMRI data by ensembles of ELM," *Neural Networks,* vol. 68, pp. 23-33, 2015.

[18]　R. Schlösser *et al.*, "Altered effective connectivity during working memory performance in schizophrenia: a study with fMRI and structural equation modeling," *Neuroimage,* vol. 19, no. 3, pp. 751-763, 2003.

[19]　L. Deserno, P. Sterzer, T. Wüstenberg, A. Heinz, and F. Schlagenhauf, "Reduced prefrontal-parietal effective connectivity and working memory deficits in schizophrenia," *Journal of Neuroscience,* vol. 32, no. 1, pp. 12-20, 2012.

[20]　E. Kirino *et al.*, "Simultaneous resting-state functional MRI and electroencephalography recordings of functional connectivity in patients with schizophrenia," *Psychiatry and clinical neurosciences,* vol. 71, no. 4, pp. 262-270, 2017.

[21]　The Center for Biomedical Research Excellence (COBRE) http://fcon_1000.projects.nitrc.org/indi/retro/cobre.html (accessed.

[22]　J. Ashburner *et al.*, "SPM12 manual," *Wellcome Trust Centre for Neuroimaging, London, UK,* 2014.

Brain Atlas Registration With Optimization Algorithms

BURAK YILMAZ[1] and GÜZİN ÖZMEN[2]

[1] Konya Food And Agriculture University, Konya/Turkey, burak.yilmaz@gidatarim.edu.tr
[1]Selcuk University, Konya/Turkey, gozmen@selcuk.edu.tr

Abstract - **A variety of methods have been developed to provide standardization in both intensity and shape in the processing and analysis of biomedical images. One of these methods is to register images to atlases or standard models. By registering biomedical images, it is possible to determine how much the tissue under examination conforms to the anatomical model or the amount of deterioration. In the literature, there are different image registration algorithms based on various methods, the algorithm developed in this study is designed to be based on non-rigid, affine transformation. Also optimization methods used for determining the conversion parameters. The algorithm has been developed to use both shape properties and density properties at the same time. In order to provide maximum correlation between the input image and the atlas, both images were processed with Cellular Artificial Neural Networks to reveal basic shape properties. The method was tested and compared with 3 different optimization algorithms.**

Keywords – **CNN, ABC, Genetic Algorithms, Particle Swarm Optimization, Affine transform, biomedical image registration**

I. INTRODUCTION

It is important to follow certain steps in the analysis of brain MR images. A general workflow has been identified in the literature thanks to the studies on this subject [1]. One of the important steps in the workflow is brain image registration to certain brain atlases [2], [3].

By registration of biomedical images, it is possible to determine how much the tissue under examination conforms to the anatomical model or the amount of deterioration [4], [5]. In the literature, different image registration algorithms based on various methods are available. We can classify algorithms according to their characteristics [6]:

• Dimensionality (spatial or space-temporal, 2D / 2D, 2D / 3D, 3D / 3D)

• By registration method (external, internal, non-image based)

• According to transformation method (solid, affine, reflective, inclined)

• By conversion base (general, local)

• Depending on the degree of interaction (interactive, semi-automatic, automatic)

• According to the optimization method

• According to image modality (single, multiple, model-modality, patient-modality)

• By subject (internal, external, atlas based)

• According to the object (brain, heart, etc.)

The algorithm developed in this study is designed to use non-rigid, affine transformation based optimization methods for determining the transformation parameters. The algorithm has been developed to use both shape properties and intensity properties at the same time. In order to provide maximum correlation between the input image and the atlas, both images were processed with Artificial Cellular Neural Networks to reveal basic shape properties.

II. MATERIAL AND METHOD

The proposed method has two key algorithms, Cellular Neural Networks for defining the shape parameters of the images and optimization algorithms for detecting the affine transform parameters.

Cellular Neural Networks (CNNs) are two dimensional cell arrays with local cell interconnections. Chua and Yang introduced CNNs in 1998 [7], [8]. Every cell is related with the neighboring cells presented as in Figure 1. [7], [8]. The CNNs have a property which called local connectivity property which gives CNNs to perform image processing and pattern recognition abilities [9], [10].
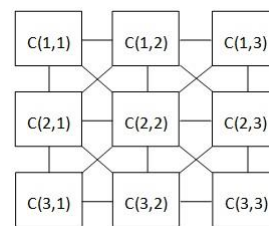
Figure 1 CNN cell structure

The constant 'r' represents neighborhood level of each cell where r = 1 means 3x3 neighborhood, r=2 means 5x5 neighborhood and so on. This is called sphere of influence and r means the radius of the sphere [11]

Each CNN cell is described with a normalized differential state equation (1).

$$\frac{d}{dx}x_{i,j}(t) = \sum_{k,l \in N} A_{kl} y_{i+k,j+k}(t) + \sum_{k,l \in N} B_{kl} y_{i+k,j+k}(t) + I \quad (1)$$

Nonlinearity of output is defined by Eq. (2), this equation represents a trapezoidal function limited between

$(-1,+1) \in \mathbb{Q}$ and used as output of the CNN

$$y(x) = \frac{1}{2}\left[|x-1|-|x+1|\right] \tag{2}$$

The input, state, and the output of the CNN, are represented as $u_{i,j}$, $x_{i,j}$ and $y_{i,j}$ respectively. The i,j values are defined in $0 \le i \le N_1$ and $0 \le j \le N_2$. In the equation (1) N_1 and N_2 represents length and width of the input image. In the equation (2) x is the same as Equation (1). A, B and I are special matrices which define patterns to be detected. The A,B and I triplet is named as template and template used in this study is chosen as in Equation (3)

$$A = \begin{bmatrix} -0,372 & 0,656 & 0,090 \\ 0,603 & 0,398 & 0,603 \\ 0,902 & 0,656 & -0,372 \end{bmatrix} \quad B = \begin{bmatrix} -0,982 & 0,647 & 0,242 \\ 0,127 & 1,126 & 0,127 \\ 0,242 & 0,647 & -0,982 \end{bmatrix} \quad I = [0,1430] \tag{3}$$

The Affine transform allows you to convert from (x, y) coordinates to (x', y') coordinates by scaling, shifting, rotating and shearing. The relationship between objects in the image continues to be preserved during the transformation. For example, the two parallel lines will remain parallel after the transformation, but the angles will change [12] The Affine conversion can be performed in both 2D and 3D. The method is described in Equation 4 - 13.

$$\begin{bmatrix} x' \\ y' \end{bmatrix} = s \begin{bmatrix} cos\alpha & sin\alpha \\ -sin\alpha & cos\alpha \end{bmatrix} \begin{bmatrix} x - x_0 \\ y - y_0 \end{bmatrix} \tag{4}$$

$$\begin{bmatrix} x' \\ y' \end{bmatrix} = s \begin{bmatrix} cos\alpha(x - x_0) & sin\alpha(y - y_0) \\ -sin\alpha(x - x_0) & cos\alpha(y - y_0) \end{bmatrix} \tag{5}$$

By reconsidering the equations :

$$x' = (s\cos\alpha)x + (s\sin\alpha)y - s(x_0 \cos\alpha + y_0 \sin\alpha) \tag{6}$$

$$y' = (-s\sin\alpha)x + (s\cos\alpha)y + s(x_0 \sin\alpha - y_0 \cos\alpha) \tag{7}$$

The equations can also be written as

$$a = s\cos\alpha \tag{8}$$

$$b = -s\sin\alpha \tag{9}$$

$$x' = ax - by + c \tag{10}$$

$$y' = bx + ay + d \tag{11}$$

Scaling factor s:

$$s = \sqrt{a^2 + b^2} \tag{12}$$

Rotation angle α:

$$\alpha = \tan^{-1}\left(-\frac{b}{a}\right) \tag{13}$$

In order to calculate the affine transform parameters optimization algorithms are used. These algorithms are, Genetic Algorithms (GA) [13], Particle Swarm Optimization (PSO) [14] and Artificial Bee Colony Algorithm (ABC) [15] .

A special fitness function is designed for using with all three optimization algorithms. Optimization algorithms were run 20 times and the results were averaged and compared. The general flow diagram of the method is as in Figure 2
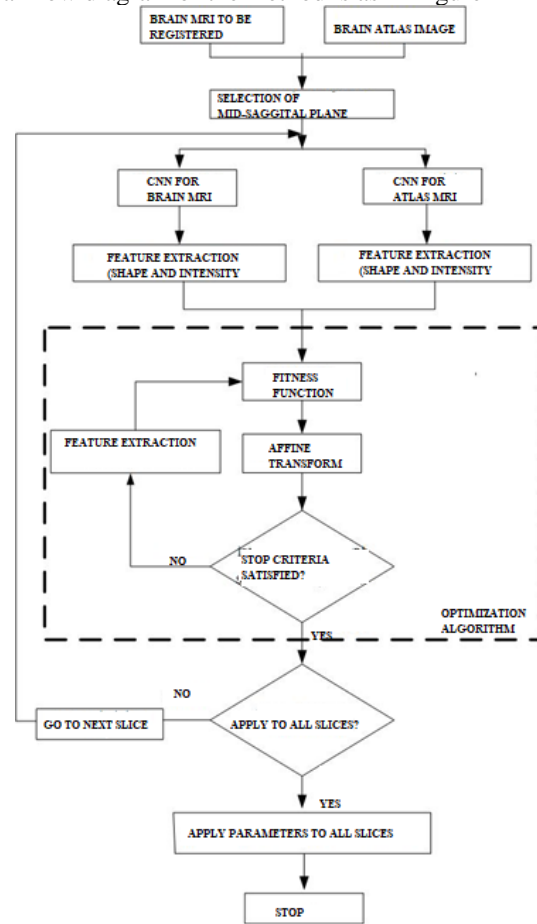
Figure 2: Flowchart of the proposed algorithm

The fitness function takes the previously generated data sets and the affine transform coefficients as parameters. The coefficients are calculated and updated by the optimization algorithm at each step and the affine transform according to the parameters is performed. After transform, the newly acquired images are used as parameters for the next step. For the calculation of registration success, the finess function uses the image correlation function and the Jaccard coefficient.

The correlation function produces a value in the range [0 - 1] by comparing the two images according to the gray level values [16]. "0" indicates that the two images are completely incompatible and "1" indicates that the two images are exactly the same. The mathematical expression of the correlation function is as in Equation 14.

$$r = \frac{\sum_m \sum_n (A_{mn} - \bar{A})(B_{mn} - \bar{B})}{\sqrt{(\sum_m \sum_n (A_{mn} - \bar{A})^2)(\sum_m \sum_n (B_{mn} - \bar{B})^2)}} \qquad (14)$$

In this Equation, the images to be compared A and B are $\bar{A}$, the 2D average value of the A image, and $\bar{B}$ is the 2D average value of the B image.

The Jaccard coefficient is used to measure the fitness of the shape properties of the two overlapped images. The Jaccard coefficient also produces a value between [0 - 1], "0" means that two images do not overlap, "1" means that two images are perfectly matched. The Jaccard coefficient is calculated according to Equations 15 and 16.

$$D = \frac{2|S \cap R|}{|S| + |R|} \qquad (15)$$

$$J = \frac{|S \cap R|}{S \cup R} = \frac{D}{2 - D} \qquad (16)$$

In this equation, S is the image obtained as a result of affine transformation, R is the image of the atlas. The value expressed by D in Equation 15 is another comparison coefficient called Dice coefficient.

By using these two parameters, the conformity function returns the image to the ABC algorithm for the next step, calculating the success of the registration according to the parameters from the ABC. Here the output of the fitness function is calculated as in Equation 17.

$$f = 1 - (\alpha r + \beta J) \qquad (17)$$

In the equation, f corresponds to fitness, r correlation, α correlation coefficient, J Jaccard value and β Jaccard coefficient. Here, the α and β values are in the range [0 - 1], which is determined by the user and indicates which coefficient is more important.

The first step in the algorithm is to select the MRI image and atlas images to be overlapped. The algorithm can work both on 3D MRI images and on each individual image slice. If only one image is to be omitted, it must be ensured that the same slice is selected in the atlas and MRI image. If 3D overlapping is to be done, MRI data and atlas data should be obtained with the same parameters and sequaencing technique. Thus, the number of slices in the data sets will be synchronized.

In the next step, the image to be overlapped with the original image is manually selected, if no special operation is performed, the midsaggital plane, which is considered to be the center of the images, is preferred to capture symmetry in both images to be overlapped. The midsagittal plane is also considered the starting point of the Talairach coordinate system [3].

After selecting the images to be registered, the images must be made available for processing. Brain atlases are obtained using brain MRI images obtained from multiple individuals [17], therefore, although the anatomical boundaries are clearly

quantified, the generated atlas images have noiseless and fuzzy structure. In the study, both images are processed with CNN algorithm to minimize the difference caused by blur, thus revealing the image properties that can be used as reference. The atlas image to be overlaid is shown in Figure 6.5 (a) and the MRI image is shown in Figure 6.5 (b). Figure 6.6 shows the same images obtained after CNN algorithm.
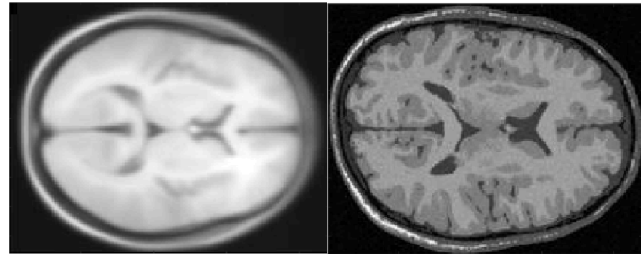
(a)   (b)

Figure 3 Atlas image to be overlapped (a) and brain MRI image (b)

In addition to the fact that both images to be overlapped were obtained by the same shooting technique, the fact that they are close to each other in terms of noise and density values will increase the success of registration. Therefore, in the next step, both images are passed through the CNN algorithm and new images are obtained to reveal the shape properties. Figure 4 shows the images obtained by CNN. CNN is preferred over a thresholding process to zoom in on image properties, because it preserves the structure based on the shape and texture properties of the image to achieve the closest possible shape.

For the comparison of the algorithm, two separate data sets of four images are created. The first data set is gray-level images and the second data set is binary images with preserved shape features.

(a)   (b)

Figure 4 (a) an atlas image to be overlapped, and (b) brain MRI image.

The registration process is terminated by the optimization algorithm when it reaches the predetermined number of steps or error value. At the end of the process, if the parameters found are to be applied to all slices, the affine transform according to the parameters found in each slice is applied, otherwise the algorithm is terminated. Slice 90 of subject52 data recorded with the T1 technique selected from the BrainWeb [18] database is shown in Figure 3 (a), Slice 78 of the atlas of T1 weighted Talairach average 305 is shown in Figure 3 (b) and slice 90 of the image obtained from

registration Figure 3 (c)).

<div align="center">
(a)   (b)   (c)
</div>
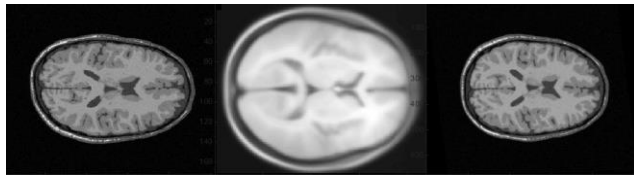
Figure 3 Result of registration algorithm (a) Slice 90 of subject52 data recorded by the T1 sequencing technique selected from the BrainWeb database;

III. RESULTS

The evaluation was performed on normal T1-weighted MRI images obtained from Brainweb database. Images are registered to T1 weighted Talairach average 305 brain atlas. Each optimization algorithm has run for 20 times and average values of elapsed time, Jaccard and Correlation coefficient values are tested. The tests were performed on Intel Core™ i5-8250U CPU @1.60 GHz and 8 GB Ram with 64 bit operating system. Results of the test are shown in Table 1

Table 1: Average results of optimization algorithms for image registration task

Parameter	PSO	ABC	GA
Elapsed Time (seconds)	11.7	18.4	21.7
Jaccard	0.89	0.92	0.96
Correlation	0.72	0.87	0.88

IV. CONCLUSION

In this study a methodology has been developed by using Affine Transform, Cellular Neural Networks and Optimization algorithms. The proposed method tested with 3 different optimization algorithms. In general perspective it can be seen that Genetic Algorithms gave more accurate results than the other algorithms. On the other hand, PSO is faster than the other algorithms. Yet the ABC algorithm can be considered as optimum method amongst these 3 algorithms.

The accuracy of the results depends on CNN algorithm and correlation coefficient. In the future experiments by focusing on finding proper template matrices for CNN, getting better results is aimed.

REFERENCES

[1] B. H. Menze *et al.*, "The Multimodal Brain Tumor Image Segmentation Benchmark (BRATS)," pp. 1–32.

[2] M. V Wyawahare, P. M. Patil, and H. K. Abhyankar, "Image Registration Techniques : An overview," *Int. J. Signal Process. Image Process. Pattern Recognit.*, vol. 2, no. 3, pp. 11–28, 2009.

[3] M. Xu and W. L. Nowinski, "Talairach – Tournoux brain atlas registration using a metalforming principle-based finite element method," *Med. Image Anal.*, vol. 5, pp. 271–279, 2001.

[4] R. Shams, P. Sadeghi, R. Kennedy, and R. Hartley, "A survey of medical image registration on multicore and the GPU," *IEEE Signal Process. Mag.*, vol. 27, no. 2, pp. 50–60, 2010.

[5] B. Glocker, A. Sotiras, N. Komodakis, and N. Paragios, "Deformable Medical Image Registration: Setting the State of the Art with Discrete Methods," *Annu. Rev. Biomed. Eng.*, vol. 13, no. 1, pp. 219–244, Jul. 2011.

[6] J. B. A. Maintz and M. a Viergever, "An Overview of Medical Image Registration Methods (Cited by: 2654)," *Nature*, vol. 12, no. 6, pp. 1–22, 1996.

[7] L. O. Chua and L. Yang, "Cellular neural networks: applications," *IEEE Trans. Circuits Syst.*, vol. 35, 1988.

[8] L. O. Chua and L. Yang, "Cellular neural networks: theory," *IEEE Trans. Circuits Syst.*, vol. 35, pp. 1257–1272, 1988.

[9] M. Kawahara, T. Inoue, and Y. Nishio, "Cellular neural network with dynamic template and its output characteristics," in *Proceedings of the International Joint Conference on Neural Networks*, 2009, pp. 1552–1558.

[10] R. Perfetti, E. Ricci, D. Casali, and G. Costantini, "Cellular neural networks with virtual template expansion for retinal vessel segmentation," *IEEE Trans. Circuits Syst. II Express Briefs*, vol. 54, pp. 141–145, 2007.

[11] A. Cerasa *et al.*, "A Cellular Neural Network methodology for the automated segmentation of multiple sclerosis lesions.," *J. Neurosci. Methods*, vol. 203, no. 1, pp. 193–9, Jan. 2012.

[12] D. Zwillinger, *CRC Standard Mathematical Tables and Formulae, 32nd Edition*. CRC Press, 2011.

[13] F. L. Seixas, L. S. Ochi, A. Conci, and D. M. Saade, "Image registration using genetic algorithms," *Proc. 10th Annu. Conf. Genet. Evol. Comput. - GECCO '08*, p. 1145, 2008.

[14] R. Poli, J. Kennedy, and T. Blackwell, "Particle swarm optimization," *Swarm Intell.*, vol. 1, no. 1, pp. 33–57, 2007.

[15] D. Karaboga, B. Gorkemli, C. Ozturk, and N. Karaboga, "A comprehensive survey: artificial bee colony (ABC) algorithm and applications," *Artificial Intelligence Review*. 2012.

[16] D. D. Sha and J. P. Sutton, "Towards automated enhancement , segmentation and classi ® cation of digital brain images using networks of networks," vol. 138, pp. 45–77, 2001.

[17] A. Gao, "Non-rigid registration between brain CT images and MRI brain atlas by combining grayscale information , point correspondence on the midsaggital plane and brain surface matching," no. Iccsee, pp. 222–225, 2013.

[18] "BrainWeb: Simulated Brain Database." [Online]. Available: http://brainweb.bic.mni.mcgill.ca/brainweb/. [Accessed: 15-Dec-2014].

A Micro-Scale Biosensor for the Detection of Bacillus Stearothermophilus Spore Germination

M.İ. BEYAZ[1] and A. SEKKOUTI[1]

[1] Antalya Bilim University, Antalya/Turkey, mibeyaz@antalya.edu.tr
[1] Antalya Bilim University, Antalya/Turkey, aissa.sekkouti@antalya.edu.tr

Abstract – **Germination of Bacillus Stearothermophilus bacterial spores is being used as a marker in sterilization monitoring systems to verify the success of sterilization processes in healthcare facilities. Such systems mainly employ optical detection techniques that are expensive and time consuming. This work presents the first micro-scale biosensing platform that is capable of detecting this specific spore germination through impedance measurements. Starting from theoretical calculations on ion concentrations, a simulation model is built on COMSOL software to analyze the conductance change of the medium during germination. It has been demonstrated that even 1% germination ion yield results in a 5-fold drop in germinant solution resistance, reaching up to more than two orders of magnitude decrease when the spores are fully germinated. A microfluidic biosensor consisting of interdigitated electrodes was designed, and a fabrication approach has been presented. This device, when fully fabricated, poses an inexpensive solution that can provide sterilization verification results in under 10 minutes.**

Keywords – **Biosensor, impedance, MEMS, lab on a chip, germination**

I. INTRODUCTION

HEAT based sterilization is a procedure frequently applied in healthcare facilities as a means to eliminate harmful organisms on medical tools. The procedure involves locating each medical tool in an oven and applying dry or wet heat at temperatures exceeding 120 °C for up to one hour. It is vitally important to ensure that such tools are completely cleaned and free of bacteria before getting in contact with the next patient. To this end, Bacillus Stearothermophilus non-pathogenic bacterial spores provide a reliable marker for the success of sterilization [1-3]. These spores are known to be one of the most heat resistant organisms [2], and are heavily used in temperature-related biological studies. During the sterilization process, these spores are simultaneously located in sterilization ovens together with other medical tools. Following the end of the process, the spores are placed in a nutrient solution at an optimal temperature to observe whether germination will occur. If the spores do not germinate into functional bacteria, this shows that the heat-resistant spores have been killed during sterilization, which indirectly demonstrates that all other bacteria on the medical tools are also eliminated since they are less heat resistant than these spores. The germination of the spores into bacterial form, on the other hand, shows that these spores and possibly other harmful bacteria on the tools were not successfully exterminated.

The germination of the Bacillus Stearothermophilus spores are currently detected using optical methods. In this respect, the spores are encapsulated in small indicators with nutrient solutions, and placed in incubators that provide optimal conditions for germination. The incubators include a UV light source together with photodiodes and electronics to detect fluorescence photon emission. The spores are exposed to UV light, which leads to fluorescence emission in the presence of germination. Read out electronics detect this phenomenon and the result is displayed on a small screen. Depending on the indicator and incubator used, the detection may take between 0.5 – 4 hours. In addition such indicators and incubators are expensive, prohibiting their wide availability in all healthcare facilities.

In this work, we present the analysis and design of an inexpensive micro-scale biosensor that can detect the germination faster than current incubators. The germination cycle of these specific spores leads to ion exchange between the spore and outside medium in 5 minutes after the start of germination [4-7]. This shows that the germination can be detected in 5-10 minutes by monitoring the conductance of the medium. Such impedance based biosensing of various biological agents have been demonstrated previously in the literature [8-10]. However, to the best of our knowledge, this is the first study on the development of a biosensor tailored for this specific bacterial spores. The sensor is designed using MEMS and lab on a chip technologies to minimize the system cost and detection time as well as to reduce the sample volume.

II. ANALYSIS AND DESIGN

The spore mineral content mainly includes dipicolinic acid (DPA), calcium, magnesium, manganese, potassium, and sodium, which are released at different phases of germination. [11-14]. Among these minerals, the highest mineral concentration belongs to DPA, and followed by calcium, and manganese as summarized in Table 1-2 [15].

Table 1: The mineral content of the spores

Content (μmol/mg [dry weight] of spores)					
DPA^{2-}	Ca^{2+}	Mn^{2+}	Mg^{2+}	K^+	Na^+
83.1	0.92	0.05	0.05	0.02	0.01

Table 2: The percentage of each ion in single spore dry weight

% dry weight of a single native spore					
DPA^{2-}	Ca^{2+}	Mn^{2+}	Mg^{2+}	K^+	Na^+
26.4	2.5	1.4	0.24	0.8	0.1

Based on the amount of each ion existing in the spore, the molar ion charge density, σ_c, have been calculated using

$$\sigma_c = e \times z \times c \times N_A \tag{1}$$

where e is the unit charge, z is the number of charges of each ion, c is the concentration of each ion calculated using the above tables, and N_A is the Avogadro's number. The calculated charge densities are listed in Table 3.

Table 3: Calculated ion charge densities

Charge density in C/m^3 × 10^6					
DPA^{2-}	Ca^{2+}	Mn^{2+}	Mg^{2+}	K$^+$	Na$^+$
-11.23	0.27	0.07	0.02	0.001	0.01

The resulting charge densities in Table 3 show that the DPA^{2-} is the dominant ion released outside the spore during the germination, and other ions can be fairly neglected to decrease the complexity of the following model. Based on this analysis, the ionic conductivity introduced by the DPA^{2-} is calculated using Einstein relation that describes the relationship between an electrolyte molar conductivity and the diffusion coefficient of the ion content. Accordingly, the molar ionic conductivity, λ, can be written as

$$\lambda = z^2 \times D \times F^2 / R \times T \tag{2}$$

where F is the Faraday constant, R is the gas constant, T is the thermodynamic temperature, and D is the diffusion coefficient that can be calculated as

$$D = k \times T / 6\pi \times \eta \times a \tag{3}$$

In this equation, k represents the Boltzmann constant, η is the viscosity of the medium (in this case germinant solution, or equivalently, water), and a is the radius of the DPA^{2-} [16]. All the parameters of equations (2-3) are known except the DPA^{2-} radius. The DPA crystal contains two molecules whose volume is 0.338 nm^3 [16]. At this point, a fair assumption is made, where this molecule has a spherical geometry and its radius can be found by using the volume of a simple sphere. Accordingly, the radius of the DPA^{2-} was calculated to be 0.343 nm. Therefore, the molar conductivity of the germinant solution containing DPA2- was determined to be 107.3 S×cm^2/mol. Assuming the worst scenario, where one droplet (0.05 ml) of germinant solution on a 1 cm^2 sensor surface results in only 10% of the spores covering the device surface, and only 10% of those spores germinate, equating a DPA yield of 1%, this value translates into a solution conductivity increase of 7.725 mS/m.

The significant increase in solution conductance can be detected using a biosensor with on-chip electrodes that can perform conductivity or resistance measurements. The general sensor configuration is shown in Fig. 1.

The device mainly consists of a set of two electrodes on an insulating substrate that measures slightly larger than 1 cm^2 in area. Although not shown in Fig. 1, the electrodes are designed in interdigitated structure, and embedded in a microfluidic chamber to perform resistance measurements. A droplet of germinant solution also containing cylindrical-shaped bacterial spores are dispensed on the electrodes. The resistance of the medium is measured by applying a voltage

and reading the resulting current between the electrodes. The detailed electrode design is shown in Fig. 2, where each electrode consists of 119 thin and long finger lines measuring 150 nm × 20 μm × 8.25 mm in thickness, width, and length, respectively. The fingers reaching to the left and right sides are connected together. This interdigitated design has been preferred over simpler electrode structures to provide a larger electro-active area for interaction, and to decrease the resistance values to an easily detectable range for readout electronics. The finger interspacing has been selected as 20 μm to decrease the microfabrication complexity.
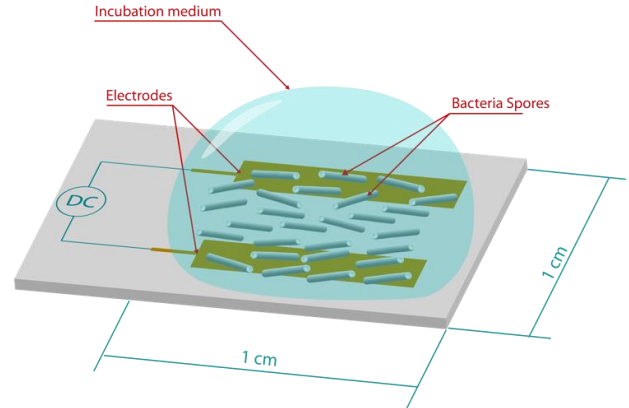
Figure 1: General biosensor design that shows the sensing principle. Electrodes are not drawn in detail for image clarity.
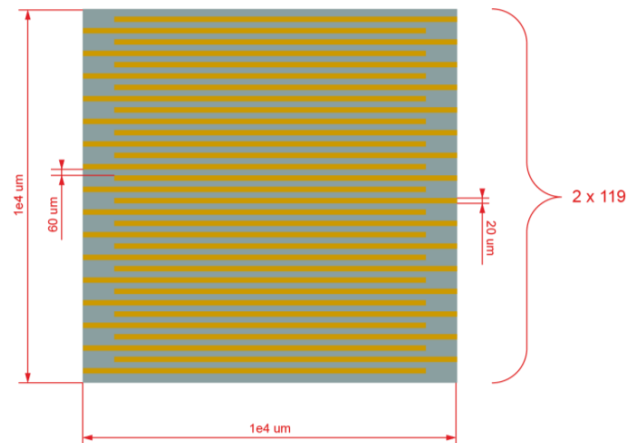
Figure 2: Detailed design of interdigitated electrodes. All the thin fingers reaching to the left and right are connected together.

III. DEVICE PERFORMANCE

The conductivity change of the germinant solution determined through the analysis presented above leads to the change in solution resistance. Since the electrodes are thin and long, their surface to volume ratio is quite high, which is observed in all devices designed in the realm of MEMS. Therefore, a simple calculation on resistance is not possible as the fingers have many edge areas, where the current density becomes higher than the rest of the electrode structure. This non-linear structure is investigated using COMSOL simulation software that can perform finite element analysis on electric currents. Specifically, the AC/DC module with Electric Current physics have been

used to model the problem. The electrode structure is drawn and a potential difference is applied. The software determines the current density throughout the device and calculates the resulting resistance. Figure 3 shows an example simulation output demonstrating that the current density is higher along the top edge of the interdigitated fingers.
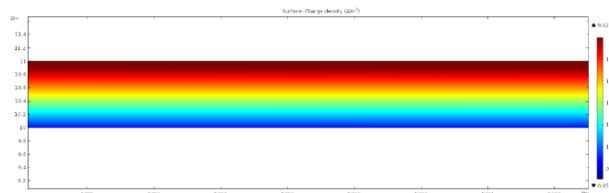
Figure 3: Current density simulation results showing the current is higher along the top edge of the interdigitated electrodes

Next, the resistance of the germinant solution has been calculated in the simulations for the cases when (i) no germination exists, (ii) germination with varying DPA2- yields. It has been demonstrated that when there is no germination, the germination solution that consists of L-alanine and inosine results in a total resistance of 320 Ω. Figure 4 below shows the decreasing resistance of the germinant solution as a result of the DPA^{2-} release during germination.
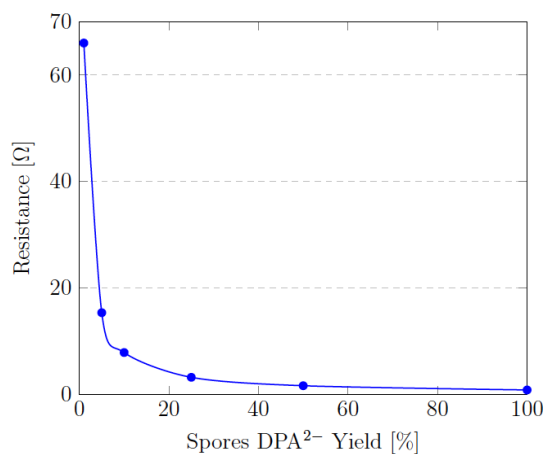
Figure 4: Decreasing trend of the solution resistance as a result of DPA^{2-} released during germination.

The resistance of the solution decreases to 66 Ω when there is only 10 % of chip area coverage and when only 10 % of the spores germinated, which was recalled as 1% DPA yield as described above. Accordingly, even this very small percentage of germination results in the resistance to drop from 320 Ω to 66 Ω, showing a 5 fold decrease in resistance. This effect is easily observable by using simple readout electronics that can perform resistance measurements. The decreasing resistance effect has been further investigated by assuming different levels of spore coverage and germination, leading to increasing DPA yields. Figure 4 shows that the resistance can decrease down to less than 1 Ω when the DPA yield is 100%, showing an even pronounced two orders of magnitude change in resistance. Considering that even small amounts of DPA can be easily observed, and

that the DPA release starts in the first five minutes of germination, the results illustrated in Fig. 4 indicate that the germination of these spores can be detected in less than 10 minutes.

IV. BIOSENSOR FABRICATION

The biosensor structure presented in this work has feature sizes down to micrometers. Accordingly, microfabrication technology is required to manufacture the device. The process flow designed for this biosensor is summarized in Fig. 5.
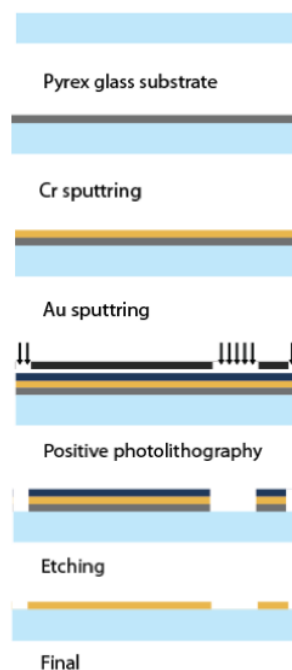
Figure 5: Microfabrication process flow for the biosensor

The device is designed to be fabricated on an insulating pyrex substrate that provides bottom electrical isolation. Initially a 50 nm-thick Cr layer will be sputtered on the substrate that will act as an adhesion layer between the Au and pyrex. Next, 100 nm-thick Au layer will be sputtered as the main electrode layer to interact with the spores and germinant solution. Au is specifically selected to prevent possible electrode corrosion due to extended exposure to germinant solution. At this point, Au electroplating to further increase the electrode thickness can be an option to decrease the internal electrode resistance and increase signal to noise ratio during resistance measurements. Following Au deposition, positive photolithography with the electrode on a mask pattern will be applied. Next, wet etching of Cr and Au will be performed sequentially. Finally, the remaining photoresist will be removed in acetone and the device fabrication will be finished. The current efforts are focused on performing this fabrication flow and demonstrating the first set of devices.

V. CONCLUSION

A biosensor that can detect the germination of Bacillus Stearothermophilus bacterial spores is presented. The device

is composed of interdigitated electrode structures integrated in a microfluidic chamber on an insulating substrate. Our design and simulations show that ion yield as low as 1% results in a 5 fold decrease in resistance, which can be easily detected by readout electronics. Further analysis demonstrated that the resistance can change more than two orders of magnitude when the spores are fully germinated, pointing out the suitability and applicability of the device. A fabrication process flow to manufacture the device was presented. Current efforts are focused on microfabricating the biosensors for testing and evaluation. The sensor structure presented in this work will enable the development of a low-cost sterilization monitoring device that can perform the process verification in less than 10 minutes.

REFERENCES

[1] D. Greenwood, R. C. Slack, M. R. Barer, and W. L. Irving, *Medical microbiology e-book: a guide to microbial infections: pathogenesis, immunity, laboratory diagnosis and control.* Elsevier Health Sciences, 2012.

[2] M. P. Doyle and R. L. Buchanan, *Food microbiology: fundamentals and frontiers.* American Society for Microbiology Press, 2012.

[3] C. Rigaux, S. Andre, I. Albert, and F. Carlin, "Quantitative assessment of the risk of microbial spoilage in foods, prediction of non-stabiliy at 55 c caused by geobacillus stearothermophilus in canned green beans," *International Journal of Food Microbiology,* vol. 171, pp. 119-128, 2014

[4] D. Xu and J. C. Cote, "Phylogenetic relationships between bacillus species and related genera inferred from comparison of 3 end 16s rdna and 5 end 16s-23s its nucleotide sequences," *International Journal of Systematic and Evolutionary Microbiology,* vol. 53, no. 3, pp. 695-704, 2003.

[5] "Bacillus stearothermoophilus bacteria spore, MicrobeWiki, https://microbewiki.kenyon.edu/index.php/Bacillus_stearothermophilus_NEUF2011, Accessed 2019-09-01.

[6] K. Reineke, "Mechanism of bacillus spore germination and inactivation during high pressure processing," Ph.D. dissertation, Technischen Universitat Berlin, Berlin, Germany, 2012.

[7] P. Setlow, "Spore germination," *Current Opinion in Microbiology,* vol. 6, no. 6, pp. 550-556, 2003.

[8] L. Yang, Y. Li, and C. F. Erf, "Interdigitated array microelectrode-based electrochemical impedance immunosensor for detection of Escherichia coli o157: H7," *Analytical Chemistry,* vol. 76, no. 4, pp. 1107-1113, 2004.

[9] Y. S. Liu, T. Walter, W. J. Chang, K. S. Lim, L. Yang, S. Lee, A. Aronson, and R. Bashir, "Electrical detection of germination of viable model bacillus anthracis spores in microfluidic biochips," *Lab on a Chip,* vol. 7, no. 5, pp. 603-610, 2007.

[10] S. Kim, G. Yu, T. Kim, K. Shin, and J. Yoon, "Rapid bacterial detection with an interdigitated array electrode by electrochemical impedance spectroscopy," *Electrochimica Acta,* vol. 52, pp. 126-131, 2012.

[11] R. S. Thomas, "Ultrastructural localization of mineral matter in bacterial spores by microincineration," *The Journal of Cell Biology,* vol. 23, no. 1, pp. 113-133, 1964.

[12] H. R. Curran, B. Brunstetter, and A. Myers, "Spectrochemical analysis of vegetative cells and spores of bacteria," *Journal of Bacteriology,* vol. 45, no. 5, pp. 485, 1943.

[13] J. F. Powell and R. Strange, "Biochemical changes occurring during sporulation in bacillus species," *Biochemical Journal,* vol. 63, no. 4, pp. 661, 1956.

[14] V. Vinter, "The effect of cystine upon spore formation by bacillus megaterium," *Journal of Applied Bacteriology,* vol. 20, pp. 325, 1957.

[15] T. C. Beaman, H. S. Pankratz, and P. Gerhardt, "Heat shock affects permeability and resistance of bacillus stearothermophilus spores," *Applied and Environmental Microbiology,* vol. 54, no. 10, pp. 2515-2520, 1988.

[16] A. Sekkouti, "A theoretical study and a micro-scale sensing platform for the detection of germination in bacillus stearothermophilus spores," Ms. Thesis, Department of Electrical and Electronics Engineering, Antalya Bilim University, Antalya, Turkey, 2019.

Modern approaches to the application of machine learning and data mining methods in the healthcare industry

A.ALTUN[1], S. CAGLAR[2] and A. TAGHIYEV[1]

[1]Selcuk University, Konya/Turkey, altun@selcuk.edu.tr
[2]Ministry of Health, Aksaray/Turkey, sona.caglar@saglik.gov.tr
[1]Selcuk University, Konya/Turkey, anart@selcuk.edu.tr

Abstract - **In recent decades, the amount of data has grown exponentially in various sectors, especially in the healthcare industry. Extracting hidden value from such massive medical data has become one of the most relevant topics for both industry and academia. Healthcare institutions are faced with the need to process big medical data at an increasing rate. Today's demands on the volume of data processed and the speed at which it is processed are such that the processes need to be almost fully automated. These requirements apply not only to direct digital processing, but also to procedures for setting up, adapting and even building appropriate quantitative models. Traditionally used models in the health care industry have been combined with new computational methods, which are referred to as machine learning and data mining. The article provides an overview of the current state of research in this field. Our goal is to classify modern methods of analysis applicable in the healthcare industry. Description of models for comparing the effectiveness of its various methods. This article presents the classification of modern methods of machine learning and data intellectual analysis used in health care. Models that use machine-learning procedures and hybrid models that use combined methods can provide the level of efficiency required in modern healthcare.**

Keywords - **Big data technology, machine learning, data mining, healthcare.**

I. INTRODUCTION

AS the world's population grows, predicting epidemics, combating existing diseases and improving treatment methods as a whole are urgent tasks for the world community. Methods should be flexible enough to test different scenarios of interaction and select the most appropriate solutions for the classification of modern methods of machine learning and data mining used in healthcare. Numerous articles are devoted to separate technologies and comparative analysis of applied methods. There are different methods of data analysis based on tools borrowed from informatics and statistics. Machine learning can find statistical correlations in a comprehensive global medical dataset that will quickly provide predictions and recommendations for patients and physicians (e.g., to identify the causes of HbA1c in patients with type 2 diabetes mellitus; disease prognosis; identification of genetic markers in oncology; infant health prognosis; forecasting risk factors in surgery) [1, 2]. Since eHealth data are still largely used and therefore wasted, there is a need to convert raw data into useful

and effective knowledge. The most valuable health data are unstructured or partially structured, and it is very difficult to obtain useful information from data with complex, dynamic and heterogeneous properties using traditional analytical tools and methods.

This review is primarily devoted to work that uses methods based on machine learning and data mining methodologies. The number of publications describing so-called hybrid methods has increased significantly in recent years. Section 1 provides a brief overview of the main methods. Sections 2 and 3 describe how to compare different models and methods used in health care. Section 4 draws conclusions and clarifies future work.

II. BASIC METHODS

A. Linear regression

Linear regression links the patient characteristics represented by the vector "$x \in R^n$" with the target variable "$y \in \{-1; 1\}$":

$$y = \beta_0 + (\beta, x) + \varepsilon \qquad (1)$$

Here, "ε" is a random error with zero mean. When deciding whether to assign "y" to a certain class, "$\beta_0+(\beta,x)$" is treated as a conditional expectation "E(y|x)". Note that in recent years, linear regression in its pure form has not been used, although it still serves as an important tool in mixed models (such as hybrid models).

B. Logistic regression (LR)

LR is one of the main methods of classification models used in healthcare [1], to calculate the probability "P(y=1|x)" of patient's disease, which has "x" characteristics. The probability is presented as

$$P(y = 1|x) = \frac{1}{1+e^{-(\alpha+\beta^T x)}} \qquad (2)$$

The maximum likelihood method is used to estimate the "α" and "β_i" coefficients ("β" vector coordinates). The estimation is carried out on the training dataset.

C. Decision Trees (DT)

This method is mainly used for classification. Let's briefly describe the essence of methods related to the construction of trees. Variable X is sequential if the numerical values it receives are ordered in a significant way for classification. Otherwise,

the variable is called categorical. The Automatic Interaction Detector (AID) algorithm, one of the first algorithms for building classification trees, sequentially splits the data in each node. In the case of an ordinal variable, branching occurs according to the conditions of the "X≤c", and in the case of a categorical variable according to the conditions of the "X∈A". Suppose that "S(t)" is a dataset numbers in a training sample related to node "t". Let's denote the average (by "S(t)") value of the explained variable "Y" in "$\overline{y_t}$". The value "$imp(t) = \sum_{i \in S(t)}(y_i - y_t)^2$" is an indication of the contamination of node "t". The AID algorithm chooses a cleavage that minimizes the sum of the contamination values of the following nodes directly. The splitting process ends when the reduction of the pollution becomes less than the preset threshold. Algorithms such as Theta Automatic Interaction Detector (TAID) extend the described method to categorical variables. Here, entropy or the Gini index is used as an indicator of contamination. More recent Classification And Regression Trees (CART) algorithms replace the stopping rules used in AID and TAID algorithms with growing and removing new branches. Chi-squared Automatic Interaction Detector (CAID) and C4.5 algorithms are also used. Rule Extraction algorithms, which are focused on working with big medical data, are adjacent to the algorithms associated with DT [3].

D. Support Vector Machine (SVM)

In healthcare SVM is used as a method of statistical classification. The essence of the method is as follows. Suppose that the training dataset "$\{(x^{(j)}, y^{(j)})\}_{j=1,2...l}$", where "$x^{(j)} \in X \subset R^n$" is a characteristic description of the object, "$y^{(j)} \in \{-1; 1\}$" is a binary classifier. An equation of the form "(w, x)-w_0=0, w∈R^n" defines a hyperplane with a normal vector "w", which in the space "R^n" separates the classes of "positive" "y$^{(j)}$=1" and "negative" "y$^{(j)}$=-1" objects. The optimal separating hyperplane is defined as the solution of the optimization problem:

$$||w|| \rightarrow min;$$
$$y^{(j)}\left((w, x^{(j)}) - w_0\right) \geq 1, j = 1,2,...l \qquad (3)$$

If there is a separating hyperplane exists, the value "$\frac{2}{||w||}$" is the bandwidth between points of different classes. The problem of finding the optimal separating hyperplane can be solved using the Kuhn-Tucker theorem. Let be "$L(w, w_0, \lambda) = \frac{1}{2}(w, w_0) - \sum_{j=1}^{l}\lambda_j(y^{(j)}((w, x^{(j)}) - w_0) - 1)$" is the corresponding Lagrange function. The object of the training sample "x$^{(j)}$" is called the support vector if "λ_j>0" and "(w, x$^{(j)}$)-w_0=y$^{(j)}$". The vector "w" is a linear combination of support vectors: $w = \sum_j \lambda_j y^{(j)} x^{(j)}$. Thus, for the actual construction of the vector "w", a relatively small number of objects of the training sample is used. This property of sparseness distinguishes the method of support vectors from the classical linear delimiters of the Fisher discriminant type. If the dividing plane does not exist (the training dataset is not linearly separable), the formulation of the optimization problem is corrected. It is also possible to switch to a nonlinear separator

using the kernel. A kernel is a function "K(x, x'),x,x'∈X" such that "K(x,x')=(φ(x),φ (x'))" for some map "φ:X→R^m". When using the map "φ", the linear separator can be built in the space "R^m". The problem of quadratic optimization in SVM can be formulated in a dual form: find "$\max_\lambda(\sum_j \lambda_j + \frac{1}{2}\sum_{i,j}\lambda_i\lambda_j y^{(i)}y^{(j)}K(x^{(i)}x^{(i)}))$" if "0≤$\lambda_j$≤C$_j$" for all "j" and "$\Sigma_j\lambda_j y_j$=0". Parameters "C$_j$" control the relative value of the indicators. The following kernel functions are most commonly used: "K(x$^{(i)}$,x$^{(j)}$)=(x$^{(i)}$,x$^{(j)}$)" is the linear model; "K(x$^{(i)}$,x$^{(j)}$)=((x$^{(i)}$,x$^{(j)}$)+1)^d" is a polynomial model of degree "d"; "$K(x^{(i)}, x^{(j)}) = \exp(\frac{||x^{(i)}-x^{(j)}||}{2\sigma^2}$" is a Gaussian radial basis function with the parameter "σ". For a new object, the prediction is built according to the formula "y=sgn($\Sigma_j\lambda_j y^{(j)}$K(x$^{(i)}$,x)+b$_j$)", here "b$_j$=$\Sigma_j\lambda_j y^{(j)}$K(x$^{(i)}$,x$^{(j)}$)". SVM relative to the nuclear family has been used for public health in many works.

E. Bayesian Networks (BN)

In healthcare, the use of the naive Bayesian method is justified when the attributes are independent. In the most general form, the BN is an acyclic oriented graph. During training, conditional probability distributions of the type "P(Y|X$_1$,...,X$_k$)" are formed, here "Y" is the vertex, and "X$_1$,...,X$_k$" are its *"parents"* on the graph. BN defines the joint distribution of vertices. For instance, the naive Bayesian method turns out to be if we take the categorical variable as the root vertex, and all the attributes - as its *"children"*. Informal learning of the BN consists in its maximum adaptation to the training dataset. Optimization is carried out relative to the functions used. These functions asymptotically lead to the same learning outcome, but the minimum description length (MDL) function has proved to be better on the final dataset. Let "B=(G,Θ)" be BN ("G" is graph, "Θ" is corresponding probability distribution), and "D={u$_1$,...,u$_n$}" is training dataset (each "u$_i$" assigns values to all vertices of the graph). "$MDL(B|D) = \frac{logN}{2}|B| - LL(B|D)$." Here "|B|" is the number of network parameters and "$LL(B|D) = \sum_{i=1}^{N}\log(P_B(u_i))$" measures the amount of information needed to describe "D" based on the probabilities distribution "PB". The MDL function is asymptotically correct.

F. Neural networks (NN)

In healthcare, this method can be used to convert a set of input variables into a set of output variables and simulate both linear and non-linear transformations. Transformations are performed with the help of neurons, which is a simplified model of brain neurons. Neurons are connected to the network by one-way information transmission channels. Each neuron can be activated by incoming input signals, and in the active state produces output signals. NN has a layer of input neurons (which receive the values of input variables), a layer of output neurons (that is, from the output signals of these neurons are formed output variables), and hidden layers. NN differ in their structure, hidden layers number and activation functions. In publications, five models of NN used in healthcare have been

analyzed: multilayer perceptron; mixture of expert; radial basic function network; learning vector quantization; and fuzzy adaptive resonance. The effectiveness of the application of NN of these types was compared with the effectiveness of parametric methods (for instance, LR), nonparametric methods and classification models of DT. The obtained results confirmed that multilayer perceptron does not show the highest accuracy, networks such as mixtures of experts and networks of radial basic functions show quite satisfactory results. Of the above methods, the most accurate was the method of LR. Networks based on fuzzy adaptive resonance proved to be the least accurate. Not inferior to other networks in recognizing patients with *"positive"* symptoms, they work much worse in recognizing patients with *"negative"* symptoms.

G. Genetic algorithms (GA)

A certain specificity of the application of GA in medicine is that classification trees form the population. Mutation and crossing algorithms are applied to trees. Otherwise, the structure of the algorithms is standard. After the initial population is created, the mutation and crossing processes are repeated and evaluated. The relative number of classification errors is used as an estimate.

H. Combined methods

Hybrid and combination methods include methods that use different methods to improve efficiency. Three methods of combining (ensemble methods) are most commonly used: bagging (bootstrap aggregating), boosting and stacking [4]. The main idea behind the bootstrap aggregating method is to build a set of predictors that together (after some aggregation) provide a better predictor [5]. Bagging is schematically applied to medicine as follows. It is assumed that there is a learning algorithm that builds a predictor "$\varphi(x,L)$" on the training dataset "L" to produce "y" at a given "x". Based on the training dataset "L", we can build a set of learning sets "$\{L_k\}_{k=1,...,K}$" (usually the same volume as "L"). These sets consist of the same objects selected randomly from "L" (possibly with repetitions). Let "K_+" be equal to the number of those "k" for which "$\varphi(x,L_k)$" gives a positive answer. The aggregated predictor "$\overline{\varphi}$" gives a positive answer if "$K_+ > \frac{1}{2}$". Bagging is particularly effective when the basic learning algorithm is unstable (i.e., it strongly depends on small changes in the learning set). The main idea of boosting is to form a strong classification algorithm based on a weak algorithm (in the sense of accuracy). In the process of forming a strong algorithm, the weak algorithm is "*retrained*" because the weights of the examples from the training sample are redistributed: (a) In the case of correct recognition, the weight decreases. (b) In case of incorrect recognition, the weight increases. The following example gives an idea of boosting. Let "X" be the space $\{(x^{(j)},y^{(j)})\}_{j=1,2,...,l}$" is a training sample. The basic algorithm runs in a series of rounds "$t=1,...,T$". Let's denote through "$D_t(j)$" the weight assigned to the object in round "t" (the initial distribution of weights "$D_0(j)$" can be taken uniformly). The task of training is to find in the round "t" such a mapping "$h_t(x)$" with values in $\{-1; 1\}$ that minimizes the probability of error "$\varepsilon_t = \sum_{h_t(x^{(j)}) \neq y^{(j)}} D_t(j)$".

Weights are updated as follows. Let "$\alpha_t = \frac{1}{2}\ln\left(\frac{1-\varepsilon_t}{\varepsilon_t}\right)$" then "$D_{t+1}(j) = \frac{D_t(j)\exp(-\alpha_t y^j h_t(x^{(j)}))}{Z_t}$", here "$Z_t$" is the normalizing factor (so that "$D_{t+1}(j)$" is a distribution). The final recognition algorithm has "$H(x) = sign(\sum_{t=1}^{T} \alpha_t h_t(x))$". This boosting method, based on the use of the exponential loss function, is called AdaBoost. It forces the algorithm to retrain in the presence of a large number of noise precedents. To minimize this effect, we can use the logistic loss function (such an algorithm is called LogitBoost). When stacking, several algorithms are combined using some kind of combiner [6]. As a rule, the role of the combiner is LR.

İ. Methods based on fuzzy logic (FL)

There are many publications on the application of FL methods in healthcare. Works in which FL is used in medicine or healthcare can be divided into two groups. The first group includes studies where elements of FL are applied in traditional methods. As a rule, these are works related to NN and the basic vector method. The second group includes studies in which the main method is borrowed from fuzzy sets theory. These are primarily works based on fuzzy inference systems, in particular, the systems of Mamdani and Takaji-Sugeno.

III. DATA SOURCE

In our study, was used the dataset which extracted from the database of Cerner Health Facts (Cerner Corporation, Kansas City, MO, USA), a national data warehouse that collects comprehensive clinical records from 130 US hospitals. This dataset is available on the UCI Machine Learning Repository [7]. The examined dataset consists of 50 attributes and 101,766 samples. This dataset contains missing, unnecessary, and noisy data as would be expected from real-world data. It also includes various features that have many missing values that cannot be directly corrected. These features were found to be useless for the analysis. One of these features is patient weight; 98% of the weight values in this dataset are missing. Only 332 out of 101,766 samples, which are 2% of the total sample size, contained weight values. The HbA1c test result values were 7% or higher for 253 samples and less than 7% for 79 samples. In the study, since the developed classification model was based on supervised learning, a filtering strategy was applied by taking the specialist doctor's opinion to determine the factors causing the increase of HbA1c in the dataset, and the classification model was developed by performing a logistic regression analysis on a total of 16 features; factors causing the increase of HbA1c have been identified.

IV. GENERAL CONCEPT OF THE MODEL

The development of the classification model by the logistic regression method is similar for both machine learning and data mining. Defining the relationship between the array of dependent and independent variables constitutes the bases for the creation of the most suitable and reasonable model. The logistic distribution function is used to describe the logistic regression model [8], with dependent and independent variables

("Y" and "X", respectively):

$$P_i = E(Y = 1 \mid (X_{i1}, X_{i2},..., X_{ik})) = \frac{1}{1 + e^{-(\beta_0 + \beta_1 X_{i1} + \beta_2 X_{i2} + ... + \beta_k X_{ik})}} \quad (4)$$

In the logistic distribution function "P_i", the probability of the feature that will make a specific choice value "i" of the independent variable "X_i" (the probability that "Y" will be "1" or "0" for the "i^{th}" sample); e is the base of the natural logarithm (e = 2.72 equals), where "P_i" is a nonlinear function with respect to both values: the independent variables ("$X_{i1}, X_{i2},...,X_{ik}$" are the *first*, *second*, and "k^{-th}" values of the independent features) and model "β"-parameters "$\beta_0, \beta_1, \beta_2,...,\beta_k$" are the regression coefficients for the corresponding variables in the model). The cumulative logistic probability distribution function shows the "S" curve, where the lower and upper bounds are zero and one, respectively. The model, which expressed as equation (4) can be linearized using the appropriate transformations, even if it is nonlinear. If in the model (4), "$\beta_0 + \beta_1 X_{i1} + \beta_2 X_{i2}...+\beta_k X_{ik}$" to interchange by "$Z_i$", so function (5) is gotten:

$$P_i = \frac{1}{1 + e^{-Z_i}} \quad (5)$$

If "P_i" is the case's occurrence probability, so "$1-P_i$" is the case's non-occurrence probability. By dividing the case's occurrence probability to the case's non-occurrence probability, function (6) is received:

$$\frac{P_i}{1 - P_i} = e^{Z_i} \quad (6)$$

If apply natural logarithm to both sides, so function (7) is obtained:

$$\ln(\frac{P_i}{1-P_i}) = \ln(e^{Z_i}) \Rightarrow L_i = \ln(\frac{P_i}{1-P_i}) = Z_i \Rightarrow$$

$$\Rightarrow Z_i = \beta_0 + \beta_1 X_{i1} + \beta_2 X_{i2} + ... + \beta_k X_{ik} \quad (7)$$

"L" is the logit model. In our case, independent variables, $X_i=(X_{i1}, X_{i2},...,X_{i15})=[race_i, gender_i, age_i, max\_glu\_serum_i, metformin_i, repaglinide_i, chlorpropamide_i, glimepiride_i, glipizide_i, glyburide_i, pioglitazone_i, rosiglitazone_i, insulin_i, change_i, diabedesMed_i]$, and $Y=[A1c\ result]$ is dependent variable.

V. EVALUATION OF THE MODEL QUALITY AND PERFORMANCE

One way to determine the quality of the machine-learning model is to divide the sample into a learning one, which is used to identify the parameters of the algorithm, and a control one, for each object that is compared the class predicted by the algorithm and the true class of the object.

Table 1. Confusion Matrix.

		Predicted	
		Positive	Negative
Actual	Positive	TP	FN
	Negative	FP	TN

The most common methods of model estimation are based on the error matrix: all objects of the control sample are divided into four categories depending on the combination of the actual and the predicted class (see Table 1. TP- True Positive, FN- False Negative, and similarly in the two remaining cases). Since the purpose of the classification model in health care is to sort objects into positive and negative ones, the effectiveness of the model is assessed by comparing for each object from the control set of class data predicted by the model with the real class of this object. The following model quality metrics are used for the tasks of data analytics in healthcare and medicine [1, 9]:

$$Accuracy = \frac{TP+TN}{TP+TN+FP+FN} \quad (8)$$

$$Precision\ (Positive\ Predictive\ Value\ ) = \frac{TP}{TP+FP} \quad (9)$$

$$Recall = \frac{TP}{TP+FN} \quad (10)$$

$$Negative\ Predictive\ Value = \frac{TN}{TN+FN} \quad (11)$$

$$F_{measure} = 2 * \frac{Precision*Recall}{Precision+Recall} \quad (12)$$

$$Specificity = \frac{TN}{FP+TN} \quad (13)$$

VI. CONCLUSIONS

This article considers the current state of research in the field of machine learning and data mining, which are combined with traditional models of computational methods. The aim of the article is the classification of modern methods used in health care and the description of models to compare the effectiveness of various methods used in medicine. This article presents the classification of modern methods of machine learning and intellectual analysis of data used in health care. In the future, models using machine-learning procedures and hybrid models using combined methods may provide the required level of efficiency in modern medicine and healthcare.

REFERENCES

[1] A. TAGHIYEV, Alpaslan A. ALTUN, et al., "A Machine Learning Framework to Identify the Causes of HbA1c in Patients With Type 2 Diabetes Mellitus," *JCEAI*, vol. 21, no 2, pp.34-42, 2019.

[2] A. A. Altun and A. Taghiyev, "Advanced image processing techniques and applications for biological objects," *2017 2nd IEEE International Conference on Computational Intelligence and Applications (ICCIA)*, Beijing, pp. 340-344, 2017.

[3] A. ALTUN and A. TAGHIYEV, "Big Data Design: Semantic Structures and Causal Models for Decision Making," *International Symposium on Human and Social Sciences (ISHSS'18),* p. 19, 2018,

[4] Wolpert D.H. "Stacked Generalization", *Neural Networks*, vol. 5, no.2, pp.241-259, 1992.

[5] Breiman L. "Bagging Predictors", *Machine Learning,* vol. 24, iss. 2, pp. 123–140,

[6] Naimi, A.I. & Balzer, L.B. "Stacked generalization: an introduction to super learning", *Eur J Epidemiol*, vol.33, no.5, pp.459-464, 2018.

[7] Strack B., et al. "Impact of HbA1c Measurement on Hospital Readmission Rates: Analysis of 70,000 Clinical Database Patient Records", *BioMed Research International*, vol. 2014, 11 pages, 2014.

[8] Hilbe Y., (2009). Logistic Regression Models. Chapman and Hall/CRC.

[9] A. ALTUN and A. TAGHIYEV, "Big Data Analytics on Cloud Based," *Inter.Symposium on Human and Social Sciences (ISHSS'18),* p.19, 2018.

Information exploitation and digital piracy

Artan Luma[1], Blerton Abazi[2], Muhamet Gërvalla[2], Azir Aliu[1] and Halil Snopce[1]

[1] South East European University, Macedonia,
a.luma@seeu.edu.mk, azir.aliu@seeu.edu.mk, h.snopce@seeu.edu.mk
[2]University for Business and Technology - UBT, Prishtina, Kosovo,
blerton.abazi@ubt-uni.net, muhamet.gervalla@ubt-uni.net

Abstract - Data is one of the most important things today and their value can not be measured, they can reinforce a business, drive new ideas, create opportunities, increase productivity etc, but in bad hands, data can be very critical and dangerous to the person who pronounces it, so everyone who keeps them online must take care of them. Here is discussed data, piracy, piracy impact, data disclosure, offensive technologies, defense technologies, preventive methods, familiar terms for computer engineers and, in general, exploitation art, art and most importantly, defense and war for their safety.

Keywords – data, information systems, piracy, exploataation

I. Introduction

Data, security, privacy, software companies and all of these similar terms have become very important terms and heard today, with increased use of the Internet and personal data storage, discrete and valid there, are create different methods and do whatever for obtaining valuable data. All these methods require extensive knowledge and great research for their creation, as to develop such methods, they must develop themselves and be discreetly maintained. Their discovery and development of counter-methods is also extremely difficult.

Most of these methods require low programming languages, unauthorized access and over-guard for each step and stage of attack or defense on the opposite side.

All these problems and disclosure of data have created the need for their "encryption", which is made by cryptography science which conceals data and makes it unreadable until the authorized person decodes and is likely to 'I read them and use them for thoughtful benefits.

A very small mistake in the source code or implementation can have a big impact if someone with "bad" knowledge enters the system and has access to those elements.

For each action, there is also the corresponding response. A protection against piracy attacks is defined as an action, process, technology, system or apparatus intended to prevent or mitigate the effects of a piracy attack on the victim, computer, server, network, or any particular device. [1]

As a licensed exploitant, a person is legally permitted to make copies of the software solely for back-up reasons. [2]

Since it is almost impossible to stop completely, software companies now issue legal claims to individuals who break these software rules.

Software piracy is a major problem in America and Europe, but in other countries is a rampant problem where routines are being copied for large applications that really require a license.

This topic will aim at describing piracy and piracy technologies, how pirated websites, torrents, P2P (Peer to Peer), protection against them, actions to be taken to prevent these technologies, piracy, piracy, some from algorithms used in these technologies, etc.

II. Literature review

Before the 1980s, everybody was able to copy computer programs and pirate them without legal constraints. U.S. the patent office knew the copyright, but only in the compiled version, not the source code. Testimony and lobbying by Microsoft founder Bill Gates in the late 1970s led to legislation that began protecting the integrity of the software.

Prior to the spread of software piracy on the Internet, thieves used Bulletin Board Systems to upload and distribute software to local computer owners. Thieves had the opportunity to authenticate via phone connection and download files on their computers.

After 1990, software piracy went far and many new methods that enabled piracy were discovered, after this time, the new millennium turned software copying illegally in a coincidence so everyone could steal copyrighted material. Peer to Peer (P2P) networks, specifically Napster and then BitTorrent, decentralized access to illegal software so that users could share files with millions of users around the world without leaving any trace of actions. [3]

Long history has data as well as security for it, many methods and many countermeasures have been developed all the time that there was a computer for breaking security doors and receiving illegal or forceful data.

Methods for data retrieval usually use low programming languages that not many people know, not so popular and notorious methods as well as people who have clear and evil goals from the attacker.

More recently, there is a growing need for data exploitation analysts, security audit people, implementation processes, and in general, work related to privacy, security, business data protection or extreme cases, government or even the army.

III. PIRACY

As in the music industry and photography industry, the software industry has problems with piracy. While digital technology for movies and music became widespread (ie 1990s and 2000s), the software was digital in nature and therefore it was all possible to copy without degradation of quality. While software piracy is "stained" by pirated movies, music, software piracy is the best example of how piracy has affected the software industry.

A teenager wants to create some graphic designs as a hobby for her new website. He browses the web and asks his friends what software he will need. Most of the answers are: Need Photoshop, all professionals use, is the most professional software, etc. So the teenager is determined that he needs Photoshop software, he goes and wants to buy this software. When he goes and sees the price of Photoshop which is 500 euros he stops and says, he can not afford to pay them all for a hobby, and even as a student. However, he still wants to enable his hob, so what does he do? Piracy is widespread and has multiple Photoshop copies on the Internet, so it runs and unloads them. After all, teenagers stay happy. At the same time, Adobe, the maker of Photoshop, does not lose any money, at the end no one is hurt. However, someone loses this act, here mostly lose Adobe's competitors because they can not compete with the cheaper prices they offer because eventually, anyone can take Photoshop without money. Take the example of GIMP, which is another software like Photoshop but at a cheaper price, but Photoshop is relatively better, so who do people choose if both are offered at a price of 0 euros (with piracy)? Photoshop, of course. So the biggest problem with piracy is that it has battered competitors and creates monopolies.

On the other hand, we will also discuss data exploitation techniques, which are related to piracy and data security.
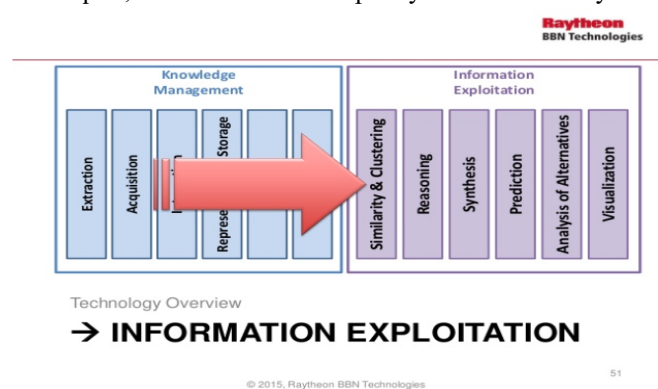
Figura 1. The stages of exploitation of information, which is divided into two main phases. [24]

IV. THE ART OF EXPLOITATION

Exploiting programs is the hunt stamp. A program is formed by a complex set of rules that follow a certain flow of executions that ultimately tell the computer what to do even if the executed program is now designed to stop that action. [5]
Developers are people, and sometimes what they write is not

entirely what they are aiming for. For example, a frequent error in development is called an off-by-one error. This is an error where the programmer miscalculated for one. This error is also known as fencepost error the cause of a case that demonstrates this error in a practical way. [6]
Often, these errors go unnoticed because the programs are not tested for any possible possibility that may occur, and the effects of this error usually do not occur during the normal execution of the program. However, when a program feeds input that makes the effect of the error manifest, the consequences of this error have a strong effect on the logic of the program. When properly exploited, an error like this can trigger a superficial safe program becomes a security vulnerability.

A classic example of this is OpenSSH, which should be a secure terminal software program, designed to turn unstable unsigned services such as telnet, rsh, and rcp. In this case, there was an off-by-one error in the exploited code, this simple error allowed further exploitation of the program so that a normal user can get administrative rights in the system. This functionality certainly was not what the developers intended for a secure program like OpenSSH, but a computer simply did what it was shown to do.

Off-by-one error and incorrect Unicode extension are all errors that may be difficult to notice in appearance but are noticeable by any developer. Again, there are some common mistakes that can be exploited in ways that are not so obvious, the impact of these security errors is not always clear, and these errors can be found in the code anywhere because the same kind of error is done in things different, and generalized exploitation techniques have evolved to take advantage of these mistakes and can be used in different situations.

V. BUFFER OVERFLOWS

In security of information and development, a buffer overflow or buffer overrun is an anomaly where a program, writing data on shock absorbers, exceeds the buffer limit and overwrites in nearby memory locations. [7]
Buffer Overflows have been present since the start of computers and they still exist. Most Internet worms use buffer overflow vulnerabilities to multiply, and today VML weaknesses on the Internet are the cause of these shock absorbers.
Take the language C example, which is a high programming language, which increases the developer's control and program output efficiency, it can also result in programs that have weaknesses to buffer buffer and memory leaks if the developer is not cautious. This means that when a variable is allocated, there is no integrated security that ensures that the contents of a variable fit into the allocated memory space. If a programmer wants to set ten bytes of data into an amortizer that was allocated only for eight space bits, this type of action is allowed, though it will usually cause the program to go bankrupt. This phenomenon is known as a buffer overflow, since the two additional bytes will overrun and spill out of the

allocated memory, overwriting whatever comes in the queue. If a critical part of the data is overwritten, the program goes bankrupt.

These types of bankruptcy programs are very common, think about how often a program has failed or has displayed a Blue Screen of Death (BSOD). A developer's mistake is when he / she does not handle something / fails, there should be a check of the length or limit on the input supplied by the user.

Program failures are annoying, but in the hands of a hacker, they can become very dangerous, a knowledgeable hacker can take control of the program when it fails and with surprising results.

These overruns can also occur in other segments of memory, such as heap and bss. If an important variable is located behind a buffer that is vulnerable to overflow, the program control flow can be changed, but the control tends to be limited. The opportunity to find these checkpoints and the lesson to use them requires creative experience and thought.

VI.   STRING FORMATION

A string format refers to a control parameter that is used by a class with functions in the string processing libraries in different programming languages. Initially, the string is written in template language, then usually printed standard, but variants exist that perform other tasks along with the result. Characters in this string format are usually copied to function output but with other values together. The string format is usually a precise and straightforward string that allows static function call analysis, but may also be the value of a variable that allows dynamic formatting but also security vulnerability known as uncontrolled string exploitation. [8]

This is another technique used to gain control of a privileged program. As the exploit of buffer overflows, the exploitation of string formatting also depends on program development errors that may appear to have no apparent security effect. Luckily for programmers, as soon as a technique is discovered and made known, it is easy to see these weaknesses of the strings and eliminate them.

Objective-C Data Types Table

Type	Example	Specifier
char	'a', 'O', '\n'	%c
int	14, -14, 780, 0xEEC0, 098	%i, %d
unsigned int	10u, 121U, 0xEFu	%u, %x, %o
long int	18, -2100, 0xfeefL	%ld
unsigned long int	13UL, 101ul, 0xfefeUL	%lu, %lx, %lo
long long int	0xe5e5e5LL, 501ll	%lld
unsigned long long int	10ull, 0xffeeULL	%llu, %llx, %llo
float	12.30f, 3.2e-5f, 0x2.2p09	%f, %e, %g, %a
double	3.1415	%f, %e, %g, %a
long double	3.5e-5l	%Lf, %Le, %Lg, %La
id	Nil	%@

Figura 2. Full list of string format specification in Objective-C. [25]

VII.   PROTECTIVE TECHNIQUES

Piracy solutions have always been a continual problem in the software industry and not just that. There are many types of technologies or techniques used by software or software

companies to take anti-piracy measures.

One of the most effective ways is licensing and product licensing management solutions.

A software license is a legal instrument (usually regulated by the law of contracts, with or without printed material) defining the use and distribution of the software. For example, the law of contracts of the United States of America all software is protected by copyright, source code, and also in the form of an object code. [22]

A typical software license allows the end-user to use one or more copies of the software in such ways that such use would potentially cause copyright infringement.

These licenses in theory that only software that is legally purchased is brave to be placed on the system. However, the reality in these systems is easily avoided and broken licenses are ready for anything and everything in the market. Recently, as piracy has risen, its response to it has increased, usually, large companies have decided to start counteracting these actions. Traditional approaches to these actions would be: site auditing, search warrants to inspect and confiscate stolen software on different computers. These methods are effective but their approaches are divisive, costly and commonly used only by large companies such as Oracle, SAP, Microsoft, Google, etc. Small software companies do not have enough resources to undertake these actions, lack the legal expertise and sufficient evidence to carry out these counteracts against pirated software.

Just knowing that your software is pirated is not enough to take legal action against it, printed proofs should also be printed in order to prosecute perpetrators of illegal acts against this software.

One of the success stories that have been pursuing software piracy is the case of Mercedes Benz, where they filed a lawsuit with a vehicle parts company that sold over $ 17 million of Mercedes Benz diagnostic software, which overtakes Mercedes's pay network, whereby Mercedes has a lot of income. Mercedesi succeeded in prosecuting these companies and permanently closing them down. [23]

VIII.   CONCLUSION

It is well known that the internet and internet technologies are growing and developing at great speeds and unpredictable. Every day new technologies, new methods, new research, inventions, discoveries, innovations emerge; All of these are of great importance in the field of technology, but some of these methodologies and technologies are also dangerous for man and the computer environment.

The Internet contains very private and sensitive information, as well as valuable for businesses, individuals, governments, military, etc. All of these are of great importance to the possessor, and especially to some of the latter.

Thieves or hackers are very knowledgeable and intelligent people but unfortunately exploit these knowledge and skills in illegal and dangerous things for the other.

Many new technologies have recently emerged about piracy, exploitation, infiltration, receipt of files without authorized permission (major cause of cryptography) but some of these technologies are for attack and theft and the rest are for protection against these things and attacks, these latest technologies, unfortunately, the only reason why they are created is the cause of illegal and robbery technologies, as with the anti-virus, every virus spurs the anti-virus to create protection and prevention methods against the virus, without that virus, even those methods would not exist.

Today, piracy is at its peak, the internet is a country that is largely uncontrolled by the state, and even if it is, it is very difficult to look after the number of websites that come out every day. These websites are not always for social benefits but for stealing, own benefits, cyber attacks etc.

However, it is good that data security has become a very central topic and is getting a lot of attention because with the increasing number of sensitive files and sensitive data on the Internet, people have learned that their privacy and security their is the main issue on the Internet today.

Piracy is growing and being alleviated, although the law is against it strictly, it is very difficult to control, people or users use VPN, false IP, overcoming security, and all possible ways to get what they want without paying any money.

Piracy can bring losses to the software company, competitors etc. but it is not as dangerous as hacking or exploiting data.

Exploitation of data today is at a very high level because new methods are emerging, automatic for data extraction, misuse, exploitation, and so on.

So, in conclusion, there is a lot of technology and methods used for attack and infiltration, and usually these methods are discrete and encapsulated so that no one else understands it, because the more they spread, the faster the methods are developed to counteract them and prevent them.

IX.   REFERENCES

[1]   Jupitermedia Corporation, «What is Software Piracy?,» 2003.

[2]   Legal Dictionary, «Free Dictionary,» 2005. [Në linjë]. Available: https://legal-dictionary.thefreedictionary.com/Software+Piracy.

[3]   R. Huesch, «History of Software Piracy,» 2008.

[4]   A. Kahsari, Metasploit Penetration Tester's Guide.

[5]   S. McCartney, në *ENIAC - The Triumphs and Tragedies of the World's First Computer and Company*, 1999, p. 16.

[6]   E. W. Dijkstra, «Why numbering should start at zero,» 2008.

[7]   Vangelis, «Stack-based Overflow Exploit: Introduction to Classical and Advanced Overflow Technique,» *Neworder,* 2004.

[8]   Oracle, «Formatting Numeric Print Output,» *The Java Tutorials,* 2017.

[9]   Team Teso, «Buffer Overflows vs Format String Vulnerabilities,» në *Exploiting Format String Vulnerabilities*, 2001, pp. 3-4.

[10] E. S. Raymond, «Daemon,» *The Jargon File,* 2005.

[11] W3C, «LogFile-960323,» në *Extended Log File Format*, W3C, 2009, p. 3.

[12] N. Biggs, në *Norman Codes: An introduction to Information Communication and Cryptography*, 2008, p. 171.

[13] J. K. Lindell, «Introduction to Modern Cryptography,» 2007.

[14] R. Richardson, «CSI Computer Crime and Security Survey,» CMPNET, 2008 .

[15] D. Czagan, «Symmetric and Asymmetric Encryption,» *SEC Institute,* 2013.

[16] W. Diffie dhe M. Hellman, në *Multi-user cryptographic techniques*, 1976, pp. 109-112.

[17] B. Schneier, Applied Cryptography (2nd ed.), Wiley, 1996.

[18] R. Cramer dhe V. Shoup, «Design and Analysis of Practical Public-Key Encryption Schemes Secure against Adaptive Chosen Ciphertext Attack,» në *SIAM Journal on Computing. ,* 2008, pp. 167-169.

[19] F. Callegati, W. Cerroni dhe M. Ramilli, në *Man-in-the-Middle Attack to the HTTPS Protocol*, 2009, pp. 78-71.

[20] J.   (.   Lohrey,   «Techwalla,»   2009.   [Në   linjë].   Available: https://www.techwalla.com/articles/how-to-stop-software-piracy.

[21] T.   (.   Miracco,   «MBTMAG,»   2016.   [Në   linjë].   Available: https://www.mbtmag.com/article/2016/02/hidden-cost-software-piracy-manufacturing-industry. [Access 2018].

[22] T. Hancock, «What if copyright didn't apply to binary executables?,» *Free Magazine,* 2008.

[23] Department   of   Justice,   Office   of   Public   Affairs,   USA   , «JUSTICE.GOV,»   2015.   [Në   linjë].   Available: https://www.justice.gov/opa/pr/auto-parts-distributor-pleads-guilty-manufacturing-and-selling-pirated-mercedes-benz-software.   [Access 2018].

[24] Raytheon   BBN   Technologies,   2014.   [Online].   Available: https://image.slidesharecdn.com/infoexploit-umdtalk-03mar15-scrubbed-150304114108-conversion-gate01/95/information-exploitation-at-bbn-51-638.jpg?cb=1425473905.

[25] Tutorials   Point,   «Tutorials   Point,»   [Online].   Available: https://www.tutorialspoint.com/objective_c/objective_c_data_types.htm. [Access 2018].

Knowledge based adaptive expert system framework for tracking water polo players based on CommonKADS methodology

VLADIMIR PLEŠTINA[1] and HRVOJE TURIĆ[2]

[1] Faculty of Science, University of Split, vlade@pmfst.hr
[2] Faculty of Science, University of Split, turich@pmfst.hr

Abstract - **Tracking players in water sports is very challenging task. Previous papers are usually based on tracking algorithms and background modeling or players extraction. In this paper it is presented expert system framework application organized from different angle. All system is described through CommonKADS methodology and it can be applied by any algorithm. This methodology is implemented and evaluated on real water polo match.**

Keywords - **expert system, CommonKADS, tracking players, water polo, computer vision**

I. INTRODUCTION

Tracking and understanding movements of sport players based on computer vision is in focus of interest for well over a decade [1], [2]. Although it is not so new, importance of research in this field is rising due to demands in modern age and increasing number of visual sensors. Processing and understanding of surveillance video data is considered as the most demanding part of Big Data problem.

Team and players movements and movement analysis during a game can be used for providing consumer with additional information during broadcast as well as for after match statistics. Trainers and managers can use facts about tactical and physical performance of the players and team to improve game results. In the literature, several approaches and applications dealing with players tracking can be found. Mainly, solutions were given for popular and commercially interesting sports such as football [3], basketball [4], hockey [5] and tennis [6]. Also, each solution was oriented mainly towards a particular sport. Aspogamo [7] system is framework that can be applied on any sport, but mainly is used with football.

In this paper, we propose adaptive expert system framework for tracking players. Based on proposed system, we present application on water polo based on CommonKADS [8] methodology. As an example, in this paper is presented rather demanding example – water polo. Tracking water polo players wasn't considered for automatic tracking using computer vision until now. Water polo is very challenging for computer vision tracking application. It has some interesting demands that should be resolved [9]: multiple occlusions between players, dynamic background and extreme variations of players' occurrence during tracking period. Therefore, approach and framework that will be presented could be considered as a representative example that will prove applicability to other sports and even to other areas such as beach and pool surveillance etc.

II. TRACKING PLAYERS IN SPORTS

As players in different sport has different characteristics, it is important to choose correct method for tracking. There are lots of variables that should be considered, such as position of the players [10], occlusions among players [11], fast changes of position and appearance of the players [12], etc. Logical step is to include knowledge about the players and the game, i.e. the expert knowledge. This way a computerized system for tracking tries to best simulate a person - an observer, expert for specific sport. Computer vision tracking players system described in [13] cites three basic steps that should be considered from the beginning: Camera system, players' detection and players' tracking.

Cameras system refers to the image acquisition method. One or more, fixed or mobile cameras can be used. The number and the position of the cameras depend on the field size. In water polo one camera is enough to cover the pool.

One of the important elements for player detection methods is background modelling. It can be utilized during the whole process of tracking, or only for the beginning players' segmentation. With sports such as football, the background is known (green grass) and there are multiple algorithms proposed for background separation. With indoor sports, background is also known and subtraction methods of current frame from known background can be used. Also, background refreshing method during a game can be used. Unlike majority of sports that have known backgrounds, for water sports the known background is changeable, i.e. it changes due to interactions between the players and pool water. In this case, background modelling methods are important for detecting players as well as for the tracking itself. In [9] is presented different methods for classification features analysis for tracking players in water polo. It emphasizes that extracting pool as background is one of challenging tasks.

III. ADAPTIVE EXPERT SYSTEM FRAMEWORK

Adaptive expert system framework consists of three main parts: Tracking module, Expert module and Database. Fig 1. shows an adaptable expert system's framework for tracking players. The main component of the framework is a database that
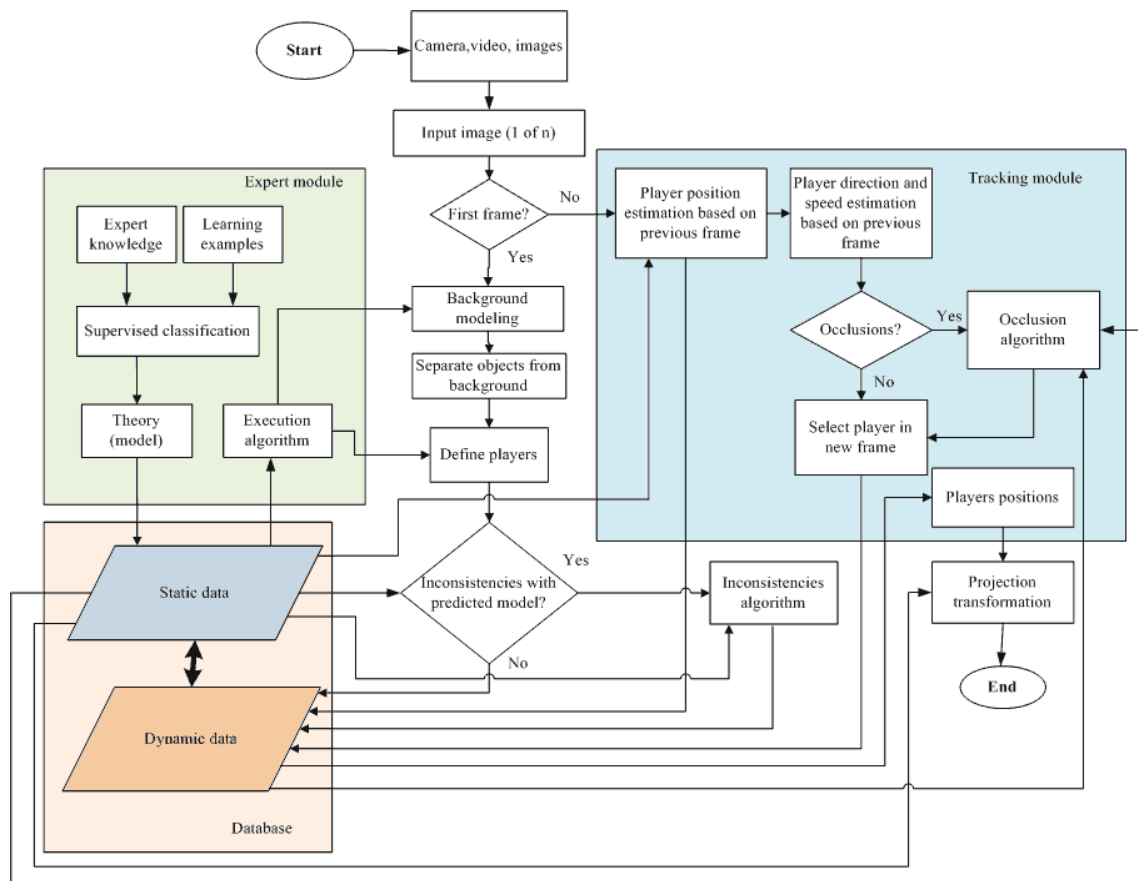
Fig 1. Adaptive expert system framework

contains static and dynamic data within the system. Database represents a knowledge base that contains facts (knowledge about sports, players, background, and game), experience-based knowledge of the expert (heuristic, expert knowledge), and meta-knowledge, which represent a basis for how to use knowledge. Different types of knowledge are linked by rules that refer to conditions and actions.

The expert module represents a component of the system used for expert knowledge acquisition and knowledge representation. When dealing with machine learning systems it is important to distinguish learning algorithm and execution algorithm [14]. The learning algorithm generates new knowledge or modifies existing knowledge from the set of learning data and background knowledge. In this framework, model (theory) present new knowledge generated from learning examples as learning data and expert knowledge as background knowledge. The execution algorithm uses the generated knowledge for solving new problems.

Theoretical models adapted to a certain system are created from knowledge of one or more experts with the help of data for learning. The knowledge is stored in the system before work begins and it forms static data that can be upgraded and utilized in further tracking. Described system is referred to image processing from one angle of view. Input image can come from a camera, a video, or series of images stored on a computer. Algorithm begins with the first input frame. According to database, and through executed algorithm, the background is

modelled with the help of background modelling algorithm. Depending on the sport, background modelling can be executed for a green field in football [15], known background in the gym [16], or modelling of the pool for the water sports [17]. By background modelling, the objects in foreground are isolated, and it is expected from those objects to be the players. If there are inconsistencies with defining players, an inconsistency solving algorithm is actuated. This algorithm includes application of knowledge about the sport and the player as well as experience-based expert knowledge. An inconsistency according to provided model represents a difference between the expected after defining the player and the knowledge from database (for ex. defining expected number of players on the field). Data about marked players are dynamic data obtained during the game. Every next image is processed in tracking module. The tracking module includes one of the tracking methods [18]. According to dynamic data from previous frame, position of the players can be estimated as well as direction and speed of the movement. If there is an occlusions among players, an algorithm for solving occlusions is activated [19], [20]. The players are then defined in a new frame by the tracking method. Information obtained during tracking is stored into data base as dynamic data. The positions of the players in any given time during tracking are obtained from database, and the players real-world positions obtained by projection transformation of coordinates. A general model defines the core of the tracking system and it is constructed based on analysis of knowledge-
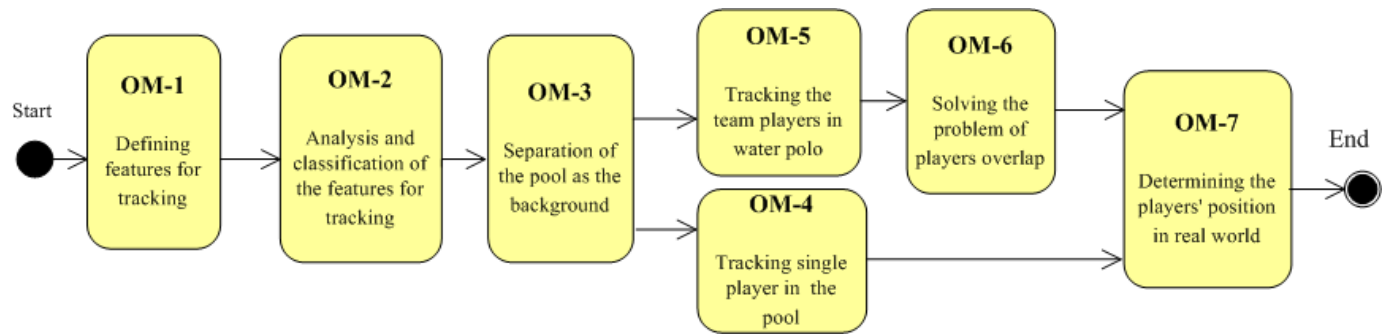
Figure 2: Organizational models

based system [21], players tracking system, and persons tracking system [5] [13].

IV. PROPOSED APPROACH BASED ON COMMONKADS METHODOLOGY

Mostly all up to date tracking systems are applicable to football. The systems that process other sports are very rarely utilized, while the tracking systems for water sports are non-existing. That is one of the motives for developing this kind of system. Development of the system is described using CommonKADS methodology.

According to available literature, it is determined that there is no adequate and flexible, general system for players tracking in team sports, especially not the ones tracking the players in water sports. Therefore, it is necessary to approach the creation of the system by analyzing research linked to given issue.

The goal of the tracking system is to obtain an accurate position of each player in time t. An adaptable experimental tracking system is utilized as a frame for developing the system of interest. Critical points that come up in system analysis are: defining features for tracking, background modelling, overlap of the players, disappearing of the players from the visual field due to water splashing, changeable shape and appearance of the players due to swimming style, and including the expert knowledge about water polo and computerized vision [9].

System development is organized through seven organizational models (OM). By solving tasks in each model, knowledge is obtained. Previous knowledge is used in the following organization model or in design model.

Figure.2 show organizational models and structure of the system.

A. OM-1: Defining Features for Tracking

In water polo object is a player and it is necessary to define tracking features. Shape of the player in water polo is changeable and depend on situation so, an observer has to define all the features according he visually recognizes and tracks players in a water pool. In the first organization model (Figure 3) observer has to analyze water polo match and parse fields of observation that are intuitively close to him. The observer describes all observations (how he recognizes the pool, the players, players' swimming, and critical situations). A system expert analyses previous research that include tracking players, recognizing persons, and applying computer vision in

sports. The expert control and connects existing knowledge with features defined by the observer. Together they define general knowledge about the water polo match.
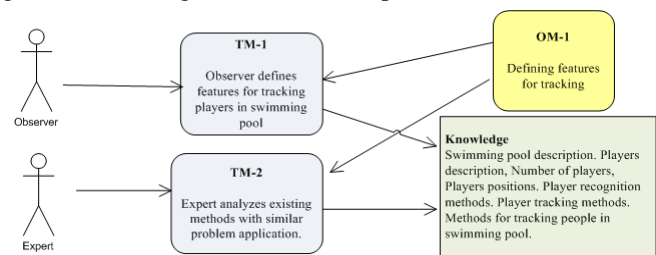
Figure 3: OM-1: Defining Features for Tracking

B. OM-2: Analysis and Classification of features for Tracking

In second organization model tracking features are analyzed through four models, and the optimal method for classification is defined. The observer's task is to define categories which describe the area of observation. With LabelMe annotation tool [22] the observer separates areas and assigns the areas to a certain category, which classifies distinguished templates. One group of templates is used to create theoretical model, and the other group is used for testing classification methods. The following four categories are defined based on which the observer finds and tracks a player: pool, player's swim cap, player's body, and player's splashing. Since there is no stable shape of players in water polo, color is the only feature to distinguish categories.

Therefore, a system expert analyses features in RGB, HSI, and YCbCr color models using Matlab program package. The selection of these models is based on analysis of previous scientific research [23], [24], [25], [26]. After defining color models, the best classification method is chosen.
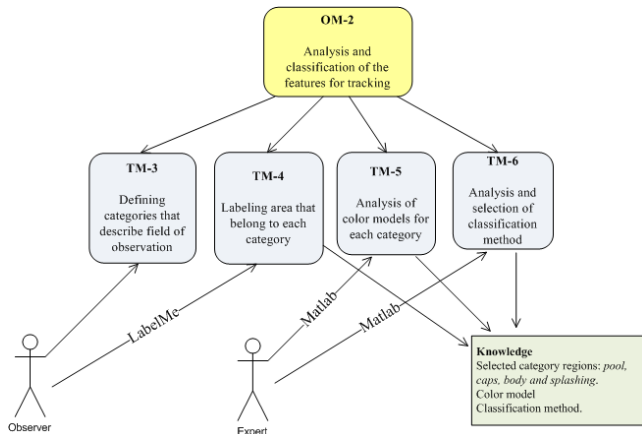
Figure 4: OM-2: Analysis and Classification of features for Tracking

C. OM-3: Separating Pool as Background

Separating background is a common method used in computer vision. However, unlike indoor sports and football, in water sports the background is changeable during the game and it is affected by the player. The expert has two tasks in this organization model. The first one is to analyze a method for separating the pool as the background. The second one is to test the method and to select the best method for separating the pool and players. In this system, it is used method for separating pool as the background [27].
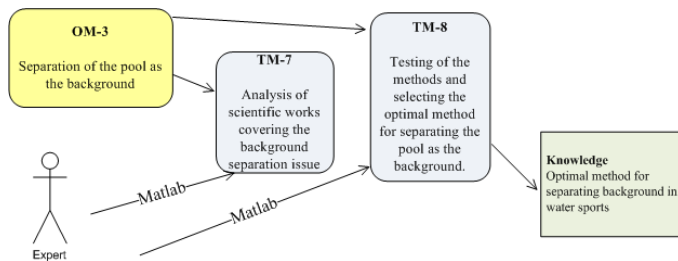
Figure 5: OM-3: Separating Pool as Background

D. OM-4: Tracking one Player in the Pool

By revising area of tracking it is determined that methods based on particle filters [28]–[29] and point tracking with high quality observational model gives the best speed to precision ratio. The expert task is to create an algorithm based on division of particles which uses as an observational model previously obtained method for classification. Proposed algorithm must be tested on sequence of input frames and it has to be compared to the correct underlying values which have been defined by the observer for the same sequence of frames.
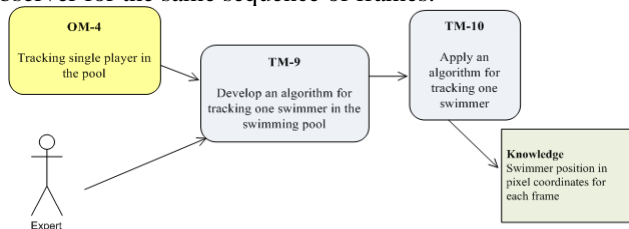
Figure 6: OM-4: Tracking one Player in the Pool

E. OM-5: Tracking the Team Players in Water Polo

Although there is no system for tracking multiple players in water sports, in this case there can be applied tracking methods for team players in other sports. Each player has unique ID and tracking consists of multiple independent tracking of each player. The expert task is to design an algorithm for tracking multiple players based on the previous knowledge, and to compare the algorithm with ground truth data.
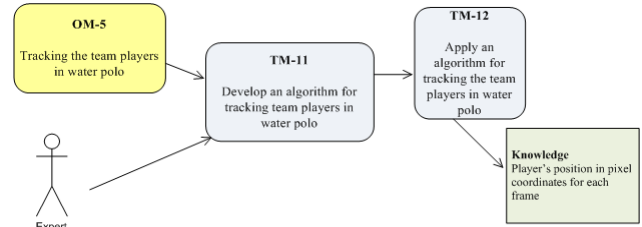
Figure 7: OM-5: Tracking the Team Players in Water Polo

F. OM-6: Solving the problem of Players overlap

While tracking multiple players there is often an overlap. According to knowledge defined by the observer, the overlap of players in water polo can be divided to overlap with the background (splashing) and occlusion among the players. The system expert's task is to create an algorithm for solving mutual overlaps based on previous knowledge, and to test it in critical situations.
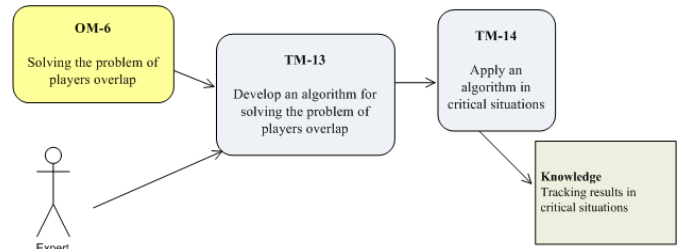
Figure 8: OM-6: Solving the problem of Players overlap

G. OM-7: Determining Players Position in Real World

Since the results of tracking one or multiple players are obtained in values of pixels, it is important to get true values. Projection transformations on known points and dimensions of the pool is performed. The system expert's task is to show the results of previous tracking in a measurable unit (cm).
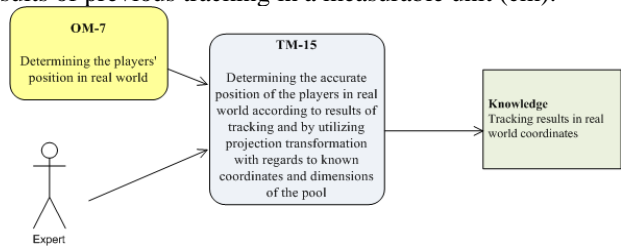
Figure 9: OM-7: Determining Players Position in Real World

V. IMPLEMENTATION AND EVALUATION

The system for tracking team players in water polo is based on adaptive expert system framework (Figure 1). System was created and tested using MATLAB, Data was stored in XML files. System was based on described seven organizational models. One camera was used with field of view (FOV) that covers the entire pool area. Independent observer was water polo expert that observes the game and transfers the observations to an expert for the system.

In water polo, two teams have caps of different colors. A player is tracked by color of the cap and his body. However, during swimming splashing occurs so the cap or the body are not visible in some cases. In that case it is necessary to follow the area of splashing until the player appears again. The expert for the system analyses utilized methods for tracking, notices critical situations that the observer pointed out, and codes knowledge into the system. First organization model is concluded by defining features for tracking and by analyzing the expert's knowledge.

In second organization model the observer (expert) utilizes input videos, and with LabelMe annotation tool, on 10 000 test images separates 100 templates for areas that describe categories "pool ", "caps", "body", and "splashing". The expert for the system analyses the components of color model for a certain category by using program tool MATLAB. Histograms of RGB, YCbCr and HSI color models are analyzed. Beside histograms, considered is a range of values for histogram's pixels. Based on the results the expert for the system chooses colors model for describing features and test classification methods. 800 randomly chosen pixels are used for testing; 200 for each category that the observer manually classified in order to have accurate baseline data. Based on the classification results, the best classification method is chosen. This organizational model is referring to experimental module of the system in which theoretical models for background isolation, defining players, and tracking players are created. Supervised classified information, ranges in defined color model for each category, and data about game defined by the observer are stored as static data in database.

In third organization model, the expert for the system utilizes knowledge from previous organizational model and defines the best method for background separation. A method for separating the pool as background is defined in this model, and it is based on knowledge about analyzed color models. To test the best method, 100 different images of the pool with swimmers are selected. In order to compare obtained results, for each image there is a model baseline values. For methods testing precision-recall diagram, F-measurement, correlating with accurate baseline values, and measurement of methods' precision were used.

In fourth organization model it is defined algorithm for tracking single player. Algorithm is based on the methods for tracking points. However, as observational model for certain point, classification method from the third organizational model is used. This ensures that points do not have weight value as the points with particle filter have. Rather, area for each category is defined.

In fifth organization model, tracking of multiple players is applied as multiple independent tracking of single player. However, overlaps are possible when there are multiple players. This issue is solved in the sixth organization model.
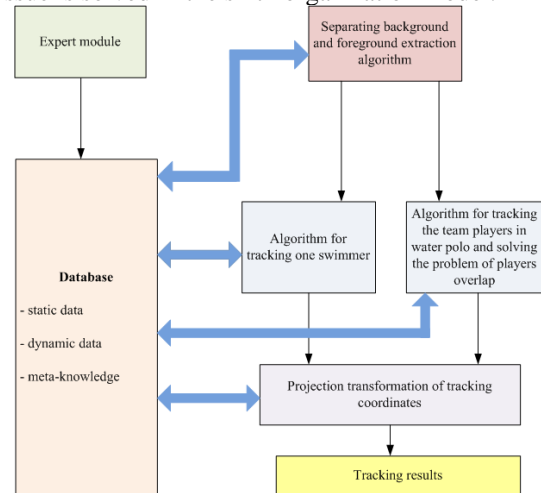
Figure 10: System flow

The result is real position of player in pool using projection transformation and known dimensions of the pool. Static knowledge data is stored as XML files. Through expert module expert's knowledge is stored in knowledge base - That knowledge is represented by the tracking features according to which the theoretical models are defined. Figure 10 depicts a diagram of system flow.
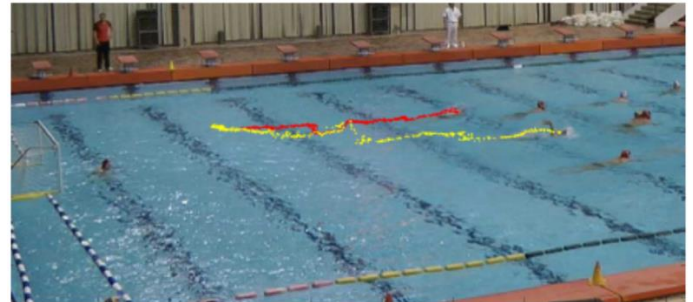
Figure 11: Tracking two players with overlap

VI. CONCLUSION

This work present application of adaptive expert system framework for tracking players based on expert knowledge of water polo. A framework for creating an adaptable system for players tracking is presented with CommonKADS methodology. As an example, players tracking system in water polo is developed.

Knowledge base in proposed system has two main types of data: the static data which is previously stored and the dynamic data which is obtained during the tracking. The result is obtained by fusing the static data from the knowledge base with dynamic data that refers to the current direction, speed, and position of the player. When tracking the team players, multiple independent tracking paths of a single player are applied, and problem of overlap is solved by utilizing movement matrix.

This work present theoretical model which is applied on real data. It includes CommonKADS methodology for developing

and testing expert system with seven organizational models. Every expert can use its own data, tracking algorithm, background modelling method or classification method in each organizational model.

REFERENCES

[1]   J. Perš and S. Kovačič, "Computer vision system for tracking players in sports games," *IWISPA 2000. Proc. First Int. Work. Image Signal Process. Anal. conjunction with 22nd Int. Conf. Inf. Technol. Interfaces. (IEEE Cat. No.00EX437)*, vol. 1, pp. 177–182, 2000.

[2]   C. J. Needham and R. D. Boyle, "Tracking multiple sports players through occlusion, congestion and scale," *Br. Mach. Vis. Conf.*, 2001.

[3]   J. Ren, J. Orwell, G. a. Jones, and M. Xu, "Tracking the soccer ball using multiple fixed cameras," *Comput. Vis. Image Underst.*, vol. 113, no. 5, pp. 633–642, May 2009.

[4]   M. Perše, M. Kristan, S. Kovačič, G. Vučkovič, and J. Perš, "A trajectory-based analysis of coordinated team activity in a basketball game," *Comput. Vis. Image Underst.*, vol. 113, no. 5, pp. 612–621, May 2009.

[5]   W.-L. Lu, K. Okuma, and J. J. Little, "Tracking and recognizing actions of multiple hockey players using the boosted particle filter," *Image Vis. Comput.*, vol. 27, no. 1–2, pp. 189–205, 2009.

[6]   X. Yu, N. Jiang, L.-F. Cheong, H. W. Leong, and X. Yan, "Automatic camera calibration of broadcast tennis video with applications to 3D virtual content insertion and ball detection and tracking," *Comput. Vis. Image Underst.*, vol. 113, no. 5, pp. 643–652, May 2009.

[7]   M. Beetz *et al.*, "Aspogamo: Automated sports game analysis models," *... Sci. Sport*, 2009.

[8]   J. K. . Kingston, "Designing knowledge based systems: the CommonKADS design model," *Knowledge-Based Syst.*, vol. 11, no. 5–6, pp. 311–319, 1998.

[9]   V. Pleština and V. Papić, "Features analysis and Fuzzy-SVM classification for tracking players in water polo," *WSEAS Trans. Comput.*, vol. 13, 2014.

[10]   P. J. Figueroa, N. J. Leite, and R. M. L. Barros, "Tracking soccer players aiming their kinematical motion analysis," *Comput. Vis. Image Underst.*, vol. 101, no. 2, pp. 122–135, Feb. 2006.

[11]   Z. Zhang and M. Piccardi, "A Review of Tracking Methods under Occlusions," in *Proc. of the IAPR Conf. on MVA*, 2007, pp. 146–149.

[12]   P. J. Figueroa, N. J. Leite, R. M. L. Barros, I. Cohen, and G. Medioni, "Tracking soccer players using the graph representation," in *Proceedings of the 17th International Conference on Pattern Recognition (ICPR '04)*, 2004, vol. 4, pp. 787–790.

[13]   V. Pleština, H. Dujmić, and V. Papić, "A modular system for tracking players in sports games," *Int. J. Educ. Inf. Technol.*, vol. 3, no. 4, pp. 197–204, 2009.

[14]   I. Kononenko and M. Kukar, *Machine learning and data mining*. Chichester, West Sussex, UK: Horwood Publishing Limited, 2007.

[15]   H.-S. Yoon, Y. Bae, and Y. Yang, "A soccer image sequence mosaicking and analysis method using line and advertisement board detection," *ETRI J.*, vol. 24, no. 6, pp. 443–454, 2002.

[16]   M. Kristan, J. Perš, M. Perše, and S. Kovačič, "Closed-world tracking of multiple interacting targets for indoor-sports applications," *Comput. Vis. Image Underst.*, vol. 113, no. 5, pp. 598–611, May 2009.

[17]   L. Fei, W. Xueli, and C. Dongsheng, "Drowning Detection Based on Background Subtraction," *2009 Int. Conf. Embed. Softw. Syst.*, vol. 339, no. 1, pp. 341–343, 2009.

[18]   A. Yilmaz, O. Javed, and M. Shah, "Object tracking: A survey," *Acm Comput. Surv.*, vol. 38, no. 4, 2006.

[19]   T. Misu, M. Naemura, and W. Zheng, "Robust tracking of soccer players based on data fusion," *16th Int. Conf. Pattern Recognition, 2002. Proc.*, vol. 1, pp. 556–561, 2002.

[20]   P. Figueroa, N. Leite, and R. Barros, "Background recovering in outdoor image sequences: An example of soccer players segmentation," *Image Vis. Comput.*, vol. 24, no. 4, pp. 363–374, Apr. 2006.

[21]   V. Papić, N. Rogulj, and V. Pleština, "Identification of sport talents using a web-oriented expert system with a fuzzy module," *Expert Syst. Appl.*, vol. 36, no. 5, pp. 8830–8838, Jul. 2009.

[22]   B. C. Russell, A. Torralba, K. P. Murphy, and W. T. Freeman, "LabelMe: A Database and Web-Based Tool for Image Annotation," *Int. J. Comput. Vis.*, vol. 77, no. 1–3, pp. 157–173, Oct. 2007.

[23]   N. Vandenbroucke, L. Macaire, and J.-G. Postaire, "Color image segmentation by pixel classification in an adapted hybrid color space. Application to soccer image analysis," *Comput. Vis. Image Underst.*, vol. 90, no. 2, pp. 190–216, May 2003.

[24]   P. Sebastian, Y. V. Voon, and R. Comley, "Colour Space Effect on Tracking in Video Surveillance," *Electr. Eng.*, vol. 2, no. 4, pp. 298–312, 2010.

[25]   H. Stokman and T. Gevers, "Selection and fusion of color models for image feature detection.," *IEEE Trans. Pattern Anal. Mach. Intell.*, vol. 29, no. 3, pp. 371–81, Mar. 2007.

[26]   M. Mignotte, "Segmentation by fusion of histogram-based k-means clusters in different color spaces," *IEEE Trans. image Process.*, vol. 17, no. 5, pp. 780–787, May 2008.

[27]   V. Pleština and V. Papić, "Object classification in water sports," in *Computers and Communications (ISCC), 2013 IEEE Symposium on*, 2013, pp. 839–844.

[28]   K. Okuma, A. Taleghani, N. Freitas, J. J. Little, and D. G. Lowe, "A boosted particle filter: Multitarget detection and tracking," *Comput. Vision-ECCV*, 2004.

[29]   A. Dearden, Y. Demiris, and O. Grau, "Tracking football player movement from a single moving camera using particle filters," *3rd Eur. Conf. Vis. Media Prod. (CVMP 2006). Part 2nd Multimed. Conf. 2006*, pp. 29–37, 2006.

Remote Home Control Using Arduino with Android Based Application

E. AVUCLU[1] and s. TASDEMIR[2]

[1]Department of Computer Technology and Computer Programming, Aksaray University, Aksaray Turkey
emreavuclu@aksaray.edu.tr
[2]Department of Computer Engineering, Technology Faculty, Selçuk University, Konya Turkey
stasdemir@selcuk.edu.tr

Abstract - **Technology has brought many innovations and conveniences to human life. Nowadays, some applications are frequently used to make people's lives easier. In this study, a model house was developed in order to make it easier for people to meet their needs in daily life. The doors and lights of this model house were controlled wirelessly by the phone. Arduino's wireless communication technology is used in the control process. Application we use daily in our house door, lamp, etc. the tools are remotely controlled thanks to the android supported phone. The application is very convenient for everyone, especially disabled-elderly people.**

Keywords - **Arduino, Remote control, Home control, Android, Blueterm.**

I. INTRODUCTION

As a result of the development of technology, things have changed rapidly in our lives. Today's technology is based on the necessary arrangements for people to live more comfortably. Mankind has developed the technology it has developed so far in some applications to its own benefit. The increasing use of technology in every field and age has made it indispensable. Today, technology can be defined as an effective part of guiding discoveries by using data sharing in the most effective way.

Different studies have been conducted in the same field in the literature;

Korkmaz controlled the electrical home appliances and security systems with a mobile phone and used the remote control for home automation [1]. Ardam showed that remote control of the telephone could also be used for the workplace [2]. Bekiroğlu and Daldal controlled the drive system of an ultrasonic motor via a mobile phone [3]. Emiroglu has implemented an inspection system that enables the operation and control of gasoline engines with RF (Radio Frequence) remote control [4]. Sevinç performed the remote control of the DC motor speed by using micro controller. It has used RF communication in the remote control system [5]. Kaplan designed a remote control system that provides control of the engine rotation direction and speed [6]. Using two microcontrollers, Kahraman developed a remote controlled, sleep mode and programmable climate control. In the remote control system, an infrared communication system was used

[7]. Using the PIC16F877 microcontroller, Karakuş provided remote control of an RF-based writing board erase system [8]. Using the PIC16F877 microcontroller, Güğül controlled the processes such as home lighting, garden irrigation and opening the garage door with the help of DTMF (Dual Tone Multi Frequency) signals [9]. Koyuncu processed DTMF signals and performed the remote control of the vehicles via the computer via turbo basic software [10]. Artificial Neural Networks and Dynamic Time Bending algorithms are used separately by using voice command home applications (light on and off, etc.) [11]. They conducted studies on remote controlled automatic irrigation system and its application [12]. SMS-controlled irrigation automation control unit was developed [13]. Arduino and Rasberry Pi were used in the system they developed. With this system, energy saving was achieved and smart drip irrigation system was designed at low cost [14].

The system developed in this study is designed to facilitate the daily life of people in general. It can be easily used to eliminate people living with disabilities, elderly or bedridden patients in their daily lives depending on the continuous people.

II. MATERIALS AND METHODS

In this section, general information about Arduino's work and pin leap is given and the interior mechanism of the model house is introduced. The implementation is carried out by a series of operations. The flow diagram showing the order of occurrence of these processes is shown in Figure 1 below.
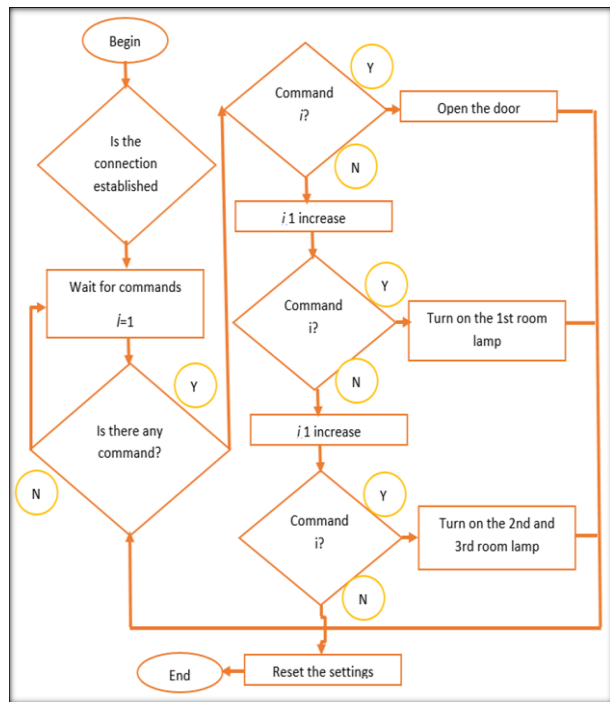
Figure 1. Flow diagram of the application

2.1. Arduino Uno and Technical Specifications

Arduino Uno controller was used in the study. The Arduino Uno controller provides control of the units in the house according to the information received from the phone. Arduino is an input / output programming board developed by electronic engineers as open source. Arduino can also be called a physical programming platform. The programming of systems that interact with the outside world is called physical programming. Anyone can create their own circuits using Arduino pre-printed circuits. Arduino is an easy-to-use, flexible and software-based electronic prototype platform. The Arduino Uno controller shown in Figure 2 provides control of the system.

Figure 2. Arduino Uno controller used in the study

These microcontrollers on the Arduino development board are programmed with an Arduino-specific programming language.

With Arduino, basic systems can be designed. Arduino cards have microcontroller. These microcontrollers are in the same category as the PIC. Microcontrollers can be easily programmed with their own libraries. There are inputs for processing digital and analog data to the card. It can receive and process data from a computer or other device and react to the incoming data, and can also send data such as light and sound to the external environment. There are 14 digital input / output pins on the Arduino Uno board. 6 of these pins can be used to obtain PWM output. There are 6 analog inputs on the Arduino Uno board. There is also a 16 MHz crystal oscillator, power input (2.1mm), USB connection, reset button. All elements required to support the microprocessor are on the Arduino Uno card. An adapter or battery is enough to power the Arduino Uno. Arduino Uno's technical specifications are shown in Table 1.

Table 1. Technical specifications of Arduino Uno

Microprocessor	Atmega328
Input Voltage (recommended)	7-12V
Input Voltage (limit)	6-20V
Operating voltage	5V
Number of Analog Input Pins	6
Digital Number of Input / Output Pins	14
Current for each input / output	40 mA
Current for 3.3V Output	50 mA
EEPROM	1 KB
SRAM	2 KB
Flash Memory	32 KB
Clock Speed	16 MHz

In this study, we used the HC-06 module to communicate between Arduino and Android. The HC-06 Bluetooth-Serial Module Card is designed for the use of Bluetooth SSP (Serial Port Standard) and wireless serial communication applications. Supporting Bluetooth 2.0, this card allows communication at a frequency of 2.4GHz and has a communication distance of approximately 10 meters in open space.

2.2. Arduino Connection with Bluetooth Module

To connect the Bluetooth module to the Arduino, we must make sure that the Arduino and Bluetooth are crossed the TXD and RXD pins. Another important point is to divide the voltage from Bluetooth with a resistor. The connection diagram is shown in Figure 3 below.
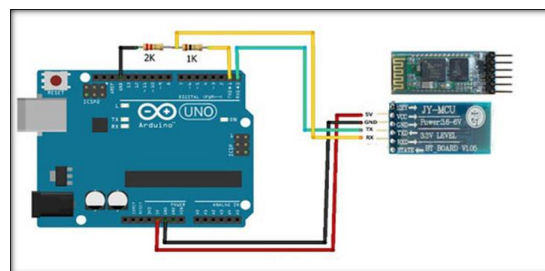
Figure 3. Arduino connection with Bluetooth module

2.3. The Blueterm Application

In this study, a terminal application, Blueterm, was used to send data from the Android device. Blueterm is the terminal emulator for communicating with any serial device using the VT-100 Bluetooth serial adapter. Communication with HC-06 is easy, the connection is faster and more stable. The user can set a specific delay in milliseconds, the number of packets to be sent, and the message to be sent to the microcontroller or microprocessor. There is a terminal that is visible to the user, the data being transmitted or received. First, the user has to start by connecting with the HC-06 /Bluetooth. The connection example is shown in Figure 4 below.
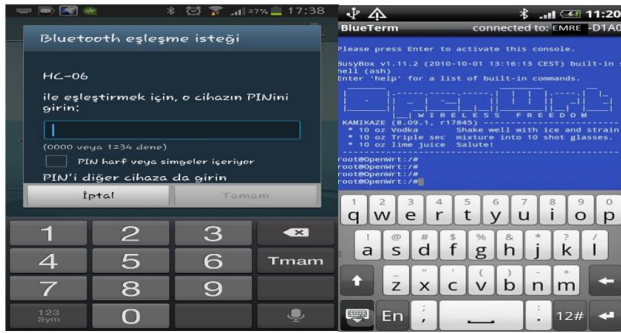
Figure 4. Blueterm connection

2.4. Sample Model Home Application

An example of the model has been developed to provide home control via phone via Arduino. Servo motor is used to open and close the doors of this model house. Figure 5 below shows a door and the servo motor connected to it with an arrow.
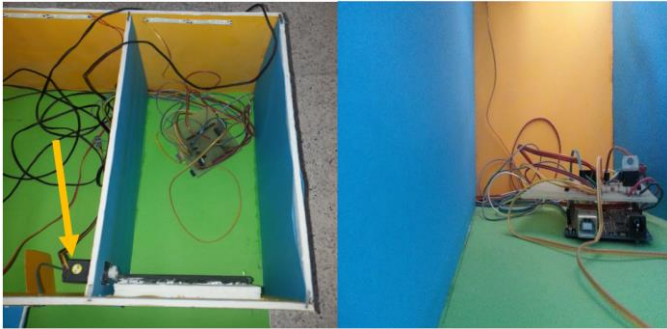
Figure 5. Home connection with Bluetooth module

Figure 6 below shows the connection of led lamps in each room. In this way, lamp control of all rooms is controlled by telephone with remote control. The general model structure showing the connection of the rooms of the house with Aurdino is shown in Figure 6 below. The white arrows indicate the LED lamps in the rooms.

Figure 6. Overview of the model house

III. CONCLUSION

In this study, some units of the house were controlled wirelessly via Arduino Uno with Blueterm application using Android operating system. The developed application was made to facilitate the social life of disabled citizens in general. It provides effortless control of all the efforts that come to mind in our daily life at home. The units of the house are much more active and designed to respond to the demands of those who want to control, as desired. It is thought that the application will be useful for people who cannot use the units of the house (lamp, curtain, door, etc.) for any reason (bedridden, elderly, etc.). With the application will be able to meet their daily needs without being connected to anyone.

REFERENCES

[1]. Korkmaz, F. "Elektrikli cihazlar ve güvenlik sistemlerinin cep telefonu ile uzaktan denetlenmesi", Yüksek Lisans Tezi, *Gazi Üniversitesi Fen Bilimleri Enstitüsü,* Ankara, 1-2 (2004).

[2]. Ardam, H. "Ev veya işyeri otomasyonunun uzaktan telefon aracıyla sağlanması", Yüksek Lisans Tezi, *Gazi Üniversitesi Fen Bilimleri Enstitüsü* Ankara, 1-2 (1996).

[3]. Bekiroğlu, E. ve Daldal, N. "Remote control of an ultrasonic motor by using GSM mobile phone", *Sensors and Actuators A: Physical*, 120 (2); 536-542 (2005).

[4]. Emiroğlu, A.O. "Benzin motorlarının uzaktan kumanda ile çalıştırılması ve kontrollerini kerçekleştiren cihazın devre tasarımı ve imalatı", Yüksek Lisans Tezi, *Gazi Üniversitesi Fen Bilimleri Enstitüsü*, Ankara, 1-3 (2002).

[5]. Sevinç, E. "DC motor hızının PIC kullanılarak uzaktan denetimi", Yüksek Lisans Tezi, *Gazi Üniversitesi Fen Bilimleri Enstitüsü*, Ankara, 1-2 (2004).

[6]. Kaplan, İ. "DC motor devrinin ve devir yönünün uzaktan kontrolünü tasarımı ve uygulaması", Yüksek Lisans Tezi, *Gazi Üniversitesi Fen Bilimleri Enstitüsü*, Ankara, 3-4 (1996).

[7]. Kahraman, H.T. "Otomatik klima tasarımı", Yüksek Lisans Tezi, *Gazi Üniversitesi Fen Bilimleri Enstitüsü*, Ankara, 1-2 (2004).

[8]. Karakuş, A. "Mikro denetleyici kontrollü yazı tahtası silme sistemi tasarımı", Yüksek Lisans Tezi, *Gazi Üniversitesi Fen Bilimleri Enstitüsü*, Ankara, 1-2 (2005).

[9]. Güğül, G.N. "Akıllı ev sistemleri ve uygulaması", Yüksek Lisans Tezi, *Gazi Üniversitesi Fen Bilimleri Enstitüsü*, Ankara, 1-2 (2008)

[10]. Koyuncu, B. "PC Remote control of appliances by using telephone lines" , *IEEE Transactions on Consumer Electronics*, 41 (1): 201-209 (1995).

[11]. Bayğın, M., Karaköse, M., "Gerçek Zamanlı Ses Tanıma Tabanlı Akıllı Ev Uygulaması" IEEE 978-4673-0056, 2012.

[12]. Çakır, A., Çalış, H. (2007) "Uzaktan Kontrollü Otomatik Sulama Sistemi Tasarımı ve Uygulaması", *Süleyman Demirel Üniversitesi, Fen Bilimleri Enstitüsü Dergisi*, 11(3), 258-261.

[13]. Fidan, U., Karasekreter, N.(2011) "GSM/SMS Tabanlı Sulama Otomasyon Kontrol Biriminin Geliştirilmesi ve Uygulaması", *e-Journal of Nem Sciences Academy*, 6(1), 71-77.

[14]. Agrawal, N., Singhal, S. (2015) "Smart Drip Irrigation System using Raspberry pi and Arduino" *International Conference on Computing, Communication & Automation*, Noida, India, 928-932.

Convolutional neural network baseline model building for person re-identification

S. HUSSIN[1], K. ELASHEK and R. YILDIRIM

[1] Yildirim Beyazit University, Ankara/Turkey, eng.saleh.hussin@gmail.com
Yildirim Beyazit University, Ankara /Turkey, k_elashek@yahoo.com
Yildirim Beyazit University, Ankara /Turkey, remzi1963@ybu.edu.tr

Abstract - **Nowadays, there has been a wide range of critical issues that made the person re-identification task as a challenging task, these issues include human pose variation, human body occlusion, camera view variation, etc. To overcome these issues, most of the modern approaches are proposed based on deep convolutional neural network (CNN). This paper, sheds light on how to utilize a pretrained CNN models which were developed for image recognition, to create a powerful CNN baseline model that could be utilized for the task of person re-identification. To build such a powerful model, this study has proposed to adjust the architecture of the CNN model by adding batch normalization and dropout layers to the classifier part of the CNN to prevent an overfitting and re-train it with the available dataset. Then this research study has utilized cosine similarity to calculate the resemblance among the extracted features. The extensive experiments conducted on the proposed CNN baseline model using the three large and well-known standard re-identification datasets to validate the performance of the proposed method, proved that the proposed approach could be compared with the state-of-the-art approaches.**

Keywords - **Computer vision, Person re-identification, Deep learning, convolutional neural network.**

I. INTRODUCTION

Recently, the process of re-identification person's identity has received more and more attention, having become a key point in intelligent surveillance systems and has wide application possibilities in many field practices. When you are given a personal image that was taken by a single camera, the task is how to identify that person from the gallery taken by other multiple cameras. It's a difficult task as a result of critical issues of the variation on human pose and camera view, and human body occlusion. Nowadays, the advance in deep convolutional neural network (CNN) architecture [1-5] utilized to build efficient person re-identification models practices. In fact, CNN's main superiority is that, it can optimize the process of feature extraction , the process of learning of metrics and the classification process jointly in an end-to-end training fashion [6].

At the current stage, most of the modern person reidentification approaches [1, 7, 8] were proposed based on CNN. Generally, fine-tuning the CNN model that pre-trained on ImageNet [9] under supervision of SoftMax loss usually serves as the baseline paradigm. Investigation on building

effective CNN baseline model is urgently in demand to benefit person re-identification research area to large extent, both from the academic and implementation frame of reference.

In this paper, deep person re-identification model architecture designed based on the pre-trained model for ImageNet problem by adjusting the architecture of the CNN model and re-train it with available dataset. This study has proposed the following key changes: Adding a fully-connected (FC) layer after the adaptive pooling layer and to prevent overfitting follow it by a batchnormalization layer and a dropout layer, then employ stochastic gradient descent (SGD) [10] as the optimizer for CNN training. The feature vector that output from the adaptive pooling is utilized as the image representation.

This research paper is structured as explained below: Second section presents a review of some associated previous studies. In third section, the definition of the person re-identification model architecture structure in this study has described. The details regarding the implementation of the experiments are provided in forth section. In fifth section this paper has presented the experimental outcomes on three large and well-known person re-identification datasets. This paper has concluded in the sixth section.

II. RELATED WORKS

Conventionally, hand-crafted feature designed based on color histogram come out on top in person re-identification [11-13], due to the consideration that color of clothes has good discriminability for tell the difference between persons. Recent researches on person re- identification mostly focus on building deep CNN models in the end-to-end learning fashion. Zheng, et. al. in [1] takes advantage of the deep convolutional models pre-trained on ImageNet [9] as well as fine-tunes it on person re-identification datasets utilizing SoftMax loss. The features that produced by the final pooling layer was utilized as an image descriptor. The learned representation achieves great performance boost against traditional hand-crafted feature. In fact, due to the favorable outcome of [1], most of the modern methods that based on deep learning technique also adopt pre-trained models as backbone network as well as have been searching other technical means to further rising the performance of re-identification framework. Therefore, for most present approaches [7, 14, 15] feature learned utilizing

only SoftMax loss commonly be in the service of as a baseline for comparison.

Various model architectures have been explored in person re-identification area. Between existing person re-identification approaches, ResNet-50 [2] is the most commonly utilized backbone network [14, 15]. Besides, GoogLeNet [5, 16], inception networks [16] and Densenet [17] have also been chosen as backbone network by some researchers. Taking advantage of the pre-trained CNN models, by further employing metric learning methods [18], using part-based CNN representation [19], otherwise carefully designing attention mechanism [20], the person re-identification performance could be further improved..

To prevent overfitting for deep CNN models when trained on relatively small datasets, several approaches have been proposed. In a specification, random cropping [3], random flipping [4], and random erase operation [21] are commonly utilized data augmentation methods in training deep CNN model. In addition, regularization methods like weight decay is also a well-known approach for prevent overfitting. In recent, batchnormalization [22] and dropout [23] are two widely utilized tricks for training CNN and have shown benefits for preventing overfitting. Dropout aims through the training process randomly with a probability, to discards the output of each hidden neuron. Batchnormalization aims at reducing internal co-variate shift by normalizing the output of each hidden neuron using minibatch mean and variance. Since person re-identification dataset are relatively small, for instance, Market1501 containing only 12,936 images for training, effective means for preventing overfitting is necessary for building high-accuracy person re-identification model.

III. PROPOSED METHOD

This section describes the research proposed approach towards building a powerful CNN based model that can be used for the person re-identification task. The pipeline of the proposed baseline model is exhibited in Figure 1. It is possible to take any CNN model designed for image classification, remove its hidden fully connected layers, and it can be used as the backbone network, for instance, Google Inception [16] and ResNet [2]. This paper utilizes the ResNet-50 [2] model, taking into account its competitive performance and its comparatively concise building style. The ResNet-50 CNN model was fine-tuned utilizing the classification framework in [1] in order, to transfer its knowledge to the domain of person re-identification. Table 1 summarizes the specifications of the ResNet-50 that is commonly utilized in person re-identification.

Table 1: Summary of ResNet-50 specifications.

CNN	ResNet-50
Release year	2015
# Layers	50
top-5 error rate	3.6%
# parameters	25.5 M
Image Input Size	224-by-224
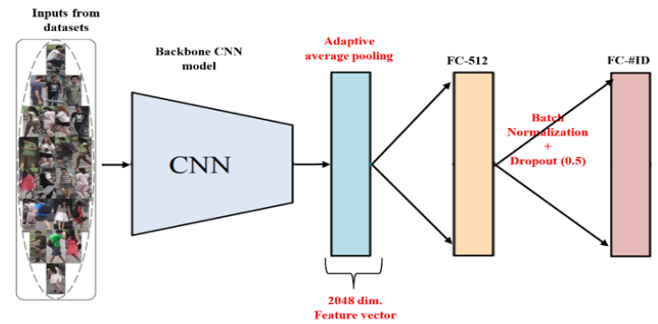
Figure 1: The pipeline of our CNN-based person re-identification model.

Taking ResNet-50 as the backbone network, we adjust its classifier architecture as following:

- Replace pool5 layer by adding an adaptive average pooling layer that can be used instead of the flatten layers that traditionally used in CNN models. This layer will output a 2048-dimensional features vector.
- After the pooling layer, a 512-dimensional FC layer is appended and then it followed by a batchnormalization layer and a dropout layer sequentially. The rate of drop in the dropout layer was adjust to the value of 0.5.
- Finally, another FC layer is appended with a SoftMax loss and dimension based on the person ID labels for training dataset, for instance, Market-1501 contains 751 ID labels.

IV. EXPERIMENTS

A. Datasets Settings

In this study, experiments were conducted on the three widely utilized person reidentification datasets, including Market-1501 [24], and DukeMTMCreID [25, 26], in addition to CUHK03 [27].

Market-1501 includes 32,668 images of a total of 1501 IDs, that were taken from 6 cameras positioned in front of a supermarket on campus. The Deformable Part Model (DPM) [28] was utilized for recognizing and cropping the images. The Market-1501 dataset is divided into three portions: the first part contains 12,936 images with 751 IDs used for training purpose, the second part contains 19,732 images with 750 IDs dedicated for the gallery, and the last part contains 3,368 images with the same 750 gallery IDs used for the purpose of querying. 64×128 is the size of all images in this dataset.

DukeMTMC-reID dataset includes 36,411 images of a total of 1,812 IDs which are taken from 8 different standpoints. In the same way as Market-1501, this dataset is also divided into three portions: the first part contains 16,522 images with 702 IDs used for training purpose, the second part contains 17,661 images with 1,110 IDs dedicated for the gallery, and the last part contains 2,228 images with 702 IDs used for the purpose of querying. Images in DukeMTMC-reID dataset are vary in size.

CUHK03 dataset includes 14,096 images of a total of 1,467 IDs. these IDs were taken by 2 cameras in the campus of CUHK

university. The CUHK03 dataset include two kinds of labeled images, one was labeled manually and the other discovered by DPM. Experiments in this work has done on the images that detected by the DPM. Originally the CUHK03 valuation protocol exactly include 20 train/test splits. However, for the purpose of compatibility with both Market-1501 and DukeMTMC-reID, the training and testing protocol that proposed in [29] is used in this paper. That is 7,365 images containing 767 IDs used for training purpose, 5,332 images containing 700 IDs dedicated for the gallery, as well as 1,400 images containing the same 700 IDs as in gallery are used for the purpose of querying. CUHK03 dataset images are also vary in size.

The details of these three datasets are listed in Table 2 as well as some images as example are exhibited in Figure 2.

B. Evaluation Metrics

For performance measurement, this study has adopted the top classification accuracy on validation data as a measurement for image classification and has adopted the cumulative matching curves (CMC) as well as mean average precision (mAP) as a measurement for re-identification accuracy. CMC curves are used to evaluate the performance of re-identification problem, this paper, reports the accuracy ranks 1, 5, as well as 10 on CMC curves rather than plotting the actual curves for easier comparison with published outcomes. Meanwhile, following the existing works [24, 25], this study also has utilized mAP to measure the efficiency of persons retrieval. The average precision for each query is measured from the curve of precision-recall. Then the mAP is computed as the mean value of average precisions across all queries. fundamentally, CMC indicates the retrieval precision, while mAP indicates the recall.

Table 2. The details of datasets.

Datasets		Market-1501	DukeMTMC-reID	CUHK03
All	# images	32,668	36,411	14,096
	# IDs	1,501	1,812	1,467
Training	# images	12,936	16,522	7,365
	# IDs	751	702	767
Gallery	# images	19,732	17,661	5,332
	# IDs	750	1,110	700
Query	# images	3,368	2,228	1,400
	# IDs	750	702	700
# cams		6	8	2

Market-1501   DukeMTMC-reID   CUHK03
Figure 2. Some example images from Market-1501, DukeMTMC-reID and CUHK03 datasets.

C. Implementation Details

Our CNN-based proposed person reidentification model was implemented utilizing the Python PyTorch framework. The ResNet-50 [2] that pre-trained on ImageNet [9] was utilized as a backbone network. Consequently, the framework of classification that was used in [1] was utilized to fine tune the proposed model, this study modify the architecture of the basic model as exhibited in section III. The input images were resized to 256x128 and then padded with zeros to size of 276x148. The required data augmentation is then performed by randomly left-right flipping images and cropping them to a final input size of 256x128. For validation purpose, this study has utilized 70% of dataset for training set and 30% for validation.

Training. This study has adopted a similar training strategy as in [30], the training epochs number was set as 60 epochs. The size of training batch was set as 32. This study has utilized the mini-batch SGD optimizer with his study has utilized the mini-batch SGD optimizer with learning rate initial value of 0.05 and momentum value of 0.9. After passing 40 epochs of training the value of the learning rate was decayed to 0.005. The backbone model is pre-trained on ImageNet [9]. With NVIDIA GeForce GTX 1050 Ti GPU and PyTorch as the platform, training of the proposed model on each one of the three widely utilized person reidentification datasets consumes about 3 to 4 hours.

Testing. In testing phase, the only image features are extracted. Consequently, after completing the training procedure, the trained model becomes ready to extract discriminative features. the pooling layer keeps the useful features and eliminates the redundant ones. Therefore, this study has utilized the output from the adaptive average pooling layer as the visual representation. This layer produces a 1x2048 dimensional feature vector. For every dataset, this study has fed all the testing images in gallery as well as query to the trained CNN model to obtain a 2048-dimensional person descriptor for each image and they are stored offline to be used in evaluation.

Evaluation. In the evaluation phase, once the descriptors for the gallery and query images are obtained, this study compute the cosine distance between the features of the query and those of the gallery to measure CMC rank-1, 5, and 10 accuracy as well as the mAP which are utilized for re-identification evaluation.

V. EXPERIMENTAL RESULTS

To verify the proposed model, this study has conducted experiments on three large and well-known datasets inclusive Market-1501, DukeMTMCreID and CUHK03. As a result, in this section this study has reported the training classification accuracy result. It reported also the CMC rank 1, 5, and 10 accuracy as well as the mAP for the three datasets. In fact, all experiments have done utilizing a single query.

Classification Accuracy Results. The overall training accuracy along with validation accuracy and loss for each dataset are exhibited in figure 3. and the outcomes of the classification accuracy on validation sets are listed in Table 3.

The outcomes presented that the performance of the

proposed model on Market-1501, DukeMTMCreID, and CUHK03 datasets are remarkably good, as shown in Table 3, this study has obtained 91.21%, 88.32%, and 94.00% validation accuracy on the three datasets respectively. Therefore, the proposed model of this experimental study can effectively reduce the impact of overfitting and can work well for person re-identification task by producing satisfactory discriminative person's features from the image.

Re-identification Evaluation Results. To validate the efficiency of the performance of the approach proposed in this study for the task of person re-identification, we report both of the accuracy ranks 1, 5, and 10 on CMC curves and the mAP for all the three datasets, and Immediately afterwards we compare the outcomes obtained to that previously obtained from the person re-identification state-of-the-art approaches that utilize the pretrained ResNet-50 CNN model as backbone model. Outcomes on the used datasets are exhibited in Table 4.

Comparison with the state-of-the-art methods. the outcomes from the model that this study proposed, were compared with the state-of-the-art approaches by means of CMC rank-1 accuracy and mAP on the three datasets, Market-1501, DukeMTMCreID, and CUHK03 as exhibited in Table 5. This study model achieved 87.7% rank-1 accuracy and 70.5% mAP on Market-1501, this achievement could be compared with the state-of-the-art 89.5% rank-1 accuracy and 71.6% mAP in [31] and it exceeds the other state-of-the-art algorithms. On DukeMTMCreID, the proposed model yielded 78.1% rank-1 and 61.1% mAP and exceeds the state-of-the-art performance. On CUHK03 dataset, the proposed model yielded 43.7% rank-1 and 40.2% mAP, which is far a little bit from the state-of-the-art 54.3% rank-1 accuracy and 50.1% mAP [31], on the other hand, it still exceeds other state-of-the-art algorithms. This demonstrates the effectiveness and generality of the proposed model. To the best of our knowledge, this study approach is the simplest one able to achieve the state-of-the-art performance.

Table 3. Model validation accuracy

Dataset	Validation accuracy
Market-1501	91.21%
DukeMTMCreID	88.32%
CUHK03	94.00%

Table 4. Model re-identification evaluation results

Dataset	Rank-1	Rank-5	Rank-10	mAP
Market-1501	87.7	95.4	96.9	70.5
DukeMTMCreID	78.1	88.5	92.3	61.1
CUHK03	43.7	63.6	72.6	40.2

Re-identification results visualization. Figure 4 exhibits some re-identification results samples on Market1501, DukeMTMCreID, and CUHK03 datasets. The query images have presented in the first column. The retrieved images are arranged from the left to the right based on the scores of similarities with the query. It could be noted that the model proposed in this study is reasonably strong to fetch the right retrieval results and go wrong in some challenging cases that are very hard due to that it shares one or more salient features with the query image
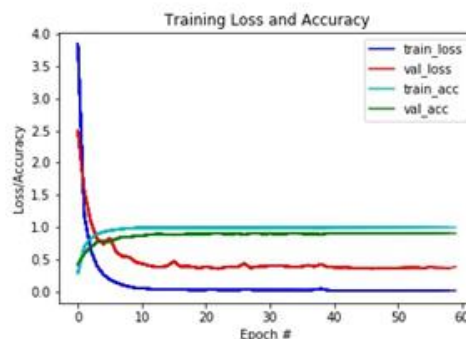
(a)
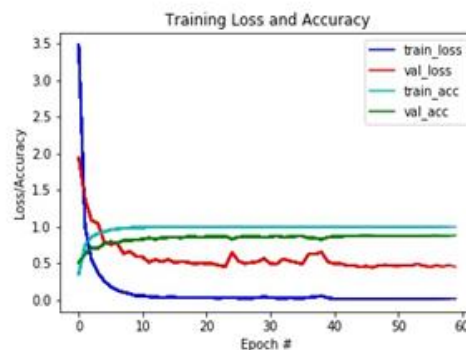
(b)
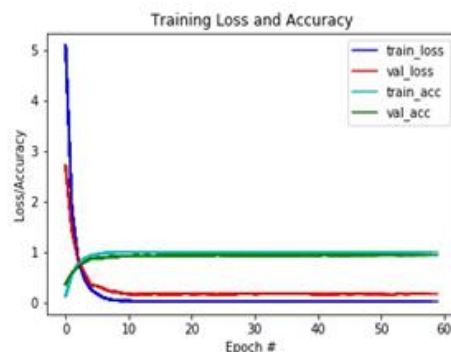
(c)

Figure 3. Model loss and accuracy results on (a) Market-1501, (b) DukeMTMCreID, and (c) CUHK03 datasets

Table 5. Comparison with the state-of-the-art approaches. CMC rank-1 accuracy and mAP are listed

Method	Market-1501		DukeMTMCreID		CUHK03	
	Rank-1	mAP	Rank-1	mAP	Rank-1	mAP
IDE [1]	73.9	47.8	65.2	45.0	21.3	19.7
Re-rank [29]	77.1	63.6	-	-	34.7	37.4
SVDNet [14]	82.3	62.1	76.7	56.8	41.5	37.3
IDE+DaF [15]	82.3	72.4	-	-	26.4	30.0
SSM [31]	82.2	68.8	-	-	-	-
DaRe [32]	86.4	69.3	74.5	56.3	54.3	50.1
CamStyle +RE [33]	89.5	71.6	78.3	57.6	-	-
ours	**87.7**	**70.5**	**78.1**	**61.1**	**43.7**	**40.2**

(a) Visual results on Market-1501

(b) Visual results on DukeMTMC-reID

(c) Visual results on CUHK03
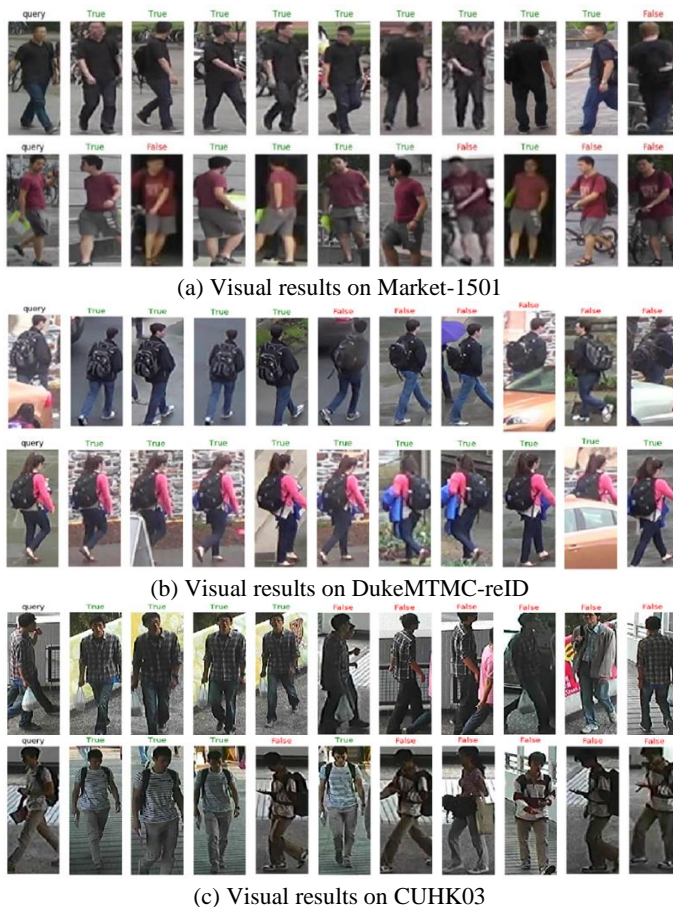
Figure 4. Top-10 person re-identification samples results on Market-1501, DukeMTMC-reID, and CUHK03 datasets. The green True word and red False word on the top of each image indicate respectively the true equivalent and the false ones.

VI. CONCLUSION

This paper sheds the light on how to utilize a pretrained CNN models that was developed for image recognition, to build powerful CNN baseline model that utilized for the task of person re-identification. This study has proposed to adjust the architecture of the CNN model by adding batch normalization and dropout layers to the classifier part of the CNN model to prevent overfitting and re-train the adjusted model with available dataset. Moreover, the experiments have exhibited that the approach proposed in this study has systematically improved the performance of the baselines model as well as was very strong to features representation. Finally, the outcomes of this experimental study showed that they remain competitive compared with the outcomes from the state-of-the-art approaches on the large and well-known re-identification datasets.

For further improvements, there is a plan to use an Adam as optimizer with the proposed model. There will be also another plan to investigate other CNN architecture that are frequently used for person re-identification task, for instance Densenet121, and Part-based Convolutional Baseline (PCB) models.

REFERENCES

[1]   Zheng, L., Y. Yang, and A.G. Hauptmann *Person Re-identification: Past, Present and Future*. arXiv e-prints, 2016.

[2]   He, K., et al. *Deep Residual Learning for Image Recognition*. arXiv e-prints, 2015.

[3]   Krizhevsky, A., I. Sutskever, and G. E. Hinton, *ImageNet Classification with Deep Convolutional Neural Networks.* Neural Information Processing Systems, 2012. **25**.

[4]   Simonyan, K. and A. Zisserman *Very Deep Convolutional Networks for Large-Scale Image Recognition*. arXiv e-prints, 2014.

[5]   Szegedy, C., et al. *Going Deeper with Convolutions*. arXiv e-prints, 2014.

[6]   Xiong, F., et al. *Good practices on building effective CNN baseline model for person re-identification*. in *Society of Photo-Optical Instrumentation Engineers (SPIE) Conference Series*. 2019.

[7]   Chang, X., T.M. Hospedales, and T. Xiang *Multi-Level Factorisation Net for Person Re-Identification*. arXiv e-prints, 2018.

[8]   Si, J., et al. *Dual Attention Matching Network for Context-Aware Feature Sequence based Person Re-Identification*. arXiv e-prints, 2018.

[9]   Deng, J., et al. *ImageNet: A large-scale hierarchical image database*. in *2009 IEEE Conference on Computer Vision and Pattern Recognition*. 2009.

[10]   Ruder, S. *An overview of gradient descent optimization algorithms*. arXiv e-prints, 2016.

[11]   Liao, S., et al. *Person re-identification by Local Maximal Occurrence representation and metric learning*. in *2015 IEEE Conference on Computer Vision and Pattern Recognition (CVPR)*. 2015.

[12]   Mignon, A. and F. Jurie. *PCCA: A new approach for distance learning from sparse pairwise constraints*. in *2012 IEEE Conference on Computer Vision and Pattern Recognition*. 2012.

[13]   Gray, D. and H. Tao. *Viewpoint Invariant Pedestrian Recognition with an Ensemble of Localized Features*. 2008. Berlin, Heidelberg: Springer Berlin Heidelberg.

[14]   Sun, Y., et al. *SVDNet for Pedestrian Retrieval*. arXiv e-prints, 2017.

[15]   Yu, R., et al. *Divide and Fuse: A Re-ranking Approach for Person Re-identification*. arXiv e-prints, 2017.

[16]   Szegedy, C., et al. *Rethinking the Inception Architecture for Computer Vision*. arXiv e-prints, 2015.

[17]   Huang, G., et al. *Densely Connected Convolutional Networks*. arXiv e-prints, 2016.

[18]   Hermans, A., L. Beyer, and B. Leibe *In Defense of the Triplet Loss for Person Re-Identification*. arXiv e-prints, 2017.

[19]   Zhao, L., et al. *Deeply-Learned Part-Aligned Representations for Person Re-Identification*. arXiv e-prints, 2017.

[20]   Li, W., X. Zhu, and S. Gong, *Harmonious attention network for person re-identification.* CVPR, 2018. **1**.

[21]   Zhong, Z., et al. *Random Erasing Data Augmentation*. arXiv e-prints, 2017.

[22]   Ioffe, S. and C. Szegedy *Batch Normalization: Accelerating Deep Network Training by Reducing Internal Covariate Shift*. arXiv e-prints, 2015.

[23]   Srivastava, N., et al., *Dropout: A Simple Way to Prevent Neural Networks from Overfitting.* Journal of Machine Learning Research, 2014. **15**: p. 1929-1958.

[24]   Zheng, L., et al. *Scalable Person Re-identification: A Benchmark*. in *2015 IEEE International Conference on Computer Vision (ICCV)*. 2015.

[25]   Zheng, Z., L. Zheng, and Y. Yang *Unlabeled Samples Generated by GAN Improve the Person Re-identification Baseline in vitro*. arXiv e-prints, 2017.

[26]   Ristani, E., et al. *Performance Measures and a Data Set for Multi-Target, Multi-Camera Tracking*. arXiv e-prints, 2016.

[27]   Li, W., et al. *DeepReID: Deep filter pairing neural network for person re-identification*. in *Proceedings of the IEEE Computer Society Conference on Computer Vision and Pattern Recognition*. 2014.

[28]   Felzenszwalb, P., D. McAllester, and D. Ramanan, *A discriminatively trained, multiscale, deformable part model.* IEEE CVPR, 2008: p. 1-8.

[29]   Zhong, Z., et al. *Re-ranking Person Re-identification with k-reciprocal Encoding*. arXiv e-prints, 2017.

[30]   Sun, Y., et al. *Beyond Part Models: Person Retrieval with Refined Part Pooling (and a Strong Convolutional Baseline)*. arXiv e-prints, 2017.

[31]   Bai, S., X. Bai, and Q. Tian *Scalable Person Re-identification on Supervised Smoothed Manifold*. arXiv e-prints, 2017.

[32]   Wang, Y., et al. *Resource Aware Person Re-identification across Multiple Resolutions*. arXiv e-prints, 2018.

[33]   Zhong, Z., et al., *Camera style adaptation for person re-identification.* CVPR, 2018: p. 5157-5166.

Aggregation of Multi-Stakeholder Preferences on Feature Models

A. KILIÇ[1] and A. ARSLAN[2]

[1] Konya Technical University, Konya/Turkey, akilic@ktun.edu.tr
[2] Enelsis Industrial Electronic Systems, Konya, Turkey, ahmetarslan@selcuk.edu.tr

Abstract - **Feature models are one of the essential techniques to manage variability and commonality for modeling the attributes of a software product line (SPL). When building an SPL, as in most practical cases, there exist multiple stakeholders with their preferences on various and optional features. In this paper, we propose using fuzzy integral operators to integrate various preferences of stakeholders in SPL. The proposed method aims to aid multi-stakeholder feature model configuration which is known to be a laborious, error-prone and time-consuming activity.**

Keywords - **Software product lines, feature models, fuzzy integral.**

I. INTRODUCTION

A Software Product Line (SPL) is a set of software systems of a domain, which share some common features but also have significant variability. SPL engineering aims to support the structured reuse of a wide range of software artifacts, including requirements, design, code, and test cases [1, 2]. Feature models are one of the most essential techniques to manage variability and commonality for modeling the attributes of an SPL [12]. Feature models are used to configure software products of a product line by selecting a set of features of a model. Selected features, in configuration activity, must respect model constraints to get valid products. As permutation of valid products of a feature model may be large, configuring a feature model, consequently, may also be hard, error-prone and time-consuming activity. Furthermore, this configuration process will be more complicated if there exist not only single stakeholder but also multiple stakeholders which geographically distributed [3, 19, 22]. Even there are many studies carried out for modeling, analyzing and configuration [4, 12], they do not focus on practical cases when there are multiple stakeholders having influences on the same product. However, in [19], they proposed giving preferences to different stakeholders, and a meta-model providing concepts to create a stakeholder configuration, which consists of hard and soft constraints among features. They used the social choice theory that is a single-winner voting system to make considerable group recommendations. Nevertheless, in order to configure a feature model to build a valid and preferred product by taking different stakeholders' preferences into consideration, instead of putting one winner forward, each stakeholders' considerations needed to combine with others. When there exist multiple sources, and if the goal is the integration of these sources, similar to human process, fuzzy integral operator will be a considerable method [6, 7, 18, 20].

In this paper, we propose a novel approach to improve configuration activity using fuzzy integral operators to aggregate all preferences of multiple stakeholders on optional features in a feature model.

II. BACKGROUND AND RELATED WORK

2.1 Feature Models

In [14], Kang et al. define features as the attributes of a system that directly affect end-users, and describe a feature model (FM) as a representation of the standard features of a family of systems in the domain and relationships between them. Feature models are simply explained as a compact representation of the products of an SPL [11]. They define the valid combinations of features in a domain.

Feature models of SPLs are arranged in a tree-like structure containing the relationships among features in a hierarchical manner. These models can be represented graphically (e.g., linking dependent features with a dependency arrow) or by textual annotations. In basic feature models, decomposition relationships and cross-tree relationships are used to represent relationships among features. Decomposition relationships determine the type of relationship between a parent feature and its children and include four relations: *mandatory, optional, alternative*, and *or*. Cross-tree relationships are used to specify cross-tree constraints, and include the relationships requires and excludes [12]. For instance, in Figure 1, there exists "DistributedFramework *requires* Networking" cross-tree relationship between two features, and "PhysicalModels must include Ownership" parent-child *mandatory* decomposition rule. "CGF" (Computer Generated Forces), "DistributedFramework" and "Networking" features are optional features. "HLA: High-Level Architecture", "DDS: Data Distribution Service" and "TENA: Test and Training Enabling Architecture" features are the alternatives of the "Distributed Framework" and just one of them can be included. However, according to the definition of *or* decomposition rule, any subset of {"Helicopter", "Aircraft", "Unmanned"} features may be included in final configuration or product.

Some features may be abstract that cannot be a part of the configured product or may be concrete similar to the object-oriented paradigm. For a complete formal definition of the feature models and detailed survey on basic and extended feature models, we refer the reader to [10, 14, 3].
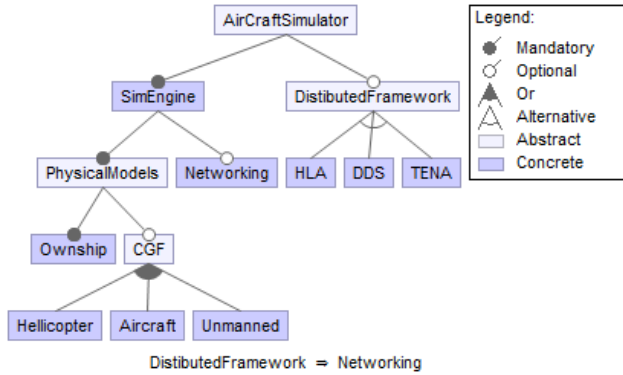
Fig. 1 Feature Model of an Aircraft Simulator.

Even basic feature models can be used in many applications in SPL, there are various extensions to handle domain problems and to meet related requirements. Related to this, Robak et al. [8] presented the employment of fuzzy logic in feature models for SPLs. They introduced the fuzzy weights of some variable features and showed some basic operations on them. Early efforts include [8, 4, 13, 15, 17], where a fuzzy logic description of costumer profiles and domain constraints is added to feature models. "Encourages" and "discourages" soft constraints have been proposed for feature models in [15]. However, these are used only to generate graphical decorations of the feature model. They did not consider stakeholders' preferences. In [16], Czarnecki et al. describe probabilistic feature models. He stated that features can be related by a probability space (PSPACE) describing probabilities of combined selection of features. In [17], Bagheri et al. describe the use of fuzzy-based soft constraints to model a stakeholder's preferred configurations. This approach differs from ours because it does not focus on multiple stakeholders having different preferences on particular feature set.

2.1 Fuzzy Integral

When building and configuring consistent feature models, system engineers, configuration managers or stakeholders which are responsible for modeling the SPL should make a decision on how different stakeholders have an influence upon alternatives and optional features, and they should aggregate all sentiments of different stakeholders on the same feature. From decision-making viewpoint, sentiments as satisfaction degrees or preferences to be aggregated are represented as fuzzy values [18]. Within aggregation operators, fuzzy integrals are known to be one of the most powerful and flexible functions as they permit the aggregation of information under different assumptions on the independence of the information sources [5].

Fuzzy integral is a nonlinear fusion method based on fuzzy intensity [18]. It combines different information considering the degree of importance or preference of components. Fuzzy integrals combine the data supplied by several information sources according to a fuzzy measure. This fuzzy measure, that represents the background knowledge on the information sources, is a set function from the set of information sources into an appropriate domain (e.g. the [0, 1] interval). Typically, this fuzzy measure represents the importance, preference, weight or relevance of the sources when computing the aggregation [5].

There are two widely used versions of fuzzy integrals: Sugeno [7] and Choquet [21] fuzzy integrals. Sugeno fuzzy integral version is the nonlinear function defined on the fuzzy measure, and it eliminates the effect of the secondary decision factors [20]. Compared with the weighted average, it enhances the effect of the main factors but completely ignores the secondary factors. Choquet fuzzy integral, however, takes various factors into consideration in order to avoid possible side effects of Sugeno fuzzy integral.

Sugeno [5, 7] first introduced the set functions using monotonicity to replace additivity called fuzzy measures. If X is a finite set of sources, i.e., $X = \{x_1, x_2, \cdots, x_k\}$, then the σ-algebra set generated by is $\{\emptyset, \{x_1\}, \{x_2\}, \{x_1, x_2\} \cdots, X\} = \Omega$.

A fuzzy measure, in the case of finite sets, is defined as a function $g : \Omega \to [0,1]$, which satisfies the following [8]:

1. $g(\emptyset) = 0, g(X) = 1$
2. $g(A) < g(B)$ *if* $A \subseteq B \subseteq X$
3. If $\{A_i\}_{i=j}^{\infty}$ is an increasing sequence of the measurable set, then
   $$\lim_{i \to \infty} g(A_i) = g(\lim_{i \to \infty} A_i).$$

Sugeno [6, 7, 4] also introduced the measure of the union of two disjoint subsets called g_λ − fuzzy measure, satisfying the following additional property: for all $A, B \subset X$ and $A \cap B = \emptyset$,

$$g(A \cup B) = g(A) + g(A) + \lambda g(A) g(B) \quad (1)$$

Let $X = \{x_{i1}, x_{i2}, \cdots, x_{im}\}$ be a finite set, and let $g^i = g(\{x_i\})$. The mapping $x_i \to g^i$ is called a fuzzy density function. λ value can be calculated by solving the following polygon.

$$\lambda + 1 = \prod_{i=1}^{n} (1 + \lambda g^i) \text{ and } \lambda > -1 \quad (2)$$

For a fixed set $g^i, 0 < g^i < 1$, there is exclusive $\lambda \in (-1, +\infty)$ and $\lambda \neq 0$. Hence, if we know the fuzzy densities g^i for $i = 1, \ldots n$, the g_λ − fuzzy measure can be

constructed. The fuzzy density value g^i can be regarded as the degree of importance of some source x_i towards the final evaluation.

Definition 1 Let g be a fuzzy measure on $(X, 2^X)$, h is a collection of input sources. Then, the Fuzzy integral of *Sugeno* version:

$$\int_S h \circ g = S_g(h) := \bigvee_{i=1}^{n} \left(h(x_{\pi(i)}) \wedge g(A_i) \right), \quad (3)$$

where $\wedge$ denotes the minimum and $\vee$ denotes the maximum, $h(x_{s(i)})$ indicates that the indices have been permutated and reordered so that

$$h \xrightarrow{\pi} h(x_{\pi(1)}) \geq \cdots \geq h(x_{\pi(n)}),$$
$$A_i = \left\{ x_{\pi(1)}, \cdots, x_{\pi(i)} \right\}_{i=1}^{n}$$

Definition 2 Let g be a fuzzy measure on $(X, 2^X)$, h is a collection of input sources. The *Choquet* Fuzzy integral of a function:

$$\int_C h \circ g = \sum_{i=1}^{n} \left(h(x_{\pi(i)}) \left[g(A_{(i)}) - g(A_{(i-1)}) \right] \right) \quad (4)$$

where $g(A_0) = 0$ and indices have been permutated and reordered as in Sugeno integral version.

Fuzzy integrals can be interpreted as a fuzzy expectation, or the maximum degree of consistency between two opposite trends or between objective evidence with the expectation affected by stakeholders' preferences and weights.

III. Motivating scenario

The features of software family members may vary according to the needs of particular stakeholders (i.e. developers, managers, experts, etc.). Similarly, the assessment of what will be common and what will be variable features of an application may result from particular needs and strategies. The same feature or feature group may be prioritized or weighted by different stakeholders.

In this section, in order to motivate and illustrate our work, we present an Aircraft Simulator case-study involving multiple stakeholders which have influenced the system in different views. An aircraft simulator's simplified feature model is shown in Figure 1, and different stakeholders having different preferences on a feature is shown in Figure 2. Although an aircraft simulator feature model is naturally much more complex and has many features, we have presented only a few features in order to focus on suggested fuzzy integral method.

As shown in Figure 1, the aircraft simulator system will consist of simulation engine and the aircraft's dynamic model as mandatory features. With these basic features, aircraft simulator can be built as standalone simulator. Similarly, simulator may have features with computer-generated forces which can be a subset of {"Aircraft", "Helicopter",

"Unmanned"}. Hence these features are represented as or-features. However, by adding distributed framework capability and networking feature because of "require" (or implies) cross-tree constraint, and selecting one of the HLA, DDS or TENA, a distributed aircraft simulation will be configured. Table 1 shows stakeholders' preferences on distributed framework alternatives and three stakeholders' different priority values as fuzzy numbers. For example, developers, managers and marketing experts as stakeholder groups (SH1, SH2 and SH3 respectively) may have different weights and importance factors.
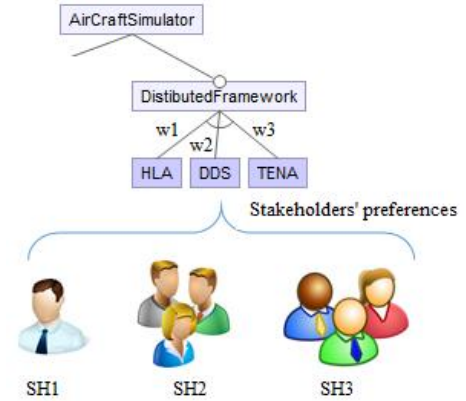
Fig. 2 Stakeholders(SHs) having preferences on alternatives of "*DistibutedFramework*" feature

Table 1 Stakeholders' preferences on the alternative feature.

Stakeholder	Importance of Stakeholder (g)	HLA (w1)	DDS (w2)	TENA (w3)
SH1	0.2	0.8	0.3	0.3
SH2	0.3	0.7	0.1	0.2
SH3	0.1	0.4	1.0	0.1

Table 2 shows integration results calculated by Sugeno and Choquet integrals using equations (3) and (4) respectively. Note that λ=3.109 value is obtained by solving the polynomial equation (2), and *g*-set is calculated with this λ by using equation (1).

Table 2 Aggregated values of alternative features

Integral Method	HLA (w1)	DDS (w2)	TENA (w3)
Sugeno	0.687	0.3	0.2
Choquet	0.626	0.242	0.189
Weighted Average	0.683	0.317	0.217

IV. CONCLUSION

When building an SPL, as in most cases, there exist multiple stakeholders with their preferences on various and optional features. Each stakeholder who has different importance factor will have their own expertise, preferences, and priorities from their viewpoints with conflicts. Hence, in order to configure a feature model to build a valid product, different stakeholders' preferences are needed to combine. In this paper, we have proposed using fuzzy integral operator to integrate all various

preferences of multiple stakeholders on optional features in feature model representation for an SPL. As future work, fuzzy integral operator may also be considered to combine soft constraints or to evaluate feature attributes when the feature model is needed to optimize multiple stakeholders' particular requirements.

REFERENCES

[1] Apel, S., Kästner. C., "An overview of feature-oriented software development", Journal of Object Technology (JOT), 8(5):49–84, 2009.

[2] Borba, P., Teixeira, L., Gheyi, R., "A theory of software product line refinement", Theor. Comput. Sci., 455:2–30, 2012. DOI:10.1016/j.tcs.2012.01.031

[3] Czarnecki, K., Helsen, S., Eisenecker, U. W., "Staged configuration through specialization and multilevel configuration of feature models.", Software Process: Improvement and Practice,10(2):143–169, 2005.

[4] Schroeter, J., Lochau, M., Winkelmann, T., "Multi-perspectives on feature models", Lecture Notes in Computer Science, 7590 LNCS, 2012. DOI:10.1007/978-3-642-33666-9_17

[5] Torra, V., Narukawa, Y. "The interpretation of fuzzy integrals and their application to fuzzy systems", International Journal of Approximate Reasoning, 2006.

[6] Sugeno, M., "Fuzzy measures and fuzzy integrals: a survey.", Fuzzy automata and decision processes:89–102, 1977

[7] Sugeno, M., "Theory of Fuzzy Integrals and Its Applications", Tokyo Inst. of Technology Tokyo, 1974

[8] Robak, S., Pieczynsky, A., "Employing fuzzy logic in feature diagrams to model variability in software product-lines", 10th IEEE Int.Conf. and Workshop on the Engineering of Computer-based Systems, 2003

[9] Durán, A., Benavides, D., Segura, S., Trinidad, P., Ruiz-Cortés, A. "FLAME: a formal framework for the automated analysis of software product lines validated by automated specification testing". Software & Systems Modeling, 2015 DOI:/10.1007/s10270-015-0503-z

[10] Schobbens, P., Trigaux, J.C., Heymans, P., Bontemps, Y., "Generic semantics of feature diagrams", Computer Networks 51(2), 456–479, 2007

[11] Segura, S., Benavides, D., Ruiz-Cortés, A., Trinidad, P., "Automated merging of feature models using graph transformations", Generative and Transformational Techniques in Software Engineering II, Springer Berlin Heidelberg, 2008

[12] Karataş, A. S., Oğuztüzün, H., Doğru, A. "Mapping extended feature models to constraint logic programming over finite domains.", Software Product Lines: Going Beyond. Springer Berlin Heidelberg, 2010

[13] Noppen, J., van den Broek, P., Weston, N., Rashid, A. "Modelling Imperfect Product Line Requirements with Fuzzy Feature Diagrams", In D. Benavides, A. Metzger, & U. Eisenecker (Eds.), 3rd Int. Workshop on Variability Modelling of Software-intensive systems: VaMos, 2009

[14] Lee, K., Kang, K. C., Lee, J. "Concepts and guidelines of feature modeling for product line software engineering", In Software Reuse: Methods, Techniques, and Tools. Springer Berlin Heidelberg, 2002

[15] Wada, H., Suzuki, J., Oba, K., "A Feature Modeling Support for Non-Functional Constraints in Service Oriented Architecture", In IEEE Int. Conf. on Services Computing (SCC 2007), 2007

[16] Czarnecki, K., She, S., Wasowski, A, "Sample Spaces and Feature Models: There and Back Again", In Proceedings of the 12th Int. Conf. on Software Product Lines, 2008.

[17] Bagheri, E., Di Noia, T., Ragone, A., Gasevic, D., "Configuring software product line feature models based on stakeholders' soft and hard requirements", In Proceedings of the 14th Int. Conf. on Software Product Lines: Going Beyond, SPLC'10, Berlin, Heidelberg. Springer-Verlag, 2010

[18] Auephanwiriyakul, S., Keller, J., Gader, P. "Generalized Choquet Fuzzy Integral Fusion" Information Fusion, Vol. 3, No. 1, 2002

[19] Stein, J., Nunes, I., Cirilo, E., "Preference-based feature model configuration with multiple stakeholders." In Proceedings of the 18th Int. Software Product Line Conf., ACM, 2014

[20] Wang, H., Fan, T., et.al., "Fuzzy Integral Based Information Fusion for Water Quality Monitoring Using Remote Sensing Data", Int. J. Communications, Network and System Sciences, DOI:10.4236/ijcns.2010.39098 , 2010

[21] Chiang, J. H.,"Aggregating Membership Values by a Choquet-Fuzzy-Integral Based Operator," Fuzzy Sets and Systems, Vol. 114, No. 3, 2000

[22] Junior, C. M., Cirilo, E., Lucena, C., "Assisted user-guidance in collaborative and dynamic software product line configuration", In CIbSE11, 2011.

Observations on the Evaluation of Dorsal Hand Vein (DHV) Recognition and Identification

K. ALASHIK[1], S. HUSSIN, and R. YILDIRIM
[1]Yildirim Beyazit University, Ankara/Turkey, k_elashek@yahoo.com
[1]Yildirim Beyazit University, Ankara /Turkey, eng.saleh.hussin@gmail.com
[1]Yildirim Beyazit University, Ankara /Turkey, remzi1963@gmail.com

Abstract - **Despite the fact that there is a demand of the optimal security framework nowadays; the dorsal venous system is a system of veins in the shallow belt on the dorsum of hand-shaped by the dorsal metacarpal veins. It is found on the back of the hand and offers to ascend to veins, for instance, the cephalic vein and the Dorsal vein. Biometrics validation is a sectional domain utilized to enhance the general self-determinations domains communicated worry over security as well as characteristic issues (Sontakke et al., 2017). This observational research will move forward on observing the electronic database to review diverse methods utilized for designing the framework has been discussed in this paper. A dorsal hand vein (DHV) recognition framework consists of the following steps, for instance, image acquisition from the database as well as post-processing, pre-processing, segmentation, finding of the region of interest, extraction of DHV pattern features as well as algorithm of DHV. Several models are utilized to enhance the accuracy as well as real-time of DHV authentication and the utilization of neural networks for the final evaluation of the testing sample as well as training samples to identify an individual has been presented in Table.A-1.1., Table.A-1.2. as well as Table.A-1.3. In addition, an outcome of this observational study will be beneficial for organizations and firms even individuals that seeking for ensuring privacy and security. In addition, this study will move to implements the accuracy compression of the Real-time DHV biometric identification utilizing faster neural networks in future.**

Keyword: Biometrics, Physical shape, Dorsal hand vein, Vein biometric feature, biometric identification framework, dorsal hand vein pattern, High security, system recognition, Dorsal hand vein recognition and identification , Feature Extraction.

I. INTRODUCTION

Recognizing an individual is an essential to recognize individuals identi-fication. Distinguishing proof through biometric remains a superior way since it partners with the individual, not with data going starting with one spot then onto the next (Alasadi and Dawood, 2017); (Sontakke et al., 2017). Moreover, a hand is a prehensile, multi-fingered member situated toward the finish of the lower arm or fore limb of primates, for instance, people. The DHV framework of the hand is a framework of veins in the shallow belt on the dorsum of hand framed by the dorsal metacarpal veins. It is found on the back of the hand and offers to ascend to veins, for example, the cephalic vein and the basilic vein (Sontakke et al., 2017). Furthermore, biometrics verification remains a developing domain in which common freedoms clusters communicated worry over protection as well as character issues (Sontakke et al., 2017). At present, biometric DHV guidelines are in procedure and biometric industry measures are being had viewed as two principle includes finishing focuses and bifurcation focuses to remove vein highlights. The highlights of the length of the vein; thickness; shape; as well as circulation of the veins remained explored to locate the most proper portrayal for the vein designs in terms of advantages and disadvantages (Sontakke et al., 2017) as presented in Table.1.1.; (Charaya and Singh, 2018). The physical state of the subcutaneous vascular tree of the back of the hand contains data that is fit for personality outcome (Badawi, 2006) which is tantamount to this investigation work. The state of the finger vein examples and its utilization for distinguishing proof (Prabu, 2017). The DHV biometrics rule is a noninvasive, automated examination of subcutaneous vein structures in the back of a hand to check the personality identification of people for biometric applications. Wiener filter as well as Smoothing filter to improve the efficiency implementation of DHV pictures (Khan, 2015). Sivakumar, (2019) have declared that the investigation on the false acceptance rate (FAR); False-Non-Match-Rate (FNMR); False Match Rate (FMR); false rejection rate (FRR); Failure to acquire (FTA) as well as Failure to enroll (FTE) (Obaidat et al., 2019). In addition, until this time, there has been no biometric verification methods that can fulfill and satisfy all these DHV features as well as requirements.
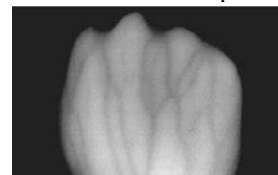
Figure.1.1. Hand veins image (Badawi, 2006).

In fact, biometric is a computerized strategy for perceiving an individual dependent on quantifiable organic as indicated by

anatomical and physiological and conduct attributes. The need the biometric framework since, presently we are living in a worldwide society of progressively frantic and unsafe individuals who can't be believed dependent on recognizable proof records, personality criminals take PIN, for example, date of birth to pull back cash from records (Sharavanan, 2016). Furthermore, DHV framework is the distinguishing proof of the individual by perceiving the vein design displayed in the front and back of the hand (Sudhakar et al., 2017). An expanding request to receive the biometric geek to limit potential security hazards, the a purchaser level biometric framework for programmed physical access control (Wang et al., 2015). In addition, through advancement of a close infrared imaging gadget for biometric procurement of DHV, examples and calculation effective picture handling strategies, they additionally announced that the proposed framework is appeared to have a scope of alluring activity attributes for certifiable utilization, which incorporate solid in recognizable proof, advantageous to utilize, high in security, quick accordingly, low in expense, and basic for establishment (Wang et al., 2015); (Benziane and Benyettou, 2016).

1.1.1.
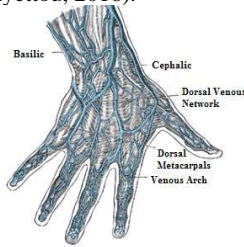
Figure.1.1. Dorsal Hand Vein Authentication adapted from (Sontakke et al., 2017).

1.1.3.

This observational study is systematized as follows: firstly Literature review in the second Section. In the third Section, the observational study. In the fourth section an outcome of the observational study. In the fifth section the conclusion.

II. LITERATURE REVIEW

2.

Biometrics verification remains an important domain in which interior liberties clusters express concern over privacy as well as identity issues. In the present day, biometric laws and regulations are in process and biometric industry standards are being tested (Sontakke et al., 2017). According to Sontakke et al., (2017) during preprocessing, Zhao et al. (2007) have utilized Match filter, Wiener filter and Smoothing filter to enhance the quality of DHV pictures. Moreover, features to reduce the dimension of the vein matrix. Moreover, to test the performance of biometric security framework, performance measures are utilized. Sanchez-Chih-Bin Hsu et al. (2012) have utilized PCA and LDA. The main objective of this techniques remains to utilize the linkage of local as well as a global INFO for DHV identification. Inshirah Rossan et al., (2014) has utilized diverse preprocessing practices that causes well defined extracted vein pattern that gives better performance and leads to an extra secure biometric authentication framework. According to Raghavendra et al., (2015) the usage of a DMK 22BUC03 monochrome CMOS camera with a resolution of 744×480 pixel for image capture which is suitable for DHV identification framework. Furthermore, the camera is equipped with a T3Z0312CS lens with a focal length of 8mm. In addition, to obtain the vein pattern, a region of interest (ROI) was defined

utilizing eight diverse feature extraction schemes that schemes include both local and global feature representation. In addition, Yiding wang et al., (2015) have explored the DHV preprocessing phase. In this observational research the vein pattern remained segmented based on simple Thresholding utilizing gray-level distribution.

According to Rossan and Khan, (2014) the Bosphorus DHV Database remains intended for several studies on biometry based DHV patterns of the hand. Furthermore, the DHV data is acquired utilizing NIR imaging techy with a monochrome NIR CCD camera (WAT-902H2 ULTIMATE) equipped with an infrared lens. In addition, the back of the hand is irradiated via two IR light sources. The pictures have 300×240 pixel size with a gray-scale resolution of eight-bit.

III. THE OBSERVATIONAL STUDY

The evolution of dorsal hand vein systems
The biometrics dorsal hand vein systems advantages and disadvantage
This section will present the biometrics DHV systems is described in Table A-1.1. which is illustrated DHV systems according to each author and which sort of systems have been described via the author and the advantages of utilizing such kind of DHV systems, disadvantages are also presented in this section.
The dorsal hand vein systems practices and usage.
This section will represent the DHV systems practices relevant to the biometrics DHV systems practices in published papers (conferences, journals,..etc.) amongst 2006-2019. The described practices in Table A-1.2 which remains describing the DHV frameworks practices according to each author.
The dorsal hand vein methods and characteristics.
This segment represents the DHV frameworks as well as the biometrics practices that relevant to the biometrics DHV frameworks practices in published papers (books, conferences, journals) amongst 2006-2019. That the described practices in Table A-1.3 which remains describing the biometrics DHV frameworks practices according to each author, as well as when can be utilized according to the evidence of each author in any venture domain or business area.
Evolution scenario of the biometrics dorsal hand vein systems
The utilization of vein systems as a biometric techy was first designed in 1992. The utilization of vein systems as a biometric techy was first designed in (1992) initiative of the EU. The origin was in the usage and the practices of DHV in a wide area of security issue and implementation which are implemented in Table A-1.1., Table-A.1.2. and Table A-1.3 respectively.

I. CONCLUSION

After observing the electronic database and according to several research papers, this study has documented that the overall declaration of dorsal hand Vein (DHV) platforms and its utilized approaches. In addition, each technique is considered to document several advantages and disadvantages as papers limitations. Furthermore, several numbers of DHV system recognition approaches has been reviewed. To sum up, there is still a scope of further developments. In fact, several authors obtained Global and Local feature by utilizing diverse approaches, for instance, ROI, RPN etc., In the future, we are trying to test the implementation of the utilization of Global feature for DHV applications.

APPENDIX A.1.1

Table A.1.1: The biometrics dorsal hand vein systems advantages and disadvantages.

The system	Description	Advantages	Disadvantages	Authors and years
A dual-modal biometrics and Graph Matching (BGM).	Learning algorithm integrating palmprint as well as DHV.	1 High accuracy as well as reliability and Liveness detection. 3. Recognize palmprint and DHV 4. Obtain three discriminant features amongst two DHV features. 5. The best experimental outcomes with Equal Error Rate equal to 0 6.Deal with the risks of complex environment data. 7. Noise eliminated as well as Reduce the quantization error transforming from the output layer to the binary code.	Storage as well as INFO retrieval	(Zhong et al., 2018) (Lajevardi et al., 2013) (Zhong et al., 2019)
A novel DHV.	The framework consists of several stages; denoising of the input picture utilizing Laplacian Scale Mixture Modeling (LSM), ROI extraction from a denoised picture utilizing the valley point detection approach, contrast enhancement utilizing pyramid based edge-aware filtering approach, contrast limited adaptive histogram equalization, binarization, several serial morphological operations as well as authentication utilizing neural networks as well as support Vector Machine (SVM).	1. The identification development and differentiating individuals for security issue that counts 2. Provides better resolution of vein platform in the picture than visible light. 3.Extended for extra utilizers will yield alike success. 4. Utilizing a dorsal vein platform utilized in security objective. 5. Uniqueness, stability as well as strong immunity to forgery of the vein platform 6.Secure as well as reliable features. 7. More reliable, secure, accurate.	1. DHV geometry problems might arise with utilizers suffering from rheumatism. 2. The need of direct contact with the sensor. 3. This causes notable deterioration in performance, factories where good-quality fingerprints remain hard to obtain for the reason that of dirt, moisture oil from the finger, etc. 4. Acquired picture remains less contaminated.	(Tazim et al., 2018) (Jain et al., 2006) (Hawkes and Clayden, 1993)
NiBlack	The algorithm acquires a clean, one-pixel-width skeleton with little distortion after a series of processes: size as well as gray normalizing, Gaussian low pass as well as median filtering.	1.Improve the recognition ratio 2. Reduce the distortion of the vein skeleton. 3. It should be normalized to a standard picture with the equal mean as well as variance gray. 4. Suitable for being utilized for recognition as well as classification.	1.The size of vein gathering region at diverse time for a similar person. 2. It remains difficult to the determination with multiple pixels wide. 3. The DHV picture contains noise, the horizontal strip scanning noise. 4. The recognition outcome remains not good	(Li et al., 2010) (Chang and Lin, 2011) (Zhu et al., 2015)

Method	Description	Points	Limitations	Reference
DHV recognition approach based on Convolutional Neural Network (CNN)	The region of interest (ROI) of the required pictures remained extracted, contrast limited adaptive histogram equalization (CLAHE) as well as Gaussian smoothing filter algorithm were utilized, Reference-CaffeNet AlexNet and VGG depth CNN to extract image feature.	1. Uniqueness, even amongst the twins, there variance in the DHV; 2. Invariance, the DHV of human is constant; 3. Difficult to forge, the dorsal vein remains a kind of biological characteristic; 4. Detection approach remains friendly, as the dorsal vein to the internal features, 5. It remains difficult to be damaged. 6. CLAHE remains characterized via contrast limiting. 6. ROI of the picture is required to enhance the contrast processing. 7. The adaptive histogram calculates the neighborhood histogram and the corresponding transform function for each pixel in the picture 8. The bilinear interpolation remains utilized to speed up the calculation of the algorithm. 9. The feature extraction, the topology of the picture content, the sequence sorts, structure type are extracted as a characterization 10. Diverse filters can learn diverse features. 11. Decrease the connection between the convolution layers, reduce the size of the input data, minimize the complexity of the operation. 12. Increase in the network structure has improved the recognition rate.	1. Needs time to describe the adjustment of sub-parameters and cannot ensure the accuracy of expression and the selection of features. 2. The conventional histogram equalization algorithm is easy to cause the loss of picture's detail data, affect the effect of recognition. 3. Requires a lot of training dates.	(Wan et al., 20 (Wang and 2017) (Jalilian and 2019)
Region Proposal Network (RPN) shares full-picture convolutional features with detection netwo detection.	An RPN is a convolutional network that simultaneously predicts object bounds and abjectness scores at each position. The RPN remains trained end-to-end to generate high-quality region proposals, which remain utilized via Fast R-CNN for detection.	1. Reduced detection networks running time. 2. RPN remains utilized end-to-end to generate high-quality region proposals 3. Achieving detection accuracy on PASCAL VOC. 4. To accelerate proposal computation is to reimplement it for the GPU.	MS COCO datasets with only 300 prop per picture.	(Ren et al., 201 (Zhang et al., 2
The region interest (ROI)	To fix ROI to be in the same position in diverse palm-dorsum pictures to ensure the stability of the principal extracted vein features. It has significant influence on the accuracy of verification. It is difficult to fix the ROI at the same position in diverse palm- accuracy of verification.	1. The image contrast is higher than in the visible area 2. The quality of the image improves after noise reduction and normalization.	1. It is difficult to fix the ROI at the same position in diverse palm-dorsum pictures without utilizing a docking device to constrain the palm position 2. Not an edge-preserving technique.	(Heenaye and Subramanian, 2009) (Pour et al., 20

Table A.1.2: The DHV frameworks practices and usage.

The system	Practices	When can be utilized	Authors and years
A dual-modal biometrics Graph Matching (BGM)	Encoding approaches, structure-based methods, subspace-based approaches as well as machine learning approaches	DHV recognition	(Zhong et al., 2018) (Lajevardi et al., 2013) (Zhong et al., 2019)
A novel DHV.	1.NIR imaging remains suitable for revealing the pattern of the blood vessels underneath the skin.	Flourishing for huge number of population.	(Tazim et al., 2018) (Jain et al., 2006) (Hawkes and Clayden, 1993)
NiBlack	1.Utilizes a template to remove eight kinds of points which composes thinned lines with multiple pixels wide.	Feature values varying widely	(Li et al., 2010) (Chang and Lin, 2011) (Zhu et al., 2015)
DHV recognition based on convolutional neural network (CNN).	1. Outcomes with DHV recognition approach to verify the effectiveness as well as feasibility. 2.The platform requires a smaller size model which is necessary on the mobile platform. 3. CNN learn pictures in a small amount of preprocessing, as well as parameter transfer makes feature extraction efficient.	1.Utilizing filters to process the input data remains utilized for several sorts of feature extraction. The picture remains passed through a filter and a representative map remains obtained.	(Wan et al., 2017) (Wang and Wang, 2017) (Jalilian and Uhl, 2019)
Region Proposal Network (RPN) with the detection network	An algorithmic change measuring proposal to an elegant as well as effective solution.	Fast R-CNN for detection	(Ren et al., 2015) (Zhang et al., 2018)
The region of interest (ROI)	Hand region segmentation, for instance, region of interest localization and background elimination, smoothing and noise reduction, local thresholding for separating veins and the post-processing.	A biometric security issue	(Heenaye and Subramanian, 2009) (Pour et al., 2015)

Table A.1.3: The dorsal hand vein methods and characteristics.

The system	Characteristics	Methods	Authors and years
A dual-modal biometrics as a biometric Graph Matching (BGM).	Vein structure surrounding human bones as well as muscle tissues.	1.The maximum curvature point to extract the skeleton of blood vessels. 2.A sub graph of two pictures. 3.A feature-level fusion based on palm print and DHV. 4.Hamming distance as well as three indexes via BGM into one vector. 5.Support Vector Machine (SVM).	(Zhong et al., 2018) (Lajevardi et al., 2013) (Zhong et al., 2019)
A novel DHV.	A Convolutional Neural Network (CNN) building remains utilized. The database remains created as well as Multi-class SVM classifier remains trained as well as then utilized for verification purpose.	High level of Correct Recognition Rate (CRR), low False Acceptance Rate (FAR) as well as low False Rejection Rate (FRR).	(Tazim et al., 2018) (Jain et al., 2006) (Hawkes and Clayden, 1993)
NiBlack	1.Utilization of the open source code, the framework remains re-programmed, as well as chooses C-SVC model. 2.Radial basis Function, one-against-one for DHV recognition.	Support vector machines (SVMs) as well as the LIBSVM software package designed via Chih-Jen Lin for implementation.	(Li et al., 2010) (Chang and Lin, 2011) (Zhu et al., 2015)
DHV recognition with Convolutional Neural Network (CNN)	1. A great research value as well as wide application prospect. 2.It performs well in solving the problem like visual recognition, talking recognition, as well as natural language processing. 3.Deep learning as well as natural language processing as well as talking recognition, the low-level features into high-level characteristics, spatial correlation amongst diverse requirements.	CNN	(Wan et al., 2017) (Wang and Wang, 2017) (Jalilian and Uhl, 2019)
Region Proposal Network (RPN)	Full-picture convolutional Features with the detection network	RPN	(Ren et al., 2015) (Zhang et al., 2018)
The region of interest (ROI)	1.The 2th and 4th finger webs as datum points to define a square ROI. 2.The requirements point of vein pattern (FPVP) remain extracted 3.The FPVP locations, gray values of the FPVPs, as well as the distance between the FPVPs determine the temperature gradient as well as the gradient direction. 4.Multiresolution analysis remains applied to decompose the feature point pictures (FPI) into multiscale FPIs	ROI	(Heenaye and Subramanian, 2009) (Pour et al., 2015)

REFERENCES

Chang, C. C., & Lin, C. J. (2011). LIBSVM: A library for support vector machines. ACM transactions on intelligent systems and technology (TIST), 2(3), 27.

Heenaye, M. M. N. M., & Subramanian, R. K. (2009). A study of dorsal vein pattern for biometric security. University of Mauritius Research Journal, 15(1), 17-25.

Hawkes, P. L., & Clayden, D. O. (1993, September). Veincheck research for automatic identification of people. In Hand and Fingerprint Seminar at NPL (pp. 230-236).

Jalilian, E., & Uhl, A. (2019, January). Enhanced Segmentation-CNN based Finger-Vein Recognition by Joint Training with Automatically Generated and Manual Labels. In 2019 IEEE 5th International Conference on Identity, Security, and Behavior Analysis (ISBA) (pp. 1-8). IEEE.

Jain, A. K., Bolle, R., & Pankanti, S. (Eds.). (2006). Biometrics: personal identification in networked society (Vol. 479). Springer Science & Business Media.

Khan, M. H. M. (2015, May). Representation of dorsal hand vein pattern using local binary patterns (LBP). In International Conference on Codes, Cryptology, and Information Security(pp. 331-341). Springer, Cham.

Li, X., Liu, X., & Liu, Z. (2010, October). A dorsal hand vein pattern recognition algorithm. In 2010 3rd International Congress on Image and Signal Processing (Vol. 4, pp. 1723-1726). IEEE.

Lajevardi, S. M., Arakala, A., Davis, S. A., & Horadam, K. J. (2013). Retina verification system based on biometric graph matching. IEEE transactions on image processing, 22(9), 3625-3635.

Obaidat, M. S., Traore, I., & Woungang, I. (2019). Biometric-Based Physical and Cybersecurity Systems (pp. 165-187). Springer.

Prabu, A. J. (2017). A Biometric Recognition System for Human Identification Using Finger Vein Patterns. Int. J. Emerg. Trends Eng. Dev., 2(7), 62-79.

Pour, A. N., Eslami, E., & Haddadnia, J. (2015). A new method for automatic extraction of region of interest from infrared images of dorsal hand vein pattern based on floating selection model. International Journal of Applied Pattern Recognition, 2(2), 111-127.

Ren, S., He, K., Girshick, R., & Sun, J. (2015). Faster r-cnn: Towards real-time object detection with region proposal networks. In Advances in neural information processing systems (pp. 91-99).

Rossan, I., & Khan, M. H. M. (2014). Impact of changing parameters when preprocessing dorsal hand vein pattern. Procedia Computer Science, 32, 513-520.

Raghavendra, R., Surbiryala, J., & Busch, C. (2015, September). Hand dorsal vein recognition: Sensor, algorithms and evaluation. In 2015 IEEE international conference on imaging systems and techniques (IST) (pp. 1-6). IEEE.

Sivakumar, S. (2019). Biometric Authentication Techniques and Its Future. In Biometric Authentication in Online Learning Environments (pp. 122-149). IGI Global.

Sontakke, B. M., Humbe, V. T., & Yannawar, P. L. (2017). Dorsal Hand Vein Authentication System: A Review. International Journal of Scientific Research Engineering & Technology, 6(5), 511-514.

Tazim, R. J., Miah, M. M. M., Surma, S. S., Islam, M. T., Shahnaz, C., & Fattah, S. A. (2018, October). Biometric Authentication Using CNN Features of Dorsal Vein Pattern Extracted from NIR Image. In TENCON 2018-2018 IEEE Region 10 Conference (pp. 1923-1927). IEEE.

Wan, H., Chen, L., Song, H., & Yang, J. (2017, November). Dorsal hand vein recognition based on convolutional neural networks. In 2017 IEEE International Conference on Bioinformatics and Biomedicine (BIBM) (pp. 1215-1221). IEE

Wu, X., Gao, E., Tang, Y., & Wang, K. (2010, August). A novel biometric system based on hand vein. In 2010 Fifth International Conference on Frontier of Computer Science and Technology (pp. 522-526). IEEE.

Wang, J., & Wang, G. (2017). Hand-dorsa vein recognition with structure growing guided CNN. Optik, 149, 469-477.

Zhong, D., Li, M., Shao, H., & Liu, S. (2018, July). Palmprint and dorsal hand vein dualmodal biometrics. In 2018 IEEE International Conference on Multimedia & Expo Workshops (ICMEW) (pp. 1-6). IEEE.

Zhu, Q., Zhang, Z., Liu, N., & Sun, H. (2015). Near infrared hand vein image acquisition and ROI extraction algorithm. Optik, 126(24), 5682-5687.

Zhong, D., Shao, H., & Du, X. (2019). A Hand-based Multi-biometrics via Deep Hashing Network and Biometric Graph Matching. IEEE Transactions on Information Forensics and Security.

Zhang, X., Xu, W., Li, J., Wang, H., & Sun, Y. (2018, August). An automatic acquisition algorithm for power distribution line based on vehicle-mounted system. In Tenth International Conference on Digital Image Processing (ICDIP 2018) (Vol. 10806, p. 108066Q). International Society for Optics and Photonics.

Dynamic Analysis of Malware in Windows Operating Systems from Previously Captured Network Packets

B.RESHITI[1] , M.HAMITI[1] , B.SELIMI[1] and B.RAUFI[1]

[1] SEE-University, Tetovo/R. North Macedonia,
bresiti@gmail.com, m.hamiti@seeu.edu.mk, b.selimi@seeu.edu.mk, b.raufi@seeu.edu.mk

Abstract - **This research gives a basic introduction to malicious software applications by describing the infection vectors. Here, we have defined the layers of malware analysis with a distinction between static and dynamic analysis. Focal point was performing dynamic malware analysis over previously captured network packets over Windows XP Operating System by building a software platform or safe environment for malware analysis with required software tools and resources. In this research, we tried to determine a working practical solution to how the malware has to be analyzed with its constraints, which standard operating procedures shall be implemented and at least how a security expert should deal to minimize the security problems infected by malicious software codes.**

Keywords – **malware, static analysis, dynamic analysis, safe environment.**

I. INTRODUCTION

MALWARE is a unified name for all kinds of threats along with viruses, worms, Trojans, rootkits, ransomware, botnet. A computer virus attaches itself to a clean file and affects machines and cross automatically from one to another machine. A worm also flows automatically by installing itself once and then checks another machine to infect. Trojans named from mythical 'Trojan horse', a malware variety impersonate itself as a useful program but in fact loads malicious activities. Rootkits hide in kernel mode and act as a device driver. While ransomware encrypts files and requests ransom for decryption, botnet creates a network of infected machines controlled by an attacker. Malware is a sophisticated threat to the digital world, which is carried by software exploits. It is a complete strategy or tactical attack on how to run malware and in case of success, there are numerous combinations for additional infections. Dealing with malware requests developing cycle of analysis under special circumstances or so-called safe environments. In this paper, there is represented static and dynamic analysis. The main goal here is to run dynamic malware analysis in Windows operating system from previously captured network packets.

Most of the time AV (Anti-Virus) companies analyses hundreds of thousands of analyses of malware samples every day by providing machine learning approaches based on behavioral and signature indicators. Studying by performing static and dynamic malware analysis leaves a backdoor to generate different artificial intelligence implementations on malware detection, classification, and even elimination, in which relays the answer on dealing with cyber-related threads.

II. MALWARE ANALYSIS PRE-REQUISITES

An operating system is that enables services for software applications to run on a computer. An important task of an operating system is taking care of the communication between the software applications and hardware devices attached to your computer. Operating systems are large programs consisting of thousands of functions, which provide services of various kinds. Often called by events in the system, the functions perform a service when needed. [1]
It is hard to pin down what an operating system is other than saying it is the software that runs in kernel mode – and even that is not always true. Part of the problem is that the operating system performs two basically unrelated functions: providing applications programmers (and application programs, naturally) a clean abstract set of resources instead of the messy hardware ones and managing these hardware resources. [2]
As a host operating system for performing malware analysis here, we used Microsoft Windows XP service pack 3.
Windows XP is a *computer operating system* and *graphical user interface* (GUI), which enables you to work with a wide variety of programs on your computer, often simultaneously. Windows XP is itself a special computer program that communicates your instructions to the actual computer hardware and displays the results. [3]
Launched in August 2001, Windows XP has been the most popular version of Windows based on the number of copies sold. [1]
According to *Spiceworks' Network and Endpoint Security* report, one-third of businesses still operate at least one device running Windows XP, which reached the end of its extended support cycle way back in 2014. (Interestingly, the final variant

of XP, *Windows Embedded POSReady 2009*, only came out of support on April 2019. This variant of XP was used as a point-of-service operating system by – for example – shops. However many XP Home and Professional users were using a hack to receive security updates intended for this lesser-known XP variant. But alas, this has now come to an end.) Of course, Windows XP doesn't get updates anymore. Including security updates. This means as crooks learn about vulnerabilities in XP, there is nothing to stop them using those exploits against XP users. As such, using Windows XP in 2019 is really one of the biggest security faux pas' you can commit. [4]

Because of high popularity, easy, user-friendly GUI, high hit and very good traceable options from malicious codes Microsoft Windows XP will be the host operating system for malware analysis in this paper.

Malware mainly is classified into two categories:

1. H**ow it spreads** or propagates to get the targets;
2. How **it payloads** or actions that malware specimen performs once a target is reached.

Malicious applications **infection routine** consists of three different classes:

A. *Installation*
B. *Propagation*
C. *Payload*

All classes have their elements and attributes in which define prospective layout about malware behavior in machines. Malware could be traced through the analysis of processes, file systems, registries and auto-start mechanism of Microsoft Windows XP operating system. While executing each application there is an equivalent process or image of a file (application) running in the memory. The registry is a hierarchical database that contains information about the various settings used by the operating system. Here very important is to point out Windows XP Auto-start registry key modification locations as shown in *Figure 1*, which malware specimen writes its path and file name to be executed during startup services.
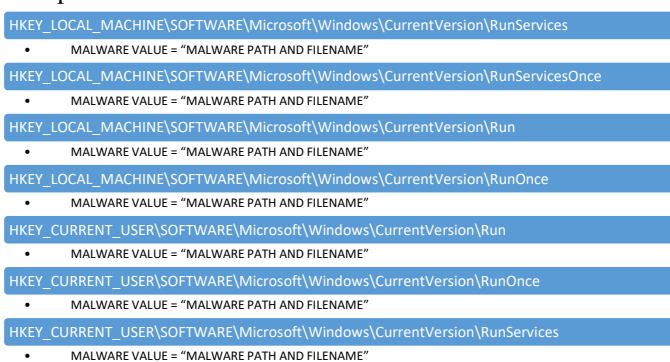
Figure 1, Common Windows XP Auto-start locations.

Exploring file system interaction can show all files that the malware creates or configuration files it uses. Malicious files are involved in nearly every major data breach and is causing growing problems for business and personal users. Microsoft Windows XP and other Microsoft Windows family of operating

systems executable file format is co-called **PE (Portable executable)** file, which consists of four sections:

- Headers - defines ho to execute a Win32 Portable Executable (PE) file;
- Sections – holds information about how a PE file is organized internally;
- Entry Point – is the starting point of program execution;
- Import Table – contains the list of functions imported by the program from dynamic-link libraries.

Most of the time, PE Files sections have pre-defined names, in which they are created while the file is compiled. The most common ones are:

- .text – Which contains the code of the file
- .rdata – Read-only data
- .data – Other data.
- .rsrc – The resource section, contain icons, menus, images, etc.

Most malware specimen it's obfuscated from their programmer using so-called packers. Before to go to malware analysis there is a need to be distinguished a packed or non-packed file. If a malicious file is packed then there is a need to be unpacked in order to extract more information while static malware analysis.

Figure 2. unpacked file versus .aspack packed file.

Before to start to analyze any malicious specimen there is a need to build a safe malware handling policy or at least to list some procedures. These procedures raise the consciousness dealing with infected specimen because it is very common while working with them you can be hit and infected. So in this topic, I listed the required safety procedures of malware handling:

- All samples should be compressed and password protected or encrypted.
- Physically transfer the Portable Device to an "Isolated Stand Alone System" for analysis.
- Once the Samples are loaded onto an isolated Stand Alone System, you may decompress the files and remove the password protection or encryption.
- You may then analyze the Samples
- Once you have completed your analysis, you must delete the Samples from the Isolated Stand Alone System by holding the "Shift" button and then pressing Delete or emptying the recycle bin or "deleted items" folder to ensure the completion of the delete process.
- Then verify that the Samples stored on the Portable Device are still compressed and password protected or encrypted, and delete the file from the Portable Device.
- Rebuild or revert the Isolated Stand-Alone System.

III.   STATIC MALWARE ANALYSIS

Static malware analyze is the analysis of malicious specimens without running or executing the code. This is usually done by determining the obfuscation of malware specimen if it is packed or not packed. If it is packed it is decompressed by various tools and techniques. Decompression leaves backdoor on malicious code in which various string searches follow dissecting detailed information about commands, IP addresses, e-mails, messages, etc, which happens during execution flow of specimen. Additionally, there is a digital signature calculation of hash value, which later can be compared with AV data hash sets.

Reliable analysis of malware requires access to infect a machine and system with malicious software piece and then using applied software monitoring tools to analyze its behaviors. To do and test malware pieces, here we used Windows XP installed as a guest operating system into an Oracle VirtualBox virtualization environment. Oracle **VirtualBox** is a free and suitable method to set a laboratory or a system that involves virtualization of software, which allows hosting multiple virtual systems in a single computer, each running a different operating system. [5].

After the successful configuration of Windows XP service pack 3 on Oracle Virtual Box v.4.3.40 environment lab, we infected our machine with a malware test sample with the name "*malware*". Right-clicking file properties of the malicious specimen, we get information about the file type that is an executable application, file description, location of the file, and information when the file is created. From this perspective of view, I know that this file is malicious but I don't know what behavior of sample has and I don't know what malicious activities do over my machine. So what I need to do is to get or extract more information from the file. With the help of tool **PEiD v.0.95** I can do more physical file analysis and file identification process. When I implement the tool I got the information shown in
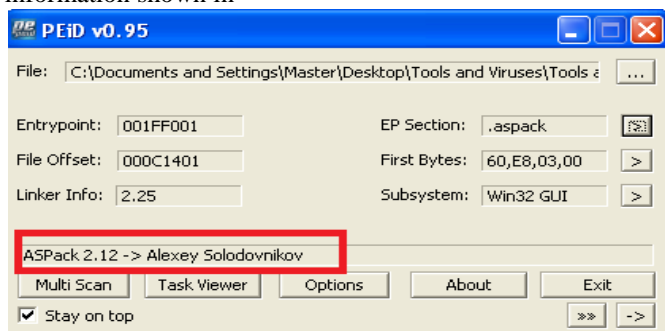
Figure 3. Detection packed malware with PEiD tool.

Information extracted over a malicious sample is a very useful and interesting indicator of the file itself. The redline block in Figure 3 shows that this sample is packed with ASPack packer. After representing the elements of packed files on manual checking for packed samples with help tool AspackDie vs 1.41, with left mouse clicking in which I selected the file and clicked

the OK button where packed specimen is unpacked to default name unpacked.exe.

Hereafter, we renamed the default output name to "*unpacked_malware1_aspackdie.exe*" to be better distinguished in further comparison. In comparison unpacked file "*unpacked_malware1_aspackdie.exe*" vs packed file "*malware1.exe*", We find out that unpacked file with size 2.02 MB is bigger than packed file and in fact, it has more user-readable information for malware analysis purpose.

With the help of **PEiD** tool, we extracted data information and verified that my malicious specimen **malware1.exe** imports the following 13 (thirteen) dynamic-link libraries (DLL's). Unpacked specimen **unpacked_malware1.exe_aspackdie.exe** imports 16 (sixteen) modules of DLL's.

In order to identify possible file behavior based on strings over our specimen, we used the Bintext v.3.0.3 tool. After the search from dozens of data we extracted some of strings such as CreateFileA, DeleteFileA, CopyFileA, FindFirstFileA, svchost.scr, "smpt.bhi.com.br", manyall@mail.com. Imported DLL functions say that test specimen tries to do modifications and searches for a file because not all the files have this ability. E-mail string tells that our malicious specimen is sending e-mail to *manyall@mail.com*, using the SMTP protocol in servers *bhi.com.br*. String svchost.scr is very famous in the malware community and it a tip that this specimen uses the Auto-start mechanism for persistence. Moreover, we validated our findings by getting the digital footprint of our malicious file using MD5 hash checksum with help hashmyfiles.exe tool and compared hash value with the online hash data set of VirusTotal.com.

When we repeated our steps over other malware samples we reached and confirmed (different AV findings) following findings:
- Malware samples static analysis have common characteristics such as:
  - Renamed sections in PE file structure,
  - compact or compressed content
  - Big difference between the virtual size and the raw data size of each section (except the section where decompression routines lie).
  - EntryPoint is not on the first section (for some samples)
  - No presence of a Digital Signature.

IV.   DYNAMIC MALWARE ANALYSIS

Dynamic analysis is the process of executing malware in a monitored environment to observe its behaviors. This technique can quickly yield information such as created files, created registry keys, contacted websites, and so on. If you're not an experienced IDA Pro user or simply don't have time to perform a thorough static analysis of the code, you can use dynamic analysis to get a quick initial perspective of the malware's capabilities. [6]

Here we used a scenario analyzing previously captured network packet with the file name **smtp.cap** and MD5 hash value **aff1528eaee1ea8d948192fac16d8db1** as a unique digital signature of the file. WireShark is a very comprehensive network traffic capture tool is. With the help of this tool, we browsed our sample to extract malicious attachment from an e-mail SMTP traffic and then run it to obtain suspicious files, processes, and registries. By implementing this cycle, we did the classification of our malicious application.

After analyzing **smtp.cap** file we found 474 captured packets. All packets have a number, timestamp, source the address where this packet is coming from, destination the address where this packet is going to, the protocol name, length of each packet and additional information about the packet content. While analyzing.

While analyzing packets we have found the following findings:

Suspicious communication between two IP addresses:

    1. IP address 10.10.5.5
    2. IP address 194.88.100.82

Host IP address 10.10.5.5 its private IP address from Class A, which is a separate set of addresses from companies, governments, etc. The second IP address 194.88.100.82 is out of range from private IP addresses with online Whois search found out that this IP address location and owner is a company in the USA. During cybercrime investigation, IP address information is very important because of its legal issuer where you can request data preservation for further ingestion.

Host and suspicious IP addresses are communicating using TCP (Transmission Control Protocol) and SMTP (Simple Mail Transfer Protocol). First, he established a connection between client IP address 10.10.5.5 sends SYN (Synchronization) flag to the server IP address 194.88.100.82. The server sends SYN-ACK (Synchronization – Acknowledged) flag and the client responds again ACK flag. After the connection is established, there is an e-mail exchange between the client and server through SMTP (a protocol responsible for delivery of mail). After filtering out just "SMTP" protocol we received 337 packets or 71.1% of total communication between the client and server.

By following TCP Stream selected in one direction of the conversation, from client 10.10.5.5 to the server 194.88.100.82, we have found a malicious email exchange between the victim's e-mail address sales@defsol.se as a sender and suspicious e-mail address rar.dutch@online.be, as a receiver. E-mail exchange happened with Subject "Incoming message" on 05 July 2004 19:50:49 and time zone -0800. Body content of exchanged e-mail tells that there is an application sent which is encoded bas64 (binary to text encoding scheme), and there is file name "Updates.com". After selecting attachment data content (see *Figure 4*) on TCP stream box and saved raw data as a new file using "extrack_email.**b64**", ".b64" as the file extension we extracted attachment. We decoded e-mail attachment using b64 tool by executing: "b64 –d extract_email.b64 update.exe", decoded extract_email.b64 file to binary file update.exe.

We used Installrite 2.5 tool and created a 'Snapshot' of changes prior to the installation and the changes after the execution of a program. After executing binary file update.exe on the Lab by following the safe malware handling policy, performed a current "Snapshot", and reviewed differences between two states with the following results:

The installation performed the following activity:

    6 files added
    2 files deleted
    4 files updated
    7 registry entries added
    0 registry entries deleted
    5 registry entries updated
    Installed 9/13/2019 12:18:10 PM
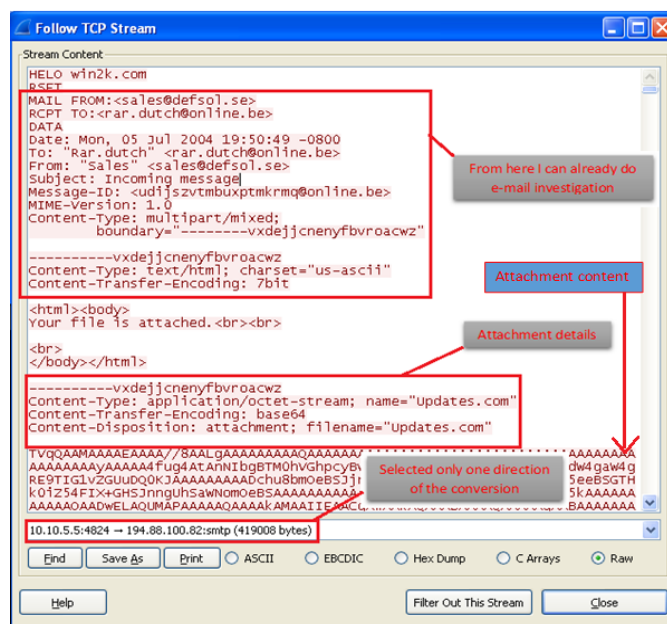
Figure 4. Following TCP stream using WireShark tool.

Followed by execution, the behavior of the malicious binary code resulted in several changes such as file deletion, adding, updating and registry entry manipulations. While installing or executing the application, file adding in some cases could be normal but file deletion without prompting to user can't be classified as normal Windows XP OS behavior. Likewise, in every installation in Windows OS's there are registry changes related to the application, but there is no registry entry adding, deleting and updating not related to the prior installation.

The following files:

    C:\WINDOWS\system32\loader_name.exe
    C:\WINDOWS\system32\loader_name.exeopen
    C:\WINDOWS\system32\loader_name.exeopenopen

are added to a very critical part of the Windows XP OS location *C:\WINDOWS\system32* where critical system files are stored. Malicious file "**loader_name.exe**" spreads itself by expanding with "**open**" string after the "**.exe**" to the disk memory.

Modified and added registry entries are so suspicious. It seems that malicious specimens, through registry manipulation in Windows XP, tried to read Internet Explorer history and

cookies. Additionally It ads malicious file and path to the registry. File "loader_name.exe" sets the following value: "C:\WINDOWS\system32\loader_name.exe" to the registry key **"HKCU\Software\Microsoft\Windows\CurrentVersion\Run"**. This confirms the theory of autostart locations that we mentioned in the first chapter. The malware specimen wants to run always when the system is on. Additionally, it attempts to create copies of itself in any folder that contains the characters **"shar"**. Additionally, we tested a malware specimen in client-server structure by date manipulation of the system and with the help of the WireShark tool we captured 1880 network packets. We filtered out captured .pcap file using "TCP" filter and we followed TCP stream (client to server) where I realized that my malicious specimen using TCP Port 53. Because port 53 is usually open, malware specimen tries to reach some suspicious web sites.

Finally, we verified our findings using hybrid-malware analysis (simultaneous analyze of malware specimen static and dynamic). With the help of **PEiD** tool find out that injected malicious file **loader_name.exe** is packed using **UPX** packer. Using command-line tool **upx.exe** (for encoding/decoding binary files) by executing the command:
upx –d loader_name.exe –o Unpacked_loader_name.exe.
unpacked our specimen and did BinText search which resulted following input strings:

> *"In a difficult world*
> *In a nameless time*
> *I want to survive*
> *So, you will be mine!!*
> *-- Bagle Author, 29.04.04, Germany."*

This is the message what malicious specimen has left in binary code. VirusTotal.com search using the hash value 3495a19bf6275f6e86f7dad561978fbc of "loader_name.exe" resulted in 55 engines from 70 engines as virus flag positive categorized as an e-mail worm with name Beagle.32 such as its author left a message on BinTex tool search previously.

V.　MALWARE ANALYSIS AUTOMATION

Every day, the AV-TEST Institute registers over 350,000 new malicious programs (malware) and potentially unwanted applications (see Figure 5). These are examined and classified according to their characteristics and saved. Visualization programs then transform the results into diagrams that can be updated and produce current malware statistics. [7]
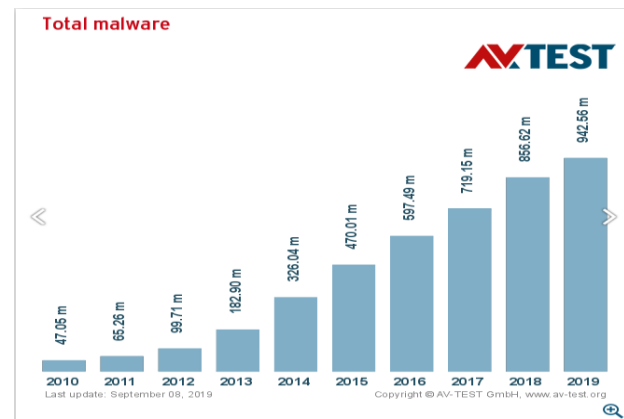
Figure 5. Malware statistics

A huge number of malware infections need to be considered as serious attacks over the privacy of home and business users. Every single moment a smart device, personal pc or server is under attack with a high risk of information to be stealth or business to be interrupted. Dealing such a type of massive invasion of security risks requires to develop methodologies or automatic responses. Detection live attacks and performing static and dynamic analysis requires automatic response. Additionally, automatic responses must be enriched using artificial intelligence. Machine learning implementation will be time-consuming, cost-effective and very strong response for eliminating the rising malware threats. Zero day exploits and validation will be always a challenge to this discipline but at least real-time detection, classification of malware, automatic generation of reports is existing on market and so many business solutions are provided by many AV vendors.

The Malware Analysis and Attribution using Genetic Information (MAAGI) system is a complete, automated malware analysis system that applies AI techniques to support all phases of traditional malware analysis work flows, including reverse–engineering, high–level functional analysis and attacker motivational characterization, clustering and family classification of malware, evolutionary lineage analysis of malware families, shared component identification, and predicting the future of malware families. An overview of the system is shown in Fig. 6. [8]
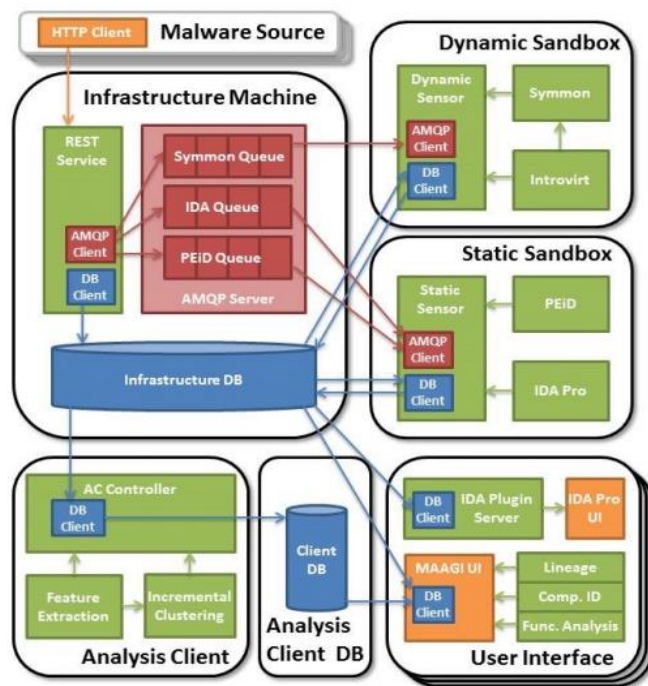
Figure 6. Architecture of MAAGI System

In addition, app.SNDBOX.com is a free online automated malware analysis system that allows anyone to upload a file and access it's static, dynamic and network analysis in an easy-to-understand graphical interface.

VI. CONCLUSION

Malware or malicious applications are in touch with every type of user (from basic to advance) and all kinds of digital platforms. The high risk of being hit by malware makes world markets to be fragile and causes a lot of material losses.

In order to deal with various types of cyber-attacks and massive produced malware variety, there is a need to be implemented scientific technics on understanding how malware specimen installs, propagates and payloads.

Before malware analysis, there is a need to build some malware prerequisites such as knowledge about operating systems, files, processes, computer networks and building safe virtual environments.

Static malware analysis and dynamic malware analysis provides the best approaches to dealing with malicious codes. While static analysis is extracting information from binary code in non-running mode, dynamic malware analysis is executing infected code to find suspicious files.

A huge quantity of malware created per day requires serious concern on developing AI (Artificial Intelligence) techniques to deal with. Automation using AI against malware is the right action but it is not all that we can do. Zero-day exploits are the weak side of the AI-based malware analysis approach. File behavior-based analysis could not close the gap, there is a need to build hardware and software (operating system level) approaches on dealing with malware specimens.

Investing in knowledge, building security protocols and standard operating procedures will keep the digital world standing up against cyber-criminals.

VII. REFERENCES

[1] E. Krogh, An Introduction to Windows Operating System, 1st ed., Bookboon, 2015.

[2] A. S.Tanenbaum, Modern Operating Systems, 3rd ed., Pearson, 2007.

[3] U. C. Town, Introduction to MS Windows XP, Center for Educational Technology, University Cape Town, 2009.

[4] C. Charles, "Report shows 32% of businesses still use Windows XP," 1 August 2019. [Online]. Available: https://www.thatsnonsense.com/report-shows-32-of-businesses-still-use-windows-xp/. [Accessed 9 September 2019].

[5] R. Singh, "A comparison of Features of VirtualBox and VMware," *International Journal of Advanced Research Computer Science and Software Engineering,* vol. 5, no. 9, pp. 467-469, September 2018.

[6] M. H. Ligh, S. Adair, B. Harstein and M. Richard, Malware Analyst's Cookbook and DVD tools and techniques for fighting malicious code, Indianapolis: Willey Publishing Inc, 2011.

[7] The Independent IT-Security Institute Magdeburg Germany, "Malware Statistics," 8 Semptember 2019. [Online]. Available: https://www.av-test.org/en/statistics/malware/. [Accessed 9 September 2019].

[8] A. Pfeffer, R. Brian, K. Lee, H. Michael, C. Catherine, O. Alison, T. Glenn, R. S. Neal, P. Terry, T. Jason, H. Robert, L. Arun, M. Craig, S. Dan and F. Jared, "Artificial Intelligence Based Malwafre Analysis," *arxive.org,* p. 38, 27 April 2017.

[9] Practical Malware Analysis, The Hands-On Guide to Dissecting Malicious Software, Michael Sikorski and   Andrew Honig, Foreword by Richar Bejtlich, published 2012

Implementation and performance of sorting algorithms in terms of time and space on Intel Core i7 (TM) processor by using C #, Java, Python, and PHP as aprogramming language

E.MOLLAKUQE[1], M.HAMITI,[2,]V.MOLLAKUQE,[3]

[1]Ss. Cyrili and Methodius Univeristy, Skopje/North Macedonia, elissamollakuqe@gmail.com
[2]SEE Univeristy, Tetovo/North Macedonia, m.hamiti@seeu.edu.mk
[3] Mother TerezaUniveristy,Skopje/North Macedonia, vesa_mollakuqe@hotmail.com

Abstract - **Data sorting is the placement of data in a particular way, such as ascending or descending. It is one of the most important computing applications. Data sorting is an intriguing problem that has attracted enormous research effort. Sorting algorithms are efficient algorithms that perform an important task by putting the elements of a list in a particular order. With the advent of computing, many data sets were born which then revealed many complexities about sorting and research problems. In 1956 came the first tests for sorting algorithms - bubble sort algorithm. The first algorithms had low capacities and used object comparison to meet the basic requirements of the form *O (n log n)* - some sequences were treated as inputs multiplying by *n log n* comparisons.**

Keywords- **performaces, sorting, algoithms, data, time complexity and space complexity.**

I. INTRODUCTION

In computing, sorting algorithms are those algorithms that place elements of a list in a certain order, and effective ordering is important for job optimizations for other algorithms, which will be applied to a computer program, such as searches, which actually require sorted lists to continue their work. Concept of sorting is very important because many of the commercial and non-commercial operations are built on a sorting basis, where conclusions have been drawn that, in data stored on different computers, sorting and searching are the two most commonly used operations which sort our data in two forms:numerical sort order (from the largest to the smallest, or vice versa) and lexical form of sorting (alphabetical ordering, ascending or descending). (Demuth, 2012)

II. SORTING ALGORITHMS

Sorting algorithms are an important part of data management. Each algorithm has specific parts of the design, processing time and sequencing method and in many cases, the best thing is to build sorting functions. For cases where building functions is impossible then we have a variety of choices of sorting algorithms. Most sorting algorithms work by comparing data. They are usually evaluated for their efficacy. In this case, efficiency refers to the size of the entries and this is based on the number of elements that require listing.

Most algorithms in use have an algorithmic efficiency such as:
- $O (n \char94 2)$
- $O (n * \log (n))$.

Based on the available efficiency then some types of sorting algorithms are implemented, such as:
- Quick Sort
- Merge Sort
- Sort Bubble
- Sort Insertion
- Heap Sort

A. Quick Sort

The Quick Sort Algorithm is probably one of the most common sort algorithms. It is characterized by implementation simplicity, operational speed and is efficient for classifications for different data types [1]. Quick Sort uses the divide and rule method for classification. It works by dividing a group into two subgroups, otherwise known as the MergeSort complement.

The idea behind Quick Sort is:
- Take an item from the list and set it as 'pivot'.
- Once overlap and split, we call it PARTITION, which rearranges entries by:
    - Place the 'pivot' in its place
    - Smaller entries than 'pivot' placed on the left side
    - Largers larger than 'pivot' placed on the right side
- Continue recursively in the left and right sections until the order is made.

B. Merge Sort

In computer science, Merge Sort is another algorithm which is specified by divisible and dominant principles [1] (Knuth, 2007). When calling this algorithm to operate on a data string with n elements first it will divide the string into two equal sequences, and then use recursiveness over the partition made, so the principle of Merge Sort work is:
- to the unreported list in n-sublists, each must contain 1 element
- rule with reclusiveness in the sub-lists creating a new change/order
- In the recurring form, join the sub-lists to find a new sub-list, and do so until you get a sub-list, which is actually the new sorted list.

Merge Sort uses the time complexity O (nlog n) using the divide and rule technique[1].

C. Bubble Sort

Bubble Sort is a simple sequencing algorithm and very slow. Here the ranking is based on comparisons of related parties and elements change place when they are noticed that they are not ranked [1]. It gets its name from the idea of "floating like a bubble" from the bottom of the list to the other side. (Niemann, 2015) Assuming that top-down rankings are being made, higher values "float" to the left, while lower values "float" to the right [1]. But what makes this algorithm inappropriate is the disadvantage it shows when we have a large set of data that needs to be sorted.

D. Insertion Sort

Insertion Sort is a simple sorting algorithm that is efficient for sorting a small number of elements [1]. The sorting here is done with the principle of "in place", by interpolating the arrays until sorting is achieved. At each position of the string, its value is checked and then placed in its place. If the value is greater, it leaves the element in its place and continues to move to the next point, but if it is smaller, it finds the appropriate position within the ordered list, respectively, all elements will move and change positions until they reach the right place[1]. Insertion Sort is the analogy of numeric or alphabetical order, let's say that in a string of letters, and the first one to draw is the letter 'S', then this will be placed at the top of the left position, the second letter which draws is the letter 'B', then we move the letter 'S' to the right, while we put the letter 'B' in place of the letter 'S', the third letter we will

draw is the letter 'V', this will be placed on the right hand side without having to change anything, the next letter is the letter is the letter 'A', this will be placed at the beginning of the list and all other letters will move to a position ... and lo this is also the work of Insertion Sort.

E. Heap Sort

Heap Sort is another sorting algorithm that is based on comparison; this can be assumed as an improved version of the Selection Sort algorithm. (PRINCETON EDU, 2017) The Heap Sort job is quite similar to the Selection Sort sorting process, here the entries are divided into two groups: the sorted and unordered group and they will be sorted by extracting the largest element and by moved it to the sorted group[1]. What makes this algorithm impractical is its slow performance, although in most cases Heap Sort replaces the Quick Sort algorithm [1]. The Heap Sort workflow process can be divided into two parts:
• Heap is built out of data and is usually placed in arrays by layout through a binary tree
• The sort string is created by moving the largest elements from the string that is in process (the data set) and inserting it into the sort string.

III.   COMPUTER ARCHITECTURE AND PROCESSOR

The processor is the main component of a computer system. He is responsible for doing all the computer calculations, logical decision making and controlling the various activities of the system. The main job of the processor is to execute low-level instructions loaded into memory (Robert Scdgwick, 2016).

Single-core processors have only one instruction processing processor. All processors manufactured by 2005 were single-core. The problems with a single-core processor are the increase in working speed and the heat produced by the chip.

Multicore processors are processors that came on the market after 2005. These processors use two or more cores to process instructions at the same time. The multi-core processor may look like a single processor, but it actually containsdual (dual-core), three (tri-core), four (quad-core), six (hexa-core), eight (octa-core) orten (deca- core) cores.

Considering the power and temperature limitations these processors are the only viable solution to increase the speed of computers in the future.Analyzing the performance of the sorting algorithms, we touched on two aspects:

Time aspect:

- Time spent on instructions
- How fast does the algorithm perform?
- What is the runtime?

Space aspect:

- Space of data structures
- What structures can be used?
- How to choose the effective structure for effective operating time.

IV.   PERFORMANCE OF ALGORITHMS IN COMPUTER ARCHITECTURE WITH INTEL CORE i7 (TM) PROCESSOR

The Intel Core i7 (TM) processor is at the forefront of the entire Core processor series. They are also more expensive. Technically the Core i7 (TM) is divided into two different types:
- processors with the LGA1156 chip set
- processors with the LGA1366 chip set.

Both offer quad core chips, virtual support, hyper thread, and turbo boost technology.
The performance of the Intel Core i7 (TM) processor is affected by these features:
- The clock frequency range ranges from 3.10 GHz to 4.10 GHz
- You have memory ranging from 4MB to 8MB
- Turbo boost technology
- Hyper-theading available with 8

The performance of the sorting algorithms in the Intel Core i7 (TM) processor is tested by analyzing data which are divided into three categories:
- Unsorted data
- Semi-sorted data
- Sorted data with repeated data,
this data is placed in three different Microsoft Office Excel 2010 files, named as un_sorted.xlsx, half_s.xlsx, and sorted_rep.xlsx [1].

Performance of the Quick Sort algorithm on Intel Core i7 (TM) processor, 8GB RAM is presented on following graph:

Figure 1.Performance of the Quick Sort algorithm on Intel Core i7

The graph below shows that in Merge Sort the shortest sorting time is when the data is half sorted while it takes much longer when the data is completely unsorted.
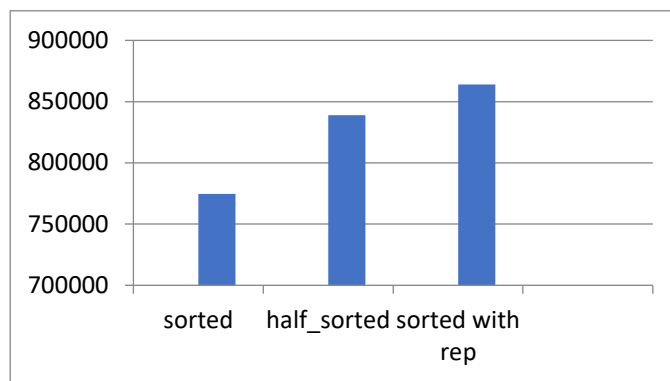
Figure 2. Performance of the Merge Sort algorithm on Intel Core i7

The graph below shows that Bubble Sort is quite slow, the shortest sorting time is when the data is sorted while it takes much longer when the data is completely unsorted.
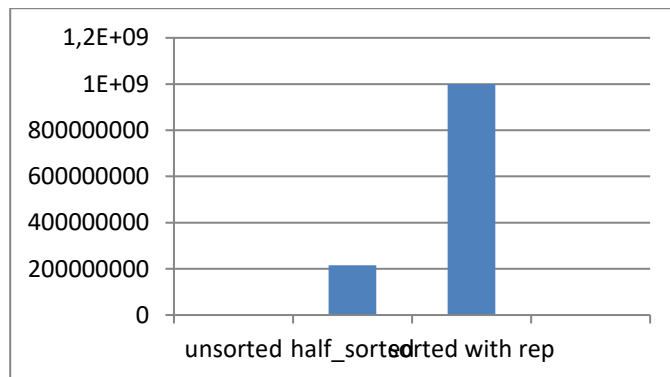
Figure 3.Performance of the Bubble Sort algorithm on Intel Core i7

The graph below shows that in Insertion Sort the shortest sorting time is when the data is sorted and half sorted while it takes much longer when the data is unsorted.
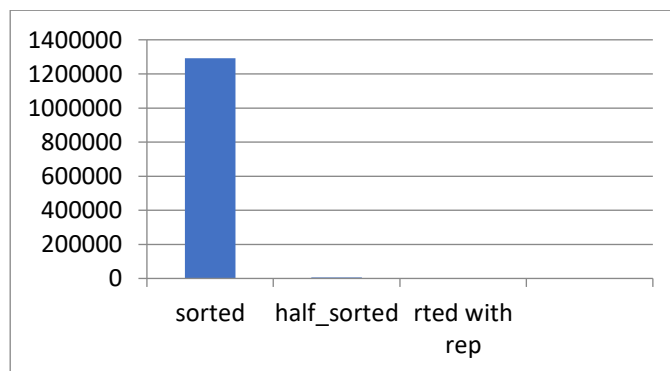
Figure 4. Performance of the Insertion Sort algorithm on Intel Core i7

The graph below shows that Heap Sort is very effective, the shortest sorting time being when the data is half sorted and sorted while it takes much longer when the data is unassorted.
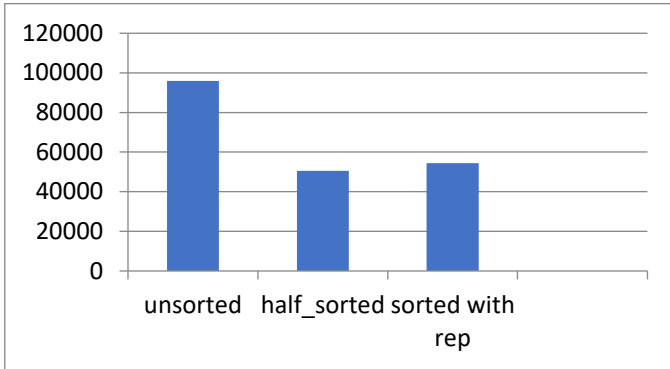
Figure 5. Performance of the Heap Sort algorithm on Intel Core i7

V.   ALGORITHM IMPLEMENTATION ON INTEL CORE I7 (TM) PLATFORM, 3.10GHz, 8GB RAM IN C # PROGRAMMING LANGUAGE, JAVA, PYTHON AND PHP

Quick Sort provided a higher sorting speed on semi-sorted data, with an average time of 32776.5 microseconds. Based on the diagram it can be noticed that the data sorted by repetition is ranked faster and the data completely un sorted
.
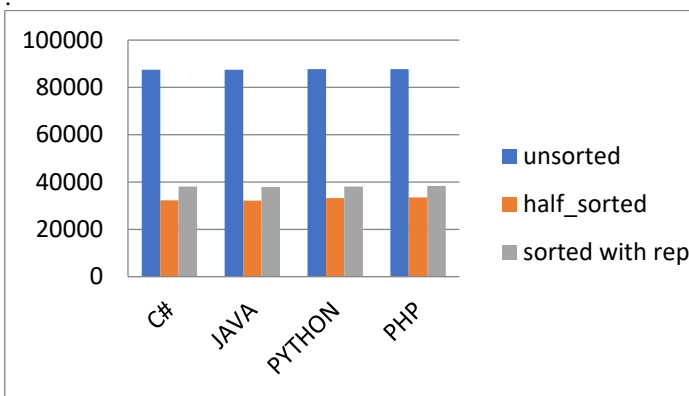
Figure 6.The runtime measured in microseconds of the Quick Sort algorithm on various programming platforms and with Intel Core i7 (TM) processor

Merge Sort is implemented in the programming languages which after compilation yielded the following results: the best execution time was for the semi-sorted data with an average time of 839025.75 microseconds, based on the diagram it is observed that the sorted data is ranked faster compared most unreported data.
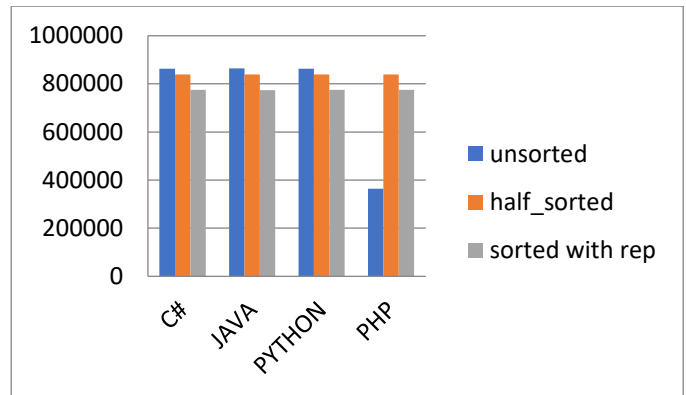
Figure 7.The runtime measured in microseconds of the Merge Sort algorithm on various programming platforms and with Intel Core i7 (TM) processor

Bubble Sort is a slow sorting algorithm, implemented and compiled in various programming languages on an Intel Core i7 processor, delivering the best time in data sorted with 755.25 microseconds of repetition.
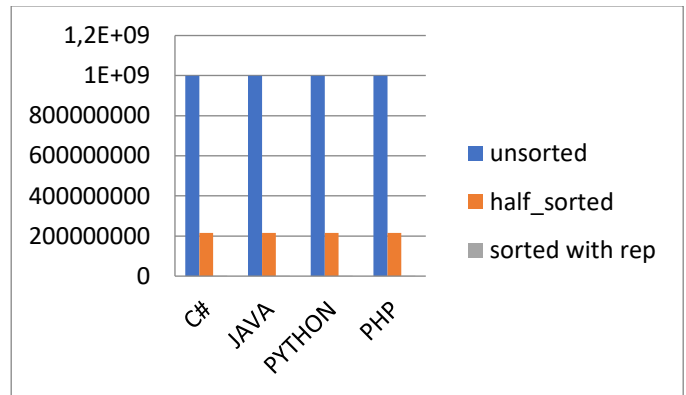
Figure 8.The runtime measured in microseconds of the Bubble Sort algorithm on various programming platforms and with Intel Core i7 (TM) processor

The performance of Insertion Sort has been shown to be the best in the data sorted by repetition, this data being sorted for approximately 2640 microseconds. Showing then a performance of 5478.75 microseconds in the semi-sorted data.
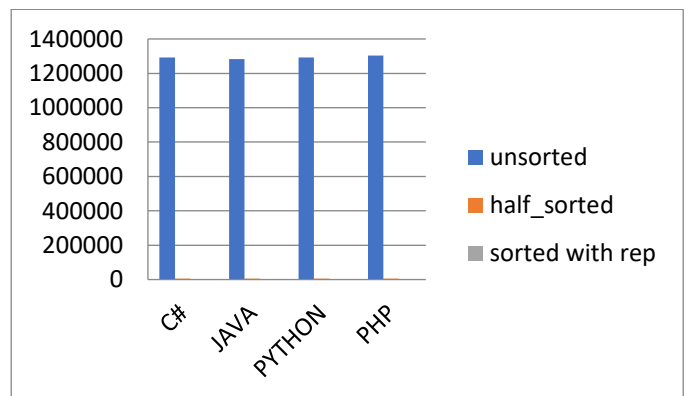
Figure 9.The runtime measured in microseconds of the Insertion Sort algorithm on various programming platforms and with Intel Core i7 (TM) processor

Based on the figure below, we can see that the Heap Sort implemented in the C #, JAVA, PYTHON and PHP programming languages, executed on the Intel Core i7 processor, gave the best performance in the semi-sorted data with an average time performance of 50596.5 microseconds.
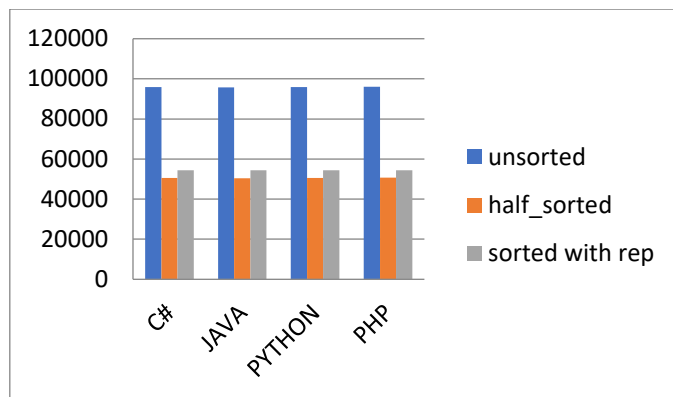
Figure 10.The runtime measured in microseconds of the Heap Sort algorithm on various programming platforms and with Intel Core i7 (TM) processor

VI. CONCLUSION

In this study, sorting algorithms written on different programming platforms and in different execution environments were analyzed, respectively execution on Intel Core i7 (TM) processors. The results were generated by analyzing a dataset of 100117, classified into three groups: semi-sorted data, non-sorted data, and repeated-sorted data. Following the analysis of performance and time complexity for each sorting algorithm (Quick Sort, Merge Sort, Bubble Sort, Insertion Sort, and Heap Sort) the following conclusions were generated:

- Quick Sort on Intel Core i7 (TM) processor, 3.10 GHz, 8 GB RAM, average output time for unsorted data is 87591.5 microseconds, for semi-sorted data is 32776.5 microseconds, and for recursively sorted data is 38100 microseconds
- Merge Sort on Intel Core i7 (TM) processor, 3.10 GHz, 8 GB RAM, average execution time for unsorted data is 864082.5 microseconds, for semi-sorted data is 839125.75 microseconds, and for recursively sorted data is 774602.25 microseconds
- Bubble Sort on Intel Core i7 (TM) processor, 3.10 GHz, 8 GB RAM, average execution time for unsorted data is 999020477 microseconds, for semi-sorted data is 215765420 microseconds, and for recursively sorted data is 755.25 microseconds
- Insertion Sort in Intel Core i7 (TM) processor, 3.10 GHz, 8 GB RAM, average execution time for unsorted data is 1292783.3 microseconds, for semi-sorted data is 5478.75 microseconds, and for recursively sorted data is 5467 microseconds
- heapSort on Intel Core i7 (TM) processor, 3.10 GHz, 8 GB RAM, average execution time for unsorted data is 95886 microseconds, for semi-sorted data is 50596.5 microseconds, and for repeats, sorted data is

54425.5 microseconds

- In Intel Core i7 (TM), 3.10 GHz, 8 GB RAM for unsorted and semi-sorted data Quick Sort algorithm work faster, followed by Heap Sort, Merge Sort, InsertionSort, and Bubble Sort
- For data sorted by iteration the Bubble Sort algorithm was more efficient, followed by Insertion Sort, Quick Sort, Heap Sort and Merge Sort
- Based on overall performance the algorithms can be sorted by Quick Sort, Heap Sort, Merge Sort, Insertion Sort and Bubble Sort.

REFERENCES

[1] M.Hamiti, E.Mollakuqe, S.Krrabaj, A.Susuri, *Performance Estimation of Sorting Algorithms Under Different Platforms and Environments,* International Conference on Engineering Technologies (ICENTE'18) October 26-28,2018,Konya/TURKEY
[2] Cormen, T. H. *Introduction to Algorithms.* Cambridge. 2009
[3] Demuth, H. *Electronic Data Sorting.* Standford University. 2012
[4] Granville Barnett, L. D. *Data Structure and Algorithms: Annotated Reference with Example.* Chicago: AWP, 2014.
[5] Lanne David & Williams Hugh,*Web Database Application with PHP and MySQL,*O'Reilly,United States of America,2004.
[6] Nixon Robin, *PHP, MySQL,JavaScript & CSS,*O'Reilly,United States of America, 2012.
[7] Welling Luke & Thomson Laura, *PHP and MySQL Web Development,*Pearson
[8] Education, USA, 2008.
[9] Ullman Larry,*PHP, and MySQL for Dynamic Web Sites,*Peachpit Press,USA,2012
[10] Powers David,PHP Solutions: Dynamic Web Design Made Easy,Spring,UK,2010
[11] Gilmore W.Jason, *Beginning PHP and MySQL,*Apress,New York,2009
[12] Guna, A. Fundamental Structure of Computer Science. NY: AWPress. 2013
[13] Kim, P. S. *Theory and Applications of Models of Computation.* UK: LNCS 2008.
[14] Knuth, D. E. *Early development of programming languages.* UK: AWP, 2007
[15] Niemann, T. Sorting and Search Algorithms. NY: Pavel Dubner, 2015
[16] Nilsson, S. *The Fastest Sorting Algorithm.* Dr. Dobbs, 2000
[17] Robert Scdgwick, K. W. Algorithms (4th Edition). Në *Algorithms* (f. 480). Library of congresse Cataloginig, 2016
[18] Rosen, S. *Programming Systems and Languages.* McGraw-Hill, 2012
[19] Sahn, E. H. *Fundamentals of Data Structures.* H. Freeman & Co, 2013
[20] Sedgewick, R.. Implementing Quicksort programs. Comm. ACM, 2009
[21] Thomas H. Cormen, C. E. *Introduction to Algorithms* (f. 1312). MIT Press, 2009
[22] Wirth, N. *Algorithms & Data Structures.* NY: Prentice-Hall, 2010

Security features of ACORN and ASCON as Competition for Authenticated Encryption: Security, Applicability, and Robustness CAESAR

E.MOLLAKUQE[1] and V. DIMITROVA[1]

[1]Ss. Cyrili and Methodius University, Skopje/North Macedonia, elissamollakuqe@gmail.com, vesna.dimitrova@finki.ukim.mk

Abstract - **CAESAR: Competition for Authenticated Encryption: Security, Applicability, and Robustness is now calling for submissions of authenticated ciphers. This competition follows a long tradition of focused competitions in secret-key cryptography[7]. CAESAR competition aims at finding authenticated encryption schemes that offer advantages and those schemes will give us more security. CAESAR tries to identify a portfolio of authenticated ciphers that [7] offer advantages over AES-GCM and [7] are suitable for widespread adoption. Now CESAR is organized into three use cases: Lightweight applications (resource-constrained environments), High-performance applications and Defense in depth. Candidates of this use case give different advantages depends on designs – block-cipher, stream cipher, functions and so on. This paper will give some characteristics of ACORN v1 ACORN v2, ACORN v3, and ASCON v1, ASCON v1.1 and ASCON v1.2by comparing security aspects.**

Keywords- **Caesar, acorn, ascon, encryption, decryption and authenticated.**

I. INTRODUCTION

Long time ago data was written, stored and processed within a computer. This computer had a monitor (screen), keyboard, mouse and main case. Much data was circulated and manipulated across different computers. On the other hand, many computers interact with each other and transfer data from one place to another, or from one country to another… etc, etc. But with the advancement of computer networks start a new era! The era of data threats. Therefore, starting with this era of humanity, start to seriously deal with these threats. These threats were the starting points for developing security aspects, including security protocols, security methods and tools, and so on. Seeing that cryptography is the efficient way to secure data, it also has its own risks, such as the loss of keys or Strength of the security of protocols, randomness of generated keys or key lifetimes, e tc. Authenticated Encryption (AE) must to provide: semantically security under CPA attack and ciphertext integrity. This method of providing privacy and integrity use key, nonce and authentication tag. Also to provide this kind of

security AE use schemes and algorithm based on block or stream cipher. The CAESAR competition is public competition for authenticated ciphers. The aim of this research is to present security features of CAESAR by using specification and security goals of ACORN v1 ACORN v2, ACORN v3 and ASCON v1, ASCON v1.1 and ASCON v1.2.

II. CRYPTOGRAPHY AND LIGHTWEIGHT CRYPTOGRAPHY

Cryptography is created as a tool to keep the privacy of information that people or computers send to each other, even if it is present an another person on the communication channel. The main purpose of cryptography is providing privacy, while the main aspects are: confidentiality, integrity, and authentication as well. Cryptography dates back to time. Since the era of Jules Caesar ....when coding was made with the rules "shift by ...” for example shift by 3, shift by 4…etc. *Cryptography* is the science of using mathematics to encrypt and decrypt data. Cryptography enables you to store sensitive information or transmit it across insecure networks (like the Internet) so that it cannot be read by anyone except the intended recipient [2]. While cryptography is the science of securing data, *cryptanalysis* is the science of analyzing and breaking secure communication. Classical cryptanalysis involves an interesting combination of analytical reasoning, application of mathematical tools, pattern finding, patience, determination, and luck. Cryptanalysts are also called *attackers. Cryptology* embraces both cryptography and cryptanalysis [2]. Lightweight cryptography is the area of classical cryptography that studies algorithms pertinent to constrained devices, such as RFID tags, sensors in wireless networks, small devices, and Internet-of-things devices [3] [lv2]. Lightweight cryptography is area of study driven by the lack of cryptographic primitives capable to run on devices with low computing power [4]. Another important characteristic of Lightweight cryptography is that it is capable of obtaining the adequate levels of security, without necessarily resorting to security-efficiency trade-offs [4]. Lightweight cryptography is based on lightweight algorithms that are based on block and stream ciphers. Lightweight algorithms based on block encryption, are Present, Katan,

Clefia, GOST 28147-89. Lightweight algorithms based on stream ciphers are listed as Grain v1, Bean, Trivium, Hummingbird.

A. Lightweight Authenticated Encryption

Whatever the current age, almost all aspects of human life are threatening. Therefore, it is imperative to protect useful information from harmful activities such as attacks. An attack can be passive or active. On passive attacks, the main purpose is to steal information by trying to secure unauthorized access to information. Passive attacks are usually done when attempting to overcome a communicating channel where they do not affect information or disrupt the communication channel. On active attacks, the main purpose is changing information by performing some information processes. These attackers do the following things: unauthorized modification of the information, initiation of unauthorized transmission, unauthorized deletion of data. Regardless of, if the attack is active or passive, the attacker has two main purposes: breaking a cryptosystem and finding the plaintext from the ciphertext [5]. Recently, we have seen many attacks that go beyond any predictions made by crypt analyzer, for example:

- Cipher text Only Attacks (COA) is a type of attack where the attacker attempts to access the set of cipher texts. The success of this attack comes when plaintext is assigned through cipher text.
- Dictionary Attack is a technique to break a computer or server with encryption and authentication mechanisms. Dictionary Attack used millions of options to reach the needed key and then put the key in a place to use then, similar to the language dictionary.
- Birthday Attack uses mathematics and probability theory to reach successful meltdown. It is an ideal attack when we want to intercept the communication between two parties. This type of attack uses hash functions and uses the hash values for different inputs. If the striker finds two inputs that give the same value of the hash then the system is break system.

Authenticated Encryption is a method for simultaneously protection of the privacy of the message and to ensure authenticity by providing confidentiality and authenticity.

Confidentiality is the ability to hide information from those people unauthorised to view it. Cryptography and Encryption methods are an example of an attempt to ensure confidentiality of data trasferred from one computer to another [5]. Confidentiality is used to make sure that nobody in between site A and B is able to read what data or information is sent between the to sites [6]. One method for providing confidentiality is through encryption. Encryption process ensures that data can only be decoded by the intended recipient. A good example of methods used to ensure confidentiality is by using User IDs and passwords constitute a standard procedure; two-factor authentication is becoming the norm. Other options include biometric verification and security tokens, key fobs or soft tokens [6].

Example 1.

Man in the Middle Attack is one of arracks that attackers uses during cybercrime. Here attacker secretly transmits and change the communication between two or more parties. The MIM attack is not very complex, as you can see on fig.1.
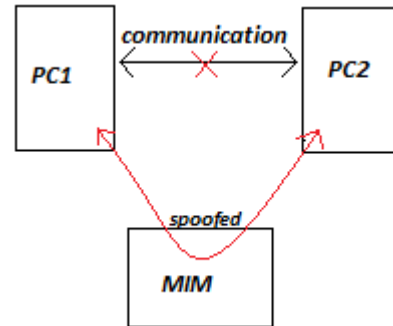
Figure 1.Man in the Middle Attack

PC1 (*know as Personal Computer*) tries to communicate with PC2 (they have to switch between them the public keys), then the attacker intervenes and exchanges his public key, so all that PC1 sends goes to the attacker and after he reads everything, he can decide to forward or to modified information, and then "he" can pass them to PC2.

III. CAESAR COMPETITION PORTOFOLIO

The United States National Institute of Standards and Technology (NIST) announced an open competition for a new Advanced Encryption Standard[7]. This competition attracted 15 block-cipher submissions from 50 cryptographers around the world, and then public security evaluations from an even larger pool of cryptanalysts, along with performance evaluations. Eventually, NIST chose Rijndael as AES. In 2004 ECRYPT, a Network of Excellence funded by the European Union, announced eSTREAM, the ECRYPT Stream Cipher Project. [7]This project called for submissions of "new stream ciphers suitable for widespread adoption". This call attracted 34 stream-cipher submissions from 100 cryptographers around the world, and then hundreds of security evaluations and performance evaluations, following the same pattern as AES but on a larger scale. Eventually the eSTREAM committee selected a portfolio containing several stream ciphers.In 2007 NIST announced an open competition for a new hash standard, SHA-3. [7] This competition attracted 64 hash-function submissions from 200 cryptographers around the world, and then a tremendous volume of security evaluations and performance evaluations. Eventually NIST chose Keccak as SHA-3.The AES competition is generally viewed as having

provided a tremendous boost to the cryptographic research community's understanding of block ciphers, and a tremendous increase in confidence in the security of some block ciphers. Similar comments apply to eSTREAM and to the SHA-3 competition and are also expected to apply to CAESAR [7.]The final CAESAR portfolio is organized into three use cases: Lightweight applications (resource constrained environments), High-performance applications and Defense in depth.CAESAR is very important on practise because here is the way of authenticated encryption which is one of the most important things on digital life. CAESAR competition is a public competition for authenticated cipher that include candidates separates on different portfolio.

IV. ACORN

ACORN is a Lightweight Authenticated Cipher submitted by Hongjun Wu. ACORN containing three version: v1, v2, and v3. As an algorithms, ACORN v1 and v2 are a bit-wise authenticated cipher that means one bit of message can processed in one step. ACORN v3 is a bit-based sequential authenticated cipher in which the difference is injected into the state for authentication for better performance [8]. ACORN-128 uses a 128-bit key and a 128-bit initialization vector. The associated data length and the plaintext length are less than 264 bits [8]. The authentication tag length is less than or equal to 128 bits[8]. The state size of ACORN-128 is 293 bits [8].In ACORN, one key, IV pair is used to protect only one message. ACORN-128 (128-bit tag) security is based on encryption 128 –bit and authentication 128-bit. Security features of ACORN v1, ACORN v2, and ACORN v3 are given on the following table:

Table 1. Features of ACORN v1

	ACORN v1
Key	generated in a **secure way**
Key and IV	Are not used to protect more than one message Are not used with two different tag size
Output	If verification fails – fails the outputs

Table 2. Features of ACORN v2

	ACORN v2
Key	generated in a **secure** and **random way**
Key and IV	Are not used to protect more than one message Are not used with two different tag size
Output	If verification fails – fails the outputs

Table 3. Features of ACORN v3

	ACORN v3
Key	generated in a **secure** and **random way**
Key and IV	Are not used to protect more than one message Are not used with two different tag size
Output	If verification fails – fails the outputs

V. ASCON

ASCON is a family of authenticated encryption and hashing algorithms designed to be lightweight and easy to implement, even with added countermeasures against side-channel attacks [9]. The family members are parametrized by the key length $k < 128$ bits, the rate r, and internal round numbers a and b. ASCON has been selected as the primary choice for lightweight authenticated encryption in the final portfolio of the CAESAR competition (2014–2019) and is currently competing in the NIST Lightweight Cryptography competition (2019–) [9]. On ASCON v1, ASCON v1.1, and ASCON v1.2 are a part of family of authenticated encryption designs by the ASCON $_{a,b}$-k where all the family members are parametrized by the key length k ≤ 128 bits and internal round numbers a,b. Security features of ASCON v1, ASCON v1.1, and ASCON v1.2 are given on the following table:

Table 4.Features of ASCON v1

	ASCON v1
Key	generated in **random way** by s-box
Key and IV	The 320-bit initial value IV is formed by the secret key K and nonce N
Output	if the verification of the tag fails – fails the outputs

Table 5. Table 4.Features of ASCON v1.1

	ASCON v1.1
Key	generated in **random way** by s-box
Key and IV	The 320-bit initial value IV is formed by the secret key K and nonce N (IV specifying the algorithm (including the key size k, the rate r, the initialization and finalization round number a, and the intermediate round number b)

Output	if the verification of the tag fails – fails the outputs

Table 6.Features of ASCON v1.2

	ASCON v1.2
Key	generated in **random way** by s-box
Key and IV	The 320-bit initial value IV is formed by the secret key K and nonce N (IV specifying the algorithm (including the key size k, the rate r, the initialization and finalization round number a, and the intermediate round number b)
Output	if the verification of the tag fails – fails the outputs

VI. CAESAR PORTOFOLIO LIGHTWEIGHT APPLICATIONS

Encryption is the method by which plaintext or any other type of data is converted from a readable form to an encoded version that can only be decoded by another entity if they have access to a decryption key [l3]. The main propose of encryption is to protect the confidentiality of data on computer systems or transmitted via the internet or any other computer network. Ecryptin can be organized as block or stream cipher. ACORN is stream cipher while ASCON is block cipher.

Security details and characteristics of ACORNv3, ACORN 128v1, ACORN 128v2 and ACORN 128 v3 are given on the following table:

Table 7. Security details and characteristics of ACORNv3, ACORN 128v1, ACORN 128v2 and ACORN 128 v3

	ACORN 128 v1	ACORN 128 v2	ACORN 128 v3
Encryption	128 bit	128 bit	128 bit
Authetication	128 bit	128 bit	128 bit
Key	128 bit	128 bit	128 bit
Nonce	128 bit	128 bit	128 bit
Tag	128 bit	128 bit	128 bit
Data limit	2^{64}bit	2^{64}bit	2^{64}bit

Security details and characteristics of ASCON 128v1, ASCON 128v1.1 and ASCON128v1.2 are given on the following table:

Table 8. Security details and characteristics of ASCON 128v1, ASCON 128v1.1 and ASCON128v1.2

	ASCON 128 v1	ASCON 128 v1.1	ASCON 128 v1.2
Encryption	128 bit	128 bit	128 bit
Authetication	128 bit	128 bit	128 bit
Key	128 bit	128 bit	128 bit
Nonce	128 bit	128 bit	128 bit
Tag	128 bit	128 bit	128 bit
Data limit	2^{64}block	264block	2^{64}block

By using the features and properties of algorithms describe previously we can conclude:

- Encryption process has been done by using 128 bit length for ACORN 128v1, ACORN 128v2, ACORN 128v3
- Encryption process has been done by using 128 bit length for ASCON 128v1, ASCON 128v1.1, ASCON 128v1.2
- Authentiaction process for ACORN 128v1, ACORN 128v2, ACORN 128v3 has been done by using 128 bit length
- Authentiaction process for ASCON 128v1, ASCON 128v1.1, ASCON 128v1.2 has been done by using 128 bit length
- ACORN 128v1, ACORN 128v2, ACORN 128v3 use a key 128 bit
- ASCON 128v1, ASCON 128v1.1, ASCON 128v1.2 use a key 128 bit
- ACORN 128v1, ACORN 128v2, ACORN 128v3 use stream data limit

ASCON 128v1, ASCON 128v1.1, ASCON 128v1.2 use block data limit

VII. CONCLUSION

We analyzed the algorithms of the lightweight cryptography ACORNv1, ACORNv2, ACORNv3 and ASCONv1, ASCONv1.1 and ASCONv1.2 from Competition for Authenticated Encryption: Security, Applicability, and Robustness CAESAR because both candidates are from the same group on CAESAR, while the ACORNv3 and ASCONv1.2 are the finalist of Competition for Authenticated Encryption: Security, Applicability, and Robustness CAESAR

since March 2019. For both of them, we analyzes their three verisons and they security details including some characteristics like key size, IV, and output.

In the analysis, the necessary features for the evaluation of the lightweight cryptography like Encryption, Authentication, Key, Nonce, tag, Data limit (Table 7,8). We analized this candidates to see what is difference between verison on the same candidates and what is difference between finalist ACORN v3 and ASCON v1.2. ACORN is designed to be efficient in hardware by using a bit-based stream cipher and also efficient in software to resist the traditional attacks and algebraic attacks. ASCON is designed to be efficient also in hardware and software by offering good performance on both platforms in more detalies ASCON is designed to allow efficient implementation of side channel resistance features. Lightweight cryptograpgy applications today is very used in many aspect, such: Small hardware area, hardware for power consumption, embedded system, etc.

In future work, we concern deeper analysis of particular features by using new proposals and new parameters for Competition for Authenticated Encryption: Security, Applicability, and Robustness CAESAR.

REFERENCES

[1] Nigel Smart, Cryptography: An Introduction-3rd Edition, University of Bristol
[2] Gpgtools Tender, https://gpgtools.tenderapp.com/kb/how-to/introduction-to-cryptography
[3] Masanobu Katagi and Shiho Moriai. Lightweight cryptography for the internet of things. Sony Corporation
[4] Santos Luan Cardos, *Software implementation of authenticated encryption algorithms on ARM processors,* http://repositorio.unicamp.br/jspui/bitstream/REPOSIP/332624/1/Santos_LuanCardosoDos_M.pdf
[5] Karvi.T, Cryprography and Network Security, PART III: Authenticated Encryption-2013: https://www.cs.helsinki.fi/u/karvi/advanced_3_13.pdf
[6] Applied Cryptography Group: https://crypto.stanford.edu/~dabo/courses/OnlineCrypto/slides/07-authenc-v2-annotated.pdf
[7] Cryptographic competitions: https://competitions.cr.yp.to/index.html
[8] Cryptographic competitions: https://competitions.cr.yp.to/round3/acornv3.pdf
[9] TU Graz: https://ascon.iaik.tugraz.at/
[10] https://competitions.cr.yp.to/round3/asconv12.pdf
[11] Libsodium documentation: https://libsodium.gitbook.io/doc/secret-key_cryptography/authenticated_encryption
[12] Cryptographic competitions: :https://competitions.cr.yp.to/round3/asconv12.pdf
[13] Cryptographic competitions: : https://competitions.cr.yp.to/round1/asconv1.pdf
[14] Cryptographic competitions: : https://competitions.cr.yp.to/round2/asconv11.pdf
[15] Cryptographic competitions: : https://competitions.cr.yp.to/round1/acornv1.pdf
[16] Cryptographic competitions: : https://competitions.cr.yp.to/round2/acornv2.pdf

Skin Disease Classification Using Convolutional Neural Networks

Ali QUTUB[1], İsmail SARITAS[2]

[1] Selcuk University, Konya/Turkey, akutub87@gmail.com
[2]Selcuk University, Konya/Turkey, isaritas@selcuk.edu.tr

Abstract— In this paper, briefly explains the approach. The LMU team will produce estimates for Task 3 (Disease Classification). The score we obtained in the 2018 ISIC validation set of the 2018 ISIC Challenge was 0.881 balanced precision. Skin cancer, the most common human malignancy is diagnosed visually by starting the first clinical screening and possibly potentially by dermoscopic analysis, biopsy and histopathological examination. Automatic classification of skin lesions using images is a challenging task due to the fine-grained variability in the appearance of skin lesions. Deep convolutional neural networks (CNNs) show potential for general and highly variable tasks in many fine-grained object categories. Here, we have demonstrated the classification of skin lesions using a single CNN, trained thoroughly from direct images, using only pixels and disease labels as inputs. We train CNN using 129,450 clinical picture data sets (two larger sizes12 larger than the previous data sets) of 2,032 different diseases.

Keywords—— Skin Disease, Classification , Neural Networks,CNN.

Introduction

A. Skin cancer has emerged as a major challenge in public health. This occurs Both skin cancer and other skin cancers have been growing over the past decades. According to the World Health Organization, more than 130,000 cases of skin cancer Between 2 and 3 million skin cancers other than skin cancer are globally diagnosed every year Injury rates are expected to increase continuously Ozone depletion and increased exposure to recreational sunshine. Low prices of cloud computing services and strong availability of powerful GPUs have led to the emergence of neural networks (CNNs), making it more accessible and learning with much larger data sets More tractable. CNNs turned out to be useful in diagnostic and decision-making So you find extensive applications in medical science. In the field of dermatology, it is applied to problems such as classification of dermatology. In this context, the International Skin Imaging Collaboration (ISIC) has established an open catalog to access the skin skin images of skin lesions. The challenges of skin diseases are regularly investigated. As reported [5], Results of skin cancer classification of ISIC Challenge 2016 and companion. A study of the reader with experienced dermatologists showed a subset of the images. That deep learning algorithms classify the images of melanoscopy more accurately than some dermatologists. In a historical publication entitled. Classification of skin diseases for skin cancer with deep neural networks, [2]

B. Prove that the Google Inception v3 structure was trained on the data set. Of c.130,000 skin lesions are capable of classifying skin cancer with level. Efficiency is similar to dermatologists.

C. In a recent publication, [4]. The Google Inception v4 CNN architecture is designed over 100,000.

D. Skin images and the results of the reader study to show that diagnostic. CNN performance outperforms most dermatologists. The main purpose of this manuscript is a brief description of this approach. Used by the LMU team to create a forecast for Task 3 of the 2018 ISIC Challenge. The mission was set to make the disease classification predictions for 1512. Skin images covering the following seven categories of diseases shown as fig (1). Abbreviations in square brackets: melanoma melanoma, melanocyte nebula [NV], Basal cell carcinoma [BCC], radial thrombosis, Bowen disease / intracellular carcinoma. Cancer [AKIEC], benign tuberosity (solar pumpkin, fatty calcification, lichen, Ureter-like ureter) [BKL], fibroblastoma [DF] and vascular lesion [VASC].
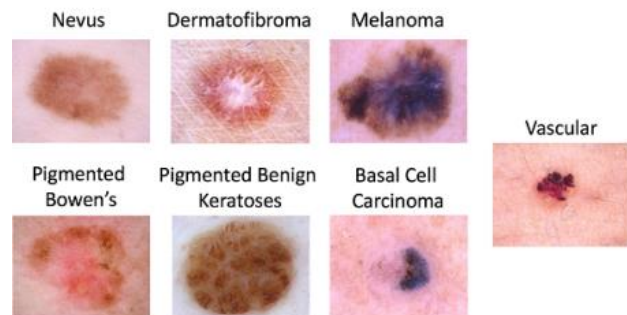
FİG.1. ISIC TASK CHALLENGE 3 CHAPTERS OF THE LESION AND IMAGES EG.

I. APPROACH

A. Our data set included 23,532 photographs, most of them by skin, from ISIC Archive (as shown in Table 1). As noted [1], the employment of additional data has led to higher performance in previous challenges. Therefore, we have updated the ISIC data sets with additional information that is publicly available. Image data sets (for example, MED-NODE, PH) and images that are not publicly available. In total we used 30,000 c. C.750 (or c.7.5%) and c.700 (or

c.7%). Randomly selected images were used for the HAM10000 dataset for test and validation sets respectively. While doing so, we have controlled the pest identifiers to confirm.

Table 1.Summary ISIC datasets used for training, validation and test kits

Dataset	NV	MEL	BKL	BCC	AKIEC	DF	VASC	All classes
HAM10000	6705	1113	1099	514	327	115	142	10015
ISIC 2017	11861	1019	575	33	7	7	15	13517
SONIC	9251	0	0	0	0	0	0	9251
MSK-2	1004	334	130	3	2	0	0	1473
MSK-4	543	215	189	0	0	0	0	947
MSK-1	532	258	57	27	5	5	11	895
UDA-1	396	159	0	0	0	0	0	555
MSK-3	123	19	83	0	0	0	0	225
MSK-5	0	0	109	0	0	0	2	111
UDA-2	12	34	7	3	0	2	2	60
Total	18566	2132	1674	547	334	122	157	23532

This table shows the number of theoretical and clinical images by ISIC category Archive (as available on 15 July 2018) Used in training, validation and testing kits Our algorithm.

He did not distribute any pictures of the same lesion on the training, validation and testing group. In order to predict strongly the performance of our model. On the invisible data, crossvalidation was used by selecting the images for. Validate the set several times, thus using all different parts of the. HAM10000 training package as check kits. A number of inverted weights are available from imagenet, but finding a good configuration to adjust them to a specific task is Exercise is very time consuming. So we just explored a subset of these Constructions for this task (such as VGG, InceptionV4, ResNet152, and NasNet) Which turned NasNet to show the best results. The use of random rotation and reflection during training is a common practice in image classification and given the limited amount of training data, this convention It was not challenged. Additional zoom techniques were tested during training. The evaluation includes magnification, shear, various color fastness algorithms And image distortions. Of the above techniques turned magnification and shear To be of limited use. We also used a number of techniques to calculate the class imbalance Problem and compensation of underrepresented classes (individual classes do not contain the same number of images). Specifically, we have integrated grade weights (Inversely proportional to the size of each chapter) in the training process and the applied threshold (ie, change of separation predictions automatically) in the test Phase based on proven rules derived from numerous confusion matrices.

Because each model produced slightly different results (not the least because Random increase during training), we used a simple average of predictions From multiple models based on different architectures. This resulted in better results From just using the best one model. This is in line with the approach taken before [7] and results [1].

The main differences between the three presentations can be summarized

Continued:

1- Describe the approach below the threshold

2- The approach described is threshold on DF and AKIEC

3- The approach is described with a more aggressive threshold on DF, AKIEC, MEL, VASC and BKL.

II. CONCLUSIONS

Figure 2 shows the performance of one model on the ISIC 2017 Challenge Test group, before including those images in the training group.
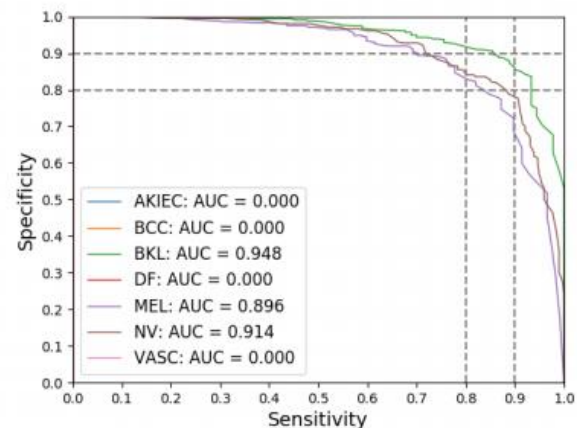
Fig. 2 (AUC) of one model on the ISIC test group Challenge 2017 Part 3: Classification of the pest. MUC AUC beats earlier. Published results, which include band approaches. The test set consists only of Photos BKL, MEL and NV. Other categories fall to zero.

After providing our test set predictions, our final results were achieved with Our developer approach will be posted on the Leaderboard and visible to everyone Participants in the ISIC

2018 Challenge. Our score on ISIC 2018 has been achieved The validation set was 0.881. The results on our test range were of the same size.

REFERENCES

[1] Codella, Noel C. F., Gutman, D., Celebi, M. E. et al. (2017). Skin Lesion Analysis Toward Melanoma Detection: A Challenge at the 2017 International Symposium on Biomedical Imaging (ISBI), Hosted by the International Skin Imaging Collaboration (ISIC). In: CoRR abs/1710.05006. arXiv: 1710.05006. URL: http://arxiv.org/abs/1710.05006

[2] Esteva, A., Kuprel, B., Novoa, R. A. et al. (2017). Dermatologist-level classification of skin cancer with deep neural networks. Nature, 542 (7639), 115118.

[3] Giotis, I., Molders, N., Land, S., et al. (2015). MED-NODE: A computer-assisted melanoma diagnosis system using non-dermoscopic images. Expert Systems with Applications, 42, 65786585.

[4] Haenssle, H. A., Fink, C., Schneiderbauer, R. et al. (2018). Man against machine: diagnostic performance of a deep learning convolutional neural network for dermoscopic melanoma recognition in comparison to 58 dermatologists. Annals of Oncology, 0, 17

[5] Marchetti, M. A., Codella, N. C. F., Dusza, S. W. et al. (2017). Results of the 2016 International Skin Imaging Collaboration International Symposium on Biomedical Imaging challenge: comparison of the accuracy of computer algorithms to dermatologists for the diagnosis of melanoma from dermoscopic images. J Am Acad Dermatol, 78 (2), 270277.

[6] Mendonca, T., Ferreira, P. M., Marques, J. S. et al. (2013). PH2 - A dermoscopic image database for research and benchmarking in 2013. 35th Annual International Conference of the IEEE Engineering in Medicine and Biology Society (EMBC), 54375440.

[7] Menegola, A. et al. (2017). RECOD Titans at ISIC Challenge 2017. In: ArXiv eprints. arXiv: 1703.04819. URL: https://arxiv.org/abs/1703.048.

[8] Tschandl, P., Rosendahl, C., Kittler, H. (2018) The HAM10000 dataset, a large collection of multi-source dermatoscopic images of common pigmented skin lesions. Sci. Data 5, 180161 doi:10.1038/sdata.2018.161.

Chest X-ray Image denoising based on Convolutional denoising autoencoder

Mohammed IBRAHIM[1] and Sait Ali UYMAZ[1]

[1] Konya Technical University, Konya/Turkey, Mohammed89shamil@gmail.com
[1] Konya Technical University, Konya/Turkey, sauymaz@ktun.edu.tr

Abstract - **Nowadays, medical imaging plays important role in medical settings to obtain high resolution images for the human body. The medical imaging techniques usually suffer from many types of noises such as gaussian, salt and pepper and speckle noises. So, getting a high-resolution body image is so difficult. The accurate medical images is necessary for diagnosis of many diseases. In this paper, medical imaging denoising technique based on convolutional denoising autoencoder is proposed. The NIH chest X-Ray dataset has been used for the training and testing of the proposed model. The model consists of 10 layers to learn the representation of the noise in the image and then reconstruct a new image without the noise. The model performance evaluated by using mean squared error and peak signal to noise ratio. For the training purpose we added gaussian noise to the dataset. The total number of images used is 25,000 splitted into training set 22,500 images and testing set 2500 images. The model achieved excellent results on the testing set with 0.01 mean squared error.**

Keywords - **Image filtering , image processing , deep learning , convolutional neural networks, autoencoder.**

I. INTRODUCTION

During the acquisition and transmission, images are always polluted with the various types of noise such as gaussian and salt & pepper that result in low-quality images. The noise removal from the images must be done before the image analysis task. Digital images plays an important role in many fields like magnetic resonance imaging, computed tomography and X-ray. The noise removal of the medical images is the significant step in the image processing. The medical images get affected by some types of noise that can be classified as substitutive noise speckle noise and Gaussian noise. Therefore the denoising of the medical images leads to a precise analysis and diagnosis of the diseases by the physicians because of medical images like CT-scan (Computed Tomography) , MRI(Magnetic Resonance Imaging),X-ray and PET(Positron Emission Tomography) encompass a very sensitive information about the brain , lung , heart and other body organs. Last years, researchers have proposed many of approaches in the field of image noise removal and filtering such as [1-7]. These methods include non-local means (NLM) [1] which is unlike the local mean which takes the mean of surrounding pixels, it takes the mean of all pixels in the image weighted by how similar are these pixels to the target pixel. The other method proposed is the block-matching 3D filtering which is a novel algorithm based on the 3D transform domain. The BM3D algorithm process blocks of image in a sliding manner and searching for

the similar blocks to the processed one [2]. In this paper we focused on the medical images filtering which is affected by the gaussian noise during the acquisition and transmission. We used the well-known dataset of The NIH chest X-Ray dataset. For the denoising technique we used the denoising convolutional autoencoder architecture to construct a model that learns the representation of the images noise and reconstruct them without the detected noise representation. We used a total of 25,000 images from the dataset splitted into 22,500 for the training set and 2,500 for the testing set. All images are corrupted with randomly gaussian noise for the training purpose. The mean squared error and peak signal to noise ratio are used in order measure the performance of the model.

II. METHODS

1. Dataset:

The NIH Chest X-ray Dataset contains a total number of images 112,120 X-ray images with disease information from 30,805 patients. the authors used Natural Language Processing To create the dataset labels, from the hospital reports of the patients. The authors mention that the labels are expected to be > 90% accurate. Figure 1 shows the samples from the dataset.
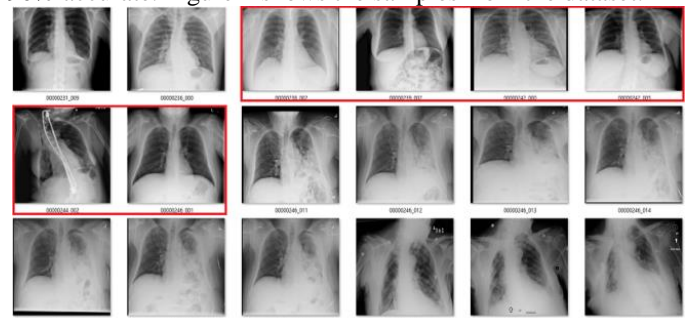
Figure 1. Dataset Samples.

2. Convolutional denoising autoencoder:

The autoencoder in general is a neural network that aim to copy the inputs to their outputs. The autoencoder compress the input into the latent space representations and then reconstruct the output using these representations. The denoising autoencoder work in the same logic by using a corrupted input (data + noise) in order to learn the representation of the noise and reconstruct a clean output. An autoencoder[8] takes input $x \in [0,1]^d$ and map this input to a hidden representation $y \in [0,1]^{d'}$ by deterministic mapping

$y = f_\theta(x) = s(W_x + b)$ that parameterized by $\theta = \{W, b\}$ where W is a d' x d weight matrix and b is the bias vector. The resulting representation is then mapped as the reconstructed output $z \in [0,1]^d$ in input space $z = g_\theta(y) = s(W'_y + b')$. The parameter of the autoencoder should be optimized using the average reconstruction error as following:

$$\theta^*, \theta'^* = \arg\min_{\theta,\theta'}\frac{1}{n}\sum_{i=1}^{n} L(x^{(i)}, z^{(i)}) =$$
$$\arg\min_{\theta,\theta'}\frac{1}{n}\sum_{i=1}^{n} L(x^{(i)}, g_{\theta'}\left(f_\theta(x^i)\right))$$
(1)

Where L is the loss function.

The idea of the denoising autoencoder is modifiying the traditional autoencoder described above by training it to reconstruct a clean input from corrupted one. This process is done by adding a noise to the real data as the input and the output will be the clean data without noise. Figure 2 shows the architecture of the denoising autoencoder.
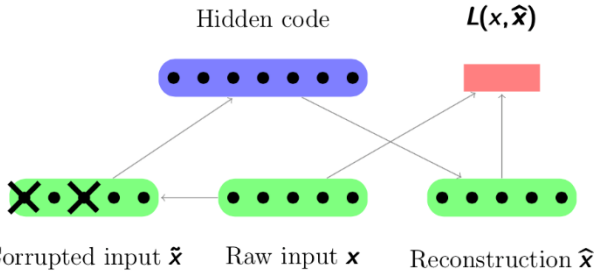
Figure 2. Denoising autoencoder basic architecture.

In this paper we propose a chest X-Ray image denoiser based on the convolutional denoising autoencoder the architecture of the model is shown in table 1. The Convolution layer is used as the main feature extractor followed by the rectified linear units (ReLU) activation function. The kernel size is 3x3 with 64 filters in all of the convolution layers. The batch normalization used to speedup the training and reduce the overfitting in the neural network.

Table 1. Model architecture.

Layer	Activation	Filters
Input Layer	None	
Conv2D	ReLU	64
Conv2D Batch Normalization	ReLU	64
Conv2D Batch Normalization	ReLU	64
Conv2D Batch Normalization	ReLU	64
Conv2D Batch Normalization	ReLU	64
Conv2D Batch Normalization	ReLU	64
Conv2D Batch Normalization	ReLU	64
Conv2D Batch Normalization	ReLU	64
Conv2D Batch Normalization	ReLU	64
Conv2D	None	1

The performance of the model evaluated using Mean squared error (equation 2) and peak signal to noise ratio (equation 3)

$$MSE = \frac{1}{n}\sum_{i=1}^{n}(Y_i - \hat{Y}_i) \quad (2)$$
$$PSNR = 10.\log_{10}(\frac{MAX^2}{MSE}) \quad (3)$$

III. RESULTS

We used the denoising model and trained on the training set that contains 22,500 images that corrupted with random additive white gaussian noise. The MSE used as loss function to measure the reconstruction error. Table 2 shows the training and validation loss for each epoch for a total of 10 epochs.

Table 2. Training and validation loss.

Epoch	Training loss	Validation loss
1	0.0742	0.0332
2	0.0292	0.0250
3	0.0236	0.0210
4	0.0208	0.0187
5	0.0188	0.0184
6	0.0177	0.0162
7	0.0165	0.0152
8	0.0158	0.0146
9	0.0150	0.0144
10	0.0144	0.0134

Figure 3 shows the results of the real image , noisy image and reconstructed image.
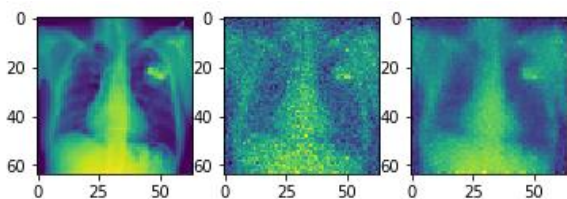
MSE: 0.0169 , PSNR: 65.8
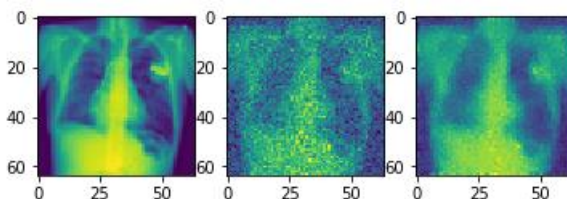
MSE: 0.0175, PSNR: :65.6
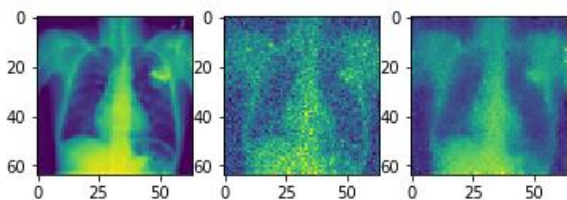
MSE: 0.0175, PSNR: 65.6
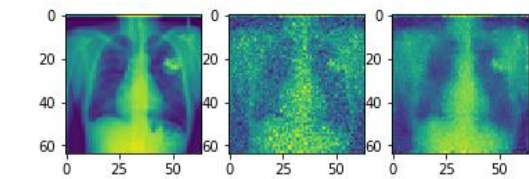
MSE: 0.0164, PSNR: 65.9
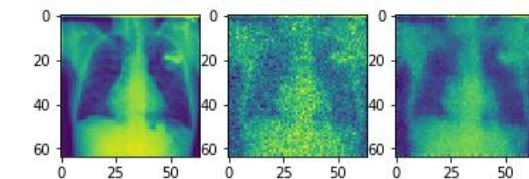
MSE: 0.0149, PSNR: 66.3

Figure 3. The results of 5 images, left image is the real clean image, the middle image is the noisy image and right image is the reconstructed image.

We use the traditional filters that used in this field such as Gaussian and median filters. Figure 4 shows the results of the Gaussian filter with PSNR and MSE results.
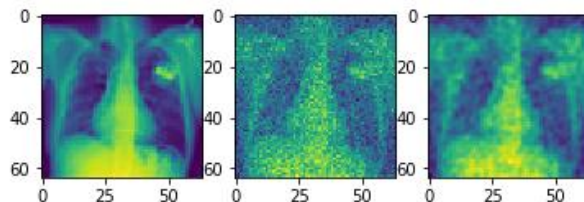
MSE: 0.0285   PSNR: 63.57
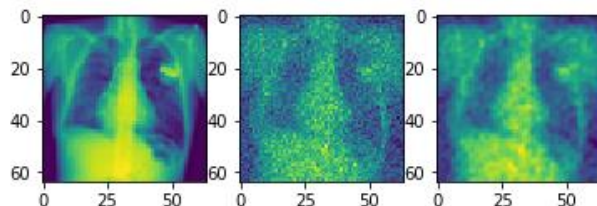
MSE: 0.0284   PSNR: 63.59
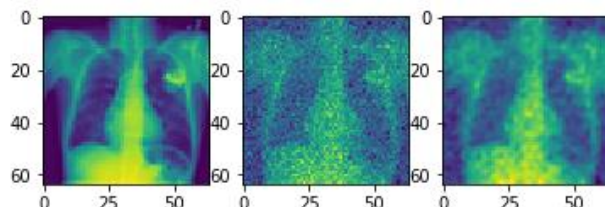
MSE: 0.0293   PSNR: 63.45
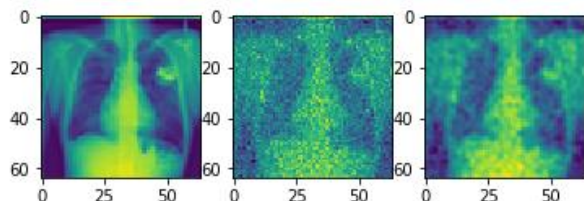
MSE: 0.033   PSNR: 62.90
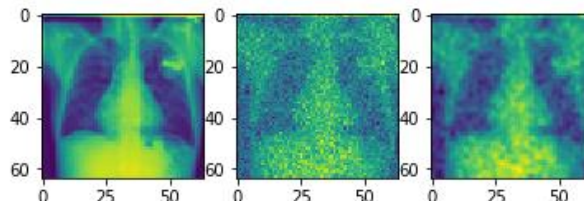
MSE: 0.031   PSNR: 63.15

Figure 4. The results of gaussian filtering, left image is the real clean image, the middle image is the noisy image and right image is the filtered image.

Figure 5 show the results of MSE and PSNR for the median filtering of the same images on the same noise scale.
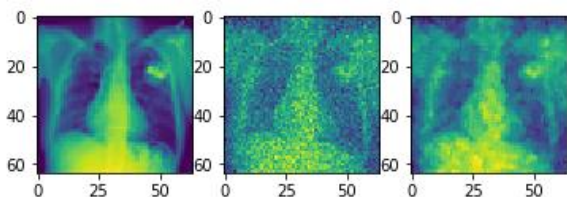
MSE: 0.0377   PSNR: 62.36
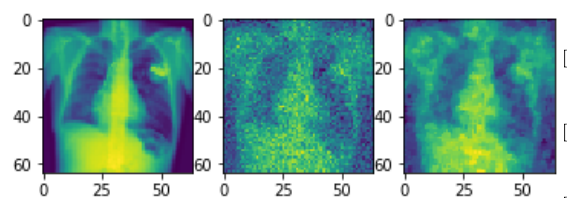
MSE: 0.0391   PSNR: 62.20
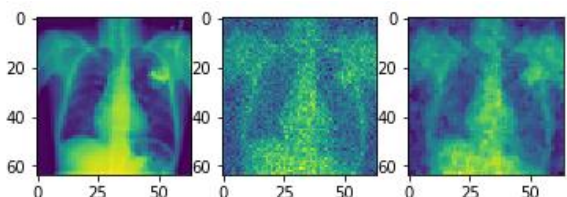
MSE: 0.0366   PSNR: 62.49
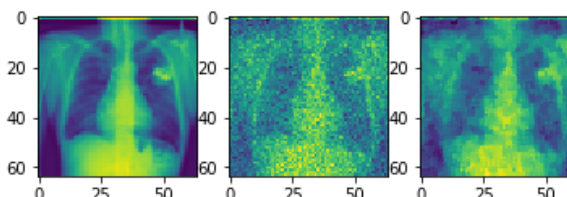
MSE: 0.0408   PSNR: 62.019

MSE: 0.0386   PSNR: 62.258

Figure 4. The results of median filtering, left image is the real clean image, the middle image is the noisy image and right image is the filtered image.
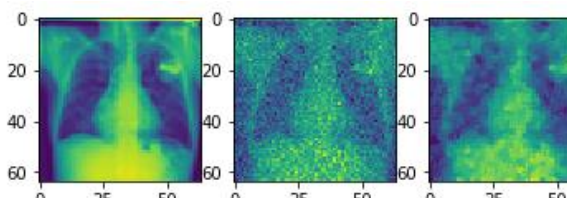
IV. CONCLUSION

In this paper, we proposed a chest X-ray image denoiser based on Convolutional denoising autoencoder. The NIH Chest X-ray dataset used for the evaluation of the model. The Mean-squared error and Peak signal-to-noise ratio (PSNR) used for measuring the performance of the filtering and reconstruction of the proposed method. In the future this work can be developed by implementing deeper architecture and using high-resolution training images will improve the results and achieving higher reconstruction resolution.

REFERENCES

[1] [1] Buades, A., Coll, B., Morel, J. M.: A non-local algorithm for image denoising. In: IEEE Computer Society Conference on Computer Vision and Pattern Recognition 2005, vol. 2, pp.60-65. IEEE (2005).

[2] [2] Dabov, K., Foi, A., Katkovnik, V., Egiazarian, K.: Image denoising by sparse 3-d transform-domain collaborative filtering. IEEE Transactions on Image Processing 16(8), 2080-2095 (2007)

[3] [3] Ng, P. E., Ma, K. K.: A switching median filter with boundary discriminative noise detection for extremely corrupted images. IEEE Transactions on Image Processing 15(6), 1506–1516 (2006)

[4] [4] Zhang, S., Karim, M. A.: A new impulse detector for switching median filters. Signal Processing Letters IEEE 9(11), 360-363 (2002).

[5] [5] . Eng, H. L., Ma, K. K.: Noise adaptive soft-switching median filter. IEEE Transactions on Image Processing 10(2), 242-51 (2001).

[6] [6] Jafar, I. F., Alna'Mneh, R. A., Darabkh, K. A.: Efficient improvements on the BDND filtering algorithm for the removal of high-density impulse noise. IEEE Transactions on Image Processing 22(3), 1223-1232 (2013).

[7] [7] Toh, K. K. V., Ibrahim, H., Mahyuddin, M. N.: Salt-and-pepper noise detection and reduction using fuzzy switching median filter. IEEE Transactions on Consumer Electronics 54(4), 1956-1961 (2008).

[8] [8] Bengio, Y. (2007). Learning deep architectures for AI (Technical Report 1312). Universit´e de Montr´eal, dept. IRO.

Implementation of moth-flame optimization algorithm for the prediction of Turkey's energy demand

A.ÖZKIŞ[1] and T. SAĞ[2]

[1] Necmettin Erbakan University, Konya/Turkey, aozkis@erbakan.edu.tr
[2]Selcuk University, Konya/Turkey, tahirsag@selcuk.edu.tr

Abstract - **In this study, a linear model based on moth-flame optimization (MFO) algorithm was developed for estimating Turkey's energy demand. Input parameters of this model consist of Turkey's gross domestic product (GDP), population, import and export data. The results of the developed *EMFO* model were compared with the results of 2 different models in the literature. Results show that the *EMFO* model is more successful than the compared models. Finally, in this study, the developed *EMFO* model was used to forecast Turkey's energy demand up to 2030.**

Keywords - moth-flame optimization, energy demand estimation, metaheuristic, optimization, Turkey.

I. INTRODUCTION

Demand for energy is increasing in all the world with the effect of developing technology and increasing population. Today, one of the most demanded energy types is electric energy. Electricity consumption per capita is considered as an important parameter indicating the development levels of countries. In order to meet the increasing demand for electricity, more and more electricity is produced. This leads to rapid depletion of non-renewable resources and damage to nature. Electricity is a source of energy that cannot be stored. For this reason, it is of great importance that the electrical energy produced is used efficiently [1]. An energy crisis can occur if the generated energy is less than the actual energy demand. If the generated energy is higher than the actual energy demand, the resources are wasted and the economy is damaged [2].

Since the 1970s, the State Planning Organization (DPT), Turkey Statistical Institute (TSI) and the Ministry of Energy and Natural Resources (ETKB) have used various mathematical models to estimate the amount of energy that will be requested in Turkey [3]. Thus, energy demand estimation has attracted the attention of many researchers and many studies have been done on this subject using statistical, metaheuristic and artificial intelligence based methods. Some of these studies are given in Table 1.

Moth-flame optimization (MFO) [4] is an optimizer proposed by Mirjalili (2015), inspired by moths' navigation behavior in nature. In this study, the energy demand of Turkey is estimated using a linear model named as *EMFO* developed by the MFO algorithm. Results of the *EMFO* model was compared with the results of similar studies in the literature.

Table 1: Some of the studies on energy demand estimation.

Researchers	Method
Kankal et al. (2011) [5]	Statistical
Dilaver and Hunt (2011) [6]	Statistical
Ediger and Tatlıdil (2002) [7]	Statistical
Ediger and Akar (2007) [8]	Statistical
Toksarı (2007) [9]	Ant colony optimization
Ozturk et al. (2005) [10]	Genetic algorithm
Unler (2008) [2]	Particle swarm optimization
Kıran et al. (2012) [11]	Particle swarm optimization
Uguz et al. (2015) [12]	Artificial bee colony
Koc et al. (2018) [13]	Gravitation search algorithm, invasive weed optimization
Sozen et al. (2005) [14]	Artificial neural network

The comparisons showed that the *EMFO* model has obtained more successful results than other compared models.

The rest of the study is organized as follows: The MFO algorithm is summarized in Chapter 2. How the MFO algorithm is implemented on the energy demand estimation model is explained in Chapter 3. Experimental results of the *EMFO* and compared models are analyzed in Chapter 4. Conclusion and advices on future works are presented in Chapter 5.

II. MOTH-FLAME OPTIMIZER

Moths are very similar to the butterfly family. Moths fly at a constant angle to moonlight with a mechanism called transverse orientation at night and can travel straight over long distances [4, 15, 16].

Although moths are oriented according to the transverse orientation mechanism, we can sometimes observe that moths fly spirally around the lights. This is because the moths are tricked by artificial lights. When moths see an artificial light, they try to fly, maintaining the same angle as that light. Since artificial lights are highly close compared to the moon, flying at an angle similar to the light source leads to a deadly spiral fly path for moths [15].

A conceptual model of transverse orientation and spiral flying path around close light sources is shown in Figure 1.
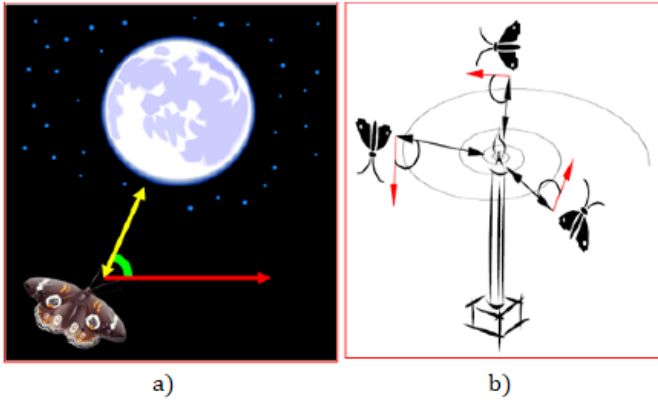
Figure 1: Conceptual model of transverse orientation (a) and spiral flight (b)

The MFO algorithm is modeled inspired by the convergence behavior of the moths to the light shown in Figure 1(b).

A. Moth-Flame Optimization Algorithm

In the MFO algorithm, candidate solutions symbolize moths and decision variables of a problem symbolizes positions of the moths. Moths can fly in 1-D, 2-D or multi-dimensional space by changing position vectors. In the MFO algorithm, a moth swarm is represented by the matrix given in Equation 1.

$$M = \begin{bmatrix} m_{1,1} & m_{1,2} & \cdots & \cdots & m_{1,d} \\ m_{2,1} & m_{2,2} & \cdots & \cdots & m_{2,d} \\ \vdots & \vdots & \vdots & \vdots & \vdots \\ m_{n,1} & m_{n,2} & \cdots & \cdots & m_{n,d} \end{bmatrix} \quad (1)$$

where n is the number of moths and d is the problem dimension. Each moth has a fitness value based on its location and it is stored in the OM array given in Equation 2.

$$OM = \begin{bmatrix} OM_1 \\ OM_2 \\ \vdots \\ OM_n \end{bmatrix} \quad (2)$$

where the index values 1,2, ...,n indicate which fitness value belongs to the which moth.

The MFO has a second matrix and array representing location and fitness values of the flames given in Equation 3 and 4 respectively.

$$F = \begin{bmatrix} F_{1,1} & F_{1,2} & \cdots & \cdots & F_{1,d} \\ F_{2,1} & F_{2,2} & \cdots & \cdots & F_{2,d} \\ \vdots & \vdots & \vdots & \vdots & \vdots \\ F_{n,1} & m_{n,2} & \cdots & \cdots & F_{n,d} \end{bmatrix} \quad (3)$$

$$OF = \begin{bmatrix} OF_1 \\ OF_2 \\ \vdots \\ OF_n \end{bmatrix} \quad (4)$$

While moths represent actual search agents in search space, flames hold the best solution points moths have achieved so far. Each moth searches around a flame and updates the flame if it finds a better solution. Thus, a moth never loses its best solution.

In the MFO algorithm, the number of flames starts equal to the number of moths. Then, using Equation 5, the number of flames is iteratively reduced to 1.

$$flame\_no = N - round\left(iter * \frac{N-1}{MaxIter}\right) \quad (5)$$

The positions of the moths are updated using Equation 6. A logarithmic spiral S function given in Equation 7 is used for updating mechanism.

$$M_i = S\left(M_i, F_j\right) \quad (6)$$

$$S\left(M_i, F_j\right) = D_i . e^{bt} . \cos(2\pi t) + F_j \quad (7)$$

where D_i is the distance between i_{th} moth (M_i) and j_{th} flame (F_j), b is a constant (1 as default) using to define the shape of the logarithmic spiral and t is a random number between [-1, 1]. Lower bound of t is linearly decreased from -1 to -2 over the course of iteration and in last iteration t is randomly generated between [-2, 1].

Pseudo code of the MFO algorithm is given in Figure 2.

```
Update flame no using Eq. (5)
OM = FitnessFunction(M);
if iteration == 1
    F = sort(M);
    OF = sort(OM);
else
    F = sort(M_{t-1}, M_t);
    OF = sort(M_{t-1}, M_t);
end
for i = 1: n
    for j = 1: d
        Update t
        Update M(i,j) using Eq. (6) and (7) with respect to the
corresponding moth
    end
end
```

Figure 2: Pseudo code of the MFO algorithm

III. IMPLEMENTATION OF THE MFO ALGORITHM TO ENERGY DEMAND ESTIMATION PROBLEM

Turkey's GDP, population, import and export data and energy demands between the years of 1979 - 2011 are obtained from [13] and used to develop a linear model based on Equation 8 for energy demand estimation.

$$E_{linear} = w_1 + w_2 X_1 + w_3 X_2 + w_4 X_3 + w_5 X_4 \quad (8)$$

in this model, X_1, X_2, X_3 and X_4 refer to GDP, population, import and export data respectively; w_1, w_2, w_3, w_4 and w_5 are the weight coefficients. The output of the model represents energy demand estimates by years. The total error of the model is calculated by Equation 9.

$$min\, f(v) = \sum_{i=1}^{R} \left(E_i^{observed} - E_i^{predicted} \right)^2 \qquad (9)$$

where R is the total number of observations, $E_i^{observed}$ and $E_i^{predicted}$ are the observed and predicted i. energy demand values.

It is intended to discover the weights w which minimize $f(v)$ error. In this study, MFO algorithm was used to find the most suitable weights.

IV. Experimental Results

A. Parameter settings

In this study, in order to make a fair comparison with the models in the literature, the number of agents of the MFO algorithm is set as 100 and the maximum number of iterations is set as 5000. The MFO algorithm was run 3 times with randomly generated seeds and w weights that produced the least error value after 3 runs were used in the *EMFO* model.

B. Comparison of the models

The *EMFO* model obtained by the MFO algorithm was compared to the *EIWO* and *EGSA* models developed by Koc et al. [13] using IWO and GSA algorithms. The obtained weight coefficients and error values are given in Table 2. When the results are examined, it is observed that the *EMFO* model has less error value than the compared models.

Table 2: Weight coefficients and error values of *EMFO*, *EIWO* and *EGSA* models

Weight Coefficients	EMFO	EIWO	EGSA
w_1	-50.13476	-28.14013	-57.15262
w_2	0.02390	0.00582	0.02461
w_3	1.75763	1.37398	1.89247
w_4	0.09997	0.13009	0.08863
w_5	-0.03636	0.05630	0.05971
$f(v)$	152.64107	367.45717	180.36962

Energy demand estimations, error and relative error values of *EMFO*, *EIWO* and *EGSA* models are given in Table 3. When the results are examined, it is observed that *EMFO*, *EIWO* and *EGSA* has the lowest error value for 13, 11 and 9 years respectively.

Table 3: Energy demand estimations, error and relative error values of *EMFO*, *EIWO* and *EGSA* models

Year	Observed energy demand (TWh)	EMFO Estimations (TWh)	EMFO Error	EMFO Relative Error(%)	EIWO Estimations (TWh)	EIWO Error	EIWO Relative Error(%)	EGSA Estimations (TWh)	EGSA Error	EGSA Relative Error(%)
1979	30.71	32.27	1.56	0.05	35.68	4.97	0.16	**31.61**	**0.9**	**0.03**
1980	31.97	**30.28**	**-1.69**	**-0.05**	34.51	2.54	0.08	29.5	-2.47	-0.08
1981	32.05	32.35	0.30	0.01	36.28	4.23	0.13	**31.87**	**-0.18**	**-0.01**
1982	34.39	**34.13**	**-0.26**	**-0.01**	37.86	3.47	0.10	33.91	-0.48	-0.01
1983	35.7	36.13	0.43	0.01	39.49	3.79	0.11	**36.06**	**0.36**	**0.01**
1984	37.43	**38.34**	**0.91**	**0.02**	41.43	4.00	0.11	38.54	1.11	0.03
1985	39.4	**40.74**	**1.34**	**0.03**	43.30	3.90	0.10	41.19	1.79	0.05
1986	42.47	**42.89**	**0.42**	**0.01**	44.82	2.35	0.06	43.45	0.98	0.02
1987	46.88	45.35	-1.53	-0.03	**46.99**	**0.11**	**0.00**	46.3	-0.58	-0.01
1988	47.91	**47.45**	**-0.46**	**-0.01**	48.72	0.81	0.02	48.69	0.78	0.02
1989	50.71	50.08	-0.63	-0.01	**50.61**	**-0.10**	**0.00**	51.48	0.77	0.02
1990	52.98	53.83	0.85	0.02	**53.45**	**0.47**	**0.01**	55.48	2.5	0.05
1991	54.27	55.58	1.31	0.02	**54.81**	**0.54**	**0.01**	57.45	3.18	0.06
1992	56.68	57.77	1.09	0.02	**56.62**	**-0.06**	**0.00**	59.88	3.2	0.06
1993	60.26	**60.79**	**0.53**	**0.01**	59.10	-1.16	-0.02	63.04	2.78	0.05
1994	59.12	60.88	1.76	0.03	**59.69**	**0.57**	**0.01**	63.58	4.46	0.08
1995	63.68	64.86	1.18	0.02	**63.25**	**-0.43**	**-0.01**	67.93	4.25	0.07
1996	69.86	67.93	-1.93	-0.03	66.02	-3.84	-0.05	**71.23**	**1.37**	**0.02**
1997	73.78	70.53	-3.25	-0.04	68.46	-5.32	-0.07	**74.22**	**0.44**	**0.01**
1998	74.71	72.67	-2.04	-0.03	69.87	-4.84	-0.06	**76.63**	**1.92**	**0.03**
1999	76.77	74.19	-2.58	-0.03	71.01	-5.76	-0.08	**78.36**	**1.59**	**0.02**
2000	80.5	77.58	-2.92	-0.04	74.31	-6.19	-0.08	**81.85**	**1.35**	**0.02**
2001	75.4	**76.52**	**1.12**	**0.01**	73.80	-1.60	-0.02	81.37	5.97	0.08
2002	78.33	79.84	1.51	0.02	**76.87**	**-1.46**	**-0.02**	85.17	6.84	0.09
2003	83.84	**84.23**	**0.39**	**0.00**	81.43	-2.41	-0.03	90.6	6.76	0.08
2004	87.82	89.52	1.70	0.02	**87.60**	**-0.22**	**0.00**	97.27	9.45	0.11
2005	91.58	95.75	4.17	0.05	**93.55**	**1.97**	**0.02**	104.56	12.98	0.14
2006	99.59	**100.51**	**0.92**	**0.01**	97.90	-1.69	-0.02	110.31	10.72	0.11
2007	107.63	99.73	-7.90	-0.07	100.10	-7.53	-0.07	**110.98**	**3.35**	**0.03**
2008	106.27	**105.76**	**-0.51**	**0.00**	107.07	0.80	0.01	119.19	12.92	0.12
2009	106.14	**106.40**	**0.26**	**0.00**	100.81	-5.33	-0.05	117.99	11.85	0.11
2010	109.27	**109.86**	**0.59**	**0.01**	108.31	-0.96	-0.01	122.16	12.89	0.12
2011	114.48	117.84	3.36	0.03	**117.70**	**3.22**	**0.03**	131.64	17.16	0.15

Finally, in this study, Turkey's energy demand between the years of 2012 - 2030 is forecasted using the *EMFO* model. For this, Turkey's GDP, population, import and export data from 2012 to 2030 is estimated with the following scenario.

Scenario: It is assumed that between 2012 - 2030, GDP increased by 4%, population by 0.5%, imports by 2.5% and exports by 3%.

Table 4: Energy demand forecasting with *EMFO* between 2012 - 2030

Year	EMFO Forecasting (TWh)	Year	EMFO Forecasting (TWh)
2012	119.65	**2022**	140.3
2013	121.5	**2023**	142.65
2014	123.39	**2024**	145.07
2015	125.33	**2025**	147.55
2016	127.32	**2026**	150.09
2017	129.35	**2027**	152.7
2018	131.44	**2028**	155.37
2019	133.57	**2029**	158.12
2020	135.76	**2030**	160.94
2021	138		

When the results in Tables 4 are analyzed, it can be said that the *EMFO* model forecasted a steady increase in the energy consumption of Turkey. According to the *EMFO* model and used scenario, energy consumption is expected to reach 160.94 TWh by 2030.

V. CONCLUSION

This study proposes a linear model based on MFO algorithm for estimating Turkey's energy demand. In this model, while Turkey's GDP, population, import and export data are used as input parameters, energy demand is resulting output. Developed *EMFO* model was compared with the *EIWO* and *EGSA* models from the literature. When the obtained results are analyzed, it is seen that *EMFO* model is more successful than the compared models.

In future studies, different models other than linear model can be developed using the MFO algorithm for energy estimation or new forecasting models can be develop for different data set.

REFERENCES

[1] A. Biçer, Enerji Talep Tahminine Yönelik Program Geliştirme ve Bir Bölge için Uygulaması, in, 2017.
[2] A. Ünler, Improvement of energy demand forecasts using swarm intelligence: The case of Turkey with projections to 2025, Energy policy, 36 (2008) 1937-1944.
[3] E. Erdogdu, Electricity demand analysis using cointegration and ARIMA modelling: A case study of Turkey, Energy policy, 35 (2007) 1129-1146.
[4] S. Mirjalili, Moth-flame optimization algorithm: A novel nature-inspired heuristic paradigm, Knowledge-Based Systems, 89 (2015) 228-249.
[5] M. Kankal, A. Akpınar, M.İ. Kömürcü, T.Ş. Özşahin, Modeling and forecasting of Turkey's energy consumption using socio-economic and demographic variables, Applied Energy, 88 (2011) 1927-1939.
[6] Z. Dilaver, L.C. Hunt, Industrial electricity demand for Turkey: a structural time series analysis, Energy Economics, 33 (2011) 426-436.
[7] V.Ş. Ediger, H. Tatlıdil, Forecasting the primary energy demand in Turkey and analysis of cyclic patterns, Energy Conversion and Management, 43 (2002) 473-487.
[8] V.Ş. Ediger, S. Akar, ARIMA forecasting of primary energy demand by fuel in Turkey, Energy policy, 35 (2007) 1701-1708.
[9] M.D. Toksarı, Ant colony optimization approach to estimate energy demand of Turkey, Energy Policy, 35 (2007) 3984-3990.
[10] H.K. Ozturk, H. Ceylan, O.E. Canyurt, A. Hepbasli, Electricity estimation using genetic algorithm approach: a case study of Turkey, Energy, 30 (2005) 1003-1012.
[11] M.S. Kıran, E. Özceylan, M. Gündüz, T. Paksoy, A novel hybrid approach based on particle swarm optimization and ant colony algorithm to forecast energy demand of Turkey, Energy conversion and management, 53 (2012) 75-83.
[12] H. Uguz, H. Hakli, Ö.K. Baykan, A new algorithm based on artificial bee colony algorithm for energy demand forecasting in Turkey, in: 2015 4th International Conference on Advanced Computer Science Applications and Technologies (ACSAT), IEEE, 2015, pp. 56-61.
[13] K. Ismail, R. NUREDDIN, H. KAHRAMANLI, TÜRKİYE'DE ENERJİ TALEBİNİ TAHMİN ETMEK İÇİN DOĞRUSAL FORM KULLANARAK GSA (YERÇEKİMİ ARAMA ALGORİTMASI) VE IWO (YABANİ OT OPTİMİZASYON ALGORİTMASI) TEKNİKLERİNİN UYGULANMASI, Selçuk Üniversitesi Mühendislik, Bilim Ve Teknoloji Dergisi, 6 (2018) 529-543.
[14] A. Sözen, E. Arcaklioğlu, M. Özkaymak, Turkey's net energy consumption, Applied Energy, 81 (2005) 209-221.
[15] K.D. Frank, C. Rich, T. Longcore, Effects of artificial night lighting on moths, Ecological consequences of artificial night lighting, (2006) 305-344.
[16] K.J. Gaston, J. Bennie, T.W. Davies, J. Hopkins, The ecological impacts of nighttime light pollution: a mechanistic appraisal, Biological reviews, 88 (2013) 912-927.

Image Processing Based Fault Detection in Elevator Circuit Boards

H. Erdinç KOÇER[*], Tevfik AKCAN[+]

[*]Selçuk Uni. Technology Faculty, Electrical and Electronics Eng. Dept. Konya 42250, Turkey

[+]Konya Technical Uni. Graduate Education Institute, Computer Engineering Dept, Konya 42250, Turkey

Abstract— In recent years, the development of electronic devices with a more compact design and more complex functions has led to electronic circuit boards becoming smaller and more intensive with circuits and components. Because bare printed circuit boards are an important part of the electronic device, they must be properly inspected before being placed on the market. Various methods are applied to detect defects in the printed circuit board (PCB). Of these, optical images are compared with reference images and errors are detected. In this study, a software has been developed to detect defects of elevator print circuit boards in transmission paths. Three types of image processing libraries are used on the Python platform. These are Scikit-Image, Pillow and OpenCV libraries. Three different types of defects (mouse bite, open circuit and pin hole) were detected by using XOR operator, structural similarity index and template matching.

Keywords - Image Processing, Fault Detection, Printed Circuit Boards

I. INTRODUCTION

A printed circuit board (PCB) mechanically supports and electrically connects electronic components using conductive tracks, pads and other features etched from copper sheets laminated onto a non-conductive substrate. PCBs can be single sided (one copper layer), double sided (two copper layers) or multi-layer (outer and inner layers) [1]. Inspection of Printed Circuit Board(PCB) is one of the important process since in the manufacturing processes there are uncertainties like tolerances, accurate position and sometimes orientation errors. The inspection system can inspect the printed circuit boards on many levels. Bare printed circuit board is a PCB without any electronic components placed on it. In order to reduce the cost which is spent on manufacturing caused by the defected bare PCB, the bare PCB must be inspected [2]. Some problems can be encountered when this examination is done manually with the human factor. As the manual visual inspection is slow, costly and the probability of scrap formation is high, instead of manual visual inspection, machine vision methods are preferred for the examination of especially complex PCBs. Machine vision (MV) is the technology and methods used to provide imaging-based automatic inspection and analysis for such applications as automatic inspection, process control, and robot guidance in industry. Machine vision is concerned with the theory behind artificial systems that extract information from images and sequence of images. The image data can take many forms, such as video sequences, views from multiple cameras, or multi-dimensional data from a medical scanner [3].

A. PCB Inspection Processes

The PCB inspection process is based on two principles: fault detection and fault classification. Fault detection also consists of contact and non-contact methods. Contact methods are based on electrical tests. Non-contact methods are classified as X-ray imaging, ultrasonic imaging, thermal imaging and optical inspection (machine vision or image processing). Today, most of the non-contact inspection methods are based on optical inspection systems.

B. Bare PCB Defects

There are some common defects on the PCB during production. These defects are divided into two categories as potential and fatal defects. Short-circuit and open-circuit faults are in the category of fatal errors. Under rupture, erosion, missing hole and wrong size hole are indicated in the category of potential defects [4]. Fatal error; Defects that the PCB does not meet the purpose for which it was produced. Potential error; They are errors that reduce PCB performance but do not affect its functionality [5]. PCB errors are classified as shown in Table I and Figure I [10].
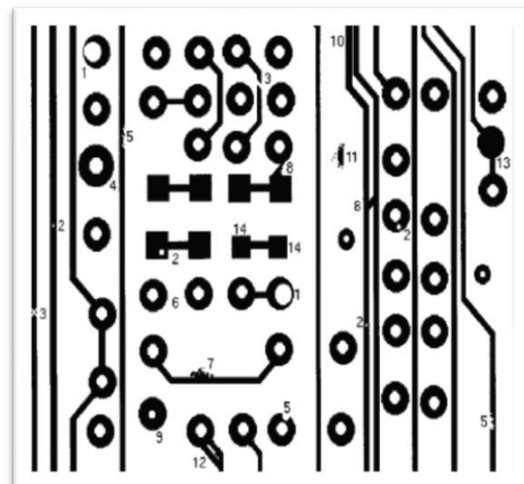
Figure 1 PCB Boards Defects

TABLE I
NAMES OF ERROR TYPES

Error No:	Errors	Error No:	Errors
1	*Leakage*	8	*Shortcut*
2	*Pin Hole*	9	*Wrong Size Hole*
3	*Open Circuit*	10	*Over Close Conductor*
4	*Lower Wear (Extreme Wear)*	11	*Fake Copper*
5	*Mouse Defect (Bite)*	12	*Extreme Short (Shortcut)*
6	*Missing Conductor*	13	*Sliding (Missing) Holes*
7	*Overhang (Mountain Arm)*	14	*Upper Wear (Partial Wear)*

II. METHODS VE TECHNIQUES

It consists of different approaches mentioned in control methods in printed circuit boards. In this study, error detection operations were performed in elevator circuit boards with reference-based approach which is one of the automatic visual control methods [6].

Some approaches are non-contact for error detection and classification; uses a reference-based, image processing approach. In these approaches, the template of a non-defective PCB image and a faulty test PCB image are segmented and compared using image extraction and other procedures. Inconsistencies between images are regarded as defects and classified by similarities and areas of occurrence.

Moganti et al. (1996) proposed three categories of PCB review algorithms: reference approaches, non-reference approaches and mixed approaches.

1. Reference approaches consist of image comparison and model-based technique.
2. Non-reference approaches or design rule validation methods are mainly based on validation of general design rules, which are the verification of the width of conductors and insulators.
3. Hybrid approaches include a combination of both reference and non-reference approaches [6].

A. Algorithms Used to Detect Pcb Errors

In general, many algorithms have been developed in methods of detecting PCB error types. In the literature, generally, a reference-based approach has been adopted and many algorithms related to this approach have been developed. Basically, the algorithm in Figure 2 was used. First, the selection of the PCB image to be tested is made. The image is then buffered to adjust the correct pixels, followed by selection of the template image compared to the defective image. The XOR process is applied with the image used to compare the template image with the PCB image. After that, it is checked whether the resulting image is error-free. Thus, practical analysis of the image followed by thresholding is performed [7].

1	• Selecting the Reference Image
2	• Image Buffering
3	• Selecting the Image to Check
4	• Performing Image Matching
5	• Matching Result Image
6	• Thresholding
7	• Part-Region Analysis
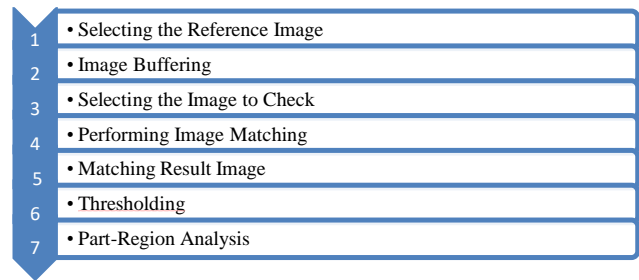
Figure 2 Reference Based Approach Algorithm

B. Image Algorithms

1) Image Extraction: Image extraction is a powerful tool for reference-based analysis. This method is quick to effectively detect the defects by subtracting pixel values from the corresponding positions of images with each other. The positive image is the result of removing the test image from the template image and the negative image is the result of removing the template image from the test image. Thus, this technique is used for defect detection. By applying this method, the two resulting negative and positive images are obtained as in Figure 3 [8].

2) Image Difference Operation: The image difference operation is performed to obtain a difference image consisting of the reference image and the test image. The process was compared using the XOR logical operator, as shown in Figure 4, with corresponding images of each pixel value. This process is similar to image extraction. The main difference between these two operations is that the positive and negative pixel images are combined in an output image of the image difference operation and the value is not negative since it is used as a logical operator [9].

3) Image separation process: The image separation process is used to compare the same and differences in properties between the two images, and then divides the objects into two image output groups. The first set of image output comprises objects having different pixel values and the second set of image output consists of objects having identical pixel values.

4) Not Operator: The process is normally used to complete the foreground and background pixel values of an image from 0 to 1. This operator completes the individual bit value of any variable and sets the corresponding bit accordingly. As a result, the object in an image is converted from black to white or vice versa as in Figure 5 [9].

C. Proposed PCB Printing Control

In this work, Anaconda platform was installed on the computer and Python language was used by using Spider interface. Three types of image processing libraries are used on the Python platform. These are Scikit-image, PILLOW and OPENCV libraries. The paths to be followed for the exemplary studies performed in elevator PCB control are presented as follows.

a) Loading elevator PCB print image to be checked
b) Error free PCB print image loading

     c)   RGB-GRI level conversion
     d)   Detection of defective areas
           i.   XOR operation
          ii.   Structural similarity index
        iii.   Template matching

error types in the elevator circuit boards were determined by applying.

1) *XOR Operation*

In this application, the reference image and the test image will be written on a new file system by taking the classical EXOR operation and finding the difference between the two cards (Figure 3-6).
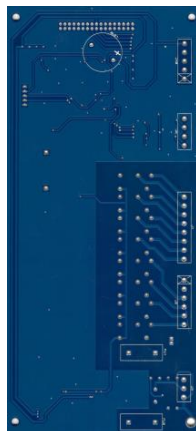
Figure 3 Error-free Elevator Circuit Board
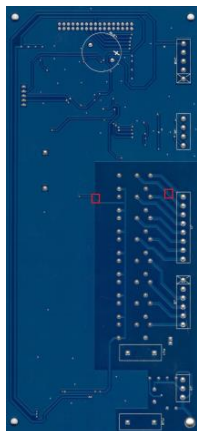
Figure 4 Faulty Elevator Circuit Board

Figure 5 Gray Level Elevator Circuit Board

Figure 6 XOR Application Result of Elevator Circuit Board

2) *Structural Similarity Index*

In this application, using the "diff" function in the classic Scikit-image library of the reference image and the test image, the difference between the two cards was found and errors were red-boxed (Figure 7-8).
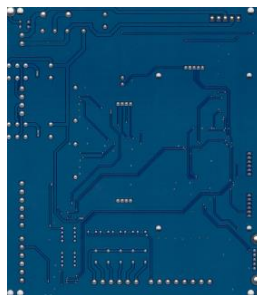
Figure 7 Error-free Elevator Circuit Board
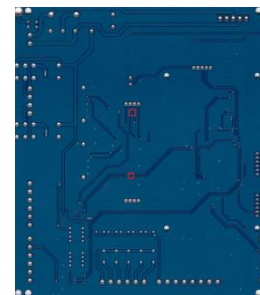
Figure 8 Faulty Elevator Circuit Board (With Red Box)

3) *Template Matching*

In this application, the reference image and the test image will be processed on a new file system by taking the classical EXOR operation and finding the difference between the two cards (Figure 9-11).

Figure 9 Error-free Elevator Circuit Board

Figure 10 Faulty Elevator Circuit Board

    (a)   (b)   (c)
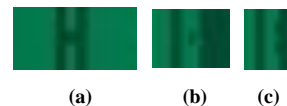
Figure 11 Faults types (a)Open Circuit (b) Pin hole (c) Mouse Bite

III. CONCLUSIONS AND RECOMMENDATIONS

In recent years, the demand for elevator circuit boards with more compact design and more sophisticated functions has made electronic circuit boards smaller and more intense with circuits and components. Since electronic circuit boards are an important part of the device in elevator systems, they must be properly inspected before being placed on the market. Various methods are applied to detect imperfections in the printed circuit board (PCB). Of these, optical images are compared with reference images and errors are detected.

In this study, the default detection rates for 20 elevator circuit boards in three types of error types are shown in Table II.

TABLE II
ERROR DETECTION METHODS ACCORDING TO ERROR TYPES

		Error Types		
		Mouse Bite	Pin Hole	Open Circuit
Methods to find the defaults	XOR	%90	%60	%100
	Structural Similarity	%80	%70	%100
	Template Matching	%70	%50	%90

As a result, the printed circuit boards are detected against to printing faults. It can be recommended according to the results taken from this study as follows:

a) It should be ensured that the image obtained from the cards is compared with different image processing methods to obtain an optimum result,

b) Color images other than gray scale should be studied,

c) Real card defects should be obtained by eliminating false defects with machine learning methods,

c) Hybrid algorithms should be tried,

d) These methods should be compared among themselves and new evaluations and results should be obtained.

REFERENCES

[1]   Anoop, K. P.; Sarath, N. S.; Kumar, VV Sasi. A review of PCB defect detection using image processing. Intern. Journal of Engineering and Innovative Technology (IJEIT), 2015, 4: pp.188-192.

[2]   Kaur, Beant; Kaur, Gurmeet; Kaur, Amandeep. Detection and classification of printed circuit board defects using image subtraction method. In: Recent Advances in Engineering and Computational Sciences (RAECS). IEEE, 2014. pp. 1-5.

[3]   Kaushik, Sonal; Ashraf, Javed. Automatic PCB defect detection using image subtraction method. International Journal of Computer Science and Network, 2012, 1.5: pp.68-73.

[4]   Chauhan, Ajay Pal Singh; Bhardwaj, Sharat Chandra. Detection of bare PCB defects by image subtraction method using machine vision. In: Proceedings of the World Congress on Engineering. 2011. pp. 6-8.

[5]   Nandanvar, V., Signh, S., Bare PCB Verification System Using Optical Inspection & Image Processing, International Research Journal of Computer Science (IRJCS) ISSN: 2393-9842, 2016, Issue 04, Vol. 3.

[6]   Moganti, Madhav; Ercal, Fikret. Automatic PCB inspection systems. IEEE Potentials, 1995, 14.3: pp.6-10.

[7]   VinitaP, M. PCB Fault Detection by Image Subtraction Method.

[8]   Putera, S. I., & Ibrahim, Z. Printed circuit board defect detection using mathematical morphology and MATLAB image processing tools. In 2nd International Conference on Education Technology and Computer. 2010, Vol. 5, pp. 359.

[9]   Khalid, N. K., Ibrahim, Z., & Abidin, M. S. Z.. An algorithm to group defects on printed circuit board for automated visual inspection. IJSSST, 2008, 9(2), pp.1-10

Hourly, Daily, and Monthly Analysis of Big Dataset of Bitcoin Blocks

A. Ş. DOKUZ[1] and A. ECEMİŞ[2] and M. ÇELİK[3]

[1] Niğde Ömer Halisdemir University, Niğde/Turkey, adokuz@ohu.edu.tr
[2] Niğde Ömer Halisdemir University, Niğde/Turkey, ecemisalper@ohu.edu.tr
[3] Erciyes University, Kayseri/Turkey, mcelik@erciyes.edu.tr

Abstract – **Recently, BlockChain network protocol is proposed for safer and more transparent communication among the peers of the networks. Bitcoin is one of the popular application of BlockChain that provide anonymity, traceability, and crowdsourcing based security to the network peers. The increasing attention in Bitcoin led wind range of usage over financial and investment domains, and the usage frequency end up a big dataset of Bitcoin transactions. In this study, we analyzed Bitcoin blocks data to answer what is the daily, weekly or monthly trends of Bitcoin transactions of dataset. The answers to these questions would provide better understanding of Bitcoin transactions and their USD value, and would become a more reliable investment option. The experimental results show that Bitcoin transactions have different characteristics on hourly, daily, and monthly scales.**

Keywords – **BlockChain, Bitcoin analysis, hourly daily and monthly analyses, Bitcoin big data, data mining.**

I. INTRODUCTION

BLOCKCHAIN is a network protocol that provides safe transaction of money, assets, and information without requiring a third party contact [1]. Bitcoin is a popular cryptocurrency application of blockchain application that is proposed by Satoshi Nakamoto [2] [3]. The anonymity, crowdsourcing based system security, and traceability of Bitcoin provides advantages over traditional banking systems.

The increasing popularity of Bitcoin over the world leads to the massive volume and velocity for Bitcoin based transactions. Daily transaction volume of Bitcoin is around 350.000 [4]. Each transaction contains several senders and receivers, and this results the Bitcoin dataset to be bigger. Bitcoin data analysis provides many insights about transactions, sender-receiver relationships, and financial and investment analyses.

However, analyzing Bitcoin dataset is challenging due to several reasons. First, the dataset is a huge dataset that contains millions of sender-receiver information daily. Second, the addresses in Bitcoin data is anonymous and a user could have more than one Bitcoin addresses and these addresses are not related to each other. Third, Bitcoin network could contain malicious activities.

In the literature, several studies are performed to analyze Bitcoin dataset for different purposes. Some of the studies focus on discovering Bitcoin price trend and predict peaks in Bitcoin price. Some of the studies focus on detecting malicious activities and accounts in Bitcoin network.

In this study, we analyzed one year of Bitcoin dataset based on hourly, daily, and monthly aspects. The main goal of this study is to answer what is the daily, weekly or monthly trends of Bitcoin transactions of dataset. Three analyses are performed for the daily, weekly and monthly analysis of Bitcoin dataset, i.e., total transaction count, total Bitcoin count, and total USD value. The results showed that hourly, daily and monthly analyses are beneficial for better understanding of Bitcoin networks and flows of Bitcoins among the network.

The rest of this study is organized as follows. Section 2 presents the literature review. Section 3 presents hourly, daily, and monthly analyses method of Bitcoin dataset. Section 4 presents the experimental results. Section 5 presents conclusions and future studies.

II. LITERATURE REVIEW

The increasing popularity of Bitcoin achieved a wide range of usage over financial and investment domains. This situation results a big dataset of Bitcoin transactions. This big dataset is analyzed on several aspects in the literature to help better understand Bitcoin price fluctuations, financial risk management in Bitcoin, etc.

In the literature, Board et al. [5] analyzed Bitcoin dataset and discovered that less than half of total Bitcoin is circulating. Reid and Harrigan [6] analyzed anonymity of Bitcoin for fraud detection and context and flow discovery using two network topologies. Haubo [7] investigated financial capacity of Bitcoin and stated that risk management of Bitcoin market could be reduced using GARCH models. Urquhart [8] proposed a clustering approach for Bitcoin price calculation. Georgoula et al. [9] proposed a Bitcoin price prediction method that is based on time series analysis and sentiment analysis techniques. Ciaian et al. [10] analyzed 6 years of Bitcoin dataset using time series analysis techniques to investigate the effect of macro financial events on Bitcoin prices. Zhu et al. [11] proposed a VEC model based approach to analyze influence of financial factors on Bitcoin prices, such as USD price, Dow Jones stock value, gold price, and concluded that highest effect on Bitcoin price is observed on USD price.

In this study, we analyzed one year of Bitcoin dataset, September 2018 – August 2019, to extract hourly, daily, and monthly Bitcoin transaction volume, Bitcoin value, and Bitcoin USD values. Based on the analyses, we found several patterns that could benefit financial experts. Also, the results of this study could be used as a decision support system.

III. METHOD

In this section, the analysis steps of this study is explained, the details of hourly, daily, and monthly analyses are presented, and information about linear trend analysis are provided.

A. Analysis Steps

In this section, the steps of hourly, daily, and monthly analyses are presented. First, the dataset preparation is presented, then the analyses are performed. The analysis steps of this study is presented in Figure 1.
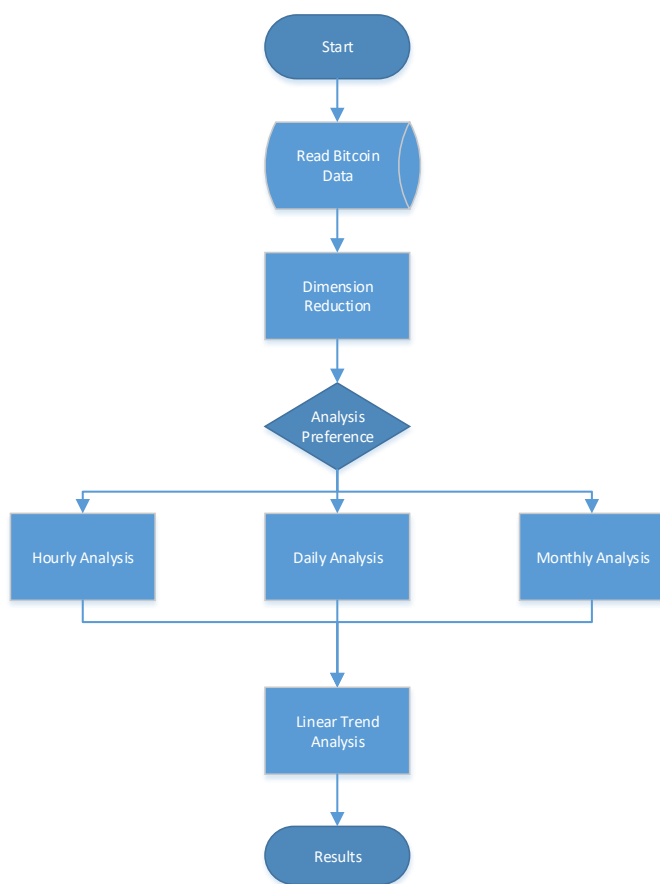
Figure 1. Analysis steps of this study

For the analysis, first, the Bitcoin blocks dataset is read (Figure 1). As the dataset has too many columns and because we do not need these information, we eliminated some of the features. Second, hourly, daily, and monthly analyses are performed. After that, linear trend analysis is performed and hourly, daily, and monthly trends of Bitcoin transaction volume, Bitcoin volume, and Bitcoin USD price volume are extracted. Finally, the results are evaluated.

B. Hourly, Daily, and Monthly Analyses

In this section, the details of hourly, daily, and monthly analyses are presented.

1) Hourly Analysis

In hourly analysis, Bitcoin block dataset is divided into 24 parts and each of them contains transactions that are processed in an hour using timestamp information of the dataset. Total transaction count, total Bitcoin count and total Bitcoin USD value are calculated based on the data of each hour.

2) Daily Analysis

In daily analysis, Bitcoin blocks dataset is divided into 7 parts and each of them contains the information of the transactions that are processed within a day of the week using day information of the blocks dataset. Total transaction count, total spent Bitcoin count, and total value of Bitcoin in USD are calculated for each day.

3) Monthly Analysis

In monthly analysis, Bitcoin blocks dataset is divided into 12 parts and each of them contains the information of the transactions that are processed within a month using timestamp information of the blocks dataset. Total transaction count, total spent Bitcoin count, and total value of Bitcoin in USD are calculated for each month in a time series manner.

C. Linear Trend Analysis

Trend analysis is a method that is used for discovering trends in time series datasets. Linear trend analysis is one of the trend analysis methods that analyzes relationships between parameters and discovers linear trend of the parameters [12]. In this study, we used linear trend analysis to discover trend and variation of the transaction count, total spent Bitcoin count, and total value of Bitcoin in USD.

IV. EXPERIMENTAL EVALUATION

In this section, first, the dataset and the properties of the dataset is provided, and then hourly, daily, and monthly experimental results are presented.

A. The Dataset

The dataset used in this study contains Bitcoin blocks information for one-year period starting from 1 September 2018 to 31 August 2019. There are 53.267 blocks and a total of 112.120.724 transaction present in the dataset. The dataset has 36 parameters in the blocks and they provide information about blocks, hash values, transactions, and spent Bitcoin count for each transaction.

1) Parameter Selection

The Bitcoin dataset has 36 parameters in total. However, we do not need most of these parameters in the analyses. Thus, we removed unnecessary parameters from the dataset to provide more refined dataset and to efficiently use the memory. We used timestamp, total spent Bitcoin count in the transactions, USD value of spent Bitcoin for each transaction in the blocks.

B. Experimental Results

We performed hourly, daily and monthly analyses on the Bitcoin dataset. Also, we extracted the trend of the analyses results. The experimental results of the analyses are provided below.

1) Hourly Analysis Results

Hourly analysis results of total transaction count, total spent Bitcoin count, and USD value of total spent Bitcoin are provided in Figures 2-4.

Figure 2 presents total transaction count with respect to each hour of day for one-year period. The trend of the dataset is also shown in the figure. As can be seen in Figure 2, total transaction count increases with respect to the increase of the hour. In addition to that a sharp decrease is observed at hour 13.
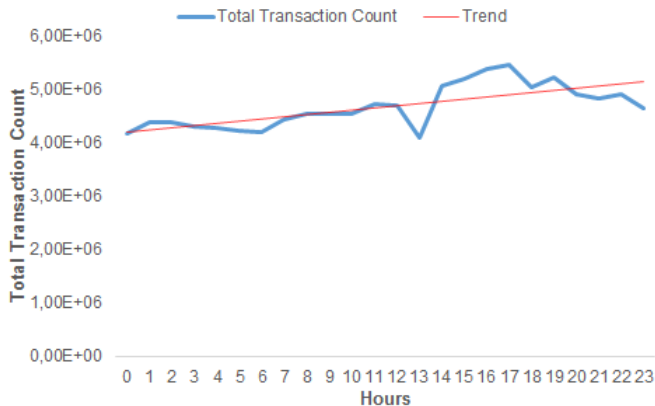
Figure 2: Hourly analysis of total transaction count
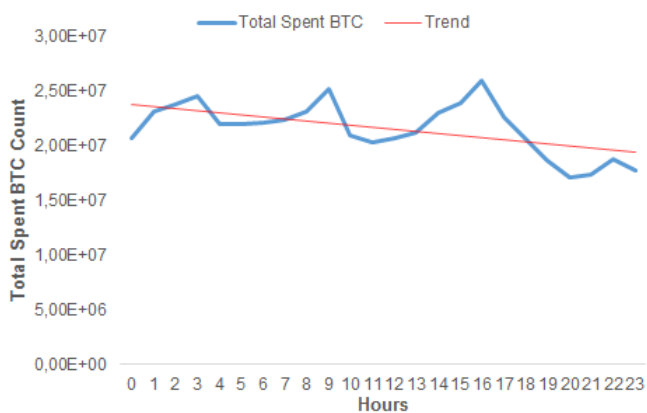
Figure 3: Hourly analysis of total spent Bitcoin count

Figure 3 presents total spent Bitcoin count with respect to each hour of day for one-year period. The trend of the dataset is also shown in the figure. As can be seen in Figure 3, there is a decreasing trend in total spent Bitcoin count. However, there are two major peaks at hours 9 and 16. At these hours, total spent Bitcoin value increases dramatically.
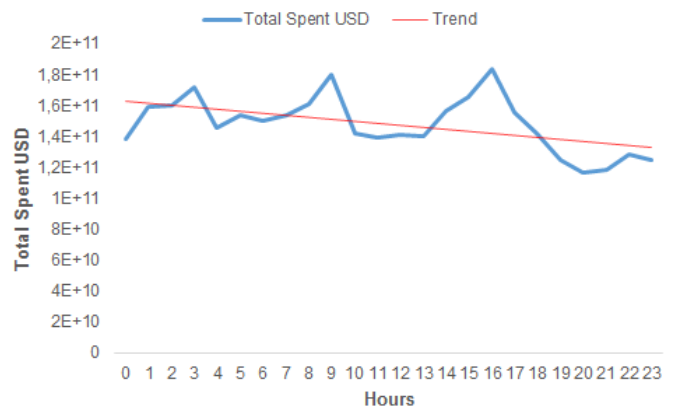
Figure 4: Hourly analysis of USD value of total spent Bitcoin

Figure 4 presents USD value of total spent Bitcoin count with respect to each hour of day for one-year period. The trend of the dataset is also shown in the figure. As can be seen in Figure 4, the trend of USD value is similar with Figure 3, as expected. Also, USD value of total spent Bitcoin has two major peaks, at hours 9 and 16.

2) Daily Analysis Results

Daily analysis results of total transaction count, total spent Bitcoin count, and USD value of total spent Bitcoin are provided in Figures 5-7.

Figure 5 presents total transaction count with respect to each day of the week from Monday to Sunday. As can be seen in Figure 5, there is a decreasing trend from Monday to Sunday. Also, weekends have less transactions than weekdays. The highest number of transactions occur at middle of weekdays and least number of transactions occur at Sunday.
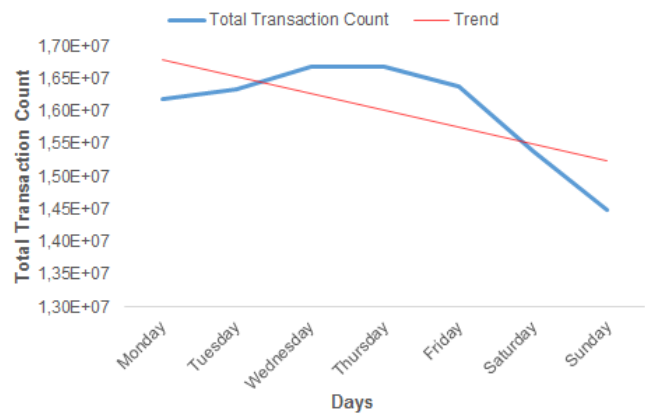
Figure 5: Daily analysis of total transaction count
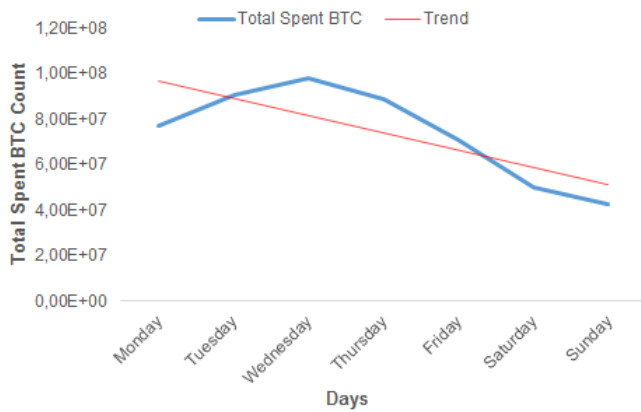
Figure 6: Daily analysis of total spent Bitcoin count

Figure 6 presents total spent Bitcoin count with respect to each day of the week. As can be seen in Figure 6, there is a similar trend with respect to transaction count. The highest spent Bitcoin day is Wednesday and the lowest spent Bitcoin day is Sunday.

Figure 7 presents USD value of total spent Bitcoin with respect to each day of the week. As can be seen in Figure 7, the trend changes with respect to total spent Bitcoin count. We can estimate that there is an evolving trend in Bitcoin spending from weekdays to weekends as the USD value of Bitcoin increases.
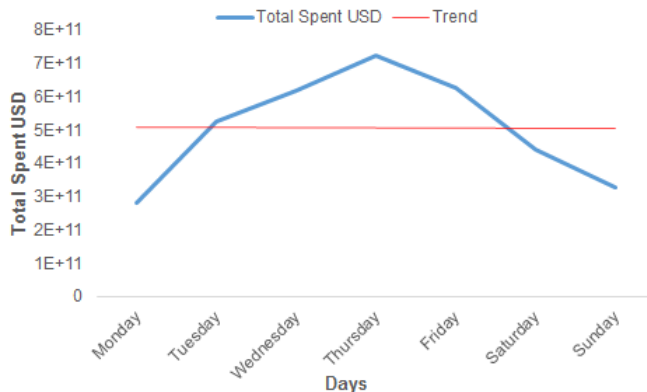
Figure 7: Daily analysis of USD value of total spent Bitcoin

3) Monthly Analysis Results

Monthly analysis results of total transaction count, total spent Bitcoin count, and USD value of total spent Bitcoin are provided in Figures 8-10.

Figure 8 presents total transaction count with respect to each month of the year from September to August. As can be seen in Figure 8, there is a decreasing trend of total transaction count. There are small fluctuations in January and May.
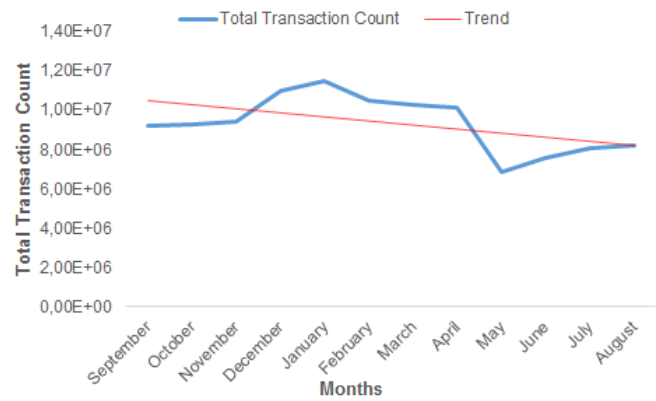
Figure 8: Monthly analysis of total transaction count
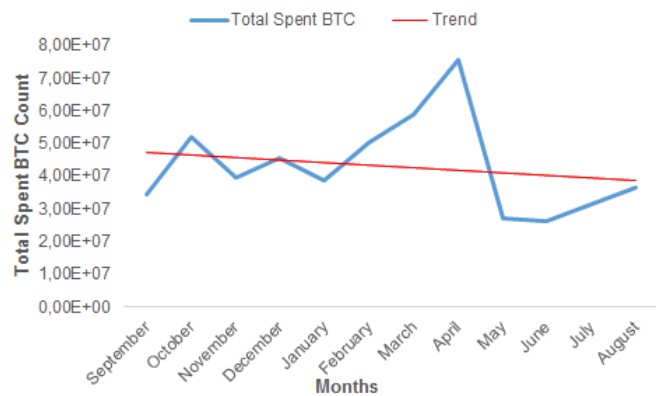
Figure 9: Monthly analysis of total spent Bitcoin count

Figure 9 presents total spent Bitcoin count with respect to the months. As can be seen in Figure 9, the trend is nearly linear. However, there are several peaks in the total spent Bitcoin count, i.e. March, April, and May. Total spent Bitcoin count increased dramatically in March and April, and suddenly falls at May.
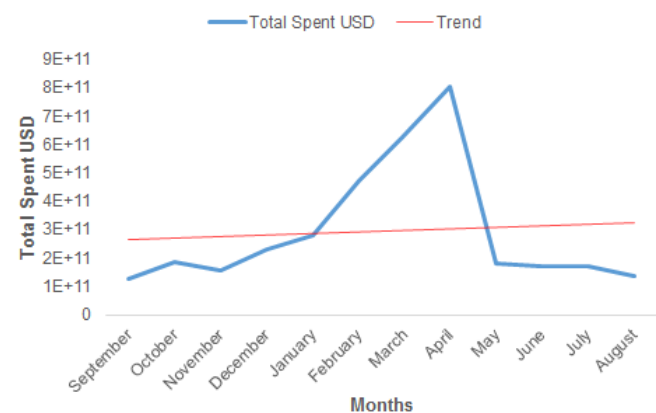
Figure 10: Monthly analysis of USD value of total spent Bitcoin

Figure 10 presents USD value of total spent Bitcoin with respect to the months. As can be seen in Figure 10, USD value of total spent Bitcoin has an increasing trend, contrary to Figures 8 and 9. The increase of total spent Bitcoin at March and April caused a peak in these months. Other months follow near linear trend.

C. Discussion

Hourly analysis shows hot hours in terms of transactions, Bitcoin and USD value of Bitcoin. In this analysis, 14-18 hours are hot hours in terms of transactions. Also, Bitcoin count and USD value has hot hours at 16-17. At hours 9 and 10, Bitcoin count and USD value of Bitcoin have increases, however, similar increase could not be observed in transaction count. This means that spent Bitcoin for transactions at these hours is higher than the other hours.

Daily analysis shows the usage pattern of Bitcoin in weekly manner. Weekdays have higher transactions and spent Bitcoin than weekends. This means that people tend to spend their Bitcoins in weekdays instead of weekends. USD value of spent Bitcoin has different trend than spent Bitcoin. This result shows that the evolution of Bitcoin spending is different among days.

Monthly analysis shows the Bitcoin spendings in monthly manner. In monthly analysis, total transaction count and total spent Bitcoin count have decreasing trends, however, USD value of spent Bitcoin has an increasing trend. Also, USD value has an increasing trend in March-April months.

When all of the results are analyzed together, there are several hours, days, and months that Bitcoin gained attention and has increasing trend. Also, some other hours, days, and months have limited fluctuations. These results could helpful for financial analysts while buying and selling Bitcoins.

V. CONCLUSION

The increasing popularity of Bitcoin and the increase in the data volume lead the need of financial analyses and predictions of Bitcoin datasets. The Bitcoin analyses would provide insight to investors and benefit their strategic planning of investment in Bitcoin. In this study, we analyzed Bitcoin blocks dataset to provide insight in hourly, daily, and monthly evolution of Bitcoin dataset in three aspects, such as, total number of transactions, total number of spent Bitcoin, and USD value of spent Bitcoin. These analyses provide the characteristics of Bitcoin usage in hourly, daily, and monthly manner. The analysis results showed that there are peaks and fluctuations in the Bitcoin usage characteristics in hourly and daily manner. The analysis results could benefit investors on when to invest in and when to leave from Bitcoin.

In the future, we are planning to perform analyses for bigger dataset. Also, anomalous activities are common in Bitcoin, and anomaly detection could be performed on Bitcoin transactions dataset.

ACKNOWLEDGMENT

REFERENCES

[1] S. Melanie, "Anticipating the Economic Benefits of Blockchain," *Technol. Innov. Manag. Rev.*, vol. 7, no. 10, pp. 6–13, 2017.

[2] S. Nakamoto, "Bitcoin: A Peer-to-Peer Electronic Cash System," 2008.

[3] P. Tasatanattakool and C. Techapanupreeda, "Blockchain: Challenges and applications," *Int. Conf. Inf. Netw.*, vol. 2018-Janua, pp. 473–475, 2018.

[4] www.blockchain.com/tr/charts, "Transactions per Day." Acsess Date: 23.09.2019 .

[5] F. R. Board, A. Badev, M. Chen, A. Badev, and M. Chen, "Bitcoin : Technical Background and Data Analysis," 2014.

[6] F. Reid and M. Harrigan, "An Analysis of Anonymity in the Bitcoin System," *IEEE Third Int'l Conf. Privacy, Secur. Risk Trust IEEE Third Int'l Conf. Soc. Comput.*, 2011.

[7] A. Haubo, "Bitcoin, Gold and the Dollar – a GARCH Volatility Analysis," *Univ. Collage Dublin. Sch. Econ.*, 2015.

[8] A. Urquhart, "Price clustering in Bitcoin," vol. 159, pp. 145–147, 2017.

[9] I. Georgoula, C. Bilanakos, and G. M. Giaglis, "Using Time-Series and Sentiment Analysis to Detect the Determinants of Bitcoin Prices," *Mediterr. Conf. Inf. Syst.*, 2015.

[10] P. Ciaian, M. Rajcaniova, and A. Kancs, "The economics of BitCoin price formation," *Appl. Econ.*, vol. 48, no. 19, pp. 1799–1815, 2016.

[11] Y. Zhu, D. Dickinson, and J. Li, "Analysis on the influence factors of Bitcoin ' s price based on VEC model," 2017.

[12] A. Hess, H. Iyer, and W. Malm, "Linear trend analysis : a comparison of methods," *Atmos. Environ.*, vol. 35, no. 30, pp. 5211–5222, 2001.

[13] www.blockchair.com, "Blockchair" Acsess Date: 23.09.2019

An Enhanced Firefly Algorithm with Opposition-Based Learning

T. SAĞ[1], A. ÖZKIŞ [2] and S. ALAN[3]

[1]Selcuk University, Konya/Turkey, tahirsag@selcuk.edu.tr
[2] Necmettin Erbakan University, Konya/Turkey, aozkis@erbakan.edu.tr
[3]Selcuk University, Konya/Turkey, salan@selcuk.edu.tr

Abstract – **This paper presents a modified Firefly algorithm (FA) improved with the opposition-based learning (OBL) method. OBL has an attractive interest in the field of metaheuristic optimization. OBL methods provide a rapid convergence to global optima without tackling local extrema. On the other hand, FA is an exclusive algorithm, which is inspired from the behaviors of fireflies. In this study, the Type-I OBL method is added to FA at two-phase and the modified version of FA is named as OBL-FA. Four well-known test problems were used to evaluate the performance. The effect of OBL methods on the FA algorithm is investigated and the results show that the proposed method has been achieved superior values than the original version of FA.**

Keywords – **OBL, FA, optimization.**

I. Introduction

THE firefly algorithm (FA) is one of the most popular swarm intelligence algorithms [1]. FA animates the behaviors of the fireflies. Although firefly algorithm method has recently developed; a significant number of studies have been cited and it has been successfully applied to many optimization problems. However, each algorithm has some drawbacks, as NFL theorem supports [2]. Therefore, it is not always possible for a single algorithm to produce the best results for all problems. Although FA can achieve successful results in many test functions and real-world problems, it is often tackled to local extrema.

To overcome this disadvantage, opposition-based learning (OBL) has emerged as the methods for improving the existing performance of the algorithms by enhancing the convergence speed and avoiding local extrema. The concept of OBL is firstly introduced by Tizhoosh in 2005 [3]. It tries to calculate the candidate solutions stated in the opposite directions of the current solutions. Thus, OBL methods provides a more effective exploration to optimization algorithms in the search space. In recent years, various studies about OBL and metaheuristics have been published [4-6]. There are lot of studies involving genetic algorithms [3], differential evolutionary algorithm [7, 8], particle swarm optimization [9, 10], artificial bee colony optimization [11], simulated annealing [12] and even multi-objective optimization techniques [13, 14].

In this study, FA is improved by aid of opposition-based learning. Type-I opposition method is adapted to FA. Then, the performance of the proposed three approach and original FA are compared with each other. Furthermore, four well-known benchmark problems involving large-scale dimensions are used to evaluate the proposed method. These are Sum Squares, Rosenbrock, Dixon & Price and Powell functions.

The rest of the paper is organized as follows. The concept of OBL and mathematical definitions are given in section-II. Then, original Firefly algorithm are briefly explained in section-II and proposed methods OBL-FA are detailed in section-IV. Next, benchmark functions are explained in section-V. After that, the experimental results are demonstrated in section-VI. Finally, the conclusions and future works are briefly considered in section-VII.

II. Opposition-based Learning

The term of opposition has been defined in many different ways for various things up to now. Since using opposition makes it easier to explain abstract concepts such as cold, hot, wet, and dry. Almost everything in the real-world can be defined by its opposition [4]. In terms of metaheuristic optimization techniques, *opposition* is used to achieve a better distribution into search space by generating the candidate solutions with their oppositions. Therefore, Opposition-Based Learning (OBL) has been an attractive research field in this specialized literature. In this context, various definitions have been made in order to express the concept of opposition numerically. The opposite number can be defined basically as below.

Definition 1 (Opposite Number): Let $x \in [a, b]$ be a real number. The opposition number $\tilde{x}$ is defined as in Eq. (1).

$$\tilde{x} = a + b - x \qquad (1)$$
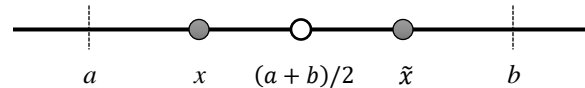
Figure 1: The illustration of opposite number with 1-D.

Type-I OBL method is defined by adapting the above definition for N-dimensional functions and its mathematical definition is given in Definition 2 below.

Definition 2 (Type-I Opposite): Let $x(x_1, \dots x_D)$ be a point in D-dimensional space and $x_i \in [a_i, b_i], i = 1, 2, \dots, D$. The opposite of x is defined by $\tilde{x}(\tilde{x}_1, \dots, \tilde{x}_D)$ as in Eq. (2).

$$\tilde{x}_i = b_i + a_i - \mathrm{x}_i \qquad (2)$$

where $x_i \in \mathbb{R}$ is the i.th candidate solution of an optimization problem with n-dimension and $x_i \in [lb_i, ub_i]$.

There are several versions of OBL methods which has been proposed in literature. Generally, these methods are divided into two categories. The methods in the first category use a mapping function for decision variables. These are modified versions of Type-I. The second category is defined according to the objective space of a problem and these methods are called as Type-2 OBL methods. Type-II opposition requires a priori knowledge of the objective space [5]. In this study, Type-I OBL method is used to improve the FA algorithm.

III. FIREFLY OPTIMIZATION ALGORITHM

Firefly Optimization algorithm was first developed by Xin-She Yang [15]. FA inspires from flashing patterns and behavior of fireflies. Three rules extracted by the nature of fireflies guide the running of the algorithm.

i.   A firefly can attract to other fireflies since all fireflies are unisex.
ii. Attractiveness is proportional to a firefly's brightness. The fireflies shine more to attract prey and share food with others. The less bright firefly will move towards the brighter. If there is no brighter one than a particular firefly, it will move randomly.
iii. The brightness of a firefly is affected or determined by the landscape of the objective function.

The brightness can be considered as the value of the objective function for a maximization problem. The basic steps of FA can be summarized as in Fig-2.

Firefly Algorithm

Objective function $f(x)$, $x = (x_1, ..., x_d)^T$.
Generate an initial population of n fireflies x_i $(i = 1, 2, ..., n)$.
Light intensity I_i at x_i is determined by $f(x_i)$.
Define light absorption coefficient γ.
while $(t < \text{MaxGeneration})$,
for $i = 1 : n$ (all n fireflies)
    for $j = 1 : n$ (all n fireflies) (inner loop)
    if $(I_i < I_j)$
        Move firefly i towards j.
    end if
        Vary attractiveness with distance r via $\exp[-\gamma r^2]$.
        Evaluate new solutions and update light intensity.
    end for j
end for i
Rank the fireflies and find the current global best g_*.
end while
Postprocess results and visualization.

Figure 2: Pseudocode of FA

IV. PROPOSED METHOD

Type-I opposition-based learning method is adapted to FA algorithm. The proposed approach is named as OBL-FA. Type-I OBL method is assembled to the original FA algorithm in two sections. The first section is the phase at which the initial population is generated. After the initial population (Pop) is

created, the opposite points of all solutions (OppPop) are calculated. Then Pop and OppPop are combined and sorted according to fitness values. Finally, the best N solutions are selected for the current population with N-members. Secondly, OBL method is applied at the beginning of each iteration depending on the jumping rate (JR).

JR is a random value in the range of [0,1]. In this study, it is taken as 0.1 for all test functions. It is checked whether a random value generated at each iteration is lower than JR. If it is so, the OBL method is applied. Otherwise, the algorithm continues to run routinely.

The flow chart of the proposed method is shown in Fig-3.
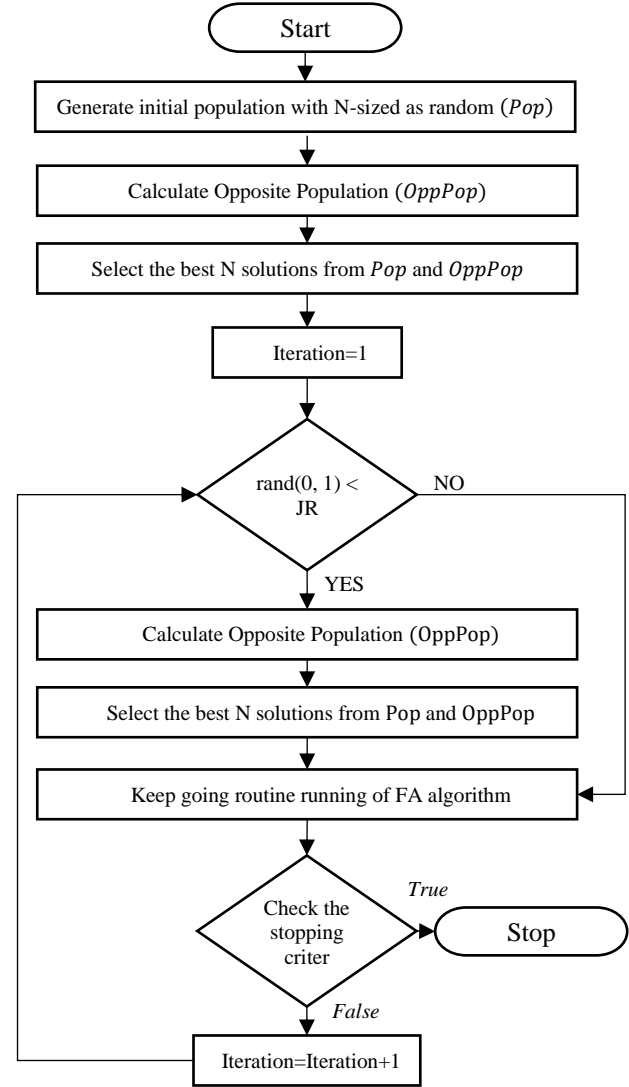
Figure 3: Flowchart of the proposed method OBL-FA

V. BENCHMARK FUNCTIONS

In order to compare the performance of the proposed approach, four test functions are used in this study. These benchmark functions are well-known and frequently used problems in the specialized literature, which are named as Sumsquares, Rosenbrock, Dixonprice and Powell. All of them are minimization functions. The functions are briefly outlined

below. Also, the range of decision variables and global extremum values of the functions can be seen in Table-1.

Table 1: The details of the functions

Function	Dimension	Lower Limit	Upper Limit	Global Optimum
Sumsquares	30	-10	10	0.0
Rosenbrock	30	-30	30	0.0
Dixonprice	30	-10	10	0.0
Powell	24	-4	5	0.0

Sumsquares function is one of the most popular test functions. It is quite simple and has not local minimum points. It is continuous, convex and unimodal. The formulation is given in Eq. (7).

$$f(x) = \sum_{i=1}^{d} i x_i^2 \tag{7}$$

Rosenbrock function is a test problem for gradient-based optimization. The function is unimodal, and the global minimum is a narrow parabolic valley. However, this valley is easy to find, but convergence to the minimum is difficult. The formulation is given in Eq. (8).

$$f(x) = \sum_{i=1}^{d-1} [100(x_{i+1} - x_i^2)^2 + (x_i - 1)^2] \tag{8}$$

Dixon and Price function is a continuous, differentiable, non-separable, scalable and multimodal minimization function. The formulation is given in Eq. (9).

$$f(x) = (x_1 - 1)^2 \sum_{i=2}^{d} i(2x_i^2 - x_{i-1})^2 \tag{9}$$

Powell function is another popular test problem, which is usually evaluated on the hypercube. The formulation is given in Eq. (10).

$$f(x) = \sum_{i=1}^{d/4} [(x_{4i-3} + 10x_{4i-2})^2 + 5(x_{4i-1} - x_{4i})^2 \\ + (x_{4i-2} - x_{4i-1})^4 \\ + 10(x_{4i-3} - x_{4i})^4] \tag{10}$$

VI. EXPERIMENTAL RESULTS

Original FA and the proposed approach which is an enhanced version of FA algorithm by Type1OBL were applied to each benchmark function for 30 times. The statistical results are given in Table 2. In this table, mean values with standard deviations and median values with interquartile ranges (IQR)

were listed to prove that OBL-FA has a more consistent running character than standard FA.

Both methods were executed under the same control parameter values. The values of alpha, beta-min and gamma parameters were assigned to 0.5, 0.2 and 1, respectively. The number of fireflies (agents) is 20. Maximum number of generations is 500. On the other hand, both methods were run for 10000 function evaluations. In OBL-FA algorithm, jumping rate (JR) value was taken as 0.1.

When the results shown in Table-1 are examined, it is understood that the proposed approach achieves more successful results than the original FA algorithm in all test functions. It is clear that the OBL technique enables the algorithm to run more consistently. As can be seen from the first section of the table which belongs to FA, the high standard deviation and IQR values indicate that FA is often tackled to local extremums. However, the proposed OBL-FA algorithm overcame this disadvantage by covering a larger distribution over the search space.

In addition, boxplot graphics are given to show the positive effect of OBL on FA. The boxplots of Sum Square, Powell, Rosenbrock and Dixon-Price functions are shown in Fig-1, Fig-2, Fig-3 and Fig-4, respectively. These figures clearly show that FA has a number of excessive points while OBL-FA has nearly no whiskers at all functions.

Table 2: Comparative Results of Original FA and OBL-FA

Test Function	FA		OBL-FA	
	Mean *Std*	Median *IQR*	Mean *Std*	Median *IQR*
Sumsquares	1.3307 *1.6257*	0.8442 *1.3156*	0.0053 *0.0137*	0.0025 *0.0017*
Rosenbrock	218.5780 *494.5319*	29.2110 *117.4829*	28.7789 *0.1629*	28.7745 *0.2438*
Dixonprice	6.8143 *6.6145*	3.6882 *8.2463*	0.7366 *0.0395*	0.7195 *0.0509*
Powell	4.8662 *3.5148*	4.1115 *5.6730*	0.9805 *0.6815*	0.7559 *1.1174*
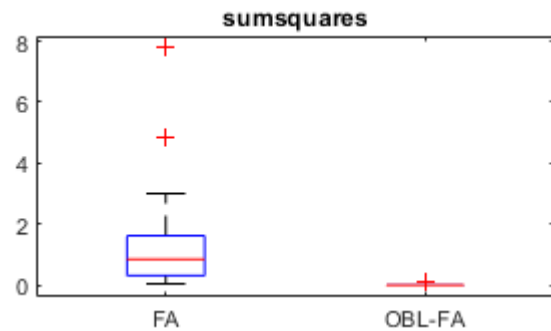
Figure 1: Boxplot graphic for Sum Square function

3
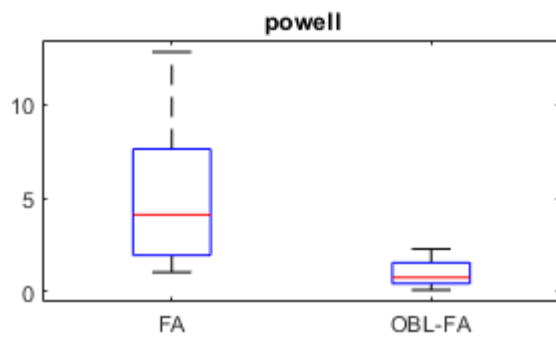
Figure 2: Boxplot graphic for Powell function
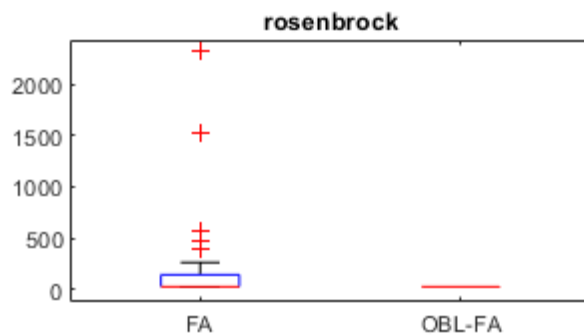
Figure 3: Boxplot graphic for Rosenbrock function
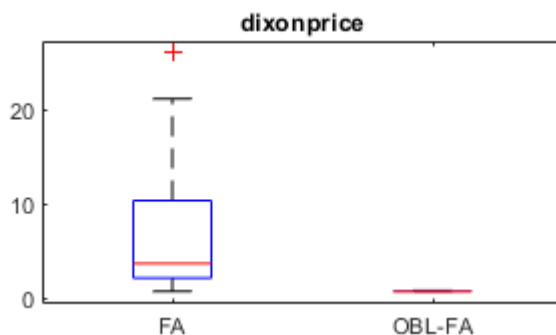
Figure 4: Boxplot graphic for Dixon & Price function

VII. CONCLUSION AND FUTURE WORKS

In this study, the performance of Firefly algorithm was improved by assembling Type-I opposition-based learning method. OBL methods have an attractive research interest in the field of metaheuristic algorithms and these methods helps to perform an effective exploration on the search space. For this purpose, Type-I OBL method is added to FA at two phase and the modified version of FA is named as OBL-FA. Four well-known test problems were used to evaluate the performance. OBL-FA and original FA were run under the same conditions for 30 times. The experimental results showed that the OBL method improved the algorithm's stable running characteristics very positively. Furthermore, OBL-FA has been obtained superior values to original FA for all test functions.

For future studies, this paper provides an encouraging

preliminary study for a comprehensive study. Various OBL methods can be applied to several metaheuristic algorithms by performing a more sensitive JR evaluation on a larger benchmark.

REFERENCES

[1] X. S. Yang, "Firefly Algorithms for Multimodal Optimization," (in English), *Stochastic Algorithms: Foundations and Applications. SAGA 2009. Lecture Notes in Computer Science,* vol. 5792, pp. 169-178, 2009, doi: 10.1007/978-3-642-04944-6_14.

[2] D. H. Wolpert and W. G. Macready, "No free lunch theorems for optimization," *Ieee T Evolut Comput,* vol. 1, no. 1, pp. 67-82, 1997, doi: 10.1109/4235.585893.

[3] H. R. Tizhoosh, "Opposition-Based Learning: A New Scheme for Machine Intelligence," in *International Conference on Computational Intelligence for Modelling, Control and Automation and International Conference on Intelligent Agents, Web Technologies and Internet Commerce (CIMCA-IAWTIC'06)*, 28-30 Nov. 2005 2005, vol. 1, pp. 695-701, doi: 10.1109/CIMCA.2005.1631345.

[4] S. Mahdavi, S. Rahnamayan, and K. Deb, "Opposition based learning: A literature review," *Swarm and Evolutionary Computation,* vol. 39, pp. 1-23, 2018/04/01/ 2018, doi: https://doi.org/10.1016/j.swevo.2017.09.010.

[5] N. Rojas-Morales, M.-C. Riff Rojas, and E. Montero Ureta, "A survey and classification of Opposition-Based Metaheuristics," *Computers & Industrial Engineering,* vol. 110, pp. 424-435, 2017/08/01/ 2017, doi: https://doi.org/10.1016/j.cie.2017.06.028.

[6] Q. Xu, L. Wang, N. Wang, X. Hei, and L. Zhao, "A review of opposition-based learning from 2005 to 2012," *Eng Appl Artif Intel,* vol. 29, pp. 1-12, 2014/03/01/ 2014, doi: https://doi.org/10.1016/j.engappai.2013.12.004.

[7] S. Rahnamayan and G. G. Wang, "Solving large scale optimization problems by opposition-based differential evolution (ODE)," *WSEAS Transactions on Computers,* vol. 7, no. 10, pp. 1792-1804, 2008.

[8] M. A. Ahandani, "Opposition-based learning in the shuffled bidirectional differential evolution algorithm," *Swarm and Evolutionary Computation,* vol. 26, pp. 64-85, 2016/02/01/ 2016, doi: https://doi.org/10.1016/j.swevo.2015.08.002.

[9] H. Jabeen, Z. Jalil, and A. R. Baig, "Opposition based initialization in particle swarm optimization (O-PSO)," in *Proceedings of the 11th Annual Conference Companion on Genetic and Evolutionary Computation Conference: Late Breaking Papers*, 2009: ACM, pp. 2047-2052.

[10] W.-f. Gao, S.-y. Liu, and L.-l. Huang, "Particle swarm optimization with chaotic opposition-based population initialization and stochastic search technique," *Communications in Nonlinear Science and Numerical Simulation,* vol. 17, no. 11, pp. 4316-4327, 2012/11/01/ 2012, doi: https://doi.org/10.1016/j.cnsns.2012.03.015.

[11] X. Yang and Z. Huang, "Opposition-based artificial bee colony with dynamic cauchy mutation for function optimization," *International Journal of Advancements in Computing Technology,* vol. 4, no. 4, pp. 56-62, 2012.

[12] M. Ventresca and H. R. Tizhoosh, "Simulated Annealing with Opposite Neighbors," in *2007 IEEE Symposium on Foundations of Computational Intelligence*, 1-5 April 2007 2007, pp. 186-192, doi: 10.1109/FOCI.2007.372167.

[13] X. Ma *et al.*, "MOEA/D with opposition-based learning for multiobjective optimization problem," *Neurocomputing,* vol. 146, pp. 48-64, 2014/12/25/ 2014, doi: https://doi.org/10.1016/j.neucom.2014.04.068.

[14] T. Niknam, M. R. Narimani, R. Azizipanah-Abarghooee, and B. Bahmani-Firouzi, "Multiobjective Optimal Reactive Power Dispatch and Voltage Control: A New Opposition-Based Self-Adaptive Modified Gravitational Search Algorithm," *IEEE Systems Journal,* vol. 7, no. 4, pp. 742-753, 2013, doi: 10.1109/JSYST.2012.2227217.

[15] X.-S. Yang, *Nature-inspired metaheuristic algorithms*. Luniver press, 2010.

Time Series Analysis with Deep Learning Approaches for Remaining Useful Life Prediction

C. N. BAS[1] and O. DURMAZ INCEL[1]

[1] Galatasaray University, Istanbul/Turkey, cerennbas@gmail.com
[1]Galatasaray University, Istanbul/Turkey, odincel@gsu.edu.tr

Abstract - **Industry 4.0, which has recently become very popular, is a term used for data exchange and automation for production technologies. The manufacturing industry produces a large amount of data which can be used to improve processes and product quality. Analyzing time series data collected from multiple sensors can provide information for active preventive maintenance, which is essential for the sustainability of the factories and automation. Therefore, in this paper, we focus on the prediction of remaining useful life of a machine and proposed a prediction model using a deep learning approach. We perform our experiments on PRONOSTIA dataset, which consist of run-to-failure bearing sensor data. Features, such as mean, kurtosis, skewness, standard deviation, root mean square, crest factor, variance, are extracted from this dataset. Also, health indicator values are calculated to determine the remaining useful life of the bearings. We construct the remaining useful life prediction model, particularly using the LSTM (long-short-term memory) neural network. Finally, we compare the results of our model with the results of previous studies on this dataset. Our results are underperformed from other studies. This dataset is not directly applicable for LSTM network and preprocessing needs high effort.**

Keywords - **Long-short term memory, deep learning, remaining useful life, active preventive maintenance.**

I. INTRODUCTION

THE current revolution of the Internet and machine-to-machine technologies has led to the emergence of the Internet of Things(IoT). The number of devices, "things" connected to the Internet increases widely [1]. IoT makes the objects smart; thus, they can share information and coordinates decisions.

Industry 4.0 contains various information technology paradigms such as cyber-physical systems, IoT, cloud computing, and cognitive computing. Nowadays, the manufacturing industry has a large amount of data which can be used to improve processes and product quality.

This large amount of data should be analyzed to extract the meaningful data, and it can be used for anomaly detection, lifetime estimation, active preventive maintenance or the amount of the used energy in the factory. These are important for the sustainability of factories and automation.

A time series is a series of data points which is a sequence taken at successive time intervals. Time series analysis is used to predict future values based on previously observed values. Time series data analysis can be beneficial for factory automation.

The methods to be used in the time series analysis may vary depending on the type of data and the information intended to be extracted. For example, simple statistical methods or several machine learning methods, such as density based, clustering based, and support-vector machine learning techniques are used to predict anomaly detection, and if it is intended to make numerical inferences, such as machine lifetime estimation, regression methods are used [9].

The active preventive maintenance is one of the most critical parts of smart factories. The purpose of the active preventive maintenance is to trigger required maintenance as early as possible and to reach just-in-time maintenance. Thus, it provides near-zero downtime. To improve productivity, rapid decision making is important.

In order to improve processes in manufacturing industry, the produced sensor data can be used. The processing of big data into significant information is fundamental for sustainable innovation. Due to the lack of smart analytic tools, big data of manufacturing industry could be analyzed in a limited way, and it prevents the provision of Industry 4.0 term. Therefore, we focus on this topic in order to create a deep learning model for such active preventive maintenance. We perform our time-series analysis on Femto-ST Bearing Dataset, which is also called as PRONOSTIA dataset [11]. Long short-term memory (LSTM) algorithm is used to create our remaining useful lifetime (RUL) prediction model. We compared the results of our model with the results of previous studies on this dataset.

This paper is organized as follows: In Section 2, there is an overview on the related work. Section 3 describes the dataset and the steps of the proposed methodology in detail. The results of our experiments are presented and discussed in Section 4. Finally, Section 5 concludes the paper with some remarks.

II. RELATED WORK

The Internet of Things is improving rapidly day by day and aiming to improve the quality of life by connecting many smart devices, technologies and applications. The IoT makes the objects smart, so these objects can see, hear, think and talk and share information among themselves and coordinate decisions.

The IoT can have significant home and business applications to improve quality of our lives [1]. Automation of the everything around us can be realized through the IoT.

The Industry 4.0 era will form a new thinking of production management and factory transformation by the teaming of inter-connected systems and intelligent analytics. The manufacturing industry has large amount of data which can be used to improve processes and product quality. This may be possible by analyzing data effectively. According to [7], advanced predictions tools are needed, in order to process data systematically and make more "informed" decisions.

Manufacturing big data consists of device data and product data. This data can be analyzed and used for active preventive maintenance, optimization of a production line and energy consumption optimization [14].

Prognostics and Health Management (PHM) is dealing primarily with component wear and degradation. Remaining useful life prediction, fault diagnosis and fault detection are targeted by PHM algorithms in order to provide factory wide transparency [8]. This can be achieved by analyzing sensory and system level data. There are many approaches to analyze the manufacturing data in Industry and to create models for prognostics, such as the learning-based and signal processing-based approaches. The learning-based approaches are very common in industrial applications, because they can learn from data without a wide expertise about the process knowledge of the analyzed data. But signal processing-based approaches require the knowledge of certain parameters of the device [4]. For the signal processing, denoising and filtering processes are necessary and important. Feature extraction from time, frequency and time-frequency domains are needed for learning based approaches. RMS, kurtosis, crest factor and standard deviation could be given as an example of these feature. In this study, we also extract these time domain features.

In order to select a suitable technique, problems from similar nature and previously used techniques to solve these problems need to be analyzed. The technique to be used may vary according to the nature of the available data. For example, neural networks can be used for analyzing manufacturing data to calculate lifetime under specific processing conditions [14].

Health condition monitoring of machines is a crucial task to guarantee reliability in industrial processes. The quality of the dataset is a critical issue for machine learning models. The real time data collected from machine in the field will help to achieve optimal flexibility and robustness for handling different situations [7]. The machine fleet data can be used to build clusters which represents different machines performances and working conditions based on similarities of the machines performing similar tasks or similar service times.

Yoo and Baek [16] present a similar study. They used the same dataset and deep learning approaches to predict RUL. In this study novel time-frequency image is proposed in order to construct health indicator (HI) and predict the RUL. The Convolutional Neural Network (CNN) is used to automatically discover useful features from the raw signal to construct the HI and the Morlet-based Continuous Wavelet Transform (CWT) was used to extract image features from the raw vibration

signal. CNN is used as a regression model to estimate the CWTCNN-HI based on training images. The HI shows the condition of the machine or component. The RUL is predicted by calculating the difference between the time at which the predicted HI reaches the threshold and the current time. A Gaussian Process Regression (GPR) algorithm has been used to predict the RUL of the bearings.

III. METHODOLOGY

In this section, we briefly describe the dataset we have used, the data manipulation steps, health indicator calculation and finally, the LSTM model created for RUL prediction.

A. Dataset

The analyzed dataset contains 17 run-to-failure data of rolling element bearings acquired from a PRONOSTIA platform [11]. The overview of the PRONOSTIA platform can be seen in Figure 1.

This dataset is constructed under 3 different operating conditions as follows:

- First operating conditions: 1800 rpm and 4000 N;
- Second operating conditions: 1650 rpm and 4200 N;
- Third operating conditions: 1500 rpm and 5000 N.

Table 1 shows the distribution of bearings under these 3 operating conditions.

The characterization of the bearing's degradation is based on two data types of sensors: vibration and temperature. The vibration sensors consist of two miniature accelerometers positioned on the vertical and the horizontal axis. The acceleration measures are sampled every 10 s for a sample period of 0.1 s at 25.6 kHz frequency, and the temperature ones are sampled at 10 Hz. Traditional fault diagnostic methods based on frequency analysis is not applicable for this dataset.

The bearings were not naturally degraded; therefore, each bearing's degradation pattern is different from each other.

This dataset has been analyzed to predict bearing's remaining useful life by other studies with many different approaches; Loutas et al. [10], e-support vectors regression, Singleton et al. [13], Extended Kalman Filtering, Ren et al. [12] sparse representation model, Wang et al. [15], proportional hazard model and Benkedjouh et al. [2] support vector regression.
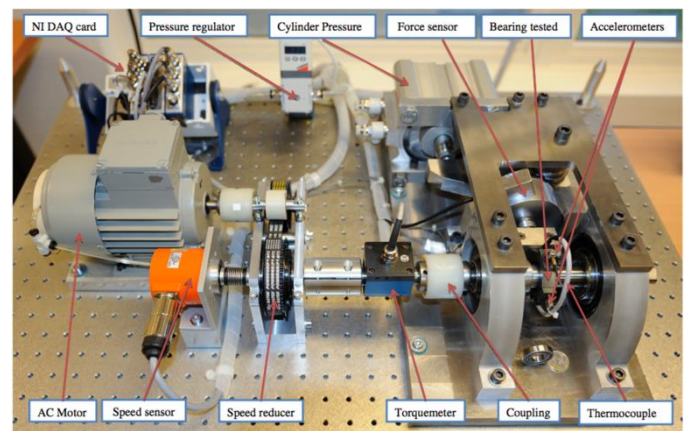
Figure 1: The overview of the PRONOSTIA platform.

Table 1: Bearing Datasets with Operational Conditions.

Datasets	Condition1	Condition2	Condition3
Training	Bearing1_1	Bearing2_1	Bearing3_1
Datasets	Bearing1_2	Bearing2_2	Bearing3_2
Test	Bearing1_3	Bearing2_3	Bearing3_3
Datasets	Bearing1_4	Bearing2_4	
	Bearing1_5	Bearing2_5	
	Bearing1_6	Bearing2_6	
	Bearing1_7	Bearing2_7	

B. Data Preprocessing

Firstly, we preprocessed the raw data by removing unnecessary fields for analysis. There are many CSV files separately for each sampling of bearing accelerometer sensors. We combined these CSV files, so there is one file for each bearing. We did not use the temperature data since it is not available for all bearings. This dataset has high-frequency noise; therefore, we applied Discrete Wavelet Transform on the horizontal and vertical accelerometer data. Figure 2 shows the smoothed accelerometer signals.

We extract many features such as mean, standard deviation, crest factor, variance, skewness, root mean square and kurtosis. While extracting these features 1-minute samples are used. We also calculated the actual RULs. Then duplicate lines are removed and all learning datasets are merged into one data frame. According to Figure 3 we can say mean of acc1 and acc2 shows rising trend after degradation started. We had to select features for all bearings to create a better model because the dataset has very variant degradation patterns for each bearing.
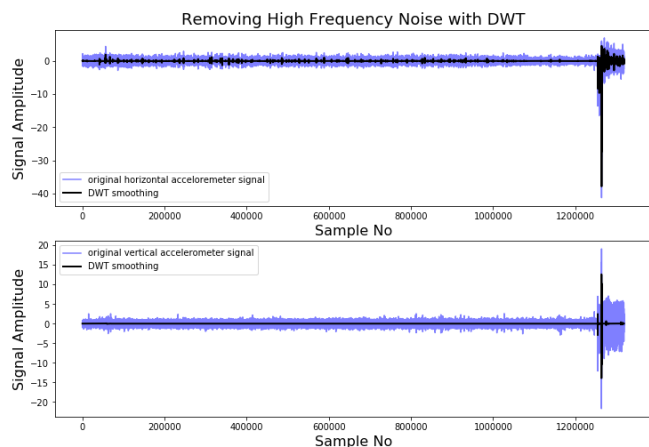
Figure 2: Accelerometer signals and their DWT smoothed versions.
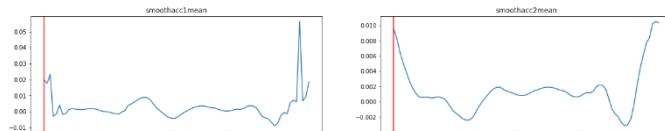
Figure 3: Mean of horizontal and vertical accelerometer.

C. Health Indicator Calculation

After feature extraction, we calculated health indicator for the bearings. Firstly, we used first 15 minutes as 1 and last 15 minutes as 0 for the health indicator values. 1 indicates healthy state and 0 indicates degraded state. Then we calculated remaining health indicator values according to correlation of features with health indicator. Table 2 presents correlation coefficient between the features and HI. None of the sensors have a remarkable high correlation with the HI. We decided to use features which has correlation coefficients greater than 0.2 to calculate other HI values. Here, we used simple ordinary least square (ols) model from stats models which is a python library. Then, we calculated health indicators for learning and test data frames. The Figure 4 shows the change of health indicator values of bearing through lifetime and it represents a degradation pattern.

Table 2: Correlation Coefficient of HI.

	HI
Acc1 Mean	-0.077
Acc2 Mean	-0.279
Acc1 STD	-0.287
Acc2 STD	-0.221
Acc1 Var	-0.194
Acc2 Var	-0.125
Acc1 Kurtosis	-0.099
Acc2 Kurtosis	-0.204
Acc1 RMS	-0.287
Acc2 RMS	-0.220
Acc1 Skew	0.138
Acc2 Skew	0.054
Acc1 Crest Factor	-0.303
Acc2 Crest Factor	-0.318
HI	1.00
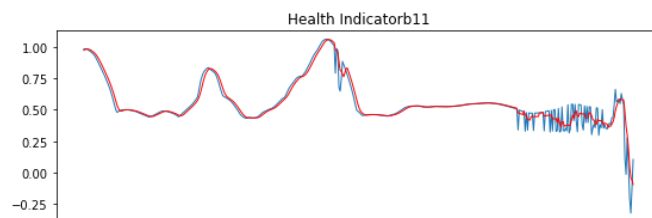
Figure 4: Bearing1_1 Health Indicator.

D. LSTM

Long short-term memory is an artificial recurrent neural network which solves the vanishing gradients problems. In a basic implementation of LSTM, the hidden layer is replaced by a complex block. This complex block is composed of gates that trap the error in the block [3]. Figure 5 shows that the layers of the recurrent neural networks and the complex structure of the LSTM block.
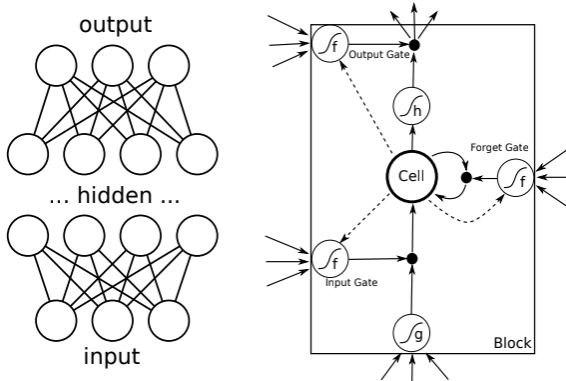
Figure 5: The structure of RNN and LSTM block.

E. Prediction Model

As a last step, we construct the deep network. The first layer an LSTM layer with 100 units and another LSTM layer with 50 units follows this layer. After each LSTM layer, we applied dropout to control overfitting. And then we add a dense output layer with single unit and linear activation since this is a regression problem. Figure 6 presents the overall structure of our prediction model.

IV. RESULTS

This section presents the results of this study. Mean absolute error is used as a performance metric of the model. For the created LSTM network, we defined batch size as 50 and epoch size as 200. Our experiments are performed on a merged dataset. This dataset contains information for each bearing. In the first epoch, mean absolute error is calculated as 147.89 in training dataset. And through the fitting process of model it reduced to 67.0041. Fitting process lasted at 121 epochs.

We also use a scoring function as a metric to compare our results with the previous studies. Percent errors and scoring function is used to compare performances.

Percent error function is defined in Equation 1:

$$Er = 100 \; x \; \frac{ActRUL - PredictedRUL}{ActRUL} \qquad (1)$$

And score is calculated, using Equation 2 and Equation 3:

$$Ai = \begin{cases} e^{(-\ln(0.5).(\frac{Eri}{5})} & if \; Eri \leq 0 \\ e^{(+\ln(0.5).(\frac{Eri}{20})} & if \; Eri > 0 \end{cases} \qquad (2)$$

$$Score = \frac{1}{11}\sum_{i=1}^{11} Ai \qquad (3)$$

In the Table 3, it can be seen the comparison of our prediction model results with previous studies. When we compared our results even we have score as 0.27, mean and standard variation values of errors are higher than the other studies. Normally, we do not need to calculate features for deep learning algorithms. PRONOSTIA dataset only consists of accelerometer data and each bearing has different degradation pattern. Therefore, we extracted features and calculated health indicator values. The results of our model need improvement. These results are not just related with our model. Each bearing has different degradation pattern and we do not know the reason of degradation. The lifetime of bearings varies between 30 minutes to 7 hours. We can say that dataset is imbalanced and the inputs are not sufficient for output. An LSTM network did not perform well on this merged dataset.

V. CONCLUSION

In order to realize the term Industry 4.0 which is related with factory automation and sustainability, lack of smart analytics tool should be removed. The big data collected from various sensors can be used for anomaly detection, life time estimation and active preventive maintenance. In this study, Femto-ST Bearing Dataset is used for time series analysis and we constructed a prediction model for remaining useful lifetime of degraded bearings. While we are constructing our model, we used LSTM network. Time domain feature extraction is also applied on dataset and health indicator values are calculated before construct the model.
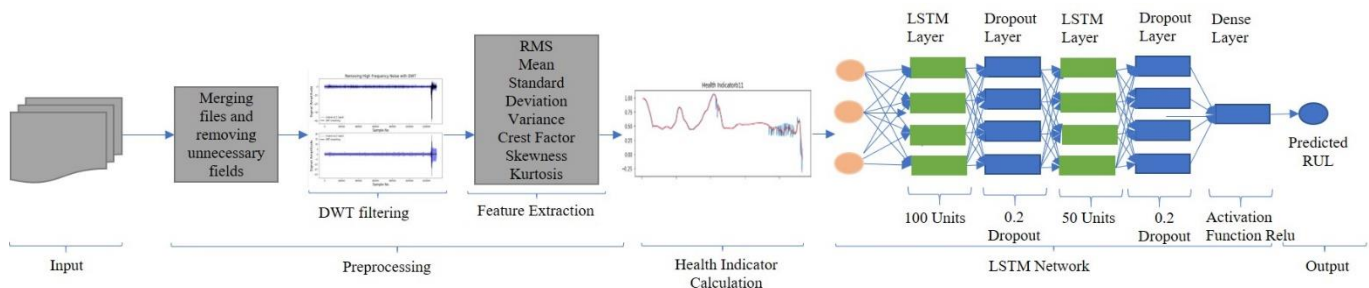
Figure 6: Overall Prediction Model

Table 3: Comparison of prediction model with other studies.

Testing Dataset	Total Time(s)	Actual RUL(s)	Predicted RUL(s)	Guo et al. [5]	Hong et al. [6]	Yoe and Baek [16]	Proposed Method
Bearing1_3	18010	5730	5805	43.28	-1.04	1.05	-1.85
Bearing1_4	11380	339	5817	67.55	-20.94	20.35	-1839
Bearing1_5	23010	1610	1286	-22.98	-278.26	11.18	17.52
Bearing1_6	23010	1460	1351	21.23	19.18	34.93	6.17
Bearing1_7	15010	7570	5817	17.83	-7.13	29.19	23.05
Bearing2_3	12010	7530	5817	37.84	10.49	57.24	22.43
Bearing2_4	6110	1390	5817	-19.42	51.8	-1.44	-321.55
Bearing2_5	20010	3090	4567	54.37	28.8	-0.65	-49.25
Bearing2_6	5710	1290	5817	-13.95	-20.93	-42.64	-361.70
Bearing2_7	1710	580	5817	-55.14	44.83	8.62	-977.30
Bearing3_3	3510	820	5817	3.66	-3.66	-1.22	-645.82
Mean				32.48	44.28	18.96	-375.22
SD				37.57	90.29	25.59	559.5423
Score				0.26	0.36	0.57	0.27

Finally, we compared our prediction model results with the previous studies, and we can say that our prediction model needs to be improved. To create a better model, we have to focus on health indicator calculation and LSTM network layers can be differently applied. Deep learning could be used to health indicator calculation.

REFERENCES

[1] Al-Fuqaha, A., Guizani, M., Mohammadi, M., Aledhari, M., & Ayyash, M. (2015). Internet of things: A survey on enabling technologies, protocols, and applications. IEEE communications surveys & tutorials, 17(4), 2347-2376.

[2] Benkedjouh, T., Medjaher, K., Zerhouni, N., & Rechak, S. (2013). Remaining useful life estimation based on nonlinear feature reduction and support vector regression. Engineering Applications of Artificial Intelligence, 26(7), 1751-1760.

[3] Gamboa, J. C. B. (2017). Deep learning for time-series analysis. arXiv preprint arXiv:1701.01887.

[4] Gillespie, R., & Gupta, S. (2017). Real-time Analytics at the Edge: Identifying Abnormal Equipment Behavior and Filtering Data near the Edge for Internet of Things Applications. Paper SAS645.

[5] Guo, L., Li, N., Jia, F., Lei, Y., & Lin, J. (2017). A recurrent neural network based health indicator for remaining useful life prediction of bearings. Neurocomputing, 240, 98-109.

[6] Hong, S., Zhou, Z., Zio, E., & Hong, K. (2014). Condition assessment for the performance degradation of bearing based on a combinatorial feature extraction method. Digital Signal Processing, 27, 159-166.

[7] Lee, J., Kao, H. A., & Yang, S. (2014). Service innovation and smart analytics for industry 4.0 and big data environment. Procedia Cirp, 16, 3-8.

[8] Lee, J., Lapira, E., Bagheri, B., & Kao, H. A. (2013). Recent advances and trends in predictive manufacturing systems in big data environment. *Manufacturing letters*, *1*(1), 38-41.

[9] Lei, Y., Li, N., Guo, L., Li, N., Yan, T., & Lin, J. (2018). Machinery health prognostics: A systematic review from data acquisition to RUL prediction. *Mechanical Systems and Signal Processing*, *104*, 799-834.

[10] Loutas, T. H., Roulias, D., & Georgoulas, G. (2013). Remaining useful life estimation in rolling bearings utilizing data-driven probabilistic e-support vectors regression. *IEEE Transactions on Reliability*, *62*(4), 821-832.

[11] Nectoux, P., Gouriveau, R., Medjaher, K., Ramasso, E., Chebel-Morello, B., Zerhouni, N., & Varnier, C. (2012, June). PRONOSTIA: An experimental platform for bearings accelerated degradation tests. In *IEEE International Conference on Prognostics and Health Management, PHM'12.* (pp. 1-8). IEEE Catalog Number: CPF12PHM-CDR.

[12] Ren, L., Lv, W., & Jiang, S. (2018). Machine prognostics based on sparse representation model. *Journal of Intelligent Manufacturing*, *29*(2), 277-285.

[13] Singleton, R. K., Strangas, E. G., & Aviyente, S. (2014). Extended Kalman filtering for remaining-useful-life estimation of bearings. *IEEE Transactions on Industrial Electronics*, *62*(3), 1781-1790.

[14] Wan, J., Tang, S., Li, D., Wang, S., Liu, C., Abbas, H., & Vasilakos, A. V. (2017). A manufacturing big data solution for active preventive maintenance. *IEEE Transactions on Industrial Informatics*, *13*(4), 2039-2047.

[15] Wang, L., Zhang, L., & Wang, X. Z. (2015). Reliability estimation and remaining useful lifetime prediction for bearing based on proportional hazard model. *Journal of Central South University*, *22*(12), 4625-4633.

[16] Yoo, Y., & Baek, J. G. (2018). A novel image feature for the remaining useful lifetime prediction of bearings based on continuous wavelet transform and convolutional neural network. *Applied Sciences*, *8*(7), 1102.

VoIP Network Security Issues via Layered Architecture

Ş.G.ŞANLIÖZ[1] and M.A.AYDIN[1]

[1] MSÜ Hezarfen Havacılık ve Uzay Teknolojileri Enstitüsü, İstanbul/Turkey, ganisanlioz@hotmail.com
[1] İstanbul Üniversitesi, İstanbul/Turkey, aydinali@istanbul.edu.tr

Abstract - **In this study, the structure of VOIP technology, it's logic, protocols and the vulnerabilities are reviewed within the layered architecture. Internet Protocol VoIP security issues, which are analyzed in five layers over the Stack architecture, are handled separately in each layer. Various vulnerabilities of VOIP security, from the physical layer to the application layer, are detailed and the possible security measures against these vulnerabilities are presented.**

Keywords – **VoIP, SIP, RTP, Layered Architecture, VoIP Countermeasures.**

I. INTRODUCTION

As a result of the rapid development of technology and the increasing number of devices connected to the Internet, the convenience in our lives has increased. Especially communication technologies are directed to the internet. The data transmitted instantly on the internet is usually multimedia data [1]. As a result, the internet structure reduces access to information to instantaneous levels. Therefore, information security vulnerability arises. This situation in particular directs the instant communication data to certain algorithms and methods. These algorithms are mostly used with multimedia data in the network structure. Text, sound, images and videos form multimedia data. A wide variety of security vulnerabilities and threats associated with these vulnerabilities affect instantaneous data transmitted on the internet and make it unusable.

With the development of IP technology, security systems, camera systems, communication systems and many other systems started to use this technology infrastructure. IP-based voice communication with VoIP technology has been increasing in recent years. The most important reason for this is the remarkable cost effectiveness and high performance of VoIP technology [2].

However, these VoIP technology protocols and architectures that operate in real time have brought additional measures for performance and security in addition to conventional network applications [3]. Examples include the creation of VLANs in the network, prioritizing some media packets with QoS [4], or the use of dynamic measures such as Session Border Controller (SBC) as well as conventional measures such as a firewall [5]. In this study, VoIP structure and protocols are examined. In addition, security vulnerabilities within the system are revealed and threats are exposed through these vulnerabilities.

In the second part of the article, VoIP working architecture, in the third part streaming protocols, in the fourth and last part the security vulnerabilities in VoIP systems and threats that may occur through these vulnerabilities are explained.

II. VOIP NETWORK STRUCTURE

VoIP (Voice over Internet Protocol) is a technology that enables real-time voice transmission by utilizing the existing internet infrastructure. Compared to traditional PSTN (Public Switched Telephone Network) based systems, VoIP technology is preferred thanks to its efficiency in integration with other systems, using the existing data line for voice transmission and much lower communication cost [6].

In VoIP technology, transactions such as registration to a SIP server, management of calls and determination of call session characteristics are performed by signaling protocols, while voice and video transmission are performed by data transfer protocols [7]. SIP is the most commonly preferred signaling protocol and RTP is the media transfer protocol.
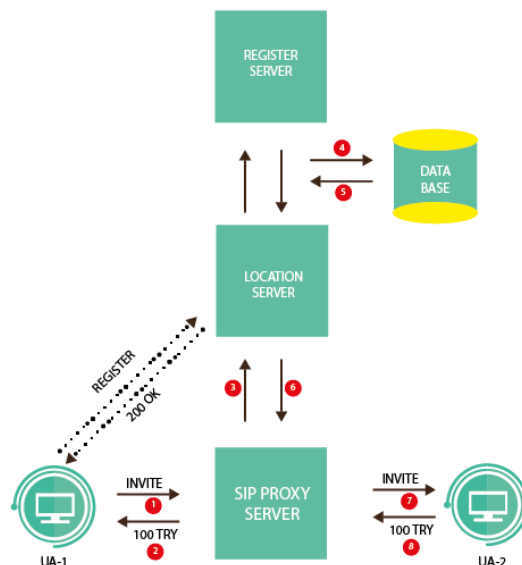
Figure 1: VOIP Operating Logic

VoIP logic is provided by a specific architecture. The VoIP user is first must be registered to a VoIP system for making calls [8]. Then, when the user attempt to call another subscriber, firstly the callee is searched in the same system; if it is in the same system, it is redirected to the relevant user; if

not, it is redirected to a system closer to the callee is registered. All of these processes occur through signaling protocols. Today, the most widely used signaling protocol is the Session Initiative Protocol (SIP). After the session is started, the media stream is provided by the Real Time Protocol (RTP). The session is terminated by SIP as in the beginning. Figure 1 clearly shows this structure.

III.　VOIP TECHNOLOGIES

Continuous data transfer over the Internet is an important concept today [9]. The main purpose of VoIP technology is to provide fast audio and video transmission. Real-Time Transport Protocol (RTP) is an Internet protocol used to manage real-time transmission over unicast and multicast services. In other words, it is a protocol developed for real-time data transfer in IP networks. Although it is mostly used in Internet phone applications, it is also used in radio, television, video conferencing etc. applications. Real-time media communication consists of applications that place a large amount of strain on the network. Delays in real-time transmissions should be minimized as much as possible. RTP is designed for real-time end-to-end multimedia application transfers. In this way, it has an important position in VoIP structure. As shown in the Fig.2. SIP and RTP participates on the transport layer.
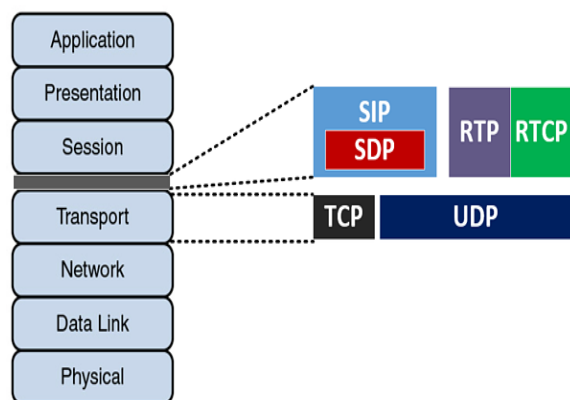
Figure 2: SIP ve RTP Protocol in OSI Referance Model

The SIP protocol provides signaling between devices. In addition, it is a widely used protocol that enables call management and session characteristics to be determined in VoIP technology. The Backus-Naur Form (BNF) syntax structure is used to encode data that the SIP protocol receives from the transport layer [10]. The transport layer is responsible for managing persistent connections over the network for transport protocols such as UDP and TCP. Established connections are shared between client and server tarnsport functions. These connections are indexed with information consisting of address, port and transport protocol.

PSTN (Public Switched Telephone Network) is a copper wired telephone network [11]. It can be converted to IP networks by using ATA (Analog Telephone Adapter). PSTN generally serves according to ITU-T standards and uses E.163-

E.164 addresses, which we know as telephone numbers. There are some special telephone lines, like military telephone lines, that are not connected to the PSTN network. In addition, some companies have private telephone networks connected to the PSTN only through limited ports (eg PBX).

IV.　VOIP SECURITY ISSUE

A.　Physical Layer Attack

The Physical Layer is the first layer of the OSI Model. The Physical Layer, also called the Hardware Layer, describes what physical and electrical infrastructure required for data transmission in computer networks. Whether the data is transmitted electrically, by light, or by radio signals is the interest of physical layer. Attacks on this layer usually occur physically. In other words, it occurs by interfering with physical cabling or the server..

B.　Data Link Layer Attack

The Data Link Layer sets the rules for accessing and processing the physical layer at the point where the data will go. Most of the data link layer is handled by Ethernet cards. The data link layer performs the task of authenticating other PCs on the network, determining who is performing instant communication, and checking for data errors comes from the physical layer. The physical address is called Media Access Control-MAC address. In this layer of VoIP technologies, ARP Cache Poisoning attacks cause great damage. These attacks are performed by changing the MAC address. In addition, MAC Spoofing attacks are another form of attack in this layer. This type of attack, which occurs when MAC addresses are displayed differently, results in the transmission of audio data to different points.

C.　Network Layer Attack

The segmented data in the transport layer, which is an upper layer, is converted to packets in the Network Layer. Furthermore, the computers that will interact need logical addressing to determine each other's locations. This layer, which uses the IP protocol, is exposed to serious attacks through this protocol. It occures by changing the source information of IP packets and connecting to the system with fake IP address. An attacker can change the IP header with a different address, making the package appear to have been sent by a different machine. IP spoofing can theoretically be performed on all protocols [12].

D.　Transport Layer Attack

It is one of the most important layers in VoIP technology due to the use of TCP and UDP protocols. In this layer, the SIP can cause availability problems by sending large amounts of TCP and UDP packets to the server. This type of attack made by delaying messages or resending them later. Attacks in this layer, which cause service disruptions, can be prevented with very high-quality solutions in VoIP technologies.

E. Application Layer Attack

In this layer, a wide variety of attacks can take place over applications. These attacks can occur when a process is unable to access the resources it needs, the consumption of IPs by sending too many requests to the DHCP server, and the attacks that can cause serious service halts, such as rendering the SIP server unavailable by sending too many ICMP packets.

V. MEASURES AGAINST VOIP ATTACKS

Since VoIP technology is located in the network structure, it can be affected by any weakness within this structure. In this respect, the general precautions to be taken in the network should be taken in VoIP. Communication must be encrypted. Calls over the Internet using VLAN technology must be provided from this line. Security measures should be taken at the port level.

Attacks on our computer usually occur in the form of disruption of service or seizure of authority. Security measures taken to ensure that the systems are not affected or are affected at lowest level should be implemented with a holistic approach. Administrator permissions must be given correctly within the VoIP structure. Firewall packet-level security must be provided. Firewalls can help a certain level for VoIP even if they cannot open the packets. Constructive safety must be ensured by using the Session Border Controller. All systems must be configured appropriately in accordance with the VoIP structure. Blocking the service can cause serious damage. For this reason, redundancy must be provided as communication or equipment. With NAT technology, IP addresses on the internal network must be hidden. In addition, one of the most effective measures is the encryption of inter-channel traffic.

In lower layers, MAC limitation, MAC authorization, firewall products with IP-MAC matching capabilities, or manageable switches can be used. In addition to all these methods, IPsec (IP Security), TLS (Transport Layer Security) and sRTP (Secure RTP) should be taken in the classical measures in different layers while VoIP architecture is being established. IPsec contributes to security by encrypting all IP communications in the network layer. TLS is used to secure the transport layer. They also have specific roles in establishing secure sessions. sRTP is a protocol specially developed for VoIP technology which makes the task of RTP protocol more secure.

VI. CONCLUSION

1) In this study, VoIP structure and the attacks against it are examined through layered architecture. It is determined which measures should be taken against these attacks. Since SIP and RTP protocol is the most widely used protocol in VoIP technology, it has been mentioned in detail in the structure. In each layer, it is explained how to protect against the attacks against VoIP systems. In addition, the weaknesses of the system are indicated and measures to be taken are suggested. In order to provide complete protection in VoIP systems, security protocols

with different functions in different layers are detailed and their place in the security framework is explained.

REFERENCES

[1] Poor, An Introduction to Signal Detection and Estimation. New York: Springer-Verlag, 1985. Trombetta, Ramon Cid, and Timothy James O'gara. "Transmit/receive data paths for voice-over-internet (VoIP) communication systems." U.S. Patent No. 7,574,353. 11 Aug. 2009.

[2] Wang, Wei, Soung Chang Liew, and Victor OK Li. "Solutions to performance problems in VoIP over a 802.11 wireless LAN." IEEE transactions on vehicular technology 54.1 (2005): 366-384.

[3] Thornton, Timothy R., et al. "Application for a voice over IP (VoIP) telephony gateway and methods for use therein." U.S. Patent No. 6,665,293. 16 Dec. 2003.

[4] Patella, James Philip, et al. "Communication buffer scheme optimized for VoIP, QoS and data networking over a power line." U.S. Patent No. 7,826,466. 2 Nov. 2010.

[5] Nory, Ravi, et al. "Uplink VoIP support for 3GPP EUTRA." 2007 IEEE 65th Vehicular Technology Conference-VTC2007-Spring. IEEE, 2007.

[6] Jiang, Wenyu, and Henning Schulzrinne. "Comparisons of FEC and codec robustness on VoIP quality and bandwidth efficiency." Networks. 2002. 537-548.

[7] Soldani, David, Man Li, and Renaud Cuny, eds. QoS and QoE management in UMTS cellular systems. John wiley and Sons, 2006.

[8] Zeadally, Sherali, and Farhan Siddiqui. "Design and Implementation of a SIP-based VoIP Architecture." 18th International Conference on Advanced Information Networking and Applications, 2004. AINA 2004.. Vol. 2. IEEE, 2004.

[9] Jiang, Wenyu, and Henning Schulzrinne. "Assessment of voip service availability in the current internet." Proceedings of the 4th International Workshop on Passive and Active Network Measurement (PAM 2003). 2003.

[10] Kwon, Ted Taekyoung, Mario Gerla, and Sajal Das. "Mobility management for VoIP service: Mobile IP vs. SIP." IEEE Wireless communications 9.5 (2002): 66-75.

[11] Pershan, Barry Paul. "Methods and apparatus for transferring from a PSTN to a VOIP telephone network." U.S. Patent No. 6,865,266. 8 Mar. 2005.

[12] Bhatia, Medhavi. "Method for responding to denial of service attacks at the session layer or above." U.S. Patent No. 7,716,729. 11 May 2010.

A Review of Web User Behavior Studies

R. SARAÇOĞLU[1*] and M. M. QADER[1]

[1] Van Yuzuncu Yil University, Van/Turkey, ridvansaracoglu@yyu.edu.tr
[1] Van Yuzuncu Yil University, Van/Turkey, mohammad_diana@yahoo.com

Abstract - Any web site logs action of its user in a file. This helpful information assists us to analyze the behavior of user. Analyzing the behavior of user makes a great opportunity for Web site to predict the behavior of its user in future sessions. In this study a brief of studies related with user behavior in literature was given. It is also given a classification of these studies. This information will provide a basis for future studies.

Keywords - Web log, web mining, Web user behavior.

I. INTRODUCTION

A website is a (location) on the WWW. Every website holds the main page, which users see the first document while they access the website. The website might also include additional files and documents. Each website is owned and administered by an individual, organization or company. A website is a combination of pages of the web (documents that are accessed via the web or Internet). A page of the web is what you see on the screen when you write in the web address, put a query or click on a link. A web page can include color, text, sound, graphics, animation and it can include any kind of information.

To have a well and clear organized site have become one of the main objectives of organizations and enterprises. Administrators of the website may want to know in any way attract visitors and which pages of the website are being accessed least or most frequently, which section of the website is most or least attractive and need improvement, etc. Of late, Analysis of data of server log can provide important and helpful information. Information provided can assists to discover user intuition. This can improve the efficacy of the websites by adapting the structure of information to the behavior of users. Most of the Web Usage Mining (WUM) approaches use Server Log Files (SLF) as crude data for the production of the patterns of user exploration [1](Kumar et al., 2014).

II. USER BROWSING BEHAVIOR

Dupret and Piwowarski [2], proposed a group of assumptions on behavior of browsing of the user that authorize the appreciation of the likelihood that a document is seen, thereby providing an unbiased estimate of relevance of document. They developed clear hypothesis on behavior of the user browsing and they derived a family of models to explain click data in search engine. The predictive ability on the same dataset they compared of the model of user browsing. The parameters of browsing model have an obvious semantic. They used this reality to compare the predicted behavior of the user with an eye-tracking experiment conclusion.

Catledge and Pitkow [3], analyzed browser user-event WLs to better known user surfing conduct. In specific, they distinguished among directed browser, general goal searching, and random (undirected) searching. They were able to describe behavior of the user in anticipation of improving design of browser.

III. PREDICT USER BEHAVIOR

Jan and Lin [4], they proposed a new model of prediction without additional information to build prediction models for a proxy server prefetching the appropriate web pages for adapting the structure of the website and improving the performance of the web. They proposed a prediction system of trend based to predict the different behaviors of the web user. A trend similarity was designed to select the patterns of suitable prediction for predicting a new behavior of user browsing.

Radinsky et al. [5], studied how to model and predict behavior of the user along time. They provided various temporal representations, procedures of learning, and represented how they can build models that predict next user behaviors from data of historical.

Sarukkai [6], described a technique for modeling log data and web server to afford foretell of visitor path next link and next page. The model is use of probabilistic making of markov chains.

Zhu et al. [7], proposed Markov Chain and web mining to predict the browsing behaviors of users. The Markov chain is proposed to predict the largest probability of future surfing page by calculating every eventuality of every link according the structure of the web and the behaviors of historical browsing.

Hu et al. [8], were capable to reliably infer limited demographic knowledge from visited websites content. Due to the sparse sample of activity used, they first fit a model to predict distributions of site-level over dimensions of demographic, after which a smoothed, reduced dimensionality was used Bayesian framework to predict user sex and age from website visits.

Liu and Kešelj [9], a study presented of the automatic classification of navigation patterns of web user and propose a new approach to classifying patterns of the user navigation

---

* Corresponding author

and predicting next requests of users'. The approach is based on the combined mining of WSL and the contents of the pages that have been retrieved of the web. The approach is implemented as an empirical system and it is evaluated performance depend on two tasks prediction and classification.

Dongre and Raikwal [10], a new model was proposed for predicting the next page of the web. The proposed system predicts the page requested for the web users. By analyzing the behavior of the user browsing, can be made the prediction next web page. They proposed different kinds of mining algorithms based on various techniques but prediction of the user future request fundamentally concern with its efficiency and accuracy.

Papoulis and Pillai [11], Markov models for the studying and understanding of stochastic processes have been used, and offered to be well-suited for modeling and predicting behavior of a user's browsing on a website. In general, the input for these problems is the web pages sequence that have been accessed by the user and the aim is to create Markov models which can be used to model and predict the page of the web that the user will most likely access future.

IV. TIME SPENT

Nagy and Gaspar [12], investigated the TSP as an indicator ignore of quality of contents of online. They introduced the idea of the sequential surfing and re visitation to more exactly restore the navigation path of users depend on TSP and the restored pile of explorer. They provided a clustering path to create groups of analogous pages of web by classifications of spent time. They introduced three activities of the user and connected spent time classifications: browsing links, backward stepping and reading.

Gündüz and Özsu [13], the problem is considered of modelling the web user behavior during a single visit to the web. They presented a novel model that uses both the sequences of visiting web pages and the TS on that web pages. As far as they know, existing tools for mining two kinds of various knowledge such as the order of visited pages of the web and the TS on those web pages, are hard to find. Therefore, in this study focused on a model that well reflects the information of structural of a user session and handles two-dimensional knowledge.

Cooley et al. [14], distinguished content pages and auxiliary depend on the reference length of the pages - the amount of time spends a user viewing a web page - for finding association rules.

V. WEB LOG

Verma et al. [15], a condition for predicting needs of the user to better the usability and the retention of user of a website can be addressed by processing WLF effectively. While browsing the sites, interactions of the users' on the web site are registered in WLF. These WLF are plentiful source of knowledge.

Iváncsy and Vajk [16], three approaches of pattern mining are investigated from the point of the WUM of view. The various paths in the mining of WL are page (graphs, sequences, and sets). Deals with the problem of finding hidden knowledge from a huge amount of WLF data collected by servers of the web. The contribution to introduce the process of the WL mining and to show how frequent pattern discovery tasks can be applied on the WLF data in order to acquire helpful information about user navigation behavior.

Srikant and Yang [17], use WLs and structure of the website to suggest reorganizations of the site. Particularly, they infer difficulties of visitor navigation from spent time of viewing pages and from inferred and actual use of the BACK button. They also make assumptions to differentiate among "navigation" pages and "content" pages. Both of these heuristic classes can be thought of as limitations to log file analysis and accurate site.

VI. SESSION

Beitollahi and Deconinck [18], proposed a defense technique against the denial of the application layer of service attacks based on user behavior model. Number of sessions, request rate per session, session duration, number of clicks per each session, mean time between two connections, favorite pages, sequence order between pages, etc. were the main factors to model the user behavior. They used a heuristic technique to model the behavior.

Bianco et al. [19], proposed clustering techniques application to a large group of actual Internet traffic traces to identify user sessions of the web. The method has been applied of proposed clustering to measurement trace data sets to study the characteristics of user-sessions of the Web, showing that process of session arrival tends to be Poisson distributed.

VII. PAGE VISITING

Román and Velásquez [20], have studied behavior of the user with a psychologically-based publishing model. They showed that the series of pages obtained by synthetic agents are found to be nearer to ~5% of the average of the visits number to every page.

Juvina and Herder [21], found that certain paths of within-session page revisits indicate that understand of users and exploit structure of the site's navigation , users that presented these paths used within navigation of site support for page re-visitation rather than the browser's back button and displayed more confidence that they could move pages to be revisited at a later stage.

VIII. CONCLUSION

This study presents an overview of the concept of user behavioral model. The web log of websites is the main source

data for our analysis. A software tool is implemented to model the behavior of users of a website. The software tool extracts various helpful information from the web logs of a website. This information assists the web site administer to improve the structure of the web and to get the most valuable information about user's behaviors.

The studies also provide the statistical analysis based on the results of the software tool. Several analysis about users are provided with this study such as access times of users, the duration of a session, number of requests per session and number of sessions per users during a day, week or month, the favorite pages of users, categorizing the pages based on the willing of users, the location of users and several other main interest information's for a website's administrator. Finally, using these data, the behavior of users can be predicted. For instance, it can be predicted when some well-known users appear in future or what a user requests in his future behavior.

ACKNOWLEDGMENT

REFERENCES

[1] T. V. Kumar, H. S. Guruprasad, I Baig,. A new web usage mining approach for website recommendations using concept hierarchy and website graph. International Journal of Computer and Electrical Engineering, 6(1): 67, 2014.

[2] G. E. Dupret,B. Piwowarski, B. A user browsing model to predict search engine click data from past observations. In Proceedings of the 31st annual international ACM SIGIR conference on Research and development in information retrieval (pp. 331-338). ACM, 2008.

[3] Catledge, J. E. Pitkow, Characterizing browsing strategies in the world-wide web. Computer Networks and ISDN systems, 27(6): 1065-1073, 1995.

[4] N. Y. Jan, N. P. Lin, Web user behaviors prediction system using trend similarity. In Proceedings of the 7th WSEAS International Conference on Simulation, Modelling and Optimization (pp. 69-74). World Scientific and Engineering Academy and Society (WSEAS), 2007.

[5] K. Radinsky, K. Svore, S. Dumais, J. Teevan, A. Bocharov, E. Horvitz. Modeling and predicting behavioral dynamics on the web. In Proceedings of the 21st international conference on World Wide Web (pp. 599-608), ACM 2012.

[6] R. R. Sarukkai, Link prediction and path analysis using markov chains. Computer Networks, 33(1): 377-386, 2000.

[7] J. Zhu, J. Hong, J. G. Hughes, Using Markov models for web site link prediction. In Proceedings of the thirteenth ACM conference on Hypertext and hypermedia (pp. 169-170). ACM, 2002.

[8] J. Hu, H. J. Zeng, H. Li, C. Niu, Z. Chen, Demographic prediction based on user's browsing behavior. In Proceedings of the 16th international conference on World Wide Web (pp. 151-160). ACM, 2007.

[9] H. Liu, V. Kešelj, Combined mining of web server logs and web contents for classifying user navigation patterns and predicting users' future requests. Data & Knowledge Engineering, 61(2): 304-330, 2007.

[10] V. Dongre, J. Raikwal, An Improved User Browsing Behavior Prediction using Regression Analysis on Web Logs. International Journal of Computer Applications, 120(19), 2015.

[11] A. Papoulis, S. U. Pillai, Probability, random variables, and stochastic processes. McGraw-Hill, 1985.

[12] I. K. Nagy, C. Gaspar-Papanek, User behaviour analysis based on time spent on web pages. In Web Mining Applications in E-commerce and E-services (pp. 117-136), 2009, Springer Berlin Heidelberg.

[13] Ş. Gündüz, M. T. Özsu, A web page prediction model based on click-stream tree representation of user behavior. In Proceedings of the ninth ACM SIGKDD international conference on Knowledge discovery and data mining (pp. 535-540), 2003, ACM.

[14] R. Cooley, B. Mobasher, J. Srivastava. Data preparation for mining world wide web browsing patterns. Knowledge and information systems, 1(1): 5-32, 1999.

[15] V. Verma, A. K. Verma, S. S. Bhatia. Comprehensive analysis of web log files for mining. International Journal of Computer Science Issues (IJCSI), 8(6), 2011.

[16] R. Iváncsy, I. Vajk. Frequent pattern mining in web log data. Acta Polytechnica Hungarica, 3(1): 77-90, 2006.

[17] R. Srikant, Y. Yang. Mining web logs to improve website organization. In Proceedings of the 10th international conference on World Wide Web (pp. 430-437), 2001, ACM.

[18] H. Beitollahi, G. Deconinck. Connection score: a statistical technique to resist application-layer DDoS attacks. Journal of Ambient Intelligence and Humanized Computing, 5(3): 425-442, 2014.

[19] A. Bianco, G. Mardente, M. Mellia, M. Munafo, L. Muscariello. Web user session characterization via clustering techniques. In Global Telecommunications Conference, 2005. GLOBECOM'05. IEEE (Vol. 2, pp. 6-pp), 2005.

[20] P. E. Román, J. D. Velásquez, Analysis of the web user behavior with a psychologically-based diffusion model. In AAAI Fall Symposium: Biologically Inspired Cognitive Architectures, 2009.

[21] I Juvina, E. Herder. The impact of link suggestions on user navigation and user perception. In User Modeling 2005 (pp. 483-492). Springer Berlin Heidelberg

Comparison the Performance of Classification Algorithms on Intrusion Detection Systems

M. H. IBRAHIM[1] and M. HACIBEYOĞLU[2]

[1]Necmettin Erbakan University, Department of Computer Engineering, Konya/Turkey,
mibrahim@erbakan.edu.tr
[2]Necmettin Erbakan University, Department of Computer Engineering, Konya/Turkey,
mhacibeyoglu@erbakan.edu.tr

Abstract - **Intrusion detection systems are security systems against attacks commonly used in internet technology and computer networks. The purpose of security systems is to identify, log and prevent malicious network traffic. The performance of intrusion detection systems depends on the classification accuracy of the classification or prediction algorithms used in these systems. In this study, Naive Bayes, decision tree C4.5 and artificial neural networks classification algorithms are used efficiently for developing machine learning based intrusion detection systems. The performances of the classification algorithms were evaluated with the confusion matrix results on the Kyoto University honeypots traffic dataset and the results of the classification algorithms were compared with each other. According to experimental results, the artificial neural networks classification algorithm enhanced better performance than Naive Bayes and decision trees C4.5 Classification algorithms for the intrusion detection system.**

Keywords - **Artificial Neural Networks, Classification, C4.5, Naïve Bayes, Intrusion Detection System.**

I. INTRODUCTION

INTRUSION detection system (IDS) and Intrusion Prevention System (IPS) products are defined as Intrusion Detection and Prevention Systems [1]. Intrusion detection systems are software or hardware security systems designed for security analysts. These security systems are used to identify dangerous and harmful attacks on traffic networks. Intrusion prevention systems are security systems that are used to prevent harmful connections or movements in the network traffic [2]. The purpose of these security systems is to stop and prevent malicious connections or movements on the network traffic. Intrusion detection systems detect and log the attack, while intrusion prevention systems hampers learning the attacks [3]. The performance of intrusion detection and prevention systems depends on the classification accuracy (CA) of classification algorithms used to identify malicious links or attacks [4]. Until today, many classification algorithms of data mining have been used by researchers and system designers in IDS. Mukkamala et al. used artificial neural networks (ANNs) and support vector machine (SVM) classification algorithms in a real-time intrusion detection system. They tested the classification algorithms on the knowledge discovery and data mining (KDD) dataset created by DARPA. They compared the performance of

ANNs and SVM classification algorithms. According to experimental results, ANNs classification algorithm obtained better results for IDS system [5]. Kim and Park, proposed a support vector machines to network-based Intrusion detection system (SVM-IDS). Evaluated the performance of the proposed SVM-IDS system with KDD dataset. The experiments results show that intrusion detection system is effective for detecting intrusions or malicious traffic [6]. Pan et al. presented a hybrid intrusion detection system with ANNs and SVM classification algorithms. They tested the presented hybrid intrusion detection system on KDD dataset, the obtained results show that the hybrid ANNs and SVM classification algorithms performed better performance in the intrusion detection system [7]. Sabhnani et al. used multi-classifier model such as ANNs, k-mean, and SVM for intrusion detection system. The performance of the used classification algorithms evaluated on KDD dataset. According to the experimental results, the classification algorithms performed well accuracy on the intrusion detection system [8]. Laskov et al. proposed a supervised learning and unsupervised learning intrusion detection system. They used ANNs, SVM, k-nearest neighbor (K-NN), and C4.5 algorithms in the supervised learning and used γ-Algorithm, single linkage clustering, and k-mean algorithms in unsupervised learning. They compared the performance of the supervised and unsupervised learning, according to the experimental results the performance of unsupervised learning is similar to the performance of supervised learning [9]. Muda et al. used the k-mean clustering and NB classification algorithm to perform intrusion detection system. In the first stage, k-mean clustering algorithm was used for labeling the sample that malicious and non-malicious activity. In the second stage, the NB classification algorithm was used to classify all data into the correct class. The performance of the k-mean and NB intrusion detection system was performed with KDD dataset, the experimental results demonstrated that the k-mean and NB intrusion detection system significantly improved the accuracy of the system [10]. Mukherjee and Sharma, proposed a novel feature selection method and used for the intrusion data set and classified the data set with the NB classification algorithm. They compared the results obtained from the proposed method with correlation-based feature selection, information gain and gain ratio

methods. The results show that the proposed method is given better results from the correlation-based feature selection, information gain and gain ratio methods and it is efficient and effective for the intrusion detection system [2]. In this paper, we used NB, C4.5, and ANNs classification algorithms to identify and log malicious network traffics. This paper is organized as follows, section 2 introduces the intrusion detection system. In section 3, we explain the experiments conducted and compare the results of classification algorithms on the Kyoto University honeypots traffic dataset. Finally, the conclusions are presented in Section 4.

II. INTRUSION DETECTION SYSTEM

An Intrusion Detection System (IDS) monitors computer networks traffic in the real time to detect malicious movements, dangerous and harmful attacks, or violations that could endanger the system [3]. Some intrusion detection systems also have the ability to stop and prevent an attack in the event of an attack, but when the prevention feature is added to the intrusion detection system, the name of the system becomes the intrusion detection and prevention system (IDPS) [3]. In generally the intrusion detection systems can be classified into host-based and network-based [5]. Since Host-based systems monitor the system with a single host, many systems use network-based intrusion detection systems. Network-based intrusion detection systems can be categorized into two categories, signature-based and anomaly-based [1]. Statistics-based, knowledge-based and machine learning-based methods are used to detect abnormal traffics in intrusion detection systems.

The intrusion detection and prevention system focuses primarily on identifying potential attacks, providing information about these attacks, and reporting attack attempts so that security analysts can better analyze them, then suspicious or dangerous entries analyzed. Data mining classification algorithms are used in intrusion detection stages of intrusion detection and prevention systems [1]. In this study, an intrusion detection system is proposed by considering the attack data set, the proposed intrusion detection system is given in Figure 1.
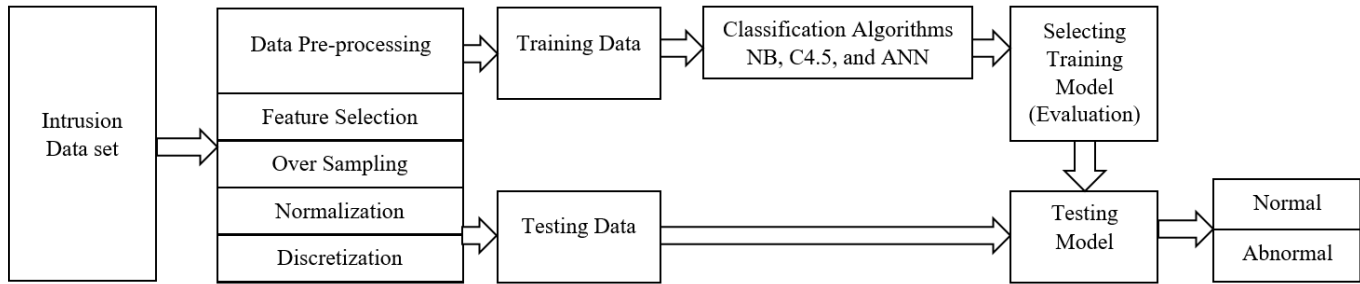
Figure 1: The proposed intrusion detection system

As shown in Figure 1, data preprocessing was performed on the attack data set. First, the feature selection process was performed on the intrusion detection data set, and the information gain method was used as the feature selection process [11, 12]. As a result of the feature selection process 19 out of 24 feature was selected. In general, intrusion detection data sets are very small in comparison to normal instances of attack data, so it is necessary to balance instances of classes. In this study, synthetic minority over-sampling technique (SMOTE) sampling technique is used as over sampling method for intrusion detection data set [13]. The number instances of normal and abnormal classes in the original dataset and the number instances of normal and abnormal classes after applied SMOTE over sampling technique is given in Table 1.

Table 1: The number instances of the Kyoto University honeypots traffic dataset

Dataset	Normal traffic (%)	Abnormal traffic (%)
Original Dataset	86	14
Dataset (SMOTE)	50	50

The normalization of the data provides data consistency to the data set, the min-max normalization method is applied for the intrusion detection data set [14, 15] according to the equation 1.

$$x' = \frac{x_i - x_{min}}{x_{max} - x_{min}} \tag{1}$$

Where, x' is the normalized data, x_i the input value, x_{min} is the smallest number in the input array and x_{max} is the largest number in the input array. Rule-based classification algorithms perform better on discrete data sets, so the intrusion detection dataset for NB and C4.5 classification algorithms is discretized using the entropy-based ID3 discretization method [15, 16]. After applying the data preprocessing methods on the intrusion detection dataset, the dataset is divided into a training dataset and a test dataset by k-Fold cross-validation [17]. The training dataset is used to obtain the training model and the test dataset is used to evaluate the test model. Finally, the test dataset is classified as normal or abnormal by the test model.

III. EXPERIMENTAL RESULTS

In this study, classification results obtained from NB, C4.5 and ANNs classification algorithms are evaluated for intrusion detection system. The confusion matrix is calculated as the evaluation criterion of the classification algorithms [18]. The confusion matrix of the classification algorithms is given in Table 2.

Table 2: The confusion matrix of the classification algorithms

Classification Algorithms	Confusion Matrix			
NB			Prediction	
			Normal	Abnormal
	Actual	Normal	4380	620
		Abnormal	311	4689
C4.5			Prediction	
			Normal	Abnormal
	Actual	Normal	4528	472
		Abnormal	261	4739
ANNs			Prediction	
			Normal	Abnormal
	Actual	Normal	4849	151
		Abnormal	180	4820

The accuracy, misclassification rate, sensitivity, specificity, and F1 Score values are calculated from the confusion matrix which are given in equations 2,3,4,5, and 6, respectively [18].

$$Accuracy\ (AC) = \frac{TP\ +\ TN}{TP\ +\ FP\ +\ FN\ +\ TN} \tag{2}$$

$$Misclassification\ Rate\ (MR)$$
$$= \frac{FP\ +\ FN}{TP\ +\ FP\ +\ FN\ +\ TN} \tag{3}$$

$$Sensitivity\ (SEN) = \frac{TP}{TP\ +\ FN} \tag{4}$$

$$Specificity\ (SPE) = \frac{TN}{TN\ +\ FP} \tag{5}$$

$$F1\ Score = 2\ * \frac{Specificity\ *\ Sensitivity}{Specificity\ +\ Sensitivity} \tag{6}$$

Evaluation criteria for classification algorithms are obtained using 10-fold cross-validation. The classification evaluation criteria obtained for NB, C4.5 and ANNs classification algorithms are compared with each other. The obtained results of the classification evaluation criteria for NB, C4.5 and ANNs classification algorithms are given in Table 3.

Table 3: The classification evaluation criteria for NB, C4.5 and ANNs classification algorithms

CA	Evaluation Criteria				
	ACC	MR	SEN	SPE	F1-Score
NB	90.69	0.0931	93.37	88.32	90.39
C4.5	92.67	0.0733	94.55	90.94	92.51
ANNs	**96.69**	**0.0331**	**96.42**	**96.96**	**96.70**

When the classification evaluation criteria of NB, C4.5, and ANNs classification algorithms in Table 3 are examined, the NB classification algorithm has achieved 90.69, 0.0931, 93.37, 88.32 and 90.39 values of accuracy, misclassification rate, sensitivity, specificity, and F1 Score on Kyoto University honeypots traffic dataset, respectively. The C4.5 classification algorithm achieved an accuracy of 92.67, the misclassification rate 0.0733, the sensitivity 94.55, the specificity of 90.94, and F1-score of 92.51 on the Kyoto University honeypots traffic dataset. ANNs classification algorithm obtained accuracy of 96.69, the misclassification rate 0.0331, the sensitivity 96.42, the specificity of 96.96, and F1-score of 96.70 on the Kyoto University honeypots traffic dataset. Generally, when the classification evaluation criteria of classification algorithms were examined, ANNs classification algorithm achieved better results than NB and C4.5 classification algorithms.

IV. CONCLUSION

Recently, we have been doing almost all of our important works through web-based applications. The number of web-based applications is increasing, but the risk security of users' important information is also increasing. Intrusion detection systems are very important for information security, so these systems need to be designed very well. The classification algorithms affect the performance of intrusion detection systems linearly. In this study, NB, C4.5, and ANNs classification algorithms are evaluated on traffic dataset of Kyoto University honeypots traffic dataset. In the evaluation process of classification algorithms, suitable classification algorithm for Kyoto University honeypots traffic dataset is determined. As a result, the ANNs classification algorithm for the Kyoto University honeypots traffic dataset performed better than NB and C4.5 classification algorithms.

REFERENCES

[1] Tsai, C.-F., et al., Intrusion detection by machine learning: A review. Expert systems with applications, 2009. 36(10): p. 11994-12000.
[2] Mukherjee, S. and N. Sharma, Intrusion detection using naive Bayes classifier with feature reduction. Procedia Technology, 2012. 4: p. 119-128.
[3] Scarfone, K. and P. Mell, Guide to intrusion detection and prevention systems (idps). 2012, National Institute of Standards and Technology.
[4] Buczak, A.L. and E. Guven, A survey of data mining and machine learning methods for cyber security intrusion detection. IEEE Communications Surveys & Tutorials, 2015. 18(2): p. 1153-1176.
[5] Mukkamala, S., G. Janoski, and A. Sung. Intrusion detection using neural networks and support vector machines. in Proceedings of the 2002 International Joint Conference on Neural Networks. IJCNN'02 (Cat. No. 02CH37290). 2002. IEEE.
[6] Kim, D.S. and J.S. Park. Network-based intrusion detection with support vector machines. In International Conference on Information Networking. 2003. Springer.
[7] Pan, Z.-S., et al. Hybrid neural network and C4. 5 for misuse detection. in Proceedings of the 2003 International Conference on Machine Learning and Cybernetics (IEEE Cat. No. 03EX693). 2003. IEEE.
[8] Sabhnani, M. and G. Serpen. Application of Machine Learning Algorithms to KDD Intrusion Detection Dataset within Misuse Detection Context. in MLMTA. 2003.

[9]   Laskov, P., et al. Learning intrusion detection: supervised or unsupervised? in International Conference on Image Analysis and Processing. 2005. Springer.

[10] Muda, Z., et al., A K-Means and Naive Bayes learning approach for better intrusion detection. Information technology journal, 2011. 10(3): p. 648-655.

[11] Reed, T.R. and J.H. Dubuf, A review of recent texture segmentation and feature extraction techniques. CVGIP: Image understanding, 1993. 57(3): p. 359-372.

[12] Yang, M., K. Kpalma, and J. Ronsin, A survey of shape feature extraction techniques. 2008, In-Tech.

[13] Chawla, N.V., et al., SMOTE: synthetic minority over-sampling technique. Journal of artificial intelligence research, 2002. 16: p. 321-357.

[14] Yavuz, S. and M. Deveci, İstatiksel Normalizasyon Tekniklerinin Yapay Sinir Ağın Performansina Etkisi. Erciyes Üniversitesi İktisadi ve İdari Bilimler Fakültesi Dergisi, 2012(40): p. 167-187.

[15] Han, J., J. Pei, and M. Kamber, Data mining: concepts and techniques. 2011: Elsevier.

[16] Yang, Y., G.I. Webb, and X. Wu, Discretization methods, in Data mining and knowledge discovery handbook. 2009, Springer. p. 101-116.

[17] Kohavi, R. A study of cross-validation and bootstrap for accuracy estimation and model selection. in Ijcai. 1995. Montreal, Canada.

[18] Yang, Y., An evaluation of statistical approaches to text categorization. Information retrieval, 1999. 1(1-2): p. 69-90.

A Different Approach to Feature Selection With Apriori Algorithm

Havva ÇETİNER ALTIPARMAK[1], Onur İNAN[2]

[1] Kuveyt Türk Participation Bank, Konya/Turkey, havva.altiparmak42@gmail.com
[2] Necmettin Erbakan University, Konya/Turkey, droinan@gmail.com

Abstract - **The rapid development of technology facilitates the recording of many transactions in digital environments and the storage of recorded data, while at the same time accelerating access to data. In business life, these data are used when making future decisions and analyzing the current situation. The data that are stored in the computer environment can be evaluated by means of data mining.**

In this article, the association rules were applied on Breast Cancer, Vote, Spect_test data sets obtained from UCI Machine Learning Repository, the results were analyzed and a method and application about the selection of qualified properties which had the most effect on the classification were explained and the algorithm details related to the application were explained. After the classification procedures performed on the data set with association algorithms, accuracy rates increased by 12.79 in Breast Cancer, 1.32 in Vote and 7.14% in Spect. Thus, more effective working on smaller data sets is provided.

Keywords - **Data Mining, Association Rules, Apriori Algorithm, Feature Selection**

I. INTRODUCTION

One of the most important developments in recent years is the increase in data volume. With this increase, the data started to be kept in larger databases. As a result, the search for Knowledge Discovery in Databases (KDD) has emerged. KDD consists of different stages, data mining is one of the most important stages of KDD. Data mining (DM) can be defined as the determination of large quantities of correlations and rules that can be used to predict the future from stored data using computer programs.

Within the large data sets, different methods are used to determine the data useful for us. In this article, some propositions have been made for the determination of the most qualified properties (which have the most effect on the classification) of data sets that contain a large number of attributes and are detailed on an application.

II. MATERIALS AND METHOD

Data produced by computer systems are worthless in themselves because they do not make sense in the naked eye.

When these data are processed for a specific purpose, they begin to make sense. [1] If we talk about many of the situations we face in daily life, technology has become an integral part of our lives. There are thousands of data stored in our computers and mobile phones, tablets, such as records made in the hospital you go to because of the illness, data of our credit cards that we use many times during the day, and the steps you take according to the records of the business you are the boss.

A. Data Mining

The concept of data mining is the formation of meaningful information by evaluating the available data. Data mining should be defined as a process; It can be said that it is the process of analyzing many and many kinds of data on the data warehouse by various methods and uncovering previously unexplored information / data. It is the process of evaluating confidential data and using it in decision-making mechanisms. Using this definition, it is possible to say that data mining studies are also a statistical study process.

In the data mining process, data preprocessing techniques can be detailed as follows:

- Data Cleaning,
- Data Integration,
- Data Selection (Reduction),
- Data Conversion,
- Application of Data Mining Algorithms,
- Patterns

].
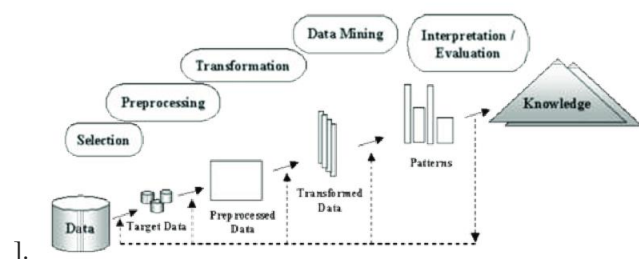
Figure 1. Data mining processes [3]

B. Feature Selection

Feature selection is the approach that aims to find a subset of the data in a way that can better express the data. This approach is applied to data sets with a large number of features and provides an increase in the overall success rate and allows the reduction of the run time of classification algorithms are preferred. The reduction in the number of features may have an impact on the success of classification algorithms on the data since noise-containing features may be present.

The preparation of the data set is only valid after a good recovery of the data obtained from the studies and observations. If the obtained data and attributes are represented by linear or matrix expression in a certain order, the data set is revealed.

The gaps in the data set without the observed result are called lost data. As the loss data increases in the values found as a result of studies and observations, the number of data that will ensure that the measured quality reaches the intended accuracy decreases. In such cases, it is difficult to draw any conclusions from the quality. Some statistical methods can be used to omit losses at a certain rate, or some methods can be used to assign values to fields with lost data. If the value loss ratio is very high, such corrections will not be realistic and may not be successful as a result. In cases where there is a lot of lost data, it may be necessary to re-observe the results. In case of missing data, re-measurement and observation is the most appropriate step. Missing data should be edited using various methods. Apart from the missing data, noisy data is also a problem. Noisy data is a set of information with different data than it should be. These data should be cleared from the data set in order to achieve successful results [4].

C. Association Rule Mining

The data mining method, which finds relationships between large data sets, supports the future studies by analyzing and revealing the possibility of events occurring together, is called Association Rules (CB). With the given transaction / transaction set, the frequency of occurrence of these elements in the next transaction is estimated from the existence of an object (or collection of objects) [5]. BK; It has wide usage in many sectors such as economy, education, e-commerce, marketing, telecommunication.

The existence of association rules in data sets is one of the important issues of the VM and serious algorithms have been designed in this field and different algorithms have been designed. Association rules provide benefits in a wide range of subjects such as sales in markets, product line-up on shelves, identification of promotions and promotions [6].

Association rule mining,
- Finding all frequently used items
- There are two stages to produce strong rules of association from these frequently occurring elements.

The Apriori Algorithm için used for the first phase of the association rule is the most popular and classic algorithm used in the mining of frequently occurring items.

D. Apriori Algorithm

Apriori algorithm was developed by Agrawal and Srikant in 1994. In data mining, association rule is the most widely known and used algorithm among inference algorithms. The basic approach in this algorithm is that "if the k-element set (candidate element set) provides the minimum support criterion, subsets of that set also provide the minimum support criterion."

Algorithm Apriori

C_k: Candidate itemset of size k
L_k : frequent itemset of size k
L_1 = {frequent items};

1. **for** ($k = 1$; L_k !=$\varnothing$; k++) **do begin**
2. C_{k+1} = candidates generated from L_k;
3.   **for each** transaction t in database do
4.   increment the count of all candidates in C_{k+1} that are contained in t
5. L_{k+1} = candidates in C_{k+1} with min_support
6. **end**
7. **return** $\cup_k L_k$;

Figure 2: Apriori Algorithm

E. Steps of Apriori Algorithm

- Minimum number of support (min.support) and minimum trust value (min.confidence)
- Support value for each item in item sets
- Disabling items with support less than the minimum support value
- Formation of bilateral partnerships by taking into account the single partnerships
- Subtracting item clusters that are less than the minimum support value
- Applying steps 4 and 5 to all data in the data set.
- Establishing association rules
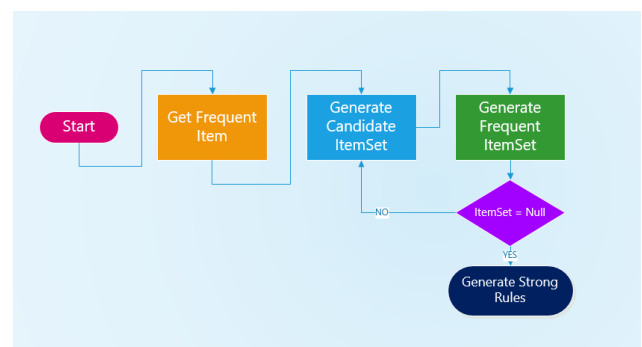
Figure 3: Apriori Algorithm Flow Chart

III. EXPERIMENTAL STUDIES

The feature selection method proposed in this study was tested with real data obtained from UCI Machine Learning Store. Table 1 shows the details of the three data sets used in our study. Each of these data sets was divided into training data set (70%) and test data set (30%). Navie Bayes algorithm is preferred for classification because of its popularity in many fields of application from scientific to business sector.

Table 1. Properties of datasets

Datasets	Num. of Instances	Num. of Attributes
Breast Cancer	286	10
Vote	435	17
Spect_test	187	23

A. Feature Selection with Apriori Algorithm

The following steps (Figure 4) were applied in order to select feature with association rules determined by Apriori algorithm [7].
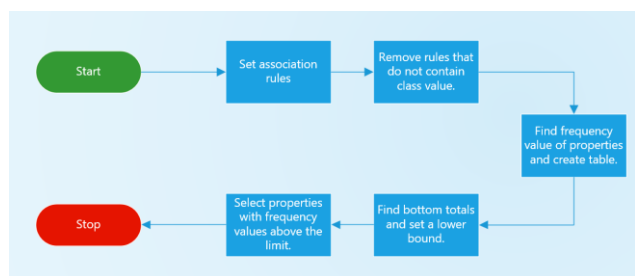
Figure 4: Feature selection steps with Apriori algorithm

These steps were implemented in a C # application. The correct classification rates of the data sets detailed and given in Table 1 before and after feature selection are given in Table 2.

Table 2. Accurate classification rates before and after feature

Data Set Name	Number of Attribute	Correctly Classified
Vote	17	90.11%
	5	91.43%
Breast-cancer	10	67.44%
	5	80.23%
Spect_test	23	66.07%
	8	73.21%

As it can be understood from this table, the classification using more qualified features is more accurate than the classification with more features. In other words, after subtracting the features that contain the data that we can call noise, the classification made with the remaining data is closer to the truth. In this way, it is aimed to save the storage unit, time

and number of transactions and thus the processor.

Figure 5 shows the screenshot of the C # application. The left panel lists all the properties of the data set. In the middle, there is a table about which feature contributes to class value according to the rules of association. In the rightmost list, the properties that are above the limit we have determined according to the frequency value in the table are listed.
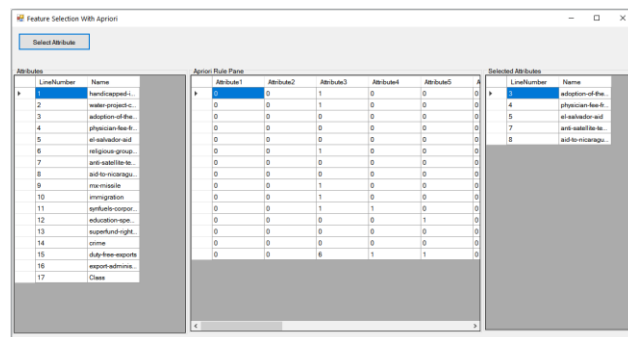
Figure 5: Feature Selection application screenshot

The results obtained from the application and classification procedures were performed. First of all, the Navie Bayes classification algorithm was run when all the features were available and the correct classification percentage was recorded. Then, the Apriori algorithm was run on our data set and the resulting rules were saved to the system. And it was observed that classification accuracy rates increased for all data sets.

IV. RESULTS

In this study, it is aimed to determine the most qualified properties required for classification, which is one of the most important methods of data mining. The aim of this process is to improve performance and to obtain effective results when working with large data sets and to determine the features that affect the result the most among the existing features. It is also possible to ignore the less common features by determining an optimal support value, which varies according to the data contained in the data sets. Through the written application, the 5 most influential features were determined among the 16 properties and it was observed that the classification process was performed at a higher accuracy rate.

REFERENCES

[1] A. Kalıkov, "Veri Madenciliği ve Bir E-Ticaret Uygulaması", *Master Thesis, Gazi University, Institute of Science and Technology,* 2006.

[2] S. Ocak, "Data Mining ve Veri Madenciliği Nedir", https://www.muhendisbeyinler.net/data-mining-ve-veri-madenciligi-nedir/, 2018.

[3] W. A. Mohotti, S. C. Premaratne, "Analysing Sri Lankan lifestyles with data mining: two case studies of education and health", *Kelaniya Journal of Management,* 6(1), pp. 1–11, 2017.

[4] A. Tunç, "Finans Sektörü İçin Yapay Öğrenme Teknikleri Kullanarak Kredi Kullanabilirliğin Tespiti", Master Thesis, *Selçuk University, Institute of Science and Technology*, 2016.

[5] A. Saygılı, "Veri Madenciliği ile Mühendislik Fakültesi Öğrencilerinin Okul Başarılarının Analizi", *Master Thesis, Yıldız Technical University, Institute of Science and Technology,* 2013.

[6] M. Azam, U. Naeem, J. Loo, S. Khan, "A Framework To Recognise Daily Life Activities With Wireless Proximity And Object Usage Data", Proceedings Of 23rd Ieee International Symposium On Personal, *Indoor And Mobile Radio Communication*, 2012.

[7] N. Kaoungku, K. Suksut, R. Chanklan, K. Kerdprasop, N. Kerdprasop, "Data Classification Based On Feature Selection With Association Rule Mining", *Proceedings Of The International Multiconference Of Engineers And Computer Scientists,* Vol I, Mart 15-17, Honkong/China, 2017.

Short Term Electrical Load Forecasting using Artificial Neural Network

Vildan EVREN[1*], İlker Ali ÖZKAN[2]

[1]Selcuk University, Konya/Turkey, evrenvildannn@gmail.com
[2]Computer Engineering Department, Faculty of Technology, Selcuk University, Konya, Turkey

*Abstract –*In the efficient operation of power systems and future planning, electrical load forecasting is very important. Load forecasting is based on the estimation of future electrical load by examining past conditions. Estimates from a few minutes to a day are called short-term forecasts. Short-term load forecasting has a decisive role in the load sharing of power plants. It also enables to overcome the deficiencies caused by sudden load increases and power plant losses. Weather conditions are effective in the short-term electrical load forecasting. Daily or hourly electricity consumption data are generally used for short-term load estimation. The last three years of daily electrical energy consumption data of Turkey used in this study. Days were categorized according to the seasons. And past electrical load values, as well as temperature values, were used to improve forecasting accuracy. In this study, a short-term electric load estimation model has been developed by using Artificial Neural Networks (ANN). The results obtained with this model were examined by statistical methods and it was found that this model has a good electrical load estimation performance.

Keywords– **Short-term electrical load forecast, Artificial Neural Network, Prediction Model, Time series forecasting**

I. INTRODUCTION

The electrical charge estimate is based on the prediction of the future status by examining previous data and conditions [1]. Some problems occur in the system that is improperly designed due to underestimated demand for electrical load. Thus, many more problems occur, such as power outages [2]. Accurate load estimation increases the safety of electrical systems [1].

Electricity load estimation is enormous importance in the efficient operation of power plants. A high estimate of the load value may lead to unnecessary use of the reserve of stored or activate to many power units. This situation provides to waste energy [3]. In the electricity markets, system load is also significantly affected by prices as well [4].

In order to make the planning work more efficiently, the demands on the electrical load should be estimated as accurately as possible. It is very important for the decision makers that the demand for electricity in the energy sector can be predicted with the least errors. Making work planning, load sharing and determining the best group and making production in the most economical way increases the importance of short term electrical load estimation. In order to make a good system planning for the future, electrical load estimates are getting more important.

The electric charge estimate is examined in three classes [5]:
- Short term (hourly, daily and weekly)
- Mid-term (monthly, quarterly)
- Long-term: (annual or longer years)

Periodic load estimates generally include estimates to be made within the period of hourly forecast to one week. Short-term load estimates are necessary for planning operations such as power generation coordination. This coordination can be used to create hourly schedules of production resources, thus minimizing the operating cost of energy power systems [3].

Three important objectives of the short-term electrical load estimation to be performed in this study. These objectives include production planning functions, evaluating the safety of system operation and providing time-dependent load information. Estimating the electric charge can play an important role for market enterprises and can also make economic decisions [4]. In the literature, there are phased studies to estimate the electrical charge.

Es and friends with Turkey by ANN net energy demand prediction study was conducted. In this study, a prediction study based on cause-effect relationship was carried out using ANN model. Researches on ANN theory have been carried out to investigate ANN and estimation models commonly used in the field of energy. In order to evaluate the success of the prediction study and to measure its performance, we developed regression and time series models and made comparisons with the ANN model established. As a result of the analysis and comparisons of ANN techniques have been able to realize more successful estimates [6].

In a study conducted by Cevik, Turkey`s short-term load prediction of power obtained. In this study, using Turkey's electricity consumption and temperature data for the years 2009-2011, estimation of electric charge in 2012 was carried out using Fuzzy Logic and ANFIS methods. Seasonal data are taken as input data. There are 4 categories, Monday model, Tuesday-Wednesday-Thursday and Friday model, Saturday model and Sunday model. There are 4 categories, Monday model, Tuesday-Wednesday-Thursday model and Friday model, Saturday model and Sunday model [7].

The main objective of this study is to minimize the error in the electrical load estimation and thus to prevent operational costs and loss of revenue. In line with this objective, a model has been created by using ANN together with categorization of day tubes according to seasons, which yields successful results in electrical load estimation. Input data of the model; previous load and temperature output data is estimated load data. Seasonal variable plays an important role in the estimation of short term electrical load. Seasonal variable is not considered as input data in this study.

Seasonal variable was used to form input data categories. In this study, 16 categories were identified. Estimation and modelling studies were performed in MATLAB software.

II. MATERIAL AND METHODS

A. *Electricity Load Data Set*

The data set is the whole formed by data elements with different attributes of the same object class [8].The short-term electrical load estimation data in this study are from 2017, 2018 and 2019. Electrical load data obtained from EPİAS [9]. Temperature data were obtained from the Turkey weather websites [10].

Electrical load data differ according to day types. Load curves on holidays and working days vary. A larger load prediction error occurs on holidays. There is a particular difficulty in predicting the demand for power, because the power consumption patterns on these holidays are quite different from those encountered during weekdays (Tuesday, Wednesday, Thursday and Friday). Load models vary from year to year. In the electricity markets, in addition to the traditional factors affecting the load such as season, day type and weather, the price of electricity is an important factor affecting the load [4].

In this study, it is aimed to estimate the load for the next year by using the temperature and load data of the previous years. Turkey's daily electricity consumption information for electricity load is used. Load data for 2017 and 2018 were obtained. Load data for 2019 are considered as test data. For example, the historical load data of the winter of Tuesday is considered as Tuesday's data of the previous week's winter month. The effect of temperature on load consumption varies according to the seasons. Temperature is the most important factor in short term electrical load estimation. Turkey`s made short-term electric load forecasting work by Cevik and the maximum power consumption within 5 city's average temperature were used in Turkey [5]. This work is handled with the greatest warmth of the city of Istanbul in Turkey's electricity consumption.

Days and seasons in load estimates are categorized as follows:
- Category 1: Tuesday, Wednesday, Thursday and Friday - Winter
- Category 2: Tuesday, Wednesday, Thursday and Friday - Spring
- Category 3: Tuesday, Wednesday, Thursday and Friday - Summer
- Category 4: Tuesday, Wednesday, Thursday and Friday on Autumn

- Category 5: Sunday - Winter
- Category 6: Sunday - Spring
- Category 7: Sunday - Summer
- Category 8: Sunday - Autumn
- Category 9: Saturday - Winter
- Category 10: Saturday - Spring
- Category 11: Saturday - Summer
- Category 12: Saturday - Autumn
- Category 13: Monday - Winter
- Category 14: Monday - Spring
- Category 15: Monday - Summer
- Category 16: Monday – Autumn

The input and output data used in the short-term electrical load estimation with ANN are shown in Figure 1. Input data:
- Temperature
- Previous load

Output data
- Estimated load
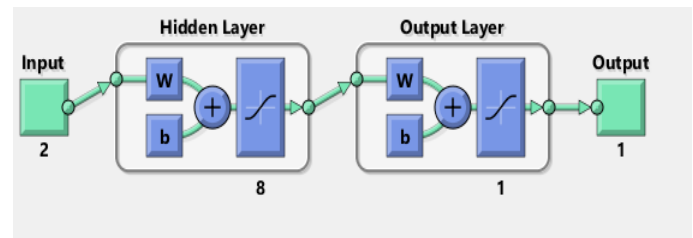
Figure1. ArtificialNeural Network Model

B. *Artificial Neural Networks (ANN)*

Artificial Neural Network, which forms a sub-branch of Artificial Intelligence, has been developed with inspiration from the working structure of the human brain [11]. Artificial Neural Network is a system developed through learning. It has self-learning ability. In addition to learning, it has the ability to relate data. It is difficult to realize what the Artificial Neural Network can do in other programming languages [12]. Therefore, Artificial Neural Network has been developed.

Artificial neural networks can be used to predict different success rates. The advantages of this are the automatic learning of the associated factors from the collected data without the need for extra information. The artificial neural network can be trained with historical data to find hidden loyalties in the data and use them to predict them. In other words, artificial neural networks are mentioned as a open model.

ANN consists of artificial nerve cells. The artificial nerve cell structure is based on biological nerve cells. Artificial Neural Network consists of three layers: input layer, hidden layer and output layer [13]. The number of artificial nerve cells in the input layer is equal to the input data. The data is processed in the input layer and the processed data is transferred to the hidden layer.

2

The number of neurons in the hidden layer varies. After processing the data from the hidden layer, it is transferred to the output layer. The output layer is the last layer. As a result, the network receives one or more inputs and outputs the number of results. The data obtained in the output layer is the solution data it generates to the problem [14].

The ANN consists of two sections, namely feed-forward and feed-back, between artificial nerve cells. In the feed-forward network, the data flows into the output section. In feed-back networks, it does not consider only a forward flow. In feed-back networks, output data is also being input data [15].

A data set is needed to train the Artificial Neural Network and then perform to test process. The data which is not used in the Artificial Neural Network training, it is used in the testing phase. The actual output data is compared with the estimated values and the average error is calculated. Input and output data which is used in this study, they are shown in Figure 2 as a three-layer Artificial Neural Network model.
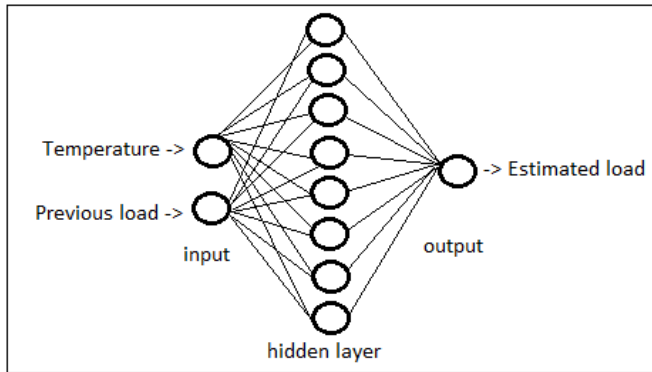
Figure 2. Feedforward Artificial Neural Network Model

C. MODELING

Data set was obtained for the training of the Artificial Neural Network. The data set was categorized according to day and season. The data were used in the training and testing of ANN. The Neural Network toolbox of MATLAB was used to train ANN. Normalized formula in Equation 1 was applied to the obtained data. Data between 0 and 1 were obtained.

$$y = \frac{x - x_{min}}{x_{max} - x_{min}} \qquad (1)$$

For example, the first category is handled on Tuesday, Wednesday, Thursday and Friday of the winter season. Turkey's Daily electricity consumption information for electricity load will be used as the output data.

Load data for 2017 and 2018 were obtained. Input data, temperature and historical load values were used. For example, Tuesday's historical load data is considered as Tuesday's data for the winter month of the previous week. In the test data, 2019 data were used.

III. RESULTS

Estimated values were obtained by using Neural Network application of MATLAB program. Category 2 (Tuesday, Wednesday, Thursday and Friday - Spring) Neural Network application as an example. Figure 3 in category 2, shows how the values in each iteration change as a result of the training using forward feed-back propagation in MATLAB program.
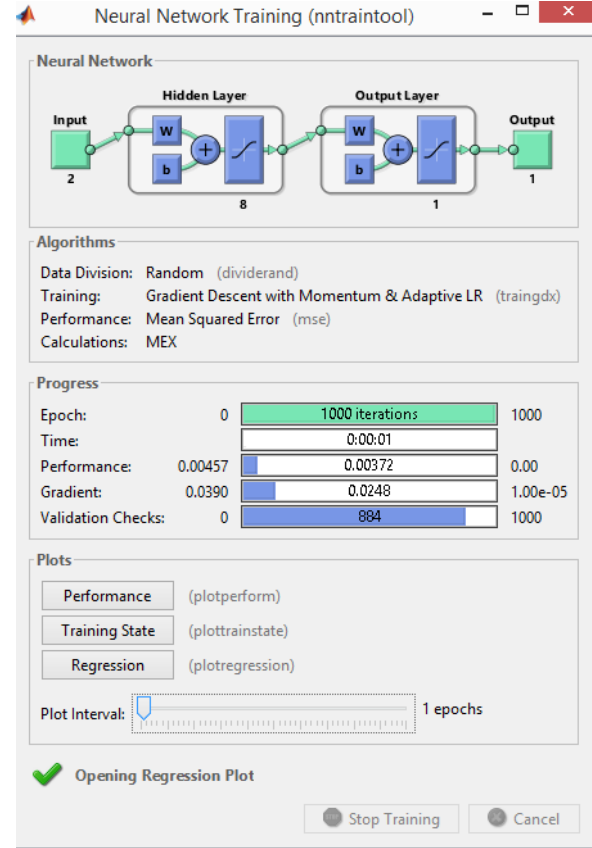
Figure 3. Category 2, Education results of the developed model

As a result of the training, the performance was obtained as 0.00457 and a successful value was obtained. Obtained Regression graph of Category 2 after learning in MATLAB is shown in Figure 4. Error rates are evaluated in the regression graph. At the same time, the success of the process is indicated by the letter R (Regression). Expected target success value is 1. It is seen that the value is very close to the target value.

The regression values of Category 2 in Figure 4 are as follows:

- Training Regression: R=0.88387
- Validation Regression: R=0.94426
- Test Regression: R= 0.73968
- All: R=0.83443
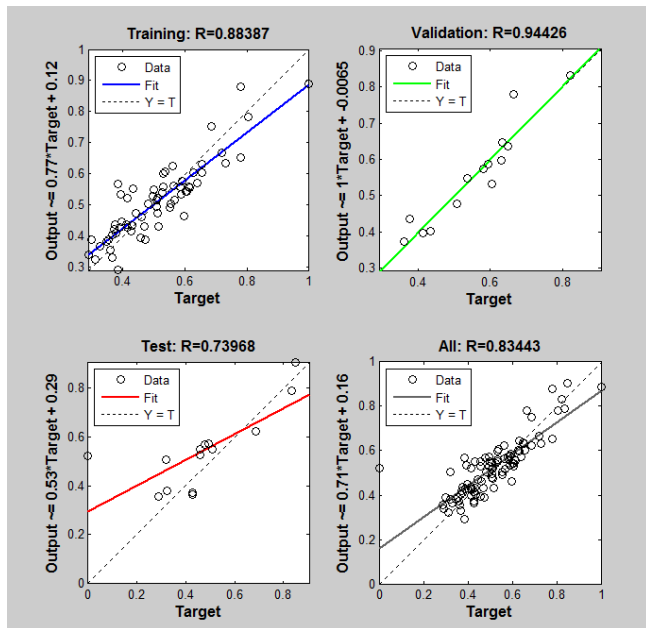
Figure 4. Category 2 Regression chart

After the network has been trained, the network is able to generate estimated test data. After the test, it is necessary to compare the test output data that the network estimates with the actual values. Table 1 below provides a comparison of the estimated and actual values. Category 2 (Tuesday, Wednesday, Thursday and Friday - spring) values were compared.

Table 1. Category 2, Comparison of estimated values with actual values

Estimated Values	Actual Values
821190,652	808466,43
809207,9556	791550,56
826807,7915	815436,85
821072,1924	826733,83
785565,3483	759309,6
789830,8761	786238,85
827300,4414	829521,38
774790,6884	776771,07
817526,0662	788588,75
775713,1009	761914,06
780622,2316	758551,26
779766,7832	779244,95
783248,6819	793522,25
804226,2521	790922,99
783297,2537	805777,61
778996,7328	814385,28
772989,8262	822231,96
753406,5717	807473,25

There is a 1.22% deviation between the total amount of the test data and the total amount of the estimated data. Table 2 shows the total comparison of the actual values and the output estimation values.

Table 2. Estimated performance by Category 2 ANN

Actual Value (Total)	Estimated Value (Total)	Total Deviation (%)
38516854,15	38988370,51	1,22

The prediction is a get some information of what will happen in the future. Almost all managerial decisions are based on forward-looking estimates. Therefore, feed-forward back propagation algorithm of artificial neural networks has been tried as a prediction tool in the solution of short term electrical charge estimation problem. The theory of artificial neural networks is investigated and the applications made on the prediction are examined. In order to measure the success of the prediction study, the actual values were compared with the artificial neural network prediction.

As a result of the studies, artificial neural network technique was found to be successful and estimated values were found for the values of test data. These values were compared with the actual data and their distance between actual values is calculated. Table 3 shows the deviation rates. For future studies, estimations can be proposed by using artificial neural network models with different architecture.

Table 3. Deviation Rates

Categories	Deviation Rates
Category 1: Tuesday, Wednesday, Thursday and Friday - Winter	%2,57
Category 2: Tuesday, Wednesday, Thursday and Friday - Spring	%1,22
Kategori 3: Tuesday, Wednesday, Thursday and Friday - Summer	%14,4
Category 4: Tuesday, Wednesday, Thursday and Friday on Autumn	%2,60
Category 5: Sunday - Winter	%1,89
Category 6: Sunday - Spring	%1,58
Category 7: Sunday - Summer	% 0,62
Category 8: Sunday - Autumn	% 0,03
Category 9: Saturday - Winter	%1,09
Category 10: Saturday - Spring	%0,14
Category 11: Saturday - Summer	%0,46
Category 12: Saturday - Autumn	%1,23
Category 13: Monday - Winter	%1,67
Category 14: Monday - Spring	%2,03
Category 15: Monday - Summer	%2,03
Category 16: Monday – Autumn	%0,03

The category consists of 4 sections according to the seasons of the week. Prediction is calculated for each day of the model. The best prediction among the categories according to the seasons of the week is category 2(Tuesday, Wednesday, Thursday and Friday - Spring). The worst prediction among the categories according to the seasons of the week is category 3 (Tuesday, Wednesday, Thursday and Friday - Summer). The deviation ratio with close values of Category 1 and Category 4 was obtained. According to seasons of the week, three categories` results were obtained as good. Table 1 shows the comparison of the estimated values with the actual values. The best result in Table 1 is 779244.95, while the estimated value is 779766.78.

As a result, low error values indicate the accuracy of the artificial neural network model is correct. There is not much deviation between the estimated values and the actual values. The categories with high error rates are thought to affect the days of public holidays. As a continuation of this study, public holidays can be considered as a separate category and the error rate can be minimized.

REFERENCES

[1] Hakan Var and Belgin Emre Türkay. *Estimation of Short Term Electric Charge Using Artificial Neural Networks.* Electronics - Computer and Biomedical Engineering Symposium, 2014.

[2] Mustafa Yavuzdemir. *Turkey's Short-Term Annual Gross Electricity Demand Forecast.* Ankara University, Institute of Social Sciences, Department of Business Administration , 2014.

[3] Tuğba AKMAN, Cemal YILMAZ and Yusuf SÖNMEZ, 06 Kasım 2018, *Analysis of Electric Load Estimation Methods*, Gazi Journal of Engineering Sciences

[4] Bülent Bilge, Short Term Load Estimation, TEİAS National Load Dispatch

[5] Coşkun Hamzaçebi and Fevzi Kutay. *Turkey Electricity Consumption Forecast to 2010 with Artificial Neural Network.* GaziUniversity, 2004.

[6] Hüseyin Avni Es. *Turkey Net Energy Demand Forecasting with Artificial Neural Networks.* Gazi University Graduate School of Natural and Applied Sciences, 2013

[7] Hasan Hüseyin Çevik. *Turkey's Short-Term Electric Load Forecasting.* Selçuk University Graduate School of Natural and Applied Sciences, 2013

[8] Ayşe Merve UZUN, Data Definition and Formation of Data Standard

[9] https://seffaflik.epias.com.tr

[10] https://www.havaturkiye.com

[11] Metin Zontul and Ayhan Yangın, *Data Mining in Educational Publishing Sector Using Artificial Neural Network Techniques*, Aurum Journal of Engineering Systems and Architecture

[12] Günay Kılıç, *Daily Demand Forecast of the Cafeteria with Artificial Neural Networks*, Pamukkale University Graduate School of Natural and Applied Sciences, 2015

[13] Mehmet Karahan, *Forecasting Tourism Demand by Artificial Neural Network Methods*, Suleyman Demirel University Journal of Faculty of Economics and Administrative Sciences, 2015

[14] Elif Erdoğan, Forecasting with Artificial Neural Networks, Fatih University, 2012

[15] Mehmet KARADENİZ, *Estimation of stator resistance in asynchronous motors by artificial neural networks*, Web address :http://www.emo.org.tr/ekler/69768b3da745b77_ek.pdf

Try on of Virtual Garments on Virtual Bodies

T.I. VASSILEV[1] and B. SPANLANG[2]

[1] University of Ruse, Ruse/Bulgaria, tvassilev@uni-ruse.bg
[2] Virtual Bodyworks S.L., bspanlang@virtualbodyworks.com

Abstract – **This paper describes a virtual try on (VTO) system which dresses a virtual human body, acquired via a 3D scanner, with digitized garments, represented by their garment panels and seaming information. The cloth is physically simulated with a mass-spring system using a velocity modification approach to overcome super elasticity. The cloth-body collision detection is based on image space tests with pre-generated depth and normal maps, used for collision detection and response. The system also checks for collisions between layers of cloth, in case the body is dressed in several garments, using the same image space approach with several maps generated. The simulation is implemented entirely on the graphics processing unit (GPU) which significantly accelerates the computations. As the results show a body can be dressed in a garment in a fraction of a second. The paper also discusses how the simulation can be implemented on a mobile device.**

Keywords – **Virtual try-on, cloth simulation, General purpose GPU programming, Collision detection, Mobile computing.**

I. INTRODUCTION

THE main aim of this paper is to present the current state of a project that developed a fast technique for cloth simulation on virtual bodies. The main application areas of garment simulation are in the entertainment and the fashion design industries and in electronic commerce where customers can shop for garments on the web and try them on in a virtual changing room.

The human body is acquired using a 3D whole body scanner, which represents accurately the body shape and size of a person and can be used to try on different garment styles and sizes. The 3D scanning technology is getting cheaper and more accessible, but still relatively accurate and a human body nowadays can be obtained even at home using a smartphone and a suitable piece of software.

The digitized garments are stored as 2D plain seaming garment patterns with their contours and seaming information. The garment panels and positioned around the virtual body, they are meshed and elastic forces are applied at the edges to be stitched together. The system uses a mass-spring elastic cloth model, which converges until the edges are sewed. The approach applies an image space based collision detection approach, which speeds up the simulation.

The rest of the paper is organized as follows. The next section reviews work in cloth simulation, collision detection, GPU implementations and cloth simulation on a mobile device. Section III describes the developed virtual try-on system. Section IV gives ideas how the simulation can be parallelized on a multicore central processing unit (CPU). Sections V and VI are dedicated to GPU and mobile device implementation. Section VII gives details about garment digitization, Section VIII shows some results and the last section concludes the paper.

II. BACKGROUND

A. Other virtual try on systems

Several research teams have developed virtual garment try on systems. There are two main approaches. Movania & Farbiz [1] and Giovanni et al [2] use geometry and image based technique to scale an existing 2D or 3D image of a garment to match the size of the customer. Kevelham & Magnenat-Thalmann [3-4] use an accurate cloth simulation accelerated on the GPU for fitting garments on a 3D customer body. As one of the goals of our work is for the customer to be able to try on different sizes of garments, our approach is also based on accurate physically based cloth simulation.

B. Previous work in cloth simulation

Physically based cloth modelling has been a problem of interest to computer graphics researchers for more than three decades. First steps, initiated by Terzopoulos et al. [5], characterised cloth simulation as a problem of deformable surfaces and used the finite element method and energy minimisation techniques borrowed from mechanical engineering. Since then other groups have been formed [6-8] challenging the cloth simulation using energy or particle based methods.

Provot [9] used a mass-spring model to describe rigid cloth behaviour, which proved to be faster than the techniques described above. Its major drawback is the super-elasticity. In order to overcome this problem he applied a position modification algorithm to the ends of the over-elongated springs. However, if this operation modifies the positions of many vertices, it may elongate other springs. That is why this approach is applicable only if the deformation is locally distributed, which is not the case when simulating garments on a virtual body.

The method, used in the addressed system, exploits a mass-spring cloth model but it introduces a new approach to overcome its super-elasticity [10]. Instead of modifying the positions of end points of the springs that were already over-elongated, the algorithm checks their length after each iteration and does not allow elongation more than a certain threshold modifying velocities of the corresponding vertices. This approach has been further developed and optimised for

the dynamic case of simulating cloth on moving objects.

C. Mass-spring model of cloth

The elastic model of cloth is a mesh of $m \times n$ mass points, each of them being linked to its neighbours by massless springs of natural length greater than zero. There are three different types of springs: structural, shear, and flexion, which implement resistance to stretching, shearing and bending, correspondingly.

Let $\mathbf{p}_i(t)$, $\mathbf{v}_i(t)$, $\mathbf{a}_i(t)$, where $i=1,\ldots,m \times n$, be respectively the positions, velocities, and accelerations of the mass points at time t. The system is governed by the basic Newton's law:

$$\mathbf{f}_i = mass_i\, \mathbf{a}_i, \tag{1}$$

where $mass_i$ is the mass of each point and $\mathbf{f}_i$ is the sum of all forces applied at point $\mathbf{p}_i$. The force $\mathbf{f}_i$ can be divided in two categories.

The **internal forces** are due to the tensions of the springs. The overall internal force applied at the point $\mathbf{p}_i$ is a result of the stiffness of all springs linking this point to its neighbours:

$$\mathbf{f}_{int}(\mathbf{p}_i) = -\sum_k k_{ik}\left(\overrightarrow{\mathbf{p}_k\mathbf{p}_i} - l_{ik}^0\,\frac{\overrightarrow{\mathbf{p}_k\mathbf{p}_i}}{\left\|\overrightarrow{\mathbf{p}_k\mathbf{p}_i}\right\|}\right), \tag{2}$$

where k_{ik} is the stiffness of the spring linking $\mathbf{p}_i$ and $\mathbf{p}_k$ and $l0\ ,ik$ is the natural length of the same spring.

The **external forces** can differ in nature depending on what type of simulation we wish to model. The most frequent ones will be:

- Gravity: $\mathbf{f}_{gr}(\mathbf{p}_i) = m\mathbf{g}$, where $\mathbf{g}$ is the gravity acceleration;
- Viscous damping: $\mathbf{f}_{vd}(\mathbf{p}_i) = -C_{vd}\mathbf{v}_i$, where C_{vd} is a damping coefficient.
- Elastic seaming forces to stitch garment panels together.

All the above formulations make it possible to compute the force $\mathbf{f}_i(t)$ applied on point $\mathbf{p}_i$ at any time t. The fundamental equations of Newtonian dynamics can be integrated over time by a simple Euler method:

$$\left|\begin{array}{l} \mathbf{a}_i(t+\Delta t) = \dfrac{1}{mass_i}\mathbf{f}_i(t) \\[2mm] \mathbf{v}_i(t+\Delta t) = \mathbf{v}_i(t) + \Delta t\,\mathbf{a}_i(t+\Delta t) \\[2mm] \mathbf{p}_i(t+\Delta t) = \mathbf{p}_i(t) + \Delta t\,\mathbf{v}_i(t+\Delta t) \end{array}\right. , \tag{3}$$

where Δt is a chosen time step. More complicated integration methods, such as Runge-Kutta [11], can be applied to solve the differential equations. This however reduces the speed significantly, which is very important in our case. The Euler Equations 3 are known to be very fast and give good results, when the time step Δt is less than the natural period of the system $T_0 \approx \pi\sqrt{m/K}$. In fact our experiments showed that the numerical solving of Equations 3 is stable when

$$\Delta t \le 0.4\pi\sqrt{\frac{m}{K}}\,, \tag{4}$$

where K is the highest stiffness in the system.

D. Accelerating the cloth simulation on the GPU

The nature of the mass-spring system is suitable for parallelization on a graphics processing unit (GPU). Zeller and NVIDIA[12] have provided a free sample demo of a mass-spring cloth simulation on their graphics processors. Their cloth model is rather simple and does not simulate resistance to bending. Rodriguez-Navarro et al. [13-14] have described two implementations of a cloth model on the GPU. The first one exploits a mass-spring system [13] and the second uses the finite element method [14]. Georgii and Westermann [15] compared two possible implementations of mass-spring systems on the GPU (point and edge centric) and tested them with cloth simulation. Other teams, working in the field of cloth modelling, have used the GPU to speed up their simulation [3, 4, 16].

E. Collision detection

Collision detection (CD) and response are the bottleneck of simulation algorithms especially when dynamically changing curved surfaces are concerned. Most algorithms for detecting collisions between cloth and other objects in the scene are based on geometrical object-space (OS) interference tests. Some apply a prohibitive energy field around the colliding objects [5], but most of them use geometric calculations to detect penetration between a cloth particle and a triangle of the object together with methods that reduce the number of checks.

Some common approaches utilize voxel or octree subdivision [17]. Other solutions use recursive subdivision with a bounding box hierarchy [18, 19]. Objects are grouped hierarchically according to proximity rules, flexible surfaces are subdivided in patches and a bounding box is computed for each object or patch. The collision detection is then performed by testing for intersections of bounding boxes. Other techniques exploit proximity tracking [20] or curvature computation [19] to reduce the large number of collision checks, excluding objects or parts which are impossible to collide.

Other approaches apply image-space tests [21, 22, 23] to detect collisions. These algorithms utilise the graphics hardware to render the scene and then use the depth map of the rendered image to perform checks for collision between objects. In this way the 3D problem is reduced to 2.5D. Vassilev et al. [10] applied a similar technique for detecting collisions between cloth and body when dressing virtual actors, which is described in more details in the next section. Vassilev & Spanlang [24] implemented this approach entirely on the GPU. They also proposed a method for collision detection and response between layers of cloth utilizing several depth and normal maps stored in 3D textures running on the GPU.

F. Cloth simulation on a mobile device

An extensive literature search showed there wasn't much work in the field of cloth simulation on mobile devices. Jeon et al. [25] proposed an implementation of cloth simulation on a mobile device, which was accelerated with the help of the mobile GPU. They used a mass-spring system and a vertex shader with transform feedback (TFB) buffers, available in

OpenGL ES 3.0. However, the shader only applies external forces and computes new positions, the spring forces are computed on the CPU using parallel threads and stored to the GPU memory. In addition, they did not offer any solution for a device supporting only OpenGL ES 2.0, on which TFB is not available. Vassilev [26] proposed solutions for virtual try-on on a mobile device, depending on the GPU hardware for devices supporting OpenGL ES 2.0, OpenGL ES 3.0 and OpenGL ES 3.1, which are described in the next section of this paper.

III. VIRTUAL TRY-ON SYSTEM

A. Velocity modification to overcome super elasticity

The main problem of the position modification approach is that first it allows the springs to over-elongate and then tries to adjust their length modifying positions. This of course is not always possible because of many links between the mass points. An alternative idea is to find a constraint that does not allow any over-elongation of springs.

After each iteration the algorithm checks for each spring whether it exceeds its natural length by a pre-defined threshold. If this is the case, the velocities are modified, so that further elongation is not allowed. The threshold value usually varies from 0.01 to 0.15 depending on the type of cloth simulated.
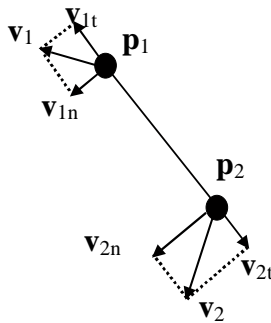
Figure 1: Velocity modification for over-elongated springs

Let p_1 and p_2 be the positions of the end points of a spring found as over-elongated, and v_1 and v_2 be their corresponding velocities (see Figure 1). The velocities v_1 and v_2 are split into two components v_{1t} and v_{2t}, along the line connecting p_1 and p_2, and v_{1n} and v_{2n}, perpendicular to this line. Obviously the components causing the spring to stretch are v_{1t} and v_{2t}, so they have to be modified. In general v_{1n} and v_{2n} could also cause elongation, but their contribution within one time step is negligible. There are several possible ways of modification:

- Set both v_{1t} and v_{2t} to their average, i.e.
  $$v_{1t} = v_{2t} = 0.5(v_{1t} + v_{2t}). \tag{5}$$
- Set only one of them equal to the other, but how to decide which one to change at the current simulation step?

Experiments showed that Equation 5 is good enough for the static case, i.e. when the cloth collides with static objects. So if a system for dressing static human bodies is to be implemented, Equation 5 is the obvious solution, because it produces good results and is the least expensive. For the dynamics, however, the way of modifying velocity proved to have an enormous influence on the cloth behaviour. For example Equation 5 gives satisfactory results for relatively low rate of cloth deformations and relatively slow moving objects. In faster changing scenes, it becomes "clumsy" and cannot give a proper respond to the environment. A solution for the dynamic case is given in [10].

B. Image space based cloth-body collision detection

Collision detection is a crucial part in fast cloth simulation. At each simulation step, a check for collision with the human body has to be performed for each vertex of the garment. If a collision between the body and a cloth point occurs, the response of that collision also needs to be calculated. The described system applies an image-space based collision detection approach. Using this technique it is possible to find a collision only by comparing the depth value of the garment vertex with the according depth information of the body stored in the depth maps. The graphics hardware is also used to generate the information needed for collision response, that is the normal vectors of each body point. This can be done by encoding vector co-ordinates (x, y, z) as colour values (R, G, B). Depth and normal maps are created using two projections: one of the front and one of the back of the model. For rendering the maps two orthographic cameras are placed at the centre of the front and the back face of the body's bounding box (BB). To increase the accuracy of the depth values, the camera far clipping plane is set to the far face of the BB and the near clipping plane is set to near face of the BB. Both cameras point at the centre of the BB. This is illustrated in Figure 2. In case of a static human body the maps are generated only once before the simulation. In case of a moving body the maps have to be generated at each animation step, although if the body movements are known, they can be pre-computed.
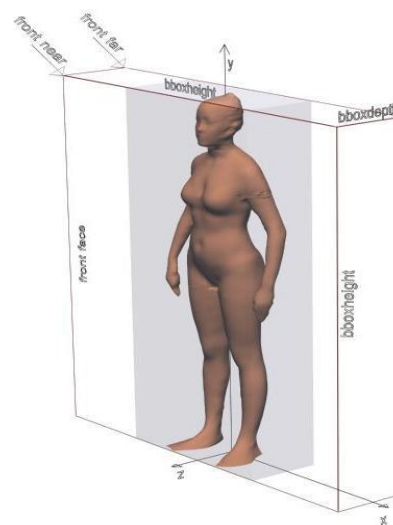
Figure 2: Front camera clipping planes
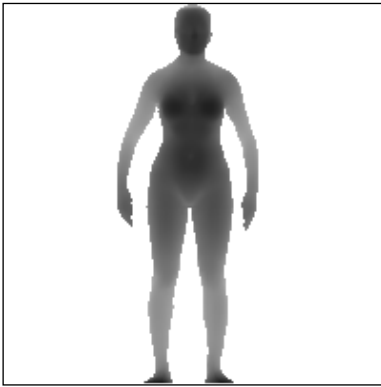
Figure 3: Front depth map: darker shades are near

When initialising the simulation two renderings are executed to retrieve the depth values, one for the front and one for the back. The *z*-buffer of the graphics hardware is moved to main memory using OpenGL's buffer-read function. The *z*-buffer contains floating-point values from 0.0 to 1.0. A value of 0.0 represents a point at the near clipping plane and 1.0 stands for a point at the far clipping plane. Figure 3 shows an example depth map.

During the two renderings for generating the depth, the normal maps are also computed. The (*Red*, *Green*, *Blue*) value of each vertex of the 3D model is substituted with the coordinates (n_x, n_y, n_z) of its normal vector **n**. In this way the frame-buffer contains the normal of the surface at each pixel represented as colour values. Since the OpenGL colour fields are in a range from 0.0 to 1.0 and normal values are from –1.0 to 1.0 the coordinates are converted to fit into the colour fields. The interpolated-shading option is turned on and so the graphics hardware interpolates between the normal vectors for all intermediate points.

More details on the implementation with equations can be found in [10].

C. Resolving collisions

When a collision has been detected, the system has to compute a proper response of the cloth so that there are no penetrations in the human body. Our approach does not introduce additional penalty, gravitational or spring forces; it just manipulates the velocities, as proposed by Eberhardt et al [7], which proved to be very efficient. However, some modifications had to be done for the dynamic case.

Let **v** be the velocity of the cloth vertex **p** colliding with the object **s** and let $\mathbf{v}_{object}$ be the velocity of this object (Figure 4). The surface normal at the point of collision is denoted by **n**. First, the relative velocity between the cloth and the object has to be computed as $\mathbf{v}_{rel} = \mathbf{v} - \mathbf{v}_{object}$. If $\mathbf{v}_t$ and $\mathbf{v}_n$ are the tangent and normal components of the relative velocity $\mathbf{v}_{rel}$, then the resultant velocity can be computed as:

$$\mathbf{v}_{res} = C_{fric}\mathbf{v}_t - C_{refl}\mathbf{v}_n + \mathbf{v}_{object}, \qquad (6)$$

where C_{fric} and C_{refl} are a friction and a reflection coefficients, which depend on the material of the colliding objects.
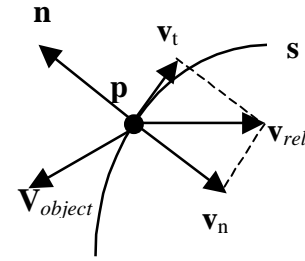
Figure 4: Resolving collisions manipulating velocities

A similar approach can be implemented to detect and find the responses not only to vertex-body, but also to face-body collisions. For each quadrangle on the cloth its midpoint and velocity as an average of the four adjacent vertices is computed. Then a check for a collision of this point with the body is performed and if so, its response using Equation 6 is computed, and the same resultant velocity is applied to the surrounding four vertices. If there is more than one response for a vertex, then an average velocity is calculated for this vertex. As the test results showed, this approach helps to reduce significantly the number of vertices, which speeds up the whole method.

In some cases the velocity collision response does not always produce satisfactory results. For example, when heavy cloth was simulated there were penetrations in the shoulder areas. In order to make the collision response smoother, an additional reaction force was introduced for each colliding cloth vertex. The force is computed in a similar way as the resultant velocity in equation 6. More details with formulation can be found in [10].

D. Cloth-cloth collision detection

The testing for cloth-cloth collisions is performed only between different garment pieces, as self-collisions in a single patch is very unlikely to occur in a virtual try-on simulation. The implemented technique is similar to the bounding box hierarchy one described by Provot [19] with some modifications. The algorithm checks for collisions between every two cloth patches. The function for collision detection between two cloth pieces is recursive. First it builds the axis aligned bounding boxes of the two patches and checks if they overlap. If this is true, every patch is subdivided in four sub-patches and the function is recursively called to check for collisions between each pair of patches.

IV. ACCELERATING COMPUTATIONS ON A MULTICORE CPU

A. Seaming of garment pieces

The Virtual Try-On system reads a body file and a garment file and dresses the body. The garment file holds information about the geometry of the garment panels, physics parameters of the cloth and seaming information. The panels are automatically positioned around the body, using body landmarks, and external forces are applied along the seaming lines. The seaming lines are discretized into groups of two or three cloth vertices to be sewn together. These are called joints and connect two vertices or vertex and an edge.

During the simulation forces are applied which pull together the corresponding vertices. When the vertices are closer than a certain threshold, they are marked as sewn and are attached to each other. The simulation ends when all seams are done, or after a pre-defined number of iterations which means the garment is too small for the body. Once collision is detected between two cloth faces, repulsive forces are applied to prevent penetration.

B. Parallelizing the cloth simulation

Most of the modern microprocessors contain several cores, which in fact are separate CPUs, so the simulation can be accelerated if the algorithm is parallelized on these cores.

One integration step of the proposed cloth simulation on the CPU can be described with the following pseudo code:

Algorithm 1: Cloth simulation on multicore CPU

```
Parallelize For each spring
  Compute internal forces
  Add forces to 2 end mass points
Endfor
Parallelize For each mass point
  Add external forces
Endfor
Parallelize For each joint
  Add joint forces
Endfor
Parallelize For each mass point
  Compute velocity
  Do collision detection and response
Endfor
Parallelize For each spring
  Correct velocities for over-elongated
springs
Endfor
Parallelize For each mass point
  Compute new positions
Endfor
```

There are six main for loops suitable for parallelization. The first one is for each spring and computes the internal forces due to the stiffness of the springs. The second loop goes for each mass and adds the viscous damping and gravity. As mentioned earlier another type of external forces used in our simulation is the seaming force applied to assemble the garment from its pattern pieces. Each seaming line between two patches is composed of "joints" and each joint connects two mass points or a mass point and an edge (the line connecting two mass-points). So, the third loop of the pseudo code is for each joint and adds joint forces to connected masses. The next loop computes the velocity of each mass, checks for collisions, and modifies velocities to respond to the detected collision. Loop 5 again goes for each spring and checks if the spring elongation is above a certain threshold. If this is the case then velocities of the masses, connected by the spring, are modified as described by Vassilev et al. [10]. The last loop again goes for each mass point and computes the new positions. In order to accelerate the cloth-cloth collision detection algorithm exploiting the multicore CPU a new parallel task is created for each recursive call of the function.

The parallelization can be implemented using the OpenMP (Open Multi-Processing) library and API.

V. GPU IMPLEMENTATION

A. Cloth-simulation on the GPU

On the modern GPU the whole cloth simulation can be implemented on the graphics processor. There are several possibilities for GPU general purpose programming: OpenGL shading language (GLSL), NVidia CUDA (however this will limit the simulation only for NVidia processors) and OpenCL. The virtual try-on system uses GLSL, as the visualization is in OpenGL and this makes data exchange between the simulation and visualization modules more efficient. In addition with the compute shaders and shader-storage (SS) buffers in OpenGL 4.3 and above the programming is as flexible as in OpenCL and CUDA.

There are two possible implementations of the cloth simulation on the graphics processor [26].

Algorithm 2: Pure point algorithm (PPA)

```
Parallelize For each mass point
  For each spring connected to this mass
    Compute and sum internal forces
  Endfor
  Add external forces
  Add joint forces
  Compute velocity
  Do collision detection and response
  Correct velocity for over-elongated
  springs
  Compute new position
Endfor
```

Algorithm 2 uses only for each mass point loops and the computation of the spring forces is the first step inside. As a result it can be implemented in only one or two compute shader execution, requires less graphics memory and is more straightforward to implement. Its disadvantage is that each spring force is computed twice, but considering the parallel nature and power of the GPU this is negligible.

Algorithm 3. Edge-point algorithm (EPA)

```
Shader 1:
Parallelize for each spring
  Compute spring force
Endfor
Shader 2:
Parallelize for each mass point
  For each spring connected to this mass
    Add spring forces
  Endfor
  Compute external forces
  Add joint forces
  Compute velocity
  Correct super-elasticity
  Do collision detection and response
  Correct velocity for over-elongated
   springs
  Compute new position
Endfor
```

A compute shader has a random access to SS buffer elements by specifying an index just like accessing array elements in any high level programming language. In addition to the pure point algorithm (Algorithm 2) it is also possible to implement the edge-point algorithm shown below and compare the performance of the two.

The EPA uses two compute shaders: the first performing parallel computations for each spring and the second – for each mass point.

B. GPU data structures for the cloth model

In a compute shader a SS buffer is accessible for both read and write operations. The following SS buffers are needed for the cloth simulation:

- one buffer for mass points velocities;
- one for mass points positions;
- one for the surface normal vectors.

The information about the springs connected to each mass point in a spring connectivity buffer, which is an array of structures and keeps the following information of a spring connected to the corresponding vertex: index of the other spring end point, natural length and spring stiffness. If the index is equal to -1, this means that the entry represents no connection. In case of edge-point algorithm (Algorithm 3) it stores information about spring indexes, to which this point is connected, and the sign with which the spring force have to be added to the sum of all forces. For the first point in a spring this sign is plus and for the second it is minus. In this way shader 1 computes the force of each spring and shader 2 adds the force with the correct sign.

The connectivity of cloth vertices into seams is stored in a similar buffer as for the springs, which we call "seam connectivity buffer". Each element of the buffer keeps information about the other mass points to which the current cloth vertex is to be sewn. During the simulation forces are applied which pull together the vertices to be connected. When the vertices are closer than a certain threshold, they are marked as sewn and are attached to each other. The simulation ends when all joints are done, or after a pre-defined number of iterations which means the garment is too small for the body.

C. Cloth-body collision detection

Cloth-body collision detection is performed in the same way as explained in Section III.B. The only difference is that there is no need to read the depth and normal maps back to the main memory, as they are accessed by the cloth simulation compute shader, which carries out the collision detection and response.

D. Cloth-cloth collision detection

The virtual try-on system tests only for collisions between different layers of cloth as collisions in one piece of cloth are less likely to happen when simulating garments on a static body. When constructing garments some pieces of cloth have to be placed on top of others, like pockets for example. When a person tries on two garments one is always on top of the other for example a T-shirt and a pair of jeans. The cloth pieces are grouped into layers, to know which layer is on top of other layers and a layer number is assigned to each cloth piece, starting from zero.

The system uses the same image-space approach for detecting collisions between layers of cloth. For this purpose several maps are generated:

- Map[0]: body depth and normal vectors
- Map[1]: body and cloth-layer 0 depth and normal vectors
- …
- Map[n]: body and cloth-layers 0 to n-1 depth and normal vectors

The number of maps, n, depends on the number of cloth layers to be simulates. Map[0] is generated only once at the beginning of the simulation, because the body does not move. All other maps have to be generated at each iteration step.
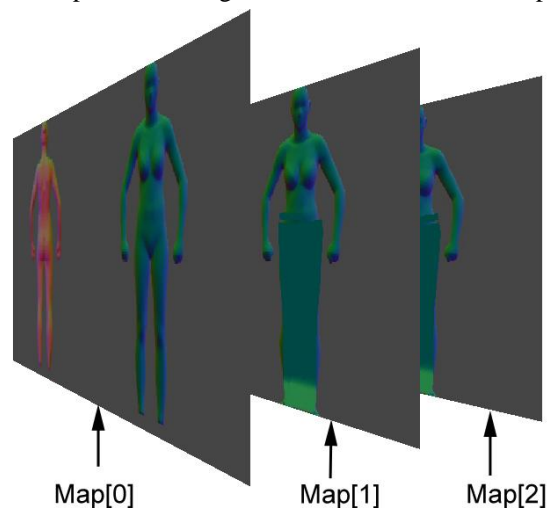
Figure 5: Normal maps generated for collision detection

When resolving a detected collision the algorithm allows simulation of impact from upper layers to lower layers, which is shown in the results section. The actual process of collision detection and response is performed as described by Vassilev & Spanlang [24].

VI. VIRTUAL TRY-ON ON A MOBILE DEVICE

The OpenGL implementation for mobile devices is called OpenGL for Embedded Systems or OpenGL ES. There are several versions of OpenGL ES, but most modern mobile devices support ES2.0, ES3.0, ES3.1 and 3.2. This section will discuss implementation on three versions of OpenGL ES.

A. OpenGL ES 2.0

The capabilities of a GPU supporting OpenGL ES 2.0 are quite limited for general purpose computations. Transform feedback and compute shaders are not supported in OpenGL ES 2.0, so the only way to make computations is to use the old well known render-to-texture technique. However, rendering to floating point textures is not possible either and in the best case one can set as a rendering target a RGBA texture with 8-bit unsigned integers per colour at maximum. This makes it impossible to utilize the GPU for cloth simulation, however it

can be used to speed up the collision detection, as described below.

1) Cloth simulation

The modern mobile devices possess a multicore CPU, so the cloth simulation can be accelerated as described in section IV.B and Algorithm 1. In addition they are based either on ARM or Intel x86 processors. Both CPU families support SIMD instructions called NEON on ARM and MMS on x86. The mass-spring cloth simulation uses quite a few operations on velocities and position which are in fact 3D vectors. So all operations on vectors (like addition, subtraction, multiplication, division, dot and vector product) can be implemented using these instructions, which speed up the computations further. There is no need to use assembly language as most compilers support the so called intrinsic operations implemented as macros or functions.

2) Collision detection

The mobile GPU can be used to accelerate the cloth-body collision detection as described in the previous section. Two orthographic cameras are placed in front and in the back of the human body and render front and back depth and normal maps. The depth maps are used for detecting collisions, while the normal map, in which the XYZ coordinates of the normal vectors are encoded as RGB colours, are used for collision response. In addition, to reduce the number of texture units, the front and back maps are placed in a single texture, as shown in Figure 6.
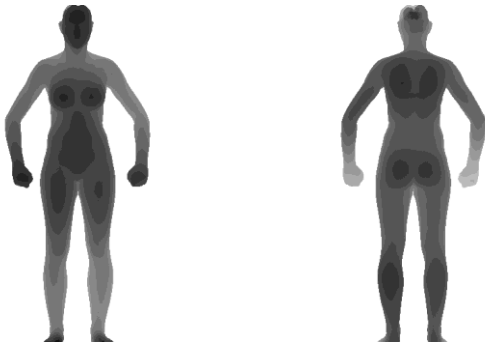
Figure 6: Front and back depth maps in one texture

As already mentioned, in OpenGL ES 2.0 one can set a rendering target with a maximum of 8-bits per channel. Although it is possible to set a depth buffer with 16 bits texture, it is not possible to read this buffer and access it for later processing. The only option is to transfer the depth values to an 8-bit channel target in a fragment shader. Therefore a RGBA texture is set as a rendering target and a fragment shader is used, which writes the XYZ normal vector coordinates to RGB and the depth value to the Alpha channel. The error of discretization can be computed as follows. Let us consider the normal vectors are stored in millimetres. Each coordinate is in the interval [-1, 1] then the error in each coordinate is

$$E_{normal} = \frac{2}{255} = 0.0078 \ mm \tag{7},$$

which is negligible.

Let us suppose the depth of the body bounding box is about 700 mm, which is discretised with 8 bits. Then the depth discretization error is

$$E_{depth} = \frac{BodyDepth}{255} = \frac{700}{255} = 2.745 \ mm \tag{8},$$

which in some cases may lead to visible artefacts and parts of the body peeking out of the garment. Therefore the following technique is proposed, in which normal vector XYZ coordinates and the depths are discretized with 16 bits. The body is rendered two times with two different fragment shaders. Shader 1 stores normal X in RG and normal Y in BA in the first render texture and shader 2 stores normal Z in RG and depth in BA of the second texture. In this way each of the normal vectors coordinates and depth are stored as 16-bit unsigned integers. This is done only once before the simulation starts and then the two buffers are read back in the main memory and converted to floats, so that XYZ coordinates of the normal vectors fall again in [-1, 1] and the depth values are in [0, 1].

In this way the depth discretization error becomes:

$$E_{depth} = \frac{700}{65535} = 0.011 \ mm \tag{9},$$

which is negligible.

The cloth-cloth collision detection and response is performed in the same way as in Section III.D and IV.B.

B. OpenGL ES 3.0

In OpenGL ES 3.0 it is possible to implement the whole simulation on the GPU by taking advantage of the transform feedback (TFB) technique.

1) Cloth simulation

With TFB it is possible to use a vertex shader that performs floating point computations on input float buffers and writes the result to an output buffer. However, the buffers cannot be accessed randomly using an array index as in compute shaders and SS buffers. Only one element of a buffer (vertex attribute) scheduled to the particular invocation of that shader is accessible. The experiments showed that the TFB approach works more efficiently with the pure point implementation of the parallel cloth simulation as shown in Algorithm 2.

2) GPU data structures for the cloth model

In a mass-spring simulation a mass point is connected with springs to several other masses, so a random access to positions and velocities in a buffer by specifying an index is needed. This cannot be achieved with transform feedback buffers, but only with textures. OpenGL ES 3.0 cannot use floating point textures as a rendering target, however it can store data in such textures. So the velocities and positions of the cloth vertices are stored in textures in the GPU memory and their new values are written to transform feedback buffers. After each iteration the newly computed data has to be copied from the buffers to the textures. The good thing is that copying from a buffer object to a texture is performed very quickly as this is an operation in the graphics memory.

Therefore two buffers and two textures are needed for the velocities and the positions and one buffer – for the normal

vectors of the cloth surface at each cloth vertex, which are also computed on the GPU.

The VTO system stores information about the springs connected to each mass point in a "spring connectivity texture". A suitable constraint on the maximum number of other vertices connected to a given mass point has to be enforced. For the cloth model this number is 12, but because of the fact that texture sizes have to be a power of two, it is simpler to reserve 16 values, and in this way there are 4 spare values for future extensions. If the textures for velocities and positions are of size (texSize × texSize), then the spring connectivity texture is of size (4*texSize)×(4*texSize). This spring matrix consists of 16 smaller matrices. Each entry in these 16 matrices has 4 channels (RGBA) and keeps the following information of a spring connected to the corresponding vertex: texture coordinates of the other spring end point, natural length and spring stiffness. If all channels are equal to -1.0, this means that the entry represents no connection.

3) Seaming of garment pieces

The connectivity of cloth vertices into seams is stored in a similar texture as for the springs, which is called "seam connectivity texture". Each entry of the texture keeps information about the other mass points to which the current cloth vertex is to be sewn. During the simulation forces are applied to the masses in a joint, which pull together the vertices to be connected. When the vertices are closer than a certain threshold, they are marked as sewn and are attached to each other. The simulation ends when all joints are done, or after a pre-defined number of iterations which means the garment is too small for the body.

4) Counting sewn vertices

In order to identify when the garment is stitched, the number of vertices still to be sewn has to be counted. In OpenGL ES occlusion queries cannot be directly used for counting as described by Vassilev & Spanlang [24]. On the PC graphics cards there is an internal counter, which is initially set to zero, and during the rendering it is increased by one for each fragment that passed the depth test. In OpenGL ES there is an internal flag, which is initially set to false and during the rendering it is set to true if any fragments have passed the depth test. So in our case this can be used to identify if there are still any vertices to be stitched.

In order to use occlusion query for this, the following steps have to be followed:
- Create a depth texture;
- Set this texture as a depth buffer for rendering;
- Render a suitable geometry and perform an occlusion query to check if any fragments have passed the depth test.

After the new positions were computed by the simulation vertex shader, another shader is called which keeps the sewn vertices together and also builds a seam depth texture with the following values: 0 if the vertex is not involved in a seam, 1 if the vertex is a part of a seam but is not sewn yet, and 0.5 if this a sewn vertex part of a seam. Then this texture is set as the default depth buffer. The z-buffer is turned to read only, otherwise the depth values will be replaced with the ones of

the incoming vertices. After that a quad with a depth value of 0.8 is rendered that covers the whole draw buffer. In this way the occlusion query will show if any fragments have a depth value greater than 0.8, that is if any vertices are still unsewn. In fact the quad can have any depth value in the interval (0.5, 1).

The function for determining if there are still unsewn vertices does not need to be called after every integration step. To speed the simulation up it could be called after every 10 or 15 iterations.

5) Cloth-body collision detection

Cloth-body collision detection is performed in the same way as explained in Section V.C. The only difference is that the depth and normal maps are accessed by the cloth simulation vertex shader, which carries out the collision detection and response.

6) Cloth-cloth collision detection

The cloth-cloth collision detection and response is performed in the same way as described in section V.D.

C. OpenGL ES 3.1

OpenGL ES 3.1 supports compute shaders and shader storage buffers as OpenGL 4.3 and above. As a result the cloth simulation and collision detection can be implemented in the same way as on a personal computer as described in section V.

VII. GARMENT DIGITIZATION

The VTO system uses a simple garment description in our own text format. The format describes global garment properties such as the mesh resolution and where the garment should arrive on the body. A garment type is used to classify the garment in order to correctly and automatically pre-position it around a body scan. Four garment categories proved to be sufficient for pre-positioning: bra, shirt, skirt, and trousers.

The exchange format also defines the set of panels comprising the garment. Garment panels are described by their cutting pattern, (Figure 7) fabric properties, Uniform Resource Locators (URL) to images that provide garment texture, and URLs to garment accessories (rigid geometry that might be attached to the garment such as buttons, cuff links, etc.). In compressed form even very complex garments can be described by less than 10KB of data in the format.

Acquiring a digital version of a garment seems to be one of the most difficult parts in a VTO system. The first option is to use an output file of a garment design CAD system like Gerber or Lectra. They export a DXF file with garment pattern information, however it cannot be used directly. There is additional seaming allowance and grading information, so it requires further manual processing. The fabric texture information has to be also acquired from other sources. However, the biggest problem of a CAD output file is that the garment designers are not willing to share these files because this is their know-how and they are afraid that it could be exposed to their competition.

So, in order to digitize garments and not depend on garment

designers a garment scanner was constructed based on the reverse engineering approach [27]. First the garment is cut into its construction panels. Then they are placed on the floor in a rectangle with known sizes. A digital photo camera, which is connected to a laptop via USB, is mounted above the rectangle and takes a picture of the garment panels. Then a piece of software processes the acquired image to undistort and rectify it. The image is imported in Adobe Illustrator (AI) and using an AI plugin, specially developed for this purpose, the garment panels are be marked-up to get their contours (Figure 7). With the help of the plugin the designed can enter garment and fabric properties, specify seaming lines and other relevant information and in the end export the garment in a format used by the VTO system.
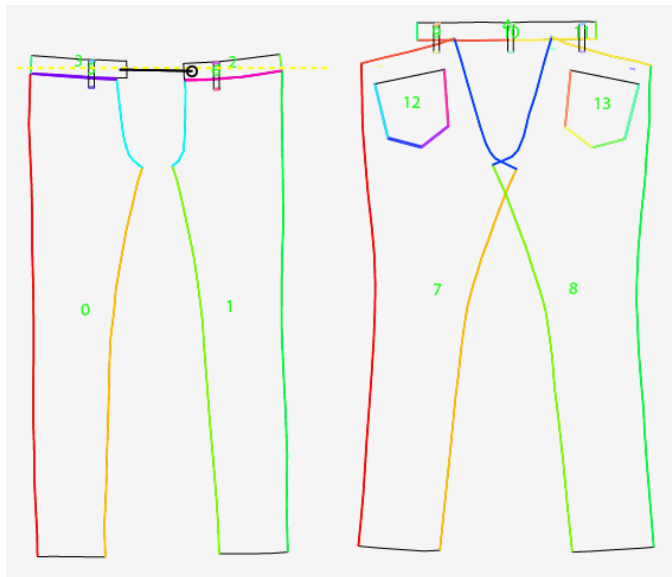
Figure 7: Garment panels of a pair of jeans

The main disadvantage of this approach is that it is too expensive. First the garment has to be destroyed in order to obtain the cutting patterns and then it takes quite a long time for shooting the images and marking-up to garment to make it suitable for the simulation.

VIII. RESULTS

The system was implemented on two platforms:
- Windows 10 with OpenGL 4.5 using Microsoft Visual Studio with C++.
- Android 5.0 and above using Android SDK and Native Development Toolkit (NDK). The interface is written in Java and the main simulation algorithms are in C++ for speed.

Figure 8 shows the result of the simulating layers of cloth. A pair of jeans is dressed on top of a T-shirt. The left picture simulates dressing the jeans with no impact of upper to lower layers. The simulation is faster, but not satisfactory. The right picture simulates impact to lower layers.

Figure 8: Layers of cloth: jeans dressed on top of a shirt; left: no impact of upper to lower layers; right: with impact to lower layers

Performance tests were executed on the following configurations:
1) Windows laptop with Intel Core i7-4702MQ quad core (with 8 threads) at 2.2 GHz and NVidia GPU GTX-760M.
2) Android mobile device with a quad core ARM Cortex-A17 1.7 GHz CPU and ARM Mali T760 GPU supporting OpenGL ES 3.0 and 3.1.
3) Android smart phone with ARM Cortex A7 quad core 1.3 GHz CPU with Mali 400 GPU supporting OpenGL ES 2.0.

Figure 9 show the results of simulating a pair of jeans on a virtual female body in five test cases: laptop GPU, laptop CPU with parallelization, mobile device (MD) CPU, MD GPU with TFB and MD GPU with compute shaders. The time was measured in milliseconds for a single iteration for different numbers of cloth vertices. In this particular case cloth-cloth collision detection was turned off as it is not likely to happen for a single garment. When executing the simulation on an Android device all processes of the operating system and widgets were running normally, but no additional applications, like listening to music or surfing the net, were running at the same time. As expected the simulation is slowest on a MD CPU, however it runs faster on a MD GPU compared to a PC CPU accelerated with parallel threads on the CPU. The implementation on a MD with compute shaders is only about 4 to 5 percent faster than the TFB implementation. This difference is probably due to the time for copying the position and velocity data from the array buffers to the textures, see section VI.B. As expected the simulation on a laptop GPU is the fastest and the time per iteration almost does not depend on the number of cloth vertices.
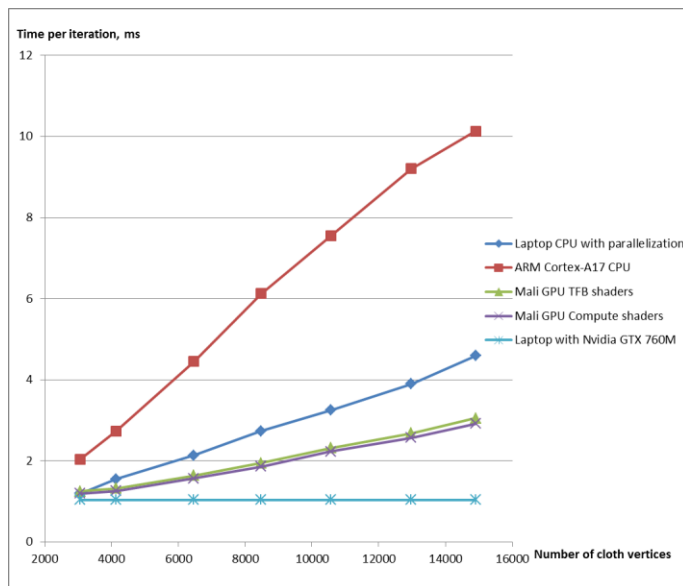
Figure 9: Time per iteration vs number of cloth vertices

The performance of the two possible implementations (PPA, Algorithm 2 and EPA, Algorithm 3) of a mass-spring system on the GPU was also tested. However they showed exactly the same times with some insignificant variations below 1%, therefore only the PPA times are shown in Figure 9.

Table 1: Time in seconds for dressing a pair of jeans with 3100 cloth vertices

Laptop GPU GTX 760M	Laptop CPU paralleli-zation	ARM Cortex-A17 CPU	Mali GPU TFB shaders	Mali GPU compute shaders	Smart phone
0.510 s	0.765 s	0.765 s	0.47 s	0.45 s	2.1 s

Figure 10: VTO of a pair of jeans simulated on a smart mobile phone

The VTO simulation starts from flat garment patterns, positioned around the body, (Figure 10 left) and converges in 350 to 500 iterations (Figure 10 right) depending on the number of cloth vertices. About 3000-3400 vertices are sufficient for a good visual quality of a garment on a mobile device. Table 1 shows the times in seconds for dressing a pair of jeans with 3100 cloth vertices. The slowest, as expected, is a smart phone CPU – about 2 s. The simulation takes below one second on all other test cases, which is quite a good performance.

IX. CONCLUSION

A complete virtual try-on system for dressing a human body in virtual garments was presented. The body is acquired via a 3D scanner and the garment is digitized using a specially designed garment scanner. The system uses physical cloth simulation running on the GPU and as a result it is very fast – a pair of jeans can be dressed on a human body for about 0.2 seconds. The following main conclusions can be drawn:

- On desktop and laptop computers with a GPU, supporting OpenGL 4.3 and above and on mobile devices with a GPU, supporting OpenGL ES 3.1 and above, the simulation can be performed entirely on the GPU using compute shaders and shader storage buffers. This speeds up the simulation very much.
- Today's mobile devices possess sufficient computational power to be used for virtual try-on garment simulation on a static human body.
- On devices with GPU supporting only OpenGL ES 2.0 the simulation can be accelerated by parallelizing the computations on the multi-core CPU, using the SIMD instructions and utilizing the GPU for collision detection.
- On devices with more powerful GPU supporting OpenGL ES 3.0 and 3.1 the simulation can be performed entirely on the GPU as described in sections 4 and 5.
- On devices with GPU supporting compute shaders two implementation of the mass-spring system are possible: pure-point and edge-point approach. However the results show that the simulation times of the two techniques are the same.
- The main drawback of the current system is the garment digitization. It is too expensive and other methods of garment digitization should be sought.

REFERENCES

[1] Movania M.M. & Farbiz F. Depth image based cloth deformation for virtual try-on. *ACM SIGGRAPH 2013 Posters*, 2013.

[2] Giovanni S., Choi Y.C., Huang J., Khoo E.T., Yin K. Virtual try-on using Kinect and HD camera. *Proceedings of Motion in Games* 7660, 2012, pp. 55–65.

[3] Kevelham B., Magnenat-Thalmann N. Fast and accurate GPU-based simulation of virtual garments. *Proceedings of VRCAI (ACM)* 2012, pp. 223–226.

[4] Kevelham B., Magnenat-Thalmann N. Virtual try on: an application in need of GPU optimization. *Proceedings of the ATIP/A*CRC Workshop*

on Accelerator Technologies for High-Performance Computing 2012, Singapore, Art.No 10.

[5]   Terzopoulos D., Platt J., Barr A., Fleischer K.: Elastically deformable models. *Computer Graphics (Proc. SIGGRAPH'87) 21, 4 (1987),* pp. 205–214.

[6]   Breen D., House D., Wozny M.: Predicting the drape of woven cloth using interacting particles. In *Computer Graphics Proceedings, Annual Conference Series* (1994), vol. 94, pp. 365–372.

[7]   Eberhardt B., Weber A., Strasser W.: A fast, flexible, particle-system model for cloth draping. *j-IEEE-CGA 16*, 5 (Sept. 1996), pp. 52–59

[8]   Carignan M., Yang Y., Thalmann N. M., Thalmann D.: Dressing animated synthetic actors with complex deformable clothes. In *Computer Graphics Proceedings, Annual Conference Series* (1992), vol. 92, pp. 99–104.

[9]   Provot X. Deformation constraints in a mass-spring model to describe rigid cloth behaviour. *Proceedings of Graphics Interface 1995*, pp. 141–155

[10] Vassilev T., Spanlang B., Chrysanthou Y.: Fast cloth animation on walking avatars. *Computer Graphics Forum 20, 3* (2001), pp. 260–267.

[11] Press W H, Flannery B P, Teukolsky S A and Vetterling W T. *Numerical Recipes in C: the Art of Scientific Computations*. Cambridge University Press 1992.

[12] Zeller C. Cloth simulation on the GPU. *Proceedings of SIGGRAPH 2005: ACM SIGGRAPH Sketches*, pp. 39-42.

[13] Rodriguez-Navarro X., Sainz M., Susin A.. GPU based cloth simulation with moving humanoids. *Actas XV Congreso Español de Informática Gráfica (CEIG'2005) 2005*, J. Regincós D. M, Thomson-Paraninfo E, pp. 147–155.

[14] Rodriguez-Navarro X., Susín A. Non structured meshes for cloth GPU simulation using FEM. *3rd. Workshop in Virtual Reality, Interactions, and Physical Simulations* (VRIPHYS) pp. 2006, 1–7.

[15] Georgii J, Westermann R. Mass-spring systems on the GPU. *Simulation Modelling Practice and Theory,* 13, pp. 693–702.

[16] Vassilev T.I. Comparison of several parallel API for cloth modelling on modern GPUs. *Proceedings of the 11th International Conference CompSysTech 2010; ACM ICPS 471*, pp. 131-136.

[17] Badler N.I. & Glassner A.S. 3D object modelling. Course note 12, Introduction to Computer Graphics, *Proceedings of SIGGRAPH* 1997, pp. 1–14.

[18] Baraff D. & Witkin A. Large steps in cloth simulation. *Computer Graphics Proceedings, Annual Conference Series*, 1998, pp. 43–54.

[19] Provot X. Collision and self-collision detection handling in cloth model dedicated to design garments. *Proceedings of Graphics Interface*, 1997, pp. 177–189.

[20] Volino P., Magnenat Thalmann N. Collision and self-collision detection: Efficient and robust solutions for highly deformable surfaces. *Computer Animation and Simulation* 1995, Terzopoulos D, Thalmann D, (Eds.), Springer-Verlag, pp. 55–65.

[21] Shinya M., Forgue M.C. Interference detection through rasterization. *Journal of Visualization and Computer Animation* 2, 1991, pp. 131-144.

[22] Myszkowski K., Okunev O.G., Kunii T.L. Fast collision detection between complex solids using rasterizing graphics hardware. *The Visual Computer* 11 (9), 1995, pp. 497–512.

[23] Baciu G., Wong W. S., Sun H. Recode: an image-based collision detection algorithm. *The Journal of Visualization and Computer Animation* 10 (4), 1999, pp. 181–192.

[24] Vassilev T.I., Spanlang B. Fast GPU Garment Simulation and Collision Detection, *20th International Conference on Computer Graphics, Visualization and Computer Vision WSCG 2012*, Plzen, pp. 19-26

[25] Jeon J.H., Min S.D., Kong M. Implementation of Cloth Simulation Using Parallel Computing on Mobile Device. *International Journal of Electrical and Computer Engineering* 5 (3), 2015, pp. 562-568.

[26] Vassilev, T.I. Garment Simulation and Collision Detection on a Mobile Device, International Journal of Mobile Computing and Multimedia Communications 7 (3), 2016, pp. 1-15.

[27] Spanlang, B. Garment Modelling and Visualisation, PhD thesis, University College London, 2005.

An Application to Provide Radio Control with Voice Commands for Visual Impaired Individuals

S. TASDEMIR[1], E. AVUCLU [2] and B. TEZCAN[1]

[1]Department of Computer Engineering, Technology Faculty, Selçuk University, Konya Turkey
stasdemir@selcuk.edu.tr, btezcan@selcuk.edu.tr
[2]Department of Computer Technology and Computer Programming, Aksaray University, Aksaray Turkey
emreavuclu@aksaray.edu.tr

Abstract - **Using technology, we can control many things in our lives. Our life has become more comfortable with technology. Some situations that were previously difficult to manage thanks to technology have become much more practical. The use of technology has made life easier especially for people with disabilities in many areas. In this study, a radio program was developed for individuals with disabilities to listen to radio via voice commands over the internet. This application was developed to address the needs of people who cannot listen to music on their own due to any disability. The application was implemented in C# programming language. In order to manage the radio program with voice commands, voice recognition libraries were first used. In the application developed, the desired radio can be listened over the internet without using keyboard and mouse.**

Keywords - **Voice recognition, Radio program, Visually impaired individuals.**

I. INTRODUCTION

Technology is an indispensable tool for people to carry out certain tasks in their daily lives. People have developed and used technology every day to meet their needs. Today it is very easy to control any application with computer software. Many applications can now be controlled with software to make people's lives easier.

In the literature, in order to facilitate the social life of people in this field, the studies on voice, speech and speaker recognition are as follows:

Separate tests were performed on male and female users with different algorithms [1]. Multiple HMM voice recognition systems were used [2].

Using artificial intelligence techniques, a voice recognition system independent of text and speaker was developed on the Turkish language [3]. The syllable-based Turkish word recognition system was developed using different voice recognition algorithms [4]. With MFCC, Euclidean Distance, Artificial Neural Networks and Dynamic Time Bending algorithms were used separately for voice commanded home applications (light on and off, shutter, etc.) [5]. In the simulation environment performed on MATLAB, the successful recognition rate for 10 people was found to be 99% [6].]. Mobile vehicle design was performed using different voice recognition algorithms [7]. They performed music and speech recognition [8]. Class Non-Principal Component Analysis was examined for the TIMIT database and compared with the Vector Quantization algorithm [9]. Linear Coding and Adaptive Algorithm-based study used different voice recognition algorithms [10]. Artificial hand design was made using HM 2007 voice recognition card. Successful results were obtained in the study which performed 40 commands [11]. Linear Predictive Coding and VQ algorithms and HMM algorithm was used separately. In the developed system, ambient noise was detected and used as threshold value. Figures 0-9 are independently detected by the sound detection system in time and then sound processing techniques are used [12]. It was controlled by voice commands of a remote controlled car [13].

In this study; An application for listening to radio with voice commands over the internet has been developed. If there is a match in the voice commands, operations can be carried out with the mouse and keyboard.

II. MATERIALS AND METHODS

The application was programmed in C # programming language. The following libraries should first be added to the system for voice recognition.

```
using System.Diagnostics;
private SpeechLib.SpSharedRecoContext objRecoContext =null;
private SpeechLib.ISpeechRecoGrammar grammar = null;
private SpeechLib.ISpeechGrammarRule menuRule = null;
```

The design of the application consists of specific stages. From the recognition of voice commands to the execution of the radio program, a number of operations are carried out. The flow diagram of the developed application is as in figure 1 below.
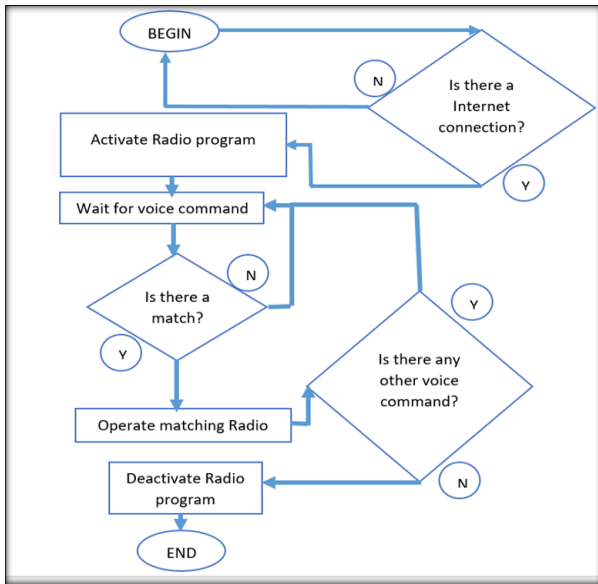
Figure 1. Flow diagram of the system

First of all, in order to listen to music in the radio program, we need to add the media player component as shown in Figure 2.
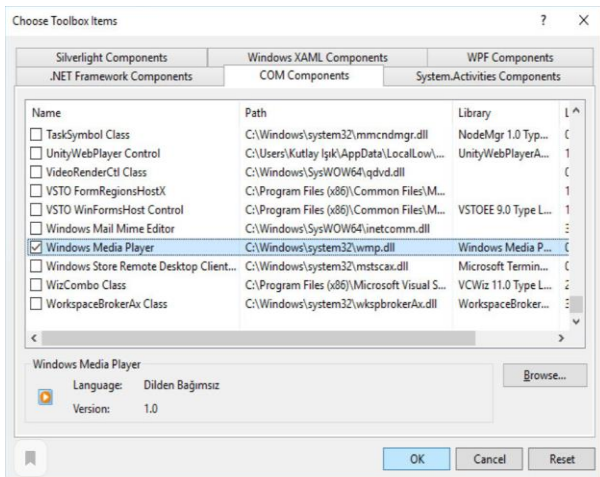
Figure 2. General structure of the system

The general form design view of the application to be managed by voice commands is shown in figure 3. We can activate or deactivate this application when we send voice commands.

Figure 3. Interface of the developed application

We need to include the following library in our system first.

```
using System.Speech.Recognition;
```

Voice detection can be performed with the methods and classes in the System.Speech library in the .Net Framework. The following code blocks are used first for voice recognition and the use of the necessary libraries in the system.

```
SpeechSynthesizer Speech = new SpeechSynthesizer();
PromptBuilder Builder= new PromptBuilder();
SpeechRecognitionEngine Recognition= new
SpeechRecognitionEngine();
```

The code block required to activate or deactivate the application is as follows.

```
avuclu.Text=Result.PhraseInfo.GetText(0, -1, true);//activate
objRecoContext = null; // deactivate
```

The definitions and their use for controlling the radio program with voice commands are shown in table 1 below.

Table 1. Commands and functions

Voice commad	Functions
One	Powertürk Fm
Two	Best Fm
Three	Dream Türk
Four	Fenomen
Five	Hit Fm
Six	Metropol Fm
Seven	Metro Fm
Eight	Moral Fm
Nine	Number 1

For the operation of the application, the internet connection

is first checked as shown in the code block below.

```
if (axWindowsMediaPlayer1.isOnline == false)
    {
 MessageBox.Show("The radio program cannot be used
because you do not have access to the Internet!");
    }
```

After verifying the voice command after the necessary definitions, the data transmission process is executed with the following code block. An audible feedback is given as to whether the radio is turned on.

```
if (avuclu.Text == "one")
    {
        axWindowsMediaPlayer1.URL =
"http://mpegpowerturk.listenpowerapp.com/powerturk/mpeg/icecast.audio";
    SpeechSynth.Speak("Radio playing");
    }
if (avuclu.Text == "two")
    {
 axWindowsMediaPlayer1.URL = "http://46.20.7.126/;stream.mp3";
    SpeechSynth.Speak("Radio playing");
    }

if (avuclu.Text == "three")
    {
  axWindowsMediaPlayer1.URL = "http://radyo.dogannet.tv/dreamturk";
  SpeechSynth.Speak("Radio playing");
    }

if (avuclu.Text == "four")
    {
        axWindowsMediaPlayer1.URL =
"http://fenomenturk.listenfenomen.com/fenomenturk/128/icecast.audio";
    SpeechSynth.Speak("Radio playing");
    }

if (avuclu.Text == "five")
    {
 axWindowsMediaPlayer1.URL = "http://yayin.turkiletisim.com.tr:1094/;";
    SpeechSynth.Speak("Radio playing");
    }

if (avuclu.Text == "six")
    {
axWindowsMediaPlayer1.URL =
"http://mfm1.webradiostreaming.de:8250/1";
    SpeechSynth.Speak("Radio playing");
    }
if (avuclu.Text == "seven")
    {
 axWindowsMediaPlayer1.URL =
"https://playerservices.streamtheworld.com/api/livestream-
redirect/METRO_FM.mp3";
    SpeechSynth.Speak("Radio playing");
    }
if (avuclu.Text == "eight")
    {
"http://yayin2.canliyayin.org:8886/;stream.mp3";
SpeechSynth.Speak("Radio playing");
    }

if (avuclu.Text == "nine")
    {
"http://nr1digitalsc.radyotvonline.com/stream/219/";
SpeechSynth.Speak("Radio playing");
    }
```

III. CONCLUSION

In this study, a radio program which can be managed by remote voice commands is developed. Radio program was managed with voice commands without using mouse and keyboard. With the voice recognition application, the radio program was also given voice feedback for visually impaired individuals. In addition, it will be possible for people with disabilities, elderly or bedridden patients to meet their radio listening needs in their daily lives. The application developed in C # using the Speech.dll library.

REFERENCES

1. Demirci, M. D., Bilgisayar Destekli Ses Tanıma Sistemi Tasarımı, Yüksek Lisans Tezi, İstanbul Üniversitesi Fen Bilimleri Enstitüsü, 2005.
2. Phoophuangpairoj, R., "Using Multiple HMM Recognizers and the Maximum Accuracy Method to Improve Voice Controlled Robots", International Symposium on Intelligent Signal Processing and Communication Systems (ISPACS), December 2011.
3. Kirişçioğlu, F., Karabacak, E., Çetintürk, Ç., "Bilgisayar Destekli Bir Dil Programı", Turkish Speech Recognition Platform TREN.
4. Aşlıyan, R., Günel, K., Yakhno, T., "Dinamik Zaman Bükmesi Yöntemiyle Hece Tabanlı Konuşma Tanıma Sistemi", Çanakkale Onsekiz Mart Üniversitesi, Akademik Bilişim, 2008.
5. Baygın, M., Karaköse, M., "Gerçek Zamanlı Ses Tanıma Tabanlı Akıllı Ev Uygulaması" IEEE 978-4673-0056, 2012.
6. Dede, G., Sazlı,M.H., "Biyometrik Sistemlerin Örüntü Tanıma Perspektifinden İncelenmesi ve Ses Tanıma Modülü Simülasyonu", Savunma Bilimleri Enstitüsü.
7. Edizkan, R., Tiryaki, B., Büyükcan, T., Uzun, İ., "Ses Komut Tanıma ile Gezgin Araç Kontrolü", Dumlupınar Üniversitesi, Akademik Bilişim, 2007.
8. Bolat, B., Küçük, Ü., Yıldırım, T., "Aktif Öğrenen PNN ile Konuşma/Müzik Sınıflandırma", Akıllı Sistemlerde Yenilikler ve Uygulamaları Sempozyumu, 2004.
9. Ertaş, F., Hanilçi, C., Konuşmacı Tanıma Sistemi İçin Yeni Bir Sınıflandırıcı, Uludağ Üniversitesi Elektronik Mühendisliği.
10. [10] Meral, O., Doğrusal Öngörülü Kodlama ve Adaptif Algoritma Tabanlı Konuşmacı Tanıma, Yüksek Lisans Tezi, İstanbul Üniversitesi Fen Bilimleri Enstitüsü, 2008.
11. Asyalı, M.H., Yılmaz, M., Tokmakçı, M., Sedef, K., Aksebzeci, B.H., Mittal, R. ,"Design and Implementation of a Voice Controlled Prosthetic Hand", Turk J. Elec. Eng. and Comp., Vol.19, No.1, 2011.
12. Babui, G., Kumar, H., Vanathi, P.T., "Performance Analysis of Hybrid Robust Automatic Speech Recognition System", IEEE 978-1-46731318-6, 2012.
13. Leechor, P., Pornpanomchai, C., Sukklay, P., "Operation of a Radio Controlled Car by Voice Commands", 2010 2nd International Conference on Mechanica and Electronics Engineering (ICMEE 2010), 2010.

FIXED AND VARIABLE ANGLE SOLAR ENERGY PLANT ANALYSIS

OYA KILCI[1] and MURAT KOKLU[2]

[1] Selcuk University, Konya/Turkey, oyautcu@gmail.com
[1]Selcuk University, Konya/Turkey, mkoklu@selcuk.edu.tr

Abstract - **Developments in science and technology cause increasing energy demand every day. Renewable energy sources already have a significant place in electricity production both around the world and also in Turkey and the share of solar energy going higher within the renewable energy sources. Solar energy is extremely easy to use, it is preferable too because it is environmentally friendly-clean energy. Solar energy plant is the energy source of the future, because the production costs of solar plants are lower than other energy sources and the economic difficulties are overcome. To get optimal production, the solar energy plant must make maximum use of the sun. In the designed system, solar panels are provided with both fixed and seasonal variations. The first variations of solar panel systems is are placed at constant 25° angle and the position angle of second variation is shifted from 10° to 30°in summer and winter accordingly. In this study, the performance of 1148 kWp PV plants which is established in Altınekin district of Konya and planned to be connected to the grid was evaluated by PVSYST analysis program. Power generation of the two different systems, specific data and performance value are calculated. Result of the study shows that the seasonal system produced 32.2 MWh more per year than the fixed system. Global irradiation in the seasonal system is 26.4 kWh/m², and the specific yield is concluded to be more than 28 kWh / kWc / year.**

Keywords - **Solar power plant, Solar energy, Fixed system, Variable angle system.**

I. INTRODUCTION

With the development of science and technology in the world and in Turkey, energy needs are increasing day by day. In order to meet the requirements of the country, the importance of alternative sources in energy production has emerged. The share of solar energy in electricity generation, which has a very important place among renewable energy sources, is increasing and the studies in this area are becoming increasingly important. Turkey trying to become one of the leading countries using solar energy in the world and aware of its solar energy production potential for very long time is trying to make the optimal use of this resource in today. Especially in recent years, Turkey has been making big investments in solar energy systems sector and many studies are being carried out on behalf the sector actors. According to European and other world states, our country's solar energy potential and annual sunny day time lengths are quite high. Solar energy is preferred because it is extremely easy to use and environmentally friendly clean energy.

One of the reasons of global warming is due to the increase in carbon dioxide (CO_2) and greenhouse gases in the atmosphere which are result of using fossil fuels for electrical energy. Due to energy crises and global warming, interest in renewable energy sources is growing against fossil fuel based production. Among these sources, the sun has become the center of attention because it is a clean and never-ending source of Energy [1].

Turkey's annual rate of electricity consumption has increased by an average of 5.4 percent in the last 15 years. At the end of 2016, Turkey's electricity production was 273,387 GWh, 184,889 GWh of which from thermal power plants, 67,268 GWh of which from hydroelectric power plants and 21,230 GWh of which from other renewable energy sources [2].

Turkey has largely renewable energy resources in terms of location. Especially solar energy has come to the fore in terms of its renewability, cleanliness, and ease of use. According to Turkey's solar energy potential Atlas (GEPA), the total annual sunny time is 2.741 hours (daily average 7.5 hours), while the total annual incoming solar energy is 1.527 kWh/m2*year (daily average 4.18 kWh/m2*day) [3]. Turkey has a solar energy potential as high as 110 days, so that if necessary investments are made, it can produce 1100 kWh of solar energy per unit square meter per day. Southeast Anatolia is the region with the highest amount of solar energy in our country, followed by the Mediterranean region and the Eastern Anatolia region [1].

STUDIES IN THIS FIELD:

In their work, Kandasamyet al. (2013) assessed the performance of the grid-connected solar system using the PVsyst analysis program. They calculated the performance ratio of 1 MW solar system in southern Tamil Nadu, India. [4]

Subhadeep Bhattacharjee and colleagues (2013) evaluated the performance of a 60 kWp PV power plant in their study. They examined various parameters for the performance estimation of 60 kWp PV power plants installed in India. They investigated various losses in the PV system, performance index, solar fraction, etc. They stated that 74.336kWh of energy per year could be obtained by the Pvsyst program. [5]

André Mermoud (2012) conducted the analysis of the mutual shading effect on PV power plants in the Pvsyst program. They have optimized the radiation in the Seville region. He has done a deep analysis of the main parameters involved in optimization, in particular the comparison of plane slope and shading boundary angle. Over the course of a year he

observed that different components (beam, propagation, albedo, and incompatibility electrical effects) were dominated by shading effects and widespread and albedo losses. Electrical effects are also important with a single string in the width of the lines. In row edits, he confirmed that the entire array is affected by this shadow when the subtypes of a string are shadowed. The analysis is based on their annual simulations. [6]

Ahsan at all. (2016) examined a 1kW PV system in small homes for rustic areas in India. The performance of the system and the cost analysis for the designed system were evaluated using PVsyst software. PVsystem produces 3101.2 kWh/year solar power. However, only 2933.4 kWh/year solar energy is given to the user. Unused 167.8 kWh of energy can be caused by a fully battery-filled or low energy demand during production. Comparing the energy generated by PV to the energy provided and needed by the user was also calculated by PVsyst. [7]

To get the most out of solar energy, you need to direct solar panels in the direction of the sun. However, there are some variables in finding the optimal direction. This study is designed to help achieve the best efficiency of solar energy. Solar panels in the northern hemisphere should always appear in the true southern direction or in the southern hemisphere in the true north direction. Installing your solar panels on a fixed slope is the easiest method. However, since the sun is higher in summer and lower in winter, it helps to get more energy all year round by adjusting the slope of the panels according to the season. In the study, we assume that either the panel is fixed or has a seasonally adjustable slope. The system designed either solar panel to be in a constant 25 degrees or to change their angles seasonally having summer to winter angles of 10-30 degrees. In the study, the efficiency of the fixed-angle or different-angle system was evaluated by the Pvsyst program.

II. MATERIAL AND METHOD

A. FIELD

The planned solar power plant in the province of Konya, Altınekin district is located Oğuzeli. It is located at 996 m altitude at coordinates 38.305597, 33.171152. The total field area is 20,000 m².

Based on data from the Solar Energy Potential Atlas (GEPA), it is understood that the insolation time is 8 hours per day on the basis of the insolation times in Konya province mentioned in figure 2.1.
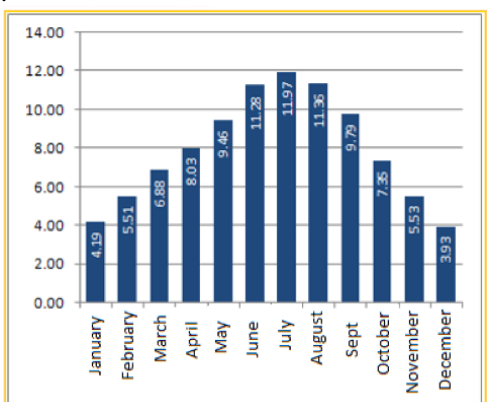
Figure 2.1: Insolation time in Konya province hour.

Insolation time and the amount of radiation per panel lead to an increase in electricity production from the sun. Therefore, the position of solar panels against the sun is important. If the panel surfaces are positioned facing south, the power obtained from solar radiation is maximum.

Two different types of panel angles have been determined for the planned solar power plant. As can be seen in Figure 2.2 and 2.3 in the fixed system, the panels placed on the fixed two metal columns to receive sun rays from a 25 degree angle throughout the year.
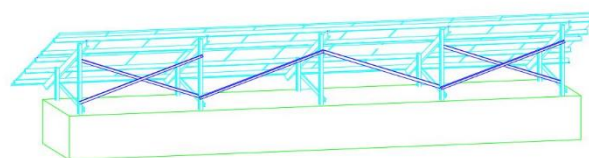
Figure 2.2: Fixed 25 Degree Table Structure
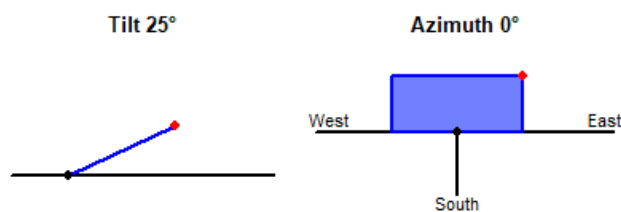
Figure 2.3: The panels overlook the south and are 25 °

As seen in figure2.4 and 2.5 variable angle system, panels placed on adjustable columns to receive sun rays throughout the year at a 10 degree angle in summer and 30 degree angle in winter. Summer winter angles are changed manually in April and September.
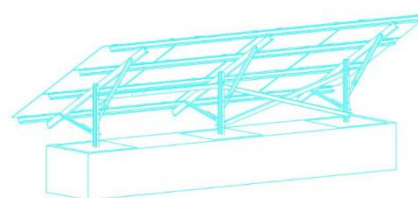
Figure 2.4: 10-30 Degree Variable Table Structure
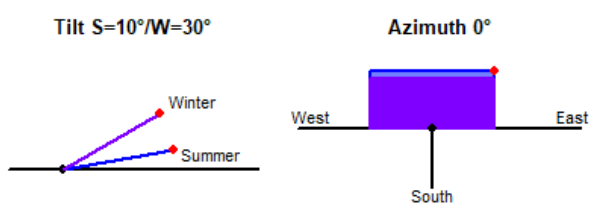
Figure 2.5: Panels overlook south and 10 °for summer, 30 ° for winter

Solar tracking systems are used to increase solar radiation from solar panels. [8] It is stated that the power obtained from a 2-axis solar tracking system at the Mugla University Campus is 30.79% higher than the fixed-slope system [9]. The adjustable 10- and 30-degree table structure is based on a kind of manual solar monitoring system.

B. MATERIALS

The planned solar plant consists of 330 Wp polycrystalline 3480 pieces of solar panels and 16 pieces of 60kWa string inverter. The panels are the PS 330P-24/T model of Smart Solar. Panels 330 Wp (Pmpp), Maximum power voltage Umpp [V] = 38.53V, Maximum power current Impp [A] = 8.57V, open circuit voltage Uoc [v] = 17.01V, short-circuit current Isc [A] = 9.15A.The panels provide 17.01% efficiency with a 12-year product 25-year performance guarantee. The inverter used is a series of 60kW rated DC power produced by Huawei and runs in the 200 to 1000Vdc (400V rated) MPPT input voltage range. The nominal power output of the facility is 1148.4kWp.

Panel and inverter forces are selected the same for both projects in the system that is constant at 25 degrees and can adjust 10-30 degrees. In a field area of 20,000 m², 3480 panels are made in a total of 20 series 174 strings. 1 string was created with 3 rows and 20 column panels for each table. Panel foot distances are important in terms of the lack of interlocking shading of the panels.

Panel foot distances are 6 meters as shown in Figure 2.4 for solar power plants. In this way, the shading effect of the panels on each other was eliminated.
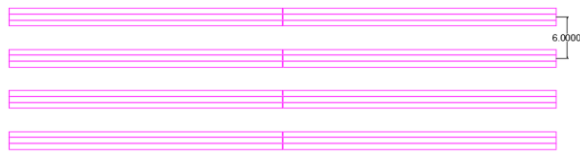
Figure 2.4: Panel Layout

C. PVSYST

Developed by Swiss physicist Andre Mermoud and electrical engineer Michel Villoz, this software is considered a standard for pv system design and simulation worldwide. Developers are designed to use this software by architects, engineers, researchers and students.

PVsyst is a software package that enables the user to use the full-featured operation and analysis of a PV project. PVsyst combines simulation of the PV system with the evaluation of pre-feasibility, sizing and financial analysis, regardless of whether it is a network-connected, independent, pumping system or dc grid system [10].

The shading status of the plant can be analyzed by Pvsyst by 3D modeling method. Panel shadows can be displayed depending on the sunrise and sunset. Thanks to the many inverter and panels in the program interface, the desired central structure is defined and analyzed.

The annual radiation values of the planned solar power plant are calculated automatically by entering coordinates in the European Union Photovoltaic Geographic Information Systems Database (PVGIS) online computing environment. The European Union Photovoltaic Geographic Information Systems Database (PVGIS) includes the European and African countries with a global radiation map prepared by the Joint Research Centre (EC JRC) within the European Union (EU) [11]. PVSYST applies the Perez model to predict radiation occurring on an oblique plane. As a result of these calculations, monthly radiation values are assigned to the PVsyst program.

III. ANALYSIS AND EXPERIMENT FINDINGS

A. FIXED SYSTEM ANALYSIS

Three main parameters were evaluated from the main simulation results. The first parameter is the total amount of energy generated in 1967 MWh / year, which is expressed as the energy generated annually from the 1148 kWp Si-poly photovoltaic system. The second parameter is the specific production per installed kWp on an annual basis and 1713 kWh/kWp/year. The third parameter is the average annual performance rate (PR) 85.33%.

Table 3.1: Balance and Main Results

Balances and main results

	GlobHor	DiffHor	T_Amb	GlobInc	GlobEff	EArray	E_Grid	PR
	kWh/m²	kWh/m²	°C	kWh/m²	kWh/m²	MWh	MWh	
January	65,3	23,60	-0,57	98,9	92,4	105,2	102,6	0,904
February	84,8	35,34	0,77	115,3	107,6	123,3	120,5	0,910
March	134,5	55,27	6,74	163,0	152,3	169,6	165,9	0,887
April	161,4	67,77	11,03	173,6	161,4	176,6	172,9	0,867
May	206,2	71,45	16,13	205,3	191,4	203,1	198,8	0,843
June	223,2	65,81	20,94	215,0	200,8	209,1	204,7	0,829
July	235,2	61,10	24,78	229,8	215,4	220,0	215,4	0,816
August	214,2	57,24	24,53	227,0	213,0	218,1	213,5	0,819
September	171,6	43,86	18,93	202,3	190,4	198,7	194,4	0,837
October	119,8	38,87	13,67	158,6	149,0	160,7	157,2	0,863
November	79,7	27,69	6,48	121,2	112,9	125,4	122,6	0,881
December	61,5	24,68	1,25	97,3	89,6	100,9	98,5	0,881
Year	1757.6	572.68	12.13	2007.3	1876.1	2010.7	1967.0	0.853

The balances and main results are shown in Table 3.1 include variables such as global radiation in the horizontal plane, ambient average temperature and global radiation in the collector plane without the optical plane, effective global radiation taking into account pollution losses and shading losses. In addition to these variables, the DC energy generated by the Sipoly photovoltaic array is calculated by taking into account the losses in electrical components, the photovoltaic array and system efficiency, as well as the energy injected into the grid. The calculated values of each variable specified in the results and the main results were obtained in monthly and annual values. The annual values of the variables are possible as the average of the sum for temperature, yield and radiation and energy. [12]

The annual spherical radiation in the horizontal plane for the workplace is 1757.6 kWh / m². Effective spherical radiation after global event energy and optical losses on an annual basis in the collector without optical corrections is 2007.3 kWh / m² and 1876.1 kWh /m². With this effective radiation, the annual DC energy generated from the PV array and the annual AC energy injected into the grid are 2010.7 MWh and 1967 MWh, respectively.

The energy generated by the PV array cannot be the same as the energy injected into the grid. The energy derived from the PV array is DC, which must be converted to AC Energy to feed the grid. In this case, some energy is lost in terms of AC cable loss. [13]

Normalized productions such as collection losses, system losses and installed kWp/day-to-day utility energy production are defined by IEC norms [14] and are standardized variables to evaluate PV system performance. Lc are collection losses or PV array capture losses, i.e. 0.7 kWh / kWp / day. Ls is the system loss and is 0.1 kWh / kWp / day. Yf, the useful energy produced is 4.69 kWh / kWp / day.

Figure 3.2: Performance Ratio (%).

The performance rate (PR) for the simulated 1148 kWp Si-poly photovoltaic system is 85.3% with an average annual PR value. There are slight differences in PR on a monthly basis, given in Figure 3.2

Various losses to be encountered while installing PV plant were obtained as a system loss diagram as a result of analysis. Loss factors are considered module quality, contamination, wiring mismatch losses, inverter efficiency, transformer, system availability and network availability, [15, 16]. The system loss diagram is seen in figure 3.3. It represents various losses in the system. The spherical teleportation in the horizontal plane is 1758 kWh / m2. However, the effective radiation on the collector is 1876 kWh / m2. This causes energy loss, i.e. 0.14% depending on the level of teleportation. When this effective radiation falls on the surface of a photovoltaic module or array, electricity or electrical energy is generated. After PV conversion, the nominal energy under standard test conditions (STC) is 2156 MWh. The yield of the PV array in the STC is 17.02%. The annual series virtual energy at MPP is 2015 MWh. Various losses at this stage are 4.18% due to temperature, 1.0% due to module array mismatch, and 0.69% due to Ohmic losses. The energy available at the inverter output facility on an annual basis is 1988.3 MWh and is injected into the same network. Two losses were possible here, one being the loss of the inverter during the operation of the inverter i.e. 1.12% and the value of the inverter is nominal inv. power is 0.21%. Transformer loss is 1.05%.
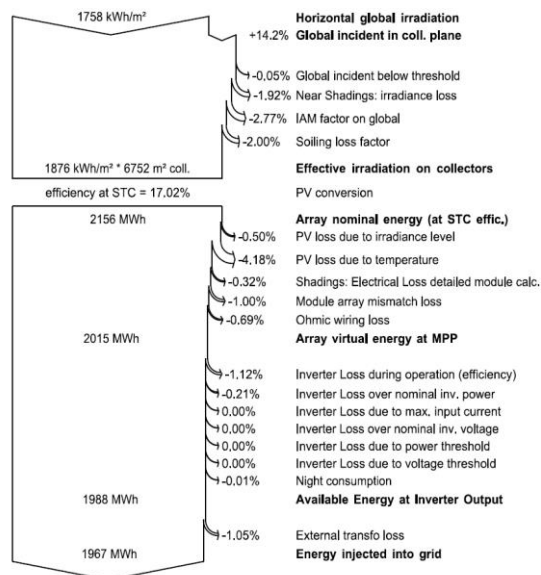
Figure 3.3: System Loss Diagram

B. VARIABLE SYSTEM ANALYSIS

The main simulation results were evaluated three main parameters for the system of 10 and 30 degrees. The first parameter is the total amount of energy generated in 1999 MWh/ year, which is expressed as the energy generated annually from the 1148 kWp Si-poly photovoltaic system. The second parameter is the specific production per installed kWp on an annual basis and 1741 kWh/kWp/year. The third parameter is the average annual performance rate (PR) 85.6%.

Table 3.2: Balance and Main Results

	GlobHor kWh/m²	DiffHor kWh/m²	T_Amb °C	GlobInc kWh/m²	GlobEff kWh/m²	EArray MWh	E_Grid MWh	PR
January	65.3	23.60	-0.57	103.9	96.3	107.8	105.1	0,881
February	84.8	35.34	0,77	119.9	110.8	126.2	123.4	0,900
March	134,5	55.27	6.74	165.8	154.0	171.0	167.3	0,879
April	161.4	67.77	11.03	169.3	159.7	175.6	172.0	0,885
May	206.2	71.45	16.13	209.6	198.4	211.0	206.6	0,858
June	223.2	65.81	20.94	223.7	212.2	220.9	216.2	0,842
July	235.2	61.10	24.78	237.2	225.1	230.0	225.2	0,827
August	214.2	57.24	24.53	223.5	212.3	218.2	213.6	0,832
September	171.6	43.86	18.93	187.5	177.5	187.5	183.5	0,852
October	119.8	38.87	13.67	163.5	153.0	164.5	160.9	0,857
November	79.7	27.69	6.48	127.4	117.8	128.9	126.0	0,861
December	61.5	24.68	1.25	102.8	93.3	101.8	99.3	0,841
Year	1757.6	572.68	12.13	2033.7	1910.4	2043.4	1999.2	0,856

The balances and main results are shown in Table 3.2 are 1757.6 kWh / m² of annual spherical radiation in the horizontal plane for the workplace. Effective spherical radiation after global event energy and optical losses on an annual basis in the collector without optical corrections is 2033.7 kWh / m² and 1910.4 kWh/m². With this effective radiation, the annual DC energy generated from the PV array and the annual AC energy injected into the grid are 2043.4 MWh and 1999.2 MWh, respectively. Lc, collection losses or PV array capture losses, 0.7 kWh/kWp/day. Ls is a system loss and 0.11 kWh/kWp/day. Yf, the useful energy produced is 4.77 kWh/kWp/day.
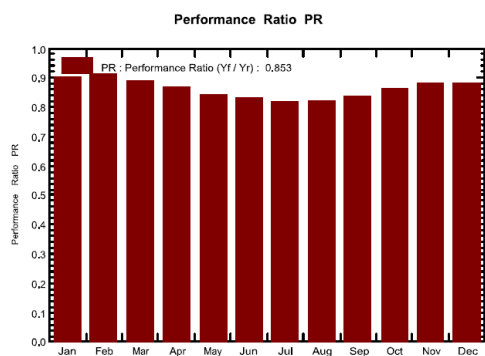
Performance Ratio PR
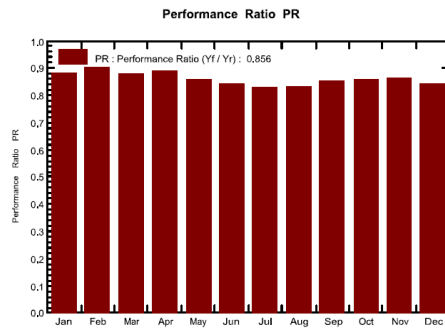
Figure 3.4: Performance Ratio (%).

The performance rate (PR) for the simulated 1148 kWp Si-poly photovoltaic system is 85.6% with an average annual PR value. There are slight differences in PR on a monthly basis and these are given in Figure 3.4.
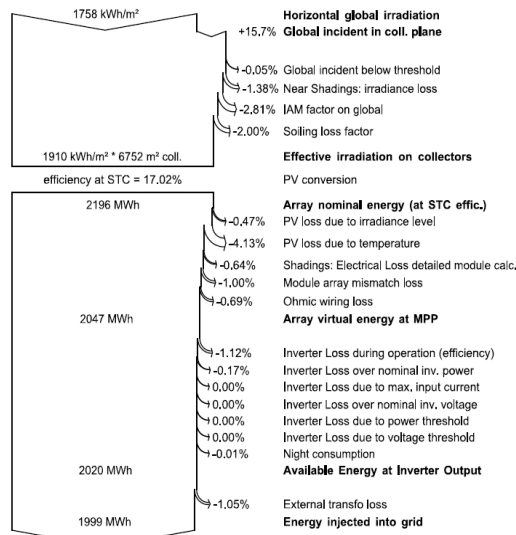
Figure 3.5: System Loss Diagram

The diagram representing the various losses in the system is given in figure 3.5. The spherical teleportation in the horizontal plane is 1758 kWh / m2. However, the effective radiation on the collector is 1910 kWh / m2. This causes energy loss, i.e. 0.15% depending on the level of teleportation. When this effective irradiation falls on the surface of a photovoltaic module or array, electricity or electrical energy is generated. After PV conversion, the nominal energy under standard test conditions (STC) is 2196 MWh. The yield of the PV array in the STC is 17.02%. The annual array virtual energy in MPP is 2047 MWh. Various losses at this stage are 4.13% due to temperature, 1.0% due to module array mismatch, and 0.69% due to ohmic losses. The current energy on an annual basis at the inverter output facility is 2020 MWh and is injected into the same grid. Two losses were possible here; one being the loss of the inverter during the operation of the inverter i.e. 1.12% and the value of the inverter is nominal inv. power is 0.17%. Transformer loss is 1.05%.

IV. CONCLUSION

This study provides evaluation of seasonal manual tracker system performance of 1148 kWp PV power plant connected to the planned network in Altinekin District of Konya province, which can be adjusted to fixed 25 streams and can be changed as summer and winter angle 10-30. Energy production, specific efficiency and performance ratio (PR) values of two different systems were analyzed. The measured data from the installed system was compared in Table 4.1. It was determined that the seasonal system produced more than 32.2 MWh per year. Global teleportation is 26.4 kWh per m2 in seasonal system; the specific yield is more than 28 kWh/kWc/year.

Table 4.1: Comparison Of Main Results

	Fixed	Seasonal
Global HorizontalIrradiation (kWh/m²)	1.757,6	1.757,6
AmbientTemperature (°C)	12,13	12,13
Global incidentIrradiation (kWh/m²)	2.007,3	2.033,7
Effective Global,corrfor IAM andshadings (kWh/m²)	1.876,1	1.910,4
Energy at theoutput of thearray (MWh)	2.010,7	2.043,4
Energyinjectedintogrid (MWh)	1.967	1.999,2
Specificenergyyield (kWh/kWc/year)	1.713	1.741
Performanceratio (%)	0,853	0,856

Through PVSYST, we conducted a comparative study between the two configurations. The two simulations were conducted under the same conditions and for the same geographic region. The tables show the energy generated by both systems, as well as the losses. The seasonal system is more advantageous in production than the fixed system.

REFERENCES

[1] ElektrikMühendislerOdası,2011,http://www.emo.org.tr/genel/bizden_detay.php?kod=8 8369. [Ziyaret Tarihi: 10 Aralık 2018.]
[2] Energyand Natural SourcesMinistryhomepage on Internet. Available: http://enerji.gov.tr/Resources/Sites/1/Pages/Sayi_15/mobile/index.html#p=3 [Ziyaret Tarihi: 16 Aralık 2018.]
[3] Enerji ve Tabii Kaynaklar Bakanlığı , http://www.enerji.gov.tr/tr-TR/Sayfalar/Gunes [Ziyaret Tarihi: 10 Aralık 2018.]
[4] Kandasamy , P. Prabu , K. Niruba (2013) , Solar potentialassessmentusing PVSYST software, 2013 International Conference on Green Computing, CommunicationandConservation of Energy (ICGCE) 2013 International Conference, 12-14 December, Chennai, India, 667-672.
[5] SubhadeepBhattacharjee, AnirudhNath, SaurabhBhowmik, Mrinmoy(2013) Performanceprediction of 60 kWp PV powerplant in an educationalinstitute.
[6] AndréMermoud, Frankfurt, Germany, 24-28 September 2012 Optımızatıon Of Row-ArrangementInPvSystems, ShadıngLossEvaluatıonsAccordıngToModulePosıtıonıngAndConnexıons, 27th EuropeanPhotovoltaic Solar Energy Conference –
[7] Shahzad Ahsan, 2016 KashifJaved, Ankur Singh Rana,MohammadZeeshan, Design andcostanalysis of 1 kW photovoltaicsystembased on actualperformance in Indianscenario,Science Direct
[8] Mutlu Boztepe, Fotovoltaik Güç Sistemlerinde Verimliliği Etkileyen Parametreler
[9] R. Eke ve A. Şentürk, Performancecomparison of a double-axis sun trackingversusfixed PV System, Solar Energy, no. 86, pp. 2665-2672, 2012.

[10] Najibhamisu Umar1, Birinchi Bora, ChandanBanerjee, B. S. Panwar, 2018　International Journal of EngineeringScienceInvention Volume 7 Issue 7 Ver II ,,PP 11-24.

[11] Pvsyst,www.pvsyst.com/Help [Ziyaret Tarihi: 14 Kasım 2018]

[12] N.ManojKumar,M.RohitKumar,P.RuthRejoice,M.Mathew, Performance Analysis of 100 kWpgridconnected Si-PolyphotovoltaicsystemusingPVsystSimulation Tool,2017, 1st International Conference on PowerEngineering,Computingand Control,Peccon-2017.

[13] IrfanJamil,J.Zhao,L.Zhang,R.Jamil,S.F.Rafiqua, Evaluation of EnergyProductionandEnergyYieldAssessmentBased on Feasibility, Design, andExecution of 3×50MW Grid-Connected Solar PV Pilot Project in Nooriabad, International Journal of Photoenergy Volume 2017, Article ID 6429581, 18 pages.

[14] IEC.PhotovoltaicSystemPerformanceMonitoring GuidelinesforMeasurement Data Exchange andAnalysis. IEC Standard 61724. GenevaSwitzerland; 1998.

[15] E. Kymakis, S. Kalykakis, and T. M. Papazoglou, "Performanceanalysis of a gridconnectedphotovoltaic park on theisland of Crete," Energy Conversion and Management, vol. 50, pp. 433–438, 2009.

[16] K. Attari, A. Elyaakoubi, and A. Asselman, "Performanceanalysisandinvestigation of a grid-connectedphotovoltaicinstallation in Morocco," EnergyReports, vol. 2, pp. 261–266, 2016.

An effective solution of ERAB problems in LTE

A.GENC[1]

[1] Isparta University of Applied Science, Isparta/Turkey, abdullahgenc@isparta.edu.tr

Abstract **- E-UTRAN Radio Access Bearer (ERAB) is an important parameter in LTE Key Performance Indicator analysis. That's why optimization engineers insist on making improvement on it. This parameter is formed by combining the S1 bearer and the corresponding radio bearer. It can be noted that this function is related to the E-RAB ID and Quality Class Identifier. The E-RAB ID parameter is used to determine the ERAB on the S1 interface. In a mobile network, there are values that affect the quality of service, such as Bit Error Rate and the end to end delay. These values define the QCI in LTE. The planned improvements are not easy; hence the ERAB parameter is composed of these different complex parameters. In this paper, ERAP and parameters related to the Handover are improved by proposed solutions of the results. As a result for downlink and uplink, ERAB Call Drop Rate is 0.05 and 72.41, respectively. Also, SINR Intra Frequency Handover is 337 and 406, respectively. All of these initiatives were successfully completed.**

Keywords **- Mobile network, LTE, radio access network, optimization.**

I. INTRODUCTION

The completion of 4G technology is calculated at the earliest in 2015. For this reason, 3G technology is developed. Then, LTE technology is obtained as a result of these studies. While this technology is called 3.9G or Pre4G, it is stated that it is the last step in the field of communication before 4G [1]. High-definition television service (HD-TV) and multiplayer comes from interactive gaming service. This requires an HD-TV 10 - 20Mbit / s communication speed (18 Mbit/s for Blue Ray standards). However, this technology is well above the capacity of the previous technology, HSPA. This situation revealed the delay problem. Multi-player interactive gaming systems have great sensitivity to delay [2]. In this low latency issue, LTE has a 10ms latency for simultaneous gamers has provided a complete key feature. Considering that the HSPA has a latency of 60ms, it can be seen how great it is.

The channel bandwidth increased from 1.25–20 MHz to 100 MHz in LTE. One of the major deficiencies of the communication systems used is the interruptions in communication and loss of data transmission while moving at high speeds. With 100Mbit/s with 4G data transfer rates of 1Gbit/s are expected [3]. Performance in antenna communications depends on improvements in an antenna system. Recently for effective communication in the 4G system, such as high speed, high reliability and long series communications antenna technologies that affect multiple

organs are emerging. Nowadays, many transmission programs can be proposed to meet the increasing data rate needs of data communication.

Spatial multiplexing has gained importance with bandwidth conservation and power efficiency in LTE technology. Spatial multiplexing requires the deployment of a wide range of antennas in the transmitter and receiver. Independent currents can be transmitted simultaneously from all antennas [4]. This increases the speed of the data in a very large number of different layers with an equal number of transmit and receive antennas. This is called multi-input multi-output communications (MIMO). Furthermore, reliability in the transmission of high-speed data in the power-down channels can be improved by using more antennas in the transmitter or receiver. Transmission-reception difference and transmission spatial multiplexing can be classified into space-time coding techniques that do not require channel information in transmission. Another category is closed loop multi-antenna technology that uses channel information in the transmitter [5].

In this paper, an effective and fast optimization study is obtained for solving network quality problems in LTE network. These have been applied in the area serving a specific region and the effects of the optimization study on the sites have been determined.

The rest of the paper is organized as follows: Section 2 describes measurement methods and DT details; Section 3 provides the brief discussion of the results, comparison of before and after optimization to see performance of this study, and finally Section 4 provides our conclusions.

II. MEASUREMENT AND DRIVE TEST

TEMS is mobile equipment (ME) to use in mobile and cellular communications by Ericsson that includes all the field information on uplink and downlink signals in the Air-interface. It covers all kinds of information about the signal level and quality between the station and the ME [8]. In order to determine the performance of the optimization, two separate drive tests are performed before and after the study. Drive test (DT) tool is given in Figure 1. It should be noted that the block diagram is shown instead of the test tool in real time as it is not allowed by the mobile operator. Here, it can be seen ME used in active and passive mode, USB Cable for connection of laptop and ME, GPS receiver, laptop and charger to determine location and coordinates. Scanner is used for to obtain all frequencies in operating band.
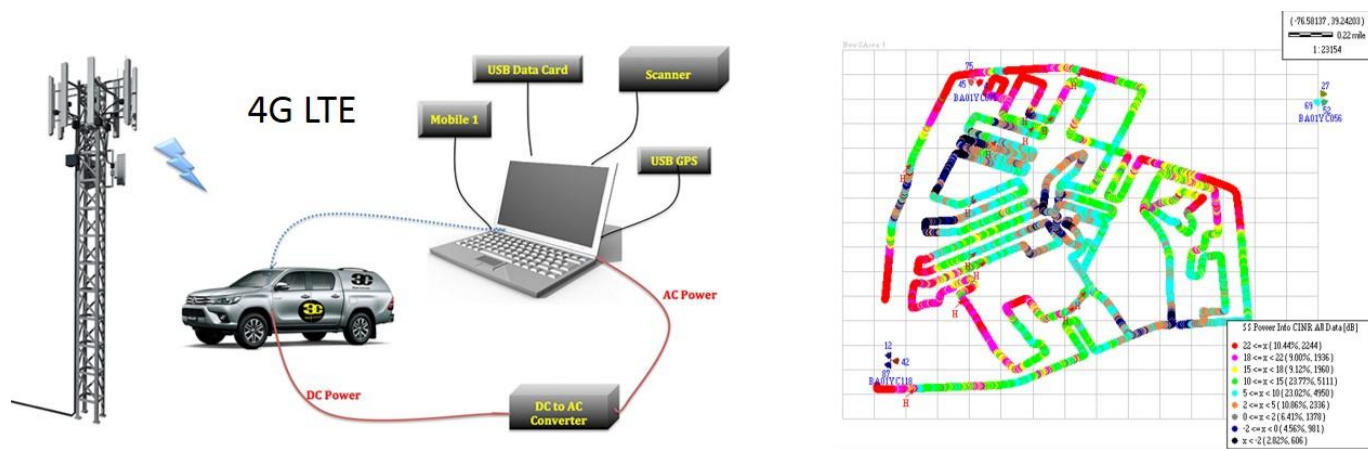
Figure 1: Drive test tool and map

As the DT Methodology, DT is performed using TEMS. There are 2 different measurement methods. All measurements are made in Singapore. In Figure 3, the DT route is given. The problematic points determined during DT in this region are conducted according to the optimization study of this paper.
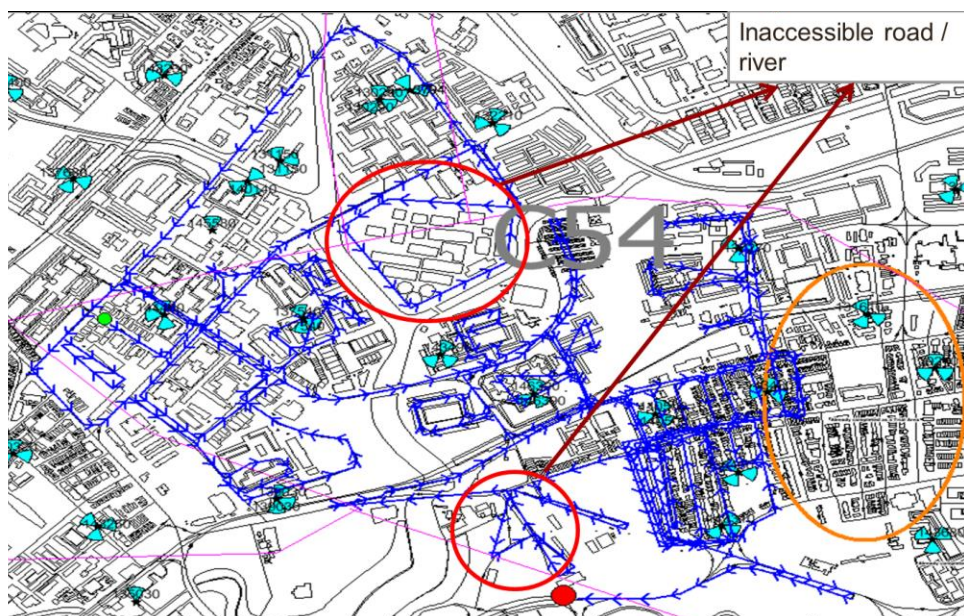
Figure 2: Cluster DT route (Planned)

III. RESULTS

E-UTRAN Radio Access Bearer (ERAB) is an important parameter in LTE KPI analysis. This parameter is formed by combining the S1 bearer and the corresponding radio bearer. It can be noted that this function is related to the E-RAB ID and Quality Class Identifier (QCI). The E-RAB ID parameter is used to determine the ERAB on the S1 interface. In a mobile network there are values that affect the quality of service (QoS), such as Bit Error Rate (BER) and end to end delay. These values define the QCI in LTE.

Another issue that makes ERAB parameter important is its effect on RRC Success Rate in LTE. Here the RRC is the Radio Resource Control. RRC Success Rate is required for service of the mobile network. And a Bearer can do that. The bearer is usually defined as Data QCI9 by default and VoLTE QCI1 as dedicated. As a result, Mostly ERAB is formed by the addition of the default bearers.

As seen in Figure 3, suspected handover (H/O) failure from PCI_85 to PCI_437 caused RRC connection reestablishment request from UE that eNodeB rejected. So that ERAB released abnormally. As a result of looking after neighbor list, both sites are neighbor each other and also H/O from PCI_437 to PCI_85 is preceded correctly. The solution of this problem is to add site id to neighbor list to increase accessibility of mobile network in site of PCI_85.
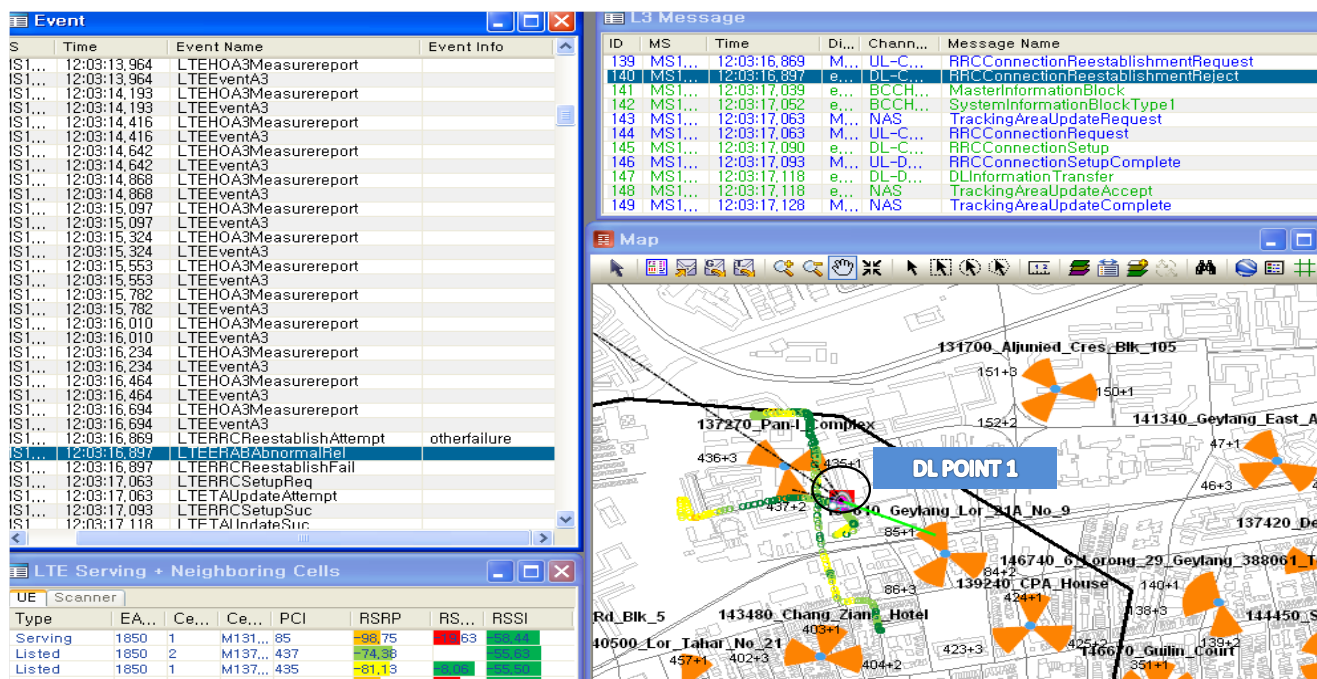
Figure 3: ERAB Abnormal Rel. Analysis (DL Point1)

With point 2, also suspected H/O failure from PCI_85 of site 3161 to PCI_86 in same site caused RRC connection reestablishment request that eNodeB rejected. So that ERAB released abnormally. Both sectors are neighbor each other.

These two abnormal release are all related to PIC_85 that strongly suspected having unknown problem. The redress of disconnection of RRC connection is increasing the power of transmitter antenna to remain of received UE data in site 3161.
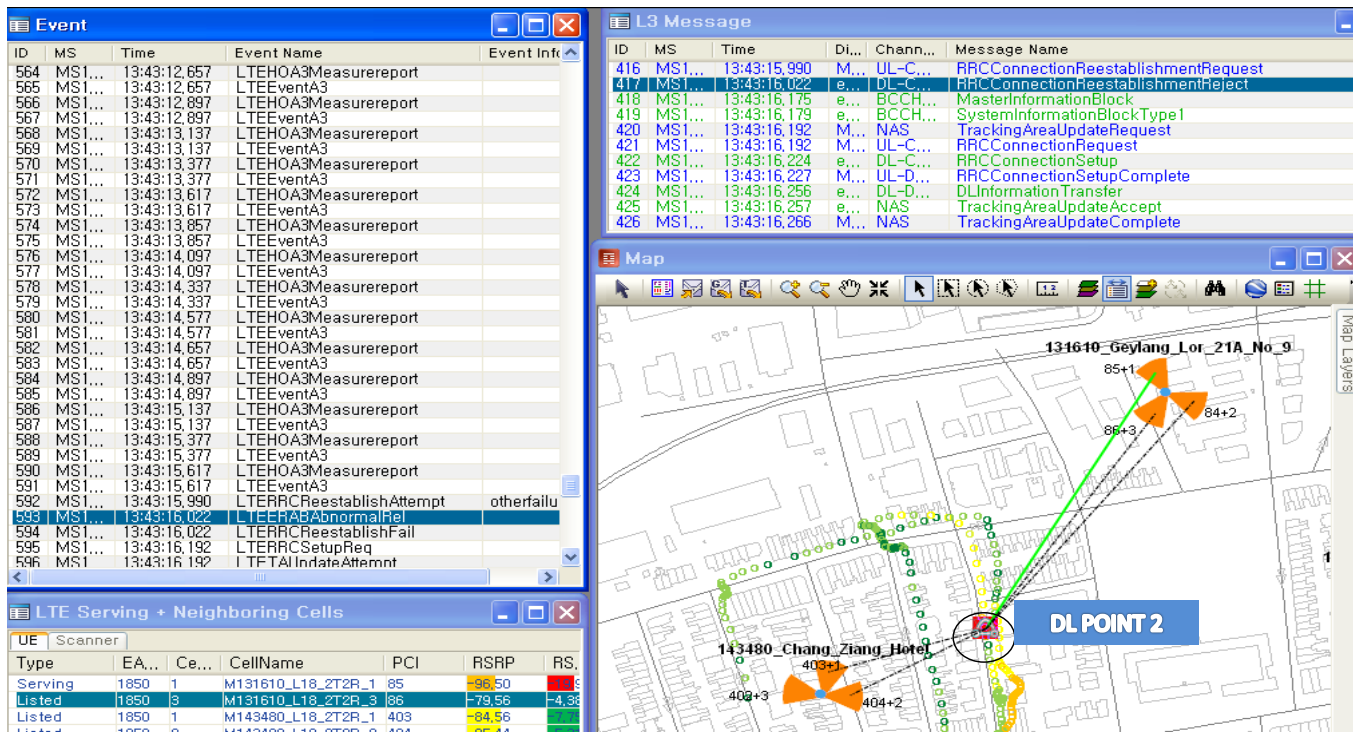
Figure 4: DL ERAB Abnormal Rel. Analysis (DL Point2)

Point suspected H/O failure from PCI_86 to PCI_404 caused RRC connection reestablishment request from UE that

eNodeB rejected. So that ERAB released abnormally. As a result of looking after neighbor list, both sites are neighbor each other and also H/O from PCI_404 to PCI_86 is preceded

correctly. On site of PCI_404 the antenna down tilt is increased to prevent overshooting problem.

Figure 5: UL ERAB Abnormal Rel. Analysis (UL Point3)

During the UL Test, we faced up frequent UE disconnected problem. After the HW check, it is observed that there is connector problem on site. When the connector is changed

with new one, UE disconnected problem is solved for UL point 4 in Figure 6.

Figure 6: UL ERAB Abnormal Rel. Analysis (UL Point4)

The Key Performance Indicators (KPI) of the mobile

network is given Table 1. The optimization study by applying proposed solutions have yielded good results. The statistics conducted after optimization can be seen and most of the KPIs

have improvement. The SINR Intra Freq HO Success Rate, ERAB Accessibility Rate, Intra Freq HO Success Rate and ERAB Accessibility Rate have the 100% success rate. Therefore, it is seen that these parameters have high and good

results in the sites where optimization changes are made. Also for downlink and uplink ERAB Call Drop Rate is 0.05 and 72.41, respectively.

Table 1: Performance results overview after optimization

Type of load way	KPI	Statistics		
		Attempt	**Success**	**Percentage**
Download	Inter FreqHO Success Rate	-	-	-
	SINRIntra FreqHO Success Rate	337	337	100
	ERAB Accessiblity Rate	34	34	100
Upload	Inter FreqHO Success Rate	-	-	-
	Intra FreqHO Success Rate	406	406	100
	ERAB Accessiblity Rate	29	29	100
Type of load way	**Performance**	**ERAB Abnormal Release**	**ERAB Setup Success**	**Rate**
Download	ERAB Call Drop Rate	2	34	0.05
Upload	ERAB Call Drop Rate	21	29	72.41

Mobile operators attach importance to the work of the different departments listed in Figure 7 to achieve KPI goals for network quality. Although the regions and methods in which these various departments study are different, they can directly affect each other's performance. For this, each unit should study efficiently within the boundary and communicate instantly with other units. However, they should work productively and result-oriented. This provides ease of work, power and time. Mobile technologies start with Design process. In this process, simulation software related to radio planning and wave propagation is used. Thus, what kind of station can be applied to which region is determined. Then, in the planning stage, the location of the stations according to the target average signal level is determined from the map of simulation. In the third stage of implementation the mobile vendors make implementation of devices and components to site. Then optimization engineers check the performance of new site in terms of related KPI values. If it's not ok, they start making optimization to improve the quality of related sites. Last they inform mobile operator the process is done or not.
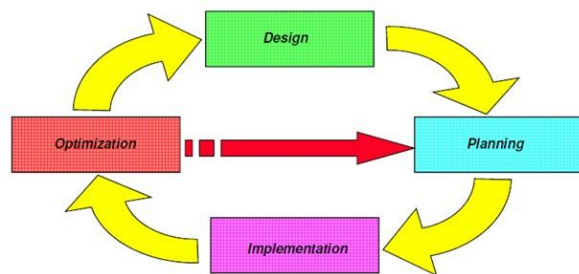
Figure 7: DT route

IV. CONCLUSION

E-UTRAN Radio Access Bearer (ERAB) is an important parameter in LTE KPI analysis. Also, it directly effect of the

RRC Success Rate of the mobile network. So, optimization engineers work with RF planners to improve this parameter. However, this improvement is not always easy, and not immediately. Therefore, the optimization method to be applied to the network should be as accurate and effective as possible. In this study, the solutions proposed in the results section is found to provide improvements in ERAB value and HO parameters. As a result The SINR Intra Freq HO Success Rate, ERAB Accessibility Rate, Intra Freq HO Success Rate and ERAB Accessibility Rate have the 100% success rate. Therefore, it is seen that these parameters have high and good results in the sites where optimization changes are made. Also for downlink and uplink ERAB Call Drop Rate is 0.05 and 72.41, respectively.

REFERENCES

[1] S.M.A. El-Atty, Z. M. Gharsseldien, "Performance analysis of advanced heterogeneous mobile network architecture with multiple small cell layers," *Wireless Networks*, vol. 23, pp. 1169-1190, 2017.

[2] R. Švraka, D. Mitić, A. Lebl, Ž. Markov, "Calculating limits of base station emission power in GSM," *Automatika*, vol. 57, pp. 774-781, 2016.

[3] A. Huerta-Barrientos, M. Elizondo-Cortés, "Optimizing the cellular network planning process for in-building coverage using simulation," *J. Appl. Res. Technol.*, vol. 11, pp. 912-919, 2013.

[4] S. Wang, C. Ran, "Rethinking cellular network planning and optimization," *IEEE Wireless Commun.,* vol. 23, pp. 118-125, 2016.

[5] A. Awada, B. Wegmann, I. Viering, A. Klein, "Optimizing the radio network parameters of the long term evolution system using Taguchi's method," *IEEE Trans. Veh. Technol.*, vol. 60, pp. 3825-3839, 2011.

[6] R. Kadiroglu, Y. Dalveren, A. Kara, "Quality of service assessment: a case study on performance benchmarking of cellular network operators in Turkey," *Turkish Journal of Electrical Engineering & Computer Sciences*, vol. 23, pp. 548-559, 2015.

[7] S.S. Zhekov, Z. Nazneen, O. Franek, G.F. Pedersen, "Measurement of Attenuation by Building Structures in Cellular Network Bands," *IEEE Antennas Wirel. Propag. Lett.*, vol. 17, pp. 2260-2263, 2018.

[8] I.K. Alabi, L. Sagir, O.A. Fatai, I.I. Alabi, "GSM quality of service performance in Abuja, Nigeria," *International Journal of Computer*

Science, Engineering and Applications (IJCSEA), vol. 7, pp. 29-40, 2017.

[9]　W.A. Hapsari, A. Umesh, M. Iwamura, M. Tomala, B. Gyula, B. Sebire, "Minimization of drive tests solution in 3GPP," *IEEE Commun. Mag.*, vol. 50, pp. 28-36, 2012.

[10]　M. Pous, M.A. Azpúrua, F. Silva, "Measurement and evaluation techniques to estimate the degradation produced by the radiated transients interference to the GSM system," *IEEE Trans. Electromagn. Compat.*, vol. 57, pp. 1382-1390, 2015.

[11]　M. Das, B. Sahu, U. Bhanja, "Coverage Analysis of Mobile Network in Nakagami Fading Channel," *Wireless Personal Communications*, vol. 97, pp. 3261-3276, 2017.

Implementation of Renewable Energy Integrated Automation Training Set

C.ŞAHİN[1], M. KARAÇOR[2] and H. ÖZBAY[3]

[1] Bilecik Seyh Edebali University, Bilecik/Turkey, cihan.sahin@bilecik.edu.tr
[2] Manisa Celal Bayar University, Manisa/Turkey, mevkut.karacor@cbu.edu.tr
[3] Bandırma Onyedi Eylül University, Bandırma/Balıkesir/Turkey, hozbay@bandirma.edu.tr

Abstract - **In today's world, the need for energy is increasing day by day with the developments in technology. This energy is mostly supplied from fossil fuels. However, the future depletion of fossil fuels, environmental damage and price increases have led people to use alternative energy sources. Although there are various alternative energy sources, Solar and Wind energy are the most widely used. The use of alternative energy sources is as important as the efficient use of these sources. Therefore, the use of control and automation technologies in alternative energy systems is of great importance. In this study, automation experiment set with integrated alternative energy source was realized. Thanks to the experimental set, the students have become interested in the alternative energy and automation world together and contributed to their development in this field.**

Keywords **– Automation, Industry 4.0, Renewable energy**

Figure 1: Stages of industrialization.

I. INTRODUCTION

Since human beings, they have constantly wanted to improve themselves and go further. This desire has been unlimited and as a result has been renewed in all areas. In particular, the innovations it has made in the industrial world have been called revolution in some points. Industrial revolutions to date are divided into four groups. These are called First, Second, Third and Fourth Industrial Revolution. The first industrial revolution continued until the end of the 18th century. During this period, the first industrial loom was established in 1784. In addition, mechanical production plants with water and steam energy were activated [1]. The second industrial revolution began in 1870 and ended with the collapse of the 1989 Eastern Bloc. During this period, the effectiveness of oil in industry and transportation was discovered and triggered the production of oil-based internal combustion engines [2, 3]. The third industrial revolution began with developments in electronics and information technologies. In 1964 the first programmable logical controller (PLC), Modicon 084 was established [1]. Nowadays, an industrial revolution called Industry 4.0, which was first introduced at the Hannover fair in 2011, was prepared by the German government for a special working group in 2012 and announced in the final report in 2013 [4]. Figure 1 shows the stages of industrialization [5].

With the Industrial 4.0 revolution; Within the scope of modular structured smart factories, it is aimed to monitor physical processes with cyber-physical systems, to create a virtual copy of the physical world and to make decentralized decisions. The internet of objects and cyber-physical systems can communicate and collaborate with each other and people in real time [6]. Figure 2 shows the structure of industry 4.0 [6].
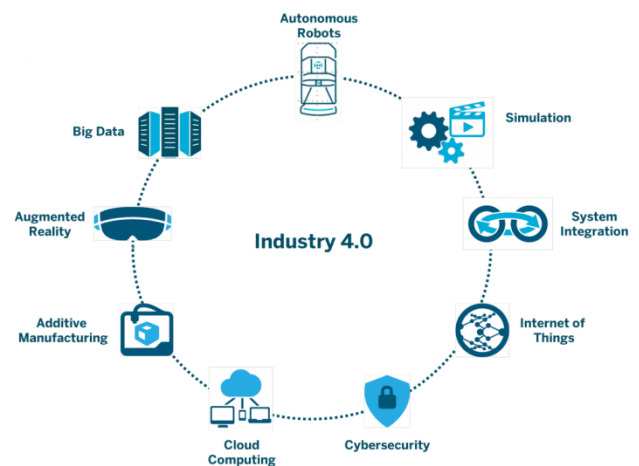
Figure 2: Structure of Industry 4.0.

In this study, PLC which is one of the basic building blocks of Industry 4.0, and solar energy from the alternative energy sources, is brought together and experiment set design are

made. With this set of experiments, it is aimed that students will be interested in both fields and understand the importance of energy efficiency.

II. MATERIAL AND METHOD

The experiment set is basically divided into three groups. The first group for the integration of solar energy system; It consists of two polycrystalline 160 Watt solar panels, one 1KVA inverter, one 12 V 100 Ah gel battery and 100 Watt IP66 Led projector. The second group is the automation group and consists of one light intensity measurement transmitter, one S7 1200 PLC, two PAC3200 energy analyzers, one Sinamics G120C motor drive and 5/1 ratio current transformers for measuring currents by analyzers. The third group consists of lighting and motor loads. 550 Watt incandescent filament lighting bulb set and there phase 1 kW induction motor test set were used for this purpose. Generator is coupled to induction motor and ohmic load is connected to generator outputs.

A. PV Solar panels

The production of electrical energy from solar energy is provided with the help of photovoltaic panels. These panels are also known as solar panels or photovoltaic cells. Photovoltaic panels; portable, ergonomic, aesthetic appearance devices that work with semiconductor technology [7]. Solar cells can be connected to each other in series or in parallel [8]. Table 1 shows the characteristics of the 160W PV modules used in the design.

Table 1: Characteristics of PV modules.

Specifications	Value
MPP Voltage	18.8 V
MPP Current	8.53 A
Open Circuit Voltage	23.2 V
Short Circuit Current	9.12 A
Power Tolerance	±3%

B. Inverter

Inverter, The inverter is centrally located in solar power systems. Charging the batteries; It ensures that the energy in the batteries is used actively in the system. In the experiment set full sine intelligent 1kVA inverter is used. Table 2 shows the characteristics of the inverter being used.

Table 2: Properties of inverter.

Mode	Specifications	Value
Inverter	Rated Power	1kVA /1kW
	DC Input	12 VDC
	AC Output	230 VAC ±5%
AC	AC Input	230 VAC / 50 Hz
	DC Output	12 VDC
Solar	Rated Power	1000 W
	System Voltage	12 VDC
	Operation Voltage	15-18 VDC
	Max. Sol. Voltage	55 DC

C. Light intensity measurement transmitter

The light intensity measuring transmitter is a sensor that measures the light intensity in the environment and produces a variable voltage at its outputs accordingly. In the use of the designed experiment set, it is aimed to make different applications depending on the light intensity in the environment with the light intensity measurement sensor. Delta Ohm HD2021T.0 - Light Intensity Measurement Transmitter was used in the experiment set. The characteristics of the sensor are shown in Table 3.

Table 3: Specifications of light intensity measurement sensor.

Specifications	Value
Measuring Range	2-200 kLux
Output Voltage	0 ÷ 10 V (0 ÷ 1 V, 0 ÷ 5 V minimum order 5 pcs)
Power supply	16 ÷ 40 Vdc or 24 Vac (0 ÷ 10 V output)
Power consumption	10 mA
Operating temperature	-20 ÷ +60 °C

D. PLC

Together with research and technological advances, PLCs are one of the leading controllers in the manufacturing industry and will remain the leader in the future [9]. PLCs, which are among the indispensables of the automation world today, have many advantages [10]. The advantages are listed in several items;

i) PLCs can read process values very quickly from input interface. In the same way, it can write the values obtained from the existing program in the PLC to the output interface.

ii) PLCs are capable of communicating with computers and other systems (SCADA, DCS and PLC systems) during the operation of the process [11].

iii) PLCs are much more durable than computers in industrial environments.

When we look at the usability of PLC systems in renewable energy systems, Dumutri et al. In 2012 performed SCADA based software for renewable energy management. Information from PLCs, RTUs and other sites from the field explained that they can be monitored and controlled at local and remote points [12]. Alphonsus et al. in 2016 is a study of the applications of PLCs in the field of renewable energy. PLCs are introduced and examples of their use in renewable energy fields such as solar, wind and photovoltaic are given. [13]. Georgescu's study in 2014 was carried out by SCADA software for referral centers for photovoltaic fields [14]. In the study conducted by Zapata et al. in 2016, SCADA system was realized by using IEC 61850 and ISA S101 international standards and OPC, Modbus TCP communication protocols [15]. In the study conducted by Zhaoxia et al. in 2017, SCADA based inspection of the system consisting of photovoltaic, wind rose and batteries was performed [16].

E. Power Analyzer

Power analyzers are monitoring devices that provide continuous monitoring and recording of electrical energy and,

where necessary, transmitting records by communicating with remote devices and software. Two power analyzers were used in the experiment set. The first power analyzer measures the amount of energy consumed by the lighting group and the second power analyzer measures the energy consumption of the motor group.

F. Sinamics G120C Motor Driver

It was used to drive the motors to be used in the experiment set. Motor drive used three phase, 0.75-1.1 Kw power range of motors can control.

III. IMPLEMENTATION AND USE OF TRAINING SET

The control panel of the experiment set is shown in Figure 3. There are energy analyzers, motor drive control screen, inverter control screen, warning lights and emergency stop button on the outer surface of the panel. Inside the panel, there are PLC, Inverter, Motor driver and ethernet switch. PLC, motor drive and energy analyzers communicate via ethernet protocol.

Figure 3: Control panel internal and external structure.

Figure 4 shows the working principle of the experiment set. The energy obtained from the solar panels is stored in the batteries via the intelligent inverter. This stored energy is used for the lighting group in the system. The PLC controls the lighting control modules according to the light intensity information received from the lux meter and provides controlled lighting in the system.
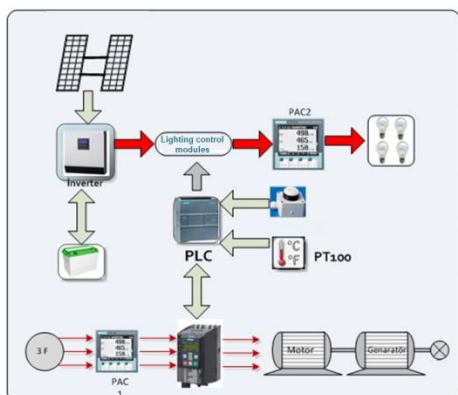
Figure 4: Developed automation based experiment set.

The motor groups in the system are considered as fan motors. The PLC sends data to the motor drive according to the temperature information it receives from the PT100, enabling the motor groups to operate in a controlled manner. Figure 5 shows the test set, solar panels and motor test set.
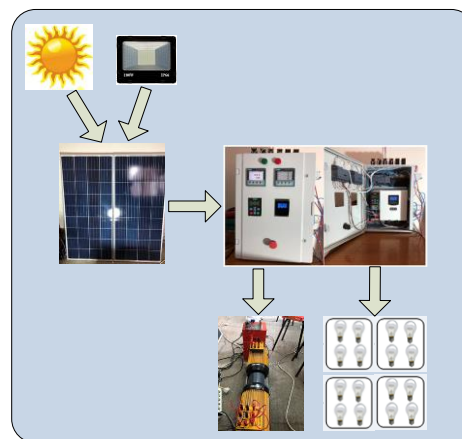
Figure 5: Designed experiment set, Solar panels and motor test set are shown.

In the case study conducted in the system, the engine group and lighting group were primarily operated independently of the automation system. n this case, the power consumption of the lighting system is 0.55 kWh and the engine group power consumption is 0.87 kWh. In the standard system; lighting group is not subject to any automation and control system. Therefore, the energy consumption is constantly constant. In the designed experiment set, the lighting group can be controlled based on automation depending on the amount of ambient light. The amount of light in the environment is measured by the light measuring transmitter and transferred to the PLC environment as an analog value. The PLC controls the relay group connected to the digital outputs depending on the measured analog value. The relay group is designed separately for four different illumination zones. In this way, which groups will be active or passive according to the amount of ambient light is determined. In other words, instead of constant energy consumption, energy consumption is realized at the required rate. Motor group is also integrated to the PLC based automation system. The PLC S7-1200 and the motor drive communicate via the Sinamics G120C ethernet protocol. The integrated motor group is controlled by PLC depending on the ambient temperature, so that an additional energy efficiency can be observed in fan group energy consumption thanks to the experiment set. The measurements show that thanks to the integration of the automation system, energy consumption is reduced in both units. In the study carried out as an example, it was seen that the energy consumption in the lighting system decreased from 0.55 kWh consumption to 0.33 kWh consumption. It was seen that the engine control system decreased from 0.87 kWh consumption to 0.48 kWh consumption.

IV. CONCLUSION

Today, the development of the automation world manifests itself in every aspect of our lives. Especially with the Industry 4.0 revolution, this effect is more evident. In today's world, a structure without automation systems is thought to be incomplete. Similarly, alternative energy sources are an important field of study for today's world. The depletion of fossil fuels leads people to use alternative energy sources. When all these are considered, new working areas are created. With this study, it was aimed to attract the attention of the students for these two important fields and to contribute to the development of the students in this field.

ACKNOWLEDGMENT

REFERENCES

[1] Y. Esmer, M. A. Alan, "Endüstri 4.0 perspektifinde inovasyon," *International Journal of Euroasian Researhes*, vol. 7, pp. 465–478, June 2019.

[2] E. Bulut, T. Akçacı, "Endüstri 4.0 ve inovasyon göstergeleri kapsamında Türkiye analizi," *ASSAM International Refereed Journal*, vol. 4, pp. 50-72, June 2017

[3] M. O. Eldem, "Endüstri 4.0 perspektifinde inovasyon," *TMMOB EMO Ankara Branch News Bulletin.,* June 2019.

[4] S. Kılıç, R. M. Alkan, "Dördüncü sanayi devrimi Endüstri 4.0: Dünya ve Türkiye değerlendirmeleri," *Journal of Research in Entrepreneurship Innovation and Marketing*, vol. 2(3), pp. 29-49, June 2018.

[5] https://hammelscale.com/industry-4-0/   time: 15:19/ 23.08.2019

[6] https://www.endustri40.com/endustri-tarihine-kisa-bir-yolculuk/ time: 15:35/ 23.08.

[7] S. Rüstemli, F. Dinçer, M. Çelik, and M.S. Cengiz, "Fotovoltaik Paneller: Güneş Takip Sistemleri ve İklimlendirme Sistemleri," *BEU Journal of Science*, vol. 2(2), pp. 141-147, December 2013.

[8] M. Grozdev, "Alternatif enerji kaynakları," Master dissertation, Dept. Elect. Eng., İstanbul Univ., İstanbul, 2010

[9] İ. Burhan, A. A. Azman, S. Talib, "Multiple Input/Outputs Programmable Logic Controller (PLC) Module for Educational Applications," in *2015 Innovation & Commercialization of Medical Electronic Technology Conference (ICMET),* pp. 39–43.

[10] C. Sahin, "Dağınık OPC sistemlerinin internet üzerinden denetlenmesi," Master dissertation, Dept. Elect. Education., Kocaeli Univ., Kocaeli, 2007

[11] C. G. Sărăcin, I. D. Deaconu, A. I. Chirilă, "Educational Platform Dedicated to the Study of Programmable Logic Controllers and the Human-Machine Interface," in *The 11th international symposium on advanced topics in electrical engineering.*

[12] C.D. Dimitru, A. Gligor, "SCADA based software for renewable energy management system," *Procedia Economics and Finance*, vol. 3, pp. 262–267, February 2012.

[13] E. R. Alphonsus, M. O. Abdullah, "A review on the applications of programmable logic controllers (PLCs)," *Renewable and Sustainable Energy Reviews,* vol. 60, pp. 1185–1205, February 2016.

[14] V. C. Georgescu, "SCADA software used in dispatch centre for photovoltaic parks," in *Proceedings of the 2014 6th International Conference on Electronics, Computers and Artificial Intelligence (ECAI),* pp. 1-4.

[15] G. Zapata, A. Salazar, D. Moreno and R. García, "Supervision of a Distributed Energy Resources Generation System Using IEC and ISA Standards," in *IEEE Colombian Conference on Robotics and Automation.*

[16] H. Poor, *An Introduction to Signal Detection and Estimation*. New York: Springer-Verlag, 1985.

Measurement of Dielectric Characteristics of Fig and Mulberry Leaves by Waveguide Transmission Line Technique

H.DOĞAN[1]

[1] Ministry of Environment and Urbanization Isparta Provincial Directorate, Isparta/Turkey,
habib.dogan@csb.gov.tr

Abstract - **Recently, the use of microwave technologies has become widespread in studies on plants. The basis of these technologies is based on the determination of the dielectric properties of the material studied. The dependence of dielectric properties to water and frequency facilitates the automation of management by remotely sensing the needs of plants to water. In this way, both yield and quality increase in plants can be achieved. In this study, dielectric parameters of the fig and mulberry leaves intensively produced in Turkey are measured by Waveguide Transmission Line Method. Measurements are conducted between 4.90-7.05 GHz (for WR159 waveguide) and the dielectric characteristics of the leaves are examined depending on the moisture content and frequency. A new model with a curve fitting method based on frequency and moisture content (MC) is proposed used dielectric measurement data of fig leaves. This model is compared with the dielectric measurement results of mulberry leaves which belong to the same family with fig type to see the accuracy of the proposed model is tested.**

Keywords - **Microwave Applications, Dielectric Measurement, Moisture Content, Fig Leaves, Mulberry Leaves.**

I. INTRODUCTION

DIELECTRIC properties are one of the main determinant parameters in the characterization of the material. The way that electromagnetic (EM) waves interact with the material in the environment depends on the dielectric properties of the material. These incident waves will be exposed to reflection, refraction, absorption and scattering. Therefore, the dielectric parameters of the material must be determined in order to predict these behaviors of the EM wave.

The complex dielectric constant of a homogeneous, isotropic and lossy material is expressed as in (1).

$$\varepsilon^* = \varepsilon' - j\varepsilon''$$
(1)

Here ε' is the real part of the dielectric constant and determines how much of the applied wave is stored in the material, while ε'' is the virtual part and represents the losses that occur. The losses in dielectric materials, also known as tangent loss, are more generally expressed as in (2).

$$\tan \delta = \frac{\varepsilon''}{\varepsilon'} = \frac{\sigma}{\omega \varepsilon_r \varepsilon_0}$$
(2)

Dielectric measurements of plants are made for the 1910s [1] but are intensified due to increasing applications in parallel with the recent technology. Even different technologies are used in the systems designed to increase the efficiency in agricultural applications carried out by conventional methods, microwave-based technologies have advantages over other technologies. These; microwaves can penetrate plants and soil, are sensitive to water content and can spread in cloudy weather or at night [2]. These features make microwave technologies stand out in application studies such as remote sensing (RS) and management in agricultural applications, drying, and heating. In particular, remote sensing studies on plants are among the topics focused on military applications. For this purpose, studies have been carried out to remote sensing and management for different vegetation canopies.

Since the dielectric properties of the plants depend on the moisture content (MC), the water content of the plant and the soil can be determined with the developed microwave applications. In this way, more or less irrigation can be prevented [3], which leads to a decrease in the yield and quality of plants. In addition, microwave heating/drying applications related to plants use the dielectric properties of the plants and both time and energy savings are achieved compared to traditional methods [4, 5]. Taking into account the dielectric properties of the plants used in the storage of microwave technologies to increase the efficiency of protection from harmful pests are obtained [6, 7].

In the dielectric measurements of plants, the leaves of the plants are predominant in determining dielectric characteristics [8]. Therefore, it is important to measure the dielectric characteristics of the leaves in determining the dielectric characteristics of the vegetation canopy. There are many studies related to the dielectric measurements of the leaves [9-13]. Some of these studies were carried out without separating the leaves from the stem and the majority of them were separated from the stem and purified from certain MC.

Another aim of dielectric measurements in plants is to use as an absorber material from natural products [14, 15] because

the absorber materials used in the current situation have a health and environmental risk. Studies have shown that fibrous plant products can be an alternative to existing absorbers supported by various additives [16]. Different techniques are used in dielectric measurements of plants. These are lumped elements, waveguide transmission line, cavity resonator, coaxial probe and free space measurement techniques [17].

Fig (Ficus Carica) and mulberry (Morus Alba) are categorized in the dicotyledonous (Magnoliopsida) and in the mulberry (Moraceae) family. According to the data of the Food and Agriculture Organization in 2018, Turkey is the first country with the highest annual fig production in the world with approximately 306,000 tons (26% percent) [18]. The mulberry in the same family has an annual production of 66.647 tons in Turkey.

Our main motivation is to determine the dielectric parameters for the use of these two plant species with wide production area in microwave applications such as RS and product monitoring automation. The results of the proposed model and dielectric measurement of mulberry leaves which belong to the same family with fig are compared to verify the accuracy of the model. Waveguide Transmission Line Method is used in measurements which are conducted with WR159 waveguides in the frequency band of 4.90-7.05 GHz. In Section 2, the dielectric measurement and test Setup is given. Section 3 consists of obtained measurement results and the proposed model, and Section 4 evaluates the results.

II. Measurement System

Measurements of fig and mulberry leave are made at Akdeniz University Industrial and Medical Applications Microwave Research Center (EMUMAM). The measurement medium is shown in Figure 1. Figure 1a shows the system that is ready for measurement with waveguides together with VNA. Figure 1b-e illustrates flanges filled with hollow and hollow Plexiglas, respectively.

In this method, the WR159 waveguide is selected in which the frequency range to be measured. The waveguide is connected to the vector network analyzer (VNA) with RF coaxial cable. Two waveguides in the transmitter and receiver state and two matching flanges are used. The sample to be measured is placed between the flanges and made ready for measurement. Measurements are made in the range of 4.90-7.05 GHz. The VNA used in the measurements is the Anritsu MS4624B model (10 MHz to 9 GHz).
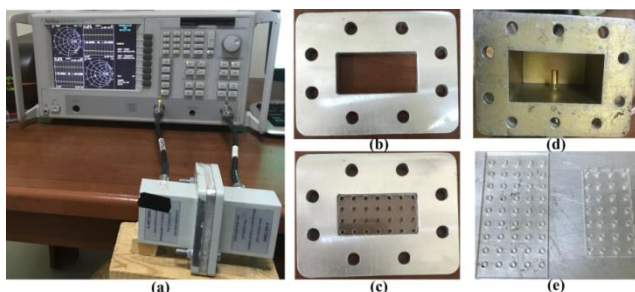
In order to prevent breakage and curling of leaves (samples) during the drying process, side holders (two transparent plexiglass) are used. Even if the effect of plexiglass on the measurement results is small, this effect is de-embedded from the results. As shown in Figure 1e, holes having the number of 9×5 and 7×4 with 1 mm diameter are drilled on the plexiglass at equal distance to allow homogeneous drying of the samples. The samples are immersed in pure (drilled) water for 48 hours before measurement to ensure full saturation of the samples. During this time, their weight is measured every 12 hours.

First of all, the fully water-saturated (fresh) samples are cut via a scalpel according to the WR159 waveguide dimensions. The water-saturated samples are dried in the microwave oven step by step. In each step, S_{11} and S_{21} parameters of the samples are measured by VNA, while their weights are measured with an electronic balance of mgr. There are different standards for dielectric measurements in terms of MC. Drying and measure steps continue until the leaves are completely dried. After the final drying step, the samples are completely dried in the oven at 70ºC for 24 hours. All measurements are performed at 24ºC.

In Figure 2, the necessary steps for preparing the fig leaves to measurement are given. Figure 2a shows the sample immersed in water for 48 hours. Figure 2b shows how the sample is cut. The sample placed between to plexiglass in Figure 2c, the sample placed in the flange in Figure 2d, the cut sample in Figure 2e, the fully-dried sample in Figure 2f and the electronic balance in Figure 2g is given. Similarly, Figure 3 shows the process of preparing the mulberry leaves for measurement.
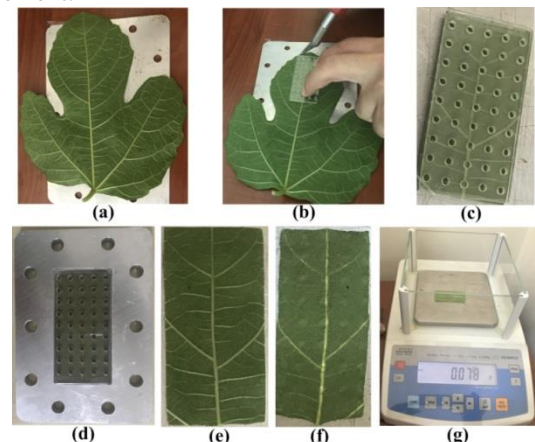
Figure 2: Preparation of fig leaves for measurement

Figure 1: Measurement System
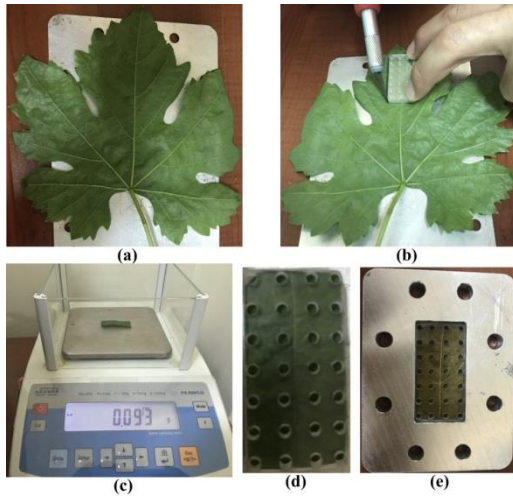
Figure 3: Preparation of mulberry leaves for measurement

As mentioned before, the drying process is carried out step by step. Table 1 shows MC calculated in the drying process for the two waveguides of the fig leaves. The weight of fresh fig leaf for WR159 is 90 mg. The weight of the fig leaves remained constant at 31 mg after 6 drying steps. This leaf weight is obtained by keeping it in the oven at 70º for 24 hours and is completely dried. Moisture amount and MC are given due to this weight reduction. The MC of fresh and completely dried leaves is calculated as 100% and 0% according to Equation 1 and Equation 2, respectively. For WR159 waveguide, the fresh mulberry leaf is 25.2 mg and the total dried sample weight is 11.2 mg. Weight of %100 water content called as absolute fresh (m_{fresh}) and dry leaves (m_{dry}) is used to calculate allowable maximum leaf water content (WaC) as in [9].

$$WaC = m_{fresh} - m_{dry} \tag{3}$$

With the help of Equation (3), relative moisture content of leaves (M_r) at current situation under investigation can be expressed as in Equation (4) where $m_{measure}$ is current mass of sample during measurements.

$$M_r = (m_{measure} - m_{dry})/WaC \tag{4}$$

Table 1. The change of MC of measured fig leaves for WR159 (4.90-7.05 GHz)

Total weight(mg)	Dried Weight(mg)	Moisture Amount(mg)	Moisture Content(%)
90	31	59	100
60	31	29	49.15
45	31	14	23.73
38	31	7	11.86
36	31	5	8.47
31	31	0	0

Table 1. The change of MC of measured mulberry leaves WR159 (4.90-7.05 GHz)

Total weight (mg)	Dried Weight(mg)	Moisture Amount(mg)	Moisture Content(%)
25.2	11.2	14	100
16.9	11.2	5.7	40.71
13.7	11.2	2.5	17.86
12.5	11.2	1.3	9.29
11.7	11.2	0.5	3.57
11.2	11.2	0	0

In each drying step, the weight of the leaf is measured on the one hand while the parameters S_{11} and S_{21} of the leaf is recorded at 4.80-7.05 GHz (WR159) 801 separate points (frequency). The Nicholson Ross Weir (NRW) derivation, a well-known and widely used analytical method, is used to calculate ε' and ε'' values from the obtained S parameters.

In order to understand the effect of MC on dielectric constant, it is necessary to calculate relative dielectric constant (ε') and dielectric loss (ε'') from the S-parameters. Even there are different algorithms in literature for this calculation, well-known and popular method is the Nicolson-Ross-Weir (NRW) algorithm [19]. In this study, complex dielectric constant of the leaves is calculated with NRW algorithm using Equations 5-12. The flow chart of the NRW algorithm is given in Figure 4 [20].
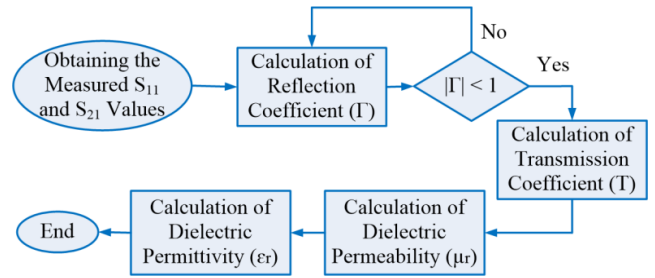
Figure 4: Flow chart of NRW algorithm

$$S_{11} = \frac{\Gamma(1-T^2)}{(1-\Gamma^2T^2)} \tag{5}$$

$$S_{21} = \frac{T(1-\Gamma^2)}{(1-\Gamma^2T^2)} \tag{6}$$

where Γ is the reflection coefficient, T is the transmission coefficient. Absolute value of reflection coefficient must be less than 1. L is the thickness of the sample.

$$\varepsilon_r = \frac{\lambda_0}{\mu_r}\left(\frac{1}{\lambda_c^2} - \left[\frac{1}{2\pi L}ln\left(\frac{1}{T}\right)\right]^2\right) \tag{7}$$

III. MEASUREMENT RESULTS AND PROPOSED MODEL

As stated in the introduction, fig and mulberry leave are used as samples in the measurements. WR159 waveguide is used for the 4.90-7.05 GHz frequency range. In the literature, the ε' values of pure water vary between 74-71 for the 4.90-7.05 GHz band [1]. The ε' and ε'' values of the water-saturated leaf in this study are considerably higher than those of the dry leaf, which is expected due to MC.

The results obtained for WR159 are given in this section. Figure 5 shows the variation of fig leaf ε' values with frequency and MC. It is seen that ε' value decreases with frequency increase and MC decrease. At 6 GHz, MC is 100%, 23.7%, 0%, while ε' is 11.90, 9.30, and 5.46, respectively. Similar changes in Figure 6 are valid for the value ε''. At 6 GHz, MC 100%, 43.8%, 0%, and ε'' are 13.00, 11.40, and 6.67, respectively.
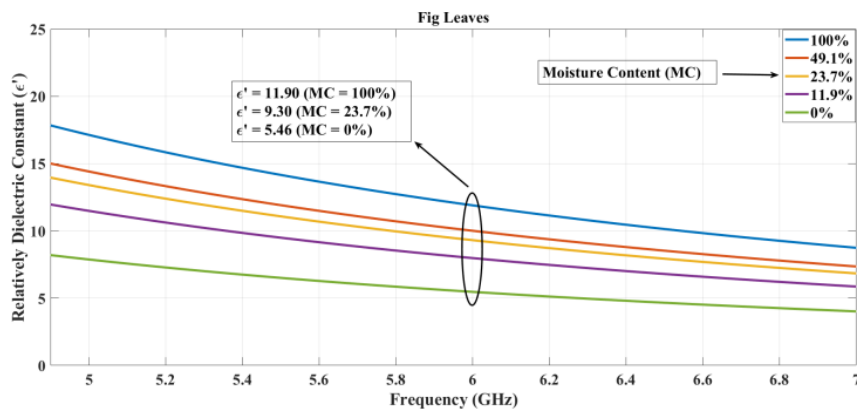
Figure 5: Variation of ε' of the fig leaves according to frequency and MC
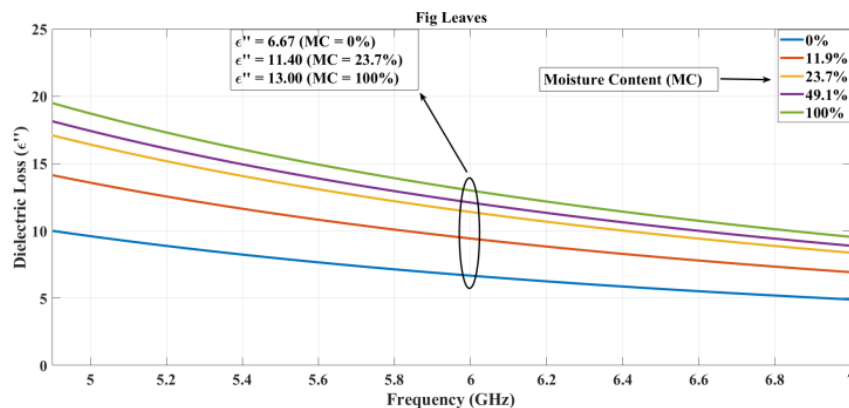
Figure 6: Variation of ε'' of the fig leaves according to frequency and MC

Figure 7 shows the variation of mulberry leaves ε' values with frequency and MC. It is seen that ε' value decreases with frequency increase and MC decrease. At 6 GHz, MC is 100%, 17.9%, 0%, while ε' is 10.72, 6.70, and 4.68, respectively.

Similar changes in Figure 8 are valid for the value ε''. At 6 GHz, MC 100%, 17.9%, 0%, and ε'' are 13.24, 8.92, and 5.56, respectively.
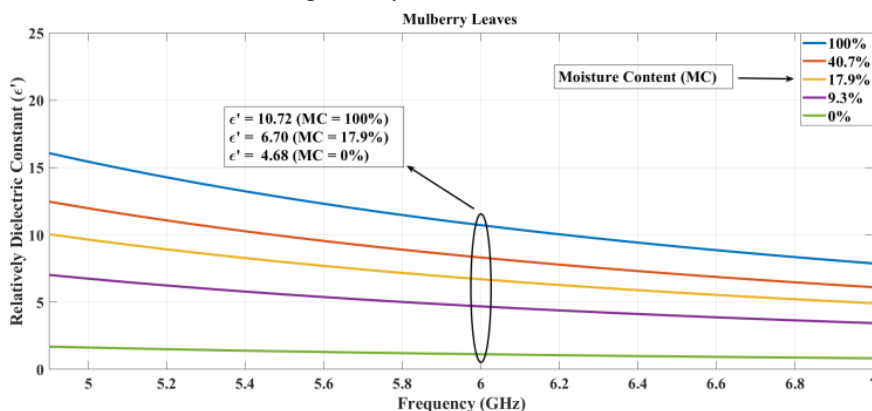
Figure 7: Variation of ε' of the mulbery leaves according to frequency and MC
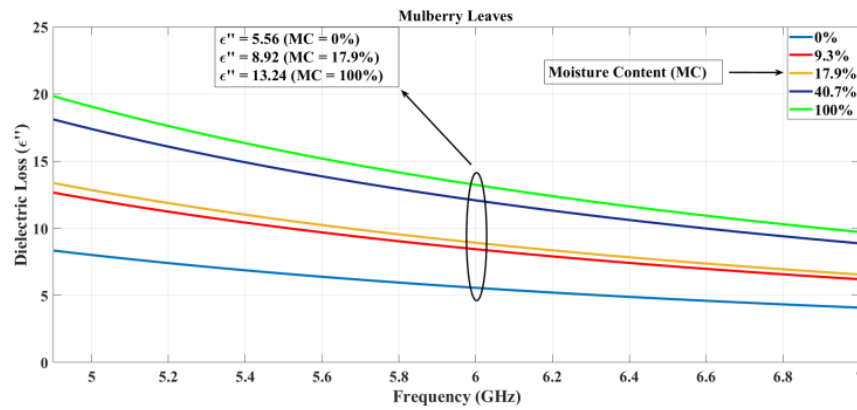
Figure 8: Variation of ε'' of the mulbery leaves according to frequency and MC

Using the fig measurement data obtained in Section 2, a new model with the curve fitting method is proposed. This model, given in Equation 9, is based on frequency and MC at constant temperature (24°C) when determining the dielectric constant and consists of a polynomial function with the second order with two variables.

$$\varepsilon_r = \sqrt{(\varepsilon')^2 - (\varepsilon'')^2} \qquad (8)$$

$$\varepsilon_r(f,m) = a + b.f + c.m + d.f^2 + e.f.m + g.m^2 \quad (9)$$

where the dielectric constant ε_r, the frequency in f GHz, m is the normalized MC ranging from 0-1. ε_r value given in (8) is

preferred in the model since it contains both real and imaginary part of the complex dielectric constant of the material. The coefficients of the model obtained in WR159 for fig leaves are $a=89.07$, $b=-20.7$, $c=13.66$, $d=1.343$, $e=-1.564$, $g=0.263$. In the model, it should be noted that 6 different MCs calculated in the drying steps in Table 1 for the fig leaves for WR159 are used as data. In Figure 9, the measurement results of the fig leaves selected for the test and the model proposed are compared and there is a good agreement between them. In addition, R^2 and Root Mean Square Error (RMSE) values of the proposed model are 0.955 and 0.836, respectively.
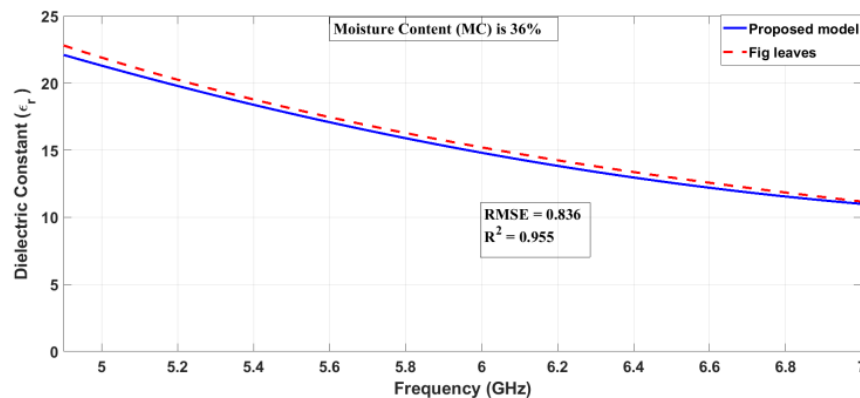
Figure 9. Comparison of dielectric constants of fig leaves with a MC of 36%

At the early this section, it is stated that the mulberry leaves are preferred unlike fig leaves. The usability of the model is tested by using the measurement data of mulberry leaves. So, the results of the proposed model having 38% MC (m=0.38) are compared with results of mulberry leaves. Figure 10 shows

that the results are very compatible with each other. This comparison shows that a model obtained from the leaves of a plant within the same family of relatives may be used for other plant species in the same family.
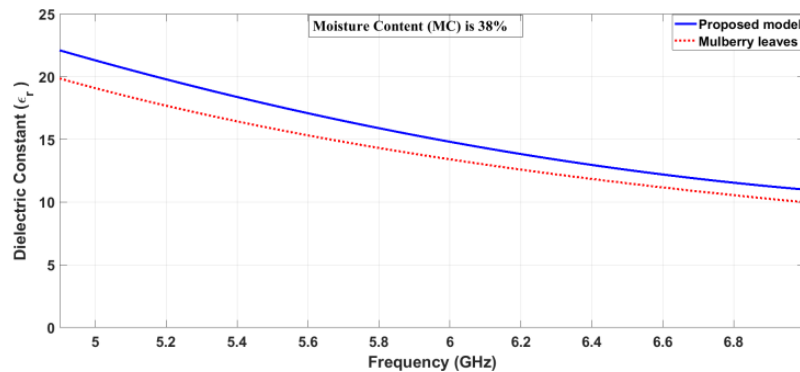
Figure 10. Comparison of dielectric constants of fig leaves with a MC of 38%

IV. CONCLUSION

Mapping the food and agriculture lands of countries is important for some institutions like The Food and Agriculture Organization. Accordingly, countries may be encouraged to invest in different agricultural activities. Remote sensing systems can provide visible and identification of plants and food. The dielectric properties of vegetation cover play important role for these kinds of systems. So, this study sheds light on related remote sensing applications by calculating the dielectric properties of fig and mulberry leaves.

In this study, the dielectric characteristics of fig and mulberry leaves from the same family depending on MC and frequency are obtained at a constant temperature. A new model is proposed by curve fitting method using just dielectric measurement data of fig leaves. The proposed model is also valid for the mulberry leaves. Waveguide Transmission Line method is used for measurements in the 4.90-7.05 GHz frequency band. For all MC values, while ε' values for fig and mulberry leaves vary between 48-7 and 50-8, ε'' values vary between 60-5 and 42-6, respectively. In the proposed model, R^2 values for WR159 is 0.998. Similarly, the RMSE values for WR159 it is 0.236.

REFERENCES

[1] S. O. Nelson, "Agricultural applications of dielectric measurements," IEEE Transactions on Dielectrics and Electrical Insulation, vol. 13, pp. 688-702, 2006.

[2] A. Kocakusak, B. Colak, and S. Helhel, "Frequency dependent complex dielectric permittivity of rubber and magnolia leaves and leaf water content relation," Journal of Microwave Power and Electromagnetic Energy, vol. 50, pp. 294-307, 2016.

[3] A. Afzal and S.-F. Mousavi, "Estimation of moisture in maize leaf by measuring leaf dielectric constant," Int J Agricul Biol, vol. 10, pp. 66-68, 2008.

[4] M. J. Kamaruddin, M. Yusof, N. Ngadi, Z. Zakaria, A. Arsad, and K. Kidam, "Dielectric Properties for Extraction of Orthosiphon Stamineus (Java Tea) Leaves," Chemical Engineering Transactions, vol. 56, pp. 1771-1776, 2017.

[5] A. Navarrete, R. Mato, G. Dimitrakis, E. Lester, J. Robinson, M. Cocero, et al., "Measurement and estimation of aromatic plant dielectric properties. Application to low moisture rosemary," Industrial Crops and Products, vol. 33, pp. 697-703, 2011.

[6] B. L. Shrestha, H. C. Wood, and S. Sokhansanj, "Microwave dielectric properties of alfalfa leaves from 0.3 to 18 GHz," IEEE Transactions on instrumentation and measurement, vol. 60, pp. 2926-2933, 2011.

[7] S. Trabelsi, M. S. Mckeown, and S. O. Nelson, "Dielectric properties-based method for rapid and nondestructive moisture sensing in almonds," Journal of Microwave Power and Electromagnetic Energy, vol. 50, pp. 94-105, 2016.

[8] H. Chuah, S. Kam, and Y. Chye, "Microwave dielectric properties of rubber and oil palm leaf samples: measurement and modelling," International Journal of Remote Sensing, vol. 18, pp. 2623-2639, 1997.

[9] T. van Emmerik, S. Steele-Dunne, J. Judge, and N. van de Giesen, "A comparison between leaf dielectric properties of stressed and unstressed tomato plants," in 2015 IEEE International Geoscience and Remote Sensing Symposium (IGARSS), 2015, pp. 275-278.

[10] A. N. Romanov and P. N. Ulanov, "Seasonal Differences in Dielectric Properties of Dwarf Woody Tundra Vegetation in a Microwave Range," IEEE Transactions on Geoscience and Remote Sensing, vol. 57, pp. 3119-3125, 2018.

[11] F. T. Ulaby and R. Jedlicka, "Microwave dielectric properties of plant materials," IEEE Transactions on Geoscience and Remote Sensing, pp. 406-415, 1984.

[12] H. Krraoui, F. Mejri, and T. Aguili, "Dielectric constant measurement of materials by a microwave technique: application to the characterization of vegetation leaves," Journal of Electromagnetic Waves and Applications, vol. 30, pp. 1643-1660, 2016.

[13] Z. Li, J. Zeng, Q. Chen, and H. Bi, "The measurement and model construction of complex permittivity of vegetation," Science China Earth Sciences, vol. 57, pp. 729-740, 2014.

[14] B. Colak, "Moisture content effect of banana leaves to radio frequency absorbing," Microwave and Optical Technology Letters, vol. 1-5, 2019.

[15] R. Kaur, G. D. Aul, and V. Chawla, "Improved reflection loss performance of dried banana leaves pyramidal microwave absorbers by coal for application in anechoic chambers," Progress In Electromagnetics Research, vol. 43, pp. 157-164, 2015.

[16] E. Jayamani, S. Hamdan, P. Ezhumalai, and M. K. Bakri, "Investigation on dielectric and sound absorption properties of banana fibers reinforced epoxy composites," Jurnal Teknologi, vol. 78, 2016.

[17] D. Khaled, N. Novas, J. Gazquez, R. Garcia, and F. Manzano-Agugliaro, "Fruit and vegetable quality assessment via dielectric sensing," Sensors, vol. 15, pp. 15363-15397, 2015.

[18] 2017 Kuru İncir Raporu. Gümrük ve Ticaret Bakanlığı. Available: http://koop.gtb.gov.tr/data/5ad0695fddee7dd8b423eb22/2017%20Kuru%20incir%20raporu.pdf

[19] A. Nicolson and G. Ross, "Measurement of the intrinsic properties of materials by time-domain techniques," IEEE Transactions on instrumentation and measurement, vol. 19, pp. 377-382, 1970.

[20] K.C. Yaw . "Measurement of Dielectric Material Properties: Application Note", Rhode & Schwarz. 2012.

Designing a System for Natural Gas Storage Facilities in Salt Caverns

Enis Murat ORHAN[1] and İlyas ÇANKAYA[2]

[1] Ankara Yıldırım Beyazıt University, Ankara/Turkey, enismuratorhan@gmail.com
[2] Ankara Yıldırım Beyazıt University, Ankara/Turkey, icankaya@ybu.edu.tr

Abstract - **Natural gas is most widely used resources for energy and is also used by people in homes for heating up. Countries cannot produce natural gas try to keep the balance between demand and supply. So, importance of natural gas storage increases and investments increase day by day.**

Generally, these facilities are operated manually. When the operation starts, operators take all decisions. Which units are working, which cavern should be used, which valves are open or close, all decisions made by operators. This type of facilities has complex process and possibility of man-made mistake is high. It is aimed that minimize the man-made mistakes, operate the facilities effectively and continuously.

Therefore, a software tool is designed for the operations. The purpose is makes a PLC programming that include definition of operating parameters for all units in natural gas storage facilities, full automatic and semi-automatic operation, programming of the parameters and create SCADA pages.

Keywords – **SCADA, Natural Gas Storage, Salt Caverns, Gas Operation**

I. INTRODUCTION

NEEDS of energy is huge and indispensable for human nowadays and increase the energy demand day by day. So, countries develop policies accordingly. In Turkey, natural gas is most widely used resources for energy and it is also used by people in homes for heating up. Moreover, distribution of electrical generation is dependent on natural gas in Turkey; it constitutes nearly 38 percentages in all energy resources. Natural gas is first and most important energy resources but our country is dependent on other countries for supply of natural gas. Nearly, %99 of natural gas is imported. So, natural gas storage becomes important.

Gas storage is generally used to meet supply-demand balances. Natural gas injected in the storage facilities when the demand is low and withdrawn from facilities when the demand is high. Moreover, it has also other advantages as below.

• It provides that cover the daily and seasonal change and in order to overcome natural gas shortage in case of decrease or stop of natural gas supply.

• It provides the control of fluctuation of price. When the demand high in the spot market, natural gas prices is very high. Therefore, the total cost can be decreased.

• And it provides the precaution of possible failure. Necessary precautions can be taken before the problem occurs.

Natural gas can be stored in depleted reservoirs, aquifers and salt caverns. According to geological studies, it is decided which storage types can be implemented and investments are going through accordingly. Also in the literature, it can be found a lot studies related with this. For example,Şener and Sözen worked on thermodynamic critics of underground natural gas storage in 2016 [1]. They calculated the compressibility factor, gas hydrate formation and maximum gas storage capacity of the natural gas stored in caverns. Anıl and Baştacıoğlu worked on solution mining in the salt layer and investigation of Natural Gas Storage Possibilities in the Occurred Cavern in 2013 [2]. They studied solution mining method that is the one of the subsurface mining methods for one of the salt mine in Turkey. Their data taken from there sort out the operation of typical salt deposits and underground natural gas storage potential.

In this study, a program is written for automatic and semi-automatic operation for natural gas storage facilities. Generally, operators control the process of these facilities manually. When the operation starts, all decisions are taken by operators. It increases the man-made mistakes. With this study, operators only decide how much natural gas should be injected or withdrawn from storage areas. It is named as semi-automatic operation. Except this decisions other process requirements controlled by logic that is programmed in PLC software. Which valves should be opened or closed, how much and which process units should be worked and which storage area is available for natural gas injection or withdrawn. All decisions taken by logic according to process parameters. In addition, SCADA screens are created.

In the literature, related with creation of SCADA and automation, a lot of studies can be found related with cyber security of SCADA systems, electrical facilities, water networks infrastructures and offshore oil and gas process etc. For example, Yurdabak and Şekkeli worked on implementation and evaluation of SCADA /DMS systems at electrical distribution networks in 2014 [3]. They reviewed an application that had been implemented on one of the electrical distribution networks in Turkey and touched on remote monitoring, analysis and control of electrical distribution on networks. Irmak and Erkek worked on Cyber Security in Industrial Control Systems and SCADA applications in 2018 [4]. They focused on the cyber security of ICS/SCADA systems and developed a software that can solve the security issue related with Modbus TCP protocol in SCADA systems for blocking the cyber-attacks. Papoutsidakis at al. worked on water networks infrastructures in the city Athens [7]. They focused on electromechanical installations and SCADA systems of the water supply network of Athens city. Prasad and Avadhani

worked on Attack Tree Design and Analysis of Offshore Oil and Gas Process Complex SCADA System [8]. They illustrated for designing attack tree in Offshore Oil and Gas Process Complex SCADA System to identify various vulnerabilities. However, it is very rare to find any study related with operation of natural gas storage facilities specifically.

In this study, a software is designed for automatic and semi-automatic operation for natural gas storage facilities. Natural gas storage methods are mentioned in section two. Process of salt cavern type natural gas storage is mentioned in section three and system design for operation is mentioned in section four.

II.   NATURAL GAS STORAGE METHODS

There are three possibilities to store natural gas in underground and with LNG (Liquid Natural Gas); natural gas can be stored aboveground. Underground storage methods are depleted gas reservoirs, aquifers and salt caverns.

Depleted reservoirs is the most prominent and common form of underground storage type. Depleted reservoirs are the formations that have already been existed in the earth and natural gas inside of these reservoirs have already been used and finished. So, this formation has already been capable of holding natural gas in natural.

Aquifers are underground natural water reservoirs. However, according to geological research, these water reservoirs can be used as natural gas storage facilities. As they are more expensive to develop than depleted reservoirs, these types of storage facilities are usually used only if no any depleted reservoirs exist nearby.

Salt caverns are human-made underground storage type. Salt in the underground melted via fresh water and caverns are created. Natural gas can be stored there. Advantages of this type of storage are high injection and withdrawal rates and cycle rates is higher than others. Natural gas in the cavern can be withdrawn and injected again 6.9 times per year as seen in Table 2.1. Moreover, the differences between them showed in Table 2.1.

Table II.1 Comparison of storage methods

	Salt Caverns	Depleted Reservoirs	Aquifers
Advantages	High injection and withdrawal rates and low cushion gas	It can be large capacity Construction cost is low because it is existing naturally	Large capacity
Disadvantages	Small volume in one cavern Brine disposal needs more cost Higher operating cost	High cushion gas requirements Slow injection and withdrawal rates	High cost Long development time Environmental problems
Cycle Rates per year	6.9	2.1	1.6
Cushion gas requirements	%20	%45	%55

Underground storage facilities contain cushion gas that is the volume of gas that must remain in the storage facility. For healthy of storage reservoirs and caverns this cushion gas remains underground every time. Otherwise, caverns or reservoirs can be collapsed.

'Working gas' is the volume of natural gas in the storage reservoir that except cushion gas. It can be extracted during the normal operation of the storage facility. This is the natural gas that is stored and withdrawn. The capacity of storage facilities generally calculated according to their working gas capacity.

In this study, salt cavern type natural gas storage is mentioned and next section is related with their process.

III.   PROCESS OF SALT CAVERN TYPE NATURAL GAS STORAGE

With the help of fresh water, salt formation in the underground melted and caverns are created (shown in Figure 3.1).
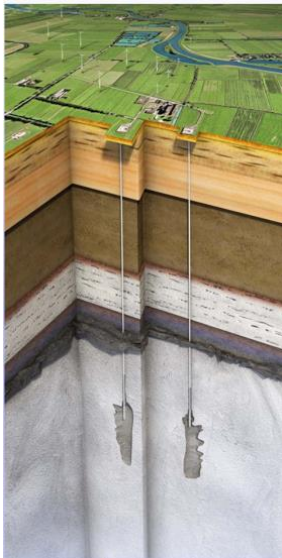
Natural gas can be stored in this formation. These formations are well suited to natural gas storage; natural gas can be incarcerated in the salt domes. The walls of a salt cavern like a steel, which makes it very resilient against any leakage. Salt cavern type natural gas storage facilities has two operation modes. One of this is injection mode that means inject the gas into caverns, in other words gas stored in the caverns. Red line in the Figure 3.2 shows the injection mode basically.

Figure 3.1: Salt caverns [5]

When the requirement of storage occurs, injection mode is used. In the injection mode, natural gas is taken from national natural gas pipeline network and inject into caverns for storage.
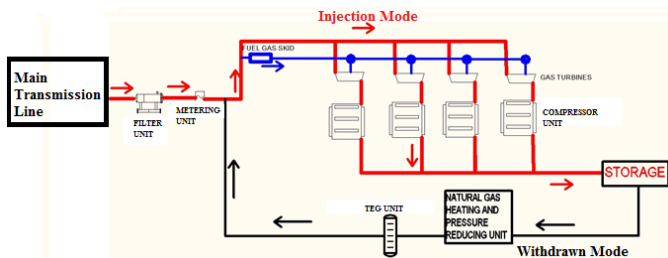
Figure III.2: Process of salt cavern facilities

Station inlet/outlet unit connects the station inlet/outlet with the main transmission pipeline. In other words, natural gas enters and exits the facility from here. In order to prevent any droplet or dust carry over to the gas plant facilities, gas coming from the transmission pipeline is filtered through a gas filter unit. Incoming liquids and dusts trapped by the filters and they are drained into condensate tank. Downstream of the inlet filter, the gas flow meters are used. This unit is most important part for commercial because thanks to this unit how much natural gas is injected or withdrawn in facility. The standard flow (energy flow, volume, etc) is calculated by these flow meters. For the purpose of the injection of natural gas, Gas compressor trains are used. It provides that pressurizing of natural gas and pressurized natural gas is injected into the caverns.

Second operation mode is withdrawn mode that provides discharge the gas from cavern to national natural gas pipeline network. Black line in the Figure 3.2 shows the withdrawn

mode. First gas discharge from cavern and reach natural gas heating and pressure reducing unit. This unit consists three parts which are water separators, gas pre-heater (boilers) and pressure reduction unit. Because natural gas discharged from caverns can consists water, water is separated from natural gas in water separators. Gas temperature drops during pressure reduction from the cavern storage pressure to the operation pressure and it cause the joule Thomson Effect. So before the pressure reduction unit, the boilers are used for heat the natural gas. After pre-heated, the gas pressure is reduced about main transmission line pressure.

Second it goes through the TEG Dehydration. In this unit, triethylene glycol (teg) is used as the absorption liquid to absorb the water in the natural gas. Last, it is metered and send from the national transmission line.

During staying in the cavern, natural gas should absorb water vapors due to contact with the remaining brine in the cavern sump. In order to meet the water dew point requirement of gas transmitting, a dehydration unit is required. In this dehydration unit, triethylene glycol (teg) need to be used as the absorption liquid to absorb the water in the natural gas. This unit mainly consists of the teg/gas absorber, the glycol regeneration skid and condensate tank. Gas and glycol meet in absorber unit and glycol takes the water in the gas. For reuse of glycol, teg regenerator is used.

For first fire of gas compressors and boilers, natural gas is used for internal use (Blue line in Figure 3.2). So, fuel gas skid unit is used.

IV.   DESIGNING A SYSTEM FOR OPERATION

In this study, designed a system for natural gas storage facility such as 500.000.000 m³ total storage capacity with 30.000.000 m³/day injection and 48.000.000 m³/day withdrawn capacity in three salt caverns. All flow values related with units are calculated by vendors based on these capacities and equipment's are chosen by mechanical engineers. So, these values will be mentioned next chapters are out of the scope of this study.

It is generated two mode for operation, automatic mode and semi-automatic mode. When automatic mode is chosen by operators, it can start the system according to determined seasons in the year. For example, in the winter, demand of natural gas high so withdrawn mode is activated and injection mode is activated in the summer. It calculates the flow rate according to main national pipeline.

With the semi-automatic mode, operators only decide which mode is used and how much flow is necessary. Because of operator intervention on flow rate and modes, it is named as semi-automatic mode. Other process in the units is full automatic both of them.

Figure 4.1 shows the created SCADA page of whole facility.
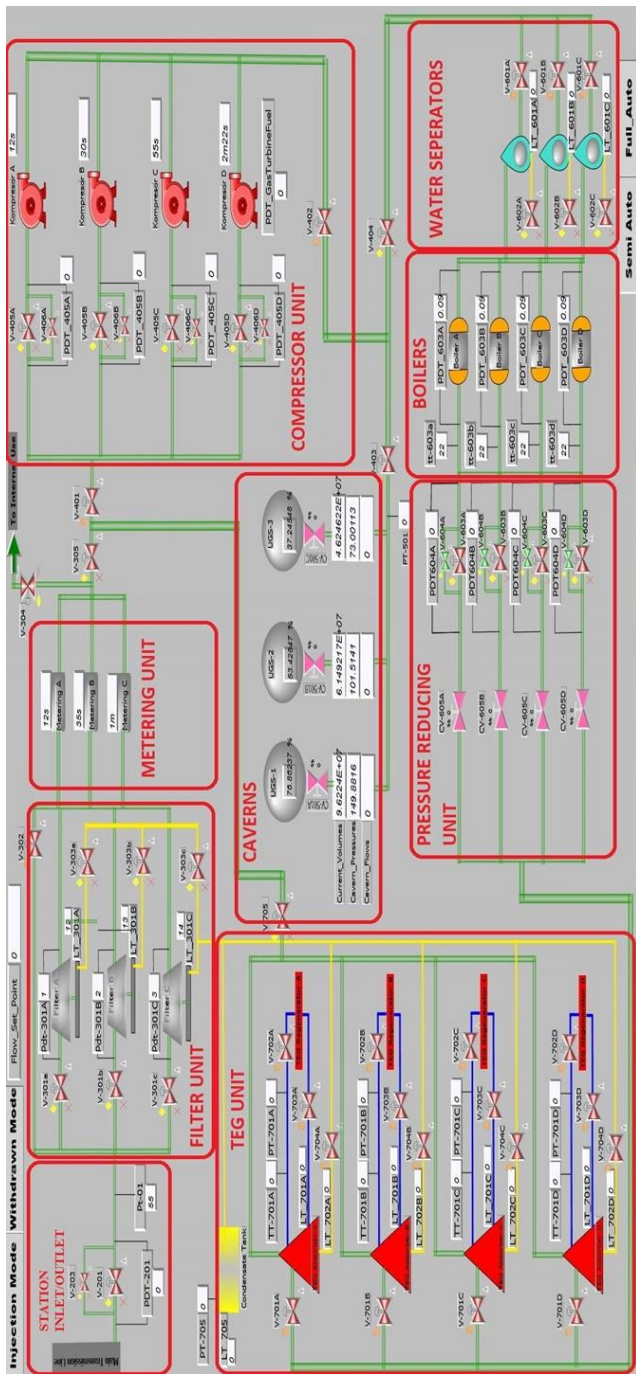
Figure 4.1: SCADA page of whole facility

A. INJECTION MODE

When the requirement of storage occurs, injection mode is used. In the injection mode, natural gas is taken from national natural gas pipeline network and inject into caverns for storage. Daily injection rate is 30.000.000 m^3, so hourly maximum injection rate is 1.250.000 m^3/h, equipment number in units is determined according to this value.

1) *Station Inlet/Outlet Unit*

When the injection or withdrawn mode is activated, Main Line Valve (V-201) open automatically. According to pressure difference between upstream and downstream of Main Line Valve opens or closes. Because of technical requirements, this valve cannot open when the pressure differences exceed 10 bar. So, bypass valve (V-203) is used in order to balance pressure differences upstream and downstream of V-201. If pressure is more than 10 bar, bypass valve opens and decrease the pressure differences. When the pressure decrease under the 10 bar, bypass valve automatically close and main line valve opens. After initiate the injection mode, Figure 4.2 shows the positions of valves (green means open, red means close).
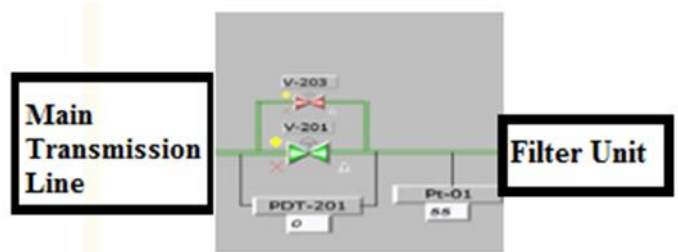
Figure 4.2 Station Inlet/Outlet Unit

2) *Filter Unit*

Filter units only used in injection mode. So, after pig sequence enable, logic control the injection mode is active or not. If withdrawn mode is activated this unit is not working. Total flow set point is limited because facilities have a daily injection capacity. If operator enters the value more than this limit, logic stop the sequence. One filter can pass 658.000 m^3 natural gas in an hour. Because total injection capacity is 1.250.000 m^3/h, two filters are enough but one more filter is installed for redundancy.

PT-01 measures the inlet pressure of the facility is limited because of compressor working range and according to this limit, logic decides to continue or stop the sequence. After these two decision, filters ready to start. According to flow set point, pressure differences between upstream and downstream of filters (PDT-301A/B/C) and liquid level of bottom tank of filters (LT-301A/B/C), logic decides which filter is working. First logic decides how much filter needs for operation. Each filter has a capacity as mentioned before. If required flow set point is below 658.000 m^3, logic decides to start one filter. Otherwise two filters are working. After logic decides which filter or filters are started. Logic compares the pressure differences between 3 filters and chooses the least one because more pressure shows the decrease of working life of filters, so, filter with less pressure is healthier.

Below the each filter, a tank is installed for collect the drain from filters. Level transmitters (LT-301A/B/C) are placed in these tanks and they measure the drain level. If it exceed the set point, related filter drain line valve (V-303A/B/C) open

automatically. Filter with this set point still continue to work but if this value still increase and reach the second set point, logic trip the related filter. For smooth operation logic switch the other filter that has the second less pressure or if two filters are in operation, it starts the spare filter automatically instead of tripped filter.

When the filters are started to work, related inlet valves (V301A/B/C) open automatically and filter sequence is ended.
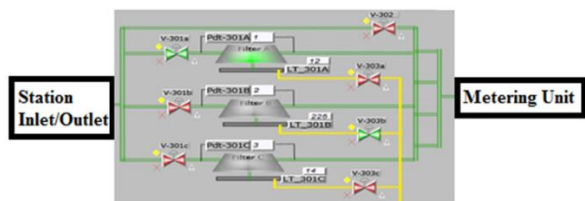
Figure 4.3 Filter Unit

After initiate the injection mode as seen in this figure 4.3 value of PDT-301A is one and less than others, for this reason logic starts this filter and related inlet valve and because value of LT-301B is higher than set point, related drain valve (V-303B) is opened automatically.

3) Metering Unit

Metering unit is used for both mode. According to metering unit capacity (one metering unit capacity is equal to 1345000 m^3/h) logic starts one metering unit or two metering unit that are the enough for injection mode.

Ultrasonic flowmeters use sound waves to determine the velocity of a fluid flowing in a pipe. Transducers installed on both bottom and upper side of pipe and travelling time of sound waves between them determined the flow rate. If no flow in the pipe, travelling time is same but when flow comes in the pipe, this time increase [12]. Because definite flow should come in the pipe for slowing down, this type of flowmeters has a threshold value. So, after injection mode is activated, logic controls this threshold value firstly.

Logic decides which metering unit is running according to running time of metering units. Timer is used for determining time for each metering unit (Figure 4.4).
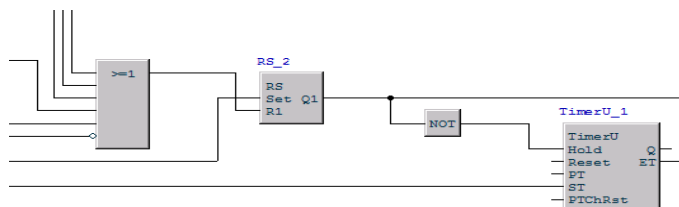
Figure 4.4 Timer and Set-Reset logic

When any metering unit is activated, timer sets and starts to count until injection mode stops or other reset events occur (general ESD, filters disable etc.). Otherwise, when the any two

or more metering times approach each other in operation, logic always change which unit works. For this reason, it is not sustainable and can be dangerous for system.

Therefore, logic compares the times in the beginning of operation and chooses underuse units. It provides uninterrupted operation.

After initiate the injection mode, Figure 4.5 shows the operation of metering. For example, in the beginning working times of metering A is 12 second, so logic starts the metering A unit. Nevertheless metering A passed metering B in this figure, metering still continue to work because of smooth operation.

Figure 4.5 Metering Unit

4) Compressor Unit

Centrifugal compressor is a machine that converts kinetic energy of the gas to high pressure thanks to its impellers because they are diffused and slow down the gas. Each centrifugal compressor has a special operating range named as compressor maps (Figure 4.6). These maps show the specific surge and chock lines that are determined by vendors. Surge is very dangerous for these compressors because it causes to increase vibration of compressor and damage to the compressor parts [6].
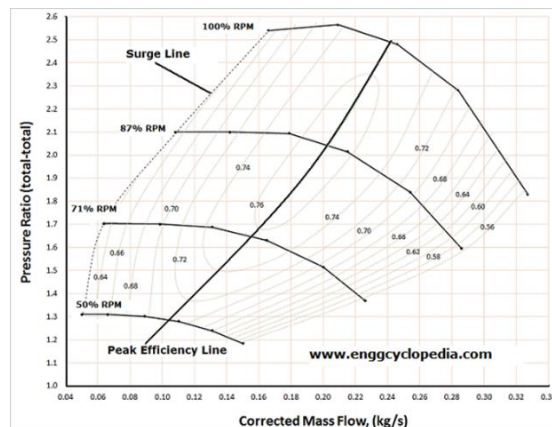
Figure 4.6 Surge line of compressors [6]

Pressure ratio is calculated as division of outlet gas pressure to inlet gas pressure. For example, if compressors can pressurize the gas from 50 bar to 100 bar, maximum pressure ratio is calculated as 2.

More pressure ratio means more gas flow as seen in Figure

4.6 for preventing to surge line. So according to facility conditions, minimum and maximum gas flow rate are calculated and determined.

After injection mode is activated, logic controls the metering enable or not and flow set point is higher than minimum gas flow rate or not. According to flow set point logic decides how much and which compressors start. According to minimum (50.000 m³/h) and maximum gas flow rate (418.000 m³/h) of compressors, logic decides how much compressors are started.

Logic decides which compressor unit is running according to running time of compressor units like metering unit. When any compressor unit is activated, timer sets and starts to count until injection mode stops or other reset events occur (general ESD or metering disable etc.) because of the reasons that mentioned in metering unit.

Therefore, logic compares the times in the beginning of operation and chooses underuse units.
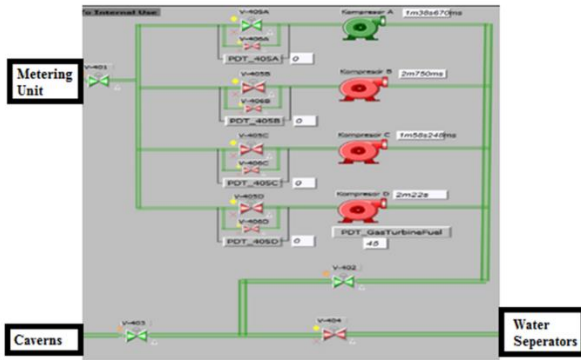
Figure 4.7 Compressor unit

After initiate the injection mode, Figure 4.7 shows the operation of compressor. According to flow set point, logic start one compressor that has the minimum operation time. Moreover, related valves are closed or open automatically by logic as seen in Figure 4.7.

5)   Caverns (Storage Units)

Each cavern has specific shape and volume according to leaching process and geological positions. So, each cavern has different volume and each of them needs different volume of cushion gas. According to total volume and current volume, fill rate and pressures of each cavern are calculated and shown on the SCADA page. According to needs of flow rate, cavern flows are calculated on the rows of cavern flows as seen in Figure 4.8. Calculations are as indicated below.

$$C_T = V_P \; x \; P_{max} \tag{1}$$

$$V_{wg} = (P_{max} - P_{min}) x \; V_p \tag{2}$$

$$\%F = \frac{V_C}{V_{wg}} x 100 \tag{3}$$

In here, C_T is Cavern Total Capacity and it is equals the multiplying of Cavern Phsyical Volume (V_P) and Maximum Pressure (P_{max}). Working Gas Volume (V_{wg}) is equals the multiplying of differences of maximum and minimum pressure ($P_{max} - P_{min}$) and Cavern Phsyical Volume (V_P) and Fill Rate (%F) is equal to the percentage of Current Cavern Volume (V_C) and Working Gas Volume (V_{wg}).
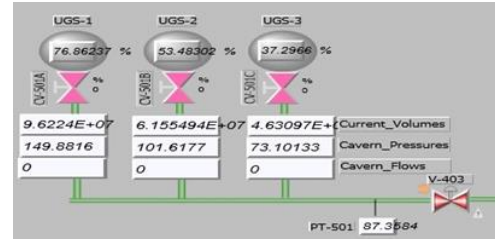
Figure 4.8 Gas Storage Unit

Each cavern has specific value and their physical volume, max pressure and min pressure are determined according to geological works. In this study, special simulation is written for visualization of injection and withdrawn of three caverns. Logic compares the fill rate of caverns and chooses least one for injection of gas. If flow rate is bigger than set point (10.000.000 m³/h) that is the maximum injection capacity of caverns, natural gas can be injected more than one cavern. After decision of which caverns are used, integrator start to accumulate cavern flows that is determined by entered flow rate for related cavern.

B.   WITHDRAWN MODE

When the demand of natural gas is increased especially winter, withdrawn mode is used. In the withdrawn mode, natural gas is taken from caverns and is sent into the national natural gas pipeline network

1)   Caverns (Storage Units)

When the withdrawn mode is activated, pressurized gas in the cavern goes the natural gas pipeline with own gravity because pressure differences between cavern and natural gas pipeline is very high. CV-501A,B and C are used for limitation of this flow. According to vendor data, logic calculates the how much percent valves should be opened or closed.

2)   Pressure Reducing and Heating Unit (Boilers)

Pressurized gas come to pressure reducing and heating unit. Logic decides how much water separator, boiler and pressure reducing line should be started according to entered flow rate. Maximum flow rate of water separators is 1.200.000 m³/h, boilers is 812.000 m³/h and pressure-reducing units is 696.000 m³/h. Each water separators have a level transmitter for measurement of the condensate level in the sump and they are used for drain the condensate liquids to condensate tank. When the liquid level exceed the set point that trigger the H (high) alarm, drain valves (V-602A/B/C) open automatically and if it exceeds the set point that trigger the HH (high high) alarm, related inlet valves of water separators close and trip the water

seperators. In this condition, logic starts other water separator that is not in trip for smooth operation. Figure 4.9 shows the operation of water seperators when withdrawn mode is activated.
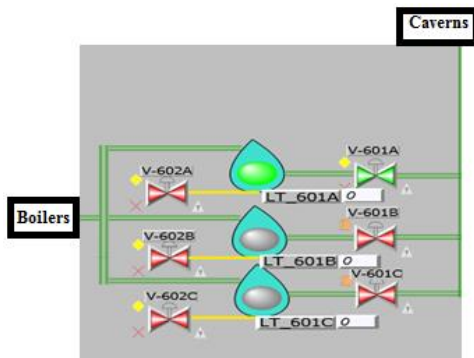
Figure 4.9 Water Separator Units

Figure 4.10 shows the operation of boilers. One temperature transmitter (tt-603a/b/c/d) that measures the outlet temperature of boiler and pressure difference transmitter (PDT-603A/B/C/D) that measures the pressure differences between inlet and outlet of boiler are installed for each boiler. For process and unit security these transmitters are used and logic shut downs the boilers according to set points of these transmitters. After decision of how much boiler starts, logic starts the boiler-A if there is not any shut down condition. If there is any problem, it starts the next one in other words boiler-B. When two, three or four boilers are working, logic works like this. Moreover, when three boilers work and problems occur on two boilers, logic trigger the emergency shut down of facility. For other combinations, it is also available.
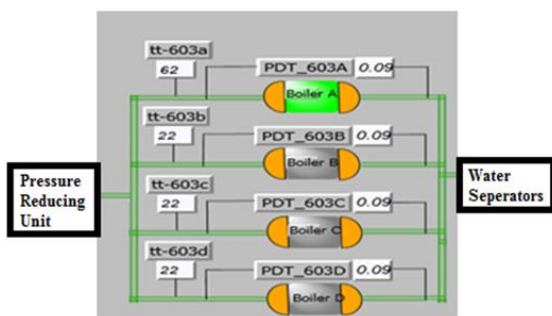
Figure 4.10 Boiler Units

High pressure natural gas coming from caverns is decreased in pressure reducing units. Pressure Transmitter (PT-01) installed in pig stations shows the not only inlet pressure of facility but also shows the pressure of main natural gas transmission line. So, according to this value and caverns pressure, logic open and close the proportional valves (CV-605A/B/C/D) installed in pressure reducing units as shown in Figure 4.11.
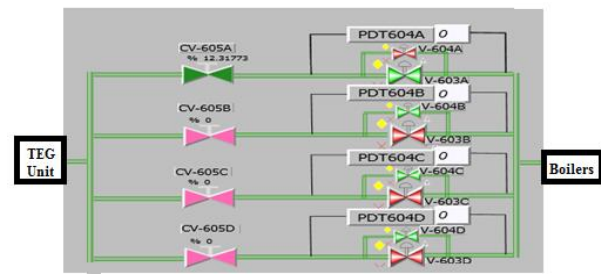
Figure 4.11 Pressure Reducing Units

Outlet pressure of Pressure Reducing Units is calculated according to PT-01 value. For providing the natural gas flow direction from facility to main natural gas transmission line, outlet pressure is set %10 more than PT-01. Proportional valves works as a formula as indicated below.

If

$$\frac{Po}{Pi} < 0,5 \qquad \%cv = \frac{f*\sqrt{(tt+273)*d}}{Cg*6,78*Pi} \qquad (4)$$

$$\frac{Po}{Pi} \geq 0,5 \qquad \%cv = \frac{f*\sqrt{(tt+273)*d}}{Cg*13,57*\sqrt{(Pi-Po)*Po}} \qquad (5)$$

Po : Outlet pressure of station

Pi : Inlet pressure

Cg: Valve coefficient of vendor

d: fluid density

tt: outlet temperature of boilers

f : flow set point

In equation (4) and (5), Po is pressure of pig station and Pi is cavern pressure. Cg and d are coefficient and other parameters are taken from the facility.

3) Teg Unit

TEG Units work principle is like boilers. After decision of how much TEG units start that is determined by maximum flow rate (844.000 m³/h) of one TEG Unit, logic starts the TEG-1 if there is not any shut down condition. These shutdown conditions are teg inlet pressure PT-701A/B/C/D, teg inlet temperature TT-701A/B/C/D, TEG level LT-701A/B/C/D and TEG bottom level LT-702A/B/C/D. Because of TEG unit capacity, these parameters shall be monitored. Figure 4.12 shows the operation of TEG Units. Because of high-pressure value of teg-a and high temperature value of teg-b, these units are in trip and teg-c unit is initiated by logic.
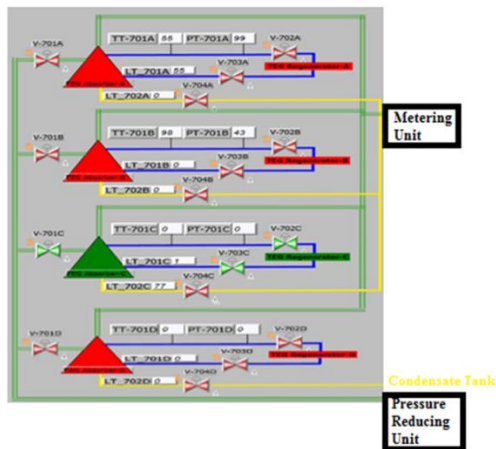
Figure 4.12 TEG Units

4) Metering Unit

After TEG units natural gas enters metering units. Work principle of withdrawn mode is same as mentioned in injection mode. Filters don't work in withdrawn mode because natural gas has already cleaned in water seperators and teg units. So, V-302 is opened automatically as shown in Figure 4.13 and natural gas are bypassed filters.
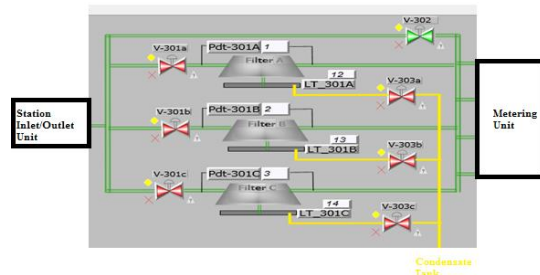
Figure 4.13 Filter Units in withdrawn mode

After pig stations whose work principle is same as injection mode, natural gas is send into main natural gas line.

V. CONCLUSION

In this study, PLC software is designed for semi and full automatic process control of sample facility that has 500.000.000 m^3 total storage capacity with 30.000.000 m^3/day injection and 50.000.000 m^3/day withdrawn rate in three salt caverns. Full Automatic mode can start the system according to determined seasons or days in the year but because of high cycle rates of salt caverns semi-automatic mode should be preferred in salt cavern type storage facilities.

With semi-automatic mode, operators only decide flow set point and which mode is used. Other requirements related with process controlled by logic that is programmed in PLC software. Which valves should be opened or closed, how much and which process units should be worked, and which storage area is available for natural gas injection or withdrawn.

When this logic is used in facilities, man-made mistakes like wrong valves or process units are opened or close on the process

can be decreased, units can be worked effectively, time loses can be prevented and financial losses can be minimized.

In the future, automatic mode can be developable more complicated according to needs and it can be implemented other type of natural gas storage facilities like depleted reservoir or aquifers. It is worked more efficiently in these types of storage facilities. Moreover, more research can be done related with characteristic of national natural gas pipeline network and statistics of natural gas usage in the seasons.

REFERENCES

[1]   1. Şener and Sözen, "Thermodynamic Critics of Underground Natural Gas Storage" , Gazi Journal of Engineering Sciences, ISSN: 2149-4916, E-ISSN: 2149-9373, Cilt 2, Sayı 1, Sayfa 21-40, August 2016.

[2]   2. Anıl and Bastacıoğlu, "Solution Mining in the Salt Layer and Investigation of Natural Gas Storage Possibilities in the Occurred Cavern", Çukurova University Journal of the Faculty of Engineering and Architecture, ISSN: 1019-1011, Vol. 28, Issue 2, pp. 149-160, December 2013.

[3]   3. Yurdabak, and Şekkeli, "Implementation and Evaluation of SCADA/DMS Systems at Electrical Distribution Networks", KSU Journal of Engineering Science, E-ISSN: 1309-1751, Cilt 17, Sayı 2, Sayfa 26-31, 2014.

[4]   4. Erdal Irmak, İsmail Erkek, "Cyber Security in Industrial Control Systems and SCADA Applications: Modbus TCP Protocol Example", Gazi University Journal of Science, Part C, E-ISSN: 2147-9526, Vol. 6, Issue 1, pp. 1-16, 2018.

[5]   5. Deep-KBB, 2018, https://deep-kbb.de/, (accessed on 16 January 2018)

[6]   6. EnggCyclopedia, 2018, Centrifugal Compressor Surge, Available online: http://www.enggcyclopedia.com/2012/01/centrifugal-compressor-surge/, (accessed on 16 January 2018)

[7]   7. Papoutsidakis et al. "SCADA Implementations to Supervise the Water Networks Infrastructures in the City of Athens". International Journal of Computer Applications. Vol 178 No 25 June 2019 pp 14-19.

[8]   8. Prasad and Avadhani, "Attack Tree Design and Analysis of Offshore Oil and Gas Process Complex SCADA System", International Journal of Computer Applications, Vol 181, No 41, February 2019, pp 12-18.

[9]   9. Cedigaz, 2018, Underground Gas Storage in the world- 2017 status(July 2017a). Available online: http://www.cedigaz.org/resources/free-downloads.aspx/, (accessed on 1 March 2018)

[10] 10. Lefond S.J.,1969, " Handbook of World Salt Resources", New York, Plenum Pres, p.384

[11] 11. Ministry of Energy and Natural Resources, 2019, Available online: https://www.enerji.gov.tr/tr-TR/Sayfalar/Dogal-Gaz (accessed on 21 March 2019)

[12] 12. Knepper GA, " Underground Storage Operations". Technology Today Series, pg:1112-1114, October 1997.

[13] 13. Gazprom, 2019, How is gas stored and what are UGS facilities, Available online: http://www.gazprominfo.com/articles/gas-storage/ (accessed on 21 March 2019)

[14] 14. TPAO,   2019,   Available   online: http://www.tpao.gov.tr/tp5/docs/ppt/Depolama-2014_en.ppsx, (accessed on 21 March 2019)

[15] ABB, 2019, Available online: https://mylearning.abb.com/, (accessed on 17 June 2019)

Inertial Measurement Unit Sensor Supported Bluetooth Based Fall Detection System for Sailors

B. AGIN[1], S. YESILPINAR[2], T. AKKAN[3], Y. SENOL[4], S. KARA[5]

[1] National Defence University, Air Force Academy, Department of Electronics Engineering, Istanbul/Turkey, bagin@hho.edu.tr
[2] Dokuz Eylul University, Department of Textile Engineering, Izmir/Turkey, sevil.yesilpinar@deu.edu.tr
[3] Dokuz Eylul University, Izmir Vocational School, Department of Mechatronics, taner.akkan@deu.edu.tr
[4] Dokuz Eylul University, Department of Electrical and Electronics Engineering, Izmir/Turkey, yavuz.senol@deu.edu.tr
[5] Dokuz Eylul University, Department of Textile Engineering, Izmir/Turkey, sukran.kara@deu.edu.tr

Abstract - **Nowadays, more people attend sports for both their health and social gains. Especially sports such as sailing and mountaineering became popular among the sportsmen who prefer to be in nature during performing a team sport. In this study, it was aimed to improve the safety of sailors by enhancing a Bluetooth based fall detection system. A previously developed fall detection system was enhanced by implementing new sensors and electronic components such as IMU (inertial measurement unit) sensor, temperature sensor, MP3 player. The designed system consisted of a master and many slave systems. The master system was planned to be located in the center of a sailor yacht and the slave systems were placed into sailor garments. The master system consisted of GSM, GPS, OLED screen and various electronical components. The slave system has heart rate sensor, temperature sensor, IMU, MP3 player, OLED screen and some controller units. In addition to all these components, both systems have Bluetooth modules to provide wireless communication. According to the developed concept, the master system continuously scans slave units by means of Bluetooth modules. Safety function of the master system is activated when any of the sailors goes out of communication range of the master system. In that case, the sailor who has the missing communication is accepted as fallen from the boat and the location of falling is found by the master by means of GPS. Then the location information is sent to rescue operation center. The sailor also gets warning signals from the electronic system, which can also detect the falling, and initiates the emergency procedure. The study was improved over a previous study with addition of new electronical technologies and new software programs. The realized waterproof tests showed that the designed system provides satisfactory results. The designed system can also be used in different sport areas which requires team activities and communications within team members such as mountaineering, entertainment activities and daily lives.**

Keywords - **Smart sailing garment, heart rate sensor, sport activity, fall detection, distress signal, embedded system.**

I. INTRODUCTION

USE of sportswear increased due to interest of people to different sportive activities. Nowadays, people expect sportswears to be functional besides their elegancy. Sportswear includes a variety of clothing designed to be worn during sports or training with their special end-use properties apart from ordinary garments. These properties may be waterproofness, breathability, lightness, water repellency, fast drying etc. [1, 2]. In addition to textiles' inherent properties, some functional properties can be added by implementing electronics to the textile structures that is referred to a class of "smart textiles" [3]. Today, smart textiles are used at different areas such as sports, medicine, military and casual activities in daily lives [4]. With improving technologies, electronic equipment become portable and smaller, therefore their implementation to textiles has become possible and feasible. So, smart functional sportswear that can be used while sailing, mountaineering and fitness are developed.

Functional garments which were developed with using electronical components and techniques are seen in literature frequently. There are some patents and articles about this type of garments. As an example, one of them includes piezoelectric transducer and electronic components that restrains the relative movement of different body parts [5]. In another study, a self-trainer fitness garment based on Silicon-MWCNT sensor was developed to track health situations of users through Android software [6]. Another study implies a smart firefighter wear with added sensors and electronics [7].

In this study, an embedded electronic system was designed and enhanced based on previous study [8] with new technologies and materials such as IMU and 433Mhz radio frequency transmitter. The embedded system was designed as two main parts. The first part was a slave system which was implemented to the garments of sports team members. The second system was a master system which communicated with slave systems and searched fall detection. The aim of the study was to enhance the safety of the sailors. During sports activity, the system evaluated some sensory information of sailors such as heart rate and body heat. In addition, the system detected the sailors who become overboard during he/she was doing sports. In case, fall detection was approved, emergency function was generated and distress signals were sent. Two embedded systems communicated each other with Bluetooth, wirelessly. Slave systems were searched by master system and the rescue procedure was begun for the sailor who fallen.

II. MATERIALS AND METHOD

Electronic part of the project contains two main systems as master and slave systems. Master system was located on the middle part of the boat in order to control slave systems in a range of defined safe area. On the other hand, each slave system were integrated to one of the sailor garment.

Slave system consists of four main parts as shown in Figure 1. First part, which includes the main circuit, was located near the shoulder of the garment. One of the added technologies to the study is IMU sensor. With this, it is possible to detect falling and gestures of sporters. Another additive innovation to the slave system was audible warning system. Audible warning system provides the sporters a more effective performance with extra information. The HC-12 433Mhz radio frequency module was also added to the system. With this module, it is possible to give emergency broadcast in free license frequency bands. Second part of slave system is the battery unit. It includes battery, charging module and measurement of battery capacity circuit. Third part of the system is a LED indicator that is used to take attention of rescue teams with visual warning system. It was located on shoulder via lens. The last part of the system is an OLED screen and located on arm part of the cloth. OLED screen shows vital information of the sporters and helps for programming and debugging of the system.
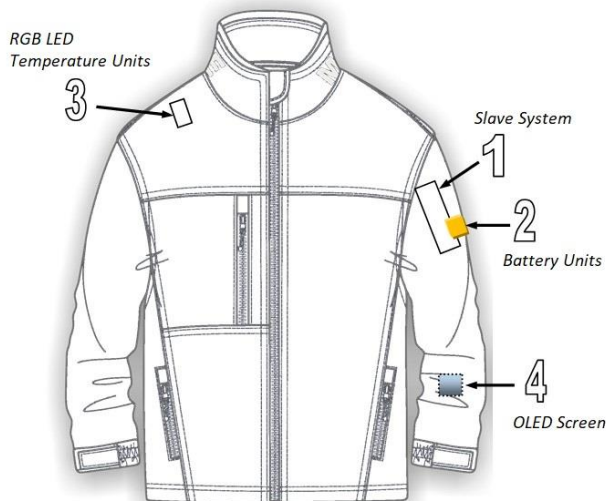
Figure 1: Slave system configuration

Master system of the project was redesigned with new technologies and waterproof design. The master system was planned to be located in the center of a sailor boat. As different from previous work [8], all electronic components and design were changed with new ones, wireless charging and magnetic on-off controller systems were also added to the system. Details of the electronic components of this study are given in the following parts.

A. Microcontrollers

Both master and slave systems of the project use the microcontroller as Sparkfun NRF52832 BLE Breakout Module. It provides Bluetooth communication and transferring information to related system thanks to its new technology. It has input and output pins which provides improvements to the project with modules. Breakout module has a chip combined with ARM Cortex-M4F microcontroller with 2.4GHz multi radio. It has also Bluetooth Low Energy technology. This feature is important for the project due to its low energy consumption and it was a big advantage for energy saving. Arduino Pro-Mini was another microcontroller that was used in slave system. The purpose of using this module was reducing extra works on Sparkfun NRF52832 BLE Breakout Module. Arduino Pro-Mini has UART, SPI, I2C analog input/output and digital input/output pins. So, Sparkfun NRF52832 Breakout Module number of connections were increased for improvements. In master system, only Sparkfun NRF52832 Breakout Module was used. So, Serial communication pins were limited. In order to solve this problem, 74HC4052 Serial Channel MUX was used. All devices which requires serial communication were connected to this integrated circuit.

Two ATTiny85 microcontrollers were also used in the project. One of them was located on battery unit in order to measure battery capacity. It could measure the battery capacity by using voltage difference inside the chip. Other ATTiny85 was used for programmer board. To come up with problem about programming Sparkfun NRF52832 Breakout Module, a programming board was improved. Thanks to ATTiny85, reset and programming mode timing was arranged and module was programmed.

B. IMU Module

Sparkfun LI3DSH accelerometer module was used as IMU in order to detect free falling of sporters. IMU was located in the center of the slave system. This module continuously observed users' gestures and detected free falling action. In case of free falling, the slave system activates the emergency procedure and distress signals are broadcasted. IMU has three degree of freedom. Module also provides interactions between user and slave system with tapping feature.

C. MP3 Player

DFPlayer Mini MP3 player module was used in the slave system. The purpose of using it was to increase interaction between system and user. Heart rate value of sporters and temperature are essential values for user. The module provided these data transfer to sporters and increased performance of them. Module supports FAT16 and FAT32 file system. It contains on chip SD card. An original file system was created inside the SD card. It contains audio files which transmit essential values and warnings. Audio files were created in different languages. So, all national sporters could interact with system in own languages which was defined to system before. A waterproof headphone was used for the module. It is possible also to upgrade this system with BLE technology in future.

D. HC-12 433Mhz Serial RF Module

One of the most important points was emergency calling function in the project. In case of free-falling detection, one of sporters falls from sailing boat and the distress signals is

generated, which is also called as S.O.S (Save Our Souls). Frequency bands of emergency signals were investigated on marine communication systems. The frequency band is 156.7Mhz for distress signals. In this marine frequency bands there is no obligation to have license for the band. So, HC-12 Serial RF Module was used to broadcast distress signals in the project. The broadcasting frequency is 433 MHz.

E. OLED Screens and RGB LED

OLED Screen was used in order to observe temperature, clock, battery capacity, heart rate value of sporters and debugging during programming. It was a significant way for interacting systems with user. OLED Screen was located on the center of the Master system in a waterproof case. On the other hand, OLED Screen was located on arm position. It was protected with a visible cover on sailor garment.

WS128B was used as RGB LED in slave and master systems. It indicates that state of the software and functional states such as emergency situation, low battery, high or low heart rate value. It also provided interaction of systems with environment.

F. GPS Module

The selected GPS Module is GY-NEO6MV2 which is a new technology. This module has high accuracy and sensitivity to detect position. It has sensitivity about -159dBm and could be able to catch lots of satellite signals. It is possible to find position with 5 meters of error by selecting 3 satellite data between existed 24 satellites. This module is important to obtain true position of fallen sailor at the falling instance. So, it is possible to find location of sailor according to the data taken from GPS module.

G. GSM Module

As a GSM Module, GSM3 Click was used in the study. As a difference from previous work, GSM3 Click has also 2.4 GHz Bluetooth antenna. It could be used in extra action with Bluetooth to transmit emergency signal. In addition, it has SIM800H-BT microcontroller different from GSM Click. SIM800H was observed to be faster than Telit GL865 microcontroller for sending SMS. GSM Module is also a critical component for the study in case of free fall detection. By using this module, it was possible to send SMS to a number which is defined before.

H. Bluetooth Module

At the beginning of the study, the Sparkfun NRF52832 BLE Breakout module was considered the main BLE module. There was not any master library existing for breakout module, BLE module was integrated to the Master system. HM-17 BLE module was used as a Bluetooth module. HM-17 has an appropriate CoD (Class of Device) to find address of Sparkfun NRF52832 BLE Breakout Module. This device could find slave BLE modules and list them. HM-17 has 100m range and Bluetooth 4.1/BLE features.

İ. Batteries & Charging

Two types of batteries were used to power up systems. One of them was 3.7V 1000mAh Li-Po battery for the slave systems. It was observed that slave systems could work up to

14 hours with fully charged batteries. Second battery was 3.7V 6000mAh Li-Po battery used for the master system. The main reason to use a high capacity battery for the master system is to response high power requirement of GSM/GSM systems. Also, it was observed that master system could work up to 12 hours with batteries charged at full capacity.

In this study, wireless charging method was added. Wireless charging has two electronic components as transmitter and receiver. Receiver was located under the board and encapsulated. The waterproof feature of this is important for the design. Another way to protect waterproof feature is the magnetic on/off reed switch which is added to the system.

J. Connectors

The Master and the slave systems are modular types. It means that modules can be installed and removed from the systems such as OLED and headphones. Connectors provided this specification. 3.5mm Audio connectors were used in the systems. Connectors were coated with silicone to reduce water permeability. Programmer, OLED screen, headphone and power cable used these connectors.

III. RESULTS

Sparkfun NRF52832 BLE Breakout Module can use Android Software of Nordic. The software was tested on a module to observe available specifications. In the test it was observed that the software can change the language of the system warnings. DF16-MP3 Player was tested in different languages and approved it works properly. LIS3DH accelerometer was also tested for free falling detection. According to the calculations S-Factor was satisfied with free falling actions.
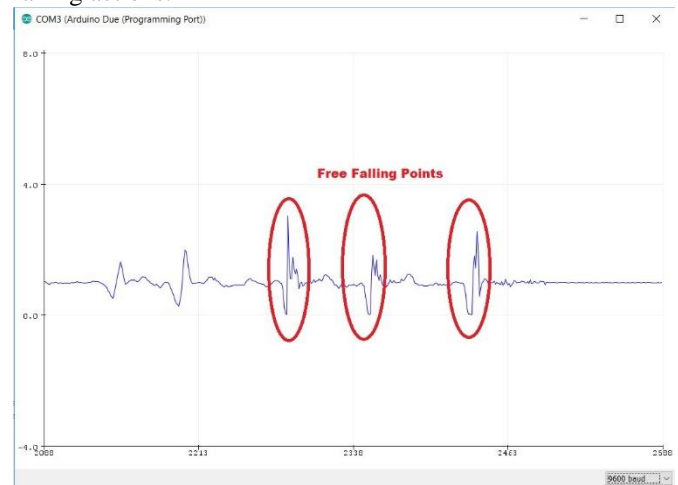
Figure 2: Free falling detection on serial monitor

HC-12 433Mhz Serial RF Module was tested by using two modules. One of them was responsible for transmitter task and other for the receiver task. The tests showed that communication between modules was established successfully. Slave system and related components accomplished their tasks properly. Heart rate value and temperature value were taken from user and ran as audio format by MP3 Player. Battery capacity and essential values were shown on OLED screen. In slave system, in case of

missing connection with master system or free fall detection, HC-12 broadcasted radio frequency in 433Mhz. Figure 2 gives multiple free fall detection which occurred during the tests.

The master system and related components were integrated to the system successfully. GPS module was tested at Dokuz Eylul University, Izmir Vocational School campus, given in Figure 3. GPS caught satellite data at least 6 and most 8. Positions were tested from Google Maps and approved its accuracy.
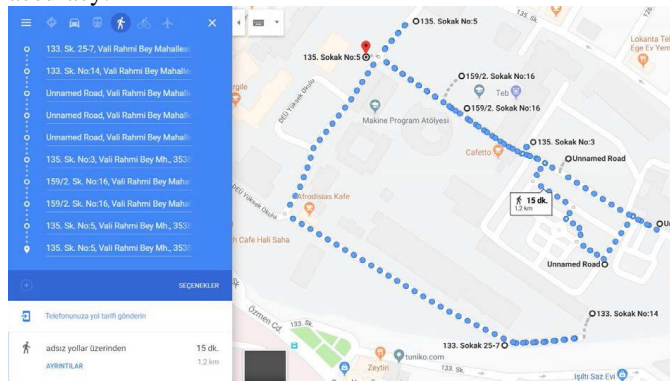
Figure 3: GPS module position verification from Google Maps

In case of the missing connection with the slave system or free fall detection, the position of the boat at the time instant of missing connection was taken and sent to defined phone number as SMS by GPS module with AT commands. So, scenario of sailor falling was simulated and planned emergency procedure was started. Wireless charging and on/off control with reed switch were tested and successful results were observed.

Figure 4: Slave and master systems with electronic boards

As a last step, schematic sketches of master and slave systems were drawn in AutoDesk Eagle in order to create electronic boards. Sketches were implemented and modules were placed on the printed boards of the slave and the master, respectively, which are given in Figure 4.

IV. CONCLUSION

The study was consisted of two main systems named as slave and master. The system was designed to provide safe sailing sport for the sporters. However, the systems is not limited to sailing. It can also be used for similar team activities, especially for mountaineering and entertainment activities. Both the master and the slave systems have lots of functional electronic boards to satisfy the safe sailing activity.

In the case of falling of the sporters from the sailing boat,

this is recognized by the available on chips modules of both the slave and the master systems. Each system starts different processes to provide the fastest search and ensuring the presence of the falling person. The master system immediately finds the location of the falling instance from the GPS module and sends the found location with SMS message to defined telephone numbers to start the rescue operation. Meanwhile, the slave system gives sound warnings to the sporters and also provides light signaling to increase the visibility of the sporters. The most importantly, RF module broadcast distress signals as the emergency broadcast in free license frequency bands. As it is clear, the designed systems will be used in sea harsh environment and therefore they are required to have waterproof feature. The master and slave systems were designed to satisfy these conditions and the realized test showed that both provides the required waterproofness.

REFERENCES

[1] Shishoo, R. Textiles in Sports. Woodhead Publishing, Cambridge England, 2005.
[2] Sukran KARA, Sevil YEŞİLPINAR (2019) Properties of 2-layered and 3-layered laminated sailing garments. International Journal of Applied Research on Textile, Special Issue CIRAT-8, 12-22.
[3] Tao X. Wearable Electronics and Photonics. Woodhead Publishing, Cambridge, England. 2005
[4] S. Jang, J. Cho, K. Jeong, G. Cho, J. Jacko, "Exploring Possibilities of ECG Electrodes for Bio-monitoring Smartwear with Cu Sputtered Fabrics," Human-Computer Interaction. Interaction Platforms and Techniques, Springer Berlin Heidelberg, 2007
[5] M. D. Pottenger, 2001. Piezzoelectrically controlled active wear, United States Patent, No: US 6,198,204 B1 dated 6.03.2001
[6] S. Cho, K. Kim, H. Cho, Y. Won, "Development of Self-trainer Fitness Wear based on Silicone-MWCNT Sensor," Journal of the Korea Academia-Industrial cooperation Society, Vol. 19, No. 7, pp. 493-503, 2018
[7] M. Dursun, E. Bulgun, Y. Şenol, T. Akkan (2019): A Smart Jacket Design for Firefighters, Tekstil ve Mühendis, 26: 113, 63-70.
[8] S. Kara, S. Yesilpinar, Y. Senol, T. Akkan, "Design of an electronically equipped sailing garment for improved safety," Industria textile, Vol. 68, No 1, pp. 23-30, February 2017

Solution of Problems on Bad Signal Quality via RF Optimization in Cellular Network

B.BASYIGIT[1]

[1]Isparta University of Applied Sciences, Electrical and Electronics Engineering, Isparta/Turkey,
bahadirbasyigit@isparta.edu.tr

Abstract - **Quality of service is a significant indicator that gives an idea of technology and success of mobile operator/vendor. Call integrity, call retainability and call set-up success rate are the important key performance indicators (KPIs) that define and create the quality of service. In addition, operators expect the complaints of customers using the network to be resolved immediately to increase customer satisfaction. The low network quality in these complaints is not easy to solve for planning and optimization engineers. The aim of this study is first to solve the quality problems by hardware configuration and changing optimization parameters in the global system for mobile communication (GSM) 900 frequency band. The second is to examine the RxQual, Speech Quality Index (SQI) and the Carrier to Interference ratio (C/I) values of the test region where voice quality problems have been solved and to determine whether the network contributed to the network quality. The network quality, which is very important for operators, has been investigated in the test regions. As a result, the average RxQual value from 7 to 3 has increased the quality of the received signal. The average SQI value from 9 to 25 has increased speech quality. The average C/I value from 7 to 13 has increased the MOS which is related to the voice quality on the grapevine.**

Keywords - **QoS, Mobile Network, KPI, Radio Access Network, Cellular Communication.**

I. INTRODUCTION

COMMUNICATION technologies have become one of the most used elements of our age. Since mobile is able to speak in motion, communication has progressed so fast. The global system for mobile system (GSM) system is the mobile communication technology that makes the most talk and the most subscribers in the world [1]. Although GSM data is insufficient to carry data, it has been the system that conveys the basic requirement of the people to the speech demand from the previous (today's) technologies. New today's systems have superiority over GSM than data transmission speed rather than voice transmission. GSM is still used by operators since it has many advantages from today's technologies in terms of voice transmission: GSM frequency region has a greater spread in terms of coverage area than the LTE frequency domain [2]. For this reason, today, GSM frequency band is still used for voice transmission in cities like long roads and small villages. Furthermore, this frequency region is more powerful against multipath fading and attenuation. It has much better speech quality and its terminal, operating and service charges are low. Since speeches are encrypted, subscriber information security is guaranteed.

Portable and mobile terminal support has low power. It is compatible with new services and networks.

The quality of service, which mobile operators pay much attention to, is not a case that can be defined as quantity [3]. But there are many factors to determine the quality of service in applications [4-6]. These factors are named as key performance indicators (KPIs) [7]. Low and bad signal quality [8, 9] affect these indicators negatively and decrease quality service. To the best of our knowledge, studies on the solution of these problems and the cause-effect relationship are limited in the literature for GSM frequency band.

The aim of this study is first to solve important problems such as low signal quality and speech quality by the improvement of the optimization parameters and doing hardware configuration in detail as a novelty. The second is to examine the RxQual, Speech Quality Index (SQI) and the Carrier to Interference ratio (C/I) values of the test region where voice quality problems have been solved and to determine whether the network contributed to the network quality. The network quality, which is very important for mobile operators, has been investigated in the test regions.

In this paper, as our study focuses on quality problems of the cellular systems, the subjects cause low signal levels are mentioned in section 2. There are drive test details in section 3. The solution of quality problems encountered in the field measurements and results is given in detail in section 4. The conclusions of results are evaluated in Section 5 and useful advice is given to field, planning and optimization engineers working in operator and vendors.

II. DRIVE TEST DETAILS

There are some important reasons for mobile operators and vendors to do drive test [10] and to analyze the network: They need this to configure the existing network to deliver optimum performance, to provide the network performance to meet the targets set by the operator. Drive test is taking place in new site integration, RF tuning and network optimization [11]. In order to solve quality problems the first drive test is needed to conduct in the network before optimization, then the second drive test is needed to see optimization results in the test region. In this study, the total duration of the drive test has been 3 days, including before and after the optimization study, including the waiting times at the traffic lights. The test length

is 24 km, including the main roads in Diyarbakir region of east of Turkey. After the optimization studies, the data for the correct analysis have been taken into consideration with the 1 week indicators as well as the most traffic hours within these data.

Transmission Environment Monitory System (TEMs) used for measurement in test region is a kind of telephone contains software that provides detailed information about all signal

Figure 1: Drive test equipment (a) test tool (ready to measure) (b) TEMs phones (c) GPS (with external antenna and data cable) (d) 12V-220V inverter (e) GPS (vehicle mounted) (f) data cable and USB for phones (g) scanner (with external antenna GPS and RF, data cable)

As shown in Figure 1, all equipment connected and ready for measurement is shown in Figure 1a. GPS has been used to see the location of the vehicle on the map during the test. GPS has been indicated with external antenna and data cables as in Figure 1c, and has been mounted on the front console of the vehicle as in Figure 1e. The inverter which converts energy from 12V to 220V can be seen in Figure 1d. Thus, both the laptop and the phones can be charged continuously. During testing, it is important to use the scanner to determine the frequency of all signals from the frequency band (GSM 900) operator serves and other frequency zones. Thus, during the analysis, interference from the same frequency or adjacent frequencies can be detected which directly disrupt network quality. The scanner used in this study with external antenna and data cables can be seen in Figure 1g. Three different telephones with TEMS software have been used as shown in Figure 1b. The first one is to collect information about the sound quality, parasites, and whether there is a dropped call during the active mode which is dedicated mode means there is conversion on phone. The second phone is for information about the signal level and quality in passive mode which is idle mode means there is no conversion on phone. The third and last phone call has been called by another telephone at 5 times per minute and ended the call. This is to examine the blocked calls and transition time from idle mode to dedicated mode. The connection of these 3 phones with USB and data cables can be seen in Figure 1f.

types, quality and level between MS, BTS and Base Station Controller (BSC) [12,13]. This is an important solution for developing and optimizing systems in wireless networks. That's why TEMs equipment has been used as a measurement tool in this study. The drive test in a vehicle is used to measure the network by giving a real image of the network's performance in the test region. In this study, the equipment used for drive test is shown in Figure 1.

III. RESULTS AND SOLUTIONS OF NETWORK QUALITY

It is important to explain the radio parameters [14] related to this study which can be seen in figures in this section in order to make the determination and analysis in the field measurement more efficiently before the solution to quality problems. RxLev shows the power level of the signal received from the BTS and received by the MS and is between -30 and -110 dBm. A voice quality measured on the basis of a Bit Error Rate (BER) [15]. Uplink and downlink radio quality (RxQual) is divided into eight levels. RxQual-0 shows the best quality while RxQual-7 shows the worst quality. When RxQual-4 is exceeded, there is a noticeable decrease in voice quality. The Frame Error Rate (FER) shows the percentage of falling frames due to a large number of uncorrected bit errors in the frame. It is an indication of the voice quality in the network. BER is the ratio of the number of bit errors to the total number of bits transmitted over a given time period and is a parameter for the voice quality in the network. The SQI, which is calculated on the basis of BER, FER and speech code is more complex than other quality parameters that take into account the reflection of the signal, and therefore is the most important parameter in the network quality parameters. C/I is the ratio of signal strength in the serving cell (carrier) to the power of unwanted disturbing signals (interference) and should have a minimum value of 9 dBm as a criterion. Finally, the MS power control level displays the power control range from 0 to 8 depending on the network design.

A. Very low RxQual and FER due to the Low Signal Strength (Poor Coverage Area)

As shown in Figure 2 during the drive test, the Rxlev value of the serving cell was -98 dBm and the Rxlev value of neighbor cells were between -99 dBm and -108 dBm which are very low signal level. Accordingly, very low quality has been observed from SQI and FER values. This is case needs to be solved urgently because it probably cause drop call and block call. Considering the cost of opening a new site in this region and the urgency of the solution, other solutions have been considered. Firstly, when the hardware configuration of the BTS has been checked, a small fault has been detected in the connectors and jumpers and replaced with a new one. Then it has been seen that signal quality is still low, although there is a certain increase in signal level. Then the antenna height of the serving cell which has the highest Rxlev value is increased

by 3m. Also with replacing the gain with another 3 dB higher antenna, lower quality has been increased.
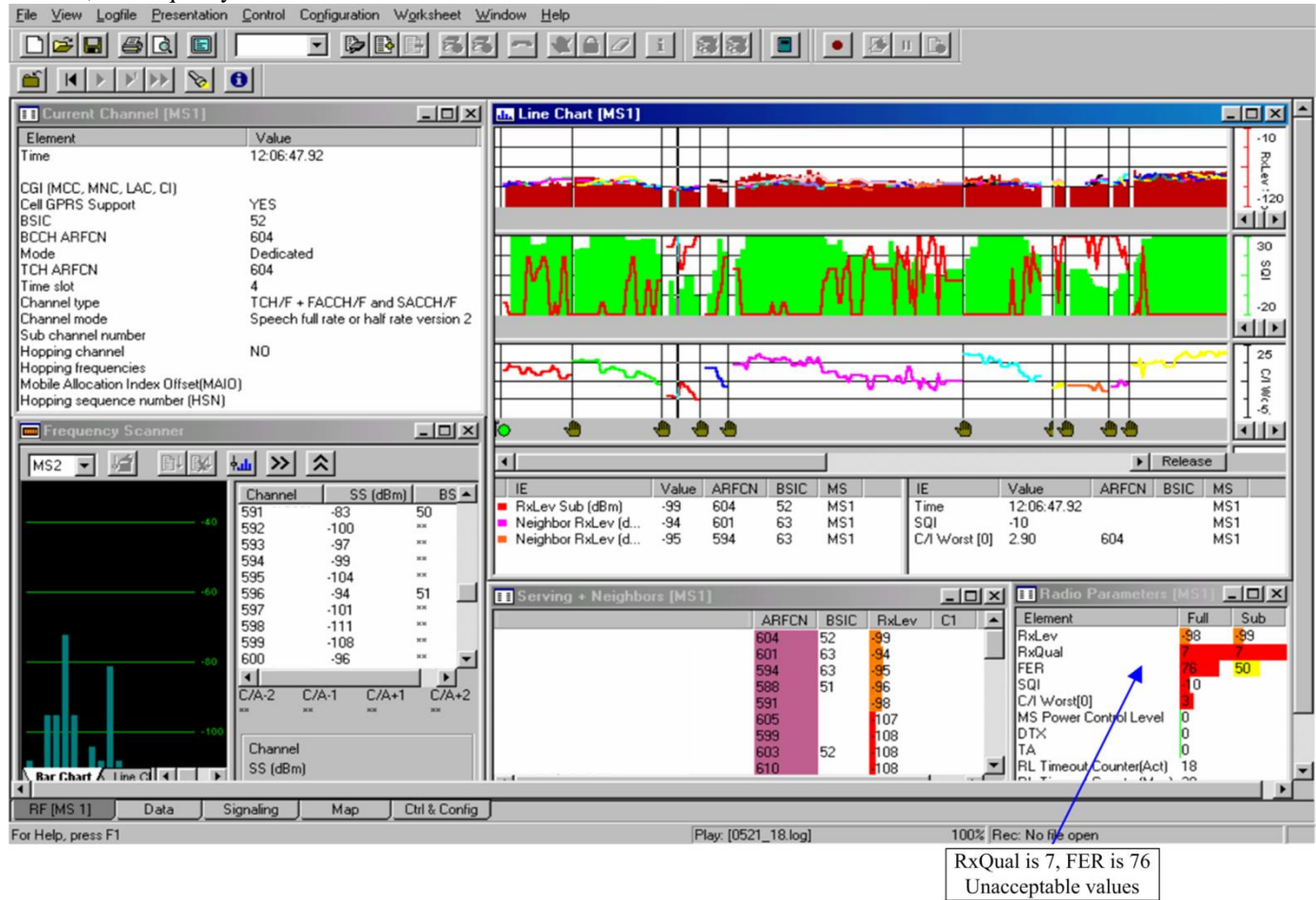
Figure 2: Very low RxQual and FER

RxQual is directly related to the quality of received signal that is based on BER. It varies between 0 and 7. Zero is the best and 7 is the worst case for network quality. For operators the RxQual value which is higher than 5 is unacceptable value. As shown in Figure 3, the RxQual has been decreased by the usage of an antenna with higher than 3 dB gain and the change of the jumper and connectors in the BTS.
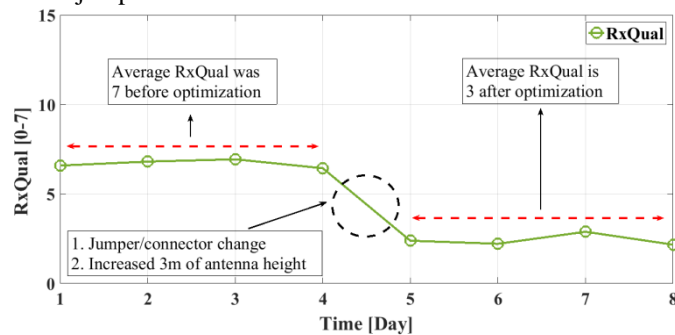
Figure 3: RxQual value before and after optimization

Measurements have been conducted by taking the average of 30 minutes values in the time period where the traffic has been the highest. As a result, while the average RXQual value before optimization was 7 for the 4 days, this value was 3 after optimization. So, the received signal quality for this test region has been increased.

B. Low SQI due to The Incorrect Frequency Assignment to TRXs

As seen in the SQI chart of Fig. 4 occasional decreases have been observed during the test. In C/I value, there has been a sudden decrease of 2 times independent of SQI. This situation should be solved because it can cause drop call in dedicated mode and call block in idle mode. The reason of this problem has been the interference caused by incorrect frequency assignment in TRXs [16] and, accordingly, C/I has been decreased. A certain offset is given to each TRX in order to prevent the TRXs in the cell from interfering with each other. The name of this parameter is Mobile Allocation Index Offset (MAIO). Each cell must contain a MAX value of up to TRX count. The frequency assignment to TRXs can be viewed in the Mobile Allocation List (MA-list). Here, there are 3 TRXs in this serving cell and it has been determined that it was defined as 0-2-3, while it should assign frequency as 0-2-4 respectively. After this correction, there has been no sudden decrease in C/I. SQI is the most important criterion of speech quality that is based on BER, FER and speech code as

mentioned before. The speech code for GSM Enhance Full Rate (EFR) is based on Algebraic Code Excited Linear Prediction (ACELP) [11]. For EFR speech code SQI varies

between 0 and 30. The best case is 30 and the worst is 0 for this parameter.
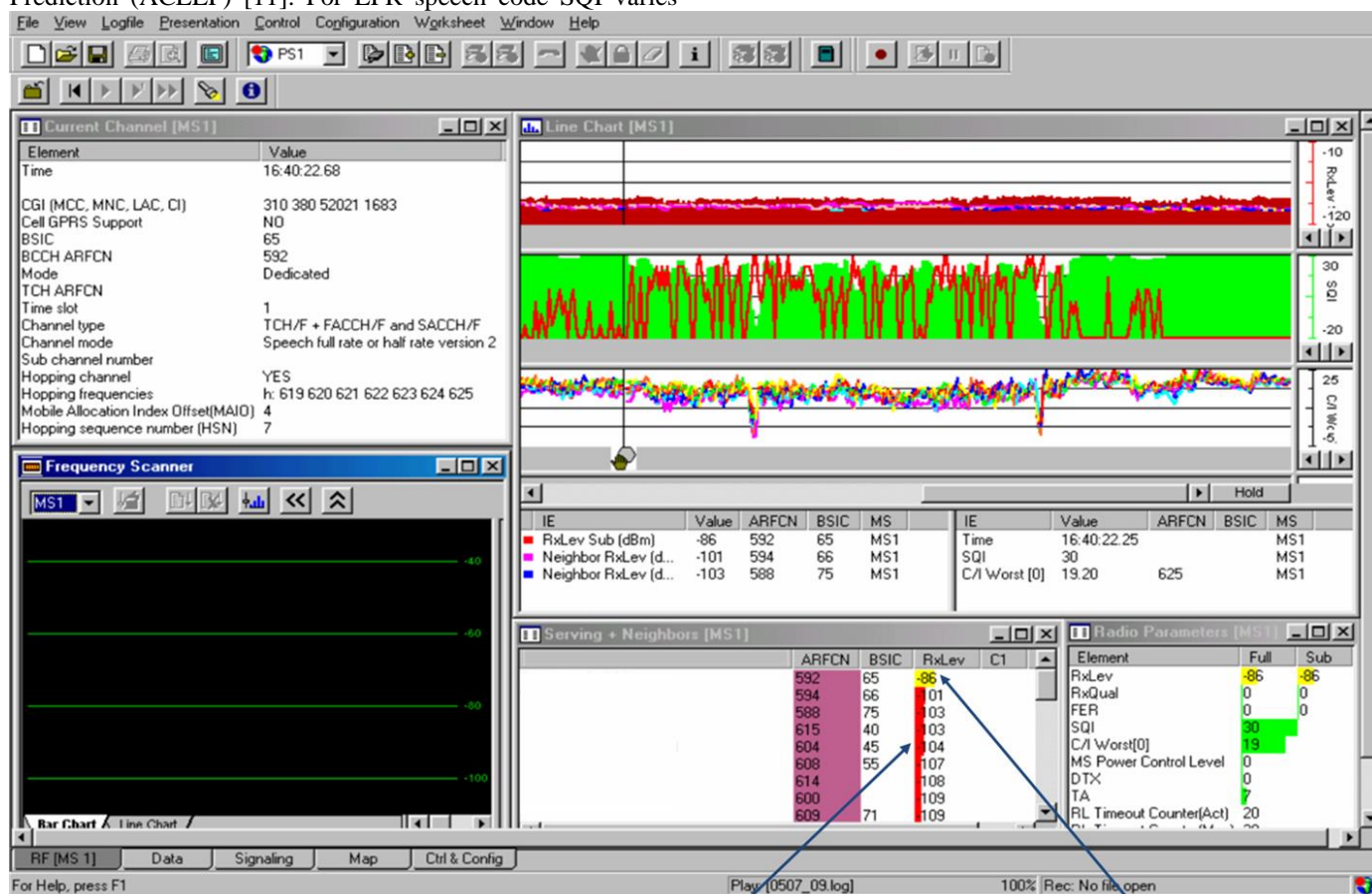
Figure 4: Very low SQI

It's important to note that for mobile vendors/operators the SQI value is unacceptable below 15. After the new assignment of frequency to the TRX, SQI value has been increased as seen on Figure 5. Here, while the average SQI value was 9 before optimization, this value was 25 after optimization. So, the speech quality of this test region has been increased.
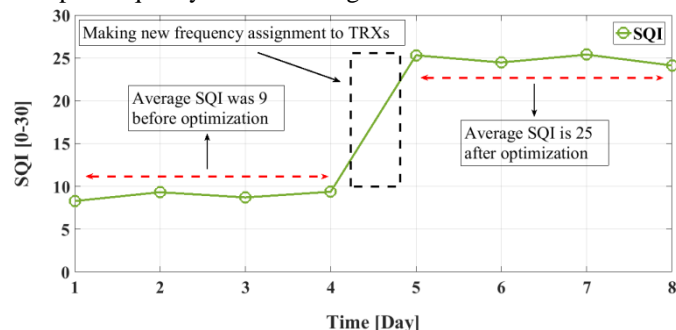
Figure 5: SQI value before and after optimization

C. Low C/I due to The Co-Adjacent Interference

As seen in Figure 6, it has been found that there was a decrease in SQI and C/I values in a certain region during the test. It is clear that the C/I value here deteriorates depending on the SQI. If this problem is not corrected, it causes disturbances in the voice quality and the network has a low Mean Opinion Score (MOS) [12]. MOS is a system that measures voice quality from ear to ear and is the measure of the network quality [13]. The reason for the poor quality in this region is co-adjacent interference. Here, serving cell with Base Station Identity Code (BSIC) 52 has the Broadcast Control Channel (BCCH) frequency 603. As seen in Absolute Radio-Frequency Channel Number (ARFCN) of Fig. 6. In the case of a neighbor cell with BSIC 54 has the BCCH frequency 604 which is not correct. In neighbor cells and in other cells that reach this region, there should be no frequency 603 (co-channel interference) and frequencies 604,605 (co-adjacent interference). This has been corrected by repeated frequency planning.

Frequency of serving cell is 603 and frequency of a neighbor cell is 604

Low C/I due to the co-adjacent interferance

Figure 6: Low C/I

After the change of BCCH frequency of neighbor cell, C/I has been increased as seen on Figure 7. For operators and vendors the C/I value that is below 9 dBm is unacceptable value. Here, while the average C/I value was 7 before optimization, this value was 25 after optimization. So, the interference negatively affect network quality has been decreased in this test region.
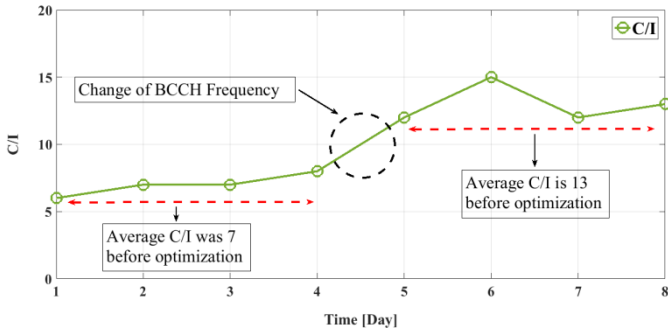
Figure 7: C/I Value Before and After Optimization

IV. CONCLUSION

The quality of service for a mobile operator/vendor is targeted in advance of certain criteria. Maximum attention should be paid to increase the quality of the network in terms of both the prestige of the operator and the increase in the number of mobile subscribers. RxQual, SQI, C/I, BER, and FER and MOS are the most important optimization parameters that directly affect network quality. Bad values of these parameters result in call drop, call block, RACH fail, SDCCH fail, and low MOS values.

It is necessary to eliminate negative situation due to the service quality problems by not only optimizing related parameters but also increasing of coverage area as opening new site, addition of sector, using repeater, site configuration change (antenna height, antenna down tilt, antenna diversity, antenna gain, turning antenna direction), frequency re-planning and BCCH change (for decreasing the co-channel and/or co-adjacent interference) and checking hardware configuration (jumpers, connectors, feeders and etc.)

In this study, RxQual, SQI and C/I values were bad and unacceptable in the area covered by 3 BTS according to the drive test measurements. The reasons of this situation have been investigated and accordingly an optimization study has been conducted. In the first location of test region it has been observed that low signal level, poor coverage area and lack of dominant serving have been caused bad RxQual value. The jumper and connector in the BTS have been replaced with a

new one, and the antenna height is increased by 3m to increase RxQual. In the second location of test region the SQI value has been low due to the false frequency allocation to TRXs which means that collusion of MA-list. Low SQI value has been corrected by re-assigning correct frequency. In the last location of test region there were unacceptable and low C/I value due to the co-adjacent interference between the neighboring cell and the serving cell was observed. This unwanted condition has been improved by changing the BCCH frequency.

As a result, the average RxQual value from 7 to 3 has increased the quality of the received signal. The average SQI value from 9 to 25 has increased the speech quality. The average C/I value from 7 to 13 has increased the MOS which is related to the voice quality from ear to ear.

ACKNOWLEDGMENT

REFERENCES

[1] Rich L., and Donner J. (2013). Mobile communication, John Wiley & Sons, New York, A.B.D.
[2] Stüber G.L. (2017). Principles of Mobile Communication, Springer International Publishing, New York, A.B.D.
[3] Qin, M., Yang, Q., Cheng, N., Zhou, H., Rao, R. R., & Shen, X. (2018). Machine Learning Aided Context-Aware Self-Healing Management for Ultra Dense Networks With QoS Provisions. IEEE Transactions on Vehicular Technology, 67(12), 12339-12351.
[4] El-Atty, S. M. A., & Gharsseldien, Z. M. (2017). Performance analysis of an advanced heterogeneous mobile network architecture with multiple small cell layers. Wireless Networks, 23(4), 1169-1190.
[5] Fraimis, I. G., & Kotsopoulos, S. A. (2011). QoS-based proportional fair allocation algorithm for OFDMA wireless cellular systems. IEEE Communications Letters, 15(10), 1091-1093.
[6] Chang, I. K., Kim, J. P., Hong, J. S., & Lie, C. H. (2010). Design of location areas with QoS considerations in a cellular network. Telecommunication Systems, 44(3-4), 333-345
[7] Kadioğlu, R., Dalveren, Y., & Kara, A. (2015). Quality of service assessment: a case study on performance benchmarking of cellular network operators in Turkey. Turkish Journal of Electrical Engineering & Computer Sciences, 23(2), 548-559.
[8] 8. Pous, M., Azpúrua, M. A., & Silva, F. (2015). Measurement and evaluation techniques to estimate the degradation produced by the radiated transients interference to the GSM system.
[9] Mossavat, I., Petkov, P. N., Kleijn, W. B., & Amft, O. (2012). A hierarchical Bayesian approach to modeling heterogeneity in speech quality assessment. IEEE Transactions on Audio, Speech, and Language Processing, 20(1), 136-146.
[10] Hapsari, W. A., Umesh, A., Iwamura, M., Tomala, M., Gyula, B., & Sebire, B. (2012). Minimization of drive tests solution in 3GPP. IEEE Communications Magazine, 50(6), 28-36.
[11] Wang, S., & Ran, C. (2016). Rethinking cellular network planning and optimization. IEEE Wireless Communications, 23(2), 118-125.
[12] Kehinde, A. I., Adunola, S. L. F. O., & Isaac, A. I. GSM quality of service performance in abuja, Nigeria, International Journal of Computer Science, Engineering and Applications (IJCSEA) Vol. 7, No. 3/4, August 2017
[13] Helhel, S., Ozen, S., Basyigit, I. B., Kurnaz, O., Yoruk, Y. E., Bitirgan, M., & Colak, Z. (2011). Radiated susceptibility of medical equipment in health care units: 2G and 3G mobile phones as an interferer. Microwave and Optical Technology Letters, 53(11), 2657-2661.
[14] Awada, A., Wegmann, B., Viering, I., & Klein, A. (2011). Optimizing the radio network parameters of the long term evolution system using taguchi's method. IEEE Transactions on Vehicular Technology, 60(8), 3825-3839.
[15] Das, M., Sahu, B., & Bhanja, U. (2017). Coverage Analysis of Mobile Network in Nakagami Fading Channel. Wireless Personal Communications, 97(2), 3261-3276.
[16] Ohatkar, S. N., & Bormane, D. S. (2014). An optimization technique for efficient channel allocation in cellular network. Journal of Communications Technology and Electronics, 59(11), 1225-1233.

DETECTING OF THYROID CANCER BY USING CONVOLUTIONAL NEURAL NETWORK

Aymen Salman Dawood Ezzat   Rahime Ceylan

Konya Technical University, Konya/Turkey, aimnsalman@gmail.com, rceylan@ktun.edu.tr

Abstract **- The thyroid gland is below the Adam's apple (called the *thyroid cartilage*) in the front of the neck. Due to increasing in the number of people who diagnose with thyroid cancer and also it has been difficult to inspect the disease within the gland.   Deep into the problem, a model of classical machine learning techniques needs to extract the feature vector first, these processes are time consuming. Besides, the techniques cannot process raw data without preprocessing and without expert assistance. The CNN algorithm features are less time consuming and higher accuracy when data is preformed which leads to the objectives of this study, to adders them, deep learning is considered to be a successful tool to solve the problem. Deep networks perform the learning process on raw data unlike the traditional techniques.**
In this study, the transfer learning method (Pre-trained Model Approach) is used to detect thyroid cancer by recalling the pretrained network (AlexNet). Results show that the deep network gives an accuracy of 100% with less time consumed. However, the data used is few in terms of number of images processed.

Keywords **- Deep learning, networks, imaging processing, transfer learning, Thyroid.**

I. INTRODUCTION

As soon as it was possible to scan medical images   and upload the scanned images to a computer, researchers created a system for automatic analysis. In the first process from the 1970s to the 1980s, analysis of medical images led to the analysis of mathematical modeling (lines and circles) by low-level pixel processing (edge and line detection filters, area-area expansion). At the same time, it is common in the field of artificial intelligence and has similarities to expert systems with many statements.

Following the end of the 1990's, guide technology for developing systems using educational data has become increasingly popular in medical image analysis. Examples include Active Form Models (for segmentation), Atlas methods (if the Atlas corresponds to new data forming training data), and the concept of functional overview and statistical classifiers (computer assisted detection and diagnosis). This building diagnostic or machine learning approach is still very popular and is the basis of many market based, successful medical image analysis systems.

Thus, from a fully human designed system, the use of sample data provided by feature vectors is witnessed as a transition to computer trained systems. The computer algorithm determines the optimal decision bounds of the high dimensional characteristic region. An important step in the design of such a system is to provide the distinctive features from these images, and this process is currently performed by researchers. The next logical step is to use a computer to learn the ability of providing the best representation of data on the immediate problem. This concept is also the basis of many deep learning algorithms.   A model (network) consists of a number of layers   that transform input data (e.g. images) into outputs   (e.g. disease / non-disease) while learning higher- and higher-level features. One of the most successful models used for image analysis today is Convolutional Neural Networks-CNN. Small CNN, its input, transform with a convolution filter that contains many layers.

Research on CNN [1], late 70's, it has already been introduced into medical image analysis [2]. This application was the first successful implementation on recognition of handwriting characters by LeNet. Contrary to these early successes, the use of convolutional neural networks has been used to develop various new techniques for effective training of deep networks. It has not gained momentum [3].

In connection with this, Milestone contributed to the December 2012 ImageNet competition. CNN, under the name of AlexNet (Convolutional Neural Networks), ended the competition ahead of its competitors [4]. In the next year, further development was done using a related but more detailed architecture [5]. In computerized imaging technology, deep convolutional networks are the preferred technology. The medical imaging community has emphasized these very important developments. Before AlexNet's turn, there are a number of different techniques that are generic in terms of learning features and allow a comprehensive review of these techniques [6]. These include basic component analysis, image fragment assembly, and dictionary approaches.

This study focuses on these deeper models,   and more traditional approaches to learn features that have been applied to medical imaging [6,7].   As an advantage, deep learning methods use effective algorithms for hierarchical feature extraction that best represent data rather than handcrafted features [8].

II. MATERIAL AND METHODS

A. Data Set

The dataset collections were formed by ultrasound images of human thyroid provided by Wilmington Endocrinology [9]. Ultrasound is one of the famous medical imaging techniques which is used for imaging thyroid gland. These images are mixed types such as images with nodules, images without nodules, images with benign lesions (non-cancerous), images with malign (cancerous) lesions (Figure 1). The dataset includes 12 images which are divided into 6 benign and 6 malign.

(a)   (b)
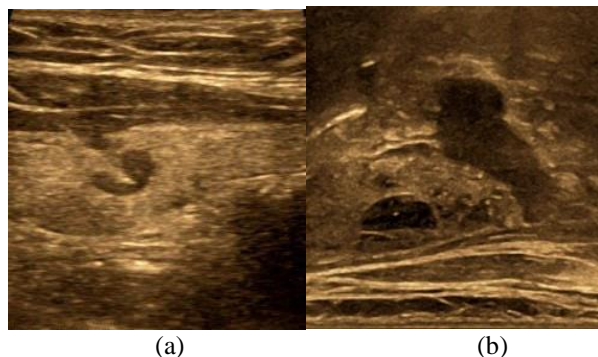
Figure 1: (a) malign, (b) benign

B. Transfer Learning

Transfer learning is a machine learning method that uses a model developed for a task. Transfer learning can be used in self-learning modeling problems. A pretrained model is a recorded network previously trained on   a large data set (usually a large image classification task). (Figure 2) as show following flowchart.
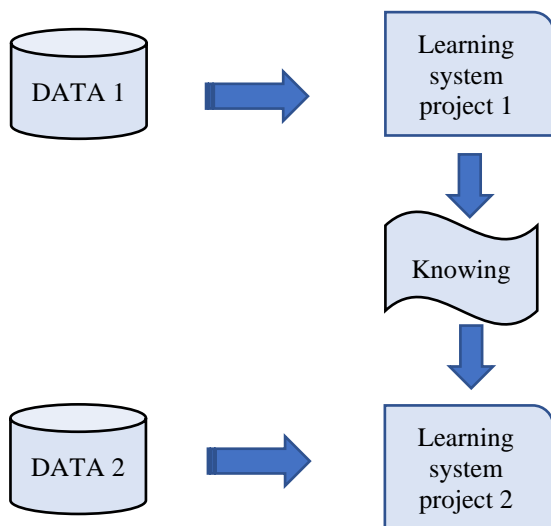
Figure 2: Flowchart for the Transfer Learning methodology

C. AlexNet

AlexNet is a convolutional neural network that is trained on more than a million images from the ImageNet database [10], where it is proved to be one of the most capable models of object detection. It has 25 layers, 5 convolution layers, 7 ReLU layers, 5 Max Pooling layers (MP), 3 fully connected layers(Fc), 2 Dropout layers and Softmax layers. The weights of model are initialized using a predefined version, as show following flowchart (Figure 3)

CNN	Conv1 55*55*96	ReLU1	MP1 27*27*96
	Conv2 27*27*256	ReLU2	MP2 13*13*256
	Conv3 13*13*384	ReLU3	
	Conv4 13*13*384	ReLU4	
	Conv5 13*13*256	ReLU5	MP5 6*6*256
	Fc6 1*1*4096	ReLU6	Drop6
	Fc7 1*1*4096	ReLU7	Drop7
	Fc8 1*1*1000	Softmax	Output
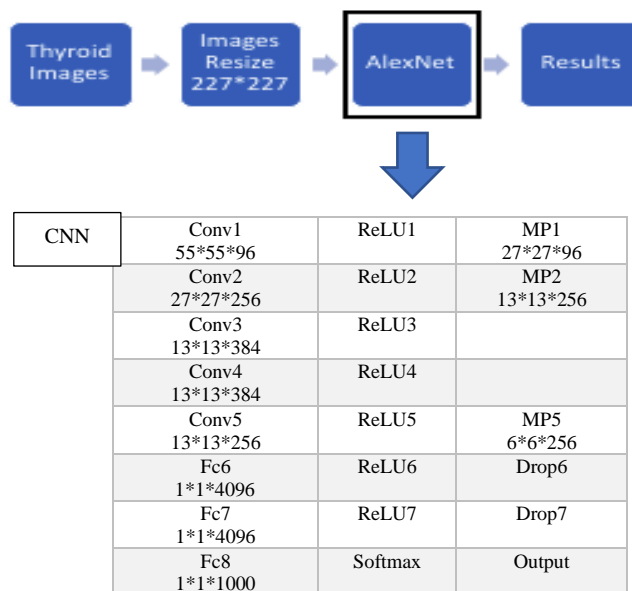
Figure 3: Flowchart for the (AlexNet) network

III. EXPERIMENTAL RESULTS

In this study; the detection of thyroid cancer disease is implemented by transfer learning. MATLAB programming language was used for examining images of the Thyroid Cancer Disease. For this purpose, Deep Learning" algorithms and "Transfer Learning" model and from Alexnet libraries.

Ultrasound images given from thyroid cancer dataset were classified as benign or malignant. These 12 ultrasound images were divided into 6 benign and 6 malignant, then all the images pixel were resized to 227x227. The training data consisted of 8 images which are formed equally as 4 benign   and 4 malignant. So, traning file and test file are   divided as 60% and 40% of dataset, respectively.   The result obtained was 100% in taking into account   the volume of data used. Figure 4 shows performance of   the convolution neural network of the pre- trained AlexNet in training. It can be seen from Figure 4 that the accuracy shows fluctuation by sharp increasing and decreasing in performance between 1 and 5 iteration. At iteration 5, the performance

reveals slightly linear increasing. At iteration 14, iteration shows a higher accuracy of 100% and the performance indicates shows stability nomatter the number of the iteration increased. Confusion Matrix for network is presented at Figure 4.
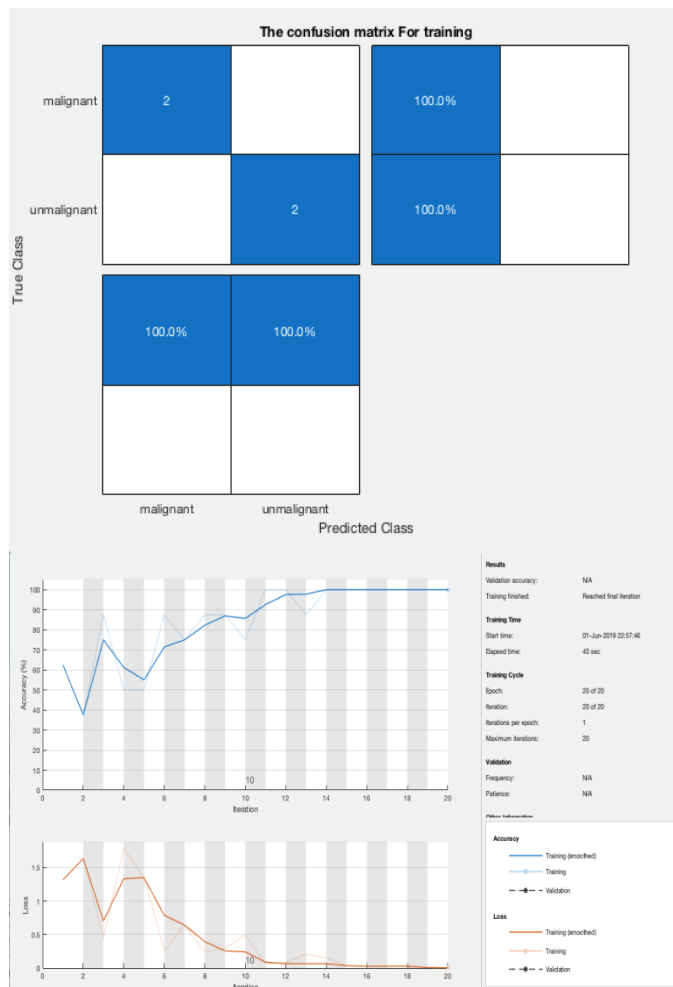
Figure 4: Training results of network

performance gives highest accuracy value of 100% whatever number of iteration after that.

As a result, thyroid Cancer can be diagnosed by using CNN that can give best result with less times consumed with higher accuracy.

REFERENCES

[1]   Fukushima, K. J. B. c., 1980, Neocognitron: A self-organizing neural network model for a mechanism of pattern recognition unaffected by shift in position, 36 (4), 193-202.

[2]   Low, L.-S. A., Maddage, N. C., Lech, M., Sheeber, L. ve Allen, N., 2009, Content based clinical depression detection in adolescents, *2009 17th European Signal Processing Conference*, 2362-2366.

[3]   LeCun, Y., Bottou, L., Bengio, Y. ve Haffner, P. J. P. o. t. I., 1998, Gradient-based learning applied to document recognition, 86 (11), 2278-2324.

[4]   Krizhevsky, A., Sutskever, I. ve Hinton, G. E., 2012, Imagenet classification with deep convolutional neural networks, *Advances in neural information processing systems*, 1097-1105.

[5]   Russakovsky, O., Deng, J., Su, H., Krause, J., Satheesh, S., Ma, S., Huang, Z., Karpathy, A., Khosla, A. ve Bernstein, M. J. I. j. o. c. v., 2015, Imagenet large scale visual recognition challenge, 115 (3), 211-252.

[6]   Bengio, Y., Courville, A., Vincent, P. J. I. t. o. p. a. ve intelligence, m., 2013, Representation learning: A review and new perspectives, 35 (8), 1798-1828.

[7]   Ravì, D., Wong, C., Deligianni, F., Berthelot, M., Andreu-Perez, J., Lo, B., Yang, G.-Z. J. I. j. o. b. ve informatics, h., 2017, Deep learning for health informatics, 21 (1), 4-21.

[8]   Şeker, A., Diri, B. ve Balık, H. H. J. G. M. B. D., 2017, Derin Öğrenme Yöntemleri ve Uygulamaları Hakkında Bir İnceleme, 3 (3), 47-64.

[9] https://wilmingtonendo.com/

[10] http://www.image-net.org/

IV. CONCLUSION

The information systems are effectively used in many scientific studies. Particularly, Convolutional Neural Network (CNN) is separated with the advantages they provided in the artificial intelligence and deep learning systems. We suggest usage of transfer learning technique (pre-training model) for classifying thyroid cancer. It was found that the algorithm path shows 3 stages of performance. The first stage is fluctuating between 1-5 iterations. This stage shows unstable performance, because of start training and extracted feature. The second stage shows linear increasing in performance between 5-14 iterations. The last stage is between 14-20 iterations and this stage shows a steady stage at which the

Use of PMSM in Electric Mobility Scooter Propulsion

F. A. KAZAN[1] and R. AKKAYA[2]

[1]Konya Technical University, Konya/Turkey, fakazan@ktun.edu.tr
[2]Konya Technical University, Konya/Turkey, rakkaya@ktun.edu.tr

Abstract –In battery-operated wheelchairs are commonly used permanent magnet direct current (PMDC) motors. However brushless motors are more efficient than brushed motors. Therefore, in this study, PMDC motor was removed in electric mobility scooter type disabled vehicle which is used as a test vehicle and permanent magnet synchronous motor (PMSM) was mounted. The PMSM was driven by a sensorless field-oriented control method. The vehicle was been successful in the outdoor tests. So, PMSM was used for the first time in a disabled vehicle with a shaft system.

Keywords – Disabled vehicle, battery-operated wheelchair, electric mobility scooter, PMDC motor, PMSM.

I. INTRODUCTION

People who lose their physical abilities to a certain degree due to disturbances in the skeleton, muscle or nervous system for any reason, and therefore need protection, rehabilitation and care are called physically disabled people.

Wheelchairs are the biggest helpers of physically disabled people in their daily activities. Wheelchairs are divided into 3 according to the source of movement energy. These are hand-operated (manual), battery-operated (electric powered) and hybrid disabled vehicles.

Hand-operated wheelchairs are used by physically handicapped people whose hands are healthy but their legs are disabled. These people are not recommended to use battery-operated vehicles. The reason is to prevent the muscles from melting by enabling the upper muscle group.

Physically disabled people who have a physical disability that cannot move the wheelchair with their hands or who need to go long distances use a battery-operated wheelchair. The movement energy of such wheelchairs is provided by the electric motor(s) fed by the battery.

In battery-operated classical wheelchairs are used permanent magnet direct current (PMDC) motors. These motors have a good speed-torque characteristic. However, since their structures contain brushes and collectors, failure probability is more and require periodic maintenance. Despite all these drawbacks, PMDC motors are the most preferred motor type in these vehicles because their speed and direction control is very easy and allow regenerative braking. The speed of the motor can be easily controlled using PWM. The motors are produced in a wide range of powers, such as 240 W, 300 W, 350 W, 400 W, 450 W, 750 W and 1500 W, depending on the type of disabled vehicle. Two low-power motors are used in standard battery-operated wheelchairs. On the other hand, there is a high-power motor in the electric mobility scooter that has a shaft system.

In wheelchairs produced in Turkey, it was determined that the PMDC motor widely used. However, it is known that the efficiency of brushed DC motors is lower than brushless AC motors of the same power. In addition, the need for compulsory maintenance due to the brush and collector in their structures is a major disadvantage for disabled users.

In the literature review, it is possible to come across studies on the use of permanent magnet synchronous motor (PMSM) in disabled vehicles. For example, there are publications where PMSM is used in disabled vehicles with two-motor [1] or PMSM is used as an in-wheel (hub) motor [2]. When scanned academic studies in Turkey it can be found in different studies related to electric wheelchairs. For example, control with head movements [3], the design of the electric motor to eliminate the gearbox [4], the collection of data such as speed, battery and temperature [5]… However, no study has been found on the use of PMSM in disabled vehicles with shaft system such as electric mobility scooter.

In this study, the PMDC motor was removed from electric scooter type disabled vehicle and the PMSM was mounted instead. Then the sensorless control of the PMSM was performed. Thus, PMSM was used for the first time in a disabled vehicle with a shaft system.

II. TYPES OF ELECTRIC POWERED WHEELCHAIRS

A wide variety of disabled vehicles is being produced for disabled people who want to use a disabled vehicle as far as their financial situation allows.

The first model that comes to mind when talking about a powered wheelchair is the standard electric-powered wheelchair in Figure 1. Therefore, the standard expression is not used when referring to these models in daily life. Two motors are used in the propulsion of these vehicles which are produced for use in indoor and outdoor environments.

Figure 1: The standard electric-powered wheelchair.

The electric mobility scooter type vehicles, which will also be used in this study, are mostly designed for outdoor use. For this reason, details such as headlamps, direction indicators and rear-view mirrors that will be needed during outdoor use are available on these vehicles. These vehicles use one but more powerful motor, unlike the standard battery-operated wheelchairs. In 3 and 4 wheels models, the direction of the vehicle is determined by the handlebar. Therefore, it is easier to use and control than a standard power wheelchair. 3 and 4 wheels models of electric mobility scooters are shown in Figure 2.

Figure 2: 3 and 4 wheels electric mobility scooters.

Physically disabled people meet numerous difficulties in their daily lives. One of these problems is to reach a high point. In order to overcome such problems, battery-operated wheelchairs which lift the user to his feet have been produced.

Stairs and high pavements are other major problems faced by physically disabled people. Although ramps are being designed for wheelchairs at building entrances, it is a known fact that many ramps are not suitable for use. Likewise, to get off at any point of the sidewalk for a physically disabled person who moves on a high sidewalk with his wheelchair may not always be possible. Academic studies aimed at solving these problems of the users [6-9] resulted. Nowadays, the disabled vehicles which can climb up and down the stairs have become commercially manufactured.

Hybrid types of wheelchairs have features of both manual and electric-powered wheelchairs and are designed as light as possible. Just like a standard battery-operated wheelchair, it has an electric motor and battery. However, this model is not suitable for use in continuous battery-operated wheelchair mode. Because the battery used in the vehicle is very small compared to the standard battery-operated wheelchair. The advantage of these models is that it provides convenience to the user who is tired or has to climb a ramp.

III. Selection of The Most Suitable Motor for Electric Mobility Scooters

Although there is a wide choice for the users, one of the biggest expectations of the users is undoubted that the vehicle travels as far as possible with a single charge. This can be achieved in two different ways. The first option is to use batteries with higher Ampere-hour (Ah) values. However, choosing this option has two disadvantages for the user. The first disadvantage is the purchase cost. Because the price of the battery increases with the Ah value. The second disadvantage is that the charging time of the high capacity battery is long. Another way to achieve far-range is to use

more efficient motors in the vehicle.

The motor used in a wheelchair should operate at an average efficiency of 75% [4]. To achieve this, motors are designed which disable the gear unit and are integrated into the wheel. Brushless dc (BLDC) motors are used in this structure called hub (in-wheel) motor. There are hub motors in different sizes and shapes suitable for use in a battery-operated wheelchair. The internal structure of hub motors and their application to different wheels are shown in Figure 3.

Figure 3: The internal structure of the hub motors and their application to different wheels.

PMDC motors are used in the propulsion of traditional battery-operated wheelchairs. However, the efficiency of these motors is lower than BLDC and PMSM. Therefore, it is more appropriate to use BLDC or PMSM instead of PMDC motor in the propulsion of these vehicles. It is seen in the literature review that high power density is an important criterion in electric vehicles [10, 11]. Consequently, this criterion will also be important for battery-operated disabled vehicles which have to be small and compact.

In a study made by analyzing the data of more than 100 motors [12], brushed DC, BLDC, PMSM and stepper motors were compared in detail. The graph of the power density plotted in light of the obtained data is shown in Figure 4. Figure 4 shows that PMSM is the motor with the highest power density in motors over 400 W.
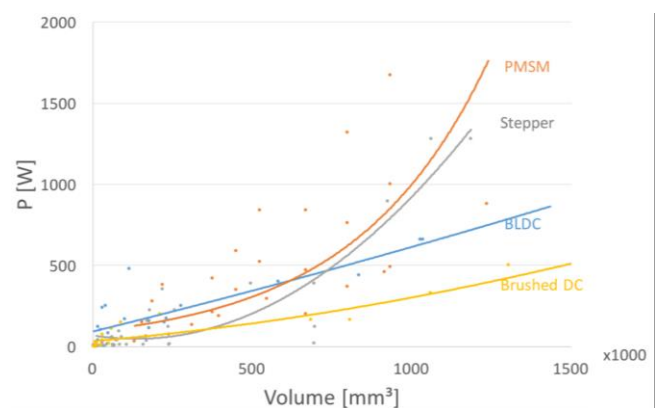
Figure 4: Power densities of brushed DC, BLDC, PMSM and stepper motors [12].

In the corresponding study, maximum motor acceleration is calculated by dividing maximum motor torque by rotor inertia. Nominal power-acceleration graphs of the motors are given in Figure 5. When the changes in the figure are examined, it is seen that the best acceleration for powers above approximately 600 W is in PMSM. PMSMs have also provided superiority in

the acceleration of motors. Therefore, considering the maximum acceleration, which is an important parameter for dynamic applications, it is more accurate to use PMSM instead of brushed DC or BLDC. Hence, PMSM will be used instead of the PMDC motor in the propulsion of the test vehicle.
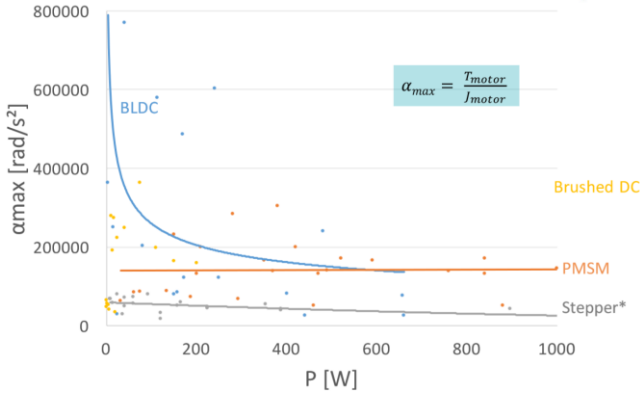
Figure 5: Acceleration in brushed DC, BLDC, PMSM and stepper motors [12].

IV. MATHEMATICAL MODEL OF PMSM

Instantaneous value equation of the voltage applied to the PMSM can be obtained in matrix form as in (1).

$$
\begin{bmatrix} v_a \\ v_b \\ v_c \end{bmatrix} = \begin{bmatrix} R_a & 0 & 0 \\ 0 & R_b & 0 \\ 0 & 0 & R_c \end{bmatrix} \begin{bmatrix} i_a \\ i_b \\ i_c \end{bmatrix} + \begin{bmatrix} L_{aa} & L_{ab} & L_{ac} \\ L_{ba} & L_{bb} & L_{bc} \\ L_{ca} & L_{cb} & L_{cc} \end{bmatrix} \frac{d}{dt} \begin{bmatrix} i_a \\ i_b \\ i_c \end{bmatrix} + \begin{bmatrix} e_a \\ e_b \\ e_c \end{bmatrix}
\tag{1}
$$

In (1), v_a, v_b and v_c are the instantaneous values of the phase voltage applied to the stator winding. R_a, R_b and R_c are the resistance of the phase winding. i_a, i_b and i_c are the instantaneous values of stator phase currents. L_{aa}, L_{bb} and L_{cc} are the total inductance of the phase windings. L_{ab}, L_{ba}, L_{bc}, L_{cb}, L_{ca} and L_{ac} are the mutual inductance between phase windings. e_a, e_b and e_c are the back emf that is induced in the stator winding by permanent magnet rotor.

R_a, R_b and R_c resistances are equal. So these resistances can be shown as R. When the back emf and inductance expressions in (1) are written in magnetic flux type, (2) is obtained. ψ_a, ψ_b and ψ_c are the flux of the phase winding.

$$
\begin{bmatrix} v_a \\ v_b \\ v_c \end{bmatrix} = \begin{bmatrix} R & 0 & 0 \\ 0 & R & 0 \\ 0 & 0 & R \end{bmatrix} \begin{bmatrix} i_a \\ i_b \\ i_c \end{bmatrix} + \frac{d}{dt} \begin{bmatrix} \psi_a \\ \psi_b \\ \psi_c \end{bmatrix}
\tag{2}
$$

Equation (2) can be written in rotor reference frame using dual axis theory as in (3) [1]. In (3), v_d and v_q symbolize the d-q components of the input voltage. i_d and i_q are the d-q components of the phase currents. R is the resistance of the stator winding. L_d and L_q are d-q axis inductances. ω_r is angular speed of the motor. Finally ψ_d and ψ_q are d-q axis magnetic fluxes.

$$
\begin{bmatrix} v_d \\ v_q \end{bmatrix} = \begin{bmatrix} R & 0 \\ 0 & R \end{bmatrix} \begin{bmatrix} i_d \\ i_q \end{bmatrix} + \frac{d}{dt} \begin{bmatrix} L_d & 0 \\ 0 & L_q \end{bmatrix} \begin{bmatrix} i_d \\ i_q \end{bmatrix} + \omega_r \begin{bmatrix} -\psi_d \\ \psi_q \end{bmatrix}
\tag{3}
$$

d-q axis magnetic fluxes of the motor were given in (4). The expression of ψ_m in (4) is the magnetic flux occurred due to the permanent magnet.

$$
\begin{bmatrix} \psi_d \\ \psi_q \end{bmatrix} = \begin{bmatrix} L_d & 0 \\ 0 & L_q \end{bmatrix} \begin{bmatrix} i_d \\ i_q \end{bmatrix} + \begin{bmatrix} \psi_m \\ 0 \end{bmatrix}
\tag{4}
$$

If (3) is written in state space form, (5) is achieved.

$$
\frac{d}{dt}\begin{bmatrix} i_d \\ i_q \end{bmatrix} = \left\{ \begin{bmatrix} v_d \\ v_q \end{bmatrix} - \begin{bmatrix} R & 0 \\ 0 & R \end{bmatrix} \begin{bmatrix} i_d \\ i_q \end{bmatrix} + \omega_r \begin{bmatrix} 0 & L_q \\ -L_d & 0 \end{bmatrix} \begin{bmatrix} i_d \\ i_q \end{bmatrix} - \omega_r \begin{bmatrix} 0 \\ \psi_m \end{bmatrix} \right\} \begin{bmatrix} \frac{1}{L_d} & 0 \\ 0 & \frac{1}{L_q} \end{bmatrix}
\tag{5}
$$

Electromagnetic torque (T_e) produced by the motor is given in (6). The expression of P in (6) is the number of pole pairs of the motor.

$$
T_e = \frac{3}{2} \cdot P \cdot \left[\psi_m \cdot i_q + \left(L_d - L_q \right) \cdot i_d \cdot i_q \right]
\tag{6}
$$

When looking at (6) it is seen that the torque that the motor produces depends on d-q axis currents. When this equation is rewritten considering the equality of d-q axis inductances [13] in surface mounted PMSM, (7) is obtained.

$$
T_e = \frac{3}{2} \cdot P \cdot \psi_m \cdot i_q
\tag{7}
$$

When (7) is examined it is seen that torque control in motor depends on q axis current. The angular speed (ω_r) and position (θ_r) expressions of the rotor are given in (8) and (9) respectively.

$$
\frac{d}{dt}\omega_r = \frac{T_e - T_l - B \cdot \omega_r}{J}
\tag{8}
$$

$$
\frac{d}{dt}\theta_r = \omega_r
\tag{9}
$$

When (7) is examined it is seen that electromagnetic torque produced by the motor can be controlled depending upon q axis current, number of poles and magnet flux. The number of poles is a parameter that cannot be changed after the motor is produced. Only q axis current remains as a control parameter because magnet flux is considered as stable [14].

V. CONTROL OF PMSM

As is known, control methods are divided into two main groups according to the controlled parameter. If only the magnitude of the parameter is controlled, this method is called the scalar control method. If the direction of the parameter is also controlled together with the magnitude, this method is called the vector control method.

The scalar control method is an open-loop method. In this method, current and torque control is not possible. The amplitude and frequency of the voltage applied to the stator winding instead of the torque are changed according to a certain V / f ratio. When the motor speed needs to be changed, the frequency of the voltage is changed. Dynamic performance

is poor because it is an open loop method. Since torque control cannot be performed in this method, motors are more affected by load changes compared to other methods [15]. For this reason, it is not appropriate to use this method to control the PMSM to be mounted in a disabled vehicle.

In the vector control method, torque can be controlled even in low-speed zones, including zero speed. It is divided into two as field weakening control (FWC) and field-oriented control (FOC).

FWC is used when the motor will be operated above the rated speed. Since a magnetic field is produced in the opposite direction to the magnetic field produced by the permanent magnet, there is a demagnetization risk of the permanent magnets. However, this risk can be minimized by using permanent magnets with large coercive force. In this method, maximum torque can be generated and motors can work at high speeds. But since there is a speed limit for the disabled vehicles, it is not necessary to run the motor above the rated speed. Therefore, it is not appropriate to use this method in the control of the PMSM to be mounted in the disabled vehicle.

FOC is particularly suitable for motors with symmetrical magnetic circuits. Therefore, it is widely used in surface mounted PMSMs. Since torque is controlled by the current in the vector control system, it is natural to use a current-controlled inverter as the driver in this system. However, a voltage command can be generated by comparing the reference current in the control system with the measured current and passing the error through a PI controller.

The control is performed by converting the stator currents to the rotating d-q axis in the vector control method. Because of the axis transformations, 3 phase stator currents of the motor and rotor position information are needed. At PMSMs, which have a symmetrical magnetic circuit and surface-mounted magnets, are used mostly FOC. FWC is preferred at PMSMs whose internal magnetic circuit is not symmetrical.

The fact that the PMSM to be mounted on the disabled vehicle is surface-mounted and that the motor will not run much above the rated speed has led to the choice of FOC as the control method.

The PMSM to be mounted on the disabled vehicle has a resolver as speed feedback. However, in order to reduce the cost of the motor commercially, the resolver was not taken into account and sensorless control was preferred. In sensorless control, different methods are used to determine the rotor position. In this study, the back-emf model was preferred. Since no innovation has been introduced in the control method, the details of the software have not presented here.

VI. Montaging of The PMSM to The electric mobility scooter and testing of the vehicle.

The test vehicle to be used in this study is seen in Figure 6. The vehicle is equipped with a PMDC motor with 750 W, 3750 rpm.

Figure 6: The electric mobility scooter to which PMSM will be mounted.

The fact that the gearbox on the vehicle is made according to the PMDC motor prevented the PMSM from being mounted to the gearbox. The flange is designed to allow the PMSM to be mounted on the gear unit, which enables the mounting of the PMSM on the gear unit. The picture of the disabled vehicle with PMDC and PMSM is shown in Figure 8.
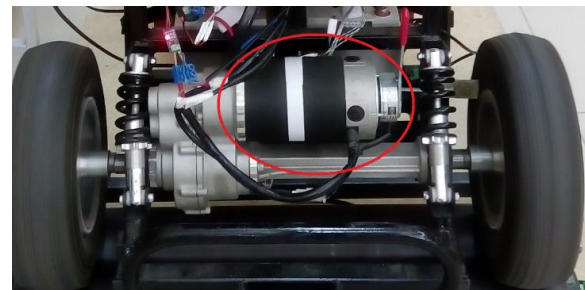
(a)

(b)
Figure 8: The case of the disabled vehicle before and after montaging of the PMSM (a) with PMDC motor (b) with PMSM.

The PMSM, which mounted to the disabled vehicle, is an 8-pole motor manufactured by Lenze with the code MCS06I41L. The motor has rated values of 640 W, 4050 rpm, 2.9 A, 175 V, 270 Hz and its efficiency is 81%. When these values are examined, it is seen that PMDC motor and PMSM are not equal power. This is due to the fact that no PMSM with the same power as on the vehicle was found. Therefore, the motor closest to it was used.

To drive the PMSM has been used the dsPICDEM MCHV-2 development board produced by Microchip. This board is designed to allow rapid development and implementation of a wide range of motor control applications using dsPIC. Thanks to the board, BLDC, PMSM and asynchronous motors can be controlled with or without sensor. The program for the board is written in the MPLAB X IDE and is installed on the board. In this way, the operating characteristics of the motors can be

determined by the user. The 220 V_{AC} voltage required for the operation of the board was obtained by using a 1.5 kW inverter that converts 24 V_{DC} to 220 V_{AC}.

Different speed values have been reached in the driven motor using corresponding hardware and control method. In the oscilloscope image in Figure 9, the variation of the phase-to-phase voltage applied to the stator windings with a frequency of approximately 312.5 Hz is given. As can be seen from Figure 9, the speed of the PMSM has achieved to over 4500 rpm. Figure 10 shows that the disabled vehicle is driven by PMSM. A picture taken during the outdoor test of the vehicle is also given in Figure 11.
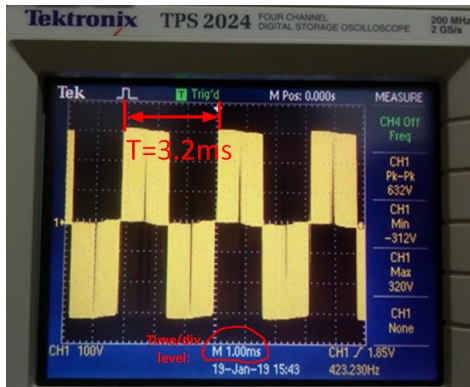
Figure 9: The phase-to-phase voltage of the PMSM.

Figure 10: Propulsion of the disabled vehicle by using the PMSM.

Figure 11: Testing the disabled vehicle which PMSM was mounted.

VII. CONCLUSION

In this study, PMDC motor was removed in electric mobility scooter type disabled vehicle which is used as a test vehicle and PMSM was mounted. The PMSM was driven by a sensorless field-oriented control method. It was seen that the disabled vehicle with PMSM was been successful in outdoor tests. However, in order to make a healthy comparison, a test

system should be designed in which these vehicles can be tested. In the system to be designed, data such as current, voltage and speed of the motor should be collected. Then, the energy consumption values per km should be compared and it should be determined by numerical data which motor driven disabled vehicle is more efficient.

REFERENCES

[1] F. P. Lopes, P. S. Oliveira, L. P. Reis, and R. E. Araujo, "An electric wheelchair as a tool for motivating students in power electronics," in *Power Electronics, Electrical Drives, Automation and Motion, 2008. SPEEDAM 2008. International Symposium on*, 2008, pp. 481-485.
[2] Y.-K. Kim, Y.-H. Cho, N.-C. Park, S.-H. Kim, and H.-S. Mok, "In-Wheel motor drive system using 2-phase PMSM," in *Power Electronics and Motion Control Conference, 2009. IPEMC'09. IEEE 6th International*, 2009, pp. 1875-1879.
[3] Ö. Deniz, A. A. Süzen, and A. Çetin, "Kafa Hareketleri İle Kontrol Edilebilen Tekerlekli Sandalye," in *4. Ulusal Meslek Yüksekokulları Sosyal Ve Teknik Bilimler Kongresi* Burdur, Türkiye, 2017.
[4] A. Akpunar, "Ergonomik Bir Elektrikli Tekerlekli Sandalye İçin Dişlisiz Ve Direkt Sürmeli Bir Elektrik Motor Tasarımı " Yüksek lisans Yüksek Lisans, Fen Bilimleri Enstitüsü, Muğla Üniversitesi, Muğla, 2007.
[5] A. Doruk, H. N. Buluş, A. Moralar, S. Çelen, and E. Uzun, "Tracing of Velocity, Battery and Temperature Values of Electric Vehicles Using Physical Programing Platforms," *Ejovoc (Electronic Journal of Vocational Colleges),* vol. 5, pp. 48-56, 2015.
[6] W. Tao, Y. Jia, T. Liu, J. Yi, H. Wang, and Y. Inoue, "A novel wheel-track hybrid electric powered wheelchair for stairs climbing," *Journal of Advanced Mechanical Design, Systems, and Manufacturing,* vol. 10, pp. JAMDSM0060-JAMDSM0060, 2016.
[7] G. Quaglia, W. Franco, and R. Oderio, "Wheelchair. q, a mechanical concept for a stair climbing wheelchair," in *2009 IEEE International Conference on Robotics and Biomimetics (ROBIO)*, 2009, pp. 800-805.
[8] M. J. Lawn and T. Ishimatsu, "Modeling of a stair-climbing wheelchair mechanism with high single-step capability," *IEEE Transactions on Neural systems and rehabilitation engineering,* vol. 11, pp. 323-332, 2003.
[9] S. Yu, T. Wang, X. Li, C. Yao, Z. Wang, and D. Zhi, "Configuration and tip-over stability analysis for stair-climbing of a new-style wheelchair robot," in *2010 IEEE International Conference on Mechatronics and Automation*, 2010, pp. 1387-1392.
[10] Z.-Q. Zhu and D. Howe, "Electrical machines and drives for electric, hybrid, and fuel cell vehicles," *Proceedings of the IEEE,* vol. 95, pp. 746-765, 2007.
[11] M. Zeraoulia, M. E. H. Benbouzid, and D. Diallo, "Electric motor drive selection issues for HEV propulsion systems: A comparative study," *IEEE Transactions on Vehicular technology,* vol. 55, pp. 1756-1764, 2006.
[12] S. Derammelaere, M. Haemers, J. De Viaene, F. Verbelen, and K. Stockman, "A quantitative comparison between BLDC, PMSM, Brushed DC and Stepping Motor Technologies," in *2016 19th International Conference on Electrical Machines and Systems (ICEMS)*, 2016, pp. 1-5.
[13] S. Juming, Z. Ming, and S. Yanmin, "Study of optimal efficient control of permanent magnet synchronous motor," in *Electrical Machines and Systems, 2003. ICEMS 2003. Sixth International Conference on*, 2003, pp. 41-44.
[14] O. Bilgin and F. A. Kazan, "The effect of magnet temperature on speed, current and torque in PMSMs," in *2016 XXII International Conference on Electrical Machines (ICEM)*, 2016, pp. 2080-2085.
[15] J.-I. Itoh, N. Nomura, and H. Ohsawa, "A comparison between V/f control and position-sensorless vector control for the permanent magnet synchronous motor," in *Proceedings of the Power Conversion Conference-Osaka 2002 (Cat. No. 02TH8579)*, 2002, pp. 1310-1315.

DESIGN AND COST of SPEED TRAIN SYSTEM WHICH GET ENERGY FROM SOLAR

M.Sertsöz

Eskişehir Technical University, Transportation Vocational School, Eskişehir, Turkey

Abstract-**The utilization rate of solar energy, which we know as a clean energy source, using in rail systems is a very popular issue. Because all possible solutions should be considered in order to meet increasing energy and transportation needs.**

In this study, it is assumed that the Ankara-Istanbul YHT train is operated entirely with solar energy except of the loss of transformers and other additional equipment. As a result of this assumption, the number of needed panels are calculated by SOLIMPLEX program and how much time this system could pay for itself are calculated according to the found number of these panels. In addition to these, CO2 emission values of the system are given and the environmental benefit is mentioned. Finally, the ways of reducing the cost of this system are mentioned and the study is finished with various recommendations.

Keywords **– Railway, Transportation, Solar Energy, Energy Efficiency, CO₂ Emission.**

I. INTRODUCTION

The sections of the study will be as follows. Firstly, this introduction section will give the information about solar energy and ways of benefiting from this energy . The second section, a literature section which describes using solar energy in the rail system, will be given. Then the third part which contains detailed of this study will be given. Finally, the results and recommendations will be given.

Solar Irradition

The sun is a necessary source in photovoltaic power systems that convert solar energy into electrical energy. This source of the sun, with the phenomenon called fusion, produces a great energy resulting from the loss of mass by the conversion of four hydrogen atmones into helium. This radiation energy emitted by the sun is 3,6x1026 W, assuming a mass of 4x109 kg per second. This energy is propagated in electromagnetic waves into energy packs, also called photons. In unit time of solar radiation, the unit quantity per unit surface is called radiation intensity or radiation power (W/m^2).

However, some amount of this radiation is absorbed or emitted by some particles in the atmosphere as it arrives. The incoming radiation is divided into three as direct radiation, diffuse radiation and reflected radiation. The sum of direct and diffuse radiation is called global radiation. Total radiation is the sum of these three radiation forms.

$$I_{GLOBAL} = I_{DIRECT} + I_{DIFFUSE} \qquad (1)$$

$$I_{TOTAL} = I_{GLOBAL} + I_{REFLECTED} \qquad (2)$$

I_{DIRECT}: Direct Irradition

$I_{DIFFUSE}$: Diffuse Irradition

I_{GLOBAL}: Global Irradition

$I_{REFLECTED}$: Reflected Irradition

I_{TOTAL}: Total Irradition
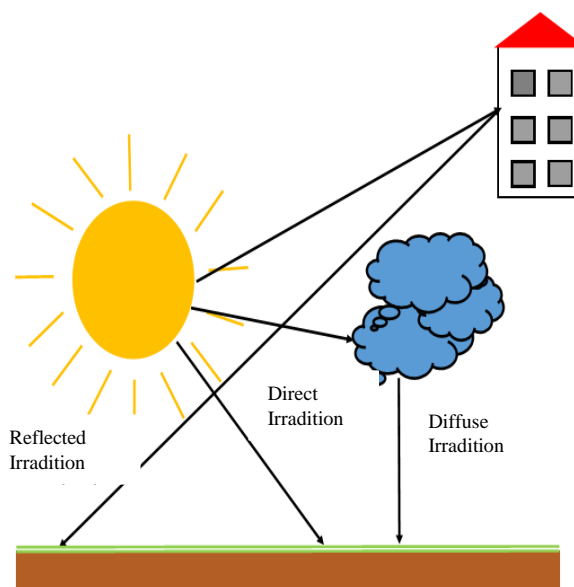
Figure 1. Solar Radiaton Types [1]

It is possible to express the maximum power obtained from solar panels as follows [2], [3], [4]:

P(t) = ηAG(t)(1 − 0. 005(T(t) − 25)) (4.55)

η, siystem efficiency;

A, total panel area (m^2);

H, Photoelectric conversion efficiency of PV array (%);

G (t), time-varying global solar radiation value (Watt / m^2);

T (t), is the ambient temperature value at time t (°C).

However, in this study, the Solimpleks program, which makes these calculations by region, is utilized. Solimpleks A.Ş was established in 2001 and manufactures Hybrid Panels that produce high efficiency Thermal Solar Collector, Thermosiphonic System, Hygienic Buffer Boilers, Photovoltaic System, Heat Pump Boiler, both electricity and hot water simultaneously. They also have their own free-use solar energy calculation tools [5].

The use of solar panels on the roof of transportation vehicles' is quite logical. A table is given below in this issue.

Table 1. Comparison of Different Vehicles According to Solar Panel Settlement Areas [6]

City bus	Alan, m2
Prius hybridcar	4
Peugeot 206 car	2,8
City bus	10
Yacht Hunter-27	15,5
Launch Bekas yacht	29
Oil tanker T2	4000
Train passeng.10 vag.	630
Train cargo	3000
Electr. train 10 vag.	750

As seen in Table 1, the area of oil tankers and trains is quite wide. However, unfortunately, it is not enough to meet all the power in vehicles that require huge powers such as high speed train. So, high speed trains need more solar panel areas.

II. LITERATURE REVIEW

3.3 GWh / year solar power plant installed on a railway tunnel near Antwerp (Belgium) [7]; Although there is not a very sunny climate (900 hours / year), the return on investments is expected to occur within 9 years. In India, solar cells were installed on railway vehicles for electricity consumption in ventilation. In Hungary, Vili that is a narrow-scale tourist ray is operated with 9.9 m^2 solar panels [8]. PV batteries are used in Switzerland to get power for rail traffic safety systems (100 % of railways are working with electricty). Solar cells are also available in airports in many countries and many projects have been initiated to integrate them with highway surface. If the full terrain strip is covered with PV modules, the railway

actually becomes an addition to such power plants, so the return of investment is considered less than 10 years for public land PV plants and several decades for railways [9].

The estimated price of the railway car that includes the solar power generation system will be 4% higher than the price of the current car. Investment in this system will be recovered in 2-3 years. Soon, aim of support of financing research and development will optimize this plan. Since the annual diesel consumption will be around 90,804 liters and considering the total number of trains running in the country, the amount of diesel fuel to be saved is large. This will not only reduce foreign oil imports, but will also be a very useful precaution to reduce global CO_2 emissions. The emission that can be avoided every year is about 239,12 tons [10].

In Italy, amorphous silicon modules were installed on five passenger cars, two locomotives and three freight cars [11]. In 2010, TER-SNCF, France's state-owned railways, tested a Diesel Multi-Unit (DMU) equipped with thin film CIGS (Copper Indium Gallium Selenite) SPV modules. The roof-mounted SPV system with a 990 Wp capacity partially provided power for the electric lighting system inside the DMU [12]. In 2011, Indian Railways installed SPV modules with a capacity of 1 kWp on the roof of trains in Pathankot, Punjab, India.

The SPV modules can meet power an electrical load for 420 W in this study. The Kalka-Simla Mountain Railway made a similar attempt and provided power to the 6 amp bulb [13]. These tests were carried out for narrow railway cars running at a maximum speed of 40 km/h. Although experiments on the establishment of the SPV system on the train have been successful, there is no scientific data available for further research and development in public areas. In 2013, a similar study in Iran showed that the SPV system could provide 74% of the power requirement of a passenger car in hot months and 25% in cold months. The maximum return of the SPV system was increased by 63.7 kWh and annual CO_2 emissions were reduced by 37 tons [14].

Indian Railways, one of the world's largest railway networks, operates about 12,000 trains per day [15]. It is also one of the largest diesel consumers in the world and it has an annual consumption of 2.7 billion liters [16]. Therefore, efforts have being made by Indian Railways to reduce fossil fuel consumption and adopt environmentally friendly technologies [17]. Solar energy can find a wide range of applications in the railways sector, especially in tropical countries. Indian Railways operates a total of 63511 railway cars, including both traditional railway cars and Linke Hofmann Busch (LHB) railway cars [18]. Most of these cars are exposed to sunlight throughout the year. This provides the opportunity to explore the possibility of utilizing solar energy nationwide to Indian Railways. This will reduce the diesel consumption of the End-Generation (EOG) system, which is the power source of the electrical load in LHB cars [19]. The statistical model developed to estimate the power output of the car per unit roof area [20]

enables the assessment of technical feasibility and economic of the Indian Railways before installing SPV modules on sun-supported cars operating on different routes in the country.

III. MATERIAL AND METHODS

Calculating of Solar Panel Data

Details about the Solimpleks program have been given before (see section 1.1). Desired power (9.474.816 kW); It is in order to meet the total need of YHT which makes ten times daily between Bozüyük-Polatlı, that is within Eskişehir province boundaries. This study is about to meet desired power by solar.
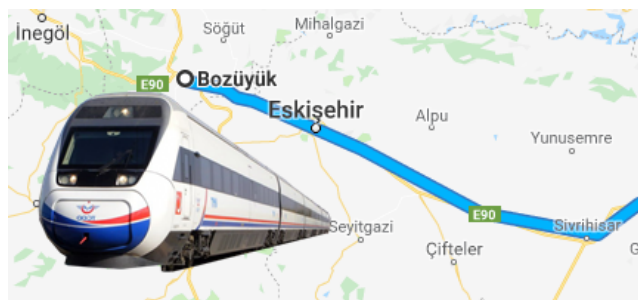
Figure 2. The route used by YHT between Bozüyük and Polatlı [21]

Results and figures are given below:
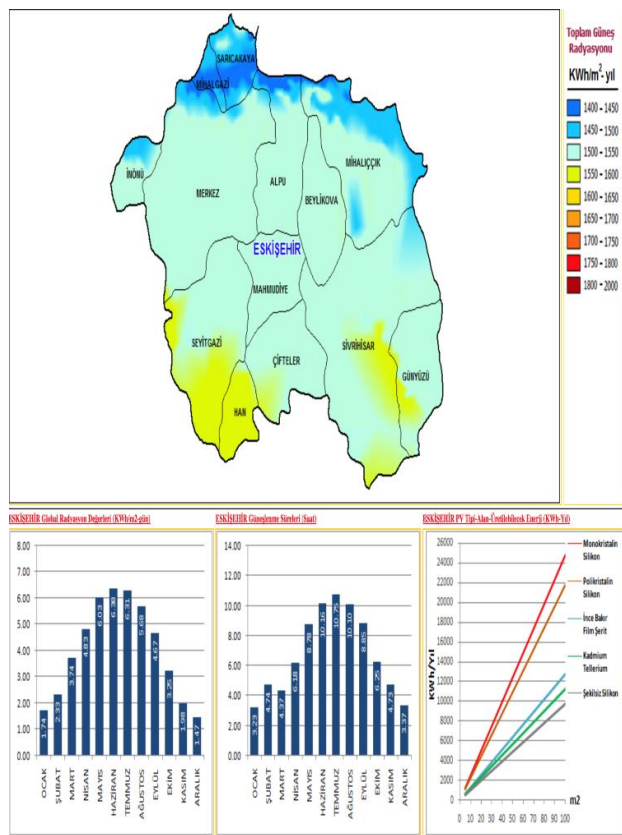
Figure 3. Solar Data of Eskişehir Province

Table 2. Solar Panel Specifications of Power Consumption Between Bozüyük-Polatlı for YHT

Weighted Usage Period	All Year Long
Panel Company	Panasonic (325W)
Panel Number	3967
Area to be Installed – Sloping Roof	8301 m^2
Area to be Installed – Flat Roof	16602 m^2
Installed Power of System	1289 Kwp

* Excluding Transformer and Sub-Consumption Losses

Installation Cost Calculation

Solar Panel Cost:

3967 number x 1930,94 TL [22] =7.660.038 TL

Inverter Cost:

13 number x150066,55 TL(100 kW inverter)=1.950.865 TL

Total Cost:

9.610.903 TL

In this study, all other costs (installation, labor cost, project cost, cabling, etc.) are not calculated. Because these parts are considered to be government-funded, the cost will be as low as possible and the calculation will not be very valid.

Starting from July 1 2019, transmission system users was determined as 0.7024 kr/kWh (EPDK) for the unit price of one-time work place energy price. In this case, the annual cost of electricity:

0,7024 kr/kWh x 9.474.816 kW = 6.655.110,76 TL

As a result, this system will start to move to profit after a short period of 1.44 years when some expenses that above mentioned are neglected.

Environmental pollution:

1054 ton-CO_2/GWh (lignite) x 9.474816 GWh = 9986 ton CO_2

23 ton-CO_2/GWh (solar) x 9.474816 GWh = 218 ton CO_2

IV. RESULT and DISCUSSION

This study was carried out with the assumption that the energy consumption of Ankara-Istanbul YHT fully benefited from solar energy. The results are as follows:

• If the system will be installed to sloping land, solar panels need 83 km^2; if the system will be installed to flat land, solar panels need 166 km^2; (For better understanding of the area: İstanbul-Pendik district is190 km^2)

• Installation, labor cost, project cost, wiring, loss of transformer, fraying shares, etc. were neglected.

• The system pays for itself in 1.44 years.

• Considering that the electricity is generated from lignite, it will produce 9986 tons of CO_2 per year on average, and will produce only 218 tons of CO_2 with this system. That is, it will have caused almost 50 times less damage to the environment.

The development of such systems is crucial for increasing energy demand and environmental pollution. The only problem is the space required for solar panels. This is expected to be overcome with the size that will get smaller and increase efficiency of the panels with the developments in power electronics.

Besides, if it will meet only amount of the power that YHT needs; it is possible to define optimization problems that will make both the need area is small and the getting power is high for solar panels. This is also planned to be carried out further studies.

REFERENCES

1. Sertsöz, M., *Raylı Sistemlerde Güneş Enerjisi Destekli Yenilikçi Enerji Modellemesi, Optimizasyonu Ve Analizi*, Doktora Tezi, Bilecik Şeyh Edebali Üniversitesi, 2018.
2. Chen, S.X., Gooi, H.B., Wang, M., *Sizing of Energy Storage For Microgrid*, IEEE Trans. Smart Grid, 3: 142–151 (2012).
3. Tao, C., Shanxu, D., Changsong, C., *Forecasting Power Output for Grid-Connected Photovoltaic Power System without using Solar Radiation Measurement*, In Proceedings of the 2010 2nd IEEE International Symposium on Power Electronics for Distributed Generation Systems (PEDG), 16(18): 773–777, Hefei, China, (2010).
4. Basaran Filik, Ü., Filik, T., Gerek, Ö.N., *A Hysteresis Model for Fixed and Sun Tracking Solar PV Power Generation Systems*, Energies, doi:10.3390/en11030603., 11(3): 603 (2018).
5. https://solimpeks.com.tr/ (accessed on 13.09.2019).
6. Vorobiev, P. and Vorobiev, Y., *About the possibilities of using the renewable energy power sources on railway transport*, J. Adv. Transp. 2013; 47:681–691 Published online 30 December 2011 in Wiley Online Library (wileyonlinelibrary.com). DOI: 10.1002/atr.189.
7. Solar power for trains dawns in rainy Belgium, http://www.reuters.com/article/ usbelgium-solar-trains-idUSTRE77B2KD20110812 (accesed on: 08.08.2018).
8. Joo, F., *Solar-powered rail vehicle ready for service*, International Railway Journal, Simmons-Boardman Publishing Inc., 2013.
9. Asanov, I.M., Loktionov, E.Y., *Possible Benefits From PV Modules Integration in Railroad Linear Structures*, Renewable Energy Focus, https://doi.org/10.1016/j.ref.2018.02.003., 25: 1-3 (2018).
10. Vasisht, MS., Vishal, C., Srinivasan, J., Ramasesha, SK., S*olar photovoltaic assistance for LHB rail coaches*, Curr Sci, 107(2): 255-9, (2014).
11. Trentini, M., *Photovoltaic systems for railways in Italy*, Tenth E.C. Photovoltaic solar energy conference, http://dx.doi.org/10.1007/978-94-011-3622-8_211, 4:826–829, Lisbon, Portugal, (1991).
12. Disasolar. SME awarded for its innovations for future transportation systems. France. Available at: http://www.idtechex.com/journal/print-articles.asp?Articleids=4922 (accessed on: 08.08.2015).
13. RailNews. *Solar powered trains in India soon on heritage Kalka-Shimla route*. RailNews media ltd. India. Available at: http://www.railnews.co.in/solarpowered- trains-inindia-soon (accesed on: 08.08.2018).
14. Rohollahi, E., Abdolzadeh, M., Mehrabian, MA., *Prediction of the power generated by photovoltaic cells fixed on the roof of a moving passenger coach: a case study*, J Rail Rapid Transit, http://dx.doi.org/10.1177/0954409714524749, 1-8, (2014).
15. Trains. Indian train. 2014-2015. Available at: http://trains.ind.in/indian-train (accesed on: 16.05.2018).
16. Vasisht, MS., Vishal, C., Srinivasan, J., Ramasesha, SK., *Solar photovoltaic assistance for LHB rail coaches*, Curr Sci, 107(2): 255-9, (2014).
17. Gangwar, M., Sharma, SM., *Evaluating choice of traction option for a sustainable Indian Railways*, Transp Res Part D, http://dx.doi.org/10.1016/j.trd.2014.08.025., 33: 135-145, (2014).
18. Bharath, V., *India's bio-diesel policy and the current turmoil*, Energetica India, 1-4, (2015).
19. Darshana, KM., Karnataki, K., Shankar, G., Ramasesha, SK., *A practical implementation of energy harvesting, monitoring and analysis system for solar photo voltaic terrestrial vehicles in indian scenarios*, IEEE international WIE conference on electrical and computer engineering. Dhaka, Bangladesh: IEEE; http://dx.doi.org/10.1109/WIECON-ECE.2015.7443989., 542-545 (2015).
20. Vasisht, MS., Vashista, G.A., Srinivasan, J., Ramasesha, SK., *Rail coaches with rooftop solar photovoltaic systems: A feasibility study*, Energy, 118: 684-691, (2017).
21. http://www.trensaat.com/polatli-bozuyuk-hizli-tren-saatleri/ (accesed on: 08.09.2018).
22. https://www.solarfirsat.com/gunes-paneli-panasonic-dunyanin-en-verimli-hit-325-wp-pmu148 (accesed on: 08.09.2019).

MOSFET-Only Current Mode BP/LP Filter

E. ARSLAN, Y. UZUN and Ş. M. KIZILIRMAK

Department of Electrical and Electronics Engineering, Faculty of Engineering,
Aksaray University, Aksaray, Turkey
emrearslan@aksaray,edu.tr, yunusuzun@aksaray.edu.tr, safakkiziirmak@gmail.com

Abstract - **In this work, a current mode dual output, analog MOSFET ONLY BP/LP filter is presented. Transconductance and gate-to-source capacitances of the MOSFET's are used instead of passive circuit components like resistors and capacitors. The proposed filter exhibits some advantages compared to classical analog filter circuits which are low voltage and low power operation, reduced chip area and wide frequency range. The functional core circuit of the proposed filter has only two MOSFET transistors. LTSpice simulations are performed to verify the theoretical results and it is shown that theoretical results are in good agreement with the simulated ones.**

Keywords – **MOSFET-only, analog filter, current-mode**

I. INTRODUCTION

GENERALLY, in active filter design, operational amplifiers with passive elements, has been used [1-28]. There are some approaches which use the internal capacitance and transconductance values of transistors instead of passive circuit elements and they are commonly called MOS-Only or MOS-C circuits design approaches. These approaches make it possible to use the parasitic components of MOS devices instead of passive circuit elements like resistors and capacitors [1]. The main advantage of MOS-Only circuits is the reduced chip area. As it is known, the circuits which are built using passive elements cover a lot of area on the chip and that kind of circuits have high costs when compared to MOS-Only circuits. Other advantage is the reduced power consumption. When compared to filter circuits that employ active and passive elements, MOS-Only circuits use very few transistors, which mean reduced power consumption in addition to reduced layout area. Therefore, using only MOS devices and their internal parasitic parameters instead of passive circuit elements [3-8] is becoming really important. Nowadays, it has gained importance to build active filters with no use of passive elements. In the last decade, low frequency filters occupy a very important part especially in biomedical applications such as Electromyographic (EMC), electrocardiogram (ECG), phonocardiographic (PCG) signals [6]. For this purpose, dual function BP/LP filter is proposed in this paper.

II. THE PROPOSED CIRCUIT

The proposed current mode BP/LP filter core circuit without biasing is shown in Fig 1. The passive resistors and capacitors in the circuit are provided by the transconductance (g_m) and parasitic gate-to-source capacitance (C_{GS}) of the MOS transistors.
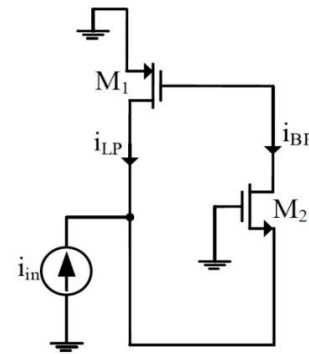
Figure 1: Functional core circuit

Current mode LP and BP filter transfer functions are achieved by the drain currents of M1 and M2, respectively. The drain current of M_1 provides lowpass filtering function, whereas the drain current of M_2 provides the bandpass filtering function. Fig 2. shows the complete schematic of the proposed circuit. Transistors M_3, M_4 are used for provided DC currents for core transistors. In order to pick upthe drain currents of M1 and M2, two additional transistors M_{lp}, M_{bp} are connected in parallel to M_1 and M_2. By doing so, the VGS voltages of M1 and Mlp, and also M2 and Mbp will be equal, which result in same drain currents through the parallel connected transistors. Transistors M_4 through M_6 serve as DC current sources for the filter transistors. The transfer functions of LP and BP filter responses can be given as;

$$\frac{I_{LP}}{I_{in}} = \frac{g_{m1}g_{m2}}{g_{m1}g_{m2} + g_{m2}C_{gs1}s + C_{gs1}C_{gs2}s^2} \quad (1)$$

$$\frac{I_{BP}}{I_{in}} = -\frac{C_{gs1}g_{m2}s}{g_{m1}g_{m2} + g_{m2}C_{gs1}s + C_{gs1}C_{gs2}s^2} \quad (2)$$

Using these transfer functions, the quality factor (Q) and the pole frequency (ω_0) of the filters can be obtained as:

$$Q = \sqrt{\frac{C_{gs2} g_{m1}}{C_{gs1} g_{m2}}} \qquad (3)$$

$$\omega_0 = \sqrt{\frac{g_{m1} g_{m2}}{C_{gs1} C_{gs2}}} \qquad (4)$$

analysis of this circuit is shown below in Fig. 5. The center frequency of the filter circuits is obtained approximately as 15kHz. In order to show the transient response, a 15kHz and 5µA sinusoidal input current is applied to the input. It is shown that, because the input signal frequency is approximately equal to the center frequencies of the filter circuits, the amplitude values are very close to the input signal amplitude. There is only change in the phases, which is the case.

Figure 2: Complete schematic of the proposed filter circuit
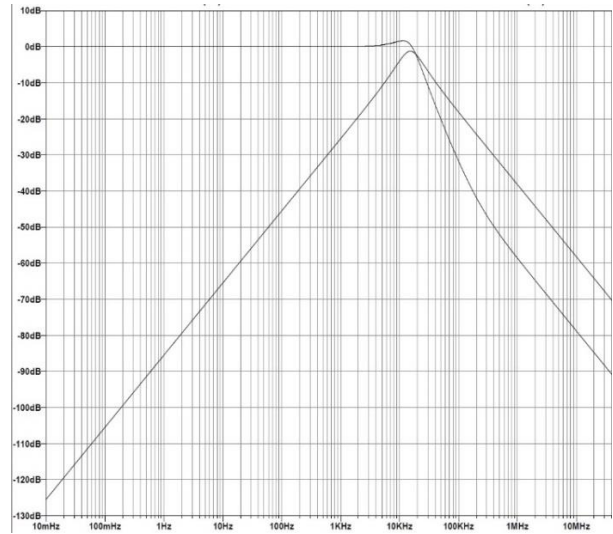
Figure 4: Frequency response of the filter circuit

In order to obtain the transfer functions of the filters, the small signal equivalent-circuit which is given in Fig. 3 is used. It is assumed that all the transistors are in their saturation region. MATHEMATICA software is used to calculate the transfer functions.

Figure 3: Small signal equivalent circuit
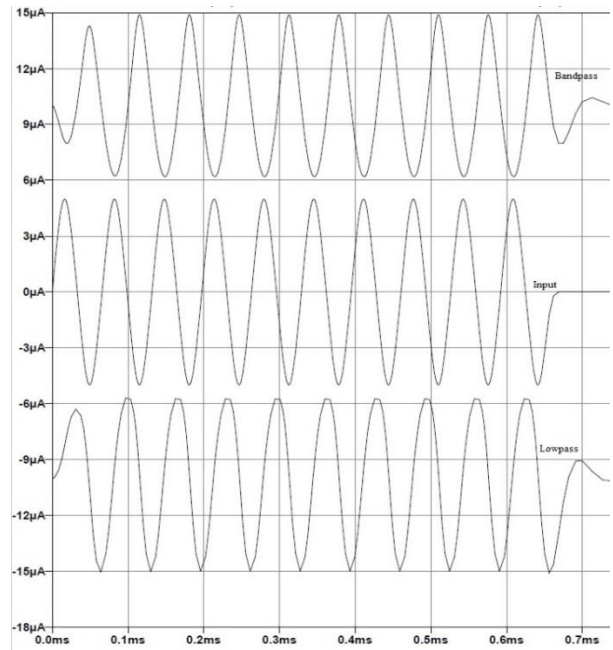
Figure 5: Time domain simulation results for a sinusoidal input signal

III.   SIMULATION RESULTS

The performance of the proposed filter circuit is examined through LTSpice simulations using 1.5V supply voltage and AMS 0.35 µm CMOS process parameters. The frequency responses of the filter circuits are given in Fig. 4. Transient

Monte Carlo simulations are also performed for the time domain simulations and simulation results are given in Fig. 6. As it is shown, the variations in the LP and BP gains are below 10%.
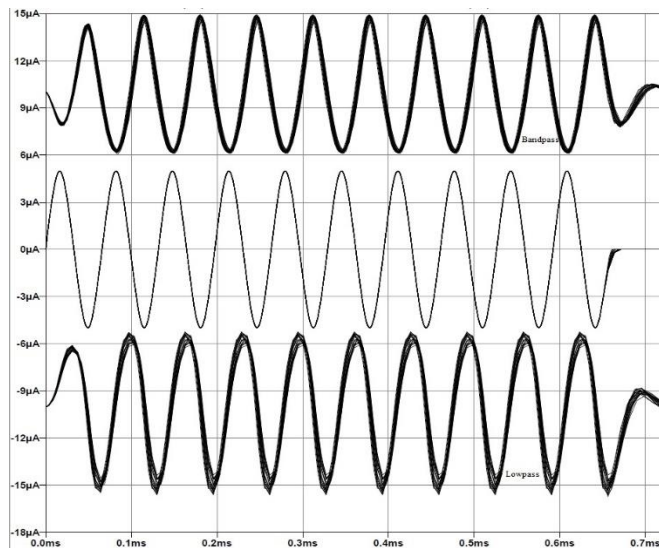
Figure 6: Monte Carlo simulations for the time domain responses

IV. CONCLUSION

In this work, a very simple structure, dual output current mode biquad filter with reduced complexity is presented using only two MOS transistors in the core circuit. The transconductance and gate-to-source capacitances are used instead of passive circuit elements. It is shown that the proposed filter is suitable for low voltage and low power operation. Depending on the integrated circuit technology parameters and also the values of the parasitic capacitance values, the circuit can operate in the GHz frequency region. The simulation results are compared with the theoretical ones and it is shown that they are in very good agreement.

REFERENCES

[1] Arslan, E., Metin, B., & Cicekoglu, O. (2015). MOSFET-only multi-function biquad filter. AEU-International Journal of Electronics and Communications, 69(12), 1737-1740.

[2] Gupta, S. S., & Senani, R. (2003). Realisation of current-mode SRCOs using all grounded passive elements. Frequenz, 57(1–2), 26–37.

[3] Chang, C. M., Soliman, A. M., & Swamy, M. N. S. (2007). Analytical synthesis of low-sensitivity high-order voltage-mode DDCC and FDCCII-grounded R and C all-pass filter structures. IEEE Transactions on Circuits and Systems I: Regular Papers, 54(7), 430–1443.

[4] Chang, C. M., & Tu, S. H. (1998). Universal current-mode filters employing CFCCIIs. International Journal of Electronics, 85(6), 749–754.

[5] Jiang, J., & He, Y. (2009). Tunable frequency versatile filters implementation using minimum number of passive elements. Analog Integrated Circuits and Signal Processing, 59, 53–64.

[6] Horng, J. W. (2009). High-order current-mode and transimpedance-mode universal filters with multiple-inputs and two-outputs using MOCCIIs. Radioengineering, 18(4), 537–543.

[7] Zhao, J., Jiang, J. G., & Liu, J. N. (2010). Design of tunable biquadratic filters employing CCCIIs: State variable block diagram approach. Analog Integrated Circuits and Signal Processing, 62, 397–406.

[8] M. Kumngern, "Realization of electronically tunable first-order allpass filter using single-ended OTAs", in 2012 IEEE Symposium on Industrial Electronics and Applications, 2012, pp. 100–103. DOI: 10.1109/ISIEA.2012.6496607.

[9] B. Metin, E. Arslan, N. Herencsar, O. Cicekoglu, "Voltage-mode MOS-only all-pass filter", in Proc. of 34th Int. Conf. Telecommunications and Signal Processing, 2011, pp. 317–318. DOI: 10.1109/TSP.2011.6043718

[10] B. Metin, O. Cicekoglu, "Tunable all-pass filter with a single inverting voltage buffer", in 2008 Ph.D. Research in Microelectronics and Electronics, 2008, pp. 261–263.

[11] S. Minaei, E. Yuce, "High Input impedance NMOS-based phase shifter with minimum number of passive elements", Circuits, Syst. Signal Process., vol. 31, no. 1, pp. 51–60, 2012. DOI: 10.1007/s00034-011-9290-0.

[12] A. Toker, S. Ozoguz, "Tunable allpass filter for low voltage operation", Electron. Lett., vol. 39, no. 2, pp. 175–176, 2003. DOI: http://dx.doi.org/10.1049/el:20030179.

[13] H. A. Yildiz, S. Ozoguz, A. Toker, O. Cicekoglu, "On the realization of MOS-Only allpass filters", Circuits, Syst. Signal Process., vol. 32, no. 3, pp. 1455–1465, 2013. DOI: 10.1007/s00034-012-9500-4.

[14] E. Yuce, "A novel CMOS-based voltage-mode first-order phase shifter employing a grounded capacitor", Circuits, Syst. Signal Process., vol. 29, pp. 235–245, 2010. DOI: 10.1007/s00034-009- 9143-2.

[15] E. Yuce, S. Minaei, "A novel phase shifter using two NMOS transistors and passive elements", Analog Integr. Circuits Signal Process., vol. 62, pp. 77–81, 2010. DOI: 10.1007/s10470-009-9324- 8.

[16] F. Yucel, E. Yuce, "A new electronically tunable first-order all-pass filter using only three NMOS transistors and a capacitor", Turkish J. Electr. Eng. Comput. Sci., vol. 24, pp. 3286–3292, 2016. DOI: 10.3906/elk-1410-95.

[17] B. J. Maundy, P. Aronhime, "A novel CMOS first-order all-pass filter", Int. J. Electron., vol. 89, no. 9, pp. 739–743, 2002. DOI: 10.1080/0020721031000083544.

[18] D. Prasad, K. Panwar, D. R., Bhaskar, M. Srivastava, "CDDITA- based voltage-mode first order all pass filter configuration", Circuits Syst., vol. 6, pp. 252–256, 2015. DOI: 10.4236/cs.2015.611025.

[19] T. Kersys, D. Andriukaitis, R. Anilionis, "VMOS, UMOS technology Simulation", in Proc. of 28th International Conference on Information Technology Interfaces (ITI 2006), Cavtat/Dubrovnik, Croatia, 2006, pp. 537–542. DOI: 10.1109/ITI.2006.1708538.

[20] A. Lahiri, A. Chowdhury, "A novel first-order current-mode all-pass filter using CDTA", Radioengineering, vol. 18, pp. 300–305, 2009.

[21] S. Maheshwari, I. A. Khan, "Simple first-order translinear-C current-mode all-pass sections", Int. J. Electron., vol. 90, no. 2, pp. 79–85, 2003. DOI: 10.1080/ 00207210310001595338.

[22] B. Metin, K. Pal, O. Cicekoglu, "All-pass filter for rich cascadability options easy IC implementation and tunability", Int. J. Electron., vol. 94, no. 11, pp. 1037–1045, 2007. DOI: 10.1080/00207210701763589.

[23] S. Minaei, E. Yuce, "All grounded passive elements current-mode all-pass filter", J. Circuits, Syst. Comput., vol. 18, no. 1, pp. 31–43, 2009. DOI: 10.1142/ S0218126609004909.

[24] J. Mohan, S. Maheshwari, "Cascadable current-mode first-order all- pass filter based on minimal components", Sci. World J., vol. 2013, no. 1, pp. 1–5, 2013. DOI: 10.1155/2013/859784.

[25] S. N. Songkla, W. Jaikla, A. B. Concept, "Realization of electronically tunable current- mode first-order allpass filter and its application", Int. Journal of Electronics and Electrical Engineering, vol. 6, no. 1, pp. 357–360, 2012.

[26] W. Tangsrirat, T. Pukkalanun, W. Surakampontorn, "Resistorless realization of current-mode first-order allpass filter using current differencing transconductance amplifiers", Microelectronics J., vol. 41, no. 2–3, pp. 178–183, 2010. DOI: 10.1016/j.mejo.2010.02.001.

[27] W. Tanjaroen, W. Tangsrirat, "Resistorless current-mode first-order allpass filter using CDTAs", 5th Int. Conf. Electrical Engineering/Electronics, Computer, Telecommunications and Information Technology, 2008, vol. 2, pp. 721–724. DOI: ECTICON.2008.4600532.

[28] L. Safari, S. Minaei, E. Yuce, "CMOS first-order current-mode all- pass filter with electronic tuning capability and its applications", J. Circuits, Syst. Comput., vol. 22, no. 3, 2013. DOI: 10.1142/S0218126613500072.

Effects of Stator Slot Optimization on Efficiency and Torque in Induction Motor

Y. UZUN and E. ARSLAN

Department of Electrical and Electronics Engineering, Faculty of Engineering,
Aksaray University, Aksaray, Turkey
yunusuzun@aksaray.edu.tr, emrearslan@aksaray,edu.tr

Abstract - **Due to a number of advantages, induction motors are the most widely used the industry. Many output parameters such as efficiency, torque and power factor of these motors can be changed thanks to changes in the motor structure. In the optimization study, the most important factor is which output parameter to change. Of course, when changing this output parameter, there will be changes in other parameters. Therefore, all parameters should be kept under control in the design to be realized. In this study, only small changes were realized in the stator slot structure and changes in the magnitudes such as current, moment, power factor and efficiency were observed. It was observed that the higher efficiency in the narrow and long slot structure. However, higher starting torque and break-down torque were obtained in the large and short slot structure for same slot volumes.**

Keywords – **induction motor, slot optimization, RMxprt, efficiency**

I. INTRODUCTION

MANY different types of motors are used to convert electrical energy into mechanical energy. Although their efficiency is relatively low compared to some motors, induction motors are still the most widely used motor types due to their simple structure, durability and lower costs [1]. A few decades ago, speed control of induction motors was quite difficult. However, the speed of the induction motors has become controllable easily thanks to the motor drives with the developments in power electronics. This has further increased the use of induction motors. It is estimated that between 80% and 90% of the electrical energy consumed in industry is used by squirrel cage induction motors [2-4]. Considering that approximately half of the electricity generated worldwide is consumed in industry, it is seen that these motors have the largest share in electricity consumption [5]. Therefore, even a small improvement in the efficiency values of these motors means enormous energy savings. There are two kinds of induction motors, winding rotor and squirrel cage rotor. Squirrel cage asynchronous motors are preferred because of their simplicity and cheapness.

It is very important to determine the parameters of the induction motor for the drive and control systems. Because the performance of the controller directly depends on the accuracy of the motor parameters used by the control algorithm [6-8].

Many studies have been carried out on the optimization of induction motors. In these studies, it is tried to get the best results by changing different parameters. Some of these studies are: Winding optimization, stator slot optimization, rotor slot optimization, core material optimization, pole optimization and size optimization.

These optimizations can be accomplished by changing many parameters such as rotor core length, rotor core diameter, stator core length, stator core diameter, stator and rotor slot shapes, core materials, and air gap length between the stator rotor. Each of these studies can be conducted separately or more than one at the same time. In addition, the aim of these optimizations can sometimes be to increase the motor efficiency, while sometimes limiting the starting current, increasing the starting torque or other purpose.

Many researches have been conducted for induction motor optimization. For example, induction motor stator winding coil step was shortened Aguiar *et al*. and the shortening value in the coil step was found to increase the efficiency value [9]. Ali et al. Have modeled 4 different stator groove geometries and found that the best starting and tipping moment is obtained by the rectangular stator groove and that the stator groove having the minimum current value at nominal shear value belongs to T type groove geometry [10]. In another study, the effect of the use of different materials on the core part of the asynchronous motor was examined and it was explained that the motor efficiency could be increased between 0.4% and 0.7% by using better quality materials [11]. Kirtley et al. Have achieved a significant increase in yield by using copper instead of aluminum in rotor rods and rings [12]. Han et al. managed to increase the efficiency by 2.9% by making changes in stator and rotor slot structures without increasing the motor volume and electrical steel grade [13].

For the modeling of the induction motor, information such as torque and current obtained from the full load test and no-load and locked rotor test data are used in general.
The electromechanical characteristics of the induction motor are directly linked to the stator and rotor slot combinations.

In this study, a 4 kW three phase squirrel cage induction motor is simulated with ANSYS software and then the stator slot parameters are changed and the effects of these changes on motor performance are investigated.

II.　Simulation Results

Only small changes in the shape of the stator slot were made and the results of this change were revealed in this work. These small changes in the stator slot structure change many output parameters of the motor. Because these changes affect the distribution of the magnetic flux. In the simulations, RMxprt tool of ANSYS program was used. 9 different stator slots structure are used, one of which is the default structure. As can be seen from Figure 1 and the dimensions in Table 1, only the length and width of the slot have been changed. While making these changes, it was taken care that the slot fill factor does not exceed 75%. Of course, many different changes can be made even on the slot. Figure 1 shows stator slot shapes used in the simulations, and Figure 2 shows dimensions' details of the stator slot.
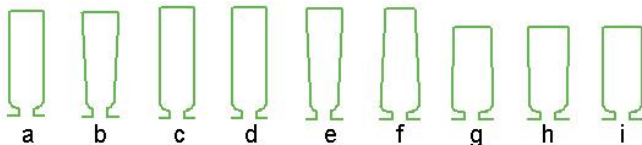
Figure 1: Stator slot shapes used in the simulation
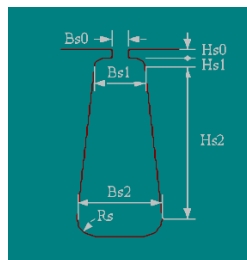
Figure 2: Stator slot dimensions' view

Table 1: Stator slot dimensions used in the simulation

Slot shape >>> Slot dimensions	a	b	c	d	e	f	g	h	i
Hs0	1.0	1.0	1.0	1.0	1.0	1.0	1.0	1.0	1.0
Hs1	1.0	1.0	1.0	1.0	1.0	1.0	1.0	1.0	1.0
Hs2	15.0	15.0	15.0	16.0	16.0	16.0	13.0	13.0	13.0
Bs0	2.6	2.6	2.6	2.6	2.6	2.6	2.6	2.6	2.6
Bs1	6.0	4.8	6.5	6.0	4.8	6.5	7.0	6.2	6.6
Bs2	6.0	6.2	5.0	6.0	6.2	5.0	6.2	7.0	6.6
Rs	0.0	0.0	0.0	0.0	0.0	0.0	0.0	0.0	0.0

As shown in Table 1, many parameters can be changed in the stator slot dimensions. However, only a limited number of changes were made in this study and the effects of these changes were observed.

The ferromagnetic materials are also important for motor efficiency. If a quality material is used, the motor efficiency increases. In the stator core, one of the most preferred materials, M19_24G, was used as ferromagnetic material. The characteristic curve B-H of this material is shown in Figure 3.
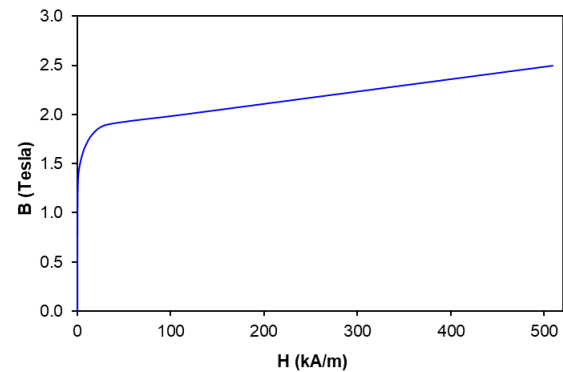
Figure 3: B-H curve of core materials

Whole-coiled winding was used in the modeling of stator windings. The whole-coiled winding is the type of winding in which the number of winding bobbins is equal to the number of slot.

Aluminum rotor rods and rings which are more commonly used in the market were preferred. If copper is used instead of aluminum, there will be an increase of 1% in the efficiency values.

Table 2 shows the effects of stator slot shapes to motor output parameters such as torque and efficiency.

Table 2: Output values for different stator slot shapes

	a	b	c	d	e	f	g	h	i
I (A)	4,865	4,751	4,845	5,033	4,913	5,009	5,781	5,290	5,399
T_s (Nm)	77,8	70,1	78,1	78,0	70,2	79,8	92,4	86,5	87,5
T_m (Nm)	127,639	121,839	129,472	128,305	122,575	130,119	140,183	134,995	135,566
T_r (Nm)	25,829	25,838	25,838	25,841	25,839	25,830	25,835	25,835	25,837
PF	0,804	0,820	0,806	0,781	0,797	0,783	0,691	0,746	0,734
η (%)	88,891	89,290	89,059	88,446	88,867	88,621	87,013	88,082	87,778

In the Table 2, I is stator current, T_s, T_m and T_r are starting torque, break-down torque and rated torque, respectively. *PF* is power factor and η is the efficiency.

As seen in the Table 2, a small change in the stator slot lead to change for many output parameters. For instance, in shape d,

only slot length is increased by 1 mm by shape a. However, the stator current increased by about 3.5% and the efficiency decreased by 0.5%.

Compared with *shape g* and *shape h*, it is seen that the slot volume is the same but that the base width is higher in *shape h*.

In this case, the efficiency increased by 1.2%, while there was a big decrease in the starting torque and the break-down torque.

These changes in the shape of the stator slot do not change the motor speed and the rated torque of the motor. However, significant changes in stator current, starting torque, break-down torque, power factor and efficiency have occurred.
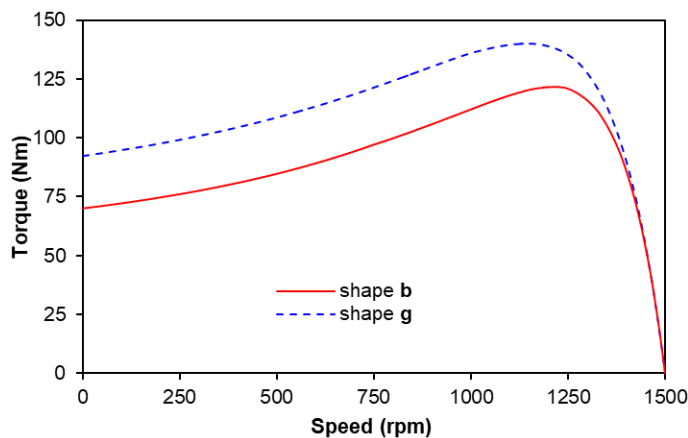
Figure 4: The speed-torque curve for *shape b* and *shape g*

Figure 4 shows torque values depend on motor speed for *shape b* and *shape g*. As it can be seen in the figure, if short and wide slot is used instead of long and narrow slot, stator current, starting torque and break-down torque increase by 21%, 32% and 15%, respectively. However, the power factor decrease by 16%.

The torque values are important parameters for electric motors. If the induction motor starts with load, which usually happens that way, the starting torque is very important. The starting torque is expected to be 1.5-2 times the normal operating torque. However, sometimes it is desirable to have an even higher starting torque under special operating conditions. If higher starting torque and break-down torque are required, *shape g* slot should be preferred.
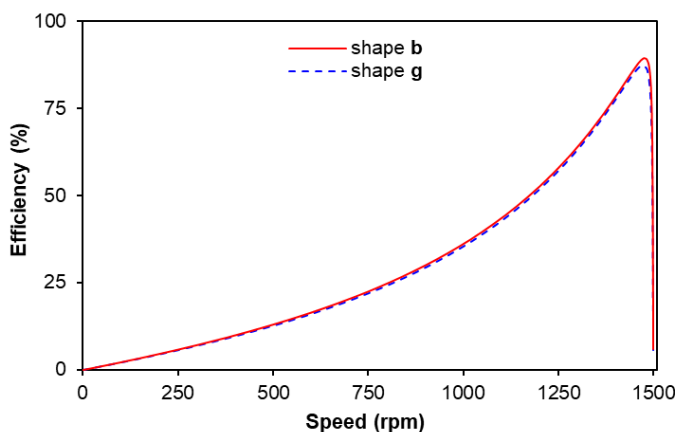
Figure 5: The speed-efficiency curve for *shape b* and *shape g*

Figure 5 shows the obtained motor efficiency versus the motor speed for *shape b* and *shape g*. For almost all motor speeds except rated value, the efficiencies close to each other were obtained. But, around the rated speed, the motor efficiency decreased by approximately 2.6%. If the starting torque and break-down moment is sufficient, the *shape b* should be preferred. Thus, a significant improvement in the motor efficiency will be achieved.

In addition, if short and wide slot is used, the starting current is measured 56.36 A. However, if long and narrow slot is used, starting current is measured 48.74 A. It corresponds to an increase by 15%.

III. CONCLUSION

Induction motors are the most widely used electric motors in the industry. Therefore, even a small improvement in the efficiency value of these motors means considerable energy savings. There are many different optimization techniques for induction motors. In this study, stator slot optimization is emphasized. The motor efficiency value increased by 2.6% with the improvement. However, there was a significant reduction in the starting torque and break-down torque. Therefore, when optimizing the induction motor, it should be well known for what purpose it is realized and other parameters should be kept under control.

REFERENCES

[1] B. Dursun, and Y. Uzun, "Design of high efficiency 4 kW induction motor", in *2018 International Conference on Innovative Research in Science Engineering and Technology*, pp. 81-86.
[2] R. Saidur, "A review on electrical motors energy use and energy saving", *Renewable and Sustainable Energy Reviews*, vol. 14, pp. 877–898, 2010.
[3] C. Verucchi, C. Ruschetti, and G. Kazlauskas, "High Efficiency Electric Motors: Economic and Energy Advantages", *IEEE Latin America Transactions*, vol. 11(6), pp. 1325-1331, 2013.
[4] P. Gnacinski, T. Tarasiuk, "Energy-efficient operation of induction motors and power quality standards", *Electric Power Systems Research*, vol. 135, pp. 10-17, 2016.
[5] C. Verucchi, C. Ruschetti, E. Giraldo, G. Bossio, J. Bossio, "Efficiency optimization in small induction motors using magnetic slot wedges", *Electric Power Systems Research*, vol. 152, pp. 1–8, 2017.
[6] L. Monjo, H.K. Jafari, F. Corcoles, J. Pedra, "Squirrel-cage induction motor parameter estimation using a variable frequency test", *IEEE Transactions on Energy Conversion*, vol. 30(2), pp. 550–557, 2015.
[7] M.A. Jirdehi, A. Rezaei, "Parameters estimation of squirrel-cage induction motors using ANN and ANFIS", *Alexandria Engineering Journal*, vol. 55, pp. 357-368, 2016.
[8] L. Monjo, F. Corcoles, J. Pedra, "Parameter estimation of squirrel-cage motors with parasitic torques in the torque-slip curve", *IET Electric Power Applications*, vol. 9(5), 377–387, 2015.
[9] V.P.B. Aguiar, R.S.T. Pontes, T.R.F. Neto, "Study and energy efficiency improvement in the design of an induction motor based on interactive CAD software", in *2013 Brazilian Power Electronics Conference*, pp. 878-883.
[10] B. Virlan, A. Simion, L. Livadaru, A. Munteanu, A. Mihai, S. Vasceanu, "External rotor shape estimation of an induction motor by fem analysis", *Bulletin AGIR*, vol. 4, pp. 27-32, 2011.
[11] E. Chiricozzi, F. Parasiliti, M. Villani, "New materials and innovative technologies to improve the efficiency of three-phase induction motors. A case study", in *2004 International Conference on Electrical Machines*, pp. 1-6.
[12] J.L. Kirtley, J.G. Cowie, E.F. Brush, D.T. Peters, R. Kimmich, "Improving induction motor efficiency with die-cast copper rotor cages", in *2007 IEEE Power Engineering Society General Meeting*, pp. 1-6.
[13] P. Han, Y. Chun, J. Choi, M. Kim, D. Koo, J. Lee, "The optimal design for improving efficiency of the three phase induction motor", in *2008 International Conference on Electrical Machines*, pp. 1-4.

A Current Limiting Control Strategy of Grid Connected Inverter for Overcurrent Protection

Mehmet Emin MERAL[1], Doğan ÇELİK[2]

[1]Van Yuzuncu Yıl University, Van/Turkey, emeral@yyu.edu.tr
[2]Van Yuzuncu Yıl University, Van/Turkey, dogancelik@yyu.edu.tr

Abstract—**With the growing proliferation of the grid connected inverter (GCI) in modern power systems, the utility grid faces the challenge of flowing excessive current under unbalanced grid fault conditions. Therefore, a proper control strategy is important for the GCI during grid faults to prevent damage to semiconductor switches of inverter. To make progress in this direction, this paper presents a current limiting control strategy for overcurrent protection. Computed peak phase currents are integrated into the reference current generator to remain the peak current in the safe limits. Control of active and reactive power oscillations are performed by using an adjustable control parameter. A set of simulation results based on PSCAD/EMTDC software confirms the accuracy of the analysis and the effectiveness of the current limiting control strategy.**

Keywords—**Grid Connected Inverter, Current Limitation Control, Overcurrent, Unbalanced Grid Fault**

I. INTRODUCTION

SHORT circuit faults result in the appearance of unbalanced voltage sags causing several adverse effects consisting overcurrent overloading of distribution transformers, overvoltage in the DC-link, higher losses and lower stability and reliability of the power system. Many control strategies have been studied to improve the performance of the inverter and to provide power delivery to loads during voltage sags [1-6]. However, safe active power production, concerning with the current limitation has rarely been discussed. The unbalanced grid faults could result in the grid tied inverter's overcurrent protection triggering if active power reference is kept at pre-value. This results in the inverter disconnection, which is incompatible with the grid codes. Therefore, a reference current generator depending positive and negative sequences (PNS) with peak current limitation control should be designed to deal with the inverter's overcurrent protection. The mentioned methods are associated with different control objectives. Shabestary et al. [5] have focused on reactive power injection to achieve voltage recovery. Some control strategies proposed in [1] and [7] provide safe active power production during voltage sags. Other interesting methods reported in [3, 8] are to mitigate the active or reactive power oscillations and to provide the balance three phase currents. On the other hand, the selection of a proper reference current proposed in [9, 10] is to meet different power quality requirements and to overcome grid faults.

In this paper, a current limiting control strategy of the grid connected inverter (GCI) is presented to avoid overcurrent during unbalanced grid faults. Calculated maximum phase currents are integrated into the reference current generator to remain within its nominal value. Oscillations or ripples in active or reactive power are mitigated by providing controllable of negative sequences using an adjustable control parameter. Performance of the current limiting control strategy is examined under various cases.

II. PROPOSED SYSTEM CONFIGURATION

The system topology of three phase inverter being connected to the utility grid is shown in illustrated in Figure 1. Distributed generation sources represent the DC-link side of three phase inverter which is connected to the utility grid with the point of common coupling (PCC) through an LC filter.
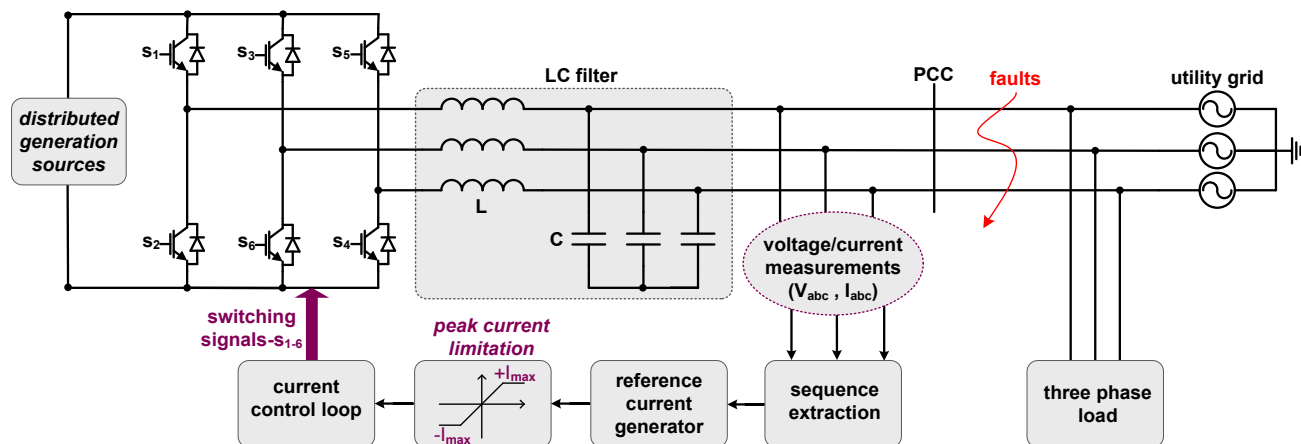
Figure 1.The proposed entire system

III. PROPOSED CONTROL STRATEGY PROPOSED CONTROL STRATEGY

Figure 2 shows the proposed control block diagram, which includes sequence analysis, a reference current generation, peak current limitation control, current control loop and switching signals. Detailed each part of the control strategy is explained as follows.
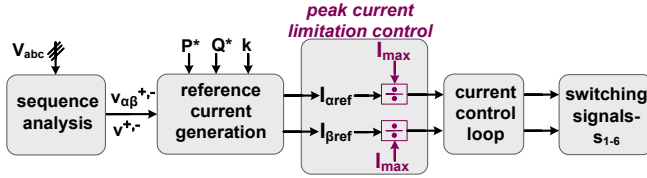
Figure 2. The proposed control scheme

A. Voltage Sag Characterization

The stationary frame representations of the PCC voltages can be expressed as:

$$\begin{bmatrix} v_\alpha \\ v_\beta \end{bmatrix} = \frac{2}{3} \begin{bmatrix} 1 & -\frac{1}{2} & -\frac{1}{2} \\ 0 & \frac{\sqrt{3}}{2} & -\frac{\sqrt{3}}{2} \end{bmatrix} \begin{bmatrix} v_a \\ v_b \\ v_c \end{bmatrix}$$

Voltages v_α and v_β are separated into symmetric components using a sequence detection method. The using voltage sequence components in stationary $\alpha - \beta$ coordinate system can be expressed as [11]:

$$v_\alpha = v_\alpha^+ + v_\alpha^- = v^+ sin(\omega t + \theta^+) + v^- sin(\omega t + \theta^-) \quad (2)$$
$$v_\beta = v_\beta^+ + v_\beta^- = -v^+ cos(\omega t + \theta^+) + v^- cos(\omega t + \theta^-)$$

where

$$v^+ = \sqrt{(v_\alpha^+)^2 + (v_\beta^+)^2}, \quad \theta^+ = tan^{-1}\left(\frac{v_\beta^+}{v_\alpha^+}\right) - \omega t$$
$$v^- = \sqrt{(v_\alpha^-)^2 + (v_\beta^-)^2}, \quad \theta^- = tan^{-1}\left(\frac{v_\beta^-}{v_\alpha^-}\right) + \omega t \quad (3)$$

B. Reference Current Generator

During unbalanced grid faults, the reference current generator of an inverter can be established in numerous different ways depending on inverter and grid requirements [11]. The current references for active and reactive power can be calculated depending on PNS voltage components in the stationary $\alpha - \beta$ coordinate system. Flexible control parameter, k is inserted in (4) and (5). The reference current generator becomes under unbalanced grid conditions as [12].

$$I_{\alpha(p)} = \frac{2}{3} \frac{P^*}{\left[(v_\alpha^+)^2 + (v_\beta^+)^2\right] + k\left[(v_\alpha^-)^2 + (v_\beta^-)^2\right]} [v_\alpha^+ + kv_\alpha^-]$$
$$I_{\beta(p)} = \frac{2}{3} \frac{P^*}{\left[(v_\alpha^+)^2 + (v_\beta^+)^2\right] + k\left[(v_\alpha^-)^2 + (v_\beta^-)^2\right]} [v_\beta^+ + kv_\beta^-] \quad (4)$$

$$I_{\alpha(q)} = \frac{2}{3} \frac{Q^*}{\left[(v_\alpha^+)^2 + (v_\beta^+)^2\right] + k\left[(v_\alpha^-)^2 + (v_\beta^-)^2\right]} [v_\beta^+ + kv_\beta^-]$$
$$I_{\beta(q)} = \frac{2}{3} \frac{Q^*}{\left[(v_\alpha^+)^2 + (v_\beta^+)^2\right] + k\left[(v_\alpha^-)^2 + (v_\beta^-)^2\right]} [-v_\alpha^+ - kv_\alpha^-] \quad (5)$$

where $I_{\alpha(p)}$ and $I_{\beta(p)}$ represent references for active power current and $I_{\alpha(q)}$ and $I_{\beta(q)}$ represent references for reactive power currents. P^* and Q^* are active and reactive power references and can be adjustable according to the inverter power capacity.

The total reference current in each channel can be given as:

$$I_{\alpha ref} = I_{\alpha(p)} + I_{\alpha(q)}$$
$$I_{\beta ref} = I_{\beta(p)} + I_{\beta(q)} \quad (6)$$

C. Peak Current Limitation Control

The reference current algorithm can be implemented in combination with the peak current limitation of the inverter to remains within its nominal value [13]. The overcurrent issue will occur during voltage sag if injected active-reactive power keeps at the desired value. To provide overcurrent issue in safety limit, injected active power should be decreased. The measured maximum injected current value from inverter output can be calculated by (7), (8) and (9) [14].

$$\begin{bmatrix} I_a \\ I_b \\ I_c \end{bmatrix} = \frac{1}{(v^+)^2 + k(v^-)^2}$$
$$\begin{bmatrix} \sqrt{A^2 + 2v^+v^+((P^*)^2 - (Q^*)^2)} \\ \sqrt{A^2 + 2v^+v^+((Q^*)^2 - (P^*)^2 - 2\sqrt{3}P^*Q^*)} \\ \sqrt{A^2 + 2v^+v^+((Q^*)^2 - (P^*)^2 + 2\sqrt{3}P^*Q^*)} \end{bmatrix} \quad (7)$$

where

$$A^2 = (P^*)^2(v^+)^2 + (P^*)^2(v^-)^2 + (Q^*)^2(v^+)^2 + (Q^*)^2(v^-)^2 \quad (8)$$

The maximum phase currents are calculated and then inserted in the reference current generator as shown in Figure 2. The maximum phase current is determined according to the expressions (9) [15].

$$I_{max} = max(I_a, I_b, I_c) \quad (9)$$

IV. PERFORMANCE EVALUATION OF THE PROPOSED CONTROL STRATEGY

In this section, a control strategy of grid connected inverter is tested with and without overcurrent protection tested during asymmetrical grid faults such as single phase to ground (SLG) and line to line to ground (LLG). A simulation model based on PSCAD/EMTDC software is used to establish the proposed system.

In this case, the LLG faults have been occurred between phase B, phase C voltages and ground. The performance of the

proposed control strategy is tested with and without current limitation control. As depicted in Figure 3a, without PCLC, generated active power is constant and injected phase currents of the inverter exceed their nominal values. However, injected phase currents are limited to rated their nominal values. Active power is curtailed to safe operation. And also, positive orthogonal currents in the synchronous $d - q$ coordinate system with respect to with or without PCLC are shown at the bottom of Figure 3a and 3b.

Similarly, in this case, the SLG fault between phase A voltage and ground have been applied to the utility grid. As can be seen in Figure 4, the proposed control stagey achieves superior performance during pre-fault and fault conditions. Generated active power and orthogonal current, I_q^+ are curtailed to safely operation of the system. The injected phase currents of the inverter are limited by the calculation of the highest phase current (see Figure 4b).
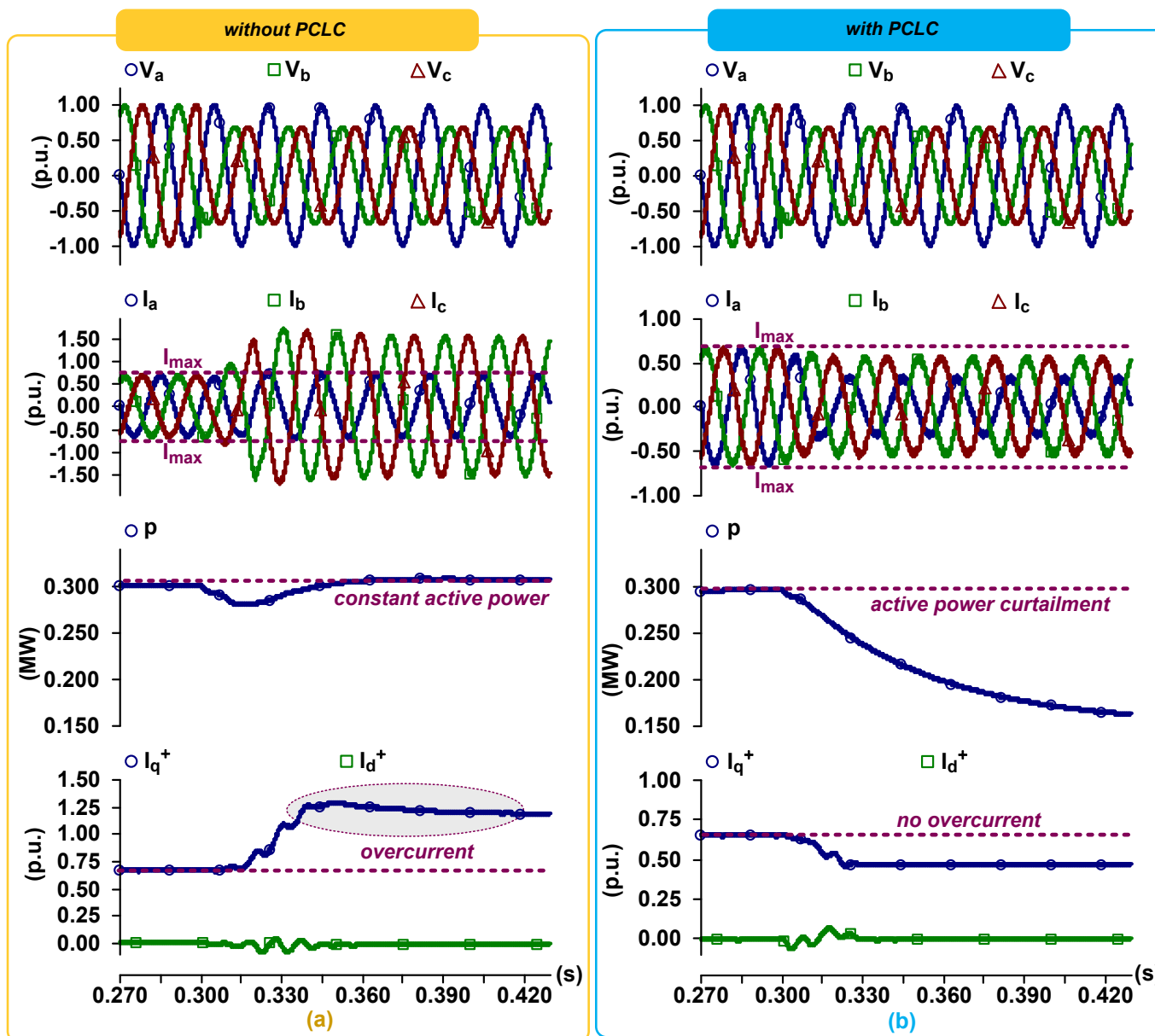
Figure 3. The performance evaluation of the proposed control strategy; a) without PCLC and b) with PCLC under LLG fault

V. CONCLUSIONS

This paper presents a multi-objective based current limiting control strategy to effectively improve the power quality requirements, to deal with inverter's overcurrent protection and to mitigate active or reactive power oscillations. The performance of the proposed control strategy with and without current limitation control is examined under SLG and LLG fault conditions. The results are reported in case studies that the proposed control strategy provides superior performance. The simulation results based on PSCAD/EMTDC software have been presented to demonstrate the effectiveness of the current limiting control strategy.
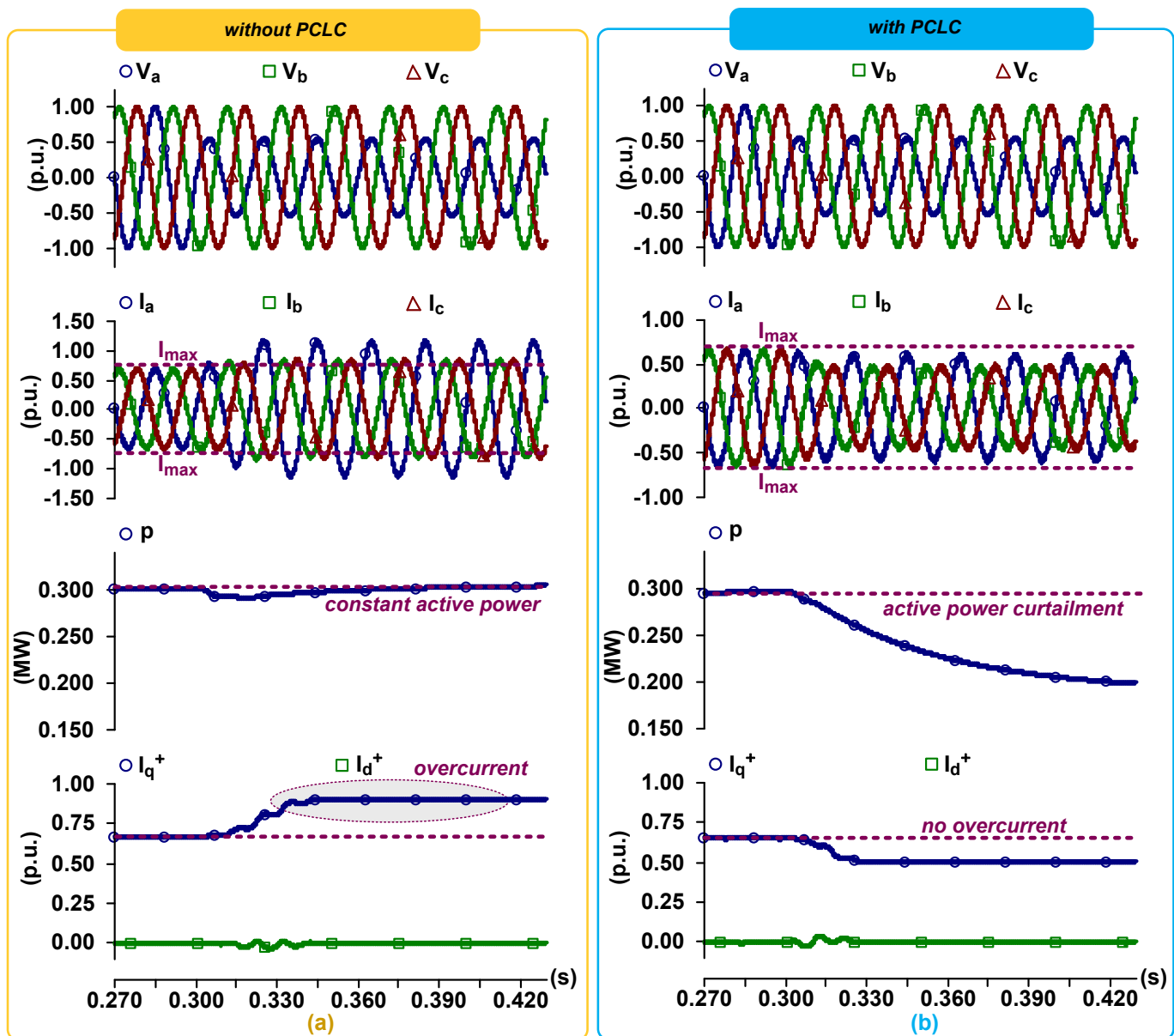
Figure 4. The performance evaluation of the proposed control strategy; a) without PCLC and b) with PCLC under SLG fault

REFERENCES

[1] M.A.G. López, J.L.G. de Vicuña, J. Miret, M. Castilla, and R. Guzmán, "Control strategy for grid-connected three-phase inverters during voltage sags to meet grid codes and to maximize power delivery capability", *IEEE Transactions on Power Electronics*, vol. 33, no. 11, pp. 9360-9374, January 2018.

[2] M. Nasiri, and R. Mohammadi, "Peak current limitation for grid side inverter by limited active power in PMSG-based wind turbines during different grid faults", *IEEE Transactions on Sustainable Energy*, vol. 8, no. 1, pp. 3-12, June 2016.

[3] D. Çelík, and M. E. Meral, "Current control based power management strategy for distributed power generation system", *Control Engineering Practice*, vol. 82, pp. 72-85, January 2019.

[4] D. Çelík, and M. E. Meral, "A flexible control strategy with overcurrent limitation in distributed generation systems", *International Journal of Electrical Power & Energy Systems*, vol. 104, pp. 456-471, January 2019.

[5] M.M. Shabestary, and Y.A.R.I Mohamed, "Advanced voltage support and active power flow control in grid-connected converters under unbalanced conditions", *IEEE Transactions on Power Electronics*, vol 33, no. 2, pp. 1855-1864, April 2018.

[6] I. Todorović, S. Grabić, and Z. Ivanović, "Grid-connected converter active and reactive power production maximization with respect to current limitations during grid faults", *International Journal of Electrical Power & Energy Systems*, vol. 101, pp. 311-322, October 2018.

[7] J.L. Sosa, M. Castilla, J. Miret, J. Matas, and Y.A. Al-Turki, "Control strategy to maximize the power capability of PV three-phase inverters during voltage sags", *IEEE Transactions on Power Electronics*, vol. *31*, no. 4, pp. 3314-3323, July 2015.

[8] R. Kabiri, D.G. Holmes, and B.P. McGrath, "Control of active and reactive power ripple to mitigate unbalanced grid voltages", *IEEE Transactions on Industry Applications*, vol. 52, no. 2, pp. 1660-1668, December 2015.

[9] P. Rodriguez, A.V. Timbus, R. Teodorescu, M. Liserre, and F. Blaabjerg, "Flexible active power control of distributed power

generation systems during grid faults", *IEEE Transactions on Industrial Electronics*, vol. 54, no. 5, pp. 2583-2592, August 2007.

[10] M. Castilla, J. Miret, J.L. Sosa, J. Matas,and L. G. de Vicuña, "Grid-fault control scheme for three-phase photovoltaic inverters with adjustable power quality characteristics", *IEEE Transactions on Power Electronics*, vol. 25, no. 12, pp. 2930-2940, September 2010.

[11] M.G. Taul, X. Wang, P. Davari, and F. Blaabjerg, "Current reference generation based on next generation grid code requirements of grid-tied converters during asymmetrical faults", *IEEE Journal of Emerging and Selected Topics in Power Electronics*, pp. 1-10, July 2019.

[12] A. Camacho, M. Castilla, J., Miret, A. Borrell, and de L.G. Vicuña, "Active and reactive power strategies with peak current limitation for distributed generation inverters during unbalanced grid faults", *IEEE Transactions on industrial electronics*, vol. 62, no. 3, pp. 1515-1525, August 2015.

[13] H.D. Tafti, A.I. Maswood, G. Konstantinou, J. Pou, and P. Acuna, "Active/reactive power control of photovoltaic grid-tied inverters with peak current limitation and zero active power oscillation during unbalanced voltage sags", *IET Power Electronics*, vol. 11, no. 6, pp. 1066-1073, May 2018.

[14] M.M. Shabestary, and Y.A.R.I Mohamed, "An analytical method to obtain maximum allowable grid support by using grid-connected converters", *IEEE Transactions on Sustainable Energy*, vol. 7, no. 4, pp. 1558-1571, May 2016.

[15] X. Du, Y. Wu, S., Gu, H. M., Tai, P., Sun, and Y. Ji, "Power oscillation analysis and control of three-phase grid-connected voltage source converters under unbalanced grid faults", *IET Power Electronics*, vol. 9, no. 11, pp. 2162-2173, September 2016.

Low Voltage Gain Boosted Two Stage CMOS Operational Amplifier

E. ALAYBEYOĞLU[1]

[1] Bartın University, Bartın/Turkey, ealaybeyoglu@bartin.edu.tr
[1] Istanbul Technical University, İstanbul/Turkey, ealaybeyoglu@itu.edu.tr

Abstract **- In this work, two-stage gain boosted CMOS operational amplifier (OPAMP) design is realized for use in analog signal processing. The input and output stages of the designed circuit have a wide dynamic range between the supply voltage and ground. The transistor sizes of the designed operational amplifier and biasing currents are selected to provide low power consumption with high gain. The designed circuit is proposed for 2kΩ resistive and 200pF capacitive load. Simulations are performed in Cadence Spectre Circuit Simulator using 180nm CMOS technology.**

Keywords **- Operational Amplifier (OPAMP), Analog Signal Processing, Analog to Digital Converter (ADC).**

I. INTRODUCTION

Operational amplifiers (OPAMP) are one of the key elements in analog processing systems. Ideally, they perform the function of a voltage controlled current source with infinite voltage gain. When used in an integrated architecture, OPAMP is often used to drive capacitive loads, that is, the gates of transistors, capacitors or capacitor arrays. Therefore, the output impedance of OPAMP structures need not be designed as high. The operational amplifier is four terminal blocks with two inputs and two outputs. One output is analog grounding. The basic function of OPAMP is to create an amplified copy of the voltage across the input terminals at the output. Ideally, the voltage gain is infinite. In addition, the input impedance is infinite and the output impedance is zero. OPAMP measures the input voltage and produces the output in the same way as an ideal voltage source. In terms of circuit theory, OPAMP performs the same function as the voltage-controlled voltage source (VCVS) [1]–[4].

In this work, two-stage gain boosted CMOS operational amplifier (OPAMP) is designed for use in analog signal processing. Performance parameters of the designed circuit such as A_d (Differential Gain), A_{cm} (Common Mode Gain), CMRR (Common Mode Rejection Ratio), Offset voltage, Phase margin, output and input oscillation, and noise are analyzed. The first stage of OPAMP consists of a folded cascode CMOS structure [5]. Differential input transistors with parallel PMOS and NMOS are used in order to realize the swing of the input signal of the designed circuit from rail to rail (supply to ground). The output stage of OPAMP is implemented with the CMOS structure of Monticelli class AB [6]. Monticelli class AB output stage is used in order to realize the output oscillation of the designed OPAMP circuit between 0V and supply voltage AVDD = 1.8V. However, to increase the gain of first stage two gain boosting CMOS amplifier structures are utilized [7]. Simple differential pair structure is used as gain boosting amplifier structure. Designs are realized in Cadence environment using 180nm TSMC technology

II. CMOS IMPLEMENTATION OF THE OPERATIONAL AMPLIFIER

The CMOS implementation of the designed OPAMP is shown in Figure 1. The transistor dimensions of the circuit are given in Table 1. The temperature independent current source is realized by combining PTAT (proportional to the absolute temperature) and CTAT (complementary to absolute temperature) current generators to produce 15µA current [8], [9]. In the selection of the transistor dimensions and the biasing current of the circuit, an approximate calculation is made via the transfer function of the single pole OPAMP given in (1). Equation (1) is obtained when a signal given in (2) is applied to a single pole OPAMP as in (3). The formula to calculate the compensation capacitance is given in (4). As a result, when τ is selected as 0.72µs, ω_0 is $1.38 Mrad/s$ for the capacitive load of $C_L = 200$pF from the equation of $\omega_0 = \frac{1}{\tau} = \frac{g_m}{C_L}$ and g_m is calculated as 276µS. From the equation (5), the current of the input transistor is selected to be about 7.5µA and the total current flowing through each branch is 15µA.

$$K_V(s) = \frac{K_o}{1 - \frac{s}{s_{p1}}} \tag{1}$$

$$v_{in}(t) = V_1 u(t) \tag{2}$$

$$v_{out}(t) = -V_1 u(t) K(1 - e^{-t/\tau}) \tag{3}$$

$$\omega_0 = \frac{g_m}{C_L} \tag{4}$$

$$g_m = \frac{2I_D}{V_{ON}} \,, g_m = \sqrt{2\mu C_{OX} W/_L I_D} \tag{5}$$

In the structure given in Figure 1, M_{13}, M_{14}, M_{15}, and M_{16} are input transistors while nMOS transistors provide positive swing and pMOS transistors are used for negative swing. The transistors of M_9, M_{10}, M_{11}, M_{12}, M_{29}, M_{30}, M_{31}, M_{32}, M_{33}, M_{34}, M_{35}, M_{36}, M_{37}, and M_{38} are used to generate the biasing current and voltage. The use of a large swing current source is preferred

to ensure the large swing by increasing the headroom. The transistors of M_{29}, M_{30}, M_{31}, and M_{32} form the wide swing current source. Resistors of R_3 and R_4 are selected as 10kΩ to provide $R_{on}I_B = 200mV$ for wide swing.

M_{39}, M_{40}, M_{41}, and M_{42} are used to increase the output resistance of the pMOS transistors M_1, M_2, M_3, and M_4 in folded cascode structure. The transistors of M_{43}, M_{44}, M_{45}, and M_{46} form the structure of gain boost amplifier used to increase the output resistance of the nMOS transistor M_5, M_6, M_7, and

M_8 in the folded cascode structure.

The KV voltage gain of a typical OPAMP is expressed in $g_m r_o$. In order to increase the gain of OPAMP, the size and current of the transistor must be increased according to the equation given in g_m (5). In addition to this, the gain boost amplifier contributes to the increase of external r_o. In this study, simple differential amplifier is used as gain boost amplifier to minimize power consumption.
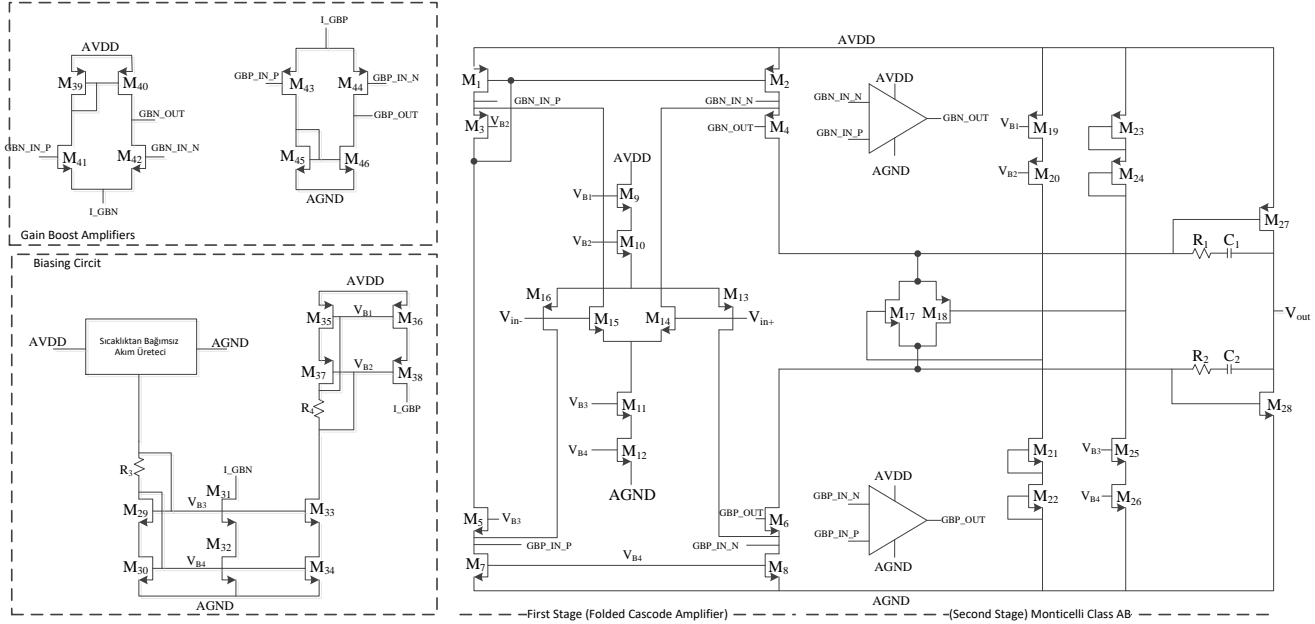
Figure 1: CMOS implementation of folded-cascode OPAMP with increased input swing and gain.

Table 1 The size of the transistors.

Transistorler	W/L	Transistorler	W/L
M_1, M_2, M_3, M_4	37μm/2μm	M_{25}, M_{26}	2.9μm/1μm
M_5, M_6, M_7, M_8	13μm/2μm	M_{27}, M_{28}	120μm/220nm
M_9, M_{10}	30μm/2μm	M_{29}, M_{30}, M_{31}, M_{32}	10μm/2μm
M_{11}, M_{12}, M_{19}, M_{20}	10μm/2μm	M_{33}, M_{34}	10μm/2μm
M_{13}, M_{14}	10μm/220nm	M_{35}, M_{36}, M_{37}, M_{38}	30μm/2μm
M_{15}, M_{16}	30μm/220nm	M_{39}, M_{40}, M_{45}, M_{46}	2μm/2μm
M_{17}, M_{21}, M_{18}, M_{24}	6μm/1μm	M_{41}, M_{42}	10μm/350nm
M_{22}, M_{23}	8μm/220nm	M_{43}, M_{44}	10μm/300nm

The dimensions of transistors M_{17}, M_{18}, M_{19}, M_{20}, M_{21}, M_{22}, M_{23}, M_{24}, M_{25}, M_{26}, M_{27}, and M_{28} are determined according to the biasing current and the proportions in the equations given in (6), (7), (8) and (9). These ratios are necessary for good matching between the transistors in the circuit. The compensation capacitances of C_1 and C_2 in the circuit are selected as = 10pF and the resistors of R_1 and R_2 are 750Ω.

Figure 2 shows the gain curve for the unloaded state of OPAMP. In the unloaded state, the gain of the circuit is 114.7dB while the gain bandwidth is 2.54GHz. Phase margin is about 82°. Figure 3 gives the gain curve for the loaded case of OPAMP with 2kΩ and 200pF. In this case, the gain of the circuit is 111.7dB while the gain bandwidth is 2.28GHz with 62° phase margin.
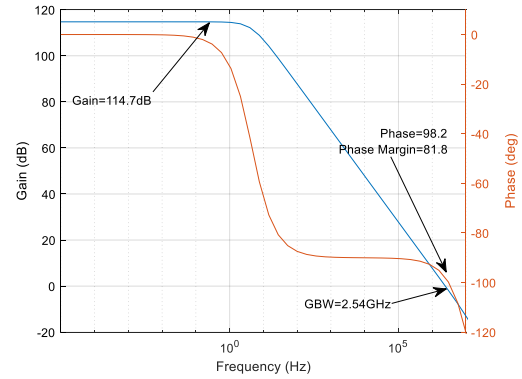
Figure 2: Open loop gain for 0.9V dc input signal.

$$\left[\frac{W}{L}\right]_{21} = \left[\frac{W}{L}\right]_{17} \tag{6}$$

$$\left[\frac{W}{L}\right]_{24} = \left[\frac{W}{L}\right]_{18} \tag{7}$$

$$I_Q \left[\frac{W}{L}\right]_{22} = \frac{I}{2}\left[\frac{W}{L}\right]_{28} \tag{8}$$

$$I_Q \left[\frac{W}{L}\right]_{25} = \frac{I}{2}\left[\frac{W}{L}\right]_{27} \tag{9}$$
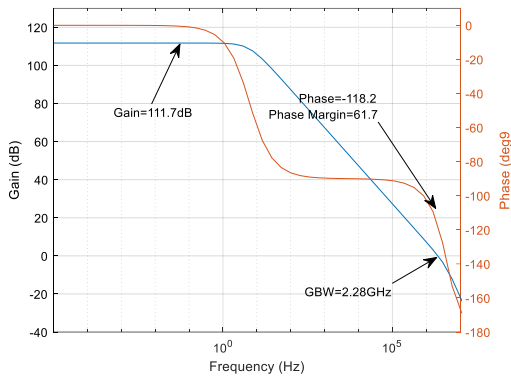
Figure 3: Open loop gain for 0.9V dc input signal with 2kΩ, 200pF load.

The common mode rejection ratio (CMRR) of OPAMP is given in Figure 4. CMRR is determined as 40.6dB. Figure 5 shows the input common mode range (ICMR). As can be seen from Figure 5, the input common mode range of the designed OPAMP is rail to rail. To calculate the settling time and slew rate of the designed circuit, a square wave of 20µs pulse width with a period of 40µs is applied. Settling time is calculated as 4.16µS while slew rate is 1.24µV / s. Figure 7 shows the spurious free dynamic range (SFDR) graph. SFDR is determined as 51.9dB. SFDR refers to the power ratio of the fundamental signal to the strongest harmonic.
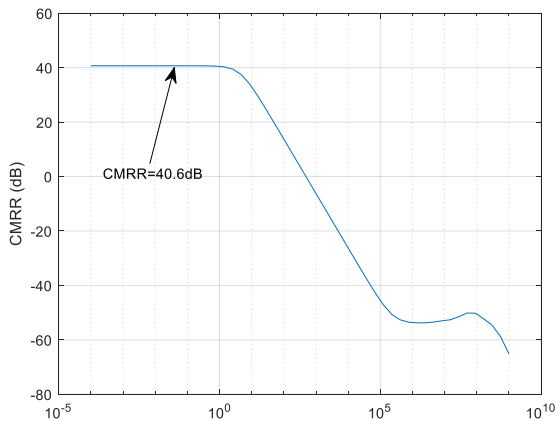
Figure 4: Common mode rejection ratio (CMRR) of the designed OPAMP.
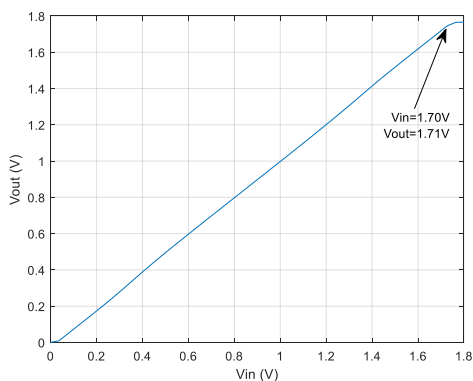
Figure 5: Input common mode range (ICMR) of the designed operational amplifier.
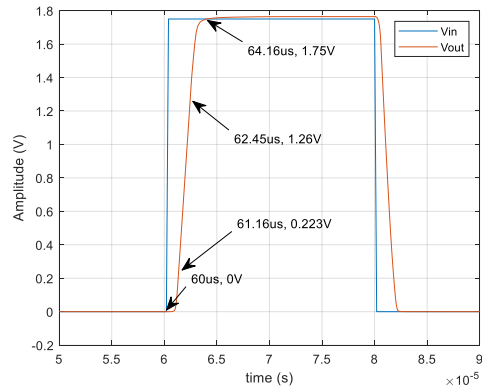
Figure 6: The simulation of settling time and slew rate of the designed OPAMP.
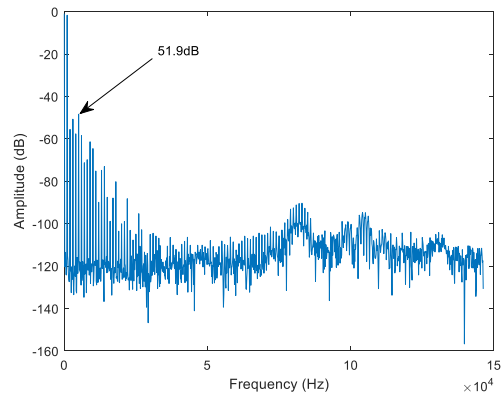
Figure 7: Spurious free dynamic range (SFDR) of the designed circuit.

Figure 8 shows the transient response of output signal obtained for the 1kHz and 0-1.7V peak-to-peak input signal. The total harmonic distortion is lower than -50dBc. Figure 9 shows the noise analysis of the circuit. The noise is reduced to the input and has a value of 67.4nV / sqrt (Hz) at $1/f$ corner frequency. The maximum value of the noise is determined as 1.28mV / sqrt (Hz).
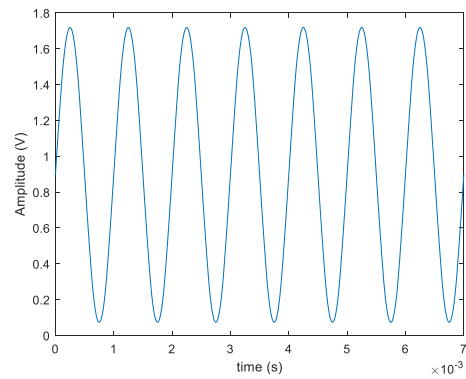
Figure 8: Transient response of the designed OPAMP for 1kHz input signal.

Table 2 shows the performance parameters of the designed OPAMP. Table 3 contains comparison of the designed OPAMP with previous works. Although the CMRR value in the designed circuit is suitable for the typical OPAMP parameters given in (1), it is important in applications where the signal amplitude of interest is lower than the offset voltage or when

voltage-aware information is found between the two signals. The CMRR of a differential amplifier determines the attenuation applied to the offset. In positive decibels, CMRR is defined as (AD) differential difference and common mode gain (AC).
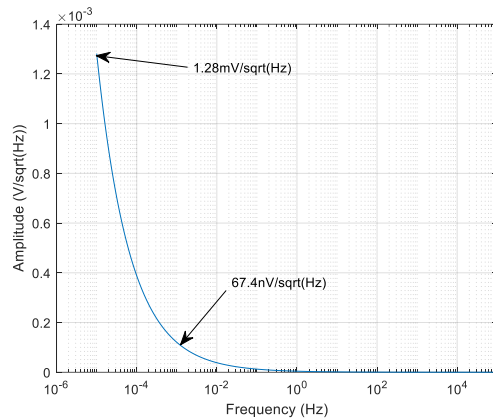
Figure 9: Noise analysis of the designed amplifier.

Table 2 The performances of the designed OPAMP.

Technology	0.18μm TSMC
Power Supply	1.8V
Input Common Mode Range	0 V to Vdd
Output Swing	200 mV to Vdd-200 mV
CMRR (DC)	> 40 dB
Gain (Open Loop R=2kΩ, C=200pF)	> 100 dB
Gain (Open Loop - Unloaded)	> 110 dB
Noise Density	$< 200\ nV/\sqrt{Hz}$
Settling Time	< 10 us
THD (1 kHz)	< -50 dBc
Offset [Temperature (-40 ºC - 85 ºC), process (ss, tt, ff, sf, fs), Supply Voltage (1.62V – 1.98)]	< 10 mV
Phase Margin	> 60º

Table 3 The comparison of the designed amplifier with state of art studies.

Parameters	[10]	[11]	[12]	[13]	This Work
Technology	90nm	0.13μm	0.18μm	0.35μm	0.18μm
Power Dissipation (mW)	-	9	0.52	7	1.08
Load (pF)	-	7.5	2	5	200
Phase Margin (º)	54	62	-	69	61
Open Loop Gain (Unloaded) (dB)	91.1	91.5	14	156	114.7

III. CONCLUSION

In the study, two-stage rail to rail input and output swing operational amplifier is designed with 180nm TSMC technology in the Cadence environment. The designed OPAMP has 111.7dB gain at 2kΩ and 200pF load while the gain bandwidth product is 2.28GHz. The designed OPAMP has a phase margin greater than 60º. The noise density of the circuit is 200 nV / √Hz. Offset voltage under the variation of temperature (-40ºC - 85ºC), process (ss, tt, ff, sf, fs), supply voltage (1.62V - 1.98V) is determined to be less than 10mV by performing a worst case analysis.

REFERENCES

[1]   W. Germanovix, E. Bonizzoni, and F. Maloberti, "Capacitance Super Multiplier for Sub-Hertz Low-Pass Integrated Filters," *IEEE Trans. Circuits Syst. II Express Briefs*, vol. 65, no. 3, pp. 301–305, 2018.

[2]   K. Kim, K. Y. Choi, and H. Lee, "a-InGaZnO Thin-Film Transistor-Based Operational Amplifier for an Adaptive DC-DC Converter in Display Driving Systems," *IEEE Trans. Electron Devices*, vol. 62, no. 4, pp. 1189–1194, 2015.

[3]   Y. C. Tarn, P. C. Ku, H. H. Hsieh, and L. H. Lu, "An amorphous-silicon operational amplifier and its application to a 4-bit digital-to-analog converter," *IEEE J. Solid-State Circuits*, vol. 45, no. 5, pp. 1028–1035, 2010.

[4]   I. M. Filanovsky and J. Zhou, "A 100-dB CMRR CMOS Operational Amplifier with Single-Supply Capability," *IEEE Trans. Circuits Syst. II Express Briefs*, vol. 54, no. 5, pp. 397–401, 2007.

[5]   M. Pourabdollah, "A new gain-enhanced and slew-rate-enhanced folded-cascode op amp," *Analog Integr. Circuits Signal Process.*, vol. 88, no. 1, pp. 43–56, 2016.

[6]   D. M. Monticelli, "A Quad CMOS Single-Supply Op Amp with Rail-to-Rail Output Swing," *IEEE J. Solid-State Circuits*, vol. 21, no. 6, pp. 1026–1034, 1986.

[7]   P. E. Allen and D. R. Holberg, *CMOS analog circuit design*, Oxford uni. 2012.

[8]   E. Alaybeyoğlu and H. Kuntman, "CMOS implementations of VDTA based frequency agile filters for encrypted communications," *Analog Integr. Circuits Signal Process.*, vol. 89, no. 3, pp. 675–684, 2016.

[9]   S. Tewari and K. Singh, "Intuitive design of PTAT and CTAT circuits for MOSFET based temperature sensor using Inversion Coefficient based approach," *19th Int. Symp. VLSI Des. Test, VDAT 2015 - Proc.*, pp. 1–6, 2015.

[10]   D. Arbet, G. Nagy, G. Gyepes, and V. Stopjaková, "Design of rail-to-rail operational amplifier with offset cancelation in 90nm technology," *Int. Conf. Appl. Electron.*, pp. 17–20, 2012.

[11]   C. Bai, J. Yang, and J. Wu, "A highly linear programmable gain amplifier with level shifter and class AB output stage for bluetooth low energy," *Asia-Pacific Microw. Conf. Proceedings, APMC*, vol. 1, pp. 6–8, 2016.

[12]   X. Liu and J. F. McDonald, "Design of single-stage folded-cascode gain boost amplifier for 14bit 12.5Ms/S pipelined analog-to digital converter," *2012 10th IEEE Int. Conf. Semicond. Electron. ICSE 2012 - Proc.*, pp. 622–626, 2012.

[13]   L. Kouhalvandi, S. Aygün, E. O. Güneş, and M. Kirci, "An improved 2 stage opamp with rail-to-rai! gain-boosted folded cascode input stage and monticelli rail-to-rail class AB output stage," *ICECS 2017 - 24th IEEE Int. Conf. Electron. Circuits Syst.*, vol. 2018-January, pp. 542–545, 2018.

An Efficient Approach to Simulation of Sepic Converter with Mutual Inductance

S. ŞOLA[1], A. B. YILDIZ[2], T. ERFİDAN[3]

[1] Department of Electrical Engineering, Kocaeli University, Kocaeli/Turkey, seckin.sola@kocaeli.edu.tr
[2] Department of Electrical Engineering, Kocaeli University, Kocaeli/Turkey, abyildiz@kocaeli.edu.tr
[3] Department of Electrical Engineering, Kocaeli University, Kocaeli/Turkey, tarik@kocaeli.edu.tr

Abstract – **DC-DC Converters are used to convert a variable or constant DC voltage level to another. According to input and output DC levels, DC-DC Converters operate as step-up or step-down. A SEPIC (single ended primary inductance converter) DC-DC converter can operate as either step-up or step-down depending on duty cycle and commonly used in photovoltaic systems and battery charger systems. In this paper, modified nodal analysis is used to analyze SEPIC Converter with coupled inductor and switching elements are modeled with two valued resistor approach. The simulation results show that two valued resistor approach is more efficient than classical modeling approaches in modeling switching elements.**

Keywords – **SEPIC, DC-DC converter, analysis, switch, model.**

I. INTRODUCTION

DC-DC Converters are used to convert a variable or constant DC voltage level to another. The conversion is carried out by periodically supplying the load with DC voltage source via switching elements. By changing switching time, the desired voltage is transferred to the load [1-2]. Voltage conversion depends on switching time which makes DC-DC Converters easy to control to achieve the desired voltage. In converters, the load is supplied continuously by using storage elements such as transformer, inductor and capacitor. There are DC-DC Converters in different topologies that serve as step-up or step-down, and they have advantages and disadvantages compared to each other based on application [3].

DC-DC Converters are widely used in industrial applications, renewable energy systems and battery chargers [4]. In applications, different types of converters are used according to the features such as voltage level, power level and cost. In the recent literature, SEPIC Converter is frequently used in photovoltaic systems (maximum power point tracking) and battery charging systems [5-9].

In this paper, the Coupled Inductor SEPIC Converter is modelled and analyzed with MNA (Modified Nodal Analysis) method by obtaining nodal equations under continuous conduction mode. Switching elements are modelled with two valued resistor approach.

II. SEPIC CONVERTER TOPOLOGY

As shown in Figure 1, the SEPIC Converter consists of a controlled switching element (MOSFET, IGBT), a fast diode, two inductors (L_1, L_2) and two capacitors (C_1, C_2) Depending on the continuous current and discontinuous current operation, different switching states occur. Two sub circuit schematics related to continuous current mode are given in Figure 2. In the first case (S_1 switch is turned on), the inductors L_1 and L_2 are charged with the voltages V_i and V_{c1}. In the second case (S_1 switch is turned off) the capacitors C_1 is discharged with the current I_{L2} and C_2 is discharged through to load. The inductors can be coupled or non-coupled.
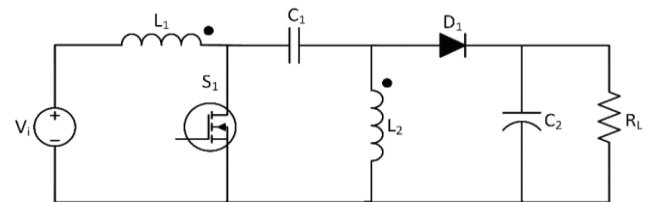
Figure 1: SEPIC Converter equivalent circuit
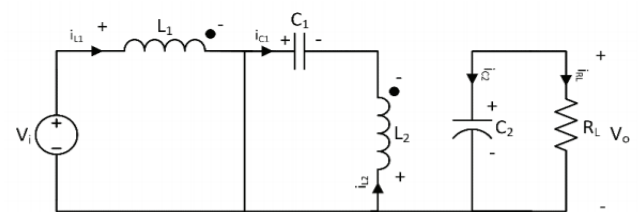
(a)
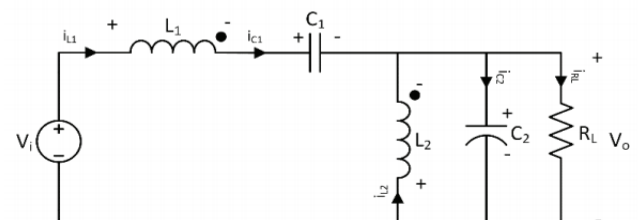
(b)

Figure 2: Equivalent circuit when (a) switch is on, (b) when switch is off.

Output voltage of sepic converter is given by;

$$\frac{Vin}{Vout} = \frac{1-D}{D} \tag{1}$$

Where D is duty cycle of a switching element.

By changing the duty cycle of switching element, the voltage at the output can be increased or decreased.

III. MODIFIED NODAL ANALYSIS OF SEPIC CONVERTER WITH COUPLED INDUCTOR

State-variable analysis or state-space analysis is one of the commonly used methods in circuit analysis. The most important advantage of this method is to have fewer unknown variables in state equations. However, due to the difficulty of obtaining state equations and solving them in circuits which use switching elements, MNA (Modified Nodal Analysis) is used. Although MNA has more unknown variable in nodal equations, it has been preferred instead of the state-variables analysis in this paper due to ease of obtaining the equations and it is flexibility in modelling the circuit elements [10].

MNA can be explained as the obtaining of nodal equations for of each node in the system by using Kirchhoff's current law and solving these equations by converting them to matrix.

Representation of modified nodal equations in s-domain and t-domain is;

$$(G + sC)X(s) = BU \tag{2}$$

$$Gx(t) + C\frac{dx(t)}{dt} = BU(t) \tag{3}$$

Where G, C and B are coefficient matrices. Passive elements such as resistance form G matrix, while storage elements such as capacitance and inductance form C matrix. The matrix U is the vector containing the independent voltage and current sources and the initial current or voltage values of inductances and capacitors that are initially energized. The matrix X(t) is the vector of unknowns in the nodal equations system which consists of current and voltage unknowns.

The modified nodal equations in the t-domain are as follows.

$$\begin{bmatrix} G_{11} & G_{12} \\ G_{21} & 0 \end{bmatrix}\begin{bmatrix} x_1(t) \\ x_2(t) \end{bmatrix} + \begin{bmatrix} C & 0 \\ 0 & L \end{bmatrix}\frac{d}{dt}\begin{bmatrix} x_1(t) \\ x_2(t) \end{bmatrix} = B\begin{bmatrix} U(t) \\ J(t) \end{bmatrix} \tag{4}$$

In equation 4, $x_1(t)$ represents unknown variable of voltages $x_2(t)$ represents unknown variable of currents.

There are two commonly used approaches to modeling switching elements: the ideal switch model and the two valued resistor model. In the ideal switch model, the switch is modeled by a short-circuit or zero-valued voltage source when it is on, and an open-circuit or zero-valued current source when it is off.

According to number of switching elements, 2^n circuit models are obtained. In the two valued resistor model, the switching element is modeled with a very low valued resistor when it is in on and very high valued resistor when it is off. The biggest difference between these two approaches is their effect on the system equations. The ideal switch model creates new unknowns to be added to the equation system and new columns to the G, C, B, U matrices. However, the two valued resistor model allows the system to be modeled only by changing the values of the G matrix for the switches. This ensures that the system equations remain the same regardless of the number of circuit model.

IV. TWO VALUED RESISTOR MODEL OF SEPIC CONVERTER

The diode and switch S in SEPIC converter have been replaced by two valued resistors and shown in Figure 3.
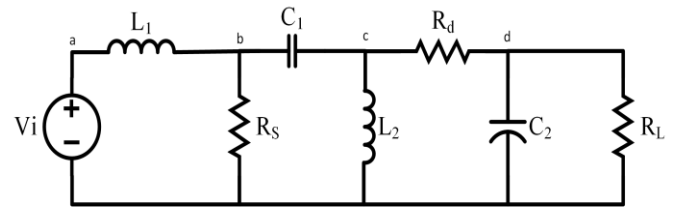
Figure 3: Two valued resistor model of SEPIC Converter

After two valued resistor conversion, coefficient matrices of modified nodal equations are;

$$G = \begin{bmatrix} 0 & 0 & 0 & 0 & 1 & 0 & 1 \\ 0 & G_{Rs} & 0 & 0 & -1 & 0 & 0 \\ 0 & 0 & G_{Rd} & -G_{Rd} & 0 & -1 & 0 \\ 0 & 0 & -G_{Rd} & G_{Rd}+G_{RL} & 0 & 0 & 0 \\ 1 & -1 & 0 & 0 & 0 & 0 & 0 \\ 0 & 0 & -1 & 0 & 0 & 0 & 0 \\ 1 & 0 & 0 & 0 & 0 & 0 & 0 \end{bmatrix}$$

$$C = \begin{bmatrix} 0 & 0 & 0 & 0 & 0 & 0 & 0 \\ 0 & C_1 & -C_1 & 0 & 0 & 0 & 0 \\ 0 & -C_1 & C_1 & 0 & 0 & 0 & 0 \\ 0 & 0 & 0 & C_2 & 0 & 0 & 0 \\ 0 & 0 & 0 & 0 & -L_1 & -M & 0 \\ 0 & 0 & 0 & 0 & -M & -L_2 & 0 \\ 0 & 0 & 0 & 0 & 0 & 0 & 0 \end{bmatrix}$$

$$B = \begin{bmatrix} 0 & 0 & 0 & 0 & 0 & 0 & 1 \end{bmatrix}^T$$

$$X(t) = \begin{bmatrix} V_a & V_b & V_c & V_d & I_{L1} & I_{L2} & I_{Vi} \end{bmatrix}$$

$$U(t) = \begin{bmatrix} V_i \end{bmatrix}$$

Where $G_{Rs} = 1/R_S$, $G_{Rd} = 1/R_d$, $G_{RL} = 1/R_L$.

When S switch is on, R_S takes very small value (Rmin) and R_d takes very high value (Rmax), When S switch is off, R_S takes very high value (Rmax) and R_d takes very small value (Rmin).

V. SIMULATION AND RESULTS

In time domain, modified nodal equations of the circuit is;

$$Gx(t) + C\frac{dx(t)}{dt} = BU(t) \tag{5}$$

For the numerical solution, Backward Euler method is used. General expression of the Backward Euler method is;

$$X_{n+1} = X_n + h * f(X_{n+1}, t_{n+1}) \tag{6}$$

Where h indicates step size.

After using Equation 5 and Equation 6, it follows:

$$X_{n+1} = K_A X_n + K_B U_{n+1} \tag{7}$$

Where;

$$K_A = K_1^{-1} C \tag{8}$$
$$K_B = K_1^{-1} hB \tag{9}$$
$$K_1 = \begin{bmatrix} C + hG \end{bmatrix} \tag{10}$$

In each iteration, the resistance values of the switches are updated according to the position of the switches. Calculations are continued by updating the G matrix and other matrices.

The parameters used for the simulation are given in Table 1.

Table 1: Simulation parameters

PARAMETER	VALUE
L_1	340µH
L_2	340µH
Mutual inductance(M)	333.2µH
C_1	20µF
C_2	680µF
R_L	5Ω
R_{min}	1µΩ
R_{max}	1MΩ
V_{in}	20V
V_{out}	30
Frequency (f)	100kHz

Duty cycle (D)	0.6
Step size (h)	10^{-6}

The simulation results obtained by entering the parameters in Table 1. into the nodal equations system and solving them using Equation 7 are given below.
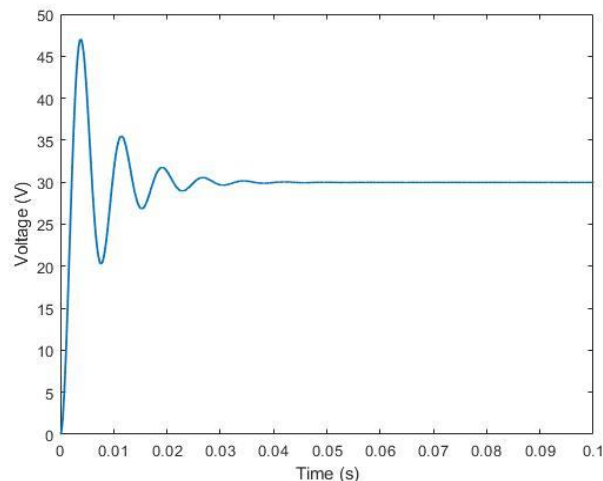
Figure 4: Output voltage versus time
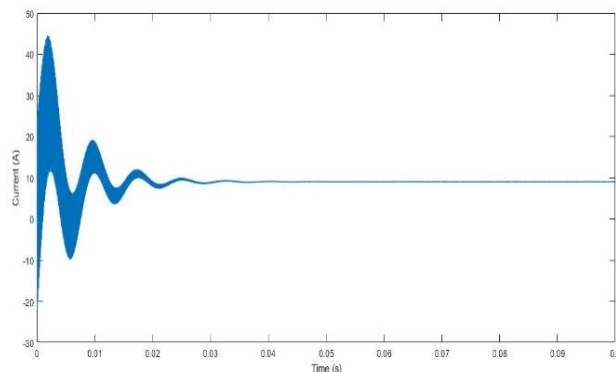
Figure 5: L_1 current versus time
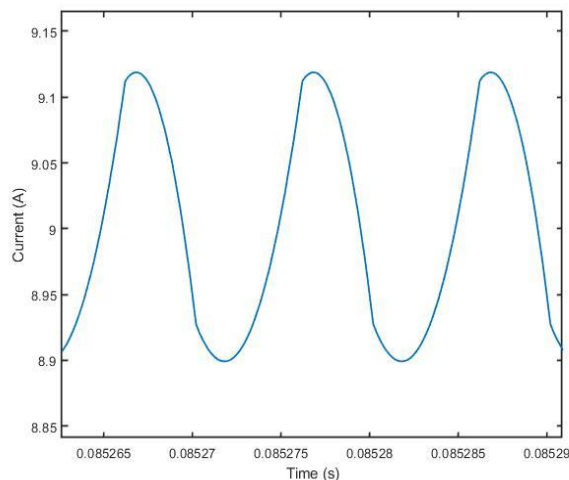
Figure 6: L_1 current versus time (zoomed)
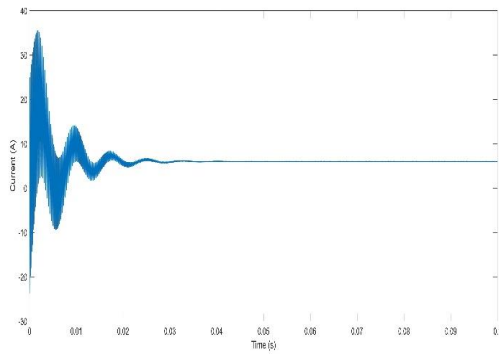
Figure 7: L₂ current versus time
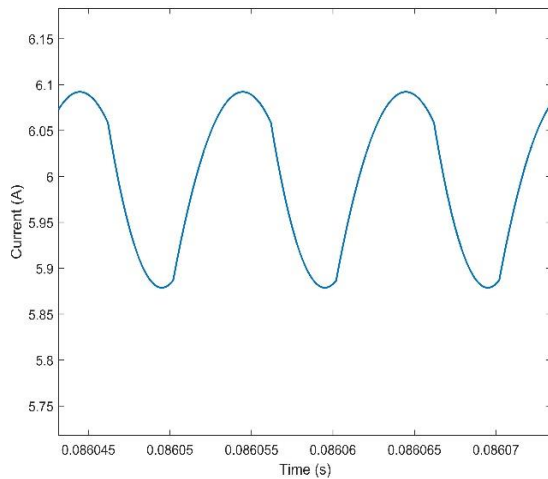
Figure 8: L₂ current versus time (zoomed)

As a result of the selected duty cycle (D=0.6), the output voltage is 30V and ΔI for I_{L1} and I_{L2} is 0.22 A.

For comparison, Equation 1 is solved with input voltage and duty cycle parameters,

$$V_{output} = \frac{20}{\frac{0.4}{0.6}} = \frac{12}{0.4} = 30 \text{ V}$$

The result confirms that simulation results are correct.

VI. CONCLUSION

In this paper, SEPIC Converter is analyzed by using modified nodal technique. The switching elements are modeled by a two valued resistor approach and this method does not need additional equations. The theoretical solution is compatible with simulation results.

REFERENCES

[1]   H. Bodur, "Güç Elektroniği", Birsen Yayınevi, İstanbul, 2010.Hart S.
[2]   D. W., "Power Electronics", McGraw-Hill, New York, 2011.
[3]   S. J. Chiang, H. Shieh and M. Chen, "Modeling and Control of PV Charger System With SEPIC Converter," in *IEEE Transactions on Industrial Electronics*, vol. 56, no. 11, pp. 4344-4353, Nov. 2009.
[4]   Rashid, Muhammed H. Rashid, Muhammad H. *Power Electronics: Devices, Circuits, and Applications*. Pearson India Education Services Pvt. Ltd., 2018.
[5]   M. Veerachary, "Power tracking for nonlinear PV sources with coupled inductor SEPIC converter," in IEEE Transactions on Aerospace and Electronic Systems, vol. 41, no. 3, pp. 1019-1029, July 2005.
[6]   H. S. -. Chung, K. K. Tse, S. Y. R. Hui, C. M. Mok and M. T. Ho, "A novel maximum power point tracking technique for solar panels using a SEPIC or Cuk converter," in IEEE Transactions on Power Electronics, vol. 18, no. 3, pp. 717-724, May 2003
[7]   R. Moradpour, H. Ardi and A. Tavakoli, "Design and Implementation of a New SEPIC-Based High Step-Up DC/DC Converter for Renewable Energy Applications," in IEEE Transactions on Industrial Electronics, vol. 65, no. 2, pp. 1290-1297, Feb. 2018.
[8]   A. El Khateb, N. A. Rahim, J. Selvaraj and M. N. Uddin, "Fuzzy-Logic-Controller-Based SEPIC Converter for Maximum Power Point Tracking," in IEEE Transactions on Industry Applications, vol. 50, no. 4, pp. 2349-2358, July-Aug. 2014.
[9]   O. Kircioğlu, M. Ünlü and S. Çamur, "Modeling and analysis of DC-DC SEPIC converter with coupled inductors," 2016 International Symposium on Industrial Electronics (INDEL), Banja Luka, 2016, pp. 1-5
[10] A.B. Yıldız., "Elektrik devrelerinin bilgisayar yardımıyla analizi", Yüksek lisans ders notları,Kocaeli Üniversitesi, (2018).

See the Wireless

Ali Yeşil [1], Radosveta Sokullu[1]

[1]Ege University, Izmir/Turkey, radosveta.sokullu@ege.edu.tr
[1]Ege University, Izmir/Turkey, aliyesil95@gmail.com

Abstract – **This paper presents the design and implementation of a system that allows visualizing the WiFi signals around us. The system is based on a Yagi antenna and a Raspberry Pi processor equipped with a camera. Using image processing techniques received signal strength is encoded into a color scale and overlaid with the corresponding image of the surrounding environment. MATLAB code ensures high conversion precision. Excluding the Yagi antenna which was custom designed from the project, the rest of the components are cheap, off-the-shelf components which make it a simple low cost solution. It can be used as a simple preliminary method to visually determine the availability and strength of WiFi signals when designing 802.11 wireless networks.**

Keywords – **Yagi-Uda Antenna, 2.4 GHz Wireless Network, Stepper Motor, Image Processing**

I. INTRODUCTION

WiFi (IEEE 802.11) is a standard for data transfer in the 2.4GHz ISM band and 5GHz band, and has become extremely popular in recent years for wireless internet connections. Today, this approach is very popular because it relieves the burden of building new infrastructures [1]. In the installation of wireless network systems, it has become desirable to serve wider areas and more users by enhancing signal quality while keeping the investment costs within desirable limits. For this reason, network planning and design decisions at an early stage are very important. To make these decisions different software tools and measurements are required. Information and support is obtained from some private IT companies during the planning stage of network projects. These companies can develop device configuration, number, layout and project budget with some methods developed by them. However, such studies sometimes do not reflect reality. Institutions may make unnecessary financial expenses at the end of the project and may have to buy many hardware and software systems that will not be actually used [2].

An example of such a situation is faced by many universities. Wireless networks in university campuses have gained great importance in recent years. Especially for large open area campuses many problems appear during the planning, design and establishment of these networks. The results of the studies conducted by private companies with their own methods for the project are not always appropriate for the institution. In this project we propose a method, based on image processing that will allow to visually represent the signal quality i.e. signal strength observed in different areas. Signal strength measurements are taken by using a directional

antenna and their values are expressed in terms of different colors which can be overlaid on a photograph of the surroundings. This simple method is fast and quite inexpensive and can provide sufficiently accurate results for the initial stages of network planning and design. The proposed system can help users in controlling the signal strength in a given environment and decide on positioning new signal sources accordingly. The project is a low-cost simple solution, which relies on a Raspberry Pi 3 to control the antenna and to process all information. The Raspberry Pi camera module is used for photographing and the image processing code is MATLAB.

II. RELATED WORKS

In the recent decade, as a result of fast technological developments, WiFi technology has managed to take its place as one of the most indispensable sides of human life. WiFi (IEEE 802.11) is a standard for data transfer which spreads over several different licensed and non-licensed bands and includes the 2.4GHz ISM band and 5GHz band. New additions to the standard for increasing data rates and the enormous availability of cheap devices have made it the most popular wireless internet connection method. While it relieves the burden of building a infrastructures [3], theoretically it can cover Theoretically, WiFi covers an area of 1.5 km, but practically good signal quality can be achieved within a radius of around 300 meters because of large scale and when used in closed areas. Above this signal quality deteriorates leading to reduction in internet speed, connectivity problems and increased delays.

Similar project can be found aiming at more complex representations. A major goal of the "Project Skittles - AR Visualization of WIFI and LTE Signal Strength" is to detect and visualize LTE/4G signals on your mobile. [4] It is a complex large scale project which involves augmented reality. Other similar work involves Android applications targeting WiFi signal strength detection and meter mapping in various visual and graphic ways for mobile devices. [12] Another augmented reality (AR) app can be found in [13]. It offers an interesting AR experience: spin your iPhone or iPad around you, and your device will act like a window into a previously invisible world. Compared to these projects the work described in this paper is less ambitious but also les complex and less expensive. It provides the most important features in a novel and yet very practical low cost solution.

From here on the paper is structured as follows: in section

III we present the system architecture and describe the main components. In section IV system software is described followed by results and discussion of the implementation. Finally the paper is concluded in Section VI.

III. SYSTEM ARCHITECTURE AND COMPONENTS

Figure 1 shows the block diagram of the designed system. It consists of an Yagi antenna, a WiFi control module, a RaspberryPi unit, a stepper motor and a camera. The signal strength detected by the antenna is processes and converted to a specific color which is mapped on the image of the surrounding area. The proposed solution system should be able to correctly detect WiFi signals from the environment and map them according to their strength and location onto the available environment image as closely as possible. This requires that the antenna is precisely rotated both horizontally and vertically to scan the whole available space. In order to achieve both ease of operation and required precision the elements are made of acrylic glass (plexiglass) with added bearings and shafts for rotation. The movements of the antenna are controlled by a step motor.
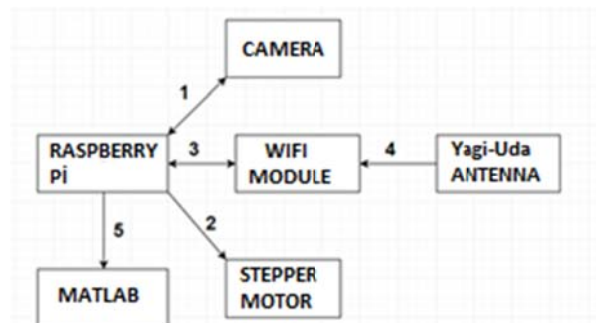
Figure 1:Major functional blocks of the proposed system

Stepper motors are electromechanical devices that convert electrical energy into physical energy by rotational movement. As the name suggests, motion is carried out in a step by step manner. They are permanent magnet pole motors that produce analog rotational motion output against pulse signals applied to their inputs, providing the step by step rotating motion with very precise control. The stepper motors consist of rotor, stator and bearings. The bearings allow the shaft connected to the rotor to move smoothly. The stator has more than one pole. The number of poles varies from engine to motor, but is usually eight. The polarity of the poles is continuously alternated by means of electronic switches. The magnetism of the rotor is generated either by permanent magnet or by external excitation techniques [5]. Since the number of steps generally provided by such a stepper motor is usually 200 and this is not sufficient to achieve the required sensitivity of rotation in our case additional power transmission control is provided by means of pulleys in the ratio of 1: 5. The designed system can rotate easily horizontally and vertically. When the

antenna is added to a 360 degree rotating system with 2000 steps, it can scan the surrounding area quite precisely. Nema 17 stepper motor controls the rotation with parameters determined by the RaspberryPi.

The camera module and WiFi module are also connected to Raspberry Pi 3. The image taken from the camera is processed with Matlab and the result is reached.

A. System Operation

In our scanning system, the control is in the processor and no external action is required during scanning. This automatic control allows the system to take the required number of samples from all points in the photographed area. A robust system with high torque is designed using stepper motors and pulleys. The L298N motor driver is used to control the stepper motors. An antenna is installed in the upper part of the system as the most suitable place to detect and measure incoming signal strength. The camera module is connected to the system for taking pictures respectively.
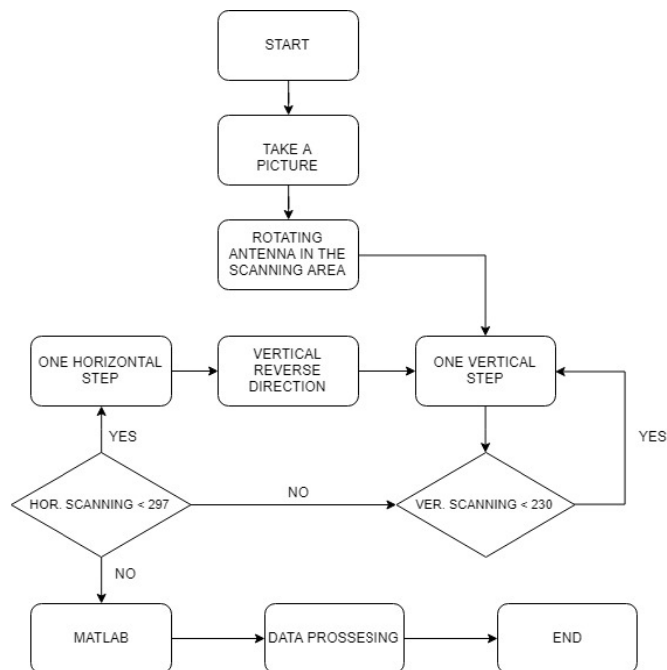
Fig. 2. System Operational Flowchart

Figure 2 shows the flowchart of the operational algorithm. The process starts with capturing the picture of the environment followed by controlled scanning of the respective area for WiFi signals. The Nema 17 stepper motor controls the rotation of the Yagi antenna by increasing the steps for vertical and then horizontal rotation. In turn the Raspberry Pi is used to determine angle values for the scanning in the range of 297 vertical and 230 horizontal steps. The designed Yagi-Uda antenna is combined with the WiFi module and connected to the processor for measuring signal strength. Thus operating the camera and the antenna in unison the surrounding environment is scanned and the wiFi signals with different strength at different frequencies are detected. After the area

where the photograph was taken is scanned and the measured signal strengths are mapped in a precisely matching manner.

B. Signal and Image Processing

In this section, the signal and image processing operations are described. The signal data received from the antenna is transferred to the computer and then the signal transformations are performed with the help of MATLAB.

To illustrate this part of the systems operation a example image is used as given in Figure 3. It is an RGB coded image. The RGB image corresponds to a 3D matrix, where each color is represented by 8 bits and 1 pixel is represented by a total of 24 color bits. In the image processing part of the system, the received signal strengths are arranged to correspond to the reception process.
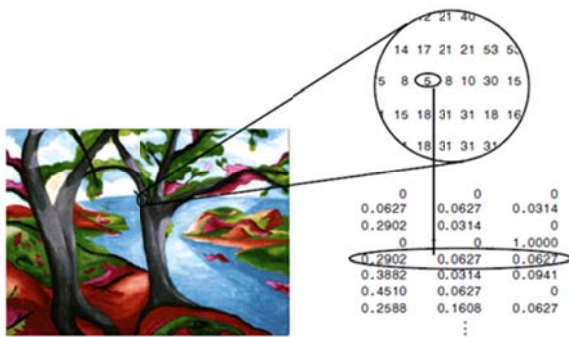
Fig. 3. RGB Coding Example

The signal strengths brought to the desired dimensions are colored according to the power levels to form a new color sequence. The color space and color code used shown in Figure 4.
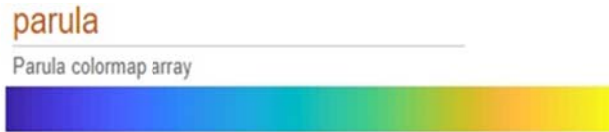
Fig. 4. PARULA Color Scale

This color sequence is matched with the photograph of the region and a map of the region with overlaid received signal strength values encoded in color is created.

The WiFi module is used to calculate the signal strength in dBm based on the detected Received Signal strength Indicator (RSSI) values. RSSI is a widely accepted parameter, used to measure the quality of a received signal at the receiver side be it a user mobile or a base station. It is usually determined as an average value over several measurements during a given time interval. Since measurements can in done as Signal-to-noise SNR in dBm it is necessary to convert them to RSSI values using the "RSSI_Max" each chip manufacturer is allocated by the defines IEEE 802.11 standard. The RSSI values range from 0 to 255 [6].

C. Yagi-Uda Antenna

An important component of the system is the Yagi-Uda antenna used to capture the WiFi signal in the examined area. In general the for the purpose of creating wireless connections using the 802.11 series stand IEEE specify different type of antennas which are omnidirectional or directional depending on the specific application. [7] [8] [9].

In our case, for the scanning process, a highly directional antenna is needed to provide good results. Therefore, a simple high-directional, cheap solution was selected.

The Yagi-Uda antenna has a very simple structure and is widely used for high gain [10] [11]. It consists of interference elements including an antenna, driver and reflector and one or more routers. In the frequency band of the antenna, the induced currents are approximately equal in amplitude and have equal step phase shift, resulting in a directed post-combustion zone. Therefore, a Yagi array can be considered a structure that supports a moving wave and is sometimes called the Yagi-Uda sequence.

The characteristics of the Yagi-Uda antenna, designed with specific parameters for the project is given in Figure 5.
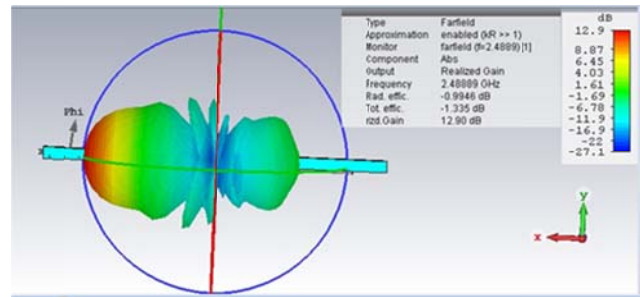
Fig. 5. Characteristics of the Yagi-Uda antenna

Antenna simulations were performed with CST (Computer Simulation Technology) program. The simulation and measurement gain results of the designed antenna are shown in Figure 6.
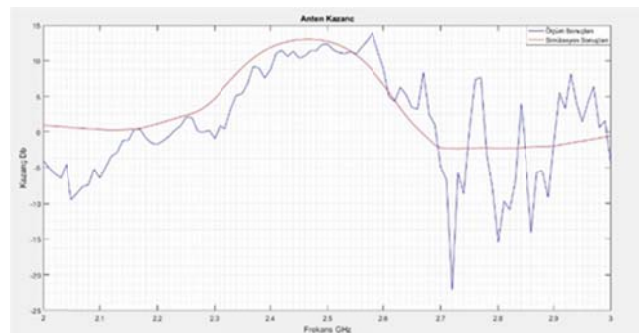
Fig. 6. Antenna Gain Results

IV. SYSTEM SOFTWARE

The software for the designed system was developed using Python, while Matlab is used for image processing. The

developed software controls the step and direction of the stepper motors which operate the antenna movement. The signal strength values are converted to the RSSI value with the WiFi module. In the following stage the signal strength values of the detected WiFi signals are processed using MATLAB and converted to a color scale. Then they are finally mapped onto the color image of the corresponding environment as shown in Figure 7. . They are mapped to color image was taken from the camera module. The signal strengths in the environment have been taken. Finally signal strengths were used to create colors on the image.
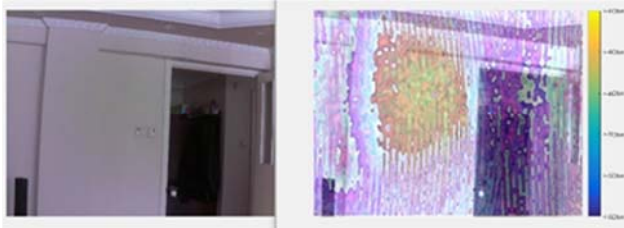
Fig. 7. Original picture and picture with mapped WiFi signals

V.   RESULTS AND DISCUSSION

In this work a system that can visualize signal strength of WiFi 2.4 GHz signals in a given area was designed. Tests in different areas were carried out. An example of the results from one of the experiments is given in Figure 7.

The WiFi signals in the area are detected by scanning with the help of a rotating Yagi-Uda antenna. The L298N motor driver circuit is used to drive the stepper motors rotating the antenna. For this experiment the motors are driven at half angle, thus 360 degree rotation is provided in 400 steps instead of 200. Rotation can be done in both directions. Furthermore the scanning is done both horizontally and vertically. The desired operations can be performed between the steps. The highest recorded value of the SNR in this experiment was -44 dBm and the lowest value is -52 dBm.

During the experiments it was observed that the scanning process is slow. This is contributed to the low processor speed and the low sensitivity of the WiFi module. The WiFi module receives signal strength with an accuracy of 1 dBm. To increase the system performance and reduce the scanning time a Software Defined Radio (SDR) module can be used instead of the WiFi module. for better results and speeding up the system. This will make the system more expensive but enable faster and more accurate measurements. It is also important to note that since the antenna can be easily separated from the system, antennas at different frequencies can be added to the system. In this way, mapping can be performed at different frequencies besides the 2.4 GHz which was used in this work.

VI.   CONCLUSION

In this paper we have discussed the design and implementation of a system that allows depicting the signal strength of WiFi signals in a visual way. The system is based on a Yagi antenna and a Raspberry Pi processor equipped with a camera. Using image processing techniques received signal strength is encoded into a color scale and overlaid with the corresponding image of the surrounding environment. MATLAB code ensures high conversion precision. Excluding the Yagi antenna which was custom designed from the project, the rest of the components are cheap, off-the-shelf components which make it a simple low cost solution. It can be used as a simple preliminary method to visually determine the availability and strength of WiFi signals when designing 802.11 wireless networks.

REFERENCES

[1]   Yücel H., Yazıcı A., Edizkan R., İç mekan lokalizasyon sistemleri araştırması2014 22. Sinyal İşleme ve İletişim Uygulamaları Konferansı (SIU), 23-25 Nisan 2014

[2]   Coşar M., Coşkun F., Ozulu I.M., İlçi V., Dış ortam kablosuz networklerde uygun sinyal dağılımının görünürlük analizi yöntemiyle belirlenmesi Sakarya Üniversitesi Fen Bilimleri Enstitüsü Dergisi, 21 Ocak 2017, 69-76

[3]   WC Chung W.C., Ha D.S., Hassas Varlık Konumunu Belirleyen Doğru bir Ultra Geniş Bant (UWB). Int. Konf. Ultra Geniş Bant Sistemleri ve Teknolojileri Üzerine, sayfa 389- 393, Reston, VA, Kasım 2003

[4]   https://www.youtube.com/watch?v=IDFRuG_D3Io

[5]   https://maker.robotistan.com/step-motor

[6]   https://itstillworks.com/calculate-average-rssi-80211-7823781.html

[7]   Gast M., 802.11 Kablosuz Ağlar: Tanımlayıcı Rehber. O'Reilly Media, Inc., 2005.

[8]   Ahson S., Wimax: Uygulamalar. Boca Raton: CRC, 2007.

[9]   https://www.wimaxforum.org/

[10]   Grajek P., Schoenlinner B., Rebeiz G., "Bir 24 GHz yüksek kazançlı Yagi-Uda anten dizisi," Antenler ve Yayılım, IEEE İşlemleri, cilt. 52, hayır. 5, sayfa 1257-1261, 2004.

[11]   Lim S., Ling H., "Yakın mesafeli, katlanmış Yagi anteninin tasarımı", Antenler ve Kablosuz Yayılım Mektupları, vol. 5, 2006

[12]   https://www.youtube.com/watch?v=j2rKAMDiW_c

[13]   https://www.theverge.com/2015/11/28/9811910/augmented-reality-app-lets-you-see-wireless-signals

Using AD7746 for high precision capacitance measurement in industrial applications

N. ÇANKAYA[1] and M. ÖZCAN[2]

[1]Necmettin Erbakan University, Konya/Turkey, ncankaya@erbakan.edu.tr
[2]Necmettin Erbakan University, Konya/Turkey, mozcan@erbakan.edu.tr

Abstract - **Capacitive sensors have been widely used in industry for many years. The basic measurement logic is to measure, analyze and linearize the changes in the dielectric coefficient of the environment. Thanks to the developing technology, these sensors have been used in new sectors in recent years. The use of these sensors has increased considerably in areas such as agriculture, biomedical devices, MEMS and mobile telephones. There are different methods of measuring the change of dielectric coefficient of the medium. Capacitive measurement is generally an inexpensive measurement method. However, there are weaknesses due to problems in capacity measurement. Magnetic noise and temperature variations adversely affect the measurement accuracy of these sensors. One of the most important reasons for this is that the measuring circuit contains a large number of elements and is susceptible to interference. However, the capacitive digital converter chips developed in recent years have made these sensors very reliable. The prices are also quite economical. The Ad7746 is one of these chips. This chip converts the capacitance in 24 bit resolution. It has temperature sensors in itself to compensate for temperature changes. The measured value from the electrodes is immediately converted to digital information. The measured values are transmitted directly to the device associated with the i2c protocol, with no distortion on the road. In this study, the characteristics of AD7746 sensor, its industrial applications and the technological features it provides are examined. It used an AD7746 circuit to measure the water level. The circuit has been tested for water presence and proportional water level. It has been found that the circuit is very successful against noise and temperature changes. It was concluded that the capacitive measurement sensor developed using AD7746 can be used reliably for liquid level measurements in the industry.**

Keywords – **AD7746, capacitance to digital, liquid level measuring**

I. INTRODUCTION

Liquid level measurement is commonly performed in many industrial plants. Electronic measurement and remote monitoring of liquid measurement is both necessary for safety and important for cost. The method used to measure the liquid level is to measure the capacity formed between the two electrodes. The capacity change with the rise of the liquid to be measured is analyzed. Capacitive measurement is used for many different processes in the industry [1-4]. This study focuses on the measurement of the liquid level. The most important problem of capacitive measurement systems is magnetic noise. Another problem is the effect of temperature changes on capacity [5-8]. These two problems have reduced the reliability of capacitive sensors. For this reason, capacitive sensors are generally used in applications where coarse measurements are performed. Sensors with different types of measuring technology are used for more accurate measurements.

Thanks to the developing technology, capacitive chips have been developed to eliminate the problems encountered in level measurement. One of the most advanced of these is AD7746. This chip is highly resistant to magnetic noise due to electronic components were fitted into a chip. The values taken from the electrodes are immediately converted to digital information in the chip. This information is also transmitted digitally by the I2C protocol. Thanks to this protocol, there is no error in transmission. Moreover, the measurement is done with very high accuracy of 24 bits. The temperature changes the dielectric coefficient of the materials. Temperature changes are therefore perceived as capacity changes, resulting in incorrect measurements. But the AD7746 has a temperature sensor. Thanks to this sensor, the chip calculates the capacity resulting from the temperature change and corrects the measurement result accordingly. As such, the AD7746 can also be used in areas where no capacitive sensor was used because it was not reliable before [9-12].

In this study, the liquid level was measured using AD7746 and the properties of the chip were analyzed.

II. MATERIAL AND METHODS

In this study, AD7746 and AD7746 Evaluation Board were used. The block diagram of AD7746 (Analog Devices 24-Bit Capacitance-to-Digital Converter with Temperature Sensor) was given in Figure 1. The function block diagram of AD7746 Evaluation Board (Analog Devices EVAL-AD7746EB) and its picture were given in Figure 2 and Figure 3. And AD7745/AD7746 Evaluation Software of Analog Devices was used to monitoring the measured values coming from EVAL-AD7746EB. The sensor designed for this study is given in Figure 4. The electrodes are made of stainless steel. Electrode dimensions are 10x10x150 mm. The capacitance was calculated by

$$C = \varepsilon_0 \varepsilon_r \frac{a \times b}{d} \tag{1}$$

A parallel-plate capacitor was characterized by
• a x b: conductor area
• d: Distance between the two conductor plates
• εr: dielectric constant for measuring environment
• εo: dielectric constant for air
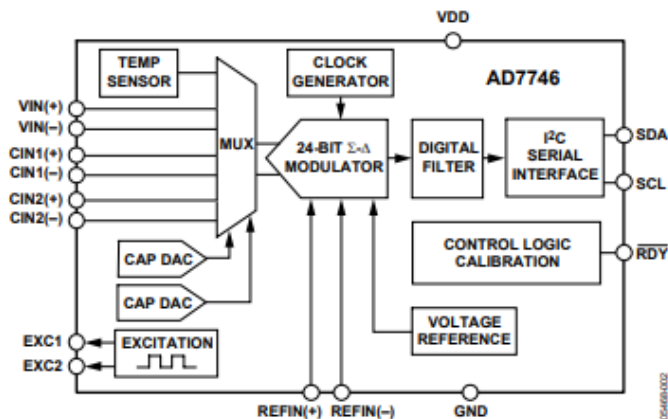
Figure 1: Functional block diagram for AD7746 [13]
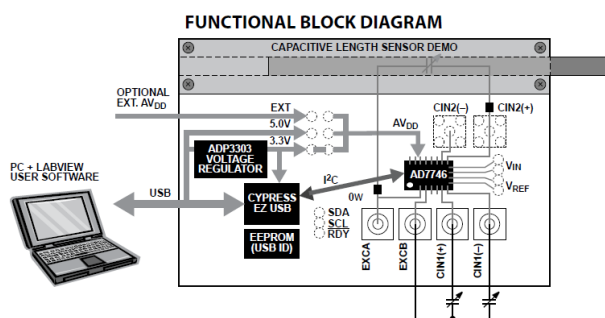
Figure 2: Functional block diagram for EVAL-AD7746EB) [14]

Figure 3: EVAL-AD7746EB) [15]

Figure 4: Sensor

This study was carried out experimentally using the equipment given above. With this equipment, measurements can be taken in the range of 0 - 4pF. Plastic and glass big cups of different sizes were used as water tanks and the principle diagram given in the figure was complied with. The distance between the electrodes was set at different values to be 4pF when the big water cup was full. By changing the water level in the water cup, the change of the liquid level was observed through the software installed on the computer. The measured accuracy was checked. The oscillations in the measured values were examined.

III.   RESULTS AND DISCUSSION

Sensor electrical configurations were given in Figure 5-7. Figure 8 shows principle diagram of liquid level measuring system.
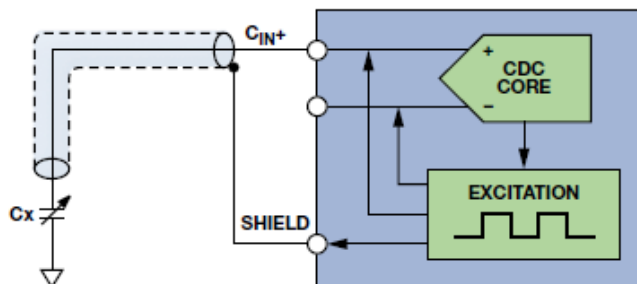
Figure 5: Single-ended grounded sensor [16].
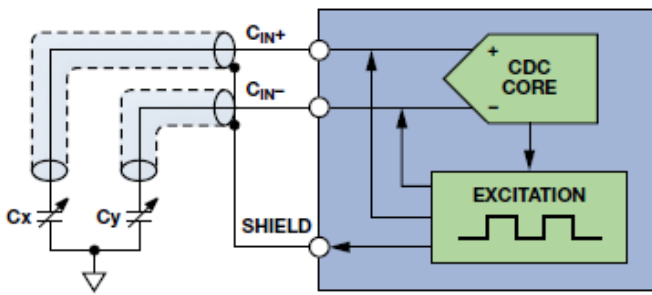
Figure 6: Differential grounded sensor [16].
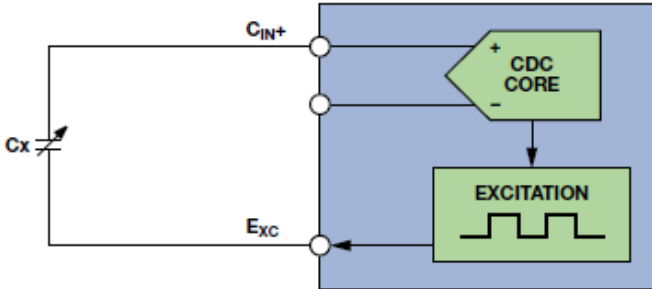
Figure 7: Single-ended floating sensor [16].
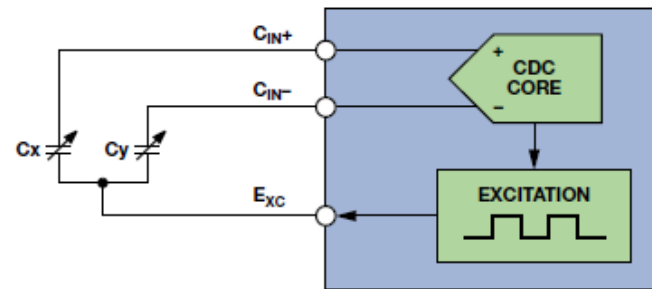
Figure 8: Differential floating sensor [16].
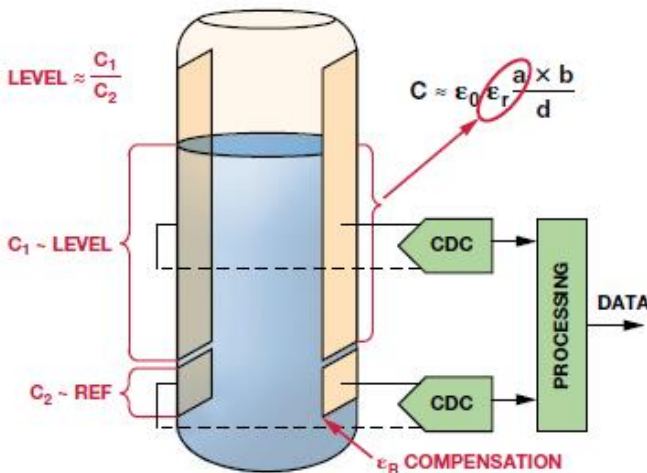
Figure 9: Principle diagram of liquid level measuring [16].

In experimental measurements, water level was measured

with high accuracy. The output was linear. The measurements were repeated near the 3 Phase 5.5kW 1500rpm induction motor to see the magnetic noise response. During the test, the motor was loaded with 50% and the measuring equipment was placed 50 cm from the induction motor. Later, the cables which comings from electrodes were shielded with thin aluminum foil, from the electrode outlet up to AD7746 input. This shielding was connected to the negative end of the feed. In this case, it was observed that the measured capacity values decreased by approximately 30%. According to these values, the water container was recalibrated for empty and full conditions. Measurements were made linearly in this interval. After this connection, it was seen that the measurement was performed with more accurate accuracy. The screenshots taken from the computer interface software showing the measured values were given in Figure 10-13.
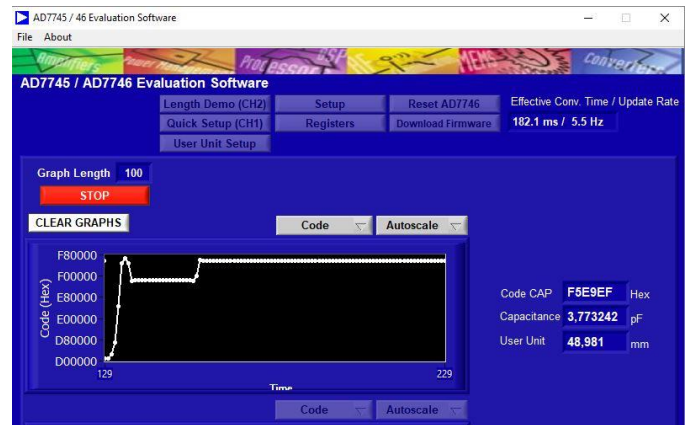
Figure 10: Screenshot a measuring for increasing water level.
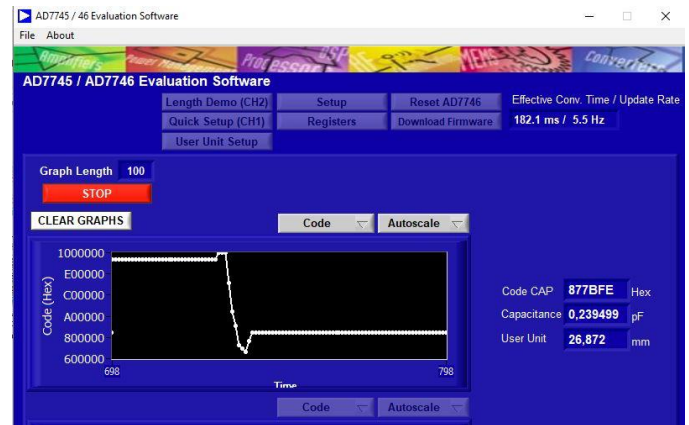
Figure 11: Screenshot a measuring for decreasing water level.
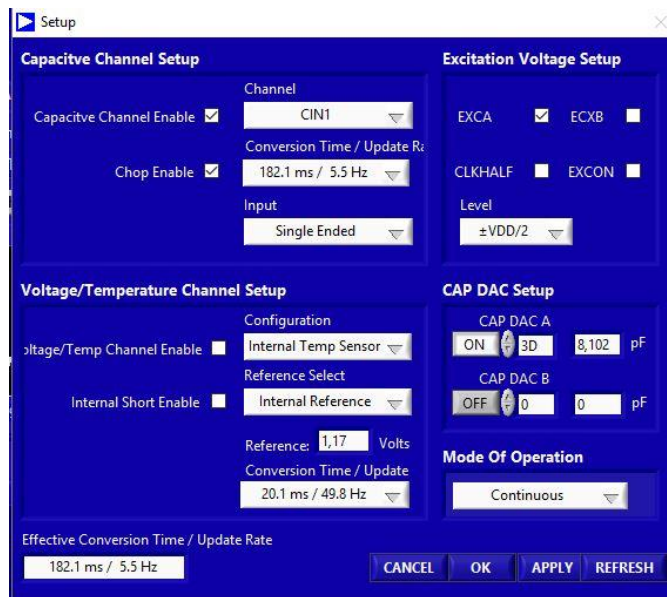
Figure 12: Screenshot for setup page.
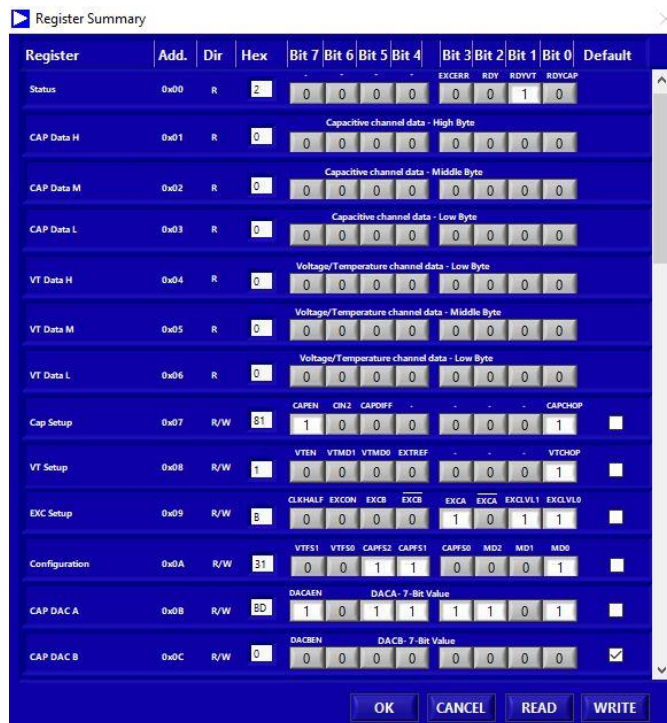
Figure 13: Screenshot for register summary.

IV. CONCLUSION

In this study, high precision capacity measurement was made by using AD7746. It was concluded that the capacitive sensors to be designed with this chip can be used successfully in industrial areas where no capacitive sensors have been used before. However, due to the price of this chip, 12-bit

resolution chips, which are a cheaper solution, can be used where 24-bit resolution is not required. With this chip, the measurements are not affected by magnetic noise and used at very high measuring speeds. Since all electronic components fit into a very small chip, the board design is simplified.

REFERENCES

[1] Oprea, A., Courbat, J., Bârsan, N., Briand, D., De Rooij, N. F., & Weimar, U. (2009). Temperature, humidity and gas sensors integrated on plastic foil for low power applications. Sensors and Actuators B: Chemical, 140(1), 227-232.

[2] Xia, S., Makinwa, K., & Nihtianov, S. (2012, February). A capacitance-to-digital converter for displacement sensing with 17b resolution and 20μs conversion time. In 2012 IEEE International Solid-State Circuits Conference (pp. 198-200). IEEE.

[3] Wang, J. (2015). Liquid level sensing using capacitive-to-digital converters. Analog Dialogue, 49(4), 1-3.

[4] Devices, A. (2005). Inc.,"24-bit capacitance-to-digital converter with temperature sensor, AD 7745/AD7746,". 2009-08-24]. http://www. analog, com/zh/analog-to-digital-converters/capacitance-to-digital-convert-ers/ad7745/products/product. html.

[5] George, B., & Kumar, V. J. (2010). Analysis of the switched-capacitor dual-slope capacitance-to-digital converter. IEEE Transactions on Instrumentation and Measurement, 59(5), 997-1006.

[6] Kim, H., Lee, B., Mun, Y., Kim, J., Han, K., Roh, Y., ... & Ko, H. (2018). Reconfigurable Sensor Analog Front-End Using Low-Noise Chopper-Stabilized Delta-Sigma Capacitance-to-Digital Converter. Micromachines, 9(7), 347.

[7] Shammeh, R. A. A., Al-Nasri, I., Walton, D., Trejos, A. L., & Price, A. D. (2019, March). Low-cost and scalable fabrication of wearable soft sensor for neck mobility measurement. In Electroactive Polymer Actuators and Devices (EAPAD) XXI (Vol. 10966, p. 109661V). International Society for Optics and Photonics.

[8] Ma, X., Guo, J., Lee, K. M., Yang, L., & Chen, M. (2019, August). A Soft Capacitive Wearable Sensing System for Lower-Limb Motion Monitoring. In International Conference on Intelligent Robotics and Applications (pp. 467-479). Springer, Cham.

[9] Paun, M. A., Schnegg, A., Joly, S., Orhan, J. B., Lepple-Wienhues, A., & Dehollain, C. (2019). Three-Dimensional Model and Evaluation of an Insulin Injection Pen for Precise Dose Capacitive Measurement. IEEE Access, 7, 117426-117435.

[10] Xia, S., & Nihtianov, S. (2018). Capacitive sensors for displacement measurement in the subnanometer range. In Smart Sensors and MEMs (pp. 87-99). Woodhead Publishing.

[11] Bednar, T., Borik, S., & Babusiak, B. (2019, May). Precise CDC based Measurement System for Biomedical Applications. In 2019 12th International Conference on Measurement (pp. 123-126). IEEE.

[12] Možek, M., Vrtačnik, D., Resnik, D., Pečar, B., & Amon, S. (2010). Digital temperature compensation of capacitive pressure sensors. Informacije MIDEM, 40(1), 38-44.

[13] https://docs-emea.rs-online.com/webdocs/0e38/0900766b80e38fa6.pdf

[14] https://docs-emea.rs-online.com/webdocs/1403/0900766b81403157.pdf

[15] https://fr.rs-online.com/web/p/kits-de-developpement-d-interface-homme-machine-hmi/8813047/

[16] Jia, N. (2012). ADI Capacitance-to-Digital Converter Technology in Healthcare Applications. Analog Dialogue, 46(2).

A Free Form Lens Design for Long Range LED Illumination

A.BİNGÜL[1] and A.J. BEDDALL[1]

[1] Gaziantep University, Gaziantep/Turkey, bingul@gantep.edu.tr
[1]Bahçeşehir University, Istanbul/Turkey, andrew.beddall@cern.ch

Abstract - **In this study, a procedure for designing a free-form lens for long-range LED illumination is presented. The geometrical form of the free-form lens is obtained by minimizing optical path lengths of the rays emitted from the light source. Also, a prototype of the proposed lens is manufactured by the plastic injection method using PMMA material whose transmittance for the visible and near infrared optical regions is greater than 90%. Optical power measurements of the lens for two different LEDs are compared with the simulations based on Zemax OpticStudio.**

Keywords - **Free-form lens, Long range illumination, PMMA, optical design.**

I. INTRODUCTION

L ED (Light Emitting Diode) is an energy-saving source providing high light efficiency and has a long life time. Despite the high light efficiency, in general, the direct light output of LEDs spread at wide angle. This results in a disadvantage in the use of LEDs when illuminating a surface being at a large distance from the source. The light intensity on a target can be improved either by using reflectors or by placing the narrow-angle free-form lenses having a suitable geometry in front of the LED.

There are many academic and engineering studies on design and production of free-form lenses in literature such as [1-6]. In this study, a free-form lens design based on optical path calculations is presented for long-range (or narrow-angle) illumination for both near infrared (IR) and visible regions. Optical simulation of the free-form lens and LED is developed in Zemax OpticStudio [7] for three different polymers; PMMA (poly(methyl methacrylate)), PC (polycarbonate) or PS (polystyrene). Simulation studies show that PMMA exhibits slightly better performance compared to others. In addition, a prototype of solid free-form lens is manufactured by using PMMA via plastic injection method. By using two different LEDs, optical measurements of the free-form lens and LED system are compared with the simulations. Results seem to be consistent if one considers mounting and manufacturing tolerances.

II. FREE-FORM LENS PROFILE

Free-form lenses are preferred mostly in illumination [2, 3] and also in imaging systems[3]. In this study, a profile of free-form lens to be used in LED illumination is proposed in order to obtain a narrow-angle beam spot at long distances.

Aim of the lens is to deflect all of the rays emitted from the source such that they are parallel to optical axis on the exit side of the lens. Figure 1a shows the required curves and three rays originating from the point source placed at origin. Optical path lengths (OPL) for rays A, B and C must be equal so that they reach the detector (or target) at the same time. This approach results in four well-known curves; a parabola, a hyperbola, an arc and a line. Three-dimensional (3D) solid form of the lens is simply obtained by rotating the lens in y-axis as shown in Figure 1b.

III. MANUFACTURING THE LENS

In the manufacturing of free-form lenses, PMMA (poly(methyl methacrylate)), PC (polycarbonate) or PS (polystyrene) are used as the lens material. Nowadays, manufacturers prefers mostly PMMA since it has lower index of refraction and better optical transparency properties [8].

A prototype of a solid free-form lens is manufactured by using PMMA via plastic injection method. Figure 2 shows the free-form lens made from PMMA.. There are some manufacturing errors such as scratches on the surface and small bubbles in the lens. These are possibly originating from the mold design and bad pre-drying condition of PMMA.

IV. OPTICAL SIMULATION

The equations derived for 2D free-form lens geometry and the point-like source are implemented in a C++ programming language to attain basic calculations related to ray tracing for single wavelength. However, in reality one needs 3D geometry and LED which is neither a point-like nor a monochromatic source.

Fortunately, there are solid (or optical) modeling softwares to obtain 3D geometry and assign desired polymeric material to the lens. Also, LED manufacturers distribute comprehensive ray-tracing data files to be used in optical simulations such as eulumdat, spectrum and ray files.

In principle, LED is considered as a point source in eulumdat files. Whereas, the spectrum file contains information about the wavelength of the light source and corresponding weight. The ray file represents actual light distribution of LED and can be used in more realistic simulations.

In Non-Squential Mode of Zemax, one can include simulation files of LED, the 3D solid free-form lens and a suitable rectangular detector which is basically a counter of rays hitting on it. Two types of LED provided by Osram Opto Semiconductors [9] are chosen in both simulations and optical measurements. The results are shown on Figure 3.

Figure 2: Manufactured free-form lens made from PMMA and two LEDs used in the study.
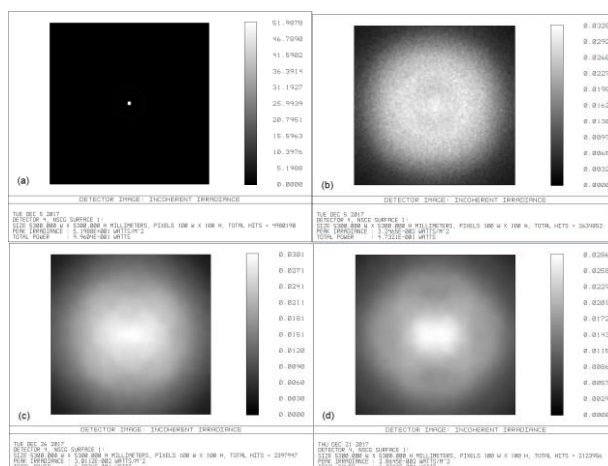
Figure 3: Spot diagrams obtained in Zemax at a distance $L = 100$ m from IR LED whose radiant power is 1 W by using (a) eulumdat file and PMMA (b) ray and spectrum fles and PMMA (c) ray and spectrum files and PC (d) ray and spectrum file and PS.

Figure 1: Schematic diagram for the surfaces of free-form lens (a) in 2D plane and (b) in 3D solid form. Four curves are obtained using the principle that OPLs of ray A, B and C are the same.

V.   OPTICAL MEASUREMENTS

In order to test the optical performance of the manufactured free-form lens two measurements are carried out using IR LED (Osram SFH4715) and white LED (Osram LUW CVBP). It is obvious that the measurement result is in good agreement with the simulation, Figure 4.

VI.   SUMMARY AND CONCLUSION

In this study, a prototype of a free-form lens which can be used for long range illumination is designed and manufactured. IR and visible LEDs are selected as light sources. Various optical polymers (PMMA, PC and PS) are concerned as lens material in Zemax simulations. Optical performance of the LED and lens system is tested on a detector placed at 100 m away from the LED.

In manufacturing of the lens, PMMA is selected since it exhibits the best performance in terms of optical power on the detector according to simulation results. Even though these defects and LED-lens misalignments in the mounting, the optical measurements are consistent with the simulations for an uncertainty about 2 degrees in the tilt angle. Hence, the illumination performance of the proposed free-form lens depend significantly on typical manufacturing errors and mounting tolerance of LED and lens.

Finally, authors suggest that an array of such free-form lenses can be used as a LED projector for the purpose of long

range illumination since angular divergence of single lens is less than 1° according to simulation results. This projector may be useful in optical wireless communication, in illumination of car parks or stadiums,

[7]　Zemax, Version June 9 2009 https://www.zemax.com
[8]　N. Sultanova et al, Acta Physica Polonica A, 116 (2009)
[9]　Osram, https://www.osram.com, (2018)
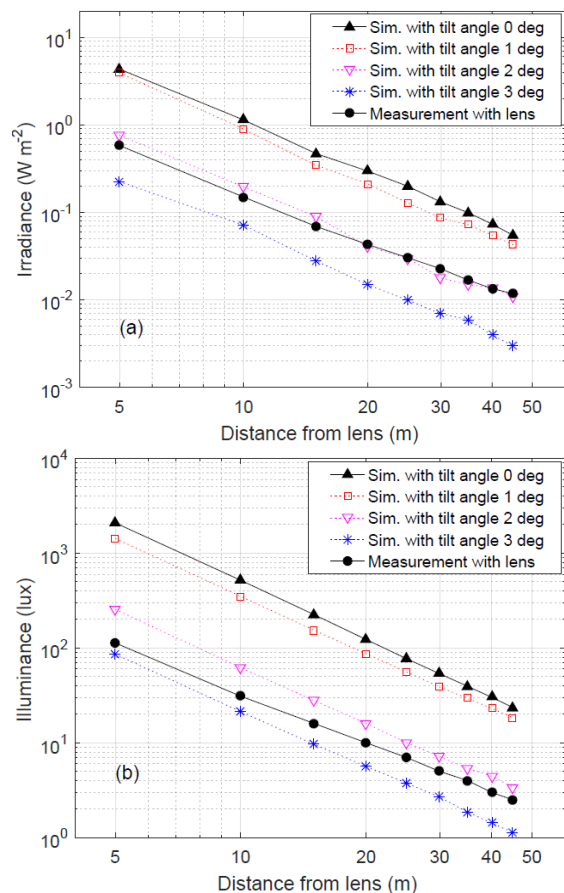
Figure 4: Simulation and measurement results of irradiance and illuminance as a function of distance from the LED and lens system for (a) IR and (b) visible LED. The misalignment of LED and lens is modeled in simulation by changing the tilt angle of the lens about y-axis at 1, 2 and 3 degrees.

REFERENCES

[1]　H. Ries and J. Muschaweck, Opt. Soc. Am. A, 19 (2002)
[2]　Y. Ding et al, Opt. Soc. Am. A, 16 (2008) 12958-12966
[3]　B. Yang et al, Optik, 120 (2009) 74-78
[4]　N.D.Q. Anh et al, Opt. Soc. Am., 53 (2014)
[5]　S. Hu et al, Appl. Opt., 54 (2015) 9990-9999
[6]　R.J. Lin and C.C Sun, Optical Engineering, 55 (2016)

Locating the Sensors Positions in WSN Based on MUSIC Algorithm

Saad S. Hreshee

University of Babylon, College of Engineering, Dept. of Electrical Engineering, Babylon-Iraq

hreshee@gmail.com

saadalkhazali@yahoo.com

Abstract - **Wireless sensor networks are often randomly deployed using an aircraft, for example, so the position of these nodes cannot be obtained previously. Therefore, we will produce a so-called site identification problem, i.e. how to obtain the site information of the unspecified node, and this is one of the most important topics of these networks. The Global Positioning System (GPS) is the most used positioning system for this time. But usually the disadvantages of these nodes are its high expenditure, its large volume, and its high cost, so the (GPS) is not applicable in these networks which are inherently self-configured low cost, and also it is impossible to install GPS for each node. In this paper, non-GPS positioning mechanisms will be used and studded for the wireless sensor networks. The effectiveness of the use of the MUSIC algorithm will be tested in the identification of signal flower angles based on SDMA technology and ESPAR antenna.**

Keywords - **Wireless sensor networks, WSN, positioning, MUSIC algorithm, SDMA technology.**

I. INTRODUCTION

Wireless sensor networks consist of hundreds or thousands of small size devices called sensors. These sensors subject to some limitations like memory, energy and limited processing capacity. Wireless sensor network is a set of sensors that are used to transmit or follow a specific physical or chemical phenomenon (e.g. heat, humidity, light, ...) [1]. Its basic idea is to deploy thousands of sensors in an environment and organize the transformation of wireless messages between them and transfer them to the data processing center to collect and use them without the need for human presence in the location of the phenomenon. These networks are expected to solve problems of surveillance, disaster relief, patient tracking, military purposes, automated warehouses and smart homes ... etc [2].

The knowledge of the site in these applications is very useful and necessary, because collecting information without knowing the location of the sensitive node is useless. Positioning can be carried out in several ways, such as providing each sensor with a GPS receiver that gives the precise location of each sensitive node but adding GPS receiver to each node is not practical for many considerations, such as high cost, energy consumption, and environmental constraints. In addition to its failure in the indoor environments and in the dense forests and underground [1].

The best solution of this problem is to self-identify the site, where each node is estimating its location using site discovery protocols. These protocols share many features, most of which use a special node called Beacon Nodes. It supposed that the locations of these nodes are known (with manual settings or using GPS receivers). These nodes are known as central nodes, references nodes, or anchor nodes, which provide us the information of the site in the broadcast messages form and give importance of the other nodes known as (blind, silent, or anonymous nodes) because the location determining of the other nodes depend on the location's information of the reference nodes [3, 4].

Locating the position in the wireless sensor networks is important and has attracted the attention of researchers in this area, due to the rapid growth in wireless technologies and sensor technologies, as well as the large spread of wireless sensor network applications. The importance of knowing the location of nodes comes from the adoption of most network functions on nodes sites such as: Routing, communication, cluster formation, network coverage and tracking goals [4].

II. THE AIM AND OBJECTIVES OF RESEARCH:

Positioning in wireless sensor networks is one of the most important researches that have been studied in several reference studies aimed at knowing the relative or precise positioning of the sensors deployed within the environment under study. The purpose of this research is to study the non-GPS positioning mechanisms used in wireless sensor networks, and to test the effectiveness of using the MUltiple SIgnal Classification (MUSIC) algorithm in determining the signal-receiving angles based on Spatial Division Multiple Access (SDMA) technology and Electronically Steerable Parasitic Array Radiator (ESPAR) antenna using computer simulations. The comparison and assessment based on [5, 6]:

- Accuracy in the design of the general plan for the distribution of sensors in the studied environment.
- The minimum amount of cross-control data between sensors, and therefore the minimum time the network can take in determining the positioning scheme.

In most applications, sensors are randomly deployed in the studied area, so it is important to know the locations of these sensors without depending on GPS technology. The algorithms used to measure the dimensions of the sensors are combined with the positioning algorithms to obtain the approximate positioning required for the sensor. The exact

position can be obtained later by knowing the exact position of a sensor and preferably the reference node [4].

III. RESEARCH METHODOLOGY AND MATERIALS

The continued development of the world of wireless sensor networks and its applications is a parallel development of simulation and design programs that help assess the performance of these networks. In addition to the high privacy required by these networks of simulators such as security requirements, downtime, quality of service requirements, and routing protocols. In this paper, MATLAB program was used for the simulation of the proposed algorithms.

A. IMPORTANCE OF POSITIONING IN WIRELESS SENSOR NETWORKS

The data provided by a sensitive node loses much of its importance when it is devoid of site-specific information, because the absence of a location may lead to a misinterpretation of the data; Because of environmental constraints, it is difficult to place the node in precisely defined places, so the node may be subject to random strew. The current positioning systems, which are good for many applications, have achieved accuracy of up to about 0.5 meters. However, for other applications, such systems had to be improved, so the problem was to create a system capable of positioning with a small error rate [6].

Positioning is defined as the combination of the three main position information that are distance estimation, location estimation and mapping. It is one of the key elements in wireless sensor networks. Most of the positioning algorithms in wireless sensor networks share three key steps:

1) Distance Estimation: This phase involves the use of measurement techniques to estimate the relative distance between nodes.
2) Location Computation: This phase includes the relative estimate of the location of the nodes (node location with respect to another site-specific node).
3) Positioning Algorithm: in this phase, the location and distance information are gathered to reduce errors and mapping the node position accurately.

B. DISTANCE ESTIMATION

Distance estimation techniques can be classified into two main categories which are range based techniques and range free techniques as shown in figure (1).

i. RANGE BASED TECHNIQUES

The range-based techniques are divided into four main parts described below [7, 8]:

a. RECEIVED SIGNAL STRENGTH INDICATOR (RSSI)

RSSI technology is cheaper and easier between distance-based technologies and does not require additional hardware, but the received signal in the real environments is largely affected by noise. In addition, they are affected by the multipath problem caused by successive signal reflections, as well as the needing of high-sensitivity receivers which due to high cost. RSSI requires a pre-survey of the site and specifying signal levels at several points of the coverage area. All of this presents challenges to the use of this technique.
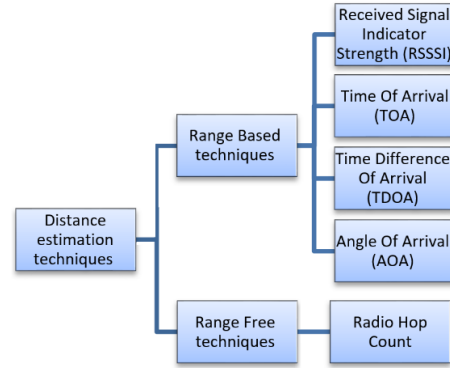
Figure (1): Classification of distance estimation techniques

The strength of received radio signal is inversely proportional to the distance between the transmitter and receiver, so the intensity of the received signal can be converted to distance information. The relationship between the distance d and the received power of the signal P_r is given by:

$$P_r = c \frac{P_{tx}}{d^\alpha} \quad \leftrightarrow \quad d = \sqrt[\alpha]{c \frac{P_{tx}}{P_r}} \tag{1}$$

Where P_r is the received power of the signal, c is the speed of light, P_{tx} is the power of the transmitted signal, d is the length of the path, and α is the path losses coefficient.

b. TIME OF ARRIVAL (TOA)

The distance between the nodes is estimated depending on the signal propagation time, where the distance between two nodes is directly proportional to the time required to propagate the signal from the first to the second node as in the equation.

$$d = v_s * t \tag{2}$$

where d is the distance between two nodes, v_s is the velocity of propagation, and t is the propagation time.

This method is usually not used because it requires precise synchronization between the transmitter and receiver, which requires additional cost and complexity for the sensitive node.

c. TIME DIFFERENCE OF ARRIVAL (TDOA)

This method is a development of the TOA technology where the node sends two different signals (radio and acoustic) to its neighbor's nodes. the distance then calculated depending on the different time of propagation of the radio and acoustic signals from the same point and the propagation velocity of each signal. The node calculates the difference between the time of arrival of both signals and the distance between tow nodes can be calculated by:

$$d = v_{sound} * (t_{sound} - t_{radio}) = v_{sound} * \Delta t \tag{3}$$

where: v_{sound} is the speed of the propagation of sound in the vacuum, t_{sound} is the sound signal propagation time, t_{radio} is the radio signal propagation time, and Δt is the time difference between the two signals.

d. ANGLE OF ARRIVAL (AOA)

In this algorithm, angles can be measured instead of measuring the distances between the nodes. This algorithm also called the Direction of Arrival Algorithm (DOA). The angle can be the link between a reference direction and the line that connects the central node with a sensor and can be the angle between two lines each connecting central node to a sensor. The usual method of measuring angles is the use of motorized directive antenna rotates on their axis (like RADAR).

Another way to measure the angle is to exploit the limited velocity of wave propagation; when multiple antennas are used separated by specific distances, the position from which the wave came from can be calculated after measuring the difference between the times of wave arrival to each antenna. Whenever the distances between these antennas are shorter, the measurement of arrival difference will be more accurate. The angle of arrival relationship is given by the following equation:

$$\Delta t = \frac{\delta}{(v*cos\theta)} \qquad (4)$$

where θ is the angle of arrival, δ is the antenna separation coefficient, and Δt is the difference between the times of wave arrival to each antenna, v is the velocity of propagation.

ii. RANGE FREE TECHNIQUES

This technique called in some references Radio Hop Count (RHC). The basic principle of its work is that if two nodes are able to communicate, the distance between them, with a high probability, will be smaller than the range of their maximum transmission that limited by a certain distance R. Its accuracy depends deeply on the node's density, the number of nodes located in known locations, and the network structure. These technologies are simple and low cost and suitable for applications where the accuracy of the site is not critical [9]. From the above review of the positioning algorithms, the DOA algorithm was selected in this paper.

IV. POSITION COMPUTATION TECHNIQUES

These techniques are used to link information with the purpose of calculating a node's location, and we will examine some of the known technologies

A. LATERATION SCANNING TECHNOLOGY

This technique is used to calculate the location of a node in the network depending on precise measurements with three adjacent central nodes, and when using this technique with 3D space, it needs four central nodes. When three central nodes are used, this technique is called trilateration (figure 2). And when using more than three central nodes, this technique

is called Multi-lateration (figure 3). The node is located by the intersection of three circles of three adjacent central nodes, and the radius is the distance from the central nodes to the required node [10].

Its disadvantages may be location information and distance information is inaccurate and this may make the three circles do not intersect.
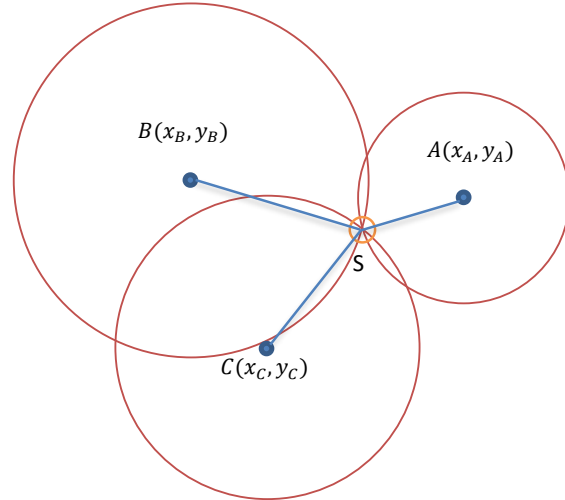
Figure (2): Triple-point scanning technique for calculating distance between nodes
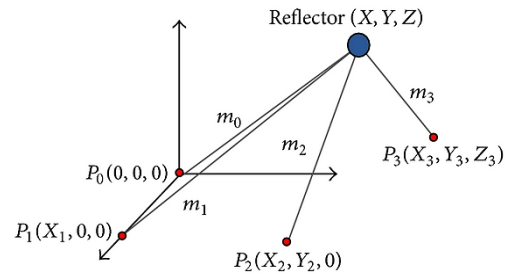
Figure (3): Multi-lateration scanning technique for calculating distance between nodes

B. TRIANGULATION TECHNOLOGY

Triangulation is a common method of calculating a node's location, it is on the angle of arrival of information instead of the distance figure (4). The node in the WSN networks estimates the angles between them and at least two central nodes, and then applies the triangle laws to calculate their location. Based on the angle of arrival (AoA) technique, the distance between the node and the central node can be estimated [10, 11].
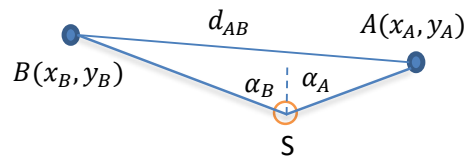
Figure 4: Spatial triangulation technique for calculating distance between nodes

C. PATTERN MATCHING LOCALIZATION

Also called the map-based algorithm or Finger Print Algorithm and includes two phases [10]:

- **First Phase (offline):** records the parameters of the received signals from the node in a database called the Radio map.
- **Second phase (online):** in which the sensors operate and the map is calculated.

Patterns matching algorithms are used to estimate the location of the anonymous node by matching the signal specifications captured with the pre-recorded values on the map. However, this method suffers from the effect of weather fluctuations because they have recorded signal parameters in the first phase and need to re-implement the first phase again in the new weather.

V. MUSIC ALGORITHM (MULTIPLE SIGNAL CLASSIFICATION)

MUSIC algorithm is a special structure algorithm with a high-resolution, widely used to create the required parameters during the process of determining the direction. There are several improved forms of the MUSIC algorithm such as the Root MUSIC algorithm and or MUSIC algorithm with spatial spectrum. These algorithms need signals from antenna array elements to form a signal correlation matrix. To apply this algorithm, it is useful to know the radiation pattern [11].

Most AoA algorithms used in the location estimation depend on the signal correlation matrix given by eq. (5).

$$\left.\begin{aligned} R_{ss} &= E\{S(t)S^H(t)\} \\ R_{xx} &= E\{X(t)X^H(t)\} \end{aligned}\right\} \tag{5}$$

where R_{xx} and R_{ss} are the correlation matrix of the received and the required signals respectively, while H represent the Hermitian transform of the matrix and $E\{a\}$ is the probability of the value a.

If the statistics of the signal and noise are unknown and the transformation processes are Ergodic signal (the stable signal called as the Ergodic signal if the time average of a function along the trajectories exists almost everywhere and is related to the space average and equals to the statistical average measured at any point in time), then the correlation matrices can be made closer by using the arithmetic mean of a limited number of monitored data and the eq.(5) become as in (6) [12]

$$\left.\begin{aligned} \hat{R}_{ss} &= \frac{1}{L}\sum_{i=1}^{L} \bar{S}(t_L)\bar{S}^H(t_L) \\ \hat{R}_{xx} &= \frac{1}{L}\sum_{i=1}^{L} \bar{X}(t_L)\bar{X}^H(t_L) \end{aligned}\right\} \tag{6}$$

where L is the number of signal samples, and with additive white Gaussian noise, the received signal matrix $\hat{R}_{xx}$ will be:

$$\hat{R}_{xx} = A(\theta)\hat{R}_{ss}A^H(\theta) + \sigma_n^2 I \tag{7}$$

where σ_n^2 is the variance of the noise signal, $A(\theta)$ is the response matrix where each element in this matrix represent the response of sensors to each signal occur, and represented by eq. (8)

$$A(\theta) = [a(\theta_1)\ a(\theta_2) \dots \dots \dots a(\theta_k)] \tag{8}$$

MUSIC algorithm is the most common algorithm among the AoA algorithms. Estimating the required AoA algorithms by defining the peaks of MUSIC spatial pseudospectrum given by eq.(9):

$$p_{MUSIC} = \frac{a^H(\theta)a(\theta)}{a^H(\theta)E_n E_n^H a(\theta)} \tag{9}$$

where $\hat{E} = [\hat{e}_1,\ \hat{e}_2,\ \dots\ \widehat{e_N}]$ is the main error vector that can be obtained by downloading main error values. The main error values are descending arranged from largest to smallest, and the main error values matrix can be divided into two matrices:

$$E = \begin{bmatrix} \widehat{E_s} & \widehat{E_n} \end{bmatrix}$$

where $\widehat{E_s}$ is the main error vectors of the signal, which have K columns and it corresponds to the partial spaces of the signal. $\widehat{E_n}$ is the main error vectors of the noise, which have N-K columns and it corresponds to the partial spaces of the noise [13].

In this paper the operation of MUSIC algorithm depending upon ESPAR antenna and on the Space Division Multiple Access (SDMA) Technique.

A. ELECTRONICALLY STEERABLE PARASITIC ARRAY RADIATION (ESPAR) ANTENNA

Figure (4) shows a typical structure of an interactive controlled steering antenna, which is called Electronically Steerable Parasitic Array Radiation (ESPAR) Antenna. Consists of an effective central element (monopole antenna) (Fed Element #0) surrounded by auxiliary elements (Parasite elements) in the form of a circle of radius R installed on a grounded circular plane (Ground Plane). Each monopole element of length L. the radius R equals to a quarter of the wavelength (λ) of the transmitting RF signal. The ground plane converts monopole antenna elements with their images to a dipole antenna elements of length 2L. The effective central monopole antenna element is connected to the RF receiver circuit and each other monopole auxiliary elements are connected to an adjustable phase-shifter.

The work principle of ESPAR antenna is different from that of other antennas. ESPAR antenna generates a directional beam based on adjustable phase-shifter $(X_1, X_2, \dots\dots, X_i)$ in the monopole auxiliary elements, where the receiver or transmitter signals at the central RF gate initiate the monopole elements, resulting in alternating currents [12, 13].
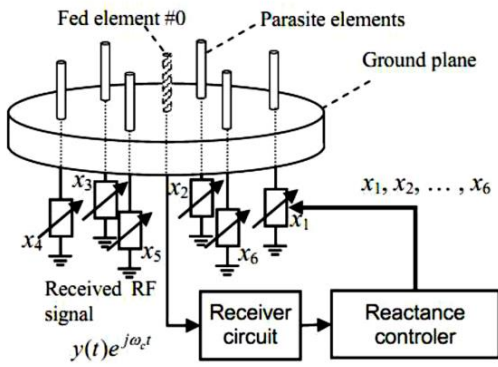
Figure (4) typical structure of a directional ESPAR antenna format [8].

By imposing the presence of signals coming at the azimuthal level, the exponential guide k will be the guide of the sources of the wave. The steering beam of the antenna is given by eq. (10) for six parasite elements (i=6):

$$\alpha(\emptyset_k) = [1 \; e_1(\emptyset_k) \; e_2(\emptyset_k) \; e_3(\emptyset_k) \; e_4(\emptyset_k) \; e_5(\emptyset_k) \; e_6(\emptyset_k)] \quad (10)$$

where $\alpha(\emptyset_k)$ represent steering beam corresponding to the signal direction which give $\emptyset_k$ corresponding to the structure of the ESPAR antenna [8].

$e_i(\emptyset_k)$ can be calculated from equation (11):

$$e_i(\emptyset_k) = exp\left\{ j\frac{2\pi}{\lambda} R \; cos\left(\emptyset_k - \frac{2\pi}{6}(i-1)\right)\right\}$$

Since $R = \frac{\lambda}{4}$

Then

$$e_i(\emptyset_k) = exp\left\{ j\frac{\pi}{2} cos\left(\emptyset_k - \frac{\pi}{3}(i-1)\right)\right\}; for \; i = 1 \; to \; 6 \quad (11)$$

and the steering beam $\hat{\alpha}(\emptyset_k)$ of the ESPAR antenna as in equation (12):

$$\hat{\alpha}(\emptyset_k) = \alpha(\emptyset_k)E_1 \quad (12)$$

$$E_1 = (I + YX)^{-1}YU_1 \quad (13)$$

$$U_1 = [1 \; 0 \; 0 \; 0 \; 0 \; 0 \; 0]^T$$

The admittance matrix Y is:

$$Y = \begin{bmatrix} y_{00} & y_{01} & y_{02} & y_{03} & y_{04} & y_{05} & y_{06} \\ y_{10} & y_{11} & y_{12} & y_{13} & y_{14} & y_{15} & y_{16} \\ y_{20} & y_{21} & y_{22} & y_{23} & y_{24} & y_{25} & y_{26} \\ y_{30} & y_{31} & y_{32} & y_{33} & y_{34} & y_{35} & y_{36} \\ y_{40} & y_{41} & y_{42} & y_{43} & y_{44} & y_{45} & y_{46} \\ y_{50} & y_{51} & y_{52} & y_{53} & y_{54} & y_{55} & y_{56} \\ y_{60} & y_{61} & y_{62} & y_{63} & y_{64} & y_{65} & y_{66} \end{bmatrix} \quad (14)$$

when there are a K incident waves, the output signal at the RF gate will be:

$$X(t) = \sum_{k=1}^{K} \hat{\alpha}(\emptyset_k)s_k(t) + n(t) \quad (15)$$

where $s_k(t)$ is the kth far field waves coming with amplitude and phase in the azimuthal level, $n(t)$ is the Additive white Gaussian noise (AWGN) with α^2 power.

Beam patterns can be formed in the desired directions by using phase shifters and attenuators in the direction of signal that causes of interference by adjusting the attenuation values. The signal is shifted depending on the angle of the coordinates of the X-Y antenna location and the receiver signal samples are represented at each m sampling period according to eq.(16) as follows:

$$X_m(t) = \sum_{k=1}^{K} \hat{\alpha}\left(\emptyset_k - \frac{2\pi}{m}(m-1)\right)s_k(t) + n_m(t) \quad (16)$$

$$\hat{\alpha}_m(\emptyset_k) = \hat{\alpha}\left(\emptyset_k - \frac{2\pi}{m}(m-1)\right) \quad (17)$$

Matrix $\hat{\alpha}_m(\emptyset_k)$ contains information number k about the signal source direction $\emptyset_k$, and $n_m(t)$ is the noise component at the period of sample m. Assuming that each independent signal source transmits instantaneous signals, and the length of the sampling period is of equal length [12].

The receiving signal samples are the same for all sampling intervals, so the receiver signal beam $X(t)$ can be written after six sampling intervals in the form of a double matrix (eq. (18)).

$$X(t) = \begin{bmatrix} X_1(t) \\ X_2(t) \\ X_3(t) \\ X_4(t) \\ X_5(t) \\ X_6(t) \end{bmatrix} = \begin{bmatrix} \hat{\alpha}_1(\emptyset_1) & \hat{\alpha}_1(\emptyset_2) & ... & \hat{\alpha}_1(\emptyset_k) \\ \hat{\alpha}_2(\emptyset_1) & \hat{\alpha}_2(\emptyset_2) & ... & \hat{\alpha}_2(\emptyset_k) \\ \hat{\alpha}_3(\emptyset_1) & \hat{\alpha}_3(\emptyset_2) & ... & \hat{\alpha}_3(\emptyset_k) \\ \hat{\alpha}_4(\emptyset_1) & \hat{\alpha}_4(\emptyset_2) & ... & \hat{\alpha}_4(\emptyset_k) \\ \hat{\alpha}_5(\emptyset_1) & \hat{\alpha}_5(\emptyset_2) & ... & \hat{\alpha}_5(\emptyset_k) \\ \hat{\alpha}_6(\emptyset_1) & \hat{\alpha}_6(\emptyset_2) & ... & \hat{\alpha}_6(\emptyset_k) \end{bmatrix} \times \begin{bmatrix} S_1(t) \\ S_2(t) \\ S_3(t) \\ S_4(t) \\ S_5(t) \\ S_6(t) \end{bmatrix}$$

$$+ \begin{bmatrix} n_1(t) \\ n_2(t) \\ n_3(t) \\ n_4(t) \\ n_5(t) \\ n_6(t) \end{bmatrix} (18)$$

Equation (18) also represent the output of any 6 elements antenna. $\hat{\alpha}(\emptyset_k)$ called as (Radiation Direction of ESPAR) and the correlation matrix at the antenna output is Rxx.

B. SPACE DIVISION MULTIPLE ACCESS (SDMA)

It is one of the most complex applications used in smart antenna technology's, that employs advanced processing techniques to identify and track mobile or fixed devices by directing broadcast signals in an adaptive manner towards user's direction without interference [25]. This technique can create several radiation patterns at the same time and for several radiation sources. The signal can reach from two different paths form a single source with the same frequency but with a phase deference caused by a variation in the length of the path, so the antenna is supplied with N beamforming networks. For each beamformer its adaptive algorithm to

control its weights (time, phase, and frequency). The adaptive algorithm is to form radiation pattern so that the main lobe is in the direction of the desired signal while the sidelobes is either reduced or zeroed [12].

VI. SIMULATION AND RESULTS

A. SIMULATION ENVIRONMENT

The main objective of this study is to model the sensors nodes used in the design of the network and to test the effectiveness of using the MUSIC algorithm to determine the angle of the received signal depending on the SDMA techniques and ESPAR antenna, which is used to determine the location of the sensor nodes used in the network, i.e. test the effectiveness of the network in detecting and locating the direction of incoming signal. The study proceeds from a network of three nodes, and one of these nodes is with known coordinates.

B. SIMULATION PARAMETERS

The set of parameters that has been taken into account during the study will be examine within this paragraph [23]

i. FREE TRACK LOSSES CALCULATION

The path loss relates to the distance travelled by the signal in the free space, which can be defined as the ratio between the power of the transmitted and the received signal measured in dB. The relationship that used to calculate the loss of the path is presented in eq.(19)

$$L_g = 10log\frac{P_t}{P_r} = 20log\left(\frac{4\pi d}{\lambda}\right) = -20log(\lambda) + 20log(d) + 21.98 \ dB \tag{19}$$

where P_t: is the transmitted power, P_r: is the received power, d : is the distance between transmitter and receiver, λ is the wavelength constant.

ii. ARRAY ANTENNA GAIN CALCULATIONS

The gain of the array antenna depends on the number of array elements (N) which given by (20):

$$G_{AR} = 10 \ log(N) + G_{EL} \tag{20}$$

where G_{EL}: is the gain of each antenna elements in dB

iii. TRANSMITTED SIGNAL TO NOISE RATIO SNR

SNR for a signal with power P is given by (21)

$$SNR = 10log\left(\frac{P}{kTB}\right) \tag{21}$$

where k: is Boltzmann constant, $1.38 \times 10^{-23} \ m^2 kgs^{-2} k^{-1}$, T: The noise temperature (Kalvin) of the system which includes the noise temperature of the antenna and the receiver, and B: effective beamwidth of the receiver noise.

iv. RECEIVED SIGNAL TO NOISE RATIO SNR

It can be defined as:

$$SNR_{AR} = SNR_{SC} - L_S - L_R + G_{AR} + G_T \tag{23}$$

where SNR_{SC}: is the transmitted signal to noise ratio, L_S: is the free space losses in dB, L_R: is the path losses due to reflection in dB, G_{AR}: is the array antenna gain in dB, and G_T: is the transmitting antenna gain in dB.

C. SIMULATION RESULTS

In this work the propagation path assumed to be ideal, that is, the received signal is the same as the transmitted signal. It is true that the situation is not perfect, but to make the study easy. The work was divided into two main parts: the first examines the efficiency of the MUSIC algorithm in estimating the angle of arrive of the received signal depending on the SDMA technique, and the second depending on the ESPAR smart antenna .

i. DEPENDING ON THE SDMA TECHNIQUE

The operating frequency of the transmitted sinusoidal wave $f=300MHz$ so that the wavelength $\lambda=1m$. When executing the simulation program, with the following parameters:
Give the number of clusters-receivers: 3; (c =3)
Give the number of elements: 8, 16, 64; (N =8, 16, 64)
Give three cases of direction of arrival as follows: DOA$_1$ = [0 35 68], DOA$_2$ = [80 82] and DOA$_3$ = [-85 -80 -77]
Give the number of Mont Carlo estimates: 100; (neurons =100)
The Figures (5) – (8) show the algorithm spectrum that shows the extent to which the spectrum peaks correspond to the angle of the signal received at high accuracy. In this test, we use three configurations of antenna with N=8, N=16, and N=64.
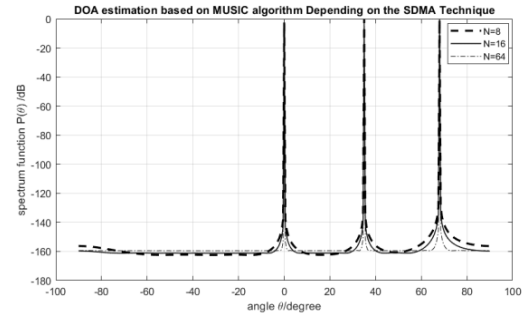
Figure (5) direction of arrival: DOA$_1$ = [0 35 68]

Figure (6) and figure (7) illustrate that even the sensors are in the same region and the deference between there AoA of the signals are closed to gather but the simulation results detect separate peak values.

ii. DEPENDING ON THE ESPAR SMART ANTENNA

Figures (5) to (8) also show the range to which the spectrum peaks correspond to the high-precision signal-input angles when testing the effectiveness of using the MUSIC algorithm based on the ESPAR smart antenna.
So we could say that we can randomly locating the nodes in the network which is suitable for many applications where we need to locate the node in inaccessible places, and then we apply one of the two methods studied above to determine the

exact location of the node, which helps to determine the location of the node with high accuracy.
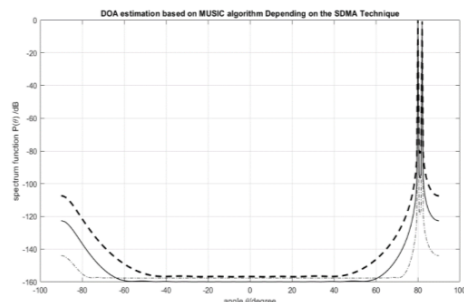
Figure (6) direction of arrival in the end terminals directions with DOA$_2$ = [80 82]
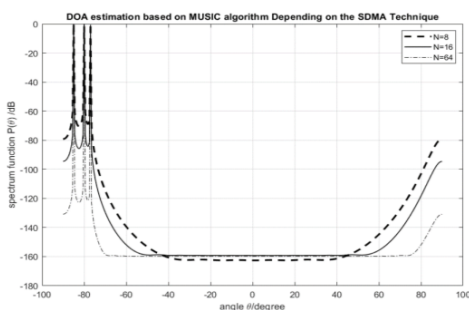
Figure (7) direction of arrival in the end terminals directions with DOA$_3$ = [-85 -80 -77]
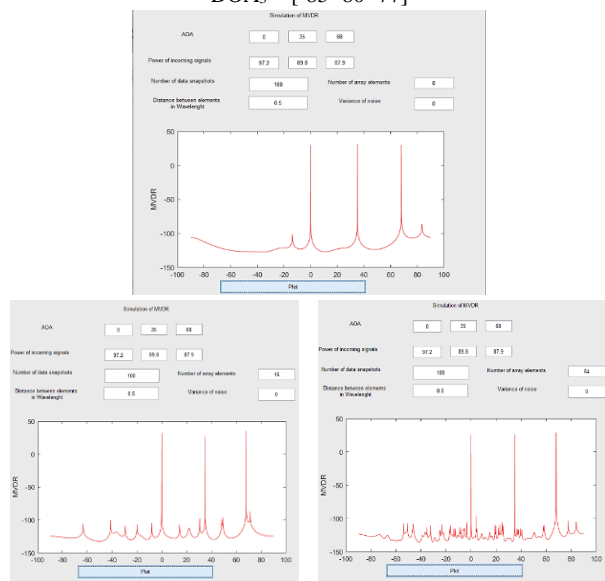
Figure (8) GUI of the simulation of the MUSIC algorithm based on SDMA technique and ESPAR smart antenna

VII. CONCLUSIONS AND RECOMMENDATIONS

In this paper, we have studied the non-GPS positioning mechanisms used in wireless sensor networks, and tested the effectiveness of using the MUSIC algorithm to determine the angle of arrival based on SDMA technology and ESPAR antenna. We have found that the use of intelligent antennas allows for increased capacity of wireless sensor networks by effectively reducing the problem of multipath and channel interference, which improves network connectivity, reduces power consumption and increases network life. The

simulation results in the considered scenario have shown that the use of intelligent antenna technology allows for accurate estimation of node locations without the need for additional components in the node as is the case when using GPS.

VIII. REFERENCES

[1] K X. Zhang, "Localization in Wireless Sensor Networks", Ph.D. Thesis, Arizona State University, 2016.

[2] N. Patwari, J. N. Ash, S. Kyperountas, A. O. Hero, R. L. Moses, and N. S. Correal, "Locating the Nodes, Cooperative localization in wireless sensor networks", IEEE Signal Processing Magazine, Vol. 22, no. 4, pp. 54–69, 2005.

[3] Z. Jin, Y. Jian-Ping, Z. Si-Wang, L. Ya-Ping and L. Guang, "A Survey on Position-Based Routing Algorithms in Wireless Sensor Networks", Algorithms, Vol. 2, 158-182, 2009.

[4] F. Benbadis, T. Friedman, M. D. Amorim, and S. Fdida "GPS-Free-Free Positioning System for Wireless Sensor Networks", Second IFIP International Conference on Wireless and Optical Communications Networks (WOCN), 2005.

[5] A. Kaur, S. Agrawal "Location Detection in Wireless Sensor Network using Classical Optimization Methodology", International Journal of Computer Science And Technology, Vol. 3, Issue 1, pp. 685-688, 2012.

[6] A. Taherkordi, "Programming Wireless Sensor Networks : From Static to Adaptive Models", PhD Thesis, Faculty of Mathematics and Natural Sciences, University of Oslo, 2011.

[7] K. Cui, W. Wu, J. Huang, X. Chen, and N. Yuan, "DOA estimation of LFM signals based on STFT and multiple invariance ESPRIT", International Journal of Electronics and Communications (AEÜ), vol. 77, pp. 10–17, 2017.

[8] D. He, "A novel methodology for planning reliable wireless sensor networks", PhD. Thesis, Departamento De automatica, Ingeniria Electronica E Informatica Industrial, Universidad Politecnica De Madrid, 2014.

[9] A. Dey, A. Nandi, and B. Basu, "Gold-MUSIC Based DOA Estimation Using ULA Antenna Of DS-CDMA Sources with Propagation Delay Diversity" International Journal of Electronics and Communications, vol. 84, pp. 162–170, 2018.

[10] M. R. Gholami, "Positioning Algorithms for Wireless Sensor Networks" MSc. thesis, Communication Systems Group, Department of Signals and Systems, Chalmers University of Technology, Sweden, 2011.

[11] M. Mohanna, M. L. Rabeh, E. M. Zieur, and S. Hekala, "Optimization of MUSIC Algorithm for Angle of Arrival Estimation in Wireless Communications" NRIAG Journal of Astronomy and Geophysics, Vol. 2, pp. 116–124, 2013.

[12] T. S. Dhope, D. Simunic, and R. Zentner "Comparison of DOA Estimation Algorithms in SDMA System" Automatika, vol. 54, Issue 2, pp. 199–209, 2013.

[13] David Poirier. "Design of A Radio Direction Finder for Search and Rescue Operations: Estimation, Sonification, And Virtual Prototyping", Ph.D. thesis, Pierre and Marie Curie University, Paris, France, 2015.

Biaxial Fuzzy Logic Based Solar Tracking System

A.M.A Shakarji[1] and M. Çunkaş[2]

[1]Ministry of Water Resources, Kirkuk /Iraq,   kirkuk_adnan@yahoo.com
[2]Selcuk University, Faculty of Technology, Department of Electrical Electronics Engineering
42075 Konya/Turkey,   mcunkas@selcuk.edu.tr

Abstract - **Solar energy is an ecologically clean, inexpensive and easy to apply energy source compared to other alternative energy sources. The efficiency of the solar panel reaches its maximum value when the sunlight is at its best angle. The aim of this study is to design a solar tracking system based on fuzzy logic that can move in two axes following the solar movement in order to increase the efficiency of the solar panel by several times. In this system, the angles of the motors used on two axes are adjusted by subjecting the current values of the LDR light sensors and the panel to the fuzzy logic rules to monitor the position of the sun. According to the experimental results, it is observed that the panel works most efficiently from sunrise to sunset.**

Keywords - **Fuzzy logic, Raspberry Pi3 B +, Solar, tracking system.**

I. INTRODUCTION

Until today, human beings have given priority to fuel energy. The most commonly used fuel energy sources are coal, oil, gas and the like. According to recent research, these sources will run out of risk in the next century [1-3]. This situation brings the world into an energy crisis. In order to prevent this, to protect the nature and to lower the price of energy, more renewable alternative energy sources have recently been given importance. Among the alternative and renewable energy sources, the potential of sunlight is quite high. To meet the annual energy needs of the world, the solar energy taken by the world in 40 minutes is sufficient [2]. More and more large areas are covered with solar farms. According to the data of 2017 5.86% of Turkey's energy needs are supplied from renewable sources [4]. The amount of energy stored depends on the quality of the panel, the intensity of sunlight and the technology used [5,6]. Since it is difficult to improve the solar energy system from a technological point of view, many studies aim to improve the contact of the panel with the sun. The panel achieves the highest solar intensity when sunlight falls vertically on the panel [7]. When the solar panel is in a static state, the solar panel receives full energy from the sun in a very short time of day. In the dynamic solar panel system, the amount of energy obtained can be increased by 50% compared to the static system [2]. There are many studies about solar tracking system until recently. Toylan (2017) proposed two-axis tracking of the sun with the help of fuzzy logic [4]. Huang et al (2016) designed a two-axis fuzzy

logic and MATLAB solar tracking system for the Taiwan climate[2]. Zakariah at el. (2015) presented a study to increase the performance of the solar system, which is completely connected to the LDR light sensor and makes its calculations with fuzzy logic, by 18.13% [3]. Sinha and Hui (2016) managed to improve the solar tracking system by 29.76% with fuzzy logic using MATLAB with PID controller [1].

In this study, a biaxial fuzzy logic based solar tracking system was designed to ensure that the light falls vertically during the sunny hours of the day. Fuzzy logic rules in the solar tracking system are performed with Raspberry Pi3 B + card. The system is designed based on the values from the light sensors and the current value from the panel. With the developed system, energy efficiency will increase and it contributes to the dissemination of solar energy systems. Therefore, when fossil fuels are gradually decreasing and greenhouse gas effects and environmental hazards are taken into consideration, the studies related to solar power plants will increase and will contribute to the development of related technologies accordingly.

II. MATERIAL AND METHODS

A. Fuzzy Logic

At the present time, we may have difficulty expressing some concepts in classical logic. Fuzzy logic can make modeling and understanding real life problems easier. Fuzzy logic is not only satisfied with the logical values 1 and 0 used by classical logic, but also uses values between logical 1 and 0 levels. For example, it not only indicates whether a distance is near or far, but also how close or how far it is. Fuzzy logic uses fuzzy set logic with classical logic. In fuzzy sets, the membership coefficients of the variables determine its membership rate [8,9].

The term fuzzy logic was introduced in 1965 by Lotfi Zadeh, later developed by Mamdani and Sugeno. The defuzzyfication method of fuzzy logic was developed by Mamdani, Sugeno. Mamdani defuzzyfication method is generally used in many problems. [9]. In addition to the defuzzyfication method, in the fuzzyfication process triangular membership functions are generally used for membership functions. The bloc diagram of fuzzy logic controller is given in Fig. 1.
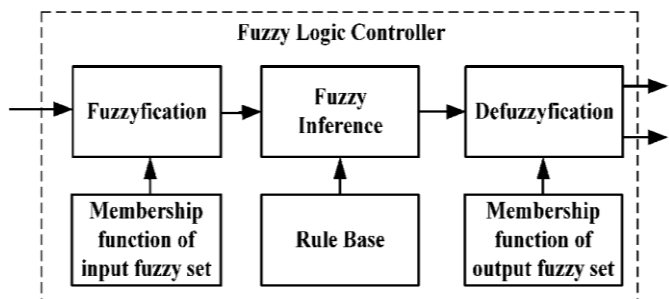
Figure 1: The working diagram of fuzzy logic

When looking at the fuzzy logic works, fuzzy logic is to match input sets to output sets. Fuzzy logic uses fuzzy rules created with If-Then in the mapping process. Fuzzy rules obtain one or more output expressions in the form of a linguistic expression using the linguistic expressions of input variables. The resulting expression is converted to a numerical value after being defuzzyfication.

B. General Structure of Solar Tracking System

In this study, four light sensors (LDR LM393), two servo motors and Raspberry PI 3 b + were used in the biaxial solar tracking system. The LDR light sensors are placed on all four sides of the panel and follow the direction of the sun. Servo motors are connected to two wheels for x-axis and y-axis and turn the solar panel to x and y sides. Fuzzy logic is used for the control mechanism, the light intensity from the light sensors and the solar panel, and according to the current values, the fuzzy logic system produces an output by subjecting them as input according to the rule table. This output determines how and to which side the x-axis and y-axis servo motors turn. Figure 2 shows the general structure of the tracking system.
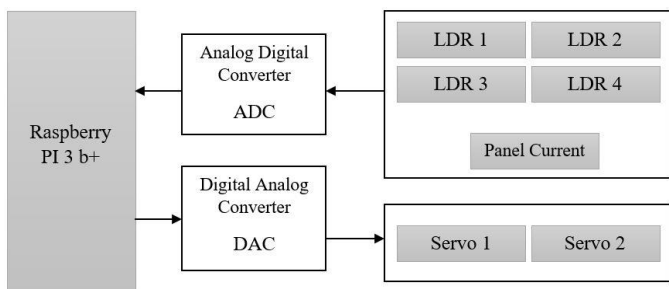
Figure 2: The general structure of the tracking system

As shown in Fig. 2, firstly the data from the sensors are transmitted to the analog to digital converter, after the necessary calculations are made, the analog to digital converter sends the values of the light sensors and the panel current to the Raspberry. The Raspberry finds the appropriate value for x-axis and y-axis motors with fuzzy logic system. The Raspberry sends the appropriate motor values to the x-axis and y-axis motors via a digital analog converter (PWM). The minimum and maximum range values for the input and output variables of the designed fuzzy based solar tracking system are given in Table 1 below.

Table 1: The minimum and maximum range values for the input and output variables

Name of variable	input/output	Minimum value	Maximum value
Light intensity (binary digit)	Input	0	1023
Panel current (A)	Input	0	1
Motor	Output	0	100

The fuzzy values and ranges of the input and output variables according to the minimum and maximum range values are given in Table 2.

Table 2: The fuzzy values and ranges of the input and output variables

Fuzzy values	Light intensity (volt)	Panel current (A)	Motor
Low (L)	0-400	0-0.5	0-40
Medium (M)	300-800	0.3-1	30-70
Big (B)	700-1023	0.8-1	60-100

According to the fuzzy values of the inputs and outputs in Table 2 and the range values, is the membership function of the system for light intensity and panel current as inputs are given in Figures 3a and 3b respectively. The membership function of the system for motor angle as output is given in Figure 4.
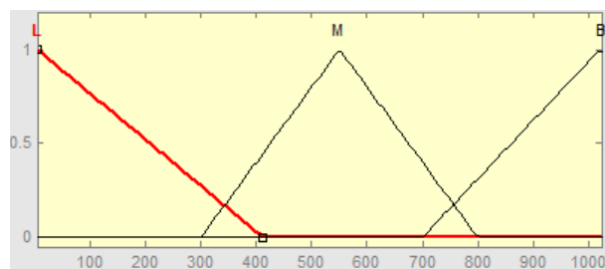
Figure 3a: Membership function of the light intensity
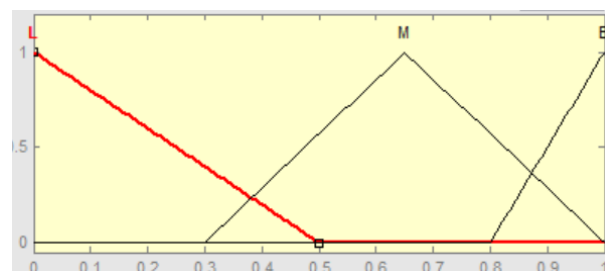
Figure 3b: Membership function of the panel current
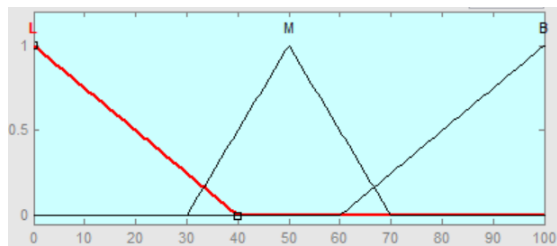
Figure 4: Membership function of the motor

In the fuzzy logic system, the accuracy of the system is directly proportional to the fuzzy rules table, so it is a great advantage for us to prepare the rule table very well. Table 3 shows a two-input and one-output fuzzy rules table of the designed solar tracking system.

Table 3: Fuzzy rules table of the designed solar tracking system

Light/Current	Low	Medium	Big
Low	Low	Big	Big
Medium	Medium	Medium	Medium
Big	Low	Low	Low

III. SYSTEM IMPLEMENTATION AND RESULTS

In the designed fuzzy logic based biaxial solar tracking system, four of the sensors placed on the panel are controlled simultaneously, so the current value of all sensors and the panel is subjected to fuzzy logic rules at the same time. Fuzzy logic rules work separately for each sensor, so the motor is directed to that side at which more volts come from. Up and down sensors are used to guide the y-axis motor and the left and right sensors to the x-axis motor. For example, the sunlight and panel current values from the right-hand sensor 178 and 0.832 respectively, this data is given to fuzzy rule and then rotate the x-axis motor 41.1 degrees to the right. The screenshot of matlab example is shown in Figure 5.
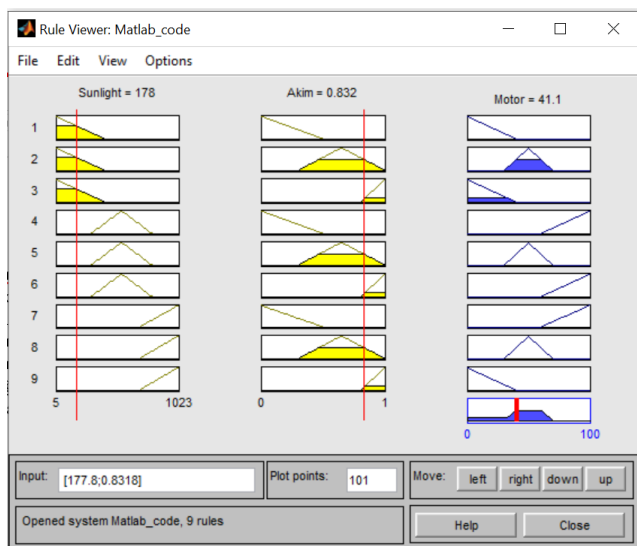
Figure 5: The screenshot of matlab example
The solar tracking system is designed according to the fuzzy

logic rules above after simulation on MATLAB FIS Editor. The structure of the designed fuzzy logic based solar tracking system is given in Figure 5. As a result of the experiments carried out in the experimental setup, it was seen that the simulation results and the experimental studies were compatible with each other.

Figure 6: The structure of solar tracking system

The following advantages can be achieved with the proposed two-axis fuzzy logic based system using Raspery-pi processor.

- This system will work fully automatically and adapt to changing conditions. This means that the system can reduce the number of starts of the engine in bad weather or in low sunlight conditions, thus preventing unnecessary energy loss.
- The system will take into account the external environment caused by a malfunction with meteorological changes. This approach will reduce unnecessary energy loss.
- Compared to traditional sensor solar tracking systems, it is easier to control the angle with this system, and it will be more sensitive and less error caused by outdoor changes.

IV. CONCLUSION

In this study, dual axis fuzzy logic based solar tracking system is designed. The designed fuzzy logic based solar tracking system has been designed to be easily applicable and has shown a higher performance than the static solar panel. The designed solar tracking system collects as much solar energy as possible except for cloudy days and night times. Fuzzy logic can also stop motor operation when solar energy is missing, thus saving energy. As a result, the designed solar tracking system uses solar energy very efficiently and works very successfully.

REFERENCES

[1] Sinha, D., Hui, N.B.: Fuzzy Logic-based Dual Axis Solar Tracking System. International Journal of Computer Applications **155**(12), 13-18 (2016).

[2] Huang, C.-H., Pan, H.-Y., Lin, K.-C.: Development of intelligent fuzzy controller for a two-axis solar tracking system. Applied Sciences **6**(5), 130 (2016).

[3] Zakariah, A., Jamian, J.J., Yunus, M.A.M.: Dual-axis solar tracking system based on fuzzy logic control and Light Dependent Resistors as feedback path elements. In: 2015 IEEE Student Conference on Research and Development (SCOReD) 2015, pp. 139-144. IEEE.

[4] Toylan, H.: Performance of Dual Axis Solar Tracking System Using Fuzzy Logic Control: A Case Study in Pinarhisar, Turkey. Makalenizi yükleyebilmek için lütfen İngilizce dilini seçiniz!!! EJENS **2**(1), 130-136 (2017).

[5] Hon, S.P., Kolte, M.: FPGA Based Sun Tracking System Using Fuzzy Logic. International Journal of Scientific & Technology Research **2**(9), 217-220 (2013).

[6] Stamatescu, I., Stamatescu, G., Arghira, N., Făgărăsan, I., Iliescu, S.S.: Fuzzy decision support system for solar tracking optimization. In: 2014 International Conference on Development and Application Systems (DAS) 2014, pp. 16-20. IEEE.

[7] Usta, M., Akyazı, Ö., Altaş, İ.: Design and performance of solar tracking system with fuzzy logic Controller. In: Sixth International Advanced Technologies Symposium (IATS'11), Elazig, Turkey, May16-18 2011.

[8] Negnevitsky, M.: Artificial intelligence: a guide to intelligent systems. Pearson education, (2005).

[9] Grigorie, T.L.: Fuzzy Controllers: Theory and Applications. BoD–Books on Demand, (2011).

Pt doped (8,0) CNT: A DFT study of Furan Detection

N. YÜKSEL[1], A. KÖSE[1], M. F. FELLAH[1,*]

[1]Bursa Technical University, Chemical Engineering Department, Bursa/Turkey, n.yuksel@btu.edu.tr
[1]Bursa Technical University, Chemical Engineering Department, Bursa/Turkey, ahmet.kose@btu.edu.tr
[1]Bursa Technical University, Chemical Engineering Department, Bursa/Turkey, mferdi.fellah@btu.edu.tr
*Corresponding Author

Abstract - **In this study, it has been investigated the use of the furan sensor at room temperature. WB97XD method with 6-31G(d,p)/LanL2DZ basis sets have been used. The charge distributions obtained for structures show that charge transfer has occurred from the adsorbed furan molecule to the Pt atom of carbon nanotube structure as an electron acceptor. The HOMO–LUMO gap of the Pt doped SWCNT decreased with adsorbing of furan molecule. As a conclusion, the electrical conductivity of Pt doped (8,0) SWCNT cluster increased after a furan molecule adsorption. Accordingly, Pt doped (8,0) SWCNT has potential for sensing of furan molecule at room temperature.**

Keywords – **DFT, CNT, Furan, Pt, Detection, Sensor**

I. INTRODUCTION

Furan molecule (C_4H_4O) is a member compound of the five-membered heterocycles which contains one oxygen atom [1]. Furan can form in food during a Maillard reaction and has been of concern because it is classified by the International Agency for Research on Cancer as potentially carcinogenic to humans [2]. The structural and energetic aspects of furan adsorption have been previously studied using various vibrational, photoelectron, and thermal desorption spectroscopies on a variety of single-crystal metal surfaces, including Cu (100), Ag (110), Ru (0001), and Pd (111) [3]. Carbon nanotubes (CNTs) which have unique electronic and structural properties have almost no study on determination of furan molecule [4] and there is no study concerning detection of furan on Pt doped CNT in either theoretical or experimental open literature. The aim of this study is to examine the activity of Pt doped CNT for the furan molecule adsorption and detection.

II. MODEL AND METHOD

In this work, the theoretical calculations were utilized in order to obtain electrical characteristics and geometry optimizations based on density functional theory (DFT) [5]. DFT calculations were made through Gaussian 09 software [6]. The applied method was the WB97XD hybrid method (including dispersion) considering the effects of change and correlation [7]. The basis set of 6-31G (d, p) was utilized for the carbon, oxygen and hydrogen atoms. LanL2DZ basis set was used for platinum atom.

The zigzag model (8,0) SWCNT structure [8] (semiconducting tube) has been modeled as a cluster which consists of 96 carbon atoms was used in this study for furan adsorption and sensing study. Hydrogen (H) atoms (totally 16 atoms) were inserted to end parts of nanotube's free carbon atoms' bonds for the purpose of neutral charge on the cluster. In addition, one carbon atom on the center of the CNT was replaced by the Pt atom in order to obtain Pt doped SWCNT cluster. In this work, all atoms were kept relaxed during all theoretical calculations.

Equilibrium geometry (EG) calculations were used to optimize geometries and obtain adsorption energies. In present study, energy difference values include zero point energy (ZPE) corrections. These energy values for furan adsorption were computed as follows:

$$E = E_{electronic} + ZPE + E_{vibrational} + E_{rotational} + E_{translational} \quad (1)$$
$$H = E + RT \quad (2)$$
$$G = H - TS \quad (3)$$

where E is the sum of the electronic and zero-point energies and thermal energies, H is the sum of the electronic and thermal enthalpies, G is sum of electronic and thermal free energy, S is the entropy and T is the temperature used for the vibrational frequency calculations. HOMO and LUMO representations, HOMO and LUMO energy values were calculated by full analysis of population. The chemical hardness, electronegativity, electrophilicity and chemical potential values were obtained to have information about the activity of cluster by using the following equations. ϵ_{HOMO} is the highest occupied molecular orbital energy and ϵ_{LUMO} is the lowest unoccupied molecular orbital energy. Following equations used to obtain these values are based on the Koopman's approach [9,10].

$$\text{Chemical hardness } (\eta) = (I-A)/2 \quad (4)$$
$$\text{Chemical potential } (\mu) = -(I+A)/2 \quad (5)$$
$$\text{Electronegativity } (\lambda) = -\mu \quad (6)$$
$$\text{Electrophilicity } (\omega) = \mu^2 / (2\eta) \quad (7)$$

where $I \cong -\epsilon_{HOMO}$ and $A \cong -\epsilon_{LUMO}$

The cluster and the furan molecule were optimized structurally by EG calculations. Below equation was used to calculate the relative adsorption energy and enthalpy values.

$$\Delta(E/H/G) = (E/H/G)_{System} - [(E/H/G)_{Adsorptive}+(E/H/G)_{Cluster}] \quad (8)$$

E_{System} was figured out the thermal energy of adsorbate on the cluster, $E_{Adsorptive}$ was calculated the adsorbing molecule's thermal energy, e.g. furan molecule and $E_{Cluster}$ was computed the initial cluster's thermal energy. Moreover, ΔH and ΔG were obtained for furan adsorption on Pt doped (8,0) carbon nanotube. The vibrational frequency calculations confirmed that the optimized structures obtained by EG have no imaginary frequency values, which means there is no number of negative eigenvalues in the Hessian matrix.

The convergence criteria are 12×10^{-4} radian for gradients of root-mean-square (rms) displacement, 18×10^{-4} bohr for max displacement, 3×10^{-4} hartreee/radian for rms force and 45×10^{-5} hartree/bohr for max force during theoretical calculations utilized in this study. Additionally, the criteria of SCF convergence criteria for RMS change in the density matrix and maximum change in the density matrix were 1×10^{-8} and 1×10^{-6}, respectively. The density of states (DOS) have been obtained by using Gaussum software [11]. Mulliken atomic charges of atoms were obtained by Mulliken population analysis.

III. RESULTS AND DISCUSSIONS

The adsorptive molecule (furan molecule here) were optimized geometrically by equilibrium geometry (EG) calculations. The detection based on adsorption of furan molecule was studied after on Pt doped CNT. Resulting optimized geometry for adsorption of furan molecule on Pt doped CNT was represented in Figure 1. The obtained adsorption energy values and geometrical parameters for furan adsorption on Pt doped (8,0) CNT cluster were listed in Table 1. This reaction is an exothermic reaction.

The chemical activity of the Pt doped carbon nanotube structure could be established by using HOMO and LUMO energy values and energy gap between the HOMO and LUMO (HLG). When the energy gap between of HOMO and LUMO is small, chemical reactivity is high [12,13]. HOMO and LUMO values, chemical hardness (η), chemical potential (μ), electronegativity (χ), electrophilicity (ω) and HLG values for both α and β molecular orbitals (spin up and spin down respectively) were obtained, and calculated results were tabulated in Table 1.

Mulliken population analysis has been utilized to obtain Mulliken charge distribution before and after adsorption of furan molecule on Pt-CNT cluster. Total charge of adsorbed furan molecule on the cluster is +0.124e. This result indicates that charge transfer has occurred from the adsorbed furan molecule to the carbon nanotube cluster. The HOMO and LUMO representations for both α and β molecular orbitals (spin up and spin down respectively) of Pt doped (8,0) CNT cluster and furan adsorbed Pt doped (8,0) CNT cluster are represented in Figure 2.
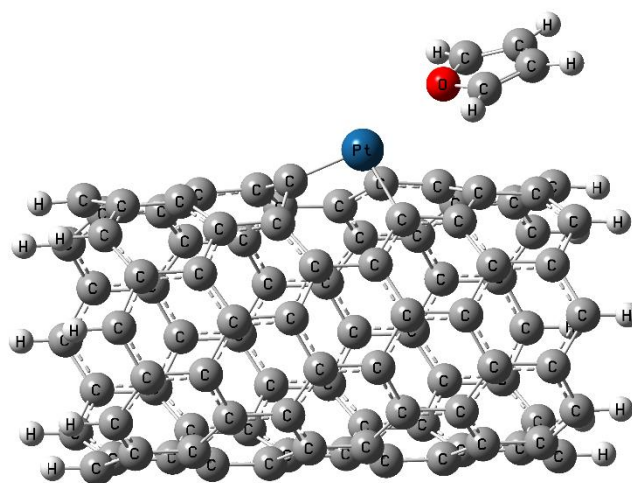
Figure 1: Optimized structure of the adsorbed furan on Pt-doped (8,0) CNT

Table 1: Structural parameters, energy values, HOMO and LUMO energy, chemical hardness, chemical potential, electronegativity, electrophilicity and HLG values for the optimized Pt doped (8,0) CNT cluster and the optimized furan adsorbed on Pt doped (8,0) CNT cluster.

Properties		Pt doped SWCNT	Furan adsorbed on Pt doped SWCNT
Distances, Å	Pt-Cs (bonded with Pt atom)	1.885 1.976 1.976	1.883 1.996 1.996
	Pt-O		2.493
Mulliken Charges, e	Pt	0.819	0.786
	Furan Molecule	0	0.124
Adsorption energies, eV	ΔE		-0.51
	ΔH		-0.53
	ΔG		-0.04
α MOs (eV)	HOMO	-5.42	-5.28
	LUMO	-1.36	-1.22
	HLG	4.06	4.06
	Chemical Hardness (η)	2.03	2.03
	Chemical Potential (μ)	-3.39	-3.25
	Electronegativity (χ)	3.39	3.25
	Electrophilicity (ω)	2.83	2.60
β MOs (eV)	HOMO	-6.11	-5.90
	LUMO	-1.81	-1.70
	HLG	4.30	4.20
	Chemical Hardness (η)	2.15	2.10
	Chemical Potential (μ)	-3.96	-3.80
	Electronegativity (χ)	3.96	3.80
	Electrophilicity (ω)	3.64	3.43

As seen from the HOMO and LUMO energy values for the structures tabulated in Table 1 and representations given in Figure 4, the HOMO-LUMO gap of Pt doped (8,0) CNT cluster reduced from 4.30 eV to 4.20 eV for β molecular orbitals (spin down) which indicates the somewhat decreasing on HLG values. Therefore, the electrical conductivity of the Pt doped (8,0) CNT cluster was increased after the furan molecule was adsorbed. This situation can be explained by the following equation [14-16].

$$\sigma = AT^{3/2} exp(-E_g/(2kT)) \qquad (9)$$

Here σ is the electrical conductivity, A is a constant (electrons/$m^3K^{3/2}$), Eg is HOMO-LUMO gap (HLG), k is the Boltzmann's constant and T is temperature. Consistent with this equation, for a given temperature, small HLG results in large electrical conductivity. Previously reported [16] that this relationship is in concordance with experimental results. Subsequently, based on this equation it can be concluded that adsorption of furan molecule has increased the electrical conductivity of Pt doped (8,0) CNT cluster which accordingly indicates that Pt doped (8,0) CNT can be a potential sensor for furan molecule [17,18].
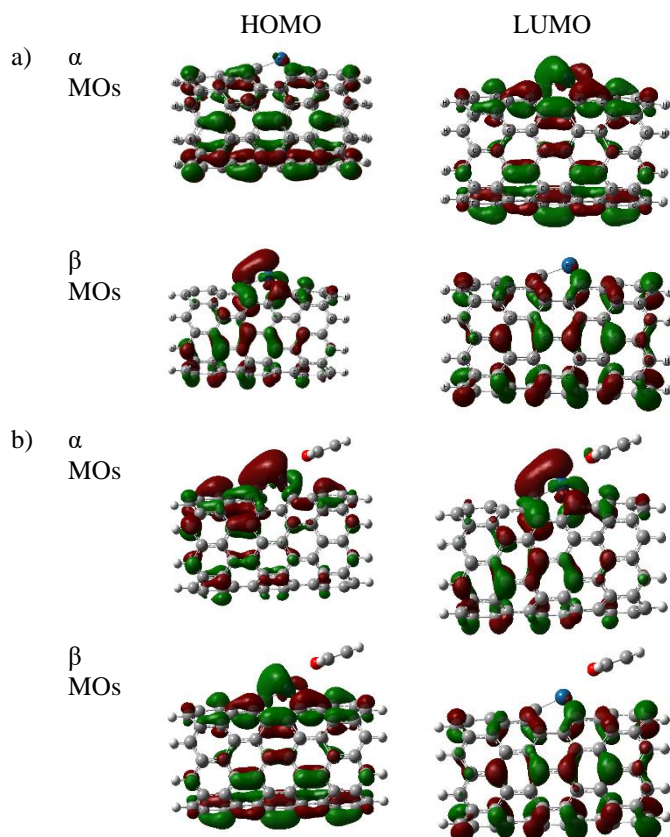
Figure 2: HOMO and LUMO representations of α and β MOs a) for the optimized structure of Pt-doped (8,0) CNT b) for the optimized structure of the adsorbed furan on Pt-doped (8,0) CNT.

The density of states (DOS) of Pt doped (8,0) CNT cluster and furan molecule adsorbed Pt doped (8,0) CNT cluster have been presented in Figure 3. As seen from Figure 3, reducing of the HOMO-LUMO gap of Pt doped (8,0) SWCNT cluster has changed in the gap of the DOS plots. This is compatible with the result that charge transfer occurred from the adsorbed furan molecule to the Pt atom of the carbon nanotube structure.

Besides, the distribution of electrostatic potential (ESP) for Pt doped (8,0) CNT cluster and furan adsorbed Pt doped (8,0) CNT cluster have been represented in Figure 4. The positive and negative regions on the van der Waals surface have been characterized by the blue and red colors on the ESP map [19,20].
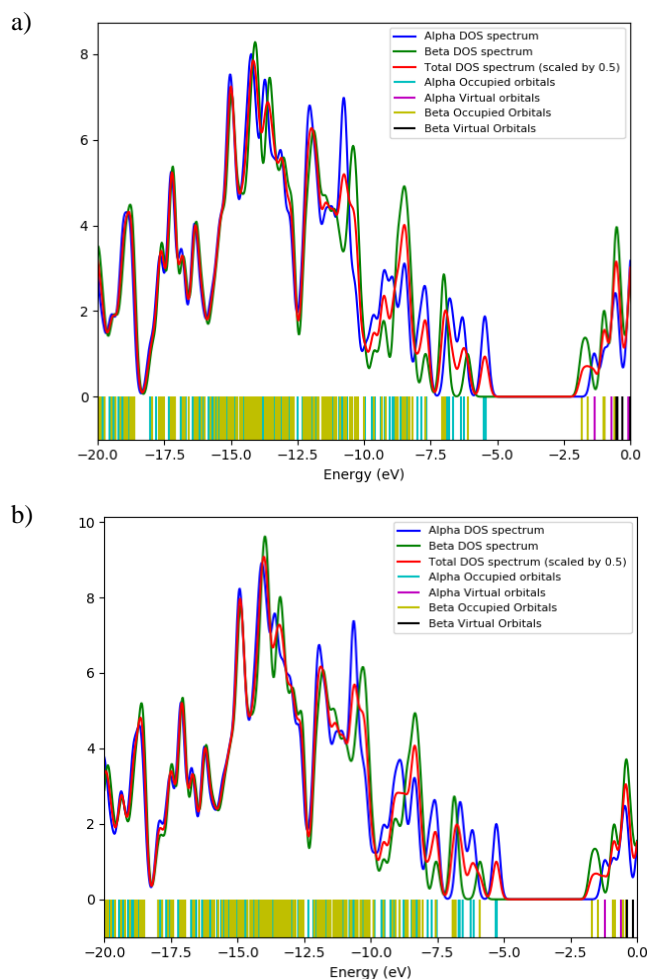
Figure 3: The density-of-states (DOS) a) for the optimized structure of Pt-doped (8,0) CNT b) for the optimized structure of the adsorbed furan on Pt-doped (8,0) CNT.

Analysis of the ESP distribution of the Pt doped (8.0) CNT cluster and the furan adsorbed Pt doped (8.0) CNT cluster clearly shows that the positive regions are localized on the Pt atoms. This is in agreement with the charge distribution of the Pt atoms. It should also be noted that some positive regions (blue) of the Pt doped (8.0) CNT cluster and furan adsorbed Pt doped (8.0) CNT cluster are located around the hydrogen atoms surrounding the rings of the CNT cluster. Nevertheless, it is not appropriate to regard this because they were used to saturate the C atoms.

a)

b)
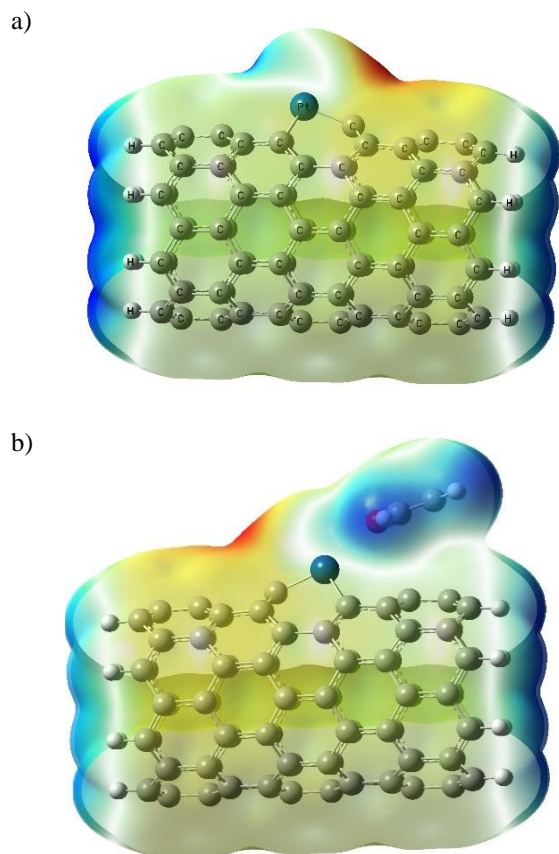
Figure 4: The electrostatic potential (ESP) distribution maps with projection a) for the optimized structure of Pt-doped (8,0) CNT b) for the optimized structure of the adsorbed furan on Pt-doped (8,0) CNT.

IV. CONCLUSION

In the present study, DFT calculations with WB97XD hybrid method (including dispersion) have been utilized for the platinum doped (8,0) CNT cluster in order to investigate the use of the furan sensor. Detailed analysis of the structural and electronic properties has been performed for both Pt doped (8,0) CNT cluster and furan adsorbed Pt doped (8,0) CNT cluster. The charge distribution shows that charge transfer has happened from the adsorbed furan molecule to the Pt atom of the CNT structure as an electron acceptor. The HOMO–LUMO gap of the Pt doped CNT decreased with adsorption of furan molecule, which indicates that electrical conductivity of the Pt doped CNT has increased. Based on the results obtained in this study, it could be concluded that the furan molecule can be adsorbed on Pt site of CNT with somewhat charge transfer. The electrical conductivity of Pt doped (8,0) CNT cluster has increased after a furan molecule adsorption. As a result, Pt doped (8,0) CNT have potential for sensing of furan at room temperature.

REFERENCES

[1] M. F. Fellah, "Direct decarbonylation of furfural to furan: A density functional theory", *Applied Surface Science*, vol. 405, pp. 395–404, May 2017.

[2] H. Hashemi-Moghaddam and M. Ahmadifard, "Novel molecularly-imprinted solid-phase microextraction fiber coupled with gas chromatography for analysis of furan", *Talanta*, vol. 150, pp. 148–154, April 2016.

[3] A. Loui and S. Chiang, "An experimental study of furan adsorption and decomposition on vicinal palladium surfaces using scanning tunneling microscopy", *Surface Science*, vol. 670, pp. 13–22, April 2018.

[4] A. Sarafraz-Yazdi, M. Abbasian, A. Amiri, "Determination of furan in food samples using two solid phase microextraction fibers based on sol–gel technique with gas chromatography–flame ionization detector", *Food Chemistry*, vol. 131, pp. 698–704, March 2012.

[5] W. Kohn and L. Shamn, "Self-consistent equations including exchange and correlation effects", *Journal of Physical Review,* vol. 140, pp. A1133-A1138, November 1965.

[6] J. Frisch, G.W. Trucks, H.B. Schlegel, G.E. Scuseria, M.A. Robb, J.R. Cheeseman, Gaussian Inc., Wallingford, CT, 2013.

[7] J. D. Chai and M. Head-Gordon, "Systematic Optimization of Long-Range Corrected Hybrid Density Functionals", *Journal of Chemical Physics*, vol. 128, pp. 84106, February 2008.

[8] M. F. Fellah, "Pt doped (8,0) single wall carbon nanotube as hydrogen sensor: A Density Functional Theory study", *International Journal of Hydrogen Energy*, Accepted, August 2019, Doi: 10.1016/j.ijhydene.2019.08.169.

[9] R. G. Pearson, "Chemical hardness and density functional theory", *Journal of Chemical Sciences*, vol. 117, pp. 369-377, September 2005.

[10] R. G. Pearson, "The electronic chemical potential and chemical hardness", *Journal of Molecular Structure: THEOCHEM,* vol. 225, pp. 261-270, March 1992.

[11] N. M. O'Boyle, A. L. Tenderholt, K. M. Langner, "cclib: A library for package-independent computational chemistry algorithms", *Journal of Computational Chemistry*, vol. 29, pp. 839-845, April 2008.

[12] B. S. Kulkarni, S. Krishnamurty, S. Pal, "Probing Lewis acidity and reactivity of Sn- and Ti-beta zeolite using industrially important moieties: A periodic density functional study", *Journal of Molecular Catalysis A: Chemical*, vol. 329, pp. 36–43, August 2010.

[13] C. K. Modi, P. M. Trivedi, J. A. Chudasama, H. D. Nakum, D. K. Parmar, S. K. Gupta, P. K. Jha, "Zeolite-Y entrapped bivalent transition metal complexes as hybrid nanocatalysts: density functional theory investigation and catalytic aspects", *Green Chemistry Letters and Reviews*, vol. 7, pp. 278–287, June 2014.

[14] Y. Yong, H. Jiang, X. Li, S. Lv, J. Cao, "The cluster-assembled nanowires based on M12N12 (M = Al and Ga) clusters as potential gas sensors for CO, NO, and NO2 detection", *Physical Chemistry Chemical Physics*, vol. 18, pp. 21431-21441, July 2016.

[15] A. Ahmadi, N. L. Hadipour, M. Kamfiroozi, Z. Bagheri, "Theoretical study of aluminum nitride nanotubes for chemical sensing of formaldehyde", *Sensors and Actuators B: Chemical*, vol. 161, pp. 1025-1029, January 2012.

[16] N. L. Hadipour, A. A. Peyghan, H. Soleymanabadi, "Theoretical study on the Al-doped ZnO nanoclusters for CO chemical sensors", *Journal of Physical Chemistry C*, vol. 119, pp. 6398-6404, March 2015.

[17] K. Li, W. Wang, D. Cao, "Metal (Pd, Pt)-decorated carbon nanotubes for CO and NO sensing", *Sensors and Actuators B: Chemical*, vol. 159, pp. 171-177, November 2011.

[18] M. T. Baei, Y. Kananib, V. J.Rezaei, A. Soltani, "Adsorption phenomena of gas molecules upon Ga-doped BN nanotubes: A DFT study", *Applied Surface Science*, vol. 295, pp. 18– 25, March 2014.

[19] P. Sjoberg and P. Politzer, "Use of the electrostatic potential at the molecular surface to interpret and predict nucleophilic processes", *Journal of Physical Chemistry*, vol. 94, pp. 3959–3961, May 1990.

[20] G. Yu, L. Lyu, F. Zhang, D. Yan, W. C. Chun Hu, "Theoretical and experimental evidence for rGO-4PP Nc as a metal-free Fenton-like catalyst by tuning the electron distribution," *RSC Advances*, vol. 8, pp. 3312-3320, January 2018.

Production of B$_4$C Reinforced Aluminum Matrix Composite by Squeeze Casting Method and Determination of Wear Resistance

A. KABİL[1], Ç. YÜKSEL[2], Serdar Osman YILMAZ[3] and M. ÇİĞDEM[4]

[1] Yildiz Technical University, İstanbul/Turkey, kblahmet@yildiz.edu.tr
[2] Atatürk University, Erzurum/Turkey, cyuksel@atauni.edu.tr
[3] Tekirdağ Namık Kemal University, Tekirdağ/Turkey, oyilmaz@nku.edu.tr
[4] Yildiz Technical University, İstanbul/Turkey, cigdem@yildiz.edu.tr

Abstract – **The expected performance values of engineering materials are increasing progressively. Today, it is becoming increasingly difficult to meet these expectations with monolithic materials. For this reason, studies in the field of composite materials are continuing intensively. Composites, which can be designed for special purposes, such as wear resistance and provide significant weight and performance gains where they are used. It is observed that the use of aluminum matrix composites is increasing gradually especially in automotive and aerospace sectors where weight reduction studies are intensified. Aluminum matrix composites which can be reinforced with various particles such as Al$_2$O$_3$, SiC and B$_4$C provide superiority to monolithic materials in mechanical properties such as wear resistance, tensile strength and hardness. In this study, aluminum matrix composite reinforced with B$_4$C is produced by squeeze casting method. The microstructural examination was made with the scanning electron microscope (SEM). The wear resistance of the composite material was evaluated with weight loss, volume loss and wear rate values. In the SEM examination, it was found that the reinforcing particles were successfully embedded in the matrix and did not cause any porosity. Results of the wear test showed that the volume loss of composite material was 1,44%, whereas the weight loss was 1,44%. Also the wear rate was 1,43x10^{-5} cm^3/m.**

Keywords – **AMMC, B$_4$C, squeeze casting, wear resistance, wear**

I. INTRODUCTION

Increasing performance expectances from engineering materials, weight reduction studies with increasing environmental concerns, and more economical process researches make up the main drivers of most material researches done today. Especially in the last century, humanity is constantly striving to achieve better in every field with the important breakthroughs of science and technique. As a projection of this situation in the field of materials, new materials and processes are being developed. Metal matrix composite materials are also a group of materials that have been developed in the last century. In some applications where monolithic materials produced by conventional methods are becoming insufficient, we see their use, such as lightweight composite brake discs for sports vehicles. One of the biggest obstacles to the use of metal matrix composites is the high cost of material production.

In order to produce composite materials in a way that does not cause material defects, the matrix metal and reinforcement must be compatible and able to make physical and / or chemical bonding. In order to promote this bond formation, the reinforcing element is often pretreated. These pretreatments also cause the process to become complex and costly. For this reason, the choice of matrix and reinforcement which has a higher chance of bonding is important.

Aluminum matrix composites have been developed for approximately 50 years and commercially used for 30 years. The main reason why aluminum matrix composites stand out among metal matrix composites is the weight reduction advantage due to their low density. In addition to light weight, high stiffness, strength and abrasion resistance make aluminum matrix composites attractive [1].

The production of aluminum matrix composites can be basically divided into 3 main headings. These; solid-state processes, liquid-state processes and semi-solid processes [2, 6].

Solid state processes; powder metallurgy, diffusion bonding and physical vapor deposition (PVD). In powder metallurgy method, the metal powders are mixed with ceramic fibers or powders in dry or wet form and then composite is produced by using extrusion and isostatic pressing methods. Diffusion bonding, this method is generally used in the production of ceramic fiber reinforced titanium matrix composites. It is achieved by diffusing the metal into the fiber. The fiber content of the structure is high and complex shapes are difficult to produce. The method of physical vapor deposition is mainly based on the vaporization of the metal to be coated and the relatively thick metal deposition on the surface by continuously passing the fiber through the medium [2].

Stir casting, squeeze casting, infiltration process, spray coating and in-situ processing make up the liquid state processes. In stir casting method, ceramic particles are added to the liquid metal, and then the liquid is stirred until homogenous distribution of the reinforcements in liquid metal is achieved. The important point here is the wettability of the particles by the liquid metal. Most of the time the particles are pre-treated to be able wet by liquid metal. Infiltration process: This

process is based on the infiltration of liquid aluminum into the preform, having a hollow structure formed by short fibers, fibers or particles. With this process, it is possible to produce composite with reinforcement ratio between 10-70%. Spray deposition process is examined in 2 different classes. These consist of a continuous melt pool or continuous supply of cold metal to the hot injection zone. It is mainly based on the injection of ceramic particles into the spray to produce a metal matrix composite. Reaction method: This method can be divided into many sub-methods; gas-gas, gas-liquid, liquid-liquid or mixed salt reactions. The general principle is to react with metal by adding substances such as salt and CO2 to produce ceramic particles in the metal [2, 4, 7].

Semi-solid processes: Relatively new fields of semi-solid casting methods are also used to produce aluminum matrix metal composites. In these methods, which are based on shaping the material after heating it to a temperature between solidus and liquidus temperature, the liquid phase (eutectic phase) should be able to wet the reinforcing element. In order to improve this wetting behavior, reinforcing elements are generally pre-treated, such as preheating or coating [2, 8].

In the squeeze casting process, which is one of the liquid state processes, the metal matrix composite material can be produced by adding and compressing the liquid metal onto the reinforcing element in the form of a preform or directly after being inserted into the metal mold. Due to the pressure applied, the liquid metal can penetrate between the reinforcing particles. In composites produced by this method, the micro porosities are minimal and production of relatively complex geometries can be done [2, 9].

The use of boron carbide (B_4C) as reinforcing element is recent than that of silicon carbide (SiC) and aluminum oxide (Al_2O_3). However, it has started to be preferred because of its higher hardness and lower density (B_4C: 2.52 g/cm^3, SiC: 3.21 g/cm^3, Al_2O_3: 3.95 g/cm^3) compared to the other two commonly used reinforcing elements [10].

II. EXPERIMENTAL PROCEDURE

The 2014 aluminum alloy, the chemical composition of which is given in Table 1, was melted in a SiC crucible with resistance furnace. The B_4C powder acquired from ESK Ceramics GmbH was spread on the bottom surface of the metal mold shown in Figure 1-a in a homogeneous thickness. Then, liquid metal was poured into metal mold at 750 °C and squeeze casting was performed by using press.

Table 1: Chemical composition of the matrix alloy

Cu	Si	Mn	Mg	Fe	Ti	Pb	Al
4,06	0,74	0,51	0,26	0,33	0,03	0,01	Bal.

After the deburring of the produced samples, they were prepared as shown in Figure 1-b for further testing.

Figure 1: a) Metal mold, b) Produced samples

As shown in Figure 2, the samples were cut to a surface area of 1x1 cm and made ready for the pin-on drum wear test.

Figure 2: Cross-section of a sample

The pin-on drum wear device, shown schematically in Figure 3, was used for the wear test. In the test, 80 mesh Al_2O_3 sand paper was used as the opposite surface. 15 N was chosen as the load.
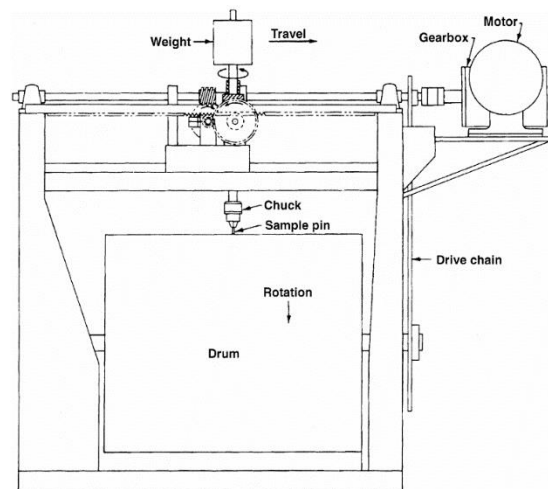
Figure 3: Schematic represantation of the pin-on drum wear test device [11]

The wear test was stopped at 400 meter intervals and the weight of the sample was measured with a precision scale.

Each time the sample was cleaned with alcohol and then weighed. This procedure was repeated 5 times and the abrasion test continued for a total of 2400 meters. After the test, weight loss, volume loss and wear rate values were calculated. SEM examination of the cross section of the material revealed the state of the reinforcing particles in the matrix.

III.   RESULTS AND DISCUSSION

The darker portion at the top of the sample in Figure 2 corresponds to the particle-reinforced black area in the electron microscope image of Figure 4. As can be seen, the B4C particles are embedded in the matrix as reinforcements. It is also observed that the reinforcing elements are homogeneously dispersed in the matrix. The particle rate was calculated with the help of the ImageJ image analysis program, which was 58.74%. Canakci et al. [12] investigated the effect of size and volume ratio of B_4C on AMMC production and microstructural change. They successfully produced B_4C-reinforced AMMC and found that increased volume ratio and reduced particle size reduced the yield of composite production. Dearnley et al. [13] developed a composite material by surface modification on an aluminum substrate using micro arc oxidation and laser alloying methods. The highest abrasion resistance value was obtained in Al_2O_3 coated material produced by micro arc oxidation method.
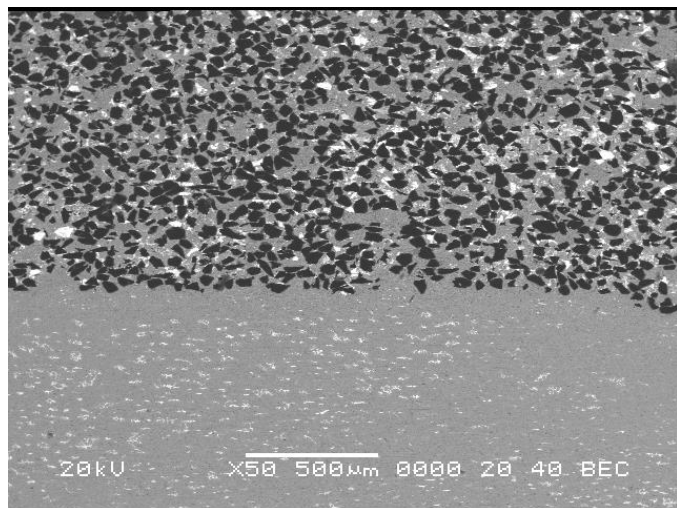
Figure 4: SEM image of the cross-section of composite

As can be easily seen from the electron microscope image with higher magnification in Figure 5, there is no porosity or interface mismatch between the reinforcing element and the matrix which will adversely affect any material property (mechanical, chemical). The results of the wear test also support these findings.
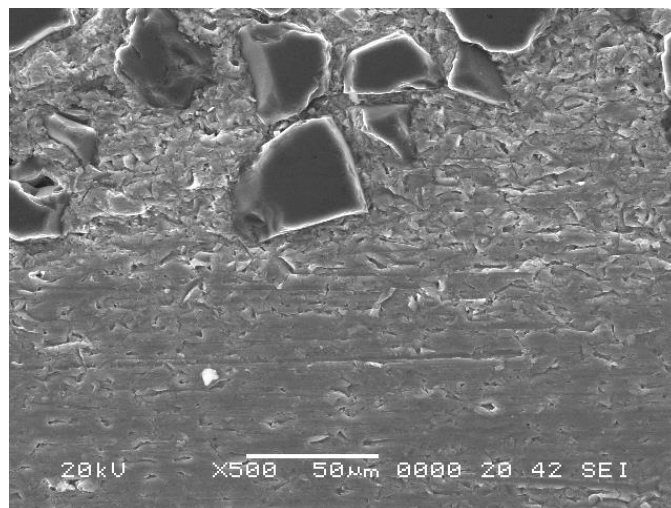
Figure 5: SEM image of the B4C particulates in Al matrix

Figure 6 shows the result of the wear test obtained at a distance of 2400 meters under the load of 15 N. Weight loss in the sample was measured in every 400 meter intervals and graph in Figure 6 was plotted. Due to the nature of the wear test, weight loss of the material is expected depending on the distance. This tendency is clearly seen in Figure 6.
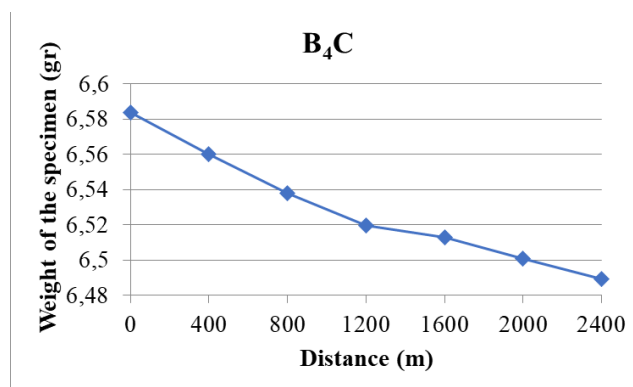
Figure 6: Weight loss-distance

However, the character of the wear resistant material will be the material which has suffered minimum mass loss depending on the distance. The wear test performance of the sample was 0.0945 gr mass loss at a total distance of 2400 meters.
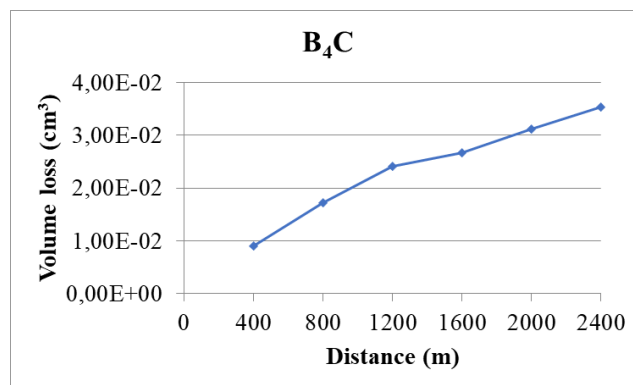
Figure 7: Volume loss-distance

The total volume loss was 0,035 cm^3 shown in Figure 7. Figure 8 shows the change in wear rate. As shown in the figure, volumetric wear rate was $1,47 \times 10^{-5}$ cm^3/m and gravimetric wear rate was $3,93 \times 10^{-6}$ gr/m. Wear rates, both volumetric and gravimetric has a trend to decrease with sliding distance. This trend is to be expected. Tang et al. [14] investigated the effect of B$_4$C reinforcement on 5083 aluminum alloy on the wear resistance of the material. The reinforcement ratio in the composite materials was 5% and 10% by weight, and they were subjected to wear testing for 3000 meters. As a result of the wear test, they found that the composite with 10% reinforcement had 40% higher wear resistance than the 5% reinforced composite. Sukumaran et al. [15] in their study, 2124 aluminum alloy and 2124 alloy with 10% SiC added composites were produced by squeeze casting method. They tested different compression pressures during production and examined the microstructure and mechanical properties of the samples and found that 100 MPa gives the best mechanical properties. They applied a wear test to the samples produced with a pressure of 100 MPa and obtained a wear rate of 8.33% less in the reinforced material.
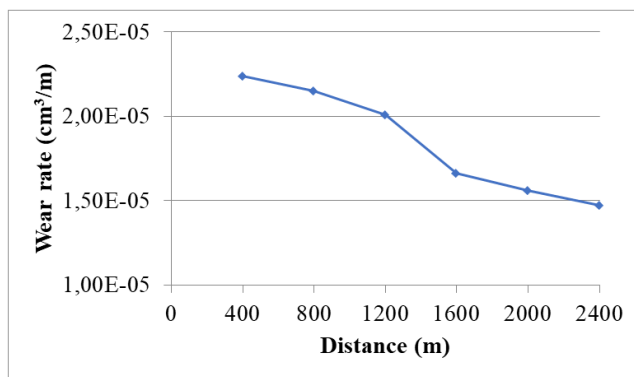
Figure 8: Wear rate

IV. CONCLUSION

To conclude;

1. The production of metal matrix composite material containing high reinforcement by compression casting method was achieved.
2. The matrix alloy which is taken as a reference in the study is not included in the results section due to the complete wear out at 170 meters. However, the reference material shows how high the wear resistance of the composite produced.
3. At a total of 2400 meters, the composite weight decreased by 0.0945 gr.
4. The volume loss at 2400 meters was 3.5×10^{-2} cm^3.
5. The wear rate was $1,43 \times 10^{-5}$ cm^3/m for 2400 meters.
6. In SEM examination, it was seen that the matrix phase completely surrounded the reinforcing elements without voids.

REFERENCES

[1] *Engineered Casting Solutions*, American Foundry Society Inc., Des Plaines, IL, 2001.

[2] M. Rosso, "Ceramic and metal matrix composites: routes and properties", *Journal of Materials Processing Technology*, 175(1-3):364-375, 2006.

[3] S. Sikder, and H.A. Kishawy, "Analytical model for force prediction when machining metal matrix composites", *International Journal of Mechanical Sciences*, 59(1):95-103, 2012.

[4] M.K. Surappa, "Aluminium matrix composites: challenges and opportunities", *Sadhana*, 28(1-2):319-334, 2003.

[5] S. Rawal, "Metal-matrix composites for space applications", *JOM*, 53(4):14-17, 2001.

[6] S. Veličković, S. Garić, B. Stojanović, and A. Vencl, "Tribological properties of aluminium matrix nanocomposites", *Applied Engineering Letters*, 1(3):72-79, 2016.

[7] J. Hashim, L. Looney, and M.S. Hashmi, "Metal matrix composites: production by the stir casting method" *Journal of Materials Processing Technology*, 92-93:1-7, 1999.

[8] D.H. Kirkwood, "Semisolid Metal Processing", *International Materials Reviews*, 39(5):173-189, 1994.

[9] N. Chawla, and K.K. Chawla, *Metal Matrix Composites*, New York, Springer, 2006.

[10] M. F. Ibrahim, H. R. Ammar, A. M. Samuel, M. S. Soliman, and F. H. Samuel, "Metallurgical parameters controlling matrix/B4C particulate interaction in aluminium–boron carbide metal matrix composites", *International Journal of Cast Metals Research,* 26:6, 364-373, 2013.

[11] J.A. Hawk, R.D. Wilson, J.H. Tylczak, and O.N. Dogan, "Laboratory abrasive wear tests: investigation of test methods and alloy correlation", *Wear,* 225–229, 1031–1042, 1999.

[12] A. Canakci, F. Arslan, and T. Varol, "Effect of volume fraction and size of B4C particles on production and microstructure properties of B4C reinforced aluminium alloy composites", *Materials Science and Technology*, 29:8, 954-960, 2013.

[13] P.A. Dearnley, J. Gummersbach, H. Weiss, A.A. Ogwu, and T.J. Davies, "The sliding wear resistance and frictional characteristics of surface modified aluminium alloys under extreme pressure", *Wear*, 225–229, 127–134, 1999.

[14] Feng Tang, Xiaoling Wu, Shirong Ge, Jichun Ye, Hua Zhu, Masuo Hagiwara, and Julie M. Schoenung, "Dry sliding friction and wear properties of B4C particulate-reinforced Al-5083 matrix composites", *Wear,* 264, 555–561, 2008.

[15] K. Sukumaran, K.K. Ravikumar, S.G.K. Pillai, T.P.D. Rajan, M. Ravi, R.M. Pillai, B.C. Pai, "Studies on squeeze casting of Al 2124 alloy and 2124-10% SiCp metal matrix composite", *Materials Science and Engineering A,* 490, 235–241, 2008.

Machinability Characteristics of Mechanically Alloyed Bronze Matrix Composites During Turning

E. SALUR[1] and A. ASLAN[1]

[1] Selcuk University, Konya/Turkey, esalur@selcuk.edu.tr
[1]Selcuk University, Konya/Turkey, aaslan@selcuk.edu.tr

Abstract - In this study, the mechanically alloyed bronze (CuSn10) matrix composite materials reinforced with 10 wt. % and 20 wt. % spheroidal cast iron (GGG-40) were produced by hot press. The turning experiments were conducted on universal turning lathe without cutting fluid. The effects of the different reinforcement ratios on the cutting force and the surface roughness of bronze matrix composites were investigated, and their effects were presented. The test results revealed that the reinforcement ratio was the highly effective on the cutting forces and surface roughness of the mechanically alloyed bronze metal matrix composites. In microstructure analyses, it was observed that mechanical alloying occurred effectively, and the reinforcement material was homogeneously distributed into matrix. It was found that as the reinforcement ratio increase cutting forces and surface roughness increase. Since GGG-40 is a harder material than CuSn10, the power consumption required for material removal increases because of increment GGG-40 amount in the structure. Considering effect of reinforcement ratio, higher proportion of GGG-40 in the composite led to increase in surface roughness because GGG-40 particles were relatively retained their form during the mechanical alloying and production process. The GGG-40 chips were broken and ruptured from the surface rather than cutting during turning and it led to rougher surface.

Keywords – Mechanical alloying, bronze matrix composites, reinforcement ratio, surface roughness, cutting forces

I. INTRODUCTION

Composite materials are extensively used in industrial applications because of their superior properties compared to traditional materials. As a result of these superior properties of composite materials, their usage rates in automotive, aerospace, space industry and nuclear energy have been increased in recent years [1-3]. There are different kinds of composite materials categorized according to matrix type. One of the most commonly used among them is metal matrix composites (MMCs). MMCs consist of two components called matrix and reinforcement materials. In MMCs, light metals such as aluminum, magnesium, copper and alloys are widely used as matrix materials. MMCs can be fabricated by various production methods. These production methods are classified into three main categories as liquid, solid-liquid and solid state [2, 4].

Although composite materials are generally produced in dimensions close to their final shape, machining is often required for most parts due to dimensional accuracy, assembly and surface precision. Machining of metal matrix composites depends on the type and properties of the reinforcement and matrix materials [5]. The mechanical and other instinctive properties of these materials have a significant impact on the machinability. In addition, the machinability characteristics of of MMCs depends on the cutting tool material, geometry and cutting parameters. The usage of MMCs are limited by their inadequate machining properties. The machining of MMCs is more hard than traditional materials due to nonuniform, anisotropic structure of MMCs [6, 7]. Therefore, same similarity is not matter on properties of MMCs in terms of mechanisms such as surface condition and tool wear in homogeneous structural materials. Although the ceramic particles used as reinforcement elements in matrix significantly enhance the mechanical properties of the composites, the high hardness values of these elements lead to tool wear and a rough surface [2, 5]. In addition, the machining of composite materials may require special demands on the wear resistance and geometry of the cutting tool. Considering these mechanisms, the selection of the right cutting tool gains great importance. The turning process is needed most attention in the machining of composite materials because of created stress concentration during machining [8, 9]. The effect of turning on the failure type and its distribution has a huge influence on the behavior of the component. Chaotic material zones occurred because of interaction of the workpiece and tool. This interaction causes to different deficiency in the material such as residual stresses and micro cracks. It is reported that the surface properties and cutting force depend on two significant constituents like the hardness and microstructure [3].

Mechanical alloying (MA) is a method which prevents segregation and agglomeration of reinforcement materials and it provides homogeneous distribution of particles into matrix [10, 11]. Work hardening occur because of excessive plastic deformation which originated from mechanical alloying process [12]. So, MA process directly affect machinability characteristics of the materials.

Most of the published researches supplies outcomes in terms of surface roughness, cutting force and tool wear during machining MMCs which reinforced with such as SiC, TiC particles. Nevertheless, no published paper available for the machining of mechanically alloyed CuSn10 matrix composites which reinforced with GGG-40. So, this study is aimed to

disclose that the effect of different feed rate and depth of cut on the machining properties such as surface roughness and cutting forces of mechanically alloyed/ball milled bronze matrix composites.

II. MATERIALS AND METHODS

In this study, spheroidal graphite cast iron (GGG-40) was utilized as reinforcement material in tin bronze matrix (CuSn10) alloy to produce MMCs. The nominal chemical compositions (wt. %) of CuSn10 and GGG-40 were given in Table 1, respectively. The beginning particle size of CuSn10 and GGG-40 metallic chips changed between 1 and 2 mm. After, these chips mechanically alloyed in high energy planetary ball milled RETSCH-PM 100 ball milled device for 1h, at 400 rpm. The ball-to-powder (BPR) mass ratio was implemented as 10:1 and 10 mm diameter WC balls were employed. Consolidation of these mechanically alloyed metallic powders was achieved by hot press and MMCs were produced with 10 wt % and 20 wt % GGG-40 reinforcement ratio. These MMCs were fabricated at 600 MPa pressure and at 500 ºC. The production parameters were settled regarding as prior tests. The metallic powders were kept in the female die for 15 min at constant temperature to uniform distribution of temperature. After the heating process, the compression stage was conducted with the synchronous displacement of the male dies. So, the time required to produce one sample lasted 25 minutes. The production stages and used equipment were illustrated in Fig.1

Figure 1: Production stages and equipment.

Different samples which reinforced with 10 wt % and 20 wt % GGG-40 namely 90B10C and 80B20C were successfully produced for further turning experiments. The turning experiments of MMCs were carried out after the fabrication process. The turning experiments were carried out on on the Tezsan T 165-MF model lathe. The experimental setup including test equipment, computer and the experimental setup of turning test were presented in Fig. 2. Mahr-M1 model surface roughness measurement device was applied to determine the surface property. All tests were executed without cutting fluid for more reliable results. In order to confirm the data, the turning tests were conducted in three repetition. Since the effect of reinforcement ratio on cutting force and surface property of MMCs were aimed to examine, other machining parameters (speed, depth of cut, diameter of tool, etc.) were chosen as constant. After turning experiments, the microstructural view of

the MMCs was monitored with a Nikon MA100 model optical microscope.
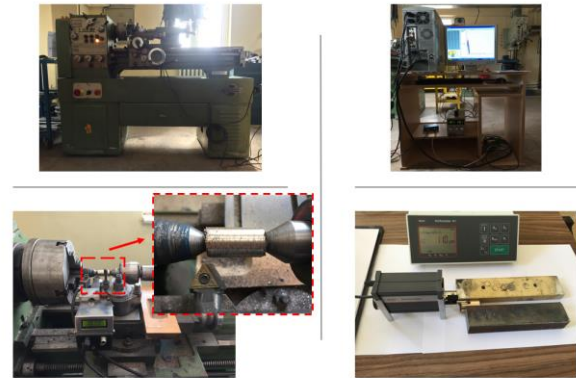
Figure 2: The turning experiments and measurement devices.

III. RESULTS AND DISCUSSION

The differences in microstructure of the samples which were produced with different reinforcement ratio were represented in Fig. 6. It was observed that convoluted lamellar structure was take place during mechanical alloying. This is expected to occur in ductile-ductile systems. In addition, this is the ideal combination material system for the mechanical alloying process. It is reported that successful alloying occurs with repeated cold welding and fracture mechanism of particles; if the particles are not ductile, cold welding will not occur. In the early stages of MA process, the ductile elements were plastically deformed by a micro forging process and particles formed convolute structures [11]. In the next step, the convoluted/flattened particles were cold welded with each other and a lamellar structure was formed within the matrix. During MA process, the composite powder particles were subjected to deformation hardening, the hardness and consequently the brittleness increased, and equiaxial particles were formed due to the repetitive fragmentation of the particles.
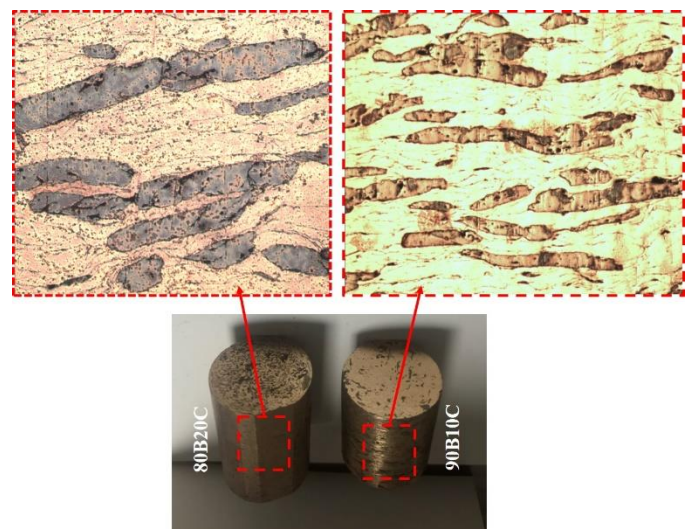
Figure 3: Microstructure of produced mechanically alloyed MMCs

with different reinforcement ratio.

As seen in the Fig.4, as the proportion of cast iron in the structure increases, the cutting forces increase. Because the harder reinforcement material (GGG-40) increases in the structure, more power consumption is required to remove the material and the cutting forces are increased. In addition, these results were compared with the previous study which deal with machinability properties of the specimens which are un-milled and produced at different production parameters [13]. It was found that the cutting forces increased by almost 100%. These results indicate that there is deformation hardening occurs in the structure as a result of severe plastic deformation of the materials by mechanical alloying.

Figure 5: The effect of reinforcement ratio on average surface roughness.

Figure 4: The effect of reinforcement ratio on average cutting forces.

According to general trend as shown in Fig.5, the average surface roughness value increases with the increment of the spheroidal cast iron ratio in the structure. This is due to the fact that the GGG-40 particles retain their shape in structure more than CuSn10 during production process. It is observed that the GGG-40 reinforcement particles which are relatively maintaining their form in structure are covered with CuSn10 matrix. As a result of the increment of GGG-40 ratio in the structure, it made difficult for the CuSn10 to perform the matrix function, the structural integrity decreased and the amount of void in the structure increased. Therefore, the average surface roughness values increased. In addition, it was observed that longer convoluted lamellar particles were formed as a function of increment of reinforcement material (GGG-40) as shown in Fig. 3. The main reason of this situation can be expressed as the flattened GGG-40 particles by deformation rather than fracturing as a result of the lubricating effect of graphite in the structure of GGG-40 reinforcement material.

IV. CONCLUSION

In this study, the effects of different reinforcement ratio (GGG-40) on cutting forces and surface roughness of mechanically alloyed bronze matrix composites during turning were investigated. The following conclusions can be drawn from the experiments.

- It was observed that convoluted lamellar structure was take place during mechanical alloying. It can be explained that this occurs as a result of fracture and cold-welding mechanisms occurring in two stages during mechanical alloying process.
- It was found that as the proportion of spheroidal cast iron in the structure increases, the cutting forces increase because of GGG-40 having higher hardness.
- It was inferred that surface roughness increase as a function of increment of the reinforcement material. The increment of reinforcement material makes it difficult to cover the reinforcement material by the matrix, resulting in a rougher structure due to the rough surface of the GGG-40.

REFERENCES

1. Davim, J.P., *Machining composites materials*. 2013: John Wiley & Sons.
2. El-Gallab, M. and M. Sklad, *Machining of Al/SiC particulate metal-matrix composites - Part I: Tool performance.* Journal of Materials Processing Technology, 1998. **83**(1-3): p. 151-158.
3. Salur, E., et al., *Experimental study and analysis of machinability characteristics of metal matrix composites during drilling.* Composites Part B: Engineering, 2019. **166**: p. 401-413.
4. Chambers, A.R., *The machinability of light alloy MMCs.* Composites Part a-Applied Science and Manufacturing, 1996. **27**(2): p. 143-147.

5. Basavarajappa, S., et al., *Drilling of hybrid aluminium matrix composites.* The International Journal of Advanced Manufacturing Technology, 2008. **35**(11-12): p. 1244-1250.
6. Barzani, M.M., S. Farahany, and V. Songmene, *Machinability characteristics, thermal and mechanical properties of Al-Mg2Si in-situ composite with bismuth.* Measurement, 2017. **110**: p. 263-274.
7. Davim, J.P., *Machining of hard materials*. 2011: Springer Science & Business Media.
8. Niknam, S.A., et al., *Turning titanium metal matrix composites (Ti-MMCs) with carbide and CBN inserts.* International Journal of Advanced Manufacturing Technology, 2018. **97**(1-4): p. 253-265.
9. Torralba, J.M., C.E. da Costa, and F. Velasco, *P/M aluminum matrix composites: an overview.* Journal of Materials Processing Technology, 2003. **133**(1-2): p. 203-206.
10. Canakci, A., T. Varol, and C. Nazik, *Effects of amount of methanol on characteristics of mechanically alloyed Al–Al2O3 composite powders.* Materials Technology, 2012. **27**(4): p. 320-327.
11. Suryanarayana, C., *Mechanical alloying and milling.* Progress in materials science, 2001. **46**(1-2): p. 1-184.
12. Nazik, C., *Alüminyum matrisli B4C parçacık takviyeli kompozitlerin toz metalurjisi yöntemiyle üretimi ve mekanik özelliklerinin incelenmesi.* 2013, Selçuk Üniversitesi Fen Bilimleri Enstitüsü.
13. Salur, E., *Investigation of machinability properties of metal matrix composites produced by recycling of waste metal chips*. 2017, Ms Thesis, Selçuk University, Department of Mechanical Engineering, Konya.

The Effect of Mechanical Alloying Process on Microstructural Evolution and Mechanical Properties of Bronze Matrix Composites.

E. SALUR[1] and A. ASLAN[1]

[1] Selcuk University, Konya/Turkey, esalur@selcuk.edu.tr
[1]Selcuk University, Konya/Turkey, aaslan@selcuk.edu.tr

Abstract - **In this study, the difference of mechanical alloying process compared to traditional production methods was investigated. In this context, 10% spheroidal cast iron (GGG-40) reinforced bronze (CuSn10) matrix composite materials were produced by two different methods and experimental studies were carried out on these specimens. Firstly, metallic chips with a particle size of 1-2 mm were hot pressed under a pressure of 700 MPa and 500 ºC without the need for a second treatment. After, these metallic chips were subjected to mechanical alloying process and hot pressed in the same production parameters. Microstructural evolution, porosity and hardness values of the specimens produced by two different methods were compared. It was found that particle sizes decreased from 1-2 mm to 200 μm in the sample subjected to mechanical alloying process. According to optical microscope images, it was observed that the broken relatively brittle particles (GGG-40) were homogenously embedded in the ductile (CuSn10) matrix. This is due to the fact that ductile metal particles become flattened by ball--powder-jar collisions and fracture of relatively brittle powders as a result of the severe plastic deformation which occurred during mechanical alloying. It was found that there was a 29,9 % increment in hardness value and a 18,5 % decrement in porosity of the mechanically alloyed sample compared to the directly pressed sample.**

Keywords – **Mechanical alloying, bronze matrix composites, mechanical properties, microstructural evolution**

I. INTRODUCTION

Rapid developments in the field of technology require the use of new materials with superior properties compared to traditional materials. For this reason, scientists have carried out various research to produce new materials with superior properties. Therefore, new material groups called "Composite Materials" have been produced which have superior qualities than traditional materials [1]. Recently, studies on composite materials have increased due to their cost, light weight, excellent mechanical and thermal properties [2, 3]. In recent years, copper and its alloy matrix composite have been used in many engineering applications especially such as superconductors owing to their good thermal conductivity, cast ability and machinability. The machinability of metal [4], metal-based alloys and metal matrix composites [5] (MMCs) materials is of great importance according to the uses of the final product and many studies have been carried out on this subject.

The final properties of composites changes depending on the properties of the matrix and the reinforcement materials, as well the distribution of the reinforcement materials in the matrix. Mechanical alloying (MA) is a method which prevents segregation and agglomeration of reinforcement materials and it provides homogeneous distribution of particles into matrix [6-8]. Mechanical alloying is a highly effective method that enables the production of homogenous composites as a result of repeated deformation, fracture mechanisms within the high energy ball milling system [9]. The MA technique is particularly suitable for the production of metal matrix composite materials (MMCs) because it allows better features than the properties obtained by other conventional methods.

According to [10], bonding materials obtained by using Cu-based alloy system have the highest physical, mechanical and working properties. Valentin et. al. found that mechanically alloyed dispersion-strengthened tin bronze grinding heads much lower diamond specific consumption when grinding harder alloys without cutting fluid [10].

Considering the published studies, it is found that there are limited studies on mechanically alloyed bronze system. Therefore, in this study the effect of mechanical alloying methods on morphologic and mechanical properties of bronze matrix system is investigated.

II. MATERIALS AND METHODS

The bronze (CuSn10) and spheroidal cast iron (GGG-40) bars produced with the desired chemical compositions and then these bars were turned, and metallic chips were obtained. These chips were mixed with double cone mixer according to German's mixture rule [11]. Firstly, wt. 10% iron reinforced bronze matrix metallic chips were pressed directly under a 500 ºC and 700 MPa without a second process. After, the metallic chips obtained by turning were mechanically alloyed (MA) in a RETSCH-PM 100 planetary mill for 1h at 300 rpm. The ball-to-powder (B:P) ratio was selected as 10:1 and the milling medium was comprised of 10 mm diameter WC balls. Methanol was chosen as a process control agent (PCA) at wt. 1 %. Mechanically alloyed metallic powders were pressed with same production parameters. Mechanical alloying process and production steps were shown in Fig.1.
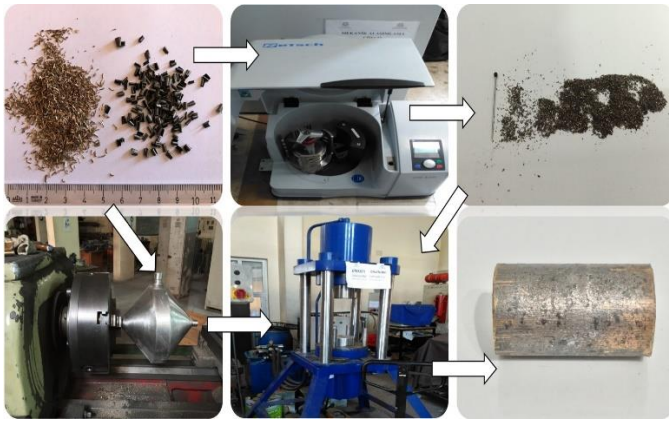
Figure 1: Mechanical alloying process and production steps

The microstructural evolution of the samples produced by different production methods was evaluated with a Nikon MA100 model optical microscope. The Brinell hardness of the samples were measured INNOVATEST NEMESIS 900 hardness tester and the porosity values of the samples were calculated according to Archimedes' rule with Precise XB220A model assay balance. The test apparatuses were shown in Fig.2.

Figure 2: Test apparatuses

Figure 3: (a) Optical microscope (OM) view of directly pressed specimen (b) OM view of mechanically alloyed and pressed specimen, with 100X magnification

III.   RESULTS AND DISCUSSION

The changes in microstructure depending on mechanical alloying process was shown in the Fig.3. It was monitored that convoluted lamellar structure was occurred during mechanical alloying. It is a typical observation for ductile-ductile components system in regard to Suryanarayana [8]. During the alloying process, as a result of collision of the balls with each other, the residual particles (metallic chips) between the balls was subjected to severe plastic deformation. This resulted in fragmentation of the particles and the particles become flattened as shown in Fig.3. During these collisions, the particles absorbed some impact energy. Due to the impact energy, the particles were flattened, cold welded, broken and welded again. This impact force deformed the powder particles, causing the particles to harden and break.

The hardness and porosity values of directly pressed and mechanically alloyed samples were measured as 137, 178 HB and % 2,43; %1,98; respectively.

As shown in the Fig.4, it was observed that the mechanically alloyed specimen exhibited superior hardness values than that of the directly pressed.   This increment can be explained by several parameters. The effect of grain size is the foremost parameter among them, as the grain size decreases the hardness increases.   Another important parameter is the lattice strain resulting from the increased dislocation density during milling.
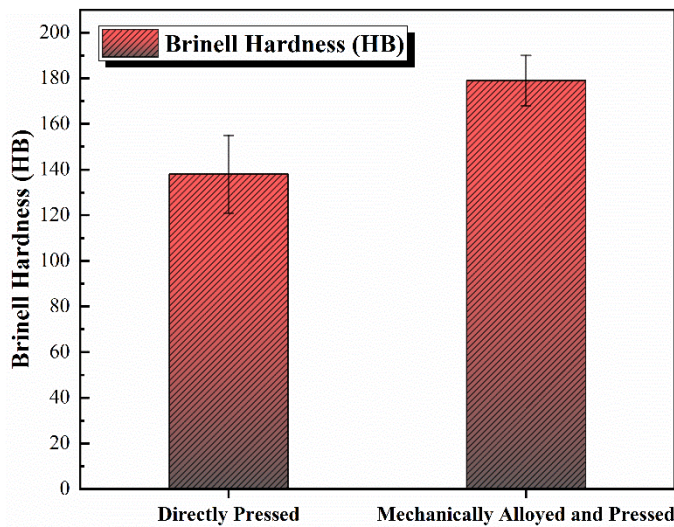
Figure 4: Brinell Hardness values of the samples fabricated with two different production methods

According to Fig.5, it was observed that porosity values of mechanically alloyed specimen was lower than directly pressed. Mechanical alloying directly affects the softening mechanism and plastic deformation behavior of the metallic chips, and it led to the successful covering of GGG-40 chips by the CuSn10 chips as providing a structural integrity. Consequently, since mechanical alloying (MA) method provided better structural integrity, the porosity value of sample was decreased in number and size.
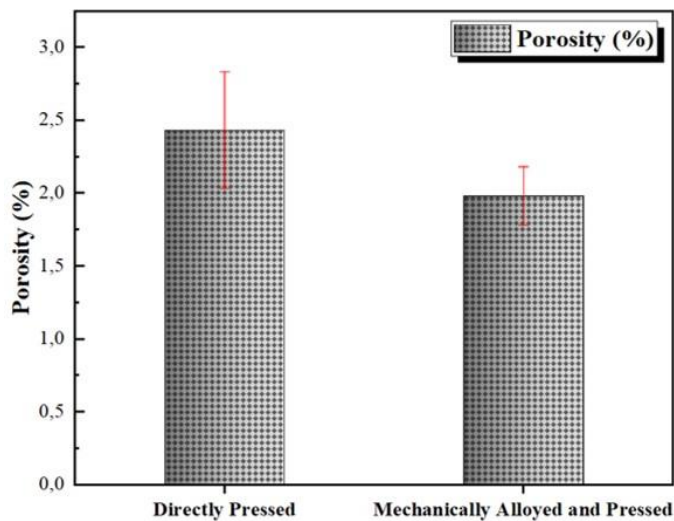
Figure 5: Porosity values of the samples fabricated with two different production methods

IV. CONCLUSION

In this study, the effects of mechanical alloying methods on mechanical properties and microstructural evolution of bronze matrix composites were investigated. The following conclusions can be drawn from the experiments.

- The metallic chips get work hardened, and the particles get fragmented because of mechanical alloying process.
- As a result of mechanical alloying, a more homogeneous structure was obtained, and the hardness values increased due to the excessive plastic deformation.
- As a consequence of better structural integrity which achieved by MA technique, the porosity values of specimen decreased.

REFERENCES

1. Guluzade, R., et al., *Fracture toughness of recycled AISI 1040 steel chip reinforced AlMg1SiCu aluminum chip composites.* Materials & Design (1980-2015), 2013. **52**: p. 345-352.
2. Erturk, A.T., et al., *Machining behavior of multiple layer polymer composite bearing with using different drill bits.* Composites Part B: Engineering, 2019: p. 107318.
3. Marani, M., et al., *Neuro-fuzzy predictive model for surface roughness and cutting force of machined Al–20 Mg 2 Si–2Cu metal matrix composite using additives.* Neural Computing and Applications, 2019: p. 1-12.
4. Kuntoğlu, M. and H. Sağlam, *Investigation of progressive tool wear for determining of optimized machining parameters in turning.* Measurement, 2019. **140**: p. 427-436.
5. Salur, E., et al., *Experimental study and analysis of machinability characteristics of metal matrix composites during drilling.* Composites Part B: Engineering, 2019. **166**: p. 401-413.
6. Canakci, A. and T. Varol, *Microstructure and properties of AA7075/Al–SiC composites fabricated using powder metallurgy and hot pressing.* Powder technology, 2014. **268**: p. 72-79.
7. Canakci, A., T. Varol, and C. Nazik, *Effects of amount of methanol on characteristics of mechanically alloyed Al–Al2O3 composite powders.* Materials Technology, 2012. **27**(4): p. 320-327.
8. Suryanarayana, C., *Mechanical alloying and milling.* Progress in materials science, 2001. **46**(1-2): p. 1-184.
9. Canakci, A., S. Ozsahin, and T. Varol, *Modeling the influence of a process control agent on the properties of metal matrix composite powders using artificial neural networks.* Powder technology, 2012. **228**: p. 26-35.
10. Smirnov, V.M. and E.P. Shalunov, *The Possibilities of Creation and the Prospects of Application of a Binder with the Matrix-Filled Structure «Tin Bronze–the Mechanically Alloyed Granules» for Production of Diamond Tools.* Materials Today: Proceedings, 2019. **11**: p. 270-275.
11. German, R.M., *Powder metallurgy science.* Vol. 105. 1984: Metal Powder Industries Federation Princeton, NJ.

Pulsed Laser Deposition System For Oxides Thin Films Deposition

A.HOUIMI[1] and S.YİĞİT GEZGİN[2] and H.Ş.KILIÇ[2,3,4]

[1] Selcuk University, Faculty of Science, Department of Nanotechnology and advanced Materials, Konya/Turkey,aminahouimi@gmail.com

[2] University of Selçuk, Faculty of Science, Department of Physics, 42031, Selçuklu, Konya, Turkey

[3] Selçuk University, Directorate of High Technology Research and Application Center, 42031, Selçuklu, Konya, Turkey

[4] Selçuk University, Directorate of Laser Induced Proton Therapy Application and Research Center, 42031, Selçuklu, Konya, Turkey

Abstract - **One of the most known transparent metal oxides is Tin oxide. It has a wild range of applications in different fields that allowed it to gain a lot of interest. In this study, we will present the composition of a mixt matrix thin films of tin oxides grown by Pulsed Laser Deposition technic. The films were produced at room temperature and with the utilization of a pure metallic tin target. The structural and optical properties were investigated using the X-ray diffraction and absorption spectrophotometry. Crystal structure and phase transformation during the deposition and annealing treatment were also explained in details.**

Keywords – **Pulsed Laser Deposition, SnO_2 , Sn_3O_4, Thin Films.**

I. INTRODUCTION

Tin Oxide is wild known metal oxide n-type semiconductor. Because of its non-toxicity, abundant availability, suitable optical and electrical properties[1] it was customarily used in Lithium-ions batteries[2], solar cells[3], sensors[4], photocatalytic activities[5]. SnO (Stannous oxide) and SnO_2 (stannic oxide) are the most used univalent forms of tin oxides with a different Sn oxidation states; Sn^{2+} and Sn^{4+} and completely dissimilar properties.

The coexistence of the two oxidation states results in other forms of tin oxides such as Sn_5O_6, Sn_2O_3, Sn_3O_4. Sn_3O_4 is an heterovalent metastable semiconductor that represents the transition phase between Stannous and stannic oxides. According to the literature, Sn_3O_4 phase is present during the synthesis of SnO_2 when SnO decompose into Sn_3O_4 and Sn (metal)[6, 7] following the next equations:

$$4 \, SnO \quad \rightarrow \quad Sn_3O_4 + Sn \qquad (1)$$
$$Sn_3O_4 \quad \rightarrow \quad 2SnO_2 + Sn \qquad (2)$$
$$Sn + O_2 \quad \rightarrow \quad SnO_2 \qquad (3)$$
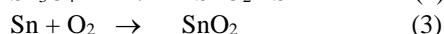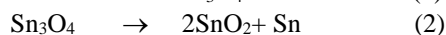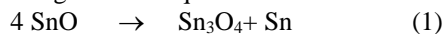
Theoretically, the optical band gap of Sn_3O_4 is in the visible range of the electromagnetic spectrum[8], this did attracts a good attention to it for a possible photo-conversion application. Despise the difficulty of obtaining a pure phase of Sn_3O_4 tin oxide but recently a good number of researches are focusing on synthesizing various morphologies of Sn_3O_4 phase; nanosheets[9], nanobelts[10], nanospheres[11], Nanoflakes[12]. Sn_3O_4 was used for photocatalyst for hydrogen generation[13, 14], gas sensors[15] , Lithium-ions batteries[16].

In this work, we tried a different Physical method for synthesizing Sn_3O_4 phase as a thin film. By Pulsed Laser Deposition technique at room temperature and using a metallic tin target we were able to deposit a well crystallized SnO_2/Sn_3O_4 thin film. Its structural and optical properties were investigated according to the deposition time and the annealing temperature.

II. MATERIALS AND METHODS:

The deposition of the thin films was effected by PLD (Pulsed Laser Deposition) technic. The laser pulses (Nd-YAG) of a 5ns duration, 10 Hz repetition rate and 1064 nm wave length were focused on a metallic Sn target (99.99% pure) using a biconvex Quartz lens (40 cm focal length). The chamber background pressure was 4×10^{-6} mbar. To assure the oxidation of the evaporated metal atoms from the target, pure oxygen gas was introduced into the chamber with a partial pressure of 3×10^{-2} mbar. To avoid the target damage and to improve the thin film homogeneity the target and the sample holders were put on circular movement with different speeds. The experiments were hold in three different time duration 1h, 1h & 30 min and 2 h (A1, B1, C1). The thin films deposited at 1h and 1h & 30 min were annealed in evacuated Quarts oven up to 400°C, denoted A2 & B2 respectively. The thicknesses were determined by profilometer (aep technology). Analyzing the Tin oxide films was done by XRD (X-ray diffraction) for structural properties and UV-VIS-NIR absorption spectrophotometry for optical properties.

III. RESULTS:

Tin oxide thin films were grown over a glass substrate by Pulsed laser deposition technic at room temperature. The evolution of thin film's thickness was presented in Table 1. The thickness increases according to the deposition time from 59 nm to 207 nm by rising ablation time from 1h to 2h.

Table 1. Thicknesses of thin film accordaning to deposition time.

Samples	Deposition time	Thickness
A1	1 hour	59 nm
B1	1 hour & 30 min	94 nm
C1	2 hours	207 nm

Figure 1. shows the X-ray diffraction (XRD) pattern of the 3 thin films A1, B1 and C1 with different deposition time measured at θ-2θ mode. All 3 films are polycrystalline and retain the monoclinic crystalline structure of Sn_3O_4 (JCPDS No. 00-016-0737 & JCPDS No. 98-017-4299) and the Orthorhombic crystalline structure of SnO_2 (JCPDS No. 00-029-1484 & JCPDS No. 98-018-1280). Using an oxide targets is the usually applied for tin oxide deposition with PLD system [17-19] also the growth temperature is generally maintained over 200°C to assure a crystal formation of the thin films [20, 21]. Stanimirova et al. [22] and Kim et al. [23] reported an amorphous structure of deposited SnO_2 thin films under 200°C, on the other hand when the substrate temperature increases crystal growth of SnO_2 thin films is ensured. At room temperature, a crystal grown SnO_2 samples was mentioned at limited rapports [24-27] and with the use of SnO_2 target. The use of Tin target was always a challenge due to difficulty of controlling the different tin oxide phases [28-30]. In our case, we are able to produce a polycrystalline Tin oxide mixt matrix thin films using a metallic Tin target and at room temperature.
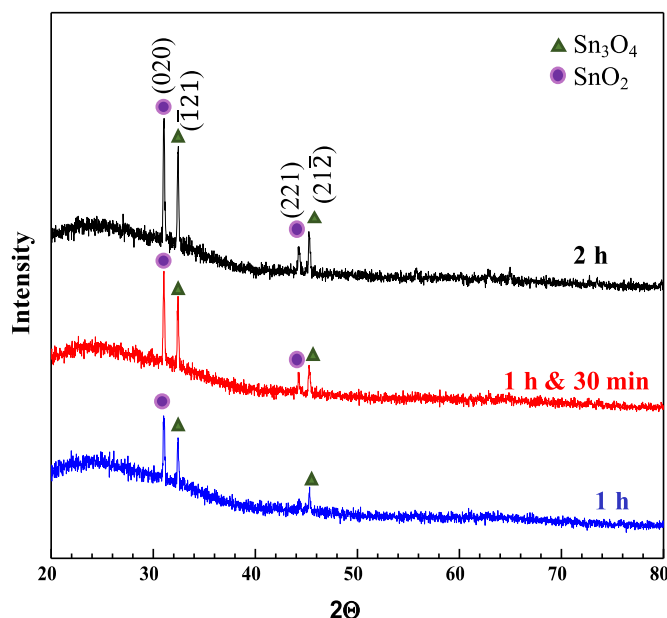
Figure 1: XRD spectra of as deposited tin oxide thin films with different deposition durations.

The deposited film during 1h exhibits a preferred orientation along the (020) plane of SnO_2 phase. $(\bar{1}21)$ & $(21\bar{2})$ peaks of Sn_3O_4 phase are also observed indicating the polycrystalline structure of the samples. By increasing the deposition time all three peaks become more intense signifying an enhancement in the crystallinity of the grown thin films[31, 32] . However, the crystalline sizes calculated using the Scherrer's formula [33] haven't seen a significant

change between the three different thicknesses intensity. The crystalline size increased from 50.4 nm to 55nm. Very small peak that belongs to SnO_2 appears in the XRD pattern after 1h & 30 min of deposition time.

The appearance of the Sn_3O_4 peak can be interpreted by the unfinished reaction of the Sn atoms with the oxygen gas in the plasma due to the genera low O_2 gas pressure. As indicated before the distance between the target and the substrate is only 4.5 cm, in this case the ablated metallic Tin (Sn) atoms won't be completely exposed to the ions of oxygen gas. Thus, the reaction between metallic atoms and oxygen gas atoms will be limited in the PLD plasma and a rich Sn oxides phases can appear [29]. Pan *et al*. [34] observed the appearance of Sn_3O_4 during the oxidation reaction of SnO to SnO_2 by changing the annealing temperature and it refer to it as an intermediate stage between the two Sn oxides. Choi et al.[35] also observed the same oxide (Sn_3O_4) as a transitional phase by changing the oxygen ratio of the reaction chamber.

To see the effect of the temperature on the structural and phase transformation of the as deposited thin films, annealing treatment was done on A1 and B1 films in atmospheric conditions. The produced thin films are called A2 and B2 respectively.
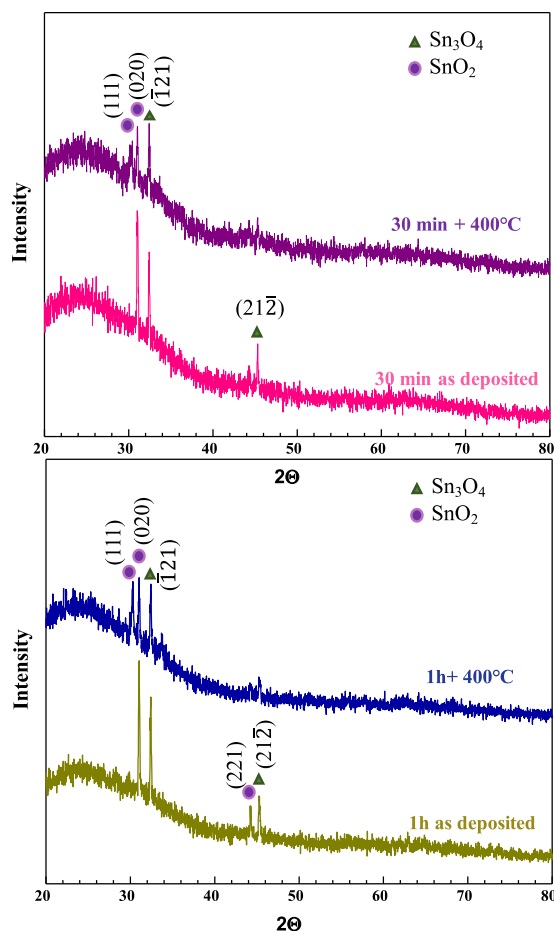
Figure 2. XRD spectra of as deposited and after annealing of (a) film deposited for 30min (b) film deposited for 1h.

The results of XRD analyse of the two annaling processes are presented in *Figure 2*. The intensity of SnO_2 (020) & Sn_3O_4 $(\bar{1}21)$ peaks decreases after the annealing the

two films at 400°C. Also, SnO_2 (221) and Sn_3O_4 $(21\bar{2})$ peaks disappear completely form the spectrum. On the other side a new SnO_2 (111) peaks appears at $2\theta{:}30.20°$. The crystalline size of A2 & B2 decreases from 50,4nm & 54,26nm to 49,01nm & 50nm respectively.

When the as deposited thin films are expose to the atmospheric oxygen a phase transformation occur by the oxidation of Sn_3O_4 to SnO_2. This phase transformation is expected because Sn_3O_4 represents a metastable phase between SnO & SnO_2. So, under annealing conditions Sn_3O_4 oxidizes to SnO_2 using the oxygen of atmosphere. Similar behavior of Sn_3O_4 films phase transformation were also reported [34, 36-38].
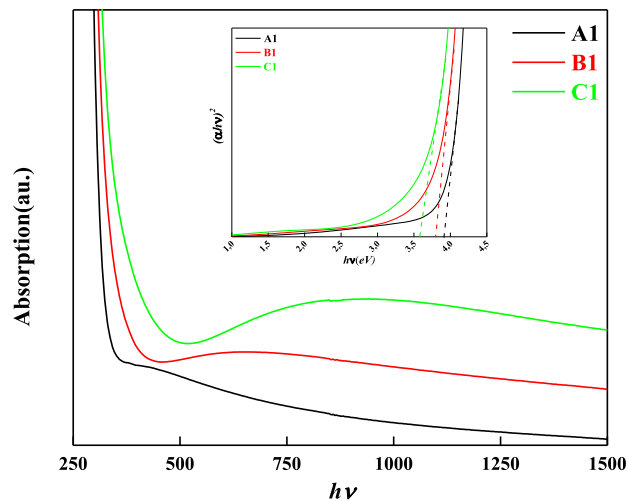
Figure 3. depicts the optical absorption and the band gap of the 3 simples with different thickness A1, B1, C1. The measurement of the absorption specter was done in the UV-Vis spectrophotometer. From Figure 3. we can see that the 3 thin films present a steep absorption edges in the UV region. The absorption of the thin films slightly increases with the deposition time due to the augmentation of the sample's thickness. The absorption edge shifts to the blue small wavelengths as the deposition time decreases. This might be attributed to the drop in crystalline size of the samples from samples C1 to A1 [39].

The band gap of the thin films was calculated from the absorption specter using the Tauc model [40]:

$$(\alpha h\nu)^2 = A (h\nu - E_g) \qquad (4)$$

Where A is a constant, α is the absorption coefficient and E_g is the optical energy gap. We can find the E_g from the intercept of $(\alpha h\nu)^2$ vs. $h\nu$ for direct transition. The values of the band gap are as the following 3.92eV, 3.78eV, 3.58eV for A1, B1 and C1 respectively. The values of the bang gap energy are similar to the reported values in the literature of the SnO_2[32, 41, 42].

A comparison between the 3 thins films indicates that by rising the deposition time the thickness increases and from the other hand the optical energy gap decreases. A similar behavior was observed by S. Yu et al.[43], H.-L. Ma et al.[32] and A. Yadav et al.[42]. It is known that the crystalline and grain size can affect the optical properties of the thin films. The difference in the atomic structure between the grains and

grain boundaries leads to a smaller different concentration of the free charge carriers and formation of potential barriers. With small grain sizes the concentration of the gain boundaries rise leading to an increase in the optical energy gap and a shifting towards the blue wavelengths of the absorption edge [44, 45].

IV. CONCLUSION

We successfully synthesized SnO_2/Sn_3O_4 thin films using PLD technique without any substrate heating and using a metallic tin target. Three different thicknesses were obtained by increasing the deposition time. The effect of the thickness on the structural was very clear by increasing crystalline size up to 55 nm and in general enhancement of the thin film's crystallinity. The optical absorption edge moved towards the small wave light by decreasing the films thicknesses. The optical band gap also experience increase in its value from 3.58eV to 3.92eV. After annealing, the thin films phase transformation has started by the oxidation of Sn_3O_4 to SnO_2.

REFERENCES

1. Kim, H., et al., *Electrical, optical, and structural properties of indium–tin–oxide thin films for organic light-emitting devices.* Journal of Applied Physics, 1999. **86**(11): p. 6451-6461.
2. Wang, Z., et al., *Fast formation of SnO2 nanoboxes with enhanced lithium storage capability.* Journal of the American Chemical Society, 2011. **133**(13): p. 4738-4741.
3. Snaith, H.J. and C. Ducati, *SnO2-based dye-sensitized hybrid solar cells exhibiting near unity absorbed photon-to-electron conversion efficiency.* Nano letters, 2010. **10**(4): p. 1259-1265.
4. Damaschio, C.J., et al., *Sn3O4 single crystal nanobelts grown by carbothermal reduction process.* Journal of Crystal Growth, 2010. **312**(20): p. 2881-2886.
5. Li, C., et al., *Z-scheme mesoporous photocatalyst constructed by modification of Sn3O4 nanoclusters on g-C3N4 nanosheets with improved photocatalytic performance and mechanism insight.* Applied Catalysis B: Environmental, 2018. **238**: p. 284-293.
6. Cahen, S., et al., *Thermodynamic modelling of the O–Sn system.* Thermochimica Acta, 2003. **403**(2): p. 275-285.
7. Lawson, F., *Tin oxide—Sn3O4.* Nature, 1967. **215**(5104): p. 955.
8. Geurts, J., et al., *SnO films and their oxidation to SnO2: Raman scattering, IR reflectivity and X-ray diffraction studies.* Thin solid films, 1984. **121**(3): p. 217-225.
9. Jun-Hua, Z., et al., *Synthesis mechanism of nanoporous Sn3O4 nanosheets by hydrothermal process without any additives.* Chinese Physics B, 2015. **24**(6): p. 066202.
10. Berengue, O., et al., *Semiconducting Sn 3 O 4 nanobelts: Growth and electronic structure.* Journal of Applied Physics, 2010. **107**(3): p. 033717.
11. Song, H., et al., *A facile synthesis of hierarchical Sn 3 O 4 nanostructures in an acidic aqueous solution and their strong visible-light-driven photocatalytic activity.* Nano Research, 2015. **8**(11): p. 3553-3561.
12. Xia, W., et al., *Visible-Light Self-Powered Photodetector and Recoverable Photocatalyst Fabricated from Vertically Aligned Sn3O4 Nanoflakes on Carbon Paper.* The Journal of Physical Chemistry C, 2017. **121**(35): p. 19036-19043.
13. Balgude, S., et al., *Sn3O4 microballs as highly efficient photocatalyst for hydrogen generation and degradation of phenol under solar light irradiation.* Materials Chemistry and Physics, 2019. **221**: p. 493-500.
14. Manikandan, M., et al., *Photocatalytic water splitting under visible light by mixed-valence Sn3O4.* ACS applied materials & interfaces, 2014. **6**(6): p. 3790-3793.
15. Ma, X., et al., *Preparation of three-dimensional Ce-doped Sn3O4 hierarchical microsphere and its application on formaldehyde gas*

sensor. Journal of Alloys and Compounds, 2017. **726**: p. 1092-1100.

16. Chen, X., et al., *Novel hierarchical flowers-like Sn3O4 firstly used as anode materials for lithium ion batteries.* Journal of Alloys and Compounds, 2017. **690**: p. 765-770.

17. Ohgaki, T., et al., *Synthesizing SnO2 thin films and characterizing sensing performances.* Sensors and Actuators B: Chemical, 2010. **150**(1): p. 99-104.

18. Preiß, E.M., et al., *Gas sensing by SnO2 thin films prepared by large-area pulsed laser deposition.* Procedia engineering, 2015. **120**: p. 88-91.

19. Dominguez, J., L. Fu, and X. Pan, *Epitaxial nanocrystalline tin dioxide thin films grown on (0001) sapphire by femtosecond pulsed laser deposition.* Applied physics letters, 2001. **79**(5): p. 614-616.

20. Tien, L., et al., *Synthesis and characterization of single crystalline SnO 2 nanorods by high-pressure pulsed laser deposition.* Applied Physics A, 2008. **91**(1): p. 29-32.

21. Sinha, S., et al., *Characterization of ZnO–SnO2 thin film composites prepared by pulsed laser deposition.* Applied Surface Science, 2011. **257**(24): p. 10551-10556.

22. Stanimirova, T., et al., *Investigation on the structural and optical properties of tin oxide films grown by pulsed laser deposition.* Journal of Optoelectronics and Advanced Materials, 2005. **7**(3): p. 1335-1340.

23. Kim, H. and A. Pique, *Transparent conducting Sb-doped SnO 2 thin films grown by pulsed-laser deposition.* Applied physics letters, 2004. **84**(2): p. 218-220.

24. Khandelwal, R., et al., *Effects of deposition temperature on the structural and morphological properties of SnO2 films fabricated by pulsed laser deposition.* Optics & Laser Technology, 2009. **41**(1): p. 89-93.

25. Chen, Z., J. Lai, and C. Shek, *Insights into microstructural evolution from nanocrystalline Sn O 2 thin films prepared by pulsed laser deposition.* Physical Review B, 2004. **70**(16): p. 165314.

26. Pereira, A., et al., *Pulsed laser deposition and characterization of textured Pd-doped-SnO2 thin films for gas sensing applications.* Thin Solid Films, 2006. **497**(1-2): p. 142-148.

27. Ding, F., et al., *Tin-Based Composite Oxide Thin-Film Electrodes Prepared by Pulsed Laser Deposition.* Journal of The Electrochemical Society, 1999. **146**(10): p. 3554-3559.

28. Kim, C., et al., *A study on thin film gas sensor based on SnO2 prepared by pulsed laser deposition method.* Sensors and Actuators B: Chemical, 2001. **77**(1-2): p. 463-467.

29. Li, M., et al., *From stannous oxide to stannic oxide epitaxial films grown by pulsed laser deposition with a metal tin target.* Applied Surface Science, 2019. **466**: p. 765-771.

30. Zhao, Y., Z. Feng, and Y. Liang, *SnO2 gas sensor films deposited by pulsed laser ablation.* Sensors and Actuators B: Chemical, 1999. **56**(3): p. 224-227.

31. Islam, M., et al., *Thickness study of Al: ZnO film for application as a window layer in Cu (In1− xGax) Se2 thin film solar cell.* Applied Surface Science, 2011. **257**(9): p. 4026-4030.

32. Ma, H.-L., et al., *Thickness dependence of properties of SnO2: Sb films deposited on flexible substrates.* Applied surface science, 2002. **191**(1-4): p. 313-318.

33. Pecharsky, V. and P. Zavalij, *Fundamentals of powder diffraction and structural characterization of materials*. 2008: Springer Science & Business Media.

34. Pan, X. and L. Fu, *Oxidation and phase transitions of epitaxial tin oxide thin films on (1012) sapphire.* Journal of Applied Physics, 2001. **89**(11): p. 6048-6055.

35. Choi, W., et al., *Oxidation process from SnO to SnO 2.* Journal of materials science letters, 1997. **16**(19): p. 1551-1554.

36. Zhang, F., et al., *Static and Dynamic Disorder in Metastable Phases of Tin Oxide.* The Journal of Physical Chemistry C, 2017. **121**(29): p. 16006-16011.

37. Min, B.-K. and S.-D. Choi, *SnO2 thin film gas sensor fabricated by ion beam deposition.* Sensors and Actuators B: Chemical, 2004. **98**(2-3): p. 239-246.

38. Zhao, J., et al., *High-performance Sb: SnO2 Compact Thin Film Based on Surfactant-free and Binder-free Sb: Sn3O4 Suspension.* Journal of Materials Science & Technology, 2015. **31**(8): p. 815-821.

39. Lin, S.-S. and J.-L. Huang, *Effect of thickness on the structural and optical properties of ZnO films by rf magnetron sputtering.* Surface and Coatings Technology, 2004. **185**(2-3): p. 222-227.

40. Tauc, J., *Amorphous and liquid semiconductors*. 2012: Springer Science & Business Media.

41. Zhang, M., et al., *SnO2 epitaxial films with varying thickness on c-sapphire: structure evolution and optical band gap modulation.* Applied Surface Science, 2017. **423**: p. 611-618.

42. Yadav, A.A., *Influence of film thickness on structural, optical, and electrical properties of spray deposited antimony doped SnO2 thin films.* Thin Solid Films, 2015. **591**: p. 18-24.

43. Yu, S., et al., *Transparent conducting Sb-doped SnO2 thin films grown by pulsed laser deposition.* Journal of Non-Crystalline Solids, 2012. **358**(23): p. 3137-3140.

44. Bao, D., et al., *Band-gap energies of sol-gel-derived SrTiO 3 thin films.* Applied Physics Letters, 2001. **79**(23): p. 3767-3769.

45. Aly, S. and A.A. Akl, *Influence of film thickness on optical absorption and energy gap of thermally evaporated CdS0. 1Se0. 9 thin films.* Chalcogenide Letters, 2015. **12**(10): p. 489-496.

Investigation on Dielectric Permittivity of PZT Manufactured by Electric Field Assisted Sintering

İ. ŞAVKLIYILDIZ[1] and Ç. OKUR[2]

[1] Konya Technical University, Konya/Turkey, isavkliyildiz@ktun.edu.tr
[2] Konya Technical, Konya/Turkey, cigdemokur@outlook.com

Abstract - **By using submicron PZT(Pb[Zr$_x$,Ti$_{1-x}$]O$_3$ ($0 \leq x \leq 1$)) materials system, we provided electric field assisted sintering at 482–520 ºC temperature range in conjunction with 60 V/mm dc electric field on the specimen. The furnace temperature increased up to 520 ºC with 10 ºC/min increment. 0.3 amp current cut off was set by dc power supply to eliminate further temperature increase on specimen due to joule heating. The electric field assisted sintering system was prepared with sandwich type experimental setup. The specimen showing initially insulator behavior, revealed current leakage at 482 ºC. Maximum current draw of 0.3 amp was reached at 502 ºC with total power absorption of 5.27 watt/mm^3 during whole experiment. The power supply spontaneously decreased the electric field 20 V/cm due to variation conductivity behavior of specimen and maximum current cut off. Reaching 95 % theoretical density was verified with FESEM micrograph and there is almost no grain growth on specimen except very good grain boundary generation. The sintered PZT specimen showed appreciable dielectric permittivity (ε_r =273) on 1 kHz at room temperature comparing with other studies. Total power absorption of 5.27 watt/mm^3 in 180 seconds decreased sintering temperature from 1200 ºC to 500 ºC. Such an effect cannot be explained with joule heating in a short period of time with very low power supply. Therefore, we ascribe this behavior to electric field related polarization of atoms rested in lattice which increases mass transport triggered with impulse electron flux thorough electric field. Thermodiffusion (Soret effect) and electromigration are few theories could explain this phenomena. With this low temperature sintering techniques, lead emission could also be restricted during manufacturing process.**

Keywords – **Electric field assisted, sintering, PZT ceramics, dielectric permittivity.**

I. Introduction

The sintering of ceramic materials, especially those that are covalently bonded, requires very high temperatures and very long times due to the low diffusivities in such materials [1-3]. For instance, piezoelectric ceramics such as PZT (Pb[Zr$_x$,Ti$_{1-x}$]O$_3$ ($0 \leq x \leq 1$)) are sintered at 1200 ºC for hours using conventional sintering to 99% density[4]. Sintering processes utilizing electrical current such as Spark Plasma Sintering (SPS) utilize a low voltage but ultrahigh current and in so doing is able to reduce the sintering time substantially to ~20 mins while the decrease in sintering temperature[4]. In SPS, Joule heating is the underlying mechanism that results sintering. In

period 2010-2013, flash sintering was discovered which utilizes not only a low voltage but also a low current. The ceramic particulate system of interest can be sintered by sudden rise in current once a certain critical temperature is reached [6-10]. Typically, the current is limited to 10 A so as to prevent Joule heating by instantaneously switching to current control, followed by current cut off [11]. Sintering takes place at temperatures that are typically 30% of the melting temperature, whereas sintering times are drastically reduced to seconds to a few minutes. Such low sintering temperatures and times cannot be explained by classical diffusion kinetics. But the work by Akdogan and Savkliyildiz, which was published in 2013, has shown by in situ synchrotron x-ray diffraction that flash sintering is accompanied by an anelastic unit cell expansion in oxide, boride and carbide ceramics indiscriminately, which is believed to be the reason for enhanced diffusivity [12]. Although a series of articles appeared in the open literature speculating on a host of mechanisms, not clear understanding exists. What is common to all flash sintering studies is that one starts with particulate matter that involves particle to particle contacts [6-10]. As such, one is suspect that tunneling at particle-particle interfaces should have a correlation to enhanced diffusion kinetics. Power absorption during field assisted sintering study lead atomic level welding between particles so that proper grain boundary formation revealed with almost no grain growth [12].

Piezoelectric ceramics such as (PbTiO3, Pb [Zrx, Ti1-x] O3 ($0 \leq x \leq 1$) (PZT), is widely used in worldwide piezoelectric applications. However, lead emission at higher temperature production is a potential thread for human health [12]. With this presented study, a healthier production technique could be presented by sintering these materials at lower temperatures by electric field assisted sintering method.

II. EXPERIMENTS

The commercial sub-micron PZT (Pb[Zr$_x$,Ti$_{1-x}$]O$_3$ ($0 \leq x \leq 1$)) powder were prepared by uniaxial cold pressing into 12 mm diameter disks with 1.5 mm thickness. PEG was used as a binder media to get proper and compact green dense specimen fort his experiment. One hour annealing process was executed on as pressed specimen to eliminate the binder before electric field assisted sintering. MPB, morphotropic phase boundary

(x=0,52) which is special composition showing higher piezoelectric and dielectric properties was chosen for this experiment. To measure density of final product, Archimedes method was used after electric field assisted sintering. FESEM (field emission scanning electron microscopy) investigation was done to assess microstructure as well as porosity. LCR meter was used to examine dielectric permittivity of sintered PZT specimen.

Figure 1 represents the electric field assisted sintering setup [12]. The specimen was positioned between ceramics insulators as sandwich type with silver electrodes on both surfaces. To provide ohmic contact on both surface, silver paste was spread properly. The electrodes was used to apply electric field on specimen during sintering. The applied electric field on specimen is set to 60 V/mm with 0.3 amp current cut off to avoid joule heating. Furnace temperature was rised 10 °C/min intervals up to 520 °C. Electric field with current draw through specimen and the furnace temperature was recorded during whole experiment.
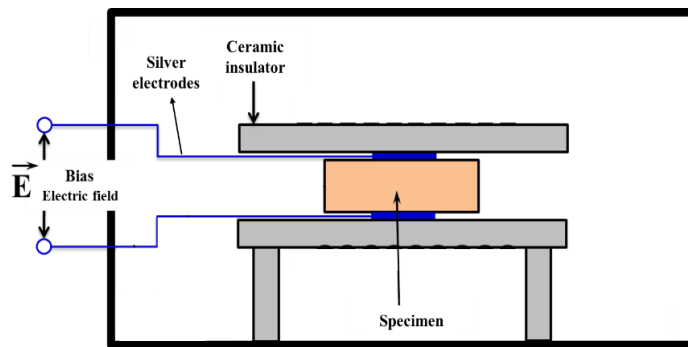
Figure 1: Schematic of sandwich model of experimental setup in furnace [12].

III. RESULTS AND DISCUSSION

Figure 2 shows history of electric field –current relation during field assisted sintering. Even though the specimen was exposed 60 V/mm electric field, no current transition was recorded up to 480 °C which means specimen behaved as an insulator at the beginning due to the lack of particle contact. As increasing temperature, the conductivity of specimen was increased and particle-particle formation was appeared so that 0.1 amp current leakage was observed at 480 °C. Further increase on temperature results increment on conductivity of specimen and current draw as well. Reaching 502 °C as furnace temperature, specimen draw 0.3 amp max. current with 60 V/mm electric field. After this point, specimen conductivity kept increase so, power supply adjusted electric field down to 20 V/mm spontaneously to keep 0.3 amp current draw.
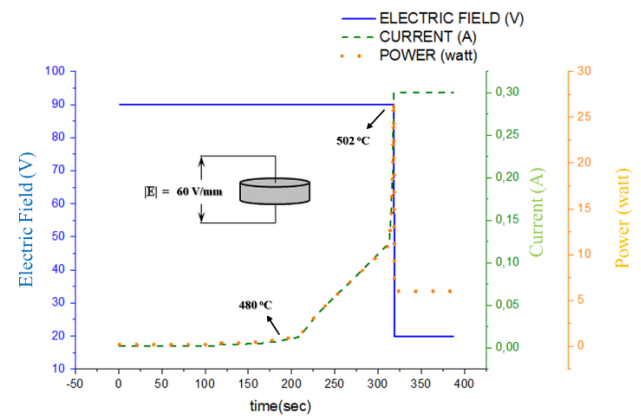
Figure 2: Electric field- current behavior of PZT as function of time

After 80 sec superimposed constant electric field with current draw was finalized to avoid joule heating of specimen. 95 % percent density was measured on sintered specimen by Archimedes method. Sintering PZT around 500 °C (conventional sintering ~1200 °C) groundbreaking outcome of this study. During experiment, specimen absorbed 5.27 watt/mm^3 power which results 10 °C extra increase on furnace temperature. This much temperature increase is not enough to achieve 95 % density so there another mechanism underlying to explain this technique.
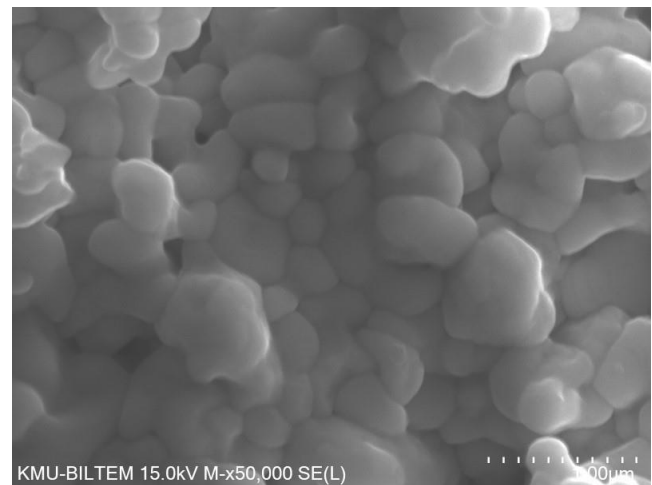
Figure 3: Microstructure of electric field assisted sintered of PZT

Figure 3 represents the microstructure of sintered specimen from fracture surface. A unimodal grain size distribution was observed with proper grain boundary formation. A closer look on microstructure suggest that sintering at low temperature limits grain growth (~700nm) beside very low porosity throughout the specimen. Starting with sub-micron powder results almost no grain growth but very good densification. Therefore, FESEM micrograph validate our density measurement.
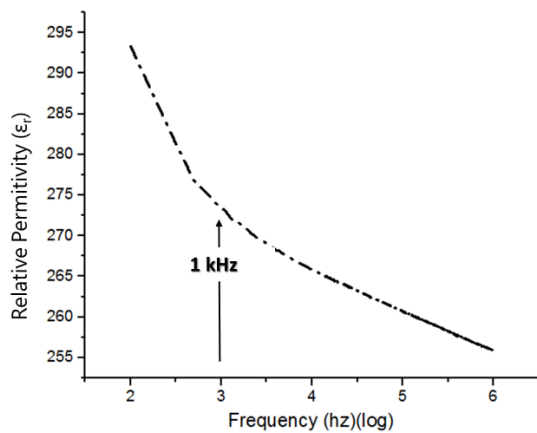
Figure 4: Dielectric permittivity behavior of PZT up to 1 MHz at room temperature

Dielectric permittivity of sintered specimen was illustrated in figure 4 up to 1 MHz at RT. Measuring 273 permittivity value is decent number comparing literature [14]. At higher frequency, specimen permittivity kept this number with little decrement. This behavior suggest that electric field assisted sintering is convenient method comparing other sintering techniques.

IV. CONCLUSION

Nonisothermal densification in sub- micron PZT powder was studied under 60 V/mm dc electric field and 10 ℃/min heating rate. Electric field assisted sintering occurred in the 482–516 ℃ range, which resulted in 95 % of the theoretical density. No local melting due to current draw at particle-particle contacts was observed in scanning electron micrographs, suggesting densification was due to solid state mass transport processes. The maximum current draw at 502 ℃ was 0.3 A, corresponding to instantaneous absorbed power density of 5.27 watt/mm^3. This much power absorption in short time period does not cause 95 % density according to literature, so we attribute this behavior to unit cell volume expansion with polarized atoms due to electric field increases mass. The electron flux during current gains enough momentum to migrate atoms which is called electromigration. Limitation of grain growth by using this technique results improvement on mechanical properties of final product according to hall-petch equation. Regarding dielectric permittivity of final product, specimen revealed 273 ε_r value which very acceptable results according to literature. Electric field assisted sintering technique decreases sintering temperature from 1200 ℃ to 500 ℃ which results very high energy saving and initial capital investment as well. Another outcome of this study is that eliminating lead emission arising at high temperature manufacturing process. Lead based piezoelectric materials is avoided due to lead emission problem at higher temperature, so our manufacture method could be a solution as a green processing technique.

REFERENCES

[1] J. E.Burke, J. H.Rosolowski, "Sintering", *Reactivity of Solids. Solid State Chemistry*. Editor: Hannay N. B., Vol. 4 Plenum, New York1976.
[2] R. L. Coble, "Sintering Crystalline Solids. I. Intermediate and Final State Diffusion Models", *Journal of Applied Physics*, 32, 787-921961.
[3] R. L. Coble, "Sintering Crystalline Solids. II. Experimental Test of Diffusion Models in Powder Compacts", *Journal of Applied Physics*, 32, 793-99, 1961.
[4] H. Maiwaa, O. Kimurab, K. Shojic, H. Ochiai, "Low temperature sintering of PZT ceramics without additives via an ordinary ceramic route," *Journal of the European Ceramic Society*, Vol. 25, Issue 12, pp. 2383-2385, 2005.
[5] B. Jaffe, W. R. Cook Jr, H. Jaffe "Piezoelectric ceramics", *Academic Press*. London and New York, 1971.
[6] M. Cologna, B. Rashkova, R. Raj, "Flash Sintering of Nanograin Zirconia in <5 s at 850°C", *Journal of American Ceramic Society*, 93, 3556–9, 2010.
[7] M. Cologna, A.L.G. Prette, R. Raj, "Flash-Sintering of Cubic Yttria-Stabilized Zirconia at 750°C for Possible Use in SOFC Manufacturing", *Journal of American Ceramic Society*, 94, 316–9, 2011.
[8] M. Cologna, J.S.C. Francis, R. Raj, "Field assisted and flash sintering of alumina and its relationship to conductivity and MgO-doping", *Journal of European Ceramic Society*, 31, 2827–37, 2011.
[9] J.S.C. Francis, R. Raj, "Flash-Sinterforging of Nanograin Zirconia: Field Assisted Sintering and Superplasticity", *Journal of American Ceramic Society*, 95, 138-46, 2010.
[10] X. Hao, Y. Liu, Z. Wang, J. Qiao, K. Sun, "A Novel Sintering Method to Obtain Fully Dense Gadolinia Doped Ceria by Applying a Direct Current", *Journal of Power Sources*, 210, 86–91, 2012.
[11] J.S.C. Francis, R. Raj, "Influence of the Field and the Current Limit on Flash Sintering at Isothermal Furnace Temperatures", *Journal of American Ceramic Society*, 96, 2754-8, 2013.
[12] E. K. Akdoğan, İ. Şavklıyıldız, H. Bicer, W. Paxton, F. Toksoy, Z. Zhong, T. Tsakalakos, "Anomalous Lattice Expansion in Yttria Stabilized Zirconia Under Simultaneous Applied Electric and Thermal Fields: A Time-resolved in situ Energy Dispersive X-ray Diffractometry Study with an Ultrahigh Energy Synchrotron Probe", *Journal of Applied Physics*, 113, 233503, 2013.
[13] J. Rödel, K. G. Webber, R. Dittmer, W. Jo, M. Kimura, D.Damjanovic, , "Transferring lead-free piezoelectric ceramics into application", *Journal of the European Ceramic Society*, 35, 1659–1681, 2015.
[14] M. Peddigari, S. Thota, and D. Pamua, "Dielectric and AC-conductivity studies of Dy_2O_3 doped $(K_{0.5}Na_{0.5})NbO_3$ ceramics", *AIP Advances*, 4, 087113, 2014.

Effect of Milling Time on Morphology and Structural Development of Cu-Cr Composite Powders

H. SÜBÜTAY[1], C. NAZİK[2], E. SALUR[3]

[1] Selcuk University, Konya/Turkey, halit.subutay@selcuk.edu.tr
[2]Selcuk University, Konya/Turkey, cnazik@selcuk.edu.tr
[3]Selcuk University, Konya/Turkey, esalur@selcuk.edu.tr

Abstract – **In this study Cu-Cr powders produced with ball milling process via high energy planetary ball milling. The planetary ball milling was chosen as being a unique tecnique for powder processing to be mechanochemical activation and mixing of powders. The ball milling jar was WC and ball to powder raito was 10/1. The ball milling time was chosen three different time (15 min., 2h, 4h). In order to determine the effects of the different milling times on the morphology of powders were utilized by particle size analysis. In addition, deformation behavior of composite powders was analyzed. The structural evolution of Cu-Cr powders produced at different milling times were evaluated from X-ray diffractometry. It was found that the milling time was powerfully effective on the particle size and its distribution. The results indicated that increasing ball milling time showed that XRD peaks were shifted to higher degrees for (111) peaks of Cu which was attributed to Cr addition.**

Keywords – **Mechanical alloying, particle Size, Cu, Cr, X-ray diffractometry**

I. INTRODUCTION

Copper is almost the earliest metal in common to be used in manufacturing industry such as power, electronics and plastic forming due to excellent ductility, thermal and electrical conductivity. However, because of relatively poor strength and wear resistance, Cu and its alloys cannot meet the application requirements of high intensity and conductivity such as vacuum circuit breaker contact materials, trams and electric trains overhead conductors. Low amount of alloying to copper makes it acceptable by means of electrical and thermal conductivities for welding electrodes, outstanding resistance to corrosion, ease of fabrication as well as good strength and fatigue resistance [1-4].

Cu-Be alloys, the high strength of the copper base alloys, are used as metallic materials with high electrical conductivity and high strength. However, since beryllium and its compounds are toxic, advanced metallic materials without hazardous substances are developed as an alternative to Cu-Be alloys [5]. For instance, alloying with Nb may increase tensile strength up to 1000 MPa and a conductivity of 70 %IACS, while Ag alloying can improve the strength to 800 MPa and

90 %IACS but Cr alloying has a strength of 1200 MPa and 75 %IACS of conductivity. Compared to Ag and Nb alloying, Cr alloying has a high cost performance but a good usability for contact wires and high-power vacuum circuit breaker [3].

The high strength and acceptable electrical conductivity is due to extremely low solubility of Cr in Cu at room temperature and the nano sized Cr-rich precipitates after aging.

In order to control the microstructure and improve the properties of such alloys and optimize the production techniques, it would be of great value to identify the composition of the phases in the Cu–Cr alloy.

Li et al. [6] found that adding 0.05% Ce into the Cu-15Cr alloy can refine the Cr dendrite and increase the tensile strength of the Cu-15Cr alloy from 850 MPa to 870 MPa. In the study of the effect of Ag and Co on the tensile strength of Cu-7Cr alloy, Song et al, [7] found that the addition of Ag and Co can reduce the thickness and spacing of Cr fiber, but Ag shows more significant influence, and the tensile strength of Cu-7Cr-0.9Ag and Cu-7Cr-0.9Cr alloy after heavy deformation can reach 798 MPa and 710 MPa, respectively. Sun et al. [8] found that the addition of 0.5% Si to Cu-15Cr alloy unfortunately increased the thickness and spacing of Cr fibers after large deformation, but the tensile strength can be improved when the deformation is small. Besides, it is unfavorable to the tensile strength of Cu-15Cr composites when the deformation is large.

Deng et al. [9] found that the addition of 0.4% Zr can refine the Cr fiber in Cu-10Cr alloy, increasing the tensile strength of Cu-10Cr alloy by more than 200 MPa and the tensile strength of Cu- 10Cr- 0.4Zr alloy to 1000 MPa. Chen et al. [10] found that 0.2% Zr can increase the tensile strength of Cu-15Cr alloy to 1020 MPa, at the same time, the anti-softening temperature can be increased by 50 °C.

The powder metallurgy can be employed for producing denser compacts and the finest grains to be consolidated up to near full densities. To produce energetic powders with laminated structure and pre-impregnation, high-energy ball-milling which is a solid-state powder processing technique, and cost-effective process, can be widely used to prepare Cu-Cr alloys conveniently [12-14]. These processes produce significant microstructural and morphological changes due to significant deformations and high temperatures introduced into the powders in microenvironment as powder-powder

contact regions to strike with Cr. These deformations, in turn, led to increased crystal defects, such as dislocations, voids, stacking faults, twin formation, a larger amount of grain boundaries, and microstructural refinement at the nanometer scale as well as impregnation of alloying phases prior to sintering. Moreover, mechanical alloying (MA) of CuCr is a highly studied manufacturing method provides wide ranges of composition for the formation of CuCr, in contrast to conventional processes [15].

Some process variables are also discussed to achieve the desired product phase or microstructure optimization of a number of variables is required and it is done by mechanical alloying that is why it is known as a complex process. Some of the important structures such as container type, speed, duration, grinding medium, atmosphere, and so on have an influence on the final constitution of the powder. The agglomeration can be increased by milling time and if the given time is more then on that case some unwanted phases can be seen [11,16].

Milling time is one of the most important parameters to be considered in mechanical alloying process as it directly affects particle size, crystal size, interplanar spacing and especially dislocation density of products. Therefore, the main aims of the present investigation is to investigate the effect of different milling time on particle size and morphology of Cu-Cr composite powders.

II. MATERIALS AND METHODS

Cu and Cr powders in metallic form were bought from Ege Nanotek company. The initial average particle sizes is approximately ~20 μm. Composite powders of Cu matrix reinforced with 5 wt.% of Cr particles were produced by mechanical alloying. The ball milling procedure was carried out in a high energy planetary ball milling (RETSCH-PM 100) using tungsten carbide (WC) jar (250 ml) and WC balls at ambient temperature. The ball mills used were 10 mm in diameter, and the weight ratio of ball to powder was chosen as 10:1. Methanol as process control agent (PCA) at 2 wt.% was also used to avoid excessive cold welding and agglomeration of the particles during the mechanical milling. The milling process was conducted with three milling times (15 min., 2, and 4 h) at 400 rpm. Schematic view of the mechanical milling principle was illustrated in Fig.1. The average particle size and particle size distribution of milled powders were calculated by Mastersize 2000. The structural evolution of the milled powders was analyzed with Rigaku ZSX Primus-II X-ray diffractometer.
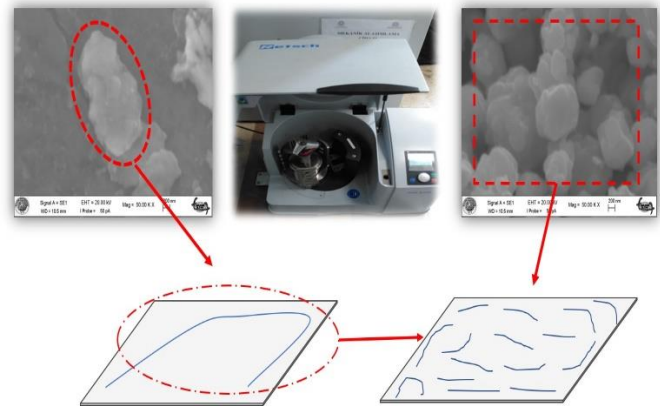
Figure:1 Schematic representation of ball milling process

III. RESULTS AND DISCUSSIONS

Figure 2 and 3 shows the change in particle size according to mechanical alloying time. In Figure 1, it is seen that the particle size decrease and the particle size distribution become more uniform during the milling time at 4 hours.

During the mechanical alloying process, the powders are exposed to ball–powder–ball collision resulted excessive plastic deformation, cold welding and fracturing of the particles. Plastic deformation and cold welding were influential during beginning stage of milling, in which the deformation caused to a variation in particle morphology and the cold welding led to an increment of particle size.
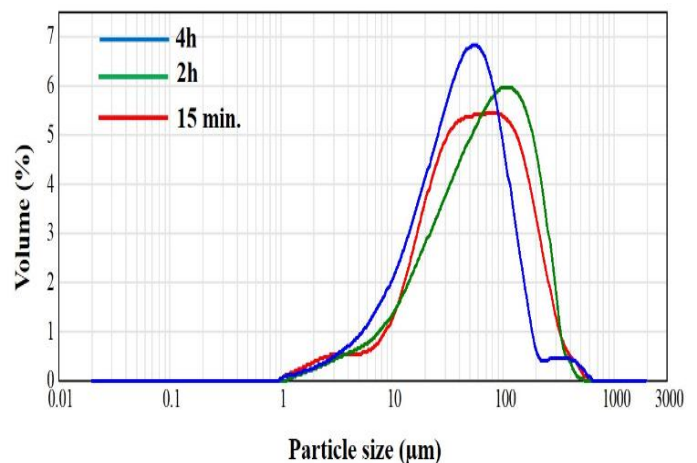
Figure 2: Particle size distribution graph of Cu-Cr powders produced at different milling times

In Figure 3, a decrease in particle size was observed for milling time over 2 hours. while an increase in particle size was observed in powders milled for 15 minutes and 2 hours In ductile- ductile milling systems, powders composed cold welding with each other, and great powder particles were composed. Clearly, it is seen from the graph that powders of flake structure are broken at milling times over two hours. In the early stage of the milling, the particles were subjected plastic deformation, their shape altering from coaxial to flattened. In the next stage of milling, the cold-welding mechanism dominates, resulting the coaxial particle shape.

Then, cold welding and fracture mechanisms extend to steadiness and the shape of particles with the unsystematic cold-welding position. The last stage is described by the steady state system, in which the fine microstructural evolution can goes on, but the particle size and size distribution continue nearly the uniform. The results achieved with the Cu-Cr ductile-ductile system which are exposed to ball milling are in good conformance with these effects of ductile-ductile system in mechanical alloying process.

Figure 3: Particle size distribution and specific surface area of Cu-Cr alloy powder as a function of milling time.

Fig. 4 shows the X-ray diffractions curves of the mechanically alloyed powder mixtures milled with different times. It can be observed in Fig.3 that, the diffraction peak of Cr is seeable in the initial stages of milling. Nevertheless, the reflection peak of Cr diminished with prolonged milling time. In addition, a shift of the Cu peak to lower 2θ angle was monitored, which is associated to the increment of the lattice parameter. Also, Fig. 3 shows that after milling for 4 h, the reflection peak of Cr can barely be observed. At the same time, the Cu peaks broadened with extended milling time
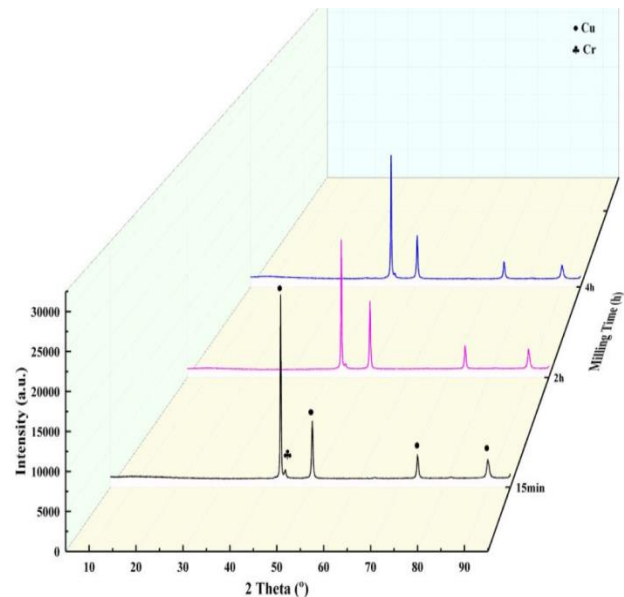
Figure 4: XRD results of ball milled Cu-Cr powders at different milling time

IV.   CONCLUSION

Cu-Cr composite powders milled with different times were successfully produced by mechanical alloying technique. The particle size and its distribution and phase evolution of milled powders were orderly investigated. Conclusions can be drawn as follows

- According to experiments, milling time was the dominant factor on the particle size in the ductile-ductile milling system.

- The particle size of Cu-Cr composite powders decreased with the increasing milling time. In addition, the results indicated that the mechanically alloying process exhibited not only to a decrement in particle size but also resulted fine dispersion of Cr into Cu matrix. After 4 h of milling, the average particle size of the Cu-Cr composite powders was diminished to 42 μm.

- Considering X-ray diffraction curves of the milled powders, it was observed that as the milling time increased, the peaks of Cu-Cr composites shifted and broadened due to increased dislocation density and lattice strain or other defects which are located in Cu-Cr composite system.

REFERENCES

[1]   Dong S., Zhang C., Cai J. Microstructure and properties of Cu-Cr powder metallurgical alloy induced by high-current pulsed electron beam. *Journal of Alloys and Compounds* 755 (2018) 251-256

[2]   Fuxiang H., Jusheng M., Analysis of phases in a Cu–Cr–Zr alloy, *Scripta Materialia* 48 (2003) 97–102

[3]   Tian W., Bi L., Ma F., Effect of Zr on as-cast microstructure and properties of Cu-Cr alloy, *Vacuum* 149 (2018) 238-247

[4]   Shangina D., Bochvar N., Effect of chromium and zirconium content on structure, strength and electrical conductivity of Cu-Cr-Zr alloys after high pressure torsion, *Materials Letters* 199 (2017) 46–49

[5]   Suzuki S., Shibutani N., Improvement in strength and electrical conductivity of Cu–Ni–Si alloys by aging and cold Rolling, *Journal of Alloys and Compounds* 417 (2006) 116–120

[6]   Popovich A., Sufiiarov V., Microstructure and mechanical properties of additive manufactured copper alloy, *Materials Letters* 179(2016)38–41.

[7]   Xu S. Fu H., Effect of Ag addition on the microstructure and mechanical properties of Cu- Cr alloy, *Materials Science & Engineering A* 726 (2018) 208–214

[8]   Joo H., Kim Y., The effect of wire drawing and aging on mechanical and electrical properties of Cu-Cr-Zr alloy. *Procedia Engineering* 207 (2017) 1129–1134

[9]   Mu G., Guo F., Study on microstructure and properties of aged Cu–Cr–Zr–Mg–RE alloy, *Materials Science and Engineering A* 475 (2008) 235–240

[10] León K., Munoz A., Optimisation of strength and ductility of Cu–Cr–Zr by combining severe plastic deformation and precipitation, *Materials Science and Engineering A* 536 (2012) 181– 189

[11] Mishnev, R., et al. "Deformation microstructures, strengthening mechanisms, and electrical conductivity in a Cu–Cr–Zr alloy." Materials Science and Engineering: A 629 (2015): 29-40.

[12] Yue H., Yao L, Effect of ball-milling and graphene contents on the mechanical properties and fracture mechanisms of graphene nanosheets reinforced copper matrix composites., *Journal of Alloys and Compounds* 691 (2017) 755-762

[13] Papillon A., Missien M., Sintering mechanisms of Cu-Cr metallic composites, Int. *Journal of Refractory Metals and Hard Materials* 65 (2017) 9–13

[14] Yamane T., Okubo H., Solid solubility of carbon in copper mechanically alloyed, *journal of materials science letters* 20, 2001, 259– 260

[15] Martínez C., Briones F., Microstructural and mechanical characterization of copper, nickel, and Cu-based alloys obtained by mechanical alloying and hot pressing, *Materials Letters 209* (2017) 509–512

[16] Kumar S., Singh S., Synthesis and Characterization of Al-alloy by Mechanical alloying, *Materials Today: Proceedings* 5 (2018) 3237–3242

Investigation of The Effect of Different Milling Times on The Characterization of Mechanically Alloyed Cu-Y$_2$O$_3$ Composites

H. SÜBÜTAY[1], E. SALUR[2], C. NAZİK[3]

[1] Selcuk University, Konya/Turkey, halit.subutay@selcuk.edu.tr
[2] Selcuk University, Konya/Turkey, esalur@selcuk.edu.tr
[3] Selcuk University, Konya/Turkey, cnazik@selcuk.edu.tr

Abstract – **In this study Cu-Y$_2$O$_3$ (ODS Copper) powders produced by mechanical alloying in planetary ball mill. The planetary ball milling was chosen as being a unique technique for powder processing to be mechanochemical activation and mixing of powders. The ball milling jar was WC and ball to powder ratio was 10/1. The ball milling time was chosen three different time (15 min., 2h, 4h). In order to determine the effects of the different milling times on the morphology of powders were utilized by particle size analysis. The crystal sizes of Cu-Y$_2$O$_3$ powders produced at different milling times were calculated from XRD results and the effect of different milling times on the structure of mechanically alloyed Cu- Y$_2$O$_3$ powders was investigated. The increasing ball milling time showed that XRD peaks were shifted to higher degrees for (111) peaks of Cu which was attributed to Cr addition. In addition, it was observed that lattice strain and dislocation density of Cu- Y$_2$O$_3$ powders increased as a function of prolonged milling time.**

Keywords – **Mechanical alloying, particle size, Cu, Y$_2$O$_3$, dislocation density, lattice strain**

I. INTRODUCTION

Copper is almost the earliest metal in common to be used in manufacturing industry such as power, electronics and plastic forming due to excellent ductility, thermal and electrical conductivity. However, because of relatively poor strength and wear resistance, Cu and its alloys cannot meet the application requirements of high intensity and conductivity such as vacuum circuit breaker contact materials, trams and electric trains overhead conductors. Low amount of alloying to copper makes it acceptable by means of electrical and thermal conductivities for welding electrodes, outstanding resistance to corrosion, ease of fabrication as well as good strength and fatigue resistance [1-4]. These materials are generally classified into two categories, based on the different enhancing mechanisms, precipitation strengthened alloys and dispersion strengthened ones. Cu-Be, Cu–Cr and Cu–Cr–Zr alloys, as representative precipitation hardened alloys, resulting from the decomposition of the supersaturated solid solutions, possess good low-temperature strength, but poor at high temperature [5].

Cu-Be alloys, the high strength of the copper base alloys, are used as metallic materials with high electrical conductivity and high strength. However, since beryllium and its compounds are toxic, advanced metallic materials without hazardous substances are developed as an alternative to Cu-Be alloys [6].

The high strength and acceptable electrical conductivity is due to extremely low solubility of Cr in Cu at room temperature and the nano sized Cr-rich precipitates after aging. In order to control the microstructure and improve the properties of such alloys and optimize the production techniques, it would be of great value to identify the composition of the phases in the Cu–Cr alloy. [7]

The solubility limit of chromium in copper is only about 0.7 wt. %, strengthening effect could be limited to a certain extent and obtained after processing and heat treatments. There is an extensive research to be put to develop new Cu-Cr alloys with addition of alloying elements alone or combined to improve the high temperature deformation resistance performance to degrade the mechanical properties, such as Be, Zr, Fe, Ti, Y and so on [8-11]. Moreover, Cu-Cr alloys are known to deteriorate from dynamic embrittlement due to segregation of elemental sulphur at the grain boundaries. Minor additions of Zr improve material's hot ductility by forming zirconium sulphides and improved high-temperature strength and ductility in both creep and low-cycle fatigue without impairing their acceptable thermal and electrical conductivities [3,6,8-10].

The particles in dispersion strengthened alloys are usually thermally stable ceramic particles. Ceramic nano-particle-reinforced copper alloys have excellent high-temperature properties; however, its reinforcement effect at ambient temperature is inferior to precipitation strengthening [12]

Oxide dispersion-strengthened (ODS) Cu-based materials have attracted extensive attention because they exhibit important engineering applications in the fields of nuclear, electronic and spot-welding electrode materials. Nanoscale Al$_2$O$_3$ and Y$_2$O$_3$ particles are frequently chosen as dispersion hardeners to strengthen Cu, or other metallic materials such as Ni and ferritic alloys at room and elevated temperatures via interacting with both dislocations and grain boundaries [12].

Yitria (Y_2O_3) and many rare earth oxides are potentially attractive as dispersions for copper alloys owing to their excellent thermodynamic stability, which is superior to that of γ-Al_2O_3. Besides, these oxide-forming elements have much larger atomic radii than aluminum, relative to copper, and consequently exhibit a low solubility and diffusivity in the metallic matrix, which would enhance the microstructural stability against coarsening

In general, the low solubility of rare earth elements in copper substantially limits the application of conventional internal oxidation in the preparation of oxide-strengthened copper alloys, in which the oxide-forming element must be in the form of solid solutions, like the type of Cu–Al2O3. Although the cast Cu–Y alloy is readily amenable to internal oxidation, a highly inhomogeneous oxide distribution in the scale of the parent dendritic structure is very easily yielded [5].

The powder metallurgy can be employed for producing denser compacts and the finest grains to be consolidated up to near full densities. To produce energetic powders with laminated structure and pre-impregnation, high-energy ball-milling which is a solid-state powder processing technique, and cost-effective process, can be widely used to prepare Cu alloys conveniently [13-15]. A planetary ball mill is known to install pots on a disk, and both are rotated simultaneously and separately at high speed. Such high-speed rotation of both the pot and the disk makes the balls to move strongly and violently, leading to large impact energy of balls that improves grinding performance [16].

These deformations, in turn, led to increased crystal defects, such as dislocations, voids, stacking faults, twin formation, a larger amount of grain boundaries, and microstructural refinement at the nanometer scale as well as impregnation of alloying phases prior to sintering. Moreover, mechanical alloying (MA) of CuCr is a highly-studied manufacturing method provides wide ranges of composition for the formation of CuCr, in contrast to conventional processes [17].
Some process variables are also discussed to achieve the desired product phase or microstructure optimization of a number of variables is required and it is done by mechanical alloying that is why it is known as a complex process. Some of the important structures such as container type, speed, duration, grinding medium, atmosphere, and so on have an influence on the final constitution of the powder. The agglomeration can be increased by milling time and if the given time is more then on that case some unwanted phases can be seen [18,19].
Milling time is one of the most important parameters to be considered in mechanical alloying process as it directly affects particle size, crystal size, interplanar spacing and especially dislocation density of products. So, in this study we investigate the effect of milling time on particle size, particle morphology, of Cu-Y_2O_3 alloy powder.

II. MATERIALS AND METHODS

Cu powders were purchased in metallic form from Ege Nanotek that have an average particle size of ~20 μm. The powders were mechanically alloyed (MA) in RETSCH-PM 100 planetary mill for 15 min, 2h, 4h at 400 rpm, respectively. The ball-to-powder ratio (BPR) ratio was chosen as 10:1 and 10 mm diameter WC balls were used. Methanol was used as a process control agent (PCA) at 2 wt.%. The average particle size of milled powders was calculated by Mastersize 2000 particle size analyzer. X-ray diffraction spectrometer (Rigaku ZSX Primus-II XRD) was used to determine the changes in the phase compositions of the powders at different milling times.

III. RESULTS AND DISCUSSIONS

Figure 1 and 2 shows the change in particle size according to mechanical alloying time. In Figure 1, it is seen that the particle size decreases, and the particle size distribution becomes more uniform during the milling time of four hours.
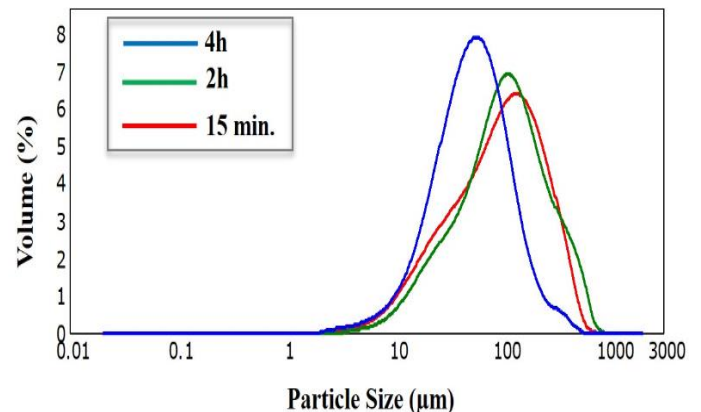
Figure 1: Particle size distribution graph of Cu- Y_2O_3 powders produced at different milling times

There is a ductile-brittle ball milling system is effective between Cu and Y_2O_3 powders. Therefore, first, ductile Cu powders are flake by ball-to-powder-jar collisions in the early stages of mechanical alloying, resulting in an increase in particle size (15 min and 2 hour milling times). Crushed brittle powders are embedded into ductile component. The brittle components settle along the cross-layer gap.
As a result of prolonged milling times, the powders be exposed to deformation hardening, the layers increase and reduce to smaller sizes (at mechanical alloying, milling times of 2 to 4 hours).
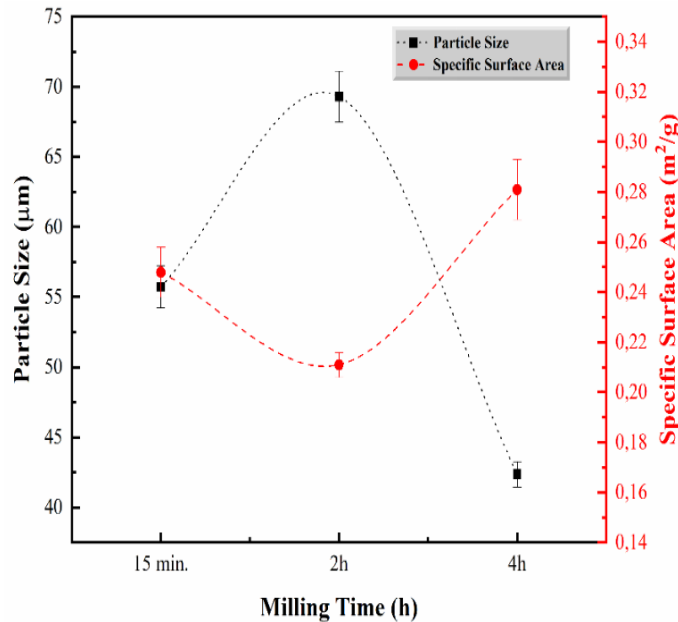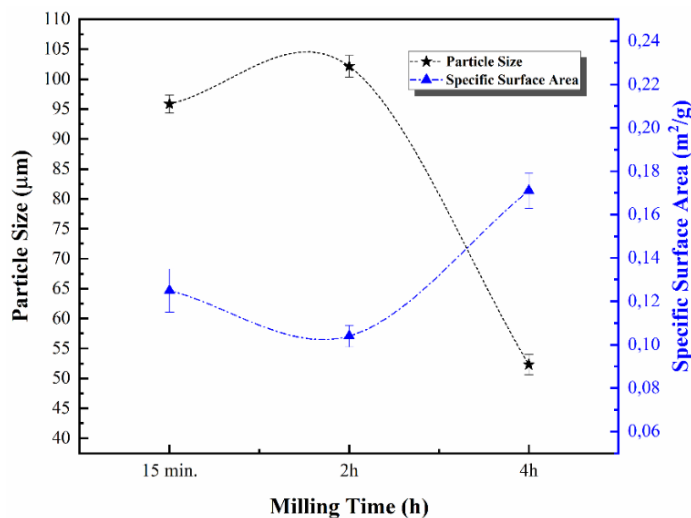
Figure 2: Particle size distribution and specific surface area of Cu-Y_2O_3 alloy powder as a function of milling time.

The corresponding X-ray diffraction curves of the milled powders are shown in Fig. 3. The reflection peaks of the Cu are observed in both initial and milled with different hours powder. Since Y_2O_3 have relatively low concentration, it is much more difficult to determine the reflection peaks of this oxide. After 15 min. of ball-milling, the reflection peaks of Cu and the intensity of this peak gradually decreases as the milling time reaches to 4h. As shown in Fig.3, increasing milling time resulted to broadening of full width at half maximum (FWHM) in the peaks of Cu.
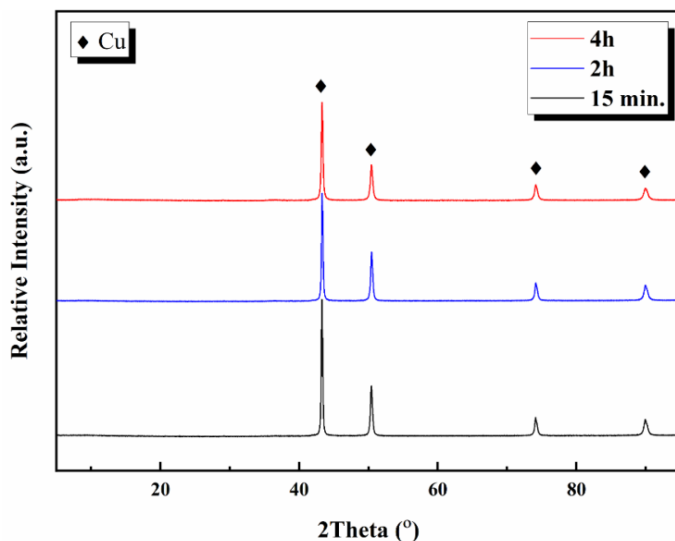
Figure 3: XRD results of mechanical alloyed Cu- Y_2O_3 powders at different milling time

Fig.4 shows the variation of the crystallite size, lattice strain and dislocation density of Cu- Y_2O_3 powders which were estimated from XRD curves using Williamson-Hall equation. It is clearly observed from Fig.4 that crystallite size decreases with prolonging milling time. Excessive and repetitive collision of powder-ball-wall changes the crystallite size from 61,49 nm to 43,42 nm. Also, it can be seen in Fig.4 that increasing milling time results in the increase of both lattice strain and dislocation density because dislocations, vacancies, interstitials, and other similar defects lead to intense plastic

deformation during mechanical milling process. So, it can be inferred that the mechanically alloyed process not only refines the particle size of the powders but also increases both lattice strain and the number of dislocations.
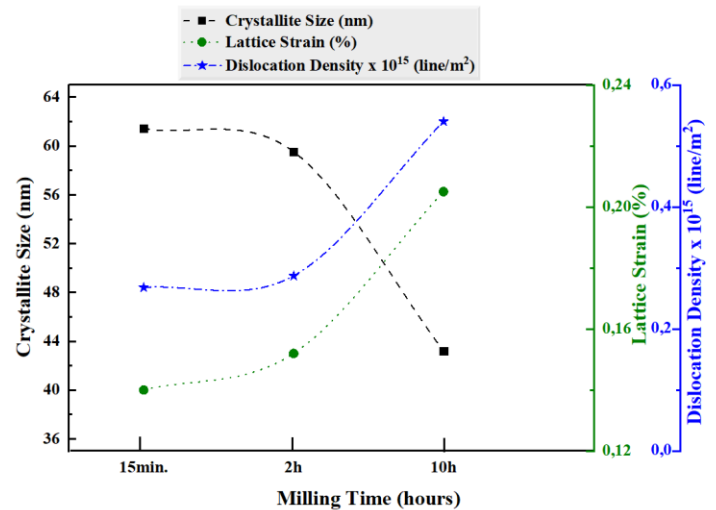
Figure 4: The changes of crystallite size, lattice strain and dislocation density with milling time

IV. CONCLUSION

In this study, the effect of different milling times on the particle size and X-ray diffraction of the milled powders were investigated. The following conclusions can be drawn from the investigations.

- As the milling time increases, the particle size of milled powders decreases, and the distribution of particle size become uniform. It was found that narrow particle size distribution occurred when the milling time reached 4h.

- It was observed that the peaks broadened with increasing milling time. Dislocations, vacancies, interstitials, and other similar defects cause to severe plastic deformation during ball milling and it results the increment of both dislocation density and lattice strain.

REFERENCES

[1] Dong S., Zhang C., Cai J. Microstructure and properties of Cu-Cr powder metallurgical alloy induced by high-current pulsed electron beam. *Journal of Alloys and Compounds* 755 (2018) 251-256

[2]   Fuxiang H., Jusheng M., Analysis of phases in a Cu–Cr–Zr alloy, *Scripta Materialia* 48 (2003) 97–102

[3] Tian W., Bi L., Ma F., Effect of Zr on as-cast microstructure and properties of Cu-Cr alloy, *Vacuum* 149 (2018) 238-247

[4] Shangina D., Bochvar N., Effect of chromium and zirconium content on structure, strength and electrical conductivity of Cu-Cr-Zr alloys after high pressure torsion, *Materials Letters* 199 (2017) 46–49

[5] Zhuo, H., Tang, J., A novel approach for strengthening Cu– Y_2O_3 composites by in situ reaction at liquidus temperature, *Materials Science & Engineering A* 584 (2013) 1–6

[6]   Suzuki S., Shibutani N., Improvement in strength and electrical conductivity of Cu–Ni–Si alloys by aging and cold Rolling, *Journal of Alloys and Compounds* 417 (2006) 116–120

[7]   [6] Peng L., Xie H., The phase transformation and strengthening of a Cu-0.71 wt% Cr alloy, Journal of Alloys and Compounds 708 (2017) 1096-1102.

[8]   [7] Cheng J. Shen B., Precipitation in a Cu-Cr-Zr-Mg alloy during aging materials characterization, 81 (2013) 68–75

[9]   [8] Zhao Z, Xiao Z., Effect of magnesium on microstructure and properties of Cu-Cr alloy, Journal of Alloys and Compounds 752 (2018) 191-197

[10] [11] Liu K., Lu D., Microstructure and Properties of a Deformation-Processed Cu-Cr-Ag In Situ Composite by Directional Solidification, JMEPEG (2013) 22:3723–3727

[11] [12] Popovich A., Sufiiarov V., Microstructure and mechanical properties of additive manufactured copper alloy, *Materials Letters* 179(2016)38–41.

[12] Zhou, D., Geng, H., Zeng, W., High temperature stabilization of a nanostructured Cu- Y_2O_3 composite through microalloying with Ti, *Materials Science and Engineering: A* Volume 712, 17 January 2018, Pages 80-87

[13] Yue H., Yao L, Effect of ball-milling and graphene contents on the mechanical properties and fracture mechanisms of graphene nanosheets reinforced copper matrix composites., *Journal of Alloys and Compounds* 691 (2017) 755-762

[14] Papillon A., Missien M., Sintering mechanisms of Cu-Cr metallic composites, Int. *Journal of Refractory Metals and Hard Materials* 65 (2017) 9–13

[15] Yamane T., Okubo H., Solid solubility of carbon in copper mechanically alloyed, *JOURNAL OF MATERIALS SCIENCE LETTERS* 20, 2001, 259– 260

[16] Mio, H., Kano, J., Saito, F., Optimum revolution and rotational directions and their speeds in planetary ball milling, *International Journal of Mineral Processing* Volume 74, Supplement, 10 December 2004, Pages S85-S92

[17] Martínez C., Briones F., Microstructural and mechanical characterization of copper, nickel, and Cu-based alloys obtained by mechanical alloying and hot pressing, *Materials Letters 209* (2017) 509– 512

[18] Mishnev R., Shakhova I., Deformation microstructures, strengtheningmechanisms, and electrica lconductivityinaCu–Cr–Zr alloy, MaterialsScience&EngineeringA629(2015)29–40

[19] Kumar S., Singh S., Synthesis and Characterization of Al-alloy by Mechanical alloying, *Materials Today: Proceedings 5* (2018) 3237– 3242

Shear Strength Performance Evaluation of Al/CFRP Adhesive Bonded Joints with Various Silane Treatments at Aluminum Surfaces

M.Ö. BORA[1], O. ÇOBAN[2], T. KUTLUK[3], E. AKMAN[4] and B. GENC OZTOPRAK[5]

[1] Kocaeli University, Kocaeli/Turkey, ozgur_bora@yahoo.com
[2] Kocaeli University, Kocaeli/Turkey, onur_coban@yahoo.com
[3] Kocaeli University, Kocaeli/Turkey, togay71@gmail.com
[4] Kocaeli University, Kocaeli/Turkey, eakman29@gmail.com
[5] Kocaeli University, Kocaeli/Turkey, genc13@gmail.com

Abstract - **Adhesive bonding offers light-weighted structures with respect to other assembly technologies such as bolted and riveted joints, particularly in aviation industries. In addition, stress concentration becomes less significant without the requirement of bolt or rivet holes, thus avoiding structure decay. The adhesive types and adherend surfaces as the main elements in adhesive bonding should have good wettability with respect to joining components, such as aluminum alloys and CFRPs (carbon fiber reinforced plastics). Surface preparation of adherends is an important prerequisite for adhesive bonding. The purpose of surface preparation is either or a combination of cleaning the surface from contamination, roughening the surface, raising the surface free energy and changing surface chemical composition in order to facilitate the chemical attachment of adhesive to the adherend surfaces. The objective of this study is to investigate the effect of silane treatment on the shear strength and failure type characteristic of Al/CFRP bonded joints using three different silane concentrations (1, 3 and 5 vol.%) on AA2024-T3 aluminum plates. Shear strength values of the Al/CFRP bonded joints were determined by using single lap shear tests according to ASTM D5868-01. From the test results, the silane concentration of 3 vol.% on AA2024-T3 aluminum plates has a significant effect on shear strength of Al/CFRP bonded joints. After mechanical tests, damage mechanisms were also observed by using the digital camera.**

Keywords -**Adhesive Bonding, Surface Treatment, Silane Concentration, Shear Strength**

I. INTRODUCTION

Modern airframes are built with significant amount of carbon fiber reinforced plastics (CFRPs) for their primary and secondary structural components, in addition to conventional metallic alloys. Most of the components made of composites must be connected with aluminum alloy structural parts directly or indirectly, as a result, CFRP-aluminum alloy joints are of increasing importance. The structural components are joined together by using either fastener or adhesive bonds [1,2]. Existing material connection technologies, such as welding, riveting and bolting, usually involve cutting fibers and introducing stress concentrations, both of which reduce structural integrity [3]. Adhesive bonding technology, a new type of structural connection joining technology, can ensure sufficient strength to connect dissimilar materials without damaging to the adherends, and it has the advantages of uniform stress distribution, good fatigue performance, and a better lightweight effect. Thus adhesive bonding has attracted extensive attention to join the dissimilar lightweight materials, especially for the CFRPs and aluminum alloy [3,4]. However, adhesive bonding is also limited for its low adhesive shear strength due to the surface quality of the adherends. In terms of this issue, surface pretreatment of aluminum alloys is an effective strategy to strengthen the interfacial bonding of CFRP/Al joints. Appropriate surface pretreatment of aluminum alloys can not only remove all contaminants on the surface (e.g., dusts, micro organisms, lubricants, etc.) but also modify the surface status such as improving the wettability, surface energy, and introducing functional groups in the surface. All these may be conducive to achieving strong combination between the molecules of the adhesive and aluminum alloy. From literature survey, some previous studies have been determined for promoting dissimilarity with the help of some surface pretreatments such as shot blasting, anodising, etching, atmospheric pressure plasma and peel ply treatment [5].

Silanes are monomeric chemicals used in the first 1940s as combining agents. If the silane contains at least one silicon-carbon bond, it is called the organosilane. The carbon-silicone bond in the silane structure is very stable and non-polar. Organo-functional silanes can be found with countless different two reactive groups of silane atom by bonding between surfaces and used as an adhesive agent [6,7]. Furthermore, it is known that due to the functionality of the silane compounds, it has industrial applications as adhesion enhancer, mineral filler, corrosion resistant layer and crosslinking agent. There are many theories about how the

silane treatment is attached to the aluminum metallic surfaces. Silanes are known as an adhesive material, which generally provides an inorganic and organic chemical bond between two dissimilar materials. The trialcoxysilane contains alkoxy groups to form a compound containing silanol. First, these groups must be hydrolyzed. When the hydrolysis reaction is complete, condensation occurs on the oligomers. When the metal surfaces are immersed in the hydrolyzed silane solution, the oligomers form a hydrogen bond with the -OH groups of the metal surfaces [8,9].
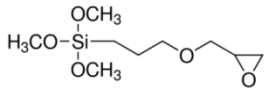
The aim of this work is to correlate the different silane concentrations (1, 3 and 5 vol.%) on AA2024-T3 aluminum alloys to the bonding strength of adhesively bonded hybrid single-lap joints (Al/CFRP). After silane treatment, single lap shear tests are applied to the CFRP/Al adhesively bonded joints. In addition, adhesive shear strengths of both abraded and untreated Al/CFRP adhesive joints are also given to determine the effect of silane concentrations on the shear strength of Al/CFRP adhesive joints. At last, failure damage mechanisms are also determined by using digital camera.

II. MATERIALS AND METHODS

In this study, unidirectional carbon fiber-reinforced epoxy composite $[0]_8$ laminates and AA2024-T3 type of aluminum alloy were used. CFRP and AA2024-T3 were supplied from Kompozitsan, Izmir/Turkey and Seykoç Alüminyum, Kocaeli/Turkey, respectively. CFRP laminates were manufactured by using resin transfer molding (RTM) method. The CFRP and AA2024-T3 samples were prepared by using waterjet and laserjet as a dimension of 2.3 mm×101 mm×25.4 mm and 1.6 mm×101 mm×25.4 mm, respectively.

All chemicals used in the study were of analytical purity and were purchased from SIGMA-ALDRICH. (3-Glycidyloxypropyl) trimethoxysilane chemical structure and its main properties are shown in Table 1.

Table 1: Silane type and basic properties used in the study.

Name	Chemical formula	Molecular weight (g/mol)
(3-Glycidyloxypropyl) trimethoxysilane	H_3CO-Si with OCH_3, OCH_3 groups and glycidyloxypropyl chain	236,34

Before silanizing, the AA2024-T3 plates were washed with methyl ethyl ketone ($C_2H_5COCH_3$) to remove impurities and to activate the surface. The pH of the hydrolyzed silane solution was adjusted to 4 by dropwise addition of 1 molar acetic acid (CH_3COOH) solution. The plates were immersed in prepared silane ponds for 15 minutes at the end of the silanization, all plates were dried at 60 °C for 1 hour. Three different silane concentrations (1, 3 and 5 vol.%) were applied to the surface of AA2024-T3 aluminum plates.

A fixture consisting of three axis linear translation stages was prepared to provide precision control of the bondline. Bondline thickness was selected as 50 μm according to Ref [10], the bondline tolerance of the samples was ±10 μm by using this fixture. Epoxy-based paste adhesive (Loctite EA 9396 AERO) was used for adhesive joining. Curing temperature was 66 ºC with curing duration as 60 min in an oven. In order to obtain statistical results, six samples were prepared for each examined parameter and average values were given. Besides, adhesive shear strengths of both abraded and untreated CFRP/Al adhesive joints were also given to determine the effect of silane concentrations on the shear strength of CFRP/Al adhesive joints.

Zwick universal test machine was used which had a capacity of 30 kN at Tubitak-MAM for determining the adhesive shear strength of untreated, abraded and silanized CFRP/Al adhesive joints. The single lap test speed was selected as 13 mm/min according to ASTM D5868-01 standard. By adding to the grips (Fig. 1) on both side of the test sample, the load transferred along the bondline region. According to the data obtained, the single lap shear strength (τ, MPa) was calculated from Eq. (1) [11];

$$\tau = \frac{F}{B.L} \tag{1}$$

where P, B and L, respectively, stand for applied load (N), overlap length (mm) and overlap width of adhesive region (mm). After single lap shear tests, the digital camera observations were performed to observe the damage mechanisms which occurred at the fractured surfaces of the Al/CFRP adhesive joints.
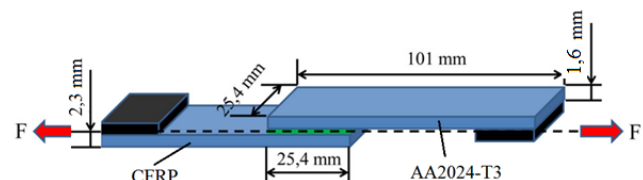
Figure 1: Dimension of single lap joint of Al/CFRP adhesive joint.

III. RESULTS AND DISCUSSION

In order to evaluate the influence of the silane surface treatment on the adhesive shear strength of Al/CFRP joints, single lap-shear tests were carried out. The results are plotted versus type of surface treatment in Fig. 2. From Fig.2, the result shows that the silane treatment at 3 vol.% and 5 vol.% produced the best bonding between the adhesive and adherends (CFRP and 2024-T3), and the mean shear strength values were obtained at 16.44 MPa and 16.52 MPa, respectively.
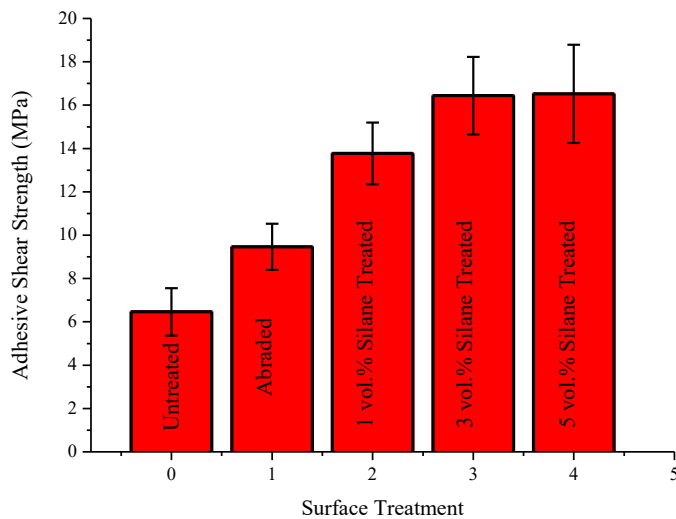
Figure 2: Adhesive shear strength values of Al/CFRP adhesive bonding joints under different surface treatments.

From single lap shear test results, it was determined that silane treatment was useful process for obtaining better adhesive bonding. But silane treatment is high cost process. By this way, the silane concentration of 3 vol.% selected the optimum silane concentration for Al/CFRP bonded joints due to cost efficiency. Beside this, when the silane concentration was 1 vol.%, the mean adhesive shear strength decreased significantly to 13.77 MPa according to 3 vol.% and 5 vol.% silane treated CFRP/Al joints. In addition, there was also an increment at adhesive shear strength values of abraded Al/CFRP joints due to the sanding application (9.46 MPa) compared to untreated samples. It can be observed that the roughness and surface area increased due to the surface treatments, which meaned the physical (abraded sample) and chemical treatments (silane treatment) on the adhesive interface should increase as similar to Ref. [12]. As stated in Ref.[13], chemical interactions in adherends-adhesive interfaces significantly contribute to adhesion between joining parts, which are usually assumed as main bonds as compared to physical interactions. For instance, van der Waals interactions are well-known as secondary force interactions. The molecules of adhesion additives, generally knows as coupling agent (based on silane molecules), promotes interfacial chemical bonds and increase the strength of adhesive joint between adherends and adhesives by forming a chemical linkage at borders. From another study, Dawood and Rizkalla [14] determined that the presence of the silane prevented ingress of moisture into the interfacial region of adhesive joints and helped to enhance the environmental durability of the bond. The presence of the silane treatment significantly enhanced the durability of the Al/CFRP joints. The enhancement of the durability could be due to the formation of primary chemical bonds at the interface between the aluminum and the adhesive due to the presence of the silane. By this way, the highest adhesive shear strength values were obtained at Al/CFRP joints by applying silane treatment on aluminum surfaces.

After single lap shear tests, digital camera observations were applied to determine the variation of damage mechanisms due to the various concentration of silane treatment on the surface of Al/CFRP adhesive bondings compared to the untreated and abraded Al/CFRP joints (Fig.3).
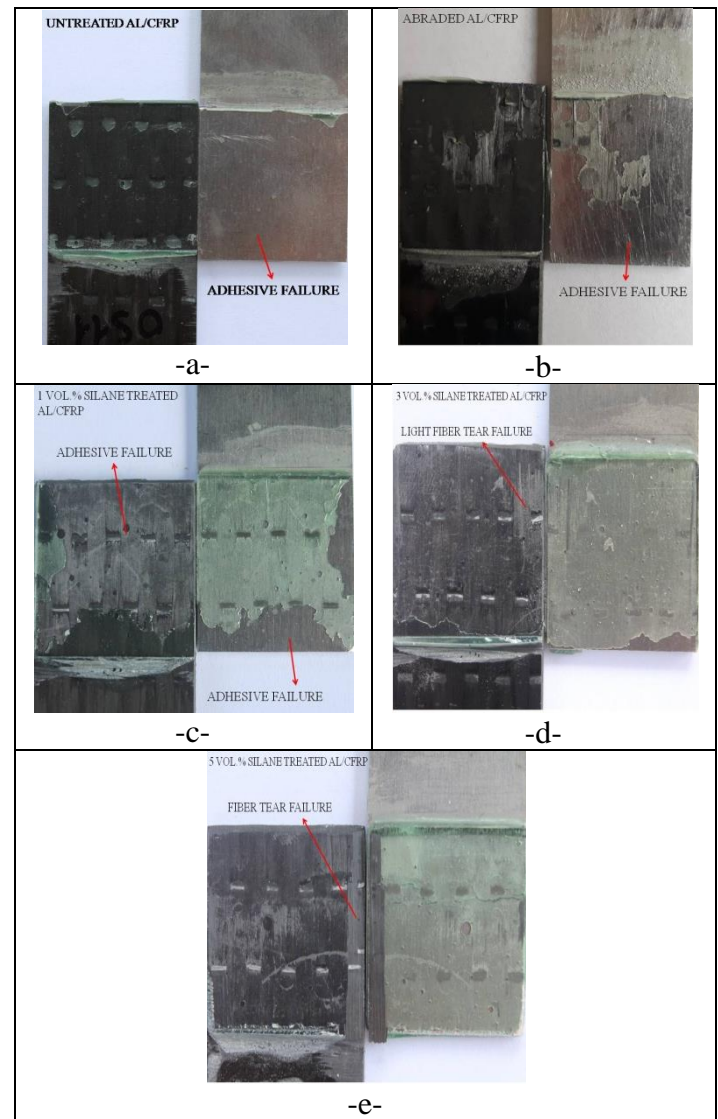
Figure 3: Damage mechanisms of various silane treatments on the Al/CFRP adhesive joints compared to the untreated and abraded samples.

The digital camera images of the fractured surface of the untreated and abraded samples shown in Fig. 3-a and b showed that adhesive failure was the dominant damage mode on the surface of the aluminum layer. Some adhesive–adherend combinations may fail by adhesive failure. If the adhesive does not wet the surface of the substrate completely, the bond is certain to be less than optimal. Internal stresses occur in adhesive joints because of a natural tendency of the adhesive to shrink during setting, and due to differences in physical properties of the adhesive and substrate [15]. In addition, Fig. 3-c, d and e showed the fractured surfaces of

Al/CFRP joints under various silane treatments. From damage observations, it was easily determined that the adhesive bonded to the surface of aluminum layers that exhibited greater adhesive shear strength of Al/CFRP joints. Beside this, fiber tear failure also occurred exclusively within the fiber-reinforced plastic matrix. This damage mode is characterized by the appearance of reinforcing fibers on both ruptured surfaces [16].

IV. CONCLUSION

The effect of the various silane treatments on the adhesive shear strength of Al/CFRP adhesive joints was investigated by single lap shear tests. Obtained results were given below;

-From mechanical test results, maximum shear strength was found as 16.44 MPa and 16.52 MPa for 3 vol.% and 5 vol.% silane concentrations. On the other hand, the silane concentration of 3 vol.% was selected the optimum silane concentration for Al/CFRP bonded joints due to cost efficiency compared to 5 vol.%.

-From digital camera observations of Al/CFRP adhesive joints, two main damage mechanisms were observed. Untreated and abraded samples were damaged as adhesive failure at the surface of aluminum layer. On the other hand, fiber tear failure and adhesive failure were determined at the surface of CFRP layer. It was predicted that silane treatment affected the aluminum surface for a better adhesion to adhesive material.

REFERENCES

[1] P.K. Sahoo, B. Dattaguru, and C.M. Manjunatha, "Strength prediction of adhesively bonded joints using plastic zone size criterion," *Procedia Engineering 173,* pp.1635 – 1641, 2017.

[2] G. Qin, J. Na, W. Mu, W. Tan, J. Yang, and J. Ren, "Effect of continuous high temperature exposure on the adhesive strength of epoxy adhesive, CFRP and adhesively bonded CFRP-aluminum alloy joints," *Composites Part B 154*, pp.43–55, 2018.

[3] W. Mu, G. Qin, J. Na, W. Tan, H. Liu, and J. Luan, "Effect of alternating load on the residual strength of environmentally aged adhesively bonded CFRP-aluminum alloy joints," *Composites Part B 168,* pp.87–97, 2019.

[4] X. Liu, X. Shao, Q. Li, and G. Sun, "Failure mechanisms in carbon fiber reinforced plastics (CFRP)/aluminum (Al) adhesive bonds subjected to low-velocity transverse pre-impact following by axial post-tension," *Composites Part B 172,* pp.339–351, 2019.

[5] Y. Li, S. Meng, Q. Gong,Y. Huang, J. Gan, M. Zhao, B. Liu, L. Liu, G. Zou, and D. Zhuang, "Experimental and Theoretical Investigation of Laser Pretreatment on Strengthening the Heterojunction between Carbon Fiber-Reinforced Plastic and Aluminum Alloy," *ACS Applied Materials and Interfaces 11*, pp.22005−22014, 2019.

[6] D. Zhu, and J.V.O. Wim, "Corrosion Protection of Metals by Water-based Silane Mixtures of Bis-[trimethoxysilylpropyl]amine and Vinyltriacetoxysilane," *Progress in Organic Coatings 49.1,* pp.42-53, 2004.

[7] S. Chandrasekaran, M.L. Tammy, and J.V.O. Wim, *"Electrodeposition of Aromatic Bis-Silanes For Pretreatment of Aluminum Alloys," Silanes and Other Coupling Agents,"* Volume 4 (n.d.), CRC Press, pp.217-30, 2007.

[8] M.f. Montemor, W. Trabelsi, M. Zheludevich, and M.g.s. Ferreira, "Modification of Bissilane Solutions with Rare-earth Cations for Improved Corrosion Protection of Galvanized Steel Substrates," *Progress in Organic Coatings 57.1,* pp.67-77, 2006.

[9] M. Mohseni, M. Mirabedini, M. Hashemi, and G.E. Thompson, "Adhesion performance of an epoxy clear coat on aluminum alloyin the presence of vinyl and amino-silane primers," *Progress in Organic Coatings 57,* pp.307–313, 2006.

[10] M.Ö. Bora, E. Akman, O. Çoban, B.G. Oztoprak, and A. Demir, "The Effect of CO_2 Laser-Induced Microhole Formations on Adhesive Bonding Strength of CFRP/CFRP Joints," *Polymer Composites 40*, pp.2891–2900, 2019.

[11] R. Wei, X. Wang, C. Chen, X. Zhang, X. Xu, and S. Du, "Effect of surface treatment on the interfacial adhesion performance of aluminum foil/CFRP laminates for cryogenic propellant tanks," *Materials & Design 116*, pp.188-198, 2017.

[12] G. Buckton, P. Darcy, and D. Mccarthy, "The extent of errors associated with contact angles. 3. The influence of surface-roughness effects on angles measured using a Wilhelmy plate technique for powders," *Colloids Surf. A Physicochem. Eng. Asp. 95*, pp. 27-35, 1995.

[13] A.Pramanik, A.K.Basak, Y.Dong, P.K.Sarker, M.S.Uddin, G.Littlefair, A.R.Dixit, and S.Chattopadhyaya, "Joining of carbon fibre reinforced polymer (CFRP) composites and aluminium alloys – A review," *Composites Part A: Applied Science and Manufacturing Volume 101*, pp.1-29, 2017.

[14] M. Dawood, and S. Rizkalla, "Environmental durability of a CFRP system for strengthening steel structures," *Construction and Building Materials Volume 24, Issue 9*, pp. 1682-1689, 2010.

[15] S. Ebnesajjad, *Surface Treatment of Materials for Adhesive Bonding (Second Edition)*, Elsevier, ISBN: 978-0-323-26435-8, USA, 2014.

[16] ASTM D5573-99(2012), *Standard Practice for Classifying Failure Modes in Fiber-Reinforced-Plastic (FRP) Joints*, ASTM International, West Conshohocken, PA 2012. www.astm.org.

Evaluation of Different Surface Treatment Methods Applied to Improve the Chemical Adhesion Mechanism of Al/CFRP Adhesive Bonding

B. GENC OZTOPRAK[1], O. ÇOBAN[2], E. AKMAN[3], M. Ö. BORA[4], T. KUTLUK[5]

[1] Kocaeli University, Kocaeli/Turkey, genc13@gmail.com
[2] Kocaeli University, Kocaeli/Turkey, onur_coban@yahoo.com
[3] Kocaeli University, Kocaeli/Turkey, eakman29@gmail.com
[4] Kocaeli University, Kocaeli/Turkey, ozgur_bora@yahoo.com
[5] Kocaeli University, Kocaeli/Turkey, togay71@gmail.com

Abstract - **Adhesive bonding has appeared to a promising technique for joining dissimilar materials. Because modification to metal surface is successfully applied to enhance material surface adhesive bonding. Many chemical (etching, anodizing, etc.) and mechanical (grinding, sand blasting, etc.) surface treatment processes are used to improve the adhesion strength of aluminum surfaces to carbon fiber reinforced plastics (CFRP). In this study, the effect of various physical and chemical treatments on the chemical composition and wetting properties of AA2024-T3 aluminum alloy surfaces was examined according to the values of untreated aluminum surfaces. Grinding process, FPL-etching and silanization methods were performed to the aluminum alloy surfaces separately. The wettability and chemical composition of the untreated, grinded, FPL-etched and silane coupled aluminum alloy surfaces were evaluated by using contact-angle goniometry and FTIR-ATR spectroscopy, respectively to compare their effects on adhesion performance of Al/CFRP adhesive bonded joints. The results show that chemical composition and wetting properties of modified aluminum adherends should be evaluated to understand the adhesion performance difference obtained for the adhesive bonded Al/CFRP joints.**

Keywords - **Adhesive Bonding, Surface Treatment, Grinding, FPL Etching, Silane Coupling, Aluminum/CFRP Adhesion.**

I. INTRODUCTION

Both aluminum alloys and carbon fiber reinforced polymers (CFRP) have been used in aerospace, marine and automotive industry due to their high strength-to-weight ratio [1-3]. Especially joining of these lightweight dissimilar materials are widely used and will becoming increasingly important in the manufacturing of hybrid structures. Joining techniques of hybrid materials include adhesive bonding, mechanical fastening and welding techniques [4]. Among these techniques, adhesive bonding has excellent fatigue strength and high corrosion resistance, however, surface properties of the adherends are played staminal role in the adhesive bonding process. In particular, the ability to bond efficiently to metal and non-metal materials can be activated by adhesive bonding.

Adhesive shear strength can be significantly improved by using different surface treatment methods. Preparation of metallic surfaces is a critical step to obtain surfaces with suitable surface properties. The purpose of the surface preparation process of the aluminum sheet is to remove the layers such as oil, glycerin and dust from the surfaces of aluminum alloy samples, to create a controlled surface roughness and to increase the surface reactivity (such as improving the wettability, surface energy, and introducing functional groups) by modifying topmost layer of the sample. [5]. If the surface preparation process is not performed, the adhesive will adhere to the layer formed by the foreign materials on the surface and therefore no real adhesion will occur to the surface, therefore it will reduce the adhesive shear strength. The controlled roughness created by the surface pretreatment will both increase the bonding surface area and contribute to the adhesion strength by mechanical interlocking [6]. Furthermore, during surface pretreatment, the surface energy of the workpieces increases, but the contact angle of the water decreases and the surface tension increases, this is desirable for spreading the adhesive on the surface.

Understanding the basis of adhesive bonded joints requires an examination on both macroscopic and microscopic levels. Many theories including mechanical, electrostatic, diffusion, physical adsorption, wetting, weak boundary layer and chemical bonding theories have been proposed to define adhesion. Among these theories, the most relevant theories of metal-polymer bonding are physical adsorption and mechanical models [7]. The strength of adhesively bonded aluminum is governed by mechanical interlocking and different form of chemical bonding between the aluminum oxide and adhesive.

Different surface treatments methods based on physical, chemical and energetic modifications have been developed to obtain both specific surface morphology and chemistry of the aluminum adherend surface in order to improve the surface adhesion activity [8]. Common steps of many surface preparation processes for aluminum alloy adhesively bonded aluminum alloys are listed in ASTM D2651. Mechanical

surface treatment methods such as grinding or sand blasting are supposed to extend surface area by increasing the roughness, however, residual debris and mechanical damage to the adherend are considered to be detrimental to bonding. Chemical surface treatment processes (etching, anodizing, etc.) are used to modify both morphology and chemistry of the sample surface. Some treatments are effective with different groups of materials, i.e. metals, glasses, plastics, elastomers, etc., tend to have their own specific treatments. The use of chromic acid-based FPL-Etch processes and varieties was a very practical method for military and industrial applications. However, with the change of materials and the increasing industrial expectations, researchers have further improved alternative chromate-free methods because of the toxicity, therefore silane coupling agents have been developed for surface treatments [2]. It is known that due to the functionality of the silane compounds, it has industrial applications as adhesion enhancer, mineral filler, corrosion resistant layer and crosslinking agent. There are many theories about how the silane coating is attached to the metal surface. Silanes are known as an adhesive material, which generally provides an inorganic and organic chemical bond between two dissimilar materials. The strong bond between these components is responsible for high thermal stability and compatibility with metal surfaces. If they are functionalized with organic components they can provide a link between the metallic surface and paints or adhesives.

In this study, grinding process, FPL-etching and silanization methods were performed to the aluminum alloy surfaces, separately. The effect of various physical and chemical treatments on the chemical composition, wetting properties and roughness of AA2024-T3 aluminum alloy surfaces was examined according to the result of single lap-shear test values compared with the untreated aluminum surfaces.
.

II. MATERIALS AND METHODS

In this study, AA2024-T3 type of aluminum alloy and unidirectional carbon fiber-reinforced epoxy composite (CFRP) $[0]_5$ laminates were used. AA2024-T3 and CFRP materials were supplied from Seykoç Alüminyum and Kompozitsan, respectively. The AA2024-T3 and CFRP samples were prepared by using laserjet and waterjet as a dimension of 1.6 mm×101.6 mm×25.4 mm and 2.3 mm×101.6 mm×25.4 mm, respectively.

Nonsystematic study to optimize the mechanical abrasion treatment has been identified in the mechanical treatment of the aluminum adherend by using sandpaper. AA2024-T3 adherend was prepared by roughening their surface with sandpaper 220 grit size to compare untreated and chemical treatment methods such as FPL-etching and silane coupling process.

In the FPL-etching method, the first step is to remove the impurities on the surface of the metals by washing the metal surface with the aid of different alcohols or solutions. This washing is usually carried out at atmospheric pressure and at room temperatures. The FPL-Etch solution consists of 30 parts

(water) H_2O, 10 parts (sulfuric acid) H_2SO_4 and 2 parts (Sodium di chromate) $Na_2Cr_2O_7$. The aluminum plates to be treated are immersed in the solution bath for a certain period of time. The copper and acid in the solution helps the formation of deep pores by acting on the aluminum surface. This increases the ability of the surface to adhere with a suitable adhesive agent. During the FPL-Etch process, two main reactions take place on the surface below.

$2Al+H_2SO_4+Na_2Cr_2O_7 \rightarrow Al_2O_3+Na_2SO_4+Cr_2SO_4+4H_2O$ (1)
$Al_2O_3 + 3H_2SO_4 \rightarrow Al_2(SO4)_3 + 3H_2O$ (2)
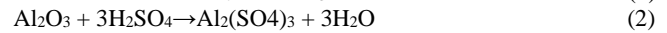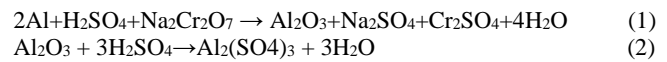
Reaction 1 shows the reaction of the chemicals in the FPL-Etch solution with the aluminum alloy, which forms an alumina (Al_2O_3) surface layer. The reaction represents the dissolution of sulfur by the sulfuric acid in the alumina solution formed in the reaction. As a result of the reaction, aluminum oxide is formed and adheres in a controlled manner on the surface of the alloy, thus forming a porous structure on the surface [2]. All chemicals used in the FPL-etching surface treatment were analytical grade and were purchased from MERCK. The pre-treated aluminum plates were washed with pure acetone at room temperature. The cleaned plates were immediately immersed in FPL-Etch solution baths at 60 ° C temperatures prepared from 30 parts (water) H_2O, 10 parts (sulfuric acid) H_2SO_4 and 2 parts (Sodium di chromate) $Na_2Cr_2O_7$. After 20 minutes waiting time, the plates were removed from the bath and washed with pure water. Finally, it was dried at 60 ° C for 1 hour.

In the silane coupling process; trialcoxysilane contains alkoxy groups to form a compound containing silanol. First, these groups must be hydrolyzed. When the hydrolysis reaction is complete, condensation occurs on the oligomers. When the metal surfaces are immersed in the hydrolyzed silane solution, the oligomers form a hydrogen bond with the -OH groups of the metal surfaces. Then, during the curing process, the water is removed and a covalent bond is formed with the metal surface.

The main reactions on the metal surface are as follows;

$RSi–OH + OH–Al$ (surface) $\rightarrow RSi–O–Al + H_2O$ (3)
$RSi–OCH_3 +OH–Al$ (surface) $\rightarrow RSi–O–Al + CH_3OH$ (4)
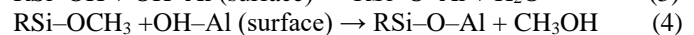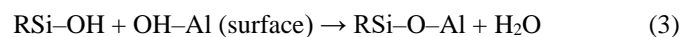
3 rd reaction is faster than 4 th reaction. Thus, the condensation of silane-binding agents on metal surfaces is also supported. During the silanization, these steps take place quickly. The covalent bonds of MeOSi and SiOSi are known to provide this adhesion [9]. When silanization is complete, silicon and oxygen in the surface is a rich network. The thickness of this film depends on the concentration of the siloxane solution. If small cracks or holes occur in the film during the process, some corrosion can be observed [10]. All chemicals used in the silane ((3-Glycidyloxypropyl) trimethoxysilane) coupling process were of analytical purity and were purchased from SIGMA-ALDRICH.

Before silanization, the aluminum plates were washed with methyl ethyl ketone (MEK) ($C_2H_5COCH_3$) to remove impurities and to activate the surface. The pH of the hydrolyzed silane solution was adjusted to 4 by dropwise addition of 1

molar acetic acid (CH_3COOH) solution The plates were immersed in prepared silane ponds for 15 minutes at the end of the silanization, all plates were dried at 60 ° C for 1 hour.

For the characterization of all untreated and treated AA2024-T3 surfaces, surface topographies and contact angles were obtained by non-contact Ambios Xi-100 optical profilometer and contact angle measurement system, respectively.

Fourier Transform Infrared (FTIR) spectra were recorded by Perkin Elmer Spectrum 100 instrument using universal attenuated total reflectance (ATR) sampling accessory used Germanium crystal with a resolution of 4 cm^{-1}, averaging 5 scans in the range from 4000 cm^{-1} to 600 cm^{-1}. Spectra recording was carried out firstly subtraction of the background in order to eliminate the effects of atmospheric effects, spectrum scanning, baseline correction and smoothing to reduce the remaining noise in the spectrum. FTIR-ATR spectra was used to investigate the chemical changes occurred on the AA2024-T3 aluminum surfaces untreated, abraded, FPL-etched and silane coupled samples, separately. All the surface characterization process were performed before the Al/CFRP adherends adhesive adhesion step.

A fixture consisting of three axis linear translation stages was prepared to provide precision control of the bondline as shown in Fig. 1. Two component structural epoxy paste adhesive (Loctite Hysol ® EA 9396™ AERO) was used to bond the AA2024-T3 and CFRP adherends. All samples were jointed at a bonding thickness of 50 μm because highest strength was obtained at 50 μm for CFRP/CFRP adhesive bonding in our previous study [11], the bondline tolerance of the samples was ±10 μm by using this fixture. Curing temperature was 66 ºC with curing duration as 60 min in an oven. In order to obtain statistical results, six samples were prepared for each examined parameter and average values were given.
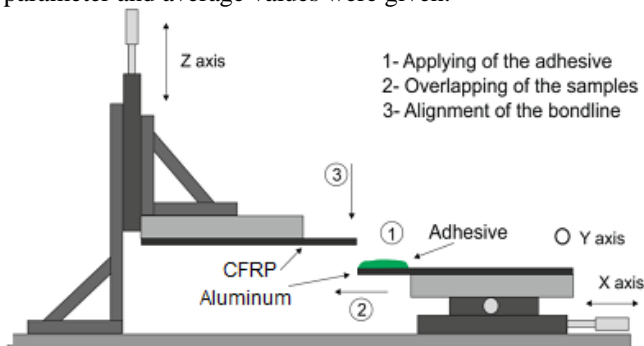
Figure 1: Shematic representation of bonding fixture used for adhesive adhesion of AA2024-T3 and CFRP adherends.

In order to perform single lap shear test Zwick universal test machine was used which had a capacity of 30 kN at TUBITAK-MAM for determining the adhesive shear strength of untreated, abraded, FPL-etched and silane coupled CFRP/Al adhesive joints. The single lap test speed was selected as 13 mm/min according to ASTM D5868-01 standard.

III.   RESULTS AND DISCUSSION

Large area of contact surfaces, good wettability and high surface energy are recommended for a better adhesive adhesion. The wettability of the adherend both depends on surface roughness and chemical composition of the surface. Increasing surface roughness on changing surface chemistry or producing of a macro/microscopically rough surface can be obtained by using suitable surface pretreatment on aluminum alloys. According to the results measured from the profilometer average roughness (Ra) was determined as 257, 4981.1, 954.2 and 726.5 nm for untreated, abraded, FPL-etched and silane coupled of the AA2024-T3 aluminum surface, as seen Fig. 2, respectively.
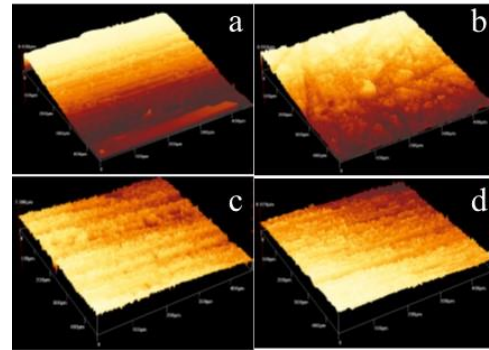
Figure 2: Optical profilometer images obtained from samples; a) untreated, b) abraded, c) FPL-etched and d) silane coupled.
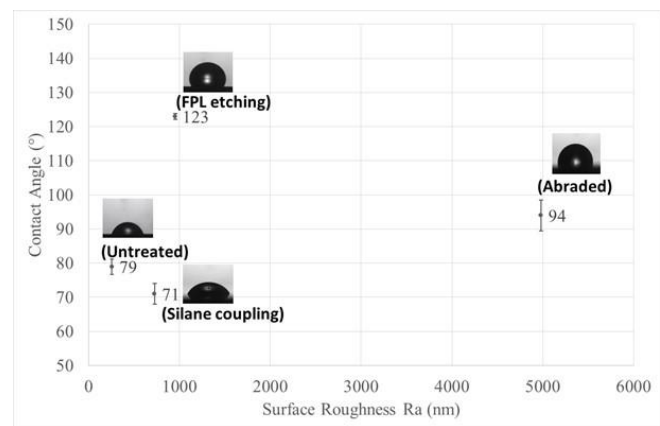
Figure 3: Effect of the surface roughness to the contact angle of various surface treated aluminum adherend.

The effect of roughness of the solid surface is to increase the actual area of contact between solid and liquid but also to increase the un-wetted solid per unit geometric area: increasing roughness of hydrophilic surface ($\theta < 90°$ increased roughness improve wetting $\theta << 90°$) leads to increased hydrophilicity while increasing roughness for hydrophobic surfaces ($\theta > 90°$ increased roughness lowered wetting $\theta >> 90°$) leads to increased hydrophobicity in the same surface treatment condition. [12]. From the literature, the contact angle of untreated aluminum alloy is around 82.2° (water as the probe liquid) without changing surface topography and energy [13].

The wettability of untreated and various pretreated AA2024-T3 aluminum surface was investigated with the water contact angle. Nine contact angle tests was recorded in different surface location of the aluminum sample and the average contact angle was calculated, the deviation of contact angles was about 2 ~ 5°. Contact angle of untreated aluminum was measured 79°, that sample has smallest nanoroughness value (257 nm). It was seen that surface roughness was not directly affects the contact angle linearly as seen Fig. 3.

The reason of this result may be due to the application of different surface treatments to the aluminum surface. Because, surface wettability and surface adhesion are affected by surface roughness, contamination and surface chemistry. Surface tension can be increased by producing a surface free from contaminants or removal of the weak cohesion layer. Suitable oxide layer or introduction an increased number of chemical functions can contribute to improvement of the wettability and of the adhesive properties of the surface [14]. Grinding process is a mechanical abrasion process that removes material from the sample surface by using fixed abrasive particle paper. The major disadvantage of the sanding process is that it does not show a uniform surface distribution and repeatability. Tezcan et al. [15] studied the effect of surface roughness on the adhesive bond strength using a cylindrical specimen of steel adherend, when the adherend surface roughness was in the range of 1.5 to 2.5 μm, maximum bond strength was obtained in that range. Although abraded aluminum surface was prepared by roughening the surface with sandpaper only 220 grit size, roughness has obtained the highest value (4981 nm) with this treatment. It is thought that the most important reason of being one of the methods which obtained low shear strength is both uncontrolled and high roughness on the abraded surface and additional residual debris to the surface contamination. Highest contact angle (CA:123°) and minimum standard deviation (0.8) was measured in the FPL etched sample, and the surface roughness was determined 954.2 nm. Venables et al. [16] reported the presence of the whiskers that has 5 nm thick and sticking out of the surface to about 40 nm. This is a thin oxide layer and better mechanism of mechanical interlocking for the FPL etched treated samples. Garnish et al. [17] added small quantities of various metals to a chromic acid bath, and reported the effect of copper among the others considerably increased the etch rate, the porosity of the surface and the resultant peel strengths. The chemical treated surface results obtained by FPL etching support this information that in addition of copper to the bath was produced optimized FPL etch. Various treatment procedure has very different contact angle result, contact angle was reached the lowest value silane coupled surface that was 71° lower than the untreated surface Fig. 3. is shown that, different treatment was produced varying degree of roughness, therefore different mechanical interlocking effect is expected. However, the contact angle is expected to decrease as the surface roughness increases. Surface chemistry and contaminants also contributes to contact angle and adhesion. Before the single lap shear test, the various treated adherend samples surfaces were analyzed by using FTIR-ATR spectroscopy to understand of the chemical bond contribution to the adhesion. Direct comparison between the spectra of

untreated and abraded, FPL etched and silane coupled AA2024-T3 samples as seen Fig. 4., respectively.
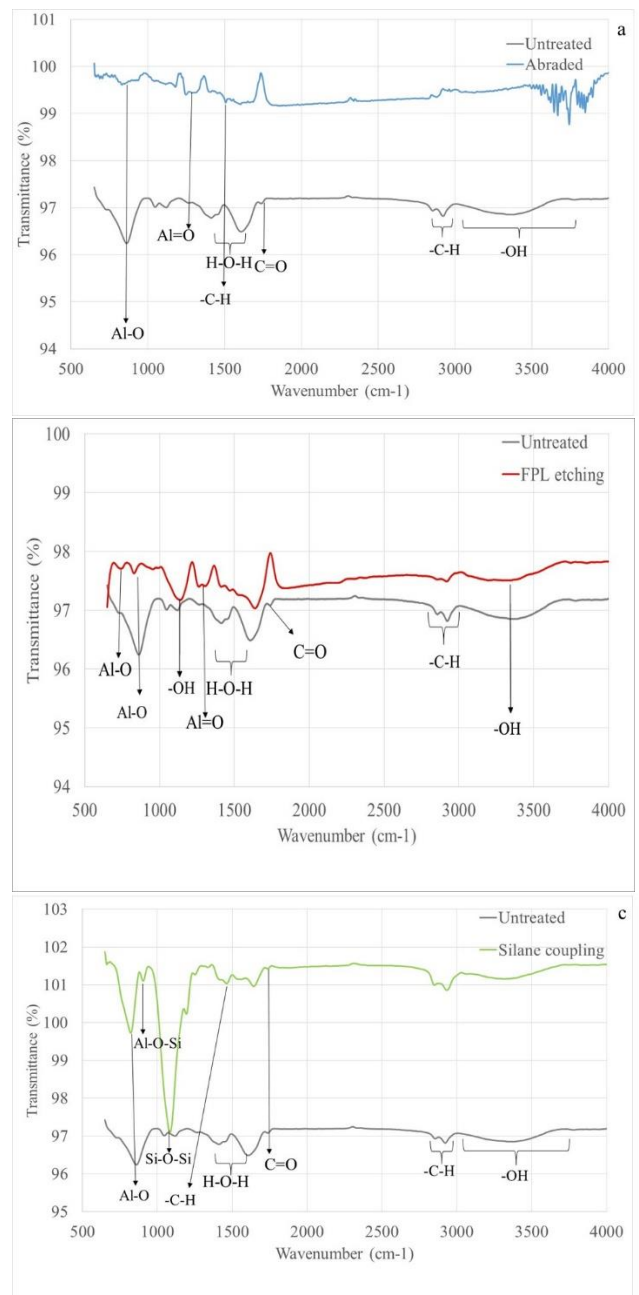
Figure 4: The comparative FTIR-ATR spectra of a) untreated and abraded aluminum surface, b) untreated and FPL etched aluminum surface and c) untreated and silane coupling of aluminum surface.

FTIR-ATR spectra were recorded to investigate the dependence of abraded, FPL-etched and silane coupled of the AA2024-T3 surface chemical composition. The bands at 870 cm^{-1} corresponded to the Al-O [18]. This band was decreased abraded and FPL-etched treatments, out of the silane coupling treatment, that peak was increased as seen Fig. 4c. The bands at 1089 cm^{-1} and 3094 cm^{-1} are the δ(OH) hydroxyl bending and ν(OH) hydroxyl streching have increasing intensity for the FPL etched samples. The bands at 1316 cm^{-1} was associated to Al=O

bond for the determining both abraded and etched treated surface [19]. Bands detected at 1410 cm^{-1}, 2864 cm^{-1} and 2921 cm^{-1} were assigned to the deformation and the asymmetrical stretching of C-H of CH$_2$ groups. Bands at 1436 cm^{-1} and 1615 reflected the bending of H$_2$O (OH stretching vibration of the adsorbed water) in the bohemite network or Al─OH and were only observed untreated and silane coupled surface of the AA2024-T3 sample [20]. The band at labeled only 1742 cm^{-1} was assigned C=O stretching vibrations for untreated and silane coupled samples spectra [21]. The band 1316 cm^{-1} corresponded to Al=O formation was detected in the spectra obtained from the grinding process treated surface, and there was a decreased trend in the intensity of the other bands, especially hydroxyl groups.

The band ~3550 cm^{-1} in the Figure 4c is due to the O-H stretching of silanol (Si-OH). The silicon atom in the silane can form three bonds with the aluminum surface to the high reactivity of silanol groups (Si–OH) with the aluminum hydroxyl groups (Al–OH). This results in Al–O–Si bonds at the metal/silane interface [22]. Siloxanes (Si-O-Si) groups formed as the result of the hydrolysis and condensation reactions of silane coupling agents were observed at 1095 cm^{-1} band by FTIR-ATR spectroscopy. It can act as a chemical bridge between the metallic surface and adhesive. Si-O stretching vibration occurred at 908 cm^{-1}. The peak at 1650 cm^{-1} is due to C=C stretching of vinyl benzene of the coupling agent [22]. As shown Figure 4c., the spectral band was concluded that Al surface were coated with siloxane. Yan et al. [23] reported that the -SiOCH$_2$CH$_3$ group would be hydrolyzed into –SiOH, and then it will condense with the -SiOH which is on the surface of the glass and in that case the hydrophilic chain would go toward the outside of the substrate so that the surface would turn into hydrophilic. The oxygen containing functional group hydroxyl, carbonyl and carboxyl groups are high polar and serve as hydrophilic character. C-C(H) bond is non-polar and serves as hydrophobic regions on the surface [24]. The FTIR-ATR result was supported to the contact angle measurement, hydroxyl (-OH) and carboxylic acid (-(C=O)-OH) group are the greatest prometer of the surface wettability. Although, silanization process was presented more intense -C-H (hydrophobic functional groups) band in the spectra than the other treatment process, surface has served hydrophilic (CA:71°) character.

Single lap shear tests were performed in order to evaluate the effect on the shear strength of the Al/CFRP adhesive bonding by using different surface treatment methods on the AA2024-T3 aluminum adherend. Shear strength result was shown in Fig. 5., from the test result grinding process was given lower shear strength values when compared to the chemical treatment methods.
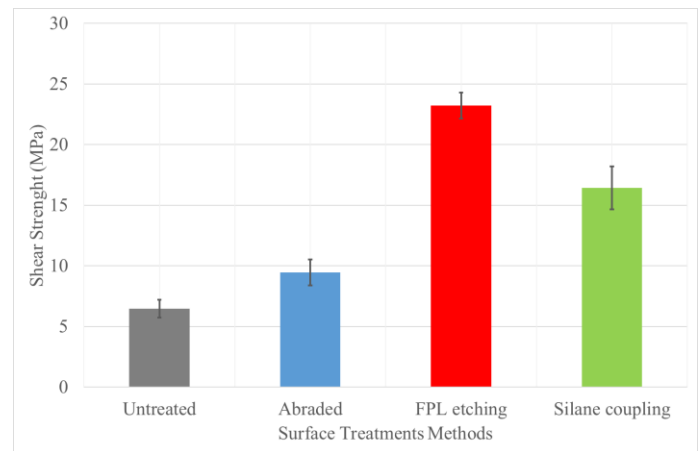
Figure 5: Effect of various suraface treatment methods on the single lap shear strengths.

Shear strength values were obtained 6.46 MPa, 9.46 MPa, 23.22 MPa and 16.44 MPa for untreated, abraded, FPL-etching and silane coupling various surface treatment process, respectively. By using FPL-etch surface treatment %154 increment was obtained according to the untreated bonding value.

IV.   CONCLUSION

Modified AA2024-T3 aluminum adherends were prepared by using grinding process, FPL etching and silane coupling process to compare their effects on adhesion performance of Al/CFRP adhesive bonded joints. Their surface was characterized via roughness, water contact angle measurements and FTIR-ATR spectroscopy.

The result concluded that surface adhesion and surface wettability were affected by surface roughness and oxide structure of the surface. Neither mechanical interlocking nor surface chemistry is not sufficient alone for best adhesion, there should be a balance between them. It is thought that the most important reason of being one of the methods which obtained low shear strength is both uncontrolled and high roughness on the abraded surface and additional residual debris to the surface contamination. In the abraded surface FTIR-ATR spectra (as seen Fig. 4a) there is a decreased trend in the intensity of the other bands, especially hydroxyl groups. FPL-etched sample has a more hydrophobic character [CA:123°] comparatively to the abraded surface while abraded sample has rougher surface than FPL-etched sample. The FPL etching is very efficient and removes the aluminum alloy hydrated oxide layer (as seen Figure 4b) and fabricates the cellular oxide structure (whiskers) on the aluminum alloy substrates. This specifically fabricated surface structure also can be provide a better mechanical interlocking to enhance adhesive penetration and increased surface area for secondary mechanism for chemical bonding or improved wetting. While FPL-etcing treated surfaces had low surface energy, the surface was free from all contamination through etching. At the same time, the disappearance of the H$_2$O line observed in the FTIR-ATR spectra was supported the disappearance of the moisture problem on the FPL-etched adhesion surface. These mechanisms are provided significant

contribution (%154 increment) towards the Al/CFRP adhesive shear strength.

Si-O-Si group can act as a chemical bridge between the metallic surface and adhesive, silane couling agents are observed at 1095 cm^{-1} band by FTIR-ATR spectroscopy (as seen Fig. 4c), the spectra concluded that Al surface were coated with siloxane. The presence of a large number of OH groups and carboxylic acid on the silane coupled surface may lead to hydrophilic behavior as the affinity of water is higher with hydroxides.

Future work will focus on the design controlled both large area surface and surface chemistry, and   free from surface contamination to obtain better Al/CFRP adhesive adhesion by using hybrid treatment (FPL-etching+silane coupling or laser processing+silane coupling) process.

ACKNOWLEDGMENT

REFERENCES

[1] A. Higgins, "Adhesive Bonding of Aircraft Structures." International Journal of Adhesion and Adhesives 20 pp.367-376, 2000.

[2] R.F. Wegman and J.V. Twisk, "Surface Preparation Techniques for Adhesive Bonding", Second Edition, Elsevier, Chapter 2, 2013.

[3] J. Barkhimer, M. Erich, and G. Nair "Effect of Time Delay Between Etching and Adhesive Bonding ("Outlife" Time) on Lap-Shear Strength of Aluminum Alloys Using Environmentally-Friendly P2 Etch", , Project report, https://www.semanticscholar.org/paper/Effect-of-Time-Delay-Between-Etching-and-Adhesive-(-Barkhimer-Erich/6180c49e752c94d869d9abf5a83e1146b6e32784.

[4] P. Kah, R. Suoranta, J. Martikainen, C. Magnu, "Techniques For Joining Dissimilar Materials: Metals And Polymers", Rev. Adv. Mater. Sci.36, pp.152-164, 2014.

[5] Y. Li, Shun Meng, Q. Gong,Y. Huang, J. Gan, M. Zhao, B. Liu, L. Liu, G. Zou, D. Zhuang, "Experimental and Theoretical Investigation of Laser Pretreatment on Strengthening the Heterojunction between Carbon Fiber-Reinforced Plastic and Aluminum Alloy", ACS Applied Materials and Interfaces, 11, 22005−22014, 2019.

[6] M. A. Şenyurt, "Grafen ve Naylon 6.6 Nano Elyaf Katkılı Yapıştırıcıların Alüminyum-Karbon Elyaf Takviyeli Kompozit Levhaların Yapıştırma Bağlantılarına Farklı Sıcaklık Koşulları Altında Etkisi", Selçuk Üniversitesi, (2017).

[7] H. Kollek, "Some Aspects Of Chemistry İn Adhesion On Anodized Aluminium", International Journal of Adhesion and Adhesives, 5(2): pp. 75-80, 1985.

[8] C. Mandolfino, E. Lertora, S. Genna, C. Leone, C. Gambaro, Effect of laser and plasma surface cleaning on mechanical properties of adhesive bonded joints, Procedia CIRP 33, pp.458-463, 2015.

[9] M. Montemor, W. Trabelsi, M. Zheludevich, and M.g.s. Ferreira. "Modification of Bissilane Solutions with Rare-earth Cations for Improved Corrosion Protection of Galvanized Steel Substrates." Progress in Organic Coatings 57.1, pp.67-77, 2006.

[10] B. Díaz-Benito, F. Velasco, M. Pantoja, "Mechanical Properties Of Polyester Films Painted After Silanization Of 6063 Aluminium Alloy With Different Pretreatment Conditions", Progress in Organic Coatings 70, 287–292, 2011.

[11] E. Akman, Y. Erdoğan, M.Ö. Bora, O. Çoban, B. Genc Oztoprak, A. Demir, "Investigation Of Accumulated Laser fluence And Bondline Thickness Effects On Adhesive Joint Performance Of CFRP Composites", International Journal of Adhesion and Adhesives 89, pp.109-116, 2019.

[12] S. Oyola-Reynoso, Z. Wang 1, J. Chen S. Çınar, B. Chang and M. Thuo, "Revisiting the Challenges in Fabricating Uniform Coatings with Polyfunctional Molecules on High Surface Energy Materials", Coatings 5, pp.1002-1018, 2015.

[13] Y. Wang, X. W. Liu, H. F. Zhang, and Z. P. Zhou, "Fabrication Of Super-Hydrophobic Surfaces On Aluminum Alloy Substrates By Rfsputtered Polytetrafluoroethylene Coatings", AIP ADVANCES 4, pp.031323, 2014.

[14] A. Baldan, Review Adhesively-Bonded Joints And Repairs İn Metallic Alloys, Polymers And Composite Materials: Adhesives, Adhesion Theories And Surface Pretreatment, Journal of Materials Science 39, pp.1–49, 2004.

[15] S. Tezcan, R. Hikmet, G. Alper, C. Meran, The Effect Of Surface Roughness On Strength Of Adhesively Bonded Cylindrical Components, Journal Of Material Processing Technology 142, pp.82-86, 2003.

[16] J.D. Venables, D.K. McNamara, J.M. Chen, T.S. Sun and J.L. Hopping, "Oxide morphologies on aluminum prepared for adhesive bonding", Applied Surface Science, 3, pp. 88, 1979.

[17] E.W . Garnish, "The Influence of Metal Surface Structure on The Adhesion of Thermosetting Resin", J. Oil Col. Chema. Ssoc., ,60(2), pp.69-74, 1977.

[18] R.S. Alwitt. In: Diggle JW, Vijh AK, eds. "Oxides and Oxide Films". Vol. 4 New York: Marcel Dekker, pp.169-254, 1976.

[19] V. Cicek, "Characterization Studies Of Aluminum Alloy Substrate Surfaces Treated By Oxyanion Esters Of A-Hydroxy Acids And Their Salts". Amer Chem Sci J.3(3), pp.264-286, 2013.

[20] M. Mrad, Y. Ben Amor, L. Dhouibi, M. F. Montemor, "Effect of AA2024-T3 Surface Pretreatment On The Physicochemical Properties And The Anticorrosion Performance Of Poly(γ-glycidoxypropyltrimethoxysilane) Sol-Gel Coating", Surf Interface Anal.1–11, 2017.

[21] L.E.M.P., Z. Pászti, I.V. Aoki, H. G.de Melo, "Comparative Investigation of the Adhesion of Ce Conversion Layers and Silane Layers to a AA 2024-T3 Substrate Through Mechanical and Electrochemical Tests", Materials Research 10, 4, pp.399-406, 2007.

[22] Aslı Guruscu, "Joining And Interfacial Properties Of Aluminum/Glass Fiber Reinforced Polypropylene Sandwich Composites", MSc Thesis, Graduate School of Engineering and Sciences of İzmir Institute of Technology, 2009.

[23] H. Yan, W. Yuanhao, Y. Hongxing, TEOS/Silane-Coupling Agent Composed Double Layers Structure: A Novel Super-hydrophilic Surface, The 7th International Conference on Applied Energy – ICAE2015.

[24] J. Long, M. Zhong, H. Zhang, P. Fan, "Superhydrophilicity to Superhydrophobicity Transition of Picosecond Laser Microstructured Aluminum İn Ambient Air", Journal of Colloid and Interface Science 441,1–9, 2015.

FPL Etching Parameter Optimization for Adhesion Performance of Al/CFRP Adhesive Joints

O. ÇOBAN[1,*], M.Ö. BORA[2], B.G. OZTOPRAK[3], E. AKMAN[4] and T. KUTLUK[5]

[1] Kocaeli University, Kocaeli/Turkey, onur_coban@yahoo.com
[2] Kocaeli University, Kocaeli/Turkey, ozgur_bora@yahoo.com
[3] Kocaeli University, Kocaeli/Turkey, genc13@gmail.com
[4] Kocaeli University, Kocaeli/Turkey, eakman29@gmail.com
[5] Kocaeli University, Kocaeli/Turkey, togay71@gmail.com

Abstract - **Chemical pretreatments are often used to improve adhesion of aviation structural joints. The FPL (Forest Products Laboratories) process for preparing aluminum for structural adhesive bonding has been used in the aerospace industry since the early 1950's. However for a novel Al/CFRP adhesive bonding, an optimization should be done with FPL etching parameters which were applied to 2024-T3 aluminum alloy. In this study, FPL etching parameters such as etching temperature and immersion time were investigated with single lap shear tests according to ASTM D5868-1. Additionally failure analyses of aluminum surfaces after mechanical tests are performed by using optical microscope to discuss the FPL etching parameter optimization. All results show that for a new dissimilar material adhesive bonding with aluminum, it is suggested to optimize the chemical pretreatment parameters according to the adhesion performance.**

Keywords - **Aluminum alloy, CFRP, FPL etching, adhesive bonding, shear strength.**

I. INTRODUCTION

Combinations of different lightweight materials such as carbon fiber reinforced plastics (CFRP) and lights metals such as aluminum alloys are developed to perfectly match the requirements of innovative lightweight structures for aerospace applications. However, the combination of these hybrid structures needs a suitable and cost effective joining technology. Conventional mechanical fastening and adhesive bonding as well as the combination of both technologies are generally used to combine CFRPs and aluminum alloys. Mechanical fastenings using bolts or rivets usually provide adequate joining strength; however, it suffers from weight increase and low sealing capacity. In addition, the cross-sectional area of structures decreases due to the presence of fastener holes with the stress increase. In addition, drilling process towards the formation of bolt holes causes cracks in composite structures. In view of that, adhesive joints are more favorable in that the process offers sealing effect with the adhesive layer which acts as an electrical insulator between the CFRP and aluminum alloy and thus, helps to prevent galvanic corrosion. In addition it does not generate significant stress concentration around the joints [1, 2]. The durability of the adhesive bond strength and the long service life under demanding conditions necessitates the pre-treatment of the aluminum surfaces before adhesive bonding. Because aluminum surfaces are usually covered with a weakly bound naturally formed surface oxide layer and adsorbed contaminations like water and release agents, which needs to be removed to establish a durable bond between the aluminum surface and adhesive [2, 3].

Various mechanical (abrading and grit-blasting), chemical (acid and/or alkaline etching) and electrochemical (anodizing) surface pre-treatment methods have been reported for aluminum substrates before adhesive bonding. The strength and its durability of the adhesive bonded joints with mechanical treated or alkaline cleaned aluminum substrates are not sufficient enough compared to chemical or electrochemical treatments for structural aerospace applications. The most exploited chemical pre-treatment for aluminum adherents is based on chromic-sulphuric acid etching which generates a suitable oxide layer on the substrate surface and can produce strong and durable adhesive bonds [3-6].

There are different chromic-sulphuric acid treatments and they differ in the concentrations of compounds, the used temperature and the immersion time [5]. In addition to this, the original etching is known as FPL (Forest Products Laboratory) [6], which involves low chromate concentrations and short treatment times [5]. In the U.S., the etch bath generally consists of a solution of 30 parts of deionized water, 10 parts of sulphuric acid and 1 to 2 parts of sodium dichromate, all by weight. The bath is usually held at 160°F (71°C) and the etching time is usually 10 minutes. The rinse water is normally tap water. In Europe, the etch is often referred to as "pickling," and frequently chromic acid is substituted for sodium dichromate, the etching time is often longer and the rinse water is often specified to be deionized [7]. These are general descriptions and there are probably as many variations in the procedure of Al/CFRP adhesively bonded joints. However, there is a lack of FPL process parameter optimization knowledge that could significantly enhance the adhesion strength of Al/CFRP joints.

In this study, the effect of FPL etching parameters such as etching temperature and etching immersion time on the adhesion performance of AA2024-T3/CFRP joints were investigated with microscopic analysis, topographic images, contact angle measurements, single lap shear tests and failure analysis with digital camera images.

II. MATERIALS AND METHODS

The adherend materials selected for this study are 2024-T3 aluminum alloy with a thickness of 1.6 mm and unidirectional carbon fiber reinforced epoxy polymer (CFRP) $[0]_5$ laminated composite with a thickness of 2.3 mm. All chemicals used in the study for chemical surface treatment of AA2024-T3 were analytical grade and were purchased from MERCK. The aluminum samples with the dimensions of $1.6 \times 25.4 \times 101.6$ mm^3 were cut from the plates and were washed with pure acetone at room temperature. The cleaned aluminum samples were immediately immersed in FPL-etch solution baths at different temperatures (60-70-80 °C) prepared from 30 parts of water (H_2O), 10 parts of sulfuric acid (H_2SO_4) and 2 parts of sodium di-chromate ($Na_2Cr_2O_7$). After immersion time (10-15-20 min), the aluminum samples were removed from the bath and rinsed with pure water. Finally, they were dried at 60 °C for 1 hour. After FPL etching treatment of AA2024-T3 samples firstly, weight loss measurements were performed with a laboratory balance and surface analyses were done with microscopic evaluations. Surface roughness topography of FPL etched samples was obtained by Nanovea PS50 non-contact 3D laser profilometer. Lastly, contact angle measurements were determined using an instrument developed in-lab which gave resolution $\pm 2°$. All measurements were made at $20\pm2°C$, the liquid used was triply-distilled water.

Two-component structural liquid adhesive "Hysol® EA 9396 TM" was chosen to bond the Al/CFRP adherends together. This adhesive has a low viscosity and its mixed density is 1.14 g/ml. At least six coupons were prepared at the same time by a manually stage micrometer controlled apparatus. All adhesive bonded Al/CFRP coupons were cured at 66 °C for 1 h in an electrical furnace. The FPL etching parameter optimization for better adhesive strength of Al/CFRP adhesive bonded joints was performed according to the single lap shear tests. These tests were applied according to the ASTM D5868-01 with the crosshead speed of 13 mm/min. After mechanical tests, a digital camera was used to determine the damage mechanisms which were occurred on the aluminum and composite surfaces.

III. RESULTS AND DISCUSSION

In this work, the effect of FPL-etching parameters of temperature, immersion time and also the time between the etching treatment and the adhesive bonding process on the adhesion strength of Al/CFRP joints were investigated. First of all, weight loss results were given in Table 1 for FPL etching processes which have varied parameter levels. It was observed that with the increment of the etching temperature and immersion time the weight loss percent of AA2024-T3 was increased from 0.26% to 1.05%. Chemical treatments such as FPL etching are based on corrosion phenomenon from the harsh environment in order to dissolve the natural thin oxide layer, to clean and activate the aluminum surface, and to help in generation of a new porous and thicker oxide layer that will well adhere. It is clear that with the increment of etching temperature and etching time this corrosion phenomenon dissolved much more material from the aluminum surface.

Table 1: Weight loss results obtained for the different FPL etching processes due to varied parameter levels

FPL etching type	Weight before etching (gr)	Weight after etching (gr)	Weight loss (gr)	Weight loss percent (%)
60 °C – 10 min	11.53	11.500	0.030	0.26
60 °C – 15 min	11.57	11.534	0.036	0.31
60 °C – 20 min	11.56	11.524	0.036	0.31
70° C – 10 min	11.63	11.593	0.037	0.32
70 °C – 15 min	11.51	11.438	0.072	0.63
70 °C – 20 min	11.56	11.490	0.070	0.60
80 °C – 10 min	11.60	11.500	0.100	0.86
80 °C – 15 min	11.57	11.440	0.130	1.12
80 °C – 20 min	11.51	11.389	0.121	1.05

This material loss from the surface was analyzed with microscopic images that were taken from the FPL etched aluminum surfaces (Fig. 1). The surfaces of aluminum substrates etched with different parameter levels seem compositionally homogeneous in Fig. 1. Weight loss increment due to the FPL etching treatment is confirmed by the surfaces of etched substrates with elevated parameters that are more rugged and bumpy with the increased number of pits generated by the chemical etch. Roughness is a direct metric of surface topography; for example the untreated AA2024-T3 adherend surface roughness was obtained as 0,257 μm. Surface topography of FPL etched samples were also analyzed and given in Fig. 2. It can be seen from the surface topography images, roughness values were increased with the increment of etching temperature and immersion time. Therefore, more rugged and bumpy surface topographies were obtained.

The wetting behavior of these resultant FPL etched surfaces prepared with different parameter and levels was evaluated by static water contact angle measurements. Fig. 3-a shows the change in static water contact angles with FPL etch temperature and immersion time. It is clear that untreated sample of AA2024-T3 is a hydrophilic material with a native thin oxidized layer that has a contact angle of approximately 79°. Additionally, on the day measurements it was observed that etching immersion time has a significant effect on contact angle measurements. After etching immersion for 10 min the contact angles were significantly increased from 79° to approximately 124°, 104° and 113° respectively for 60 °C, 70 °C and 80 °C etching temperatures. This increment trend continued slightly with the increment of immersion time to respectively 15 and 20 min. As a result; contact angles for 20 min immersion time of three etching processes were obtained between 117° and 123°. This significant contact angle increment is interestingly similar with the increment of roughness obtained after the etching treatments.
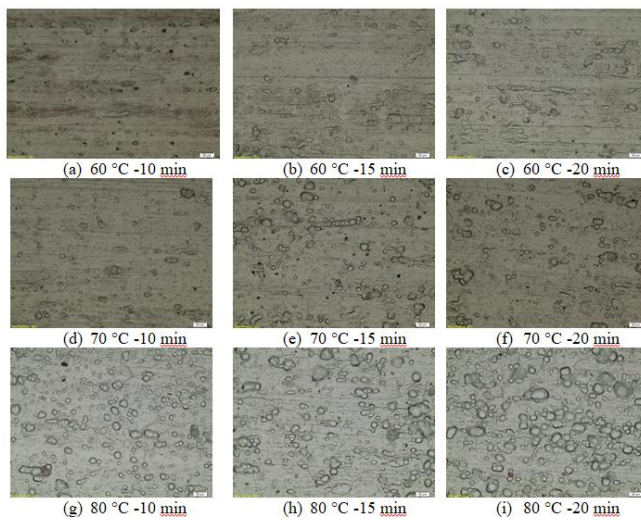
Figure 1: Microscopic images of FPL etched aluminum surfaces (50x).

The static water contact angle appears to be dependent on the surface roughness from various anodization times. The water contact angle change can be understood theoretically by the Cassie-Baxter equation (Eq. 1).

$$\cos\theta_W = f_1 \cos\theta_R - f_2 \qquad (1)$$

where θ_R is the solid-water receding contact angle and θ_W is the apparent receding contact angle for the rough surface. f_1 and f_2 are the fractions of solid surface and air in contact with air, respectively (i.e. $f_1 + f_2=1$) [8, 9]. The higher surface roughness can trap more air in the bumpy microstructures as shown schematically in Fig. 4 [10] to reduce the f_1 value, thus leading to a larger contact angle for a hydrophobic surface. The surface roughness plays an important role in determining the wetting state of solid surface. The two wetting states on rough solid surfaces are famously known as Wenzel's [11] and Cassie-Baxter's wetting states [8, 12]. In Wenzel's state the liquid drop could easily penetrate and wet the rough structure, resulting in high adhesion towards the surface. However, in Cassie–Baxter's state, the liquid does not penetrate due to the trapped air pockets in between the rough structure, and the liquid drop sits on the top asperities of the structure, maintaining a high contact angle [12]. It is well known that hydrophobic enhancement of metal substrates can be easily achieved by chemical etching treatments. The etching of metals in acid or base solutions can simply create dual scale rough structures required to achieve superhydrophobicity after surface chemical modification by low surface energy materials. This strategy has been widely used to achieve superhydrophobicity on metal substrates like steel [13], copper [14], aluminum [15] and zinc [16]. The large number of high energy dislocation sites present in crystalline metals is prone to destruction when immersed in chemical etchants, leading to the formation of micron scale surface roughness [12]. In this study hydrophobicity increment up to 123° by FPL etching can be attributed especially to the cellular oxide structure with a regular array of protrusions (Fig. 4) which can trap more air

were obtained with the immersion time of 20 min for all etching temperatures. This result predicts lower wettability and shear strength. Therefore, adhesive performance of FPL etched samples with 20 min immersion times was investigated with single lap shear tests in accordance with the untreated sample.
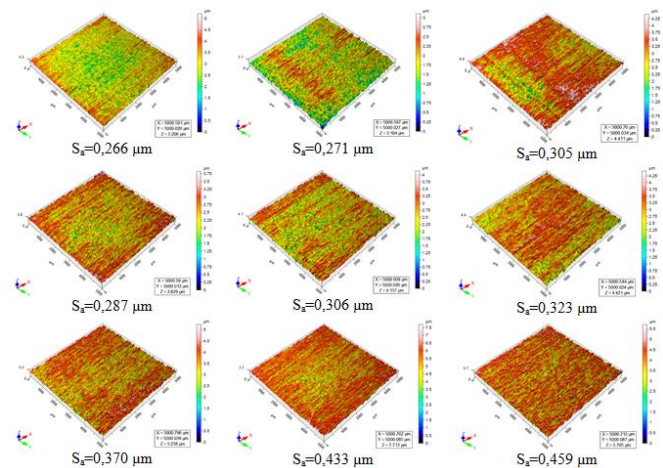
Figure 2: Surface topography analyzes of FPL etched aluminum surfaces.
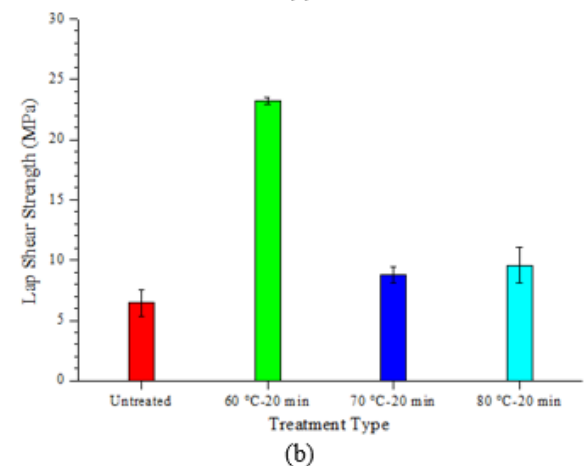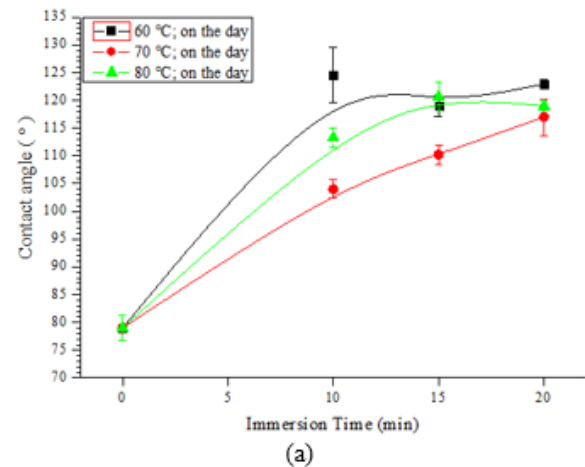
Figure 3: Static water contact angle (a) and lap shear strength (b) results of FPL etched aluminum surfaces.

Lap shear strength results of untreated and FPL etched samples were given in Fig. 3-b. Single lap adhesive bonded joint with untreated AA2024-T3 samples has 6.46 MPa shear strength. With the FPL etching treatment of 60 °C-20 min, this shear strength was significantly increased to 23.22 MPa. However, FPL etching treatment with 70 °C and 80 °C for 20 min, decreased the shear strength a little bit higher levels as 8.81 and 9.59 MPa, respectively.

After single lap shear tests of Al/CFRP joints, digital camera observations were performed to determine the variation of failure modes occurred due to the various FPL etching treatments on the CFRP and AA2024-T3 fractured surfaces (Fig. 5). It was observed from the macroscopic image of fractured untreated Al surface as shown in Fig. 5-a, that failure mode is dominantly occurred as adhesive failure. It occurs at the interface between the adhesive and the adherend. There will be very few residual adhesive remaining at any location on only one substrate. As is expected from the adhesive bonding of aluminum substrate (as known as inorganic material) and epoxy adhesive (as known as organic material) would has weak bonding strength because of their different chemical structures. In addition to this if the adhesive does not wet the surface of the substrate sufficiently, the bond will also be expected to be weak. Therefore it was tried to enhance the adhesion mechanisms of mechanical interlocking and chemical bonding with FPL etching treatment.
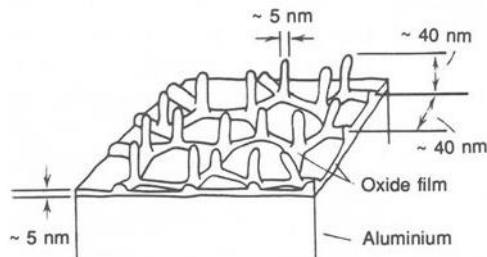
Figure 4: Schematic illustration of surface morphology on aluminum following FPL etching [10]
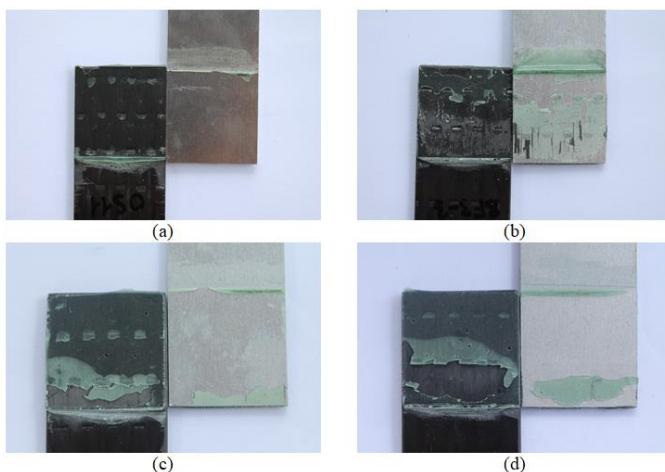
Figure 5: FPL etching effect on failure modes of Al/CFRP adhesive joints such as: untreated (a), 60 °C-20 min (b), 70 °C-20 min (c) and °80 C-20 min (d)

Failure mode analysis was applied on the aluminum substrate of FPL etched with 60 °C-20 min that was illustrated in Fig. 5-b, it can be clearly seen that a strong bonding can be observed with dominantly cohesive bonding and fiber tearing regions. This result supports the obtained maximum shear strength value among the all FPL etching processes. Beside this, with the increment of etching temperature to 70 and 80 °C for the same immersion time, bonding strength again significantly decreased as can be seen on the failure surface of substrates illustrated in Fig. 5-c and d. It is obvious that, very little region of adhesive failure was observed on etched aluminum substrate contrary to the large adhesive failure that obtained on the fractured CFRP surface. These failure results indicate that adhesive could not be bonded strongly to the aluminum despite the FPL etching application.

IV. CONCLUSION

In this work the effect of FPL etching parameters such as temperature and immersion time on the adhesion performance of Al/CFRP adhesive bonded joints was investigated by surface analysis and single lap shear tests. FPL etching effects on the aluminum surfaces were analyzed by weight loss measurements, optical microscopic images, profilometer topographies and single lap shear tests. According to these analyzes these following conclusions can be drawn:

- Increment of the etching temperature and immersion time causes increment of weight loss percent of AA2024-T3 from 0.26% to 1.05%.
- The weight loss and so the roughness increment was also observed by the optical microscope and profilometer topography investigations.
- Contact angle measurements were increased with the increment of etching immersion time for all the etching temperatures.
- Hydrophobicity increment up to 123° by FPL etching was attributed especially to the cellular oxide structure with a regular array of protrusions which can trap more air that was explained theoretically by the Cassie-Baxter model.
- The maximum shear strength was obtained with the FPL etching of 60 °C-20 min treatment.
- As a result it can be suggested that AA2024-T3 should be FPL etched with the temperature of 60 °C and the immersion time of 20 min to obtain the best adhesion strength for the Al/CFRP joint with epoxy matrix and epoxy adhesive.

REFERENCES

[1] A. Pramanik, A.K. Basak, Y. Dong, P.K. Sarker, M.S. Uddin, G. Littlefair, A.R. Dixit, S. Chattopadhyaya, "Joining of carbon fibre reinforced polymer (CFRP) composites and aluminium alloys-A review", *Composites Part A: Applied Science and Manufacturing*, vol. 101, pp. 1-29, October 2017.

[2] V. Reitz, D. Meinhard, S. Ruck, H. Riegel, V. Knoblauch, "A comparison of IR- and UV-laser pretreatment to increase the bonding strength of adhesively joined Aluminum/CFRP components", *Composites Part A: Applied Science and Manufacturing*, vol. 96, pp. 18-27, May 2017.

[3] K. Leena, K.K.Athira, S.Bhuvaneswari b, S.Suraj a, V.Lakshmana Rao, "Effect of surface pre-treatment on surface characteristics and adhesive bond strength of aluminium alloy", *International Journal of Adhesion&Adhesives*, vol. 70, pp. 265–270 2016.

[4] J.A. Bishopp, "Surface pretreatment for structural bonding", Handbook of Adhesives and Sealants, vol.1, Cognard, P.(ed.), Amsterdam: Elsevier, pp.163–214.

[5] S.G. Prolongo, A. Urena, "Effect of surface pre-treatment on the adhesive strength of epoxy–aluminium joints", *International Journal of Adhesion & Adhesives*, vol. 29, pp. 23–31, 2009.

[6] G.W. Critchlow, D.M. Brewis, "Review of surface pretreatments for aluminium alloys", *International Journal of Adhesion and Adhesives*, vol. 16, pp. 255–75, 1996.

[7] A.V. Pocius, "The Electrochemistry of the FPL (Forest Products Laboratory) Process and its Relationship to the Durability of Structural Adhesive Bonds", *Journal of Adhesion*, vol. 39. pp. 101-121, 1992.

[8] A.B.D. Cassie, S. Baxter, "Wettability of Porous Surfaces", *Transactions of the Faraday Society*, vol. 40, pp. 546-551, 1944.

[9] F. Xiao, S. Yuan, B. Liang, G. Li, S.O. Pehkoen, T. Zhang, "Superhydrophobic CuO nanoneedle-covered copper surfaces for anticorrosion", *Journal of Materials Chemistry A*, vol. 3, pp. 4374-4388, 2015.

[10] J.D. Venables, D.K. McNamara, J.M. Chen, T.S. Sun and J.L. Hopping, "Oxide morphologies on aluminum prepared for adhesive bonding", *Applied Surface Science*, vol. 3, 88, 1979.

[11] R.N. Wenzel, "Resistance of Solid Surfaces to Wetting by Water", *Industrial and Engineering Chemistry*, vol. 28, pp. 988-994, 1936.

[12] S.S. Latthe, P. Sudhagar, A. Devadoss, A.M. Kumar, S. Liu, C. Terashima, K. Nakata and A. Fujishima, "Mechanically bendable superhydrophobic steel surface with its self-cleaning and corrosion-resistant properties", *Journal of Materials Chemistry A*, vol. 3, pp. 14263-14271, 2015.

[13] L. Li, V. Breedveld and D.W. Hess, "Creation of Superhydrophobic Stainless Steel Surfaces by Acid Treatments and Hydrophobic Film Deposition", *ACS Applied Materials&Interfaces*, vol. 4, pp. 4549-4556, 2012.

[14] S. Yuan, S.O. Pehkonen, B. Liang, Y.P. Ting, K.G. Neoh, E.T. Kang, "Superhydrophobic fluoropolymer-modified copper surface via surface graft polymerisation for corrosion protection", *Corrosion Science*, vol. 53 (9), pp. 2738-2747, 2011.

[15] M.Yeganeh, N. Mohammadi, "Superhydrophobic surface of Mg alloys: A review", *Journal of Magnesium and Alloys*, vol.6-1, pp. 59-70, March 2018.

[16] B. Qian and Z.S. Langmuir, "Fabrication of superhydrophobic surfaces by dislocation-selective chemical etching on aluminum, copper, and zinc substrates", *Langmuir*, vol. 21, 9007-9009, 2005.

Surface Preparation of the Al 2024 Alloy for Adhesive Bonding of Al/ CFRP Using Fiber Laser Treatment

E. Akman[1,*], M. Ö. Bora[2], O. Çoban[3], B. Genc Oztoprak[4]

[1]Kocaeli University, Kocaeli /Turkey, erhan.akman@kocaeli.edu.tr
[2]Kocaeli University, Kocaeli /Turkey, ozgur_bora@yahoo.com
[3]Kocaeli University, Kocaeli /Turkey, onur_coban@yahoo.com
[4]Kocaeli University, Kocaeli /Turkey, genc13@gmail.com

Abstract - **Adhesive bonding is an alternative method for bonding dissimilar materials to traditional mechanical joining techniques such as rivet or bolted joints, widely used in structural applications of aviation industries. In adhesive bonding, surface preparation is one of the most important pre-treatments that need to be studied to improve the adhesion quality. In this study, the surface of the Al 2024 sample has been prepared using fiber laser to obtain the maximum single lap shear strength at Al/ CFRP adhesive joints. It is necessary to determine the optimum laser parameters such as laser power, frequency and scanning speed for obtaining the better surface quality of aluminium surfaces in order to bond to the CFRP. By this way, L9 orthogonal array Taguchi method (3 variables and 3 levels) was used to determine the significance of variables and to reduce the number of experiments. Furthermore, a statistical analysis of variance (ANOVA) was performed to determine which process parameter is statistically significant for each laser parameter.**

Keywords - **Adhesive Bonding, Laser Surface Treatment, Shear Strength, Taguchi analysis**

I. INTRODUCTION

A multi-material design in the aviation industry is one of the key methods to achieve lightweight construction, because the material type of each element that meets the minimum weight requirements for applications can be selected [1]. In joining different materials, joints are naturally the weakest part of the structure and therefore the manufacture of joints is very important in design. The traditional method used for joining the parts is screws or rivets that need holes which cause the stress concentrations. In that case, structural integrity and also the lightweight advantages of the materials reduce [2]. An alternative method that fully utilizes the advantages offered by lightweight materials is the adhesive bonding. The surfaces of the materials to be bonded play an important role in the bonding process, which is perhaps the most important parameter determining the quality of the bonding [3]. In industrial applications, to achieve strong and stable adhesion the surface of the Al samples must be pretreated [4]. The reduction of surface impurities, removal of poor layers, enhancement of the roughness to provide mechanical interlock and increasing surface energy are the target of the suitable surface treatment method. Chemical and electro-chemical pretreatment of Al surfaces are methods that provide favorable results for this purpose [4]. However, the disposal of chemicals involved, long pretreatment times and high operating costs are the disadvantages of those methods. So, using of chemicals is on the decrease as a result of new environmental regulations and changing environmental behavior [5]. Laser surface treatment is an alternative to chemical methods. The variation in the application parameters of the laser (such as pulse duration, energy, repetition rate) allows the processing of almost all materials when appropriate parameters are used. However, this necessitates an optimization depending on the material.

So, in this study surface of the Al 2024 series materials have been processed using pulsed fiber laser to increase the adhesive joint strength between Al/CFRP joint.

II. MATERIALS AND METHODS

The adherend materials selected for this study are 2024-T3 aluminum alloy with a thickness of 1.6 mm and unidirectional carbon fiber reinforced epoxy polymer (CFRP) composite with a thickness of 2.3 mm. The dimensions of the samples were prepared according to ASTM D5868-01 standard as seen in Fig 1-a. The surface of the aluminum samples were processed using max. 50 W pulsed fiber laser. This laser operates at 1064 nm wavelength with a pulse duration 100ns and repetition rate range between 20 kHz and 80 kHz. To ablate the desired surface area on the samples, a galvanometric system which provides the computer controlled movement of the laser beam to the desired area was used, together with a 160 mm focal length F-Theta lens to focus the laser beam (as seen Fig. 1-a)

Two component structural liquid adhesive "Hysol® EA 9396 TM" was chosen to bond the Al/CFRP adherends together. This adhesive has a low viscosity and its mixed density is 1.14 g/ml. At least six coupons were prepared at the same time by a manually stage micrometer controlled apparatus (see Fig 1-b). All adhesive bonded Al/CFRP coupons were cured at 66°C for 1 h in an electrical furnace.
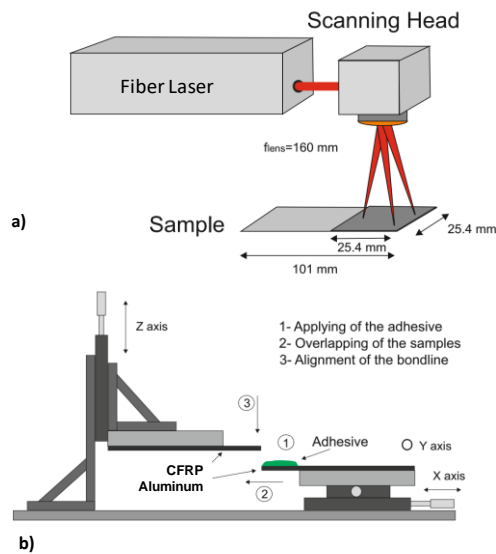
Figure 1: Experimental setup.

Adhesive strength of Al/CFRP adhesive bonded joints was performed according to the single lap shear tests. These tests were applied according to the ASTM D5868-01 with the crosshead speed of 13 mm/min. After mechanical tests, a digital camera was used to determine the damage mechanisms which were occurred on the aluminum and composite surfaces.

III. RESULTS AND DISCUSSIONS

The main parameters affecting surface morphology of the materials in laser material processing are laser power, frequency and beam travelling speed. Laser power, frequency and scanning speed were chosen in orthogonal array as control factors (see Table 1.). These factors were evaluated over 3 levels. Taguchi L9 orthogonal array was used to determine the experiment set. Six replications were carried out for each treatment.

Table1:Experimental design matrix by using Taguchi Method

Sample No	Frequency (kHz)	LaserPower (W)	ScanSpeed (mm/s)	ShearStrength (MPa)	S/N
D1	20	20	100	18.45984	25.29165
D2	20	35	800	19.04476	25.50043
D3	20	50	1500	12.30424	21.78071
D4	50	20	800	15.6634	23.81634
D5	50	35	1500	13.51512	22.59173
D6	50	50	100	18.06704	24.94462
D7	80	20	1500	10.13504	20.10242
D8	80	35	100	22.63472	27.08201
D9	80	50	800	23.61731	27.44541

When the lasers have been used for the texturing, surfaces are affected in two ways depending on the laser fluence. Laser-induced periodic surface structures (LIPPS) are

observed on the surface in the case of low-level fluences of polarized pulses near the threshold fluence for laser ablation. In the second approach performed in high laser fluences, polarization is not very important, overlapping spots form microchannels and hierarchal structure due to melting and oxidation [6]. Microchannel and micro holes are observed on almost all surfaces since this work is performed in high laser fluences as seen in Fig 2.
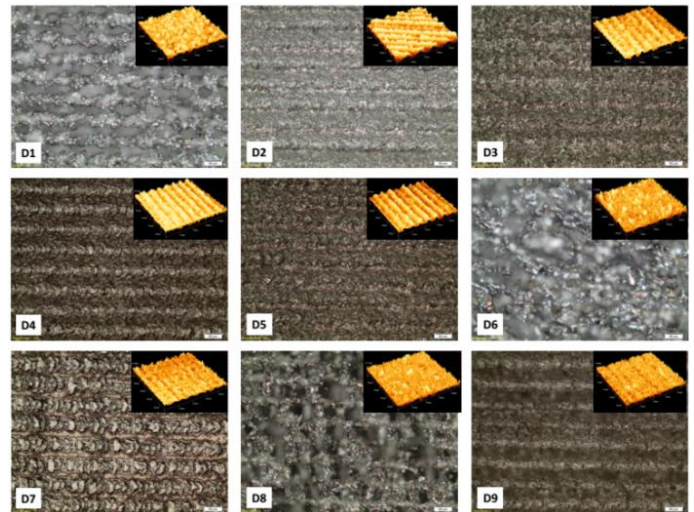
Figure 2: Optical microscope images and the surface profile of the laser textured Al surfaces.

When the microscope images are examined, only the structure of the sample in D7 is different from the others. Since the D7 sample is processed comparatively at low laser power (20W) and high scanning speed (1500 mm/s), the depth of the structures formed on the surface is very low also sparse. The roughness of these shallow structures is, as expected, the lowest compared to the other samples (1,6μm). Due to the surface roughness that can provide mechanical interlocking has been low, the shear strength of the D7 is the lowest level relatively as seen in Fig. 3.
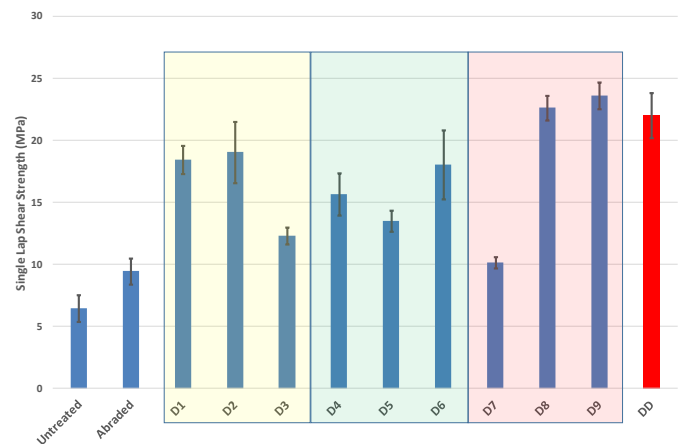
Figure 3:Single lap shear strength of the adhesively joint Al/CFRP samples.

The adhesion strength of the surfaces is not only depended roughness of the surfaces, chemical composition, and contact angle is also important. According to the literature, the better adhesion is usually obtained by higher wettability [7]. The contact of the untreated sample is 80°.While almost all samples are hydrophilic (<20°), only the D7 sample exhibited a superhydrophobic behavior as seen in Fig. 4.
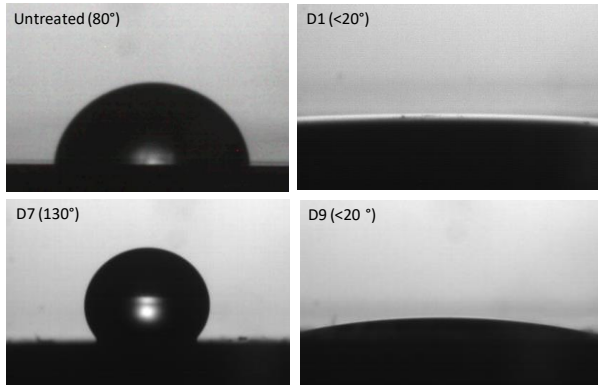
Figure 4: Contact angle of the surfaces.

The damage mechanisms of both untreated and various fiber laser treated CFRP/Al adhesive joints were displayed in Fig. 5. From Fig.5-a, it was easily shown that the relatively small strength of the untreated CFRP/Al joints with adhesive failure showed the bad influence of contamination such as a release agent, and proved the necessity for surface treatment as similar to Ref.[8].
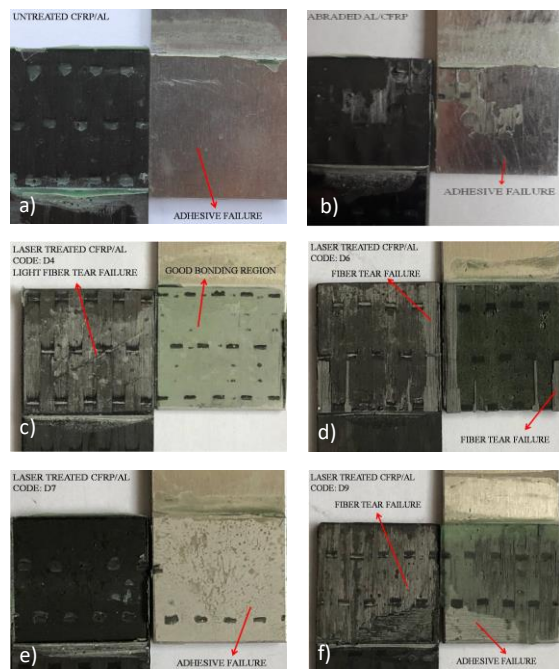
Figure 5: Damage mechanisms of various laser treatments on the CFRP/Al adhesive joints compared to the untreated and abraded samples.

Due to mechanical treatment by using sand paper (Fig.5-b), epoxy based adhesive bonded locally to the surface of aluminum. By this way, the adhesive shear strength value of Al/CFRP joints was improved. Focusing the damage types of the laser treated CFRP/Al adhesive joints to identify a sensitive treatment intensity, it was determined that already at high power laser treatments occurred fiber tear failure (Fig.5-d and f) at CFRP surface region which leaded a significant increase of the adhesive shear strength values compared with the untreated CFRP/Al joints. In addition, good adhesion also occurred at the aluminum surfaces with adhesive at low power laser treatments (Fig.5-c). It was predicted that laser treatment affected the aluminum surface for a better adhesion to adhesive material. Beside this, for laser treated samples with high velocities (Fig.5-e), adhesive failure was obtained as similar to untreated samples. This type of treatment affected the aluminum surfaces badly.

IV. ANALYSIS OF VARIANCE (ANOVA)

The contribution of each factor on the multiple performance characteristics on laser surface treatment process for Al/CFRP adhesive bonding was determined using analysis of variance (ANOVA). The analysis was done at a significance level of a α=0.05 (confidence level of 95%). F-test was used to determine the change in which laser surface treatment parameter significantly influences the single lap shear results as shown Table 2. ANOVA results was shown that the investigation with 80 kHz frequency, 50 W laser power and 100 mm/s has the highest levels and was recommended result from the ANOVA table. The shear strength of the sample treated using ANOVA's recommended parameters has been shown in figure 3 as DD sample (21,99 Mpa). Scan speed has the highest contribution (%68.86) of the laser surface treatment parameters which affect the adhesion performance.

Table 2: ANOVA result for optimization of laser process parameters

Source of variation	A Freque ncy	B LaserPo wer	C Scanspe ed	Error	Total
Degrees of freedom	A	B	C		
Level 1	24,19	23,07	25,77		
Level 2	23,78	25,06	25,59		
Level 3	24,88	24,72	21,49		
Sum of thesqueres	1,83	6,80	35,14	3,83	47,59
Meansquares	0,91	3,40	17,5689	0,0813	
Percent Contribution (%)	3,8430	14,2838	73,8355	8,04	100
F	47,2202	175,508	907,238		

V. CONCLUSION

In this study, the surface of the Al 2024 series aluminum material has been textured using pulsed fiber laser to increase the joining strength of Al / CFRP bonding. The process parameters of the laser frequency, power and scanning speed

was used as variables and optimized with the Taguchi method. According to the results, it is concluded that the most effective parameter is the scanning speed. It is seen that the adhesion strength can be increased approximately 3.4 times by using laser surface texturing process when suitable laser parameters are used. The results of the approval test realized to test the optimal setting obtained from the Taguchi method are satisfactory.

REFERENCES

[1] D. Meinhard, V. Reitz, S. Ruck, V. Knoblauch, H. Riegel, "A comparison of IR- and UV-laser pretreatment to increase the bonding strength of adhesively joined Aluminum/CFRPcomponents," LIM 2007, pp.1-7.

[2] E. Akman, Y. Erdoğan, M. Ö. Bora, O. Çoban, B. GencOztoprak, A. Demir, Int. J. Adhes. Adhes, 89, 2019, pp.109-116.

[3] M. D. Banea, L. F. M. da Silva, "Adhesively bonded joints in composite materials: an overview," Proc. IMechE Vol. 223 Part L: J. Materials: Design and Applications, pp.1-18.

[4] N. Anagreh, A. Al Robaidi, "Improvement in Adhesion Behavior of Aluminum Due to Surfaces Treatment with Arc Discharge," Jordan Journal of Mechanical and Industrial Engineering, Volume 4, Number 2, March. 2010, pp.330-339.

[5] R. Rechner, I. Jansen, E. Beyer, "Optimization of the aluminum oxide properties for adhesive bondingby laser surface pretreatment," J. Laser Appl., Vol. 24, No. 3, August 2012, pp.032002-1-9.

[6] P. Gregorčič, B. Šetina-Batič, M. Hočevar, "Controlling the stainless steel surface wettability by nanosecond direct laser texturing at high fluences," Appl. Phys. A (2017) 123:766,pp.1-8.

[7] A. Buchman, M. Rotel, H. Dodiuk-Kenig, "Nd:yag laser surface treatment of various materials to enhance adhesion" K.L. Mittal, T. Bahners (Eds.), Laser surface modification and adhesion, Wiley, New York (2015), pp. 3-54.

[8] F. Fischer, S. Kreling, P. Jäschke, M. Frauenhofer, D. Kracht& K. Dilger (2012) Laser Surface Pre-Treatment of CFRP for Adhesive Bonding in Consideration of the Absorption Behaviour, The Journal of Adhesion, 88:4-6, 350-363.

Investigation of the use of fly ash additive in aerated concrete production and its effects

S. AKPINAR[1], A. EVCİN [1], Ç. ÖZTÜRK[2], İ. AKŞEN[1]

[1]Afyon Kocatepe University, Afyonkarahisar/Turkey, akpinar@aku.edu.tr

[1]Afyon Kocatepe University, Afyonkarahisar/Turkey, evcin@aku.edu.tr

[2]Necmettin Erbakan University, Konya, Turkey, cozturk@erbakan.edu.tr

[1]Afyon Kocatepe University, Afyonkarahisar/Turkey, ibrahim.aksen@gmail.com

Abstract - **Aerated concrete, is a lightweight construction material that is resistant to fire and earthquake as well as having high thermal insulation properties, and does not harm the environment. Nowadays, the rapid increase in demand for raw material resources and the limited natural resources make it necessary to investigate the reusability of industrial wastes. In this study, the possibility of using fly ash wastes in aerated concrete production as an additive was investigated. For this purpose, the fly ash taken from Kütahya Cement Plant was added to the standard aerated concrete recipe, used by AKG aerated concrete company, at the proportions 3, 5, and 7 wt.%. The effects of fly ash addition on compressive strength and density of the samples were investigated. Present phases and microstructures of the samples were characterized by XRD and SEM analyses, respectively. The results indicate that the production of higher strength and lower density aerated concrete is possible with the addition of 3 wt% fly ash.**

Keywords - **Fly ash, Aerated concrete, Strength, Density**

I. INTRODUCTION

AERATED concrete is produced by introducing gas bubbles into conventional concrete which provides material of lower density [1]. It is used not only as an insulating material for heat and sound but also as a fire-resistant material [1, 2]. Lightweight aerated concrete can be used to decrease the dead load, reduce the inertia effect during earthquakes and minimize the sections of the building members. Thus, the structural foundations become less demanding, and the building cost is decreased. However, this type of concrete has lower mechanical properties, and more cement may be required for the same strength as normal concrete. Typical lightweight concrete has densities from 1000 to 2000 kg/m^3 and compressive strengths from 1 to 100 N/mm^2 [1].

Aerated concrete is a lightweight concrete consist of independent air cells, where a finely ground silica material is bonded with an inorganic binder and then expanded with a porous material and finally cured [3].

Due to the air trapped inside the small pores, aerated concrete shows effective thermal insulation. Aerated concrete is in the lightweight concrete group and various raw materials mainly including quartz-rich sand, cement, lime and gypsum are used in its production. Water and expanding agent (e.g. aluminium) are added to these starting materials and the mixture is poured into mould trolleys. After casting, the mixture is allowed to harden in the waiting tunnel whose temperature is continuously controlled. When the hardness of cutting is reached (after 3-4 hours), the concrete is taken to computer-controlled cutting benches and cut to desired dimensions. Aerated concrete from the cutting process is put into autoclaves and subjected to saturated steam at 12 atm. pressure and 190 °C for 12 hours for the curing process [4].

In the autoclave process, the reaction given in equation 1, yields a product having a porosity of 75-85% and a high density. This process directly affects the property of the material [5].

$$5Ca(OH)_2 + 6SiO_2 + 5,5H_2O \rightarrow 5CaO.6SiO_2.5,5H_2O + 5H_2O \quad (1)$$
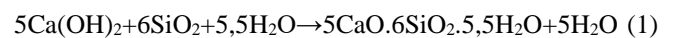
After the quality control process, steam-cured concrete is presented to the market with their light, porous and high-pressure resistance properties [4].

The benefits of implementing effective recycling of waste include reduced environmental pollution, lower disposal costs and landfill volume, advancements in recycling technology, and economic gains [6].

Fly ash is an important waste from industries such as cement factories and thermal power stations that generates a great deal of pollution to the environment due to its fineness and soluble ions. The growth of power plants around the world and a further increase in cement production due to the dynamism of the construction sector results in an increasing amount of fly ash that causes high environmental impact, especially in Turkey. Today, annual fly ash generation reaches 15 million ton in Turkey. Fly ash is mainly utilized in the construction industry, concrete and cements production as an additive material; however, the utilization ratio is still very limited [7].

Many researchers around the world are looking at methods of gainful utilization and disposal of fly ash. However, the construction materials industry is the most suitable way to mass consumption of fly ash waste [7].

Although silica-based filler is generally used in commercial aerated concrete production, it is a good alternative for the mass use of industrial wastes rich in SiO_2 and CaO [7]. Many researchers have investigated the possibility of replacing conventional raw materials of aerated concrete with industrial waste such as coal bottom ash, natural zeolite, blast furnace slag, lead-zinc wastes, copper deposits, iron ore residues, gasification wastes and sand-phosphorus slag-lime [8-16].

Fly ash is a very fine-grained waste material of dark colour. The colour of fly ash can vary from tan to grey to black, depending on the amount of unburned carbon in the ash; the lighter the colour, the lower the carbon content. The main components of fly ash are; silica (SiO_2), alumina (Al_2O_3), iron oxide (Fe_2O_3) and CaO, the amount of which varies according to the type of fly ash. However, the essential compounds of fly ash are silica and alumina. It is reactive when fly ash, lime and water are together. This reactivity is largely based on the glassy structure of the fly ash. It is stated that the glassy (amorphous) structure in fly ash is between 50-90% [17].

Due to its fineness and amorphous mineralogy, fly ash is a pozzolanic material and exhibits pozzolanic properties just like fine-grained natural pozzolans; when combined with calcium hydroxide in an aqueous medium, they have hydraulic bonding. Therefore, they are used directly in the production of portland-pozzolan cement as well as a concrete admixture. Generally, they can be used in very large quantities as concrete additives. The amount of fly ash in the concrete mixture can vary between 15% and 50% of cement weight [17].

Different approaches are used to accelerate the pozzolanic reaction of fly ash, and these approaches increase the early strength of concrete containing fly ash. Within these approaches; grinding, curing acceleration (autoclave curing) and chemical activations [17].

While most of the studies aimed at evaluating wastes in aerated concrete production are relatively high-density concrete (> 0.5), the effects of fly ash additive on low-density concrete composition were investigated in this study. Besides, those studies were carried out in the laboratory conditions, and aerated concrete production was realized in industrial autoclave conditions of AKG gas concrete company in this study.

II. Material and Method

Materials:
In the experimental study, the usability of fly ash as an additive in autoclaved aerated concrete (AAC) production was investigated. In this context, silica sand, Portland cement, lime, gypsum and aluminium powder were used in standard recipes of AKG Company. Fly ash from Kütahya Cement Plant added instead of silica sand ratio.

In the experimental study, CEM I 42,5 R class portland cement was used. This cement was consisting of 44-48% C_3S phase, 10% C_3A phase and max. 12% C_4AF phase. The setting time of the cement is 60 minutes, the percentage of over 90 micron sieve is less than 2%, the Blaine is 3939 cm^2/g, and the specific gravity is 3.10 g/cm^3. Unslaked lime having CaO content more than 80% and grain size less than 42 μm was used. Aluminium powder of purity 90% and size less than 45 μm was used as a foaming agent.

Fly ash has a specific gravity of 1.98 g/cm^3 and the percentage residue left on the screen of 45 micron sieve is 23.25, and its specific surface area is 4020 cm^2/g. Besides, the use of fly ash as an additive in structural materials such as cement and concrete at a rate of maximum 40% is acceptable limit by Atomic Energy Authority as it does not cause radiological hazards.

Preparing of Aerated Concrete Compositions:

The chemical analyses of the raw materials, used in the preparation of the aerated concrete compositions, are presented in Table 1.

Table 1. The chemical analyses of the raw materials.

Oxide (%)	Silica sand	Cement	Gypsum	Lime	Fly ash
SiO_2	80.51	19.55	1.04	-	53.69
Al_2O_3	10.01	5.12	0.25	-	20.29
Fe_2O_3	3.57	3.08	0.30	-	11.83
CaO	0.04	63.38	33.40	>80	3.40
MgO	0.38	1.16	0.30	-	4.09
Na_2O	0.11	0.11	0.02	-	-
K_2O	3.21	0.68	0.02	-	2.53
Cr_2O_3	0.02	0.23	-	-	-
SO_3	0.10	3.06	45.50	-	0.99
LOI	2.04	3.43	19.17	<5	2.01

*LOI: Loss of Ignition

The compositions were prepared based on the AKG aerated concrete standard recipe. Fly ash powders were added to the raw material mixture by partial substitution with silica sand up to 7 wt% to examine their potential effects on the finished aerated concrete. Thus, three extra formulations were designed

by the addition of the fly ash up to 7 wt%. The designed formulations were encoded as FA0, FA3, FA5, and FA7 where, 'FA' stands for fly ash while '0, 3, 5, and 7' stand for wt% additive amount. The composition of the designed formulations is given in Table 2.

Table 2. The designed aerated concrete formulations

Raw Materials	Compositions (wt.%)			
	FA0	FA3	FA5	FA7
Silica sand	59.4	56.4	54.4	52.4
Fly ash	0	3	5	7
Lime	9.25			
Portland Cement	28			
Gypsum	3.25			
Aluminium	0.1			
W/S ratio	0.70	0.73	0.74	0.77
Total	100	100	100	100

The water/solid ratios of the standard recipe used in AKG aerated concrete production were taken as the basis. However, with the use of fly ash having a finer grain size instead of silica sand, the need for water increased due to increased surface area. Therefore, as the amount of fly ash increased, the water / solid ratio was also increased.

Sample Preparation:

According to the designed aerated concrete formulations, first, lime and water were mixed in the mixer for 5 minutes, then silica sand and fly ash were added and mixed for a further 10 minutes. Aluminium powder was then added to the mixture and stirring was continued until the mixture was homogeneous. The resulting mixture was filled into oiled 10 x 10 x 10 cm plastic moulds and placed in a well-fixed surface. The shaped samples were then stored in an oven at 50 °C for 16 hours and then removed from the mould and autoclaved and cured in an autoclave at 190 °C at 12 atm. vapour pressure for 12 hours.

The samples taken from the autoclave were sized and kept in the oven at 60 °C for one day, and then cooled to ambient temperature and the initial density values were measured. Test specimens were prepared according to TS EN 678 standard, and were kept in a dry oven at 105 °C until constant weight in the oven and their weights were recorded. Similarly, the dimensions were measured by a calliper. After 28 days of retention, the samples were made ready for use in the characterization step. In Figure 1, a flowchart of fly ash added AAC production is given.
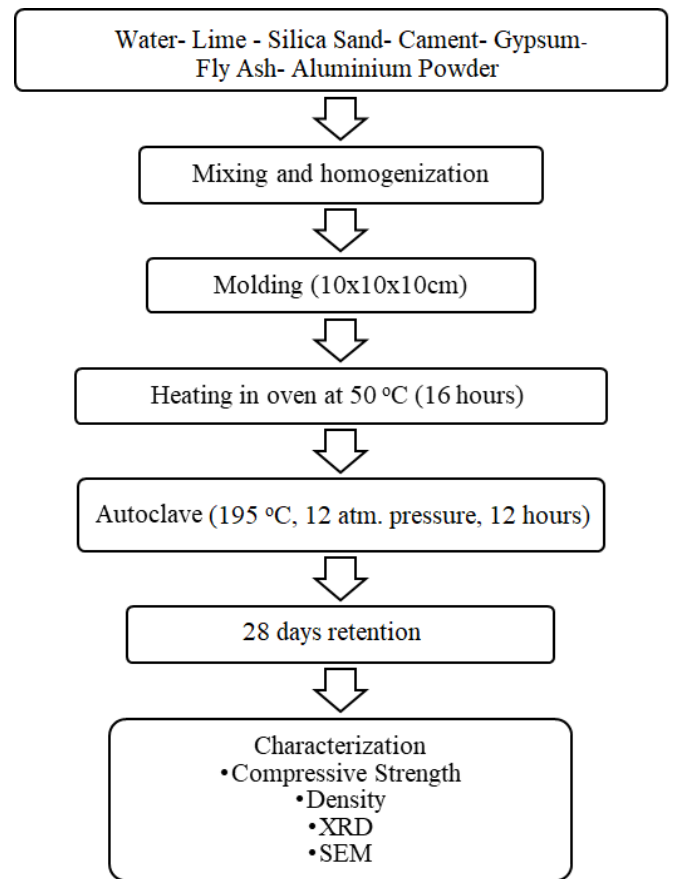
Figure 1. Flow chart of fly ash added AAC production

The test specimens were characterized by physical tests, and the mineralogical and microstructure analyses. Compressive strength and density tests were performed according to TS EN 772-1 and TS EN 678 standards, respectively. For phase and microstructural analyses Shimadzu XRD-6000 and LEO 1430VP-SEM devices were used, respectively. Figure 2 shows the standard and fly ash-added aerated concrete used in the characterization tests.

Figure 2. Macro images of the shaped aerated-concrete samples; a) F0 and b) F3

III. Results

Effect of Fly Ash Addition on the Compressive Strength of Aerated Concrete

The compressive strength values of aerated concrete samples are given in Table 3. According to Table 3, the

compressive strength values of 3 wt% (FA3) and 5 wt% (FA5) fly ash added aerated concrete increased compared to the standard recipe (FA0) used by the company AKG aerated concrete, whereas the strength decreases with 7 wt% (FA7) additive. The compressive strength results of the samples prepared from different fly ash-added compositions revealed that the best results were achieved in the samples prepared from 3 wt% fly ash containing composition. In addition, according to TS-EN 772-1 norms, the aerated concrete should have a compressive strength of 25 kN/mm^2. Thus, it is understood that aerated concrete samples with 3 wt% fly ash additive have a higher strength value than the desired strength value in TS-EN 772-1 norms.

Table 3. Compressive strength values of aerated concrete samples.

Recipes	Fly Ash Amount (%)	Compression Strength (kN/ mm^2)
FA0	0	23.0
FA3	3	26.6
FA5	5	23.9
FA7	7	20.5

Effect of Fly Ash Addition on the Density of Aerated Concrete

The density values of aerated concrete samples are given in Table 4. According to Table 4, with increasing fly ash additive, the density of the aerated concrete decreased.

Table 4. Density values of aerated concrete samples.

Recipes	Fly Ash Amount (%)	Density (kg/dm^3) (T:60 °C)	Density (kg/dm^3) (T: 105 °C)
FA0	0	0.429	0.394
FA3	3	0.419	0.387
FA5	5	0.412	0.380
FA7	7	0.405	0.378

Effect of Fly Ash Addition on the Phase Structure of Aerated Concrete

In Figure 3, X-ray diffraction (XRD) patterns showing the comparison of mineralogical structures of the standard aerated concrete sample (FA0) and 3 wt% fly ash-added aerated concrete (FA3) samples are given.
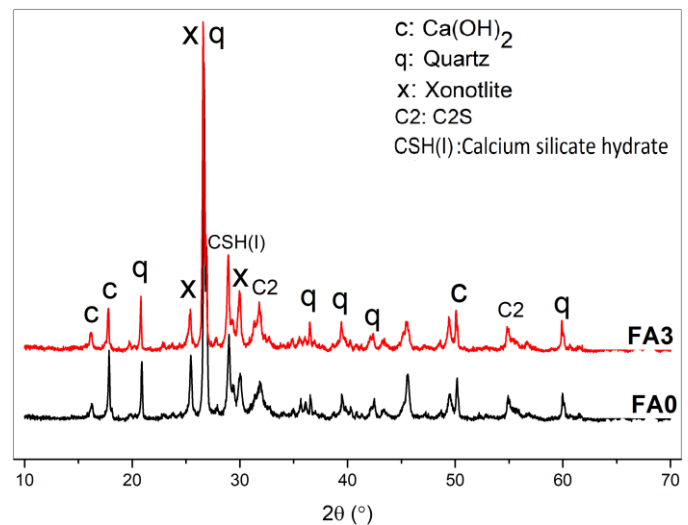
Figure 3. XRD patterns of fly ash added and non-added aerated concrete samples.

As shown in Figure 3, the standard sample consists of the phases Xonolite, Quartz, Ca(OH)$_2$, CSH(I) and C$_2$S. The peak intensity of CSH(I) and Xonolite phases increased in the 3 wt% fly ash-added aerated concrete sample compared to the standard one. No significant change was observed in the peak intensity of the quartz.

Effect of Fly Ash Addition on the Microstructure of Aerated Concrete

In Figure 4, scanning electron microscopy (SEM) images showing the comparison of the microstructure of standard aerated concrete sample and 3 wt% fly ash-added aerated concrete samples are given.
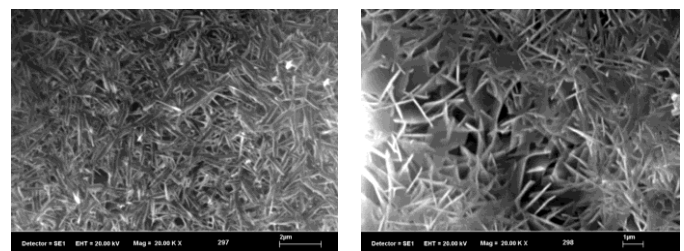
Figure 4. SEM images of non-added (left) and fly ash-added (right) aerated concrete samples.

SEM microstructure analysis indicated that an increase in the needle-like structure with fly ash additive. There are also differences between the needle-like structure in the standard aerated concrete and the needle-like structure in the fly ash-added sample. Needle-like CSH(I) (tobermorite) crystals are denser in fly ash-added aerated concrete. CSH(I) crystals were concentrated to 2 μm. In addition, the pores formed in the structure are clearly seen as in a similar study in the literature [18].

IV. DISCUSSION AND RESULTS

Aerated concrete compressive strength, which should be 25 kN/mm^2 according to TS-EN 772-1 standard, has increased to 26.6 kN/mm^2 with the addition of 3 wt% fly ash. This value is also higher than that of the standard recipe of AKG aerated concrete (23 kN/mm^2). The density of the aerated concrete decreased with the addition of fly ash. As a result, it is possible to produce more strength, and low density aerated concrete with the addition of 3 wt% fly ash.

This study indicated that fly ash which flue gas waste from cement plants can be evaluated in aerated concrete by adding 3 wt%.

ACKNOWLEDGEMENT

REFERENCES

[1] Shabbar R, Nedwell, P., Al-Taee M., and Wu Z., Effect of Different Aluminium Powder Content on the Behaviour of Aerated Concrete: Experimental and Finite Element Validation, International Journal of Materials, Mechanics and Manufacturing, Vol. 6, No. 2, April 2018
[2]Narayanan N., Ramamurthy K., Structure And Properties of Aerated Concrete: A Review, Cement and Concrete Composites, 22 (5), 321-329, 2000
[3] TS 453, Gaz ve Köpük Beton Yapı Malzeme ve Elemanları, Türk Standartları Enstitüsü, Ankara. 1988
[4] AKG Gaz beton Tasarım ve Uygulama El Kitabı, 2005
[5] GüçlüerK., Uçucu Külden Üretilen Silis Dumanı Katkılı Gazbeton Özellikleri Üzerine Kür Etkisinin Araştırılması, Afyon Kocatepe Üniversitesi, Fen Bilimleri Enstitüsü, Yüksek Lisans Tezi, Afyonkarahisar, 2011
[6] Walczak P., Malolepszy J., RebenM., Szymański P., RzepaK., Utilization of Waste Glass in Autoclaved Aerated Concrete, Procedia Engineering 122, 302 – 309, 2015
[7] Baspinar M. S., Demir İ., Kahraman E., Görhan G., Utilization Potential Of Fly Ash Together With Silica Fume in Autoclaved Aerated Concrete Production, Journal of Civil Engineering 18(1):47-52, 2014
[8] Pachideh G., and Gholhaki M., Effect Of Pozzolanic Materials on Mechanical Properties and Water Absorption of Autoclaved Aerated Concrete, Journal of Building Engineering, 26, 2019
[9] Liu Y., Leong B. S., Hu Z.T., Yang E. Y., Autoclaved Aerated Concrete Incorporating Waste Aluminum Dust as Foaming Agent, Construction and Building Materials, 148, 140-147, 2017
[10] Różycka A., Pichór W., Effect of Perlite Waste Addition on The Properties of Autoclaved Aerated Concrete, Construction and Building Materials, 120, 65-71, 2016
[11] Pehlivanlı Z. O., Uzun İ., Yücel Z.P., Demir İ., The Effect of Different Fiber Reinforcement on The Thermal and Mechanical Properties of Autoclaved Aerated Concrete, Construction and Building Materials, 112, 325-330, 2016
[12] Drochytka R., Helanová E., Development of Microstructure of The Fly Ash Aerated Concrete in Time, Procedia Engineering, 108, 624-631, 2015
[13] Jerman M., Keppert M, Výborný J., Černý R., Hygric, Thermal and Durability Properties of Autoclaved Aerated Concrete, Construction and Building Materials, 41, 352-359, 2013
[14] Karakurt C., Kurama H., Topçu İ. B., Utilization of Natural Zeolite in Aerated Concrete Production, Cement and Concrete Composites, 32 (1), 1-8, 2010
[15] Kurama H., Topçu İ. B., Karakurt C., Properties of The Autoclaved Aerated Concrete Produced From Coal Bottom Ash, Journal of Materials Processing Technology, 209 (2), 767-773, 2009
[16] Mustafa Albayrak M., Abdulkerim Yörükoğlu A., Serdar Karahan S., Sema Atlıhan S., Aruntaş H. Y., Girgin İ., Influence of Zeolite Additive on Properties of Autoclaved Aerated Concrete, Building and Environment, 42 (9), 3161-3165, 2007
[17] Görhan G., Kahraman E., Baspinar M. S., İsmail İ., Uçucu Kül Bölüm II: Kimyasal, Mineralojik ve Morfolojik Özellikler, Yapı Teknolojileri Elektronik Dergisi, 5(2), 33-42, 2009
[18] Özel G., Uçucu Külün Gazbeton Özellikleri Üzerine Etkisinin Belirlenmesi, Kırıkkale Üniversitesi, Fen Bilimleri Enstitüsü, Yüksek Lisans Tezi, Kırıkkale, 2013

Effect of Inoculant Type on Microstructure of A206 Aluminum Alloy

S. ÇETİNTÜRK[1] N. TARAKÇIOĞLU[2] and M. ACARER[3]

[1]Konya Technical University, Metallurgical and Materials Engineering, Konya / Turkey, selmanct@yahoo.com
[2]Selçuk University, Faculty of Technology, Metallurgical and Materials Engineering, Konya / Turkey, ntarakcioglu@selcuk.edu.tr
[3]Selçuk University, Faculty of Technology, Metallurgical and Materials Engineering, Konya / Turkey, macarer@selcuk.edu.tr

Abstract - In this study, AlSr10, Al-3Ti-1B and Al-5Ti-1B grain refiner master alloys have been entered into A206.0 aluminum copper casting alloy and casting has been made to the gravity mold. Thus, the effects of different grain refiners on the microstructures of aluminum copper alloys were investigated. Grain refining alloys were added to aluminum copper alloy in 0.20%, 0.40%, 0.60% and 0.80% by weight. Optimum results were achieved when the grain refiner master alloys were entered at 0.60% by weight. The microstructures of the samples were examined by optical microscope and scanning electron microscope. The results were compared. AlSr10 added alloys were found to be finer grained than aluminum copper alloys without grain refiner. However, it has been found that AlSr10 grain refiners are not as effective as titanium and boron. In terms of grain size thinning effect, Al-5Ti-1B and Al-3Ti-1B grain refiners were compared; Al-5Ti-1B was found to be more effective than Al-3Ti-1B. As the boron ratios of these two master alloys were equal, titanium was found to be more effective in grain thinning.

Keywords - A206 Al-Cu alloys, master alloys, Al-5Ti-1B alloy, grain refinement, microstructure.

1. INTRODUCTION

The use of aluminum alloys in the automotive, aerospace and defense industries has been increasing recently. Aluminum is preferred because of its lightness, resistance, thermal conductivity, corrosion resistance, recyclability, easy formability and high performance. Especially copper containing aluminum alloys are more preferred in places requiring high strength although they are easily formed [1]. Ming-Yu Xie et al. [2] studied grain refining of Al-5% Cu aluminum copper alloy. Al5Ti1B grain refiner master alloy in 0.2%, 0.4%, 0.6% and 0.8% were added in four different proportions. Solution heat treatment at 535^0C for 12 hours and quenching in 30^0C water followed by 18 hours at 175^0C'de made artificial aging are applied. As a result, when 0.6% Al5Ti1B master alloy was entered, they found average grain size as 70µm, tensile strength as 435 MPa and percent elongation as 11%. In this study conducted in 2014, only Al5Ti1B master alloy was used. In my study, Al-5% Cu alloy and three different grain refiners AlSr10, Al3Ti1B and Al5Ti1B master alloys were entered. Sigwort G. K. and Kuhn T. A. [3] studied the effects of Al-Ti-B grain refiner master

alloy on aluminum alloys such as Al-Si, Al-Si-Cu, Al-Cu, Al-Mg and Al-Zn-Mg. When the Al-5Ti-1B and Al-3Ti-1B master alloys entered as grain refiner were entered, they obtained the best grain refinement results when 10-20 ppm B was entered.

In this study by Sigwort et al., three different master alloys have been entered into the A356 Al-Si alloy and which inoculant is more effective in grain refinement has been compared. According to this; Using Al-5Ti-1B, Al-5Ti and Al-4B master alloys, they found that the Al-4B inoculant had higher grain refiner effect for Al-Si alloys than others.

According to the results of this study, average grain size values of 900 µm for Al-5Ti-1B, 500 µm for Al-5Ti and 200 µm for Al-4B were obtained with grain refiners entered at 0.06%Ti and 0.06%B ratios. In this study, Al-Si system titanium element easily soluble $AlTi_3$ compound and insoluble stable TiB_2 titanium boride compounds stated that they act as nucleolus in grain refinement process. They showed that titanium was the most effective ratio of 0.10% Ti in grain refinement. They stated that adding more titanium than this value had no effect on grain refinement.

Fan Z. et al. [4] showed that by using 0.2% Al-5Ti-1B master alloy as grain refiner in aluminum alloys, TiB_2 compound binds two-dimensional Al_3Ti compound to itself and increases the nucleolus effect. They have shown that the addition of grain refiners to the molten liquid metal, the titanium element which dissolves from the master alloy and increases the conversion of the alloy structure from colonic dendritic structure to coaxial grain structure. They also stated that Al_3Ti is stable in dense Al-Ti solutions and unstable in dilute solutions.

Talamentes-Silva M. A. et al [5] studied the effect of solidification rate and heat treatment on the microstructure and tensile stress conditions of aluminum copper alloys. They showed that these parameters increased with the reduction of solidification rate by examining the effects of secondary dendritic arm distance, grain size and porosity on microstructure. In this study, the distance between the secondary dendrites was found to be 50 µm in T4 heat treatment and 30 µm in T7 heat treatment conditions.

Kashyap K. T. et al. [6] affects phase diagram theory, peritectic hulk theory, hyper nucleation theory and double layer nucleation theory are some of them. They have expressed the grain refinement mechanism in aluminum alloys

as heterogeneous nucleation and growth of nucleus in the follow-up. They also stated that the solute effect together with nucleolus is also important in grain refinement mechanism.

In this study, microstructures of Al-5% Cu alloy were investigated by entering three different grain size thinner inoculants. AlSr10, Al-3%Ti-1%B and Al-5%Ti-1%B master alloys were selected as grain thinners and were entered in 0.20%, 0.40%, 0.60% and 0.80% by weight. The effects of Sr, Ti and boron elements in grain size thinning will be examined. From the Ti:B ratio of the Al-3Ti-1B and Al-5Ti-1B master alloys, the effectiveness of the increase in titanium content will be investigated by keeping the ratio of boron element constant.

2. MATERIALS AND METHODS

2.1 Materials

Inputs for the casting of aluminum copper alloy; pure aluminum ingot (99.7% Al) Etial E7, magnesium ingot (99% Mg), manganese (60% Mn), copper wire (99% Cu), three different grain refiners (AlSr10, Al-5Ti-1B, Al-3Ti-1B grain refiner master alloys) 100 grams in the form of metal rods. Melting process was performed in Selcuk University Metallurgical and Materials Engineering Department Metallurgical Laboratory with electric resistance digital thermocouple furnace. After the aluminum copper alloy was melted in SiC crucible, copper, magnesium and manganese were entered and mixed for 20 minutes and slag was removed. Afterwards, grain refiner master alloys were entered and poured into gravity mold at 750^0C temperature. Each alloy group was entered separately by choosing three different grain refiner master alloys such as AlSr10, Al-3Ti-1B and Al-5Ti-1B.

Table 1: Chemical composition of the materials used in experimental studies. Commercial purity (99.7 wt % Al) Seydişehir Etial E7 / EN AC 46200 pure aluminum ingot.

%Si	%Fe	%Cu	%Mn	%Mg	%Al
0.10	0.15	0.03	0.02	0.02	rest

Table 2: Chemical composition of A206.0 aluminum copper alloy with (%) weight.

% Si	% Fe	% Cu	% Mn	% Mg	% B	% Ti	% Al
0.20	0.20	5.09	0.43	0.17	0.0002	0.006	93.8

Our goal here; the aim of this course is to investigate the effects of strontium, titanium and boron materials on the refinement of crystal grains by grain size measurements. Seydişehir Etial E7 (99.7% Al) pure aluminum primary ingot and other inlets were melted in SiC crucible in an electrically resistant furnace at 750^0C. Slag removal of the molten liquid metal was carried out with Na_2SiF_6 flux. According to the process, degasser tablet degassing process and grain refiner master alloys were entered after this step. The samples to be examined were obtained from three different grain refiner alloys and one unalloyed Al-5%Cu material in four different groups.

The microstructure of the alloys was investigated by using Nikon T1-SM Eclipse MA100 brand reverse material microscope. Microstructure pictures were taken with TCA 300-A microscope camera. Image analysis method was used to calculate grain size. Grain size was calculated as the number of grains per unit distance and the number of grains per unit area. For scanning electron microscopy (SEM), Zeiss EVO LS10 was used. For energy distribution spectrum (EDX) studies; 1.23 eV Bruker EDX Detector was used. Metallographic procedures were performed on the samples prepared for optical microscopy and scanning electron microscopy (SEM) analysis.

Metallography was carried out with Metkon Forcipol 2V grinding and polishing machine. Duopat-M brand monocrystalline diamond polisher has been used as polisher. The surfaces of the samples were etched for 10 seconds with the Keller etch (1% HF, 1.5% HCl, 3% HNO3 and remaining water) to obtain an image from the surface of the aluminum alloys. Hardness measurements were made with brinel hardness tester. For hardness measurements, mean values were obtained from five different points from each sample.

2.2 Grain Refiner Master Alloys

AlSr10, Al-3Ti-1B and Al-5Ti-1B, three different grain refiner master alloys are cast separately by entering separately. Master alloys are in the form of metal rods with a diameter of 10 mm and a weight of 100 g. The following chemical compositions by weight of these grain refiner master alloys are as follows. AlSr10, Al-3Ti-1B and Al-5Ti-1B grain refiner master alloys were cast by entering 0.2%, 0.4%, 0.6%, and 0.8% by weight aluminum copper alloy.

Table 3: Chemical composition of AlSr10 grain refiner alloys by (%) weight.

% Si	% Fe	% Sr	% Ca	% Al
0.20	0.30	9-11	0.03	Rest

2.3 Preparation of Samples

In order to obtain microstructure and scanning electron microscope samples, spheroidal GGG50 material was molded. Eight sample pieces were cast in each casting. Castings were

made twice for each different alloy. In addition, the samples were painted with mold paint for easy separation from the mold. The parts obtained after casting process are classified according to alloy type and numbered with brand.

Table 4: Chemical composition of Al-3Ti-1B grain refiner alloys by (%) weight.

% Si	% Fe	% B	% Ti	% Cu	% Mg	% Zn	% Al
0.05	0.10	0.9-1.1	2.8-3.4	0.02	0.02	0.10	Rest

Table 5: Chemical composition of Al-5Ti-1B grain refiner alloys by (%) weight.

% Si	% Fe	% B	% Ti	% Cu	% Mg	% Mn	% Zn	% Al
0.10	0.30	0.9-1.1	4.5-5.5	0.02	0.02	0.02	0.10	Rest

3. RESULTS AND DISCUSSIONS

3.1 Hardness Measurements

Hardness measurements were applied to four alloy groups. These; Al-5%Cu alloy without grain refiner. Al-5%Cu alloy with AlSr10 grain refiner master alloy. Al-5%Cu alloy with Al-3%Ti-1%B grain refiner master alloy and Al-5%Cu alloy with Al-5%Ti-1%B grain refiner master alloy. In addition, while the hardness values of the alloy without grain refiner were the lowest, the highest hardness values were observed in the material with Al-5% Ti-1%B grain thinner master alloy. Brinell hardness values obtained from four different alloys are shown in the Table 6. Below.

Table 6: Comparison of Brinell hardness values of the samples which were added into three different grain refiner master alloys.

Brinell Hardness Values (HB)				
Alloys	**Measurement**			
	1.	**2.**	**3.**	**Average**
Al-%5Cu Alloy	70	72	73	**71,6**
Al-%5Cu + AlSr10	88	89	92	**89,6**
Al-%5Cu + Al-3Ti-1B	91	92	96	**93,0**
Al-%5Cu + Al-5Ti-1B	96	101	103	**100**

3.2 Microstructure Research

0.6% by weight of three different grain refiner master alloys and one grain refiner is not entered into Al-5%Cu alloys are shown at 100 magnification images in Figure 1. The grain size thinner master alloys used were AlSr10, Al-3%Ti-1%B and Al-5%Ti-1%B. Accordingly, the grain size of the alloy with AlSr10 grain refiner was significantly improved and thinner than the Al-5%Cu alloy without grain refiner. (Fig. 1: (a) and

(b)). However, the grain size thinning effect of AlSr10 is not at the level of Al-Ti-B grain refining alloys. Ti and boron are more effective than strontium in grain refining. Figure 1.(c) shows that the grain refining effect of Al-3%Ti-1%B alloy is higher than AlSr10.

However, the grain refining effect of Al-3%Ti-1%B is not at the level of the Al-5%Ti-1%B alloy. Figure 1.(d) shows that grain refining effect is obtained with Al-5%Ti-1%B grain refiner. Titanium and boron elements support each other in grain refining. Al-5%Ti-1%B and Al-3%Ti-1%B alloys have equal boron ratios, but Al-5%Ti-1%B has a higher grain refining effect. Thus, it is seen that titanium is the most effective element in grain refining. (Figure 1. (c)).

(x100)   (x100)
(a)   **(b)**

(x100)   (x100)
(b)   **(d)**
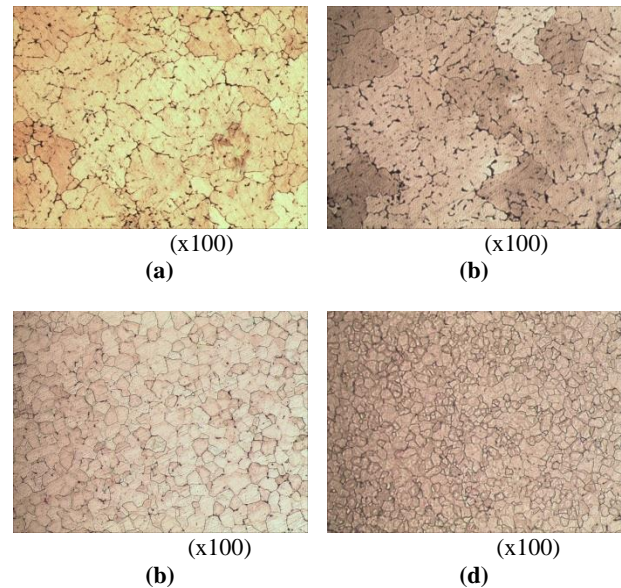
Figure 1: Different grain refiner master alloys were entered at 0.6% by weight; Microstructure images of Al-5% Cu alloys at 100 magnification: **(a)** Al-5% Cu alloy without grain thinner; **(b)** Al-5% Cu + AlSr10 alloy, **(c)** Al-5% Cu + Al-3Ti-1B alloy, **(d)** Al-5% Cu + Al-5Ti-1B alloy.

3.3 Grain Size Measurements

Grain size measurements of the samples can be seen in Fig 2-5. As seen, the grain size of the sample with Al-5Ti-1B inoculant is finer than the others.

(a) (x100)   **(b)**
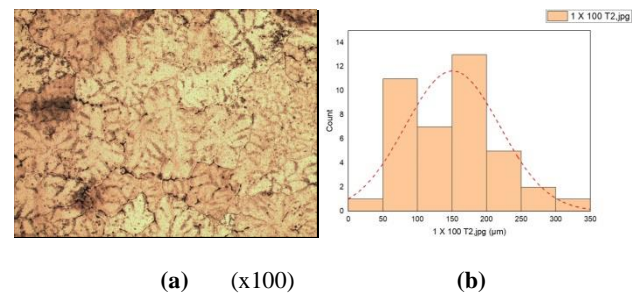
Figure 2: Al-5% Cu alloy without grain refiner. **(a)** Grain structure image at 100 magnification. **(b)** Grain size distribution is shown by Image analysis method. There are 13 number of 200 μm sizes per unit area.

(a)　　(x100)　　　　　　　　**(b)**
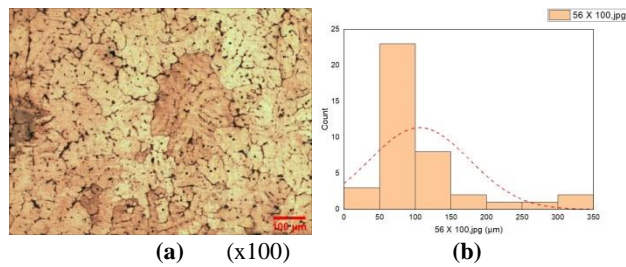
Figure 3: Al-5% Cu alloy with AlSr10 grain refiner. **(a)** Grain structure image at 100 magnification. **(b)** Grain size distribution is shown by Image analysis method. There are 23 number of 100 µm sizes per unit area.

(a)　　(x100)　　　　　　　　**(b)**
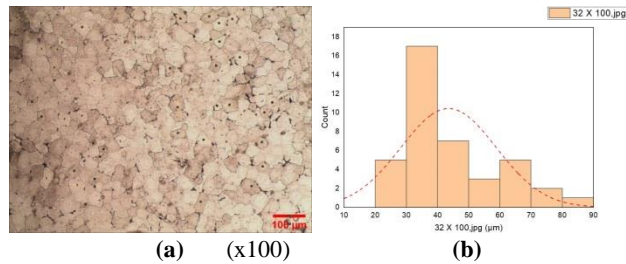
Figure 4: Al-5% Cu alloy with Al-3%Ti-1%B grain refiner. **(a)** Grain structure image at 100 magnification. **(b)** Grain size distribution is shown by Image analysis method. There are 17 number of 40 µm sizes per unit area.

(a)　　(x100)　　　　　　　　**(b)**
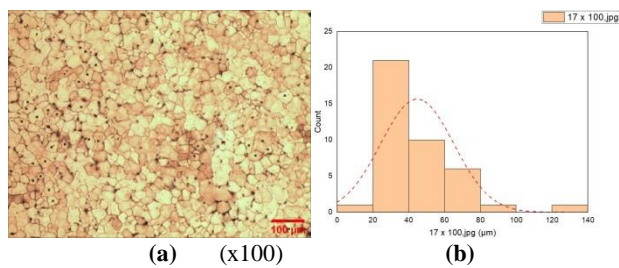
Figure 5: Al-5% Cu alloy with Al-3%Ti-1%B grain refiner. **(a)** Grain structure image at 100 magnification. **(b)** Grain size distribution is shown by Image analysis method. There are 22 number of 40 µm sizes per unit area.

4. CONCLUSIONS

In this study, the grain size thinning effects of aluminum copper alloy of three different inoculants were 23 pieces from 100 µm for AlSr10 alloy, 17 pieces from 40 µm for Al-3%-Ti-1%B alloy and 22 pieces from 40 µm for Al-5%Thi-1%B alloy were found.

The grain thinning effect of the AlSr10 alloy was obtained as 23 pieces from 100 µm grain sizes compared to copper-aluminum alloys having a grain size 13 pieces from 200 µm.

The grain sizes of Al-5% Ti-1% alloy and Al-3% Ti-1%B alloy were equal to 40 µm but the number of grains in the same unit area is more than 5 pieces of Al-5%Ti-1%B alloy.

Al-5%Ti-1%B grain refiner is the most effective of three different inoculants in grain size thinning.

REFERENCES

[1] R. E. Sanders, T. H. Sanders, and I. T. Stalley, 1983, ''Relationship Between Microstructure, Conductivity and Mechanical Properties of Alloy 2024-T4 (1),'' Aluminum, 59, Jarg, 13-17.

[2] M. Y. Xie, S. H. Ao and X. Wang, 2014, ''Effect of Al5Ti1B Master Alloy on Microstructure and Mechanical Properties of Al-5wt.%Cu Based Alloy,'' *Advanced Materials Research Vol. 1051 (2014) pp. 195-198*

[3] G. K. Sigwort, and T. A. Kuhn, 2007. ''Grain Refinement of Aluminum Casting Alloys,'' *American Foundry Society, Schaumburg, IL USA, Paper 07-067(02), Page 1 of 12.*

[4] Z. Fan, T. Wang, Y. Zhang, T. Qin, X. R. Zhou, G. E. Thompson, T. Pennycook, and T. Hashimoto, 2015. ''Grain Refining Mechanism in the Al/Al-Ti-B System,'' *Acta Materialia 84, 292-304.*

[5] M. A. Talamantes-Silva, A. Rodriguez, J. Talamantes-Silva, S. Valtierra, and R. Cola's, 2008. ''Effect of Solidification Rate and Heat Treating on the Microstructure and Tensile Behavior of an Aluminum-Copper Alloy,'' *The Minerals, Metals & Materials Society and ASM International 2008, doi: 10.1007/s11663-008-9204.*

[6] K. T. Kashyap, and T. Chandrashekar, 2001. ''Effects and Mechanisms of Grain Refinement in Aluminium Alloys,'' *Bull. Mater. Sci., Vol. 24, No.4, pp. 345-353.*

Design and Analysis of PI Controller Based Four-Quadrant DC Motor Drive with Bipolar and Unipolar Switching Methods

K. TUTUNCU[1] and R. OZCAN[2]

[1] Selcuk University, Konya/Turkey, ktutuncu@selcuk.edu.tr
[2]Selcuk University, Konya/Turkey, recaiozcan@selcuk.edu.tr

Abstract - **In this study, the closed loop speed control of the separately excited Direct Current (DC) motor controlled by a four-quadrant DC motor drive circuit was performed in MATLAB / SIMULINK software. For this purpose, two control circuits were designed using PI controller. The first one is the bipolar switching circuit and the second one is the unipolar switching circuit. The control signals obtained from these circuits were applied to the single-phase four-quadrant DC chopper power circuit to drive the separately excited DC motor at reference speed. Comparison of the both switching methods has been implemented based on the data obtained from the simulation results of four-quadrant operation of the DC motor. As a result of the comparison, it has been seen that output voltage and frequency responses were better than the bipolar switching method (BSM) due to doubling of switching frequency of output voltage of the unipolar switching method (USM).**

Keywords - **DC motor drive, PI Control, Four-quadrant operation, Bipolar switching, Unipolar switching**

I. INTRODUCTION

NOWADAYS, DC motor drives are widely used in applications requiring deceleration, acceleration and reversal operation due to their simple structure and low cost. Four-quadrant DC motor drive systems are required for speed control and braking applications to be faster, more efficient and economical [1-4]. High performance is an important element for the industry. DC motors need to be controlled in industry where the high performance is important [5]. Some of these control methods are PI, PID, fuzzy logic, reference model, and artificial neural networks [6].

Advances in semiconductor technology have resulted in tremendous progress in power electronics. Thus, Pulse Width Modulation (PWM)-based applications for generating variable frequency and voltage have become popular [7]. There are various applications in the literature depending on circuit structures and control methods: speed control of chopper fed DC motor with PI and fuzzy logic proportional integral controllers [5], modeling and implementation of four-quadrant DC motor drive [1] and DC motor control application with double cycle support for electric vehicles [6].

In this study, closed loop speed control of the separately excited DC motor controlled by a four-quadrant DC motor drive circuit in MATLAB / SIMULINK software was performed by using BSM and USM, respectively. The PI controller was used in both switching methods.

The rest of the study was organized as follows: Section 2 gives information about the concept of the study and the design of the control system. Section 3 shows the results of the simulations. The study was concluded in Section 4.

II. METHODS

A. Conceptualization

1) Four-Quadrant DC Chopper Power Circuit

Full bridge (H-Bridge) is used for DC motor to operate in forward motoring, reverse motoring and braking (four-quadrant) [4]. The four-quadrant DC chopper circuit feeding the DC motor shown in Figure 1 was constructed using four semiconductor switches (IGBT). The circuit has two legs and each leg has two switches. One of the switches on the same leg of the circuit, operates with the turned on and the other switch turned off.
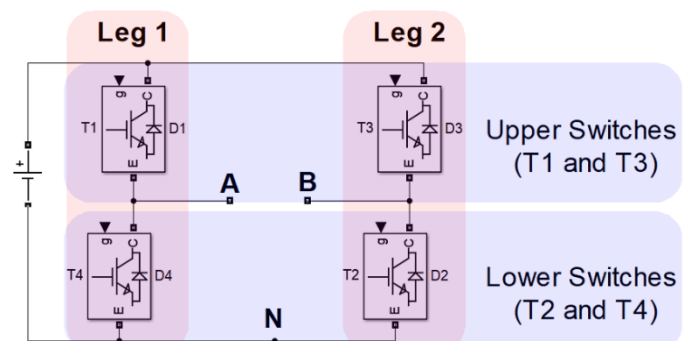
Figure 1: Four-quadrant DC chopper power circuit

By switching the IGBTs appropriately, the average values of the output voltage and current as well as the polarity can be set. This enables the DC motor to be operated in four-quadrant. This topology let the system has, the advantages such as rapid response and control flexibility [1]. Figure 2 shows the four-

quadrant operation of drives.
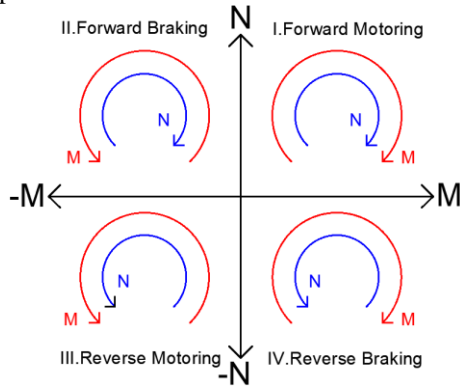
Figure 2: Four-quadrant operation (N is the speed and M is the torque)

2) Switching Methods

The main idea of unipolar and bipolar switching is to compare the triangular carrier signal (V_{tri}) and the control signal (V_c) as defined in Eq. (1,2).

$$V_c > V_{tri} \implies Logic\ 1 \tag{1}$$
$$V_c < V_{tri} \implies Logic\ 0 \tag{2}$$

IGBTs are switched depending on the values of the comparison of V_{tri} and V_c, [8].

a)   BSM

In this switching method, one V_c signal is required to compare with V_{tri}. In the four-quadrant DC chopper circuit shown in Figure 1, one of the upper switches of leg 1 and leg 2 operates with the turned on and turned off mode, respectively. This also applies to the lower switches. That is, the four switching devices are turned on or turned off simultaneously. The polarity of the switches and the output voltage are defined in the Eq. (3,4).

$$V_c > V_{tri} \implies V_o = +V_{dc}\ (T1\ and\ T2\ is\ on) \tag{3}$$
$$V_c < V_{tri} \implies V_o = -V_{dc}\ (T3\ and\ T4\ is\ on) \tag{4}$$

In the BSM, the drive output voltage varies between $+V_{dc}$ to $-V_{dc}$. The bipolar switching patterns are shown in Figure 3.
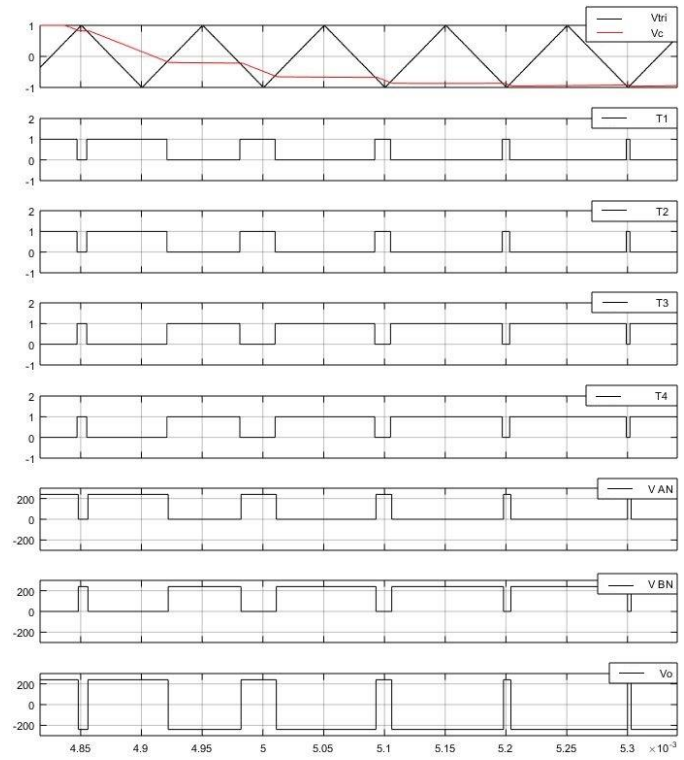
Figure 3: Waveforms of BSM

The output voltage for bipolar switching is as follows:

$$V_o = V_{AN} - V_{BN} \tag{5}$$

b)   USM

In this switching method is required two reference signals (+V_c and -V_c) with the same frequency and amplitude. There is a 180° phase difference between these two signals [7].

The comparison of +V_c with V_{tri} controls the switches in leg 1, and the comparison of -V_c with V_{tri} controls the switches in leg 2. The comparison of +V_c and -V_c with V_{tri} is defined in Eq. (6-9).

$$V_c > V_{tri} \implies V_o = +V_{dc}\ (T1\ is\ on) \tag{6}$$
$$V_c < V_{tri} \implies V_o = -V_{dc}\ (T4\ is\ on) \tag{7}$$
$$-V_c > V_{tri} \implies V_o = +V_{dc}\ (T3\ is\ on) \tag{8}$$
$$-V_c < V_{tri} \implies V_o = -V_{dc}\ (T2\ is\ on) \tag{9}$$

In the forward motoring mode of the DC motor, the drive output voltage varies between 0 and $+V_{dc}$, and in reverse motoring mode the drive output voltage varies between 0 and $-V_{dc}$ [9]. Unlike bipolar switching, in unipolar switching, the switches do not turned on or turned off simultaneously [10]. The unipolar switching patterns are shown in Figure 4.
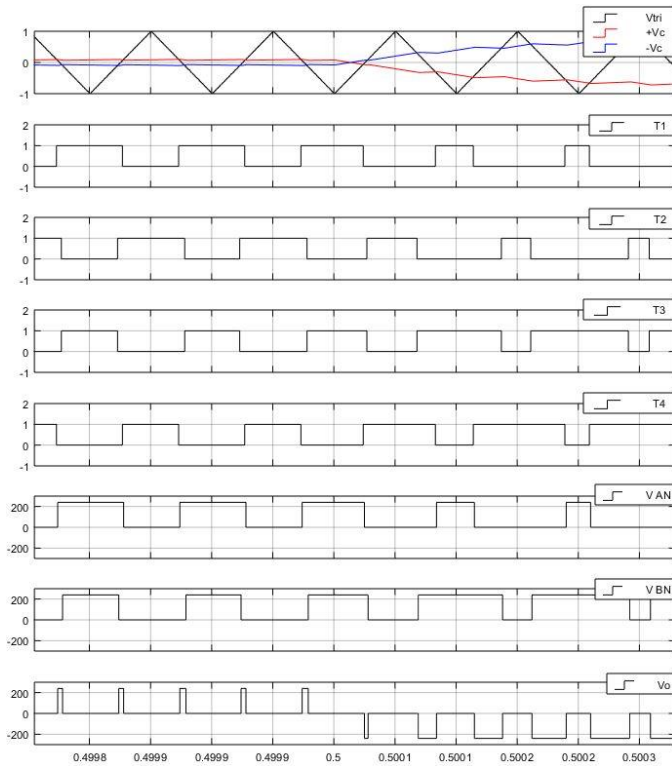
Figure 4: Waveforms of USM

The output voltage is calculated as in Eq. (5) used in the BSM.

3) PI Controller

PI controller was used in the designed system. In order to achieve good control performance, the controller parameters must be selected correctly. Otherwise, it may cause unstable operation of the system [9]. Increasing the proportional gain of the speed controller allows the system to react more quickly to small speed errors. The faster response of the current reference given by the speed controller, enables better tracking of the speed reference. This property ensures a smooth approach to the reference speed and reduces speed overshooting. When the desired speed is reached, the armature current decreases. The effect of the proportional controller on the system decreases as the error becomes smaller. This causes a constant error. The integral gain eliminates constant error and helps the system to keep the speed at the reference level. Excessive increase in proportional and integral gains leads to insensitivity and instability of the system [11,12].

B. Designing Control System

Four-quadrant DC motor drive systems, which are formed by BSM and USM, consist of 3 parts. The first one is the mode control unit, the second one is the power circuit and the third one is the control circuit.

1) Mode Control Unit

The mode control unit is shown in Figure 5. When both switches are set to 1, forward motoring and braking mode (1st

and 2nd quadrant) are activated. The motor starts at 500 rpm with a torque of 8 Nm, after 0.5 seconds the torque becomes -8 Nm.

When both switches are set to 2, reverse motoring and braking mode (3rd and 4th quadrant) are activated. The motor starts at -500 rpm with a torque of -8 Nm, after 0.5 seconds the torque becomes 8 Nm.
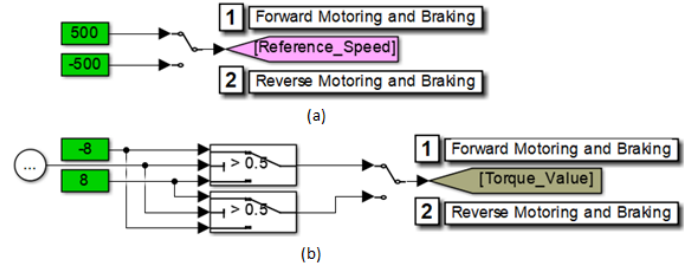
Figure 5: Mode control unit: (a) Reference speed value, (b) Torque value

The values from Figure 5(a) are assigned as the reference speed values to the bipolar switching control circuit shown in Figure 7 and to the unipolar switching control circuit shown in Figure 8. The values from Figure 5(b) are assigned to the DC chopper power circuit shown in Figure 6 as the torque values.

As can be seen from Figure 2, the positive and negative values of the speed and torque ensure four-quadrant operation of the motor. The plus and minus signs of speed and torque for the four-quadrant operation of the motor are defined in Table 1 with respect to the clockwise direction.

Table 1: Signs of speed and torque for the four-quadrant operation.

Four-quadrant operation	N (speed)	M (torque)
I. Forward Motoring	+	+
II. Forward Braking	+	-
III. Reverse Motoring	-	-
IV. Reverse Braking	-	+

2) Power Circuit

The power circuit provides voltage which is adjustable average value and has polarity to the DC motor. The power circuit shown in Figure 6 was used for both the BSM and the USM.
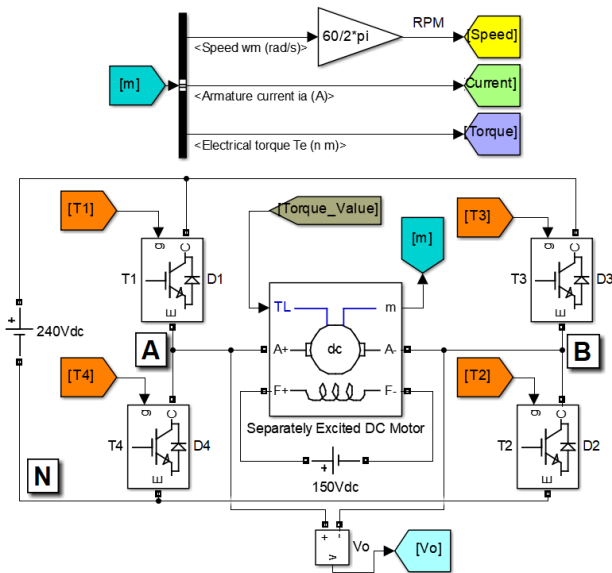
Figure 6: DC chopper power circuit with separately excited DC motor

The parameters of the separately excited DC motor used in Figure 6 are shown in Table 2.

Table 2: The parameters of separately excited DC motor.

Parameters	Values
Armature resistance and inductance	0.78 (Ω) - 0.016 (H)
Field inductance and inductance	150 (Ω) – 112.5 (H)
Field-armature mutual inductance	1.234 (H)
Motor inertia	0.08 (kg.m^2)
Viscous friction	0.01 (N.m.s)

3) Control Circuit

The systems designed using the BSM and the USM are shown in Figure 7 and Figure 8, respectively. The control circuit generates drive signals that provide the necessary switching to the drive circuit. In other words, it generates gate signal for IGBTs.
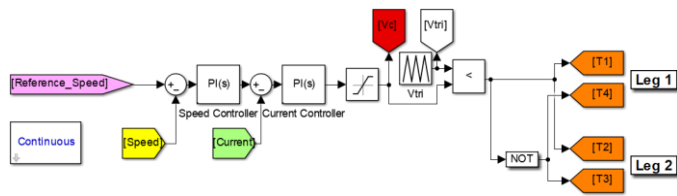
Figure 7: Bipolar Switching Control Circuit
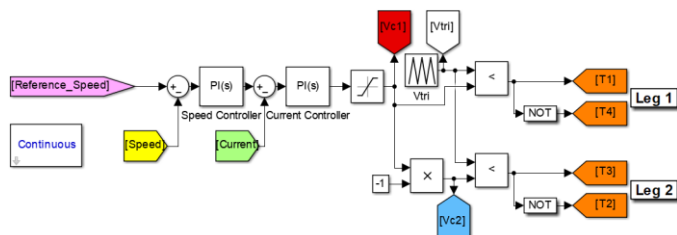
Figure 8: Unipolar Switching Control Circuit

In both switching techniques a V_{tri} with a frequency of 10 KHz was used. This signal was used when comparing the control signals. Thanks to the signal obtained as a result of the comparison, the IGBTs were switched. As previously mentioned in the switching methods heading, a single control signal is required in the BSM, whereas two control signals are required in the USM.

In the system where PI is used as the controller, K_p and K_i constants were determined by trial and error. Proportional constant (K_p) and Integral constant (K_i) for the speed controller are 0.08 and 1.1, respectively. Proportional constant (K_p) and Integral constant (K_i) for the current controller are 0.5 and 5, respectively.

III. SIMULATION RESULTS

Simulation results were obtained by using the same frequency V_{tri}, K_p and K_i constants of PI controller in both switching techniques.

The simulation results of BSM and USM are shown in Figure 9 and Figure 10, respectively. Figure 9 shows the results obtained in forward motoring and braking mode (I. and II. Quadrant), and Figure 10 shows the results obtained in reverse motoring and braking mode (III. and IV. Quadrant).

Simulation results obtained from BSM and USM in forward motoring and braking mode are shown in Figure 9 (a) and Figure 9 (b), respectively.

From top to bottom, Figure 9 and Figure 10 include V_{tri} and control signals in the first row, power circuit output voltages in the second row, instantaneous speed values in the third row, and armature current and torque values in the fourth row.

As can be seen from the Figure 9, the DC motor starting to run when the torque sign and the speed sign are both positive. While the speed sign remains constant, the motor speed increases when the torque sign is negative, but the controller quickly reduces the motor speed to the reference value.
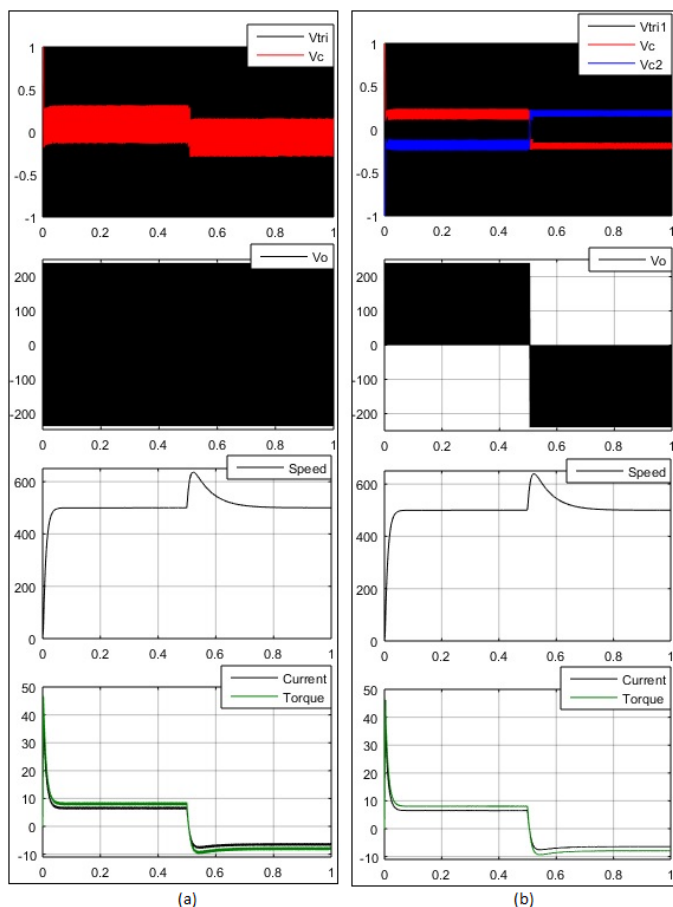
Figure 9: Forward motoring and braking mode (I. and II. Quadrant) for 500 rpm reference speed : (a) BSM, (b) USM

Figure 10: Reverse motoring and braking (III. and IV. Quadrant) for 500 rpm reference speed : (a) BSM, (b) USM

As shown in Figure 10, the DC motor starting to run when the torque sign and the speed sign are both negative. While the speed sign remains constant, the motor speed reduces when the torque sign is positive, but the controller quickly increases the motor speed to the reference value.

IV. CONCLUSION

In this study, two different circuit models were designed by using BSM and USM for a four-quadrant DC motor drive in MATLAB / SIMILINK software. The control signals generated from these circuits were applied to the single-phase DC chopper power circuit with closed loop control. In this way, the DC motor was simulated in four-quadrant with both switching techniques. When the simulation results are examined;

- Although the two-level output voltage was obtained by applying the BSM, it has been observed that the three-level output voltage was obtained by applying the USM.
- In the USM, it has been observed that the fluctuations in armature voltage decreased compared to the BSM.
- It has been seen that the USM output voltage was closer to DC voltage than BSM.
- USM has been seen to give better frequency response than BSM.
- It has been seen that the reference speed was reached in both switching techniques.

REFERENCES

[1] H. Altun, Ö. Aydoğmuş and S. Sünter, "Gerçek Dört-Bölgeli Bir DC Motor Sürücüsünün Modellenmesi ve Tasarımı," *Fırat Üniv. Fen ve Müh. Bil. Dergisi.* 20(2), pp. 295-303, 2008.

[2] Y. S. Ettomi, S. B. M. Noor, S. M. Bashi, and M. K. Hassan, "Micro controller based adjustable closed-loop dc motor speed controller," *Student Conference on Research and Development,* pp. 59-63, August 2003.

[3] L.E. Davis, H. H. Moghbelli and A. Ahmed, "Microprocessor control of DC motor drives," *Industry Applications Society Annual Meeting,* pp. 1782-1786, October 1992.

[4] İ. Çolak, M. Soysal and R. Bayındır, "DA Motorunun Dört Bölge Denetiminin Eğitim Amaçlı Gerçekleştirilmesi," *Politeknik Dergisi,* 10(3), pp. 219-227, 2007.

[5] E. Sesli, Ö. Akyazı and A. Çora, "Kıyıcı Beslemeli DA Motorun Oransal İntegral ve Bulanık Mantık Oransal İntegral Denetleyicilerle Hız Kontrolü Karşılaştırılması," *Elektrik-Elektronik-Bilgisayar ve Biyomedikal Mühendisliği 13. Ulusal Kongresi ve Fuarı Bildirileri,* Ankara 2009.

[6] A. M. Sharaf, İ. H. Altaş and E. Özkop, "Elektrikli Araçlar İçin Çift Çevrim Destekli DA Motor Kontrol Uygulaması," *XII. EEBB Mühendisliği Ulusal Kongresi ve Fuarı*, Eskişehir Osmangazi Üniversitesi, Eskişehir 2007.

[7] E. H. E. Aboadla, S. Khan, M. H. Habaebi, T. Gunawan, B. A. Hamidah and M. B. Yaacob, "Effect of modulation index of pulse width modulation inverter on Total Harmonic Distortion for Sinusoidal," *2016 International Conference on Intelligent Systems Engineering (ICISE),* pp. 192-196, January 2016.

[8] M. Bilge, M. Salihmuhsin, S. Yılmaz and S. Doganay, "Tek ve İki Kutuplu, Düzenli Örneklenmiş Sinüsoidal Darbe Genişlik Modülasyonu (SPWM) ile Kontrol Edilen İnverterin Matlab/Simulink ile Tasarım ve Analizi," *International Journal of Scientific and Technological Research*, vol 1, no.1, pp. 101-108, 2015.

[9] P. Karpagavalli,and A. E. Ebenezer, "PID Controller Based Full Bridge DC-DC Converter For Closed Loop DC Motor With Unipolar Voltage Switching," *University Politehnica of Bucharest Scientific Bulletin Series C-Electrical Engineering and Computer Science,* 77(1), pp. 59-72, 2015.

[10] A. Namboodiri and H. S. Wani, "Unipolar and Bipolar PWM Inverter," *International Journal for Innovative Research in Science & Technology (IJIRST),* vol 1, no 7, pp. 237-243, December 2014.

[11] B. Prashansa, P. K. S. Chinamalli and R. Yanamshetti, "Digital Control Strategy for Four Quadrant Operation of DC Motor using DSPIC30F4011," *International Journal of Recent Technology and Engineering (IJRTE),* vol 3, no 1, July 2014.

[12] A. Gören, Kontrol Sistemleri Available: http://kisi.deu.edu.tr/aytac.goren/MAK3026/h5.pdf, August 2019.

Design, Manufacturing and Control of Mini-Size Rotary Swing Compressor

K. TUTUNCU[1] and S. TASAR[2]

[1] Assitant Prof. Dr., Electrical and Electronics Engineering, Faculty of Technology, Selcuk University, Konya/Turkey, ktutuncu@selcuk.edu.tr.
[2] Mechatronics Teacher, Automation Department Adil Karaagac Technical High School, Konya/Turkey, selmantsr@hotmail.com

Abstract - **Today, it is possible to find many types of compressors according to the manufacturing capacity and size. However, the diversity for mini-size compressors is drastically reduced. It causes serious problems for small systems where compressed air is needed. In this study, design and manufacturing of a mini-size rotary swing type compressor were carried out in order to contribute to the solution of the related problem.**

In the phase of design, the value of pressure to be created by the compressor and the energy to be consumed by it were calculated. After the manufacturing was carried out by using industrial counters, various pressure experiments were performed on the compressor. As a result of the experiments carried out by using brushless DC motor and semi-hermetic tank at 4000 rpm, the compressor operating with 23,7% efficiency created 6 bar pressure by consuming 120 W power.

The compressor manufactured for small systems will be able to be used easily in various sectors that can work up to 6 bar pressure. By changing the piston size without changing the compressor size, high pressures such as 12-13 bar will be obtained and it will be possible to be used in many sectors including cooling systems.

Keywords – **Compressor, rotary, swing, power, cooling, efficiency**

NOMENCLATURE

DC	: Direct Current
BLDC	: Brushless Direct Current
KW	: Kilowatt
V	: Volt
T	: Temperature (C°)
R	: Ideal gas constant for air (0,287 kJ/kgK)
k	: The ratio of specific heat (1,4)
F	: Force (Newton)
M	: Motor Torque (Nm)
S	: Surface Area (cm2)
P	: Pressure (bar)
h	: Height (mm)
x	: Eccentric Runout (mm)
fs	: Service Factor (1,30)
d	: Moment Length (mm)
r	: Radius (mm)
η	: Efficiency (%)
$\dot{m}$	: Mass Flow Rate (kg/s)
Wmeasured	: Measured Power (W)
$\dot{W_s}$	: Isentropic Power (kW)
n	: Revolutions per Minute (rev/min)
v	: Volume (cm3)
ρ	: Density of flow material (kg/m3)
w_s	: Isentropic Work per Unit Mass (kj/kg)

I. INTRODUCTION

Today, we use compressed air-generating systems both in industrial and many personal fields. Compressor is named after the word compression and is called the gas compressing machine. Compressors are devices that provide the flow of gas with the force applied against pressure and convert mechanical energy to pneumatic energy [1].

According to compression mechanisms, compressors can be examined under 5 titles as piston, rotary, screw, scroll and turbo [2]. Rotary compressors obtain the power required to perform the process of compression by means of single or multiple rotating eccentric shafts. The process of compression is carried out as intermittent due to the nature of the rotary compressors. However, the fluctuation of the intermittent flow is almost ignored as if there is a continuous flow due to the frequency of compression periods [3].

There are three types of rotary compressors:

- Rotary piston

- Sliding valve

- Swing

The principle of compression of the rotary piston compressors is based on the shaft movement and the out-of-axial movement of the piston on the eccentric shaft. While the rotary piston rotates by touching the circumference of the cylinder with the out-of-axial movement, the wing makes the compression of the fluid. In this type of compressor, the lift and force chambers are separated with the help of the spring-loaded dividing wing. The working principle of the sliding valve type compressors is as follows; wings more than one ensure compression of the cooling fluid by touching the

circumference of the cylinder with a rotary piston. The working principles of rotary piston compressors and sliding valve compressors are shown in Figure 1.1 [2].

Figure 1.1. Rotary piston compressors and sliding valve
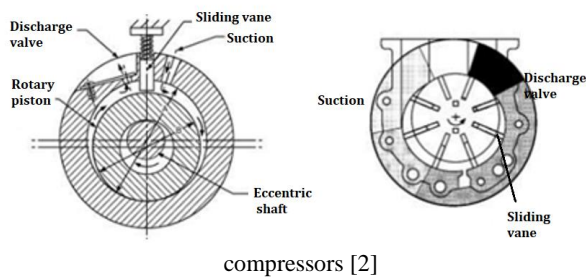
compressors [2]

These two types of rotary compressors don't have suction valves and the fluid inlets are continuous. Therefore, their vibration is less than other types of compressors. It contains less parts compared to piston compressors. Although this may seem to be an advantage, the components in the rotary compressor must be manufactured with high precision to prevent wear. This increases the cost of manufacturing of components. Piston rotary compressors, the most commonly used among rotary compressors, are gradually being replaced by swing type compressors nowadays [2].

The cross-sectional view of a swing compressor is given Figure 1.2. Rotation of the shaft causes the piston to move eccentrically. The piston compresses the gas taken from the suction chamber in the compression chamber by the out-of-axial movement and discharges it from the force chamber. The piston must be supported with brushes and piston rod so that it can make the necessary linear and rotational movement [4].

Figure 1.2. Cross-sectional view of swing compressor [4]
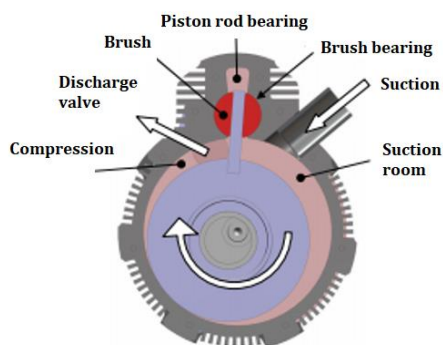
In this study, design, manufacturing and control of rotary swing compressor were carried out. The design of the components required for the mini rotary swing compressor was made using a computer-aided drawing program. The designed components were manufactured with the help of industrial counters, the necessary experiments were performed and the results were analysed.

II. LİTERATURE REVİEW

In the study performed by Masuda et al. (1996), calculations related to the durability and performance of swing compressors were made and compared with the experimental results. Durability and performance tests were performed using alternative refrigerant gasses (R134a, R32/ 134a and R410A). In the performance and leakage tests, a yield of 2% to 9% was obtained [5].

In the study conducted by Bayir (2008); capacity and efficiency of scroll and piston type compressors were compared according to working conditions and hermetic and semi-hermetic conditions. It was concluded that the losses in the volume of suction caused by increasing pressure in piston compressors are higher than scroll compressors and that increasing pressure of evaporation and compressor power remain constant in scroll compressors while it is leading to increasing amount of power required in piston compressors. Scroll compressors have high efficiency at low pressure ratios, and as the ratio of pressure increases, the efficiency decreases while the piston semi-hermetic compressors are efficient as the ratio of pressure increases [6].

Sahin (2011) examined the impact of dead storage on the performance of compressor in hermetic compressors in his master's thesis. He stated that the impact of the refrigerant gas (dead storage) that cannot be supplied to the system in the compressor is great on the performance. In this study, the performance values of the compressor were investigated experimentally. It was concluded that the performance values decrease as the amount of dead storage increases in the compressor piston and the performance values increase as it decreases [7].

Hugenroth (2014) developed an oil-free rotary swing compressor for the portable oxygen concentrator used by patients in need of additional oxygen. Comprehensive analytical and experimental studies were conducted in the manufacturing of compressor. In the application of the rotary swing compressor, a power reduction of 24% was observed as well as an abatement of 24% compared to the piston compressors used in previous systems. In addition, the volume level of the system was reduced by 2 db, 37% in other words [4].

In the study of Ma et al. (2016), mathematical modelling of the design was performed to optimize the energy efficiency of the double-wing rotary swing compressor. Optimum structural parameters were determined on the basis of modelling results by significantly reducing loss of friction of the optimized compressor. Accordingly, if the rotor diameter is 42,4 mm, the rotor length is 46,2 mm and the wing length is 20,3 mm, the efficiency was found to reach 0,8757 [8].

In the study conducted by Cakmak (2017), evaluations were made about the exergy yields of scroll and semi-hermetic piston compressors. In the evaluations made, it was determined that the use of scroll compressors in climatic conditions and semi-hermetic piston compressors in colder climatic conditions yield more efficient results [9].

In the study done by Xu Yang et al. (2017); the working principle of the newly designed oscillating rotary compressor was introduced. In this new compressor, centrifugal force was used to separate the oil and coolant in the exhaust slot unlike conventional compressors. The oil supply system allows the

use of air conditioning systems without valves. In addition, adiabatic yield of 98% was achieved [10].

In the study done by Kun Liang (2017), a compilation of linear compressors for cooling systems was presented and different linear compressor designs and models were examined. Accordingly, it was stated that linear compressors can be used easily in steam compression systems thanks to its high motor efficiency and small size. It was concluded that the efficiency reaches 90% in compressors using brushless DC motors, but gets behind linear compressors due to friction in crank mechanisms [11].

III. CALCULATION OF THE COMPRESSOR DIMENSIONS

In this section, the compressor dimensions required to manufacture at 6 bar pressure were determined. The volume of the compressed air that the pistons in the compressor sends to the hermetic tank at each revolution and the motor torque directly affect the pressure value to be created. Calculations were made considering that the motor to drive the compressor has a torque value of 0,18 Nm.

In the rotary swing compressors, the rotation of the shaft causes the piston to move eccentrically. The piston compresses the gas taken from the suction chamber in the compression chamber by the out-of-axial movement and discharges it from the force channel. The piston must be supported with brushes and piston rod so that it can make the necessary linear and rotational movement [4].

Considering that the motor used is at constant torque, the pressure value can be increased by changes to the surface area where the piston applies force. In this context, the calculations required to reach a pressure value of 6 bar are given below.

Problem Inputs:
M : Motor Torque (Nm)
S : Surface Area (cm2)
P : Pressure (bar)
h : Height (mm)
x : Eccentric Runout (mm)
fs : Service Factor (1,30)
d : Moment Length (mm)

When calculating the surface area where the pressure has an impact on, eccentric runout and piston height were utilized. The piston height and the eccentric runout were respectively determined 8 mm and 3 mm here. In this case, the surface area was calculated in (2) using the equation in (1).

$$S = h \times x \tag{1}$$

$$S = 8mm \times 3mm = 24mm^2 = 24 \times 10^{-6} m^2 \tag{2}$$

Using the moment formula in (3), the force applied by the motor to the surface was calculated in Newton in (4). Here, the torque length was taken as 11 mm.

$$F = \frac{M}{d} \tag{3}$$

$$\frac{0,18Nm}{0,011m} = 16,36N \tag{4}$$

By using the equation (5) with obtaining the force and surface area, the expected pressure value was calculated in bar in (6).

$$P = \frac{F}{S} \tag{5}$$

$$\frac{16,36N}{24 \times 10^{-6} m^2} = 0,681 \times 10^6 \frac{N}{m^2} = 6,81bar \tag{6}$$

If the service factor is included in the calculations, the minimum pressure value to be obtained at ambient temperature was found in (7).

$$\frac{P}{fs} = \frac{6,81bar}{1,15} = 5,92bar \tag{7}$$

Considering the piston diameter (22 mm), piston bearing diameter (25 mm) and piston bearing height (8 mm), the volume of compressed air generated at each revolution was calculated in (9) by using the equation (8).

$$Piston\_yatak\_hacmi - Piston\_hacmi$$
$$= (\pi \times r_1^2 \times h_1) - (\pi \times r_2^2 \times h_2) \tag{8}$$

$$(3,14 \times 12,5^2 \times 8) - (3,14 \times 11^2 \times 8)$$
$$= 3925mm^3 - 3039mm^3 = 0,885cm^3 \tag{9}$$

Since there are 2 pistons in the compressor, 1,77 cm3 of compressed air is generated at each revolution. As result of the rotation of the motor at 4000 rpm, the amount of air generated per minute was found in (10).

$$1,77 \times 4000 = 7080cm^3 = 7lt \tag{10}$$

IV. PHASES OF DESIGN AND MANUFACTURING

The compressor to be planned to be manufactured was designed to be 53 mm in diameter and 57,7 mm in length using the computer-aided drawing program (Solidworks 2013). After the motor connection was made in the design, if

the shaft lengths and coupling are considered, the total length of the compressor was 187 mm. After the design was completed, it was manufactured by using industrial counters. When the final product appeared, the motor was checked and placed in the hermetic tank and the test setup was made ready.

A. Phase of Design

There are three products that should be used in the manufacturing of compressor and are procured from the market in standard sizes. These are the oil seal used for sealing, coupling and compressor-driving motor. Other parts were designed using the computer-aided drawing program (Solidworks 2013).

Vibration and oscillation in compressors should be kept at a low level. In single-piston rotary compressors, fixed load is connected to the motor rotor in the opposite direction of the piston movement to prevent vibration. In this way, the balance to be formed can be minimized. In this study, two pistons that move as opposed to each other on a single body were used in order to prevent the balance and increase the efficiency. These two pistons on the body were completely insulated from each other and worked as two separate compressors. The only point where these two pistons are connected to each other was the eccentric shaft. Considering all these specifications, body, eccentric shaft, piston and reed valve were designed.

The compressor was designed to consist of five body elements for ease of manufacturing. These elements are respectively the sealed rear cover, the part with the first piston, the central part providing the insulation of the two pistons, the part with the second piston and the sealed front cover. The wall thickness of each part is 8 mm. Technical drawings of the body elements are given in Figure 1.1.

Drawing of the compressor designed is given in Figure 4.1.
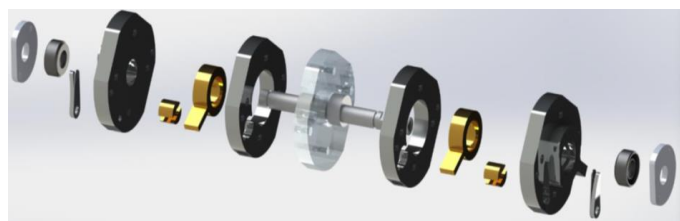
Figure 4.1. Body elements of the compressor

Ready-supplied oil seals have a domino effect in determining the compressor component dimensions in our design. The inner diameter of the oil seal provided the determination of the camshaft diameter (8 mm) and the outer diameter provided the determination of the piston diameter (22 mm). The emergence of the outer diameter of the piston was effective in determining the air ducts to be sent to the tank, so the part where the reed valve is located. By determining the optimal wall thickness, the outer diameter of the piston also revealed the inner diameter of the piston (14 mm) and eccentric movement revealed the diameter of the shaft (14 mm). In addition, the bearing diameter of the piston (25 mm) and the external dimensions of the compressor (Ø53 mm) were determined with the determination of the volume of

compressed air (1,77 cm3) that the compressor sends to the tank. While determining all these dimensions, it was considered that the compressor occupies the least space and that the precision faults that may arise during manufacturing are minimized.

B. Phase of Manufacturing

In order to minimize friction and unnecessary voids in the manufacturing of the compressor parts whose 3-D solid modelling is completed, manufacturing with a tolerance of error between 0.2% - 0.5% was realized.

Cold work steel with DIN 1.2379 quality cementation was used due to the low coefficients of friction and of expansion in the manufacturing of compressor block and moving parts inside it (piston, metal brushes, eccentric shaft).

Body blocks, pistons, eccentric shafts and metal brushes were cut from a single piece of steel block with a wire-erosion machine in order to avoid the difference in thickness between the parts. The compressor parts obtained after the process of cutting are given in Figure 4.2.
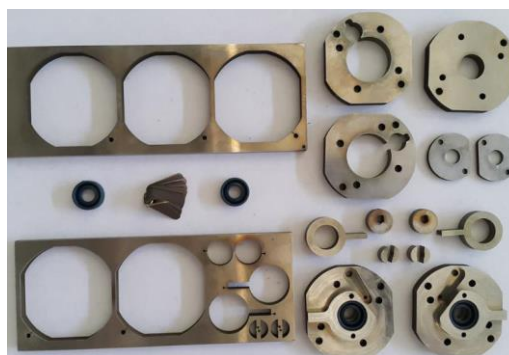
Figure 4.2. Compressor parts after the process of cutting

Piston and metal brushes

Piston and metal brushes processed with 5-micron precision were coated with 10-micron titanium using PVD technique because they are seen as insufficient due to surface roughness and heat that may arise. The specifications of titanium are given in Table 4.1 and the products manufactured are given in Figure 4.3.

Figure 4.3. Piston and metal brushes coated with titanium

Table 4.1. Specifications of the titanium coating used

Colour	Golden yellow
Hardness	200-2300 HV
Thickness	7-10 micrometers
Coefficient of Friction	0,6
Surface roughness	0,2

Eccentric shaft

The eccentric shaft was machined in 6 pieces with CNC wire erosion machine in line with the possibilities. Then, these parts were combined with laser welding and an eccentric shaft was obtained. It was determined in the measurements that the manufacturing was performed with 2% accuracy. The eccentric shaft manufactured is given in Figure 4.4.

Figure 4.4. Eccentric shaft

Reed valve (flap)

Three different experiments were performed during the application phase of the compressor. In these experiments, 0.10 mm, 0.20 mm and 0.40 mm thick sheets were used to ensure that there is no air leakage problem caused by the Reed valve. Because the opening and closing time of the valves varies with values such as the hardness and thickness of the sheet to be used and its distance from the point of connection. In this direction, it was determined that there is no air leakage when using 0.40 mm sheet thickness reed valve. The reed valves manufactured are given in Figure 4.5.

Figure 4.5. The reed valve manufactured

Semi-hermetic tank

After the manufacturing of rotary swing compressor, design and manufacturing of the semi-hermetic tank were carried out in order to perform the experiments. In the phase of manufacturing, CK-45 manufacturing steel was used.

A connection was provided with connection screws from 6 points for the sealing of the tank. A general purpose NBR oring (nitrile oring) with 3 mm diameter that is resistant to oil

and grease was used on the joint surface of the tank consisting of 2 parts. The processed version of the semi-hermetic tank is given in Figure 4.6.

Figure 4.6. Semi-hermetic tank

After all these processes, compressor parts were combined and placed in the tank and manufacturing was completed as shown in Figure 4.7.

Figure 4.7. Compressor and motor placed in the semi-hermetic tank

Control of the motor

Among the types of brushless DC motor (BLDC), 42BLF-03 series was used for this study. This model works with 24 V. While it rotates at 5000 rpm in case of no load, it rotates at 4000 rpm in case of load. The main reason for preferring can be said that it is long life, silent, low volume and can go up to high speed. The operating values of the preferred motor are given in Table 4.2.

Table 4.2. Specifications of the preferred BLDC motor (42BLF03)

Nominal voltage(V)			24
Input Voltage(V)	Peak Current(A)	Nominal Current(A)	Temperature(ºC)
20V-50V	30A	15A	0-50 ºC
No-load speed(rpm)			5000
Nominal current(A)			0,47
Load speed(rpm)			4000
Nominal torque(Nm)			0,18
Peak current(A)			18
Mechanical power (W)			78

BLDC-8015 series driver was used to control the BLD motor selected for the semi-hermetic compressor experiment. Speed control is also possible with this driver. Specifications of the driver are given in Table 4.3.

Table 4.3. Specifications of the preferred BLDC motor driver (BLDC-8015)

8 cables from the BLDC motor placed in the semi-hermetic tank were carried out of the tank by a circular connector. In this way, the air trapped inside the tank was prevented from leaking out. After making the supply and driver connections of the BLDC motor, the test setup was made ready by placing the motor and compressor into the semi-hermetic tank as shown in Figure 4.8.
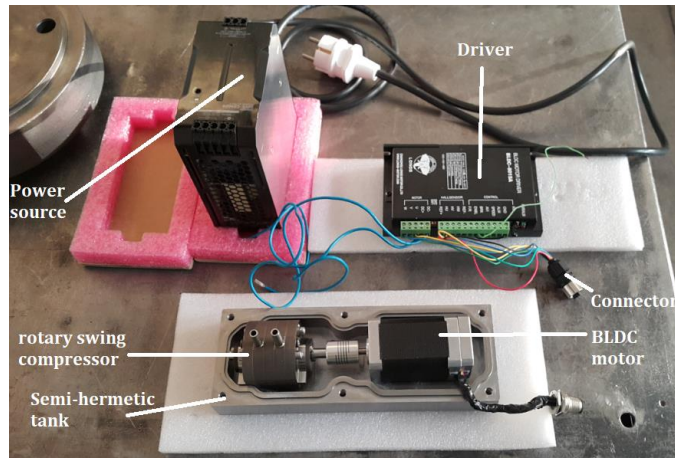
Figure 4.8. Test setup of the semi-hermetic compressor

V. DATA ANALYSIS

In this section, the data obtained from the experiments performed on the compressor manufactured were examined and compared on the graphs.

Pressure values ranging from 5.5 to 6.5 bar were read on the pressure sensor when the current drawn by the motor used to drive the compressor was at 5 A.

The fact that the eccentric shaft was manufactured with 2% accuracy greatly affected the accuracy in eccentric runout. The leakage occurred in the pistons with reaching 6 bar that was the expected value of pressure according to the calculations. Therefore, there were changes in pressure values according to torque and speed of the motor. These changes are given in Figure 5.1.
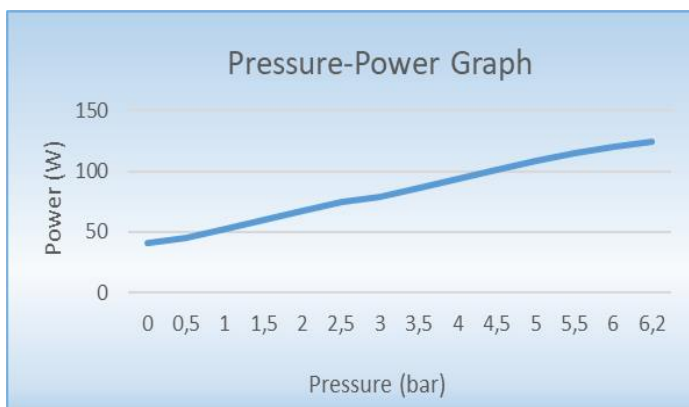
Figure 5.1. Pressure-motor speed graph obtained in the phase of experiment

In the power analysis, while the motor rotates at 4000 rpm, the current drawn increases as the pressure value increases. As

shown in Figure 5.2, the motor that consumes 120 W of power creates compressed air between 5.5 and 6.5 bar.
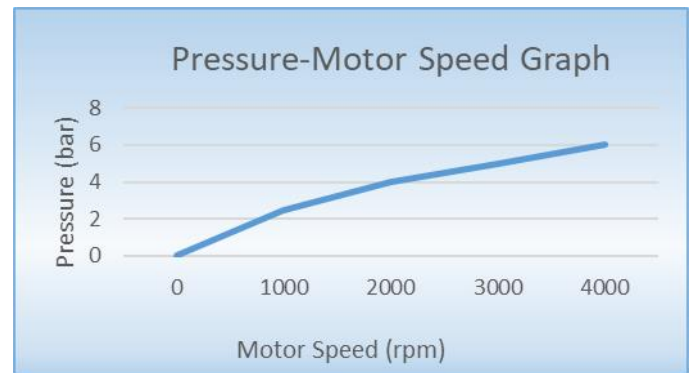
Figure 5.2. Pressure-power graph obtained in the phase of experiment

A. Calculation of Efficiency

In the light of the data obtained in this section of the study, the efficiency of the compressor at 4000 rpm was calculated. Since the temperature of the compressed air created by the compressor couldn't be found, the inlet and outlet pressures were used according to the isentropic ideal gas relation.

Isentropic work or power is something calculated according to the assumption that the compression process of a compressor is performed without increasing the entropy. If air is accepted as ideal gas; the temperature and pressure of the air in the working range allow for this assumption; then, isentropic work for the unit mass can be calculated using the equation (11). k represents the ratio of specific heat and R represents the ideal gas constant for air. The temperature T2 is not known here because this temperature must be read from within the volume of compression. Instead, the temperature T2 is written in terms of the temperature T1 using the ideal gas relations. This process is shown in the relation (12) [12].

$$w_S = \frac{k \times R \times (T_2 - T_1)}{k - 1} \tag{11}$$

In the relation (12), there is no T2 in the part in the right side of the equation and all other parameters are known. Therefore, the isentropic work is calculated as in the relation (13) [12].

$$w_S = \frac{k \times R \times (T_2 - T_1)}{k - 1} = \frac{k \times R \times \left[T_1 \left(\dfrac{T_2}{T_1} - 1 \right) \right]}{k - 1}$$

$$= \frac{k \times R \times T_1}{k - 1} \times \left(\frac{T_2}{T_1} - 1 \right) = \frac{k \times R \times T_1}{k - 1} \times \left[\left(\frac{P_2}{P_1} \right)^{\frac{k-1}{k}} - 1 \right] \tag{12}$$

$$w_s = \frac{k \times R \times T_1}{k-1} \times \left[\left(\frac{P_2}{P_1} \right)^{\frac{k-1}{k}} - 1 \right]$$

$$= \frac{1,4 \times 0,287 \frac{kj}{kgK} \times 298K}{1,4-1} \times \left[\left(\frac{600 kPa}{101,325 kPa} \right)^{\frac{0,4}{1,4}} - 1 \right] \quad (13))$$

$$= \frac{119,7364}{0,4} \times \left((5,92)^{0,285} - 1 \right)$$

$$= 299,34 \times 0,66 = 197,56 \frac{kj}{kg}$$

Note that the unit obtained from the relation (13) is the work-per-mass value and the work at the unit time must be determined to obtain the power value. Therefore, if the values obtained from the relation (13) with the mass flow value are multiplied, the power value is calculated. The relation (14) is used to calculate the mass flow [13].

$$\dot{m} = n \times v \times p \quad (14)$$

The mass flow rate calculated for the motor speed of 4000 rpm is given by (15). If the mass flow obtained by the equation (15) is multiplied by the work per unit mass obtained by the equation (13), isentropic compressor power in (16) is calculated [13].

$$\dot{m} = 66,66 \frac{devir}{sn} \times 1,77 \times 10^{-6} m^3 \times 1,225 \frac{kg}{m^3} \quad (15)$$

$$= 0,0001445 \, kg/s$$

$$\dot{W}_s = \dot{m} \times w_s = 28,55W \quad (16)$$

In the formula (17), the concept of efficiency is defined for the compressor. When the isentropic power calculated by the measured compressor power is replaced in the equation (17), the efficiency value of the compressor expressed in the equation (18) is obtained.

$$\eta = \frac{\dot{W}_s}{W_{ölçülen}} \quad (17)$$

$$\eta = \frac{28,55W}{120W} = \%23,7 \quad (18)$$

Accordingly, the efficiency of the BLDC motor used to drive the compressor is calculated as 23,7% since it consumes 120 W of energy while rotating at 4000 rpm.

VI. CONCLUSION AND RECOMMENDATIONS

In this study, design and manufacturing of the rotary swing compressor that can be used for mini systems and creates 6 bar pressure were carried out. The dimensions required for the compressor for 6 bar pressure value were determined with the calculations made in the phase of design. A compressor that consumes 120 W power and creates 6 bar average pressure was obtained with the manufacturing in this direction. Efficiency of the compressor was calculated as 23,7% in the creation of 7 l compressed air per minute.

Excluding eccentric shaft in the phase of manufacturing, other parts were manufactured with 0,5% accuracy. The eccentric shaft was manufactured with 2% accuracy. The fact that the eccentric shaft was not manufactured with sufficient accuracy caused leakage after a certain pressure. It will be possible that the compressor rises to higher pressures at low speeds with an eccentric shaft to be manufactured with 0,3% accuracy.

The compressor manufactured can be used easily in pneumatic systems that need low pressure due to its silent operation and small dimensions. However, manufacturing should increase to 11-12 bar for high pressure cycles such as refrigeration systems. For this, it is necessary to reduce the amount of compressed air created per unit time, i.e. the surface area on which the pistons act. Accordingly, there is a need for special production cast moulds and accurate eccentric machining counters in order to transfer the desirable accuracy and measurements to manufacturing without any problem.

The reducer to be used both for the existing compressor being manufactured and for the compressor to be able to be manufactured in new dimensions will provide high pressures with the energy consumed and thus increase the efficiency. In this way, a mini compressor with low power consumption and a wide range of usage will be obtained.

REFERENCES

[1] Sarıibrahimoğlu, K., Hermetik kompresörler için ileri yatak malzemeleri geliştirilmesi, İstanbul Teknik Üniversitesi Fen Bilimleri Enstitüsü, İstanbul, Turkey,2009.

[2] Arslan, A.E., Toprak kaynaklı ısı pompası ile doğal gazlı kombi birleşik sisteminin enerji verimliliği yönünden araştırılması, Trakya Üniversitesi Fen Bilimleri Enstitüsü, Edirne, Turkey,2014.

[3] Brown, R.N., *Compressors: selection and sizing*. Gulf Professional Publishing. Unites States of America, 1997.

[4] Hugenroth, J.J., Oil-Less swing compressor development, *International Compressor Engineering Conference*, *Louisiana USA*. (2014), pp. 1668,1-10

[5] Masuda, M., *et al.*, Development of swing compressor for alternative refrigerants, *International Compressor Engineering Conference*. (1996),

[6] Bayır, E.,S. Küçüka, Scroll ve pistonlu tip soğutma kompresörlerinin kapasite ve verimlerinin çalışma şartları ile değişimi, Dokuz Eylül Üniversitesi Fen Bilimleri Enstitüsü, İzmir, Turkey,2008.

[7] Şahin, Ç., Hermetik kompresörlerde ölü hacim miktarının kompresör performansına etkisinin incelenmesi, İstanbul Teknik Üniversitesi Fen Bilimleri Enstitüsü, İstanbul, Turkey,2011.

[8] Ma, J., *et al.*, Optimal structural design of swing double-vane compressor, *International Compressor Engineering Conference*. (2016), pp. 1468,1-9

[9] Çakmak, Ç., Pistonlu ve scroll tipi kompresörlerin soğutma performansının karşılaştırmalı enerji ve ekserji analizi, Bilecik

Şeyh Edebali Üniversitesi Fen Bilimleri Enstitüsü, Bilecik, Turkey,2017.

[10]   Yang, X.*, et al.*, Design and dynamic analysis of a novel double-swing vane compressor for electric vehicle air conditioning systems*, International Journal of Refrigeration*, *76*. (2017), pp. 52-62

[11]   Liang, K., A review of linear compressors for refrigeration*, International Journal of Refrigeration*, *84*. (2017), pp. 253-273

[12]   Çengel,   Y.A.,M.A.   Boles,   *Termodinamik-Mühendislik yaklaşımıyla*. Palme yayıncılık. İzmir, Turkey, 2013.

[13]   Çengel, Y.A.,J.M. Cimbala, *Akışkanlar mekaniği temelleri ve uygulamaları*. Güven bilimsel. İzmir, Turkey, 2008.

Segmentation of Capillaroscopic Images

K. TUTUNCU[1] and M. BUBER[1]

[1] Selcuk University, Konya/Turkey, ktutuncu@selcuk.edu.tr
[1]Selcuk U
niversity, Konya/Turkey, mbuber@selcuk.edu.tr

Abstract- **Capillaroscopy device shoot videos of capillaries of oral mucosa and nailfold of patient over the related skin without any pain. The image frames of videos are used by experts for early detection or treatment of some diseases such as diabetics, rheumatism and etc. Since this process is implemented in manually, decision support systems that helps the experts for diagnosis have been subjects of studies of biomedical researches. First step of these systems is the successful segmentation process on these images that will be used for classification of disease depending on 8 parameters such as the number of capillaries in a certain area, the distance between the two vessels, the size of the capillaries and etc. This study aims to contribute decision support system for experts by presenting a successful segmentation. In this study Otsu, Fuzzy C-mean, Fast Marching, Region Growing and H-Minima methods have been used for segmentation of capillarocopic images. The segmentation accuracy ratios of upper mentioned methods were obtainedas %80,47, %67,44, %63,23, %44,11 and 96.76%, respectively. When the results were examined, it was observed that the H-Minima method, which had not previously been applied in capillary images, reached the highest accuracy parameter value.**

Keywords: Image Processing, Capillaroscopy, Capillary Video, Capillary, Segmentation, H-Minima Method.

I. INTRODUCTION

Image segmentation is a very challenging problem that needs to be specifically designed according to the application area. The success of algorithms developed for this purpose also depends largely on the correct identification of similarity criteria used for zone homogeneity. Image segmentation techniques are often classified as threshing-based, edge determination, region-based, and clustering-based techniques [1-3].

Image segmentation, which is used in many fields, is also heavily used in the medical field and is of great importance in the diagnosis and treatment of many diseases [4]. The tests performed with a capillaroscopy device are one of these samples. Capillaroscopy is the process of taking pictures or video images of capillaries with the help of a device. With these images, capillaries are examined and changes in veins can be a precursor to some diseases. In particular, nailfold capillaroscopy makes it easy to diagnose rheumatological and diabetic diseases [5].

II. LITERATURE REVIEW

Tama et al. (2015) conducted a study to measure morphological parameters for each capillary by image processing. Morphological parameters were determined by preprocessing, dualization, skeletal (skeleton) inference and skeletal (skeleton) segmentation. These parameters are the width of the capillary, the height of the capillary, the morphology of the vascular nodes, the width of the terminal nodes, the calibre and the curvature. With the application they developed, up to 96% sensitivity was achieved in the automatic measurement of all parameters [6].

Vucic (2015) in his thesis work used the support vector machine method as an image processing technique, resulting in an accuracy parameter of 92% [7].

Bellavia et al. (2014) prefixed images with wavelet analysis and mathematical morphology. Later they applied segmentation in order to minimize in-class lighting value differences of capillary and background images. Mean sharpness, mean recall and Jaccard index were calculated as 0.924, 0.923 and 0.858, respectively [8].

Isgrò et al. (2013) also performed segmentation on sequential videos of capillaries at the tip of the nail. First, rough segmentation was applied, then a series of automatic thresholds were passed and a segmentation map was drawn with the STAPLE algorithm. The accuracy, sensitivity and authenticity parameters compared to manually segmented images were obtained as 97%, 96% and 98% respectively [9].

Goffredo et al. (2012) developed a new method for parsing the color field in digital nailfold bottom capillaroscopy analysis. The threshold values of the image were determined using Otsu technique and 7x7 median filter. In nailfold capillary images, segmentation is indicated to have the highest performance predictably in the green channel. As a result, values of 75~87%, 85~90% and >80% were found for sensitivity, authenticity and accuracy parameters, respectively [10].

Kwasnicka et al. (2007) presented a preliminary study of the use of automatic note insertion methods for computer aided diagnosis and analysis of capillary images. In summary, capillary images were taken, their features were removed, these features were processed with a predefined note splitter and they obtained an automatic note spliced capillary image. As a result of the study, five separate images were obtained. A total of six images were created with the first image passed through the Gaussian filter. These images were applied grid segmentation to create all regions together with the segmentation. After that, automatic note insertion system was applied to images using multiple class machine learning, balanced average and continuous relevance model. As a result of this application, the accuracy parameter value was obtained as 77% [11].

Riaño-Rojas et al. (2007) conducted a study to infer

segmentation and morphological features in nailfold capillaroscopic images. To segment images, the Laplace and commitment threshold of the most contrasting component in each color space have been added. Morphological feature inferences were obtained by using PCA (Principal Components Analysis), fractal geometry and tortuosity index techniques. The accuracy parameter value was calculated between 88~91%. [12].

III. MATERIAL

The intra-oral capillaroscopic images used in this study was obtained from the authors of the study of (Bellavia et al., 2014) "a non-parametric segmentation methodology for oral video-capillaroscopic images". They had ethics permission (Comitato bieoetico Dell'azienda ospedaliera Policlinico di Palermo. Verbale n.5/2012 del 16/05/2012.) for these images [13]. Necessary correspondence was provided with them and images were obtained. Additionally for this study, a GUI (Graphical User Interface) and software were implemented by using MathWorks tools of Matlab (Matrix Laboratory) package to provide segmentation of images and to make comparisons with previous studies.

IV. METHOD

In this study, previously obtained images were transferred to the developed software by MATLAB. Then the images were segmented with Otsu, Fuzzy C-mean, Fast Marching, Region Growing and H-Minima methods. The accuracy parameter ratios of the methods applied by the expert were subsequently determined by the hand segmented images (Ground Truth). The stages of this practice are as follows;

- Retrieval of the image to be processed by the software,

- Choice of method to be applied,

- Processing the image segment,

- Detection of vessel edges-boundaries by software

- Comparison of segments performed by expert and system for calculation of accuracy and other parameter values.

A. Otsu Method

This method introduces a nonparametric and unsupervised automatic threshold selection method for image segmentation. To maximize separability of the resulting classes at Gray levels, the optimal threshold is chosen by the distinguishing criterion. The procedure is very simple, using only the zero and first order cumulative moments of the gray-level histogram to perform the segmentation process. It is easy to extend the method to multivariate problems. Various experimental results have also been presented to support the validity of the method [14].

B. Fuzzy C-Mean Method

A pioneering application of fuzzy sets theory to cluster analysis was carried out by Ruspini in 1969. Until 1973, Dunn and Bezdek's work on the Fuzzy ISODATA (or fuzzy c-tool) method played an important role in the theory of cluster analysis. The important issue regarding the convergence of such methods is better understood as a result of the recent studies described in the monograph [15].

C. Fast Marching Method

FMM (Fast Marching Method) was first introduced to find numerical approximations of solutions to the stationary eiconal equation. More generally, it shows that this method allows to find solutions of numerical schemes that satisfy a definite causality conjecture. To apply this method, by presenting the shape from the shading problem, they introduced the concept of viscosity solutions in the stationary eiconal equation and took into account finite difference schemes. They also presented various comparison principles for ecological equations and schemes [16].

D. Region Growing Method

In areas such as computer image processing, image segmentation has been and is still a relevant area of research due to its widespread use and application. Image segmentation and the use of techniques in different areas have explored a review of achievements, problems encountered and open issues in the field of research. The researchers in [17] considered techniques under three groups; threshold-based, Edge-based, and Zone-based. Zone growth is an approach to image segmentation in which neighboring pixels are examined and added to a zone class if no edge is detected. This process is repeated for each border pixel in the region. If adjacent regions are found, a zone join algorithm is used where weak edges are dissolved and strong edges are left in tact. This method is very stable in terms of noise [17].

E. H-Minima Method

This method is applied before the watershed segmentation is carried out. H-minima transform is the method proposed to replace the Wolf pruning [18]. H-minima transform suppresses all regional minima in I, whose depth is less than or equivalent to H. I is the areal surface topography dataset, while H is the height threshold value (non-negative scalar) [19]. Besides, regional minima are connected components of pixels with the same dataset value, t, whose external boundary pixels all have a value greater than t [20]. To eliminate all regional minima, except the significant minima, H-minima transforms can be applied to specify a height threshold value by using the following equation:

$$H = N*Z \tag{1}$$

Where:

H = height threshold value

Z = maximum height from mean plane

N = percentage from maximum height (%)

From the Equation 1, it is observed that height threshold value depends on N (percentage of maximum height). The value of N depends on the irregularities of the measured surface topography data (~5%-20%). H-minima transform only affects the regional minima; as none of the other pixel values is changed. The significant minima remains, although their heights are increased. Moreover, the size of the significant

minima tends to increase and the number of regional minima decreases. Figure 1 shows the overview of H-minima transform function applied on the structured surface.
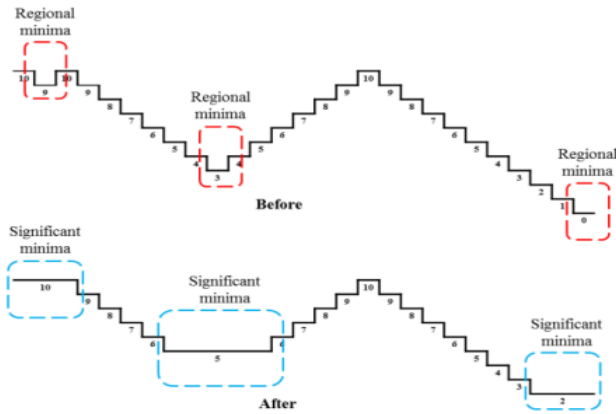
Figure 1. Overview of H-minima transform algorithm for 1-dimensional diagram. [21].

Before application of H-minima transform, numbers 9, 3, and 0 (inside the dotted red box) were the regional minima. For number 9, its depth was 1 (from 9 to 10), while for number 3, its depth was 7 (from 3 to 10), and for 0, its depth was 10 (from 1 to 10). For example, by taking 20% of the maximum height, the height threshold value becomes 2 (also called as depth). After the application of the H-minima, the result showed that H-minima transform removed all the regional minima, which were insignificant with depth smaller or equal to 2, and increased the height of the regional minima by 2. As per figure display, before and after application of H-minima transform, the regional minima (9, 3, and 0) are merged with the adjacent minima to become significant minima. Hence, all regional minima that had been less significant were transformed by 'flattening out' any insignificant regional minima into the required significant minima. Thus, H-minima transform is defined as the reconstruction by erosion of f, and increased by a height, H as in the Equation 2 [22-23]:

$$\text{Hmin}_H \, (f) = R_{\cdot f}(f + H) \qquad (2)$$

Where:

$\text{Hmin}_H \, (f)$ = H-minima transform

$R_{\cdot f}(f+H)$ = reconstruction by erosion of f increases by height threshold H

F. Segmentation Flowchart

The flow diagram of the segmentation algorithm performed in this study is presented in Figure 2. Looking at the flow diagram, it is seen that the algorithm consists of three stages. The first stage is the processing of the image. At this stage, the capillaroscopic image is first uploaded to the program. The contrast values of the image are improved at the desired level and the external background images of the image to be processed are removed. The second phase involves filtering and converting. Firstly, the average filtration of the filtered image is implemented at this stage, and it is converted to the image to be processed by Otsu, Fuzzy C-mean, Fast Marching, Region Growing and H-Minima methods. In the third and final stage,

the thresholds of the vessels in the image are subtracted and the vessels are determined.
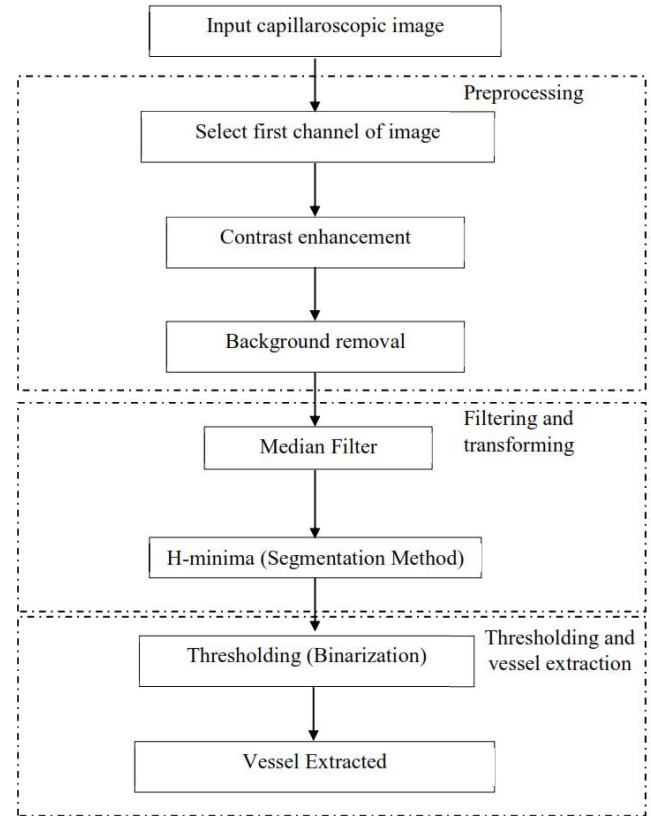
Figure 2: Segmentation flow diagram

V.　Research Results and Analysis

The accuracy parameter ratios were compared with the segmented image obtained by the expert by applying Otsu, Fuzzy C-mean, Fast Marching, Region Growing and H-Minima methods. It should be noted here that H-Minima method has not been used in the studies of capillaroscopic image segmentation. After applying the segmentation methods, determination of the method with the highest accuracy parameter ratio was performed. In addition, the original images, each hand-segmented by the expert, were divided into 16 equal parts. Then, 5 methods were applied on the pictures in 1/16 scale. The accuracy parameter ratios were averaged and compared with the results obtained by application of same methods on full scale images.

The average of the results obtained by segmenting the images in the data set for Otsu, Fuzzy C-mean, Fast Marching, Region Growing and H-Minima methods are presented in Table-1.

Table 1: Segmentation parameters on full scale images

Method	Sensitivity (%)	Specificity (%)	Accuracy (%)	Processing time (Second)
Otsu	52,8952	83,1945	80,4734	0,2063
Fuzzy C-mean	6,12879	73,39620	67,44145	9,691
Fast Marching	37,39774	65,42173	63,22977	0,112
Region Growing	81,19214	39,69065	44,11263	7,294
H-Minima	81,11151	98,43124	96,75916	0,221

Table 2 includes the values of parameters of Otsu, Fuzzy C-mean, Fast Marching, Region Growing and H-Minima segmentation methods on 1/16 scale images. The values are obtained as follows:
1) Segmentation method was applied to 1/16 scale image (dividing each image into 16 equal parts on the data set)
2) The average parameters' values of segmentation is calculated for related full scale image
3) For each full scale image step 1 and step 2 were repeated
4) Final values of segmentation parameters were calculated by taking the average of parameters obtained by step 3
5) For each of 5 segmentation method step 1 to 4 were repeated

Table 2: Segmentation parameters on 1/16 scale images

Method	Sensitivity (%)	Specificity (%)	Accuracy (%)	Processing time (Second)
Otsu	47,3226	85,7178	82,1045	0,0331
Fuzzy C Mean	31,8480	75,3284	71,4306	0,3841
Fast Marching	52,8748	62,9617	62,5182	0,0105
Region Growning	74,3036	59,8206	61,7682	0,1091
H-Minima	71,1363	97,3344	94,8380	0,0713

The worst result obtained among 1/16 scale images using the H-Minima method is shown in Figure 3.
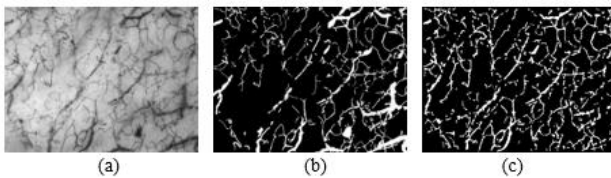
Figure 3: The worst result of the H-Minima method on 1/16 scale images; a) Original image, b) Expert hand segmentation, c) The result of the applied method

The best result obtained among 1/16 scale pictures using H-Minima method is shown in Figure 4.
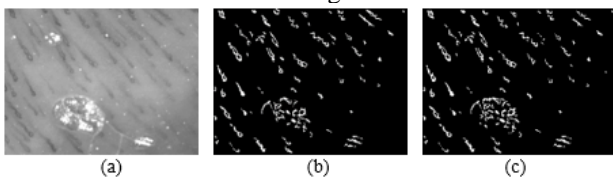
Figure 4: The best result of the H-Minima method on 1/16 scale images; a) Original image, b) Expert hand segmentation, c) The result of the applied method

A graphical comparison of the sensitivity, specificity and accuracy parameter values of the 5 segmentation methods applied on full scale images is shown in Figure 5. As can be seen from Figure 5, the highest accuracy ratio is obtained by H-Minima segmentation method.
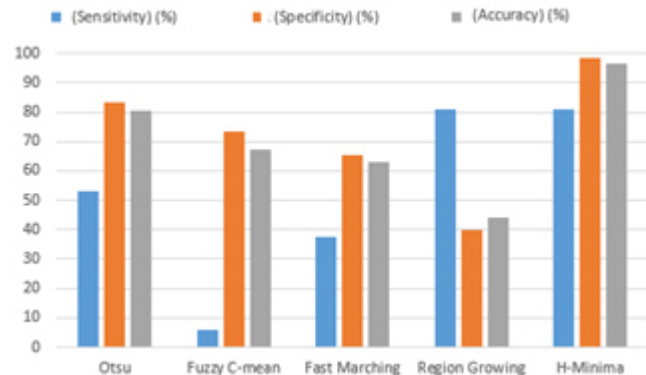
Figure 5: Comparison of all methods respect to processing time

The processing time of 5 segmentation methods is shown in Figure 6. The Fuzzy C-mean method has the maximum whereas the Otsu method has minimum processing time.
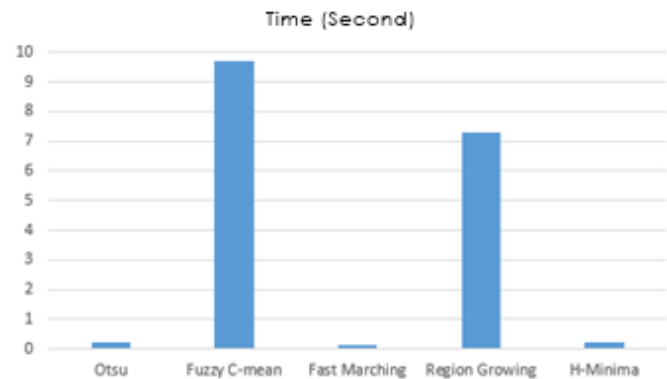
Figure 6: Processing time expenditure for all methods

VI. RESULTS

In this study, it's aimed to develop a software for segmentation of capillaroscopic images. It includes H-minima segmentation algorithm, which had not been used before in this field. This software can contribute to the infrastructure of the decision support system to be developed for the experts of diabetic and rheumatology in the early diagnosis process and also during the treatment process.

In the software that is developed in MATLAB platform, Otsu, Fuzzy C-mean, Fast Marching, Region Growing and H-Minima methods were applied separately and the following results were obtained;

- When Otsu method was applied, the diagnostic accuracy parameter was found to be 88.6725% as maximum, 73.020% as minimum, and the average value was 80.4734%.
- When the Fuzzy C-mean method was applied, the diagnostic accuracy parameter was found to be 74.5787% as maximum and 56.7998% as minimum and the average value was 67.4414%.
- When Fast Marching method was applied, the diagnostic accuracy parameter was found to be 88,135% as maximum

and 13,5143% as minimum, and the average value was 63,2297%.

- When the Region Growing method was applied, the diagnostic accuracy parameter was found to be 86,0065% as maximum and 7,6783% as minimum and the average value was 44,1126%.
- When the H-Minima method was applied, the diagnostic accuracy parameter was found to be 99,6796% as maximum and 90,9075% as minimum and the average value was 96,7591%.

The segmentation results that are performed on 1/16 scale images are as follows;

When Otsu method was applied, the diagnostic accuracy parameter was found to be 90,2347% as maximum and 67,9906% as minimum and the average value was 82,1045%.

When the Fuzzy C-mean method was applied, the diagnostic accuracy parameter was found to be 80.7386% as maximum and 66.9137% as minimum and the average value was 71.4306%.

When Fast Marching method was applied, the diagnostic accuracy parameter was found to be 86.2718% as maximum and 49.3792% as minimum and the average value was 62.5182%.

When the Region Growing method was applied, the diagnostic accuracy parameter was found to be 88,1556% as maximum and 39,6263% as minimum, and the average value was 61,7682%.

When the H-Minima method was applied, the diagnostic accuracy parameter was found to be 97.0065% as maximum and 90.77552% as minimum and the average value was 91.7412%.

When the results in Table 3 were examined, it has been seen that the accuracy parameter ratios increased for 3 of segmentation methods namely Otsu, Fuzzy C-mean and Region Growing when 1/16 scale images were used. Fast Marching and H-Minima segmentation methods have lower accuracy ratios when it comes to 1/16 scale images. This means that the there is no generalization of increase in accuracy ratio of all segmentation methods when they are applied and combined to smaller parts of an image instead of applying full scale image itself.

Table 3: Accuracy parameter ratios of segmentation on full scale and 1/16 scale images

Method	Full scale Images Accuracy (%)	1/16 scale images Accuracy (%)	Difference (%)
Otsu	80,4734	82,1045	1,6311
Fuzzy C-mean	67,4414	71,4306	3,9892
Fast Marching	63,2297	62,5182	-0,7115
Region Growing	44,1126	61,7682	17,6556
H-Minima	96,7591	91,7412	-5,0179

In Table 4, sensitivity, specificity, accuracy and Jaccard-Index parameter values are presented in order to compare the different methods used in the literature and the H-Minima method that has not been used in the literature but in this study. It was found that H-Minima method produced compatible results with Staple (Isgrò et al. (2013)) and Wavelet Analysis (Bellavia et al. (2014)) methods.

Table 4: Comparison of H-Minima and literature studies

Researcher (Year Of Study)	Method	Sensitivity (%)	Specificity (%)	Accuracy (%)	Jaccard index
(Vucic, 2015)	Support Vector Machine	-	-	92	-
Isgrò et al. (2013)	Staple	96	98	97	-
Goffredo et al. (2012)	Otsu	75~87	85~90	>80	-
Tama et al. (2015)	Binarization	-	-	96	-
Bellavia et al. (2014)	Wavelet Analysis	92,3	92,4	-	0,858
Kwasnicka et al. (2007)	Tophat-Hessian	-	-	77	-
Riaño-Rojas et al. (2007)	Regions Growth by Threshold	-	-	88~91	-
Buber, (2019)	H-Minima	81,11	98,43	96,76	

REFERENCES

[1] Lucchese, L. ve Mitra, S. K., 2001, Colour image segmentation: a state-of-the-art survey, Proceedings-Indian National Science Academy Part A, 67 (2), 207-222.
[2] Gonzales, R., Woods, R. ve Eddins, S., 2002, Digital Image Processing, Prentice Hall, New Jersey, 567-642.
[3] Narkhede, H., 2013, Review of image segmentation techniques, International Journal of Science and Modern Engineering, 1 (8), 54-61.
[4] Altuntas, V., Altuntas, S. ve Gok, M., 2018, Automatic Colony Segmentation on Agar Surface by Image Processing.
[5] Doğdu, D. M., 2015, Bağ Dokusu Hastalıklarında Tırnak Kıvrımı Kapiller Yapısının Dermatoskop ile Değerlendirilmesi, Tıpta Uzmanlık, Selçuk Üniversitesi, Konya.
[6] Tama, A., Mengko, T. R. ve Zakaria, H., 2015, Nailfold capillaroscopy image processing for morphological parameters measurement, 2015 4th International Conference on Instrumentation, Communications, Information Technology, and Biomedical Engineering (ICICI-BME), 175-179.
[7] Vucic, V., 2015, Image Analysis for Nail-fold Capillaroscopy.
[8] Bellavia, F., Cacioppo, A., Lupaşcu, C. A., Messina, P., Scardina, G., Tegolo, D. ve Valenti, C., 2014, A non-parametric segmentation methodology for oral videocapillaroscopic images, Computer methods and programs in biomedicine, 114 (3), 240-246.
[9] Isgrò, F., Pane, F., Porzio, G., Pennarola, R. ve Pennarola, E., 2013, Segmentation of nailfold capillaries from microscopy video sequences, Proceedings of the 26th IEEE International Symposium on Computer-Based Medical Systems, 227-232.
[10] Goffredo, M., Schmid, M., Conforto, S., Amorosi, B., D'Alessio, T. ve Palma, C., 2012, Quantitative color analysis for capillaroscopy image segmentation, Medical & biological engineering & computing, 50 (6), 567-574.
[11] Kwasnicka, H., Paradowski, M. ve Borysewicz, K., 2007, Capillaroscopy image analysis as an automatic image annotation problem, 6th International Conference on Computer Information Systems and Industrial Management Applications (CISIM'07), 266-271.
[12] Riaño-Rojas, J., Prieto-Ortiz, F., Morantes, L., Sánchez-Camperos, E. ve Jaramillo-Ayerbe, F., 2007, Segmentation and extraction of morphologic

features from capillary images, 2007 Sixth Mexican International Conference on Artificial Intelligence, Special Session (MICAI), 148-159.

[13] Spera, E., Tegolo, D., & Valenti, C. (2015, June). Segmentation and feature extraction in capillaroscopic videos. In Proceedings of the 16th International Conference on Computer Systems and Technologies (pp. 244-251). ACM.

[14] Otsu, N., 1979, A threshold selection method from gray-level histograms, IEEE transactions on systems, man, and cybernetics, 9 (1), 62-66.

[15] Bezdek, J. C., 2013, Pattern recognition with fuzzy objective function algorithms, Springer Science & Business Media, p.

[16] Monneau, R., 2010, Introduction to the fast marching method.

[17] Kamdi, S. ve Krishna, R., 2012, Image segmentation and region growing algorithm, International Journal of Computer Technology and Electronics Engineering (IJCTEE), 2 (1).

[18] Wolf, G. W., 1991, A Fortran subroutine for cartographic generalization, Computers & Geosciences, 17 (10), 1359-1381.

[19] Raimondo, F., Gavrielides, M. A., Karayannopoulou, G., Lyroudia, K., Pitas, I. ve Kostopoulos, I., 2005, Automated evaluation of Her-2/neu status in breast tissue from fluorescent in situ hybridization images, IEEE Transactions on Image Processing, 14 (9), 1288-1299.

[20] C. P.Documentation and N.Agreement, "Installation Guide R 2014 b," (2014).

[21] Zaini, T. R. M., Jaafar, M., & Pin, N. C. (2016). H-minima transform for segmentation of structured surface. In MATEC Web of Conferences (Vol. 74, p. 00025). EDP Sciences.

[22] Bleau, A. ve Leon, L. J., 2000, Watershed-based segmentation and region merging, Computer Vision and Image Understanding, 77 (3), 317-370.

[23] surface topography maps," Surf. Topogr. Metrol. Prop., vol. 1, no. 1, p. 015005, Oct. (2013).

A Shadow Mask Implementation for MEMS Sensors Requiring Formation of a Sensing Layer

S. TEZ[1] and M. KAYA[2]

[1]Pamukkale University, Department of Electrical and Electronics Engineering, Denizli, Turkey, stez@pau.edu.tr
[2] Pamukkale University, Graduate School of Natural and Applied Sciences, Denizli, Turkey, mkaya145@posta.pau.edu.tr

Abstract **- This paper introduces fabrication of a shadow mask wafer. The formed shadow mask is a standard silicon wafer having <100> crystal orientation, and its thickness approximately 300 μm-thick after fabrication process completed. The formed aperture on the shadow mask as small as 37 μm, which can probably allow deposition of different sensing layers on sensors.**

Keywords **- MEMS, Silicon based shadow-mask, KOH etch, sensing layer formation, DRIE.**

I. INTRODUCTION

MEMS technology presents unique solutions for various sensor implementations. However, some of MEMS applications needs for the formation of specific sensing layer. These layers provide a change in electrical or physical parameters in presence of the target species desired detect. Furthermore, it is necessary to deposit these layers to the optimum position on sensor to improve performance [1]. Especially, the cantilever based sensor applications suffer from this situation [2].

The sensing layers can be formed before or after releasing of the structure. However, when the sensor yield is taken into account, the formation of the sensing layer should be completed before release process [3]. The photolithography based lift-off method can also be an option for the formation of sensing-layers before sensor release process; however, if the sensing layers are vulnerable to chemicals used during this method like polymers, another choice can be using of a shadow mask [4]. Therefore, the current study introduces a fabrication process flow and presents a reusable Silicon based shadow mask, which can be utilized to deposit not only polymer based sensing layers but also different materials on the sensors.

II. FABRICATION PROCESS

For this implementation, a front-side of Silicon wafer having 500 μm-thick is deposited with 2 μm-thick SiO_2 layer (Figure 1-a) and then, this wafer is thinned to approximately 300 μm by using KOH solution (Figure 1-b). Afterwards, the rear-side of the wafer is again deposited with 2 μm-thick SiO_2 layer (Figure 1-c). From this step, the rear side of the Silicon wafer is utilized to continue to the fabrication process. Next, the patterning of the wafer is performed by using a fabrication mask and

photolithographic steps (Figure 1-d). After patterning of photoresist, firstly the SiO_2 layer on the front-side is patterned by using BHF (Figure 1-e), and the SiO_2 layer on the rear-side is also completely removed in this step (Figure 1-f). Finally, the Silicon wafer is etched-away by using DRIE to form apertures as small as 37 μm (Figure 1-g). After completing the fabrication process, the alignment of fabricated shadow mask wafer and a sensor wafer can be possible to form different sensing layers on the sensors. (Figure 1-h).

By using process steps shown in the Figure 1, the fabrication of the shadow mask wafer is completed. Figure 2 shows the fabricated shadow mask in the wafer and die level, respectively. For the wafer level, there are marks formed on the edge, which can be used for adjusting of coarse alignment. When the front
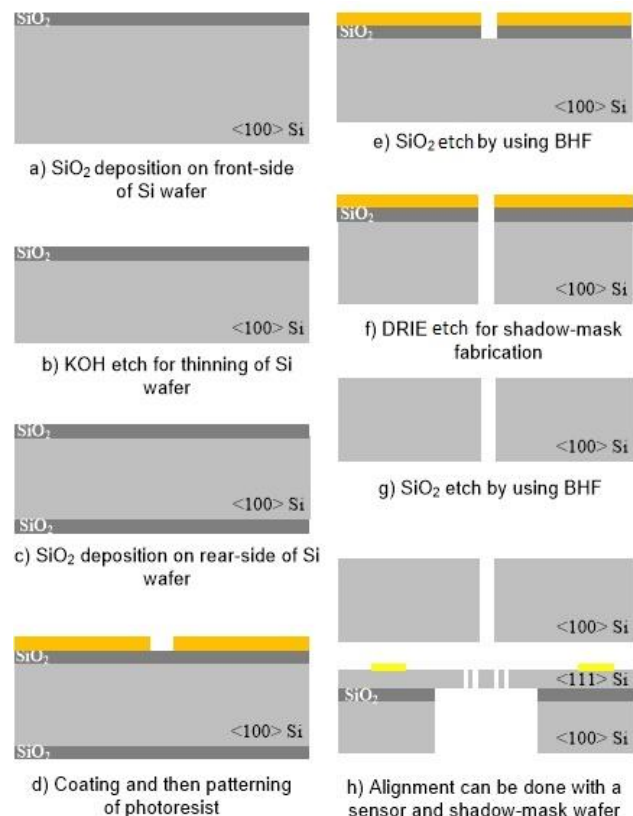
Figure 1: The shadow-mask fabrication process steps.
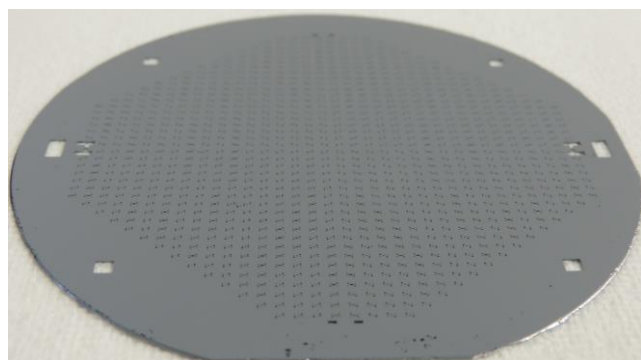
a)
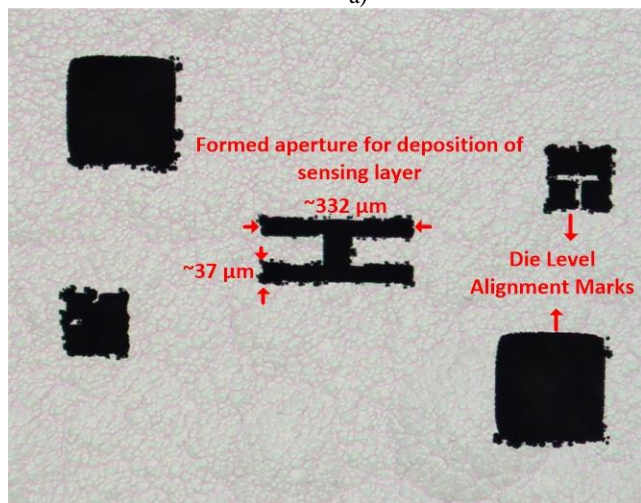
b)
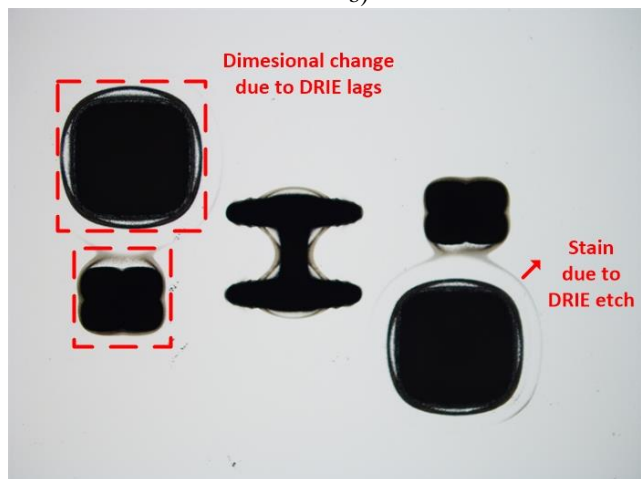
c)

Figure 2 a): The fabricated shadow mask b) Front side of the shadow mask c) Rear side of the shadow mask.

side of the wafer shown in Figure 2 b) is examined, it can be seen that the size of formed aperture is as small as 37 μm for the front side of the wafer etched by DRIE. This measurement is performed by using a 3D digital microscope. However, the dimension formed on the shadow mask for the rear side is slightly different from the front side. The reason of this can be explained with DRIE lags. Furthermore, an etch stain can be observed as a result of DRIE etch. Table I gives a comparison between the size of the aperture for the drawn in

the fabrication mask and obtained after fabrication for the front side.

Table 1: A comparison between the size of the aperture for front side of the shadow mask wafer

Aperture size	
Drawn in fabrication mask	Obtained after fabrication
30 μm	37 μm
330 μm	332 μm

It is also possible to use fabricated shadow mask for wafer level sensor implementations. However, the dicing of the shadow mask gives more opportunity to research various candidate materials for sensor applications. Thus, after fabrication is completed, the shadow mask wafer is diced (Figure 3). The dicing size of the shadow mask is nearly 2380 μm × 2000 μm. It can also be possible to use the fabricated shadow wafer for die level coating.

Figure 3: The fabricated shadow mask and a SOI based sensor in the die level.

A handmade alignment setup is formed to show the feasibility of the proposed method. For this, a silicon on insulator (SOI) based sensor and a shadow mask can be successfully aligned in the die level by using alignment marks formed during the fabrication. Figure 3 shows the alignment result. Due to the formed aperture, the fabricated shadow mask is successfully placed on the top of the sensor in the die level, allowing to deposition of any material on the proof mass region of the sensor. Thus, the shadow mask can contribute to obtain a sensor having independent sensing characteristic from the position of the sensing layer on the prof mass, compare with literature.

When the fabrication results and the outcome of alignment

with a sensor are taken into consideration, the fabricated shadow mask can also provide flexibility for the formation of different thin film layers with various deposition methods such as spray coating and sputtering.
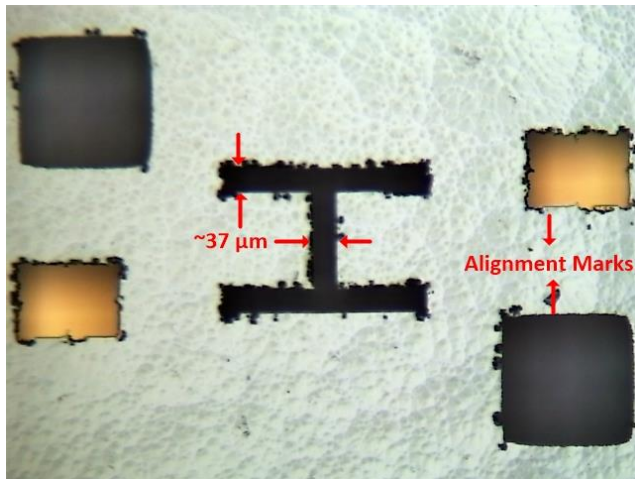
a)
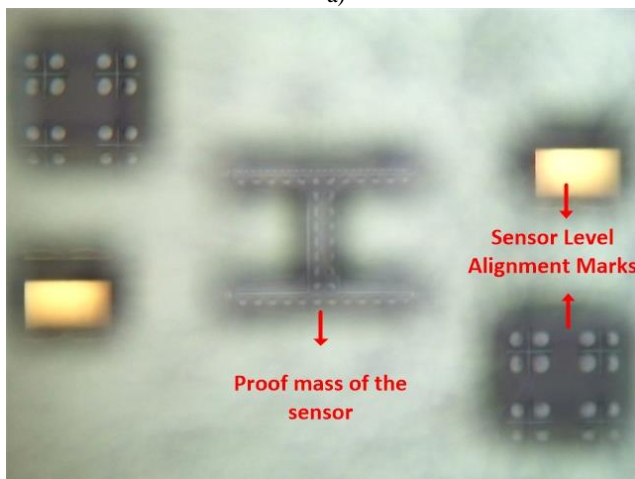
b)

Figure 4 a) The focus on shadow mask b) The focus on the sensor showing the proof mass region and die level marks.

III. CONCLUSION

The proposed method is useful to provide sensing layer for the resonance based capacitive sensors which generally needs for a polymer based material providing change in the mass by swelling. Although there is difference in the size of aperture of the shadow mask formed on rear and front sides, this dimensional difference is in the mask tolerance, and it does not cause a problem for material deposition process. Moreover, the fabricated shadow mask is reusable for different material deposition process.

ACKNOWLEDGMENT

This study is supported by the Scientific and Technological Research Council of Turkey (TUBITAK) under the grant number 116E231. The authors would like to thank TUBITAK.

REFERENCES

[1] B.N. Johnson and R. Mutharasan, "Biosensing using dynamic-mode cantilever sensors: A review", Biosen. and Bioelect. 32, 1-18, 2012.
[2] F Patocka, M Schneider, N Dörr, C Schneidhofer and U Schmid, "Position-dependent mass responsivity of silicon MEMS cantilevers excited in the fundamental, two-dimensional roof tile-shaped mode", J. Micromech. Microeng. 29 045009, 2019.
[3] Arash Hajjam ; Siavash Pourkamali, "Fabrication and Characterization of MEMS-Based Resonant Organic Gas Sensors", IEEE Sensors Journal, vol. 12 No.6, 2012.
[4] Ching-Chang Tseng, Chen-Wei Chiu, Kai-Xiang Zhung, Jiun-Haw Lee, and Guo-Dung John Su "Thin silicon shadow masks for organic light-emitting diodes (OLED) deposition processes", Proc. SPIE 6414, Smart Structures, Devices, and Systems III, 64141G (8 January 2007).

Computational Investigation of Turbulent Flow in Single-Sided Backward-Facing Steps

T. KARASU[1]

[1]Eskişehir Osmangazi University, Meşelik, 26480 Eskişehir/Turkey, tkarasu@ogu.edu.tr

Abstract - **The present original paper deals with computational investigation of steady, incompressible, two-dimensional, separating and reattaching turbulent flow in single-sided backward-facing steps at three different Reynolds numbers. Employing the finite-volume method with a hybrid scheme, a computer program based on the SIMPLE (Semi-Implicit Method for Pressure Linked Equations) algorithm has been developed. Numerical solution of conservation equations of mass and momentum, together with the standard k-ε turbulence model, are obtained using an iterative numerical solution technique. Near the solid boundaries, wall-functions are employed. Numerical predictions for local streamwise velocity, turbulence kinetic energy, turbulence kinetic energy dissipation rate, effective viscosity profiles, locus of flow reversal, bottom wall static-pressure coefficient, wall-shear stress and friction coefficient distributions along top and bottom walls of the single-sided backward-facing step flow configurations are presented and compared with experimental measurements. The results of computational investigation are generally in good agreement with experimental data.**

Keywords - **Turbulent flow, k-ε turbulence model, Predictions.**

I. INTRODUCTION

THE separating and reattaching turbulent recirculating flow in a two-dimensional single-sided backward-facing step shown in Figure 1, is of great practical importance. It is an excellent case for analysing the basic physical phenomena of separation and reattachment because it is the simplest such flow. As depicted in Figure 1, three fundamental flow regimes are present: a reattaching shear-layer, a recirculating region, and a stagnation flow region. These regimes rigorously test the validity of turbulence models, which are, for the most part, tuned to specific homogeneous shear flows. Turbulent flow in single-sided backward-facing steps, sudden expansions and pipes have been studied both experimentally and theoretically by numerous investigators, among the most interesting ones are the works of [1-37]. In the present computational investigation, the experimental measurements of [7,8,10] have been employed for comparison with the numerical predictions. The main objective of this original investigation is to obtain numerical predictions for steady, incompressible, two-dimensional turbulent recirculating flow in single-sided backward-facing steps using the standard k-ε turbulence model [38] with a wall-functions boundary condition, and to compare the results of numerical computations with available experimental measurements in the literature for validation.

II. MATHEMATICAL AND PHYSICAL MODEL

A. Governing Equations and Turbulence Model

With reference to Figure 1, the mathematical and physical model employed in the computational investigation of steady, incompressible, and two-dimensional separating and reattaching turbulent flow in single-sided backward-facing steps, requires the simultaneous solution of the governing equations, together with the turbulence model equations. The transport equations representing the conservation of mass, momentum, turbulence kinetic energy and its dissipation rate in steady state cartesian coordinate system are cast into the following general form:

$$\frac{\partial}{\partial x}\left(\rho u \phi\right) + \frac{\partial}{\partial y}\left(\rho v \phi\right) - \frac{\partial}{\partial x}\left(\Gamma_\phi \frac{\partial \phi}{\partial x}\right) - \frac{\partial}{\partial y}\left(\Gamma_\phi \frac{\partial \phi}{\partial y}\right) = S_\phi \quad (1)$$

This equation represents a transport equation for a general variable ϕ. The variables u and v are the local time-averaged velocity components in the horizontal (x) and normal (y) directions, respectively, ρ is the fluid density and Γ_ϕ is the transport coefficient. The final term, S_ϕ, is the source term. The variables, ϕ, necessary in this numerical investigation are u, v, k and ε. Here, k and ε stand for the kinetic energy of turbulence and its dissipation rate, respectively. The turbulence model employed in the present study is the k-ε model of [38]. If ϕ is set equal to unity and Γ_ϕ and S_ϕ to zero, equation (1) reduces to the equation of continuity. Pressure is derived from the pressure correction equation [39,40]. The transport equations, coefficients and the source terms are summarised in Table 1.
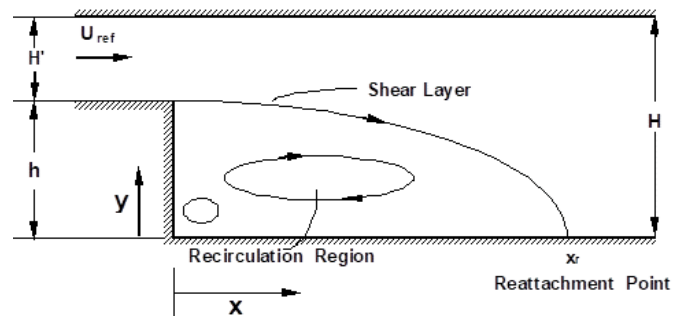
Figure 1: Cartesian coordinate system and geometry of single-sided backward-facing step flow.

Table 1: Transport equations, coefficients and source terms.

Variable ϕ	Γ_ϕ	S_ϕ
1	0	0
u	$\mu_e = \mu + \mu_t$	$-\dfrac{\partial P}{\partial x} + \dfrac{\partial}{\partial x}\left(\mu_e \dfrac{\partial u}{\partial x}\right) + \dfrac{\partial}{\partial y}\left(\mu_e \dfrac{\partial v}{\partial x}\right)$
v	μ_e	$-\dfrac{\partial P}{\partial y} + \dfrac{\partial}{\partial x}\left(\mu_e \dfrac{\partial u}{\partial y}\right) + \dfrac{\partial}{\partial y}\left(\mu_e \dfrac{\partial v}{\partial y}\right)$
k	μ_e / σ_k	$G - \rho\varepsilon$
ε	$\mu_e / \sigma_\varepsilon$	$\dfrac{\varepsilon}{k}(C_1 G - C_2 \rho\varepsilon)$

Note:
1. $\mu_t = \rho C_\mu k^2 / \varepsilon$
2. Turbulence model constants are assigned the following values (Launder and Spalding, 1974):
$C_\mu = 0.09$, $C_1 = 1.44$, $C_2 = 1.92$, $\sigma_k = 1.0$, $\sigma_\varepsilon = 1.3$
3. $G = \mu_t\left\{2\left[\left(\dfrac{\partial u}{\partial x}\right)^2 + \left(\dfrac{\partial v}{\partial y}\right)^2\right] + \left(\dfrac{\partial u}{\partial y} + \dfrac{\partial v}{\partial x}\right)^2\right\}$

B. Boundary Conditions

With reference to Figure 1, the boundary conditions for two-dimensional separating and reattaching turbulent flow in a single-sided backward-facing step studied are given below. Three different boundary conditions were used: inlet plane, outlet plane, step, bottom and top solid walls. At the step inlet plane either streamwise velocity distribution or a uniform velocity distribution from the experimental measurements is specified, while the velocity in the normal direction is set equal to zero. Empirical relationships are employed to assign uniform entrance values to turbulence quantities k and ε; that is, $k=(0.001\text{-}0.002)\,u_b^2$ and $\varepsilon = (C_\mu k^{3/2} / 0.03h)$, where u_b is the bulk velocity at inlet and h is the step height. The outlet plane was located sufficiently far away from the recirculation region so that fully-developed conditions could be assumed to prevail at the outlet; that is, all the streamwise gradients of the dependent variables vanish at the outlet plane and the normal velocity is assumed zero. At the step, bottom and top solid walls, velocity components u, v and turbulence quantities k and ε are set to zero. The values of k and ε at the near-wall grid points are evaluated using the wall-functions of [38]. Initial field values throughout the computational domain were specified properly so as not to cause numerical divergence.

C. Numerical Solution Procedure

In this computational investigation, employing the finite-volume approach, a computer program based on the SIMPLE algorithm of [39] has been developed. The partial differential equations (1) are discretised by a control-volume-based finite-difference method with a hybrid scheme. The finite-volume forms of the partial differential equations coupled with the boundary conditions are solved iteratively using a line-by-line solution procedure in conjunction with a tridiagonal matrix form [41].

D. Computational Details

The numerical computations were carried out on a Pentium 4 CPU 1.60 GHz personal computer. The computational grid distributions for all of the single-sided backward-facing step flows studied are depicted in Figures 2, 13 and 24. All the computational grids employed were non-uniformly distributed with dense grid-line concentrations in the recirculation region and near the walls of the single-sided backward-facing step configuration. Staggered control volumes were used for streamwise and normal velocity components. All other quantities of interest were calculated at the grid points. The line-by-line method was used to obtain converged solutions iteratively. Underrelaxation factors were employed to procure numerical stability with values of 0.4, 0.4, 0.6, 0.6, 0.5 and 0.5 for u, v, k, ε, P and μ_e, respectively. The convergence criterion adopted in the present computations was that the summation of the absolute values of the mass residual in the entire computational domain be less than a prescribed value of 10^{-5}. Grid tests were performed with different grid sizes to obtain an optimum grid-independent solution for each flow case studied. All the computations presented in this study are grid-independent. Table 2 summarises details of computational requirements for all flow cases investigated. In this table, Re is the Reynolds number and N is the number of iterations performed to obtain a converged solution.

Table 2: Flow case, Reynolds number, grid size and number of iterations.

Flow case of	Re	Grid Size (x) × (y)	N
Ruck and Makiola [10]	64 000	40 × 30	484
Kim et al. [7]	44 500	40 × 30	326
de Groot [8]	174 071	40 × 30	309

III. PRESENTATION AND DISCUSSION OF RESULTS

Numerical computations were carried out for two-dimensional separating and reattaching turbulent flow in single-sided backward-facing steps at three different Reynolds numbers, and the results of computations were compared with the experimental measurements of [7], [8], and [10]. With air used as the working fluid in the single-sided backward-facing step, the experimental measurements of [10] are first selected as the comparison basis for this computational study. The single-sided backward-facing step flow configuration has an expansion ratio of H / H' = 2. The Reynolds number of the flow at the inlet is Re = 64 000 (Re = u_o h / v, where u_o is the maximum velocity in profile before step and h is the step height). For this flow situation, the computational domain is extended to a streamwise distance of x=25h downstream from the inlet plane of the single-sided backward-facing step. The numerical grid distribution for the single-sided backward-facing step flow geometry of [10] is displayed in Figure 2. The predicted local streamwise velocity profiles along the single-sided backward-facing step flow channel in dimensionless form u/u_o, and normal distance y, at streamwise locations ranging from x/h=1 to 15 across the channel have been compared with the experimental measurements of [10] in Figure 3. Examination of Figure 3 indicates that the predicted non-dimensional streamwise velocity profiles exhibit good

qualitative agreement with the corresponding experimental ones, and as the flow develops along the channel the agreement becomes better. The predicted locus of flow reversal (u=0) for the backward-facing step flow channel is presented in Figure 4. The normal distance y measured from the bottom wall is normalised to step height (h) and plotted as a function of downstream distance normalised to step height (x/h). In this figure, the streamwise velocity (u) is zero on the circles, positive above the circles and negative below the circles. As can be seen from the figure, the predicted flow reattachment length is found to occur at about $x_r/h=6.76$ downstream from the inlet plane, whereas the experimental flow reattachment length occurs at about $x_r/h=8$. The source of this problem is a limitation of the standard k-ε turbulence model. The model does not account for the time lapse between extra turbulent energy being supplied and the effect being felt in the dissipating motions. Figures 5, 6 and 7 reveal the predicted profiles of turbulence kinetic energy, turbulence kinetic energy dissipation rate and effective viscosity, respectively, along the backward-facing step flow channel of [10] at the same downstream locations as in Figure 3. Here, the predicted profiles are normalised, respectively, with respect to square of maximum velocity in profile before step u_o^2, maximum values of turbulence kinetic energy dissipation rate ε_{max} and effective viscosity $\mu_{e\ max}$ in the flow field. These figures show how the predicted turbulence kinetic energy, dissipation rate of turbulence kinetic energy and effective viscosity profiles develop along the channel. The predicted wall-shear stress distribution along the single-sided backward-facing step flow channel bottom-wall in terms of τ_{wb}/τ_{wdb}, as a function of downstream distance x/h, is depicted in Figure 8. Here, the wall-shear stress has been made dimensionless with respect to its value at the outlet plane (τ_{wdb}). As can be seen from the figure, starting from the inlet plane of the channel until at about x/h=6.75 the wall-shear stress is negative. This is due to the negative streamwise velocities (-u) in the recirculation zone. The bottom wall-shear stress, as it takes negative values, increases rapidly until it attains its maximum negative value, and then decreases sharply to its zero value at about x/h=6.75, afterwhich it takes positive values and increases continuously.
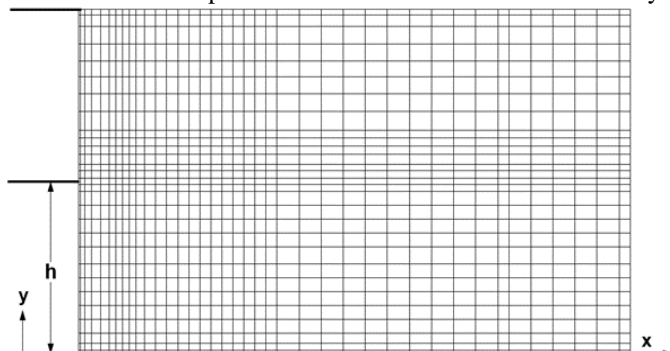
Figure 2: Numerical grid distribution for single-sided backward-facing step flow geometry of [10].
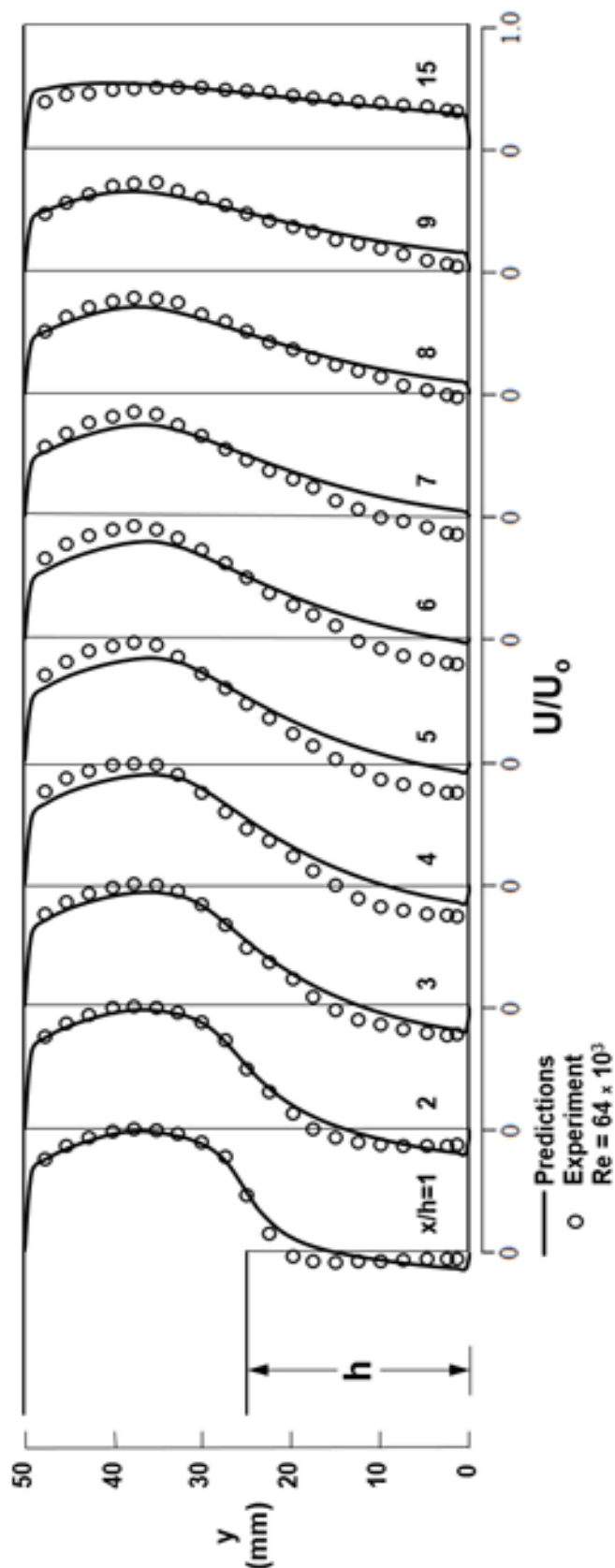
Figure 3: Comparison of predicted dimensionless streamwise velocity profiles along single-sided backward-facing step flow channel with experimental measurements of [10].
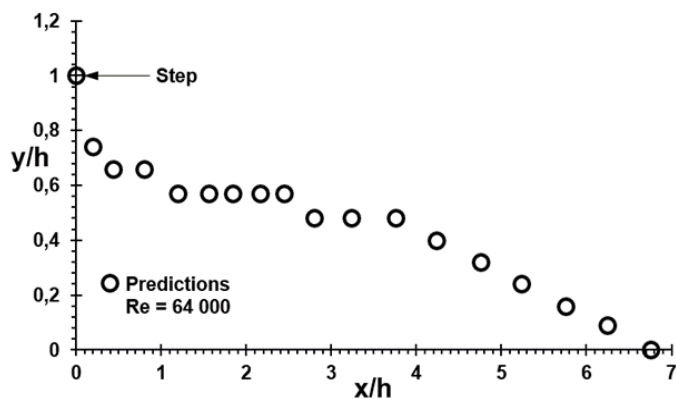
Figure 4: Predicted locus of flow reversal (u=0) for single-sided backward-facing step flow of [10].

Figure 5: Predicted profiles of normalised turbulence kinetic energy along backward-facing step flow channel of [10].

Figure 6: Predicted profiles of normalised turbulence kinetic energy dissipation rate along backward-facing step flow channel of [10].

The predicted distribution of friction coefficient ($C_{fb} = 2\,\tau_{wb} / \rho\,u_o^2$) along the channel bottom-wall, as a function of downstream distance x/h, is plotted in Figure 9. As seen from the figure, the friction coefficient exhibits the same trend as the wall-shear stress shown in Figure 8. The predicted variation of wall static-pressure coefficient [$C_p = (P - P_{ref}) / 0.5\,\rho\,u_o^2$] along the channel bottom-wall, as a function of downstream distance x/h, is given in Figure 10. As seen from the figure, the bottom-wall static-pressure coefficient takes negative values just from the inlet plane of the channel, and due to the recirculating flow, it shows sudden increase up to downstream location x/h=18. Beyond this location, it remains nearly constant. In Figure 11, the predicted distribution of wall-shear stress along the channel top-wall in dimensionless form of τ_{wt} / τ_{wdt}, as a function of

downstream distance x/h, is displayed. Here, the wall-shear stress has been normalised with respect to its value at the outlet plane (τ_{wdt}). As can be seen from the figure, starting from the inlet plane of the channel until at about x/h=1 the wall-shear stress increases sharply until it reaches its maximum positive value, and thereafter decreases up to x/h=24.5. Finally, the computed variation of friction coefficient ($C_{ft} = 2\ \tau_{wt}\ /\ \rho\ u_o^2$) along the channel top-wall, as a function of downstream distance x/h, is presented in Figure 12. As seen from the figure, the friction coefficient reveals the same trend as the wall-shear stress shown in Figure 11.

Figure 8: Predicted distribution of dimensionless wall-shear stress along bottom-wall of backward-facing step flow channel of [10].
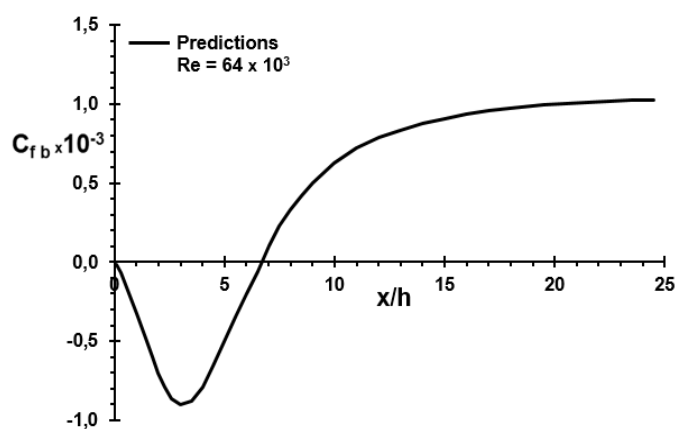
Figure 9: Predicted distribution of friction coefficient along bottom-wall of backward-facing step flow channel of [10].
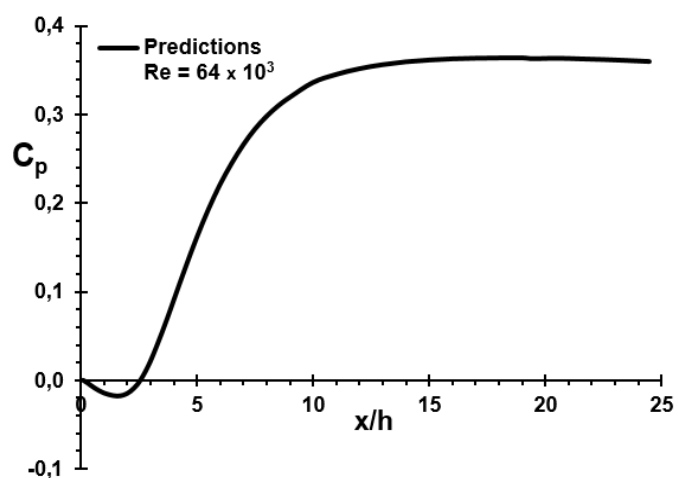
Figure 10: Predicted variation of wall static-pressure coefficient (C_p) along bottom-wall of backward-facing step flow channel of [10].

Figure 7: Predicted profiles of normalised effective viscosity along single-sided backward-facing step flow channel of [10].
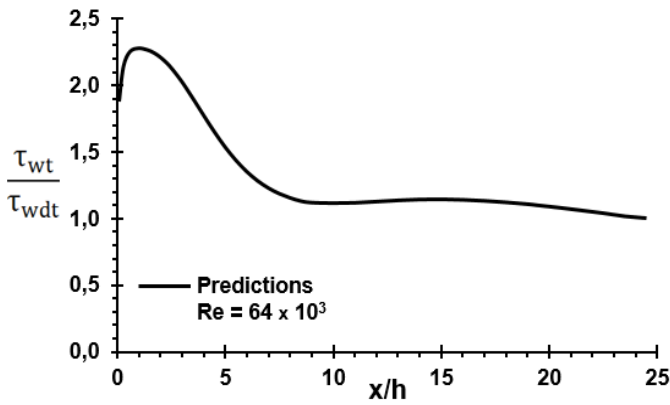
Figure 11: Predicted distribution of dimensionless wall-shear stress along top-wall of backward-facing step flow channel of [10].
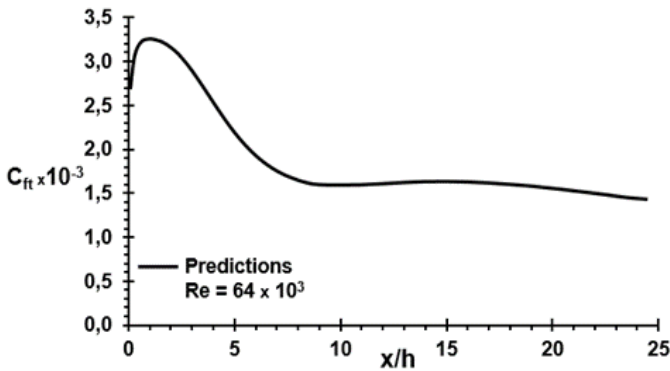
Figure 12: Computed variation of friction coefficient along top-wall of backward-facing step flow channel of [10].

The second flow configuration corresponds to the two-dimensional single-sided backward-facing step flow experimental study of [7] with air used as the working fluid. The single-sided backward-facing step flow geometry has an expansion ratio of H / H' = 1.5. The Reynolds number of the flow at the inlet is Re = 44 500 (Re = u_o h / ν, where u_o is the reference free-stream velocity measured at x=-15.24 cm upstream of the step and h is the step height). For this flow case, the calculation domain is extended to a streamwise distance of x=25h downstream from the inlet plane of the backward-facing step. The computational grid distribution for the backward-facing step flow of [7] is depicted in Figure 13. The predicted local streamwise velocity profiles for the step flow in terms of u/u_o, and transverse distance y/h, at streamwise positions ranging from x/h=0.3 to 25 across the channel are presented in Figure 14 and compared with experimental data of [7].
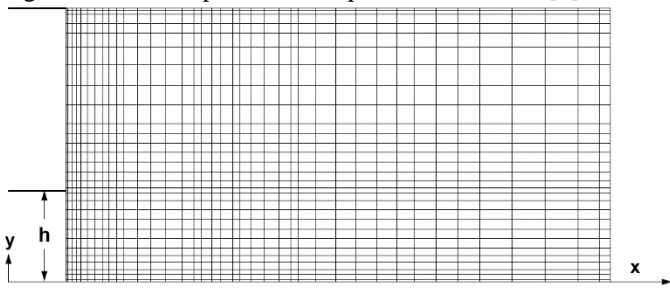
Figure 13: Computational grid distribution for single-sided backward-facing step flow geometry of [7].

As seen from the figure, the predicted streamwise velocity profiles are in good qualitative agreement with the corresponding experimental ones. In addition, this figure also shows how the predicted streamwise velocity profiles develop along the single-sided backward-facing step flow channel.
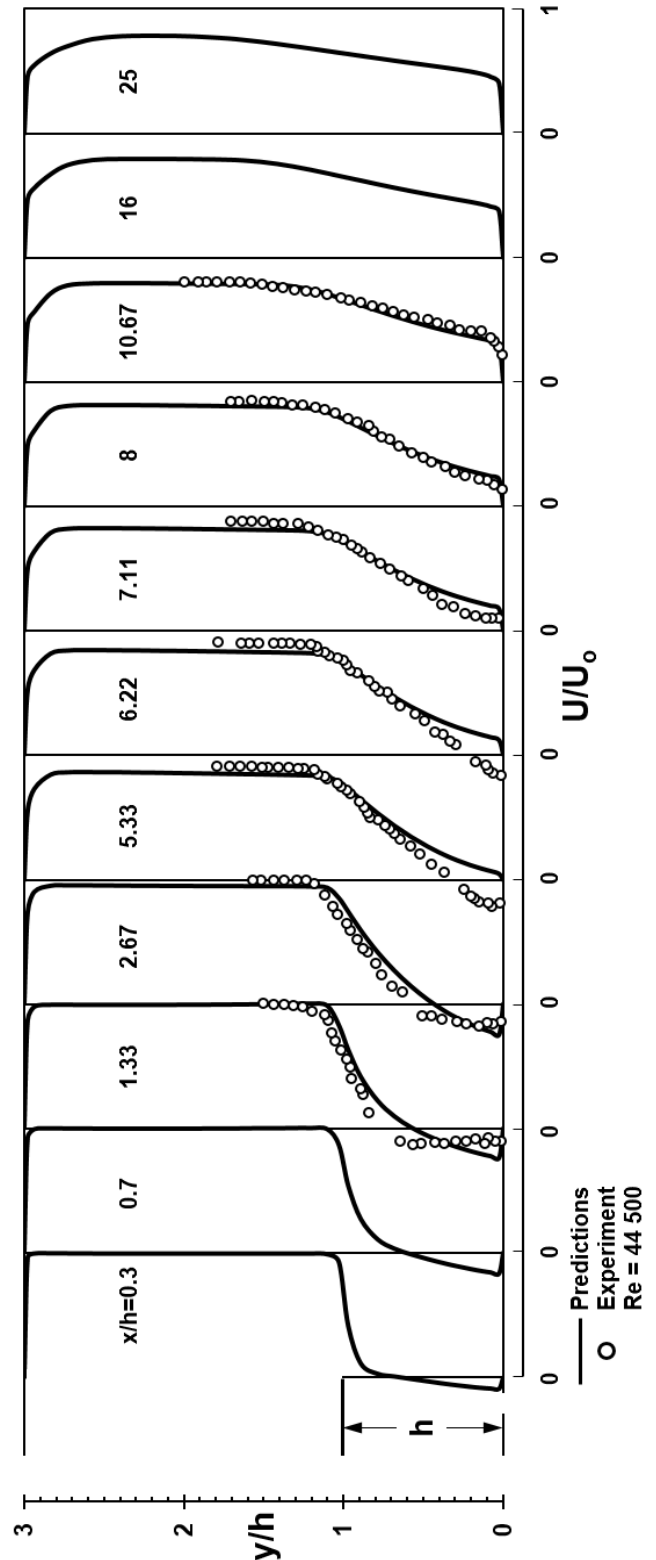
Figure 14: Comparison of predicted dimensionless streamwise velocity profiles along single-sided backward-facing step flow channel with experimental data of [7].

The predicted locus of flow reversal (u=0) for the single-sided backward-facing step flow is given in Figure 15. In this figure, the streamwise velocity (u) is zero on the circles, positive above the circles and negative below the circles. For this flow situation, as seen from the figure, the predicted flow reattachment length is found to occur at about x_r/h=4.965 downstream from the inlet plane, while the experimental flow reattachment length is reported to occur at x_r/h=7±1. The source of this problem is a limitation of the standard k-ε turbulence model. The model does not account for the time lapse between extra turbulent energy being supplied and the effect being felt in the dissipating motions. Figures 16, 17 and 18 exhibit the predicted profiles of turbulence kinetic energy, turbulence kinetic energy dissipation rate and effective viscosity, respectively, along the channel of [7] at the same downstream positions as in Figure 14. Here, the predicted profiles of dissipation rate of turbulence kinetic energy and effective viscosity are normalised, respectively, with respect to maximum values of turbulence kinetic energy dissipation rate ε_{max} and effective viscosity $\mu_{e\ max}$ in the flow field. These figures indicate how the predicted turbulence kinetic energy, dissipation rate of turbulence kinetic energy and effective viscosity profiles develop along the channel. The predicted wall-shear stress distribution along the single-sided backward-facing step flow channel bottom-wall in dimensionless form of τ_{wb}/τ_{wdb}, as a function of downstream distance x/h, is displayed in Figure 19. Here, the wall-shear stress has been made dimensionless with respect to its value at the outlet plane (τ_{wdb}). As seen from the figure, starting from the inlet plane of the channel until at about x/h=5.3 the wall-shear stress is negative. This is due to the negative streamwise velocities (-u) in the recirculation region. The bottom wall-shear stress, as it takes negative values, increases rapidly until it reaches its maximum negative value, and then decreases sharply to its zero value at about x/h=5.3, afterwhich it takes positive values and increases continuously. The computed distribution of friction coefficient $(C_{fb} = 2\,\tau_{wb}\,/\,\rho\,u_o^2\,)$ along the channel bottom-wall, as a function of downstream distance x/h, is manifested in Figure 20. As seen from the figure, the friction coefficient reveals the same trend as the wall-shear stress shown in Figure 19. The predicted variation of wall static-pressure coefficient $[C_p = (P - P_{ref})\,/\,0.5\,\rho\,u_o^2\,]$ along the channel bottom-wall, as a function of downstream distance x/h, is plotted in Figure 21. As seen from the figure, the bottom-wall static-pressure coefficient takes negative values just from the inlet plane of the channel, and due to the recirculating flow, it shows sudden increase up to downstream location x/h=17. Beyond this location, it remains nearly constant. In Figure 22, the predicted distribution of wall-shear stress along the channel top-wall in terms of $\tau_{wt}\,/\,\tau_{wdt}$, as a function of downstream distance x/h, is presented. Here, the wall-shear stress has been normalised with respect to its value at the outlet plane (τ_{wdt}). As can be seen from the figure, starting from the inlet plane of the channel until at about x/h=0.5 the wall-shear stress increases sharply until it reaches its maximum positive value, and thereafter decreases up to x/h=24.5. Finally, the computed variation of friction coefficient (C_{ft}=2τ_{wt}/$\rho\,u_o^2$) along the channel top-wall, as a function of downstream distance x/h, is depicted in Figure 23. As seen from the figure,

the friction coefficient exhibits the same trend as the wall-shear stress indicated in Figure 22.
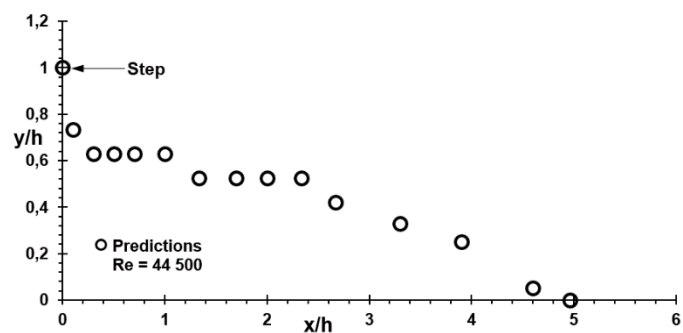
Figure 15: Predicted locus of flow reversal (u=0) for single-sided backward-facing step flow of [7].
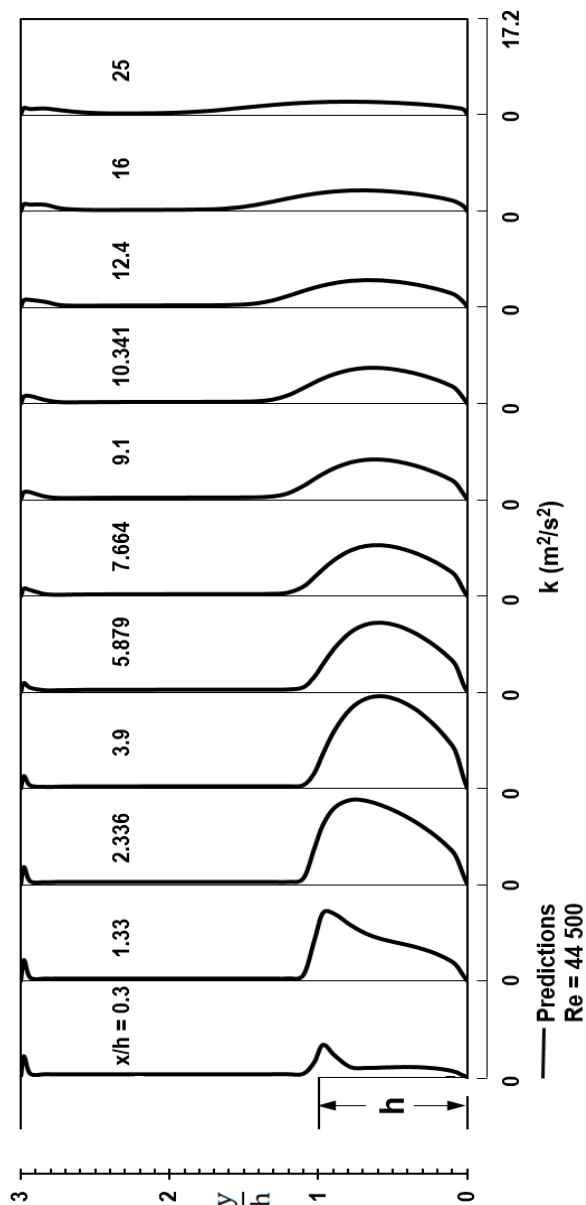
Figure 16: Predicted profiles of turbulence kinetic energy along single-sided backward-facing step flow channel of [7].
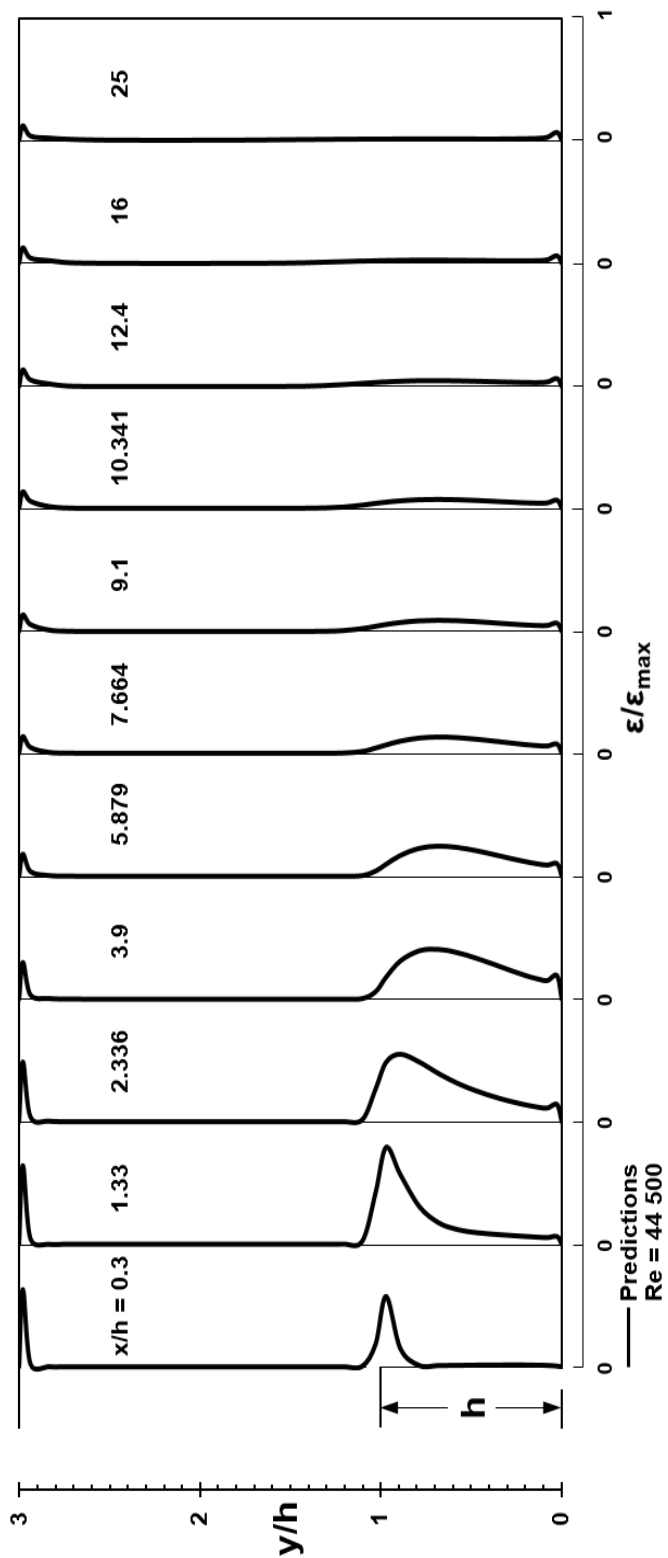
Figure 17: Predicted profiles of normalised turbulence kinetic energy dissipation rate along single-sided backward-facing step flow channel of [7].
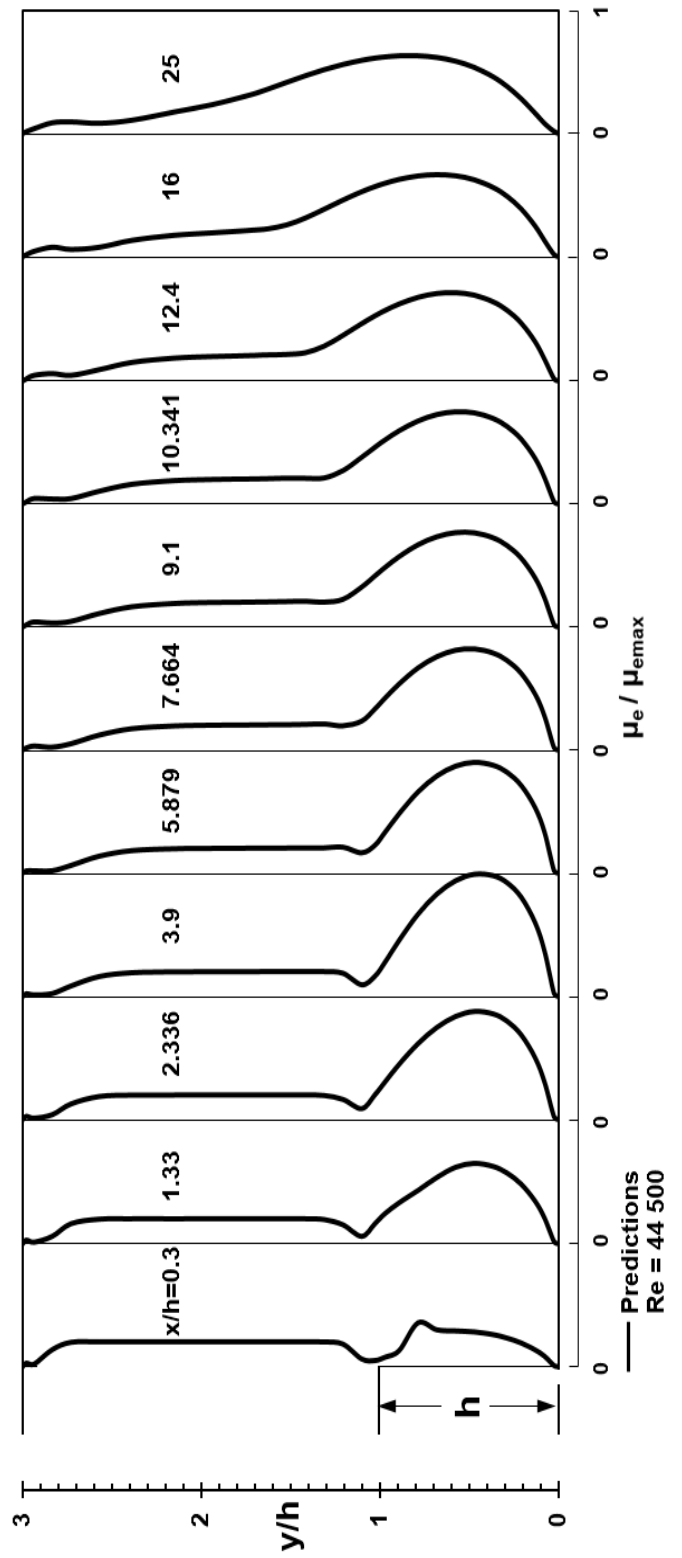
Figure 18: Predicted profiles of normalised effective viscosity along single-sided backward-facing step flow channel of [7].
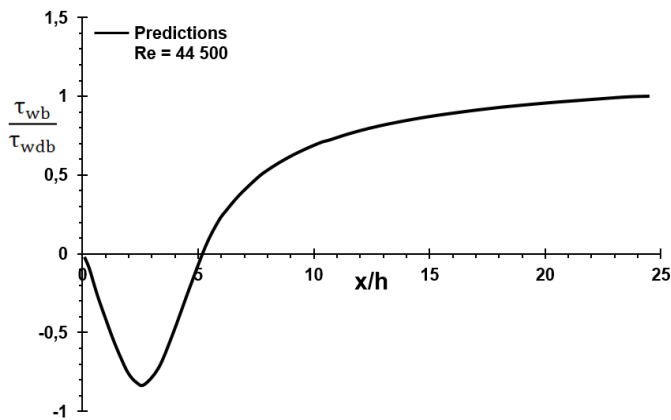
Figure 19: Predicted distribution of dimensionless wall-shear stress along bottom-wall of single-sided backward-facing step flow channel of [7].

Figure 20: Computed distribution of friction coefficient along bottom-wall of single-sided backward-facing step flow channel of [7].

Figure 21: Predicted variation of wall static-pressure coefficient (C_p) along bottom-wall of single-sided backward-facing step flow channel of [7].
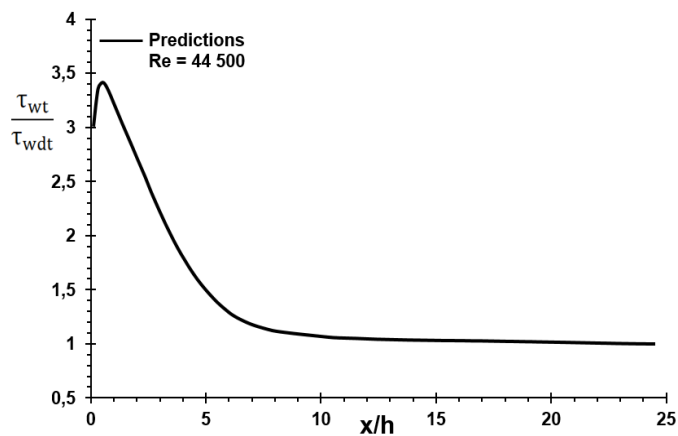
Figure 22: Predicted distribution of normalised wall-shear stress along top-wall of single-sided backward-facing step flow channel of [7].
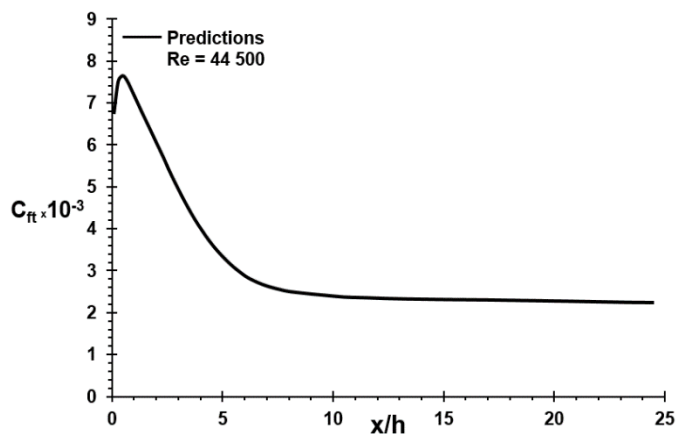
Figure 23: Computed variation of friction coefficient along top-wall of single-sided backward-facing step flow channel of [7].

With air used as the working fluid in the single-sided backward-facing step flow channel, the experimental study for turbulent flow conducted by [8] is thirdly selected as the test case for this computational study. The single-sided backward-facing step flow channel has an expansion ratio of H / H' = 1.5. The Reynolds number of the flow at the inlet is Re = 174 071 (Re = u_b h / ν, where u_b is the bulk velocity at inlet and h is the step height). For this flow situation, the computational domain is extended to a streamwise distance of x=25h downstream from the inlet plane of the backward-facing step. The numerical grid distribution for the backward-facing step flow of [8] is presented in Figure 24. The predicted local streamwise velocity profiles along the singl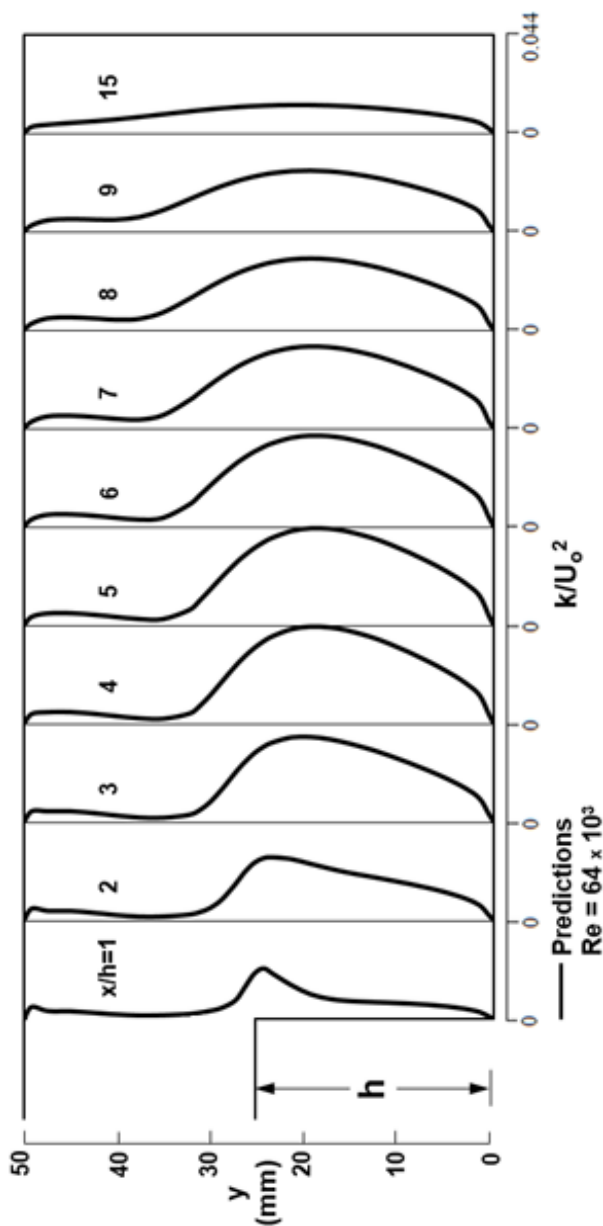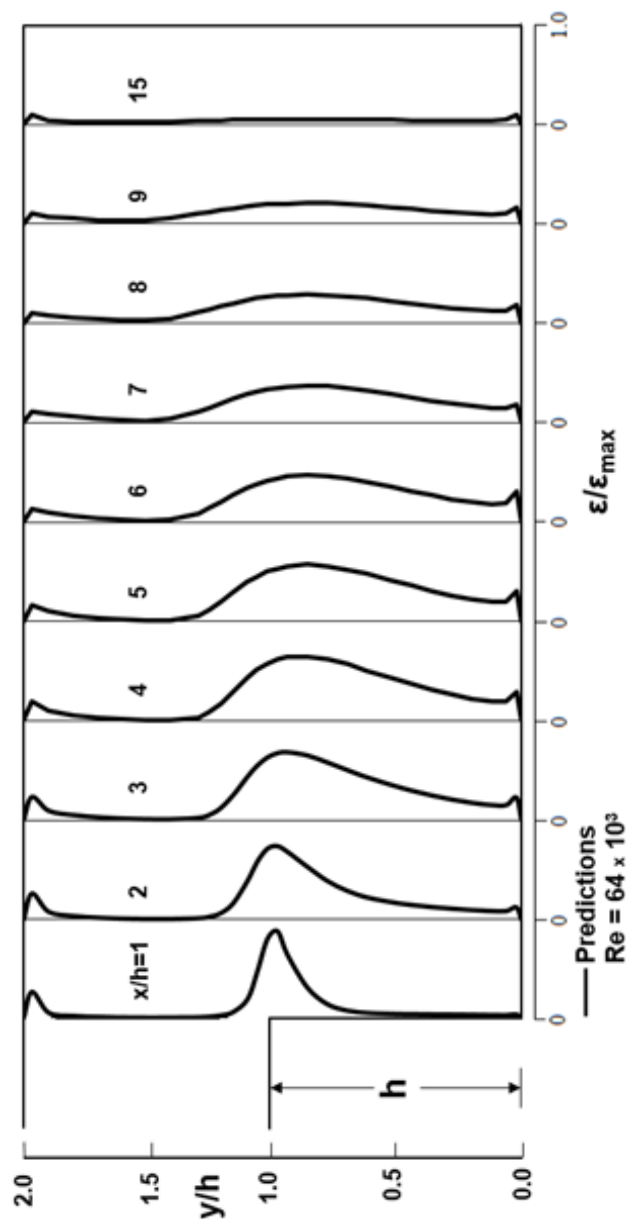e-sided backward-facing step flow channel in dimensionless form u/u_b, and normal distance y/h, at streamwise locations ranging from x/h=0.1 to 25 across the channel have been compared with the experimental measurements of [8] in Figure 25. As seen from the figure, the predicted non-dimensional streamwise velocity profiles reveal good qualitative agreement with the corresponding experimental ones, and as the flow develops along the channel the agreement becomes better. The predicted locus of flow reversal (u=0) for the single-sided backward-facing step flow

is indicated in Figure 26. In this figure, the streamwise velocity (u) is zero on the circles, positive above the circles and negative below the circles. For this flow case, as seen from the figure, the predicted flow reattachment length is found to occur at about $x_r/h=5.415$ downstream from the inlet plane, whereas the experimental flow reattachment length is reported to occur at $x_r/h=7.33$. Figures 27, 28 and 29 display the predicted profiles of turbulence kinetic energy, turbulence kinetic energy dissipation rate and effective viscosity, respectively, along the backward-facing step flow channel of [8] at the same downstream locations as in Figure 25. Here, the predicted profiles are normalised, respectively, with respect to square of bulk velocity at inlet u , maximum values of turbulence kinetic energy dissipation rate ε_{max} and effective viscosity $\mu_{e\,max}$ in the flow field. These figures show how the predicted turbulence kinetic energy, dissipation rate of turbulence kinetic energy and effective viscosity profiles develop along the channel. The computed wall-shear stress distribution along the backward-facing step flow channel bottom-wall in terms of τ_{wb}/τ_{wdb}, as a function of downstream distance x/h, is manifested in Figure 30. Here, the wall-shear stress is nondimensionalised with respect to its value at the outlet plane (τ_{wdb}). As seen from the figure, starting from the inlet plane of the channel until at about x/h=5.415 the wall-shear stress is negative. This is due to the negative streamwise velocities (-u) in the recirculation zone. The bottom wall-shear stress, as it takes negative values, increases rapidly until it reaches its maximum negative value, and then decreases sharply to its zero value at about x/h=5.415, afterwhich it takes positive values and increases continuously. The computed variation of friction coefficient ($C_{fb} = 2\,\tau_{wb}\,/\,\rho\,u$) along the channel bottom-wall, as a function of downstream distance x/h, is plotted in Figure 31. As seen from the figure, the friction coefficient indicates the same trend as the wall-shear stress shown in Figure 30. The predicted distribution of wall static-pressure coefficient [$C_p =$ (P - P_{ref}) / 0.5 ρ u] along the channel bottom-wall, as a function of downstream distance x/h, is given in Figure 32. As seen from the figure, the bottom-wall static-pressure coefficient takes negative values just from the inlet plane of the channel, and due to the recirculating flow, it shows sudden increase up to downstream position x/h=17.5. Beyond this position, it remains nearly constant. In Figure 33, the predicted distribution of wall-shear stress along the channel top-wall in dimensionless form of τ_{wt} / τ_{wdt}, as a function of downstream distance x/h, is displayed. Here, the wall-shear stress is normalised with respect to its value at the outlet plane (τ_{wdt}). As can be seen from the figure, starting from the inlet plane of the channel until at about x/h=0.3 the wall-shear stress increases sharply until it reaches its maximum positive value, and thereafter decreases up to x/h=24.5. Finally, the computed variation of friction coefficient ($C_{ft} = 2\,\tau_{wt}\,/\,\rho\,u$) along the channel top-wall, as a function of downstream distance x/h, is presented in Figure 34. As seen from the figure, the friction coefficient reveals the same trend as the wall-shear stress shown in Figure 33.
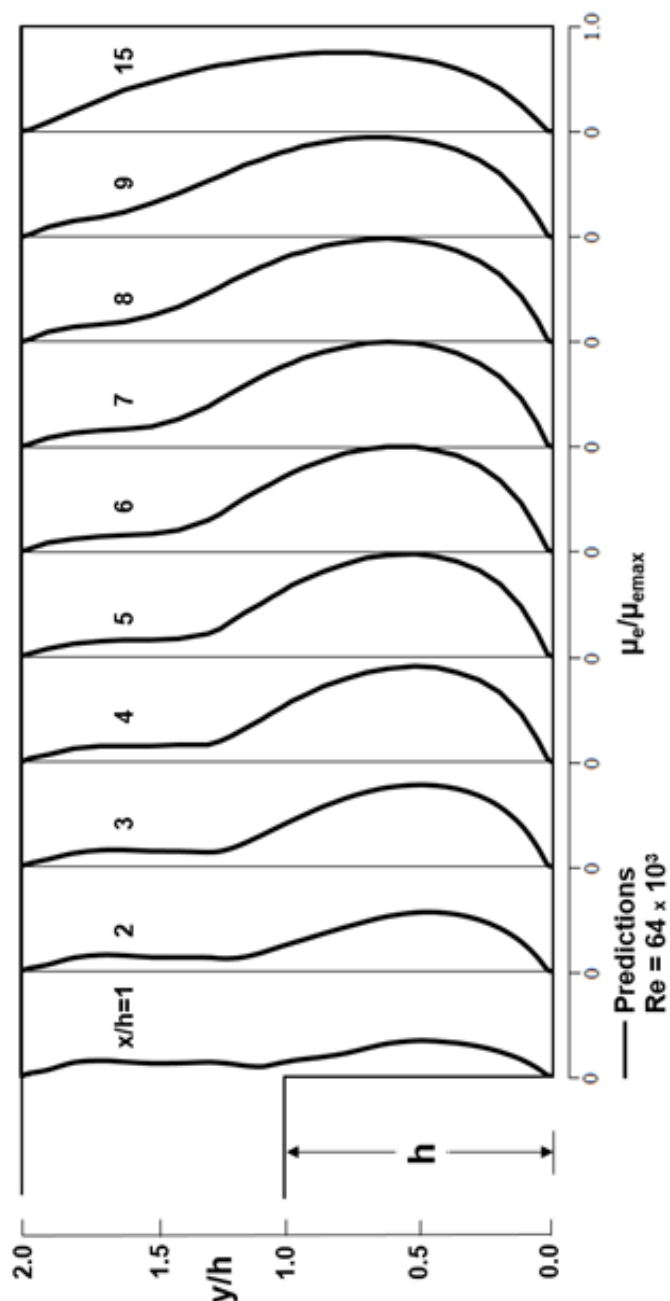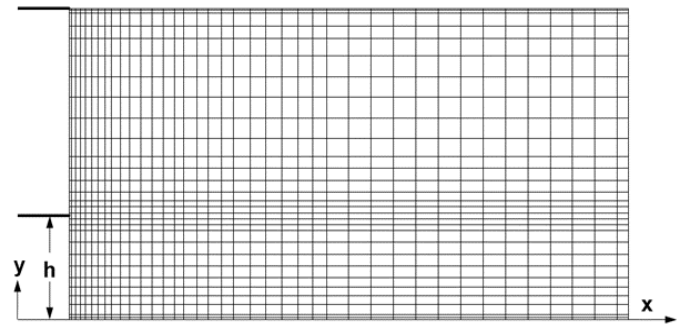

Figure 24: Numerical grid distribution for single-sided backward-facing step flow geometry of [8].
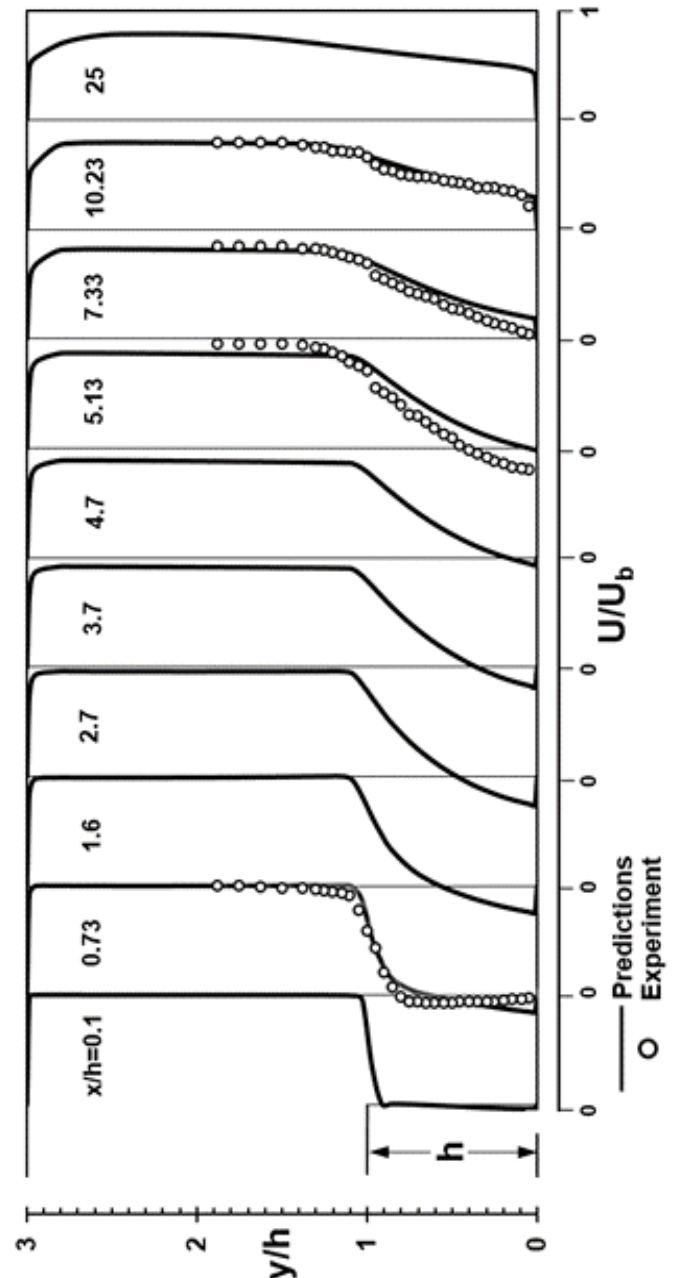
Figure 25: Comparison of predicted dimensionless streamwise velocity profiles along single-sided backward-facing step flow channel with experimental measurements of [8].
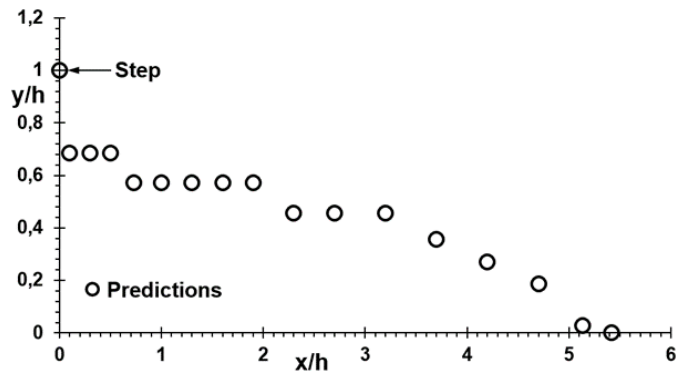
Figure 26: Predicted locus of flow reversal (u=0) for single-sided backward-facing step flow of [8].
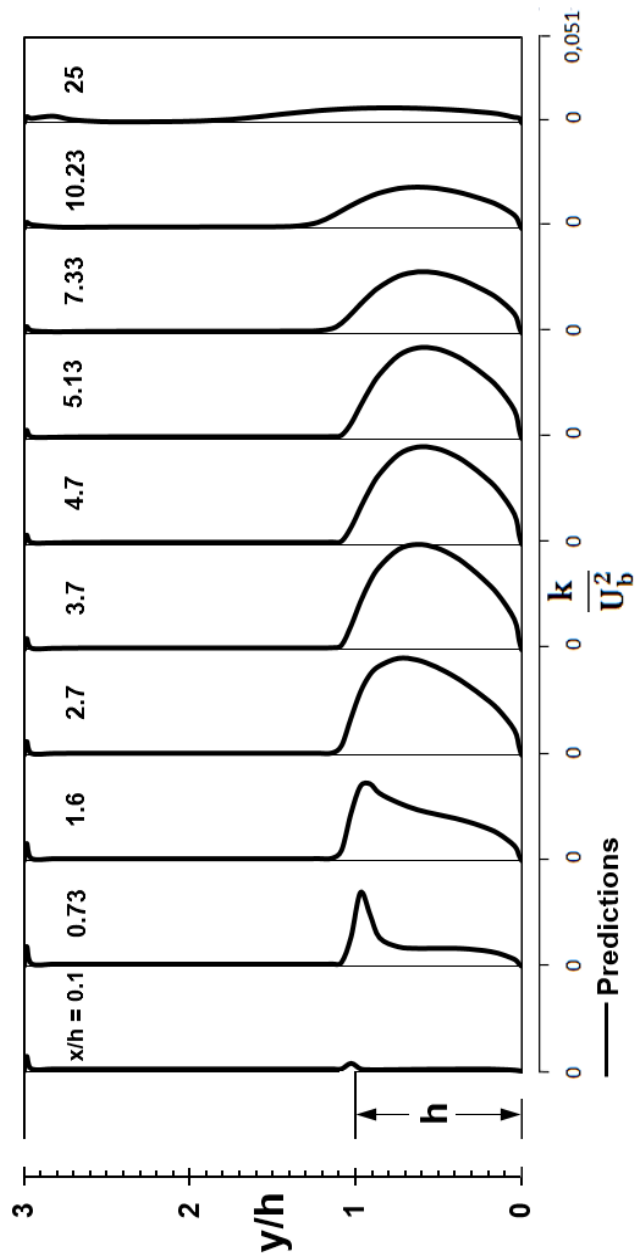
Figure 27: Predicted profiles of normalised turbulence kinetic energy along single-sided backward-facing step flow channel of [8].
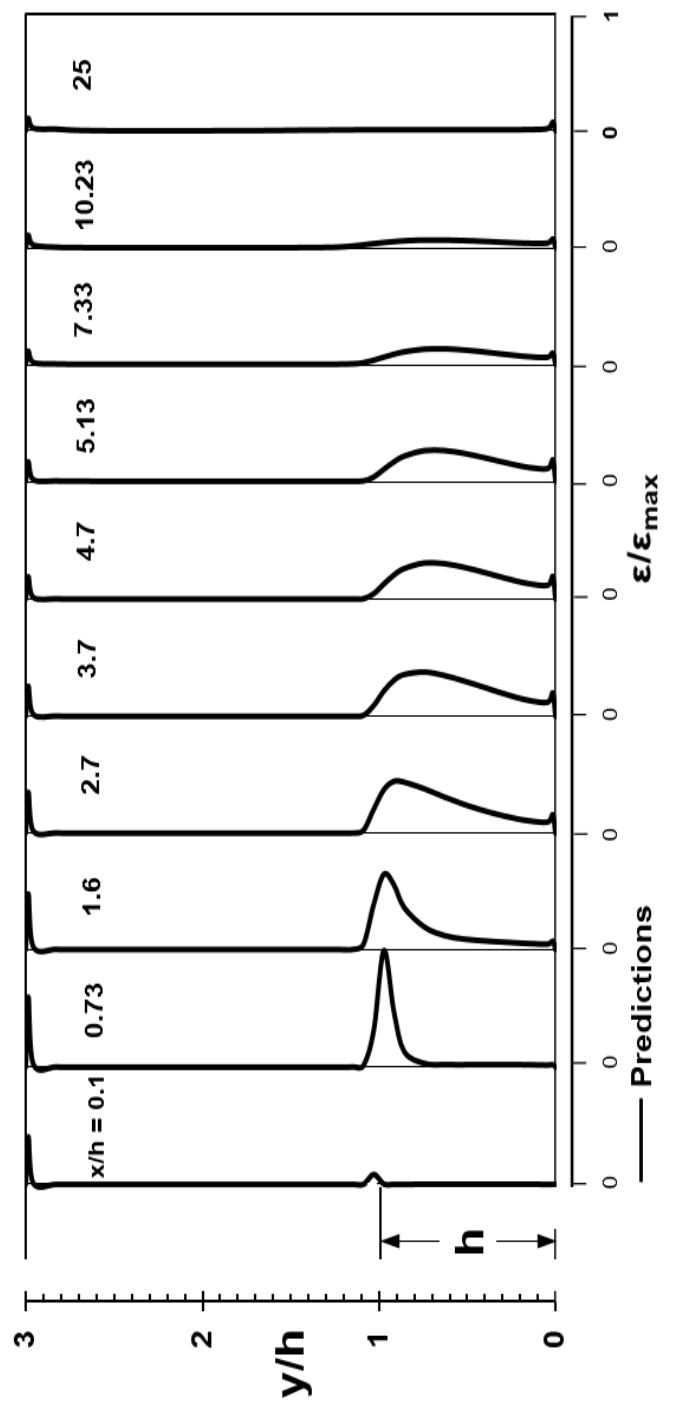
Figure 28: Predicted profiles of normalised turbulence kinetic energy dissipation rate along single-sided backward-facing step flow channel of [8].
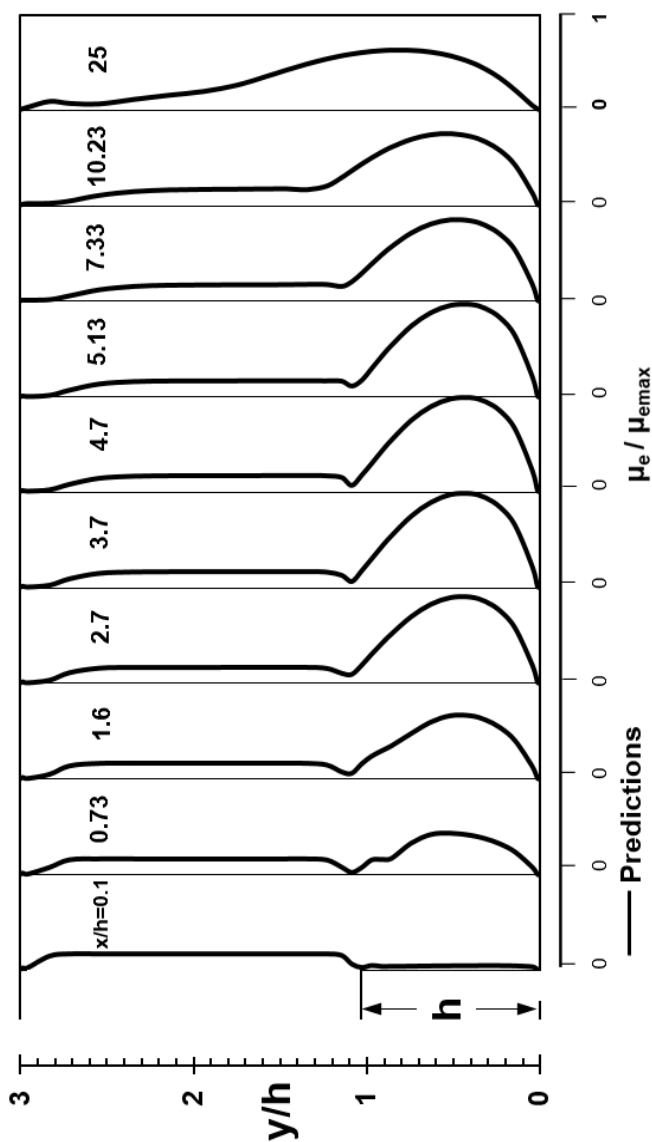
Figure 29: Predicted profiles of normalised effective viscosity along single-sided backward-facing step flow channel of [8].
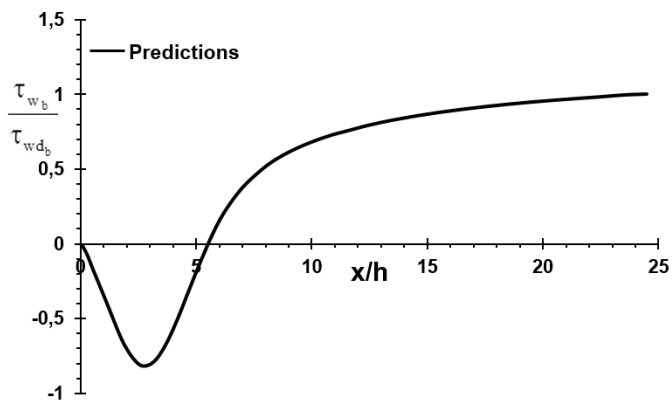
Figure 30: Computed distribution of dimensionless wall-shear stress along bottom-wall of single-sided backward-facing step flow channel of [8].
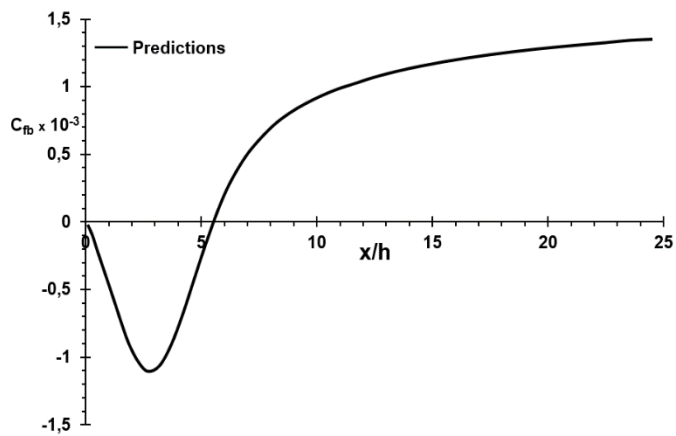
Figure 31: Computed variation of friction coefficient along bottom-wall of single-sided backward-facing step flow channel of [8].
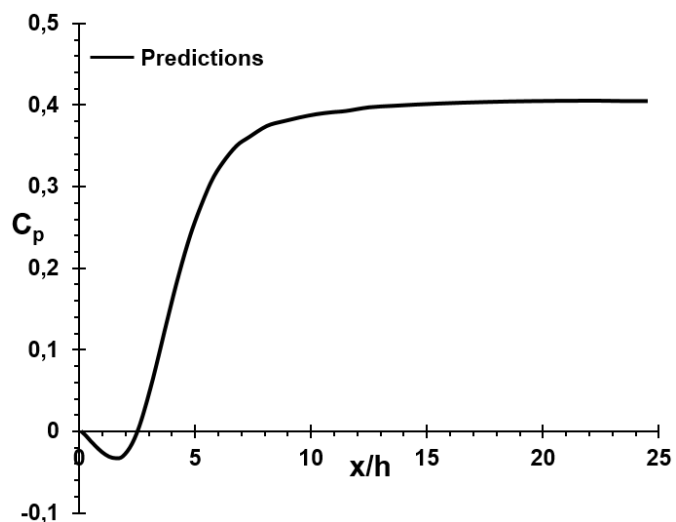
Figure 32: Predicted distribution of wall static-pressure coefficient (C_p) along bottom-wall of single-sided backward-facing step flow channel of [8].
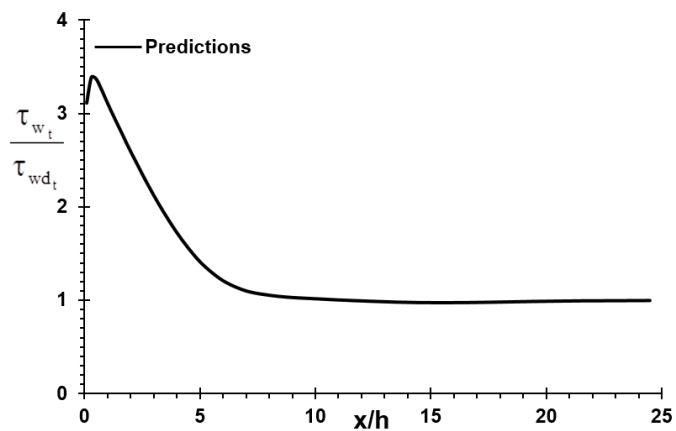
Figure 33: Predicted distribution of dimensionless wall-shear stress along top-wall of single-sided backward-facing step flow channel of [8].
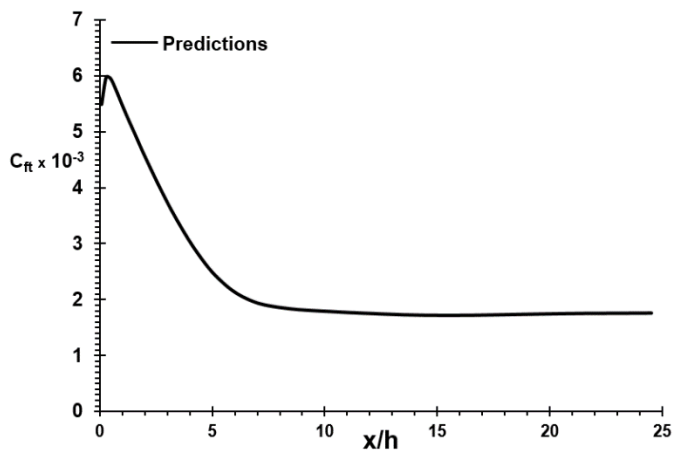
Figure 34**:** Computed variation of friction coefficient along top-wall of single-sided backward-facing step flow channel of [8].

IV. CONCLUDING REMARKS

The main concluding remarks from the computational investigation of the present original research work can be summarised as follows. Steady, incompressible, two-dimensional, separating and reattaching complex turbulent recirculating flow in single-sided backward-facing step flow channels at three different Reynolds numbers has been computed numerically employing the standard k-ε turbulence model. Using the finite-volume approach, a computer program based on the SIMPLE algorithm of Patankar [39] has been developed. The performance of the standard k-ε turbulence model has been investigated for three different single-sided backward-facing step flows. Numerical predictions for local streamwise velocity, turbulence kinetic energy, turbulence kinetic energy dissipation rate, effective viscosity profiles, locus of flow reversal, wall-shear stress, friction coefficient and wall static-pressure coefficient distributions along the single-sided backward-facing step flow channels top and bottom walls are presented and, wherever availlable, compared with experimental measurements reported in the literature. The results of computational investigation are generally in good agreement with experimental measurements.

REFERENCES

[1] E. W. Adams, and J. K. Eaton, "An LDA study of the backward-facing step flow, including the effects of velocity bias," *ASME J. Fluids Eng.*, 110, pp. 275-282, 1988.

[2] M. K. Denham, P. Briard, and M. A. Patrick, "A directionally sensitive laser anemometer for velocity measurements in highly turbulent flows," *J. Physics E: Scientific Instruments*, 8, pp. 681-683, 1975.

[3] W. H. Stevenson, H. D. Thompson, and R. R. Craig, "Laser velocimeter measurements in highly turbulent recirculating flows," *ASME J. Fluids Eng.*, 106, pp. 173-180, 1984.

[4] J. R. Fessler, and J. K. Eaton, "Particle response in a planar sudden expansion flow," *Experimental Thermal and Fluid Science*, 15, pp. 413-423, 1997.

[5] J. C. Vogel, and J. K. Eaton, "Combined heat transfer and fluid dynamic measurements downstream of a backward-facing step," *ASME J. Heat Transfer*, 107, pp. 922-929, 1985.

[6] K. B. Chun, and H. J. Sung, "Control of turbulent separated flow over a backward-facing step by local forcing," *Experiments in Fluids*, 21, pp. 417-426, 1996.

[7] J. Kim, S. J. Kline, and J. P. Johnston, "Investigation of a reattaching turbulent shear layer: flow over a backward-facing step," *ASME J. Fluids Eng.*, 102, pp. 302-308, 1980.

[8] W. A. de Groot, "Laser doppler diagnostics of the flow behind a backward-facing step," Ph.D. Thesis, Georgia Institute of Technology, Atlanta, GA, 1985.

[9] R. V. Westphal, and J. P. Johnston, "Effect of initial conditions on turbulent reattachment downstream of a backward-facing step," *AIAA Journal*, 22(12), pp. 1727-732, 1984.

[10] B. Ruck, and B. Makiola, "Particle dispersion in a single-sided backward-facing step flow," *Int. J. Multiphase Flow*, 14, pp. 787-800, 1988.

[11] M. V. Ötügen, "Expansion ratio effects on the separated shear layer and reattachment downstream of a backward-facing step," *Experiments in Fluids*, 10, pp. 273-280, 1991.

[12] N. Kasagi, and A. Matsunaga, "3-D particle-tracking velocimetry measurement of turbulence statistics and energy budget in a backward-facing step flow," *Int. J. Heat and Fluid Flow*, 16, pp. 477-485, 1995.

[13] J. T. Yang, B. B. Tsai, and G. L. Tsai, "Separated-reattaching flow over a backstep with uniform normal mass bleed," *ASME J. Fluids Eng.*, 116, pp. 29-35, 1994.

[14] D. M. Driver, and H. L. Seegmiller, "Features of a reattaching turbulent shear layer in divergent channel flow," *AIAA Journal*, 23(2), pp. 163-171, 1985.

[15] T. Karasu, *Numerical prediction of incompressible turbulent swirling flows in circular-sectioned ducts and annuli*, Ph.D. Thesis, University of London, London, U.K., 1980.

[16] T. Karasu, P. R. Choudhury, and M. Gerstein, "Prediction of some turbulent flows using upwind and hybrid discretisation schemes and the two-equation turbulence model," *Proc. 4th Miami international symposium on multi-phase transport and particulate phenomena*, Miami Beach, Florida, U.S.A., 5, pp. 105-124, 1988.

[17] T. Karasu, "Prediction of turbulent flow with heat transfer in an annulus with rotating inner cylinder," *Proc. 8th Miami international conference on alternative energy sources*, Miami Beach, Florida, U.S.A., vol. 2, pp. 361-385, 1989.

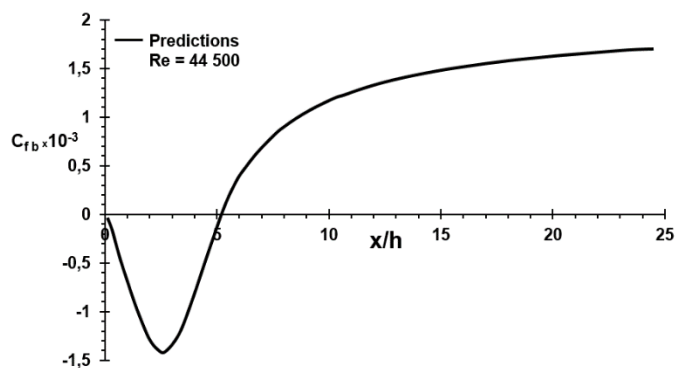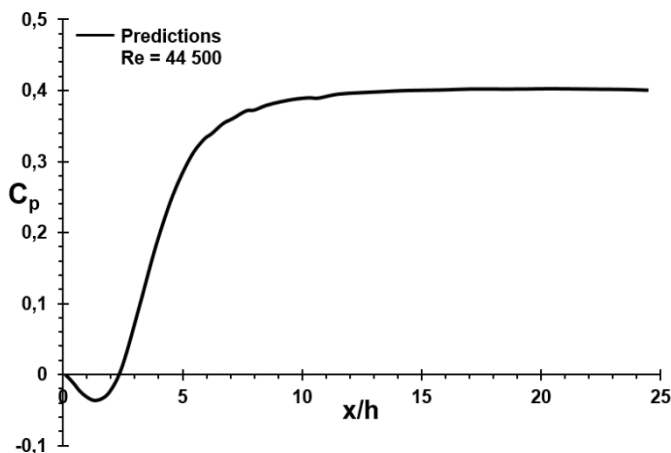[18] T. Karasu, "Numerical prediction of turbulent swirling flows in circular-sectioned annuli," *Proc. 5th Miami international symposium on multi-phase transport and particulate phenomena*, Miami Beach, Florida, U.S.A., vol. 1, pp. 149-174, 1990.

[19] T. Karasu, "Numerical study of turbulent flow in pipes," *Proc. 6th Miami international symposium on heat and mass transfer*, Miami, Florida, U.S.A., 1990.

[20] T. Karasu, "Numerical prediction of turbulent recirculating flow through axisymmetric sudden expansions," *10th International Conference on Numerical Methods in Laminar and Turbulent Flow*, 21st –25th July 1997, Swansea, U.K., Proceedings Book, Vol. 10, pp. 357-368, 1997.

[21] T. Karasu, "Numerical computation of turbulent flow in pipes," *Doğa-Tr. J. of Engineering and Environmental Sciences,* 17, pp. 29-38, 1993.

[22] T. Karasu, "Numerical solution of turbulent flow with heat transfer in an annulus with rotating inner cylinder," *Turkish Journal of Engineering and Environmental Sciences*, Vol. 12, No. 3, pp. 250-272, 1988.

[23] T. Karasu, "Numerical prediction of turbulent flow in circular pipes," *9th International Conference on Numerical Methods in Laminar and Turbulent Flow*, Atlanta, Georgia, U.S.A., Proceedings Book, Vol. 9, Part 2, pp. 1329-1339, 1995.

[24] T. Karasu, "Kapalı türbülanslı akışların modellemesi ve bilgisayarlı simülasyonu," *20. Ulusal Mekanik Kongresi*, 05-09 Eylül 2017, Uludağ Üniversitesi, Bursa, Türkiye. Bildiriler Kitabı, s. 1-12, 2017. ISBN 978-975561491-5.

[25] T. Karasu, "Numerical investigation and modelling of confined turbulent recirculating flows," *International Conference on Engineering Technologies (ICENTE'18)*, 26-28 October 2018, Selçuk University, Konya, Turkey, Proceedings Book, pp. 419-433, 2018. E-ISBN: 978-605-68537-3-9.

[26] T. Karasu, "Computational investigation of turbulent flow in pipes," *3rd International Conference on Advanced Technology and Sciences (ICAT'16)*, 01-03 September 2016, Selçuk University, Konya, Turkey, Proceedings Book, pp. 939-948, 2016.

[27] T. Karasu, "Numerical computation of developing turbulent flow between two parallel plates," *21. Ulusal Isı Bilimi ve Tekniği Kongresi (ULIBTK'17)*, 13-16 Eylül 2017, Hitit Üniversitesi, Çorum, Türkiye, Bildiri Kitabı, ss. 11-20, 2017.

[28] T. Karasu, "Numerical study of turbulent flow in circular-sectioned pipes," *8th Atmospheric Sciences Symposium (ATMOS'2017)*, 01-04 November 2017, Istanbul Technical University, Istanbul, Turkey, Proceedings Book, pp. 663-674, 2017. ISBN**:** 978-975-561-490-8.

[29] T. Karasu, "Numerical investigation of turbulent recirculating flow through plane symmetric sudden expansions," *IV. Uluslararası Katılımlı*

Anadolu Enerji Sempozyumu (AES'2018), 18-20 Nisan 2018, Trakya Üniversitesi, Edirne, Türkiye, Bildiri Kitabı, part 3, ss. 2044-2056, 2018.

[30] T. Karasu, "Kapalı türbülanslı çevrintili akışların modellemesi ve sayısal araştırılması," *14. Ulusal Tesisat Mühendisliği Kongresi (TESKON 2019)*, 17-20 Nisan 2019, MMO Tepekule Kongre ve Sergi Merkezi, İzmir, Bildiriler Kitabı, ss. 1276-1297, 2019.

[31] T. Karasu, "Numerical simulation of internal turbulent flows," *International Conference on Engineering Technologies (ICENTE'17)*, 07-09 December 2017, Selçuk University, Konya, Turkey, Proceedings Book, pp. 679-688, 2017.

[32] T. Karasu, "Computer simulation and modelling of cofined turbulent flows," *21. Ulusal Isı Bilimi ve Tekniği Kongresi (ULIBTK'17)*, 13-16 Eylül 2017, Hitit Üniversitesi, Çorum, Türkiye, Bildiri Kitabı, ss. 1-10, 2017.

[33] T. Karasu, "Borularda türbülanslı akışların sayısal simülasyonu," *VIII. Ulusal Hidrolik Pnömatik Kongresi,* 22-25 Kasım 2017, İzmir. Bildiriler Kitabı, ss. 69-83, 2017. MMO Yayın No: E/MMO/678. ISBN 978-605-01-1088-3.

[34] T. Karasu, "Paralel iki plaka arasında gelişen türbülanslı akışın sayısal araştırılması," *20. Ulusal Mekanik Kongresi*, 05-09 Eylül 2017, Uludağ Üniversitesi, Bursa, Türkiye. Bildiriler Kitabı, ss. 13-24, 2017. ISBN 978-975561491-5.

[35] T. Karasu, "Computer simulation of turbulent recirculating flow through circular-sectioned sudden expansion pipes," *7th International Conference on Advanced Technologies (ICAT'18)*, April 28-May 1, 2018, Antalya, Turkey, Proceedings Book, pp. 752-763, 2018. E-ISBN: 978-605-68537-1-5.

[36] T. Karasu, "Numerical investigation of turbulent recirculating flow in double-sided planar sudden expansions in channels," *7th International Conference on Advanced Technologies (ICAT'18)*, April 28-May 1, 2018, Antalya, Turkey, Proceedings Book, pp. 764-773, 2018. E-ISBN: 978-605-68537-1-5.

[37] T. Karasu, "Computer analysis and modelling of confined turbulent recirculating flows," *4th International Conference on Advances in Mechanical Engineering (ICAME'2018)*, 19-21 December 2018, Yıldız Technical University, Istanbul, Turkey, Proceedings Book, pp. 363-382, 2018. ISBN 978-605-9546-13-3.

[38] B. E. Launder, and D. B. Spalding, "The numerical computation of turbulent flows," *Comp. Meth. Appl. Mech. Engng*, 3, pp. 269-289, 1974.

[39] S. V. Patankar, *Numerical heat transfer and fluid flow*, Hemisphere, McGraw-Hill, Washington, D.C., Chapters 5 and 6, 79-138, 1980.

[40] S. V. Patankar, and D. B. Spalding, "A calculation procedure for heat, mass and momentum transfer in three-dimensional parabolic flows," *Int. J. Heat Mass Transfer*, 15, pp. 1787-1806, 1972.

[41] D. B. Spalding, "A general-purpose computer program for multi-dimensional one-and-two phase flow," *Math. Comput. Simulation*, XXIII, pp. 267-276, 1981.

Effects of surface roughness on strength of adhesive joints

A. ASLAN[1], E. SALUR[1], M. KUNTOĞLU[1]

[1] Selcuk University, Konya/Turkey, aaslan@selcuk.edu.tr

Abstract –**Adhesives are often used both in the production of composite materials and as joint element. Adhesives can be used in order to adhere different materials such as steel-aluminum, aluminum-composites, metal-woods…etc. Although there are a lot of parameters which can affects the bond quality, one of the most important parameters is surface roughness. Surface roughness values may vary according to the type of surface to be bonded. There are a lot of surface preparation techniques which can be used in adhesive joints. In this study, surface roughness values of adhesive surfaces were determined and optimized in aluminum-aluminum joints. Etching method was used as surface preparation techniques. After the surfaces were prepared, surface roughness measurements were occurred. In addition, micro structure views were taken from the surfaces by the help of optical microscope. It is said that optimal surface roughness values (R_a) were determined as approximately Ra=2.91 μm for aluminum-aluminum joints. Similarly, Rz μm values were measured as 12.1 The highest strength was obtained via etching method.**

Keywords – **Adhesives, adhesive joints, surface roughness, surface preparation.**

I. INTRODUCTION

Adhesive joints are frequently used in many academic and industrial applications. Recent developments in the field of composite materials have gained momentum with the presence of adhesives and adhesive joints. Due to the engineering approaches based on energy efficiency, the lightness of the designed machine element has become an important design criterion. Therefore, the use of adhesive joints in place of conventional fasteners has become widespread [1, 2]. Adhesive joints provide the external forces acting on it by means of its own cohesion and adhesion resistance on the part surface. It is preferred because of its ease of application, absence of irregularities such as holes and notches on the elements to be connected, which may cause stress accumulation, connection of different materials, providing sealing, having good damping properties, low risk of fatigue damage and good strength weight ratio [3].

With the help of the studies on adhesives, it is aimed to increase the adhesive strength and the joint quality between adhesive and adhesion surfaces. For this, the joint conditions and the place where the joint is used should be analyzed and a suitable joint type should be determined [4].

The free energy of the bonding surfaces must be higher than the surface tension of the adhesive. In some cases (especially when the materials to be bonded are polymers or polymer matrix composites), the free energy of these surfaces needs to be modified to be compatible with the adhesive. Therefore, it is necessary to apply surface preparation processes in order to homogenize the surfaces, form certain chemical groups, bring the surface roughness to the desired level or remove weak boundary layers [5, 6]. Many different types of surface treatments are used, including mechanical (sandblasting, sanding), chemical (anodizing, etching) and energy-based (plasma, laser) [7]. Surface preparation of aluminum joints is a difficult and long-term process [8]. Although the surface preparation process in aluminum alloys varies according to the type of aluminum and the type of adhesive, the etching process is suitable for bonding aluminum with epoxy [9]. Similarly, it is reported that sanding is a best method for preparation of composite adhesive joint surfaces. Not only roughness of adhesive surfaces but also homogeneity of roughness is another important condition [10].

In this study, three types of aluminum surface were compared in terms of joint quality (strength). Three different surfaces (only cleaned, sanded, etched) were prepared and surface roughness were measured. After the measurements, specimens were adhered with epoxy resin. SLJ tests were occurred and strength of joint were compared. Comparison of the specimens revealed that optimum surface roughness values were Ra=2.91, Rz=12.61 Rmax=16.4 μm for adhesive joints. Homogeneity of the surface roughness examined with micro structures views.

II. MATERIALS AND METHODS

Aluminum SLJ joints were used as test specimen. Firstly, aluminum sheets were cut to 101,6 x 25 mm dimensions. Adhesion surfaces were prepared three different ways which are cleaned, sanded and etched. Before adhesion process, surface roughness of surfaces was measured (Fig 1).

Figure 1: Surface roughness measurements

Aluminum parts were adhered with commercial epoxy resin and cured according to curing process. SLJ tests were made in order to determine strength of joints. Fig 2 and 3 showed that specimens and test.
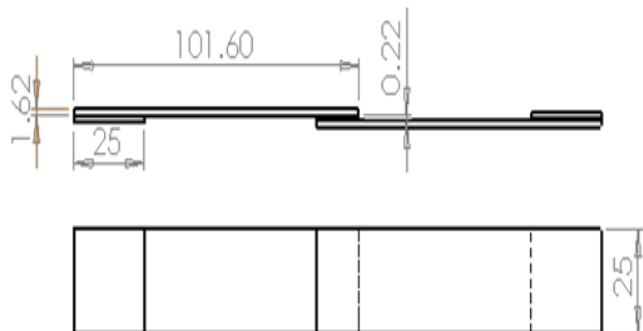
Figure 2: Test specimen

Figure 3: SLJ test

III. RESULTS AND DISCUSSION

Figure 4 show that surface roughness results of aluminum joints. As seen in the fig 4, the lowest surface roughness values were obtained from cleaned surfaces. When residues such as oil, humidity, were cleaned, bright and smooth surfaces arose. Surface roughness measurements showed that etching process increase roughness significantly. Ra increase from 0.224 to 2.029. Over etching process showed that another important parameter was etching time. If the optimum etching time is exceeded, surface roughness values increase. The highest roughness values were observed in sanded process which was 4.28.
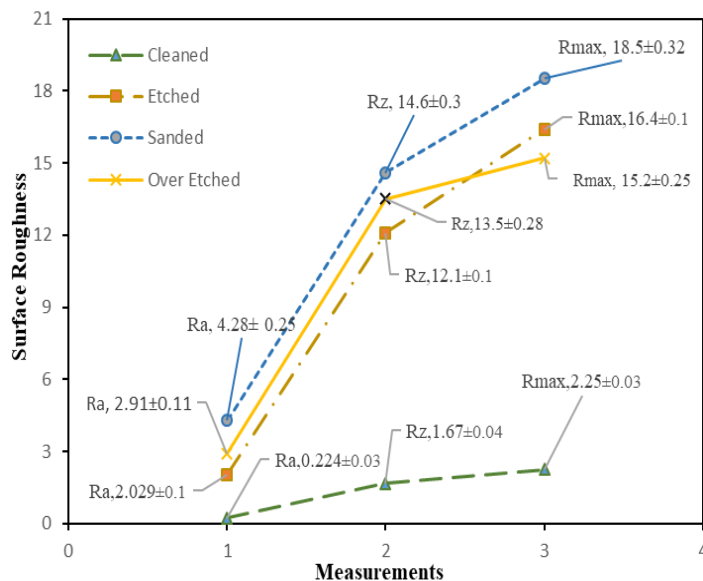
Figure 4: surface roughness values

The effects of surface roughness on strength of joint results showed in figure 5. The highest strength was obtained from etched specimen. It is higher than nearly 300% from cleaning process, 30% from sanding process, 26% from over etching process. Adhesion mechanism of epoxy-aluminum joint were examined, the most effective adhesion mechanism was mechanical interlocking according to literature [11]. The test results support the literature. There is an optimum surface roughness value which can enhance the mechanical interlocking mechanism. The higher or lower surface roughness values have negative effects on mechanical interlocking mechanism, and it causes decrease of joint strength.
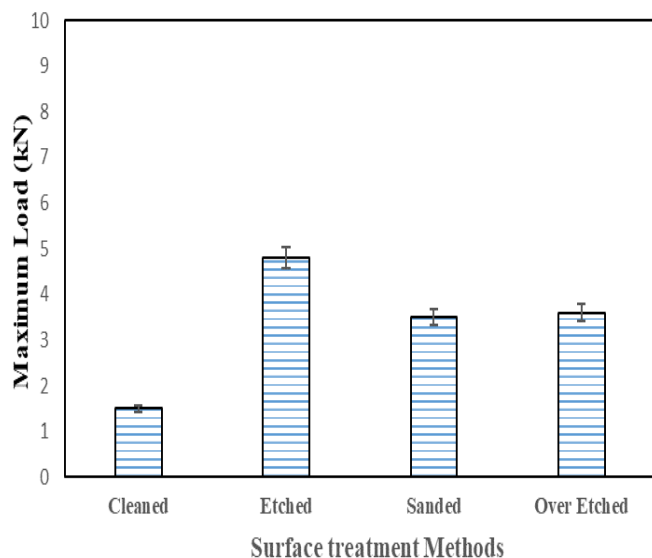
Figure 5: Strengths of aluminum joints

Fig 6 a, b, c, d, show cleaned, etched, sanded and over etched specimen surfaces. When the aluminum surface was cleaned, there were only micro and scratches which stem from production or transportation. After the etching process were applied, there were spheroidal alumina oxides on the surface homogeneously. Strength of alumina oxides are higher than aluminum. Therefore, the aluminum oxides on the surface facilitate the adhesion of the epoxy resin to the aluminum surface [12]. Sanding process cause deep scratches on the surface. However, it cannot increase the strength as far as etching process [13].
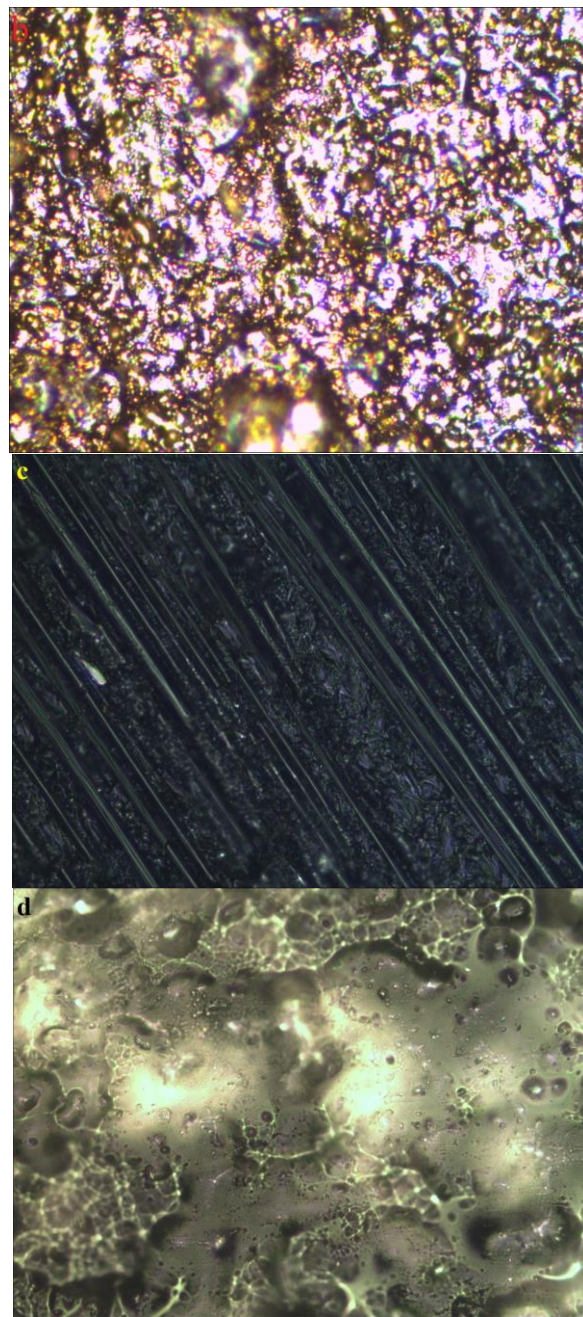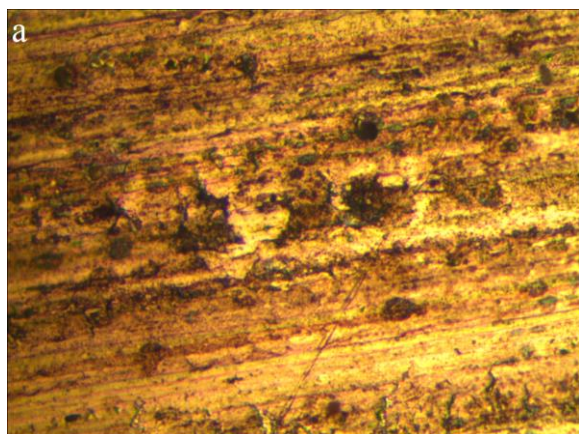
Figure 6: Micro structures, **a-**Cleaned **b-** Etched **c-** Sanded **d-** Over Sanded

IV. CONCLUSION

In this study, effects of surface treatment methods (via surface roughness values) on strength of aluminum joints were determined. The important points obtained from the experiments are shown below:

- The optimum surface roughness was obtained from etching process.
- Over etching may cause the decrease of strength owing to loss of homogeneity of surface roughness.
- Only cleaning is not enough in order to obtain a good aluminum joint.

- Sanding process can be preferred in some applications which can not be needed high strength bonding.

REFERENCES

1. Kaya, *Ana Hatlarıyla Yapıştırıcılar*. 2004, İstanbul: Birsen Yayınevi. 240.
2. Da Silva, L.F., A. Öchsner, and R.D. Adams, *Handbook of adhesion technology*. 2011: Springer Science & Business Media.
3. Higgins, A., *Adhesive bonding of aircraft structures.* International Journal of Adhesion and Adhesives, 2000. **20**(5): p. 367-376.
4. Pocius, A.V. and D.A. Dillard, *Adhesion science and engineering: surfaces, chemistry and applications*. 2002: Elsevier.
5. Van Ooij, W., *Industrial Adhesion Problems*. 1985, Orbital Press Oxford.
6. Verbruggen, M.L., *Aramid reinforced aluminium laminates: Arall: adhesion problems and environmental effects. Volume A: Adhesion and delamination.* 1987.
7. Sabbineni, K., *Investigation of polymer nanocomposites reinforced with nanocarbon*. 2015: Lamar University-Beaumont.
8. Lunder, O., B. Olsen, and K. Nisancioglu, *Pre-treatment of AA6060 aluminium alloy for adhesive bonding.* International journal of adhesion and adhesives, 2002. **22**(2): p. 143-150.
9. Prolongo, S., et al., *Effects of dispersion techniques of carbon nanofibers on the thermo-physical properties of epoxy nanocomposites.* Composites Science and Technology, 2008. **68**(13): p. 2722-2730.
10. Miracle/Donaldson, *ASM Handbook volume 21: Composites*. 2001: ASM International.
11. Davis, J.R., *Aluminum and aluminum alloys*. 1993: ASM international.
12. Petrie, E., *Plastics and adhesives as adhesives.* Handbook of plastics and elastomers, 1975.
13. Petrie, E.M., *Plastics and elastomers as adhesives.* Handbook of Plastics, Elastomers, and Composites, 2002: p. 397.

Taguchi based optimization in high speed turning

A. ASLAN[1]

[1]Selcuk University, Konya/Turkey, aaslan@selcuk.edu.tr

Abstract – **Turning is one of the most widespread and basic machining method. There are a number of expectations from the turning process such as, high efficiency, low cutting forces, low tool wear, long-term tool life …etc. However, one of the most significant machining output is quality of machined surface. The machined surface quality can be evaluated by means of surface roughness parameters such as Ra and Rz. Surface roughness parameters not only gives information about the workpiece but also about the tool. Therefore, if the machining parameters can be optimized sensitively, both effective tool condition monitoring and workpiece with desired surface quality can be obtained. In this work, optimization of the surface roughness has been realized during the turning of 5140 steel material under dry cutting conditions. Taguchi L$_8$ orthogonal array design based 8 experiments were performed with 2-level parameters (cutting speed, feed rate, depth of cut and approaching angle) and statistical analysis was carried out with ANOVA. 3 different measurements were taken from the beginning, middle and at the end of the workpiece in order to provide measurement reliability. Detailed investigation of results showed that both Ra and Rz are affected from depth of cut mostly (25% and 27%). After that, the cutting speed (21%), feed rate (16% and 17%) and approaching angle (25% and 27%) have significant contribution on surface parameters Ra and Rz respectively.**

Keywords - **Surface Roughness, Taguchi design, AISI 5140, Turning,**

I. INTRODUCTION

History of the manufacturing show that decreasing human intervention on production process increase the efficiency. The most important reason of this is the possibility of making a mistake owing to tiredness, carelessness etc. As the rivalry has increased day by day, the continuous development of manufacturing in parallel with new demands emerged today's industry, minimal error, maximum efficiency and lowest cost principles should be preferred in order to compete. Surface roughness control of workpiece has been usually preferred in order to tool wear monitoring and optimisation of cutting forces, cutting speed, feed rate and depth of cut.

Literature review showed that as the worn surface of the cutting edge remains, it should be changed whether the surface roughness values are critical or not [1-3]. A number of method ,which are the multiple regression technique [4], mathematical modelling based on the physics of the process [5], the fuzzy-set-based technique [6], and neural network modelling, [7-9] were developed in order to prediction of surface roughness.

Effects of machining parameters on surface roughness were studied by researchers [10, 11]. Aouici et al. indicated that the cutting force components were influenced principally by the depth of cut and workpiece hardness. In addition both feed rate and workpiece hardness have statistical importance on surface roughness [11]. Another study revealed that a linear model best fits variation of cutting forces with feed rate and depth of cut and depth of cut is a dominant contributor to the feed force. Besides, a non linear quadratic model can describes the variations of surface roughness [12]. Bouacha et al. said that how the thrust forces and feed rate influence the surface roughness. In addition, the depth of cut affects the cutting forces as compared to the feed rate and cutting speed [13]. It is revealed by some researchers that prediction of proper cutting conditions and surface topography were calculated by means of an algorithm which is developed by themselves [14]. There are a strong relationship between surface roughness and work piece properties such as tribological, sealing, hydrodynamic, electrical and thermal conduction. High quality surfaces can be obtained from machining parameters which are decreasing depth of cut, low feed rate, high cutting speed , increased delivery of cutting fluid, higher rake angels, and nose radius [15].

Modern-day industry sector claims maximum productivity in minimum time. To achieve this, optimization methods should be preferred. Produced surface during machining operations become quite important according to in-service conditions. In this context, to obtain demanded quality provides reliable and durable appearance to manufacturer. This study includes experimental work, optimization and statistical analysis of surface roughness in high speed dry turning of AISI 5140 carbon steel. To optimize surface roughness parameters namely Ra and Rz, Taguchi based experimental design was constituted firstly. And lastly, the effects of cutting speed, feed rate, depth of cut and approaching angle on surface roughness parameters were investigated. The selected two-phase methodology provides substantially information with minimum labour with Taguchi and advice for academic and industrial concerns about high speed turning for future studies.

II. EXPERIMENTAL SET UP

The effects of machining parameters on surface roughness are examined in this study. A lathe was used in order to machine work piece. Turning process was carried out under dry conditions. Cutting parameters were selected as shown in

table 1. Komet branded cutting tools were used for turning operation.

Table 1: Cutting parameters

Factors / Levels	Cutting speed (v) (m/min)	Feed rate (f) (mm/dev)	Depth of cut (d) (mm)	Approaching Angle (κ) (°)
Level 1	350	0.1	2.0	90
Level 2	240	0.05	1.5	60

In order to measure of surface roughness, MAHR surf test profilometer was used (Fig 1). The measurement length was 6 mm and the profilometer gave a one value for each surface parameter by averaging the all measurements taken from distances of 6 mm.   To ensure the test reliability, measurements were made from there different locations (first, middle and last region of the workpiece). As it is known there are two types of surface roughness values which are Ra, Rz. All of three surface roughness values were measured and averaged.

Figure 1: Surface roughness measurements

Taguchi method used for optimization of this manufacturing process. An orthogonal array design was made for two-level for variables (L_8) experiments were made. Analysis of variance (ANOVA) provides to understand how much the effect of each parameter (independent variable) on quality characteristics (dependent variable). Besides, Taguchi based ANOVA ensures to obtain the optimum parameters for expected output. This is determined with S/N ratios and objective function which can be "smaller is better", "larger is better" or "nominal is the best" according to the situation of result.

The workpiece used in this study is AISI 5140 steel and it is used for production of engine parts, axels tubes, front axels, steering shaft, crank shaft, construction and agriculture machines, machine tools, bolt, screw nut. Besides, it is suitable for surface hardening. It is known that high toughness.

The dimensions of workpiece is 55x35 mm (Ø x L) and its chemical composition was shown in table 2.

Table 2: Chemical composition of AISI 5140 steel

C	Mn	Pmax	Smax	Cr
0,38-0,45	0,6-0,9	0,035	0,035	0.9-1.2

Taguchi L_8 orthogonal array design is demonstrated in Table 3. This approach aims to reduce the number of experiment which directly affects experimental burden, waste materials and energy loss. In this study, instead of 16 experiments, 8 experiments were carried out and significant time and cost income were obtained. Using Taguchi method, to calculate the standard deviation from the surface roughness parameters objective functions were used. Besides, to reduce the error rates noise factors were decreased with orthogonal arrays. In this paper, smaller is better type S/N ratio was preferred because of the aim of the little surface roughness results. Smaller is better type S/N ratio is calculated with this equation:

$$S/N = -10\log 1 / n \left(\sum y^2\right)$$

Table 3: Taguchi L_8 orthogonal design

Parameter / E. N.	κ (°)	v (m/dak)	f (mm/dev)	d (mm)
1	1	1	1	1
2	1	1	2	2
3	1	2	1	2
4	1	2	2	1
5	2	1	1	2
6	2	1	2	1
7	2	2	1	1
8	2	2	2	2

III.   RESULTS AND DISCUSSION

The experimental design and surface roughness results are shown in Table 4. Using L_8 orthogonal design Table 4 is constituted and contains 2-level approaching angle, feed rate, depth of cut and cutting speed. According to experimental results, minimum surface roughness results are obtained at 8. Experiment for Ra (0.511 μm) and Rz (2.87 μm).

ANOVA results for S/N ratios for Ra and Rz are demonstrated in Table 5 and 6 respectively. The effect of cutting parameters and tool geometry were calculated with sum squares (SS) and the percent contributions were obtained to demonstrate the rate of influence on Ra (d>v>f>κ) and Rz (d>v>f>κ). F and P-values verify these results.

Response table for S/N ratios for Ra and Rz are demonstrated in Table 7 and 8 respectively. Response table results also confirm the dominant effect of depth of cut (Δ=4.94358 for Ra and Δ=4.99 for Rz). S/N ratios state that the bigger value demonstrate optimal value for each level of

parameter. Therefore, second level of cutting speed, feed rate, depth of cut and approaching angle should be selected for optimum or minimum surface roughness values.

Table 4: Experimental design and results

E.N.	κ (°)	v (m/dak)	f (mm/dev)	d (mm)	Ra (μm)	Rz (μm)
1	90	350	0.1	2.0	3.454	19.3
2	90	350	0.05	1.5	0.628	3.39
3	90	240	0.1	1.5	0.522	3.43
4	90	240	0.05	2.0	0.739	4.203
5	60	350	0.1	1.5	0.787	4.35
6	60	350	0.05	2.0	0.693	4.466
7	60	240	0.1	2.0	0.727	3.996
8	60	240	0.05	1.5	0.511	2.87

Table 5: ANOVA Results for S/N Ratios for Ra

Source	Dof	SS	MS	F	P	PC (%)
κ	1	18.98	18.98	1.02	0.386	10
v	1	42.09	42.09	2.27	0.229	21
f	1	31.79	31.79	1.71	0.282	16
d	1	48.88	48.88	2.64	0.203	25
Error	3	55.64	18.55	-	-	-
Total	7	197.37	-	-	-	-

Table 6: ANOVA Results for S/N Ratios for Rz

Source	Dof	SS	MS	F	P	PC (%)
κ	1	19.63	19.63	1.25	0.345	10
v	1	39.23	39.23	2.5	0.212	21
f	1	31.95	31.95	2.03	0.249	17
d	1	49.9	49.9	3.18	0.173	27
Error	3	47.15	15.72	-	-	-
Total	7	187.85	-	-	-	-

Table 7: Response Table for S/N Ratios for Ra

Level	Approaching Angle	Cutting Speed	Feed Rate	Depth of Cut
1	0.38235	-0.37118	-0.07073	-0.54294
2	3.46276	4.21628	3.91584	4.39434
Delta (Δ)	3.08041	4.58746	3.98657	4.94358
Rank	4	2	3	1

Table 8: Response Table for S/N Ratios for Ra

Level	Approaching Angle	Cutting Speed	Feed Rate	Depth of Cut
1	-14.87	-15.52	-15.31	-15.8
2	-11.74	-11.09	-11.31	-10.81
Delta (Δ)	3.13	4.43	4.00	4.99
Rank	4	2	3	1

IV. CONCLUSIONS

In this study, experimental and statistical work has been performed in high speed dry turning of AISI 5140 steel. Taguchi based ANOVA approach provided the dominant parameters on surface roughness parameters namely Ra and Rz. Besides Taguchi method gives the optimal results to obtain minimum surface roughness. According to results, the following deductions can be done:

1. During turning, with the effect of high speeds and relative motion of workpiece and cutting tool new surface is produced and causes high temperature and pressure. Specifically for high speed turning, some extreme results can be appear in terms of temperature and pressure. Deviations at workpiece-cutting tool contact area become highly fluctuated. In this context, surface roughness value was investigated.

2. The interacted variables make difficult to predict the results in machining operations. Therefore, to achieve optimum results wide range of machining parameters should be experienced.

3. ANOVA results showed that depth of cut is the most effective parameter on Ra and Rz with 25% and 27% contribution rate. High cutting speeds prevent BUE formation and the traditional effects of parameters change. Besides, Mn and Cr involved AISI 5140 effects tool wear characteristics and indirectly changes surface roughness parameters. On the contrary of literature, feed rate or cutting speed seem less effective compared to depth of cut.

4. After depth of cut, cutting speed (21% and 21%), feed rate (16% and 17%) and approaching angle (10% and 10%) seem influent on Ra and Rz respectively according to variance analysis. The rate of effectiveness was confirmed by F-values.

5. Responses for S/N ratios showed that second level cutting parameters will be the optimum choices to obtain minimum surface roughness results. According to S/N ratio results, v_2 (240 m/min), f_2 (0.05 mm/rev), d_2 (1.5 mm) and $κ_2$ (60°) will be the best options to optimize Ra (0.511 μm) and Rz (2.87 μm).

REFERENCES

1. Gong, F., et al., *Fatigue failure of coated carbide tool and its influence on cutting performance in face milling SKD11 hardened steel.* International Journal of Refractory Metals and Hard Materials, 2017. **64**: p. 27-34.
2. Mikołajczyk, T., et al., *Neural network approach for automatic image analysis of cutting edge wear.* Mechanical Systems and Signal Processing, 2017. **88**: p. 100-110.
3. Salur, E., et al., *Experimental study and analysis of machinability characteristics of metal matrix composites during drilling.* Composites Part B: Engineering, 2019. **166**: p. 401-413.
4. Arbizu, I.P. and C.L. Perez, *Surface roughness prediction by factorial design of experiments in turning processes.* Journal of Materials Processing Technology, 2003. **143**: p. 390-396.
5. Jurkovic, Z., G. Cukor, and I. Andrejcak, *Improving the surface roughness at longitudinal turning using the different optimization methods.* Tehnicki Vjesnik, 2010. **17**(4): p. 397-402.
6. Ali, Y. and L. Zhang, *Surface roughness prediction of ground components using a fuzzy logic approach.* Journal of materials processing technology, 1999. **89**: p. 561-568.
7. Tsao, C. and H. Hocheng, *Evaluation of thrust force and surface roughness in drilling composite material using*

Taguchi analysis and neural network. Journal of materials processing technology, 2008. **203**(1-3): p. 342-348.

8. Zain, A.M., H. Haron, and S. Sharif, *Prediction of surface roughness in the end milling machining using Artificial Neural Network.* Expert Systems with Applications, 2010. **37**(2): p. 1755-1768.

9. Asiltürk, I. and M. Çunkaş, *Modeling and prediction of surface roughness in turning operations using artificial neural network and multiple regression method.* Expert systems with applications, 2011. **38**(5): p. 5826-5832.

10. Lin, W., B. Lee, and C. Wu, *Modeling the surface roughness and cutting force for turning.* Journal of Materials Processing Technology, 2001. **108**(3): p. 286-293.

11. Aouici, H., et al., *Analysis of surface roughness and cutting force components in hard turning with CBN tool: Prediction model and cutting conditions optimization.* Measurement, 2012. **45**(3): p. 344-353.

12. Lalwani, D., N. Mehta, and P. Jain, *Experimental investigations of cutting parameters influence on cutting forces and surface roughness in finish hard turning of MDN250 steel.* Journal of materials processing technology, 2008. **206**(1-3): p. 167-179.

13. Bouacha, K., et al., *Statistical analysis of surface roughness and cutting forces using response surface methodology in hard turning of AISI 52100 bearing steel with CBN tool.* International Journal of Refractory Metals and Hard Materials, 2010. **28**(3): p. 349-361.

14. Bouzakis, K.-D., P. Aichouh, and K. Efstathiou, *Determination of the chip geometry, cutting force and roughness in free form surfaces finishing milling, with ball end tools.* International Journal of Machine Tools and Manufacture, 2003. **43**(5): p. 499-514.

15. Cakir, M.C., C. Ensarioglu, and I. Demirayak, *Mathematical modeling of surface roughness for evaluating the effects of cutting parameters and coating material.* Journal of materials processing technology, 2009. **209**(1): p. 102-109.

Tool Condition Monitoring with Sensor Fusion in Turning AISI 5140

M. KUNTOĞLU[1] A. ASLAN[2] H. SAĞLAM[3]

[1]Selcuk University, Konya/Turkey, mkuntoglu@selcuk.edu.tr
[2]Selcuk University, Konya/Turkey, aaslan@selcuk.edu.tr
[3]Selcuk University, Konya/Turkey, hsaglam@selcuk.edu.tr

Abstract – **The existence of high temperature and pressure make cutting area highly hard-to-access in machining operations. The changes occurring at workpiece-cutting tool contact should be monitored in turning operations. A tool condition monitoring system (TCMS) embodies sensors, data acquisition unit and data processing software. Also, sensors providing consistent information with each other generate sensor fusion. This paper aims to investigate surface roughness parameters (Ra and Rz) via resultant cutting force and vibration during dry turning of AISI 5140 material. Experimental data and statistical analysis outcomes demonstrated that to achieve the optimum Ra and Rz, higher cutting speeds and lower feed rates should be selected. Cutting speed is the most effective about 49% and 61% while feed rate have influence about 36% and 28% on Ra and Rz respectively. Newly produced surface reflects directly the condition of cutting tool and indirectly cutting forces, tool tip temperature, chatter vibration etc. As a result, the findings for optimizing surface roughness were verified with vibration and resultant cutting force analysis impressed mostly from cutting speed (66%) and feed rate (61%) respectively. Finally, vibration and resultant cutting force data comprises reliable and robust sensor fusion according to regression analysis result (90,8% for Ra and 89,1% for Rz)**

Keywords – **Tool Condition Monitoring, Sensor Fusion, Vibration, Cutting Force, Surface Roughness**

I. INTRODUCTION

Increasing expectation from manufacturing industries incite the manufacturers low cost, high productive and short time production methods. The assistance of developing technology makes easy the detection of error providing reliable process. The requirement of high quality product guides the producers to understand the behaviour of tool and workpiece during chip removing under different conditions. Several factors (machine tool, cutting speed, feed rate, tool geometry, cutting fluid, depth of cut, tool hardness, workpiece quality) and variables (cutting temperature, power, chatter, cutting force, vibrations) should be kept under control from the start to last second.

Aforementioned parameters can be classified as dependent and independent variables. The independent variable states the changes at variable occurring with the interference of operator while the dependent variable fluctuates according to the independent variables and noise factors. Actually, optimization process requires a complete design and knowledge saving. Therefore, following instructions should be performed respectively for obtaining a whole optimization.

- Independent variables should be chosen correctly after the preliminary tests.
- Dependent variables should be monitored in real time with several sensors and measurement equipments.
- The relationship between inputs and results should be established correctly.
- The noise factors should be eliminated to prevent erroneous results.

TCMSs include sensors, monitoring device, data logger and software to collect and evaluate the information to decide about the process. On the other hand, using multiple sensors in TCMSs brings significant advantages as accuracy, reliability and comparability. The sensors showing consistent information compose a sensor fusion. There are several researchers investigated TCMSs and sensor fusion approach in literature. Ahmed et. al. [1] used acoustic emission and cutting force data to monitor build-up-edge formation during turning of AISI 304 steel. The authors imported that both AE and cutting force signals can successfully detect the build-up-edge wear. Guo and Ammula [2] used AE signal parameters to investigate surface damage and surface integrity during turning of AISI 52100 material. AE signal structure reflects the surface damage and surface integrity. Prasad et. al. [3] developed a temperature and vibration signal based TCMS using coated and uncoated carbide inserts during turning 316L steel. According to progressive tool wear, the changes in temperature and vibration were investigated. Caggiano et. al. [4] presented force, torque, AE and vibration signal based condition monitoring study during drilling. Besides, neural network based prediction approach was implemented and diagnosed tool wear successfully. Panda et. al. [5] proposed an accelerometer based tool wear and surface roughness monitoring system in hard turning. They expressed the correlation between vibration and surface roughness-tool wear. Saglam and Unuvar [6] applied a neural network based milling operation using cutting forces for tool wear and surface roughness. The results showed that additional to cutting parameters cutting forces provide a close relationship for estimating Ra and tool wear. Azouzi and Guillot [7] proposed a sensor fusion system to estimate the dimensional deviation and Ra parameter includes feed rate, depth of cut and cutting force components. Sick [8] reviewed monitoring of indirect and on-line tool wear monitoring systems with

neural networks. Saglam [9] studied a neural network based milling operation to predict the surface roughness and tool wear. The developed model includes cutting parameters namely cutting speed, feed rate and depth of cut and cutting force components can successfully predict dependent variables. Kuntoğlu and Sağlam [10] proposed an on-line monitoring system based on cutting force and AE signals to optimize tool wear in turning. Implemented system showed the sensorial data detected the tool wear progression and possible tool breakage. Ratava et. al. [11] performed an experimental study to detect tool breakage with acceleration sensor. The method successfully predicts the tool breakage preventing waste and catastrophic failure. Saglam et. al. [12] used dynamometer and temperature sensor to investigate the cutting parameters and tool geometry. Kuo [13] presented a multi-sensorial data based tool wear estimation approach. To validate the results neural network and fuzzy logic based prediction approaches were used. According to results tool wear was successfully calculated.

In this study, to optimize the surface roughness parameters, a sensor fusion approach based on cutting force and vibration was utilized. A tool condition monitoring system was generated to obtain and evaluate sensorial data. Lastly, statistical analysis was carried out to determine the effectiveness of sensors on surface roughness parameters. In this context, AISI 5140 material was machined under dry cutting conditions with three levels of cutting speed, feed rate and depth of cut. A dynamometer and an accelerometer were mounted to a conventional lathe. The data collected from cutting area transferred to a computer. The results showed that a dynamometer and an accelerometer built a strong sensor fusion to utilize for the future work.

II. EXPERIMENTAL SET UP

In this study, AISI 5140 carbon steel having Ø75 x 500 mm in length was used as workpiece material. As cutting tool geometry (WCMT 06T308) and tool type (P25) Achteck products were selected. Experiments were performed at a conventional lathe (De-Lorenzo S547-8899). Experiments were performed under dry cutting conditions and three cutting speeds (660, 870 and 1400 rev/min), three feed rates (0.06, 0.12, 0.24 mm/rev) and three depth of cuts (1, 1.5, 2 mm) (Table 1).

For each experiment a newly cutting tool and workpiece bar were used. During machining, each cutting tool used for four pass to obtain cutting force and vibration data then average values were calculated. After each pass, additional to vibration and cutting forces surface roughness parameters were also measured and recorded.

Measurement of vibration was carried out with an accelerometer (Kistler 8692C50) and transmitted by a data acquisition card (National Instruments USB-6003) to computer. Collected data were processed in detail using Signal Express software. On the other hand, cutting forces were measured by a dynamometer (TLC DKM2000A) and the data transferred directly to computer with devices special software (TelC XKM). Surface roughness was measured with a perthometer (Mahr M1) and gives Ra and Rz values simultaneously.

Table 1: Experimental Parameters

Cutting speed (m/min)	Feed rate (mm/dev)	Depth of cut (mm)
150	0,06	1
200	0,12	1,5
330	0,24	2

Taguchi based experimental design was selected and L_9 orthogonal array was implemented to cutting parameters. Also, experimentally obtained results for vibration, cutting force and surface roughness are demonstrated in Table 2. Taguchi method is extensively preferred from many researchers in manufacturing [14-18] because of providing reliable and robust design. Decreasing the experiment number ensures significant time, waste, cost and labor gain. In this study, experimental burden was reduced 66% using this methodology and quite convincing results were acquired. Taguchi method uses several approaches to calculate the S/N ratio according to objective of experiment. The equations are calculated below:

For larger is better:

$$S/N= -10 \log 1 / n \left(\sum 1/y^2\right) \quad (1)$$

For smaller is better:

$$S/N= -10 \log 1 / n \left(\sum y^2\right) \quad (2)$$

For nominal is best:

$$S/N= -10 \, y / s^2 y \quad (3)$$

In this work, because of the requirement of obtaining minimum vibration, cutting forces and surface roughness, the second equation was chosen. Higher vibration deteriorates the surface roughness and reduces tool life, low quality and high cost production occurs. Meanwhile, higher cutting forces affect tool life and machining quality. By the way, resultant cutting force was utilized in statistical analysis can be calculated following equation:

$$F_r = \sqrt{F^2_c + F^2_f + F^2_b} \quad (4)$$

Table 2: Experimental design and results

E.N.	f	d	v	Ra(μm)	Rz(μm)	V(Hz)	F(N)
1	0,06	1	150	1,6222	7,7850	66,854	140,63
2	0,06	1,5	200	0,4867	3,1650	49,966	229,42
3	0,06	2	330	0,4342	2,4575	52,241	303,22
4	0,12	1	200	1,0005	5,2350	55,677	221,49
5	0,12	1,5	330	0,6267	3,5150	49,961	308,98
6	0,12	2	150	1,0532	6,2850	53,975	423,61
7	0,24	1	330	0,8630	3,9175	49,990	408,63
8	0,24	1,5	150	2,3615	10,900	66,116	429,59
9	0,24	2	200	1,7892	8,8050	49,974	602,52

III.　RESULTS AND DISCUSSION

The statistical analysis results for S/N ratios calculated with analysis of variance (ANOVA) and responses for S/N ratios are demonstrated in Tables 3-10. Tables contain statistical elements state the importance of source. Percent contribution (PC) value is calculated with divide of sum of square (SS) value of each parameter to total SS value. Higher PC values impress that the source has bigger influence on quality characteristic. F-value also reflects the dominance of a parameter should be compatible with PC. Lastly, P-value demonstrates the reliability of each parameter in a specified range (interval of 95%).

According to analysis results, cutting speed is the dominant factor (49%) after feed rate (36%) on arithmetic average roughness parameter (Ra). F-values also support this situation (4,01 > 2,95) shown at Table 3. To achieve optimal value of Ra, the necessary parameters should be $f_1d_2V_3$ (0,06 mm/rev-1,5 mm-330 m/min) can be seen at Table 4. For the maximum average roughness parameter, the similar comments can be done. Considering Table 5 and table 6, cutting speed is clearly effective on Rz and minimum value can be obtained with $f_1d_2V_3$ which is the same as Ra.

Table 3: ANOVA Results for S/N Ratios for Ra

Source	Dof	SS	MS	F	P	PC (%)
f	2	74,936	37,468	2,95	0,253	36
d	2	6,266	3,133	0,25	0,802	3
v	2	101,895	50,947	4,01	0,2	49
Error	2	25,438	12,719	-	-	12
Total	8	208,536	-	-	-	100

Table 4: Response Table for S/N Ratios for Ra

Level	Feed Rate	Depth of Cut	Cutting Speed
1	3,0996	-0,9755	-4,0387
2	1,2014	0,9499	0,3991
3	-3,7457	0,5809	4,1949
Delta (Δ)	6,8453	1,9255	8,2336
Rank	2	3	1

Table 5: ANOVA Results for S/N Ratios for Rz

Source	Dof	SS	MS	F	P	PC (%)
f	2	43,113	21,556	2,69	0,271	28
d	2	0,96	0,4801	0,06	0,943	1
v	2	95,274	47,862	5,97	0,143	61
Error	2	16,03	8,015	-	-	10
Total	8	155,828	-	-	-	100

Table 6: Response Table for S/N Ratios for Rz

Level	Feed Rate	Depth of Cut	Cutting Speed
1	-11,88	-14,69	-18,18
2	-13,75	-13,89	-14,43
3	-17,17	-14,22	-10,20
Delta (Δ)	5,29	0,8	7,98
Rank	2	3	1

Table 7 shows ANOVA results and Table 8 demonstrates responses for S/N ratios for vibration data. The results indicated that cutting speed has domination (66%) on vibration while feed rate and depth of cut have no significant effect. In Table 8, it can be seen that third level of cutting speed and depth of cut and second level of feed rate should be selected for minimum vibration.

Table 7: ANOVA Results for S/N Ratios for Vb

Source	Dof	SS	MS	F	P	PC (%)
f	2	0,2912	0,1456	0,18	0,847	3
d	2	0,9778	0,4889	0,61	0,622	12
v	2	5,5315	2,7657	3,44	0,225	66
Error	2	1,6077	0,8039	-	-	19
Total	8	8,4082	-	-	-	100

Table 8: Response Table for S/N Ratios for Vb

Level	Feed Rate	Depth of Cut	Cutting Speed
1	-34,95	-35,13	-35,85
2	-34,51	-34,78	-34,29
3	-34,79	-34,33	-34,10
Delta (Δ)	0,44	0,80	1,75
Rank	3	2	1

In table 9, the effectiveness of cutting parameters on resultant cutting force can be seen. Feed rate seems the dominant factor (61%) followed by depth of cut (35%). Both F-value (29,89) and P-value (interval of 95% or 0,05>0,032) verify the significance of feed rate on Fr. For minimum cutting force, first levels of cutting speed, feed rate and depth of cut should be chosen according to Table 10. And cutting speed has no important effect on resultant cutting force.

Table 9: ANOVA Results for S/N Ratios for Fr

Source	Dof	SS	MS	F	P	PC (%)
f	2	71,443	35,722	29,89	0,032	61
d	2	40,985	20,493	17,15	0,055	35
v	2	2,048	1,024	0,86	0,539	2
Error	2	2,390	1,195	-	-	2
Total	8	116,866	-	-	-	100

Table 10: Response Table for S/N Ratios for Fr

Level	Feed Rate	Depth of Cut	Cutting Speed
1	-46,60	-47,37	-49,39
2	-49,75	-49,89	-49,91
3	-53,50	-52,59	-50,55
Delta (Δ)	6,89	5,23	1,17
Rank	1	2	3

The regression analysis has been performed to understand the rate of effectiveness between vibration, cutting force and surface roughness parameters. According to regression analysis results, a strong correlation has been found demonstrated in equation 5 and equation 6. The analysis of variance results for the regression analysis demonstrated that the correlation between Ra and Rz and cutting force-vibration

couple seem significantly high as 90,8% and 89,1% respectively in Table 11 and Table 12.

Ra= -4,75 + 0,00316 Fr + 0,0876 Vb   (5)

Rz= -19,8 + 0,0141 Fr + 0,377 Vb   (6)

Table 11: ANOVA Results for Regression for Ra

Source	Dof	SS	MS	F	P
Regression	2	3,1213	1,5606	29,55	0,001
Residual Error	6	0,3168	0,0528	-	-
Total	8	3,4381	-	-	-

Table 12: ANOVA Results for Regression for Rz

Source	Dof	SS	MS	F	P
Regression	2	59,144	29,572	24,41	0,001
Residual Error	6	7,269	1,212	-	-
Total	8	66,413	-	-	-

IV. CONCLUSIONS

A real time monitoring system which can detect failures and track machining stability are demanded in today's manufacturing technologies. Especially in machining operations, TCMS were preferred for on-line monitoring via sensor systems. In this study, a sensor fusion was constituted using an accelerometer and a dynamometer for monitoring surface roughness parameters namely Ra and Rz in dry turning of AISI 5140 material. The undermentioned conclusions can be executed:

1. To realize sensor fusion, provided information from cutting area should be supported and affirmed by existing sensors.
2. Because of the high temperatures and pressures the difficulty to reach cutting zone in turning makes the sensorial data valuable for understanding the operation.
3. According to results, cutting speed has the most influence on Ra (49%) and Rz (61%), followed by feed rate (36% and 28%). For the minimum surface roughness values, minimum feed rate and maximum cutting speed should be selected.
4. Through investigation process, the authors observed that the depth of cut has no significant impact on optimization tools.
5. For the minimum vibration during machining, the dominant parameter cutting speed (66%) should kept maximum while for the minimum resultant cutting force, the effective parameter feed rate (61%) should be discerned as minimum value.
6. When 3 important quality characteristics are observed, to optimize surface roughness is dependent higher cutting speed and lower feed rate providing minimum vibration and resultant cutting force simultaneously.
7. As a result, dynamometer and accelerometer data seem to be robust and reliable information sources to state surface roughness situation that proved by

regression analysis both Ra (90,8%) and Rz (89,1%).

REFERENCES

[1] Y. S. Ahmed, S. Alam and A. F. M. Arif, S. C. Veldhuis, "Use of acoustic emission and cutting force signals to monitör built-up edge formation in stainless steel turning," *The International Journal of Advanced Manufacturing Technology*, vol. 103, pp. 2257-2276, 2019.
[2] Y. B. Guo, S. C. Ammula, "Real-time acoustic emission monitoring for surface damage in hard machining," *International Journal of Machine Tools & Manufacture*, vol. 45, pp. 1622-1627, 2005.
[3] B. S. Prasad, K. A. Prabha, P. V. S. G. Kumar, "Condition monitoring of turning process using infrared thermography technique – An experimental approach" *Infrared Physics & Technology*, vol. 81, pp. 137-147, 2017.
[4] A. Caggiano, R. Angelone, F. Napolitano, L. Nele, R. Teti "Dimensionality Reduction of Sensorial Features by Principal Component Analysis for ANN Machine Learning in Tool Condition Monitoring of CFRP Drilling," *Procedia CIRP,* vol. 78, pp. 307-312, 2018.
[5] A. Panda, A. K. Sahoo, I. Panighani, R. Kumar, "Tool condition monitoring during hard turning of AISI 52100 Steel: A case study," *Materials Today: Proceedings*, vol. 5, pp.18585–18592, 2018.
[6] H. Saglam, A. Unuvar, "Tool condition monitoring in milling based on cutting forces by a neural network," *Int. J. Prod. Res.*, vol. 8, pp. 1519-1532, 2003.
[7] R. Azouzi, M. Guillot, "On-line Prediction of Surface Finish and Dimensional Deviation in Turning Using Neural Network Based Sensor Fusion" *Int. J. Mach.Tools Manufact.*, vol. 37, pp. 1201-1217, 1997.
[8] B. Sick, "On-line and Indirect Tool Wear Monitoring in Turning with artificial neural networks: a review of more than a decade of research" *Mechanical Systems and Signal Processing*, vol:16, pp. 487-546, 2002.
[9] H. Saglam, "Tool Condition Monitoring based on Multi-Component Force Measurement Using Artificial Neural Network in Milling," *Phd Thesis, Selçuk University Natural and Applied Sciences Department*, 2000.
[10] M. Kuntoğlu, H. Saglam, "Investigation of progressive tool wear for determining of optimized machining parameters in turning," *Measurement*, vol. 140, pp. 427-436, 2019.
[11] J. Ravata, M. Lohtander, J. Varis, "Tool condition monitoring in interrupted cutting with acceleration sensors," *Robotics and Computer–Integrated Manufacturing*, vol. 47, pp. 70-75, 2017.
[12] H. Saglam, F. Unsacar, S. Yaldiz, "Investigation of the effect of rake angle and approaching angle on main cutting force and tool tip temperature*," International Journal of Machine Tools & Manufacture* vol.46, pp. 132–141, 2006.
[13] R. J. Kuo, "Multi-sensor integration for on-line tool wear estimation through artificial neural networks and fuzzy neural network," *Engineering Applications of Artificial Intelligence*, vol. 13, pp. 249-261, 2000.
[14] S. Dolinsek, J. Kopac, Acoustic emission signals for tool wear identification, *Wear* vol.225–229, pp. 295–303, 1999.
[15] G. Zheng, R. Xu, X. Cheng, G. Zhao, L. Li, J. Zhao, Effect of cutting parameters on wear behavior of coated tool and surface roughness in high-speed turning of 300M, *Measurement*, vol.125, pp. 99–108, 2018.
[16] N. Mandal, B. Doloi, B. Mondal, R. Das, Optimization of flank wear using zirconia toughened alumina (ZTA) cutting tool: taguchi method and regression analysis, *Measurement* vol.44 pp. 2149–2155, 2011.
[17] S. Debnath, M.M. Reddy, Q.S. Yi, Influence of cutting fluid conditions and cutting parameters on surface roughness and tool wear in turning process using taguchi method, *Measurement* vol. 78, pp. 111–119 2016.
[18] A.K. Parida, K. Maity, Modeling of machining parameters affecting flank wear and surface roughness in hot turning of Monel-400 using

response surface methodology (RSM), *Measurement*, vol. 137, pp. 375–381, 2019.

A Combined Fuzzy Logic and Optimization Approach for Tool Wear in Surface Milling

M. KUNTOĞLU[1] H. SAĞLAM[2]

[1]Selcuk University, Konya/Turkey, mkuntoglu@selcuk.edu.tr
[2]Selcuk University, Konya/Turkey, hsaglam@selcuk.edu.tr

Abstract – **It is important to monitoring of on-line tool condition to determine optimized machining parameters and obtain reduced costs in industrial applications. Tool wear affects surface quality and accuracy of workpiece which stands ultimate aim of a production line. Artificial intelligence methods provide prediction of machining performance with reduced experiments and contribute to enhancing of productivity. In this work, a combined statistical analysis (ANOVA) and fuzzy logic approach is implemented into surface milling operation to obtain minimum tool wear state with minimum experiment. Experiments were performed in dry cutting conditions and cutting speed, feed and depth of cut were chosen as input parameters. A Mamdani-Type fuzzy logic based model was developed and compare with the experimental results. The results showed that the developed model is reliable (R^2=0.9) and successfully implemented to similar applications. Finally, the most effective machining parameter (feed rate with 50%) on tool flank wear and optimal milling parameters (v_1=113 m/min, f_2=250 mm/min, d_3=2.5 mm) were determined with statistical analysis using data obtained from experiments. The aim of the study is obtaining of high quality materials with high efficiency and low costs.**

Keywords – **Tool Wear, Tool Condition Monitoring, Analysis of Variance, Fuzzy Logic, Taguchi Method**

I. INTRODUCTION

Milling is one the most preferred machining process performing the operation with rotating tool and linear moving workpiece material. The process enables machining of several materials with wide-range of tool materials. The machinability rating in milling increases with using soft or brittle materials such as aluminum, mild steel or cast iron and carbide inserts appear to be the most commonly used cutters [1].

Tool wear is inevitable phenomenon occurring different locations on cutting tool. Developing tool wear generates fresh surface with removing chips. Different type of tool wear occurs according to machining process, tool-workpiece material and cutting parameters. Monitoring tool wear in real time provides to keep the quality characteristics in safe ranges [2]. Especially for surface roughness parameters, dimensional deviations, chatter vibrations and cutting forces, the critical threshold values should be observed during machining.

Progressive tool wear cause undesired results in terms of high cutting forces, deteriorated surface quality, high cutting temperatures, uncontrolled chip generation [3]. To decide the changing time of a cutting tool, tool wear condition becomes important. Flank wear taking place on flank surface of a cutting tool considered an important information source about tool life [4, 5].

To increase the productivity and reduce machining costs requires technological infrastructure based optimization and modeling methods [6]. The artificial intelligence based modeling [7-9] and optimization [10-12] based design methods provide decreasing the labor, waste material and idle time during manufacturing and researching [13].

Kuram and Ozçelik [14] presented a Taguchi and fuzzy logic based study during milling of AISI 304 steel. The effect of cutting speed, feed rate and depth of cut on tool wear were examined. Besides, tool wear can be efficiently predicted with fuzzy modeling. Das et. al. [15] proposed to develop a model based on optimize milling operation with Taguchi and fuzzy logic approach. Ratnam et. al. [16] performed an experimental study in turn-milling to investigate the effect of parameters and optimal cutting conditions. Ren et. al. [17] carried out a fuzzy logic based modeling for predicting cutting forces in milling process. The developed model can successfully predict the cutting forces. Cuka and Kim [18] performed a fuzzy logic based tool wear monitoring.

In this study, a combined artificial intelligence and statistical analysis approach were integrated to milling of AISI 1040 material. In this context, an optimization and modeling were performed using fuzzy inference system and Taguchi design. Matlab and Minitab softwares were utilized to model and analyze the experimental results. First, Taguchi based experimental design L_{16} was constituted and experiments were carried out. Then, ANOVA based statistical analysis were performed and lastly fuzzy logic based prediction was done. Experiments were carried out in universal milling machine under dry cutting conditions. The effects of feed rate, cutting speed and depth of cut were investigated. To obtain the minimum tool wear, optimal cutting parameters were determined. The proposed model can be successfully used for prediction and analysis for future studies.

II. EXPERIMENTAL SET UP

The experiments were carried out with no cutting fluid on universal milling machine (Taksan). The used tool holder (Takımsaş-A2 45 89 R05-12) capable of mounting 5 cartridge to hold cutting tools (SPMW 12 04 08 SBF (HW) P15-P30) in the experiments. The workpiece material was AISI 1040 material had 167 x 65 x 40 mm dimensions. The experimental summary was shown in Table 1. The composition of AISI 1040 material was demonstrated in Table 2. The experiments

were performed in three four levels of cutting speed (A) (113-140-178-226 m/min), feed rate (B) (200-250-315-400 mm/min) and depth of cut (C) (1-1.5-2-2.5 mm). The factors and levels are shown in Table 3.

Table 1: Experimental Conditions

Material	Feature
Machine Tool	Taksan-Universal Milling Machine
Cutting Tool Holder	Takımsaş-A2 45 89 R05-12
Tool Tips	SPMW 12 04 08 SBF (HW) P15-P30
Workpiece Material	AISI 1040
Dimension of Workpiece	167 x 65 x 40 mm
Cutting Fluid	-

Table 2: Material composition of workpiece

C	Si	Mn	P	S	Cr	Ni	Cu
0,42	0,24	1,77	0,023	0,016	0,15	0,08	0,338

Table 3: Factors and levels

Levels	Cutting Speed (A) (m/min)	Feed Rate (B) (mm/min)	Depth of Cut (C) (mm)
1	113	200	1
2	140	250	1,5
3	178	315	2,5
4	226	400	3,5

In spite of the $4^3=64$ experiments, with the aid of Taguchi design only $4^2=16$ experiments were executed. Taguchi orthogonal array design provides to reduce the number of experiment and obtain the best results with minimum experiment. Aforementioned reasons which cause to increase the experimental costs, labor and idle time can be prevented with this method. Taguchi method is a robust, reliable and low-cost and energy consumer approach. The widely usage prove the reliability and importance. L_{16} orthogonal array is demonstrated with factors and their levels in Table 4.

Table 4: Taguchi L_{16} orthogonal array

Number of Exp. / Factors	A (v)	B (f)	C (d)
1	1	1	1
2	4	4	4
3	2	2	4
4	3	3	1
5	3	1	4
6	2	4	1
7	4	2	1
8	1	3	4
9	4	3	2
10	1	2	3
11	3	4	3
12	2	1	2
13	2	3	3
14	3	2	2
15	1	4	2
16	4	1	3

A Mamdani type fuzzy inference system was constituted to model cutting tool wear. Matlab 18 software was used for fuzzy inference interface. Four levels of cutting speed, feed rate and depth of cut were described as membership functions. 16 rules were identified to determine the relationships between input parameters (cutting parameters) and results (tool wear).

To describe the type of inference system min. for and method, max. for and method, min. for implication, max. for aggregation, centroid for defuzification were chosen. Additional to fuzzy prediction, Taguchi based estimation was executed and compared with each other with regression analysis.

During the experiments, flank wear and surface roughness measurements were performed after each pass. The variation for surface roughness and development of flank wear were followed. Surface roughness values decrease while flank wear values increase during the machining in the beginning. Flank wear values increases through the experiments but after some point, surface roughness values increase. The data used in this paper was selected for each cutting tool reached 3 minutes during machining.

III. RESULTS AND DISCUSSION

Taguchi based ANOVA and fuzzy logic-based prediction were implemented to milling operation for optimization. In this context, 16 experiments were carried out to investigate the effects of cutting parameters on tool wear and optimum choices for minimum wear. Besides if designed fuzzy model was correct then some of the experiments can be estimated. By this way a significant work can be avoided for the future studies. The experimental results can be seen in Table 7.

ANOVA is a statistical analysis approach providing the effects of cutting parameters on quality characteristics. In table 5, the dominance of cutting speed, feed rate and depth of cut on tool flank wear can be seen. Sum of square (SS) value is an indicator for the effectiveness of each factor. To divide the SS value for each factor to total SS value gives the percent contribution (PC) which reflects the dominance of factor. Feed rate is the most effective (50%) factor on tool flank wear followed by depth of cut (31,9%) and cutting speed (12,4%). These results are verified with F-value (21,76 > 13,64 > 5,3) and P-value (0,001 < 0,004 < 0,04).

Response table for S/N ratios are shown in Table 6. Taguchi method provides to minimize the noise factors and robust design can be obtained. Several methods can be selected to calculate the S/N ratios according to expectation from quality characteristic. For smaller is better type, followed equation should be selected:

$$S/N = -10 \log 1 / n \left(\sum y^2\right) \tag{1}$$

Table 5: Anova table

Source	DOF	SS	MS	F	P	PC
A	3	16,347	5,449	5,3	0,04	12,4
B	3	67,047	22,349	21,76	0,001	50
C	3	42,065	14,022	13,65	0,004	31,9
Error	6	6,163	1,027	-	-	
Total	15	131,622	-	-	-	

Because of the minimum tool wear is expected from machining operations, equation 1 was selected as objective function. Calculated results are demonstrated in Table 6. According to results, to obtain minimum tool wear, first order

of cutting speed, first order feed rate and third order of depth of cut should be selected. Maximum delta value also verifies the dominant effect of feed rate.

Table 6: Response table for S/N ratios

Level	Cutting Speed	Feed Rate	Depth of Cut
1	**11,607**	**13,185**	7,837
2	11,058	11,104	11,224
3	10,799	10,629	**12,008**
4	8,920	7,466	11,315
Delta	2,687	**5,719**	4,171

Table 7 shows the experimental results for flank wear and predicted with two different methods namely Fuzzy Logic and Taguchi method. The results were evaluated by regression equation. Regression results for Taguchi and fuzzy logic results calculated with analysis of variance are demonstrated in Table 8 and Table 9. Besides, calculated results were compared with experimental results to observe the reliabilities in Figure 1 and Figure 2. According to results, fuzzy logic based approach predicts the tool wear with 90% success rate while Taguchi method predicts with 96% success rate.

Table 7: VB results for experimental and predicted

Number of Exp. / Factors	VB (Exp.)	VB (Fuzzy)	VB (Taguchi)
1	0,305	0,282	0,280
2	0,498	0,48	0,475
3	0,268	0,271	0,260
4	0,403	0,387	0,397
5	0,177	0,198	0,197
6	0,522	0,442	0,523
7	0,422	0,432	0,451
8	0,231	0,246	0,240
9	0,359	0,365	0,336
10	0,211	0,215	0,190
11	0,385	0,39	0,371
12	0,196	0,239	0,184
13	0,224	0,257	0,242
14	0,252	0,346	0,250
15	0,321	0,354	0,356
16	0,218	0,218	0,233

Table 8: Analysis of Variance for Regression for Fuzzy Logic

Source	DOF	SS	MS	F	P
Regression	1	0,110208	0,110208	126,17	0,000
Error	14	0,012229	0,000874	-	-
Total	15	0,122438	-	-	-

Table 9: Analysis of Variance for Regression for Taguchi

Source	DOF	SS	MS	F	P
Regression	1	0,171593	0,171593	420,64	0,000
Error	14	0,005711	0,000408	-	-
Total	15	0,177304	-	-	-
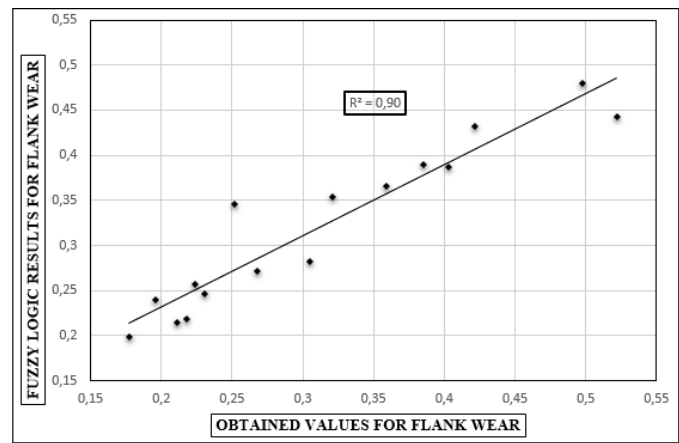
Figure 1: The comparison between obtained and predicted values by fuzzy logic
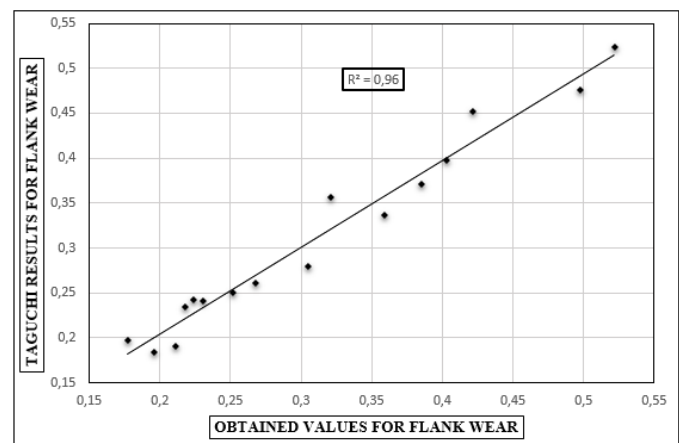
Figure 2: The comparison between obtained and predicted values by Taguchi method

The obtained results from fuzzy inference system are demonstrated in graphs in Figure 3a, 3b and 3c. The combined effects of feed rate and cutting speed, cutting speed and depth of cut and feed rate and depth of cut on flank wear as 3d plots can be seen.

At lower cutting speeds, lower feed rate (3a) and higher depth of cut (3b) values cause lower flank wear rates. At higher cutting speeds, higher feed rates and lower depth of cuts, highest flank wear rates occur. ANOVA supported result can be verified with graphs.

The highest value of flank wear appears in 3c at lowest depth of cut and highest feed rate. Similarly at lowest feed rate and highest depth of cut, lowest flank wear value appears.

During intermittent cutting, each cutting tool enters and exits from workpiece which cause a hammering effect. Chip section becomes important because of the repetitive hits. Therefore, feed rate and depth of cut determine the chip section. Lower depths of cut values prevent the contact between tool and workpiece that should be adequate area. Increasing depth of cut provides sufficient section area but with the aid of feed rate. But higher feed rate affects tool wear increasingly negative. As a result, to eliminate the high tool wear effects, feed rate and depth of cut should be arranged in

milling operations.
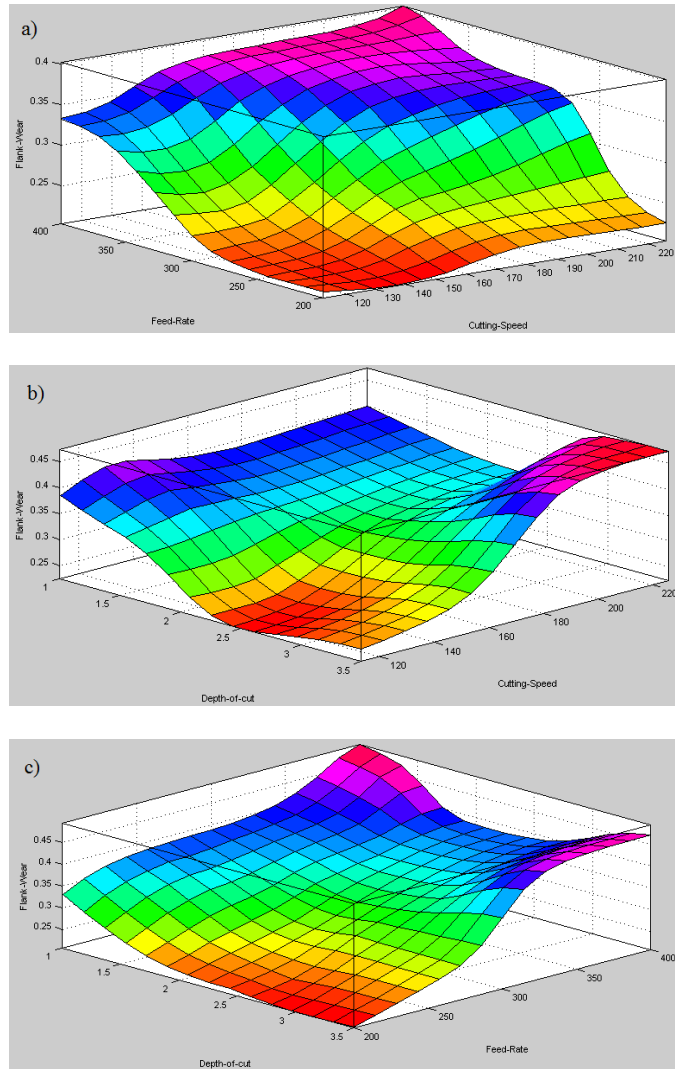
Figure 3: The predicted fuzzy logic 3D plots combinations of a) Cutting Speed-Feed Rate, b) Cutting Speed-Depth of Cut, c) Feed Rate-Depth of Cut

IV. CONCLUSIONS

This study presents tool wear based tool condition monitoring system during milling operation predicting flank wear with developed fuzzy model. Besides, optimal machining parameters and the most dominant factor on tool wear were determined using analysis of variance and S/N ratios. Previous studies focused on surface roughness investigations while flank wear prediction and analysis were barely found in literature. Therefore, following implications can be useful for similar applications both in academic and industry.

- The most important parameter to affect tool wear appears to be feed rate (50%) followed by cutting speed (31.9%) and depth of cut (12.4%) according to ANOVA results. The reason is that the pulsed interaction between tool and workpiece produce small chips on the contrary of turning process. Coefficient of friction has higher effect than

temperature on flank wear. The intermittent process cause instant contact and feed rate increases the coefficient of friction mostly.

- Minimum tool flank wear can be obtained with optimal cutting parameters found by S/N ratios. The first level of cutting speed (113 m/min), second level of feed rate (250 mm/min) and third level of depth of cut (d_3=2.5 mm) were determined giving the best response value.

- The developed fuzzy logic model illustrations show the combined effect of factors and levels successfully proved by regression equation (R^2=0.9). Flank wear should increase inevitably as a nature of machining. Cutting speed-feed rate graph fits and confirms for this definition considering the ANOVA results.

- The results of statistical analysis showed that Taguchi method can be successfully used to decrease experiment number and find main effects of factors. Taguchi method was also used for prediction and showed good relation between experimental values (R^2=0.96).

REFERENCES

[1] R. H. Todd, D. K. Allen, L. Alting, *Manufacturing Processes Reference Guide*. New York: Industrial Press Inc-200 Madison Avenue, 1994.
[2] H. Saglam, "Tool Condition Monitoring based on Multi-Component Force Measurement Using Artificial Neural Network in Milling," *Phd Thesis, Selçuk University Natural and Applied Sciences Department*, 2000.
[3] H. Saglam, A. Unuvar, "Tool condition monitoring in milling based on cutting forces by a neural network," *Int. J. Prod. Res.*, vol. 8, pp. 1519-1532, 2003.
[4] M. Kuntoğlu, H. Saglam, "Investigation of progressive tool wear for determining of optimized machining parameters in turning," *Measurement*, vol. 140, pp. 427-436, 2019.
[5] W. Yan, Y.S. Wong, K.S. Lee, T. Ning, An investigation of indices based on milling force for tool wear in milling, J. Mater. Process. Technol. 90 (1999) 245–253.
[6] H. Saglam, F. Unsacar, S. Yaldiz, "Investigation of the effect of rake angle and approaching angle on main cutting force and tool tip temperature*," International Journal of Machine Tools & Manufacture* vol.46, pp. 132–141, 2006.
[7] D. Kim, D. Jeon, Fuzzy-logic control of cutting forces in CNC milling processes using motor currents as indirect force sensors, *Precision Engineering*, vol. 35, pp. 143-152, 2011.
[8] T. P. Manesh, R. Rajesh, Optimal Selection of Process Parameters in CNC End Milling of Al 7075-T6 Aluminium Alloy Using a Taguchi-Fuzzy Approach, *Procedia Materials Science*, vol. 5, pp. 2493-2502, 2014.
[9] A. Iqbal, N. He, N. U. Dar, L. Li, Comparison of fuzzy expert system based strategies of offline and online estimation of flank wear in hard milling process, *Expert Systems with Applications* vol.33, pp. 61–66, 2007.
[10] E. Salur, A. Aslan, M. Kuntoğlu, A. Gunes, O.S. Sahin, Experimental study and analysis of machinability characteristics of metal matrix composites during drilling, Compos. Part B 166 (2019) 401–413.
[11] T. Kıvak, Optimization of surface roughness and flank wear using the Taguchi method in milling of hadfield steel with PVD and CVD coated inserts, *Measurement* vol. 50, pp. 19–28, 2014.
[12] I. Asilturk, H. Akkus, Determining the effect of cutting parameters on surface roughness in hard turning using the taguchi method, *Measurement* vol. 44, pp. 1697–1704, 2011.
[13] A. Aslan, A. Gunes, E. Salur, O.S. Sahin, H.B. Karadag˘, A. Akdemir, Mechanical properties and microstructure of composites produced by recycling metal chips, Int. J. Miner. Metall. Mater. 25 (9) (2018) 1070–1079.

[14] E. Kuram, B. Ozçelik, Micro-milling performance of AISI 304 stainless steel using Taguchi method and fuzzy logic modelling, *J. Intell. Manuf.* vol. 27, pp. 817-830, 2016.

[15] B. Das, S. Roy, R. N. Rai, S. C. Saha, Application of grey fuzzy logic for the optimization of CNC milling parameters for Al–4.5%Cu–TiC MMCs with multi-performance characteristics, *Engineering Science and Technology, an International Journal*, vol. 19, pp. 857-865, 2016.

[16] C. Ratnam, K. A. Vikram, B. S. Ben, B. S. N. Murthy, Process monitoring and effects of process parameters on responses in turn-milling operations based on SN ratio and ANOVA, *Measurement*, vol. 94, pp. 221-232, 2016.

[17] Q. Ren, M. Balazinski, K. Jemielniak, L. Baron, S. Achiche, Experimental and fuzzy modelling analysis on dynamic cutting force in micro milling, *Soft Comput*, vol. 17, pp.1687–1697, 2013.

[18] B. Cuka, D. Kim, Fuzzy logic based tool condition monitoring for end-milling, *Robotics and Computer–Integrated Manufacturing*, vol. 47, pp. 22-36, 2017.

Investigation of the combined TLC-ORC and the combined ORC-ORC power systems

M.ÖZÇELİK[1], N. BİLİR SAĞ[2]

[1] Konya Technical University, Konya/Turkey, mehmetozcelik61@hotmail.com
[2] Konya Technical University, Konya/Turkey, nbilir@ktun.edu.tr

Abstract **- One of the best performances in waste heat and power generation systems is the organic Rankine cycle. The difference of the Organic Rankine Cycle from the basic Steam Rankine Cycle is the use of organic fluids as the working fluid. Power generation can be achieved from low temperature heat sources (80-90ºC) with organic fluids. In this study, studies on dual loop combined power systems and system structures were investigated. As a result of the investigations, it was concluded that higher thermal efficiency and lower exergy destruction were obtained from combined Trilateral Cycle-Organic Rankine Cycle power system.**

Keywords **– Organic fluids, Organik Rankine cycle, Trilateral cycle, Combined power systems.**

I. INTRODUCTION

ENERGY is one of the necessities of the one in which we operate it in our daily lives. With the increase of the world population, the energy demand in both daily and industrial areas have increased. With the insufficient reserves of fossil fuels, new energy sources are searched for. The Rankine cycle is one of the most widely used methods for converting high capacity thermal energy into power and the system uses water as working fluid. Power can be generated from high-temperature heat sources with the Rankine cycle, but power generation from low-temperature sources (solar, geothermal, biomass technology, renewable etc.) with the Organic Rankine cycle.

Organic Rankine Cycle (ORC) uses a low-temperature waste heat source; Concentrating solar energy systems generate power from the exhaust gases and gas turbines of diesel engines, waste heat in industrial processes, geothermal energy and waste heat produced by biomass [1]. For this reason, ORCs are widely used around the world and their usage continues to increase.

A. Organic Rankine Cycle

When water is used as the working fluid in small and medium power cycles, there is a risk of corrosion in turbine blades, high pressure operation in the evaporator, and the use of complex turbines. The problems encountered with the use of water can be partially reduced by the use of appropriate fluid [2]. Fluids with a higher molecular weight and lower critical temperature than water are called organic fluids. Rankine cycles using these fluids are also called Organic

Rankine Cycle (ORC). The working principle of ORC is the same as the Rankine cycle. ORC has pump, evaporator, turbine and condenser elements. ORC is used for heat recovery from low temperature heat source. The yield of ORCs varies between 8-20% [3].
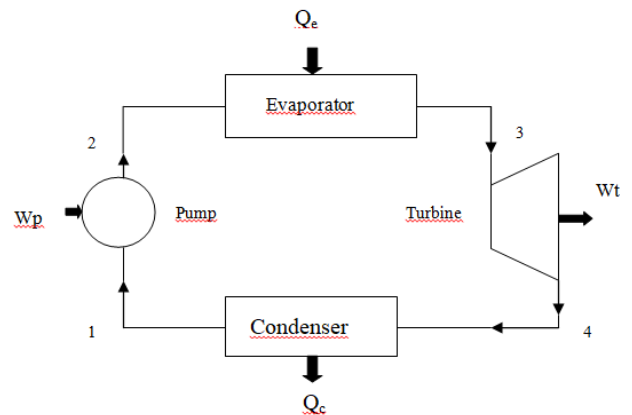
Figure 1: System stracture of simple ORC.
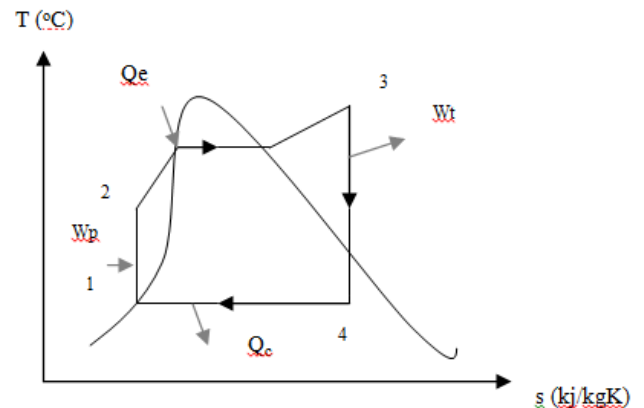
Figure 2: T-s diagram of the simple ORC.

In the cycle, respectively;
1-2: Isentropic compression in the pump
2-3: Heat input at constant pressure in the evaporator
3-4: Isentropic expansion in the turbine
4-1: Steps of throwing heat at constant pressure in the condenser take place.

B. Trilateral Cycle

Trilateral Cycle (TLC) generates power from low-temperature waste heat, such as ORC. TLC basically has the

same elements as the Rankine cycle, but unlike the Rankine cycle, the working fluid is heated without evaporation and enters the expander in its saturated phase. A two-phase expander is used in the cycle. The working fluid exits the expander as liquid vapor mixture or saturated vapor. As the working fluid enters the expander without evaporation, a better temperature match is achieved with heat transfer from the heat source to the working fluid. In other words, low exergy degradation occurs according to ORC and thermal efficiency increases. System components of TLCs are pump, evaporator, two-phase expander and condenser. The thermal efficiency of the cycle is around 19-24%.
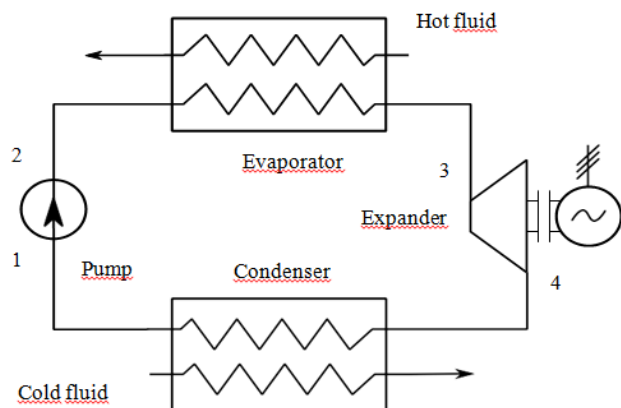
Figure 3: TLC system structure [4]
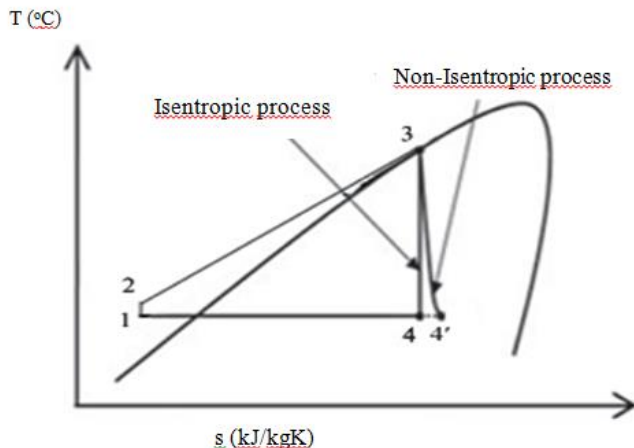
Figure 4: T-s diagram of TLC [5].

II. COMBINED POWER SYSTEMS

A. The Combined ORC-ORC Power Systems

Great efforts have been made by different organizations, including the government, research institutes, companies and colleges, to draw more attention to energy conservation today, facing environmental and energy challenges such as global warming and fossil fuel shortages. In a typical industrial country, internal combustion engines (ICE) are the primary consumers of fossil fuel. However, in an ICE, about 55-70% of the fuel heat is not used and is exhausted [6], so that to

recover energy from ICE's waste heat to save energy: including the Organic Rankine cycle many thermodynamic cycles [7], Kalina cycle [8] and Brayton cycle [9] have been considered effective methods. Among these, ORC has received great attention due to its safety, high efficiency, high reliability and flexibility, low costs and easy maintenance [10].

This system includes two cycles, one high temperature cycle and one low temperature cycle, and ORC is used in both cycles. With the high temperature cycle, the engine exhaust waste heat and fuel waste heat are passed through the evaporator of the cycle and used by the working fluid and the fluid exits the evaporator and continues to cycle. In the low temperature cycle, while the working fluid is circulated in the cycle, the refrigerant passing through the condenser gives heat to the fluid and condenses into a saturated liquid. In this way, waste heat is recovered. The efficiency of ORC – ORC systems is in the order of 18 -19%.
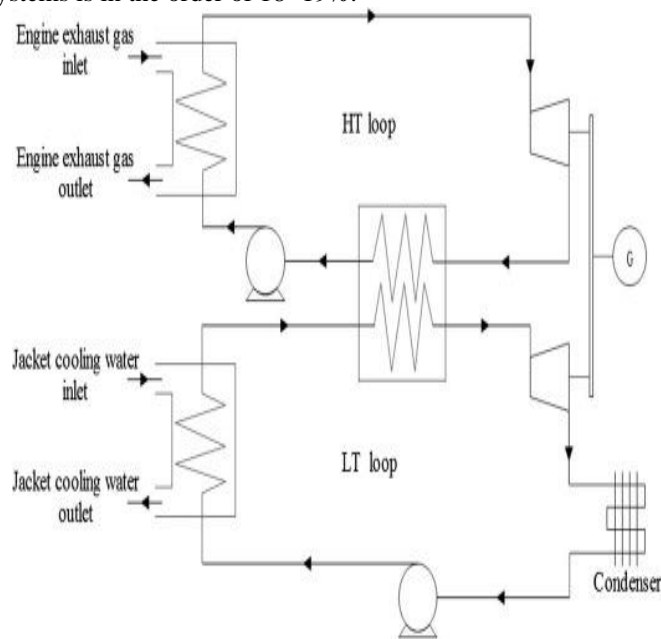
Figure 5: ORC-ORC system structure [11].
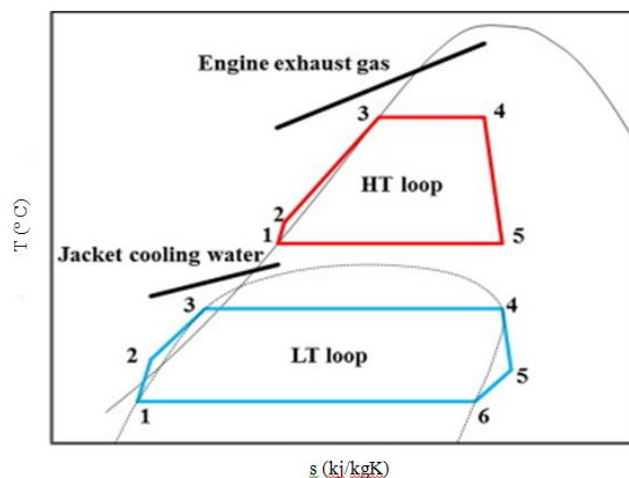
Figure 6: T-s diagram of ORC-ORC system [11].

Zhang et al. examined a system that combines a diesel engine with an ORC-ORC power cycle and recovers heat from the engine exhaust, inlet air and coolant. They found that the net power of the low temperature cycle was higher than that of the high temperature cycle and that the thermal efficiency increased by 16 - 43% [12].

Tian et al. proposed a regenerative transcritical ORC-ORC system in order to recover the exhaust waste heat and the whole waste heat of the engine coolant. Among the working fluids, it was found that if the use of toluene in high temperature cycle and R134a in low temperature cycle, the system thermal efficiency was 12.77% and exergy yield was 51.92%. The increase in temperature of the HT cycle reduces system performance by reducing net power and energy conversion efficiency. The condenser of the LT cycle and turbine of the HT cycle also has the least irreversibility [13].
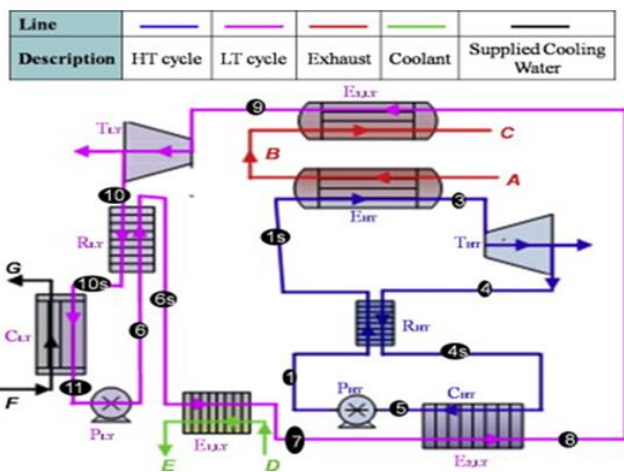
Figure 7: Regenerative ORC-ORC system structure [13].
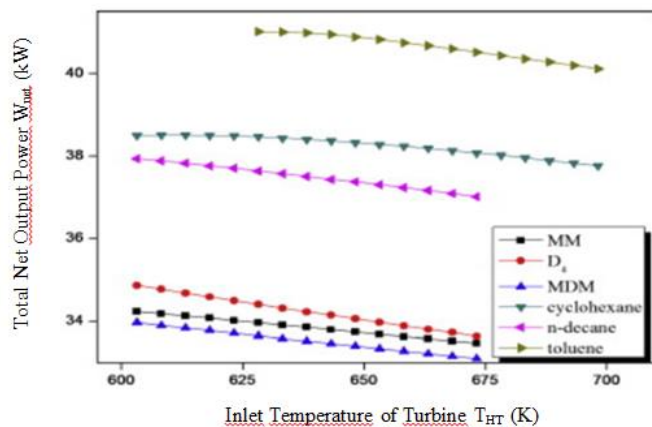
Figure 8: Variation of turbine inlet temperature and net power output [13].

Chen et al. proposed a cascade expansion ORC (CCE-ORC) system that is more suitable for the engine waste heat recovery, which has a simpler architecture, smaller volume and higher efficiency than the traditional ORC-ORC system. The thermodynamic simulation method was created by considering the non-design performances of the main

components of the system and the working fluid pressure drop in the condenser. System performance simulations under full engine operating conditions have been found to be able to increase the thermal efficiency of the engine from 45.3% to 49.5% when applied to a heavy duty truck diesel engine. Compared to the traditional ORC-ORC system, the CCE-ORC system produces net power more than 8%, while the total heat exchanger volume is less than 18% [14].
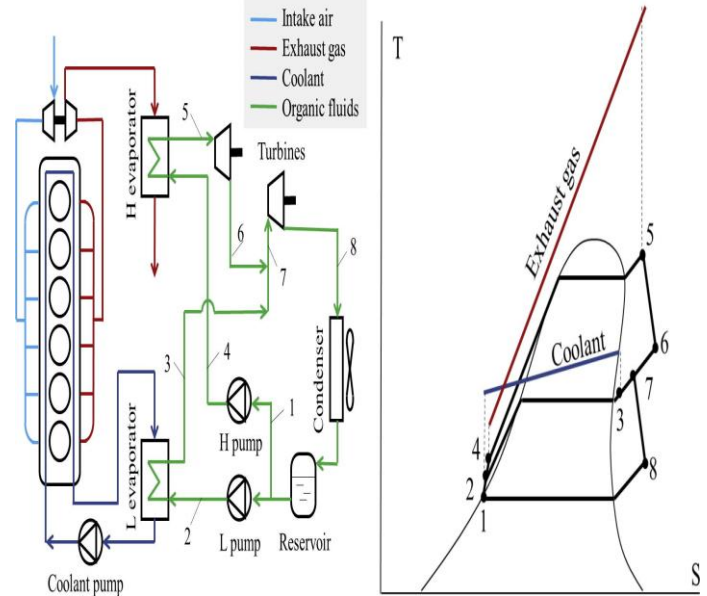
Figure 9: CCE-ORC system structure and T-s diagram [14].

Wang et al. (2018) examined the thermo-economic performance of the system by using isobutane as the working fluid for ORC-ORC and single-pressure evaporating ORC. A performance comparison was made between the two systems for the same source inlet temperature and optimized state. The results showed that the net power output of the ORC-ORC is higher at the low heat source temperature. [15].

B. Combined TLC-ORC Power Systems

Heat recovery technologies; the increase in fuel prices, meticulous emission regulations and the related increase in environmental problems related to the use of existing energy systems have received increasing attention worldwide [16, 17]. The heat transfer process in the evaporator of a conventional ORC system is a low temperature match between the heat source and the working fluid, depending on the evaporation process of the phase change. This leads to high exergy destruction and low thermodynamic performance [18, 19]. The characteristic of TLC is that the working liquid enters the expander directly after being heated in the evaporator without any evaporation process. Therefore, the temperature difference between the working fluid and the heat source in the evaporator may be smaller than that of a conventional ORC, which in general may result in a smaller exergy loss in the evaporator [20]. Johann Fischer (2011) compared the performance of a TLC and an ORC for waste heat recovery. The results showed that under the same operating conditions, the exergy efficiency of TLC could be 14-29% higher than that of a conventional ORC [21].

In the TLC - ORC system, higher thermal efficiency is aimed by using TLC instead of ORC as high temperature cycle. In TLC, the working fluid is heated without evaporation and then enters the turbine as a saturated liquid. Heat passes from the heat source to the working fluid, thereby providing a better temperature match between the heat source and the fluid than the ORC. In other words, low exergy destruction occurs according to ORC in the turbine. Therefore, thermal efficiency is increased.

Thermal efficiency of TLC-ORC systems varies between 17-25% [22].
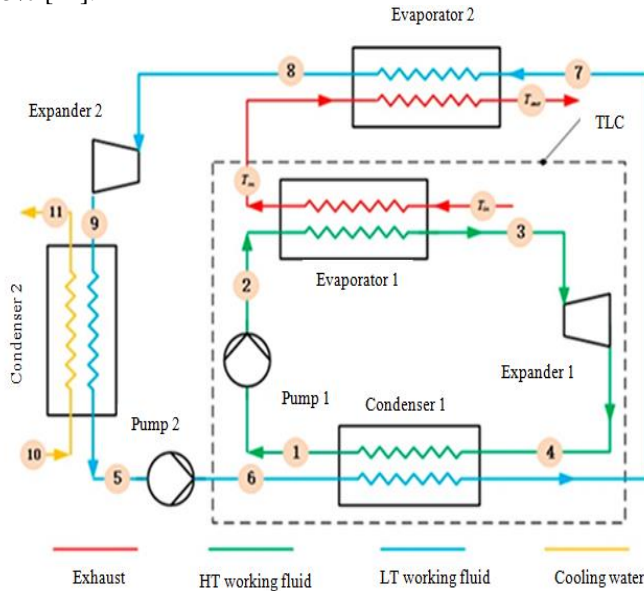
Figure 10: TLC-ORC combined power system structure [22].

Yu et al. articles, comprehensive comparisons between ORC-ORC and TLC-ORC systems have been made by using first and second law analysis. The values of the TLC-ORC system are 34.1%, 33.7% and 31.2% higher than the values of ORC-ORC, respectively [22].

Li et al. proposed a TLC-ORC combined power system for better thermal mapping between heat source and working fluid and for waste heat recovery. By selecting four different working fluids for the high temperature cycle, thermodynamic analysis of the system was performed under different evaporation temperatures for high temperature cycle and low temperature cycle. The results show that toluene has the best performance of fluids of other studies. The maximum net power output for toluene was 11.3 kW, thermal efficiency was 24.2% and exergy efficiency was 63.2% [23].
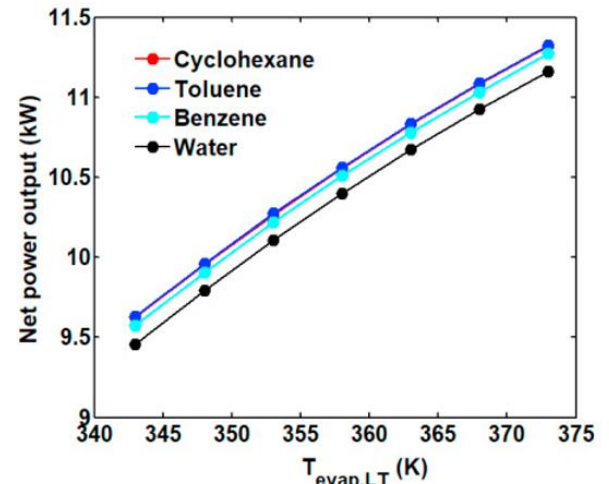
Figure11: Net power output variation of high temperature work fluid at different evaporation temperatures [23].

III. CONCLUSION

Waste heat recovery applications with ORCs are quite common today. The fact that it is one of the most effective methods for generating power from low and medium heat sources undoubtedly indicates that the use of ORC technologies will continue.

In this paper, the combined ORC - ORC and combined TLC - ORC power systems have been searched for waste heat recovery and the structures of the systems have been investigated. The only challenge of the combined TLC-ORC power system compared to the combined ORC-ORC power system is to use a dual-phase expander in the system. As a result of this research, it is seen that the combined TLC – ORC power system loops from these two different combined power systems work with higher thermal efficiency than ORC - ORC systems since two phase expander is used.

REFERENCES

[1] Yaşar, S., Altunbaşak, B. ve Biber, M. S., Düşük Sıcaklıkta Organik Rankine Çevrim Uygulamalarından Faydalanılarak Farklı Akışkanların Verimlerinin Karşılaştırılması, Süleyman Demirel University, Isparta, 2016.

[2] F. Çanka Kılıç, M. Ö. Sert, M. Eyidoğan, D. Kaya and N. C. Özdemir, *Endüstriyel Tav Fırınlarında Bir ORC Sistemi Uygulaması ile Enerji Tasarrufu*. GU J Sci, Part C, 6 (1), pp. 33-43, 2018.

[3] H. Yağlı, ''Baca Gazı Atık Isısı İçin Organik Rankine Çevrimi Tasarımı ve Ekserji Analizi,'' M. S, Mustafa Kemal University Institute of Science and Technology, Hatay, 2014.

[4] R. McGintya, G. Bianchi, O. Zaher, S. Woolass, D. Oliver, C. Williams and J. Miller, ''Techno-economic survey and design of a pilot test rig for a trilateral flash cycle system in a steel production plant,'' in *1st International Conference on Sustainable Energy and Resource Use in Food Chains,* pp. 281-288.

[5] M. Ahmadi, S. Vahaji, M. A. Iqbal, A. Date, and A. Akbarzadeh, ''Experimental study of converging-diverging nozzle to generate power by Trilateral Flash Cycle (TFC),'' Appl. Therm. Eng., 147, pp. 675-683, 2019.

[6] V. Chintala, S. Kumar and J. K. Pandey, ''A technical review on waste heat recovery from compression ignition engines using organic Rankine cycle,'' Renew. and Sustain. Energy Rev., 81, pp. 493–509, 2018.

[7] L. Shi, G. Shu, H. Tian and S. Deng, ''A review of modified Organic Rankine cycles (ORCs) for internal combustion engine waste heat

recovery (ICE-WHR),'' Renew. and Sustain. Energy Rev., 92, pp. 95–110, 2018.

[8]   T. Eller, F. Heberle and D. Brüggemann, ''Second law analysis of novel working fluid pairs for waste heat recovery by the Kalina cycle,'' Energy, 119, pp. 188–98, 2017.

[9]   F. Crespi, G. Gavagnin, D. Sánchez and G. S. Martinez, ''Supercritical carbon dioxide cycles for power generation: A review,'' Appl. Energy, 195, pp. 152–83, 2017.

[10] K. Rahbar, S. Mahmoud, R. K. Al-Dadah, N. Moazami and S. A. Mirhadizadeh, ''Review of organic Rankine cycle for small-scale applications,'' Energy Convers. and Manage., 134, pp. 135–55, 2017.

[11] J. Song, and C. Gu, ''Performance analysis of a dual-loop organic Rankine cycle (ORC) system with wet steam expansion for engine waste heat recovery,'' Applied Energy, 156, pp. 280-289, 2015.

[12] H. G. Zhang, E. H. Wang and B. Y. Fan, ''A performance analysis of a novel system of a dual loop bottoming organic Rankine cycle (ORC) with a light-duty diesel engine,'' Applied Energy, 102, pp. 1504-1513, 2013.

[13] H. Tian, L. Liu, G. Shu, H. Wei and X. Liang, ''Theoretical research on working fluid selection for a high-temperature regenerative transcritical dual-loop engine organic Rankine cycle,'' Energy Conversion and Management, 86, pp. 764-773, 2014.

[14] T. Chen, W. Zhuge, Y. Zhang and L. Zhang, ''A novel cascade organic Rankine cycle (ORC) system for waste heat recovery of truck diesel engines,'' Energy Conversion and Management, 138, pp. 210-223, 2017.

[15] M. Wang, Y. Chen, Q. Liu and Z. Yuanyuan, ''Thermodynamic and thermo-economic analysis of dual-pressure and single pressure evaporation organic Rankine cycles,'' Energy Conversion and Management, 177, pp. 718-736, 2018.

[16] M. E. Demir and İ. Dinçer, ''Performance assessment of a thermoelectric generator applied to exhaust waste heat recovery,'' Appl. Therm. Eng., 120, pp. 694–707, 2017.

[17] B. Orr, A. Akbarzadeh, M. Mochizuki and R. Singh, ''A review of car waste heat recovery systems utilising thermoelectric generators and heat pipes,'' Appl. Therm. Eng., 101, pp. 490–495, 2016.

[18] H. Y. Lee, S. H. Park and K. H. Kim, ''Comparative analysis of thermodynamic performance and optimization of organic flash cycle (OFC) and organic Rankine cycle (ORC),'' Appl. Therm. Eng., 100, pp. 680–690, 2016.

[19] H. Chen, D. Y. Goswami, M. M. Rahman and E. K. Stefanakos, ''A supercritical Rankine cycle using zeotropic mixture working fluids for the conversion of low-grade heat into power, Energy, 36, pp. 549–555, 2011.

[20] Z. Li, Y. Lu, Y. Huang, G. Qian, F. Chen, X. Yu, and A. P. Roskilly, ''Comparison study of Trilateral Rankine Cycle, Organic Flash Cycle and basic Organic Rankine Cycle for low grade heat recovery,'' Energy Procedia, 142, pp. 1441–1447, 2017.

[21] J. Fischer, ''Comparison of trilateral cycles and organic Rankine cycles,'' Energy, 36, pp. 6208–6219, 2011.

[22] X. Yu, Z. Li, Y. Lu, R. Huang and A. P. Roskilly, ''Investigation of an Innovative Cascade Cycle Combining a Trilateral Cycle and an Organic Rankine Cycle (TLC-ORC) for Industry or Transport Application,'' Energies, 11, 3032, 2018.

[23] Z. Li, R. Huang, Y. Lu, A. P. Roskilly, and X. Yu, ''Analysis of a combined trilateral cycle - organic Rankine cycle (TLC-ORC) system for waste heat recovery,'' 10th International Conference on Applied Energy (ICAE2018), 22-25 August 2018, Hong Kong, China, 2019.

DETERMINATION OF SOME PARAMETERS FOR INFRARED FREE ELECTRON LASER

Suat ÖZKORUCUKLU[1], Serap YİĞİT GEZGİN[2]

[1] Istanbul University, Istanbul /Turkey, suat.ozkorucuklu@gmail.com

[2] Selcuk University, Konya/Turkey, serap3207@hotmail.com

Abstract *-* **In this study, the peak magnetic field (B_o) and the force parameter (K) have been calculated based on the gap between poles of U90 undulator to be used for IR-FEL intended to be produced in Turkish Accelerator Center. It has been shown that the gap between the poles of the undulator increases and the B_o and K values decrease. The wavelength range of the radiation produced in U90 undulator and U30 undulator with a shorter period length which were calculated, and the graphs of the wavelength range vs the gap of the undulator were obtained and interpreted for the electron beam with energy of 20 MeV and 40 MeV. The radiation with shorter wavelength is produced by decreasing the energy of the electron beam, the period length, and the gap of the undulator. In the this study, by the energy of the electron beam entering in to the undulator, the undulator gap and the period length which are adjusted at appropriate values, it has been shown that the radiation can be produced in the wavelength range of 2.45µm-344µm by U90 an U30 undulators.**

Keywords **- FEL, undulator, IR, radiation, wavelength**

I. INTRODUCTION

LASERS are consistent sources of electromagnetic radiation covering a wide range of spectrum between near infrared and ultraviolet. However, the wavelength region in about 10 µm -1 mm of the electromagnetic spectrum (typically this region is called as infrared near the terahertz region), which cannot be easily achieved with conventional lasers having disadvantages such as limited wavelength adjustability and low intensity. Therefore, there is great interest in alternative sources of coherent radiation in this electromagnetic spectrum and a lot of research is being done with this aim. [1].

Free Electron Laser (FEL) is known as an adjustable high power radiation source in which a portion of the energy are carried by an electron beam moving at relativistic speed is transferred resonant to a co-emitted electromagnetic wave in the presence of a spatially periodic magnet array (called an undulator). FEL was first produced by Madey et al. in 1976 and since then FELs have been produced in between the millimetre (mm) and X-ray wavelength region of the spectrum [2]. The coherent radiation can be provided anywhere in the electromagnetic spectrum by FEL. Furthermore, the wavelength of the radiation can be adjusted continuously, its intensity is very high and its pulse length can be very short.

These properties make the FEL quite remarkable as a consistent source of the radiation [3].

FEL system consists of three parts: *i-* an electron accelerator is used to accelerate electrons to the speed of light, *ii-* an undulator is used to convert the kinetic energy of the electron into electromagnetic energy and to obtain undulating electron motions, *iii-* an optical resonator is used to amplify consistent light beams and limit the radiation [4, 5]. FELs with adjustable high-power has excellent beam quality which they are used in many fields such as basic science research, medical applications, life sciences, nuclear industries, defence industry, materials science and nanotechnology[5]. Infrared FELs (IR-FELs) are currently used in many places around the world, such as CLIO (Infrared Laser Center of Orsay) in France [6], FHI-FEL (Fritz Haber Institute-FEL) in Germany [7], FELIX (Free Electron Lasers for Infrared experiments) in Netherland [8]. FELs are particularly effective devices in the IR region, since they typically produce laser pulses with high power at MW levels for peak power and several hundred mJ levels for macro pulse energy [1].

The Turkish Accelerator Complex (TAC) Project wasproposed by a group of scientists from Gazi and Ankara Universities in 2000, was accepted by the State Planning Organization (SPO) in 2006. The installation of the IR-FEL plant in oscillator mode is intended as the first step of this accelerator complex. IR-FEL plant is planned to include medium and far infrared radiation wavelengths and will be produced based on superconducting linear accelerator (LINAC)[9, 10]. The possible use of FEL to be produced which is considered in processes such as non-linear optics, semiconductors, biotechnology, medicine and photochemical.

In this study, the peak magnetic field (B_o) and force parameter (K) were calculated and plotted depending on the inter-poles gap (g) of the U90 undulator with a period length of $\lambda_u = 9$ cm for IR-FEL intended to be installed in the Turkish Accelerator Center (TAC). In addition, the radiation wavelengths based on the gap among the poles of the undulator were calculated and plotted for the electron beams in 20 MeV and 40 MeV energy entering into U90 undulator and U30 undulator with a period length of $\lambda_u = 3$ cm.

II. THE WORKING PRINCIPLE OF FEL

FEL system consists of an electron gun, an electron accelerator, an undulator and an optical cavity as shown in Fig. 1a. Electrons are ejected from the electron gun rise to relativistic speeds in the accelerator and then they enter the undulator. The sinusoidal magnetic field is formed among the poles of the undulator formed by the alignment of the opposite poles. As a result of the oscillation movement of electrons at relativistic velocity passing through this field, they lose their kinetic energy and form the radiation. Then, this radiation is reflected several times in the optical cavity which they are formed by two mirrors to exchange energy between the electron beam and the laser radiation. Thus, the intensity of the radiation in the magnet reaches the saturation point as a result of reflections between the mirrors and exits to outside by a permeable mirror [5, 11].
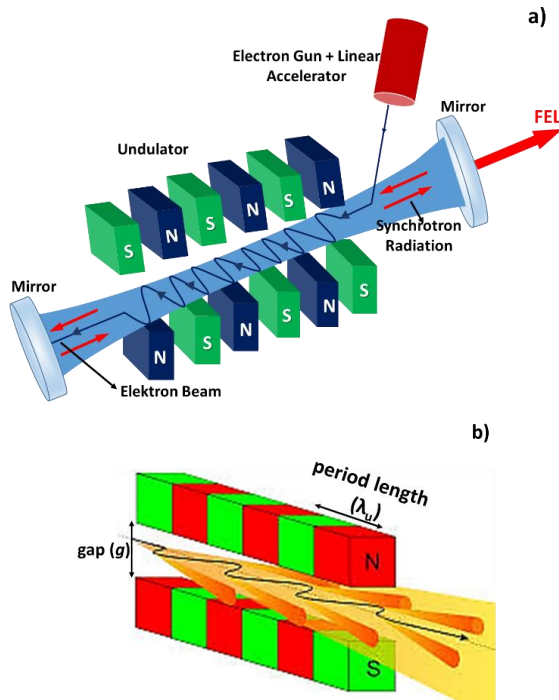
Figure 1: **a)** The working image of FEL, **b)** the gap (g) and period length (λ_u) of the undulator

III. RESULTS AND DISCUSSION

In this study, it is mainly considered the U90 undulator with a period of λ_u = 9 cm. Since the SmCo material offers very high magnetic properties, the undulator consists of hybrid type magnets made of Sm_2Co_{17} material [12]. The peak magnetic field (B_o) formed among the poles of this magnet,

$$B_o = 2B_r \frac{sin(E\pi M)}{(\pi/4)}\left(1 - e^{-2\pi h/\lambda_u}\right)e^{-\pi g/\lambda_u}$$

(1)

is expressed by equation (Eq.) (1). Where A is the remanent area of the magnet and its value is 1.5 T. M is the block number and its value is 4. E is the packaging factor and has a

value of 1. λ_u is period length of the undulator, h is the block height of magnet, g is the gap among the poles of the undulator [5, 13].
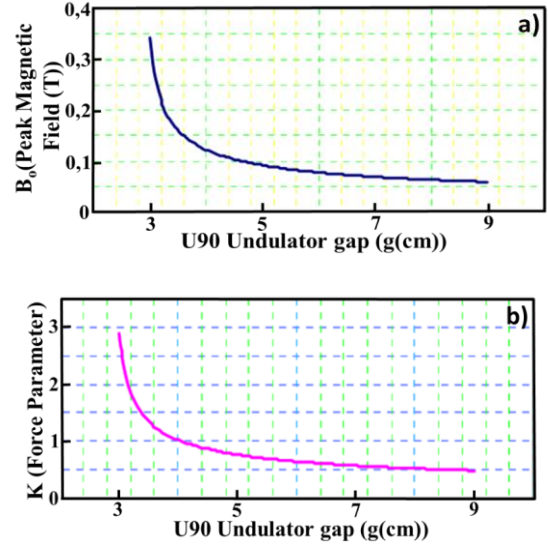
Figure 2: The plots of a) peak magnetic field and b) force parameter depending on gap of U90 undulator

The peak magnetic field is calculated based on the gap of U90 undulator and its graph is expressed in Fig. 2a. According to the graph, it is seen that the peak magnetic field is limited by gap of the undulator. B_o is about 0.34 T for g=3 cm. B_o value decreases exponentially to about 0.06 T when the undulator gap is increased to 9 cm [1, 5].

The force parameter of the undulator (K),

$$K = \frac{e B_o \lambda_u}{2\pi m c}$$

(2)

is expressed by Eq. (2). Where e is the particle charge, m is the electron mass and c is the velocity of light. According to Eq. (2), the force parameter of the undulator is directly proportional to the period length and the peak magnetic field of the undulator. In addition, if Eq. (1) is defined in Eq. (2), the undulator gap can be expressed as one of the main factors determining the force parameter.

It is given that the plot of the change of the force parameter (K) of U90 undulator in the range of 3 cm and 9 cm in Fig. 2b. It is calculated that K is about 2.09 for g = 3 cm by using Eq. (2) depending on Eq. (1), and K is about 0.5 when g is increased to 9 cm [14]. As the gap between the poles of the magnet increases and B_o decreases, K value decreases.

The electron beam oscillating in the undulator and the generated radiation wave continuously interact with each other under resonance conditions in FEL. The basic resonance wavelength of radiation obtained in the undulator used,

$$\lambda_s = \frac{\lambda_u}{2\gamma^2}\left(1 + \frac{K^2}{2}\right)$$

(3)

is expressed with Eq. (3). γ=E/mc^2, is the Lorentz Factor of the electron beam [4, 15, 16]. The simplest way to adjust FEL

wavelength is to change K value of the undulator corresponding to the undulator gap change. FEL can be obtained in the desired wavelength region by adjusting the electron energy, the oscillatory period length and the gap of the undulator [1]. Using the Eq. (1) and (2) in Eq. (3), the obtained plots of the radiation wavelengths generated based on the gap of U90 undulator for electron beams with 20 MeV and 40 MeV which they are shown in Fig. 3a and 3b.

Table 1: Parameters for U90 and U30 undulators

Parameters	U90	U30
Undulator Material	Sm_2Co_{17}	Sm_2Co_{17}
Period Length [cm]	3	9
Undulator gap (g)[cm]	2-3	3-9
Period Number	56	40
Undulator Length	1.68	3.6
Electron Beam Energy	40 MeV	40 MeV
Wavelength range (µm)	74-88 µm	2.50-2.45 µm
Electron Beam Energy	20 MeV	20 MeV
Wavelength range (µm)	295-340 µm	9.8-10 µm
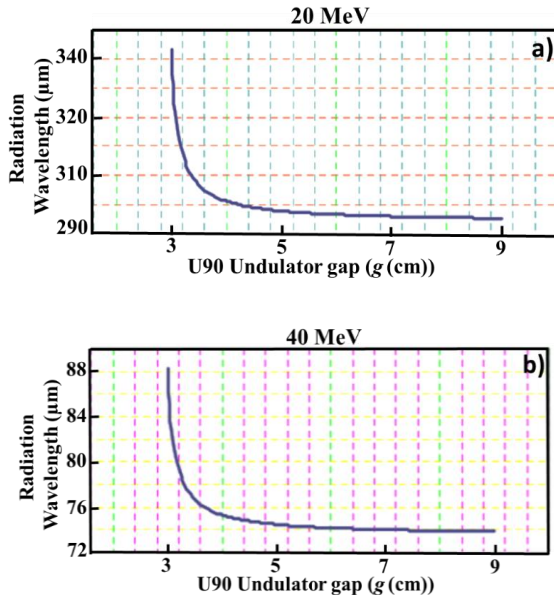
Figure 3: The plots of the radiation wavelength depended on the gap of U90 undulator for the electron beam of **a)** 20 MeV and **b)** 40 MeV

The radiation is generated in FIR wavelength region by U90 undulator for the electron beam at 20 MeV energy, according to the plot shown in the Fig. 3a. As gap among the poles of the undulator increases, the wavelength range of the laser produced in the cavity decreases. When the radiation wavelength for $g = 3$ cm which is about 340 µm, the gap is increased to $g = 9$ cm and the radiation wavelength decreases to about 295 µm. While there is no significant reduction in laser wavelengths between $g = 7$ cm and 9 cm, an evident decrease occurs between $g = 3$ cm and 6 cm. As a result, as the gap between the poles of the undulator increases, the radiation wavelength produced decreases.

The wavelength of the radiation produced by U90 undulator which shifts towards MIR (middle infrared) region for the electron beam of 40 MeV energy, according to the graph in Fig. 3b. The radiation wavelength is 88 µm while the gap of the undulator is $g = 3$ cm for U90 undulator. When g is increased to 9 cm, the value of the radiation wavelength decreases to 74 µm. No significant change in laser wavelength has been observed for the undulator range of $g = 6$ cm and 9 cm. When the energy of the electron beam has been increased from 20 MeV to 40 MeV, the radiation wavelength value produced in U90 undulator which decreased by about 1/4. This indicates that shorter wavelength radiation can be generated in the undulator while increasing the electron beam energy.

The undulator with short period length should be used to generate radiation in the shorter wavelength region depending on the area of application. Therefore, in this study, in addition to U90 undulator, it has been calculated that the radiation wavelength to be produced in U30 undulator with a period length of $\lambda_u = 3$ cm. The graphs (plotted using Eq. (3)) of the radiation wavelength produced by the electron beam at 20 MeV and 40 MeV energy oscillating in U30 undulator that are shown in Fig. 4.
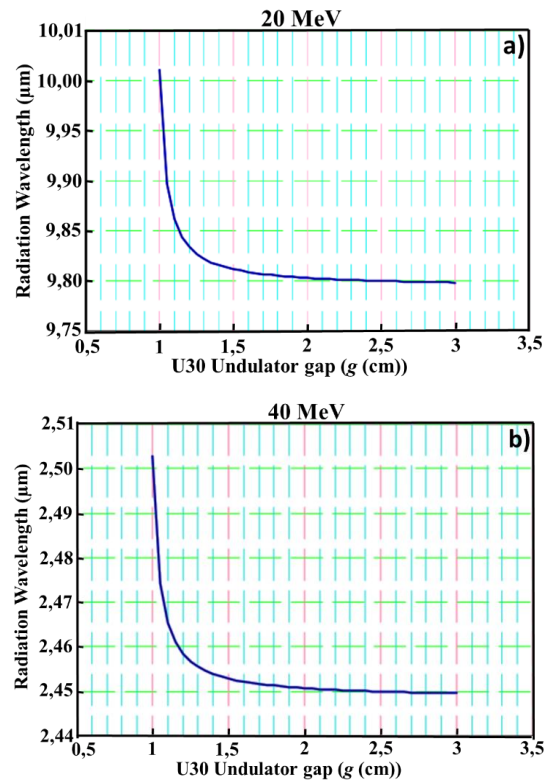
Figure 4: The graphs of the radiation wavelength based on the gap of U30 undulator for electron energy of **a)** 20 MeV and **b)** 40 MeV

The graph of the radiation wavelength based on the undulator gap given in Fig.4a which shows that the radiation can be produced in MIR wavelength region by U30 undulator for electron energy of 20 MeV. As the gap between the poles of the undulator increases, it is reduced to the radiation

wavelength range produced in the cavity. While the laser wavelength produced for g = 1 cm in U30 undulator that is about 10 μm, when it is increased to g = 3 cm, the laser wavelength decreased parabolically to about 9.8 μm as seen Fig.4a. In particular, there was no significant change in the laser wavelength between g = 2 cm and 3 cm. In other words, the reduction in laser wavelength was between g = 1 cm and 2 cm.

The wavelength of the radiation generated by U30 undulator shifted towards NIR (near infrared) region, according to the radiation graph depended on the undulator gap shown in Fig. 4b. For the gaps of g = 2 and 3 cm of U30 undulator, the generated radiation wavelength is about 2.50 μm and 2.45 μm for electron energy of 40 MeV, respectively. The radiation wavelength between g = 2 cm and 3 cm which showed no significant change. When the energy of the oscillating electron beam in the undulator was increased from 20 MeV to 40 MeV, the radiation wavelength values produced by U30 undulator that decreased by ~ 1/4.

In conclusion, in this study, it is shown that the shorter wavelength radiation production can be realized by decreasing the period length of the undulator and increasing the electron beam energy in FEL undulator. [4, 5, 9, 14]. Furthermore, the wavelength of the radiation produced decreases with increasing gap of the undulator. As a result, by this adjustability on the generated radiation wavelength, IR-FEL can be used in in medical applications such as human brain surgery; in material sciences such as semiconductors; in bio-technology such as the investigation of radiation effects on biological samples, in photochemistry and non-linear optic applications such as research on radiation absorption spectroscopy of surfaces by total frequency generation method [9, 10].

IV. CONCLUSION

In this study, U90 undulator with a period length of λ_u = 9 cm is mainly used to produce IR-FEL at the Turkish Accelerator Center. The peak magnetic field and the force parameter of the undulator has been decreased by increasing gap of U90 undulator. For the electron beam at 20 MeV and 40 MeV energy, U90 undulator produced the radiation at FIR wavelength. The wavelength of the radiation produced in the undulator was reduced by 1/4 as the electron beam doubled its energy. In addition, the radiation in MIR wavelength was generated for electron beam at 20 MeV and 40 MeV oscillating in U30 undulator with a period length of λ_u = 3 cm. The radiation produced by the reduction of the period length which shifted to the shorter wavelength region. As a result, in this study, U90 and U30 undulators produced the radiation in the wavelength range of 2.45μm and 340 μm. It has been shown that radiation can be produced in the desired wavelength region by adjusting the period length of the undulator, electron energy and gap of undulator at appropriate values.

REFERENCES

[1] 1. Li, H.-T., et al., *Design of FELiChEM, the first infrared free-electron laser user facility in China.* Chinese Physics C, 2017. **41**(1): p. 018102.
[2] 2. Pant, K. and V. Tripathi, *Free electron laser operation in the whistler mode.* IEEE transactions on plasma science, 1994. **22**(3): p. 217-223.
[3] 3. Pełka, J., et al., *Applications of Free Electron Lasers in Biology and Medicine.* Acta Physica Polonica A, 2010. **117**(2): p. 427-432.
[4] 4. ALTAN, H. and H. KESKIN, *SPECIAL PROBLEMS IN PHYSICS.* 2010.
[5] 5. Gezgin, S.Y., *Serbest elektron lazeri parametrelerinin belirlenmesi.* 2009, SDÜ Fen Bilimleri Enstitüsü.
[6] 6. Ortega, J., *Operation of the CLIO infrared laser facility.* Nuclear Instruments and Methods in Physics Research Section A: Accelerators, Spectrometers, Detectors and Associated Equipment, 1994. **341**(1-3): p. 138-141.
[7] 7. Schöllkopf, W., et al. *The new IR and THz FEL facility at the Fritz Haber Institute in Berlin.* in *Advances in X-ray Free-Electron Lasers Instrumentation III.* 2015. International Society for Optics and Photonics.
[8] 8. Van Amersfoort, P., et al., *First lasing with FELIX.* Nuclear Instruments and Methods in Physics Research A, 1992. **318**: p. 42-46.
[9] 9. Mete, O., O. Karslı, and O. Yavas. *An Optimization Study for an FEL Oscillator at TAC Test Facility.* in *EPAC06.* 2006.
[10] 10. Aksoy, A., Ö. Karslı, and Ö. Yavaş, *The Turkish accelerator complex IR FEL project.* Infrared Physics & Technology, 2008. **51**(5): p. 378-381.
[11] 11. Feldhaus, J., J. Arthur, and J. Hastings, *X-ray free-electron lasers.* Journal of Physics B: Atomic, molecular and optical physics, 2005. **38**(9): p. S799.
[12] 12. Yildiz, H., *Infrared Free Electron Laser, Resonator Parameters Optimization with GENESIS, OPC and GLAD Codes.* Mathematical and Computational Applications, 2011. **16**(3): p. 659-668.
[13] 13. Tanaka, T., et al., *Tunability and power characteristics of the LEBRA infrared FEL.* FEL2004, Trieste, Italy, 2004.
[14] 14. Socol, Y., *High-power free-electron lasers–technology and future applications.* Optics & Laser Technology, 2013. **46**: p. 111-126.
[15] 15. Couprie, M.E., *Towards compact Free Electron–Laser based on laser plasma accelerators.* Nuclear Instruments and Methods in Physics Research Section A: Accelerators, Spectrometers, Detectors and Associated Equipment, 2018. **909**: p. 5-15.
[16] 16. Yavaş, Ö., *Serbest Elektron Lazeri-Çekirdek Çarpıştırıcılarının Nükleer Spektroskopi Açısından Önemi.* 2007.

Investigation Of Exhaust Emissions From A Diesel Engine Fuelled With Biodiesel Diesel Blends

A.E. ÖZÇELİK[1] H. AYDOĞAN[1] and M. ACAROĞLU[1] and M.N. KILIÇARSLAN[2]

[1] Selcuk University, Mechanical Engineering, Konya/Turkey, eozcelik@selcuk.edu.tr
[1] Selcuk University, Mechanical Engineering, Konya/Turkey, haydogan@selcuk.edu.tr
[1] Selcuk University, Mechanical Engineering, Konya/Turkey, acaroglu@selcuk.edu.tr
[2]Konya Technical University, Environment Engineering, Konya/Turkey, mnkilnçarslan@ktun.edu.tr

Abstract **- Energy production is heavily dependent on fossil fuels that are not only diminishing, but also are considered the main cause of harmful emissions and global warming. Therefore using vegetable oils as alternative fuels in diesel engines has drawn a great attention.**

Trans-esterified vegetable oil derivatives also called 'biodiesel' appear to be the most convenient method of utilizing bio-origin vegetable oils as replacement fuels in diesel engines. In the present study, biodiesel was prepared from 60% canola, 20% sunflower, 20% safflower through the trans-esterification process.

The emission characteristics were compared in an unmodified diesel engine.

Keyword **- Walnut, biodiesel, engine, emissions**

I. INTRODUCTION

Renewable fuels have recently started to play an important role in meeting the world's energy needs [1,2]. The use of fossil fuels leads to economic, environmental and resource problems [3,4]. In order to solve these problems, countries are encouraged to use liquid biofuels instead of petroleum-derived fuels, and increasingly biofuels are gaining a great deal of attention[5,6]. Among biofuels, biodiesel is preferred for reasons such as its easy degradation in nature, its environmental friendliness and its ability to be used in a diesel engine without requiring any modifications [7]. Long chain fatty acid methyl ester, renewable oils (vegetable and animal oils) derived biodiesel as alternative fuel to petroleum diesel and can be used as an additive [8,9].

Biodiesel is usually produced by the alkaline catalyzed transestirification method of vegetable and animal fats with methanol [10]. After removal of glycerin, residues such as alcohol, catalyst, free fatty acids, glycerin, water may exist in biodiesel[11]. In order for biodiesel to be commercially acceptable, certain requirements in biodiesel standards such as EN 14214 and ASTM d6751 must be adhered to. For this reason, it is necessary to use purification and drying processes to ensure biodiesel quality [12]. The purification phase requires removal of various impurities from raw biodiesel to prevent combustion from damaging emission quality as well as engine performance, robustness and safety. This purification stage is therefore among one of the most important for commercial biodiesel production [13].

In this study, the effects of biodiesel and diesel mixtures obtained in a four-stroke, common-rail fuel system, water-cooled, 4-cylinder diesel engine with 60% canola, 20% sunflower, 20% safflower oil mixture on engine exhaust emissions were investigated. The results were compared and evaluated [14].

II. MATERIAL AND METHOD

Biodiesel used in this study, 60% canola, 20% sunflower, 20% safflower oil mixture obtained from oil was produced using transestrification method. Using these biodiesel and eurodiesel, B7 (7% mixture biodiesel by volume - 93% Eurodiesel), B20 and B100 fuel mixtures were prepared. Engine exhaust emissions tests were performed on the engine with these mixtures prepared.

The test mechanism used in this study is seen in Figure 1. The experimental engine is a 4-cylinder diesel engine with a common-rail fuel system, supercharged and decooled. Technical specifications of the engine are given in Table 1. The technical specifications of the engine dynamometer and exhaust emission device used in the study are also given in Table 2 and Table 3.
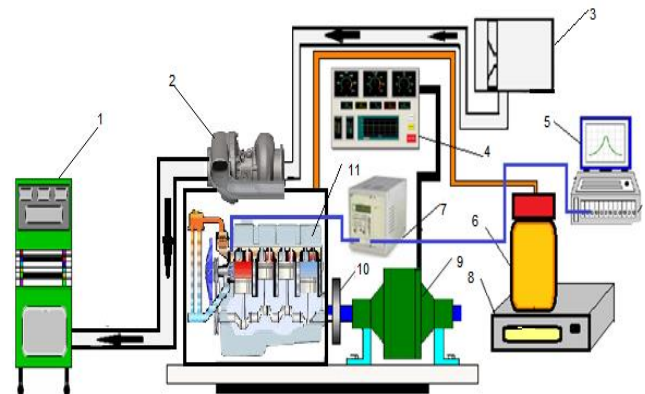
1. Exhaust Emissions Device	5. AVL cylinder pressure meter	9. Hydraulic Dynameters
2. Turbocharger	6. Fuel Tank	10. Clutch
3. Orifice Plate	7. Charge Amplificatory	11. Engine
4. Control Panel	8. Digital Scales	

Fig. 1. Experimental setup

Table 1
Technical characteristics of the engine used in the study

Engine	1.9 Multijet
Number of cylinders and layout	4, a single row of the front transverse
Cubic capacity (cc)	1910
Compression ratio	5.18: 1
Maximum power hp - d / d	105 - 4000
Maximum torque Nm (kgm) - d/d	200 - 1750
Fuel	diesel
Fuel supply	Electronically controlled Common Rail type
	MultiJet direct injection, turbocharger and intercooler
Ignition	compressional
Bore x Stroke (mm)	82 x 90.4

Table 2
Motor dinamometresinin teknik özellikleri

Model	BT-190 FR
Capacity	100 kW
Maximum speed	6000 rpm
Maximum torque	750 Nm

Table 3
Technical specifications of exhaust emission device used in study

Measurement Range	Unit	Value
CO	%	0-9.99
CO_2	%	0-19.99
HC	ppm	0-2500
Λ	%	0-1.99
O_2	%	0-20.8
NOx	ppm	0-2000

The experiments were carried out at different revs, with the engine in full throttle position. Before starting measurements, the engine was heated to a working temperature of. After the engine fan is turned on and off twice, experiments have started.

III. RESULTS AND DISCUSSION

In Figure 2, the co values of the fuels are given depending on the engine speed. According to the results, the CO values of B100 fuel are lower than other fuels due to the fact that it is better to burn biodiesel due to the oxygen contained in it than eurodiesele. Among the reasons for the lowest output of this fuel are the high rates of biodiesel in it. In addition, because

the increased intake air speed at high revs increases the turbulence density within the combustion chamber, the fuel air mixture may have mixed better and improved combustion. As a result, the amount of CO may be reduced. CO effects on human health include fatigue, decreased working efficiency, headache, dizziness, shortness of breath, loss of consciousness, even lethal effects when the amount in the air reaches a limit of 0.3%.
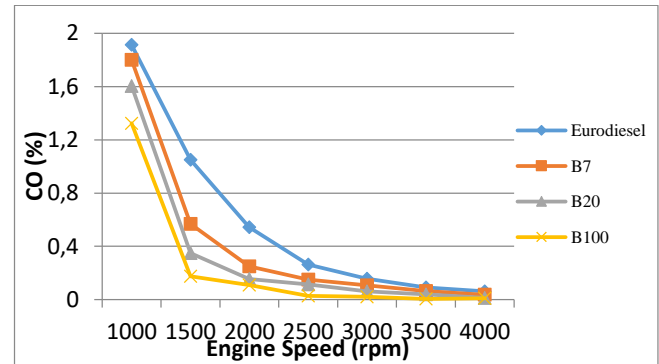
Şekil 2. CO emission

The CO_2 generated by the combustion of renewable energy origin fuels is retained by plants. Plants divide CO_2 into carbon and oxygen. Oxygen is released back into the atmosphere. The use of renewable energy thus ensures a natural balance in CO_2 emissions. In Figure 3, the CO_2 values of the fuels are given depending on the engine speed. According to the results, the CO_2 value of eurodiesel fuel is higher than that of biodiesel mixed fuels. The most load CO_2 value is seen to be at 2000 rpm. In this period, the CO_2 value of the engine fuel decreased by 15.56% in the B100 fuel compared to eurodiesel fuel. This reduction is due to the fact that biodiesel has a lower carbon-hydrogen ratio depending on the presence of oxygen atoms.
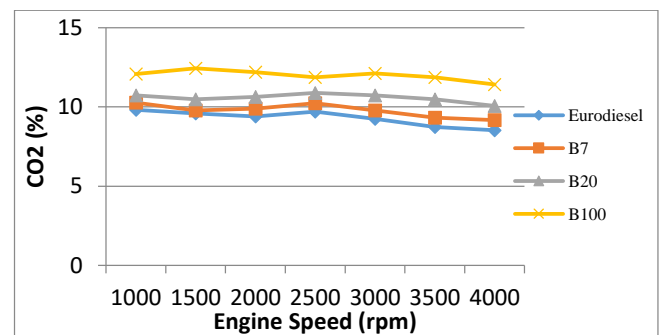
Şekil 3. CO_2 emission

Figure 4 shows the HC values of the fuels depending on the engine speed. When the chart is examined, the highest HC value is seen in eurodiesel fuel. The reason for this is that the formation of hydrocarbons among unburned products is because the fuel is not oxidized or semi-oxidized due to the fact that it does not reach the ignition temperature or is insufficient. For this reason, the HC values in eurodiesel fuel were high. According to the chart the lowest HC was achieved in B100 fuel for all cycles. This reduction in HC emissions may have been due to improved combustion of the oxygen in

the structure of biodiesel and its mixtures. Another reason is that biodiesel and its mixtures have a high value of cetane compared to eurodisele. This will shorten the ignition delay and alter the reaction timing of the mixture. As a result, the HC emission level will be reduced.
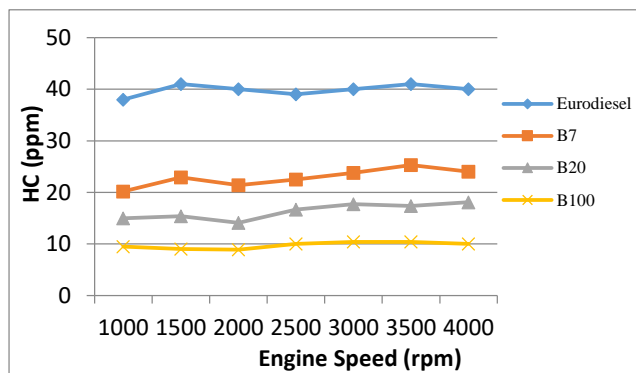
Şekil 4. HC emission

Figure 5 shows the change in the amount of O_2 in the exhaust gases depending on the engine speed. O_2 values were measured in eurodiesel fuel at the lowest 2000 rpm and in B100 fuel at the highest. Looking at the average values, it was observed that the O_2 percentage of B100 fuel increased by 50% compared to eurodiesel fuel. Biodiesel and bioethanol in comparison to eurodiesele oxygen content because of the excess O_2 values in biodiesel mixed fuels increased so much.
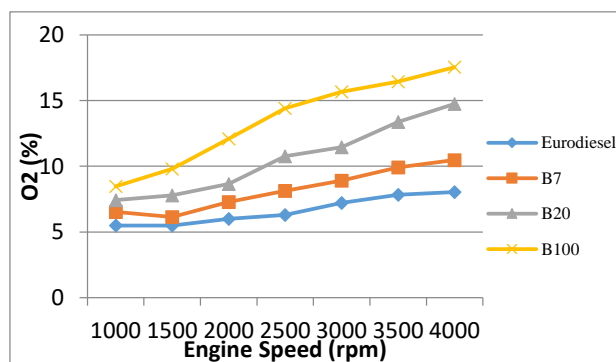
Şekil 5. O_2 emission

In Figure 6, NOx values of fuels are given depending on engine speed. On average, NOx values for Eurodiesel fuel increased by 21.48% in B7 fuel, 42.75% in B20 fuel and 89.72% in B100 fuel. This is due to the fact that vegetable oils contain oxygen. The high heat that occurs as a result of the combustion of fuel in the engine, the nitrogen in the air combines with oxygen to form nitrogen oxides. In addition, NOx increase occurs because the combustion time is extended in the fuels that ignite quickly. NOx values are high due to this high temperature in the oxygen contained in vegetable fuels.
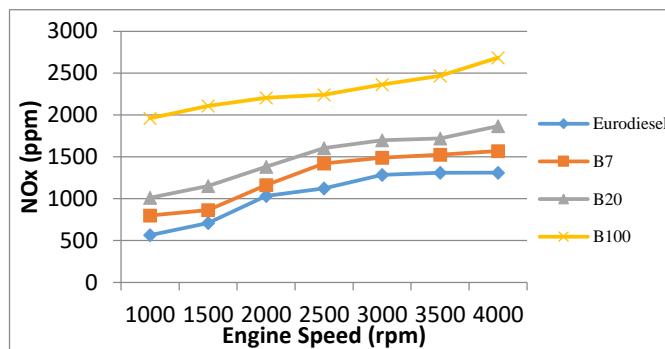
Şekil 6. NO_x emission

Figure 7 shows the change of mistiness values according to motor speed. The smoke values were highest at 1000 rpm and 1500 rpm revs. At high revs the values have been very close. Especially in the B100 fuel, smoke values are the lowest. The reason for this is that the amount of oxygen in biodiesel is more than the amount of eurodiesel is good to burn.
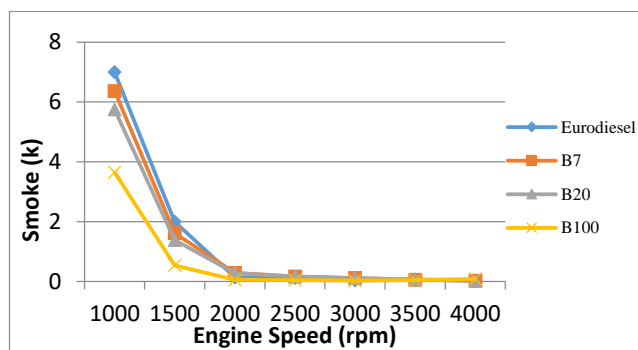
Şekil 7. Smoke (k) emission

IV. RESULTS

In this study, biodiesel was obtained from pirina oil with eurodiesel fuel by transestrification method. B7, B20 and B100 mixtures of biodiesel fuel obtained from Eurodiesel fuel have been prepared. Biodiesel fuel mixtures were used separately, respectively, with no modifications to the engine with the common-rail fuel system. The engine exhaust emission characteristics of these fuels were tested at full load and different engine revs. According to the data obtained, engine exhaust emission change graphs of each fuel were obtained and these graphs were compared with each other.

The main factor in the changes in engine performance when biodiesel is used is that the thermal value of the fuel is lower than eurodiesel fuel. Under partial load conditions, the oxygen in biodiesel improves the oxidation of the fuel, resulting in an increase in engine power. Changes in emission values are in line with eurodiesel, which is the reference fuel in terms of the emissions produced by alternative fuels, while there are differences in the rate of increase and decrease. Because the engine used in the experiments kept the fuel under very high pressure thanks to the Common-rail fuel system, HC

emissions were lower than eurodiesel fuel compared to other fuels. At the same time, CO and CO2 emissions were lower than eurodiesel fuels. The use of biodiesel increased the amount of NOx and O2 in the exhaust gases due to the presence of oxygen in the fuel content. In this study, it was observed that NOx amount in exhaust gases is at most in B100 fuel. Again, the smoke values of biodiesel mixtures were found to be quite low compared to the engine, especially at low revs.

The production of biodiesel from the mixture oil and the use of the mixtures of biodiesel with eurodiesel fuel in diesel engines as an alternative fuel creates a positive effect in reducing the dependence on external energy. Besides this, it contributes to the formation of new business areas. As a result, the use of vegetable and waste vegetable oils as an alternative fuel in diesel engines has a positive ecological and economic impact.

V. RESOURCES

[1] Singh, A.P., Agarwal, A.K., Combustion characteristics of diesel HCCI engine: An experimental investigation using external mixture formation technique,
Applied Energy, Volume 99 (2012) Pages 116–125

[2] Singh, G., Singh, A.P., Agarwal, A.K., Experimental investigations of combustion, performance and emission characterization of biodiesel fuelled HCCI engine using external mixture formation technique, Sustainable Energy Technologies and Assessments, Volume 6 (2014) Pages 116–128

[3] Sükran Efe, Mehmet Akif Ceviz, Hakan Temur, Comparative engine characteristics of biodiesels from hazelnut, corn, soybean, canola and sunflower oils on DI diesel engine, Renewable Energy, 119 (2018) 142-151.

[4] Sivaramakrishnan, K., Ravikumar, P., Determination of cetane number of biodiesel and It's influence on physical properties, ARPN Journal of Engineering and Applied Sciences (2012) vol. 7, no. 2

[5] Ali Aminian, Bahman ZareNezhad, Accurate predicting the viscosity of biodiesels and blends using soft computing models, Renewable Energy, 120 (2018) 488-500

[6] Aleksandra Sander, Mihael Antonije Koscak, Dominik Kosir, Nikola Milosavljevic, Jelena Parlov Vukovic, Lana Magic, The influence of animal fat type and purification conditions on biodiesel quality, Renewable Energy, 118 (2018) 752-760

[7] Dıraman, H., 2016, "Zeytinyağı, Yemeklik Pirina Yağı ve Bazı Önemli Yemeklik Bitkisel Yağlarda Oksidatif Stabilitenin Karşılaştırılması Üzerine Çalışmalar." Hasad GIDA (2006) pg 12-17.

[8] Mohan, B., Yang, W., Raman, V., Sivasankaralingam, V., Chou, S.K., Optimization of biodiesel fueled engine to meet emission standards through varying nozzle opening pressure and static injection timing, Applied Energy, Volume 130 (2014) Pages 450–457

[9] Azbar, Nuri, et al., "A review of waste management options in olive oil production." Critical Reviews in Environmental Science and Technology (2004) 34.3: 209-247.

[10] Seiji Kosemura, Kazuki Niwa, Hideyuki Emori, Kaori Yokotani Tomita, Koji Hasegawa, ShosukeYamamura, Light-induced auxin-inhibiting substance from cabbage (Brassica oleacea L.) shoots, Volume 38, Issue 48 (1997) Pages 8327-8330

[11] Beken, Yeliz, and Ahmet Sahin., "The effect of prina (olive cake) feeding methods on growth performance and behaviour of awassi lambs." Int. J. Agric. Biol (2011) 13: 423-426.

[12] Mohammad Ali Rajaeifar, Asadolah Akram, Barat Ghobadian, Shahin Rafiee, Reinout Heijungs, Meisam Tabatabaei, 2016, Environmental impact assessment of olive pomace oil biodiesel production and consumption: A comparative lifecycle assessment, Energy, Volume 106 (2016) Pages 87-102

[13] Antonio Lama-Muñoz, Paloma Álvarez-Mateos, Guillermo Rodríguez-Gutiérrez, María Montaña Durán-Barrantes, Juan Fernández-Bolaños, 2014, Biodiesel production from olive–pomace oil of steam-treated alperujo, Biomass and Bioenergy, Volume 67, (2014) Pages 443-450

[14] Franklin Che, I. Sarantopoulos, Theocharis Tsoutsos, Vasileios Gekas, Explorina promising feedstock for biodiesel production in Mediterranean countries: A study on free fatty acid esterification of olive pomace oil, Biomass and Bioenergy, Volume 36 (2012) Pages 427-431

COOLING TOWERS DESIGNS AND APPLICATIONS

İrfan UÇKAN

Van Yuzuncu Yil University, Van / TURKEY, irfanuckan@yyu.edu.tr

Abstract **- Cooling towers are one of the most important industrial equipment used in industrial facilities to discharge unwanted process heat from heat exchangers to the atmosphere through cooling water. The phenomenon of heat exchange in the cooling tower has a complex structure involving simultaneous heat and mass transfer. Reuse and for environment, cooling of hot waste water and process water is important. There are many factors affecting cooling tower performance. The main factors affecting cooling tower performance are air flow, water flow, cooling load, incoming air conditions, water temperature and tower design. The aim of the study supported by the BAP department of Van Yuzuncu Yil University with FAP-2019-8610 project name aims to examine the studies and researches about cooling tower in order to make cooling towers used in industrial facilities more economical and efficient and to increase efficiency and power saving.**

Keywords **- Cooling towers, heat rejection, evaporation, tower design**

I. INTRODUCTION

Cooling towers play an important role in the chemical industry, air conditioning and refrigeration plants and in many plants. In industry, two types of auxiliary elements are generally used. These are the elements that perform heating and cooling. Cold water is required for condensers, heat exchangers, reactors and many other elements that need cooling. Cooling towers are used to remove heat from Steam and heat exchangers and maintain reaction conditions among hot plants that produce heat. Cooling towers are used in the cooling operations required by various such applications. Water coming from various applications at high temperature can be cooled and reused. In cooling towers, air and water are simultaneously passed through the cooling tower. The heat gained from the air is the heat lost by the water. The efficiency of the cooling tower varies depending on air and water flow rates and operating temperatures. Several researchers have conducted research and investigations on various aspects of the cooling tower that affect the efficiency and operation of the cooling towers.

Zavaragh et al. [1] analyzed the application of wind breaker in natural draft dry cooling towers. They found that the efficiency values of natural air-draft dry cooling towers were influenced by wind speed when their design and geometry were higher than a critical level. Khan et al. [2] used a detailed model to investigate the performance characteristics of counterflow wet cooling towers. According to this model, the thermal performance of cooling towers is explained by different air and water temperatures. In this study, the variation of air and water temperature along the height of the tower is explained in psychometric tables. In addition, they showed that evaporation was effective on heat transfer. Li et al. [3] investigated the effects of cross flow on a natural draft dry cooling tower in a solar thermal power plant. Tower performance was investigated under different ambient temperatures and cross wind speeds. Unlike high cooling towers, it has been shown that short cooling tower efficiency does not decrease monotonously with increasing cross wind speed. Fisenko et al. [4] developed a new mathematical model for the performance evaluation of a mechanical draft cooling tower and described heat and mass transfer processes and drop dynamics of droplets. They determined that the thermal efficiency of a mechanical air-drawn cooling tower depends on the ratio between the mass flow rates of water and air.

Soylemez [5] presented a thermo-hydraulic performance optimization analysis and estimated a simple algebraic formula for the optimum performance point of counterflow forced draft cooling towers. He used the NTU method to work with the derivation of the psychometric properties of moist air, based on a numerical approach method for thermal performance analysis.

Milosavljevic et al. [6] used equilibrium equations to estimate temperature changes of water and air as a function of the height of the tower. In the pilot experiments, the efficiency of cooling tower elements such as water spray nozzles and droplet separators was investigated. Computational fluid dynamics was also used to estimate the flow structure and properties, and was used to estimate the outside air flow around the cooling tower in cold and hot weather conditions. Lemouari et al. [7] presented an experimental investigation of the thermal performances of a forced-draw counterflow wet cooling tower filled with a VGA (Vertical Grid Assembly Apparatus) packaging. They examined the effects of air and water flow rates on cooling water range and tower characteristics for different inlet water temperatures.

Cooling towers are heat dissipation devices used to transfer waste heat to the atmosphere by cooling a water stream. Cooling towers are mainly used to cool the circulating water used in power plants. A number of numerical and experimental studies have been conducted on cooling towers. Jose [8] described the dynamic efficiency of thermofluid that can be used to compare and select a filler material for a given application. Thermo-fluid dynamic efficiency means maximum heat transfer with minimum pressure drop in the cooling tower. To illustrate this, heat transfer related to the pressure drop in isolated fills with different water cooling towers was evaluated. The experimental results obtained from commercial fillings showed that thermal fluid dynamic efficiency values were obtained, it was concluded that this efficiency is not a function of the height of the filling.

Naik et al. [9] considered the effect of operating parameters such as relative humidity, water inlet temperature, dry air temperature, heat load, and tower efficiency, and proposed an analytical model to estimate the amount of water taken from ambient air in cross-flow wet cooling. They revealed that these parameters had a significant effect on the efficiency of the cooling tower, except for the dry bulb temperature.

Cutillus et al. [10] applied an optimization control strategy to a cooling tower to reduce both energy and water consumption in the TRNSYS program. They also compared the three typical capacity control methods and examined the configurations involving different water distribution systems.

II. APPLICATION AREA AND WORKING PRINCIPLE OF COOLING TOWER

A cooling tower is a device used to cool a water stream while also removing heat to the atmosphere. In systems involving heat transfer, a condenser is used to condense a fluid passing through the gaseous state into a liquid. Cooling of the fluid passing through the condensers of high capacity power plants is generally provided by a cooling tower. Cooling towers are generally used in heating and cooling applications in large office buildings, hospitals and schools. In addition, cooling towers are much larger than conventional cooling systems and are used to extract heat from cooling tower water systems in petrochemical plants, oil refineries, natural gas processing plants, and other industrial processes and facilities (Fig. 1).

Cooling towers are generally used in the following businesses.

1. HVAC (Heating Ventilation and Air Conditioning), to remove heat from the chillers
2. To provide process cooling in manufacturing plants
3. For cooling the condenser in electricity generation plants
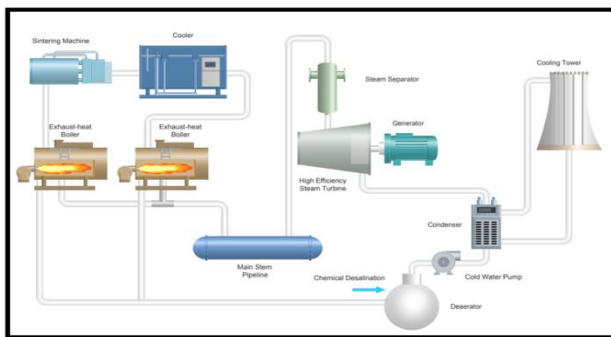
Fig.1 Process flow diagram for a power plant

The operating principle of the cooling tower (Fig. 2) is a form of cooling which takes place by evaporative cooling as well as sensible heat exchange. During evaporative cooling in a cooling tower, a small amount of cooled water is evaporated in a moving air stream to cool the remaining water.

Furthermore, when the hot water comes into contact with the cold air, there is a reasonable sensible heat transfer which allows the water to cool. While most of the heat transfer to air is carried out by evaporative cooling, only 25% of the heat transfer is carried out by sensible heat.
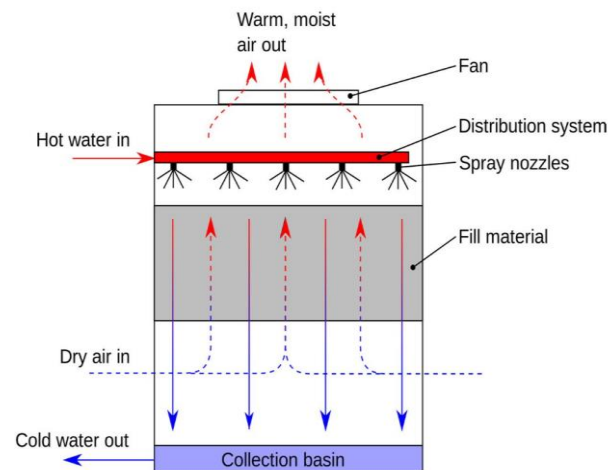
Fig. 2. Working principle of cooling tower Factors

III. AFFECTING COOLING TOWER PERFORMANCE

Factors affecting the performance of a cooling tower include Hill [11]:

➢ *Range -* The difference between the temperature of the water entering the tower and the temperature of the water leaving the tower.

➢ *Approach-* Cooling tower designers often used two temperature differences to characterize cooling tower operation. These are the cooling range and the approach as shown in Fig. 3. The range is the difference between the water inlet and outlet temperatures. Accordingly, the range is not determined by the size or capability of the tower, but it is determined by the heat load and water flow rate. This approach is defined as the difference between the temperature of the water leaving the cooling tower and the wet-bulb temperature. It is used as an indicator of how close the water from the tower is to the wet bulb temperature. In other words, the approach is basically defined as how close the outlet cold water temperature is to the entering air wet thermometer temperature. The approach is the most important parameter of cooling tower performance. Regardless of the size, range or heat load of the cooling tower, it determines the theoretical limit of the leaving water temperature throughout the tower. The approach is a function of a cooling tower capacity. Therefore; a large cooling tower will produce a closer approach to a given heat load, flow

rate and entering air condition.
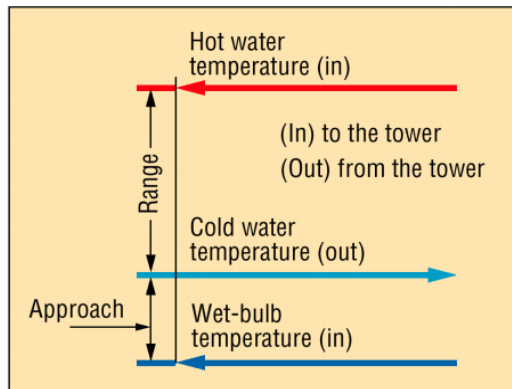
Fig.3 Process of range and approach

➢ ***Capacity*** - Capacity is the total amount of heat of a cooling tower that can remove at a given flow rate, approach and wet thermometer temperature. Usually it is measured in tons.

➢ ***Heat load***-When selecting the cooling tower, the waste heat load should be determined with a geographic area and design wet thermometer temperature for the desired range. The heat load is the amount of heat to be extracted from the circulating water in the tower. The size of the cooling tower is proportional to the cost. If the heat load is low, the cooling tower will likely be small, otherwise the equipment will be overly costly.

➢ ***Cell -*** It is the smallest tower sub-section which can work independently. Each cell of a tower can have different water flow and air flow.

➢ Filler - Heat transfer medium or surface contact area designed to maximize air and water surface contact area

➢ ***Additional water -*** The amount of additional water required to balance the water lost by evaporation, drift, discharge and other losses.

➢ ***Dry bulb temperature -*** The temperature of the air measured by a thermometer that is freely exposed to air but protected from moisture and radiation.

➢ ***Wet bulb temperature –*** The temperature of the air is measured when the thermometer is covered with wet wick, referred to as wet bulb temperature (WBT). When the air comes in contact with the wet wick, it absorbs some moisture and gives some heat. As the air passes through the wet wick, the water in the wick evaporates. If the air is too humid (moist), only a small amount of moisture will evaporate from the wick. A non-wetted thermometer measurement gives us a dry bulb temperature (DBT) reading. The comparison of wet and dry bulb readings allows the determination of the air properties from a psychometric chart and the air properties table. It is not possible or impractical to design a cooling tower that can provide cooling water equal to or lower than

the current wet bulb temperature of the air. Each tower system is specifically sized for the current summer wet thermometer temperature of each geographical region. Therefore, the wet-bulb temperature is the lowest temperature that water can reach by evaporative cooling. It is a critical parameter for measuring the performance of evaporative cooling tower systems. The cooling towers are specified and designed to achieve a certain degree of "wet-bulb approach" during the circulation of a certain amount of cooling water.

IV. COOLING TOWER CLASSIFICATION

Cooling towers can be classified in many different ways as follows

❖ Classification by structure
➢ Package Type
➢ Tower type built in the field

,

❖ Classification according to heat transfer method
➢ Wet cooling tower
➢ Dry cooling tower
➢ Liquid Cooler

❖ Classification by fill type
➢ Spray Filler
➢ Bounce Filler
➢ Film Filler

❖ Classification according to air intake
➢ Atmospheric tower
➢ Natural Traction Tower
➢ Mechanical drive tower
➢ Forced airflow tower
➢ Towing air flow tower

❖ Classification by air flow order
➢ Cross-flow cooling tower
➢ Opposite flow cooling tower

❖ Classification by structure

Package type cooling towers are pre-assembled and can be easily transported and installed in place of use. They are generally suitable for applications where the heat load to be exhausted is not very large (most HVAC and process load applications). The types of towers built on the site are often much larger to remove larger heat loads and are custom-built to customer requirements. Most of the tower construction and installation takes place in the area where the tower is located (Fig.4)
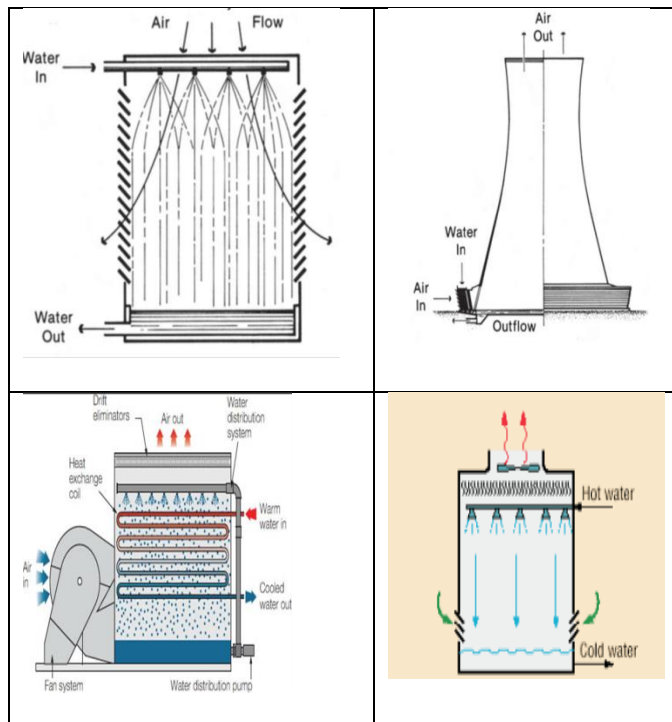
Fig. 4 Different type of cooling tower by structure

❖ **Classification according to filler type:**

In the spray fill tower, the water is divided into small droplets, thereby increasing the contact area between the water surface and air. Small water drops are produced by spraying water from the nozzles in the tower body and which have air flow through it. Disadvantages of this type of filling are low efficiency, large tower size and large airflow requirement.
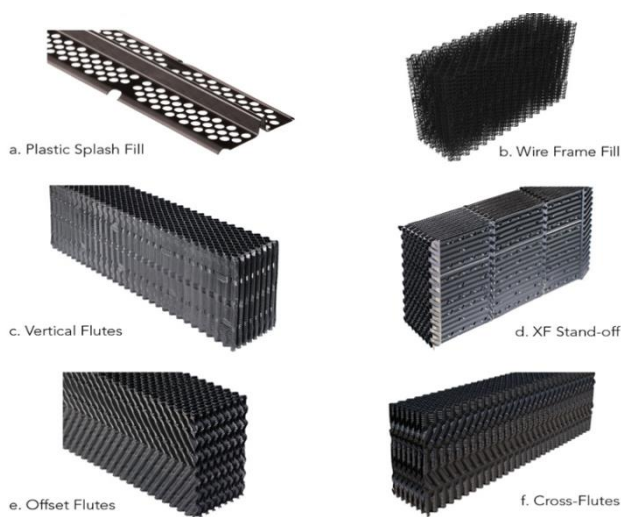
Fig. 5 Type of Fill for Cooling Tower

In a splash fill tower there is a stepped structure of wood, PVC or ceramic material where the water goes down the

tower. When water splashes onto slices, it creates small droplets that provide better tower performance.

In a film filler, a large surface area is provided for water to flow, resulting in a thin film. Due to this large contact area between the water surface and air, effective evaporative cooling occurs.In such a tower, the pressure drop when air flows through the tower is lower than in the previous types and therefore less fan power is required to move the air inside the tower. Film filling is cheaper and more efficient than splash filling and is widely used in cooling towers. An example of a type of fill for a cooling tower is shown in Fig. 5.

❖ *Classification according to air intake*

Atmospheric cooling tower: In an atmospheric tower, air enters the blinds driven at its own velocity. This kind of tower is cheaper. The performance is greatly influenced by wind conditions and is largely inefficient. It is rarely used when clear and constant cold water temperatures are required.

The natural draft cooling tower: The natural draft cooling tower (also known as the hyperbolic cooling tower) is similar to an atmospheric tower; wherein there is no mechanical device to generate air flow from the tower. However, unlike an atmospheric tower, it is reliable and consistent. The air flow through the tower is a result of the difference in density between the hot and less dense air inside the tower compared to the relatively colder and more dense ambient air outside the tower. While the warm air rises through the tower, cool ambient air is drawn in through the inlets under the tower. Natural draft towers are widely used in power generation plants and in areas with higher relative humidity. These towers are much more expensive than other tower types and are notable for their hyperbolic shape.

Mechanical Air Draft Cooling Towers: Sometimes natural air-draft towers are equipped with fans to increase air flow and are called air-assisted natural air-draft towers or hybrid air-draft towers. Mechanical air-draft towers have one or more propellers used to move air through the tower and make them the preferred tower for most HVAC and process applications to provide predictable and consistent performance. It can be divided into two types as mechanical draft cooling towers, *forced flow towers* and *pressure towers*. If the fans are arranged to blow air to the tower, the tower is called *a forced-flow tower*. Thus, there is a positive pressure in the tower fill relative to the outside. In this case, the fans are usually located at the point where air enters the tower. If the fans are arranged to remove air from the tower, the tower is called an induced attraction tower. Therefore, there is a negative pressure in the tower fill relative to the outside. The fan is located at the point where the air leaves the tower.
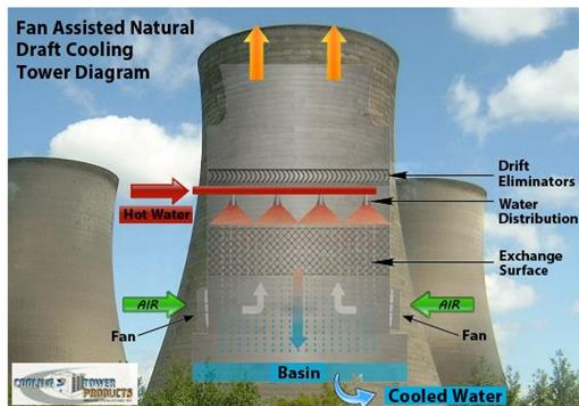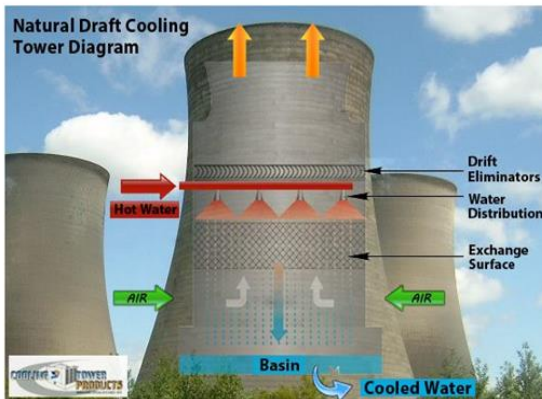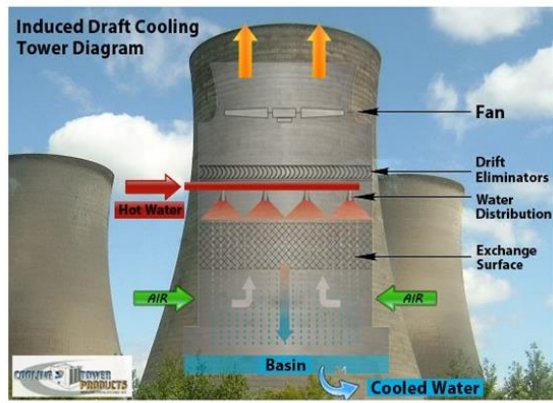
Fig. 6 Different type of cooling tower by air intake

❖ *Classification according to air flow pattern:*

In a cross-flow tower, the air flow direction is perpendicular to that of the water flow, namely the water flows vertically downward through the filling, while the air flows horizontally through the filling. In a counter-flow tower, the air flow direction is the opposite of the water flow, nameley, the water flows vertically downward through the filling, while the air flows vertically upward through it.

Fig. 7 Schematic view of Crossflow and Counterflow Cooling Towers

V. CONCLUSION

In this study, a lot of literature review has been made and the most important information has been given about the design and application of cooling towers. Cooling towers are cooling systems installed near power plants instead of mandatory power plants that have been established on the banks of the river or sea for a long time. Cooling towers are an evaporative cooling technique and prevent waste of water, environmental and energy saving systems. After understanding that cooling towers have many advantages, designers have expanded the range of applications of cooling towers by designing more efficient cooling towers where there are no large water sources. Therefore, in this study, a wide literature search has been done about the designs and application areas that affect the performance of cooling towers.

Acknowledgements

VI. REFERENCES

[1]   Zavaragh, H. G., Ceviz, M. A., Tabar, M. T. S. Analysis of windbreaker combinations on steam power plant natural draft dry cooling towers. Applied Thermal Engineering, 99, 550-559 (2016).

[2]   Khan, J.R., Yaqub, M., Zubaır, S.M. Performance characteristics of counter flow wet cooling towers, Energy Conversion and Management, (2003) 44:2073-91.

[3]   Li, X., Gurgenci, H., Guan, Z., Wang, X., Duniam, S. Measurements of crosswind influence on a natural draft dry cooling tower for a solar thermal power plant. Applied Energy, 206, 1169-1183 (2017).

[4]   Fisenko, S. P., Brin, A. A., Petruchik, A. I. Evaporative cooling of water in a mechanical draft cooling tower.

International Journal of Heat and Mass Transfer, (2004), 47(1), 165-177 (2004).

[5]   Soylemez, M. S., Theoretical and experimental analyses of cooling towers, ASHRAE Trans., (1999), 105:330-337.

[6]   Milosavljevic, N., Heikkilä, P. A comprehensive approach to cooling tower design. Applied Thermal Engineering, (2001), 21(9): 899-915.

[7]   Lemouarı, M., Boumaza, M., Mujtaba, I.M. Thermal performances investigation of a wet cooling tower, Applied Thermal Engineering, (2007), 27:902-909.

[8]   Jose, A.S., The use of thermo-fluid dynamic efficiency in cooling towers, Heat Transfer Eng., (2002), 23:22-30.

[9]   Naik, B. K., Muthukumar, P. A novel approach for performance assessment of mechanical draft wet cooling towers". Applied Thermal Engineering, (2017) 121: 14-26.

[10]   Cutillas C.G., Ramírez J.R., Miralles M.L. Optimum Design and Operation of an HVAC Cooling Tower for Energy and Water Conservation, Energies (2017), 10(299):1-27

[11]   Hill, G.B., Pring, E., and Osborn, P.D., Cooling Towers: Principles and Practice, Butterworth-Heinemann, (1990).

[12]   Stanford H.W. HVAC Water Chillers and Cooling Towers Fundamentals, Application,and Operation, NEW YORK, 2003.

Selection of a Sustainable Third-Party Reverse Logistics Provider Based on VIKOR

T. GEDIKLI[1] and B. CAYIR ERVURAL[1]

[1] Konya Food and Agriculture University, Konya/Turkey, tolga.gedikli@gidatarim.edu.tr
[1] Konya Food and Agriculture University, Konya/Turkey, beyzanur.ervural@gidatarim.edu.tr

Abstract – **Return of used products is becoming an important logistics activity to protect the environment and reduce waste products. For companies, the management of return flow often requires a special infrastructure. Since this infrastructure is an extra cost for the company, they are turning to third-party reverse logistics providers (3PRLP). However, the availability of more 3PRLPs makes it difficult to evaluating and selecting the most efficient 3PRLPs. The problem of 3PRLP selection is considered a multi-criteria decision making (MCDM) problem because the problem involves a number of difficulties, such as uncertainty and complexity. In this study, the VIKOR method, which is one of the MCDM methods, is used for the selection of the best 3PRLP. Finally, the application of the VIKOR method with a numerical example is performed.**

Keywords – **third-party reverse logistics, reverse logistics, multi-criteria decision making, VIKOR.**

I. INTRODUCTION

REVERSE logistics (RL) focuses on the backward flow of materials from the customer to the supplier in order to maximize the value gain from the returned product or to minimize the total RL cost [1]. RL is performed in many industries such as magazines, computers, plastics, mobile phones, books, steel, aircraft, electronics, automobiles, chemicals, and medical items [1], [2]. Customers demand solutions to defective products. The number of product returns can account for more than 50% of sales in some industries [1], [2].

An effective RL process can help organizations use energy resources efficiently and maintain a healthy balance between the environment and economy. RL has important environmental aspects as well as recovery-related dimensions [1], [2].

The main factor to consider for RL is whether a suitable third-party reverse logistics provider (3PRLPs) is available. Third-party logistics has become a significant player in RL. Because the implementation of return processes requires special information systems for monitoring / capturing data, special equipment for processing returns and a specialized infrastructure that requires trained specialists in standard production processes. Therefore, these companies outsource all or part of the RL process to 3PRLP [2].

The selection problem of the RL supplier may include various criteria and alternatives, the combination of different decision models and various uncertainties. For these reasons, it is difficult to evaluate and select a 3PRLP. Companies use various methods [3], [4] to cope with this challenge. Therefore, the most important issue in choosing and evaluating the right 3PRLP is to use an appropriate method [2].

When the literature is examined, it is seen that many multi-criteria decision making (MCDM) methods are used for 3PRLP selection. However, the most commonly used methods for the 3PRLP selection problem are Analytic Hierarchy Process (AHP), Analytic Network Process (ANP), and Technique for Order Preference by Similarity to Ideal Solution (TOPSIS). The motivation of this study is the application of Vise Kriterijumska Optimizacija Kompromisno Resenje (VIKOR) method in 3PRLP selection problem. In this study, the previous study with TOPSIS method is discussed. Using the same data, VIKOR method is applied and the results are compared.

The rest of the paper is organized as follows. In section II, the studies on 3PRLP are summarized. In section III, VIKOR methodology is described. In section IV, VIKOR methodology is implemented. Finally, possible research directions are presented in section V.

II. REVIEW OF LITERATURE ON THIRD-PARTY REVERSE LOGISTICS

RL first appeared in the 1990s. In the last two decades, RL has attracted both industrial applications and academic research [5].

Figure 1 graphically illustrates a fundamental flow diagram of RL activities [6].
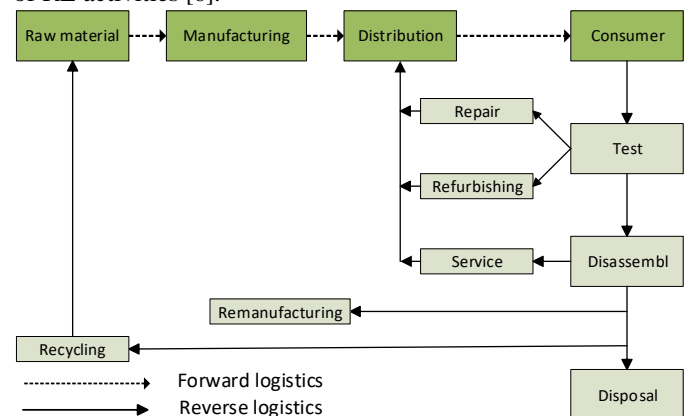
Figure 1: Fundamental flow diagram of RL activities [6].

Table 1: Literature review for RL

[5]	An integrated model based on ANP was proposed for the evaluation and prioritization of evaluation criteria and TOPSIS for the selection of RL providers.	Electronic industry
[7]	An integrated model based on fuzzy AHP was proposed for the prioritization of evaluation criteria and TOPSIS for the selection of RL providers.	Electronic industry
[8]	ANP method was used.	Composite pipe manufacturer
[2]	AHP method and fuzzy TOPSIS method were integrated. Then, a sensitivity analysis was performed for criterion weights.	Plastic recycling industry
[9]	3PRLP was selected and evaluated using the Data Envelopment Analysis (DEA) method.	Numerical Example
[1]	Interpretive Structural Modeling (ISM) and fuzzy TOPSIS methods were used.	Battery industry

Table 1 is shown some studies in the literature. The 3PRLP selection problem has been applied in many fields in the literature. Li et al. [5] and Prakash and Barua [7] in electronic industry, Tavana et al. in composite pipe manufacturer, Senthil, Srirangacharyulu, and Ramesh [2] in plastic recycling industry, Govindan et al. [10] in tire industry, Ravi [11] in computer company, Govindan and Murugesan [12] and Kannan, Pokharel, and Sasi Kumar [1] in battery industry, have chosen the 3PRLPs. Also, as a result of the literature research, the most commonly used methods in the selection of 3PRLP is found to be AHP [2], [7], ANP [5], [8], TOPSIS [7], DEA [9] and Mathematical Models [13], [14].

III. METHODOLOGY

A. VIKOR

The VIKOR method was first introduced by Serafim Opricovic in 1998 [15]. On the basis of the method, there is the creation of a conciliatory solution within the framework of alternatives and evaluation criteria. This conciliatory solution is the closest solution to the ideal solution. In the method, by creating a multi-criterion ranking index for alternatives made, the closest decision to the ideal solution under certain conditions is made. By comparing the proximity values to the ideal alternative, the conciliatory order is achieved [15], [16].

VIKOR algorithm has the following steps:

1. The best (fi^*) and worst (fi^-) values determined for each evaluation criterion. If the criteria i is a criterion in terms of "benefit", for $i = 1, 2, …, n$; fi^* and fi^- are expressed as follows. $fi^* = max_j f_{ij}, fi^- = min_j f_{ij}$

2. S_j and R_j are calculated for each alternative. w_i, represents the weight criteria.

$$S_j = \sum_{i=1}^{n} w_i(f_i^* - f_{ij})/(f_i^* - f_i^-) \qquad (1)$$

$$R_j = \max[w_i(f_i^* - f_{ij})/(f_i^* - f_i^-)] \qquad (2)$$

3. Q_j values are calculated for each alternative.
$$Q_j = v(S_j - S^*)/(S^- - S^*) + (1 - v)(R_j - R^*)/(R^- - R^*) \qquad (3)$$

where $S^* = min_j S_j$; $S^- = max_j S_j$; $R^* = min_j Rj$; $R^- = max_j R_j$ and v is introduced as the weight of strategy of "the majority of criteria" (or "the maximum group utility"), here v =0,5

4. Q_j, S_j, R_j values are sorted. The alternative with the smallest Q_j value is chosen as the best alternative.

5. Two conditions must be met for the result to be accepted as valid. Only the alternative with minimum Q value can be the best alternative.

• Condition 1 (C_1) – Acceptable advantage: It states that there is a significant difference between the best and the closest option.

$$Q(P_2) - Q(P_1) \geq D(Q) \qquad (4)$$

In this inequality, P_1 is the alternative with the smallest Q value, and P_2 is the second-best alternative. It is expressed as $D(Q) = 1 / (j - 1)$. j, indicates the number of alternatives. If the number of alternatives is less than four $D(Q) = 0.25$.

• Condition 2 (C_2) - Acceptable stability in decision making: The alternative P_1 with the best Q value should have achieved the best score in at least one of the S and R values.

If one of the two specified conditions cannot be met;

• If C_2 condition is not met, alternatives P_1 and P_2 are chosen as best alternative.

• If C_1 condition is not met P_1, P_2 , ……, P_m alternatives are chosen alternatives based on $Q(P_m) - Q(P_1) \geq D(Q)$ inequality [15].

IV. NUMERICAL EXAMPLE

The data set for this application is taken from Kannan, Pokharel, and Sasi Kumar [1]. Kannan, Pokharel, and Sasi Kumar applied their work to the problem of selecting 3PRLPs in a battery recycling industry in India. They used IMS and TOPSIS methods in this study [1].

A. Identifying the criteria

The seven evaluation criteria for the 3PRLP problem defined as follows [1], [2]:

• Quality (Q): It includes product performance, quality as well as 3PRLPs quality awareness, timeliness of service, inspection methods and ability to deal with problems.

• Delivery (D): It covers the ability of 3PRLP to meet delivery schedules.

• Reverse logistics cost (C): Refers to costs that may arise as a result of selecting 3PRLP. For example, transportation cost, inspection cost, packaging cost, stock cost etc.

• Rejection rate (R): Indicates whether it complies with quality specifications for the recycling process.

• Technical/engineering capability (T): Includes the technical and engineering infrastructure required for the job. For example, advanced equipment level, handling capability, availability of technical workforce, ability to perform RL function, etc.

• Inability to meet future requirement (I): It means whether the expected demand will be met.

• Willingness and attitude (W): It means the attitude and willingness of 3PPs to do business.

The hierarchical structure for the 3PRLP selection problem is shown in Figure 2.
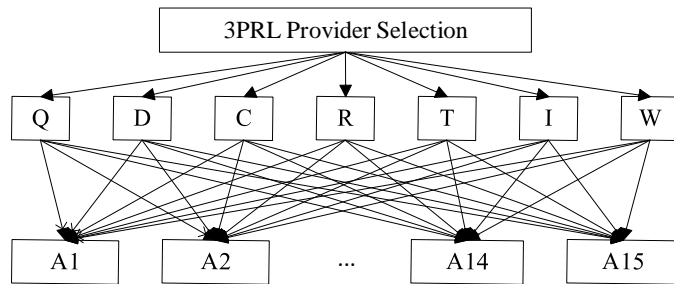
Figure 2: Hierarchical structure of decision problem

B. Identifying the alternatives

15 3PRLP alternative companies are selected for the problem. These are listed as A1, A2, A3, A4, A5, A6, A7, A8, A9, A10, A11, A12, A13, A14, A15.

C. Application of VIKOR

Criteria weights and alternative significance levels from five decision-maker opinions are aggregated with the arithmetic mean operator. Table 2 is shown the criterion weights aggregated with the arithmetic mean and Table 3 is shown the aggregated weight of the alternatives for each criterion.

Table 2: Normalized criteria weights

Criteria	Q	D	C	R	T	I	W
Weights of Criteria	0.160	0.168	0.184	0.136	0.128	0.088	0.136

Table 3: Weights of alternatives aggregated with arithmetic mean

Alternatives / Criteria	Q	D	C	R	T	I	W
A1	4.2	5.6	5.6	5.4	2	6	4.4
A2	1.6	1.6	4.8	4.8	5.6	5.8	3
A3	3	5.6	5.8	2.2	5.8	3.8	4.4
A4	5.8	3.8	2	6.4	6	6	2
A5	6.2	3.6	3.8	4.6	5.6	6	2
A6	2.2	3	4.4	1.6	4.8	2	2.8
A7	6	5.2	2.2	2	6	4.6	3
A8	4.6	2.4	5.4	4.8	5.6	6	5.6
A9	4.6	5	6	3.4	3.2	4.6	4.4
A10	5.4	5.2	5.4	6	4.8	3.4	5
A11	4.8	2	5.8	2.6	5.2	6.2	5.2
A12	4.6	4.2	5.8	4.8	2.2	5.4	5.6
A13	1.8	2.2	5.8	2	5	4.8	5.6
A14	6	5.6	3.6	4.4	5.8	5	6.4
A15	4.6	5.2	3.4	4.8	5.4	2.2	3

The best (fi^*) and worst (fi^-) values determined for each evaluation criterion are presented in Table 4. The weighted normalized matrix is shown in Table 5.

Table 4: Best (fi^*) and worst (fi^-) values

Criteria	Q	D	C	R	T	I	W
fi^*	6.2	5.6	6	6.4	6	6.2	6.4
fi^-	1.6	1.6	2	1.6	2	2	2

Table 5: The weighted normalized decision matrix

Alternatives / Criteria	Q	D	C	R	T	I	W
A1	0.07	0.00	0.02	0.03	0.13	0.00	0.06
A2	0.16	0.17	0.06	0.05	0.01	0.01	0.11
A3	0.11	0.00	0.01	0.12	0.01	0.05	0.06
A4	0.01	0.08	0.18	0.00	0.00	0.00	0.14
A5	0.00	0.08	0.10	0.05	0.01	0.00	0.14
A6	0.14	0.11	0.07	0.14	0.04	0.09	0.11
A7	0.01	0.02	0.17	0.12	0.00	0.03	0.11
A8	0.06	0.13	0.03	0.05	0.01	0.00	0.02
A9	0.06	0.03	0.00	0.09	0.09	0.03	0.06
A10	0.03	0.02	0.03	0.01	0.04	0.06	0.04
A11	0.05	0.15	0.01	0.11	0.03	0.00	0.04
A12	0.06	0.06	0.01	0.05	0.12	0.02	0.02
A13	0.15	0.14	0.01	0.12	0.03	0.03	0.02
A14	0.01	0.00	0.11	0.06	0.01	0.03	0.00
A15	0.06	0.02	0.12	0.05	0.02	0.08	0.11

Table 6: Results of VIKOR

Alternatives	S_j	R_j	Q_j
A1	0.310	0.128	0.368
A2	0.555	0.168	0.787
A3	0.358	0.119	0.383
A4	0.414	0.184	0.701
A5	0.389	0.136	0.484
A6	0.696	0.139	0.821
A7	0.462	0.175	0.716
A8	0.305	0.134	0.388
A9	0.351	0.090	0.258
A10	0.224	0.059	0.000
A11	0.379	0.151	0.534
A12	0.332	0.122	0.366
A13	0.516	0.153	0.686
A14	0.206	0.110	0.187
A15	0.445	0.120	0.478

According to Equations 1, 2 and 3, the S_j, R_j and Q_j values are calculated, and the obtained results are shown in Table 6. The S, R, and Q values are sorted from small to large (ascending order) and three ranking lists are created for the 3PRLPs. The order of alternatives is given in Table 7.

Table 7: Ranking by S_j, R_j ve Q_j values

Ranking	S_j	R_j	Q_j
1	A14	A10	A10
2	A10	A9	A14
3	A8	A14	A9
4	A1	A3	A12
5	A12	A15	A1
6	A9	A12	A3
7	A3	A1	A8
8	A11	A8	A15
9	A5	A5	A5
10	A4	A6	A11
11	A15	A11	A13
12	A7	A13	A4
13	A13	A2	A7
14	A2	A7	A2
15	A6	A4	A6

Condition 1 and condition 2 should be checked after the ranking is performed. According to the data in Table 7, the A8, A9, A10 and A11 3PRLPs have an acceptable advantage because they meet condition 1. In other words, $Q(P_2) - Q(P_1) \geq D(Q)$ equation is provided for these alternatives. On the other hand, condition 2 is provided for the A2, A5, A6 and A10 3PRLPs. 3PRLP A10 that provides condition 1 and condition 2 simultaneously. Therefore, the best 3PRLP is chosen as A10.

D. The Comparison

Table 8 shows the results of the paper of Kannan, Pokharel, and Sasi Kumar. Using the TOPSIS method, the best alternative A14 was chosen as the result of the study conducted by Kannan, Pokharel and Sasi Kumar [1]. In this study using the same data, A10 is chosen as the best alternative. According to the results of these two studies, there are small differences. Therefore, it may be advantageous for companies to use different methods in order to see a comparative and satisfactory result.

Table 8: Results of the paper of Kannan, Pokharel, and Sasi Kumar [1]

Rank	Alternatives
1	A14
2	A10
3	A8
4	A12
5	A1

6	A9
7	A4
8	A5
9	A11
10	A3
11	A15
12	A7
13	A2
14	A13
15	A6

V. CONCLUSION

The selection of 3PRLP is a hot topic surveyed by managers and researchers. Inappropriate selection of 3PRLP can create adverse situations for companies. For the 3PRLP selection and evaluation problem, one of the most important issues is the usage of the appropriate method. Because, as the number of 3PRLP increases, the selection becomes difficult. Each method can choose a different 3PRLP as the best alternative. Since each of the alternatives is subjective, it is difficult to control accuracy. Using a single method or the most commonly used methods may not always be accurate. Therefore, different methods should be used. In this study, the VIKOR method is proposed for 3PRLP selection. With the proposed method, the most suitable one among the fifteen alternatives is selected. In future studies, more MCDM methods can be used for 3PRLP selection. In addition, because uncertainty is high, better results can be achieved by integrating MCDM methods with fuzzy logic [4], [17].

REFERENCES

[1] G. Kannan, S. Pokharel, and P. Sasi Kumar, "A hybrid approach using ISM and fuzzy TOPSIS for the selection of reverse logistics provider," *Resour. Conserv. Recycl.*, vol. 54, no. 1, pp. 28–36, Nov. 2009.

[2] S. Senthil, B. Srirangacharyulu, and A. Ramesh, "A robust hybrid multi-criteria decision making methodology for contractor evaluation and selection in third-party reverse logistics," *Expert Syst. Appl.*, vol. 41, no. 1, pp. 50–58, Jan. 2014.

[3] T. Gedikli and B. Cayir Ervural, "Selection Optimum Maintenance Strategy Using Multi-Criteria Decision Making Approaches," in *Industrial Engineering in the Digital Disruption Era*, F. Calısır and O. Korhan, Eds. Springer, 2019.

[4] B. Cayir Ervural, S. Zaim, O. F. Demirel, Z. Aydin, and D. Delen, "An ANP and fuzzy TOPSIS-based SWOT analysis for Turkey's energy planning," *Renew. Sustain. Energy Rev.*, vol. 82, pp. 1538–1550, Feb. 2018.

[5] Y. Li, D. Kannan, K. Garg, S. Gupta, K. Gandhi, and P. C. Jha, "Business orientation policy and process analysis evaluation for establishing third party providers of reverse logistics services," *J. Clean. Prod.*, vol. 182, pp. 1033–1047, May 2018.

[6] S. K. Srivastava, "Network design for reverse logistics," *Omega*, vol. 36, no. 4, pp. 535–548, Aug. 2008.

[7] C. Prakash and M. K. Barua, "An analysis of integrated robust hybrid model for third-party reverse logistics partner selection under fuzzy environment," *Resour. Conserv. Recycl.*, vol. 108, pp. 63–81, Mar. 2016.

[8] M. Tavana, M. Zareinejad, F. J. Santos-Arteaga, and M. A. Kaviani, "A conceptual analytic network model for evaluating and selecting third-party reverse logistics providers," *Int. J. Adv. Manuf. Technol.*,

vol. 86, no. 5–8, pp. 1705–1721, Sep. 2016.

[9]   M. Azadi and R. F. Saen, "A new chance-constrained data envelopment analysis for selecting third-party reverse logistics providers in the existence of dual-role factors," *Expert Syst. Appl.*, vol. 38, no. 10, pp. 12231–12236, Sep. 2011.

[10]   K. Govindan, M. Palaniappan, Q. Zhu, and D. Kannan, "Analysis of third party reverse logistics provider using interpretive structural modeling," *Int. J. Prod. Econ.*, vol. 140, no. 1, pp. 204–211, Nov. 2012.

[11]   V. Ravi, "Selection of third-party reverse logistics providers for End-of-Life computers using TOPSIS-AHP based approach," *Int. J. Logist. Syst. Manag.*, vol. 11, no. 1, p. 24, 2012.

[12]   K. Govindan and P. Murugesan, "Selection of third-party reverse logistics provider using fuzzy extent analysis," *Benchmarking An Int. J.*, vol. 18, no. 1, pp. 149–167, Mar. 2011.

[13]   A. Ç. Suyabatmaz, F. T. Altekin, and G. Şahin, "Hybrid simulation-analytical modeling approaches for the reverse logistics network design of a third-party logistics provider," *Comput. Ind. Eng.*, vol. 70, pp. 74–89, Apr. 2014.

[14]   H. Min and H.-J. Ko, "The dynamic design of a reverse logistics network from the perspective of third-party logistics service providers," *Int. J. Prod. Econ.*, vol. 113, no. 1, pp. 176–192, May 2008.

[15]   S. Opricovic and G.-H. Tzeng, "Compromise solution by MCDM methods: A comparative analysis of VIKOR and TOPSIS," *Eur. J. Oper. Res.*, vol. 156, no. 2, pp. 445–455, Jul. 2004.

[16]   S. Opricovic and G.-H. Tzeng, "Extended VIKOR method in comparison with outranking methods," *Eur. J. Oper. Res.*, vol. 178, no. 2, pp. 514–529, Apr. 2007.

[17]   B. C. Ervural, B. Ervural, and Ö. Kabak, "Evaluation of Flexible Manufacturing Systems Using a Hesitant Group Decision Making Approach," *J. Intell. Syst.*, vol. 28, no. 2, pp. 245–258, Apr. 2019.

Evaluation of Wind-Solar Hybrid Renewable Energy Systems using Loss of Power Supply Probability

A. ECEMİŞ[1] and H. DEMOLLİ[2] and M. GÖKÇEK[3] and A. Ş. DOKUZ[4]

[1] Niğde Ömer Halisdemir University, Nigde/Turkey, ecemisalper@ohu.edu.tr
[2] University of Prishtina, Prishtina/Kosovo, halil.demolli@uni-pr.edu
[3] Niğde Ömer Halisdemir University, Nigde/Turkey mgokcek@ohu.edu.tr
[4] Niğde Ömer Halisdemir University, Nigde/Turkey, adokuz@ohu.edu.tr

Abstract – **Renewable energy sources are one of the most popular and strong alternative to conventional energy generation systems due to their availability at many locations, clean and cheap energy production capability, and relatively lower operating costs. Although renewable energy systems are more preferable than conventional ones, they have several weaknesses. One of the main weaknesses of renewable energy systems is that they could produce energy when the renewable source is present, i.e. wind speed or solar irradiation. In the literature, hybrid renewable energy systems are proposed to handle this weakness. In this study, we propose a method to determine hybrid potential of candidate locations in terms of hybrid energy generation capacity. Wind and solar energy systems are used as renewable energy sources, and several combinations of these systems are selected. The experimental evaluation of the selected systems are performed on two selected locations in Turkey with two different load demands. The experimental results show that one of the locations has better hybrid potential than other one in terms of wind-solar renewable energy system.**

Keywords – **Renewable energy, hybrid energy systems, wind-PV hybrid system.**

I. INTRODUCTION

WITH the availability at many locations in the earth, environmental friendly nature, lower operating costs, and recent successful applications, renewable energy sources are getting attention in energy production and consumption domains [1]. Also, renewable energy sources require no raw material for energy production other than naturally present sources, such as, wind speed and solar irradiation.

Renewable energy sources are a good alternative to conventional energy production systems. However, they could not produce energy for each time slices interval, and when the load demand of the power system requires constant energy generation, using only one renewable energy source is not sufficient [2]. In this case, two or more renewable energy sources can be used in hybrid manner to meet load demand of the energy systems.

However, there are several challenges that hybrid renewable energy sources encounter. First of all, renewable energy sources can produce energy when the renewable source is present, such

as wind speed, and solar irradiation. Second, installation costs are higher with respect to conventional energy sources. Third, every location has a different renewable energy characteristics and energy production capability, and finding renewable energy efficient locations are challenging. Finally, when hybrid renewable energy sources are used, the hybrid potential of the candidate locations could not be observed easily.

In the literature, there are several studies performed for optimal sizing and techno-economic analysis of hybrid energy systems. Some of these studies used optimization algorithms for hybrid sizing of the renewable sources, while some other studies consider using software tools. Among the literature studies, limited number of studies consider optimal location selection for hybrid renewable energy systems, and evaluating hybrid efficiency of different locations in terms of renewable energy sources.

In this study, we used a method for discovering hybrid energy potential of two selected locations in terms of wind and solar renewable energy sources. Three options for each renewable energy source is selected for comparison with each other, and also two load demand scenarios are applied on generated energy. The evaluation of renewable energy potential is performed using Loss of Power Supply Probability (LPSP) metric that is widely used in the literature for determining the performance of energy systems with respect to load demands.

The rest of this study is organized as follows. Section 2 presents the related works. Section 3 presents our method in this study. Section 4 presents the experimental evaluation of the method. Finally, Section 5 presents the conclusions.

II. RELATED WORK

The availability of renewable energy sources in all around the world and the potential for clean and cheaper energy production led researchers analyze and investigate hybrid energy potentials of different locations. For this purpose, many studies are conducted to discover wind, solar, hydrothermal, biomass, or other renewable energy source efficient locations. Also, another important study area for renewable energy domain is to discover hybrid energy efficient locations, that have more chance to produce energy with respect to only one energy source, such as wind, or solar.

In the literature several studies are performed for hybrid renewable energy systems. Yang et al. [3] proposed an optimal sizing method for solar-wind-battery hybrid system that uses genetic algorithm to achieve lower LPSP value. Belfkira et al. [4] proposed a deterministic optimization algorithm based optimal sizing methodology for wind-PV-diesel hybrid power generation systems. Xu et al. [5] designed a PV-wind-hydropower hybrid renewable energy system that use the flow of the river and store extra energy generated from wind and PV by pumping water from the lower reservoir to the upper one. In their experimental results, LCOE can be reduced as low as 0.091 $/kWh when LPSP value is set at 5%. Javed and Ma [6] proposed a sizing method for solar-wind-battery hybrid system based on cost of energy and system reliability and outlined that genetic algorithm is more efficient than HOMER in terms of economic sizing, optimization time, and system reliability. Wu et al. [7] proposed an optimal location selection method based on multi criteria decision making approach for wind-PV-seawater pumped storage plant in offshore areas. Spiru and Lizica-Simona [8] analyzed PV-wind-diesel hybrid power systems in terms of technical and economic aspects for a remote area. Mizani and Yazdani [9] Ngan and Tan [10], Ma et al. [11] and Sen et al. [12] used Hybrid Optimization Model for Electric Renewables (HOMER) software for optimal sizing of hybrid renewable energy systems.

In this study, we used wind and solar renewable energy sources for selected two locations and used three different sizing options for each energy source. Also, we added two different load demands for analyzing performances of proposed hybrid methods. We experimentally evaluate performances of two selected locations in terms of LPSP metric and concluded that one of the locations is more efficient and comparably better than other one in terms of wind-PV hybrid renewable energy systems.

III. Method

In this section, the proposed hybrid sizing method is presented. First, the renewable energy components of hybrid system are introduced, then the load demand is presented, and finally proposed hybrid method is presented. Figure 1 presents the method of this study.
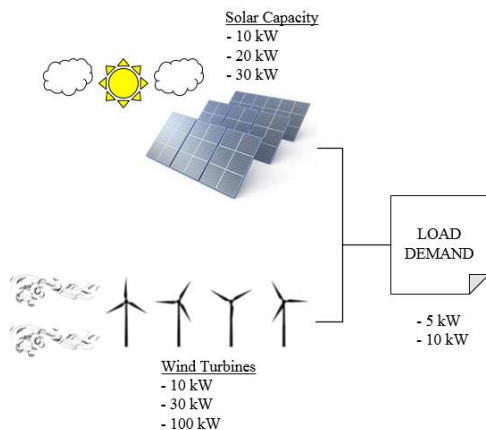
Figure 1: This caption is centered.

A. Renewable Components

In this study, wind and solar energy sources are used as renewable energy sources. For wind energy source, three different wind turbine is selected each of them have different energy production capability. As wind turbines BWC Excel (10 kW), Fuhrlaender FL 30 (30 kW), and Fuhrlaender FL 100 (100 kW) wind turbines are selected. Wind turbine power calculation was carried out using methodology in literature [13].

For solar energy source, three different sizes are selected each of them has different number of PV panels and have different energy production capability. As PV panel capabilities, 10 kW, 20 kW, and 30 kW configurations are selected. Solar energy power calculation was carried out using methodology in literature [14].

B. Load Demand

In this study, we used two different load demands, i.e. 5 kW and 10 kW, respectively. The load demands are constant for each hour of days for both of the demands. By using two different loads, we have the chance to monitor the hybrid potential for smaller and bigger loads.

C. Proposed Hybrid Method

For hybrid sizing of renewable energy sources, we used combinations of selected wind and solar energy capabilities and monitored if the produced energy meets load demands. Figure 2 presents proposed 9 different hybrid combinations of solar and wind energy sources.
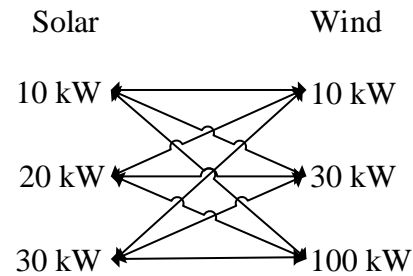
Figure 2: Proposed hybrid combinations of solar and wind energy.

For analyzing hybrid performance and potential of renewable energy sources, we used Loss of Power Supply Probability (LPSP) [15] metric. LPSP is calculated by using number of time slices that load demand could not be met by the energy sources divided by total number of time slices. The formulation of LPSP is provided in Eq. (1). In Eq. (1), produced power of each energy source is calculated, and addition of the time slices that the total energy production is smaller than the load demand, and finally the value is divided by 8760, which is hourly value of one-year period. As the LPSP value gets lower, the performance of the renewable energy source is seen better.

$$LPSP = \frac{\sum_{t=1}^{8760}(P_{pv}(t) + P_{wt}(t) < P_{Load})}{8760} \qquad (1)$$

Based on LPSP value, energy production potential of each renewable energy source is calculated using meteorological data and renewable component capabilities. After, for each load

demand and for each hybrid combinations, LPSP values are calculated for each time for two selected locations. Finally, the hybrid potentials of selected locations are discussed.

IV. Experimental Evaluation

In this section, experimental evaluation of hybrid renewable energy potential for two selected locations are performed. For both locations, solar, wind, and hybrid performances of selected components are evaluated. First, the dataset of this study is presented, and then experimental results are provided.

A. Dataset

The dataset in this study has meteorological parameters that are used for calculating solar and wind power with respect to given component configurations. Four parameters are present in the dataset, namely, time, solar irradiance, ambient temperature, and wind speed, for two selected locations, namely, Bozcaada, and Nigde. Figure 3 presents the selected locations in a map. The locations are presented with a red star in Figure 3.
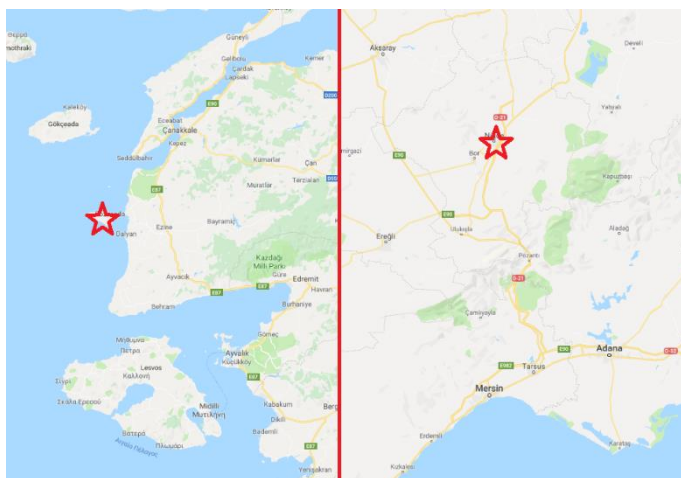
Figure 3: The selected locations for this study.

B. Experimental Results

In this section, the experimental results of this study is presented. Solar, wind, and hybrid potential of selected two locations are tested using LPSP metric. The experimental results of both locations are provided separately, and a discussion of results are presented.

1) Results for Nigde

The experimental results for Nigde are provided below. First, the LPSP results of solar and wind energy sources are provided in Figures 4 and 5, and then hybrid combinations of solar and wind energy sources are presented in Figure 6.
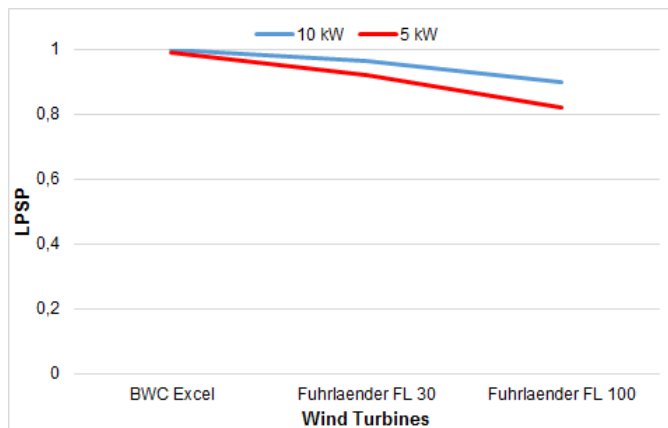
Figure 4: LPSP results of wind turbine components for Nigde.

As can be seen in Figure 4, the wind turbine performances are not good for Nigde, especially for 10 kW load demand. Their performances could reduce LPSP value to only 0.8 LPSP level for a 100 kW wind turbine and for 5 kW load demand. The best performance could be observed in Fuhrlaender 100 wind turbine because it has highest energy production capacity, as expected. Also, both load demands could not be supplied by wind turbines. Based on this result, we could infer that Nigde is not a suitable location for wind turbine installation.
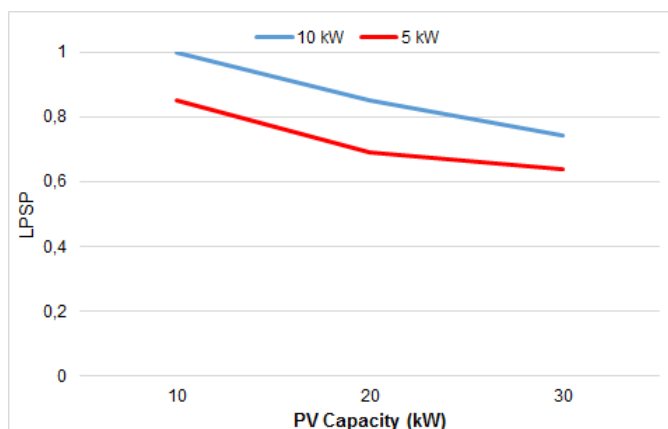
Figure 5: LPSP results of solar components for Nigde.

As can be seen in Figure 5, the solar performances are higher with respect to wind turbines in Nigde. As the solar capacity increases, the LPSP value could be reduced up to 0.6. 5 kW load demand could be supplied at more times than 10 kW load demand by the solar components. Based on this result, we could infer that Nigde has a potential for solar energy installation.
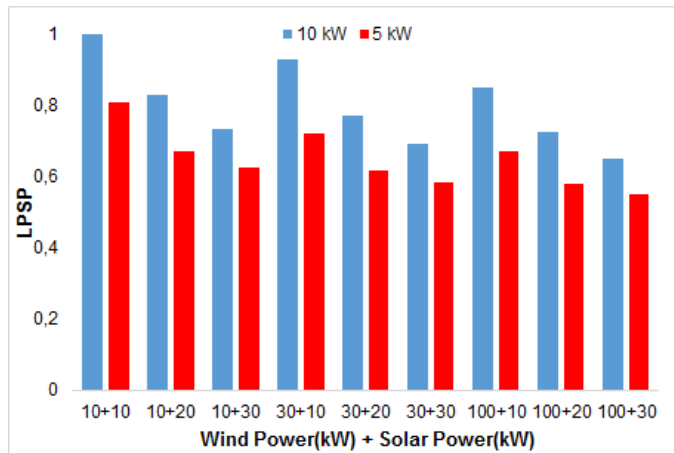
Figure 6: LPSP results of hybrid combinations for Nigde.

As can be seen in Figure 6, proposed hybrid combinations are observed for the load demands. As the component capacities increase, the LPSP value gets lower, as expected. The lowest LPSP value is observed for 100 kW wind and 30 kW solar energy combination, and the value is 0.65 and 0.55 for 10 kW, and 5 kW load demands, respectively. Based on hybrid combinations of wind and solar components, Nigde can be said to be a modest location for hybrid renewable energy installation.

2) Results for Bozcaada

The experimental results for Bozcaada are provided below. First, the LPSP results of solar and wind energy sources are given in Figures 7 and 8, and then hybrid combinations of solar and wind energy sources are presented in Figure 9.
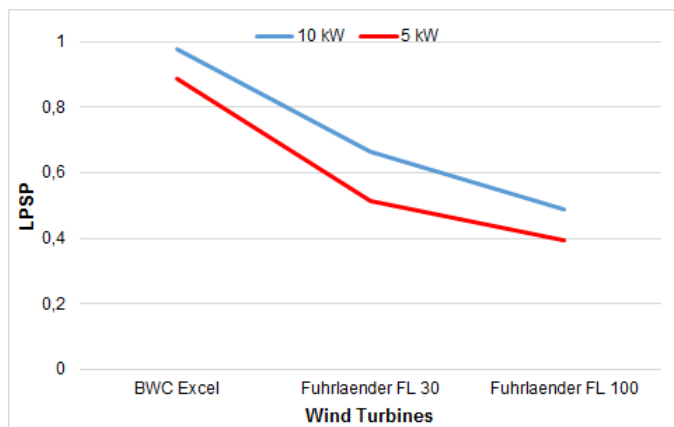
Figure 7: LPSP results of wind turbine components for Bozcaada.

As can be seen in Figure 7, LPSP values of selected wind turbines are efficient for Bozcaada. The highest performance is observed in 100 kW wind turbine, and the LPSP value is around 0.4 for 5 kW load demand, and around 0.5 for 10 kW load demand. Based on this result, we could infer that Bozcaada is a wind energy efficient location.
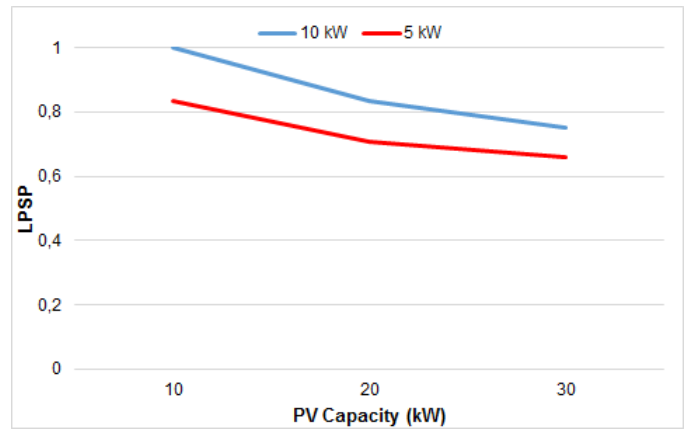
Figure 8: LPSP results of solar components for Bozcaada.

As can be seen in Figure 8, the performances of solar components are not good as wind components. Although, the results can be seen as modest for solar capacities. The LPSP value could be reduced up to 0.6 levels for 5 kW load demand, and 0.8 level for 10 kW load demand. Based on this result, Bozcaada can be seen as a modest location for solar energy installation.

As can be seen in Figure 9, the LPSP values of proposed hybrid components gets lower, and the performances of hybrid components gets more satisfying. The best hybrid performance is observed for 100 kW wind and 30 kW solar energy combination, and the LPSP values are 0.37 and 0.29, for 10 kW, and 5 kW load demands, respectively. Based on hybrid combinations of wind and solar energy sources, Bozcaada can be seen as an efficient location for hybrid renewable energy sources, because it could reduce LPSP value more than single renewable energy sources.
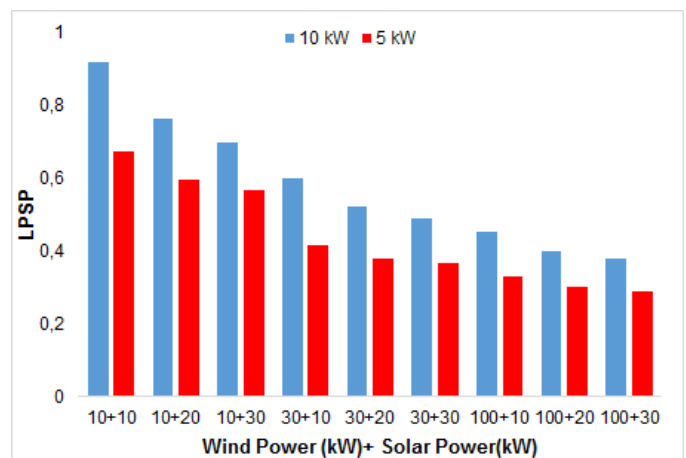
Figure 9: LPSP results of hybrid combinations for Bozcaada.

3) Discussion

In this section, the hybrid renewable energy performances of both locations are evaluated with respect to the experimental results. In terms of wind energy, the LPSP value of Bozcaada for 100 kW wind turbine and 10 kW load demand is around 0.5. The LPSP value of Nigde for 100 kW wind turbine and 10 kW load demand is around 0.9, which is much higher than Bozcaada. When the experimental results for Nigde and

Bozcaada are evaluated, Bozcaada is more efficient location for wind energy production.

In terms of solar energy, the LPSP value of Bozcaada for 30 kW solar capacity and 10 kW load demand is around 0.75. The LPSP value of Nigde for 30 kW solar capacity and 10 kW load demand is around 0.75 which is similar to Bozcaada. When these results are evaluated, both locations can be seen as modest locations for solar energy production.

In terms of hybrid energy, the LPSP value of Bozcaada for 100 kW wind turbine and 30 kW solar capacity, and 10 kW load demand is 0.37. The LPSP value of Nigde for 100 kW wind turbine and 30 kW solar capacity, and 10 kW load demand is 0.65. Based on this information, we could observe that Bozcaada is more hybrid efficient location than Nigde in terms of hybrid renewable energy production. Also, the higher performance for Bozcaada with respect to Nigde occurs because of wind efficiency of the location.

V. CONCLUSION

Renewable energy sources are one of the most popular and strong alternative to conventional energy generation systems due to their availability at many locations, clean and cheap energy production capability, and relatively lower operating costs. Hybrid renewable energy sources play an important role in generating energy at remote locations. However, hybrid renewable energy sources are not practical for every location due to the dependency of renewable energy sources, higher initial investment costs, and difficulty on discovering hybrid potential of candidate locations.

In this study, we focused on developing a hybrid renewable energy system using wind and solar energy sources. For this purpose, Bozcaada and Nigde regions are used as candidate locations and 9 different combinations have been examined for the hybrid system to be installed. Furthermore, the analysis of hybrid system was carried out in two different load demands of 5 kW and 10 kW. The best LPSP value is obtained from a hybrid renewable energy system that used 100 kW wind turbine and 30 kW solar PV panels in two regions and for two load demands. In addition, Bozcaada has the best performance of LPSP in terms of hybrid renewable energy potential, because it has more efficient wind energy potential than Nigde.

ACKNOWLEDGMENT

REFERENCES

[1] H. A. Kazem, J. H. Yousif, and C. Miqdam T., "Modeling of Daily Solar Energy System Prediction using Soft Computing Methods for Oman," *Res. J. Appl. Sci. Eng. Technol.*, vol. 13, no. 3, pp. 237–244, 2016.

[2] L. Bird, M. Milligan, D. Lew, Integrating Variable Renewable Energy : Challenges and Solutions," *Natl. Renew. Energy Lab.*, 2013.

[3] H. Yang, W. Zhou, L. Lu, and Z. Fang, "Optimal sizing method for stand-alone hybrid solar – wind system with LPSP technology by using genetic algorithm," vol. 82, pp. 354–367, 2008.

[4] R. Belfkira, L. Zhang, and G. Barakat, "Optimal sizing study of hybrid wind / PV / diesel power generation unit," *Sol. Energy*, vol. 85, no. 1, pp. 100–110, 2011.

[5] X. Xiao, H. Weihao, C. Di, H. Qi, C. Cong, and C. Zhe, "Optimized Sizing of a Standalone PV-wind-hydropower Station with Pumped-storage Installation Hybrid Energy System," *Renew. Energy*, 2019.

[6] M. S. Javed and T. Ma, "Techno-economic assessment of a hybrid solar-wind-battery system with genetic algorithm," *Energy Procedia*, vol. 158, pp. 6384–6392, 2019.

[7] W. Yunna, Z. Ting, X. Chuanbo, Z. Buyuan, Y. Lingwenying, LicYimingKeYudong, and X. Ruhang, "Optimal location selection for offshore wind-PV-seawater pumped storage power plant using a hybrid MCDM approach: A two-stage framework," *Energy Convers. Manag.*, vol. 199, 2019.

[8] P. Spiru and P. Lizica-simona, "Technical and economical analysis of a PV/wind/diesel hybrid power system for a remote area" *Energy Procedia*, vol. 147, pp. 343–350, 2018.

[9] S. Mizani and S. Member, "Design and Operation of a Remote Microgrid," *2009 35th Annu. Conf. IEEE Ind. Electron.*, no. 2, pp. 4299–4304, 2009.

[10] M. S. Ngan and C. W. Tan, "Assessment of economic viability for PV / wind / diesel hybrid energy system in southern Peninsular Malaysia," *Renew. Sustain. Energy Rev.*, vol. 16, no. 1, pp. 634–647, 2012.

[11] T. Ma, H. Yang, and L. Lu, "A feasibility study of a stand-alone hybrid solar – wind – battery system for a remote island," *Appl. Energy*, vol. 121, pp. 149–158, 2014.

[12] R. Sen and S. C. Bhattacharyya, "Off-grid electricity generation with renewable energy technologies in India : An application of HOMER," *Renew. Energy*, vol. 62, pp. 388–398, 2014.

[13] H. Demolli, A. S. Dokuz, A. Ecemis, and M. Gokcek, "Wind power forecasting based on daily wind speed data using machine learning algorithms," *Energy Convers. Manag.*, vol. 198, no. March, p. 111823, 2019.

[14] M. S. Javed, A. Song, and T. Ma, "Techno-economic assessment of a stand-alone hybrid solar-wind-battery system for a remote island using genetic algorithm," *Energy*, vol. 176, pp. 704–717, 2019.

[15] D. Abbes, A. Martinez, and G. Champenois, "Life cycle cost , embodied energy and loss of power supply probability for the optimal design of hybrid power systems," *Math. Comput. Simul.*, 2013.

Vibration Fatigue Analyses of a Cantilever Beam in Transportation Based on Military Standard

Mehmet Sefa GUMUS[1], Muhammed Arif SEN[2], Mete KALYONCU[3]

[1]Konya Technical University, Konya/Turkey, msgumus@ktun.edu.tr
[2]Konya Technical University, Konya/Turkey, masen@ktun.edu.tr
[3]Konya Technical University, Konya/Turkey, mkalyoncu@ktun.edu.tr

Abstract – **This study includes the vibration fatigue analyses of a cantilever beam exposed random vibration while transporting based on the specified military standard using Miner's Cumulative Damage technique. The theory of Miner is introduced in detail. Finite element model is used to obtain the stresses on the designed cantilever beam under random vibration. Response Power Spectral Density is presented in graphical form at critical points. The fatigue life of the cantilever beam is calculated by using the stresses obtained by random vibration analysis.**

Keywords – **Miner's Cumulative Damage, Vibration Fatigue, Military Standard, Power Spectral Density.**

I. INTRODUCTION

Predicting the accurate fatigue life of designed parts within the shortest time is rising in importance every passing day because fatigue tests bring extended period of time and high costs. In periodic vibration environment, signal can be defined in time domain because the loads are cyclic. It is easy to find the amplitudes in certain time. The repetition of loads and resultant stresses could be determined thanks to the order of periodic loads. However, designed parts are mostly exposed to random vibrations in nature. In this type of vibration environments, calculating stress values and repetitions is not possible if we want to predict the fatigue life of a part in a short time.

It is not easy to define random vibrations in time domain. There is a lot of overlapping sinusoidal waves repeating different frequencies. As a consequence of this characteristic of random vibrations, frequency domain data is used to define the random vibration. In frequency domain, the vibration amplitudes can be seen for certain frequency but it is still very difficult to determine the maximum stress values, instantaneous stresses on certain locations, and repetitions of peaks in certain time intervals. In order to encounter this disorder coming from random vibration environments, analyses is carried out by using some statistical approaches or the spectral moments of the power spectral density.

In this area, there are several complicated techniques and study to predict the fatigue life faster and more accurate [1]. One of the basic techniques developed by Bendat is *Narrow-Band* which is not capable of predicting life in broad-band

vibration environment [2]. There are lots of different approaches developed by improving *Narrow-Band* technique to predict life in broad-band excitations such as *Wirching* [3], *Tunna* [4], *Hancock* [5], *Kam and Dover* [6] and *Dirlik* [7]. In addition to these techniques, Steinberg [8] developed a time saving method to predict life in shorter time using Three-Band technique based on Gaussian distribution. The Three-Band Technique Gaussian probability distribution is used with *Miner's Cumulative Damage* technique [9] in this study to get result in shorter time In order to obtain more realistic results, rather than using white noise, the standard real road data set [10] is used while transporting military equipment on a highway. First, the modal analysis is done for the cantilever beam. Then, random vibration analysis is carried out to obtain 1-σ, 2-σ and 3-σ stresses. RPSD (Response Power Spectral Density) graph is obtained on the critical point. The number of cycles that cause the failure for 1-σ, 2-σ and 3-σ stresses from S-N diagram. After that, Miner's Cumulative Damage technique is used to predict the life of the cantilever beam under defined random vibration.

In the following sections, firstly, the Miner's theory of fatigue life for a cantilever beam is introduced in Section II. In Section III., the specimen is designed, the PSD (Power Spectral Density) data of the random vibration for military equipment is given, the analysis is performed and the calculation of fatigue life is carried out. Finally, the study is concluded in Section IV.

II. THEORY OF FATIGUE LIFE

According to the Miner's Technique, the modal analysis is performed first on the part subjected to vibration. It is modeled and analyzed by entering the material properties using finite elements considering the data in the PSD graph. 1- σ stress is observed after this analysis. Afterwards, 2-σ and 3-σ values are determined according to Gaussian probability distribution. The probability of occurrence of these amplitudes is shown on Table 1.

After this analysis, RPSD graph can be obtained at the point where maximum stress is observed on the part. The maximum amplitudes on this graph are expected to coincide with the natural frequencies of the part. Miner's Total Damage Ratio can be calculated by using 3-band technique.

Next step is the determination of the number of cycles that cause damage according to 1-σ, 2-σ and 3-σ stresses. S-N graph [9] is used in fatigue analysis to determine the number of cycles needed to fail. When determining the slope of S-N graph, the stress concentration factor should be determined. The slope of the graph is revised according to the stress concentration factor. The S-N Graph for Aluminum (*Al6061-T6)* is given Figure 2.

Table 1: Occurrence of Stresses

Standard Deviation	1-σ	2-σ	3-σ
Percentage of Occurrence [%]	68.3	27.1	4.33
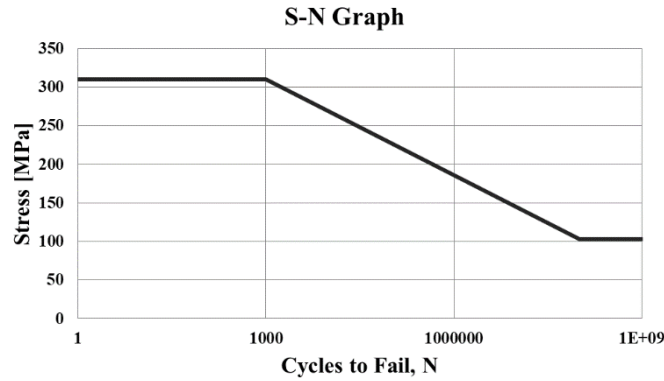
Figure 1: S-N Graph.

The number of cycles that cause failure for 3-band stresses could be calculated using the Eq.1 where; N_1, number of cycles to failure, S_1, 3-band stresses, N_2, ref. point, S_2, stress at ref. point. The total damage in a certain period *"t"* can be shown as Eq. 2 where; n is the stress cycle which is experienced, N is the life under the certain stress. The number of repetitions for 1-σ, 2-σ and 3-σ stresses in the time *"t"* is calculated separately by using Eq.3 where; f is the frequency value corresponding to the maximum stress which is observed in the RPSD graph.

$$N_1 = N_2 \cdot \left(\frac{S_2}{S_1}\right)^b \tag{1}$$

$$E[D] = \sum \frac{n}{N} = \frac{n_{1\sigma}}{N_{1\sigma}} + \frac{n_{2\sigma}}{N_{2\sigma}} + \frac{n_{3\sigma}}{N_{3\sigma}} \tag{2}$$

$$1\sigma \rightarrow f_n\left(\frac{cyc}{sec}\right) * t(hr) * 3600\left(\frac{sec}{hr}\right) * 0.683 = n_{1\sigma}$$

$$2\sigma \rightarrow f_n\left(\frac{cyc}{sec}\right) * t(hr) * 3600\left(\frac{sec}{hr}\right) * 0.271 = n_{1\sigma} \tag{3}$$

$$3\sigma \rightarrow f_n\left(\frac{cyc}{sec}\right) * t(hr) * 3600\left(\frac{sec}{hr}\right) * 0.043 = n_{1\sigma}$$

$$E[D] = \frac{n_{1\sigma}}{N_{1\sigma}} + \frac{n_{2\sigma}}{N_{2\sigma}} + \frac{n_{3\sigma}}{N_{3\sigma}} = 1 \tag{4}$$

The fatigue life of the beam *"t"* under defined vibration can be calculated by equalizing the total damage to 1 as Eq.4.

III. RANDOM VIBRATION ANALYSIS

The dimensions of the specimen are given in Figure 2. The material of the specimen is *Al6061-T6* (E=68.9GPa, γ=0.3, thickness: 2.5mm).
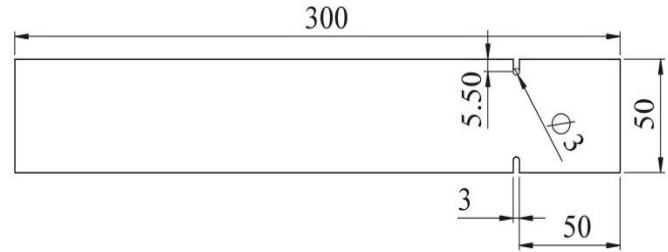
Figure 2: Dimensions of the Specimen.

As a first step, 3D model is constructed and the modal analysis of specimen is carried out in *Ansys.* Observed natural frequencies of the specimen are given in Table 2.

Table 2: Natural frequencies of the specimen

Modes	1	2	3	4	5	6
Frequencies [Hz]	22.6	143.9	267.9	405.2	407.6	797.0

The PSD input which is taken from *USA Department of Defense Test Method Standard (MIL-STD-810G)* are defined by Table 3. PSD input diagram is shown in Figure 3.

Table 3: PSD Data [10]

Vertical		Transverse		Longitudinal	
Frequency [Hz]	PSD [g²/Hz]	Frequency [Hz]	PSD [g²/Hz]	Frequency [Hz]	PSD [g²/Hz]
10	0.01500	10	0.00013	10	0.00650
40	0.01500	20	0.00065	20	0.00650
500	0.00015	30	0.00065	120	0.00020
		78	0.00002	121	0.00300
		79	0.00019	200	0.00300
		120	0.00019	240	0.00150
rms = 1.04 [g]		500	0.00001	340	0.00003
				500	0.00015
		rms = 0.20 [g]		rms = 0.74 [g]	
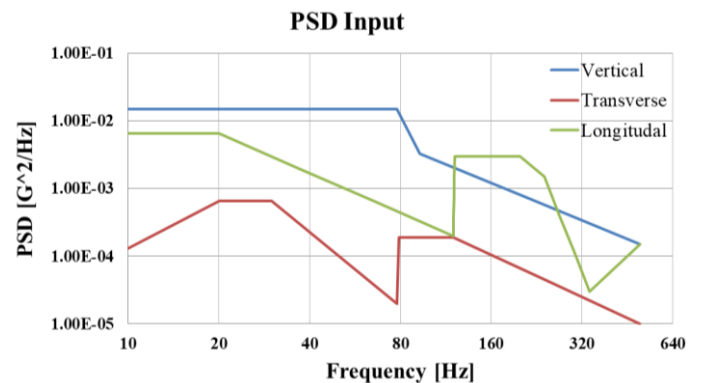
Figure 3: PSD Input.
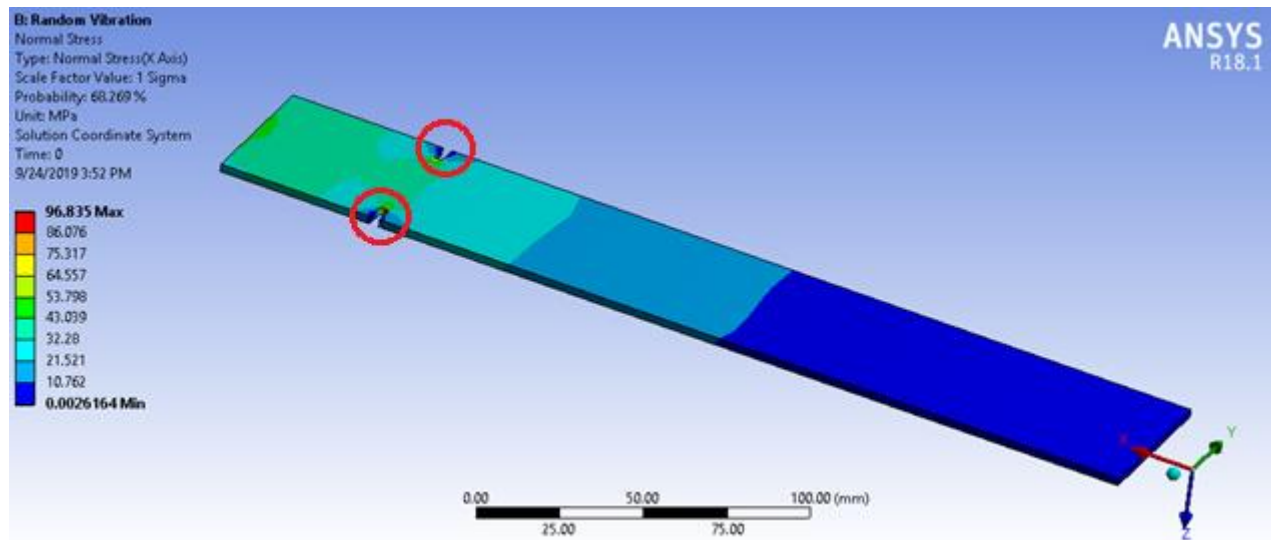
Figure 4: Screen Shot from Random Vibration Analysis using Ansys

The random vibration analysis is carried out in *Ansys* after defining PSD Inputs. Results are shown on Figure 4. Maximum stresses are occurred on notches (red circles) as expected. According to Gaussian probability distribution, 1-σ, 2-σ and 3-σ stresses are determined as shown on Table 4.

Table 4: Random Vibration Analysis Results

Standard Deviation	1-σ	2-σ	3-σ
Bending Stress [MPa]	96.84	193.68	290.49

The number of cycles that cause the failure is obtained by using $S_{1-\sigma}$=96.84 [MPa], $S_{2-\sigma}$=193.68 [MPa], $S_{3-\sigma}$=290.49 [MPa] separately according to Eq.1 as follows; $N_{1-\sigma}$=1,91.10^8, $N_{2-\sigma}$= 1,36.10^5, $N_{3-\sigma}$=1,97.10^3.

After random vibration analysis, RPSD graph is obtained at the point where maximum stress is observed on the part. The maximum amplitudes on this graph are coincident with the first natural frequency at 22.6 [Hz]. RPSD graph is shown on Figure 5.
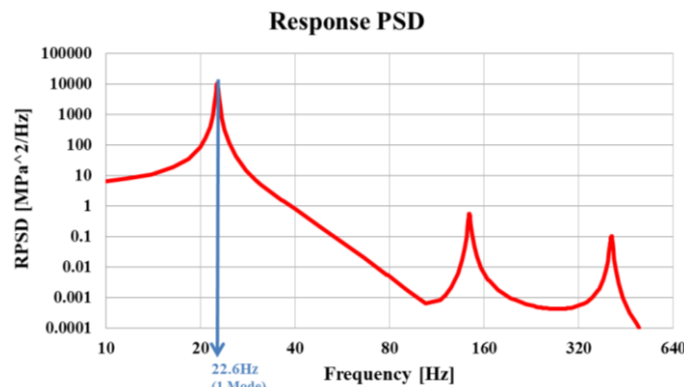
Figure 5: Response PSD at Critical Point

Consequently, by equalizing the cumulative damage ratio to one, vibration fatigue life of the cantilever beam is calculated as *1,846.10^3 seconds (30.77 minutes)* according to Miner's theory under the vibration based on specified military standards.

IV. CONCLUSION

In the paper, the vibration fatigue life of a cantilever beam is calculated while transporting according to military standard by using Miner's Cumulative Damage method. It is understood that Miner's Theory is a time saving method to analyze the fatigue life. The paper could contribute to next studies about vibration fatigue life.

REFERENCES

[1] N. W. M. Bishop and F. Sherratt, "Finite Element Based Fatigue Calculations," NAFEMS, Germany, 2005.

[2] J. S. Bendat, "Probability functions for random responses", *NASA report on contract NAS-5-4590*, Technical Report (ID 19640008076), 1964.

[3] P. H. Wirsching, M. C. Light, "Fatigue under wide band random loading*", Journal of Structural Division*, ASCE (American Society of Civil Engineers), vol. 106, pp. 1593–1607, 1980.

[4] J. M. Tunna, "Fatigue Life Prediction for Gaussian Random Loads at the Design Stage," *Fatigue Fact Engineering Mat. Struct*, vol. 9, no. 3, pp. 169–184, 1986.

[5] J. C. P. Kam, and W. D. Dover, "Fast Fatigue Assessment Procedure for Offshore Structures under Random Stress History", *Proceedings of the Institution of Civil Engineers*, vol. 85, part 2, pp. 689–700, 1988.

[6] G. K. Chaudhury and W. D. Dover, "Fatigue analysis of offshore platforms subject to sea wave loading," *International Journal of Fatigue*, vol. 1, no. 1, pp. 13–19, 1985.

[7] T. Dirlik, "Application of computers in Fatigue Analysis,", Ph.D. dissertation, Dept. Computer-Aided Eng., University of Warwick. 1985.

[8] D. S. Steinberg, "Vibration Analysis for Electronic Equipment", John Wiley & Sons, 3rd edition, USA, 2000.

[9] Kumar, S. M. "Analyzing random vibration fatigue", ANSYS Advantage 2.3, pp. 39-42, 2008.

[10] *MIL-STD-810G*, Department of Defense Test Standard for Environmental Engineering Considerations and Laboratory Tests, Washington, D.C., See Method 514.6 Annex C, 2008.

PARALLEL DISASSEMBLY LINES WITH SOME CONSIDERATIONS

Seda Hezer[1*] and Yakup Kara[1]

[1] Konya Technical University, Konya/Turkey, shezer@ktun.edu.tr

[1] Konya Technical University, Konya/Turkey, ykara@ktun.edu.tr

ABSTRACT

Disassembly is the crucial process of the product recovery operations and it can be defined as removing the parts of the discarded products through a series of operations. A disassembly line contains sequential workstations with a material handling system. Disassembly line balancig problem (DLBP) is defined as assigning the tasks to the workstations to minimize the number of workstations and to utilize the available resources as efficiently as possible while meeting the demand for recovered parts. More than one parallel disassembly lines are balanced simultanously to increase the efficiency and effectiveness. Balancing problem of these lines is called Parallel Disassembly Line Balancing Problem. There are some considerations which complicate the disassembly. Negative effects of these considerations can be reduced by considering parallel disassembly lines. In this study, these considerations and PDLBP is simply defined and discussed and future directions are proposed.

Keywords: Disassembly, Disassembly line balancing problem, Disassembly actions, Parallel disassembly line balancing problem

I. INTRODUCTION

Product recovery is growing in importance due to regulations about environment, augmented cost of landfills, consumer awareness for saving resources. It provides minimising the amount of waste sent to landfills. Disassembly is the main step of the recovery activities [1]. It decomposes a returned product or subassembly into two or more subassemblies and/or parts using systematic methods [2, 3]. Disassembly is ususaly performed on disassembly line to provide the highest productivity. A disassembly line consists of workstations which are arranged along a material handling belt. Disassembly lines should be designed effectively for the efficient operations. However, many problems arise over disassembly lines to design. Balancing of disassembly lines is one of the most important problem among these problems [4]. This problem is called Disassembly Line Balancing Problem (DLBP) which is assigning tasks (disassembly tasks) to successive workstations by satisfying some constraints and optimizing a performance measure like minimisation of total workstations or line cost or maximisation of total profit of the line [5].

Disassembly lines can be categorized as simple straight and U-shaped by means of the line shape and single model and multi/mixed model with regard to the number of products disassembled on the line.

The simplest version of DLBP (single product and straight layout) was first studied by [5, 6] and has been studied by many researchers to date such as [3, 7-26]. For an overview of disassembly, product recovery and DLBP, see [27-31].

The majority of the DLBP (approximately 96%) focused on the straight line type [30]. In straight disassembly line, products are disassembled on a straight line that has an ordered sequence of workstations. An operator works on each workstation within the same cycle time [9, 32]. But in some cases, the capacity of a straight line is not sufficient due to high demand of the parts. Therefore, it is highly desirable to increase capacity in order to meet the part demand. One of the ways to do this is balancing the several parallel lines simultaneously [33]. Parallel assembly line balancing problem was first introduced by [34]. Since the original study of [34], many other references have developed different approaches [35-43] to solve the problem. Reference [44] presents a literature review on parallel assembly lines.

In disassembly literature, only one study [33] considered parallel diassembly line balancing problem (PDLBP). In parallel lines, two or more lines are balanced simultaneously with common resources. This paper deals with some special considerations related to the disassembly actions. Our main purpose in this paper is to discuss these actions and its considerations in terms of parallel lines. Also, we aim to provide a different point of view for interested researchers for DLBP.

The remainder of the paper is structured as follows: Section 2 presents PDLBP. Disassembly actions are explained in Section 3. Finally, some concluding remarks and opportunities for further research are presented.

II. PARALLEL DISASSEMBLY LINE BALANCING

Balancing problem of more than one parallel disassembly line is PDLBP. The objective of the PDLBP is assigning disassembly tasks to workstations to find the minimum number of workstations while satisfying the precedence relations among the tasks and the cycle time constraints [33, 34].

There are many advantages of balancing of parallel lines simultaneously by considering the resource (e.g. equipments, assistants, workers etc.) requirements. These advantages are summarized as follows [33, 40]:

- It can provide to disassemble similar products or different types of the same product on adjacent lines,
- It can reduce the idle time and so, increase the efficiency of the disassembly lines,

- It can improve visibility and communication skills between operators,
- It can reduce resource requirements.
- In cases where the disassembly line stops or break down due to uncertainties specific to the disassembly process, the disassembly task may continue in the parallel line, which allows for preventing setbacks of any kind and avoiding situations where facility can not meet demands.

In Figure 1, a parallel disassembly line is given. It consists of simultaneously balanced two parallel disassembly lines.
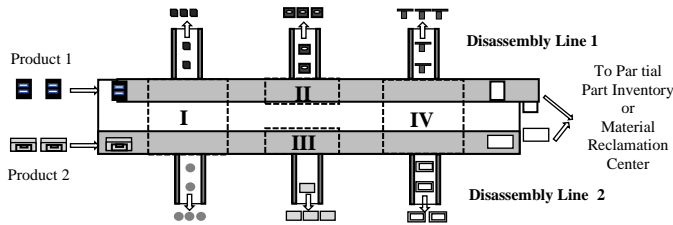
Figure 1: An example of the parallel disassembly line layout

Figure 1 shows a recovery facility that consists of two parallel lines and four workstations. The workstations I and IV are 'common' workstations. Operators first perform the tasks on line 1 then walk to line 2 and finally return to line 1 at the end of the cycle (Hezer and Kara 2015).

III. SPECIAL CONSIDERATIONS ABOUT DISASSEMBLY ACTIONS

A part or multiple parts of the product is disassembled through specific disassembly actions at each step of the disassembly process. These actions are categorized as unfastening and destructive actions. *Unfastening action (UA)* involves removing fasteners and breaking off connections. It is possible to cause damage on fasteners by the UA. This action is performed with or without using various equipments. A list of these equipments are given in Table 1 [45].

Table 1: List of equipments of UA

Standart list of UA equipments	
None	Chisel
Powered screw driver	Shear cutter/Scissors
Manual screw driver	Hammer
Wrench	Tie rod/Lever
Spanner	Pins
Pliers	Hacksaw
Ring pliers	

Destructive action (*DA*), on the other hand, results in breaking the product into parts. DA is applied to fasteners and/or parts. For this reason, it may damage the both fasteners and parts. DA have generally different equipments and processes unlike UA. It has many desructive processes according to the proporties of the fasteners. Table 2 provides these processes [45].

Table 2: List of destructive processes

Standart list of DA processes	
Axial pulling	Crushing and bending
Levered pulling	Chemical dissolution
Hammering	Shredding
Adhesive separation	Impact breakage
Shearing cut	Suction and drainage
Saw cutting	Paint removal
Flame cutting	

There are two significant factors that influence the performance of both actions and needs to be taken into account: *fasteners* which allows for joining parts and the *fastening structure* between parts.

Fasteners are components which provide the connection between the parts. They can be discrete components such as screw, nail, and pin or nondiscrete components such as snap-fits or virtual components such as welding and soldering [29]. A list of fastener types which are generally used to connect the parts from disassembly perspective is given in Table 3 [45].

Table 3: Fastener types which are generally used

Fastener Types	
Nail with head	Welded
Nail w/o head or Pin	Velcro/Zipper
Screw/Bolt standart head	Releasable clips
Screw/Bolt speciality head	Cyclindirical snapfit
Nut and Bolt	Cantilever snapfit
Rivets/Staples	Seam/Crimp joint
Retaining rings/Circlips	Interference fit
Tape	Integrally threaded part
Adhesive	Socket and plug

Each fastener type given in Table 3 has the relative unfastening difficulty rate which describes the disassembly effort associated with unfastening action and each destructive process given in Table 2 has the relative disassembly effort rate [45, 46, 47]. Both of two rates affect the disassembly time of removal of fasteners and performance of the disassembly system.

Fastening structure is related with how two or more parts are connected to each other using fasteners. According to the study of [45], for any pair of mating parts three possible mating relationships are identified as follows:

Type 1 mating is defined that parts are connected with separate fasteners. In Type 2 mating, parts are connected with fasteners integral to one of the parts. Finally, if parts are mating but there is not direct fastening involved, this mating is called as Type 3 mating. *Fastening structure* is described with two important parameters, *access difficulty* and *accessibility*, which affect the efficiency and profitability of disassembly. Access difficulty is the degree to which we can reach the starting point of the fastener. It is related with position of the fastener relative to the part. The closer the fastener is located on the surface of the part, the easier it is accesible and removed. For this situation UA is generally performed for this

fastener. When feasible access to the fastener is not available, a destructive process must be used [45, 46].

A disassembly task may be carried out with unfastening only, with destructive action only, or alternatively with both depending on properties of fasteners and the fastening structure. Each action presents alternative options depending on whether equipments are used or the type of equipment to be used. For example, if a screw is located on the surface of the part and it is not damaged, it can be disassembled with manual or powered screw driver. Disassembly with both equipments are unfastening actions. However, if it is stucks to the part, it needs desructive processes such as saw cutting or flame cutting. For this situation each process is a DA.

In such cases, different process alternatives (source combinations) may emerge depending on the task and the type of equipments[48]. The task time, the revenue from parts, and the equipment cost for a task with more than one process alternative vary depending on these alternatives. For example, if the part is removed using the UA, a higher revenue is obtained compared to the DA. This is because the unfastening action is applied to the fastener instead of the part, therefore the part is not damaged.Comparing both actions in terms of task time, we can say that the DA takes less time. Although it is wrong to compare two actions in terms of equipment cost, it is possible to say that the cost of equipments used to apply UA is usually higher [46].

According to the information above, disassembly actions are inevitable processes for disassembly of the products and for efficient disassembly, for each disassembly task it is necessary to choose one process alternative which provides the best return with respect to revenue, time and cost parameters. However, disassembly should be performed if it is profitable due to the high costs of workers, equipment and similar resources required for disassembly. For this reason, the layout of the line should be designed considering the cost, time and revenue parameters. Design becomes even more important particularly in recycling plants where multiple lines are used. In this case two individual lines can be used. However, the costs will also increase due to the increase in the number of resources used. Therefore, as previously described, it is possible to achieve common resource use by balancing these lines simultaneously instead of balancing them separately. Common resource use is possible at common stations. Tasks using the same resource on the same lines can be assigned to the same station if the precedence relationships are provided, while tasks with the same resource on opposite lines are assigned to common stations, reducing the number of resources. Considering all these features, a suitable model should be designed by developing PDLBP. The relevant model, with which the total net profit is intended to be maximized, should be designed to determine the selection of tasks and resources to be assigned to stations, to ensure that the number of resources available is compatible with the number of resources used, and most importantly, to determine the most appropriate process alternative for each task. In addition, considering the difficulties of accessing the fasteners and their accessibility status, the cost and time parameters

caused by these features should be included in the disassembly task costs and time, and reflected in the model.

CONCLUSION

In this paper, the specific actions for disassembly are discussed to adapt these actions to the concept of PDLBP. The disassembly actions cover many factors such as fasteners, fastening structure, accessibility. These factors increase the cost of the line and complicate removing the parts of the products. This paper aims to provide future research directions in terms of PDLBP which involves the actions and the factors. New mathematical and metaheuristic methods can be considered and real applications can be presented as a future research.

REFERENCES

[1] S. M. McGovern, and S. M. Gupta, *The Disassembly Line: Balancing and Modeling*, New York: McGraw Hill, 2011.

[2] S. M. Gupta, and K. N. Taleb, "Scheduling Disassembly", *International Journal of Production Research*, 32 (8), pp.1857-1866. 1994.

[3] S. M. McGovern, and S. M., Gupta, "A balancing method and genetic algorithm for disassembly line balancing", *European Journal of Operational Research*, 179 (3), pp. 692-708, 2007a.

[4] M. Bentaha, L. Battaia, O. and A. Dolgui, "A sample average approximation method for disassembly line balancing problem under uncertainty", *Computers & Operations Research*, vol.51, pp. 111-122, 2014.

[5] A. Gungor, and S. M. Gupta, "Disassembly line in product recovery", *International Journal of Production Research*, 40 (11), pp. 2569-2589, 2002.

[6] A. Gungor, and S. M. Gupta, "A solution approach to the disassembly line balancing problem in the presence of task failures", *International Journal of Production Research*, 39 (7), pp.1427-1467, 2001.

[7] S. M. Mcgovern, and S. M. Gupta, "Combinatorial optimization analysis of the unary NP-complete disassembly line balancing problem", *International Journal of Production Research*, 45 (18-19), pp. 4485-4511. 2007b.

[8] F. T. Altekin, L. Kandiller, and N. E. Ozdemirel, "Profit-oriented disassembly-line balancing", *International Journal of Production Research*, 46 (10), pp. 2675-2693, 2008.

[9] S. Agrawal, and M. K. Tiwari, "A collaborative ant colony algorithm to stochastic mixed-model U-shaped disassembly line balancing and sequencing problem", *International Journal of Production Research*, 46 (6), pp.1405-1429, 2008.

[10] A. Koc, I. Sabuncuoglu, and E. Erel, "Two exact formulations for disassembly line balancing problems with task precedence diagram construction using an AND/OR graph", *Iie Transactions*, 41 (10), pp. 866-881, 2009.

[11] C. B. Kalayci, and S. M. Gupta, "Ant colony optimization for sequence-dependent disassembly line balancing problem" *International Journal of Agile Management Systems merged into Integrated Manufacturing Systems*, 24 (3), pp. 413-427, 2013a.

[12] C. B. Kalayci, and S. M. Gupta, "Artificial bee colony algorithm for solving sequence-dependent disassembly line balancing problem", *Expert Systems with Applications*, 40 (18), pp. 7231-7241, 2013b.

[13] C. B. Kalayci, and S. M. Gupta, "A particle swarm optimization algorithm with neighborhood-based mutation for sequence-dependent disassembly line balancing problem", *The International Journal of Advanced Manufacturing Technology*, 69 (1), pp. 197-209, 2013c.

[14] C. B. Kalayci, and S. M. Gupta, "A tabu search algorithm for balancing a sequence-dependent disassembly line", *Production Planning & Control*, 25 (2), 149-160, 2013d.

[15] C. B. Kalayci, O. Polat, and S. M. Gupta, "A variable neighbourhood search algorithm for disassembly lines", *Journal of Manufacturing Technology Management*, 26 (2), pp.182-194, 2015a.

[16] C. B. Kalayci, A. Hancilar, A. Gungor, and S. M. Gupta, "Multi-objective fuzzy disassembly line balancing using a hybrid discrete artificial bee colony algorithm", *Journal of Manufacturing Systems*, vol. 37, pp. 672-682, 2015b.

[17] M. L. Bentaha, O.Battaia, and A. Dolgui, "An exact solution approach for disassembly line balancing problem under uncertainty of the task processing times", *International Journal of Production Research*, 53 (6), pp. 1807-1818, 2015a.

[18] M. L. Bentaha, O.Battaia, A. Dolgui, and S. J. Hu, "Second order conic approximation for disassembly line design with joint probabilistic constraints", *European Journal of Operational Research*, 247 (3), pp. 957-067, 2015b.

[19] E. G. Kalaycilar, M. Azizoglu, and S. Yeralan, "A disassembly line balancing problem with fixed number of workstations", *European Journal of Operational Research*, 249 (2), pp. 592-604, 2016.

[20] C. Zhang, and M. Chen, "Designing and verifying a disassembly line approach to cope with the upsurge of end-of-life vehicles in China", *Waste Manage.*, vol. 76, pp. 697–707, 2018.

[21] K. Liu, and Z. Zhang, "Capacitated disassembly scheduling under stochastic yield and demand", *European Journal of Operational Research*, 269 (1), pp. 244–257, 2018.

[22] J. Liu, Z. Zhou, D. T. Pham, W. Xu, C. Ji, and Q. Liu, "Collaborative optimization of robotic disassembly sequence planning and robotic disassembly line balancing problem using improved discrete Bees algorithm in remanufacturing"*, Robotics and Computer-Integrated Manufacturing*, vol. 61, doi:10.1016/j.rcim.2019.101829, 2020.

[23] Y. Fang, Q. Liu, M. Li, Y. Laili, and D. T. Pham, "Evolutionary many-objective optimization for mixed-model disassembly line balancing with multi-robotic workstations", *European Journal of Operational Research*, vol. 276, pp. 160–174, 2019.

[24] Y., Ren, C. Zhang, F. Zhao, G. Tian, W. Lin, L. Meng, and H. Li, "Disassembly Line Balancing Problem Using Interdependent Weights-Based Multi-Criteria Decision Making and 2-Optimal Algorithm", *Journal of Cleaner Production,* 174 (1), pp. 1475–1486, 2018.

[25] J.Li, X. Chen, Z. Zhu, C. Yang, and C. Chu, "A branch, bound, and remember algorithm for the simple disassembly line balancing problem", *Computers & Operations Research*, vol. 105, pp. 47-57, 2019.

[26] W. Kaipu, L. Xinyu, G. Liang and A. Garg, "Partial disassembly line balancing for energy consumption and profit under uncertainty", *Robotics and Computer-Integrated Manufacturing*, vol. 59, pp. 235-251, 2019.

[27] A. Gungor, and S. M. Gupta, "Issues in environmentally conscious manufacturing and product recovery: a survey", *Computers & Industrial Engineering*, 36 (4), pp. 811-853, 1999.

[28] M. A. Ilgin, and S. M. Gupta, "Environmentally conscious manufacturing and product recovery (ECMPRO): A review of the state of the art", *J Environ Manage*, 91 (3), pp. 563-591, 2010.

[29] A. J. D. Lambert, and S. M. Gupta, *Disassembly modeling for assembly, maintenance, reuse, and recycling* London, CRC Press, p. 419, 2005.

[30] E. Ozceylan, C.B. Kalayci, A. Gungor, and S.M. Gupta, "Disassembly line balancing problem: a review of the state of the art and future directions", *Int. J. Prod. Res.*, 1e23. https://doi.org/10.1080/00207543.2018.1428775, 2018.

[31] N. Deniz, and F. Ozcelik, "An extended review on disassembly line balancing with bibliometric & social network and future study realization analysis", *Journal of Cleaner Production*, https://doi.org/10.1016/j.jclepro.2019.03.188, 2019.

[32] C. Becker, and A. Scholl. "A Survey on Problems and Methods in Generalized Assembly Line Balancing." *European Journal of Operational Research*, 168 (3), pp. 694–715, 2006.

[33] S. Hezer, and Y. Kara, "A network-based shortest route model for parallel disassembly line balancing problem", *International Journal of Production Research*, 53 (6), 1849-1865, 2015.

[34] H. Gokcen, K. Agpak, and R. Benzer, "Balancing of parallel assembly lines", *International Journal of Production Economics*, 103 (2), pp. 600-609, 2006.

[35] R. Benzer, H. Gokcen, T. Cetinyokus, and H. Cercioglu, "A network model for parallel line balancing problem", *Mathematical Problems in Engineering*, 2007.

[36] A. Baykasoglu, L. Ozbakir, L. Gorkemli, and B. Gorkemli, "Balancing Parallel Assembly Lines via Ant Colony Optimization", *Cie: 2009 International Conference on Computers and Industrial Engineering, Vols 1-3*, pp. 506-+

[37] H. Cercioglu, U. Ozcan, H. Gokcen, and B. Toklu, "A Simulated Annealing Approach for Parallel Assembly Line Balancing Problem", *Journal of the Faculty of Engineering and Architecture of Gazi University*, 24 (2), pp. 331-341, 2009.

[38] A. Scholl, and N. Boysen, "Designing parallel assembly lines with split workplaces: Model and optimization procedure", *International Journal of Production Economics*, 119 (1), pp. 90-100, 2009.

[39] Y. Kara, H. Gokcen, ve Y. Atasagun, "Balancing parallel assembly lines with precise and fuzzy goals", *International Journal of Production Research*, 48 (6), pp.1685-1703, 2010.

[40] Ozcan, U., Cercioglu, H., Gokcen, H. and Toklu, B., 2009, "A Tabu Search Algorithm for the Parallel Assembly Line Balancing Problem", *Gazi University Journal of Science*, 22 (4), 313-323.

[41] U. Ozcan, H. Cercioglu, H. Gokcen, and B. Toklu, "Balancing and sequencing of parallel mixed-model assembly lines", *International Journal of Production Research*, 48 (17), 5089-5113, 2010.

[42] L. Ozbakir, A. Baykasoglu, B. Gorkemli, and L. Gorkemli, "Multiple-colony ant algorithm for parallel assembly line balancing problem", *Applied Soft Computing*, 11 (3), pp. 3186-3198, 2011.

[43] A. Baykasoglu, L. Ozbakir, L. Gorkemli, and B. Gorkemli, "Multi-colony ant algorithm for parallel assembly line balancing with fuzzy parameters", *Journal of Intelligent & Fuzzy Systems*, 23 (6), pp. 283-295, 2012.

[44] A. Lusa, "A survey of the literature on the multiple or parallel assembly line balancing problem", *European Journal of Industrial Engineering*, 2 (1), pp. 50-72, 2008.

[45] S. K. Das, and S. Naik, "Process planning for product disassembly", *International Journal of Production Research*, 40 (6), pp. 1335-1355, 2002.

[46] S. K. Das, P. Yedlarajiah, ve R. Narendra, "An approach for estimating the end-of-life product disassembly effort and cost", *International Journal of Production Research*, 38 (3), pp. 657-673, 2000.

[47] R. Sodhi, M. Sonnenberg, and S. Das, "Evaluating the unfastening effort in design for disassembly and serviceability", *Journal of Engineering Design*, 15 (1), pp. 69-90, 2004.

[48] Y. Kara, C. Özgüven, N. Yalçın, and Y. Atasagun, "Balancing straight and U-shaped assembly lines with resource dependent task times", *International Journal of Production Research*, 49 (21), pp. 6387-6405, 2011.

Investigation of Exergy Performance of Fluids Used in ORC for Waste Heat Recovery from Aluminum Production Plants

A.KAHRAMAN[1], R. ŞAHİN[2] and S.ATA[2]

[1] Necmettin Erbakan University, Konya/Turkey, akahraman@erbakan.edu.tr
[2]KTO Karatay University, Konya/Turkey, remzi.sahin@karatay.edu.tr
[2]KTO Karatay University, Konya/Turkey, sadik.ata@karatay.edu.tr

Abstract - **In this study, exergy analysis of Organic Rankine Cycle (ORC) technology applied in waste heat recovery from aluminum production plants was carried out. Exergy performance of 20 organic fluids of different structure used in high temperature applications of ORC was determined. Performance parameters were determined as recovered exergy, total irreversibility and exergy efficiency of the system. n-hexane, n-octane, n-decane, n-dodecane, n-nonane, n-heptane, isohexane, cyclohexane from the group of alkanes; benzene, ethylbenzene, toluene, m-xylene, P-xylene, o-xylene from the aromatic hydrocarbons; D4, D5, MM, MDM, MD4M and HFE7500 fluids were selected from the siloxanes group. With EES (Engineering Equation Solver) software, different models of turbine inlet temperature ranging from 160 °C to 200 °C have been created. The waste heat source temperature of ORC is 240 ºC. The effect of the turbine inlet temperature change on the exergy performance of the ORC was determined. The recovered exergy values were determined for each fluid. The irreversibility values of the pump, evaporator, turbine and condenser were determined, and the total irreversibility value was calculated. Then, exergy efficiency of the system was determined according to the recovered and expended exergy values. Fluids that achieve the best exergy efficiency were determined in each fluid group. In this study, it is determined how the waste heat at different temperatures in aluminum production plants can be evaluated in best conditions by using which fluid with ORC. Therefore, it is aimed to determine the optimum fluids that the system will work under different waste heat temperatures.**

Keywords - **Organic Rankine Cycle (ORC), Aluminum Plants, Waste Heat, High Temperature, Exergy Performance**

I. INTRODUCTION

What makes Organic Rankine Cycle (ORC) systems different from other Rankine cycles is not the system equipment but the type of fluid used in the system. In ORC, the organic working fluid has a lower boiling point and a higher vapor pressure than the working fluid in the traditional Rankine cycle. As this fundamental difference increases the efficiency of the cycle, the lower the boiling point of the selected working fluid and the higher the vapor pressure, the higher the energy obtained from the turbine [1].

In this study, exergy performance of fluids used in high temperature applications of ORC was investigated. The exergy analysis of the ORC system applied in the waste heat recovery of the aluminum production plant was carried out. The results of the literature research on fluids used in high temperature applications of ORC are summarized below.

Wang et al.; have studied thermodynamic analysis of ORC system designed using hydrofluoroethers. They have benefited from the Engineering Equation Solver (EES) software. The HFE7000, HFE7100 and HFE7500 organic fluids were compared in terms of the turbine inlet temperature change and the first-second law efficiency, net power and turbine size factor. The best thermodynamic performance was observed in HFE7000 fluid. It is stated that the minimum value of the turbine dimension factor calculated by taking into account the volumetric flow value at the turbine outlet and the enthalpy difference realized in the turbine is in HFE7000 fluid [2].

Li et al.; evaluated the performance of the ORC system designed to recover the heat of the waste gas from the industrial boiler with zeotropic fluids. They made thermodynamic and thermo-economic analysis under different mixing compositions and different operating conditions. They stated that the components of the mixture had a significant effect on ORC system performance. They concluded that mixtures do not always improve ORC system performance. In mixtures, the temperature difference in the heat exchanger increases the overall cost of the ORC system while causing a larger heat transfer area. For this reason, they found that mixtures were also economically weaker compared to pure fluids [3].

Dong et al., investigated the effect of zeotropic fluids on the system using Siloxanes hexamethyldisiloxane (MM) and octamethyltrisiloxane (MDM) fluids for high temperature ORC applications. The temperature gradients of heating and cooling fluids were examined for ORC performance. They achieved the best performance when the MM / MDM ratio was 0.4/0.6. It was found that the hot source temperature should be between 20 ºC or slightly higher between the inlet and outlet temperature. They stated that condensation affects system efficiency more than evaporation. They emphasized that high pressure ratios are important in high temperature ORC applications. As a result, they stated that zeotropic fluids performed better than pure fluids [4].

Han et al.; studied the waste heat applications of ORC. They made the thermodynamic and economic analysis of ORC with heat exchanger using flue gas as heat source at 160 ºC using MATLAB. The effect of volumetric flow rate, evaporation temperature and superheating temperature on system performance was determined by using different organic fluids.

The highest net power values were observed in systems with isohexane and butane fluids due to high latent heats. The lowest volumetric flow rate was also observed in the system with butane. At the end of the study, the optimum evaporation temperature was 100 ºC and the superheating temperature was 5 ºC [5].

Shu et al., studied fluid determination for waste heat recovery applications of high temperature ORC. Mixtures of three pure hydrocarbons, cyclopentane, cyclohexane and benzene and R11 and R123 in different proportions were investigated. In this study, simple ORC and ORC with recuperators were compared. Zeotropic fluids have been reported to give better results than pure fluids. As a result of their study, the best results were obtained in the case of benzene / R11 (0.7 / 0.3) and recycled ORC. They stated that with the addition of heat exchanger, the efficiency increased between 7.12% and 9.72%. In the study, they reached the maximum thermal efficiency value of 16.7% [6].

Kahraman et al.; tried to determine the ideal fluid by conducting energy analysis on ORC applied in waste heat recovery from aluminum production plants. High temperature organic fluids are discussed in 3 different structures. The best performing fluids in terms of thermal efficiency are cyclohexane in the alkanes group; benzene in the aromatic hydrocarbon group and in the siloxanes group it was determined as D4 [7].

In this study, exergy analysis of ORC system applied in waste heat recovery of aluminum production plant was performed. The heat source temperature was determined as 240 ºC. The exergy performance of organic fluids used in high temperature applications was determined by changing the turbine inlet temperature between 160 ºC and 200 ºC. Organic fluids were evaluated in three different groups. These; alkanes, aromatic hydrocarbons and siloxanes. 20 different organic fluids recovered in these three groups were compared in terms of recovered exergy values, total irreversibility values and exergy efficiency. The main purpose of this study is to determine the exergy performances of fluid groups used in high temperature applications of ORC.

II.   MATERIALS AND METHODS

The organic fluid used in ORC is pressurized by the pump and sent to the evaporator, the element used as the evaporator is a heat exchanger, which transfers the heat from the hot source to the organic fluid. The organic fluid then passes to high temperature and pressure. It is then sent to the turbine and converted into mechanical work. Then it returns to the condenser and becomes liquid again. The cycle continues in this cycle.

The schematic drawing and the T-s diagram describing the operating principle of the ORC operating on a basic principle is given in Fig. 1-2 [8].
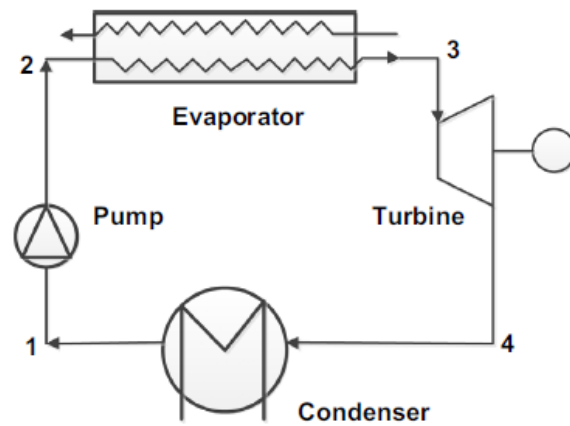
Figure 1. ORC working principle
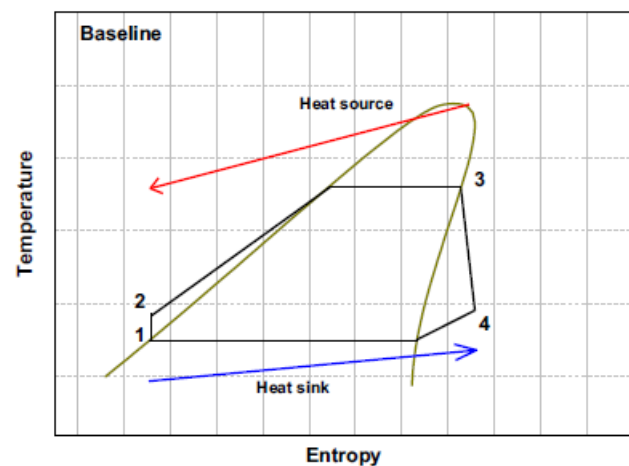
Figure 2. ORC T-s diagram

The equations required for the thermodynamic analysis of the classical ORC are given between Equation 1 and Equation 7. These equations are introduced to EES software and thermodynamic simulation study is performed for different fluids.

The reason for using EES software is that it contains thermophysical properties of many organic fluids in the database. When the equations required for thermodynamic analysis are entered into the system, the desired results can be obtained in response to the change of many parameters at the same time. The effect of using different fluids on system performance is easily seen. By processing irreversibility relations in the EES, a component whose irreversibility value reaches a negative value in a given temperature or pressure range can be detected. In this way, the conformity of the model to the second law of thermodynamics is checked.

Irreversibility of ORC components;

Pump

$$I_p = T_0\dot{m}(s_2 - s_1) \qquad (1)$$

Evaporator

$$I_{evap} = T_0\dot{m}[(s_3 - s_2) - (h_3 - h_2)/T_H)] \qquad (2)$$

Turbine

$$I_T = T_0\dot{m}(s_4 - s_3) \qquad (3)$$

Condenser

$$I_{con} = T_0\dot{m}[(s_1 - s_4) - (h_1 - h_4)/T_L)] \qquad (4)$$

Total irreversibility;

$$I_{total} = \sum I_{ORC\ Components} \qquad (5)$$

Exergy Efficiency

$$\eta_{II} = \frac{Exergy\ Recovered}{Exergy\ Expended} = 1 - \frac{I_{total}}{I_{expended}} \qquad (6)$$

$$I_{expended} = \left(\left(1 - \left(\frac{T_L}{T_H}\right)\right) * Q_{evap}\right) + W_p \qquad (7)$$

The constant values, independent variables, high temperature organic fluids and performance parameters used in this study are given in Table 1.

In this study, exergy performance of three different groups of fluids indicated in Table 1 was determined. The waste heat source temperature of ORC is 240 ºC. The effect of turbine inlet temperature changing between 160 ºC and 200 ºC on different fluids was determined.

III. RESULTS AND DISCUSSIONS

In Fig. 3-5, exergy analysis results of n-hexane, n-octane, n-decane, n-dodecane, n-nonane, n-heptane, isohexane and cyclohexane fluids of alkanes group are given.

Figure 3 shows the effect of the turbine inlet temperature variation on the recovered exergy value. It was stated that the highest recovered exergy value was in cyclohexane fluid. At an inlet temperature of 200 ºC turbine, 15.4% more recovered exergy was obtained in cyclohexane ORC than isohexane ORC.

Table 1. Fixed values and independent variables for the thermodynamic design model

Constant Values	Turbine Isentropic Eff.	75%
	Pump Isentropic Eff.	75%
	Heat Source Temp.	240 ºC
	Sink Temperature	25 ºC
	Pump Temperature	40 ºC
Organic Fluids	Group I: Alkanes	n-hexane; n-octane; n-decane; n-dodecane; n-nonane; n-heptane; isohexane; cyclohexane
	Group II: Aromatics	Benzene; ethylbenzene; toluene; m-Xylene; p-Xylene; o-Xylene
	Group III: Siloxanes	D4; D5; MM; MDM; MD4M; HFE7500
Independent Variables	Turbine Inlet Temperature	160 ºC – 200 ºC
Performance Parameters	Exergy Recovered (kJ/kg) Irreversibility (kJ/kg) Exergy Efficiency	
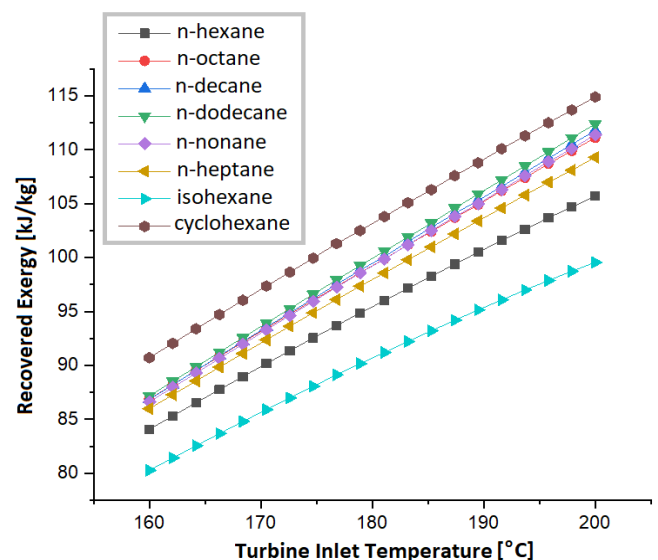
Figure 3: Effect of turbine inlet temperature change on recovered exergy for alkanes

Figure 4 shows the effect of turbine inlet temperature variation on irreversibility values. As the turbine inlet temperature increases in the Alkanes group, the rate of increase of irreversibility value is different. With the 40 °C turbine inlet temperature change, the irreversibility of cyclohexane ORC increased by 1.5%, while the irreversibility of n-dodecane ORC increased by 8%. The least irreversibility was observed in cyclohexane fluid and the most in n-dodecane fluid.
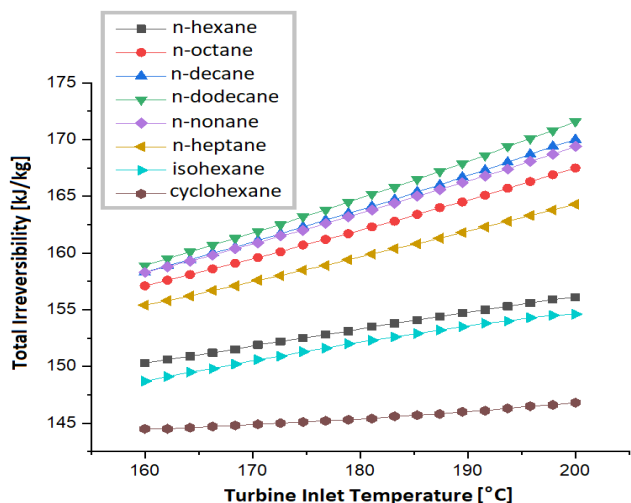
Figure 4: Effect of turbine inlet temperature change on total irreversibility for alkanes

Figure 5 shows the effect of turbine inlet temperature variation on the exergy efficiency of the system. The exergy efficiency of cyclohexane ORC is very high compared to alkanes. Since the recovered exergy value is higher than the other fluids and contains the least irreversibility, the highest exergy efficiency was observed in cyclohexane ORC. The lowest exergy efficiency was obtained with isohexane ORC. At 200 °C turbine inlet temperature, 12% more exergy efficiency was obtained in cyclohexane ORC than isohexane ORC.
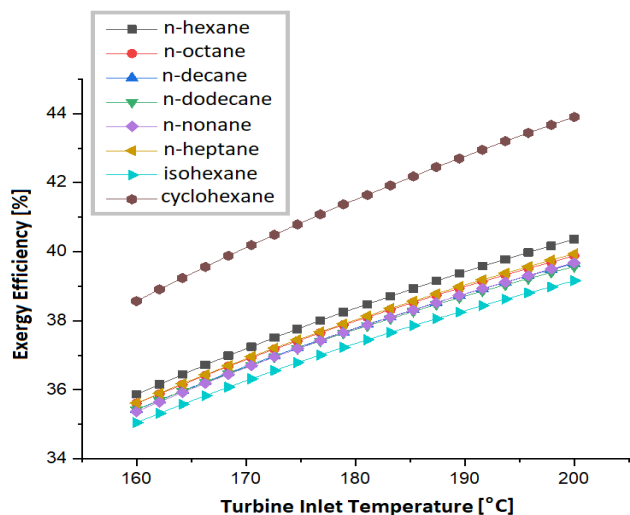
Figure 5: Effect of turbine inlet temperature change on exergy efficiency for alkanes

In Fig. 6-8, exergy analysis results of aromatic hydrocarbon group fluids like benzene, ethylbenzene, toluene, m-Xylene, p-Xylene and o-Xylene are given.

Figure 6 shows the effect of turbine inlet temperature variation on the recovered exergy value. The recovered exergy values are stated as the best fluid benzene at 160 °C turbine inlet temperature. It was determined that the system with o-Xylene performs better as the turbine inlet temperature increases.
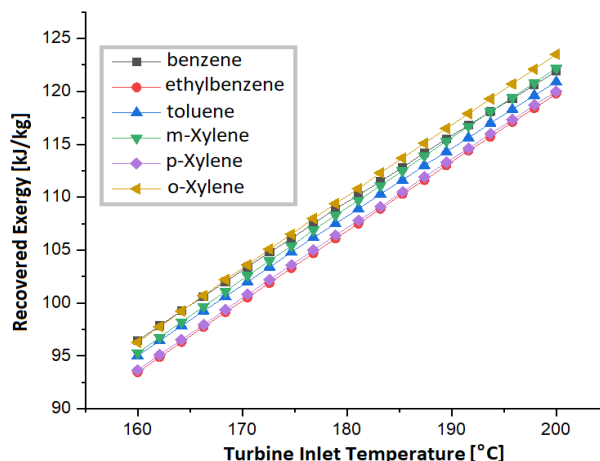
Figure 6: Effect of turbine inlet temperature change on recovered exergy for aromatics hydrocarbon

Figure 7 shows the effect of turbine inlet temperature variation on irreversibility values. In contrast to the alkanes group fluids, irreversibility did not increase as the turbine inlet temperature increased in aromatic hydrocarbon group fluids. While the irreversibility values of the ORC with benzene and toluene decreased, no significant change was observed in the other fluids. With the 40 °C turbine inlet temperature change, irreversibility values of toluene and benzene ORC decreased 1.2% and 2.84%, respectively.
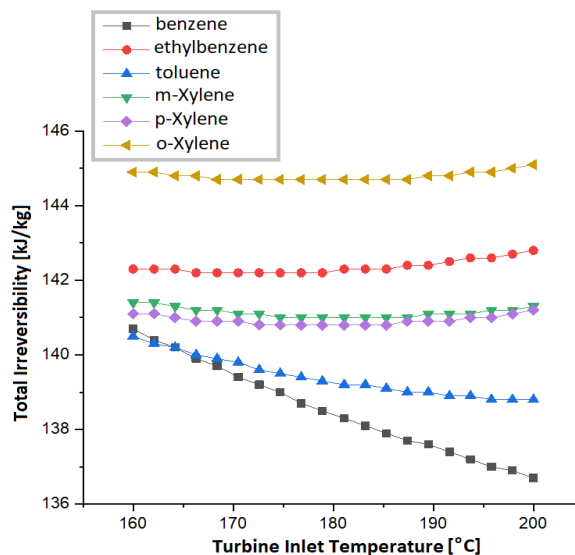
Figure 7: Effect of turbine inlet temperature change on total irreversibility for aromatics hydrocarbon

Figure 8 shows the effect of turbine inlet temperature variation on the exergy efficiency of the system. The highest exergy efficiency was obtained in the benzene fluid where the least irreversibility value was observed. Although the highest irreversibility value was observed in o-Xylene fluid, the worst performance in exergy efficiency was obtained in the ORC system with ethylbenzene. A higher exergy efficiency than ethylbenzene was obtained due to the higher recovered exergy in the ORC with o-Xylene.
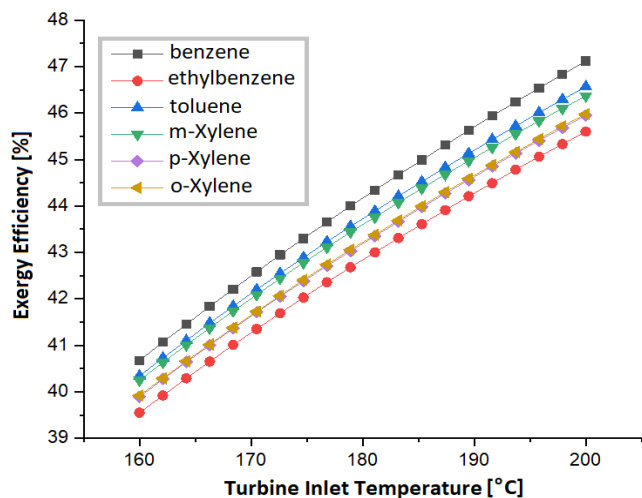
Figure 8: Effect of turbine inlet temperature change on exergy efficiency for aromatics hydrocarbon

In Fig. 9-11, exergy analysis results of siloxane group fluids D4, D5, MM, MDM, MD4M and HFE7500 are given.

Figure 9 shows the effect of the turbine inlet temperature variation on the recovered exergy value. It is seen that MM is the best fluid in recovered exergy values. At 200 °C turbine inlet temperature, 97% more exergy recovery was achieved in MM with ORC than HFE7500.
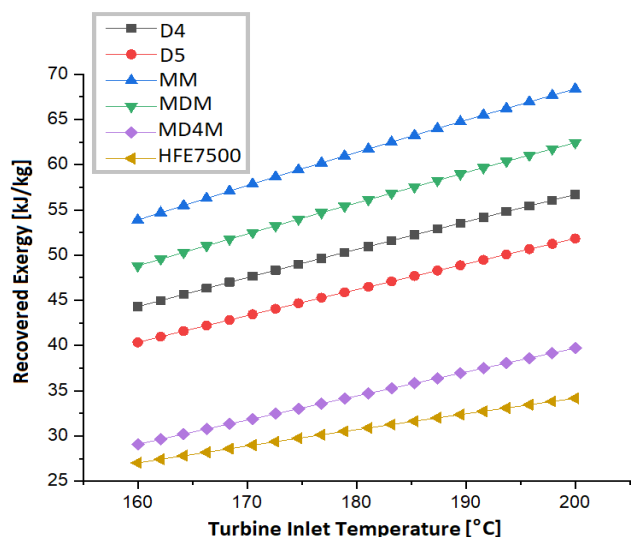
Figure 9: Effect of turbine inlet temperature change on recovered exergy for siloxanes

Figure 10 shows the effect of turbine inlet temperature variation on irreversibility values. The irreversibility increased as the turbine inlet temperature increased for all fluids. It is seen that ORC systems with MM, MDM and MD4M have high irreversibility values. The ORC with HFE7500 has a very low irreversibility value compared to other siloxane fluids. At 200 °C turbine inlet temperature, the ORC with MM contains 70.6% more irreversibility than the ORC with HFE7500.
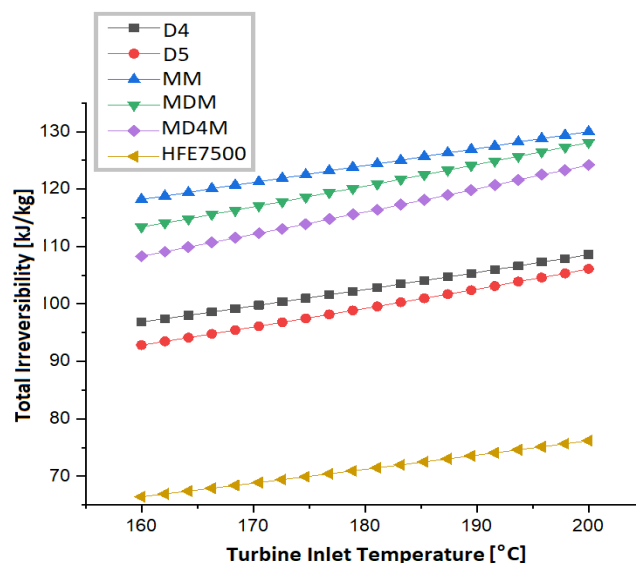
Figure 10: Effect of turbine inlet temperature change on total irreversibility for siloxanes

Figure 11 shows the effect of turbine inlet temperature variation on the exergy efficiency of the system. The highest exergy efficiency was obtained in MM and D4 systems. Although the irreversibility value of the ORC with MM is high, it is stated that the exergy efficiency is better than the other fluids due to the high recovered exergy value.
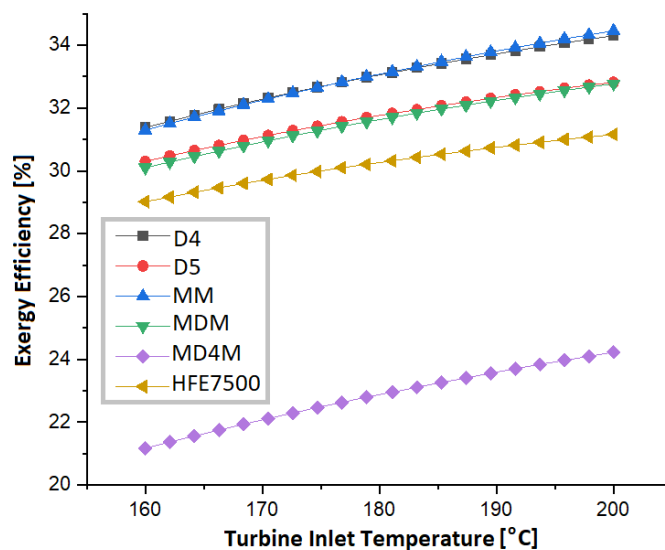
Figure 11: Effect of turbine inlet temperature change on exergy efficiency for siloxanes

Table 2 shows the fluids that achieve the highest exergy efficiency for 200 °C turbine inlet temperature in three different groups. In this study, it is seen that aromatic hydrocarbons are in the best condition in terms of exergy performance. The ORC system with benzene in the aromatic hydrocarbon group reached the highest exergy efficiency with 47.12%.

Table 2. Comparison of fluids with the highest exergy efficiency values in three different organic fluid groups

High Temperature Organic Fluids		Exergy Efficiency for 200 °C turbine inlet temp.
Alkanes	1-) Cyclohexane	43.9%
	2-) n-hexane	40.36%
Aromatics	1-) Benzene	47.12%
	2-) Toluene	46.57%
Siloxanes	1-) MM	34.46%
	2-) D4	34.3%

IV. CONCLUSIONS

In this study, exergy analysis of Organic Rankine Cycle applied in waste heat recovery from aluminum production plants was performed. ORC is designed using 20 different organic fluids. Organic fluids used in high temperature applications of ORC were evaluated under three different groups. These are alkanes, aromatic hydrocarbons and siloxanes. The effect of turbine inlet temperature variation on exergy performance of fluids identified in three different groups were compared. Exergy performance parameters were determined as recovered exergy, total irreversibility and exergy efficiency. Aluminum production plant waste heat source temperature has been considered constant as 240 °C. The results obtained by evaluating the case where the turbine inlet temperature is 200 °C are indicated below.

The highest exergy efficiency of alkanes was obtained from cyclohexane (43.9%) and n-hexane (40.36%) fluids. Although the recovered exergy value in the n-hexane ORC system was low, the exergy efficiency was found to be higher than the others since the irreversibility value was not high.

The highest exergy efficiency of aromatic hydrocarbon group fluids was obtained in benzene (47.12%) and toluene (46.57%) fluids. Although o-Xylene showed good performance in recovered exergy values, exergy efficiency was lower than benzene and toluene due to its high irreversibility value.

The highest exergy efficiency from siloxane group fluids was obtained in MM (34.46%) and D4 (34.3%) fluids. The least irreversibility is achieved in the HFE7500 ORC system. However, as the exergy recovered in this system is very low, the exergy efficiency is lower than MM and D4.

As a result, when the three different fluid groups used in high temperature applications of ORC were evaluated, it was found that the best exergy performance fluids were benzene and toluene in aromatic hydrocarbon group. The least irreversibility value was obtained in MM and D4 ORC systems in siloxanes group.

As a continuation of this study, it is recommended to determine the thermodynamic sustainability indexes (waste exergy ratio, exergetic sustainability index, environmental effect factor, availability ratio) of high-performance fluids.

REFERENCES

[1] M. Pelit, "Biyokütle Kaynaklı Organik Rankine Çevrimli Güç Ünitesinin Termoekonomik Analizi," Yüksek Lisans Tezi, Karabük Üniversitesi Fen Bilimleri Enstitüsü, Karabük, 2015.
[2] H. Wang, H. Li, L. Wang, X. Bu, "Thermodynamic Analysis of Organic Rankine Cycle with Hydroluoroethers as working fluids," *Energy Procedia*, vol. 105, pp. 1889-1894, 2017.
[3] Y.-R. Li et al., "Potential of organic Rankine cycle using zeotropic mixtures as working fluids for waste heat recovery," *Energy*, vol.77, pp. 509-519, 2014.
[4] B. Dong et al., "Analysis of zeotropic mixtures used in high-temperature Organic Rankine cycle," *Energy Conversion and Management*, vol. 84, pp. 253-260, 2014.
[5] Z. Han et al., "Thermo-Economic Performance Analysis of a Regenerative Superheating Organic Rankine Cycle for Waste Heat Recovery," *Energies*, vol. 10, pp.1-23, 2017.
[6] G. Shu et al., "Study of mixtures based on hydrocarbons used in ORC (Organic Rankine Cycle) for engine waste heat recovery," *Energy*, vol. 74, pp. 428-438, 2014.
[7] A. Kahraman, R.Şahin, S.Ata, "Comparison of the Performance of Organic Fluids of Different Structure in Organic Rankine Cycle for Waste Heat Recovery From Aluminum Production Plants," *The International Aluminum-Themed Engineering and Natural Sciences Conference (IATENS'19)*, Seydişehir/Turkey, October 4-6, 2019 (Accepted).
[8] G. Li, "Organic Rankine cycle performance evaluation and thermoeconomic assessment with various applications part I: Energy and exergy performance evaluation," *Renewable and Sustainable Energy Reviews*, vol. 53, pp. 477-499, 2016.

EFFECT OF VEHICLE SPEED AND MASS ON VIBRATION DAMPING

A. KARABULUT[1], H.ŞAHMAN[2], Ü.CAN[3]

[1] Afyon Kocatepe University, Afyonkarahisar/Turkey, akarabulut@aku.edu.tr
[2] Afyon Kocatepe University, Afyonkarahisar/Turkey, hsahman@gmail.com
[3]Secant Engineering, Eskisehir/Turkey, canumitcan@gmail.com

Abstract - Vibrations to the driver and passenger have been a problem in vehicles due to road roughness. Driver and passengers are adversely affected by these vibrations. The vibration forces that the vehicles take from the ground while traveling are damped with the suspension system in the vehicle and the remaining part is transmitted to the driver and passengers. In this study, one and two degree of freedom car model is studied. Calculations were made in Matlab and LMS Amesim and the results were shown on the graph. Displacement and frequency values of the behavior at two different masses and four different speeds were found in a single degree of freedom car model. Two degree of freedom car models are given and motion differential equations are formed and state variables are defined. Matlab program was prepared according to the state variables. In the LMS Amesim software, two degree of freedom quarter car system is modeled. In addition, parameters have been assigned and graphs have been taken on a single degree of freedom model. The effect of vehicle speed on displacement is seen in the graphs. As a result of the analysis of the graphs, it is seen that there is an important link between mass and natural frequency. It was found that there was an inverse ratio between mass and natural frequency. However, the natural frequency varies with the broadcast constant used in the suspension system. It has been observed that the natural frequency increases with increasing spring constant. According to the values found, the suspension system plays a very important role in controlling the vehicle mass. It has been concluded that the mass, spring and damping element on the suspension system must consist of appropriate values to achieve the desired movement.

Kewords **- LMS Amesim Sofware, Vehicle Vibrations, Road Roughness, Acceleration and Speed Chart, Vibrations Analysis , Matlab**

I.   INTRODUCTION

Since the emergence of transportation vehicles, driving comfort and safety have come to the forefront. Comfort and safety need to be improved with the increase in vehicle speeds with the development of technology. The roughness of the road surface exposes the vehicle to vibrations. Many different designs and methods are being developed to minimize these effects. Vehicle wheel characteristics, suspension characteristics, vehicle mass and vehicle speed determine the amplitude and frequency of these vibrations.

In road transport vehicles, vibrations from the road have to be reduced to improve driving comfort. For this, the vibration analysis should be done first. The movements in the vertical direction are the most effective vibration movements. Suspension systems are used to damp vibration movements in vehicles. For the design of the suspension system, an analytical model of the system should be formed, and mathematically expressed, path input should be given. The driving comfort of the vehicles is only possible if the vehicle's ergonomics, aerodynamic structure and vibration are at the appropriate forum. Furthermore, the fact that vibrations do not disturb the passenger during a long journey determines the comfort of the vehicle [5].

The passenger traveling inside the vehicle may be covered by bumps, pits, road roughness, etc. caused by the ground. It is aimed to prevent any discomfort caused by external effects and to improve driving comfort. During this effect, it is aimed to keep the position change and acceleration values in the vertical direction relative to the ground transmitted by the suspension to the vehicle body as low as possible [6]**.** There is a significant relationship between the vehicle mass and vibration. The higher the mass of the vehicle, the lower the vibration frequency, the lower the vibration acceleration. As the acceleration decreases, the vibration magnitude, which bothers the person and causes fatigue, will lose its effect. Accordingly, the increase and decrease of the mass directly affect the vibration frequency [2].

II.   METHOD

The methods used in the study will be explained under several titles. The mathematical model of the vehicle was created and necessary calculations were made.

A.   Groud Caution

The physical quarter car model of a car moving on the unevenness of the road surface is given. The system has a single degree of freedom. Mass m, suspension damping constant c, vehicle mass displacement x, damping mass displacement y, road roughness $y = \sin \omega t$ profile [4].
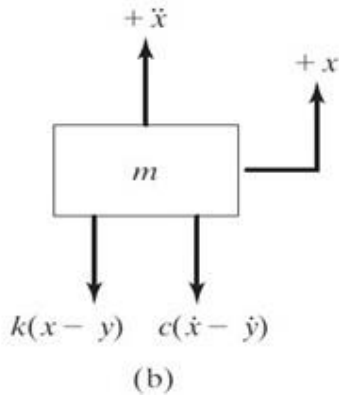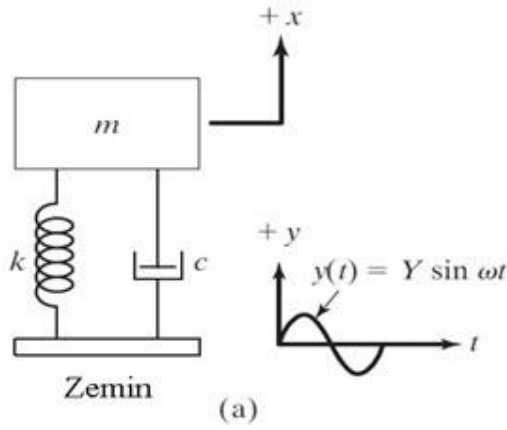
Figure 1: Vibration model [1].

When Newton's law of motion was applied using the vibration model, an equation was found that gives the displacement in the vertical direction. The change of mass was calculated using this equation.

$$x(t) = e^{-\zeta\omega_n t}\left\{ x_0\cos\sqrt{1-\zeta^2}\,\omega_n t + \frac{\dot{x}_0 + \zeta\omega_n x_0}{\sqrt{1-\zeta^2}\,\omega_n}\sin\sqrt{1-\zeta^2}\,\omega_n t \right\} \tag{1}$$

The mathematical model of the vibration motion between the vehicle and the ground is shown in Figure 1. The movement of the mass in the vertical direction due to ground roughness is shown in the graph in Figure 2. Vibration movement due to the damping of the system will cease over time.
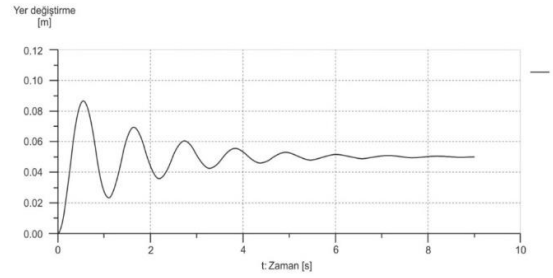
Figure 2: Variation of damped system displacement over time

The displacement of the mass according to the ratio of the damping constant stops its movement after a certain period.

B.　Analysis of Car Model in LMS Program

A single degree of freedom car model was modeled in LMS Amesim program and the behavior of the system according to time was determined. The model of the system is shown in Figure 3. The blocks created in the program were defined and numerical data were converted to graphs using the equations.
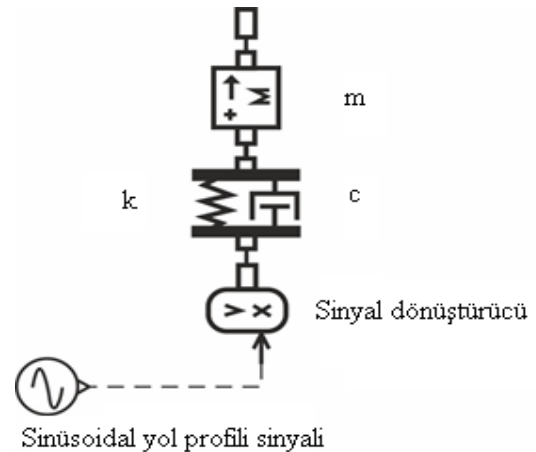
Figure 3: LMS Amesim is a single degree of freedom car model at the input of the sinusoidal profile

The car model is defined as a road-sine curve. The signal converter converts the signal into position. k and c values are assigned parameters in the system. The vehicle mass is defined as m. The vertical axis is selected as the direction of movement. LMS Amesim program obtains the graphic value by using the equations defined in the software. Equations defined in the software are the equations of motion of the mass.

III.　　RESULTS

A.　Impact of Road Profile on the System

In this study, the path profile is sinusoidal and firstly the effect of the system on wavelength and wave height is compared. Then the effect of the change of the road period on the system was kept by keeping the wave height constant. Using the equation (1) the values in Table 1 were obtained.

Table 1: Vehicle speed and mass effect on displacement

Speed (km/h)	ω_b (rad/s)	r_1	r_2	X_1 (cm)	X_2 (cm)
30	5,236	0,9069	1,0139	32,68	39,26
50	8,7266	1,5115	1,6899	8,04	5,72
82	14,3117	2,4789	2,7714	2,37	1,83
110	19,1986	3,3253	3,7178	1,37	1,08

The parameters used in the calculation are given in the graph in Figure 4. Traffic values were obtained by calculating the program according to these values.
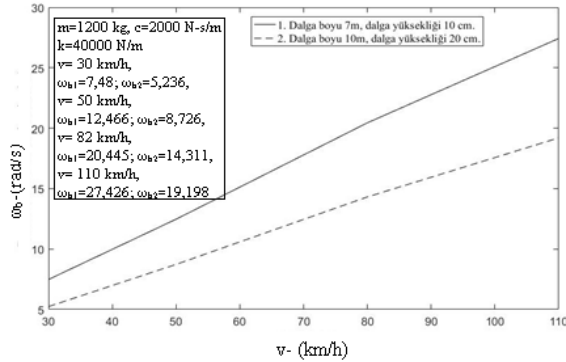
Figure 4: Variation between speed and caution frequency

Figure 4 shows the variation of vehicle speed and natural frequency. Both curves were found to increase in direct proportion to natural frequency depending onvehicle speed.
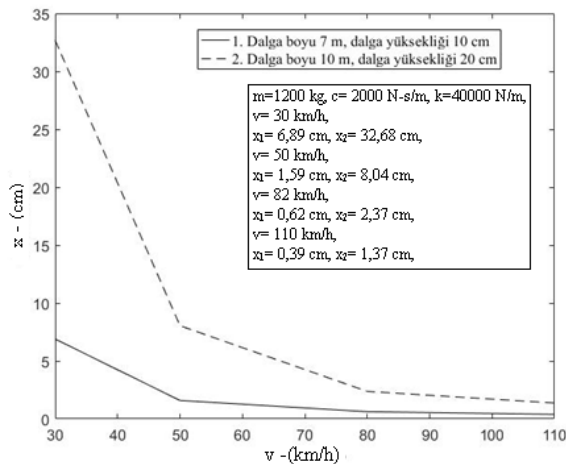
Figure 5: Variation between speed and amplitude [4]

Figure 5 shows the variation between speed and amplitude of the vehicle. As the speed of the vehicle increases, the amplitude decreases dramatically and we see that the amplitude decreases as a hyperbolic curve.
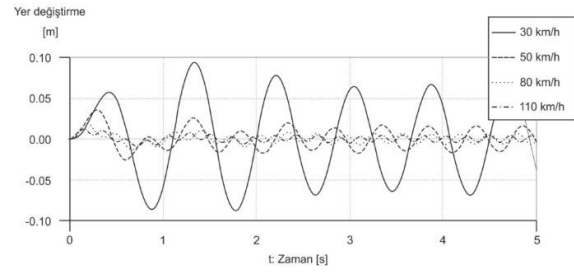
Figure 6: Amplitude changes in different masses [4].

As the mass of the vehicle increases, the amplitude values decrease. In the study conducted on three different masses, it was seen that the amount of amplitude decreases as the amount of mass increases. As the mass increases, the natural frequency will decrease, and since the decrease in the natural frequency causes the amplitude amount to decrease, the mass amount is inversely proportional to the amplitude of the vehicle. [3].

B.　Effect Of Vehicle Mass On Damping

When the mass of the vehicle increases, damping effect is exacerbated. It is known that the damping value varies between $0 < \zeta < 1$ for weak damping. The suspension of the system will soften as it approaches zero, and the suspension system will not bring a large proportion of the caution forces coming from underneath the vehicle. As shown in Figure 7, the numerical value of the damping ratio decreases as the amount of mass increases, which will cause the damping effect of the structure of the system to be greater.
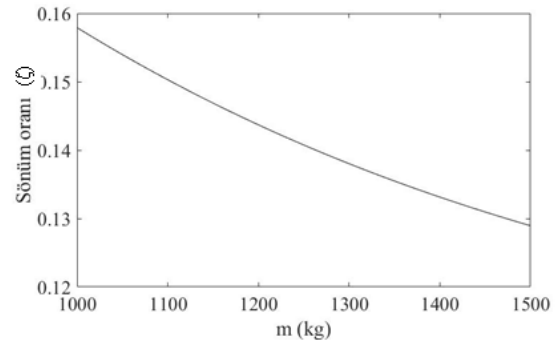
Figure 7.　Change of mass and damping ratio

Table 2. Mass and damping ratio values

m (kg)	ζ
1000	0,158
1100	0,150
1200	0,144
1300	0,138
1400	0,133
1500	0,129

The damping ratio is neither hard nor too soft. It must be determined at a rate that can filter the excitation forces from the bottom in proportion to the size of the mass.
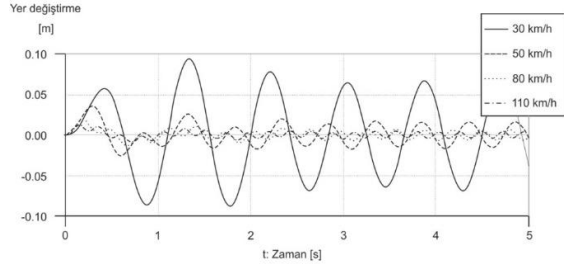
Figure 8: Amplitude change at different speeds [4].

As the speed of the vehicle increases, the amplitude values change (Figure 8). The displacement amplitude of the vehicle was examined by giving four different speed values. Amplitude decreased as speed value increased. Conversely, it is seen that the amplitude values increase as the speeds decrease. As a result, the fast passing of the vehicles from the bowl reduces the bouncing of the vehicle. On the other hand, the force on the undercarriage of the vehicle increases and severely damages the vehicle. If possible, the vehicle must pass through the bumps as quickly as possible.

IV.   CONCLUSION

It is the ground roughness that affects the vibration amplitude of the vehicle. Ground roughness is considered as a periodic curve, even in the form of a sinusoidal curve. In general, ground roughness values are considered as sine curves in scientific studies. When the measured values of the ground roughness were calculated analytically using the forier series, the total curve was found to be equivalent to a periodic curve. Therefore, it is suggested that the use of sinus curve is suitable in scientific studies. In this study, graphs were drawn by using LMS Amesim program on vehicle suspension system considering vehicle values and road roughness conditions. Different results were obtained by increasing and decreasing the variables. In addition, these parameters were analyzed analytically and the mathematical models were analyzed with Matlab. Both results were compared with each other. It is the suspension system that determines the comfort of vehicles. It is the suspension system that determines the comfort of the passenger in the vehicle and keeps them vigorous for a long time. The suspension system affects the damped circular frequency of the vehicle. As the mass increases, the natural frequency decreases. It was reached

that the natural frequency of a vehicle with a high mass would decrease. The spring constant changes in proportion to the natural frequency. It has been observed that the natural frequency increases with increasing spring constant. In line with these changes, we see that the suspension system plays a very important role in controlling the vehicle mass. The mass, spring and damping element on the suspension system must consist of appropriate values to achieve the desired movement. The damping system must be selected according to the vehicle mass. The spring coefficient should be selected according to the mass and damping element. As it is known, springing stores potential energy and the damping element tries to stop the movement in the system during energy exchange. Therefore, mass, spring coefficient and damping element should be designed together.

V.   REFERENCES

[1]   Rao, S.S., (2011). Mechanical Vibration, fifth edition pearson, Singapure.

[2]   Karabulut, A.,(2009). Kütlenin Taşıt Titreşimine Etkisinin Modal Analizi Kullanarak Belirlenmesi , Makine teknolojileri elektronik dergisi, 6-1, 17-23

[3]   Karabulut, A. ve Dahil, L.,(2016). Assessment Of The Vibration On The Foam Legged And Sheet Metal-Legged Passenger Seat. Metalurgija, 55(1), 41-43

[4]   Can, Ü., (2019). Araç Hızı Ve Kütlesinin, Süspansiyon Sistemindeki Yerdeğiştirme İletgenliğinin Araştırılması.Yüksek Lisans Tezi, Fen Bilimleri Enstitüsü, Makine Mühendisliği Anabilim Dalı, Afyonkarahisar.

[5]   Çetinkaya, S., (2014). Taşıt Mekaniği. Nobel Akademik Yayıncılık Eğitim Danışmanlık Tic. Ltd. Şti, 7. Baskı, İstanbul.

[6]   Delen G. (2014). İki Serbestlik Dereceli Aktif Süspansiyon Sisteminin Kontrolü. Yüksek Lisans Tezi, İstanbul Üniversitesi, Fen Bilimleri Enstitüsü, İstanbul.

Investigation of Vibration Effect of Vehicle Engine on Chassis

A. KARABULUT[1], H.ŞAHMAN[2], İ.AKKUŞ[3]

[1] Afyon Kocatepe University, Afyonkarahisar/Turkey, akarabulut@aku.edu.tr
[2] Afyon Kocatepe University, Afyonkarahisar/Turkey, hsahman@gmail.com
[3] Danet Et İşleme Tesisleri, Afyonkarahisar/Turkey, isaakkus@gmail.com

Abstract - **In vehicles, the oscillating motion of the engine affects the chassis. In order to prevent the vibration transmitted by the engine to the chassis of the vehicle, it is aimed to reduce the vibration to the chassis by using vibration wedges in the connection between them. In this study, the displacement and acceleration values of the engine and chassis were measured simultaneously with the help of a four channel Datalogger. According to the graphs obtained, the engine speed is directly proportional to the amount of vibration produced. This causes serious discomfort to the driver and passengers in the vehicle. In order to prevent this, the vibration between the engine and the chassis is tried to be prevented by using damping elastic material. Thanks to the damping wedge used, it has been observed that the transmission of the engine vibration to the chassis is reduced by approximately 50%. It is seen that the spring coefficients are proportional to the engine speed due to the liquid in the structure of the hydraulic wedges. It is observed that the spring coefficient decreases at low speeds. In addition, it was observed that vibration amplitude increases at low engine speeds and vibration amplitude decreases at high engine speeds. When the numerical values of the new and used vibration wedges used in the study were taken into consideration, it was found that the new vibration wedge was a better insulating material than the used wedges.**

*Keywords***: Vibration, Engine Vibration, Engine Vibration Damping, Engine Vibration Wedges**

I.   INTRODUCTION

As a result of increased use of automobiles it has been an increase in a person's request. As a result of the large number of vehicle manufacturers and vehicle types, users started to make their preferences according to their needs and comfort performance characteristics of the vehicle. With the increase in the use of automobiles, we can say that automobiles have some negative effects on human health. One of these effects is vibration. A high amount of vibration occurs in vehicles used today. The resulting vibrations affect the driving comfort and health of the occupants and cause serious health problems. Vibrations in vehicles are caused by ground and engine. The vibrations caused by road roughness are low frequency and high amplitude. Engine vibrations are relatively high frequency and low amplitude vibrations [4]. It is known that diesel vehicles produced are more vibratory than gasoline vehicles [2].

It is necessary to dampen vibrations that occur in vehicles for comfort. Vibration from the ground damper and coil spring (Suspension System), such as damping elements by using vibration-damping elements are highly damped. The vibration in the engine is damped by the engine wedges used to connect the engine to the vehicle body [1]. Almost every automobile manufacturer is working on engine wedges and new wedges are made and used with different types and different damping rates [7]. In this study, it is aimed to reduce the amount of vibration transmitted from engine to chassis by using different types of engine wedges. In this context, the vibration movements of the engine and chassis were measured at the same time. It was found out that the vibration wedges used were plotted according to acceleration and amplitude values affect vibration isolation. In order to increase the comfort by reducing the amount of vibrations coming from the engine to the people in the vehicle, a study was carried out to provide healthier driving pleasure.

II.   MATERIALS AND METHODS

A.   Engine Vibration Wedges

The ideal engine suspension system is to isolate vibrations caused by engine irregularities and prevent excessive oscillation of the engine caused by shock drives. Conventional rubber wedges do not meet all requirements of the engine wedge. However, it is still widely used because of its low cost, easy productionability, no maintenance and reliability. Passive hydraulic wedges perform better at low frequencies than hydraulic wedges. Semi-active hydraulic wedges have better characteristics because they can be adjusted more easily. Active engine wedges isolate vibrations by showing hard spring hardness at low frequencies and soft spring hardness at high frequencies. Correct placement of the dynamic engine wedges is important for a balanced engine suspension system. In addition, the loads coming to the wedges should be optimized and the wedges should have a long life. Optimum design can be found by testing various wedges and layouts. Computer aided optimization techniques will facilitate engine suspension system design [4]. Hydraulic engine couplings are used in the automotive industry because they offer a frequency and amplitude response. Such nonlinear dynamic properties are examined using analytical and experimental methods,

both at the device level and in the context of a simplified instrument model.
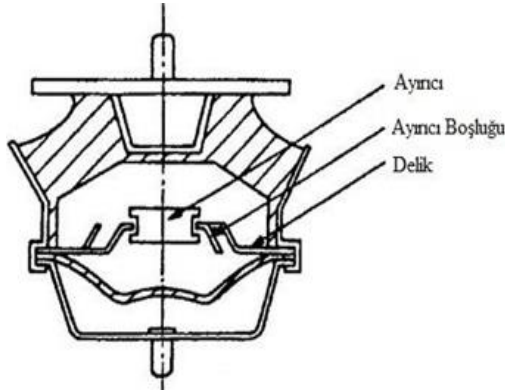
Figure 1: Hydraulic wedge with separator [6].

B. *Mathematical Model*

It can be shown as a vibration model in Figure 2 considering the suspension feature of the vehicle's engine and chassis wedge. Time-dependent force,

$$F(t) = F_0 \cos \cos \omega t \tag{1}$$

Equality of movement of the system,

$$m\ddot{x} + c\dot{x} + kx = F(t) \tag{2}$$

1 and 2 equations,
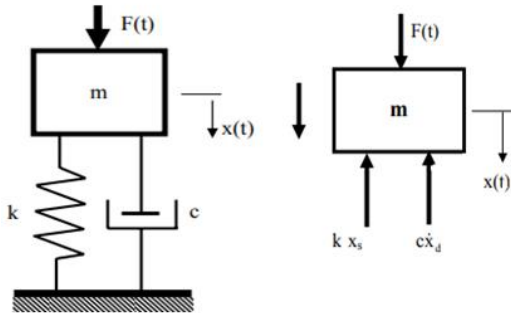
Figure 2: Vibration Model [5]

$$m\ddot{x} + c\dot{x} + kx = F_0 \cos \cos \omega t \tag{3}$$

equation is created. Form of solution,

$$x_p(t) = X\cos(\omega t - \emptyset) \tag{4}$$

Through two equalities,

$$X[(k - m\omega^2) \cos \cos (\omega t - \emptyset) - c\omega \\ \sin \sin (\omega t - \emptyset)] = F_0 \\ \cos \cos \omega t \tag{5}$$

Taking advantage of trigonometric relations,

$$X[(k - m\omega^2) + c\omega \sin \sin \emptyset] = F_0 \tag{6}$$
$$X[(k - m\omega^2) - c\omega \cos \cos \emptyset] = 0$$

after cartesian products,

$$X = \frac{F_0}{\sqrt{(k - m\omega^2)^2 + c^2\omega^2}} \tag{7}$$

$$x(t) = X_0 e^{-\zeta\omega_n t} \cos(\omega_d t - \emptyset_0) + X\cos(\omega t - \emptyset) \tag{8}$$

equation is obtained. Here X0 from homogeneous solution ω_d presumed circular frequency and $\emptyset$ is defined as phase angel [5]. The displacement amplitude of the engine in the vertical direction at different speeds can be obtained.

Table 1: Displacement and spring coefficient values

Engine RPM	900 rpm	2500 rpm
Mass	127 kg	127kg
Impact Mass	1240,87 N	1240,87 N
Damping Constant	465 N.s/m	465 N.s/m
Acceleration	1,59 rad/s	4,37 rad/s
Replacement	6,68x10-4 m	1,08x10-4 m
Spring Constant	1,88x106 N/m	1,17x107 N/m

It is seen that the wedge spring is soft at low speeds and the spring stiffness increases as the speed increases. We see that the wedge behaves differently according to the number of revolutions.

C. *Engine Vibration*

Vibration measurement is a topic that is addressed in all industrial applications, especially in the context of maintenance work. Engine, shaft bearings, fans, pumps, rotating machines, etc. are the concept of vibration at many critical points. As a result of the necessary investigations, a four-channel vibration meter with a suitable measuring range was provided for the vehicle.

Figure 3: Engine Vibrations Measurement [3]

Vibration meter (Datalogger) can measure acceleration and displacement values from 4 different points separately. It is a vibration meter that complies with ISO norms and quality standards.

III.   RESULTS

A used vibration wedge on the motor and a new vibration wedge were measured. The displacement and acceleration values of the engine and chassis were obtained. As a result of the graphical comparison of the results found, the changes occurred between used vibration wedge and new vibration wedge were observed.

A.   Used Engine Wedge

A damaged wedge is intended to mean a long-term used vibration wedge. In some parts of the wedges used in the study, the ones with weakened insulation properties and less insulation feature were preferred.
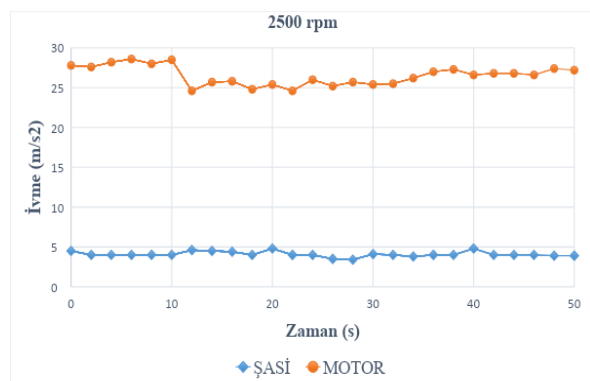
Figure 4: Acceleration-time graph of worn wedge at 2500 cycles [3]

The acceleration values of the engine at 2500 rpm are measured in the acceleration graph shown in Figure 4. There have been small changes in the acceleration values of the engine. On the chassis, the acceleration value is fixed. We can say that the vibration wedge dampens a significant part of the vibration of the engine.

Acceleration values are important parameters in vibration. The greatest effect of damage to vehicles occurs with acceleration values. According to the graph, the acceleration value is around 4.5 m/s^2, which shows the vibration of the existing wedge from the engine to the chassis. The reason for this is that the value of the constant acceleration is not sufficiently felt by the passenger. If there was a continuously variable acceleration, it would cause the passenger and driver to notice and disturb these vibrations. In other words, the constant acceleration is a positive factor for passenger and driver comfort. However, high acceleration values have a negative effect on the fasteners in the vehicle.
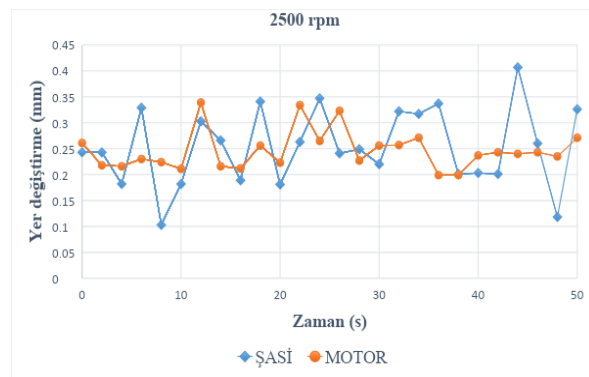
Figure 5: Displacement-time graph of used wedge at 2500 rpm

In the displacement-time graph shown in Figure 5, the graph of the engine and chassis at high speed is very close to each other. We can almost see that the vibration isolation of the wedge has completely disappeared, that it does not perform its function or that the vibration of the wedge has disappeared. This is the opinion that worn wedges should not be used in vehicles. It can be said that this wedge damages all parts of the vehicle. It is seen that the drivers and passengers in the vehicle are highly exposed to vibrations from the engine at 2500 rpm.

B.   New Engine Wedge Values
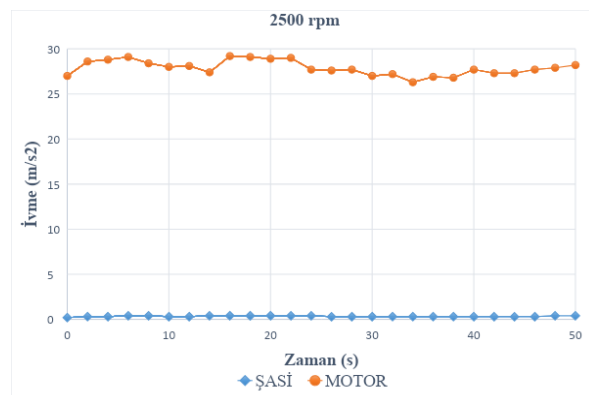
Figure 6: Acceleration-time graph of the new wedge at 2500 cycles

As shown in Figure 6, a significant decrease was observed in the acceleration value of the chassis when the wedge with good insulation properties was used. When we compare used wedge and new wedge, it is seen that there is a big difference between the two. When we look at the acceleration values of the used wedge in Figure 4, it is seen that the acceleration value in the new wedge decreases to a great extent while the acceleration values formed in the engine and the measured values in the new wedge are the same. In other words, the new wedge has decreased the acceleration values formed on the chassis. This decrease also shows that the amount of vibration in the chassis is reduced. In terms of numerical graphs, the vibration acceleration of the used wedge on the chassis is approximately twenty times higher than the new wedge. This is how the vibration oscillations in the chassis are different with the use of a new wedge and an old wedge. Based on these results, it was concluded that used wedges should not be used in the vehicles in order not to wear the driver, passenger and vehicle.
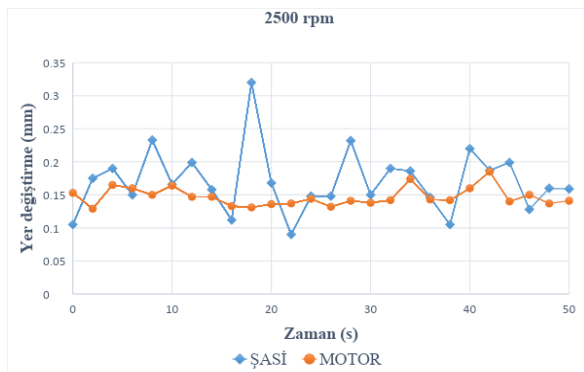
Figure 7. Displacement-time graph of the new wedge in 2500 cycles [3]

The displacement graph in Figure 7 shows that the movements of the engine and chassis are close to each other. We see that the chassis peaks at high speeds from the measured values. We can say that the way the engine works affects these values. The temperature during the measurement of the engine or the irregularity in the combustion of the current fuel in the engine may have caused such a graph. Considering the obtained graph values, another result is that the new engine wedge does not perform well at high speed. This is undesirable. Compared to the high speed values of the used wedge in Figure 5, the displacement values transmitted to the frame decreased. The new wedge performs better than the damaged wedge. However, this performance is not enough for the driver, passenger and vehicle. Considering the values obtained, it is more appropriate to use different types of wedges for this vehicle which provide better performance at high speeds [3].

IV.   CONCLUSION

The vibrations of the vehicles are very important for the driver and passengers. The comfort of the vehicle is related to vibration isolation. In other words, the comfort of the vehicle increases when vibration is minimized. Vibration affects human health negatively. The vibration movement makes you tired. When the vibration

movement reaches further values, it will cause damage or malfunction of the vehicles. In order to get rid of these negativities, vibration should be minimized. Apart from these, we can say that the vehicle engine shakes the vehicle's chassis when it is running at idle speed and high speed. The connection between the engine and the chassis of the vehicle must therefore consist of flexible elements instead of rigid elements. The flexible elements will absorb some of the movement of the engine as it undergoes energy exchange. Vibration blocks between the engine and the chassis serve this purpose. The vibration wedges have an elastic material. The spring coefficient of the material varies depending on the mass of the engine and the intensity of the force it produces. A wedge must be used as the connecting element. We see that the wedges are worn over time. After a certain time, we can say that the wedges should change [3].

The vehicle must be on a level surface during the test. The inclined surface adversely affects the working results. In order to prevent the vibration transmitted by the vehicle engine to the chassis, vibration reduction to the chassis was investigated by using vibration wedges in the connection. In this study, the displacement and acceleration values of the engine and chassis were measured simultaneously with the help of a four-channel Datalogger. The obtained graphs were interpreted. Vibrations produced by the engine in vehicles are disturbing. Vibration wedges are used as connecting elements between the engine and chassis. The vibration wedge prevents the engine from passing the vibration to the chassis. As the engine speed changes, the vibration size it produces changes. The unbalance of the rotating elements in the internal structure of the engine creates the oscillating motion of the engine. Again, when the old and new wedges are compared, it is seen that the vibration isolation of the old wedges is considerably weakened and the appropriate wedges should be selected according to the engine condition.

It has been observed that there is a difference in both displacement and acceleration between engine movement and chassis. In other words, it is observed that the values in the chassis are lower than the values in the engine. It has been observed that vibration amplitude changes according to engine speed in hydraulic wedges. It is seen that the spring coefficients are proportional to the engine speed due to the liquid in the structure of the hydraulic wedges. It is observed that the spring coefficient decreases at low speeds. In addition, it has been observed that vibration amplitude increases at low engine speeds and vibration amplitude decreases at high engine speeds.

REFERENCES

[1] Coşkun, G. (2004). Kauçuk Gövdeli Motor Takozunun Sonlu Elemanlar Yöntemiyle Modelleme, Simülasyon ve Testleri. Yüksek Lisans Tezi. İ.T.Ü. Fen Bilimleri Enstitüsü, İstanbul.

[2] Gültekin, G., Mayda, M. ve Milit, M. (2017). Benzin ve Dizel Motorlarda Devir Sayısının Titreşime Olan Etkisinin İncelenmesi. *Journal of Science*, 6: 39-43.

[3] Akkuş, İ., (2017) Araç Motorlarının Şasiye Bağlantı Takozlarının Titreşim Sönümleme Etkisinin İncelenmesi, Yüksek Lisans Tezi, Afyon Kocatepe Üniversitesi Fen Bilimleri Enstitüsü, Afyonkarahisar.

[4] Korkmaz, İ. (2007). Araçlarda Motor Askı Sistemlerinin İncelenmesi, Yüksek Lisans Tezi. İ.T.Ü. Fen Bilimleri Enstitüsü, Makine Mühendisliği Anabilim Dalı, İstanbul.

[5] Rao, S.S., (2004)Mechanical Vibration, fifth edition pearson, Singapure.

[6] Naganathan, N. G., Yu, Y. and Dukkipati, R.V. (2001). A Literature Review of Automotive Vehicle Engine Mounting Systems. Mechanism and Machine Theory, 36: 123-142.

[7] Ünlüsoy Y. S., Bilal, H. ve Çalışkan, K. (2010). Motor Destek Takozlarının Optimizasyonu. Bursa 5. Otomotiv Teknolojileri Kongresi, Bursa.

Survey of Engineering Students' Cognitive Level of Industry 4.0

Hakan SAHMAN[1], Abdurrahman KARABULUT[2], Mehmet Akif SAHMAN[3],
Murat KOKLU[4], Kemal TTUTUNCU[3]

[1] Institute of Natural and Applied Sciences, Mech Engineering Dep., Afyon Kocatepe University, AFYONKARAHISAR
[2] Faculty of Technology, Mechanical Engineering Dep., Afyon Kocatepe University, AFYONKARAHISAR
[3]Faculty of Technology, Electrical-Electronics Engineering Dep., Selcuk University, KONYA
[4]Faculty of Technology, Computer Engineering Dep., Selcuk University, KONYA

Abstract - **Growth on the world is slowing down and this is emerging as a very important issue. The growth of the global economy stops. In fact, this is not a new situation. The growth of the economy has been decreasing for 50 years. Growth matter a lot. As a result, a new industrial revolution began in 2011. This new production revolution is called Industry 4.0. Industry 4.0 is known as the interaction between the physical and cyber worlds. In other words, mechanical systems and cyber systems can work together and communicate within themselves to produce flexible production at optimum level. This allows us to produce economical, quality and flexible production in less time. The greatest need for countries to move their production systems to the Industry 4.0 platform is the need for trained personnel, especially in engineering fields. Students must be trained in the fields of engineering in accordance with the new industrial revolution. In this study, a questionnaire was applied to measure the cognitive level of engineering students about Industry 4.0. The target engineering areas of the survey are Mechanical, Electrical-Electronics, Mechatronics and Computer engineering.**

Keywords - **Industrial Revolutions, Industry 4.0, Survey, Engineering Studenst, Cognitive Level, Cyber and Physical Worlds**

I.   INTRODUCTION

Industry 4.0 is known to work interactively between the physical and cyber worlds. In other words, mechanical systems and cyber systems work together and communicate within themselves to produce flexible production at optimum level. This allows us to produce economical, quality and flexible production in less time. This is how industry 4.0 is briefly described.

Growth on the world is slowing down and this is emerging as a very important issue. The growth of the global economy stops. In fact, this is not a new situation. The growth of the economy has been decreasing for 50 years. If this continues, we will have to learn to live in a world without growth in the next 10 years. Because if the economy doesn't grow, we'll all get a share of the smaller pie and fight for the bigger slice. This will cause conflicts in the world. It is important to grow by looking at these reasons ahead. If we look at the history of growth, great growth has always been due to the large production revolutions in the industry. The reason for this is to produce more to grow and to add more to the economy. Industrial revolutions so far have occurred every 50-60 years and have occurred three times so far [1].

The most important factor in all industrial revolutions leading to growth in the world is increasing productivity. Producing more products in a short time has enabled growth. But at this point, the growth of the economy is at a standstill. Because there is no growth in the industry. Therefore, there was an expectation for growth from the sector other than production. The expected sector was the technology sector. It was the sector with many innovative solutions. The simplest example of this is the Internet. Efforts have been made to achieve growth with the internet we use today. However, this has been a factor in human life rather than growth in the industry. There have been unsuccessful efforts to improve the production area. Technological developments are moving away from the production. In order to prevent this, it has been decided to combine the existing production system with technological innovations. This merger initiated the Fourth Industrial Revolution. For the first time in the merger process at the 2011 Hannover-Messe in Germany, Robert Bosch GmbH, Henning Kagermann, and the Federal Government of Germany published a statement declaring the beginning of this revolution. Industry 4.0 is a revolution that will produce 1/3 growth in production. Each country has given different names to Industry 4.0. Industry in our country is called 4.0. Industry 4.0 has nine main titles. For a system to be designated as an Industry 4.0 production system, it must contain at least four of the subheadings. The subheadings of Industry 4.0 are as follows; Simulation, System Integration, Internet of Things, Cyber Security, Cloud Computing, Additive Manufacturing, Augmented Reality, Big Data, Autonomous Robots.

Industry 4.0 is known to work interactively between the physical and cyber worlds. In other words, mechanical systems and cyber systems work together and communicate within themselves to produce flexible production at optimum level. This allows us to produce economical, quality and flexible production in less time. Industry 4.0 is briefly described [1].

Universities around the world are developing strategies to include into their curricula trend topics from

Industry 4.0, such as Cyber Physical Systems, robotics, process virtualization and advanced IT tools. However, at the state of the art in literature there is few evidence for educational environments in which all these components are fully integrated [2].

The vision of Industry 4.0 will be bring not only new approaches but also the methodologies and technologies, which will have to be introduced into companies. The transition to such a sophisticated production will not be possible immediately. The main reasons are high financial costs and the lack of qualified employees [3].

Industry is facing a historic turning point. In industry 4.0, people, machines and products communicate with one another via the internet. This means the convergence of industry and Internet technology. Modern machines allow companies to exploit the potential of digitalization in their production facilities and to unlock new business fields. The mechanical engineering sector have to know how new technologies can be successfully integrated for the benefit of the customer. Production processes and supply chains will become more efficient, with advances in productivity and huge savings in material and energy. Digitalization goes hand in hand with the growing importance of platforms for data exchange, customer contact and services. Online platforms facilitate market access, reduce transaction costs and enable innovation through new business models. Machines are connected around the world, so Industry 4.0 would not be possible without networks and data traffic [4].

The degree of Mechanical Engineering allows the labor insertion of the graduate as industrial Technical Engineer. At the same time, the degree must allow access to a high level of specialization due to its subsequent incorporation into the labor market. This engineer is a professional trained in industrial design, management, construction, assembly and maintenance of industrial systems and installations in the mechanical field [4].

The Degree plan of Mechanical Engineering aims to achieve the previous objectives through a training program that combines a basic scientific and technical training with a common training in the industrial sector, with a strong specialization in the field of mechanical engineering. In other words, it is intended to guarantee the development of these professionals who are specialists in mechanics [4].

Manufacturing, through the Industry 4.0 concept, is moving to the next phase of digitalization. Industry 4.0 supported by innovative technologies such as Internet of Things, Cloud technology, Augmented and Virtual Reality will also play an important role in manufacturing education, supporting advanced life-long training of the skilled workforce. Advanced education, also called Education 4.0, and networked ecosystems will develop skills and build competences for the new era of manufacturing [5].

The developed framework aims to support the Education 4.0 concept, where the trainers utilize Industry 4.0 technologies to actively involve the aspiring engineers in realistic simulations that increase the perception of the studied material. Additionally, teaching factories 4.0 serve as an introduction for the aspiring engineers to the newly developed and implemented technologies, through workshops that call the participants to utilize these technologies as a mean that will improve the quality and the effectiveness of their tasks, potentially unlocking new capabilities. The implementation of these technologies in the teaching factories will also boost their integration in manufacturing, as the new engineers that have familiarized themselves with the true potential and the capabilities offered by Industry 4.0 will seek for opportunities to consider these technologies in their works [5].

Complex and fast changing production processes represent a major challenge for universities, since appropriate didactic concepts for authentic reaching methods are necessary. Especially digitalization and the interaction of interdependent disciplines are difficult to comprehend. The modular smart production lab has been developed precisely for the education of the industrial engineers of tomorrow [6].

II.   METHOD

Some multiple choice questions were asked to determine the cognitive level of technology faculty students. While determining the target students, university students in the city of Konya where the industry is developed and the developing cities of Afyonkarahisar were preferred. The questions directed to the target audience are given below. Each of the questions was determined to measure the level of cognition towards the students.

1.   Which faculty do you study??

It is for comparison of participants from different faculties. There are engineering, technology and technical education faculties in both cities.

2.   What is your department?

It was asked to measure the level of cognition between departments.

3.   What grade do you study?

The students were asked to understand the differences between the first and last year students..

4.   What is the Industrial Revolution?

It was asked to measure knowledge of the word meaning and content of the industrial revolution.

5.   How many industrial revolutions have taken place to date?

Asked to learn about the number of industrial revolutions that took place.

6.   Which of the following is the definition of Industry 4.0?

Asked to measure information about entry level definition about Industry 4.0.

7. Which of the following is the year and country in which Industry 4.0 started?

Industry 4.0 was asked to measure information on which country it started**.**

8. What name is Industry 4.0 named in our country?

It was asked to check the knowledge of the name given in the state policy of industry 4.0 in our country.

9. How many subheadings does Industry 4.0 have?**?**

Asked to measure cognitive level of Industry 4.0 topics**.**

10. What is the Internet of Things (IoT)?

It was asked to measure information about IoT, an important topic in Industry 4.0.

11. What is the relationship between Big Data and Cloud Computing?

It was asked to measure the viewpoint of the interaction of Big Data and Cloud Computing.

12. What is Augmented Virtual Reality?

It was asked to measure information about the definition of Augmented Virtual Reality.

13. Should Augmented Virtual Reality be used for education in universities?

They were asked to learn the idea of integrating education into Industry 4.0.

14. What is an autonomous system?

They were asked to question the definition of Autonomous Systems confused with automation.

15. What is flexible production?

The definition of flexible production, which is the main theme of Industry 4.0, was asked to measure information.

16. What is the Dark Factory?

Another definition of factories in accordance with Industry 4.0 was asked about knowing the term Dark Factory.

17. What is the industrial level of our country?

We were asked to measure the industrial production level of our country.

18. Is Industry 4.0 required for our country?

Industry 4.0 has been asked to question the necessity of our country.

19. Are Automation Systems and Industry 4.0 Systems different?

It was asked to measure the difference between Automation systems, which is a definition of Industry 3.0, and Industry 4.0.

20. Do you believe that autonomous systems will prevent humanity in the future?

Robots, a utopian thought, were asked to control the view of the thought that would destroy humanity.

21. Does the system become part of Industry 4.0 by integrating robots into the Production Line?

It was asked to understand the industry level of the robot.

22. What is the difference between the 3rd Industrial Revolution and the 4th Industrial Revolution?

Because of the high difference between the two industrial revolutions, it was asked to measure its awareness.

23. What does machine learning mean?

It was asked to measure the cognitive level of Machine Learning which is a name of artificial intelligence or expert system.

24. What is Predictive Maintenance?

It was asked to measure the cognitive level of Predictive Maintenance, which is used to detect machine failures and to take precautions with Big Data.

25. Are there courses in accordance with Industry 4.0?

It was asked to measure the quality of education and its suitability to Industry 4.0.

III.   RESULTS

A total of 285 students participated in the survey. The answers to each question were checked individually. The findings of the control were shared.

285 participants answered the first question. All participants selected option A. This shows that all participants are students of the Faculty of Technology.

In the second question, 282 out of 285 participants selected option A, namely Mechanical Engineering. The remaining 3 participants marked Electrical and Electronics Engineering.

In the third question, 6 out of 285 participants selected A 1st Class, 5 B second class, 86 C third class and 188 D fourth class. The majority of the participants are senior students.

285 participants answered the fourth question. 68 participants selected A, 126 selected B, 80 selected C and 11 selected D. According to these results, the majority of the participants think that an industrial revolution has been made to increase production. Other participants considered improving machinery and society.

285 participants answered the fifth question. Twenty-two participants selected A, 76 selected B, 90 selected C and 97 selected D. Accordingly, the majority of respondents think there are 4 industrial revolutions.

285 participants answered the sixth question. 62 participants selected A, 17 selected B, 93 selected C and 113 selected D. According to this result, the majority of

participants perceived Industry 4.0 as an automated or robotic system. There are very few participants who know it as flexible production systems.

285 participants answered the seventh question. 50 participants selected A, 106 selected B, 59 selected C and 70 selected D. The majority of the participants considered B as Japan. In general, because Japan is considered as a city of technology, the participants chose this option. The right option is D, which is Germany.

285 participants answered the eighth question. 84 participants selected A, 85 selected B, 104 selected C and 12 selected D. The majority of the participants knew that Industry 4.0 is called Industry 4.0 in our country.

285 participants answered the ninth question. 96 participants selected A, 65 selected B, 102 selected C and 22 selected D. Accordingly, the majority of the participants thought that there were 8 subheadings. This is because they may have confused autonomous robots with industrial robots. Industry 4.0 has nine subheadings.

285 participants answered the tenth question. 48 participants selected A, 48 selected B, 152 selected C and 37 selected D. The majority of the participants have correctly understood what IOT systems mean. IoT is an important title of Industry 4.0. It is an important criterion for cognition level.
285 participants answered the eleventh question. 124 participants selected A, 56 selected B, 74 selected C and 31 selected D. Participants often ticked the correct option for Big Data and Cloud Computing. However, the second majority perceived and marked the artificial intelligence and expert system differently.
285 participants answered the 12th question. 91 participants selected A, 60 selected B, 111 selected C and 23 selected D. The majority of participants confused the Augmented Virtual Reality with the VR used from the game consoles. For this reason, option B is highlighted more. This is because the use of Augmented Virtual Reality or Virtual Reality samples in game consoles is often used in advertisements.
285 participants answered the thirteenth question. 162 participants selected A, 59 selected B, 24 selected C and 40 selected D. The majority of the participants think that it is beneficial to use Augmented Virtual Reality in education. The reason for this is that the generation of the participants is more inclined to visual education than written education.
285 participants answered the fourteenth question. 102 participants selected A, 56 selected B, 60 selected C and 67 selected D. It was understood that the majority of the participants knew what the meaning of the Autonomous Systems was.
285 participants answered the fifteenth question. 66 participants selected A, 43 selected B, 120 selected C and 56 selected D. Most of the participants think that Flexible Production will come from different materials on the same line. Accordingly, participants know the general meaning of Flexible Production correctly.
285 participants answered the sixteenth question. 29 participants selected A, 138 selected B, 65 selected C and 53 selected D. Participants answered the fact that the Dark

Factory is an unmanned factory with artificial intelligence, mostly by selecting the B option.

285 participants answered the seventeenth question. 70 participants selected A, 114 selected B, 56 selected C and 48 selected D. Participants showed the industrial level of our country by mostly selecting B option. Industry of our country is at 3.0 level. Work and support for Industry 4.0 is ongoing.

285 participants answered the eighteenth question. 147 participants selected A, 48 B, 42 C and 48 D. The majority of the participants considered Industry 4.0 necessary for our country.

285 participants answered the nineteenth question. 105 participants selected A, 84 selected B, 42 selected C and 54 selected D. Participants saw both industry 4.0 and automation systems differently. The new revolutionary name for automation systems is industry 4.0. It is also confused with the word meaning of automation with autonomy.

285 participants answered the twentieth question. 107 participants selected A, 90 selected B, 43 selected C and 45 selected D. With the effect of the artificial intelligence captured in the science fiction films, the majority of the participants both supported this idea and cast undecided votes.

285 participants answered the twenty-first question. 62 participants selected A, 92 selected B, 74 selected C and 57 selected D. Participants made approximately marking each other in the options. But the majority confuses robot 4.0 with industry.
285 participants answered the twenty-second question. 95 participants selected A, 65 selected B, 102 selected C and 23 selected D. The participants decided that there was a 75% difference between the new industrial revolution and the old revolution.

285 participants answered the twenty-third question. 65 participants selected A, 84 selected B, 71 selected C and 65 selected D. Participants mostly chose the C option because the name of the problem and the similar name in the options. However, the number of participants who know machine learning properly is high.

285 participants answered the twenty-fourth question. 65 participants selected A, 113 selected B, 67 selected C and 40 selected D. Participants perceived Predictive Care as literally disconnecting the system and performing maintenance. Predictive maintenance, however, is the artificial intelligence that constantly checks the machine and decides the failure state in advance.
285 participants answered the twenty-fifth question. 125 participants selected A, 71 selected B, 28 selected C and 61 selected D. Participants see the course content close to Industry 4.0.

IV.   CONCLUSION

The majority of the students in the survey were Mechanical Engineering students. Industrial 4.0 British electrical-electronic and computer engineering designs were made. However, Mechanical Engineering is the unit to design and produce a mechanical integrated project that will be controlled by software and electronic hardware innovations. For this reason, mechanical engineering constitutes the main body of industry 4.0 within the engineering fields. Because all innovations will be integrated on the machines. The important result reached in the survey is that the industrial 4.0 cognition level of the students who continue their education in the developing city of Konya and the developing city of Afyonkarahisar is the same. In the survey, it was observed that the participant students did not fully understand the concepts of Industry4.0 in general. In order to prevent this situation, they can be solved by seeing a course on contemporary technologies related to them in all engineering branches starting from the first year. The adaptation process is prolonged when an engineer candidate who does not know or follow current technologies is graduated. The company, which does not have a competent engineer, is also difficult to progress. Explaining some courses with Augmented Virtual Reality for the best learning by Industry 4.0 students will change the perspective and level of cognition. At this point the faculties will have improved themselves. In a country where education develops, production increases and welfare level rises accordingly. Industry 4.0 is a necessary phenomenon for our country. The level of cognition of current engineer candidate students should always be high.

V.   REFERENCES

[1] Şahman, H., (2017) Bal Sağım Ünitesinin Endüstri 4.0 Yardımıyla Modernizasyonu ve Analizi, Yüksek Lisans Tezi, Afyon Kocatepe Üniversitesi Fen Bilimleri Enstitüsü, Afyonkarahisar.

[2] Sauza Bedolla, Joel & D'Antonio, Gianluca & Paolo, Chiabert. (2017). A Novel Approach for Teaching IT Tools within Learning Factories. Procedia Manufacturing. 9. 175-181. 10.1016/j.promfg.2017.04.049.

[3] Benešová, Andrea & Tupa, Jiri. (2017). Requirements for Education and Qualification of People in Industry 4.0. Procedia Manufacturing. 11. 2195-2202. 10.1016/j.promfg.2017.07.366.

[4] Suárez Fernández-Miranda, Susana & Marcos-Bárcena, Mariano & Peralta, María Estela & González, Francisco. (2017). The challenge of integrating Industry 4.0 in the degree of Mechanical Engineering. Procedia Manufacturing. 13. 1229-1236. 10.1016/j.promfg.2017.09.039.

[5] Mourtzis, Dimitris & Vlachou, Katerina & Dimitrakopoulos, George & Zogopoulos, Vasilios. (2018). Cyber- Physical Systems and Education 4.0 –The Teaching Factory 4.0 Concept. Procedia Manufacturing. 23. 129-134. 10.1016/j.promfg.2018.04.005.

[6] Mayer, Barbara & Rabel, Birgit & Sorko, Sabrina Romina. (2017). Modular Smart Production Lab. Procedia Manufacturing. 9. 361-368. 10.1016/j.promfg.2017.04.025.

HYDROGEOCHEMICAL PROPERTIES AND POLLUTABILITY OF NATURAL WATER RESOURCES IN WEST OF KONYA

GülerGöçmez[1] and Sarah Fakhrulddın Ahmed[2]

[1,2]Konya Technical University, Faculty of Engineering and Natural Sciences, Department of Geological Engineering, Konya, Turkey

ggocmez@ktun.edu.tr. sara92can@gmail com

*Abstract-*Freshwater resources are located in the west of Konya and about 6 km away (Figure 1). Beypınarı and Mukbil resources were closed during AlaaddinKeykubat period. Dutlu spring catchment was built by Yavuz Sultan Selim in the 16th century, and Çayırbağı spring catchment was built in 1902 by Konya Governor FeritPaşa. Spring water has been transported to the city center by pipes in order to meet the water needs of the city. Since 1990, the water of the spring has been given to 1000 fresh water fountains.

In recent years, the structure of the resources within the feeding area, social areas, ring road works and unimposed settlements affect the resources and cause water pollution. Spring water temperatures 14-16 oC, flow rates 1.5l / s-51,l / s, pH 7.72-8.67 hardness 16-19 Fs, Total dissolved matter amount is between 188-324 mg / l. The aquifer of the waters is Upper Cretaceous Çayırbağı ophiolite and Hatip ophiolite complex and Lorasdağılimestones. Water is rich in Ca, Mg and HCO_3 ions. In the hydrochemical analyzes, Nitrate is between 3.52-10.44 mg / l, boron 25-66.5 mg / l, chromium is between 2.91-3.55 mg / l and is above the limit values.. Due to the high permeability of the units around the springs and the absence of a protective covering layer on the aquifer layer, all kinds of pollutants reach the source waters directly and cause the water pollution. Protected areas around the welds and the precautions to be taken should be followed and construction within the feeding area of the welds should not be allowed.

Keywords **- Konya, Source, Pollution, Catchment, aquifer.**

I. INTRODUCTION

Fresh water resources are located to the west of Konya and about 6 km away (Figure 1). In order to meet the water needs of the city in 1900, the water was transferred to the warehouses in the city center. Today, it is used in the city center from around 1000 fresh water fountains.

In recent years, low rainfall has caused ground water levels to decrease and resource flow rates to decrease. In addition, the beginning of construction around the resources, the creation of picnic areas, garbage waste areas, and the continuation of mining activities threaten the future of resources in terms of pollution. In this study, the hydrochemical properties and contamination of fresh water resources were aimed. Studies in and around the study area were conducted [1], [2], [3] . Conserving resources and feeding area against all kinds of pollution is very important for the future of Konya .

Figure 1:Locatıon map in the study area

II. GEOLOGY AND HYDROGEOLOGY

At the bottom of the study area is Kızılören formation consisting of Upper Permian - Upper Triassic carbonate rocks. This formation is overlain by the Upper Triassic-Upper Cretaceous aged, the Lorasdağı formation and the Upper Cretaceous aged radiolarite and chert intercalated limestones. These units are tectonically overlain by Upper Cretaceous Hatip ophiolite mixture and two mappableolistoliths which are mappable in size. The units continue with an angular unconformity with the Sille formation, the Ulumuhsine formation made of lacustrine limestone and crumbs, and the Küçükmuhsine formation consisting of tuff, tuffite and volcanic brest. These formations cover the Lower Pliocene aged Yürükler formation consisting of conglomerate, sandstone and conglomerate with angular unconformity. All these units are Upper Pliocene -It is covered by Quaternary aged soil formation[4], [5],

and current alluvial deposits.

The aquifer of the waters is Upper Cretaceous Çayırbağı ophiolite and Hatip ophiolite complex and Lorasdağı limestones. The groundwater flow direction in the study area is north-west to southeast, west-east to west, and south-north to the south.

There are 5 fresh water springs in the study area. Beypınarı and Mukbil sprıng were catchments Alaaddin Keykubat period. The Dutlu spring was built by Yavuz Sultan Selim in the 16th century, while the Çayırbağı spring was built by the Governor of Konya Ferit Pasha in 1902. Spring water has been transported to the city center by pipes in order to meet the water needs of the city. Since 1990, the water of the spring has been given to 1000 fresh water fountains. Spring water temperatures 14-16 °C, flow rates 1.5 l /s -51,l / s, pH 7.72-8.67 hardness 16-19 Fs, Total dissolved matter amount is between 188-324 mg / l. The aquifer of the waters is Upper Cretaceous Çayırbağı ophiolite and Hatip ophiolite complex and Lorasdağı limestones.

Beypınarı spring (K1) and Mukbil spring (K2) are discharged from the Mesozoic aged Çayırbağı ophiolites on the western slope of the Beypınarı stream. The water of the springs is taken by the galleries opened into the Çayırbağı ophiolites. Spring waters are rich in Ca $^{++}$, Mg $^{++}$ and HCO$_3$ $^=$ ions.

The Çayırbağı spring (K3) is discharged from the serpentines in the stream bed to the west of Çayırbağı settlement center to the south of the investigated area. The water of the source is rich in Mg HCO$_3$ ions.

Dutlukırı spring (K4) is discharged from limestones in Hatip ophiolite complex. The water of the spring is taken by the catchment in the stream bed to the east of the lime kiln. Spring water is rich in Mg, Ca HCO$_3$ ions

. Kırankaya Spring (K5) The chromium magnesite is taken from the Çayırbağı ophiolites near the mine site, and the spring water is rich in Mg and HCO$_3$ ions (Table 1).

III. HYDROCHEMISTRY AND POLLUTION

Fresh water sources are used as drinking water. In recent years, the structure of the resources within the feeding area, social areas, environmental road works and unimposed settlements affect the resources and cause the pollution of the spring water. Due to the high permeability of the units around the springs and the absence of a protective covering layer on the aquifer layer, all kinds of pollutants reach the source waters directly and cause the water pollution.

Physico-chemical analyzes of water samples collected periodically from the sources to determine the hydro-chemical properties and contaminants of the sources have been performed and the results obtained by performing bacteriological analyzes in the Water Chemistry Laboratory of Konya Metropolitan Municipality have been interpreted. The waters are rich in Ca ++, Mg ++, HCO3 = ions. In our country, French hardness degree is used. The hardness of spring waters is between13-17(Fs) and it is soft-medium hardness.

According to the Schoeller diagram, the lines connecting the ions pass close and parallel to each other and the waters are of the same origin (Fıgure2) [6],. According to the Piper diagram it falls to the 5th zone. According to this, the waters are CaCO3 and MgCO3 and are in the group of waters with a carbonate hardness of more than 50% (Fıgure3) [7],

Tablo 1: hydrochemical analysis of spring waters

Ions	K1	K2	K3	K4	K5
Ca^{++}	6.72	4.28	6.54	25.12	8.04
Mg^{++}	35.23	34.66	31.24	26.68	27.71
Na$^+$	10.08	1.62	1.68	2.33	0.96
K$^+$	1.45	<0.5	0.95	<0.5	0.4
Cl$^-$	9.43	2.30	3.40	4.76	1.85
SO$_4^-$	2.82	3.26	3.04	6.44	1.84
HCO$_3^-$	96.82	111.86	122.20	152.75	123.14
CO$_3^-$	59.22	48.88	39.48	33.84	23.50
NO$_3$	3.56	3.66	6.49	10.67	5.41
Hg	0.07	<0.07	<0.07	-	-
B	18.51	19.32	24.70	23.50	24.46
AL	12.5	<12.5	<12.5	<12.5	<12.5
As	18.51	<1	<1	<1	<1
Cd	0.5	<0.5	-	<0.5	-
Cr	2.78	2.04	2.86	3.09	2.19
Cu	2	<2	<2	<2	<2
Fe	9	-	<9	<9	10.69
Mn	1	<1	<1	<1	<1
Sb	0.5	-	-	-	-
Temprature	14	15	16	15	14
Ph	8.73	8.71	8.52	7.70	8.49
Ec	292.00	262.00	280.0	337.00	245.00
Tçm	260.00	136.00	256.00	324.00	228.00
Fs	16	15	14	17	13
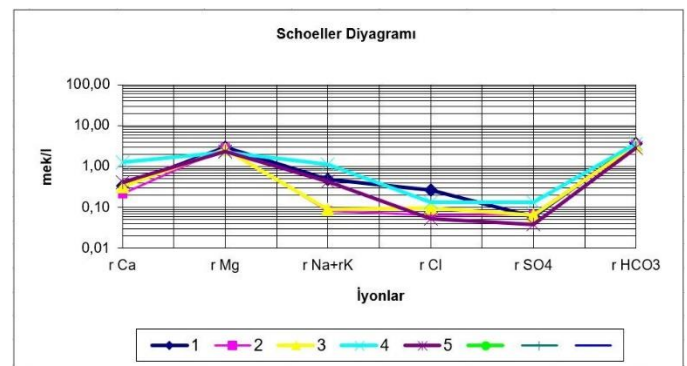
Fıgure 2. Schoeller diagram of waters in the study area
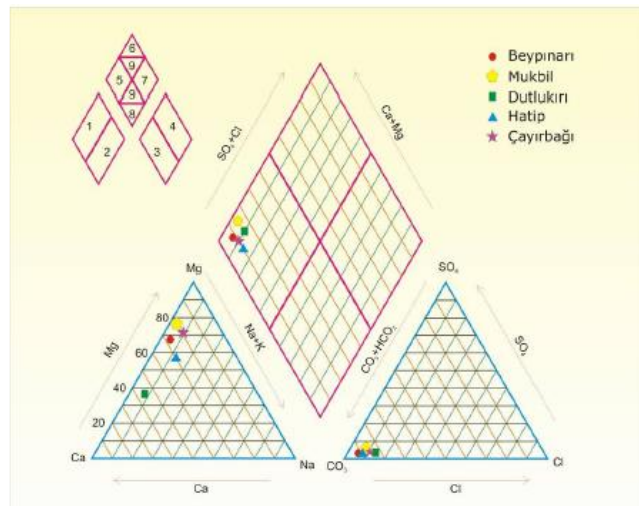
Fıgure 3. Piper diagram of waters in the study area

Table 2. WHO and USEPA drinking water standards

Parameter	WHO 2006 (ppm)	USEPA 2006 (ppm)
Al	0,2	0,2
As	0,01	0,01
Cu	2	1,3
Fe	0,3	0,3
Cd	0,003	0,005
Pb	0,01	0,015
Mn	0,4	0,05
pH	6,5-8,5	6,5-8,5

When the results of physicochemical analysis of spring waters were evaluated according to WHO and USEPA drinking water standards, Al, Cu, Fe, Mn, As values were found to be above the limit values (Table 2).

Beypınarı in bacteriological analysis of spring waters. Dutlu and Çayırbağı Kırankaya sources are thought to be the reason for the presence of bacteria as a result of fattening activities carried out in the resource environment.

IV.CONCLUSION

In recent years, there is little rainfall in the area. Lack of precipitation causes groundwater level to decrease and the flow rates of resources decrease. Due to the high permeability of the units around the springs and the absence of a protective covering layer on the aquifer layer, all kinds of pollutants reach the source waters directly and cause the water pollution. In addition, the structures within the feeding area of the resources, social areas, ring road works and unimposed settlements affect the resources and cause pollution of the source water and threaten the future of the resources. In the physicochemical analyzes, Nitrate is between 3.52-10.44 mg / l, boron 25-66.5 mg / l, chromium is between 2.91-3.55 mg / l and is above the limit values. precautions should be followed and construction within the feeding area of the resources should not be allowed.

REFERENCES

[1] Göçmez.G., Güzel. A., Çayırbağı- Hatip-Beybes-Kozağaç (Konya) yöresinin Hidrojeoloji İncelemesi. Ahmet Acar Jeoloji Sempozyumu bildiriler s.125-134.1991

[2] Özdemir A, A., Aydın. ME., Chemical properties of groundwater in the Konya residential area. 1998.

[3] Öztürk. A.,Baykal, A., Hatıp-çayırbağı (Meram-Konya) bölgesinde yüzeylenen ofiyolitik kayaçlarda jeofizik yöntemlerle ağır ve kıymetli metal aranmasıS.Ü. Müh.- Mim. Fak. Derg., c.27,s.4, 12.2012

[4] Eren Y., Eldeş – Gökçeyurt – Derbent (Konya Kuzeybatısı) Dolaylarındaki Kocaçaldağı Yükseltisinin Jeolojisi, S.Ü. Araştırma Fonu, Proje No: 88-026. 1993.

[5] Ekdur. E. Konya Batısındaki tatlı su kaynakları çevresinin jeoloji- hidrojeoloji ve izotopik incelemesi. S.Ü.Fen Bilimleri Enstitüsü Yüksek Lisans tezi. 104 s.(Yayınlanmamış).2008

[6] Schoeller, H., , Les eaux souterraines masson et cie Paris (Çeviren, Karadağ, K.,1973) Yeraltı sulan Matbaası) İstanbul.1962.

[7] Piper, A.M..A Grafhic procedure in the geochemical interretation of water analyses .Transaction, American Geophysical Union 25:914-23.1944

[8] Erguvanlı. K, Yüzer. E.~, Yeraltısuları Jeolojisi (Hidrojeoloji),İstanbulTeknikÜniversitesi,Yayın No:23, İstanbul, Nisan 1987.

[9] WHO, Guidelines for Drinking-Water Quality Vol 2. (Health Criteria and Other Supporting Information) Geneva, 1984.

[10] USEPA (2006) Current Drinking Water Standards, , http://www .USEPA National Drinking Water Standards. htm, Erişim Tarihi: 22.07.2007.

Improving the Tribological Resistance of Inconel 600 Alloy by Electrodeposition

H.MINDIVAN[1]

[1]Bilecik Seyh Edebali University, Bilecik/Turkey,:hmindivan@gmail.com

Abstract - **An electrodeposition process was performed to improve the tribological resistance of Inconel 600 alloy. Nickel (Ni) coating was electrodeposited on Inconel 600 alloy from a Watts electrolyte. The microstructure of the coating was investigated using SEM and XRD. The mechanical property of Ni coating was studied by microhardness tester. The tribological behavior of Inconel 600 alloy and pure Ni coating was revealed, using a reciprocating ball-on-plate tribometer. Pure Ni coating exhibited a distinctly low friction coefficient and a small wear rate as contrasted with Inconel 600 alloy.**

Keywords – **Coating, Electrodeposition, Inconel 600 alloy, Nickel, Tribology.**

I. INTRODUCTION

Nickel-base superalloys are widely used in a variety of fields including aircraft, automobile and chemical industries due to their good plastic, fatigue and corrosion properties [1, 2]. In contrast to their superior chemical and mechanical stability at high operating temperatures, poor wear performance limits the practical use of superalloys as sliding components under dry sliding conditions. In this respect, protection of the surfaces by a coating appears an essential role for enhancing the wear performance of superalloys [2]. Among the coating techniques, electrodeposition is one of the most convenient approaches available in producing coatings used in applications requiring high resistance to friction and wear [1]. In this regard, one of the non-expensive wear-resistant coatings is pure nickel (Ni) based coating. This kind of coating has a wide range of application in different industries such as military, aviation, automotive, marine, instrumentation, medical industries, etc. [3].

In this paper, pure Ni coating was electrodeposited on Inconel 600 alloy from a Watts electrolyte to evaluate their properties from the view of tribological properties at room temperature as contrasted with the Inconel 600 alloy.

II. EXPERIMENTAL PROCEDURE

Pure Ni coating were electroplated with a current density of 2 A/dm^2 in an electrolyte containing 300 g/L $NiSO_4.6H_2O$, 60 g/L $NiCl_2.6H_2O$ and 30 g/L H_3BO_3. The pH of solution which measured with pH tester. Deposition time was fixed at 90 min and temperature was kept constant during the experiment at 40°C. The cathode used in this study was made of disc-shaped Inconel 600 alloy sheet while a nickel plate (~99.99 % purity)

was employed as soluble anode. Before plating, the substrate surface was mechanically polished with abrasive paper and then were degreased in an alkaline solution containing 30 g/L NaOH and 20 g/L Na_2CO_3 for 5 min and then etched with $HCl:H_2O=2:1$ for 4 min. Prior to final electrodepositing, pre-electrodeposited with a current density of 2 A/dm^2 in a solution of 200 ml/L HCl and 200 g/L $NiCl_2.6H_2O$ for 4 min.

Phase analysis and surface morphology of pure Ni coating were determined by X-Ray Diffraction (XRD) and Scanning Electron Microscope (SEM), respectively. The thickness of the deposited coating was measured by the Nikon Eclipse LV150 Light Optical Microscope (LOM). Hardness measurement in the cross-section of coating was conducted on a Shimadzu HMV2 microhardness tester by applying an indentation load of 25 g with a Vickers indenter.

Friction and wear tests were performed by using a reciprocating ball-on-plate tribometer against a 10 mm Al_2O_3 ball. The tests were carried out under the following conditions: a load of 5 N, a sliding speed of 1.7 cm s^{-1}, a sliding stroke of 12 mm on the plate and a duration time of 45 min for wear tests under dry sliding conditions. All tests were conducted in laboratory air, and the test atmosphere has a relative humidity of 50 % at room temperature. The wear tracks after sliding tests were examined by using a surface profilometer (Surftest SJ 400). The wear of the Al_2O_3 balls was evaluated by a LOM examination of their contact surfaces. To evaluate wear mechanisms, wear tracks were further studied using a SEM.

III. RESULTS AND DISCUSSION

The surface and cross-section morphologies of pure Ni coating are illustrated in Figure 1. The pure Ni coating exhibited irregular polyhedral crystals on the top surface. The thickness of the pure Ni coating was about 17 μm.

Figure 2 displays the XRD patterns of the Inconel 600 alloy and pure Ni coating. It can be noticed that low-intensity Inconel 600 alloy substrate peaks could be identified from the pure Ni coating in the as-deposited state as consequence of the high intensity of Ni diffraction peaks corresponding to pure Ni deposition with crystallographic planes of (111), (200), (220).

(a)

(b)
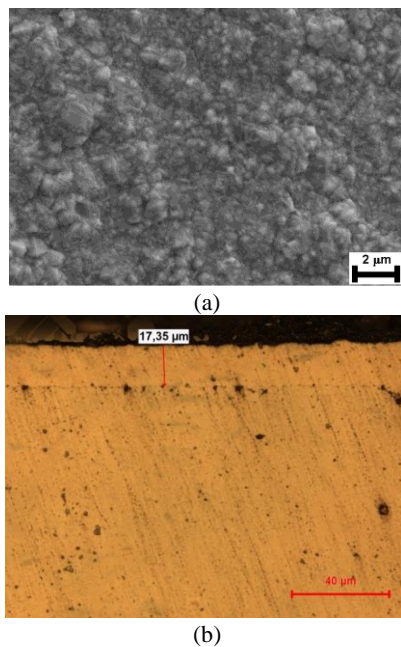
Figure 1: (a) Surface and (b) cross-section morphologies of pure Ni coating.
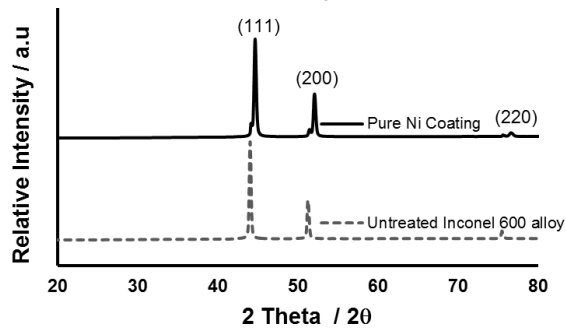
Figure 2: XRD patterns of the Inconel 600 alloy and pure Ni coating.

The friction coefficients vs sliding distance curves of the Inconel 600 alloy and pure Ni coating are shown in Figure 3. Clearly, the friction coefficient of the pure Ni coating was distinctly lower than that of the Inconel 600 alloy. The stable friction coefficient of the Inconel 600 alloy was about 1.3-1.5 while it was 0.4–0.5 for pure Ni coating. As can be seen from Fig. 3, the sliding curves of the untreated Inconel 600 alloy exhibited larger fluctuation than the pure Ni coating. The wear rate of the pure Ni coating was 2.47×10^{-5} mm^3/Nm, which was much smaller than that of Inconel 600 alloy (63.7×10^{-5} mm^3/Nm) under identical wear condition.
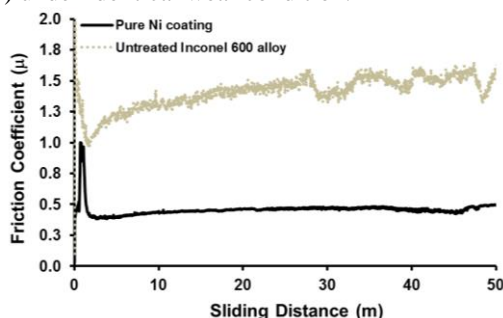
Figure 3: Relationships of coefficient of friction against sliding distance for the Inconel 600 alloy and pure Ni coating.

Figure 4 presents the SEM micrographs of the worn surfaces of the untreated Inconel 600 alloy and pure Ni coating generated through testing at a normal load 5 N. Obviously, the wear track width for the pure Ni coating (Fig. 4 (b)) was much narrower than that of the untreated one (Fig. 4 (a)). The difference observed in the width of wear tracks between the Inconel 600 alloy and pure Ni coating showed that the pure Ni coating prevented the expansion of wear due to increased hardness of the pure Ni coating compared with the Inconel 600 alloy. The Inconel 600 alloy had a microhardness of 220 ± 9 HV$_{0.025}$. The microhardness value of electrodeposited pure Ni coating was 282 ± 19 HV$_{0.025}$. From higher magnification of Fig. 4 (a), a large extent of plastic deformation and severe adhesive wear was observed on the worn surface of the Inconel 600 alloy, which resulted in large wear rate, high friction coefficient and large fluctuation in the sliding curve of the untreated Inconel 600 alloy. The worn surface of pure Ni coating shown in Fig. 4 (b) exhibited shallower furrows and slight scratches, which can be characterized as slight abrasive and adhesive wear.

(a)

(b)
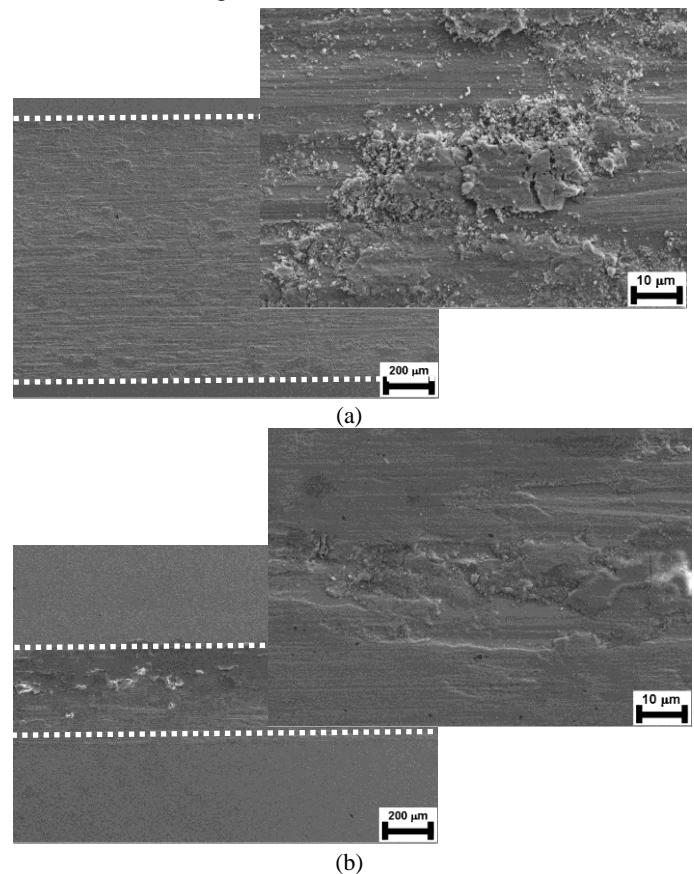
Figure 4: Low and high magnification SEM micrographs of the worn surfaces of (a) the untreated Inconel 600 alloy and (b) pure Ni coating against an Al$_2$O$_3$ ball in a reciprocating wear test.

Figure 5 shows the morphologies of the wear tracks on Al$_2$O$_3$ balls after the friction test. The Al$_2$O$_3$ ball displays a smaller wear track after sliding against pure Ni coating than sliding against the Inconel 600 alloy. This may be related to the increased hardness in the coating, which can reduce the wear of coating.

(a)

(b)
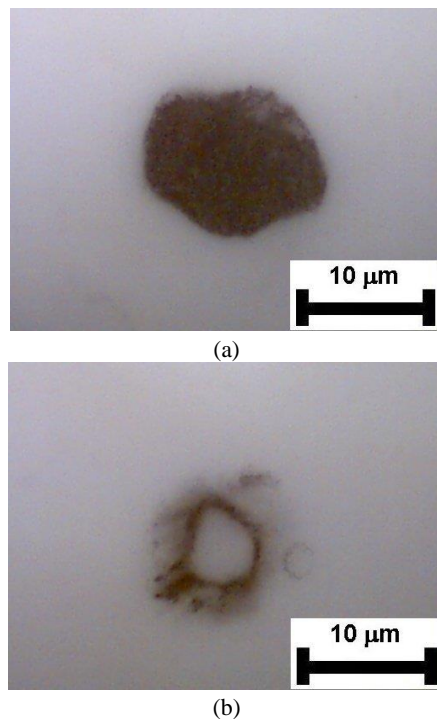
Figure 5: Morphologies of the Al_2O_3 balls after sliding test against (a) Inconel 600 alloy and (b) pure Ni coating.

IV. CONCLUSION

The following conclusions can be drawn:

-After the electrodeposition, the microhardness measured on the outer surface of Inconel 600 alloy increased from 220 ± 9 $HV_{0.025}$ to 282 ± 19 $HV_{0.025.}$

-The electrodeposition resulted in the formation of a dense and uniform Ni coating layer with thickness of ~17 μm on the surface of Inconel 600 alloy.

-The results of the wear tests indicated that the stable friction coefficient of the pure Ni coating was lower than that of the Inconel 600 alloy.

-The wear rate of the pure Ni coating decreased remarkably compared with that of the untreated one. The wear mechanism for the pure Ni coating was a slight abrasive and adhesive wear.

REFERENCES

[1] X.S. Liang, J.H. Ouyang, Y.F. Li, Y.M. Wang. (2009). Electrodeposition and tribological properties of Ni-SrSO₄ composite coatings. *Appl. Surf. Sci*. 255. pp. 4316–4321.

[2] T. Borowski, A. Brojanowska, M. Kost, H. Garbacz, T. Wierzchon. (2009). Modifying the properties of the Inconel 625 nickel alloy by glow discharge assisted nitriding. *Vacuum*. 83. pp. 1489-1493.

[3] Z. Mahidashti, M. Aliofkhazraei, N. Lotfi. (2018). Review of nickel-based electrodeposited tribo-coatings. *Trans. Indian. Inst. Met*. 71. pp. 257-295.

An Investigation on Roll-in Formation in Hemming Operation

Selim GÜRGEN

Eskişehir Vocational School, ESOGU, 26110, Eskişehir, Turkey, sgurgen@ogu.edu.tr

Abstract - **Roll-in formation, which is an inward motion of hemming line, is an inevitable phenomenon in roller hemming operations. Therefore, it results in a visual defect along the closures on the products. However, it can be controlled by tuning the process parameters such roller diameter, flange height, hembed overhang and bending angles. Tailoring the bending angles in roller hemming process is one of the most important method to overcome excessive roll-in formations. Restricting the roll-in formation in curved regions is highly tedious in comparison to straight edge parts. For this reason, a curved edge model was built and roll-in formation in this geometry was investigated in the presented study. A bake hardening steel, BH220, was selected for the hemming components and the material data was taken from the software library. BH220 is extensively used in automotive industry especially in the automobile skins. Three different bending angle pairs were selected to close the flange angle of 100° in a two-stage roller hemming process. A 15 mm diameter cylindrical roller was utilized in the designed operation. Based on the results, it is better to divide the flange angle into equal amounts to complete the hemming process because this lowers the accumulated strains in the hemming zone and thereby avoiding sudden fracture due to excessive plastic deformation. For this reason, the bending angle pair of (50°/50°) yields the minimum roll-in values since the flange angle was 100° in our numerical work. For the (50°/50°) process, the roll-in values were found as 0.254 mm and 0.284 mm after the pre-hemming and final hemming respectively.**

Keywords - **Hemming, roll-in, metal forming.**

I. INTRODUCTION

ROLLER hemming process has been widely utilized in automotive industry due to its flexible manufacturing advantages [1]. This process consists of folding of outer sheet metal onto inner sheet metal. The folded section of outer metal sheet is called flange [2]. Flange is formed by a previous operation namely flanging. In general, doors, sunroofs, hoods, tailgates and wheel arches are benefited from roller hemming operation in automotive industry. Since these parts make up the exterior of automobiles, roller hemming is highly important for visual appearance. One of the most common defects is excessive roll-in formation in the components. Roll-in is defined as a displacement of hemming line toward part center. In the excessive roll-in cases, the gap between the doors or in the other automobile components becomes wider which results in a low visual quality [3]. In order to minimize roll-in formation, different approaches are tried in the industry such as optimizing roller diameter or roller geometry.

Optimization of bending angles is another method to keep roll-in values at lower levels. In the present study, roll-in formation in the roller hemming operation of a curved part was investigated. The study was carried out using a numerical approach and bending angle pairs in a two-stage roller hemming process was analyzed. In the numerical model, flange angle was 100º and three bending angle pairs such as (40º/60º), (50º/50º) and (60º/40º) were utilized to close the flange onto the inner sheet metal. Roll-in measurements were conducted from the mid-point of the part and each roll-in value was reported both after pre-hemming and final hemming stages. According to the results, roll-in formation becomes pronounced by increasing the bending angle in the operation. Therefore, equal bending angles such as (50º/50º) to close the flange angle of 100º are required to minimize the roll-in values in the process.

II. NUMERICAL MODELING

In this work, a curve geometry was created as seen in Figure 1. As seen in the figure, the numerical model consists of four components which are outer, inner, flange and hembed. Flange is the folded edge of the outer which has a height of 5 mm. Flange angle, which is the angle between flange and outer, is 100° in the model. The thickness of the parts is 0.5 mm and the material is BH220, which was modeled using power law plasticity model, for the flange and outer. The material data was supplied from LSTC material library. The inner, hembed and roller were modeled as rigid since there is no deformation in these components. In the analyses, two-stage process was designed by using the bending angle pairs as (40º/60º), (50º/50º) and (60º/40º) for closing the flange angle of 100°. To close the flange onto the inner, a 15 mm diameter roller was utilized. Shell elements were utilized in the modeling and adaptive remeshing option was enabled to increase the accuracy. Explicit time scheme was used in the simulations.
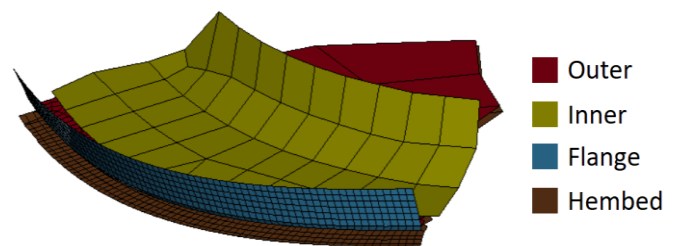
Figure 1: Numerical model and components.

III.   RESULTS AND DISCUSSION

Figure 2 shows the deformation of flange after pre-hemming stage of the (50º/50º) process. As seen in the image, the flange is folded onto the inner and therefore, hemming line moves inward and consequently roll-in formation is seen in the flange. Figure 3 shows the schematic illustration of roll-in. In this study, roll-in formation along the hemming line was investigated. Figure 4 shows the roll-in values for pre-hemming and final hemming stages. From this chart, it can be mentioned that roll-in increases as the bending angle increases in the pre-hemming stage. Because hemming line exhibits a sharp motion toward the center of the components due to enhanced bending. On the other side, the increase in the roll-in values decelerates from (40º/60º) to (60º/40º) process in the final hemming stage. This is due to the lower remaining opening angle as the bending angle increases in the pre-hemming stage. However, considering the final roll-in values, it is seen that (50º/50º) process yields the minimum roll-in value amongst the investigated processes. This is associated to the equal dividing of the flange angle of 100º. Therefore, it is possible to state that in order to keep the roll-in values low, flange angles should be divided into two equal parts for two-stage hemming operations.
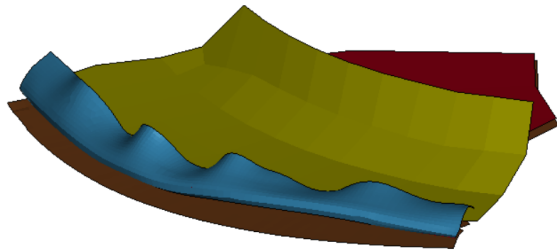
Figure 2: Deformation of flange after pre-hemming stage of the (50º/50º) process.
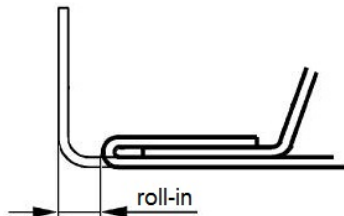
Figure 3: Schematic illustration of roll-in [4].

IV.   CONCLUSIONS

In the present work, roll-in formation in roller hemming operation was investigated. A curved geometry, which simulates the corner regions on automobile parts, was selected in the numerical simulations. A two-stage process was designed including one pre-hemming and one final hemming stage. Bending angle pairs were varied in the operation to close a flange angle of 100º. According to the results, roll-in values increase by increasing the bending angle in the hemming process. For this reason, it is better to divide the flange angle into equal parts to complete the operation. Therefore, the bending angle pair of (50º/50º) yields the

minimum roll-in formation amongst the investigated ones since the flange angle was 100º in our geometry. For the (50º/50º) process, the roll-in values are 0.254 mm and 0.284 mm after pre-hemming and final hemming respectively.
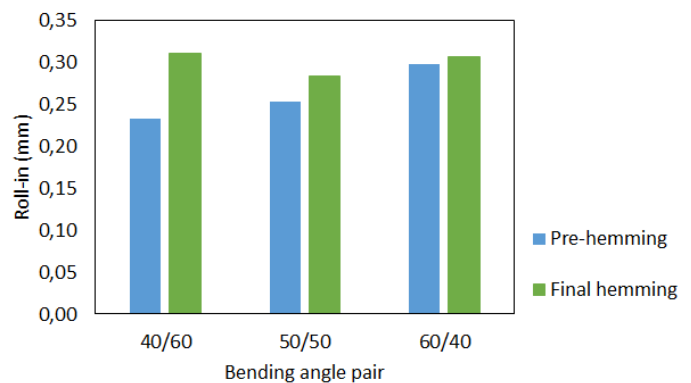
Figure 4: Roll-in values in the operations.

REFERENCES

[1]   S. Gürgen, Numerical simulation of roller hemming operation on convex edge-convex surface parts, Advanced Engineering Forum, 15, 75-84, 2016.
[2]   B. Jonkers, Simulation of the Robot Roller Hemming Process, University of Twente, Master Thesis, 2006.
[3]   S. Gürgen, A parametric investigation of roller hemming operation on a curved edge part, Archives of Civil and Mechanical Engineering, 19, 11-19, 2019.
[4]   S. Gürgen, M.İ. Gökler, H. Darendeliler, Ç.C. Çelikkaya, K. Erden, Analysis of roller hemming process for a vehicle tailgate closure, AIP Conference Proceedings, 367-374. 2013.

Spall Liner Composites for Armored Vehicles

Selim GÜRGEN

Eskişehir Vocational School, ESOGU, 26110, Eskişehir, Turkey, sgurgen@ogu.edu.tr

Abstract - **Spall liner is an essential protective structure in armored vehicles. This structure is designed for interior usage in the vehicles and protects the crew from spalling in case of penetrating threats. Spall liner systems use soft composites which are made from various kinds of high performance fibers. Soft composites also serve as interior lining for the vehicle as well as providing flexibility during an impact and thereby stopping the spalling from emission to the crew cabin. This study gives an overview of spall liner and utilized materials in this structure.**

Keywords - **Spall liner, high performance textiles.**

I.   INTRODUCTION

IN the design of armored vehicles, designers focus on the exterior design of the vehicles to protect the vehicle from the attacking threat. In order to do this, different types of armor are developed such as metallic, ceramic or composite based armor while increasing the protection level and reducing the areal density of the armor. Although armor designers work hard to improve the protection performance of the current systems, armored vehicles may be subjected to heavy attacks at which the projectiles perforate the vehicle armor and strike the crew inside the vehicle. In order to reduce the effect of perforating projectiles inside the vehicle, spall liner covers the interior walls of armored vehicles. Spall liner is not utilized to stop the projectile at all, the purpose of a spall liner is to restrain the emission of Behind Armor Debris (BAD) arising from the spalling of armor during projectile penetration stage and thus, the spall-affected area inside the vehicle is reduced. Figure 1 shows a schematic for the utilization of spall liner.
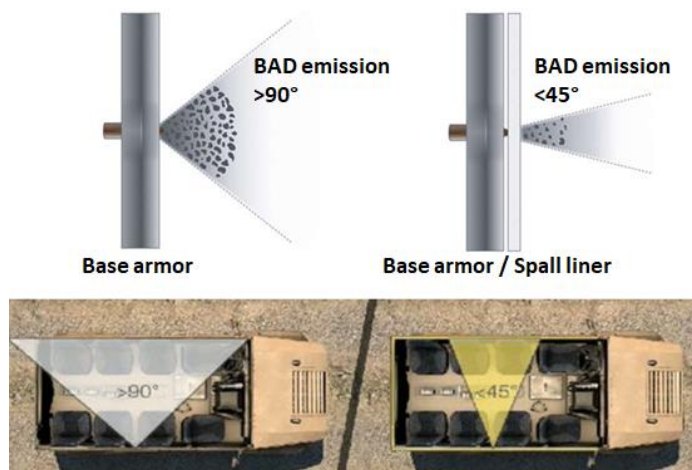
Figure 1: Effect of spall liner on BAD emission [1,2].

II.   MATERIAL SELECTION FOR SPALL LINER

Aramid is extensively utilized in protective applications due to its advanced properties. The best-known trademark amongst the aramid products is Kevlar. Aramid products were fabricated in 1960s and DuPont produced the first commercial product with the trademark of Kevlar in 1971. Apart from Kevlar, different commercial products made from aramid are now available in market such as Twaron, Technora and Nomex. Aramid fibers provide high modulus, advanced strength and improved toughness for the users. Furthermore, aramid is resistant to cutting which makes it an ideal material for spall liner applications. Aramid shows a thermal degradation at around 400°C [3] and therefore, it can serve under high temperature exposure. However, as temperature increases, mechanical properties of aramid have a loss of performance. For example, there is a 20% loss in strength at temperatures up to 180°C [2]. On the other hand, aramid is susceptible to ultraviolet light exposure. Another alternative material is ultrahigh molecular weight polyethylene (UHMWPE) for spall liner applications. Spectra Shield and Dyneema are the most known two commercial products made from UHMWPE in the market. This polymer has improved chemical and biological resistance as well as advanced fatigue strength and wear resistance [4,5]. Therefore, spall liner systems benefit from UHMWPE on a large scale. This product also provides very light structures because the density of UHMWPE is 0.93-0.97 g/cm³ whereas it is 1.41-1.44 g/cm³ for aramid. Another advantage of UHMWPE is excellent chemical resistance. UHMWPE is resistant to acidic medium and therefore, products made of UHMWPE can be utilized in acidic environments without heavily compromising the strength. The most important drawback is limited processing temperature for UHMWPE which is around 120°C [2]. Because of the lower temperature requirement, UHMWPE systems have a small number of matrix choice which can be cured at low temperatures. S-glass is also extensively utilized in spall liner applications as well as other protective systems. Aircraft or advanced building applications also take advantage of the mechanical properties of S-glass. This material has a typical composition of 65wt% SiO_2, 25wt% Al_2O_3 and 10wt% MgO. In comparison to E-glass, S-glass provides 40% higher strength which makes this material favorable for high tensile applications. Beside tensile strength, S-glass has a significant fatigue performance as well as considerable creep resistance. Fibers made from polybenzobisoxazole (PBO) are another alternative for spall liner applications. PBO fibers have advanced tensile strength and for this reason, they have high impact performance in comparison to UHMWPE fibers. However, PBO is lack of an improved compressive strength. Zylon is the most known commercial product in the market for

the utilization within various protective structures. Temperature effect on PBO is slightly lower than aramid because the decomposition point of PBO is around 550°C which is quite higher with respect to that for aramid [2].
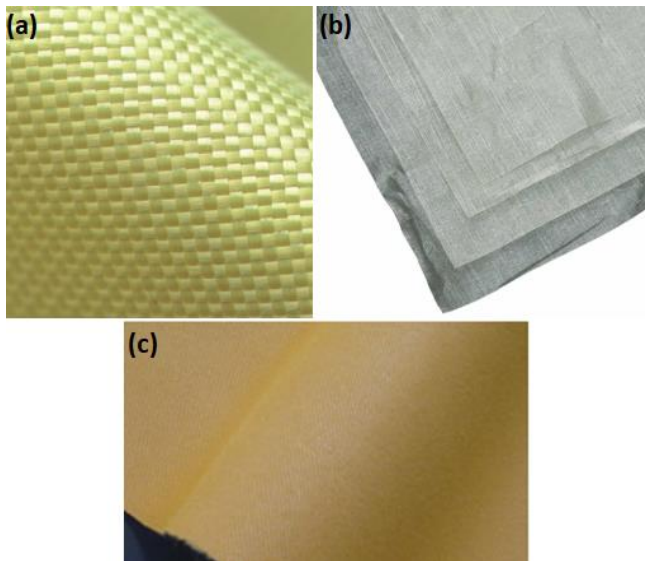
Figure 2: Spall liner materials (a) aramid [6], (b) UHMWPE [7] and (c) PBO [8].

III. CONCLUSIONS

Spall liner is an important component in armored vehicles since it ensures the protection of crew in the vehicles. Due to low weight and advanced protective properties, high performance textiles are extensively preferred for spall liner applications. Main textiles for spall liner systems are made from aramid, UHMWPE, glass fibers and PBO in the market. These materials exhibit different advantages over each other however, all of them are beneficial to the protective performance of spall liners.

REFERENCES

[1] https://www.defence-industries.com, last access: 25 June 2019.
[2] Y. Erbil, A.K. Ekşi, D.A. Bircan, Spall Liner: From Fiber to Protection, 6th International Advanced Technologies Symposium, Turkey, 378-382, 2011.
[3] M.I. Sarwar, S. Zulfiqar, Z. Ahmad, Organic–inorganic nanocomposites prepared from fluoro-aramid and silica, Colloid and Polymer Science, 285, 1733-1739, 2007.
[4] R.A. Scott, Textiles for protection. Cambridge: Woodhead Publishing; CRC, 2005.
[5] S. Gürgen, High Performance Fabrics in Body Protective Systems, Materials Science Forum, 880, 132-135, 2016.
[6] https://www.teijinaramid.com, last access: 03.07.2019.
[7] https://www.dsm.com, last access: 03.07.2019.
[8] https://www.toyobo-global.com, last access: 03.07.2019.

Evaluation of the F2 Peak Parameter (hmF2) Prediction Performance of IRI-2016 Model

S. ALCAY[1]

[1] Necmettin Erbakan University, Konya/Turkey, salcay@erbakan.edu.tr

Abstract – **This study aims to validate the height of F2 peak (hmF2) prediction performance of IRI-2016 model using AMTB2013 and SHU-2015 options over San Vito station, Italy, (Lat:40.6, Long: 17.8). The analysis covers a period of one month (April 2019), which includes quiet days. The results of the comparison of observed hmF2 with IRI2016 (AMTB2013) and IRI2016 (SHU-2015) options based hmF2 estimates indicate that the predicted values of hmF2 overestimate the observed ones. In addition, it is found that SHU-2015 option produces monthly averages of the hourly data in better agreement with observed data.**

Keywords – **AMTB2013, hmF2, IRI-2016, SHU-2015.**

I. INTRODUCTION

The International Reference Ionosphere (IRI) is a joint project of Committee on Space Research (COSPAR) and the International Union of Radio Science (URSI) which is regularly improved and released. The latest version of the model is IRI-2016. For a given location, time and date, IRI provides various parameters including electron density, electron temperature, ion temperature, total electron content, height of F2 peak (hmF2) etc. Several researchers have focused on the performance of IRI model [1-11].

In [1], the variations in F2 peak electron density [NmF2], its height (hmF2) and the thickness parameter B_0 were examined using the measurements of Jicamarca digisonde. The monthly averages of the parameters were compared with the IRI-2001 model values. The results showed that while higher hmF2 values during daytime were responsible for the greater values of NmF2 and B_0, the nighttime lower hmF2 were responsible for the smaller NmF2 and B_0. In [6], hmF2 parameters at the conjugate points near the magnetic equator of Southeast Asia were studied and compared with the IRI model. The monthly hourly medians of hmF2 parameters were calculated and compared with the predictions from the IRI-2007 from January 2004 to February 2007. According to the results the observed hmF2 showed better agreement with the IRI predictions during daytime than during nighttime. In order to validate the IRI model in predicting peak height of F2 layer (hmF2), [7] examined the seasonal hourly means of the hmF2 parameter above Roquetes station and compared the results with IRI-2001, IRI-2007 and IRI-2012. It was found that the predicted values of hmF2 overestimated the observed ones during all seasons, except summer. In [10], the results of ionospheric measurements from DPS-4 installed at Multan,

were reported. The peak height hmF2 were studied during the deep solar minimum between cycles 23-24 and compared with the IRI versions 2012 and 2016. The results of the comparison of the observed hmF2 with the IRI models indicated that IRI-2016 with URSI/CCIR SHU-2015 options predicted well for nighttime hours. However the IRI-2012 CCIR option produced better agreement with data during daytime hours. In order to investigate the hmF2 prediction performance of the IRI-2016 [11] used three hmF2 models (SHU-2015, AMTB-2013, and BSE-1979). The results showed that SHU-2015 was consistently and significantly lower in values that the ionosonde hmF2, AMTB-2013 and BSE-1979 models. Consequently, AMTB-2013 and BSE-1979 models were recommended for equatorial region over West African longitude sector.

In this study, hmF2 prediction performance of IRI-2016 model was examined. Two options (AMTB2013 and SHU-2015) were used and the results compared with the observed values from San Vito, a mid-latitude station.

II. DATA AND METHODS

For the purpose of this study, the variations in hmF2 during April 2019 were analyzed. Since the IRI model has deficiency during active ionospheric conditions, geomagnetic and solar quiet days were selected. Figure 1 gives the geomagnetic storm (Kp), geomagnetic activity (Dst) and solar activity (F10.7) index values [12]. According to the index values there is no geomagnetic/solar activity in April 2019. The observed height of F2 peak (hmF2) parameters were obtained from ionograms of digisonde DPS4D at San Vito. The location of this station is given in Figure 2. This digisonde acquires data 24 h at 15 min intervals. In this study, hmF2 parameters at 1 hour intervals from April 01, 2019 to April 30, 2019 were used.

IRI-2016 has three options for the hmF2: AMTB2013, SHU-2015 and BSE-1979. The AMTB2013 model is based on data from 26 digisonde stations from the Global Ionosphere Radio Observatory (GIRO) network for the time period 1998–2006 [13]. The SHU-2015 model is based on a large amount of radio occultation data from CHAMP (years: 2001–2008; ~300,000 values), GRACE (2007–2011; ~100,000) and COSMIC (2006–2012; ~3,500,000) and with hmF2 data from 62 digisondes for the years 1987–2012 [13]. In this study AMTB2013 and SHU-2015 options were chosen in order to find out which can provide the best representation of the

realistic ionospheric condition. Besides the common input parameters, URSI option for the Ne F-peak were selected with F-peak storm model, using the "off" option. The model based

hmF2 values over San Vito were derived at 1 hour interval corresponding to observed data.
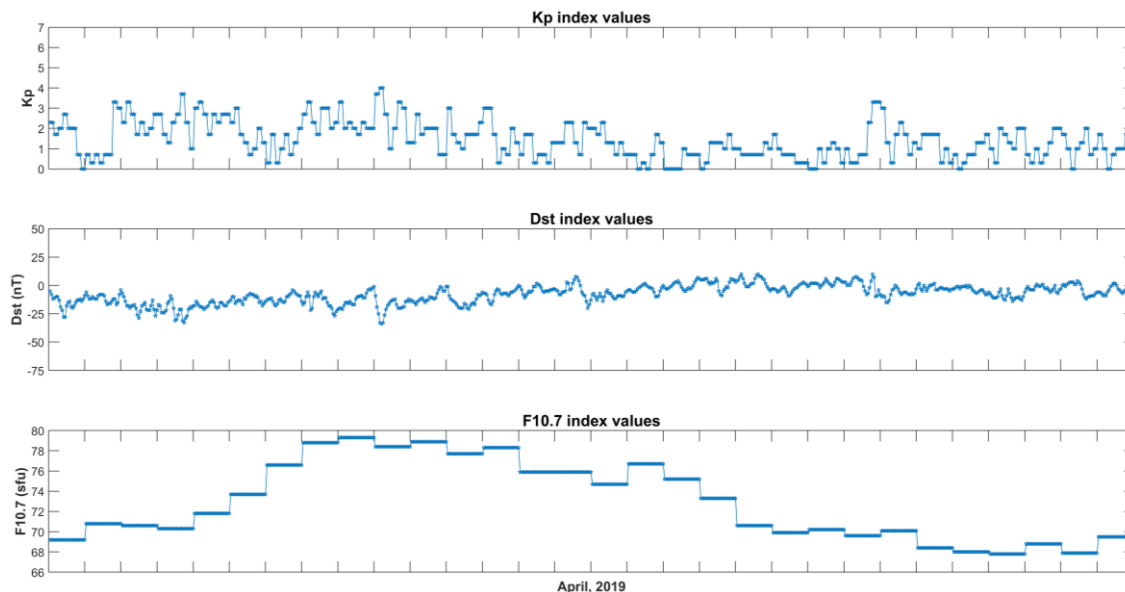
Figure 1: Kp, Dst and F10.7 index values in April 2019
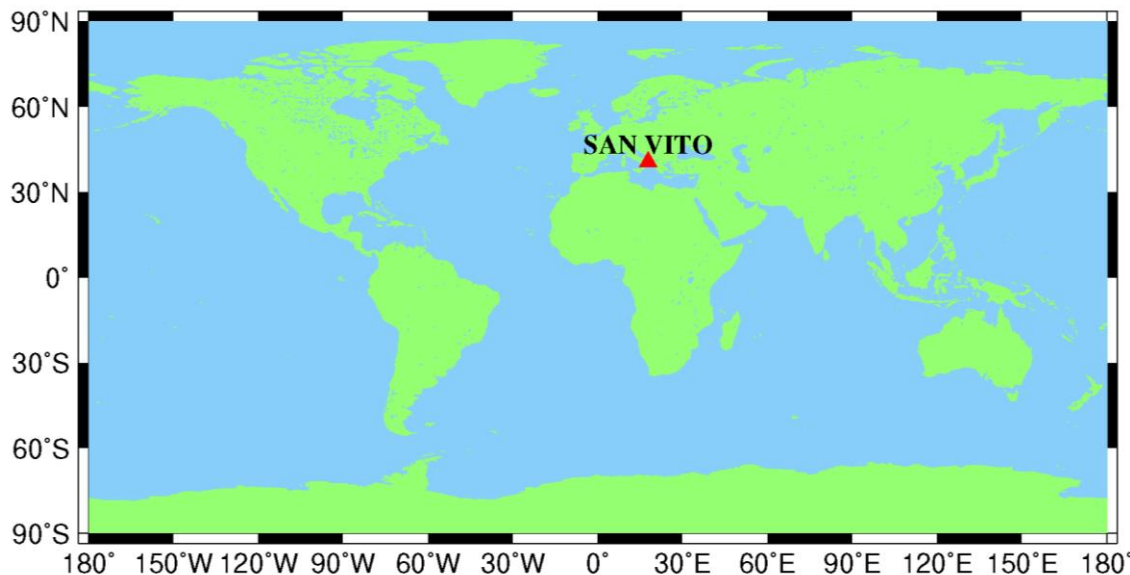
Figure 2: Location of the San Vito station (Italy)

III. RESULTS

The general behavior of hmF2 based on observations and models shows similar trend (Figure 3). As depicted in Figure 3 IRI 2016 derived hmF2 using AMTB2013 option overestimate the observed hmF2 values at almost all hours. However, SHU-2015 based hmF2 values are higher than the observed hmF2 at some times and lower at other times. The monthly averages of the hourly differences between predictions of two IRI2016

hmF2 options and the digisonde observed hmF2 are provided in Figure 4. As depicted in Figure 4 SHU-2015 derived hmF2 are closer to the observed values than other option and differences are mostly within ±10 km which shows normal distribution. Moreover mean of the hmF2 differences between observed and AMTB2013 are high (~30 km), except 16-19 UT. It is noticed that the results obtained during daytime and nighttime are similar.
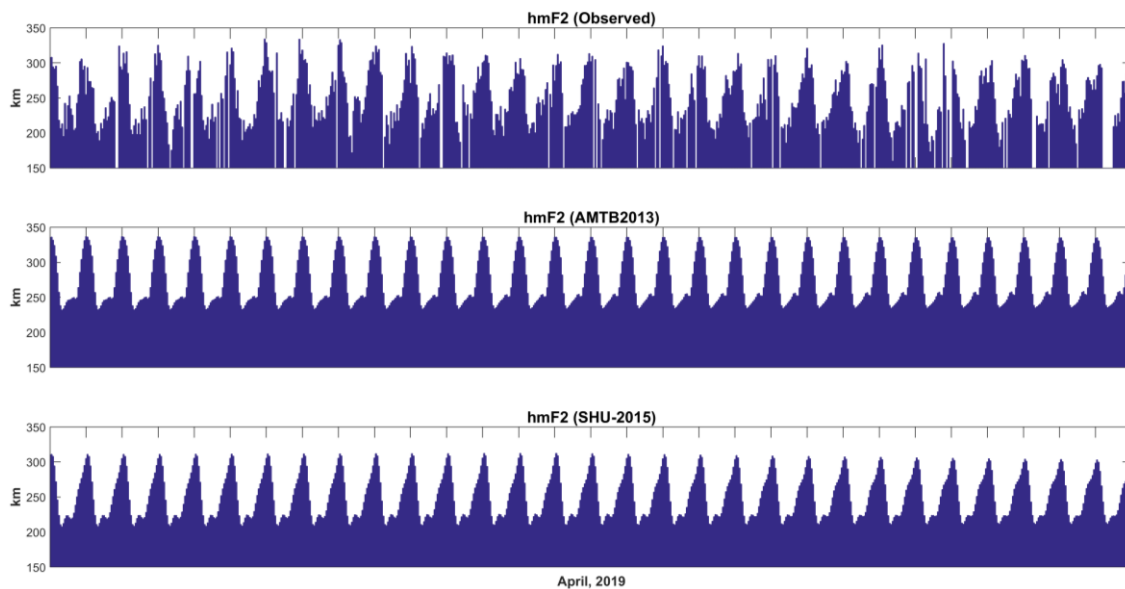
Figure 3: Comparison of observed and predicted hmF2 values
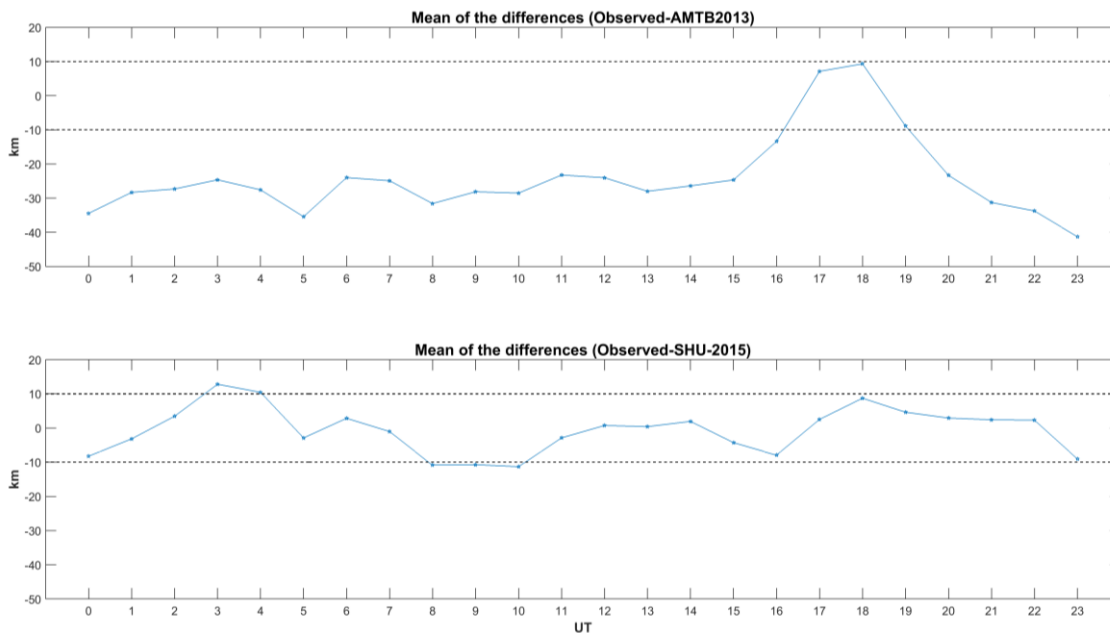
Figure 4: Comparison of hourly means of observed and predicted hmF2 values in April 2019

Besides the hmF2 differences, in an attempt to examine the results in more detail, basic statistical values of the differences, including mean, standard deviation (std), absolute maximum, absolute minimum and range values representing the difference between the maximum and minimum values were calculated and provided in tables 1, 2. As given in tables 1-2, the superiority of the SHU-2015 model is apparent in mean and max (abs) values. The maximum difference between the

observed and AMTB2013 derived hmF2 is 110.2 km, while maximum difference between observed and SHU-2015 based hmF2 is 103.6 km. The std values for each hour are at similar level for both models and they are less than 18 km, except 6, 10, 12, 20, 21, 23 UT. Moreover, when the absolute minimum values are examined, it is seen that the hmF2 values obtained by using the AMTB2013 model are closer to the observation values than the hmF2 obtained using SHU-2015.

Table 1: Basic statistical values of the differences between observed and AMTB2013 based hmF2 values.

Observed - (IRI-2016/AMTB2013)					
Hour	Mean	Std	Max	Min	Range
0	-34.5	16.0	79.9	2.8	77.1
1	-28.3	12.7	58.1	2.5	55.6
2	-27.3	12.4	64.3	4.1	60.2
3	-24.6	17.9	73.7	4.2	77.9
4	-27.6	14.5	55.0	14.0	69.0
5	-35.4	11.1	52.7	11.0	41.7
6	-24.0	30.8	76.3	54.6	130.9
7	-24.9	14.0	55.2	5.2	60.4
8	-31.6	17.7	76.5	8.3	68.2
9	-28.1	16.5	65.5	4.6	70.1
10	-28.5	24.1	110.2	26.9	137.1
11	-23.2	15.9	53.9	3.2	57.1
12	-24.0	22.2	104.0	9.8	113.8
13	-28.0	13.1	54.1	2.9	51.2
14	-26.4	10.8	48.4	4.8	43.6
15	-24.7	12.0	45.9	0.6	45.3
16	-13.4	10.8	41.0	4.3	45.3
17	7.1	11.4	30.1	10.0	40.1
18	9.3	15.3	64.2	19.2	83.4
19	-8.9	15.2	35.5	24.6	60.1
20	-23.3	21.7	81.7	17.9	99.6
21	-31.3	24.7	81.8	16.1	97.9
22	-33.8	16.5	81.2	4.0	85.2
23	-41.3	24.3	95.1	7.5	87.6

Observed - (IRI-2016/SHU-2015)					
Hour	Mean	Std	Max	Min	Range
0	-8.3	15.2	55.0	21.5	76.5
1	-3.2	12.9	34.3	22.1	56.4
2	3.4	12.7	34.6	25.3	59.9
3	12.8	18.0	41.2	36.6	77.8
4	10.4	14.6	52.5	16.5	69.0
5	-2.9	11.2	22.4	19.4	41.8
6	2.8	30.6	103.6	27.2	130.8
7	-1.0	14.1	31.4	29.2	60.6
8	-10.9	17.5	55.4	11.6	67.0
9	-10.7	16.4	47.8	23.6	71.4
10	-11.3	24.1	93.8	43.6	137.4
11	-2.9	16.1	34.3	24.1	58.4
12	0.7	22.6	80.2	34.9	115.1
13	0.4	13.4	26.0	25.2	51.2
14	1.9	10.9	24.5	19.7	44.2
15	-4.3	12.2	25.5	21.2	46.7
16	-7.9	10.4	31.7	12.2	43.9
17	2.5	10.7	24.4	16.3	40.7
18	8.7	14.2	60.8	16.2	77.0
19	4.6	15.8	40.9	22.5	63.4
20	2.9	22.0	56.0	44.3	100.3
21	2.4	24.9	50.1	48.4	98.5
22	2.3	16.3	46.1	39.6	85.7
23	-9.1	23.6	59.1	23.7	82.8

IV. CONCLUSION

In this study, two options of IRI-2016 model, AMTB2013 and SHU-2015, were used to predict hmF2 parameter. The model derived hmF2 values were given in a comparative approach with the values obtained from the observations. It is found that:
 - Predicted values of hmF2 using both option are higher than the observed ones over a mid-latitude station (SAN VITO) at most of the hours during April 2019.
 - The differences between the hmF2 values obtained from the observations and the model using AMTB2013 range between 0.6 km and 110.2 km.
 - The differences between the hmF2 values obtained from the observations and the model using SHU-2015 range between 11.6 km and 103.6 km.
 - Monthly averages of the hourly values illustrate that the SHU-2015 option generates better results.

Table 2: Basic statistical values of the differences between observed and SHU-2015 based hmF2 values.

In view of the results, it can be concluded that although the superiority of SHU-2015 option is clear in the mean of the results, both options provide similar data in terms of the range of the differences.

REFERENCES

[1] C.C. Lee, B.W. Reinisch, "Quiet-condition hmF2, NmF2, and B0 variations at Jicamarca and comparison with IRI-2001 during solar maximum", *J. Atmos. Sol. Terr. Phys*. vol. 68 (18), pp.2138–2146, 2006.

[2] M.L. Zhang, J.K. Shi, X. Wang, S.P. Shang, S.Z. Wu, "Ionospheric behavior of the F2 peak parameters foF2 and hmF2 at Hainan and comparisons with IRI model predictions", *Adv. Space Res*. vol. 39, pp. 661–667, 2007.

[3] Kh. Karami, S. Ghader, A. Raeen, "Comparison of peak characteristics of F2 ionospheric layer over Tehran region at a low solar activity period

with IRI-2001 and IRI-2007 models predictions". *Adv. Space Res.* vol. 48 (6), pp.1049–1055, 2011.

[4]   C.C. Lee, B.W. Reinisch, "Variations in equatorial F2-layer parameters and comparison with IRI-2007 during a deep solar minimum", *J. Atmos. Sol. Terr. Phys.* vol. 74, pp. 217–223, 2012.

[5]   M.C. Mbambo, Lee-Anne McKinnell, J.B. Habarulema, "The variability and IRI-2007 predictability of hmF2 over South-Africa". *Adv. Space Res.* vol. 52, pp. 1798–1808, 2013.

[6]   N. Wichaipanich, P. Supnithi, T. Tsugawa, T. Maruyama, T. Nagatsuma. "Comparison of ionosphere characteristic parameters obtained by ionosonde with IRI-2007 model over Southeast Asia", *Adv. Space Res.* vol. 52, pp.1748–1755, 2013.

[7]   Fahmi, A. Mohammed, "Comparsion of peak height of the F2-layer (hmF2) measurements with IRI-2012, IRI-2007 and IRI-2001 models prediction above Roquetes station (Spain) during the ascending phase of the solar cycle 24", *J. Atmosph. Solar-Terrest. Phys.* vol. 132, pp. 101–105, 2015.

[8]   M. Szwabowski, B. Dziak-Jankowska, M. Pożoga, L. Tomasik, "The 2009-2012 ionosonde and IRI2012 variability of foF2, hmF2, M3000F2, B0, B1 parameters over Warsaw", *Acta Geophys.* Vol. 64 (4), pp. 1211-1223.

[9]   X. Zhao, B. Ning, M.-L. Zhang, L. Hu, "Comparison of the ionospheric F2 peak height between ionosonde measurements and IRI2016 predictions over China". *Adv. Space Res.* vol. 60, pp. 1524–1531, 2017.

[10] M.A. Ameen, H. Khursheed, M.A. Jabbar, M.S. Ali, F. Chishtie, "Variation of hmF2 and NmF2 deduced from DPS-4 over Multan (Pakistan) and their comparisons with IRI-2012 & IRI-2016 during the deep solar minimum between cycles 23 & 24". *Adv. Space Res.* vol.61, pp. 1726–1735, 2018.

[11] O.S. Oyekola, "Comparison of IRI-2016 model-predictions of F2-layer peak density height options with the ionosonde-derived hmF2 at the equatorial station during different phases of solar cycle" *Adv. Space Res.* https://doi.org/10.1016/j.asr.2019.04.022.

[12] Web interface of kp, Dst and F10.7 indices. Available: https://omniweb.gsfc.nasa.gov/form/dx1.html.

[13] D. Bilitza, D. Altadill, V. Truhlik, V. Shubin, I. Galkin, B. Reinisch, X. Huang, "International Reference Ionosphere 2016: From ionospheric climate to real-time weather predictions", *Space Weather*, vol. 15, pp.418-429, 2017.

Landsat imagery and GIS based evaluation and monitoring desertification process surrounding Kirkuk City, Iraq

SUZAN ATTA BAKR[1] and KAMALADIN F. HASAN[2] and QAYSSAR MAHMOOD AJAJ[3]

[1]Selcuk University, Konya/Turkey, suzanatta70@gmail.com
[2]North technical university kirkuk/Irak, Sofia0703@yandex.com
[3]North technical university kirkuk/Irak, qayssarrsgis@gmail.com

Abstract – **Desertification implies land degradation in areas arising from different variables, including climatic variations and human operations. Controlling and monitoring the phenomena and calculating the regions that have been transformed to desert required adequate management. Likes another hazard, the desertification phenomena can be modeled and identified. Kirkuk City located in north of Iraq. A town situated at longitude 44° 00′E to 44° 50′ E and latitude 35 ° 13′N to 36 ° 29′ N with a total area of 96.79 km2 .it is 236 kilometers north of the capital, Baghdad. Kirkuk's average elevation is 346 m. This area lies in the North Temperate Zone which the weather in this region characterizes by very low humidity and low clouds in the most days of the year. For this study, three set of Landsat image which are Landsat-5 TM, Landsat-7 ETM+, and Landsat-8 OLI for 1987, 2002, and 2017 were used. To classify images, the Maximum Likelihood algorithm was used. Change detection analysis makes possible monitoring and detecting the environmental changes among different times. The result of change detection discussed to; short term (1987-2002) and (2002-2017) and long term (1987-2017) change detection. The amount of desertification has decreased during the period 1987 to 2002 and has increased significantly during the period 2002 to 2014. The main reasons of the changes that happened in land cover from 1987 to 2002 due to the changes in climate conditions faced by the potential of government by supporting the farmers and provide them the necessary materials and machines to develop the agriculture in Iraq. On the other hand, the period from 2002 to 2017; the region suffered from the military operations and carelessness of the government about farmers as well as the rising of fuel cost prevents them from farms product.**

Keywords - **Classification, Change detection, GIS, Land cover, land degradation, Remote sensing.**

I. INTRODUCTION

Surveillance involves field survey, available records and acquisition of information through remote sensing [1]. GIS and remote sensing are good tools for control, reveal and analysis changes in land use/cover [2]. The method of identifying changes over time is change detection. In order to detect change, multi-date imagery is needed as each picture indicates land use and coverage at particular moments. Change detection is a practical illustration of human-environmental relationships, helping to enhance the management of environmental resources. Detection of change in land cover using remote sensing methods is heavily dependent on the sensor's spatial, spectral and temporal features [3].

II. METHOD

A. Study area

Kirkuk City located in north of Iraq. A city situated at longitude 44° 00′E to 44° 50′ E and latitude 35 ° 13′N to 36 ° 29′ N with a total area of 96.79 km2 (fig.1)
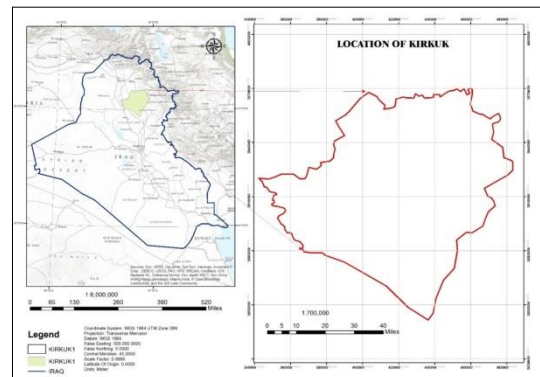
Figure 1: study area

B. Data user

Remote sensing data and various ancillary data were collected in order to study land changes. As shown in Table (1).

Satellite Image

The landsat image over the study areafrom 1987 to 2017 were downloaded from United geological survey (USGS) as free of charge.

C. Preprocessing of satellite image

Sensors are mounted on satellite platforms and supply remote sense draw data; generally the sensor has faults and drawbacks. Deficiencies in the data can be improved by some ways known as pre-processing methods. Pre-processing

involves the initial processing of image data to correct geometric distortions, examine the data radiometric, and eliminate noise present in the data. Three methods of pre-processing that must be considered to obtain an interesting input of satellite images are geometric, radiometric, and atmospheric correction methods.

Table 1: satellite data that used for this study.

No.	Image source	Acquisition Date	Path/Row	Map Projection
1	Landsat-5 TM	1987-05-23	169/35	UTM/WGS 84
2	Landsat-7 ETM+	2002-05-24	169/35	UTM/WGS 84
3	Landsat-8 OLI	2017-05-25	169/35	UTM/WGS 84

D.　Processing

Fusion process

Popular pan-sharpening techniques enable elevated spatial or spectral quality of the output picture to be maintained. A noticeable connection exists in that the spectral quality reduces along with an enhancement in spatial quality [4]. The suggested technique guarantees the sharp image's elevated spectral quality while at the same moment preserving high spatial resolution.

Classification scheme

The classification scheme is a structure that can be obtained from picture information to organize and categorize land cover / land use classes [5]. In this research, four kinds of land use/cover were recognized as water bodies, vegetation, urban land, and barren land. In this study we use the maximum likelihood classification it is one of the most popular methods of classification in which a pixel with the maximum likelihood is classified into the corresponding class.

Accuracy assessment

The accuracy assessment for each classification is testing to reveal the trust level in the results of classification and that done by finding out the overall and user accuracy, Kappa coefficient, as well as Producer accuracy for each classification algorithm in three years with using ENVI software. In this study, 92.2405% and 89.2857% 94.0741% accuracy was obtained in 1987, 2002 and 2017, respectively. The result of accuracy assessment and Kappa coefficient illustrate in table 2 below

Change detection

This study detected changes through the post-classification comparison method. ıt provides a method to extract the change detection matrix that explains how each category changes to another and amount this change occurs in that range.

Evaluation of environmental degradation indicators

Not all factors have equal importance for the determination of degradation based on spatial location. Different weights were therefore identified for different factors. Analytic Hierarchy Process was used to calculate the weight of the criterion [6]. ArcGIS was used to determine the level of environmental degradation. The determination of criteria is depends on the availability of data for the study area. In this study, vegetation change, wasteland, urbanization, water surface, and population pressures were the main criteria for assessing environmental changes. In order to give precise evaluation, within the main criteria, there are sub-criteria should be considered.

A weighted linear combination (WLC) will be used in this research. This weighted linear combination is used for the weighted criteria sum calculation. An analytical hierarchy process, known as pairwise comparisons, is used to perform the weighted linear combination technique. It is implemented within a GIS environment in two steps: First, the weights Connected with the layers of the criteria map are determined. The second thing is; Priority is combined for all hierarchical levels, including levels that represent levels [6]. Multi criteria decision making is based on the weight of each factor making the determination of weight a main step in defining the decision maker's preferences [6]. For the selection of criteria weights, a multi-criteria assessment (MCE) module is used. The comparison technique for pairs includes comparing each variable with each other in the pairs.

To calculate the weightages of criteria, the following steps should be followed:

- In this step, the sum of the values in each column is computed in the even comparison matrix show in (table 4). In this research, five criteria and priority criteria were considered

- In this step, the normalized matrix is calculated to fill the values of normalized matrix, dividing each cell in Table 4 by the sum of the column. Then the average of each row is calculated from the resulting in the (Table 5). These averages constitute the comparative weights of the criteria.

The accuracy of the pairwise comparison is assessed by the Consistency Ratio (CR) calculation (see equation 1). The consistency ratio is used to assess the comparative weights of each criterion.

Table 2 Classification accuracies of the satellite images for 1987, 2002, and 2017

Classes	1987		2002		2017	
	Producer's Acc. %	User's Acc.%	Producer's Acc. %	User's Acc.%	Producer's Acc. %	User's Acc. %
Urban	59.83	88.61	78.72	94.87	100	85.71
Vegetation	95.12	95.12	81.75	100	100	98.46
Sand	98.52	91.08	99.08	81.82	80.25	100
Water	80.85	92.68	95.74	93.75	100	100
Overall accuracy	92.2405%		89.2857%		94.0741%	
Kappa coefficient	0.8691		0.8435		0.9182	

The comparison between the variables is acceptable if the outcome of the consistency ratio is less than 10 percent. Otherwise, the consistency ratio enables comparisons to be re-evaluated.

$$CR = (\frac{CI}{RI}) \qquad (1)$$

CI: Consistency Index
RI: Random Index

Table 3: Shows average random consistency index (RI).

Number of criteria	2	3	4	5	6	7	8
Random Index	0.00	0.58	0.90	1.12	1.24	1.32	1.41

The consistency Index (CI) can be calculated using equation 2

$$CI = (\frac{\lambda max - n}{n-1}) \qquad (2)$$

Where:
λmax=(Weight1*S1+Weight2*S2+Weight3*S3+)　　(3)
n = number of criteria
After calculating CI, apply CR equation, if the result less than 10%, depends the weights.

Table 4: show the of pairwise comparison matrix

Criteria / factors	Veg. to sand	Water to sand	Urb. to sand	Veg.to urban	Water to urb.
Veg. to sand	1	2	3	6	7
Water to sand	0.5	1	2	5	6
Urb. to sand	0.3333	0.5	1	4	5
Veg. to urb.	0.1666	0.2	0.25	1	2
Water to urb.	0.1428	0.1666	0.2	0.5	1
Sum	2.1428	3.8666	6.45	16.5	21

Table 5: show normalized matric calculation

Criteria	Vegetation to sand	Water to sand	Urban to sand	Vegetation to urban	Water to urban	Weight %*
Veg. to sand	0.4666	0.5172	0.4651	0.3636	0.3333	0.4291
Water to sand	0.2333	0.2586	0.31007	0.30303	0.2857	0.2781
Urban to sand	0.1555	0.1293	0.15503	0.2424	0.23809	0.18408
Veg. to urban	0.0777	0.05172	0.03875	0.060606	0.09523	0.06482
Water to urban	0.0666	0.0431	0.031007	0.030303	0.0476	0.04373
sum	1	1	1	1	1	1

III. RESULTS AND DISCUSSIONS

A. Classification results of 1987
Figure 2(a) states the four land-cover classes and their spatial distribution. It can be seen that the big class is the sand represented %58.78 of study area with 695.2797 Km². In contrast, the urban class around 96.8472 Km² which represented %8.19 of study area. A second proportion of the study region was in vegetation around %31.71 which covers approximately 375.1497 Km². Finally, the water bodies represented with %1.32 percentages of the study area and around 15.615Km2.

B. Classification results of 2002
Figure 2(b) shows the four land-cover classes ' spatial distribution. The dominant class can be seen as the sand depicted around %47.79 of study area with 565.2576 Km². In contrast, the urban class has around 213.1812 Km² which represented %18.2 of study area. Vegetation had percentage of study area around %27.34 which covers approximately 323.361 Km². Finally, the water bodies represented with %6.86 percentage of the study area and around 81.09 Km².

C. Classification results of 2017
Figure 2(c) states the percentage of the land-cover classes and their spatial distribution. It is possible to see that the dominant class is the sand around 42.02% of study area with 497.083 Km2. In contrast, the urban class around 95.778 km which represented %8.10 of study area. Vegetation

represented %46.73 of study area which covers approximately 552.7593 Km2. Finally, the water bodies represented %3.15 percentage of the study area and around 37.2645 Km^2.
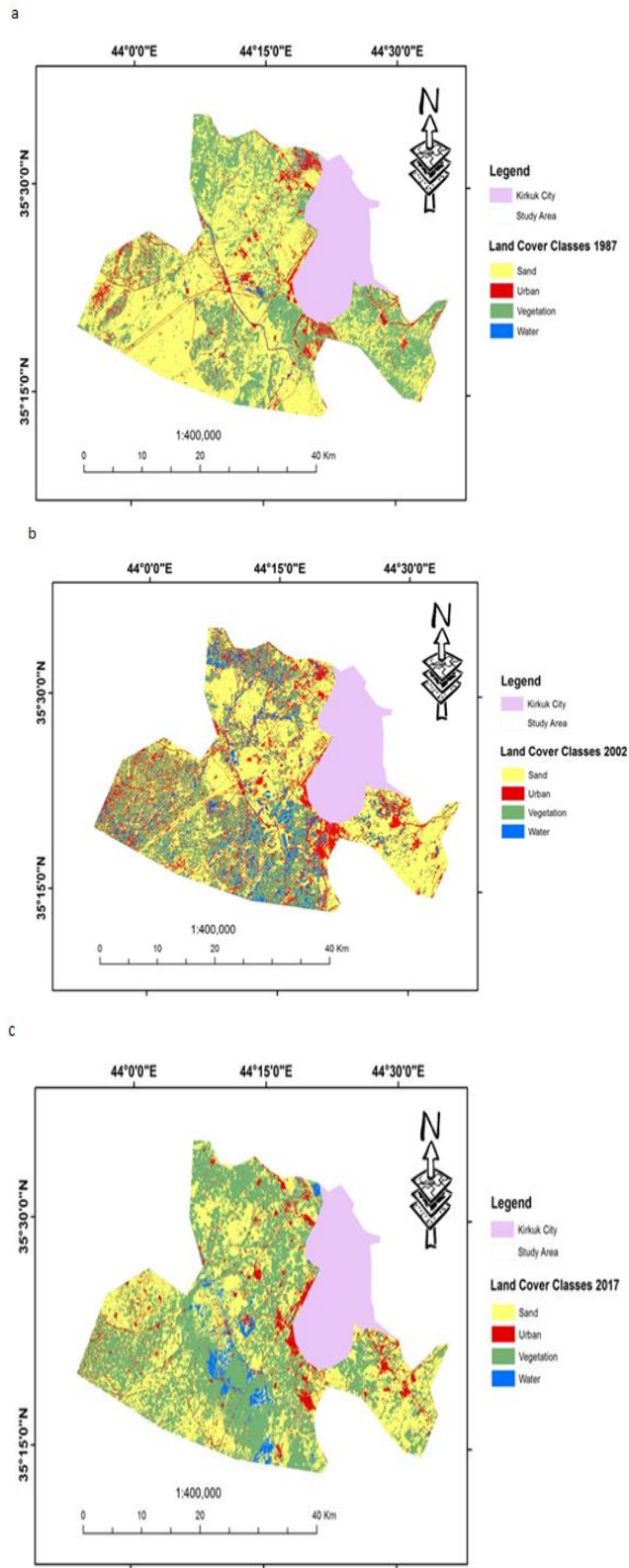
Figure 2: Show Classified maps of land cover in a- 1987, b- 2002, c-2017

D.　Change detection outcome

The result of change detection will be discussed in two terms; short and long term change detection analysis.

Short term change detection analysis

This term included two period of time; 1987-2002 and 2002-2017. The modifications that have occurred have been recognized and analyzed based on Figure 3(a) and 3(b) and Tables (6 and 7) information. In the first period, the noted changes were the decrease in the sand class from 695.279 km2 to 565.257 km2 which converted to other classes mostly vegetation and water classes. This decrease of sand is assigned to the development of the irrigation that supported by government in that period. In second period, sand decreased around 68.1735 km2 as net change. The urban class notably elevated in the first period then decreased along the second period with the net change percentages of 8.18% to 18.02 % and then to 8.09%, respectively. This vibrate was noted in vegetation belong to the vibrated support of government for the farmers as well as the war conditions. In contrast, in the first period, water class increased and decreased in the second period of study +5.5% and - 3.7% respectively because of unstable policy of water. During first period, the vegetation increased (9.84 %) as result of the growth of the irrigation systems in which used to convert around 13.8 % of sand to be planted areas. Over the second period there was deterioration in vegetation area in which reduced around 9.93% because agriculture has been neglected and dependent on import of agricultural products as well as the reduction in the amount of precipitation.

Long term change detection analysis

In this section, the period of 30 years it was examined in order to understand the long term of change. Figure 3(c) and table 8, changes that happened during this period. Among these changes, sand decreased about 16.755% with net change approximately 198.1962 km2 which is huge area compare with other classes. This decreased can be attributed to different factors, including the increasing of rain, neglect agriculture lands because of the situation after 2003 war, and the changes of climate. Also, urban class decreased from 96.8472 km^2 to 95.778 km^2 as a normal result of the war conditions of U.S.A as well as of ISIS. By contrast, during the entire periods studied, water and vegetation classes increased. Vegetation growth about 177.6096 km^2 because of around 38.859 % of sand area was converted to vegetation area. Besides that, water increased from 15.615 km^2 to 37.2645 km^2 to record 1.83% rising.

Land degradation outcome

The purpose of this research is to detect changes in land cover and environmental degradation. This research given quantitative and qualitative assessments on land cover and environmental changes in Kirkuk city, Furthermore, remote sensed data and GIS modeling, thematic maps showing rates of environmental degradation in the region of job, may be useful in future planning and improvement of the environment and quality of life in the city. As shown in Figure (3).The

results of this study show that the city of Kirkuk threatens further environmental deterioration in the future due to the increasing deterioration of climate circumstances in the region and population growth. The future proposal of this study uses high spatial resolution to use field data that adds factors that contribute more to the impact on the level of environmental degradation as well as achieving more land use/land cover classes.

Table 6: The confusion matrix of change area between 1987- 2002

	class	1987				
		Urban	Vegetation	Sand	Water	Class total
2002		Area km^2	Area km^2	Area km^2	Area km^2	Area km^2
	Urben	5043.96	5619.78	10221.57	432.72	21318.03
	vegetation	1276.29	12512.7	18224.1	322.92	32336.01
	Sand	2974.05	15909.57	37208.7	4333.35	56525.67
	Water	390.42	3472.65	3873.42	372.51	8109
	Total class	9684.72	37514.97	69527.97	1561.5	

Table 7: The confusion matrix of change area between 2002- 2017

	class	2002				
		urben	vegetation	sand	water	total
2017		Area km^2	Area km^2	Area km^2	Area km^2	Area km^2
	urben	4685.67	904.32	634.27	345.24	9577.8
	vegetation	8759.7	19183.59	21674.16	5658.12	55275.57
	sand	7164.09	11137.86	29780.46	1625.85	49708.26
	water	70.848	1110.24	1427.94	47979	3726.45
	Total class	21318.12	32336.01	56525.76	8109	

Table 8: The confusion matrix of change area between 1987- 2017

	class	1987				
		urben	vegetation	sand	water	total
2017		Area km^2	Area km^2	Area km^2	Area km^2	Area km^2
	urben	3154.05	2090.07	4172.49	161.19	9577.8
	vegetation	2412.54	19775.97	32448.06	639.36	55275.93
	sand	3719.7	14578.02	3097.701	433.62	49708.35
	water	398.43	1070.73	1929.96	327.33	3726.45
	Total class	9684.72	37514.97	69527.97	1561.5	
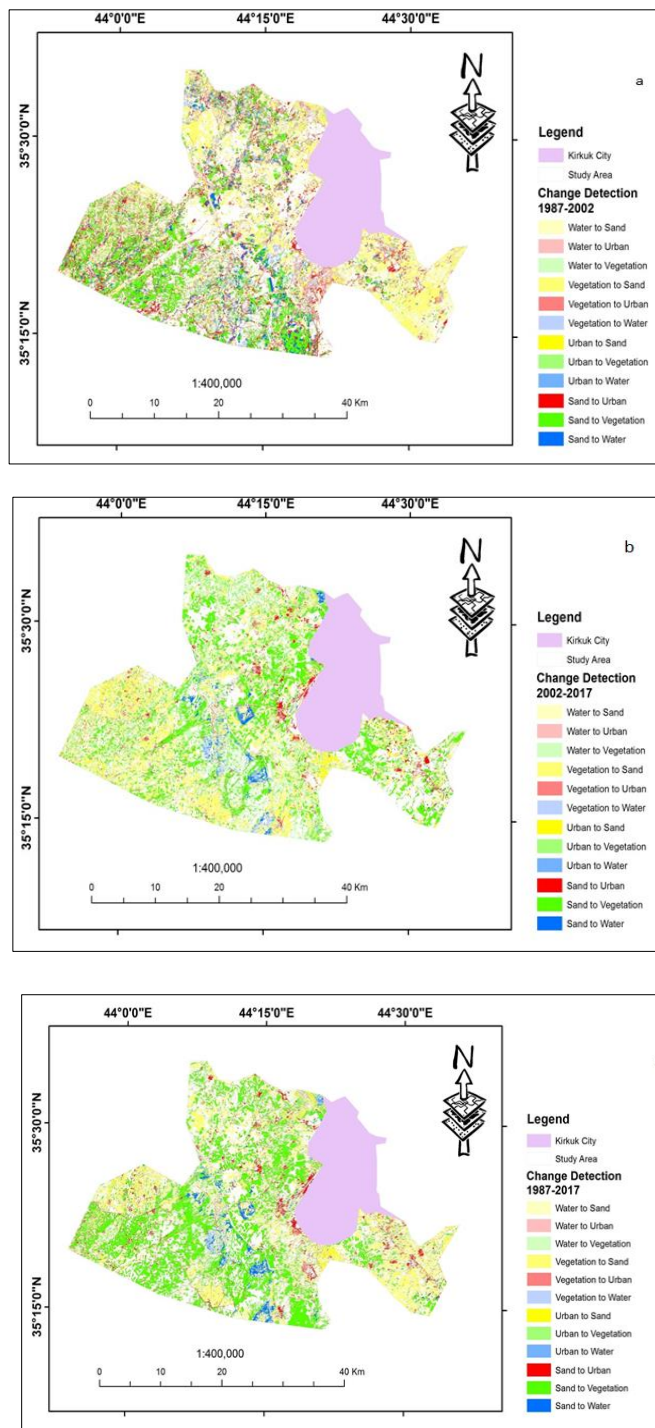
Figure 3: Spatial pattern of land use and land cover changes during (a) 1987–2002, (b) 2002–2017, and (c) 1987–2017.
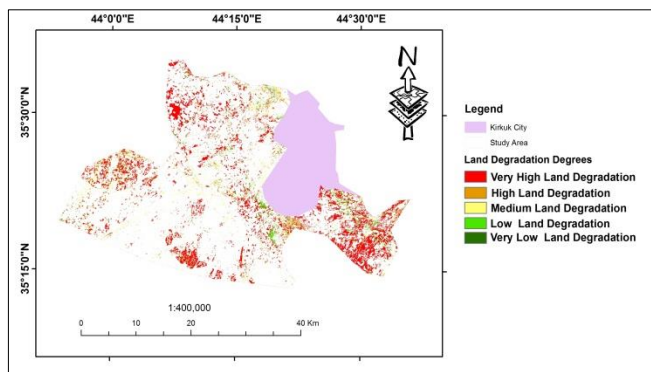
Figure 4: shows the degree of land degradation

IV. CONCLUSION

This research has attempted to demonstrate different methods for extracting four land class using both spectral and spatial attributes and to use the outcomes in the assessment of post-classification changes. Landsat images were acquired in the city of Kirkuk, Iraq, in 1987, 2002 and 2017, and were classified using pixel-oriented maximum likelihood (ML) and support vector machine (SVM) classifiers. Before 1987, the region was significantly stable, but later as a result of changes in circumstances weather and ware conditions; it affected the land cover of the region, leading to increased desertification. The main purpose of this study is to determine the degree of desertification in the north of Iraq. Landsat images with a spatial resolution of 30 m and different spectral bands connected to the sensors were used. In determining land cover classes, the maximum probability and support vectors were used machine algorithms. The result of the support vector machine (SVM) was not valid and the classification contained very wrong, the maximum probability method achieving better results than SVM. Therefore, classification analysis classes are based on maximum likelihood method. Calculation of the amount of class changes Change provided by the ENVI program detection analysis (Change Detection Statistics). The amount of desertification decreased in 1987-2002 periods and the increased. The main reasons for the changes in the land were the changes in climate conditions; the state provided support to farmers and provided the necessary materials and machinery to improve agriculture in Iraq. On the other hand, the period from 2002 to 2017; farming has decreased due to the fact that the state has stopped supporting farmers due to military action and fuel costs have risen.

REFERENCES

[1] Vogt, J., Safriel, U., Von Maltitz, G., Sokona, Y., Zougmore, R., Bastin, G., & Hill, J. (2011). Monitoring and assessment of land degradation and desertification: Towards new conceptual and integrated approaches.

Land Degradation & Development, 22(2), 150-165.

[2] Manonmani, R., & Suganya, G. M. D. (2010). Remote sensing and GIS application in change detection study in urban zone using multi temporal satellite. *International Journal of Geomatics and Geosciences, 1*(1), 60-65.

[3] Burnett, C., & Blaschke, T. (2003). A multi-scale segmentation/object relationship modelling methodology for landscape analysis. *Ecological Modelling, 168*(3), 233-249.

[4] Lillo-Saavedra, M. and Gonzalo, C., 2006, Spectral or spatial quality for fused satellite imagery? A trade-off solution using the wavelet à trous algorithm, *International journal of remote sensing*, 27 (7), 1453-1464.

[5] Thapa, R. B., & Murayama, Y. (2009). Examining spatiotemporal urbanization patterns in kathmandu valley, nepal: Remote sensing and spatial metrics approaches. Remote Sensing, 1(3), 534-556.

[6] Drobne, S., & Lisec, A. (2009). Multi-attribute decision analysis in GIS: weighted linear combination and ordered weighted averaging. *Informatica*, *33*(4).

[7] Ajaj, Q. M., Pradhan, B., Noori, A. M., & Jebur, M. N. (2017). Spatial Monitoring of Desertification Extent in Western Iraq using Landsat Images and GIS. *Land Degradation & Development*, *28*(8), 2418-2431.

Assessing the Shear Strength Reduction Factor in Geopolymer Concrete Beams Without Stirrups

G. ARSLAN[1], S. ALACALI[2] and M. ÖZTÜRK[3]

[1] Yıldız Technical University, Istanbul/Turkey, gurayarslan@gmail.com
[2] Yıldız Technical University, Istanbul/Turkey, noyan@yildiz.edu.tr
[3] Yıldız Technical University, Istanbul/Turkey, mehdioztrk@gmail.com

Abstract - **In the design of strength, the strength reduction factor decreases from ductile to brittle to increase safety with decreasing ductility. In the codes, it is intended to provide the target failure probability by means of safety factors that are load factors and strength reduction factors. But, the literature related to the safety factor of geopolymer concrete materials has not been observed. This paper presents how to determine the reduction factor for shear strength of reinforced geopolymer concrete beams according to ACI318 code. In the reliability-based design, the reliable prediction of the shear strength of reinforced geopolymer concrete beam is assured by the use of reduction factors corresponding to different target reliability index. In this study, for different variation coefficients of the concrete strength, the shear strength reduction factor has been investigated by using experimental studies available in the literature. In the reliability analysis part of the study, the first-order second moment approach has been used to determine the reduction factor. ACI 318 [1] code suggests a strength reduction factor value of 0.85 for shear. However, in ACI 318 [2], the strength reduction factor value for shear is decreased to 0.75. It is found that a strength reduction factor of 0.75 for shear is valid in design according to ACI318 for a coefficient of variation of concrete compressive strength of 0.12 and a failure probability of 10^{-7}.**

Keywords – **Geopolymer concrete, shear strength, failure, probability, reduction factor.**

I. INTRODUCTION

IN view of sustainable development in the construction industry, it can be noticed that cement-based concrete are replacing with geopolymer concrete in next years. The manufacture of geopolymer concrete is carried out using the traditional concrete technology methods. As in the portland cement concrete, the aggregates occupy the largest volume, that is, approximately 75 to 80% by mass, in geopolymer concrete. The silicon and the aluminum in the fly ash are activated by a combination of sodium hydroxide and sodium silicate solutions to form the geopolymer paste that binds the aggregates and other unreacted materials [3]. Geopolymer concrete is considered as a highly sustainable material since it can be manufactured from industrial waste materials. Previous studies on the structural behaviour of reinforced geopolymer concrete beams have covered the flexural behaviour of members. Further studies are needed to investigate other aspects of the structural behaviour of geopolymer concrete. The performance of reinforced geopolymer concrete beams depends on tensile strength of low calcium fly ash-based geopolymer concrete. Shear strength of geopolymer reinforced concrete beams is essential to prevent shear failures which are brittle in nature.

There is, however, a relatively limited number of studies available on the structural behaviour of reinforced geopolymer concrete members, particularly those failing in shear. Moreover, of the work currently available in the literature there is to the authors' knowledge none focusing on predicting the concrete component of the shear capacity [4].

In design according to ACI318, the strength reduction factors are used to reflect the importance of the member in the entire structure and other constructional inaccuracies. The ACI 318 [1] Code suggests strength reduction factor of 0.85 for shear. However, in ACI 318 [2,5], the strength reduction factor for shear is decreased to 0.75 [6]. In the study of Rakoczy and Nowak [7], the resistance factors is investigated and compared with the updated data. Arslan et al. [8] assessed the reliability of shear strength prediction equations based on the performance functions by using second-moment approach. This paper assesses ACI318's response to the change of the strength reduction factor in predicting the contribution of concrete to shear strength by using second-moment approach. The change in the strength reduction factor against the coefficient of variation of concrete compressive strength and the failure probability was investigated through the database of five shear test results given from literature. The results are limited to the beams with the slenderness ratio greater than 2.5 are considered.

II. REDUCTION FACTOR FOR SHEAR DESIGN

Design Codes [1,2,5,9] indicated that the design shear strength of a member must exceed the shear demand as shown in Equation 1.

$$\phi v_n \geq v_u \tag{1}$$

in which ϕ is the shear strength reduction factor and given as 0.75, v_u and v_n are the ultimate and nominal shear strength, respectively. The nominal shear strength is the sum of concrete and stirrup contribution. According to the ACI318 [2], the cracking shear strength of RC beam without stirrup is defined as follows;

$$v_c = \frac{1}{6}\sqrt{f_c} \qquad \frac{a}{d} \geq 2.5 \qquad\qquad (2)$$

in which f_c is the concrete cylinder compressive strength in MPa.

In this study, the change in the shear strength reduction factor considered in predicting the contribution of concrete to shear strength according to ACI318 [2] is investigated and compared for different coefficient of variation of concrete compressive strength and failure probability.

III. DETERMINATION OF PARTIAL SAFETY FACTORS

The reliability analyses have been carried out using the first-order reliability method (FORM). FORM is considered to be one of the most reliable computational methods for structural reliability. The advantage of this method provides physical interpretations and do not require much computation time. FORM leads to results that can be considered sufficiently accurate for most cases in structural buildings. In this study, the determination of the partial safety factor according to the probability-based design is described by the first-order second moment approach [6]. In this study, it is assumed that the distributions of variables in performance function are lognormal. It is also assumed that the random variables are statistically independent. The performance function is expressed as

$$g(X) = \gamma_1 \cdot v_{c,ACI318} - \gamma_2 \cdot v_{c,\text{exp.}} \qquad\qquad (3)$$

in which $v_{c,exp.}$ is the experimental cracking shear strength and $v_{c,ACI318}$ is the cracking shear strength defined in Equation 3. γ_1 and γ_2 are the safety factors corresponding to the related variables and it is assumed that the safety factor γ_1 corresponds to the shear strength reduction factor (ϕ). The change in the strength reduction factor considered in predicting the contribution of concrete to shear strength according to ACI318 [2] against the different values of coefficient of variation (0.10, 0.12, 0.15, 0.18) and failure probabilities (10^{-7}, 10^{-6}, 10^{-5}, 10^{-4}, 10^{-3} and 10^{-2}) was investigated by using experimental studies available in the literature. In reliability analysis, the reliability indexes β corresponding to the different failure probabilities p_F (10^{-7}, 10^{-6}, 10^{-5}, 10^{-4}, 10^{-3}, 10^{-2}) are taken as 5.2, 4.75, 4.27, 3.72, 3.09, 2.33, respectively.

Arslan et al. [6], Tabsh and Nowak [10], Du and Au [11], Schlune et al. [12], and Akiyama et al. [13] used lognormal distribution for strength in their studies. Accordingly, lognormal distribution for strength is used in this study.

IV. STATISTICAL VARIATIONS OF THE VARIABLES

The parameters related to the shear strength were modelled as random variables, and the values of coefficient of variation were determined based on the studies available in the literature and the codes. The values of the coefficient of variation taken into account in the calculations were determined by considering the previous statistical studies for traditional construction materials, so, it hasn't been studied on this subject for geopolymer concrete. The coefficient of variation of concrete compressive strength (V_{f_c}) under average construction quality control usually depends on the concrete strength and varies in between 0.10 and 0.21 through the literature [6]. In this study, the coefficient of variation of concrete compressive strength (V_{f_c}) ranges from 0.10 to 0.18. It is assumed that the coefficient of variation of strength is 0.01, which is the value used in this study.

V. PROPERTIES OF BEAMS

The properties of the beams in the database of five shear test results are shown in Table 1 [4,14]. As seen in Table1, varies from 21 MPa to 63.1 MPa. In this study, high strength concrete (HSGC) is defined as compressive strength of concrete higher than 50 MPa. The experimental beams of experimental cracking shear strength ($v_{c,\text{exp.}}$), concrete cylinder compressive strength ( ), shear span-to-depth ratio (a/d), and flexural reinforcement ratio (ρ) are given in Table 1.

Table 1: The properties of the beams

Beams	b_w (mm)	d (mm)		(MPa)	(%)	f_y (MPa)	$v_{c,\text{exp.}}$ (MPa)
B2-T1*	150	250	2.5	24	1.07	880	1.92
B3-T1*	150	200	2.5	33	1.34	880	2.75
B4-T1*	150	300	2.5	21	0.89	880	1.15
B-0.0-1**	120	204	3.67	63.1	3.28	540	1.43
B-0.0-2**	120	204	3.67	49.1	3.28	540	1.43
*[4], **[14]							

Table 2 summarizes the change in the shear strength reduction factors obtained from the analysis. According to ACI318 [2], the shear strength reduction factor considered in predicting the contribution of concrete to shear strength equals to 0.75. It is indicated that this value corresponds to the target values of $p_F = 10^{-7}$ ($\beta = 5.2$) and $V_{f_c} = 0.12$. It is observed that it is on the safe side for $p_F > 10^{-7}$ and a variation coefficient of 0.12. It can be noted that it is conservative for   on the range 10^{-7} to 10^{-2} and a variation coefficient of 0.12.

Table 2: The average values of shear strength reduction factors

V_{f_c}	Reliability index β and failure probability p_F						Beams
	$\beta=5.2$ $p_F=10^{-7}$	$\beta=4.75$ $p_F=10^{-6}$	$\beta=4.27$ $p_F=10^{-5}$	$\beta=3.72$ $p_F=10^{-4}$	$\beta=3.09$ $p_F=10^{-3}$	$\beta=2.33$ $p_F=10^{-2}$	
0.10	0.793	0.808	0.825	0.844	0.868	0.898	NSGC (4beams)
0.12	0.751	0.769	0.789	0.812	0.840	0.875	
0.15	0.694	0.715	0.738	0.766	0.800	0.843	
0.18	0.641	0.665	0.691	0.723	0.762	0.812	
0.10	0.777	0.794	0.812	0.834	0.859	0.891	HSGC (1beam)
0.12	0.737	0.756	0.777	0.802	0.832	0.869	
0.15	0.681	0.703	0.728	0.757	0.793	0.838	
0.18	0.625	0.654	0.682	0.715	0.756	0.808	
0.10	0.790	0.805	0.822	0.842	0.866	0.896	NSGC & HSGC (5beams)
0.12	0.749	0.767	0.786	0.810	0.838	0.874	
0.15	0.691	0.713	0.736	0.764	0.799	0.842	
0.18	0.637	0.663	0.689	0.722	0.761	0.811	

The effects of experimental cracking shear strength $(v_{c,\exp.})$, concrete cylinder compressive strength ( ), slenderness ratio (   ), and flexural reinforcement ratio ( ) on the shear strength reduction factors are discussed below.

ϕ is calculated for each experimental beam using the performance function given by Equation 3, and the results are shown in Figure 1 for $(\beta=5.20)$ and   . The experimental cracking shear strength for existing test data with the variation of shear strength reduction factor is shown in Figure 1a for $p_F=10^{-7}$ $(\beta=5.20)$ and   . For relatively low cracking shear strength values ($v_{c,\exp.}<1.50$ MPa), where the corresponding shear strength reduction factors are mostly less than 0.75 for $p_F=10^{-7}$ $(\beta=5.20)$ and   (Figure 1a). Figure 1b shows the shear strength reduction factor with the variation of   for $p_F=10^{-7}$ $(\beta=5.20)$ and   . Only one of the HSGC beam test was conducted for $f_c \geq 50$ MPa. Since the test data for HSGC members are very limited, further research is required to verify the founded   for HSGC beams. The shear strength reduction factor is not influenced significantly by   for all (NSGC & HSGC) beams. Figure 1c and Figure 1d show the shear strength reduction factor with variation of the reinforcement ratio   and slenderness ratio (   ) for $p_F=10^{-7}$ $(\beta=5.20)$ and   , respectively. It is generally observed that the   increases with increasing   except for an experimental beam for NSGC beams.

a)

$\beta=5.20$
$V_{fc}=0.12$

■ NSGC
△ HSGC

Experimental shear strength ($v_{c,exp.}$)

b)

$\beta=5.20$
$V_{fc}=0.12$

■ NSGC
△ HSGC

Compressive strength of geopolymer concrete (f_c)

c)

$\beta=5.20$
$V_{fc}=0.12$

■ NSGC
△ HSGC

Reinforcement ratio (ρ, %)
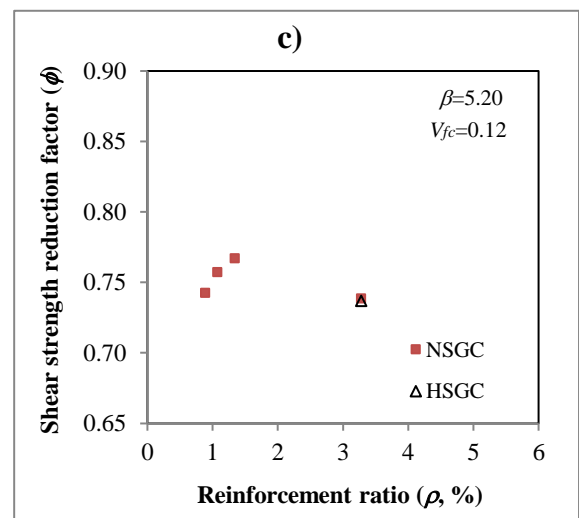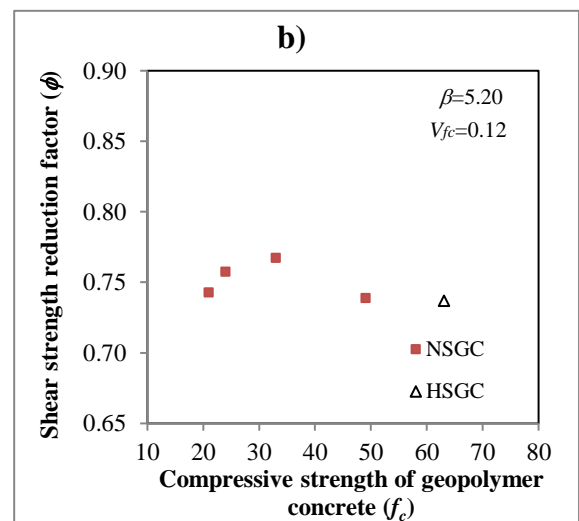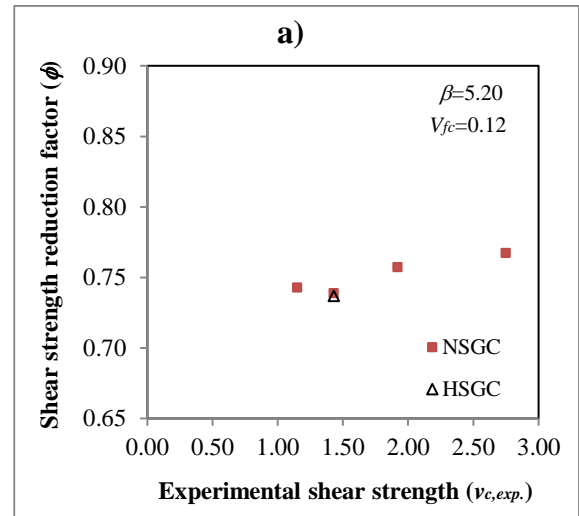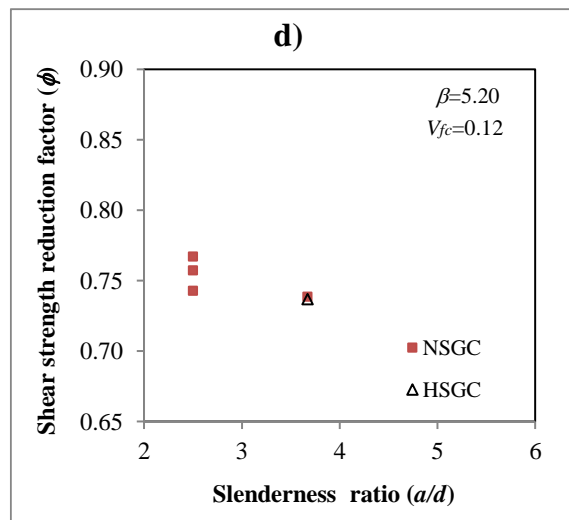
Figure 1: Range of ϕ values determined using evaluation database for $\beta = 5.2$ ($p_F = 10^{-7}$) and $V_{f_c} = 0.12$

VI. CONCLUSIONS

This study was conducted to calculate the shear strength reduction factor (ϕ) for geopolymer concrete beams without stirrups. On the basis of results obtained in this study, the following conclusions can be drawn.

- For the traditional concrete, ACI 318 [2] Code suggests strength reduction factor of 0.75 for shear. This reduction factor considered in predicting the contribution of geopolymer concrete to shear strength is valid for a   of 0.12 and a failure probability of 10^{-7}.

- For relatively low cracking shear strength values ($v_{c,\text{exp.}} < 1.50$ MPa), where the corresponding shear strength reduction factors are mostly less than 0.75 for $p_F = 10^{-7}$ ($\beta = 5.20$) and   .

- It is shown that the shear reduction factor generally increases with increasing f_c except for an experimental beam for NSGC beams. So, this result means that the shear reliability of the beam increases as the strength of the geopolymer concrete increases.

- For a given V_{f_c}, when   increases or vice versa p_F decreases, shear reduction factor ϕ decreases. Therefore, this result can be explained by the increase of shear reliability of the beam.

- For a particular p_F, the shear reduction factor   is reduced with the increase of   coefficient of variation related to the   . As a result, the shear strength of the beam decreases with increasing coefficient of variation of geopolymer concrete.

- It is generally observed that the   increases with increasing   except for an experimental geopolymer beam for NSGC beams.

- Since the test data for NSGC and HSGC members are very limited, further research is required to verify the founded   for HSGC beams.

REFERENCES

[1] ACI, "Building code requirements for structural concrete (ACI 318M-95) and commentary", *American Concrete Institute*, Farmington Hills, MI, USA, 1995.

[2] ACI, "Building code requirements for structural concrete (ACI 318M-11) and commentary", *American Concrete Institute*, Farmington Hills, MI, USA, 2011.

[3] D. Hardjito, S.E. Wallah, D.M.J. Sumajouw, and B.V. Rangan, "On the Development of Fly Ash-Based Geopolymer Concrete", *ACI Materials Journal,* 2004.

[4] P. Visintin, M.S. Mohamed Ali, M. Albitar M, W. Lucas, "Shear behaviour of geopolymer concrete beams without stirrups", *Construction and Building Materials,* 148, 10–21, 2017.

[5] ACI, "Building code requirements for structural concrete (ACI 318M-02) and commentary", *American Concrete Institute*, Farmington Hills, MI, USA, 2002.

[6] G. Arslan, S.N. Alacali, and A.Sagiroglu, "Assessing reduction in concrete shear strength contribution", *Proceedings of the Institution of Civil Engineers Structures and Buildings* 169(4), pp. 237–244., 2015.

[7] A.M. Rakoczy, and A.S. Nowak, "Resistance factors for lightweight concrete members", *ACI Structural Journal*, 111(1): 103–111, 2014.

[8] G. Arslan, A. Ibis and S.N. Alacali, Assessment of reliability of existing equations predicting the shear strength of reinforced concrete beams without stirrups. Teknik Dergi 25(1): 6601–6623, 2014.

[9] TS-500, "Requirements for design and construction of reinforced concrete structures", *Turkish Standards Institute*, Ankara, Turkey (in Turkish), 2000.

[10] S.W. Tabsh, and A.S. Nowak, "Reliability of highway girder bridges", *ASCE Journal of Structural Engineering*, 117(8): 2372–2388, 1991.

[11] J.S. Du, and F.T.F. Au, "Deterministic and reliability analysis of prestressed concrete bridge girders": comparison of the Chinese, Hong Kong and Aashto LRFD Codes, *Structural Safety*, 27(3): 230–245, 2005.

[12] H. Schlune, M. Plos, and K.Gylltoft, "Safety formats for nonlinear analysis tested on concrete beams subjected to shear forces and bending moments" *Engineering Structures*, 33(8): 2350–2356, 2011.

[13] M. Akiyama, H.Matsuzaki, H.T. Dang, and M. Suzuki, "Reliability-based capacity design for reinforced concrete bridge structures", *Structure and Infrastructure Engineering* 8(12): 1096–1107, 2012.

[14] T.S. Ng, A. Amin, and S.J. Foster, "The behaviour of steel-fibre-reinforced geopolymer concrete beams in shear", *Magazine of Concrete Research*, 65(5), 308-318, 2013.

Decision Parameters Supplied by Mining Engineering Students: Are They Creative

M.K. GOKAY

Technical University of Konya, Turkey, mkgokay@ktun.edu.tr

Abstract – **What is creative thinking and how it influence mining engineering students? This question needs to be answered to analyze educational improvements in mining engineering departments. What can be reasonable answers if we ask basic mining questions to the students who are not graduated yet. In order to determine students' creative thinking a survey study was performed. Total number of students who attended this study was 54. They were students at different Grades of Selcuk University, Mining Engineering Department, Konya, Turkey. The survey included one question and it was about the decision parameters for common mining engineering design. Students' answers were filed according to their Grade and decision parameters. Their survey papers were evaluated in seven different categories including one category for "creative ideas". It was resolved that students had been influenced by mining engineering lectures as it was expected. However, it was also concluded that, maximum influences of mining related knowledge and information on these students had been realized at Grade 2 and Grade 3 levels of the department. Parameters selected as the product of original thinking, creative brainstorming, of students were also determined. It was determined that creative thinking in students had been decreased as their Grades in the department are increased.**

Keywords – **Education, Engineering education, Creative engineers, Real-world engineering applications.**

I. INTRODUCTION

Engineering education covers several theoretical and laboratory lectures including practical summer practice at Selcuk University, Mining Eng. Department in Konya-Turkey. Students have prepared mining related projects and full design assignments during Grade 3 and Grade 4 years of their education. After several modifications put forward in curriculum in this department, graduates become more ready for real sector in mining. However, it has been felt by lecturers that, some graduates have obtained their BSc degree but, they are not ready (mentally) for real mining sector. These students have common characteristics; they are unsocial usually, they got knowledge and information related with mining but, they have limited capacity of creative thinking. These graduates feel confident in mining sector after a few years of mining engineering experiences gained in mine conditions. Then, what is critical and creative thinking in general and why mining business and mining engineering environment has been looking for these parameters. In the world, number of engineering faculties and their graduates are gradually increased in last decades.

Due to the requirement recognized in US, engineering standard has been introduced in US to rank engineering departments according to predetermined rules. This is reasonable if one country has several engineering faculties with similar departments. The questions should be asked here, "Are the education in engineering departments standard? Are the graduates of same profession having minimum level of engineering? What are the differences in engineering graduates originated from their education? Standardization in engineering has then started with optional ABED checks for engineering departments in US. This standardization action has gradually been accepted by most of the universities in the world as well. There is another standardization offered for engineering education in Turkey. It is called MUDEK and evaluation organized by National Committee of Engineering Faculty Deans. Both standardizations are active in Turkey and engineering departments can apply one or both of them to obtain their standardization reports. Departments have been informed for their powerful and weak points in their engineering education. Then, engineering departments can act accordingly to eliminate their weak points to require re-evaluation in succeeding year.

Recent research have pointed that standardization in engineering education is necessary but, good engineers have still required especial education. This should not be based on pure mathematics, physics, geometry, chemistry, mechanics etc. Engineers should be innovative and genius at the beginning. Therefore original thinking capacity and its improvements are important in engineering education. Several methods and systems have been offered here to facilitate students' curiosity, innovation in addition to basic engineering educations.

II. CREATIVE THINKING AND ENGINEERING EDUCATION

When creativity in human ideas is the subject in discussions, architectural and artistic projects are in general found more related. Since their obligations and success in architectural design business have been directly related with their originality in their projects & products, they have been lectured about creativity already in their university times. Students in other engineering departments on the other hand, they have tried to present their originality in their projects without getting creativity related lectures. At this point the research performed by Sola etal. [1] must be mentioned. They pointed wide range of knowledge and information which engineering education systems should handle progressively for their students. Engineers ought to be creative, skillfully, practical and knowledgeable nowadays to solve more complex

real world engineering problems. After stressing on creativity and critical thinking abilities of students, which were given as essential parameters of engineering success, Sola etal. wrote also that *"there is evidence of decreasing creativity and critical thinking in senior engineering students. This study sought to understand if freshman engineering students are measurably more creative, but less capable of critical thinking, than senior undergraduate engineering students".* Knowledge intensive engineering education, which have been performed sometimes through pure science information, forces students concentrates on details of scientific realities but less engineering design activities in some universities. But, engineering problems and designs requires mostly socially-related technical creativity as well. Supplying heavy information drains students' critical thinking and creativity, because numbers of design lectures are getting decreased in this kind of engineering educations. This is pointed also by Atwood & Pretz [2] in different manner. They determined that *"students who view themselves as highly creative are less likely"* to complete their engineering degrees. Because their results showed *"creativity is not appropriately taught or rewarded in some engineering curricula".* These results present the fact realized by lecturers and engineering design companies in last decades. That is the declining creative ability of graduates in engineering. Kim [3] performed a study and used archived TTCT data covered 272599 people (included kindergarten kids to Grade 12 students and adults) in US. This research presented that *"a downturn in creative thinking skills (i.e. fluency, originality and elaboration within the TTCT) from 1966 through 1974, and from 1990 to the present"*, [1].

Wilbur, [4] pointed also that, there was a problem in engineering education. He wrote about *"the lack of creativity coming from recently graduated engineering students".* He argued that some universities graduated engineers without *"a better understanding of the issues".* Wilbur stated that *"many classes are content driven leaving little time for the students to explore actual uses for the formulate they learn but rather plug-and-chug. The result is a higher focus on getting good grades than fully understanding the material and knowing how to implement it innovatively".* According to him curriculum was not only the problem, there was also problems in expressing "the value of creativity". Another problem is the courses which are heavy enough so creative applications are difficult to insert into them. According to Wilbur, if the education methods in engineering departments have not been reevaluated, graduates from them *"may find it difficult to exhibit the main characteristics of a good engineer that companies are searching for-becoming an innovator and a thinker".*

In order to evaluate engineering education deeply, education practices at architecture and art departments are also need to be analyzed. Students there are assumed to deal more creative circumstances. Architectures and artists in fine art and music have been lecturing in many universities on the basis of repeated work of practices. Training of students may have been obtained by supplying practical studio & project type lecturing hours but there is always hesitation about the students' creativity capacity gained there. For instance, Potur

and Barkul [5] performed a study at Faculty of Architecture (Yildiz Tech. University, Istanbul-Turkey) and supplied TTCT test (Torrance test of creative thinking) results obtained from students. They said that t-test results obtained from their tests demonstrated; *"last year students were notably more creative than the first year students".* They noted also that this may be results of their studio-based education system where students had projected and they have worked on their own studies during these studio lecture times. On the contrary, Sola etal. [1] performed a survey to test engineering students' creativity at University of Central Florida, US. Freshman engineering students from EGS1006C coded lecture and senior engineering students from EGS4624 coded lecture were surveyed through TCT-DP (Test of creative thinking-drawing production) tests. These researchers concluded this study provided *"strong evidence that incoming freshmen were more creative than senior engineering students".* These results show *"a decline in creativity between the freshman and senior years of engineering students".* Sola etal. pointed engineering curriculum as main influences on these result and they said that *"studies show evidence of a definite lack of creativity training within the engineering curriculum".*

Creative thinking in education is familiar subjects for all educators. Fisher, [6] warned about "critical thinking" fact and teaching activities about it. According to Fisher, one of the earlier teachers about "creative thinking" was Sokrates at 2000 years ago. That means, original thinking, innovations, creative ideas have been valuable assets in history as well. Societies have always required innovative individuals who think differently to solve complex, messy, troubles and offer easier way of living.

III. CREATIVE THINKING AND MINING ENGINEERING

As an engineering branch mining engineering requires original thinking to imagine rock masses in underground without seeing them. In addition, excavation of rocks and earth type materials are very difficult when the amount of moving materials think about. Therefore miners use big machines which need careful design and careful operational plans in mining sites. One of the leading mining companies around the world is "Rio Tinto", and it has several coal, energy minerals and metal mines around the world. This company has interested engineering education and announced their expectations in its web-page [7]. Researchers partnering with Rio Tinto Company had reached following evaluations after analyzing the mine engineering working conditions; *"a) Technology, society and markets are moving in a dramatic way which demands a fundamental shift in the way we think, b) Tomorrow's mining workforce – as in many other industries – will require an* increasing focus on problem solving skills, creative thinking and digital savvy, *c) It is estimated that 70 % of future jobs will be STEM (*science, technology, engineering, and mathematics) *related and these will be the key to sustaining economic growth and development".* Since "creativity" has long been realized by engineering companies and universities, some departments have already been rearranged their educations accordingly to handle creativity as well. Mining is powerful sector in Rep.of South Africa (SA). When "Carrier Guide" booklet published

by Mining Qualification Authority in SA was checked carefully, several advices were observed [8]. In this guide, job applicants in mining sectors were advised to have more than 10 critical cross-fields skills in addition to their technical skills. First 3 advises here were related with original thinking capacity; they were; *i) Identifying and solving problems, ii) Display responsible decisions, iii) Use critical and creative thinking*. These recommendations stress also mainly on team works and responsibilities as well. Currently, some universities are mentioned in their WebPages about creative engineering education in addition to their practical and theoretical education capacities. For example; School of Construction and the Environment, Mining and Mineral Resource Engineering department at British Columbia Institute of Technology, Canada, [9], have introduced itself in related webpage with following lines *"...the degree will have a strong practical focus built upon a broad foundation of engineering theory, analysis and design. Throughout this program, students will be challenged to develop their critical thinking skills and exercise their creative abilities"*. Educational features supplied by mining engineering departments are generally different in character. Besides the location, department facilities, elective lectures, scholars and practical application opportunities might be diverse among them. In some departments lectures are given by especial scholars who ignite students' creative capacities. In some other cases, scholars even destroy critical and creative thinking abilities of students by facilitating memorization. Creative students are usually ready for difficult circumstances, because they are confident about their problem searching and design habits. These students sure that problems in future might be complex and unusual. They may feel upset during problem solving time and they may lose the way out. But they are sure to work on it without hesitating, even with satisfaction.

IV. SURVEY QUESTION TO CATCH CREATIVITY OF MINING ENGINEERING STUDENTS

In order to catch creativity and wideness of mining related knowledge of students in Mining Engineering Department of Selcuk University (Konya-Turkey), a survey was performed. This study was not a standard survey type; it had only one question to answer. It was aimed to determine creative thinking clues by asking unexpected one survey question to the students who accept to attend. The survey question required basic culture of mining to replay. It could also be answered by assisting advance level of mining engineering knowledge as well. It was open also imaginative solutions which might have activated brainstorming in students. That means creative and logical reasoning was also possible to replay this kind of questions. The answers were free style texts, story writing in character. They were analyzed line by line for their content. Since the survey was a "content analyses" type research, students' reasoning and decision parameters mentioned in their answers were then evaluated and listed according to predetermined 7 decision groups.

Creativity of engineers and engineering students could be activated when they are put into extraordinary decision circumstances. These decision situations could be a kind of

simulation cases like our ancestors pass through the troubles in history. For instance; how you get water to drink at arid flat area if the water is in 15 meters deep in underground? How you collect fruits from long coconut trees? We may add many similar questions which had possibly been answered already by our ancestors. Have you ever think about early human societies which had a few members and they had to find out solutions for their everyday troubles. One should bear in mind that those troubles might be life threaten types (lack of food, heated coverage, animal attacks etc.) as well. Miners are pioneering frontier in excavation, currently at earth surface or in underground, in future they may do similar operations at other planets and moons. They organize works and workers to dig minerals from earth everyday. Therefore they definitely come across original decision cases daily bases and that decision should be given by shift mine engineers. Those decisions (work orders) should be reasonable and legislatively correct. Thus, mine engineers must open minded, original thinker, innovative, critical and creative at their workplaces to design or organize mining activities in/on such a surprising earth crust.

In this study undergraduate students were surveyed and they were suddenly, (without giving them any earlier notice) asked if they would like to answer one survey question. The question was as follows: *"Flat elongated surface area has flat coal seam opportunity beneath (Fig.1). The coal seam thickness is 2 meters and its horizontal dimensions in underground are 7.5 x10.0 kilometers. This seam is located 200 meters below the surface. Think that; the density of the coal is about 1.7 ton /m³ and the selling price of coal is 500 TL/metric ton in local energy market. How you mine out this seam to get profit? This is legal mine operation. There will be no marketing problem, as much as you mine out, you will sell all of them in cash through the same mine run-out price. Feel free to answer this question; you may prefer not to write your name on the survey sheets".*
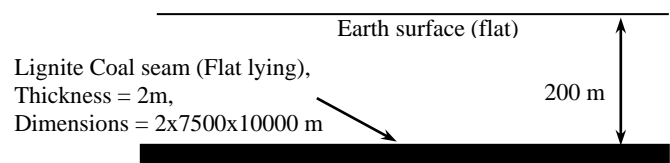
Figure 1. Survey question (sketch).

Students were surveyed in Jan. 2018 and they were requested to finish their reasoning in 15 minutes time. Students who would like to attend the survey were also warned during the survey with the following words; *"there may be different and numerous solutions, please write freely and follow your imagination to think about to reach your answers"*.

V. DECISION PARAMETERS OBTAINED

In this survey study, students wrote their answers in free text format. There was no pre-determined format to follow. The texts, (they supplied), were analyzed and decision parameters they supplied were subtracted one by one as they mentioned in their texts. Students wrote their reasoning in free style. They wrote as they thought and scheduled their mining operations. Their texts were accepted as products of their reasoning originated from their knowledge and creativity. The decision parameters they supplied were grouped in 7 categories. These

categories were decided according to mining design and operation steps, (Table 1).

Table 1. Decision parameter groups to categorize the students' reasoning in this survey study.

Groups	Group concepts
1	Early stage-mining ideas,
2	2.1 Office works (earlier data), 2.2 Site data, 2.3 Data evaluation,
3	Decision about mining methods,
4	4.1 Mining related risks (workplace safety), 4.2 Mining related risks (financial & operational),
5	Mining related factors,
6	Results,
7	Different facts stated (creative facts).

Question asked in survey has many ways to answer. This question can even be asked to secondary or high school students. Answers given can be imaginary also, but it can include professional reasoning as well. Numbers of decision parameters obtained from students in this survey are summarized according to their categories and Students Grades in Table 2. Total number of decision parameter obtained was 633 in this survey. Students attended to the survey were 9, 7, 12, 16 in Grade 1, 2, 3, 4 respectively (totally 54 students). Decision parameters (Table 3) obtained from them were 69, 56, 144 and 364 in Grade 1, 2, 3 and 4 respectively. Grade 4 students supplied more decision parameters as it was expected before the survey. Average values representing the "numbers of decision parameter/students" were found more significant in the evaluation. Decision parameter group which has maximum average value (5.667) was determined for Category 2 parameters from Grade 3 students' survey sheets. Decision parameters supplied by surveyed Grade 1 and Grade 4 students are listed in Table 3.

VI. EVALUATION OF THE SURVEY RESULTS

Decision parameters listed above were obtained from volunteer surveyed students. Since they were not warned before, about the survey, these obtained decision parameters can be considered as their background knowledge. Students used their creativity to supply valuable reasoning and decision parameters during the survey. However, it was realized also that, students were influenced unintentionally during survey applications. Since the survey question was directed to the students at the beginning of lectures (it took first 15 minutes of the lectures) which were related with mining operations, soil mechanics and rock mechanics, decision parameters obtained in the survey were slightly more related with these lectures. Since the survey question did not cover any intention about coal cleaning, most students did not mention about this subject and related decision parameters. Similarly the question given them summarized the coal seam dimensions in underground; therefore some students did not include exploration parameters in their decision parameters supplied in their texted answers. These were cited for students as positive approaches. That

means they did not listed whole decision parameters as they are given in some text-books. This is marked as "positive" manner (descriptive selection made by some students during answering sessions of survey question). During survey performance, it took 15 minutes for students, but each of them spent time for; understanding, reasoning, thinking, logic checking, listing, writing, while texting thinking again etc. Figure 2 and 3 summarized the survey decision parameters outputs in graphs. The decision parameters categories, total and average decision parameters supplied by students are presented here to show their differences more clearly. Figure 2 present that surveyed students supplied maximum numbers of decision parameter in group-2, totally 207 parameters. The numbers of decision parameters supplied by students are listed in descanting order as follows; 207, 194, 77, 67, 60, 16, 12 for decision group 2, 5, 3, 4, 7, 6, 1 respectively.
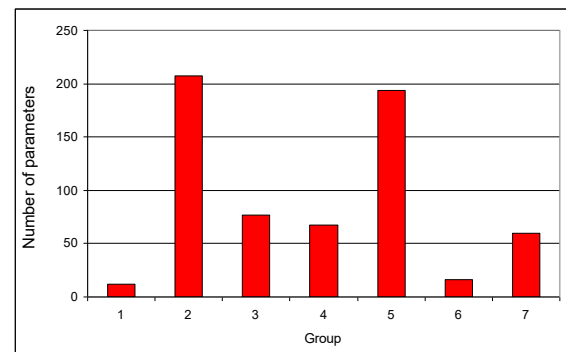
Figure 2. Total number of parameters determined for different decision parameter groups.
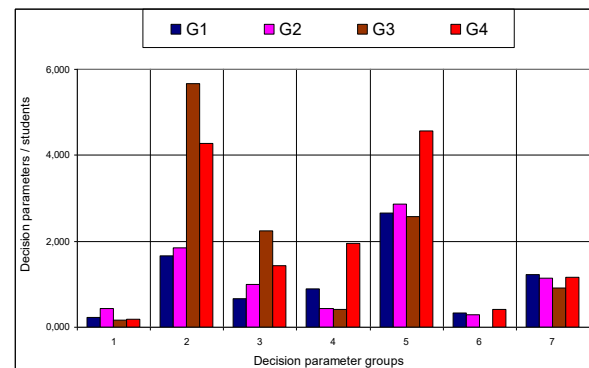
Figure 3. Survey outputs presenting decision parameters/student ratio for surveyed students.

Table 2. Analyses of decision parameters obtained from the surveyed students.

Decision	Grade 1	Grade 2	Grade 3	Grade 4

Parameter	Total	Average	Total	Average	Total	Average	Total	Average
1	2	0.222	3	0.429	2	0.167	5	0.192
2	15	1.667	13	1.857	68	5.667	111	4.269
3	6	0.667	7	1.000	27	2.250	37	1.423
4	8	0.889	3	0.429	5	0.417	51	1.962
5	24	2.667	20	2.857	31	2.583	119	4.577
6	3	0.333	2	0.286	0	0.000	11	0.423
7	11	1.222	8	1.143	11	0.917	30	1.154
TOTAL	69	7.667	56	8.000	144	12.000	364	14.000

Table 3a. Some decision parameters obtained from the Mining Eng. Department's Grade-1 students.

Dec. Group-1	Dec. Group-2.1	Dec. Group-2.2	Dec. Group-2.3
Mine location.	Required machineries, Collect the data.	Exploration drilling, Coal strength, Strength of country rocks, Analyses of country rocks, Hardness, Water conditions.	Mining method selection, Thick overburden, Stable shaft, Planning.

Dec. Group-3	Dec. Group-4.1	Dec. Group-4.2	Dec. Group-5
Suitable method, Explosive selection, Machinery selection, Underground mining method, Open pit mining.	Work safety, Workplace safety, Precautions.	Roof collapsing, Roof failure risk, Prevention of roof failure, Cost of liquid pumping, Powerful shaft.	Shaft sinking, Reach the coal seam, Lifting, Gallery excavation, Two shafts excavated, Tunnels, Rails at galleries, Divide the seam into slices, Mine the slices, Excavate.

Dec. Group-5	Dec. Group-6	Dec. Group-7	Dec. Group-7
Coal excavations, Haul the coal, Construct conveyors, Conveyors for hauling, Haul the coal outside, Ventilations, Machinery operations, Fillings, Drill pipe holes, Pump chemicals to coal seams.	Earn money without mining, Mine out the whole seam.	Selling the mining rights, Mine out locations, Construct and sell apartments there, Slicing like a cake, Liquefaction of coal.	Pump liquid-coal up, Condensate liquid-coal, Ask reasonable cost of coal mining, Exploration drillings are important, Careful steps in planning.

Table 3b. Same decision parameters obtained from the Mining Eng. Department's Grade-4 students.

Dec. Group-1	Dec. Group-2.1	Dec. Group-2.1
High value reserve, Mine the seam, do not let it laying down, Mining or unnoticing, Best mining method, selection, Basic coal seam data are known.	Pre-works, Location of seam is known, Overburden quantity is huge, Deep seem, Seam dimension is known, Location conditions, Seam thickness is good.	Control if there is any pre-reports on this site, Overburden rocks , Check the problems for this seam. Engineers got the required lectures, Work experiences are encountered.

Dec. Group-2.2	Dec. Group-2.2	Dec. Group-2.2
Rock mechanic tests for coal, Rock mech. tests for country rocks, Limit values for open pit mining, Exploration drillings, Carrot analysis for coal quality & value, Coal seam structure, Country rocks structures, Determine roof and floor laying rock formations, Study on machinery capital and operation costs.	Hauling problems, will be encountered, Many variables and parameters, Controls the rocks' cavebility, Geology, Geophysical explorations, Coal reserve, volume calculations, Panel reserves, Underground water conditions, Underground mining tests, Required, (enough) tests.	Roof loads. Gallery, unsupported time period, Open pit is not efficient for deeper seams, Fault search around the faces, Coal hardness, Environmental conditions, Energy supply conditions, Roof dead loads, Ventilation conditions.

Dec. Group-2.3	Dec. Group-2.3	Dec. Group-2.3
Decide open pit or Underground	Select cutting machines,	Select support types,

mining, Method advantages and disadvantages, checked, Market value of whole coal 33,12 billion US\$, Pit mining is not good, Underground mines, %100 of seam cannot be mined, Planning with obtained data, For 200m Underground mining is costly then apply open pit, Decide coal mine life (Duration of mining), Feasibility Works, Calculate pit and Underground mining costs.	Coal hardness Select hauling machineries, Cut-off grade calculation, Plan for the coal mine, Divide coal seam into panels, Panel design for longwall faces, Panel dimensions, Mine life calculation, Cost analyses, profitability, Stability analyses, Suitable bench slope angle, Decide excavation type, Select production methods, Select mine machineries.	Steel supports related with rocks, Mechanized coal cutter dimension, Seam suitability for panel, Longwall designs, Select suitable machineries, Coal selling price & reserves, Calculate earnings, cash money, Coal cleaning plant required, Country rock conditions are suitable, Decide load on supports, Support types, If it is suitable timber supports.

Dec. Group-3	Dec. Group-3	Dec. Group-3
Select mine method, Underground mining methods, Longwall mining, Retreat longwall mining, Longwall with caving, Room & pillar mining methods, Rocks are stable, Decide pit or underground mining, Open pit mining method.	Try to select open pit, Decide underground mining so overburden moving is out of consideration, Cut-off grade determined so Underground mining method, Decide on mine operations, longwall mining method, Mine plan include hauling & ventilation system.	Caving methods with weak rocks, Filling methods with weak rocks, Decide support system & types, Select excavation method, If required so pellet production, Apply methods to increase recovery ratio.

Dec. Group-4.1	Dec. Group-4.2	Dec. Group-4.2
Work safety, Workplace safety, Follow the safety rules, Obey precautions to mine coal seam, Mine accident possibilities, Safety is important, Measure mine gases, Ventilate mine properly, Prevent mine explosion, Roof support problems, Underground water and Methane problems, Control the workers like at open pit, Open pit operation is safer.	Decide if mine is profitable, Suitable mining condition check, Cost analysis, Fast production, Decrease cost and increase profit, Decreasing cost by obtained data, Mine at upto 200m with minimum cost, Mine gas and coal dust problems, Dust due to mechanized mining, Mine fire dangers, Flat seam, 200 m Underground mine is economic, Underground development cost is high, Full mechanized face, less workers, Roof falling dangers, Produced coal size and market differentiation, Drum coal cutter selection for energy plant market, Coal selling procedures, Lost of reserve is minimum in open pits.	Accident risk is lower in open pit Operations, Prepare side galleries for work safety purposes, Obtain machines is important, Water jets and continuous face ventilation, For profitability, calculate costs & profits, Too many variable then untouched, Lost should be encountered, physical and mental problems, Coal supplied to market, sell it with good price, Economic cost calculations, If no profit then no mining, Supports and workers cost in minimum at faces, Cost for workers and machines.

Dec. Group-5	Dec. Group-5	Dec. Group-5
Shafts sinking, Inclined shaft sinking, Shaft sinking at the mid point of seam, Ventilation shaft, additional, Develop the seam start mining, Mine entrances, natural ventilation possible, Two ventilation galleries, Excavate, Excavate after obtaining suitable conditions, Excavate according to data evaluation, Excavate in panels, Daily high production, Production according to market requirement.	Drum coal cutter, Daily product rate, Mine out periods for panels, Ventilation, together with small fans in the mine, Ventilation (natural and with fans), Ventilation doors, Coal size arranged by coal crusher, Coal crusher at transfer point from chain to band conveyors, Band conveyor hauling upto surface, Supply coal 7/24 through the band conveyors, Mine cars for coal hauling, Transport coal, haul, to surface, Lift system, Main galleries, Galleries to reach coal.	Excavate through O/pit benches, Dragline usage, Rock hauling trucks, Suitable pit machineries, Open pit efficiency may be higher, Underground mining, pillars then lost of reserve, Underground mining, extra costs, Overburden excavate, Machineries, Haul and dump mine trucks, Pit blasting, Overburden materials, moved to dump sites, Coal cleaning for cleaner coal, Calculate this plant cost, Sell clean coal expensive, Screen the coal into sizes.

Dec. Group-5	Dec. Group-5	Dec. Group-5
Production rate depends mining	Coal hauling,	Pellet production with calorie

method, Arrangement of longwall faces, Machine excavation, Mechanized coal mining, Half mechanized mining, Chain face conveyors, Advancing hydra. face supports, Double drum coal cutter.	Haul through ramp, Support the galleries, Supports, Timber supports, Supports to help roof rocks, Roof rocks carry the dead loads, Supports according to method type, To excavate coal seam, excavate 　　rock volumes.	modification, Employ experienced workers, If there is no profit, then, no 　mining.

Dec. Group-6	Dec. Group-7	Dec. Group-7
Mine out valuable coal seam, Mine out and sell the coal, Mine out the coal and clean 　the coal, Mine out the coal for power plant, If it is okay start mining, Start mining in suitable way, Considering parameters, Accept the lost of reserve, 　mine out the seam.	Environ. friendly mine design, Safe operation for creatures, Company efficiency & success, Panel layouts, (sketch), Less workers then low risk, Weather conditions, Transportation, road & accessibility, Main exploration data are given, Domestic purposes, pellets, calorie 　modification.	Small sized coal production for 　power plant, Mine out valuable coal seam, Mine out and sell the coal, Mine out the coal and clean 　the coal, Mine out the coal for power 　plant, If it is okay start mining.

Dec. Group-7	Dec. Group-7	Dec. Group-7
Start mining in suitable way, Considering parameters, Accept the lost of reserve, 　mine out the seam, Data known exploration steps out, May be, company ,boss, differences 　influence the results.	Knowledge can be obtained, field 　experience can be gain, Follow your mine workplace safety first, Face, crusher, conveyors in 　(sketch).	Advancing face support in 　(sketch), Select mining method according 　to coal demand, Our problem is production, Any idea about earnings, As a student we got the same 　information, but we will have 　different mining ideas.

These decision parameters suggest also that the importance of groups for students. They put group 1 parameters at the end of list. That means surveyed students paid less attention to the works performed at the early stage of mining ideas. Similarly they seemed to be less concentration on the results of mining activities. However, since the survey question was under analyses, students were not asked directly about these two decision parameters. They were asked how to manage the mining and put the coal out for selling. Therefore students naturally supplied more parameters on decision group of 2, 3, 4 and 5. Students mainly concentrated on pre-mining and mining factors and supplied decision factors mainly on these decision groups (groups 2 and 5). Since the main objective of this survey was the creativity of the students, parameters related with creative thinking circumstances were listed in decision group 7 in Fig.2. Students supply totally 60 creative parameters. Number of creative parameters which supplied through the mining engineering Grades can be listed as; 30, 11, 11, 8 for Grade 4, 3, 1, 2 respectively. Since the number of students who attended the survey was different for Grades, ratios representing average number of creative parameters supplied per students were also determined as follows; Grade1: 1.222, Grade2: 1.143, Grade3: 0.917, Grade4: 1.154 That means creative decision parameters per students were determined highest for Grade 1. Then the value decreased up to 0.917 in Grade 3 passing through the value 1.143 for Grade 2. This value 1.154 was found for Grade 4.

Therefore creativity assumed to be declined slightly From Grade 1 to Grade 3. This result coincides with the theoretical lecture intensity of the mining engineering students. Second semester of Grade 3 and Grade 4 years includes design and seminar lectures as well. This seems influence thinking capacity of the students, their creativity raised from 0.917 to 1.143 creative decision parameters/students. Students must show their original thinking capacity in full manner. In some case, students feel surrounded by knowledge given in lectures. When they are asked something original, they assumed it is better to answer with the gained knowledge before. They are not get used to present their own ideas. However, it was observed that "seminar" and "design lectures" which have been supplied to students influenced them positively.

VII. Conclusion

Creative statements, ideas, parameters and designs are the products of innovative individuals who help themselves positively. History recorded these kinds of achievements originated by creative original thinking. Creative ideas are necessary for mining engineering applications as well. Therefore, students at Mining Engineering Department of Selcuk University (Konya-Turkey) were surveyed in this study for their creative ideas. It was found that creative parameters supplied per students in the performed survey work at Grade 1 level were higher than the other grades. This ratio (creative parameters supplied per students) was determined lower for Grade 2 and lowest for Grade 3 students. The ratio was found slightly higher than Grade 2 for Grade 4. As the other researchers determined before it can be concluded here as well that, theoretical lectures and heavy subjects included in them have forced students concentrate only the knowledge they

have been getting. When the design lectures starts in second semester of Grade 3, they were found out more creative in producing innovative decision parameters. Creativity concept supplied by Grade 4 students was slightly different than Grade 1 students. Because age, social perceptions, culture, mining knowledge and information they have collected were positively differentiated.

REFERENCES

[1] E. Sole, R. Hoekstra, S. Fiore and P. McCauley, "An investigation of the state of creativity and critical thinking in engineering undergraduates", *Creative Education*, ISSN Online: 2151-4771, doi:10.4236/ce.2017. 89105, vol 8, 1495-1522, 2017.

[2] S.A. Atwood and J.E. Pretz, "Creativity as a factor in persistence and academic achievement of engineering undergraduates", *Journal of Engineering Education*, doi:10.1002/jee.20130, vol 105, 540-559, 2016.

[3] K. Kim, "The creativity crisis: The decrease in creative thinking scores on the Torrance Tests of Creative Thinking", *Creativity Research Journal*, doi: 10.1080/10400419.2011.627805, vol 23, 285-295, 2011.

[4] R. Wilbur, "Boxed in: The lack of creative thinking in engineering students", *Undergraduate Research Posters*. 2013, http://scholarscompass. vcu.edu/uresposters/10, Virginia Commonwealth University, Scholars Compass, Poster 10, Retrieved Nov. 21st, 2017.

[5] A.A: Potur and O. Barkul, "Creative thinking in arhitectural design education", *1st International CIB Endorsed METU Postgraduate Conference, Built Environment & Information Technologies,* 113-125, Ankara, Turkey, 2006.

[6] A. Fisher, "*Critical thinking, An Introduction"*, Cambridge University Press, The Edinbugh building, Cambridge, UK, ISBN 0-521-00984-7., 2001.

[7] Rio Tinto, "*What will the mining workforce of the future look like? Why science-based skills are critical for the industry's pioneers of tomorrow"*, Web page, http://www.riotinto. com/ourcommitment/ spotlight-18130_22976.aspx, Retrieved 23th March 2018

[8] MQA, "*Career Guide, Mining and minerals sector*," Mining Qualifications Authority, South Africa, www.mqa.org.za, Retrieved Nov, 22cd 2017.

[9] BCIT, "British Columbia Institute of Technology, School of Construction and the Environment, Mining and Mineral Resource Engineering", Web page; https://www.bcit.ca /study/programs/8610beng, Retrieved 23th March 2018.

Benefits of Micro Scale Deformation Detection

M. UZBAS[1] and M.K. GOKAY[2]

[1]Technical University of Konya, Turkey, muzbas@ktun.edu.tr
[2]Technical University of Konya, Turkey, mkgokay@ktun.edu.tr

Abstract – **Deformation measurements are important for rock strength tests. There are mechanic and electronic methods to measure micro scale rock strain related displacements. Moreover, deformations which can not be measured through electro-mechanical or optical apparatus are also valuable assets in engineering decisions. Digital image correlation (DIC) method is one of the methods used to realize and calculate very fine (micro) scale deformation in engineering applications. Compressive strength tests and indirect tension (Brazilian) strength tests were performed in this study to visualize vertical and horizontal micro displacements of tested specimen surfaces to evaluate behavior of the sample (breakages) during these tests.**

Keywords – **Digital image correlation, Rock strength tests, Micro scale rock deformation, Rock mechanics.**

I. INTRODUCTION

Rock mechanics applications cover field and laboratory tests. Main aims to perform these strength and physico-mechanical tests are observing behavior of the rock materials and rock masses through their strength and physical property differences. Rock masses are natural solid materials around tunnels, mine galleries and mine stopes. Concrete which can be thought as a kind of reconfigured carbonate rock are main load carrying materials in construction industry. Rock and concrete types and their strength values and mechanical behaviors are governing factors in stability evaluations of engineered designs (rock foundations, tunnels, mine galleries, buildings, dams, bridges, ports, roads etc.) for civilization. Laboratory tests to define rock & concrete strength properties include also compressive and indirect tensile tests. These tests have been performed to obtain stress-strain diagrams for related rock and concrete types (tested samples). Rock mechanic tests performed according to suggested method, [1], are referenced in different mine engineering designs to define rock mass behaviors on rock related stability problems (at underground or open pit mines). Rock-related engineering has also interested in vertical and horizontal displacements occurred at test samples. These strain values are used to define elastic modulus and Poisson's ratios of the samples. Engineers have recently concentrated on micro scale displacement at these samples, because these movements are initiations of micro level fractures at the test samples. Fracture propagation at rock and concrete materials are special research areas in

rock and structural mechanics for stability evaluation. Machine parts which have micro fractures due to production inaccuracy, mismatches, have analyzed through x-ray analyses, finite element calculation methods, thermal camera evaluations etc. Likewise, stability problems at mine and construction related features require similar examinations. All the cases require these studies are important for the safety of men at their work and civil life.

Study performed here includes micro scale displacement determination during basic strength tests, which are compressive and indirect tensile (Brazilian) strength tests. Deformations which were measured from test samples (rock or concrete) have different in directions and these displacements depend on the types of rock and concretes. Deformation of some rock samples can be seen during strength test by naked eyes. Some rocks supply vertical and horizontal strain level which can be measured by electro-mechanical instrumentation. Some others produce very fine micro displacement until their breakage (brittle rocks for example) which can not be detected at all. Either ductile or brittle tests samples, their micro scale displacements (vertical and horizontal) during the tests produce valuable data for engineers. Therefore digital image correlation, DIC, method has been applied for several years in rock and civil engineering cases to understand the rock and concrete behaviors under stressed conditions, [2, 3].

Application of DIC method at strength tests of rock and concrete materials starts with adding random dotted paint matrix on selected test samples. Then dotted surface of the test specimens have continuously been photographed (numerous digital photo frames should be taken for each second of testing time). These photos supply size and location data for dots observed on the test samples. Concurrent images are correlated (Fig.1) through time for any differences which are interpreted as the results of micro scale displacements. DIC methods and related applications have been reported already for different application areas [4]. Mechanical and civil engineers are also facilitating related DIC methodologies for their strength related analyses. Toughness of solid materials which have been tested by facture initiations & propagation cases are common research subjects in these engineering fields.
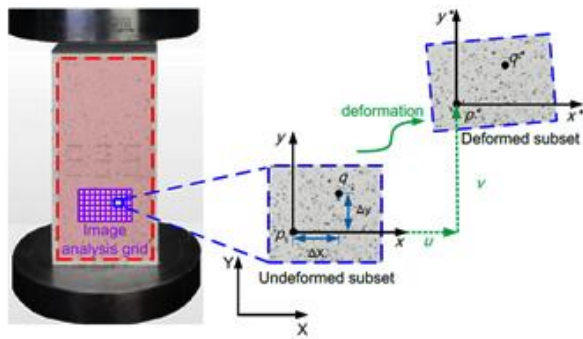
Figure 1: Detection of compressive test sample (which had been painted with dots) deformation by using DIC analyses [3].

II. DIGITAL IMAGE CORRELATION

Digital image correlation method is based on image processing techniques and according to Dai etal. [5], DIC method first offered by Peters and Sutton etal. [6, 7]. It is optical method and based on digital pixel properties (differentiation in properties, locations etc. in testing times). Pixels in simultaneous digital photos (photographs obtained by high speed cameras, Fig.2) have been compared for any differences [8]. One or certain groups of referenced pixels in selected images might have then been replaced during test times. These movements can be recognized when the pixels (supplied by simultaneous images) are compared. Thus randomly but homogeneously distributed diverse sized dots on tested sample surfaces are very helpful in DIC analyses. These dots, points, help DIC calculation programs in their correlation procedures. Strain development on the surface of the tested samples due to applied stress levels can be shown by DIC methods after correlating the progressive images' pixel data. Determination of strain levels on the appeared surface of the test samples can provide information about strains in the tested samples as well. Displacements (vertical and horizontal) determined on the surface of the test samples open new dimensions in understanding of strain accumulation and progressive differentiation.

Figure 2: Test apparatus including digital cameras for direct tensile strength testing of titanium alloy plate [8].

III. DISPLACEMENTS AT TESTED SAMPLES

Displacements observed at test samples of compressive and indirect tensile strength tests were used here for evaluation of related micro scale displacements. In order to understand strain developments during these tests, travertine and light weight concrete samples were selected as tested materials. Both of them were porous solid materials. Light weight concrete samples are especially produced for heat and sound isolation purposes and these structural members molded by using a concrete type which contains numerous small (2-5 mm in diameter) voids. Travertine rock was other test material in this study which contains also many natural voids. These two solid materials have widely been used at modern constructions in Turkey. Therefore, these materials were purposely selected for DIC based strain evaluation through compressive and indirect tensile strength tests (Fig.3) in this study.
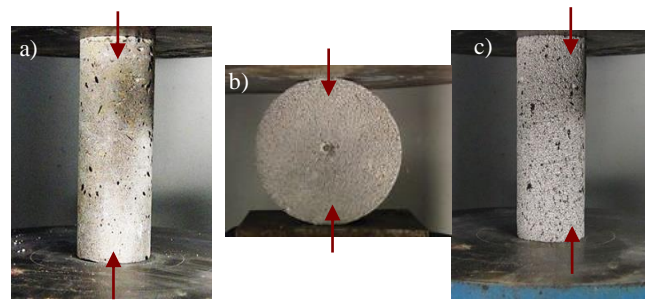
Figure 3: Test samples at their location between hydraulic press platens just before vertical loading.

Vertical loading for travertine (Fig. 3a) and light weight concrete (Fig. 3c) at hydraulic press had been arranged according to standard test procedures suggested for their compressive strength tests except vertical loading rate. It was kept at minimum level to catch solid material micro displacements before fracturing. Test samples for Brazilian test (Fig. 3b) have small holes at the center of the samples as well. Fractures originated due to tensile stresses in these samples are expected in vertical axis covering these holes. Thus, these small holes were drilled to understand their influences on strain developments at indirect tensile test samples. Vertical and horizontal displacements which had been observed during the performed tests were analyzed for their rock behavior properties.

Data for DIC evaluation in this study were obtained remotely through one camera under enough light obtained from artificial daylight lighting. Rock strength tests and camera recordings did not interrupt, influence, each other. After each test, DIC data were transferred to computer to follow Matlab calculation procedures to obtain digital image correlations which supply micro level vertical and horizontal displacements (Fig. 4, 5 and 6).

a)　　　　　　b)　　　　　　c)

Level of the vertical displacements on the sample surface.

d)　　　　　　e)　　　　　　f)

Level of the horizontal displacements on the sample surface.

Figure 4: Displacements observed during compressive strength test of travertine sample. (Progressive phases; at the beginning of the test (a,d); at the mid level of loading (b, e); just before the breakage of the test sample (c, f). Displacement levels are scaled according to color change: Blue color (- direction), Red color (+ direction).

a)　　　　　　b)　　　　　　c)

Level of the vertical displacements on the sample surface.

d)　　　　　　e)　　　　　　f)

Level of the horizontal displacements on the sample surface.

Figure 5: Displacements observed during compressive strength test of light weight concrete sample. (Progressive phases; at the beginning of the test (a,d); at the mid level of loading (b, e); just before the breakage of the test sample (c, f). Displacement levels are scaled according to color change: Blue color (- direction), Red color (+ direction).

a)　　　　　　b)　　　　　　c)

Level of the vertical displacements on the sample surface.

d)　　　　　　e)　　　　　　f)

Level of the horizontal displacements on the sample surface.
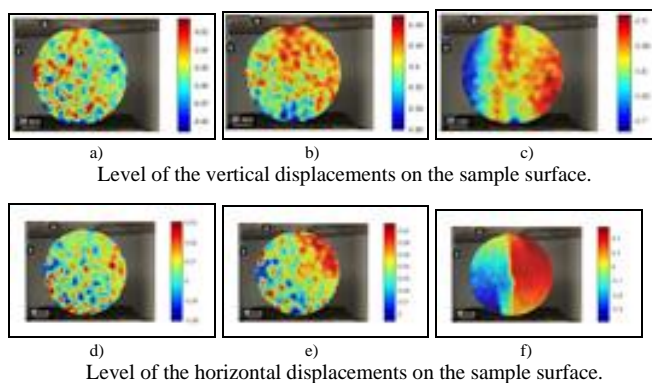
Figure 6: Displacements observed during indirect tensile (Brazilian) strength test of light weight concrete sample. (Progressive phases; at the beginning of the test (a,d); at the mid level of loading (b, e); just before the breakage of the test sample (c, f). Displacement levels are scaled according to color change: Blue color (- direction), Red color (+ direction).

IV. EVALUATION OF TESTS

Displacements occurred due to hydraulic press loading at selected strength tests have visualized by using DIC methods. While loading had been applied, strain gained in the test samples and displacements observed through DIC had been recorded progressively. Results presented in Fig.4, 5 and 6 are computer evaluation outputs of collected digital images. There are several ready-to-use software programs and Matlab program steps which could be used to obtain DIC displacement outputs like presented. Each output screen has its own separate displacement scale which present negative, (-), direction (blue colored) and positive (+) direction (red colored) of movements for the selected time periods. DIC procedures can produce numerous output graphics (screen views) which basically depend on obtained simultaneous digital images through cameras. Brittle materials, for instance produce sudden breakage at the end of the strength tests which can only be captured by high speed cameras. DIC outputs for the tests performed for this study were illustrated here for their progressive phases. Micro displacements (which were detect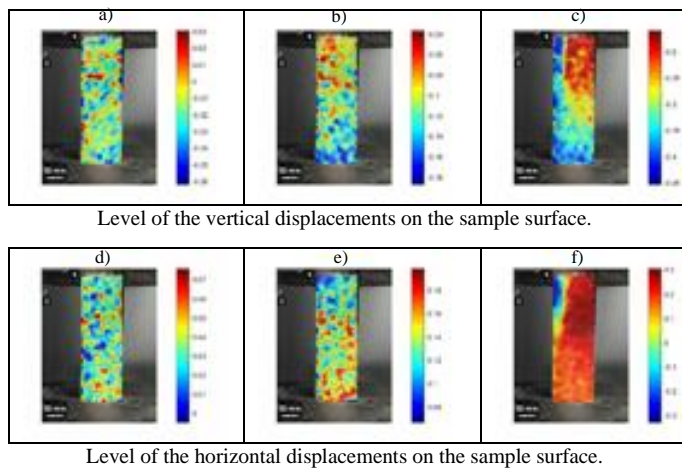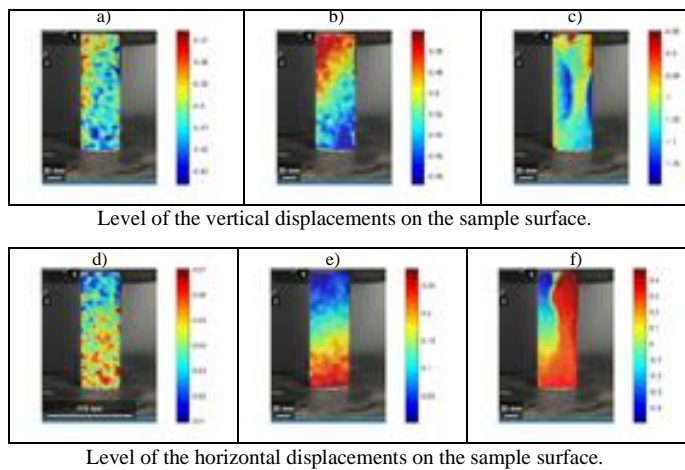ed for vertical and horizontal deformations) were presented in Fig. 4, 5 and 6. In these figures, 3 phases in deformations were illustrated; these phases are; phase-1: just after the starting moments of the tests (a and d labeled graphs); phase-2: at the mid-levels of the tests (b and e labeled graphs); and phase-3: just before the breakage of the samples (c and f labeled graphs). Vertical and horizontal displacements presented in these figures were acquired from simultaneous digital images of the performed tests.

It is important to point here that, displacement occurred on the surface of the test samples might sometimes be different than the displacements occurred in the samples. However, in most of the cases, surface displacements resemble with actual deformations behavior of samples. Observing micro scale displacements (through the test loading phases until the breakage) on the surfaces of tested samples causes new dimensions, understandings, in strength test evaluations. For example, Figure 4 and 5 include displacements occurred on the surface of the travertine and light weight concrete samples (during uniaxial compressive strength test) simultaneously. Hydraulic press used in this study increase its boom from bottom. Therefore, each test sample in this hydraulic press has stressed by raising this hydraulically activated boom. Upper parts of the samples are backed, (passively opposed, resisted) by counteraction steel platen of the hydraulic press. There was no hydraulic boom there to push test samples from their upper surfaces.

It was detected that, uniaxial compressive strength tests of porous samples, (travertine and light weight concrete), have certain similarities in vertical and horizontal displacement behaviors at the performed tests in this study. Gradual differentiation of vertical displacements (in negative, (−), direction and positive, (+), direction) were observed at tested samples' surfaces. Micro vertical displacements in (−) direction were observed at the bottom parts of the samples, and (+) direction in vertical displacements were detected at upper parts of the samples. Horizontal displacements on the other hand were obtained in (almost) opposite manners. These (horizontal) deformations were determined at (+) direction

near bottom parts of those porous uniaxial strength test samples. Displacements observed for Brazilian test were also remarkable in character. Stressed light weight concrete sample had been produced (+) direction vertical displacements at upper side of the test sample. When indirect tensile actions had started to influence the sample, (+) direction vertical displacements had also been become obvious at vertical loading axis of the test sample. At the beginning of the test, horizontal displacements were observed randomly, (horizontal displacements in (-) direction and (+) direction were not concentrated) on the surface of the tested sample. When the Brazilian test was progressed and indirect tensile stresses had been influenced the sample, horizontal displacements (either in (-) direction or (+) direction) have also been concentrated on the tensioned vertical axis of the test sample. Horizontal displacements which were indirectly formed in the sample due to vertical loading were then easily be recognized by DIC graphics (Fig.6f) presented.

V. CONCLUSION

Digital image correlation techniques supply additional clues for the researcher in their targeted tests. Stress-strain differentiation graphics have been common results from strength tests. DIC techniques open new dimensions, understandings, in stability analyses. Vertical and horizontal displacements on the surface of the tested samples have been recorded through digital images. These displacements which can be obtained for the selected test time have been constructive for researchers. Engineers have currently new opportunities to understand and evaluate strain distributions on test sample surfaces. Observing strain differentiations on the tested sample surface during the strength tests open new windows for engineers to capture further material properties. Influences of heterogonous materials in the tested samples have then been recognized more radically through test sample surface displacement rates. Small scale fissures and defects on/in test samples can also be analyzed for their influence.

REFERENCES

[1] R.Ulusay and J.A. Hudson, *The Complete ISRM Suggested Methods for Rock Characterization, Testing and Monitoring: 1974-2006, Int. Society for Rock Mechanics, Commission on Testing Methods, 2007.*

[2] Q.Lin and J.F. Labuz, Digital image correlation and fracture process in rock, *"44th US Rock Mechanics Symposium and 5th US-Canada Rock Mechanics Symposium*, Salt Lake City, UT, US, June 27-30, 2010.

[3] M. Chen, S.Yang, R.P. Gamage, W. Yang, P. Yin, Y. Zhang and Q. Zhang, "Fracture processes of rock-like specimens containing nonpersistent fissures under uniaxial compression", *Energies,* vol. 12, 79, doi: 10.3390/en12010079, 2019.

[4] P. Wilbur, "Damage identification in reinforced concrete beams using digital image Correlation", Master of Applied Science, Faculty of Graduate Studies, Civil and Environmental Engineering, University of Windsor, Canada, 2011.

[5] S. Dai, X. Liu, and K. Nawnit, "Experimental study on the *fracture* process zone characteristics in concrete utilizing DIC and AE methods", *Applied Science,* vol. 9, doi: 10.3390/app9071346, 2019.

[6] W. Peters and W. Ranson, "Digital imaging techniques in experimental stress analysis", *Opt. Eng*. vol. 1, 21, pp427-431, 1982.

[7] M. Sutton and W. Wolters, "Determination of displacements using an improved digital correlation method", *Image Vis. Comput*. vol.1, pp133-139, 1983.

[8] L. Shi, X. Zhang, L. Zhang, C. Wang and J. Wang, "Application of digital image correlation technique in stress and strain measurement", *15th Asia Pacific Conf. for Non-Destructive Testing, APCNDT2017*, http://www.ndt.net/?id=22154, Singapore, 2017.

Investigation of Strength Properties of Different Cement Types on Sandy Soil

A. SENKAYA[1] and M. OLGUN[1]

[1] Konya Technical University, Konya/Turkey, asenkaya@ktun.edu.tr
[1] Konya Technical University, Konya/Turkey, molgun@ktun.edu.tr

Abstract – **In this study, strength performance of DMFC-800 fine-grained cement, CEM I Portland cement, CEM II composite cement and CEM III slag admixtured cement on sandy soil were investigated. Cement mortars in different W/C ratios were prepared and mixed with sandy ground. Unconfined compressive strength (UCS) tests were performed at the end of curing periods of 7,28 and 56 days. Fine-grained cement showed early strength and was the best tolerant cement type for excess water. Admixtured cements gave better results than CEM I cement in the long term.**

Keywords – **Cement grout, soil stabilization, blast furnace slag, pozzolanic additives, microfine cement.**

I. INTRODUCTION

Soil improvement with cement grouts has been used for many years [1]. The development of the method to be efficient on different types of soils has continued since its first implementation [2]. While machine equipment was developed for better injecting of cement grouts into the soil, researchers have also worked on the development of cement grout mixtures used. There are many studies investigating the flow properties and penetration capabilities of cement grouts [3-4-5-6-7].

Fine-grained cement injections can achieve high strengths at a lower cost than chemical injection types. [8]. Furthermore, in fine-grained cement injections, no loss of strength over time, such as old-type chemical injections, is observed [3]. The use of pozzolanic additives has been increased to improve hydration properties of cement injections and to further reduce costs. Pozzolanic additives does not binding when used singularly. Through the SiO2 and Al2O3 compounds they contain, they improve the hydration reaction of cement. The contribution of the pozzolanic additive to strength is achieved by improving the chemical reaction. In this study, fine - grained cement and CEM I type Portland cement, which are frequently used in soil improvement studies, were used. In addition to these cements, CEM II natural pozzolan and limestone admixtured cement and CEM III blast furnace slag (BFS) admixtured cement were used. The aforementioned cement types have been used to improve sandy soil at different W / C ratios. At the end of the curing periods of 7,28 and 56 days, the UCS test results were evaluated.

II. MATERIAL AND METHOD

A. Sandy Soil

The sandy soil used in this study was obtained from natural sand quarries located in Eğribayat District of Selçuklu District of Konya Province. Sieve analysis was performed according to ASTM D6913-04 standard [9].
As a result of sieve analysis, components of sandy soil;•
  %3.75 gravel,
- %94.5 sand,
- %1.72 silty and clayey.
  According to the drawn granulometry curve of sandy soil garanulometry parameters determined as follows;
- The uniformity coefficient Cu = 6,8
- Coefficient of gradation Cc = 0,84.
  According to the USCS classification system, the class of sandy soil is determined as SP, ie poorly graded sand. Pycnometer test was carried out to determine the grain unit weight of sandy soil. According to the result of the pycnometer experiment, the unit weight per unit volume of soil γs; 26.6 kN/m3.

The maximum and minimum unit volume weights according to the compactness of the soil and the calculated void ratios are given in Table 1. Maximum and minimum void ratios were determined according to ASTM D4253 and ASTM D4254 standards, respectively [10-11].

Table 1: Mass-volume relation parameters of soil.

$\gamma_{k,min}$ (kN/m^3)	1,55
$\gamma_{k,max}$ (kN/m^3)	1,98
e_{min}	0,34
e_{max}	0,72

B. Cement Types

In this study, CEM I 42.5 R, CEM II / A-M (P-L) 42.5 N, CEM III / A 42.5 N and DMFC-800 fine grain cement imported from China are used. All types of binder materials are cements with a characteristic strength of 42.5 MPa and different grain size distributions.

CEM I 42.5 R ordinary Portland cement. It contains Portland clinker and gypsum. It does not contain additives. It contains C3S, one of the main constituents of cement, and provides early strength of the cement material used due to this component.

CEM II / A-M (P-L) is classified as admixtured cements according to TS EN 197-1: 2012 standard [12]. Contains

limestone and natural pozzolanic admixtures. Due to these mineral additives, it has high long-term strength, higher durability than Portland cement. This type of cement reduces the permeability by tightening the micro pores in the cemented mass thanks to the thin filling materials it contains. This cement, provides long term durability thanks to its trass content.

CEM III / A 42.5 N cement contains a high proportion of slag. Blast furnace slag (BFS) is a by-product obtained during the production of iron in blast furnaces. The slag obtained as a by-product contains large amounts of calcium oxide, alumina and silica. The slag removed from the blast furnace in molten state has a crystalline structure when subjected to slow cooling in air; however, if cooling is carried out too quickly (by pouring into water or by another process), it becomes granulated with the size of coarse sand grains and has an amorphous structure. Since granulated blast furnace slag is amorphous and contains sufficient amount of silica and alumina, it may show pozzolanic properties if pulverized to fine grained state [13]. The mass component ratios of the cements produced in our country are given in Table 2.

Table 2: The mass component ratios. (Data from manufacturer.)

Cement Type	Clinker %	Pozzolan %	BFS %	Other
CEM I	94	-	-	6
CEM II	80	20	-	-
CEM III	45	-	55	

DMFC-800 fine grain cement is not produced in our country and is imported from China. The maximum grain size limitation (D95) is the limit value that separates micro-fine cements from standard cements. According to EN 12715: 2000 European "Injection" standard, micro-fine cements can be defined by vertical and homogeneous grain size distributions [14]. The maximum particle size D95 should not exceed 20 microns. DMFC-800 is a Portland clinker based cement. Grain sizes are quite small compared to normal portland cement. 95% of its total mass is less than 16 microns (D95 <16μm).

Through to its small grain size, cement injection can easily penetrate into the gaps between very small cracks, fissures and particles and can be used in soil improvement works. Specific surface area The Blaine value is greater than 800 m2 / kg, which makes it possible to interact electrically with aggregates and other soil components. This type of cements are especially preferred and used for injection into loose floors, cracked rocks and concretes.

C. Specimen Preparing Procedure

The type of cement chosen as binder on the soil improved by cement injection, has an effect on the results to be obtained. The rheological property tests were performed to determine the water/cement (W / C) ratios of the grout mixtures used in the preparation of the samples. Marsh funnel flow time, sedimentation and Lombardi plate cohesion meter experiments were performed in various W / C ratios (from 0.5 to 4.0) for

each cement. Samples were prepared using grouts with W/C ratios which are 0.75, 1.00, 1.25, 1.50. Since fine grained DMFC-800 cement has a high water tolerance, grouts with a W / C ratio of 2.00, 2.50 and 3.00 were also used. Samples were prepared in cylinder molds. The cylinder molds have a diameter of 50 mm (inner diameter 47 mm) and a length of 100 mm.

The water content of the sandy soil specified as 5% in terms of being close to the natural stuation. The relative density of the soil was determined as 50% with medium density. When designing the mixing ratios of the samples, the following procedure was followed in order to fully represent the designs;

1- Preliminary tests were carried out to allow the sand with a 5% water content to be compacted at a density of 50% and a placement method was determined in order to ensure that the density of each sample was approximately the same and each sample was prepared in the same way. The sand used was sieved through a 4.75 mm sieve. According to the calculations, it was calculated that the mold must be completely filled with 113 cm3 sand in order to ensure relative density 50% for each mold and 61 cm3 injection mixture should enter into the cavities of sand. The sand and injection mixture were mixed in the indicated volumes and placed in the molds in 3 layers. Sand-injection mixture was placed in each layer by gently tapping the mold 5 times from outside.

2- The void ratio of the untreated sand prepared by the determined technique was calculated and the volume of the void in the mold was determined. In this way, the amount of injection that each sample can hold is calculated and the ground is prepared using this amount of injection fluid.

3- After the samples were prepared, they were kept in the mold for 48 hours to maintain their integrity (Figure 1.). After 48 hours, the samples were removed from the mold and stored in individual plastic bags.
The plastic bags were soaked to prevent the sample from drying out and the mouths were sealed to allow air. Samples were stored in sunlight-free compartments at a temperature of about 23 ° C.

Figure 1: Cylinder specimens removed from the molds.

D. Test Procedure

Unconfined Compressive Strength (UCS) test was applied on samples prepared using different cements. Tests were performed according to ASTM C-4219-02 standard [15]. Two samples were tested for each design. The experiments were carried out at the end of the curing periods of 7, 28 and 56 days.

III. TEST RESULTS

At the end of the seven-day curing period, the UCS test results showed that the samples prepared with fine-grained DMFC-800 cement showed significantly higher strength. In designs with a W / C ratio of 0.75, the strengths of CEM cemented samples range from 85% to 65% of the DMFC-800, whereas when the W / C ratio is 1.5, the ratio was seen 50%. Due to its large specific surface area, fine-grained cement exhibited a faster hydration reaction compared to other cement types and provided high early age strength. The stress-strain (σ-ε) relationship of UCS experiments of 7-day samples prepared with DMFC-800 cement is given in Figure 2. Samples using CEM I type cement after fine-grained cement gave higher strength values than other cements. Since CEM I type cement is Portland cement without admixture, it contains a higher percentage of clinker than other cement types with mineral admixture and thus showed higher early age strength. The stress-strain (σ-ε) relationship of UCS experiments of 7-day samples prepared with CEM I cement is given in Figure 3. CEM II type cement, also called Portland composite cement, contains a higher proportion of clinker than CEM III cement. Therefore, it gave higher strength than CEM III cement in 7 days. Since the clinker ratio of CEM III cement was between 35-40%, it was the cement that gave the lowest strength in 7-day strength tests. The stress-strain (σ-ε) relationship of UCS tests of 7-day samples prepared with CEM II and CEM III cement is given in Figure 4 and Figure 5.

Figure 3: UCS test results of CEM I specimens at the end of 7 days of curing period.

Figure 4: UCS test results of CEM II specimens at the end of 7 days of cure time.

Figure 2: UCS test results of DMFC-800 specimens at the end of 7 days of curing period.

Figure 5: UCS test results of CEM III specimens at the end of 7 days of curing period.

When the 28 day strength of samples was examined, the order of strength changed according to cement types. Samples prepared with CEM II and CEM III cements containing pozzolanic additives yielded higher results than those with CEM I cement (Figure 6 and Figure 7). Samples prepared with fine-grained cement gave the highest strength results (Figure 8).

It has seen that CEM II and CEM III cements gave very close results to fine-grained DMFC-800 cement. The strength of the samples prepared with CEM I type cement about 85% of the strength of the samples prepared with other cement types (Figure 9). In the samples prepared with DMFC-800 and CEM I cement which are in the class of unadulterated cement, when the curing period is increased from 7 days to 28 days, it is seen that the strength increase is about 2 times. It was observed that the strength increase was approximately 2.5 times in samples prepared with CEM II cement and approximately 3.3 times in samples prepared with CEM III cement. CEM II cement contains natural pozzolan. CEM III cement contains YFC. Through the pozzolanic reaction, these mineral admixtures provided more strength increase compared to unadulterated cement during the 28-day curing period. CEM III cement resulted very close to the DMFC-800 cement. It was found that the samples prepared with DMFC-800 cement were break down at lower deformation values than the samples prepared with CEM I cement, that is, they showed a brittle fracture behavior. It was observed that the fracture behavior of the samples was more ductile as the W/C ratio of the injections increased for all cement types. At the end of the 28-day curing period, it was observed that admixtured CEM II and CEM III cements showed close performance to DMFC-800 fine-grained cement and performed better than CEM I cement, which is unadulterated Portland cement.

Figure 7: UCS test results of CEM III specimens at the end of 28 days of curing period.
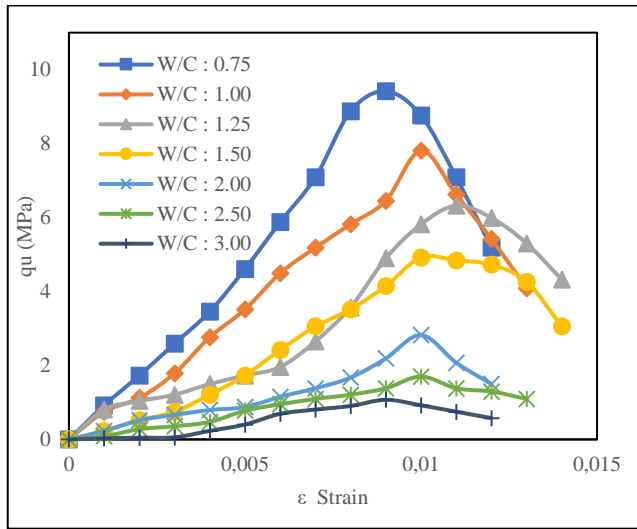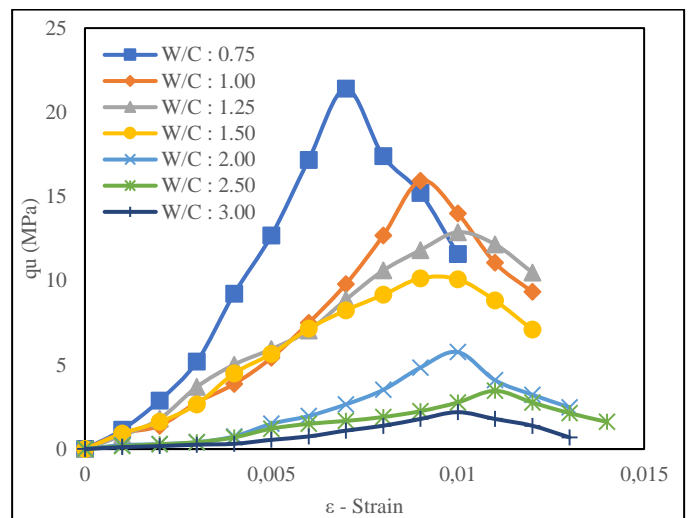

Figure 8: UCS test results of DMFC-800 specimens at the end of 28 days of curing period.
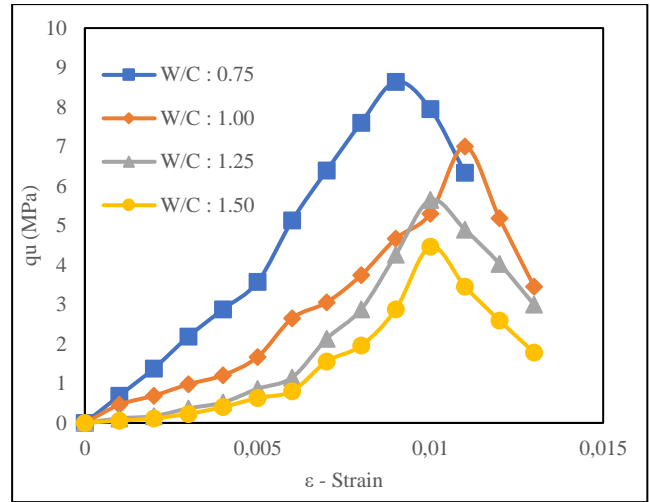

Figure 6: UCS test results of CEM II specimens at the end of 28 days of curing period.
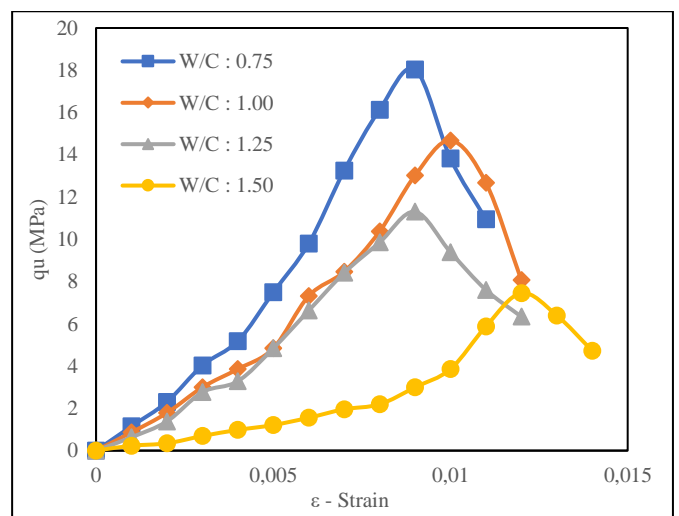
Figure 9: UCS test results of CEM I specimens at the end of 28 days of curing period.

UCS tests were performed at the end of the 56-day curing period in order to evaluate the long-term performance of the cements. The 56-day UCS values of CEM I unadulterated Portland cement showed a 5% strength increase compared to the 28-day UCS values. The stress-strain relationship of the pressure tests of 56-day-old samples prepared with CEM I cement is given in Figure 10.

When the 56-day UCS values of fine-grained DMFC-800 cement were compared with 28-day UCS values, it was observed that the strength increase was approximately 9%. Although fine-grained cement does not contain mineral additives due to its high specific surface area, it shows more strength increase compared to normal Portland cement. The stress strain relationship of UCS tests of 56-day-old samples prepared with DMFC-800 cement is given in Figure 11.

When 56 days UCS values of CEM II Portland composite cement were compared with 28 days UCS values, it was seen that the strength increase was approximately 16%. It was found that this cement containing natural pozzolan showed much more strength increase than unadulterated and fine grained cements due to pozzolanic reactions. Samples prepared with CEM II cement showed higher strength values than CEM I cement and DMFC-800 fine grain cement after 56 days curing period. The stress-strain relationship of UCS tests of 56-day-old samples prepared with CEM II cement is given in Figure 12.

Samples prepared with CEM III BFS admixtured cement were the cement which gave the highest strength results in long term strength tests. The pozzolanic reactions of BFS persisted after 28 days and it was observed that the strength of the free compressive strength values of 56 days compared with the UCS values of 28 days increased by 17%. The stress strain relationship of UCS tests of 56-day-old samples prepared with CEM III cement is given in Figure 13.

Figure 11: UCS test results of DMFC-800 specimens at the end of 56 days of curing period.

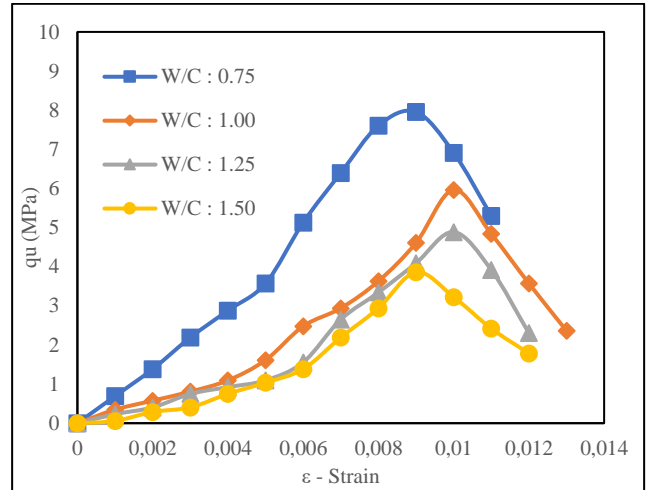Figure 12: UCS test results of CEM II specimens at the end of 56 days of curing period.
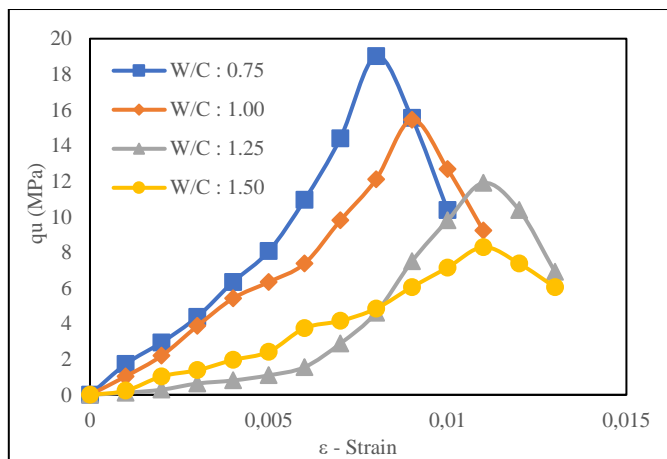
Figure 10: UCS test results of CEM I specimens at the end of 56 days of curing period.
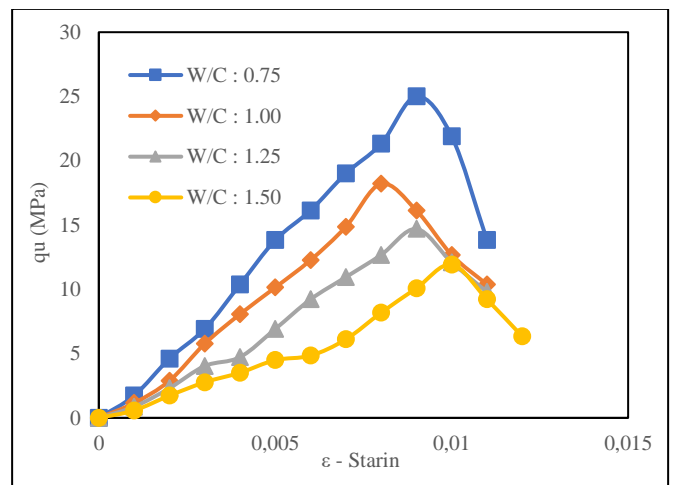
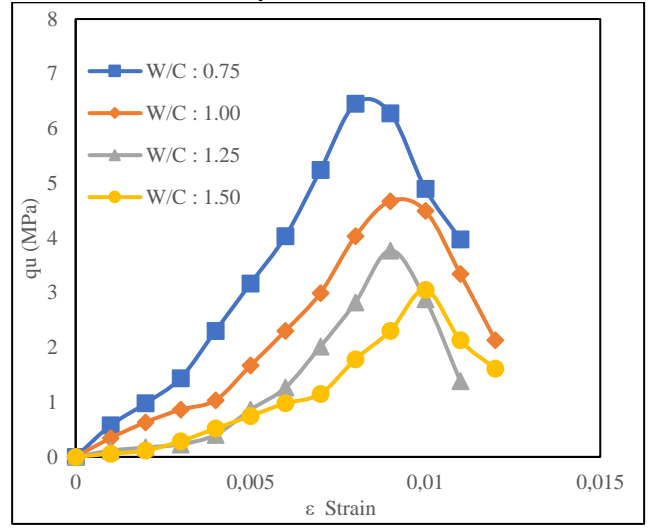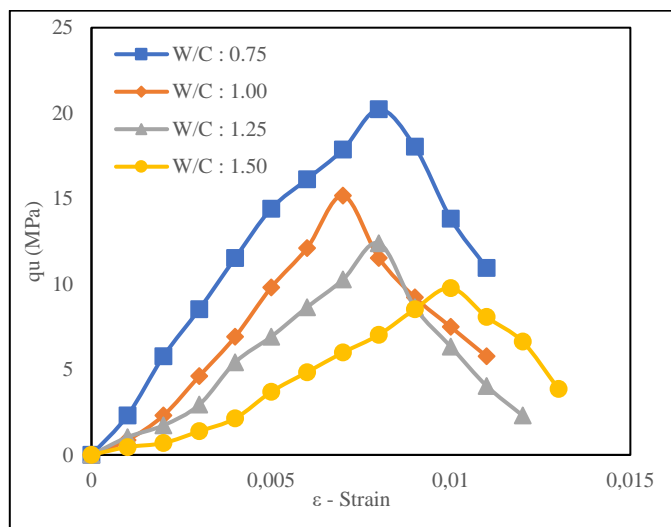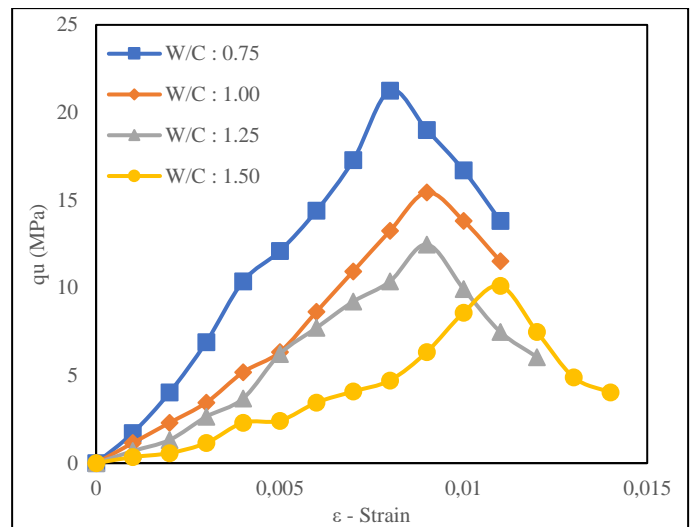Figure 13: UCS test results of CEM III specimens at the end of 56 days of curing period.
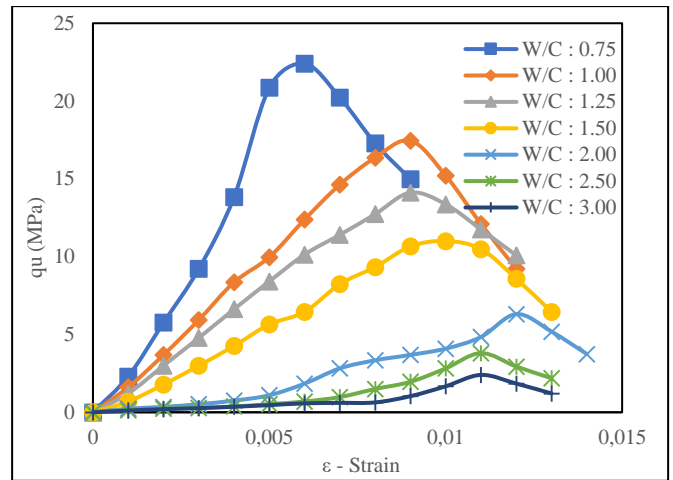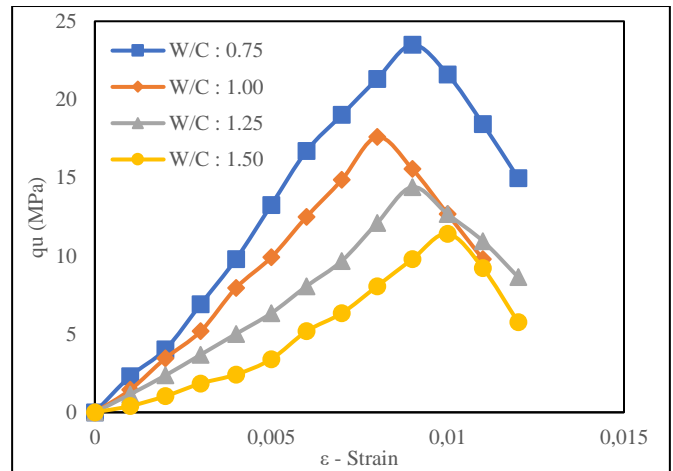
IV. Conclusion

The results of the research can be listed as follows:

• Fine-grained cement provides early strength and the hydration residue water is the best tolerant cement type. It can give more effective results with finely ground pozzolanic additives.

• Water requirement is high due to pozzolanic additives in CEM II cement. W / C ratio increased and water was tolerated better than CEM I and CEM III cements. It did not show the desired strength properties at the 7 days of curing time. The strength of CEM II samples increased during the curing time of 28 and 56 days.

• CEM III cement is the type of cement containing the least amount of clinker and did not show the desired strength in 7 days curing period. At the end of the 28-day curing period, it showed the desired strength. At the end of the 56-day curing period, it showed very high strength. Since BFS reduces water requirement, CEM III showed high strength at low W / C ratios. However, when W / C increased, residue hydration water caused strength loss.

In this study, CEM I cement was selected as a reference for interpretation of different components of other cements. Although natural pozzolan additives and BFS additive are disadvantageous for early strength, it has been found that they can provide the desired results in the long term. In addition, these additives reduce costs and reduce carbon emissions from cement production.

Appendix

Appendixes, if needed, appear before the acknowledgment.

Acknowledgment

References

[1]   Essler R, Yoshida H. Jet grouting. In: *Moseley M. P, Kirsh K*., editors, Ground improvement. pp. 160-96. 2004.

[2]   Shibazaki M. "State of practice of jet grouting" *Grouting and Ground Treatment*. p. 198-217. 2003.

[3]   Mollamahmutoğlu, M., "Treatment of Medium-to Coarse-Grained Sands by Fine-Grained Portland Cement (FGPC) as an Alternative Grouting Material to Silicate-Ester Grouts", *Cement, Concrete and Aggregates*, 25(1), 1-6. 2003.

[4]   Park, C.K., Noh, M.H. and Park, T.H., "Rheological properties of cementitious materials containing mineral admixtures",*Cement and Concrete Research*, 35(5), 842-849.2005.

[5]   Mollamahmutoglu, M. and Yilmaz, Y., "Engineering properties of medium-to-fine sands injected with microfine cement grout", *Marine Georesources and Geotechnology*, 29(2), 95-109.2011.

[6]   Pantazopoulos, I. A., Markou, I. N., Christodoulou, D. N., Droudakis, A. I., Atmatzidis, D. K., Antiohos, S. K., & Chaniotakis, E., "Development of microfine cement grouts by pulverizing ordinary cements", *Cement and Concrete Composites*, 34(5), 593-603.2012.

[7]   Mollamahmutoglu, M. and Avcı, E., "Effectiveness of Microfine Portland Cement Grouting on the Strength and Permeability of Medium to Fine Sands", *Periodica Polytechnica Civil Engineering*, 319-326.2015.

[8]   Zebovitz S., Krizek, R. J. ve Atmatzidis, D. K., "Injection Of Fine Sands With Very Fine Cement Grout", *Journal Geotechnical Engineering*, 115 (2), 1717-1733. 1989.

[9]   ASTM. D6913-04, "Standard test methods for particle-size distribution (gradation) of soils using sieve analysis". West Conshohocken, PA, USA: ASTM international. 2009.

[10] ASTM. D4253-00, "Standard test methods for maximum index density and unit weight of soils using a vibratory table". PA, USA: ASTM international. 2006.

[11] ASTM. D4254, "Standard test methods for minimum index density and unit weight of soils and calculation of relative density." PA, USA: ASTM international. 2006.

[12] TS EN 197-1. "Cement-Part 1: General Cements-Composition, Properties and Compliance Criteria", Turkish Standards Institute. 2002.

[13] [13] Erdogan, S.T. and Erdogan, T.Y., "Pozzolanic Mineral Additives and Historical Backgrounds", 2nd Symposium on Chemical Additives in Structures, Ankara, 263-275. 2007.EN, BS. 12715. "Execution of special geotechnical work: Grouting. British-Adopted European Standard." 2000.

[14] ASTM C4219-02. "Standard test method for unconfined compressive strength index of chemical-grouted", Annual Book of ASTM Standards. ASTM. 2002.

Physical Properties of Recycled Concrete Aggregates as Granular Road Base and Sub-base Material

E.B. TOKA[1] and M. OLGUN[1]

[1] Konya Technical University, Konya/Turkey, ebtoka@ktun.edu.tr
[1] Konya Technical University, Konya/Turkey, molgun@ktun.edu.tr

Abstract - **Recycled concrete aggregates (RCA) are obtained from waste concretes which are emerged as one of the construction and demolition wastes. As in many fields of civil engineering, the use of RCAs as granular road base (GRB) and granular road sub-base (GRSB) material eliminates their adverse effects such as big landfill area needs and environmental pollution and contributes greatly to economic sustainability. However, in order for these materials to become GRB and GRSB material, they must comply with the technical specifications. In this study, the suitability of RCAs to the conditions of GRB and GRSB was investigated by flakiness index, particle density and water absorption, Los Angeles (LA) abrasion and magnesium sulfate soundness tests. 3 different RCAs were obtained by crushing the concrete blocks of the debris of the demolished buildings. Natural aggregates (NA) and crushed aggregates (CA) were used to compare the RCAs with conventional aggregates. Tests were carried out for 23 different designs, which were formed with pure forms of these 5 different materials and their mixtures in certain proportions. As a result of the tests, it was found that the RCAs had very good properties in terms of flakiness index. It was found that the RCAs had lower particle density and higher water absorption values than the conventional aggregates. For LA abrasion and magnesium sulfate soundness tests, too much material loss was observed for the RCAs, which shows that the RCAs are in some cases disadvantageous. However, the poor properties of the RCAs largely eliminated by mixing them with the CA and NA.**

Keywords - **Recycled concrete aggregate, granular road base, granular road sub-base, physical properties.**

I. INTRODUCTION

AS a result of construction and demolition process, many waste materials are produced. Wood, plastic, marble, tiles, steel and concrete are some of them. It is aimed to ensure that these waste materials are stored regularly and to minimize the pollution they will cause to the environment. However, with the increasing population in the modern world, construction activities have accelerated, thus a large amount of construction and demolition waste has started to occur in mass. It is clear that there will be problems with the landfilling of all these wastes in the future. Therefore, these wastes should be handled in a different way.

Demolition concretes constitute a large part of construction and demolition wastes. By reusing this waste, the landfill area problem can be solved and can contribute to the sustainability of the economy. For this purpose, demolition concrete is converted into recycled concrete aggregate (RCA) by suitable crushing processes and can be used in different fields of civil engineering as well as in road constructions. However, it must be proven that RCAs can provide sufficient performance for this and the areas where they can be used should be determined. For this purpose, many researchers have conducted studies to determine the characteristics of RCAs compared to conventional aggregates which are natural aggregates (NA) and crushed aggregates (CA). Cyclic triaxial tests simulating the traffic load of RCAs as a result of higher resilient modulus compared to conventional aggregates and lower plastic deformation of the RCA mixture compared to conventional aggregates has been reported [1]. As a compaction behavior, it was observed that RCAs had higher optimum moisture content (w_{opt}) and lower maximum density than conventional aggregates [2]. RCAs were found to be highly suitable for being GRSB material in terms of California Bearing Ratio (CBR), Los Angeles (LA) abrasion and flakiness index characteristics [3]. RCAs generally had higher water absorption and lower particle density values than conventional aggregates [4], which adversely affects their use in GRB.

In this study, in order to determine the physical properties of RCAs, the suitability of the physical properties of the RCAs to the requirements of GRB and GRSB materials given in Highway Technical Specification-2013 (HTS-2013) [5] was investigated with a series of laboratory test.

II. MATERIAL

The CA was obtained from a quarry in Egribayat region of Konya-Turkey and the NA was obtained from a natural quarry from Egribayat region from Konya-Turkey. The RCAs were obtained from 3 different buildings that were demolished by Meram Municipality from the Meram region of Konya within the scope of urban transformation practices. Compressive strengths of the core samples of the concrete blocks where RCAs were produced were determined as 18.5, 15.2 and 11.7 MPa. The RCAs were named R1, R2 and R3 from high compressive strength to low compressive strength. The concrete blocks were adjusted to the selected granulometry by using jaw crusher in the laboratory, with maximum particle

diameter of 25 mm, within the appropriate gradation limits given in HTS-2013 [5] for GRB and GRSB materials. Grain size distribution plots obtained from sieve analysis are given in Figure 1 for 5 different materials. AASHTO M-145-91 [6] classes were found to be A-1-a for the CA and RCAs, and A-2-4 for the NA. Accordingly, the materials can be classified as excellent to good for subgrade layer.
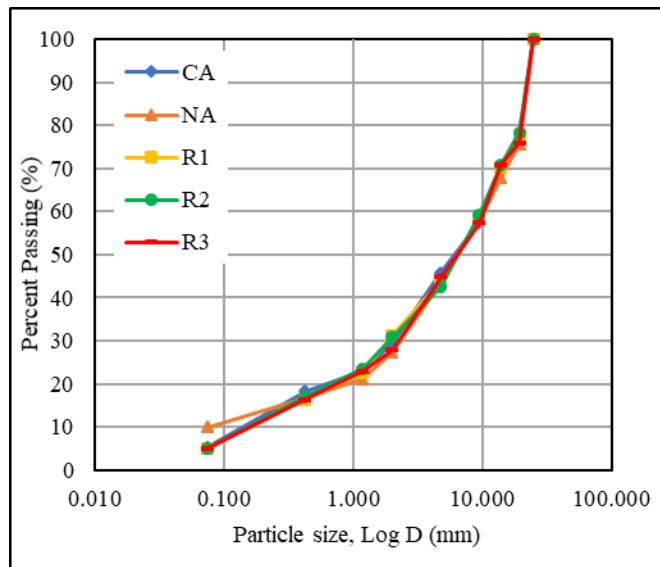
Figure 1: Grain size distributions.

III. METHOD

A. Design

In order to determine the physical properties, 23 different designs were established. 5 of these designs were made of pure forms of the materials. The other 18 designs were made by mixing each RCA with CA and NA at 25-50-75% ratios. Table 1 presents each design. Accordingly, for example, "50CA 50R1" design includes 50 percent of the CA and 50 percent of the R1.

Table 1: Designs.

Design No	Design Name	Design No	Design Name
1	100CA	13	25CA 75R2
2	100NA	14	25CA 75R3
3	100R1	15	75NA 25R1
4	100R2	16	75NA 25R2
5	100R3	17	75NA 25R3
6	75CA 25R1	18	50NA 50R1
7	75CA 25R2	19	50NA 50R2
8	75CA 25R3	20	50NA 50R3
9	50CA 50R1	21	25NA 75R1
10	50CA 50R2	22	25NA 75R2
11	50CA 50R3	23	25NA 75R3
12	25CA 75R1		

B. Flakiness Index Test

Flakiness index tests were performed according to TS EN 933-3 [7] for 23 different designs. According to this test, each particle size fraction (di/Di) is sieved through the appropriate grid sieve given in TS EN 933-3 [7]. In this test, the material in each particle size fraction passing through the sieve is weighed. As a result, the sum of all (di/Di) particle size fraction masses are calculated. The sum of the masses of the particles in each of the particle size fractions (di/Di) passing through the sieve Di/2 is calculated. For each partical fraction, flakiness index can be calculated separately, or total flakiness index can be calculated directly.

C. Particle Density and Water Absorption Test

Following the TS EN 1097-6 [8] test procedure, particle density values and water absorption percentages were determined for 23 different designs. Two different water absorption and particle density values were determined separately for particle fractions of 4-25 mm (coarse aggregates) and particle fractions of 0.075-4 mm (fine aggregates).

D. Los Angeles Abrasion Test

The LA abrasion test for 23 different designs was carried out according to the TS EN 1097-2 [9]. For this purpose, the abrasion resistance of the material weighing 5000 g with 10 to 14 mm particle size is determined and the percent material loss is calculated as LA abrasion value.

E. Magnesium Sulfate Soundness Test

The magnesium sulfate soundness test was carried out for 23 different designs according to the method given in TS EN 1367-2 [10]. Magnesium sulfate soundness test was performed as an alternative to freeze-thaw effect which is one of the resistance properties of the materials and the material loss values obtained as a result of this test helped to evaluate the resistance of the materials against the bad environmental conditions. This test is mainly based on the determination of the loss of material which is immersed in magnesium sulfate solution for a certain period.

IV. RESULTS AND DISCUSSION

In this section, the measured physical properties of the materials are examined and discussed.

A. Flakiness Index Test Results

The results of flakiness index tests for 23 different designs are shown in Figure 2. It was observed that the flakiness index of 100CA was the highest with 19.14%. Although the flakiness index values of the NA and RCAs are similar to each other, they are very low compared to the CA. Flakiness index values of 100R1, 100R2, 100R3 and 100NA were found to be 6.72%, 7.20%, 6.34%, 5.94%, respectively. In previous studies, 16.78% [11], 4-9% [12] and 11.68% [13] values were obtained for RCAs. The flakiness index values obtained in this study were similar to the previous studies. The flakiness index

varies depending on the crushing stages and crusher equipment in the crushing plant [14]. The low flakiness index value of the NA is related to the use of this material in its natural state without any crushing process and to the phases of the geological formation of the material. For the RCAs, the low flakiness index values were obtained; because in this study, especially in laboratory, crushing process was done with the jaw crusher which had a maximum jaw opening of 10 mm in order to obtain particles less than 10 mm and a maximum jaw opening of 25 mm in order to obtain particles between 10 and 25 mm. This caused the particles to spend more time in the crusher jaw and more fracture on all surfaces, thereby reducing the flakiness. However, when the CA was obtained in the quarry, the crusher in the crushing plant separated the particles passing through 38 mm into fractions of different particle sizes. In other words, since the material was obtained by using maximum 38 mm jaw opening and not with separate jaw opening for each particle fraction for the CA, particles spent less time in the jaw crusher during the crushing process and consequently the flakiness index became high. Since all materials have flakiness index values of 25% and less than 30%, which are the limit flakiness index value requirements of the GRB and GRSB materials in the HTS-2013 [5], respectively, their use as GRB and GRSB material is not a disadvantage in this respect.

presents the results of water absorption tests obtained for 23 different designs.

The water absorption values of 100R1, 100R2 and 100R3 were obtained as 4.63% (6.59% for fines), 2.88% (6.00% for fines) and 3.56% (6.75% for fines), respectively. The water absorption values of 100CA and 100NA were 0.63% (0.78% for fines) and 2.49% (3.49% for fines), respectively. In previous studies, some researchers obtained similar results with regard to RCAs. In some of these studies, 1.43% to 6.77% [15], 5.1% [16], 4.66% to 9.75% [3], 4.19% to 9.23% [4] water absorption values for RCAs were obtained. These water absorption values are similar to the results of this study.

An opposite trend was observed with water absorption values for particle density values. Accordingly, the particle density for 100CA and 100NA (coarse - fine aggregate) were found to be 2.75-2.48 g/cm^3 and 2.74-2.48 g/cm^3 respectively and for 100R1, 100R2 and 100R3, 2.62-2.35 g/cm^3, 2.67-2.39 g/cm^3, and 2.69-2.40 g/cm^3, respectively, were obtained for coarse and fine aggregates. In previous studies, particle density for RCAs were 2.051-2.435 g/cm^3 [17]; specific gravities were 2.1-2.4 [18], and 2.29-2.53 [19]. Accordingly, in the literature, results close to the values obtained in this study. These results are due to the fact that RCAs are more hydrophilic than NA and CA because of their adhered cement mortar and porous structure [12].

Figure 2: Change of flakiness indexes for designs.

Table 2: Particle density values.

Design	Density of Coarse Particles (g/cm^3)	Density of Fines (g/cm^3)
100CA	2.75	2.48
100NA	2.74	2.48
100R1	2.62	2.35
100R2	2.67	2.39
100R3	2.69	2.40
75CA 25R1	2.73	2.44
75CA 25R2	2.74	2.45
75CA 25R3	2.75	2.46
50CA 50R1	2.70	2.41
50CA 50R2	2.72	2.43
50CA 50R3	2.73	2.44
25CA 75R1	2.66	2.38
25CA 75R2	2.70	2.41
25CA 75R3	2.72	2.42
75NA 25R1	2.72	2.44
75NA 25R2	2.73	2.45
75NA 25R3	2.73	2.45
50NA 50R1	2.69	2.41
50NA 50R2	2.71	2.43
50NA 50R3	2.72	2.43
25NA 75R1	2.66	2.38
25NA 75R2	2.69	2.40
25NA 75R3	2.71	2.41

B. Particle Density and Water Absorption Test Results

Table 2 presents the results of particle density and Table 3

Particle density values were also lower in the RCA compared to the NA and CA due to this adhered mortar. The particle density of cement mortar generally varies between 1-

1.6 g/cm³, which causes the particle density values for RCA to be lower than pure aggregate particle [20]. In HTS-2013 [5], it is stated that GRB and GRSB materials should have water absorption values less than 3% and 3.5% for both coarse and fine aggregate, respectively. Accordingly, the RCAs had water absorption values above this limit values when used alone, while water absorption values of more than 3% water absorption values have been obtained in all designs except 75CA designs.

Table 3: Water absorption values.

Design	Water Absorption of Coarse Particles (%)	Water Absorption of Fines (%)
100CA	0.63	0.78
100NA	2.49	3.49
100R1	4.63	6.59
100R2	2.88	6.00
100R3	3.56	6.75
75CA 25R1	1.64	2.24
75CA 25R2	1.18	2.09
75CA 25R3	1.36	2.28
50CA 50R1	2.62	3.67
50CA 50R2	1.76	3.40
50CA 50R3	2.10	3.77
25CA 75R1	3.64	5.12
25CA 75R2	2.33	4.70
25CA 75R3	2.82	5.27
75NA 25R1	3.03	4.27
75NA 25R2	2.58	4.12
75NA 25R3	2.76	4.29
50NA 50R1	3.57	5.05
50NA 50R2	2.70	4.73
50NA 50R3	3.03	5.11
25NA 75R1	4.09	5.82
25NA 75R2	2.79	5.37
25NA 75R3	3.29	5.92

C. Los Angeles Abrasion Test Results

LA abrasion test results for 23 different designs are given in Figure 3. It is seen that the lowest LA abrasion values were obtained with 31.09% and 33.76% for 100CA and 100NA, respectively. The highest LA abrasion values were obtained for 100R1, 100R3 and 100R2 with 46.66%, 45.03% and 40.39%. In previous studies, some researchers found LA abrasion values for RCAs as 21-25% [21], 32.9-43.6% [15], 42.7% [22], 29-34% [23]. In this study, LA abrasion values obtained for the RCAs were generally higher than those obtained in literature studies. Since LA abrasion value is related to the rock properties from which the material is obtained and the CA is generally used as GRB and GRSB material, the LA abrasion value for the CA is lower than the maximum limit conditions for both GRB and GRSB given in HTS-2013 [5] that are 45% and 35%, respectively. Therefore, it had sufficient results in terms of abrasion resistance. The NA was also desirable in terms of these limit conditions.

However, not all RCAs had LA abrasion values above the limit LA abrasion value of the GRB material, so they are not suitable for use in the GRB. However, with the exception of 100R1 and 100R3, 100R2 and mixtures of the RCAs with the NA and CA had favorable results in terms of the desired LA abrasion value for the GRSB material, all of which had a LA abrasion value under this limit condition. The reason for such abrasion loss in RCAs can be explained by the adhered mortar in RCAs. As the concrete from which RCAs were obtained deteriorated over time and exposed to bad environmental conditions for a long time after the demolition of the building, it was easier to separate the adhered cement mortar from the aggregates in the RCAs under heavy impact. According to this, LA abrasion loss in RCAs is caused by separation of adhered cement mortar from aggregate [24]. With this separation, resistance to abrasion of the RCAs was low.
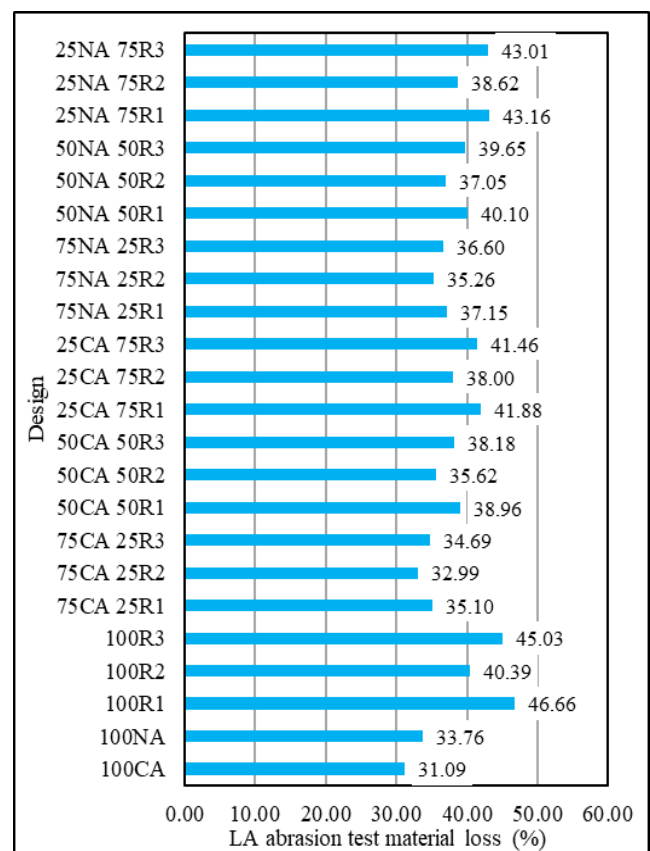
Figure 3: Change of LA abrasion material losses for designs.

D. Magnesium Sulfate Soundness Test Results

Test results of 23 different designs for magnesium sulfate soundness are given in Figure 4. As a result of these tests, the maximum material loss occurred in 100R1, 100R2 and 100R3 with 26.94%, 25.31% and 22.94% respectively. The least material loss was obtained in 100CA and 100NA with 2.33% and 9.69%. In previous studies, for the sulfate soundness tests, material losses were observed as 34% [25], 16.17% [26] and 14.3-15.7% [27]. It can be said that the values obtained for the RCAs within the scope of this study are between the loss values found in the wide range of the literature.
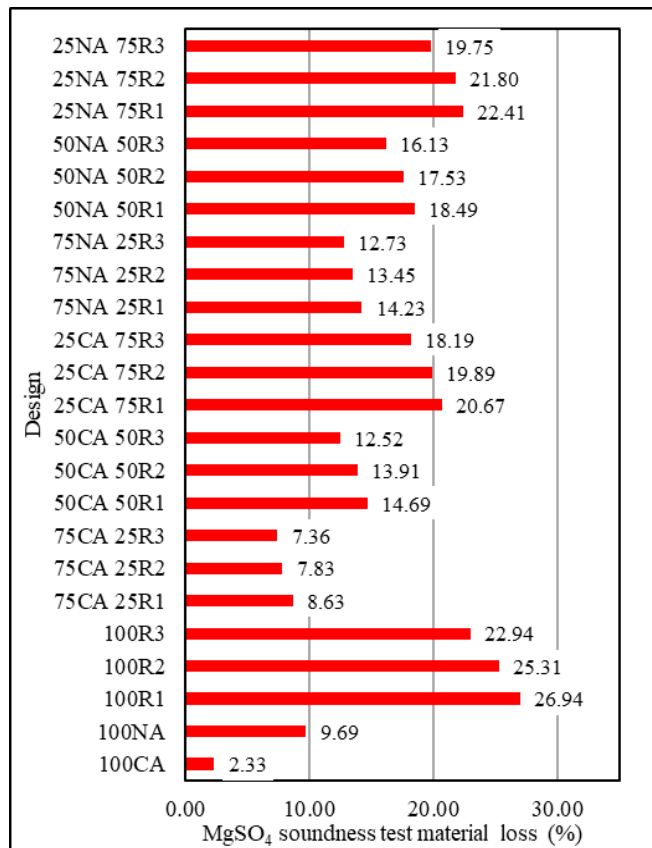
Figure 4: Change of MgSO₄ soundness material losses for designs.

Material losses were higher for the RCAs than the CA and NA due to the degradation of the adhered cement mortar contained in these materials as a result of sulfate attack. Sulfate attack is a harmful environmental effect that can also be dangerous for concrete and adhered cement mortar found in RCAs is more affected by sulfate attack than CA and NA [28]. This suggests that a further test should be used to determine the resistance of RCAs to freeze-thaw [25], and that in the areas with harmful groundwater may cause sulfate attack on GRB and GRSB. It shows that there may be disadvantages to use RCAs in GRB and GRSB. According to this; When the limit values of magnesium sulfate soundness test material loss value given - which are %20 and %25 - for GRB and GRSB in HTS-2013 [5] is compared with the material losses of the RCAs, it is not a drawback that the RCAs are used in GRSB for this property; however, it was found to be unfavorable to use them in GRB. Since the material losses in the mixtures were below the limit value required for both GRB and GRSB except for a few designs, it is not disadvantageous to use mixtures of the RCAs and CA in GRB and GRSB in this respect.

V. Conclusion

In this study, in which the physical properties of RCAs were compared with the NA and CA and their suitability to be used in GRB and GRSB based on HTS-2013 [5] was examined, the following conclusions can be drawn:

- In terms of the flakiness index, the RCAs were suitable for use in both GRB and GRSB, either alone or when used with conventional aggregates mixed. Crushing stage controls the flakiness index.

- The RCAs had higher water absorption and lower particle density than the CA and NA. Although the water absorption values were high for 100RCAs, it was obtained below the upper limits for GRB and GRSB in some mixtures. Particle density and water absorption were highly influenced by the adhered cement mortar in the RCAs.

- The RCAs suffered excessive material loss in the LA abrasion test due to the separation of the adhered cement mortar under impact. In some mixtures, this loss amount was less, thus making it suitable for GRB and GRSB.

- The loss of material in magnesium sulfate soundness test for the RCAs was much higher than for the NA and CA. Sulfate attack to adhered cement mortar caused this; however, losses in the mixtures were lower than the upper limit for GRB and GRSB.

References

[1] T. Bennert, W. J. Papp, A. Maher, and N. Gucunski, "Utilization of construction and demolition debris under traffic-type loading in base and subbase applications," *Recycled and Secondary Materials, Soil Remediation, and in Situ Testing,* pp. 33-39, 2000.

[2] C. S. Poon and D. X. Chan, "Feasible use of recycled concrete aggregates and crushed clay brick as unbound road sub-base *Construction and Building Materials,* vol. 20, pp. 578-585, Oct 2006.

[3] A. Arulrajah, J. Piratheepan, M. M. Y. Ali, and M. W. Bo, "Geotechnical properties of recycled concrete aggregate in pavement sub-base applications," *Geotechnical Testing Journal,* vol. 35, pp. 743-751, Sep 2012.

[4] J. O. Bestgen, M. Hatipoglu, B. Cetin, and A. H. Aydilek, "Mechanical and environmental suitability of recycled concrete aggregate as a highway base material," *Journal of Materials in Civil Engineering,* vol. 28, Sep 2016.

[5] Highway Technical Specification, *General Directorate of Highways*, Ankara, Turkey, 2013.

[6] AASHTO M-145-91, "Classification of soils and soil-aggregate mixtures for highway construction purposes," *American Association of State Highway and Transportation Officials (AASHTO)*, Washington D.C., USA, 2004.

[7] TS EN 933-3, "Tests for geometrical properties of aggregates - Part 3: Determination of particle shape - Flakiness index," *Turkish Standards Institution*, Ankara, Turkey, 2012.

[8] TS EN 1097-6, "Tests for mechanical and physical properties of aggregates - Part 6: Determination of particle density and water absorption," *Turkish Standards Institution*, Ankara, Turkey, 2013.

[9] TS EN 1097-2, "Tests for mechanical and physical properties of aggregates - Part 2: Methods for the determination of resistance to fragmentation," *Turkish Standards Institution*, Ankara, Turkey, 2010

[10] TS EN 1367-2, "Tests for thermal and weathering properties of aggregates- Part 2: Magnesium sulfate test," *Turkish Standards Institution*, Ankara, Turkey, 2010.

[11] Y. H. Cho, T. Yun, I. T. Kim, and N. R. Choi, "The application of recycled concrete aggregate (RCA) for hot mix asphalt (HMA) base layer aggregate," *Ksce Journal of Civil Engineering,* vol. 15, pp. 473-478, Mar 2011.

[12] A. Barbudo, F. Agrela, J. Ayuso, J. R. Jimenez, and C. S. Poon, "Statistical analysis of recycled aggregates derived from different sources for sub-base applications," *Construction and Building Materials,* vol. 28, no. 1, pp. 129-138, Mar 2012.

[13] B. Ok and A. Demir, "Investigation of the usability of construction and demolition wastes in road bases," (in Turkish) *Omer Halisdemir University Journal of Engineering Sciences,* vol. 7, pp. 224-236, 2018.

[14] B. Estes and G. Fensome, "Crushing for particle shape," *Aggregates Manager Magazine,* vol. 19, 2014.

[15] T. Park, "Application of construction and building debris as base and subbase materials in rigid pavement," *Journal of Transportation Engineering-Asce,* vol. 129, pp. 558-563, Sep-Oct 2003.

[16] M. H. Shehata, C. Christidis, W. Mikhaiel, C. Rogers, and M. Lachemi, "Reactivity of reclaimed concrete aggregate produced from concrete affected by alkali–silica reaction," *Cement and Concrete Research,* vol. 40, pp. 575-582, 2010.

[17] J. R. Jimenez, F. Agrela, J. Ayuso, and M. Lopez, "A comparative study of recycled aggregates from concrete and mixed debris as material for unbound road sub-base from," *Materiales De Construccion,* vol. 61, pp. 289-302, 2011.

[18] J. Sharma and S. Singla, "Study of recycled concrete aggregates," *International Journal of Engineering Trends and Technology (IJETT),* vol. 13, p. 123, 2014.

[19] A. H. Aydilek, *Environmental suitability of recycled concrete aggregate in highways*, Report, Maryland State Highway Administration. Office of Policy & Research, Maryland, 2015.

[20] V. W. Tam and K. N. Le, "Aggregate testing using 2nd-, 7th-and 10th-order interpolation polynomials," *Resources, Conservation and Recycling,* vol. 52, pp. 39-57, 2007.

[21] A. Nataatmadja and Y. L. Tan, "Resilient response of recycled concrete road aggregates," *Journal of Transportation Engineering-Asce,* vol. 127, pp. 450-453, Sep-Oct 2001.

[22] N. Fonseca, J. de Brito, and L. Evangelista, "The influence of curing conditions on the mechanical performance of concrete made with recycled concrete waste," *Cement & Concrete Composites,* vol. 33, pp. 637-643, Jul 2011.

[23] P. Jitsangiam, K. Boonserm, T. Phenrat, S. Chummuneerat, P. Chindaprasirt, and H. Nikraz, "Recycled concrete aggregates in roadways: Laboratory examination of self-cementing characteristics," *Journal of Materials in Civil Engineering,* vol. 27, Oct 2015.

[24] T. B. Edil, J. M. Tinjum, and C. H. Benson, *Recycled unbound materials,* Final Report, Minnesota Department of Transportation, Minnseota, 2012.

[25] A. R. Chini, S. S. Kuo, J. M. Armaghani, and J. P. Duxbury, "Test of recycled concrete aggregate in accelerated test track," *Journal of Transportation Engineering-Asce,* vol. 127, pp. 486-492, Nov-Dec 2001.

[26] R. Kumar, "Influence of recycled coarse aggregate derived from construction and demolition waste (CDW) on abrasion resistance of pavement concrete," *Construction and Building Materials,* vol. 142, pp. 248-255, 2017.

[27] I. Haider, B. Cetin, Z. Kaya, M. Hatipoglu, A. Cetin, and H. A. Ahmet, "Evaluation of the mechanical performance of recycled concrete aggregates used in highway base layers," in *Geo-Congress 2014: Geo-characterization and Modeling for Sustainability*, Atlanta, 2014, pp. 3686-3694.

[28] R. Cardoso, R. V. Silva, J. de Brito, and R. Dhir, "Use of recycled aggregates from construction and demolition waste in geotechnical applications: A literature review," *Waste Management,* vol. 49, pp. 131-145, Mar 2016.

Permeability and Compaction Properties of Recycled Concrete Aggregates as Granular Road Base and Sub-base

M. OLGUN[1] and E. B. TOKA[1]

[1] Konya Technical University, Konya/Turkey, molgun@ktun.edu.tr
[1] Konya Technical University, Konya/Turkey, ebtoka@ktun.edu.tr

Abstract - **Recycled concrete aggregates (RCA) can be used as granular road base (GRB) and granular road sub-base (GRSB) in highway constructions. Thus, the use of RCAs which are waste materials contributes to sustainable economy. But RCAs must meet certain requirements for use in GRB and GRSB. Adequate drainage capability, which is one of these conditions, is important for draining surface water. In this study, drainage capabilities of RCAs produced from concrete from 3 different buildings were compared with crushed aggregate (CA) and natural aggregate (NA). In order to carry out the tests, 23 different designs consisting of mixture and pure forms of the materials were established. The permeability tests were carried out with falling head and constant head permeability equipment to evaluate permeability coefficients. The samples were prepared in the permeability molds by compression at maximum dry unit weight (γ_{kmax}) and optimum moisture content (w_{opt}), which are the compaction parameters obtained from modified Proctor test. For this reason, w_{opt} and γ_{kmax} were determined by modified Proctor test before conducting the permeability tests. As a result, it was observed that RCAs had higher w_{opt} values and lower γ_{kmax} values than the NA and CA. It was determined that the permeability coefficients obtained by the permeability tests of the NA were very low and the permeability coefficients of the CA and RCAs were close to each other and higher than the NA. The fact that the RCAs had a permeability coefficient close to the CA indicates that drainage capability can be sufficient if RCAs are used in GRB and GRSB.**

Keywords - **Recycled concrete aggregate, granular road base, granular road sub-base, permeability coefficient, compaction.**

I. INTRODUCTION

RAPID urbanization and population growth in the world countries cause the construction sector to grow and thus increase the construction and demolition wastes arising from construction process. Landfilling of these wastes is a major problem; because in the coming years there may not be sufficient landfill area for the large amounts of these wastes. In addition, such a large amount of construction practices may cause the danger of depletion of natural resources that are natural aggregate (NA) and crushed aggregate (CA) in the future. Therefore, the use of recycled concrete aggregates (RCA), one of construction and demolition wastes, reduces unnecessary landfill and natural resource consumption and contributes to sustainable economy. However, the use of RCAs must comply with the requirements of the specifications according to the field in which it is used in civil engineering. Many researchers have therefore investigated the usability of RCAs as granular road base (GRB) and granular road subbase (GRSB) materials which are road layers and have determined the advantages and disadvantages of RCAs. Most of the tests applied to natural aggregates other than sulfate resistance tests can be applied to RCAs [1]. Material losses of Los Angeles (LA) abrasion and sulfate soundness tests are higher than the natural aggregate [2]. In one study, it was reported that although the permeability coefficients of RCAs were low, they still remained within the limits required for GRSB [3].

In this study, in order to determine the permeability coefficients of RCAs, permeability tests were performed, and the permeability of RCAs was compared with conventional aggregates. Thus, the permeability behavior of RCAs was investigated in detail.

II. MATERIAL AND METHOD

A. Materials and Design

CA and NA were obtained from Egribayat region-Konya. The CA was obtained from a crushing plant and the NA from a quarry. The RCAs were obtained from 3 different buildings from Meram region-Konya that were demolished within the projects of urban transformation. The materials were adjusted and stored in a maximum size of 25 mm in accordance with the gradation limits given for GRB and GRSB materials in Highway Technical Specification-2013 (HTS-2013) [4]. In order to adjust the RCAs to the appropriate gradation, the concrete blocks brought from the demolished buildings were crushed with laboratory type jaw crusher. Some physical properties of the materials are given in Table 1.

In order to determine the compaction parameters and permeability, 23 different designs were formed from these 5 different materials. The performance of the materials in the case of being used alone was examined with 5 designs consisting of pure (100%) forms of the materials. The remaining 18 designs were made by mixing the RCAs with the CA and NA at 25-50-75% ratios by mass. Thus, it was aimed to examine the use of these materials when they are mixed. The RCAs were named as R1, R2 and R3, respectively, from

higher to lower core sample compressive strength of the buildings from which they were obtained; thus, RCAs were distinguished according to strength criteria. The core strengths of the buildings where R1, R2 and R3 were obtained were determined as 18.5, 15.2, 11.7 MPa, respectively. The established design is shown in Table 2. As an example nomenclature in the designs, "75CA 25R3" design includes 25% of the CA and 75% of the R3 by mass.

Table 1: Physical properties of the materials.

Property	Material				
	CA	NA	R1	R2	R3
Particle Density (g/cm^3) (Coarse-Fines)	2.75-2.48	2.73-2.48	2.62-2.35	2.67-2.39	2.69-2.40
Water Absorption (%) (Coarse-Fines)	0.63-0.78	2.49-3.49	4.63-6.59	2.88-6.00	3.56-6.75
LA abrasion (%)	31.09	33.76	46.66	40.39	45.03
MgSO$_4$ soundness (%)	2.33	9.69	26.94	25.31	22.94
Plasticity Index (%)	NP	7.44	NP	NP	NP
Flakiness Index (%)	19.14	5.94	6.72	7.20	6.34

Table 2: Established designs.

Design No	Design Name	Design No	Design Name
1	100CA	13	25CA 75R2
2	100NA	14	25CA 75R3
3	100R1	15	75NA 25R1
4	100R2	16	75NA 25R2
5	100R3	17	75NA 25R3
6	75CA 25R1	18	50NA 50R1
7	75CA 25R2	19	50NA 50R2
8	75CA 25R3	20	50NA 50R3
9	50CA 50R1	21	25NA 75R1
10	50CA 50R2	22	25NA 75R2
11	50CA 50R3	23	25NA 75R3
12	25CA 75R1		

B. Modified Proctor Tests

In order to determine the compaction parameters of 23 different designs, modified Proctor tests were performed. In accordance with the method of TS 1900-1 [5], modified Proctor test was carried out in compaction molds with a volume of 2100 cm^3.

C. Permeability Tests

According to ASTM D5856 [6], it is stated that a constant head permeability test can be performed on materials with permeability coefficient greater than 10^{-5} m/s, and falling head permeability test can be performed on materials with a permeability coefficient less than 10^{-5} m/s. Accordingly, in some designs, the falling head permeability tests and in some designs the constant head permeability tests were performed.

Falling head permeability tests were performed according to ASTM D5856 [6].

According to ASTM D2434 [7], constant head permeability

test was carried out in designs that do not require falling head permeability test.

In a design, whether the falling head or constant head permeability test is carried out was determined by switching to the falling head permeability test equipment when the difference between the two piezometers cannot be seen (the energy of the water traveling through the sample becomes very low due to high friction between particles of the materials.) in the constant head test equipment of the material placed in the permeability mold.

III. RESULTS AND DISCUSSION

A. Modified Proctor Test Results

Modified Proctor test results are given in Table 3 for 23 different designs. This table shows the optimum moisture content (w_{opt}) and maximum dry unit weight (γ_{kmax}) values obtained from each test.

Table 3: Compaction parameters of the materials.

Design	Optimum Moisture Content, w_{opt} (%)	Maximum Dry Unit Weight, γ_{kmax} (kN/m^3)
100CA	5.35	21.97
100NA	4.40	22.22
100R1	9.75	19.48
100R2	8.60	19.69
100R3	9.60	19.70
75CA 25R1	6.40	21.62
75CA 25R2	6.20	21.78
75CA 25R3	6.47	21.64
50CA 50R1	7.20	20.73
50CA 50R2	6.60	21.14
50CA 50R3	6.60	21.26
25CA 75R1	7.75	20.38
25CA 75R2	7.30	20.58
25CA 75R3	9.20	20.24
75NA 25R1	6.42	21.76
75NA 25R2	6.95	21.49
75NA 25R3	5.40	21.71
50NA 50R1	7.50	20.99
50NA 50R2	7.40	21.33
50NA 50R3	8.35	20.96
25NA 75R1	7.23	20.42
25NA 75R2	7.80	20.64
25NA 75R3	7.10	20.52

When the tests results were examined, it was observed that w_{opt} values were higher than 100NA and 100CA for the designs of 100RCAs and the mixtures of RCAs with NA and CA. Accordingly, the highest w_{opt} values were obtained in 100R1 and 100R3 with 9.75% and 9.60%, respectively. The lowest w_{opt} values were obtained in 100CA and 100NA with 5.35% and 4.40%. For the mixtures of NA and CA with RCAs, w_{opt} values increased with the increasing percentage of

RCAs by mass. In previous studies for RCAs, 9-12.8% [8], 11.8% [9], 12% [10], 5.5-7.5% [11], 7.44-14.64% [12] w_{opt} values were obtained. The w_{opt} values obtained in this study are consistent with previous studies. The fact that RCAs have high w_{opt} values can also be explained by the fact that these materials have high water absorption values [13]. In addition, the reason for the high water absorption values of RCAs is due to the adhered cement content present in these materials [14]. Adhered cement from the main concrete has caused RCAs to have more porous [15] and hydrophilic properties.

When the γ_{kmax} values obtained from the modified Proctor test results in Table 3 are examined, it is seen that RCAs had lower γ_{kmax} values than the CA and NA. It was observed that these values decreased more with increasing percentage of the RCA in mixtures. The highest values of γ_{kmax} were 22.22 kN/m^3, 21.97 kN/m^3 for 100NA and 100CA; The lowest values of γ_{kmax} were 19.48 kN/m^3, 19.69 kN/m^3 and 19.70 kN/m^3 for 100R1, 100R2 and 100R3, respectively. In previous studies, maximum dry density values of RCAs were 2.0 g/cm^3 [16], 1.81-2.21 g/cm^3 [8] and γ_{kmax} values of RCAs were 18.9 kN/m^3 to 19.8 kN/m^3 [17], 20.2 kN/m^3 [18]. In these studies, the values obtained for RCAs are consistent with the values obtained in this study. The reason that γ_{kmax} values are lower in RCAs is that the particle density of RCAs is lower than CA and NA [9] and adhered cement mortar present in RCA is caused low particle densities [14]. Another reason for the lower values of γ_{kmax} in RCAs may be that the adhered cement mortar, which makes the RCA rougher, makes it difficult for RCA particles to settle in the voids during the modified Proctor test, resulting in less material filling.

B. Permeability Tests Results

For 23 different designs, in Table 4 the permeability methods are given and in Figure 1 the results of permeability tests are shown.

Table 4: Permeability test methods used for the designs.

Design	Permeability Test Method	Design	Permeability Test Method
100CA	Constant Head	25CA 75R2	Constant Head
100NA	Falling Head	25CA 75R3	Constant Head
100R1	Constant Head	75NA 25R1	Falling Head
100R2	Constant Head	75NA 25R2	Falling Head
100R3	Constant Head	75NA 25R3	Falling Head
75CA 25R1	Constant Head	50NA 50R1	Falling Head
75CA 25R2	Constant Head	50NA 50R2	Falling Head
75CA 25R3	Constant Head	50NA 50R3	Falling Head
50CA 50R1	Constant Head	25NA 75R1	Constant Head
50CA 50R2	Constant Head	25NA 75R2	Constant Head
50CA 50R3	Constant Head	25NA 75R3	Constant Head

When the results are examined, it was determined that the design with the highest permeability coefficients was 100CA with 1.411x10^{-5} m/s. The lowest permeability coefficient was obtained in 100NA with a value of 5.435x10^{-7} m/s. The reason for the lowest permeability of 100NA; although the fines

ratios did not change much in the gradation of the materials, the fines of the 100NA were plastic and the mineral structure of the particles was composed of clay minerals. Accordingly, the plastic material interacted with water, became viscous, increased some volume and caused some gaps in the sample matrix to be blocked or reduced. The fines forming the CA and RCAs was close to the silt structure and had "non-plastic (NP)" plasticity. Therefore, the particles did not undergo any volume increase and did not interfere with the passage of water.
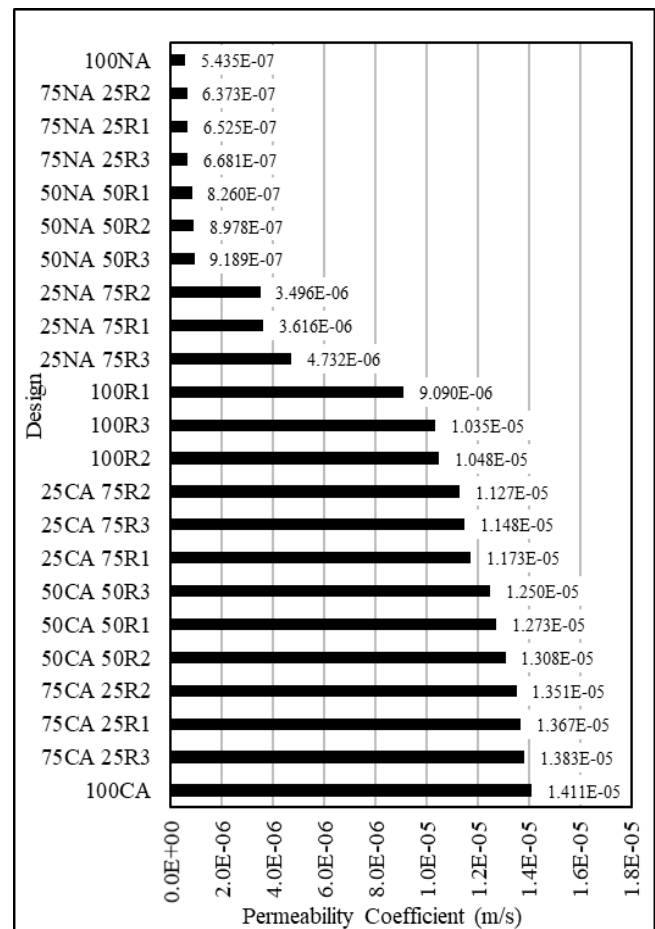
Figure 1: Change of the permeability coefficients for designs.

The permeability coefficients of the RCAs were obtained as 9.090x10^{-6} m/s, 1.048x10^{-5} m/s and 1.035x10^{-5} m/s for 100R1, 100R2 and 100R3, respectively. Some researchers found that the permeability coefficients for RCAs were 2.67x10^{-3} m/s [13], 3.3x10^{-8} m/s [10], 1.6x10^{-5}-2.6x10^{-5} m/s [17]. Although the difference between the permeability coefficient values in the literature is very high, it is seen that the permeability coefficients obtained in this study are within the limits of the results in the literature. Although there is not a big difference between the RCAs and 100CA in general, it was observed that the permeability coefficient values of the RCAs were lower than 100CA. This can be explained by the fact that RCAs become hydrophilic due to adhered cement mortar [19] and tend to retain water. On the other hand, in the mixture designs, the permeability coefficients were generally decreased in

designs with high NA ratio and the permeability coefficients were increased in designs with high CA ratio. However, the effect of the NA on the permeability made a significant difference due to the change in the NA ratios in the mixtures and changed the permeability properties of the mixtures very much. In AASHTO [20] pavement design guide, the ability of the materials used for GRB and GRSB to drain water plays an important role in determining the drainage coefficients used in directly for thickness calculation of pavement layers. The fact that the permeability coefficients of the RCAs were close to the CA and generally high values indicate that their ability to drain water when used in GRB and GRSB will be adequate. This shows that RCAs will not be a problem in terms of draining surface water both when mixed with CA and when used alone in GRB and GRSB.

IV. Conclusion

In this study, the permeability of RCAs was investigated, and the results were compared with the conventional aggregates CA and NA. The study results can be summarized as follows:

- The RCAs had higher w_{opt} values and lower γ_{kmax} values than the NA and CA. Adhered cement mortar was the most important factor in this situation. The w_{opt} values increased and γ_{kmax} values decreased as the RCA ratio increased in the mixtures.

- The permeability coefficients of the RCAs were significantly higher than those of the NA. As the RCA ratio in the mixtures increased, the permeability coefficients also increased. The fines of the NA which have plastic nature caused the permeability coefficients to be so low.

- The permeability coefficients of the CA and RCAs were obtained very close to each other, although the RCAs had slightly lower permeability coefficients. Since the CA is widely used in GRB and GRSB as crushed aggregates, the fact that the RCA had similar permeability to the CA shows that RCAs can have good drainage capabilities when used in GRB and GRSB.

Acknowledgment

References

[1] A. Saeed and M. Hammons, "Use of recycled concrete as unbound base aggregate in airfield and highway pavements to enhance sustainability," in *Airfield and Highway Pavements Conference*, Washington, 2008, pp. 497-508.

[2] A. R. Gabr and D. A. Cameron, "Properties of recycled concrete aggregate for unbound pavement construction," *Journal of Materials in Civil Engineering,* vol. 24, pp. 754-764, Jun 2012.

[3] A. Arulrajah, J. Piratheepan, and M. M. Disfani, "Reclaimed asphalt pavement and recycled concrete aggregate blends in pavement subbases: Laboratory and field evaluation," *Journal of Materials in Civil Engineering,* vol. 26, pp. 349-357, Feb 2014.

[4] Highway Technical Specification, *General Directorate of Highways*, Ankara, Turkey, 2013.

[5] TS 1900-1, "Methods of testing soils for civil engineering purposes in the laboratory – Part 2: Determination of physical properties", *Turkish Standards Institution*, Ankara, Turkey, 2006.

[6] ASTM D5856, "Standard test method for measurement of hydraulic conductivity of porous material using a rigid-wall, compaction-mold permeameter," *ASTM International*, West Conshohocken, USA, 2015.

[7] ASTM D2434, "Standard test method for permeability of granular soils," *ASTM International*, West Conshohocken, USA, 2006.

[8] T. Park, "Application of construction and building debris as base and subbase materials in rigid pavement," *Journal of Transportation Engineering-Asce,* vol. 129, pp. 558-563, Sep-Oct 2003.

[9] C. S. Poon and D. X. Chan, "Feasible use of recycled concrete aggregates and crushed clay brick as unbound road sub-base,", *Construction and Building Materials,* vol. 20, pp. 578-585, Oct 2006.

[10] A. Arulrajah, J. Piratheepan, M. M. Y. Ali, and M. W. Bo, "Geotechnical properties of recycled concrete aggregate in pavement sub-base applications," *Geotechnical Testing Journal,* vol. 35, pp. 743-751, Sep 2012.

[11] M. Arshad and M. F. Ahmed, "Potential use of reclaimed asphalt pavement and recycled concrete aggregate in base/subbase layers of flexible pavements," *Construction and Building Materials,* vol. 151, pp. 83-97, Oct 2017.

[12] T. G. Townsend, P. Chadik, N. Gupta, M. Kluge, T. Vinson, and J. Schert, *Concrete debris assessment for road construction activities,* Final Report, Florida Department of Transportation Research Center, Florida, 2016.

[13] C. S. Poon, X. C. Qiao, and D. X. Chan, "The cause and influence of self-cementing properties of fine recycled concrete aggregates on the properties of unbound sub-base," *Waste Management,* vol. 26, pp. 1166-1172, 2006.

[14] J. R. Jimenez, J. Ayuso, F. Agrela, M. Lopez, and A. P. Galvin, "Utilisation of unbound recycled aggregates from selected CDW in unpaved rural roads," *Resources Conservation and Recycling,* vol. 58, pp. 88-97, Jan 2012.

[15] M. Arm, "Self-cementing properties of crushed demolished concrete in unbound layers: results from triaxial tests and field tests," *Waste Management,* vol. 21, pp. 235-239, 2001.

[16] A. Nataatmadja and Y. L. Tan, "Resilient response of recycled concrete road aggregates," *Journal of Transportation Engineering-Asce,* vol. 127, pp. 450-453, Sep-Oct 2001.

[17] K. Nokkaew, J. M. Tinjum, and C. H. Benson, "Hydraulic properties of recycled asphalt pavement and recycled concrete aggregate," in *GeoCongress 2012: State of the Art and Practice in Geotechnical Engineering*, Oakland, 2012, pp. 1476-1485.

[18] J. Lewis, B. Cetin, and A. H. Aydilek, "Effect of pH on the leaching of elements from highway base layers built with recycled concrete aggregates," in *IFCEE 2015*, San Antonio, 2015, pp. 2758-2766.

[19] T. B. Edil, J. M. Tinjum, and C. H. Benson, *Recycled unbound materials,* Final Report, Minnesota Department of Transportation, Minnesota, 2012.

[20] AASHTO Guide for design of pavement structures, *American Association of State Highway and Transportation Officials (AASHTO)*, Washington D.C., USA, 1993.

Stability of Layered Cylindrical Shells with FGM Interlayer Subjected to Combined Load under Mixed Boundary Conditions

R.P.BAYRAMOV[1] , A.H. SOFIYEV[2], F. DIKMEN[3]

[1]Department of Automobile Transportation and Organization of Transport,
Azerbaijan Technical University, Baku, Azerbaijan bp.razim@gmail.com,
[2]Department of Civil Engineering, Suleyman Demirel University, Isparta, Turkey
*E-mail: abdullahavey@sdu.edu.tr
[3]Student of Graduate School of Natural and Applied Sciences of Suleyman Demirel University, Isparta, Turkey fatihdikmen32@gmail.com

Abstract- In this study, the stability of functionally graded (FG) layered cylindrical shells (LCYLSs) with mixed boundary conditions under the combined load (combination of lateral and axial loads) is investigated. The fundamental relations and governing equations of functionally graded three-layered cylindrical shells consisting of an FGM interlayer between ceramic and metal layers (MFGC-CYLS) are derived in the framework of Donnell-type shell theory and solved using by Galerkin's method. The expression for the critical combined load of MFGC-CYLSs within the classical shell theory (CST) is found. Finally, the influence of the FGM interlayer on the values of the critical combined load for MFGC-CYLSs is investigated numerically.

Keywords: Layered cylindrical shells, FGM interlayer, Stability, Combined load, Critical loads.

I. INTRODUCTION

It is well known that a sudden change in the properties of the material at the interfaces of the layers of various materials constituting a multilayer structure leads to the appearance of large stresses [1, 2]. These stresses are even more effective at various pressure loads and at high temperature and cause the separation of some layers forming the structural element. It is more convenient to use a new generation of composite materials whose properties are continuously changing to prevent such destructive effects. One type of new-generation material is called functionally graded materials (FGMs) [3]. FGMs are composite materials made up of a mixture of ceramics and metals that characterized by the smooth and continuous changes of mechanical properties [4]. FGMs are specifically designed to reduce heat loss from engine exhaust system components, including exhaust manifolds, turbocharger housings, exhaust caps, downpipes, and tailpipes. FGMs are also used in machine tools, forming and cutting tools, metal casting, forging, combustion chambers, engine cylinder liners, diesel engine pistons, drive shafts and flywheels. When using FGM in multilayer composite components, this significantly reduces interface problems and provides a more even voltage distribution [5, 6]. The development of modern technologies, the use of FGMs as interlayers increased interest in the investigation of stability and vibration behavior of layered shells containing an FGM layer with different boundary conditions [7-11]. The studies on the stability and vibration of pure FGM and sandwich shells with FGM interlayer under various separately loads with mixed boundary conditions are proposed in refs. [12-14]. The literature review reveals that the stability of layered shells containing an FGM core under combined loads is not sufficiently studied. The aim of this study is to investigate this problem in the framework of the CST.

II. FORMULATION OF THE PROBLEM

Fig.1 shows a layered cylindrical shells consisting of an FGM interlayer between ceramic and metal layers having a radius R and a length L and subjected to a combination of lateral pressure (P) and axial load (T). As shown in Figure 1b, (1) a ceramic substrate, (2) an FGM interlayer and (3) a metal coating. The total thickness of the MFGC-CYLS is indicated as follows: $h = h_c + h_{FG} + h_m$ in which h_c, is the thickness of the ceramic, $h_{fg} = 2a$ is the thickness of the FGM interlayer and h_m is the thickness of the metal coating. The coordinate system $(Oxyz)$ on the middle-layer of the MFGC-CYLS is shown in Fig.1.
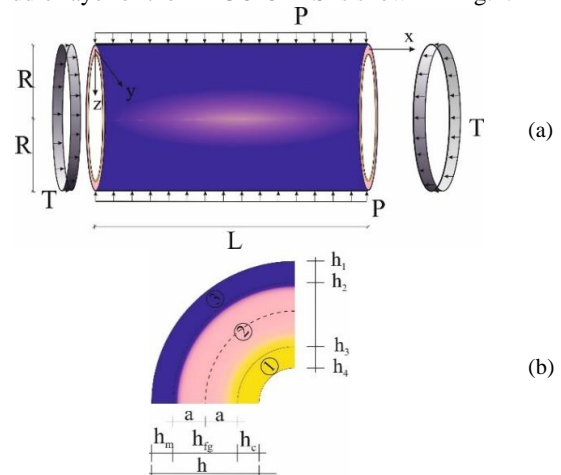

Figure 1: (a) MFGC-CYLS under the combined load and (b) cross section

III. FUNDAMENTAL RELATIONS AND GOVERNING EQUATIONS

The effective material properties, such as Young's modulus and Poisson's ratio of the coating, FGM interlayer and substrate of MFGC-CYLSs, in accordance with Voight rule mixture, are expressed as [6-12]:

$$E(\bar{z}), \nu(\bar{z}) = \begin{cases} E_m, \nu_m \quad for \ -h_1 \leq z < -h_2, \\ E_{fg} = (E_c - E_m)V_c + E_m, \ \nu_{fg} = (\nu_c - \nu_m)V_c + \nu_m \ for \ -h_2 \leq z \leq h_3, \\ E_c, \ \nu_c \ for \ h_3 < z \leq h_4 \end{cases} \tag{1}$$

where $\bar{z} = z / h_{fg}$, E_m, E_c and ν_m, ν_c are Young's modulus and Poisson's ratio of the metal and ceramic surfaces of the FGM interlayer, and V_c is the volume fraction of the ceramic phase and is defined as the inverse quadratic function [5]: $V_c = 1 - (0.5 - \bar{z})^2$.

The stresses-strains relationships of the *k-th* layer for MFGC-CYLSs within the CST are expressed as:

$$\begin{bmatrix} \sigma_{11}^{(k)} \\ \sigma_{22}^{(k)} \\ \sigma_{12}^{(k)} \end{bmatrix} = \begin{bmatrix} Q_{11}^{(k)} & Q_{12}^{(k)} & 0 \\ Q_{12}^{(k)} & Q_{11}^{(k)} & 0 \\ 0 & 0 & Q_{66}^{(k)} \end{bmatrix} \begin{bmatrix} e_{11} - z \dfrac{\partial^2 w}{\partial x^2} \\ e_{22} - z \dfrac{\partial^2 w}{\partial y^2} \\ \gamma_{012} - 2z \dfrac{\partial^2 w}{\partial x \partial y} \end{bmatrix} \tag{2}$$

where $Q_{ij}^{(k)}$ (i,j $= 1, 2, ..., 6; k = 1, 2, 3)$ are the material properties in the *k-th* layer, w is the displacement of the mid-surface in the normal direction which is positive towards the axis of the cylindrical shell and e_{ij} are the strains on the mid-surface [7].

The governing equations of MFGC-CYLSs within the CST can be derived as:

$$\begin{bmatrix} D_{11} & D_{12} \\ D_{21} & D_{22} \end{bmatrix} \begin{bmatrix} \psi \\ w \end{bmatrix} = 0 \tag{3}$$

where $D_{ij}(i, j = 1, 2, ..., 4)$ are differential operators, depending on the MFGC-CYLSs characteristics and ψ is the Airy stress function [13].

IV. SOLUTION OF GOVERNING EQUATIONS

The following mixed boundary conditions are used. At left end of the MFGC-CYLS is satisfied, i.e. for $x = 0$ is satisfied the following boundary condition [14],

$$v = w = N_x = M_x = 0 \tag{4}$$

and the right end i.e., for $x = L$ is satisfied the following boundary condition,

$$u = \frac{\partial w}{\partial x} = Q_x = N_{xy} = 0 \tag{5}$$

where N_x, N_{xy}, Q_x and M_x are shear forces and bending moment, respectively, and u is the displacement in the direction x.

Under these boundary conditions the solution of the governing Eqs. (3) can be described by [14]:

$$\psi = \psi_1 \sin(m\pi x / 2L) \sin(ny / R),$$
$$w = w_1 \sin(m\pi x / 2L) \sin(ny / R) \tag{6}$$

where ψ_1 and w_1 are amplitudes, in which $m = 1, 3, 5, ...$ is the wave number in axial direction and n is the circumferential wave number.

Substituting (6) into Eq. (3), after applying the Galerkin method for the critical lateral pressure and critical axial load of MFGC-CYLSs, the following expressions are found:

$$P_{cr} = \frac{1}{b_{PL}} \left(b_2 + \frac{b_1 b_4}{b_3} \right) \tag{7}$$

and

$$T_{cr} = \frac{1}{b_{ax}} \left(b_2 + \frac{b_1 b_4}{b_3} \right) \tag{8}$$

where $b_j (j = 1, 2, ..., 4)$ and b_{PL} and b_{ax} are parameters depending on the MFGC-CYLSs characteristics, lateral pressure and axial load under mixed boundary conditions [13].

In the framework of CST, the following equation is used to find the critical combined axial compression and lateral pressure for the cylindrical shells [15]:

$$\frac{T_1}{T_{1cr}} + \frac{P_1}{P_{1cr}} = 1 \tag{9}$$

where T_1 is dimensionless axial compressive load, P_1 is dimensionless lateral pressure and the following definitions apply:

$$T_1 = T / E_c h, \ P_1 = P / E_c \tag{10}$$

If $T_1 = \mu P_1$ is considering in Eq. (9), the expression for critical combined load (combination of lateral pressure and axial load) of the MFGC-CYLSs under mixed boundary conditions is obtained as:

2

$$P_{1cr}^{cb} = \left(\frac{\mu}{T_{1cr}} + \frac{1}{P_{1cr}} \right)^{-1} \tag{11}$$

where μ is the load-proportional parameter and it is a positive number.

The minimum values of the critical combined load for MFGC-CYLSs are obtained by minimizing Eqs. (11) with respect to circumferential wave number, (m,n).

V. NUMERICAL ANALYSIS

The mixture of materials of an FGM interlayer is considered to be nickel (Ni) and zirconium oxide (ZrO₂), referred to as Ni/ZrO₂. The MFGC-CYLS is composed of Ni, ZrO2 and Ni/ZrO₂ is shown as follows: Ni/FGM/ ZrO₂. The Young's moduli and Poisson's ratio of the FGM interlayer can be expressed as, $E_c = 1.68063 \times 10^6 (MPa)$, $E_m = 2.05098 \times 10^6 (MPa)$, $\nu_c = 0.297996$, $\nu_m = 0.31$ [4].

The variation of critical combined loads for nickel (Ni), zirconium oxide (ZrO₂) and Ni/FGM/ZrO₂ cylindrical shells under mixed boundary conditions versus the ratio h/h_{fg} for R/h=75, $L/R = 1$ and $\mu = 500$ are given in Table 1. The values of critical combined loads for Ni, ZrO₂ and Ni/FGM/ZrO₂ shells increase with increasing of the h/h_{fg}. It is observed that the values of critical combined loads for Ni and ZrO₂ shells remain constant, whereas those for Ni/FGM/ZrO₂ shells increase for the FG-inverse quadratic profile of the interlayer with the increasing of from 1.1 to 1.5 with the step 0.1. As the critical combined loads for Ni/FGM/ZrO₂ shells compared with ceramic and metal cylindrical shells, the influences of the FGM inverse-quadratic profile of the interlayer on the critical combined loads increase from (+9.06%) to (+10.03%) and decrease from (-11.06%) to (-10.27%), respectively, as increases from 1.1 to 1.5.

Table 1. The variation of critical combined loads for Ni, ZrO₂ and Ni/FGM/ ZrO₂ cylindrical shells versus the ratios h/h_{fg}

=75	$P_{1cr}^{cb} \times 10^6 (n)$		
	ZrO₂	Ni/FGM/ ZrO₂	Ni
1.1		7.135(5)	
1.2		7.158(5)	
1.3	6.542(5)	7.175(5)	8.022(5)
1.4		7.188(5)	
1.5		7.198(5)	

The variation of critical combined loads for nickel (Ni), zirconium oxide (ZrO₂) and Ni/FGM/ZrO₂ cylindrical shells under mixed boundary conditions versus the ratio R/h for $L/R = 1$, $h/h_{fg} = 1.1$ and $\mu = 500$ are plotted in

Fig.2. The values of critical combined loads for Ni, ZrO₂ and Ni/FGM/ZrO₂ shells diminish with increasing of the . Comparing Ni/FGM/ZrO₂ cylindrical shells to ZrO₂ and Ni cylindrical shells with mixed boundary conditions, the effects of the FGM inverse quadratic profile on the critical combined load remain almost constant (-11%) and (+9.3%), respectively, as R/h increases from 50 to 150.
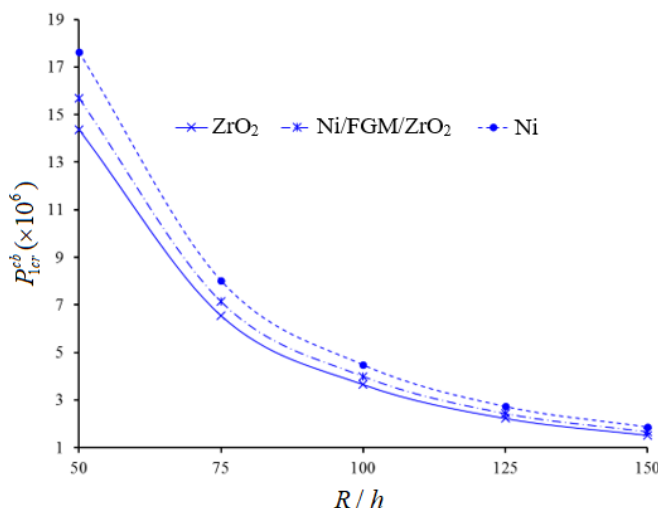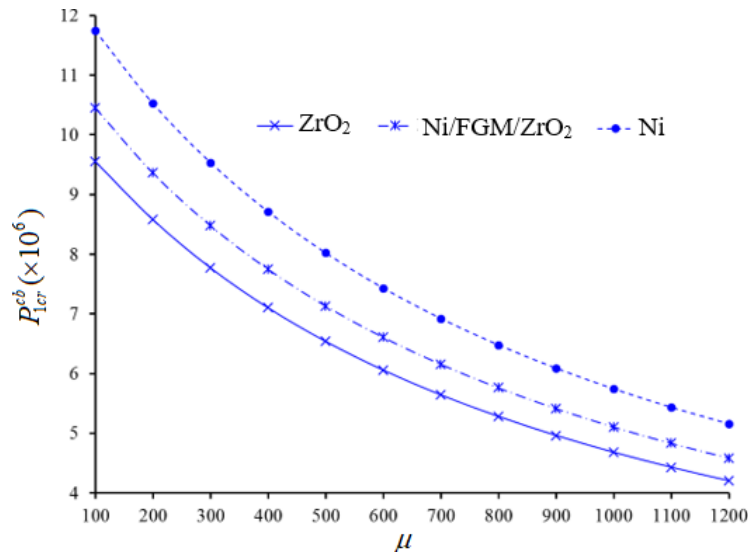

R/h

Figure 2: The variation of critical combined loads for Ni, ZrO₂ and Ni/FGM/ ZrO₂ cylindrical shells versus the ratios R/h

The distribution of the magnitudes of critical combined loads for nickel (Ni), zirconium oxide (ZrO₂) and Ni/FGM/ZrO₂ cylindrical shells under mixed boundary conditions versus the load-proportional parameter for $R/h = 75$, $L/R = 1$ and $h/h_{fg} = 1.1$ are illustrated in Fig.3. It is seen that the magnitudes of critical combined loads for Ni, ZrO₂ and Ni/FGM/ZrO₂ cylindrical shells

decrease, as the increases from 100 to 1200. Comparing Ni/FGM/ZrO₂ cylindrical shells to ZrO₂ and Ni cylindrical shells with mixed boundary conditions, the effects of the FGM inverse quadratic profile on the critical combined load change slightly, since with increasing μ from 100 to 200, these effects remain almost constant, as μ increases from 200 to 1200.

Figure 3: The variation of critical combined loads for Ni, ZrO₂ and Ni/FGM/ ZrO₂ cylindrical shells versus the μ

VI. CONCLUSION

In this study, the stability of MFGC-CYLSs with mixed boundary conditions under the combined load is investigated. The governing equations of MFGC-CYLS are derived in the framework of Donnell-type shell theory and solved using by Galerkin method. The expression for the critical combined load of MFGC-CYLSs within the CST is found. Finally, the influence of the FGM interlayer with inverse quadratic profile and the load-proportional parameter on the values of the critical combined load for MFGC-CYLSs with different characteristics is investigated.

REFERENCES

[1] F.J. Plantema, *Sandwich Construction*. New York: Johen Wiley & Sons Inc., 1966.
[2] H.G. Allen, *Analysis and Design of Structural Sandwich Panels*. London: Pergamon Press, 1969.
[3] T. Hirai, M. Sasaki, "Vapor-deposited functionally gradient materials", *JSME International Journal*, vol.34, pp. 123-129, 1991.
[4] H.S. Shen, *Functionally Graded Materials: Nonlinear Analysis of Plates and Shells*. Florida: CRC Press, 2009.
[5] S. Pitakthapanaphong, E.P. Busso, "Self-consistent elasto-plastic stress solutions for functionally graded material systems subjected to thermal transients", *Journal of Mechanics and Physics Solids*, vol.50, pp. 695-716, 2002.
[6] A.M. Zenkour, "A comprehensive analysis of functionally graded sandwich plates: Part 2- Buckling and free vibration", *International Journal of Solids and Structures*, vol.42, pp. 5243-5258, 2005.

[7] A.H. Sofiyev, "Vibration and stability of composite cylindrical shells containing a FG layer subjected to various loads", *Structural Engineering and Mechanics an International Journal*, vol.27, pp. 365-391, 2007.
[8] U. Icardi, L. Ferrero, "Optimization of sandwich panels with functionally graded core and faces", *Composites Science and Technology,* vol.69, pp. 575-585, 2009.
[9] S.R. Li, X.H. Fu, R.C. Batra, "Free vibration of three layered circular cylindrical shells with functionally graded middle layer", *Mechanics Research Communications,* vol.37, pp. 577-580, 2010.
[10] R. Sburlati, "An axisymmetric elastic analysis for circular sandwich panels with functionally graded cores", *Composites Part B Engineering,* vol.43, pp. 1039-1044, 2012.
[11] F.A. Fazzolari, E. Carrera, "Refined hierarchical kinematics quasi-3D Ritz models for free vibration analysis of doubly curved FGM shells and sandwich shells with FGM core", *Journal Sound and Vibration*, vol.333, pp. 1485-1508, 2014.
[12] A.H. Sofiyev, "The buckling and vibration analysis of coating-FGM-substrate conical shells under hydrostatic pressure with mixed boundary conditions", *Composite Structures*, vol.209, pp. 686-693, 2019.
[13] A.H. Sofiyev, D. Hui, "On the vibration and stability of FGM cylindrical shells under external pressures with mixed boundary conditions by using FOSDT", *Thin-Walled Structures*, vol.134, pp. 419-427, 2019.
[14] L.G. Agenosov, A.V. Sachenkov, "The stability and vibration of circular conical and cylindrical shells at different boundary conditions", *Research on the Theory of Plates and Shells*, Kazan State University, Kazan, vol. 2, pp.111-126, 1964 [in Russian].
[15] A.S. Volmir, *Stability of Elastic Systems*. Nauka: Moscow. English Translation: Foreign Tech. Division, Air Force Systems Command. Wright-Patterson Air Force Base, Ohio, AD628508, 1967.

4

Experiment Investigation of Internet Use of Objects in Fire Detection and Extinguishing Systems

O. MUSTAFA[1] and M. ALTIN[2]

[1] Selcuk University, Konya/Turkey, omaryawiz@gmail.com
[2] Konya Technical University, Konya/Turkey, maltin@ktun.edu.tr

Abstract - **Fire, one of the greatest inventions in the history of humanity, on the other hand, fire can lead to major disasters. The human know that he was the only organism capable of controlling fire and was also aware of the magnitude of disasters when he is unable to control it so he work to solve it by harnessing engineering information and modern technologies. The fire explodes very quickly in very short periods so it was found that the fire detection and rapid intervention to solve the problem before the exacerbation is critical. This project was practically tested in a specially prepared room to measure the success rate and efficiency. The completed construction, fire alarm and fire monitoring systems will be integrated into the Internet of Things (IoT) platform and necessary instructions will be created by means of smoke, flame, visual motion and temperature sensors, and when the system reaches that the result is fire, then, extinguishing systems will be started before the fire starts. The system will fire the fire alarm with the sound and light in the right place during the first response to the fire and thus will save time to evacuate people and save what they can from the important things they can in the building where they are located. The system also sends a fire notification via the Internet to the emergency department by calling their numbers or sending a notice on the location. The design here aims to determine the exact location of the fire starting point through the sensors and aims to conduct the initial intervention in the target point to reduce its spread. Since this system adopts wireless communication, it will be an important economic system that can be used in industrial plants.**

Keywords - **Fire, IOT, Internet of things, Wireless, Connection systems.**

I. INTRODUCTION

The Internet of Things (IoT) is a network of devices such as electronics, software, sensors, actuators, and tools and the appliances that allow these things to connect, interact and exchange data[1]IoT is a newly emerging term for the new generation of the Internet (network) that allows understanding between interconnected devices (over IP).These devices include tools, sensors, various AI tools and more.This definition goes beyond the traditional concept of people communicating with computers and smartphones over a single global network and through traditional IP. What distinguishes the Internet of Things is that it allows people to be free from the place, that is, a person can control the tools without having to be in a specific place to deal with a particular device.

The concept of the network of smart devices was discussed as early as 1982; A modified Coke vending machine at Carnegie Mellon University was the first device connected to the Internet [2]to report inventory and whether the freshly loaded drinks were cold. [3]Mark Weiser's article on ubiquitous computing 21, The Computer of the 21st Century and academic sites such as UbiComp and PerCom produced IoT's contemporary vision [4] In 1994, Reza Raji described the concept of IEEE Spectrum as vehicle moving small data packets from home appliances to a wide range of nodes to integrate and automate all factories [5].Between 1993 and 1997, several companies proposed solutions such as Microsoft's Work or Novell's NEST. Bill Joy gained momentum when he envisioned Device-to-Device (D2D) communications as part of the "Six Networks" framework presented at the World Economic Forum in Davos in 1999.

The term "Internet of Things" was written by Kevin Ashton of Procter & Gamble, and later in MIT's Auto-ID Center (1999) [6], although he preferred "Internet for things". At this point, he saw radio frequency identification (RFID) as the basis for the Internet of things that would allow computers to manage all the individual things[7]. The comprehensive suite of applications for IoT devices [8]is generally devoted to consumer, commercial, industrial and infrastructure. [9]. A growing number of IoT devices have been created for consumer use, including connected tools, home automation, wearable technology (as part of the Internet of Wearable Objects (IoWT) [10], devices with health-related and remote monitoring capabilities. IoT devices are part of a wider home automation concept that can include lighting, heating and air conditioning, media and security systems. [11]Long-term benefits can include energy savings by automatically turning off lights and electronic devices.

A smart home or an automated home can rely on a platform or hub that controls smart devices and devices. [12]For example, manufacturers using Apple's HomeKit can control their home products and accessories by an app on iOS devices such as the iPhone and Apple Watch. This can be a custom app or iOS native apps like Siri. This can be demonstrated in the case of Lenovo's Smart Home Essentials, a series of smart home devices controlled without the need for a Wi-Fi bridge through Apple's Home app or Siri. There are also smart home hubs available as stand-alone platforms for connecting different

smart home products. These include Amazon Echo, Google Home, Apple's HomePod, and Samsung's SmartThings Hub.

II. METHODS

Two fire rooms 300 x 350 cm and 190 x 620 cm controlled and observation room were constructed in order to carry out the experimental studies. Figure 1 shows the plan of the building under construction and shows the current situation of the building.

Figure 1. Fire Room

We used Arduino which is an open source electronic platform based on easy-to-use hardware and software. Arduino boards can read inputs - the light in a sensor, the finger of a button. Over the years, Arduino has been the brain of thousands of projects, from everyday objects to complex scientific tools. Students, hobbies, artists, programmers and professionals - a worldwide producer community gathered around this open source platform. Arduino Uno will be used as the main microprocessor of the system, all gas sensors will be controlled by it ([13]

Figure 2. Arduino

Smoke sensor module is an easy tool to detect any type of gases or smoke occurred so we included The Gas Sensor (MQ5) module which is useful for detecting gas leakage (in the home and industry). Suitable for H2, LPG, CH4, CO, Alcohol detection. Thanks to its precision and fast response time, measurements can be taken as soon as possible. The sensitivity of the sensor can be adjusted using the potentiometer. MQ-5 gas sensor will be used to detect smoke caused by fire and controlled by Arduino It will be[14]

Figure 3. MQ-5 Gas sensor

And so on The Mini WIFI IP Camera 1.3MP HD imager will be used to monitor the room and locate the fire. It also sends live video[15]

Figure 4. . Mini WIFI IP Camera 1.3MP HD

The liquid and crystal display will be used to display the signals of temperature and gas sensors [16]

Figure 5. LCD Display

And now we have the fire Ball, Classic fire extinguishing guns are thrown into the fire flame and after 3-4 seconds, the fire intervenes with explosion. It is known to be effective in extinguishing the fire by drowning the fire in an area of approximately 10 m³ and dry chemical powders and A, B, C and D type fires. Super Fire Ball is a fire extinguisher that operates automatically with electrical activation for the first time in the world, in addition to conventional fire extinguishers. Works flame-free, works with smoke, heat or system you want to work with 1-24 volts. It can be connected to fire detection and extinguishing systems or used alone. Super Fireball is the only fireball in the world that operates with electric activation. It will be used in our experimental studies. [17]

Figure 6. Fire Ball

The Arduino GSM SIM800L used here is a miniature cellular module which allows for GPRS transmission, sending and receiving SMS and making and receiving voice calls. Low cost and small footprint and quad band frequency support make this module perfect solution for any project that require long range connectivity. [18]

Figure 7. Arduino GSM sim800l

Also we must use Neo-7M Dual Antenna Interface GPS Module the Global Positioning System (GPS) which is a satellite navigation system that provides location and time information in all weather conditions anywhere on or near Earth where there is an unobstructed sight line for four or more GPS satellites[19]

Figure 8. Neo-7M Dual Antenna Interface GPS Module

The sound sensor module provides an easy way to detect sound and is commonly used to detect sound intensity. In this project it was used to give alarm when a fire occurred [20]

Figure 9. Sounds sensor

The relay module is an electrically operated switch that enables you to switch on or off a circuit using voltage or current that is much higher than a microcontroller could handle. There is no link between the microcontroller's low voltage circuit and the high power circuit [21]

Figure 10. Relay module

Finally, Flame Sensor a flame detector is a sensor designed to detect and respond the presence of a flame or fire. The Flame sensor is used to detect fire flames. The module makes use of Fire sensor and comparator to detect fire up to a range of 1 meter. [22]

Figure 11. Sounds sensor

The project is an integrated system for the detection of fires and methods of control and extinguishing them with minimal losses. Through this project are detected fires at the moment of fire and extinguish automatically to ensure the reduction of human and material losses and inform the people and the fire brigade at the scene by sending the coordinates of the site to them. The mechanism of operation of this system is shown in Figure 12.
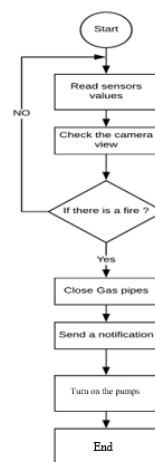
Figure 12. The diagram of this system

III.   RESULTS AND FINDINGS

In this research, a fire and gas leak detection system has been developed using special sensors to detect heat and gas using Arduino. It was practically applied in a pre-equipped experimental chamber, where a small fire was fabricated in the chamber for the purpose of ensuring the sensors distributed throughout the chamber. Initially, the heat sensor was tested to detect the fire and the sources of fire. After the fire was detected, the fire was extinguished after a very short time by the fire ball. As shown in the Figure 13, 14.

Figure 13. SMS Messenger   Figure 14. Logic (Google Maps)
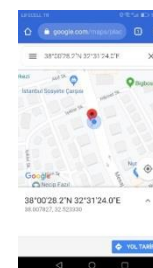
In the second stage, a special sensor was used to detect the leaked gases .In addition to all the above, a camera was used to view the fire place via the Internet from anywhere in the world and to make sure that there is no body in the room.

IV.   CONCLUSION AND RECOMMENDATIONS

Wireless sensor network play important role in save people and valuables, Here in this study the fire alarm system was developed by the use of small Arduino Uno control unit. The prototype developed provided a feature that enabled us to verify that a fire actually occurred. The fire alarm system will then warn the user by sending an alert first and request

confirmation before sending a report / alert to the "firefighter". Low cost and reliable tools were used to develop the fire alarm at a reasonable cost, thus enabling students to apply the knowledge gained during the engineering program while working on this project.

I recommend that this project be used for its cost-effectiveness and great utility in reducing the risk of fire, and thus reducing deaths. It is also a continuous development projects such as the addition of newer features such as the use of sensors for greater distances. Also large companies can take advantage of this system to reduce losses in the event of such situations.

REFERENCES

1.   Brown, E.J.U.h.w.l.c.n.w.-n.-i.-t.C.o., *Who needs the Internet of Things?(2016).* 2016: p. 3.
2.   Palermo, F.J.I.W., *Internet of things done wrong stifles innovation.* 2014. **7**.
3.   Mattern, F. and C. Floerkemeier, *From the Internet of Computers to the Internet of Things*, in *From active data management to event-based systems and more*. 2010, Springer. p. 242-259.
4.   Raji, R.S.J.I.s., *Smart networks for control.* 1994. **31**(6): p. 49-55.
5.   Pontin, J.J.M.T.R., *ETC: Bill joy's six webs.* 2005.
6.   Day, P.J.B.W.S.B.R., *Peter Day's World of Business.* 2018. **13**.
7.   Weber, R.H.J.C.l. and s. review, *Internet of things–Need for a new legal environment?* 2009. **25**(6): p. 522-527.
8.   Lochab, K., et al., *Internet of Things in Cloud Environment: Services and Challenges.* 2017. **10**(5): p. 23-32.
9.   Perera, C., C.H. Liu, and S.J.I.T.o.E.T.i.C. Jayawardena, *The emerging internet of things marketplace from an industrial perspective: A survey.* 2015. **3**(4): p. 585-598.
10.   Liberali, F. and A. Cremaschi, *Gateway, the magic mirror: IoT application for lift cars.*
11.   Meola, A.J.B.I.A.o.h.w.b.c.i.-o.-t.-s.-h.-a.-.-. *How IoT & smart home automation will change the way we live.* 2016.
12.   Lee, D., *Internet of Things: Smart Home System.* 2019.
13.   Bahrudin, M.S.B., R.A. Kassim, and N. Buniyamin. *Development of fire alarm system using Raspberry Pi and Arduino Uno*. in *2013 International Conference on Electrical, Electronics and System Engineering (ICEESE)*. 2013. IEEE.
14.   Amin, M.M., et al., *Design of cigarette disposal blower and automatic freshner using mq-5 sensor based on atmega 8535 microcontroller.* 2018. **7**(3): p. 1108-1113.
15.   Leonard III, P., *Digital 3D/360 degree camera system*. 2008, Google Patents.
16.   Krishnamurthi, K., et al., *Arduino based weather monitoring system.* 2015. **3**(2): p. 452-458.
17.   Piran, T.J.P.R., *Gamma-ray bursts and the fireball model.* 1999. **314**(6): p. 575-667.
18.   Eberspächer, J., H.-J. Vögel, and C. Bettstetter, *GSM Global System for Mobile Communication: Vermittlung, Dienste und Protokolle in digitalen Mobilfunknetzen*. 2013: Springer-Verlag.
19.   Parkinson, B.W., et al., *Global positioning system: Theory and applications, Volume II*. 1996: American Institute of Aeronautics and Astronautics.
20.   Touse, M., J. Sinibaldi, and G. Karunasiri. *MEMS directional sound sensor with simultaneous detection of two frequency bands*. in *SENSORS, 2010 IEEE*. 2010. IEEE.
21.   Lebaron, R. and L.T. Perryman, *Implantable relay module*. 2019, Google Patents.
22.   Maguluri, L.P., et al., *Efficient Smart Emergency Response System for Fire Hazards using IoT.* 2018. **9**(1): p. 314-320.

Lyapunov Exponents as a Statistical Test Tool

YILMAZ AYDIN[1] and FATİH ÖZKAYNAK[1]

[1] Fırat University, Elazığ/Turkey, y.aydin@firat.edu.tr
[1] Fırat University, Elazığ/Turkey, ozkaynak@firat.edu.tr

Abstract - **One of the application areas of chaotic systems is chaos based cryptography studies. Many design studies have been proposed using the relationship between chaos and cryptography. In this study, it has been shown that this relationship can be used in cryptanalysis of cryptographic designs. The usability of chaos analysis methods in the analysis of cryptographic protocols has been investigated. Lyapunov exponents, which are a chaos analysis method, have been used to measure the quality of random number generators. The analysis results showed that Lyapunov exponents can be used as a criterion in the evaluation of random number generators.**

Keywords - **Chaos; cryptography; cryptanalysis; random number generator; Lyapunov exponent**

I. INTRODUCTION

THE main purpose of science and engineering studies is to understand real world systems and to use these results for the benefit of mankind. During these studies, chaos theory became increasingly important. Because this phenomenon is needed to understand the logic of real world events. Therefore chaos theory has started to find its place in many applications [1]. One of the most common practical applications is the design of chaos based encryption systems [2]. In the simplest expression, chaos theory is defined as the randomness of a deterministic system. In other words, despite the fact that real world events are mathematical models, they contain an unpredictable randomness. This exciting relationship is the fundamental phenomenon desired in the cryptographic system design process [3]. A cryptographic protocol is an algorithm. However, this algorithm should provide two basic requirements, called confusion and diffusion. Chaos based cryptography studies have become increasingly popular among researchers over the last two decades, since chaotic systems have both a mathematical model and the randomness properties will provide confusion and diffusion requirements [2].

This close relationship between chaos theory and cryptography science has been used in the design process. In other words, chaotic systems have been used as an entropy source and this entropy source has been transformed into cryptographic primitives such as image encryption schema [4-8], hash functions [9-12], s-box designs [13, 14] and key generators with the help of a protocol [15-19]. When the common aspects of these cryptographic primitive studies are examined, it is seen that the hypotheses of the researchers are based on the fact that the complexity of the entropy source contributes to the design of the cryptographic primitive. In other words, it is claimed that there is a strong relationship between the complexity of the chaotic system used as an entropy source and the robustness of the cryptographic protocols [2, 3, 5].

This study deals with this hypothesis from a different perspective. The usability of chaos analysis methods in the analysis of cryptographic protocols has been investigated. The hypothesis tried to be proved in the study is that if the complexity of the chaotic system used in the protocol design contributes positively to the cryptographic protocol design, chaos analysis methods can be used to measure the quality of these cryptographic protocols. In this study, this hypothesis has been tried to be proved on cryptographic random number generators.

Lyapunov exponents, a chaos analysis method, have been used to measure the quality of cryptographic random number generators. The analysis results showed that Lyapunov exponents can be used as a criterion in the evaluation of random number generators. These results confirmed the alleged hypothesis. It has also shown that it may be an alternative to solve problems in the process of testing the statistical properties of applications that need short length sequences, especially cryptographic key generators.

The rest of the study is organized as follows. In the second section, chaos analysis methods have been mentioned briefly. In the third section, the design architecture of the chaos based random number generator is explained. In the fourth section, randomness test results and Lyapunov analyzes have been given for two different dataset. In the last section, obtained results have been summarized and suggestions have been made for future studies.

II. CHAOS ANALYSIS WITH LYAPUNOV EXPONENTS

Since chaotic behavior is an important characteristic, many researchers want to examine the existence of chaos in their systems [20, 21]. In this process, methods such as phase space portrait, power spectrum, Poincare mapping bifurcation diagram have been some of the most common methods used to determine chaotic behavior. However, the common point of these methods is that they are qualitative approaches. In other words, there is a need for an expert to interpret and evaluate the results. The chaos analysis method known as Lyapunov exponents has become more popular than others because it is a quantitative approach [21].

The idea that fixed (invariant) exponents could be used to determine the stability states of the sets of differential

equations of nonlinear dynamic systems was first shown by Sonya Kovalevskaya in 1889. Following the introduction of this hypothesis, it was based on theoretical foundations by Alexandr Mikhailovich Lyapunov. In the Lyapunov study, he explained only the basics of his thoughts about the change of trajectories of a dynamic system (as a function of time) with Lyapunov exponents. The starting point of the chaos analysis using the Lyapunov exponents is the dependence on the initial conditions and control parameters of chaotic systems. When a chaotic system is initiated from two very close neighboring initial conditions, chaos analysis can be carried out by moving the orbits away from each other or by convergence. Lyapunov exponents are a mathematical method that measures this distance between neighboring orbits. Lyapunov exponentials are likened to eigenvalues used in linear systems [21].

Lyapunov exponents can be calculated for continuous time system, discrete time systems and time series obtained from experimental or simulation results. Sensitivity to the initial conditions of a dynamic system is measured by Lyapunov exponents. Firstly, two trajectories have been determined with very close initial conditions on an attractor. If the attractor is showing chaotic behavior, the orbits are divided on an exponential rate, characterized by the largest Lyapunov exponent. The detection of a positive Lyapunov exponential is sufficient for the existence of chaos and indicates instability in a particular direction.

The TISEAN 3.0.0 package will be used for the calculation of Lyapunov exponents [22]. There are two different algorithms to make the calculations using the program. These algorithms have been developed by Rosenstein and Kantz. These algorithms are coded as lyap_r and lyap_k in the program respectively. It has been shown to give similar results in both lyap_r and lyap_k. It is stated that the small differences that can be neglected in the calculations are due to various calculation parameters such as embedding time, embedding delay, iteration number etc. The calculations in the fourth section are realized by using Kant algorithm (lyap_k).

III. Chaos Based Random Number Generator

In the proposed algorithm, chaotic system outputs are calculated for the selected initial conditions and control parameters. A threshold value function is applied to the calculated output values. The logistic map [20] has been used as the chaotic system in the study. The reason for choosing the logistics map is its simple structure. The simple structure will contribute to the faster operation of the generator.

The main premise of chaos based cryptographic designs is the complexity of entropy source (the chaotic system). In other words, more complex chaotic systems will produce better quality random numbers.
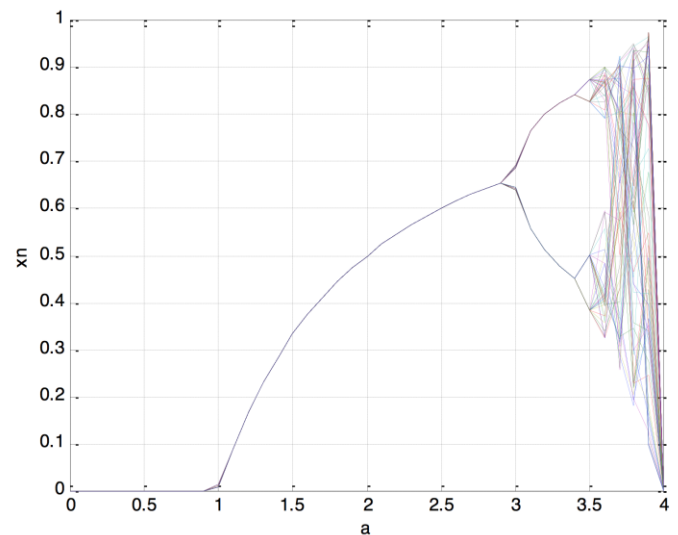
Figure 1. Bifurcation diagram of logistic maps

IV. Analysis Result

Randomness is related to probability, so that the properties of the random sequence can be defined as probabilistic. There are many statistical tests to evaluate the probabilistic properties of random numbers. These tests are used in the process of identifying samples that will ensure that the sequence is random. Because there are many statistical tests, a generator that passes all tests cannot even say randomly. Because there is a possibility that the generator will fail for a new test. Therefore, the results of statistical tests should be interpreted well.

In order for a value to be defined random, it must be arbitrarily selected from the sequence and the values must be uniformly distributed. However, when the distribution of a non-random sequence is examined, it does not seem to have a uniform distribution. Therefore, the probability distribution of the sequence is examined to test the randomness.

One of the simplest approaches to assess the randomness of a generator is the chi-square test. This test analyzes whether the data is uniformly distributed. If m random data is generated from the values between 0 and n, then it is expected that each value will be m/n units for the ideal situation.

If the calculated chi-square value is smaller than the confidence values determined for the degree of freedom, the data may be random. 16 different values ranging from 0 to 15 are produced using RNG, therefore the degree of freedom is 16. The confidence values for this degree of freedom are given in Table 1.

Table 1. Confidence values for degree of freedom 16

DF	0.20	0.10	0.05	0.025	0.02	0.01	0.005	0.002	0.001
16	20.465	23.542	26.296	28.845	29.633	32.000	34.267	37.146	39.252

Table 2. Chi-square values for different random sequences

Name of Dataset	Chi-square Value
a=3.4 and x_0=0.3	3749904.1
a=3.8 and x_0=0.3	298875.8

Table 3. The number of observed data from each value

Name of Dataset	0	1	2	3	4	5	6	7	8	9	10	11	12	13	14	15
a=3.4 and x_0=0.3	0	0	0	0	0	0	0	0	0	0	249997	0	0	0	1	2
a=3.8 and x_0=0.3	0	0	0	0	0	23760	18754	27409	0	0	23358	45952	0	45518	27580	37669

Table 4. NIST test results for twelve different dataset

Nist Test	a=3.4 and x_0=0.3		a=3.5 and x_0=0.3	
	S/F	P-Value	S/F	P-Value
Monobit test	S	0.99202	F	0'
Frequency within block test	S	1	F	0'
Runs_test	F	0	F	0'
Longest run ones in a block test	F	2.3e-159	F	8.32e-28
Binary matrix rank test	F	0	S	1
Dft test	F	0	F	3.6e-123
Non overlapping template matching test	F	0	F	0'
Overlapping template matching test	S	0.5839	S	0.5839'
Maurers universal test	S	0.014128	S	0.54998'
Linear complexity test	S	1	S	1'
Serial test	F	0	F	0 0'
Approximate entropy test	F	0	F	0'
Cumulative sums test	S	1	F	0 0'
Random excursion test	F	2.7e-12	F	3.9e-14'
Random excursion variant test	S	0.4795	S	0.83117
Total success rate	**7/15**		**5/15**	

Table 5. Lyapunov exponents for RNG sequences

Name of Dataset	Lyapunov exponents
a=3.4 and x_0=0.3	does not compute
a=3.8 and x_0=0.3	0.26141

Calculated chi-square values for two different random sequences are given in Table 2. The number of observed data from each value is given in Table 3.

The most widely used statistical test package is NIST tests [24]. This analysis method, published as a test package, is accepted as the standard in many studies. There are 15 tests in NIST test package. These tests are "Monobit test, Frequency within block test, Runs_test, Longest run ones in a block test, Binary matrix rank test, Dft test, Non overlapping template matching test, Overlapping template matching test, Maurers universal test, Linear complexity test, Serial test, Approximate entropy test, Cumulative sums test, Random excursion test, Random excursion variant test".

NIST test results for two different dataset are given in Table 4. The S and F symbols in the table indicate successful and unsuccessful test results, respectively. P symbol is the calculated probability value of the test. The test results revealed some problems of the NIST test package. The logistic map output values are periodic for control parameter less than 3.5. The periodicity of output of logistic map can be observed both in the bifurcation diagram in Figure 1 and in the distribution of numbers in Table 3. However, NIST test results for random sequences generated for a = 3.4, are better than the sequences generated for a=3.8. In other words, according to NIST test results, the values produced from periodic data are more random than the values produced from chaotic data. However, it is understood from the data distribution in Table 3 that this claim is invalid. This indicates that the NIST test package cannot be used for analysis alone.

Table 5 shows the calculated Lyapunov exponential values

for the outputs obtained by converting the chaotic system outputs to random numbers. The analysis has been shown that the NIST test results and the Lyapunov exponents calculated for both raw chaotic data outputs and random number sequence have been consistent. Another statement that the calculated Lyapunov exponential for a random number sequence is positive can be used as an indicator for the cryptographic quality of the generator.

V. CONCLUSION

There is a theoretically strong relationship between chaos and cryptography. The main characteristics of the two disciplines coincide with each other. This strong relationship has always been used in the design of new cryptographic protocols. In this study, it has been shown that this relationship can be used in cryptanalysis of chaos based cryptographic designs.

It is expected that a cryptographic design should provide confusion and diffusion requirements to be considered secure. It has been claimed that these requirements can be measured by Lyapunov exponential. Lyapunov exponents are a quantitative chaos analysis method. Considering the relationship between chaos and cryptography, it has been thought that the presence of chaos could be used to verify that mixing and diffusion requirements have been met.

In this study, it has been shown that random number generators can be analyzed using Lyapunov exponents. The successful analysis results confirmed that the proposed method could be used as a test tool for cryptographic design. It has also been shown that various problems for the NIST test suite can be eliminated.

REFERENCES

[1] S. H. Strogatz, Nonlinear Dynamics and Chaos with Applications to Physics, Biology, Chemistry and Engineering, 2nd Edition, Taylor & Francis, 2014

[2] G. Alvarez, S. Li, Some Basic Cryptographic Requirements for Chaos-Based Cryptosystems, International Journal of Bifurcation and Chaos, Vol. 16, No. 08, pp. 2129-2151 (2006), https://doi.org/10.1142/S0218127406015970

[3] C Li, When an attacker meets a cipher-image in 2018: A Year in Review, arXiv preprint arXiv:1903.11764.

[4] X. Liu, Y. Song, G. Jiang, Hierarchical Bit-Level Image Encryption Based on Chaotic Map and Feistel Network, International Journal of Bifurcation and ChaosVol. 29, No. 02, 1950016 (2019), https://doi.org/10.1142/S0218127419500160

[5] F, Özkaynak, Brief review on application of nonlinear dynamics in image encryption, Nonlinear Dynamics 92 (2), 305-313 (2018)

[6] Q. Yin, C. Wang, A New Chaotic Image Encryption Scheme Using Breadth-First Search and Dynamic Diffusion, International Journal of Bifurcation and ChaosVol. 28, No. 04, 1850047 (2018), https://doi.org/10.1142/S0218127418500475

[7] G. Ye, C. Pan, X. Huang, Z. Zhao, J. He, A Chaotic Image Encryption Algorithm Based on Information Entropy, International Journal of Bifurcation and ChaosVol. 28, No. 01, 1850010 (2018), https://doi.org/10.1142/S0218127418500104C

[8] Q. Shen, W. Liu, A Novel Digital Image Encryption Algorithm Based on Orbit Variation of Phase Diagram, International Journal of

Bifurcation and ChaosVol. 27, No. 13, 1750204 (2017), https://doi.org/10.1142/S0218127411750204

[9] Y. Li, X. Li, Chaotic hash function based on circular shifts with variable parameters, Chaos, Solitons & Fractals, Volume 91, October 2016, Pages 639-648

[10] M. A. Chenaghlu, S. Jamali, N. N. Khasmakhi, A novel keyed parallel hashing scheme based on a new chaotic system, Chaos, Solitons & Fractals, Volume 87, June 2016, Pages 216-225

[11] A. Kanso, M. Ghebleh, A fast and efficient chaos-based keyed hash function, Communications in Nonlinear Science and Numerical Simulation, Volume 18, Issue 1, January 2013, Pages 109-123

[12] H. S. Kwok, W. K. S. Tang, A Chaos-Based Cryptographic Hash Function for Message Authenticayion, International Journal of Bifurcation and ChaosVol. 15, No. 12, pp. 4043-4050 (2005), https://doi.org/10.1142/S0218127405014489

[13] E. Solami, M. Ahmad, C. Volos, M. N. Doja, M. M. Si Beg, A New Hyperchaotic System-Based Design for Efficient Bijective Substitution-Boxes, Entropy 2018, 20(7), 525; https://doi.org/10.3390/e20070525

[14] Özkaynak, F, Construction of Robust Substitution Boxes Based on Chaotic Systems, Neural Computing and Applications, DOI: 10.1007/s00521-017-3287-y.

[15] M. Bakiri, C. Guyeux, J. Couchot, A. K. Oudjida, Survey on hardware implementation of random number generators on FPGA: Theory and experimental analyses, Computer Science Review, Volume 27, February 2018, Pages 135-153

[16] M. L. Sahari, I. Boukemara, A pseudo-random numbers generator based on a novel 3D chaotic map with an application to color image encryption, Nonlinear Dyn (2018) 94:723–744 https://doi.org/10.1007/s11071-018-4390-z

[17] E. Zambrano-Serrano, J. M. Muñoz-Pacheco, E. Campos-Cantón, Chaos generation in fractional-order switched systems and its digital implementation, AEU - International Journal of Electronics and Communications, Volume 79, September 2017, Pages 43-52

[18] D. Lambic, M. Nikolic, Pseudo-random number generator based on discrete-space chaotic map, Nonlinear Dyn (2017) 90:223–232 DOI 10.1007/s11071-017-3656-1

[19] A. Kanso, N. Smaoui, IRREGULARLY DECIMATED CHAOTIC MAP(S) FOR BINARY DIGITS GENERATIONS, International Journal of Bifurcation and ChaosVol. 19, No. 04, pp. 1169-1183 (2009), https://doi.org/10.1142/S0218127409023573

[20] R. C. Hilborn, Chaos and nonlinear dynamics: an introduction for scientists and engineers, Oxford University Press, 2000.

[21] J. C. Sprott, Chaos and time-series analysis, Oxford University Press, 2001

[22] R. Hegger, H, Kantz, T. Schreiber, TISEAN Nonlinear Time Series Analysis, https://www.pks.mpg.de/~tisean/

[23] F. Özkaynak, Cryptographically secure random number generator with chaotic additional input, Nonlinear Dynamics 78 (3), 2015-2020, 2018.

[24] A. Rukhin, J. Soto, J. Nechvatal, M. Smid, E. Barker, S. Leigh, M. Levenson, M. Vangel, D. Banks, A. Heckert, J. Dray, S. Vo, A statistical test suite for random and pseudorandom number generators for cryptographic applications. NIST Special Publication 800–22rev1a (2010).

Design and Construction of Compact CNC Router

G. YALCIN[1], S. NESELI[2], H. TERZIOGLU[1] and A.C. AGACAYAK[1]

[1] Konya Technic University, Konya/Turkey, gyalcin@ktun.edu.tr, hterzioglu@ktun.edu.tr, agacayak@ktun.edu.tr
[2] Selcuk University, Konya/Turkey, sneseli@selcuk.edu.tr

Abstract - **3 axes CNC milling machine design and produce is important for creating advanced parts in industry. Designed and builded CNC router machine has single rotational speed and 3 axes movement ability. For motion on three axes to cutting operation it can be used three stepper motors. For providing machine rigidity has been used grinding bars and its suitable accuracy bedding. The generation of G codes has been made using Grbl Controller. The interaction with computer has been operated via Arduino. Motion capacity of head for X, Y and Z are 300x350x140 mm. Also there is no tool magazine so change of the tools can be performed by hand, easily. The construction of main body material is aluminum sigma profile with cross section of 20x20 mm. This machine can be used for cutting operation of polyamide, electrical circuit card and wooden materials to confidence.**

Keywords – **Arduino, CNC, Milling machine, Router, Stepper motor**

I. INTRODUCTION

CNC router lathes have become very popular lathes used today to save much more time and labor. Special CNC router lathes can be designed for many different parts that are not mass production. These parts are produced on special design CNC router lathes and mass production can be started and presented to both national and world markets. In the following literature, the importance of router design and usage is mentioned.

Neşeli et al. [1] have designed a three-axis table-type CNC router machine using SolidWorks program. In that design, they accepted the working limit dimensions of the machine as 500x600x450 mm. The most preferred stepper motors have been used in the drive systems of the machine axes, which are easily available on the market. The machine's control panel is programmable with the help of Mac 3 software, Arduino and PLC software. In this way, it is thought to contribute to education with CNC router which is designed to be used in interdisciplinary projects and design works.

Automation of any welding process is very important for controlling welding process parameters and achieving high production speed of desired quality in automotive applications. Sowrirajan et al. [2] in their study, to control welding speeds on two axes have created a computer-aided numerical control system. This system has helped to achieve various benefits in terms of welding automation in the automotive industry by effectively controlling the welding speed.

Sushama et al. [3] In order to perform asynchronous operation on CNCs, they developed a C language firmware by utilizing the intelligent features of AVR Micro controls. In this way, the motion motors were able to provide vibration-free movements up to 30 kHz and showed that they can operate with standard G codes on CNCs without any problems. This CNC control software has also made it available for free, which also supports laser mode.

In the study of Yıldırım et al. [4] determined the success of the project development and implementation training courses given to university students on their students. In this direction, theoretical and practical training was given to the students on the theoretical calculations of machine construction, machine design and manufacturing, assembly stages and system analysis and operation. As a result of this training, students were asked to design and manufacture three axis mini CNC routers. As a result of the study, it is seen that the students have successfully transferred the theoretical knowledge to the design and manufacture of CNC routers. After the manufacturing process was completed, a sample sample was processed and the functionality of the mini CNC router machine was tested and the results were evaluated. In addition, student achievement was statistically analyzed with a written exam including CNC machine design, construction principles and manufacturing processes. The results and analyzes obtained when the exam is evaluated; They found that the success rate of the exam was 77.75% in the light of the theoretical and practical knowledge that the students received during the project.

Coban et al. [5] In their studies, they have created a six-degree-of-freedom robot system called 'FBF-6 robot' designed for use in industrial areas. With this system, they realized the design of robot mechanics and drive systems as well as the system kinematics that provide the ideal system inputs to the robot for the accuracy of the end positioning. The simulations were run using the Matlab program and concluded that the entire robot should be useful for the design of static Coulomb friction and control of the drive system by minimizing the effects of nonlinear components.

Karabey [6] designed, modeled and manufactured prototype of 3 axis CNC milling machine which can be used in workshop courses in their project work. The machining limits of the CNC milling machine are 500x650x120 mm. CNC stepper motor, ball bearings, aluminum construction, ball screw and ball nut systems are used. In addition, CNC motion

systems, electronic systems, drive systems and precision have been examined. Electronic control unit; It consists of three stepper motor drives, drive control circuit and power supply. Mach 3 CNC program is used as machine control software. The theoretical accuracy and standard deviation of the machine were calculated. As a result, the prototype triaxial CNC milling machine developed for educational purposes was run smoothly.

In the study of Ekim and Cengiz [7] in their work, four axis CNC milling design and prototype manufacturing were made. The operating logic of the system is made in accordance with the four-axis CNC logic. As a result of this study, Mach 3 control has been carried out to measure accuracy in X, Y, Z and A axes. Accordingly, 9.98 mm advance against the G code given for 10 mm advancement on Z axis, 2.98 mm corresponding to the G code given for 3 mm advancement on the X axis. The sensitivity of the system was ± 0.2.

Aktan et al. [8] In order to manufacture the 3-axis CNC router system for training purposes, mechanical components are linearly connected, and electronic control interface cards and drives are produced with a mechanical and electronic approach. At the same time, an interface program has been prepared to control the router via USB. Thanks to their work, a new concept CNC machine with an easy-to-use interface for educational purposes was designed and manufactured.

Uyar et al. [9] 4 axis CNC milling machine was designed and prototyped. The body construction and axes are modeled in 3D and the table dimensions are 600x500x120 mm. Styrofoam materials are processed by CNC developed applications are made.

Yarimbas and Gökdemir [10] projects include the introduction of CNC machines to human life, the necessity of CNC machines and the application of CNC machines. Selection criteria of CNC machine are mentioned. Advantages and disadvantages of CNC machine over other machines are discussed. In addition, the features of an NC (Numerical control) and CNC machine were compared. Information is given about the parts of the CNC machine made as an application. General information about Mach 3, the interface program used in CNC operation, is explained.

Uyanık et al. [11] in their work, composite materials thickness measurements, crack detection, such as to be used in operations such as 3-axis positioning of various end components, 3-axis CNC Router design and manufacturing have made. In this study, the purpose of design, theoretical calculations of construction, drawings of manufacturing and assembly, finite element analysis and working principle of the system are explained.

Kaygısız et al. [12], in their workshops, labs and laboratories of the vocational schools can be manufactured with school facilities and low-cost, three-axis desktop CNC milling by designing, have produced prototypes. They performed experiments to determine the accuracy and accuracy of the manufactured CNC and evaluated the results. In order to determine the accuracy of the axes, groove lengths were measured and standard deviations were calculated. To test the CNC's 2.5-axis machining capabilities, the pocket element was machined and measured. They successfully processed Atatürk relief in order to test 3 axis free surface treatment ability.

In the work of Ion Nae and Tiberiu Andrei [13], a CNC milling machine using stepper motors is easy to operate, useful even for small part applications. Step motors have the advantage that they do not require feedback from the process while providing high precision and repeatability.

Kutlu [14] determined the necessary design parameters for the design and manufacture of three-axis table type CNC milling machine and made the necessary static and dynamic calculations for the design and manufacturing of the machine. In line with the calculations, it was drawn in a three-dimensional drawing program. The three-axis table-type CNC milling machine, which has been drawn and designed, has been machined in metalworking machines in the industry. Bearing systems to transmit and direct movements in the axis system of the machine have been purchased as ready. Mechanical parts were assembled and the system was made ready. The drive system of the axes of the machine is provided with stepper motors. Electronic control of three axis table type CNC milling machine is made by stepper motor drivers and control board. As a result, the three-axis table-type CNC milling machine operated smoothly and the workpiece was machined.

In the master's thesis [15], a low-cost, fully Turkish and educational set is designed for the students who are trained in CNC education. CNC training set, an electronic book that can get theoretical information about CNC, use of CNC, structure, programming, etc. a multimedia environment where topics are discussed, an editor environment where programs can be written, a simulation environment where the result of the written program can be seen on the computer, a mini CNC machine with normal machine functions, which is a medium where the actual shape of the piece will be seen.

II. MATERIAL AND METHOD

In this study, main frame of CNC router machine is designed to be a modular system by using sigma profiles which can be used on a desktop. It can be fixed to any table type (Wood, Metal, etc.) by sigma profiles. All of the axis movements which are designed in SolidWorks program and designed as solid working area with a working area of 300x350x140 mm can be simulated.

Workable materials: wood, polyamide, electrical circuit board is thought to be designed, the axis system of the designed machine to transmit and guide the bearing system is designed according to the maximum force values that can be released during operation. The drive system of the machine axes is realized with the most preferred step motors which are easily available on the market. The control panel of the three axis table type CNC router machine is made programmable by Grbl software, Arduino and PLC software. The designed device (Figure 1) consists of four main parts:

- Lower frame and part mounting table
- Upper frame
- Cuttin tool motion mechanism
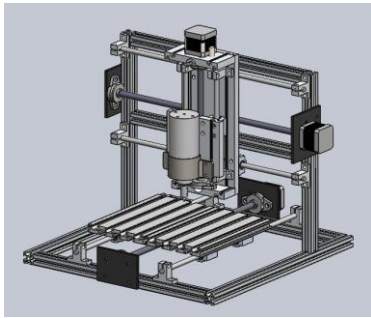- Control panel and software display

Figure 1: Designed CNC router machine

A. Lower Frame and Part Mounting Table

The lower frame is designed to carry 20x20 mm sigma profiles and processing length 300x350x140 mm in order to carry both the upper moving system and the cutting motion mechanism system. The components are assembled using M6 bolt fasteners which can be removed and installed inside. In order to provide stiffness, profiles are formed using internal corner connection elements. A stepper motor was used on the chassis to make the Y axis movement. In order to ensure tolerance within the desired limits in the direction of movement of the table to which the workpiece is to be connected, two ball screw shafts are mounted on the right and left sides and the actual movement ball screw shafts in the center. Bearing system is also used on all surfaces which are mobile and will be exposed to load. If desired, these sigma profiles can be fixed to the table or to a desired location. Figure 2 shows the subframe assembly designed.
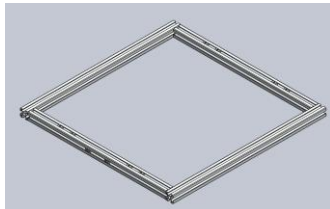

Figure 2: Lower frame assembly

B. Upper Frame

The system has been made rigid by using 20x20x140 mm sigma profiles which will eliminate the negativities (vibration, lathing, machine dynamics problems, etc.) that should be avoided in order to remain within the accepted tolerance range during tool path formation in the X axis. A stepper motor is used for X axis movement. In addition, the profile cross-section is the same to ensure dimension fit in the mounting of the upper frame to the lower frame. The bearing is designed with one screw center shaft and two column shafts. Two horizontal sigma profiles parallel to each other are used for the assembly of the cutting tool movement to be mounted on the system. Figure 3 shows the top frame assembly.
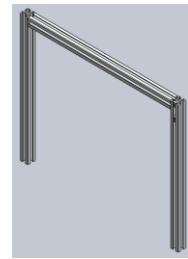
Figure 3: Upper frame assembly

C. Cuttin tool motion mechanism

It is the part that enables the cutting tool to rotate and move along the Z axis. A stepper motor is used to control the feed movement and an additional motor with a rotation speed of 5000 rpm is placed for speed adjustment. A total of three parallel spindle systems are designed with double-sided spindle and central ball screw spindle to ensure smooth and linear movement of the cutter. Each shaft is supported using suitable ball bearings to allow them to turn over and over. The system is mounted on the upper frame by means of screw connections of the main body into which it can be placed. Figure 4 shows the cutting tool movement mechanism.
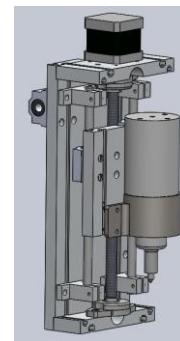
Figure 4: Cutting tool motion mechanism

Mounting picture Linear bearings and ball screw shafts were used for the transmission of motion of the three-axis table-type CNC router in Figure 5. Stepper motor is selected for all axes as the drive motor. Spindle motor was preferred as the cutter motor. Thus, the cutting forces in the X, Y, Z axes were calculated, then the cutting motor was selected. In other calculations, linear bearing, ball screw shaft, stepper motor types and dimensions required for X, Y, Z axis were determined.
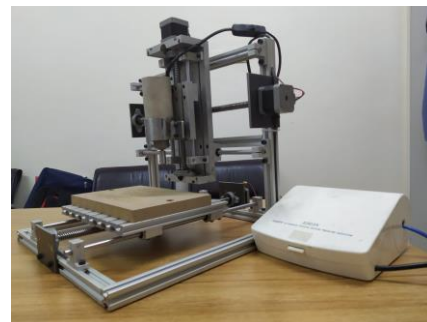
Figure 5: The view of CNC router machine

D. Control panel and software display

The control of the three-axis table-type CNC router can be performed using Arduino, PLC or electronic cards. In order to process the G codes required for CNC machines, Grbl software is provided as programmable by communicating with the control circuit. The interface used for writing CNC codes and monitoring the simulation is shown in Figure 6.

Figure 6: Interface screen of Grbl software

Through the developed interface, parameters such as tool information, cutter position and feed can be controlled inside or outside the process. Thanks to the simulation screen, process safety and operational performance will be improved according to the criteria to be determined. In addition, possible errors will be prevented by operating the tool path codes to be generated without the system running. The designed data transfer board is shown in Figure 7

III. WORKING PRINCIPLE OF EXPERIMENT DEVICE

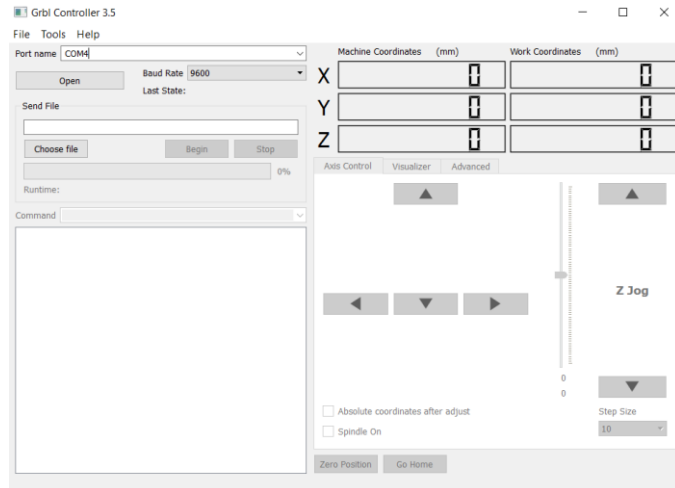The desired production process will be realized by controlling the three axis table type CNC router bench with the software. The control system can work with manual data entry or with G codes generated in any packet program (CAM). It will be able to process parts with a movement range of 300x350x140 mm. The tool path can be formed synchronously along the X, Y, Z axes. It is therefore possible to define non-linear paths via the control interface. In fact, interpolations such as pocket evacuation or island creation can be implemented with ready-made codes.

IV. RESULTS AND DISCUSSION

Almost all products in the manufacturing sector are produced using CNC lathes. CNC lathes are a system in which how and to what extent the parts to be machined are processed by a computer commanded by numerical codes. Therefore, these machines are among the indispensables of the manufacturing industry. In order to train the operators who can use and code these looms which are important for the sector, courses are given on the use of looms in schools. It is very important for students to take interdisciplinary studies in their schools by taking software, design and processing

techniques courses from different departments in terms of efficiency of their applications in industry. Giving the practical training will increase the permanence of the knowledge and thus the personnel expected by the industry will be trained. Computer, electrical and electronic program students will learn the usability of the software, machine drawing and construction program students made designs by machine program students reading through the production, all of them by seeing the return of their jobs will be provided to increase their commitment to their profession.

All departments will be able to use the produced three-axis CNC router machine in their own fields. The cost of the CNC router machine is approximately 570 US Dollars. Periodic maintenance fees for a CNC router are no longer a problem for the machine designed in this study and periodic maintenance is cost-effective and can be performed by technical personnel. It is aimed that the CNC router, which is designed within the scope of this study, will serve as an example for the workshops of other institutions that are making the same movements and will be produced and serviced for future sales.

As a result of this study, the transfer of the information given to the students during the course of project development and implementation has been accomplished successfully. Throughout this study, students had the opportunity to learn about the transfer of theoretical knowledge, the problems encountered, the difficulties and how these problems were solved from the beginning of design to production. As a result of this study, it was seen that the most important problem of the students in vocational school was self-confidence problem. In future studies, it is planned to process and analyze metallic materials by adding liquid cooling system in addition to the workshop.

In the next study, the machine dimensions can be enlarged further. By reducing the tolerance ranges, more precise parts can be machined. Tool change system can be used for mass production. It can be processed faster by adding different loop systems in CNC machines.

REFERENCES

[1] Neşeli S., Yalçın G., ve Terzioğlu H. (2018). "Üç Eksenli Masa Tipi Cnc Router Tasarımı" , VII. International Vocational Schools Symposium (UMYOS'18) ISBN: 978-605-68882-4-3 Azerbaijan, 16-18 October 2018.

[2] Sowrirajan, M., Koshy Mathews, P. ve Ashok, D. (2018). Design and Fabrication of Computer Numerical Controlled 3-Axis Welding Manipulator for Automotive Industries. International Research Journal of Automotive Technology (IRJAT), 1(1); 13-20.

[3] Sushama Kolhe, A., Deepak Varde, V., Devyani Khairnar. S., Anushka Aware, M. (2018). CNC Controller based on Microcontroller ATmega1284P. International Journal of Electronics, Electrical and Computational System (IJEECS), ISSN 2348-117X, Volume 7, Issue 3.

[4] Yıldırım F., Doğan O., Elen L., Çiçek B. (2017). Transfer of Project Development Training To Vocational High School Students to Three Axis Mini Cnc Router Design: An Applied Study. International Journal of Education Science and Technology, 3 (3), 125-134, e-ISSN:2458-8628.

[5] Çoban F., Ertuğrul A., Claudia Castillo-Berrio. (2017). Bir FBF-6 Robot Sisteminin Tasarımı, Simulasyonu ve Hareket Kontrolü Üzerine Çalışma. S-331-335, Otomatik Kontrol Ulusal Toplantısı, TOK 2017, 21 – 23 Eylül, Yıldız Teknik Üniversitesi, İstanbul.

[6] Karabey Ö., (2016). Prototip 3 Eksenli Cnc Freze Tasarimi ve Uygulaması. Yüksek Lisans Tezi, Cumhuriyet Üniversitesi Fen Bilimleri Enstitüsü Makine Mühendisliği, Sivas.

[7] Ekim B., Cengiz M.T. (2016). Dört Eksenli Masaüstü CNC Freze Tezgahı Tasarımı ve Prototip İmalatı. Karabük Üniversitesi Mühendislik Fakültesi Mekatronik Mühendisliği, Lisans Bitirme Tezi, Karabük.

[8] Aktan M.E., Akkuş N., Yılmaz A., Akdoğan E., (2016). Design and Implementation of 3 Axis CNC Router for Computer Aided Manufacturing Courses. MATEC Web Conferences 45, 05002-P.2/P.5.

[9] Uyar S., Beler F., Çetinkaya K., (2012). Eğitim Amaçlı 4 Eksenli Masa Üstü Cnc Freze Tasarımı ve Prototipi. 3. Ulusal Talaşlı İmalat Sempozyumu, 04-05 Ekim, Ankara.

[10] Yarımbaş M.A., Gökdemir V., (2011). 3 Eksenli CNC Tezgahı, Karadeniz Teknik Üniversitesi Mühendislik Fakültesi Elektrik-Elektronik Mühendisliği, Bitirme Çalışması, Trabzon.

[11] Uyanık S., Akpınarlı L., Sabancı S., Özcan R., Kuyucu M., Yıldız S. (2011). Bilgisayar Kontrollü X-Y-Z Tablası Tasarımı ve İmalatı. Ege Üniversitesi Mühendislik Fakültesi Makina Mühendisliği Bölümü, Bitirme Tezi, İzmir. Kaygısız H., Çetinkaya K., (2010). Cnc Freze Eğitim Seti Tasarımı ve Uygulaması. SDU International Journal of Technologic Sciences, pp. 53-71, Vol. 2, No 3, September.

[12] Kaygısız H., Çetinkaya K., (2010). Cnc Freze Eğitim Seti Tasarımı ve Uygulaması. SDU International Journal of Technologic Sciences, pp. 53-71, Vol. 2, No 3, September.

[13] Nae I., Andrei T., (2010). "Designing and Building a CNC Router Using Stepper Motors" , BULETINUL Universităţii Petrol – Gaze din Ploieşti, Vol. LXII, No. 1/2010 55 - 62 Seria Tehnică

[14] Kutlu M. (2006). Üç Eksenli Masa Tipi Cnc Freze Tezgâhi Tasarım ve İmalatı. Afyonkarahisar Kocatepe Üniversitesi Fen Bilimleri Enstitüsü, Yüksek Lisans Tezi, Afyonkarahisar.

[15] Alan S. (2006). Cnc Eğitim Seti Tasarımı. Selçuk Üniversitesi Fen Bilimleri Enstitüsü, Yüksek Lisans Tezi, Konya.

Design of Small Scale Fire Extinguishing Robots for Educational Purposes

H. TERZİOĞLU[1], A.C. AĞAÇAYAK[1], G. YALÇIN[1] and S. NEŞELİ[2]

[1]Konya Technical University, Konya/Turkey, hterzioglu@ktun.edu.tr, acagacayak@ktun.edu.tr, gyalcin@ktun.edu.tr
[2]Selcuk University, Konya/Turkey, sneseli@selcuk.edu.tr

Abstract **- In this study, it is aimed to intervene a fire in a closed area by a mobile autonomous robot with image processing and obstacle identification methods. Small scale fire fighting robots designed and realized for educational purposes. The robot is designed to extinguish fires in confined spaces where people can reach or cannot reach them. It acts without hitting any obstacles during the intervention in the fire zone. The robot uses HC-SR04 distance measurement and fire-sensing UV temperature measurement sensors to measure the distance to objects. The HC-06 bluetooth module is used for wireless communication and the Arduino microcontroller is used for the control of the robot. The robot car kit is controlled by DC motors using the L293D Motor Drive Module. When the robot reaches the target, it extinguishes the fire by operating the water pump. The propeller positioned in front of the robot prevents the electronic cards and parts of the robot from being affected by heat. As a result of this study, a robot prototype which performs these functions has been produced and necessary hardware and software integration has been made.**

Keywords **- Remote Control, Traveling Robot, Mini Fire Fighting Robot, Arduino.**

I. INTRODUCTION

THE security of houses, laboratories, offices, factories and buildings in every area where people live their lives is at the forefront. Fires are one of the main threats that threaten people in these habitats. Due to the silent occurrence of the fire and the flammability of the goods used in the places where people live, the fire starts and spreads rapidly. It is quite difficult and time consuming to extinguish and cool the environment after fires that have not been intervened in time. The first precautions to be taken in the fight against fire are taking measures to prevent the fire from occurring and intervening and extinguishing as soon as possible and when the fire event starts.

Today, firefighters, which are fire extinguishing units, are often notified after the fire is seen, and the time taken for them to come to the scene often leads to the loss of property, serious injuries, and death or serious injuries to people throughout their lives. In order to avoid these irreparable disasters, technology offers innovations to people. Fire extinguishing systems that are used in public places today are both costly and can spread water to large areas rather than the place where

the fire spreads, causing damage without the need to be affected by the surrounding water. For this reason, in our study, a prototype fire extinguishing robot was designed in order to intervene in the place where the fire spread with minimum damage and as soon as possible. The robot is approximately 15 * 25 * 15 cm in size.

There is progression, drive system, software development system and fire detection system with sensor on it, avoiding obstacles with distance sensor. We design the fire detection system using two flame sensors of the fire fighting robot.

Thus, 180^0 angle fire screening can be done. We design the fire detection system in the fire fighting robot and program the fire detection and combat procedure using a sensor-based method.

The robot is able to detect the fire through the flame sensor by overcoming obstacles and approach the fire with the drive system. Two methods are used for intervention. In the first method, the water in the water tank squeezes water from the hard hose and pump motor on fire. In the second intervention method, it tries to extinguish by reducing the effect of fire by providing air flow over the fire with the motor and propeller connected to the front of the robot. A modular low-cost fire prevention design is designed using the IR sensor and ultrasonic sensor in the robot.

II. MATERIALS AND METHODS

A. Microprocessor

Arduino UNO R3 is used as microprocessor in the system. In 2010, Arduino UNO was made available to the public. ATmega328 is a software based electronic prototyping platform using microcontroller. Operating between 7-12V, this platform has 14 digital input / output pins. We can use 6 of them for PWM. With Arduino UNO, we can obtain physical information from various sensors and conduct various experiments with this information. In addition, motor, LED, buzzer, such as the output can be a stimulator.

Figure 1: Arduino UNO R3 Picture.

B. UV Flame Sensor

Generally fire alarm systems are based on smoke detection. But it is designed as a project that can detect when the flame comes out with the sensor. It is also a kind of sensor used in fire extinguishing robots. The sensor has features that vary depending on the quality. They operate correctly at an average light wavelength of 760 nm ~ 1100 nm. They can detect the presence of fire at a corner of about 60 °. Operating temperature is -25 ~ +85 ° C.

C. About the Module

The fire sensor sensor board is a sensor board used to detect fire with a wavelength between 760 nm and 1100 nm. It has one IR receiver. It can be used as a fire detection sensor in fire extinguishing robots. Sensitivity can be adjusted with trimpot on it and can be output both analog and digital.

Figure 2: Flame Sensor Module.

D. HC-SR04 Ultrasonic Range Sensor

In the application, the HC-SR04 ultrasonic distance sensor is used for distance measurement. There are two surfaces on the sensor as input and output. An ultrasonic sound wave is emitted at a certain frequency from the output surface to the medium. The input surface also collects the sound waves at certain frequencies emitted by the output surface. For distance measurement, the sound wave is first emitted from the output surface to the medium. The oscillating sound wave is emitted at an angle of 15 degrees. When the emitted sound wave strikes an object in this area, it is reflected back from the object surface to the sensor.

When the reflected wave comes to the input surface, the process is completed. The distance between the wave and the exit surface is measured and the distance of the object is calculated.
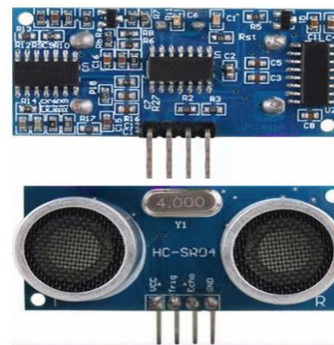

Figure 3: HC-RS04 Module.

There are 4 pins, VCC, Trig, Echo, GND on the sensor. Of these, the VCC pin supply (5 volts) is the GND pin ground line. The trigger pin is the pin that allows the wave to oscillate from the output surface. The Echo pin is the pin that notifies Arduino that the wave reflected on the input surface has reached. HC-SR04 ultrasonic distance sensor time diagram is shown below. The Trig pin should take + 5V at least 10 µS to start the measurement. This means that the 8-wave sound wave is transmitted out of the sensor at 40 kHz and is expected to reflect. When the Hc-sr04 receives the sound wave from the receiver, the Echo pin switches from 0 V to 5 V and waits for a time proportional to the distance. Here, by measuring the width of the Echo pin, we can get the distance.
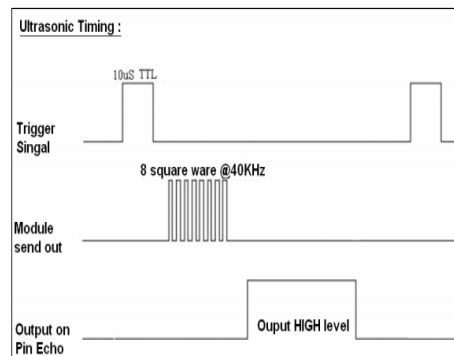
Figure 4: HC-RS04 Module Signal.

Ultrasonic timing
Trigger signal: 1 signal sent when the trigger pin is active.
Module send out: When the trigger pin is active, it sends 8 square wave signals at 40 kHz at one time.
Output on pin Echo: The signal generated by the reflected waves on the Echo pin in rotation.

E. HC05 Bluetooth-Serial Module Board

The HC05 Bluetooth Module is made for the use of Bluetooth SSP (Serial Port Standard) and wireless serial communication applications. It provides easy operation with the help of pins on it. This card supports Bluetooth 2.0, allowing communication at a frequency of 2.4GHz. There are many types of communication for remote control. The most common method used in Arduino applications is communication with bluetooth module. Bluetooth can

communicate in an open area with a radius of 10 to 100 m, as well as the speed of data transfer. In addition, audio and video data is transferred via the bluetooth module.

There are two things we need to pay attention to from the communication pins. The first is that we need to connect the rx (receive) pin on the module to the tx (transmit) pin on the Arduino and the tx pin on the module to the rx pin of the arduino. Otherwise communication will not be possible. The second thing to note is that the communication pins of the module operate at 3.3 volts. The 3.3v from the tx pin of the module does not pose any inconvenience for the Arduino. However, the tx pin (5V) module from the arduino also causes permanent damage. Therefore, voltage reducing circuit must be made to input rx of module. For voltage drop as shown in the picture 1k and 2k resistors are connected in parallel and 3.3 volts are obtained.
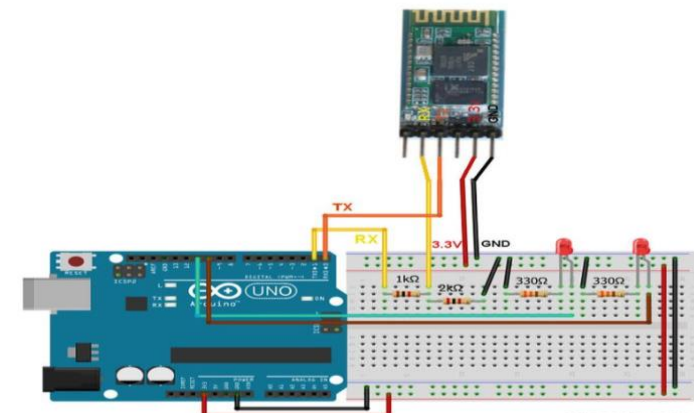

Figure 5: HC-05 Bluetooth Serial Module Board Arduino connection.

F. L293D Engine Driver

It is a H-bridge motor driver integrated in the range of 4.5-36V, capable of delivering 600mA continuous current per channel. It is often preferred in many robotics projects and motor driver boards. First of all, let's start with getting to know our engine shield in a short way. With the motor shield you have seen, we are able to run two servo motors, four DC motors and two stepper motors. We have four outputs to operate our DC motors, these are our M1, M2, M3, M4 outputs. With the EXT_PWR terminal, we must supply the voltage to feed our motors.
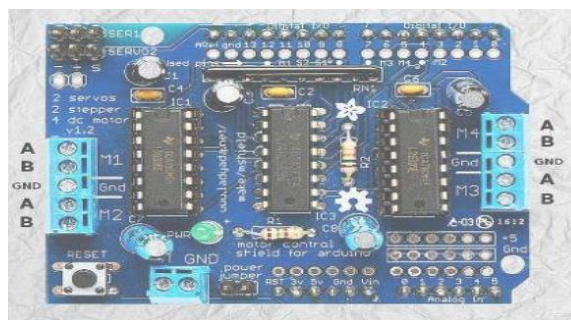
Figure 6: L293D Motor Drive Module.

Since Arduino Motor Shield has a large number of motors, the number of pins used is high. Shield; Pin 2 uses all pins except 8 pins, 13, A0-A5. That's why this motor comes with extra sensors, etc. the remaining pins should be considered if used. To drive the DC motor, you must add the adafruit motor shield library to your Arduino library.

Our scheme applies to both L293D and L293B as the connections are exactly the same. After installing our circuit, we install our code.
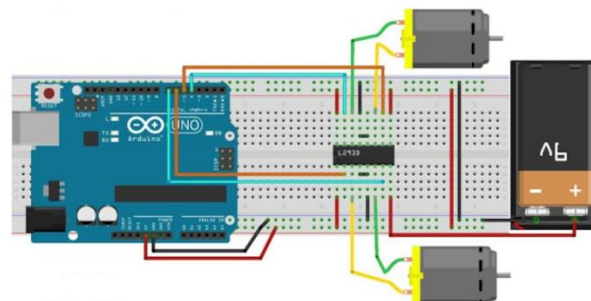
Figure 7: L293D Motor Drive Circuit Connection.

G. DC Motor

Brushed DC Motors: The most basic type is the DC motor type. They are used in many projects with or without gearboxes. Speed control can be achieved by simply changing the voltage between the two terminals of brushed DC motors with a very simple operating principle. If we want to change the direction of operation of the motor, we must change the direction of the applied voltage. For this process, we need the so-called H-bridge circuits. This type of motors can have direct shaft output or gearbox (gearbox). The biggest advantage of brushed DC motors is that speed and direction control can be done very easily by varying the magnitude and direction of the voltage applied to the motor.

Figure 8: DC Motor.

Small-sized DC motors are popularly used as affordable driver integrated circuits such as the L293D to drive with microcontroller. In this project, the fire extinguishing robot was used both in the direction controls and in front of the robotton flame removal propeller.

The system is based on the toolkit.
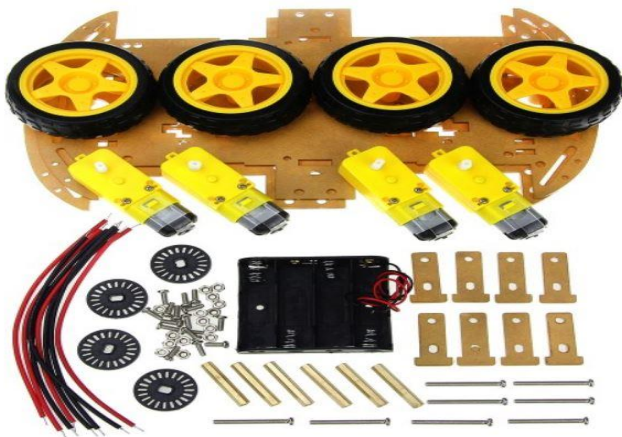
Figure 9: Used Car Kit.
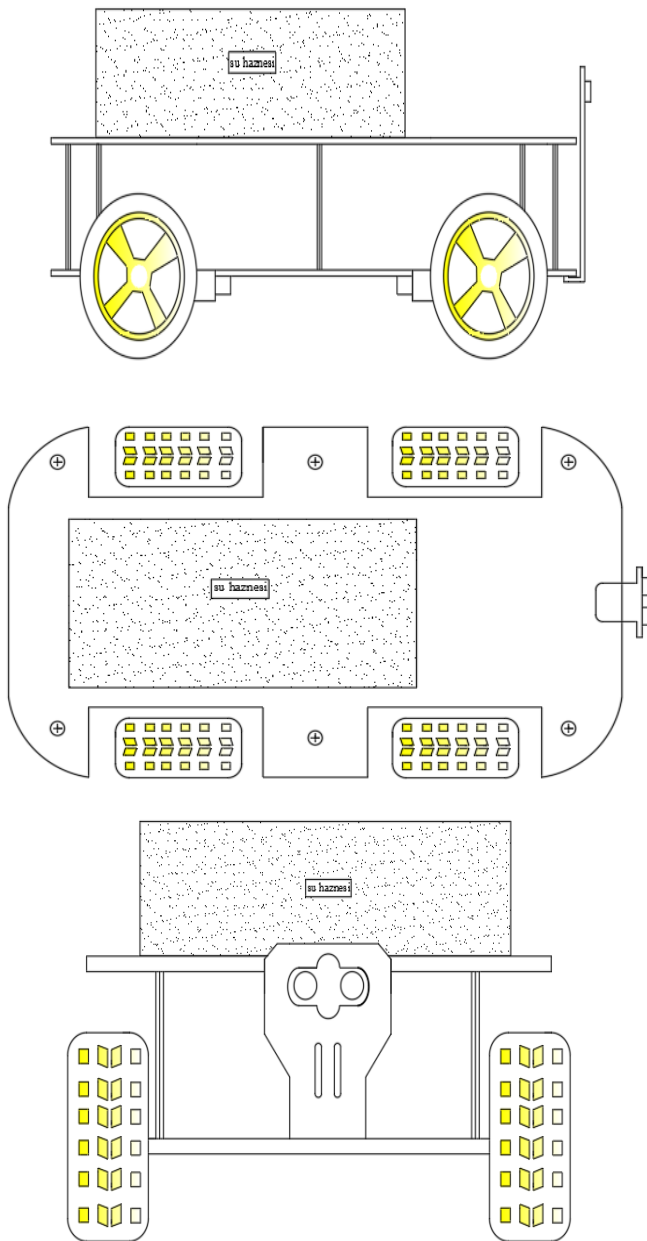
Figure 10: Top and Front View of the Car Kit.

LD293D Motor drive and Arduino connection is made as shown.

Figure 11: LD293D Motor drive and Arduino connection.

LD293D Motor driver, Arduino connection and HC-SR04 distance sensor are mounted on the car kit as shown.

Figure 12: LD293D View of the motor driver, Arduino and distance sensor in the car kit.

The fire fighting robot is designed as shown.

Figure 12: Front and Side View of Fire Fighting Robot.

III. CONCLUSION

In this study, firstly, prototype fire extinguishing robot was designed in order to intervene in the fire place with minimum damage and as soon as possible. A distance sensor is positioned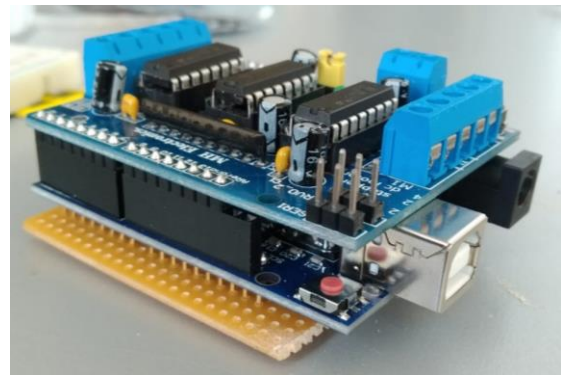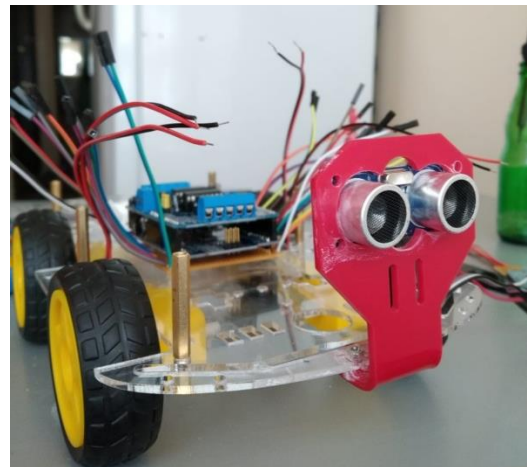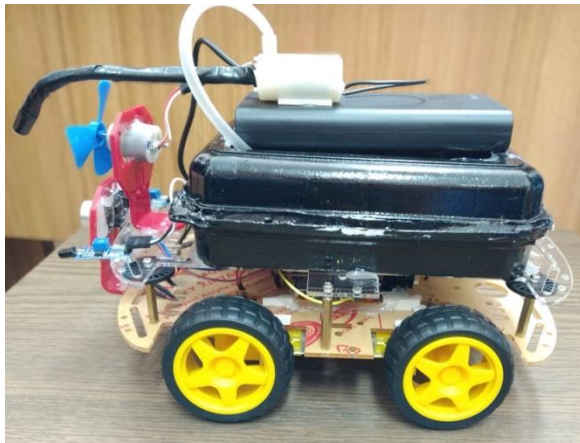 on the designed flame suppression robot to detect and overcome obstacles. For fire detection, a fire detection system has been established which can detect fire at an angle of 180 °, where a flame sensor is positioned on both sides of the robot. Thus, the fire detection and combat procedure was programmed using a sensor-based method. The robot, which detects the flame by means of a sensor, moves on top of the flame and sprayes the extinguishing chemical contained in the tank above it with a hose and pump.

With the propeller placed in front of the fire extinguishing robot, the flame and hot air coming on the robot were removed from the robot. This prevents heat damage to electronic circuits and sensors in front of the robot. In the future studies, when the robot detects the fire, it is thought that it can be made more useful by adding the design to the building authority and fire crews while informing the building authority and firefighters on the other hand by means of communication modules.

REFERENCES

[1] Badamasi, Y. A., "The working principle of an Arduino," *In Electronics, computer and computation (icecco), 2014 11th international conference,* (pp. 1-4), 2014, September.

[2] Brock, J. D., Bruce, R. F.,ve Reiser, S. L. (2009). Using Arduino for introductory programming courses. Journal of Computing Sciences in Colleges, 25(2), 129-130, 2009.

[3] Banzi, M., "O'Reilly Media. Inc. Getting Started with Arduino", 10, 978-1, 2009.

[4] Stone, W. L., "Robotics and automation handbook", *CRC Press*, Boca Raton, Florida, 2005.

[5] Siciliano, B., Sciavicco, L., Villoni, L. ve Oriola G., Robotics Modelling, "Planning and Control", Springer Verlag, London, 2009.

[6] A. Angelo, J., "Robotics: A Referene Guide to he New Technology", Greenwood Press, Westport, 2012.

[7] Spong M. W., Hutchinson, S. ve Vidyasagar, M., "Robot Modelling and Control", *John Wiley&Sons, Inc, United States of America*, 2011.

[8] AlHaza T., Alsadoon A., Alhusinan Z., Jarwali M., Alsaif K., "New Concept for Indoor Fire Fighting Robot," *Procedia - Social and Behavioral Sciences*, Volume 195, 2343-2352, 2015.

[9] Rehman A., Necsulescu D., Sasiadek J., "Robotic Based Fire Detection in Smart Manufacturing Facilities," *15th IFAC Symposium onInformation Control Problems in Manufacturing*, Ottawa, Canada,1640-1645, 11-13 Mayıs 2015

[10] Duran, F., Avuçlu, O., & Canal, M. R., "Uzaktan Denetimli Gezgin Mini Yangın Söndürme Robotu Tasarımı ve Gerçekleştirilmesi," *Gazi Üniversitesi Fen Bilimleri Dergisi Part C: Tasarım ve Teknoloji*, 4(4), 259-265.

[11] Canbay, D. E., Yolal, E., Şahan, Ö. F., Terzioğlu, İ., & Sezer, V., "Yangın Söndüren Otonom Robot Tasarımı Ve Gerçeklemesi, " Design and Implementation of Fire Fighter Autonomous Robot.

[12] Tok, Özge. "Design and manufacturing of a fireproof fire rescue robot, " *MS thesis. Izmir Institute of Technology*, 2008.

Internet Resources

[13] https://www.arduino.cc/en/Guide/ArduinoMega2560, on August 10, 2018.

[14] https://sinancanbayrak.com/hc-rs04-ultrasonik-mesafe-sensoru-nedir-nasil-calisir/, on June 06, 2019.

[15] https://sinancanbayrak.com/hc-sr04-de-kullanilan-58-nereden-geliyor/, on June 06, 2019.

[16] https://gelecegiyazanlar.turkcell.com.tr/konu/arduino/egitim/arduino-301/arduino-ile-uzaklik-olcumu, on June 06, 2019.

[17] https://static5.arrow.com/pdfs/2013/10/14/2/49/45/232/arduin_/manual/22arduino-mega2560_r3-sch.pdf, on August 12, 2018.

[18] http://techtonic10.blogspot.com/2016/06/arduino-mega-2560-pin-mapping.html, on August 15, 2018.

A New Method for Performance Improvement of Chaotic S-box Structures

YAŞAR SELİM BAHÇECİ[1] and FATİH ÖZKAYNAK[1]

[1] Fırat University, Elazığ/Turkey, yasarselimbahceci@gmail.com
[1]Fırat University, Elazığ/Turkey, ozkaynak@firat.edu.tr

Abstract - **In cryptographical protocol design, substitution boxes have an important place. One common method for creating substitution boxes is random selection based designs. Chaos-based designs are the most effective method in the literature for random selection. In this paper, it is aimed to improve performance of chaos based substitution box designs by using new methods. Nonlinearity is one of the most prominent features used as performance measurement in substitution boxes. It is aimed to improve the nonlinear criterion with the proposed method.**

Keywords - **Chaos; cryptography; s-box; nonlinearity**

I. INTRODUCTION

THE basic design principle of chaos-based substitution box (s-box) structures is based on the conversion of chaotic system outputs, which are a powerful source of entropy, to s-box values. The reason why chaotic systems are characterized as a strong source of entropy stems from the fact that these systems are highly dependent on initial conditions and control parameters. In other words, very small (negligible) changes in initial conditions and control parameters result in very different outputs. As a result, the chaotic system used in design is associated with complexity.

S-box structures, especially block ciphers, are one of the basic cryptographic building blocks used to provide the confusion feature of cryptographic protocols. There are several methods used in the s-box design process. The most widely known of these is a table proposed by Nyberg and used in AES block encryption algorithm with a size of 16x16, ranging from 0-255. After the emergence of various problems of this design approach, alternative designs were investigated. Chaos-based S-Box designs have become increasingly popular in this context. To demonstrate its practical applicability, the chaos-based S-Box designs are also designed in 16x16 size tables with values ranging from 0-255. Five basic requirements are used in the literature to evaluate the quality of these designs. These are Bijective, Nonlinearity, Sac, Bit Independence Criterion and XOR distribution.

Ref. [3] and Ref. [14] show what the highest performance values can be achieved for chaos based s-box structures. In these studies, it was stated that the maximum value that can be reached for nonlinearity is 106.75 and the lowest value that can be calculated for XOR distribution is 10. The best S-Box designs obtained using the method proposed in the Ref. [3]. In this paper, it will be examined whether performance improvements can be made by applying various post processing algorithms to experimentally obtained data in [14].

The rest of the study is organized as follows. In the second section, chaos analysis methods have been mentioned briefly. In the third section, the design architecture of the chaos based random number generator is explained. In the fourth section, randomness test results and Lyapunov analyzes have been given for two different dataset. In the last section, obtained results have been summarized and suggestions have been made for future studies.

II. LITERATURE SURVEY

Various methods for the design of s-box structures have been proposed in the literature. These methods fall into three main categories: heuristic methods, algebraic methods and random selection-based methods. Modern block encryption algorithms often use s-box design techniques based on strong algebraic relationships. The most well-known of these are suggested by Nyberg. In addition, new design techniques have been investigated with the development of new attack techniques such as side channel analysis and algebraic attacks. New design techniques based on chaotic systems are among these studies.

Chaos-based s-box design was first seen in the early 2000s. In these designs, s-box structures were produced using discrete-time chaotic systems [1, 3-15]. The most important advantage of discrete time chaotic systems is their simple mathematical models. The general approach in these group designs is to improve the performance criteria of the s-box using different chaotic maps [3-7]. The second group of studies emerged in 2010 [8]. The common point in the design logic of these group studies is to improve the s-box performance criteria by increasing the chaotic system complexity. Therefore, continuous time chaotic systems with a more complex mathematical model have been used in these group designs [2-13]. In the third group of chaos-based s-box designs, hyper-chaotic or time-delayed chaotic systems have been used to further increase the complexity of the chaotic system. Studies have also suggested that chaos merges with other structures. Another popular s-box design approach is based on the chaotic system of fractional order [14]. However, a recent study has shown that the performance of chaos-based s-box structures is independent of the chaotic system [14]. Ref. [14], the maximum nonlinear values that can be reached for chaos-based s-box structures, and the minimum maximum value are shown in the differential distribution (XOR) table. For example, it is stated

tht the non-linear criteria of s-box can be 106.75 maximum and the minimum maximum value in the differential distribution is 10.

III. PROPOSED METHOD
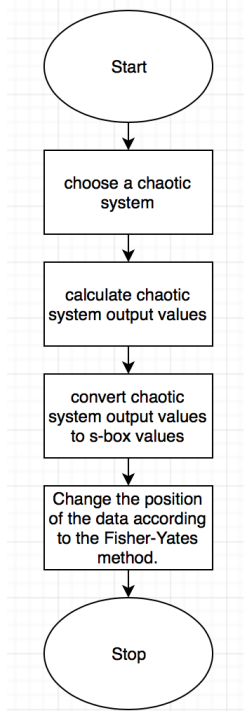
The procedure for creating the S-box is shown in Figure 1.

Figure 1. Flowchart of proposed method

As stated in the second section, there are many successful s-box generator methods. The first three steps of the algorithm whose steps are given in Figure 1 represent this process. These output values are changed according to Fisher Yates Shuffle method. The flowchart of the Fisher Yates algorithm is given in Figure 2.
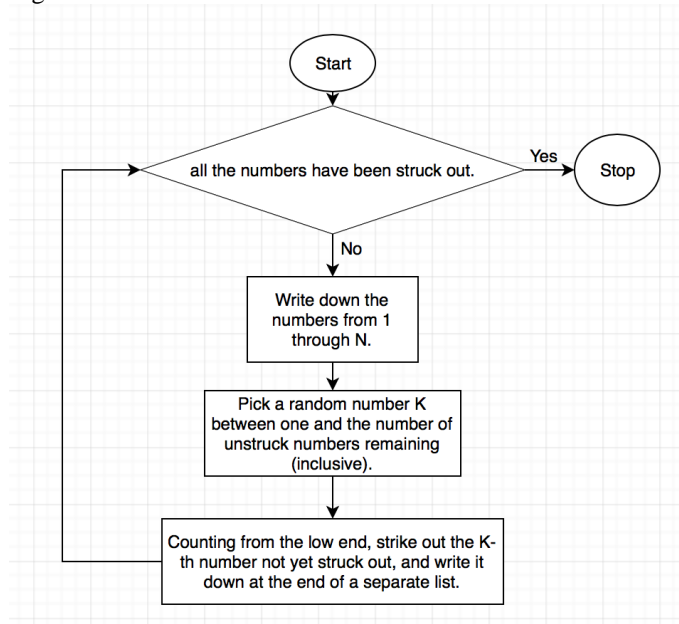
Figure 2. Flowchart of Fisher-Yates method

The step-by-step operation of the Fisher-Yates algorithm on a small example of 10 elements is shown in Figure 3.

Range	Roll	Scratch	Result
		1 2 3 4 5 6 7 8	
1–8	3	1 2 3 4 5 6 7 8	3
1–7	4	1 2 3 4 5 6 7 8	3 5
1–6	5	1 2 3 4 5 6 7 8	3 5 7
1–5	3	1 2 3 4 5 6 7 8	3 5 7 4
1–4	4	1 2 3 4 5 6 7 8	3 5 7 4 8
1–3	1	1 2 3 4 5 6 7 8	3 5 7 4 8 1
1–2	2	1 2 3 4 5 6 7 8	3 5 7 4 8 1 6
		1 2 3 4 5 6 7 8	3 5 7 4 8 1 6 2

Figure 3. The step-by-step operation of Fisher-Yates method

IV. ANALYSIS RESULT

An s-box structure has been generated using method proposed in Ref. [10]. The structure and cryptographic properties of this s-box are given in Table 1. In this study, the values in Table 1 have been shuffled using proposed method. The new values obtained are given in Table 2.

The cryptographic features of the s-box tables produced are also given in these tables. There are generally five basic criteria in s-box evaluation. These criteria are bijective, nonlinearity, strict avalanche criterion, bit independence criterion and XOR distribution. It has been shown that performance improvements can be made by using various post-processing methods from the analysis results.

V. CONCLUSION

S-box structures play an important role especially in block encryption algorithms. Since it is the only nonlinear element in many encryption algorithms, it is thought that there is strong relationship with chaos theory. In this study, a new method for the performance improvement of chaos based designs in the s-box design process is proposed. The original aspects of the thesis proposal are listed below.

- Upper limits for performance characteristics of s-box structures are given in the literature. Maybe, the validity of these limits will be proved using post-processing algorithms.
- Improvements will be made for designs whose performance measurement is below theoretical limits.
- The analysis results showed that the performance improvements yielded successfully.

REFERENCES

[1] M. S. Açikkapi, F. Özkaynak, and A. B. Özer, "Side-channel analysis of chaos-based substitution box structures", IEEE Access, vol. 7, pp. 79030–79043, 2019. doi: 10.1109/ACCESS.2019.2921708.

[2] C. Wu and D. Feng, Boolean Functions and Their Applications in Cryptography. Berlin, Germany: Springer, 2016.

[3] D. Lambi¢, ''S-box design method based on improved one-dimensional discrete chaotic map,'' J. Inf. Telecommun., vol. 2, no. 2, pp. 181–191, 2018.

[4] H. A. Ahmed, M. F. Zolkipli, M. Ahmad, "A novel efficient substitution-box design based on firefly algorithm and discrete chaotic map", Neural Computing and Applications, vol. xx, no. x, pp. xx-yy, May 2018.

[5] K. M. Ali and M. Khan, "Application based construction and optimization of substitution boxes over 2D mixed chaotic maps", Int. J. Theor. Phys., pp. 1–27, 2019. doi: 10.1007/s10773-019-04188-3.

[6] A. H. Zahid and M. J. Arshad, "An innovative design of substitution-boxes using cubic polynomial mapping", Symmetry, vol. 11, no. 3, p. 437, 2019. doi: 10.3390/sym11030437.

[7] M. F. Khan, A. Ahmed, K. Saleem, and T. Shah, "A novel design of cryptographic SP-network based on gold sequences and chaotic logistic tent system", IEEE Access, vol. 7, pp. 84980–84991, 2019. doi: 10.1109/ACCESS.2019.2925081..

[8] F. Özkaynak and A. B. Özer, "A method for designing strong S-boxes based on chaotic Lorenz system", Phys. Lett. A, vol. 374, no. 36, pp. 3733–3738, 2010.

[9] L. Liu, Y. Zhang, and X. Wang, "A novel method for constructing the S-box based on spatiotemporal chaotic dynamics", Appl. Sci., vol. 8, no. 12, p. 2650, 2018. doi: 10.3390/app8122650.

[10] F. Özkaynak, "An analysis and generation toolbox for chaotic substitution boxes: A case study based on chaotic labyrinth rene thomas system", Iranian J. Sci. Technol.-Trans. Elect. Eng., pp. 1–10, 2019. doi: 10.1007/s40998-019-00230-6.

[11] M. F. Khan, A. Ahmed, and K. Saleem, "A novel cryptographic substitution box design using Gaussian distribution", IEEE Access, vol. 7, pp. 15999–16007, 2019. doi: 10.1109/ACCESS.2019.2893176.

[12] T. Ye and L. Zhimao, "Chaotic S-box: Six-dimensional fractional Lorenz–Duffing chaotic system and O-shaped path scrambling", Nonlinear Dyn. vol. 94, no. 3, pp. 2115–2126, 2018. doi: 10.1007/s11071-018- 4478-5.

[13] A. H. Zahid, M. J. Arshad, M. Ahmad, (2019). "A Novel Construction of Efficient Substitution-Boxes Using Cubic Fractional Transformation". Entropy, 21(3), 245.

[14] F. Özkaynak, "Construction of robust substitution boxes based on chaotic systems", Neural Comput. Appl., pp. 1–10, 2017. doi: 10.1007/s00521-017-3287-y.

[15] E. Tanyildizi, F. Özkaynak, A New Chaotic S-Box Generation Method Using Parameter Optimization of One Dimensional Chaotic Maps, IEEE Access, Volume 7, Page(s): 117829 - 117838, DOI: 10.1109/ACCESS.2019.2936447

Table 1. Classical chaos based s-box structure and cryptographic features

s-box structure					
Nonlinearity Average		**Strict Avalanche Criterion Average**	**Bit Independence Creation**		**Input / Output XOR Distribution**
			BIC-SAC	**BIC-Nonlinearity**	**Max**
101.75		0.4905	0.5034	103.36	10

s-box																
	0	**1**	**2**	**3**	**4**	**5**	**6**	**7**	**8**	**9**	**A**	**B**	**C**	**D**	**E**	**F**
0	145	154	48	51	61	124	18	83	110	122	227	179	67	206	74	163
1	42	155	195	248	139	181	114	247	92	82	29	96	34	236	229	75
2	241	17	91	39	101	28	221	129	147	24	216	250	188	109	217	239
3	173	1	57	87	50	135	117	86	190	8	200	253	210	7	197	168
4	166	211	38	119	15	137	182	35	134	228	183	202	37	138	214	120
5	71	123	240	99	141	191	43	40	108	209	94	249	151	66	152	69
6	22	63	121	242	140	98	45	235	95	107	133	255	150	102	161	2
7	125	178	104	105	12	32	41	118	88	184	84	225	233	245	21	112
8	177	185	127	153	212	157	187	169	237	158	254	243	113	25	89	219
9	44	80	54	30	116	27	223	244	146	132	10	78	193	164	49	203
A	246	59	198	230	85	11	199	55	9	194	31	20	159	73	13	167
B	213	53	36	126	165	115	70	162	215	175	77	174	46	128	220	4
C	251	160	65	208	5	130	143	3	192	93	189	33	136	23	52	106
D	204	0	64	172	196	207	103	232	131	176	148	186	72	149	60	252
E	90	100	97	180	201	79	224	231	111	226	14	171	205	19	170	218
F	47	142	238	234	81	26	156	16	222	58	68	144	6	62	56	76

Table 2. Improved structure and cryptographic properties for the chaos-based s-box structure in Table 1

s-box structure							
Nonlinearity Average		Strict Avalanche Criterion Average		Bit Independence Creation		Input / Output XOR Distribution	
				BIC-SAC	BIC-Nonlinearity	Max	
104.75		0.5071		0.4981	104.14	10	

s-box																
	0	**1**	**2**	**3**	**4**	**5**	**6**	**7**	**8**	**9**	**A**	**B**	**C**	**D**	**E**	**F**
0	132	94	162	67	139	241	137	32	27	107	64	165	63	255	41	227
1	163	205	77	206	230	127	244	130	81	170	171	122	203	210	158	24
2	113	101	238	1	95	252	78	75	195	190	229	29	2	51	123	240
3	124	91	202	199	208	209	76	221	152	136	180	233	68	79	191	153
4	186	141	133	176	150	52	5	88	142	129	104	20	177	207	131	23
5	38	102	126	220	90	98	164	242	82	72	135	55	231	160	185	21
6	45	99	62	9	211	197	103	112	54	46	80	234	222	71	40	167
7	47	92	155	118	96	245	178	58	115	193	11	219	31	100	173	179
8	16	214	28	43	56	156	19	6	7	120	93	109	236	42	175	174
9	189	105	128	14	83	18	61	108	144	201	84	33	154	119	183	125
A	10	237	235	159	225	134	106	65	215	166	147	196	87	148	114	213
B	111	121	59	66	184	73	34	168	35	232	182	60	53	138	216	17
C	116	187	254	44	146	194	74	13	70	181	217	247	248	15	8	212
D	228	223	169	249	246	161	198	204	89	36	117	151	0	218	12	37
E	50	172	226	48	85	253	69	145	30	49	22	157	4	110	86	39
F	25	149	57	188	3	243	250	192	143	200	97	239	140	26	224	251

Implementation of Babylonian Square Root Computation Algorithm with VHDL

Abdulkadir SADAY[1], Ilker Ali OZKAN[2]

[1]Selcuk University, Konya/Turkey, asaday@selcuk.edu.tr
[2]Faculty of Technology, Selcuk University, Konya/Turkey, ilkerozkan@selcuk.edu.tr

Abstract - **One of the most important calculation operation in many systems is the calculation of the square root of numbers. In digital systems and digital signal processing there are some different algorithms to calculate the square root of numbers. Designing of the square root calculator depends on the algorithm or method for the programming format. The Babylonian method was examined and used as a different approach in this study. The digital square root calculator designed is mainly based on the Babylonian method and design was implemented with VHDL language.**

Keywords – **VHDL, square root, Babylonian method, FPGA**

I. INTRODUCTION

Square root is a necessary and frequently used mathematical expression in applications such as image processing, sound processing, scientific calculation. Numerous computational algorithms such as mathematical predictive method and restoring method have been developed for square root calculation. In general, algorithms have been developed in order to perform the calculation process quickly and to obtain an accurate result [1, 2].

In many applications, the Newton method is adopted for the square root calculation. In this method, the approximate value of the square root is calculated by iterations. In order to obtain the iteration equation, Newton method can be used which approximately result is obtained in iteration equation. In each iteration, multiplication, addition and subtraction operations are performed and this causes process density. In order to accelerate the multiplication in the calculation, the parallel multiplier is used by partial production and then an aggregator is used to obtain the result of the production. Since multipliers require a very large number of gates, it is impractical to use multiple multipliers to achieve exact square root calculations [3].

In many of the science and engineering applications, square root calculation has an important place. In applications, the result of an operation is not always expected to be an integer. For this reason, square root calculations with decimal numbers are studied. On FPGA, operations with decimal numbers are provided by the decimal points libraries called as floating-point and fixed-point libraries. Hasnat et al [4] presented square root and inverse square root calculation by using the Quake's algorithm. In their studies, they applied square root calculation using single precision floating point library.

The current commercial DSP and embedded processors do not provide special complex number calculation units. Instead, they use a number of real basic computational processes at the software level. This parsed form of calculation results in reduced computational performance due to process complexity. The software unit called Cordic is an advanced library that allows you to handle process with complex and trigonometric numbers. Cordic provides to done complex arithmetic operations with only summing and shifting operation [5].

In their study, Leeser and Wang designed the square root calculation with the floating-point library of variable precision. Their calculator is based on the computational algorithm called Taylor Series in the literature. In their calculator, a small lookup table and small multipliers are used to obtain the first few terms of the Taylor series. The methodology they offer is in IEEE standard format and is flexible so that different formats can be obtained from their method. They stated that their methods support zero and nearest rounding property [6].

In addition to speed, it has an important place that the field used in calculation operations. In the literature, there are studies in which the minimum field is used within the square root calculation algorithms. This algorithm is based on the formula called Dwandwa Yoga. In their study, Kachhwal and Rout presented square root calculators based on the old Indian mathematical formula [7]. Their calculator generates 16-bit floating-point output versus 24-bit floating-point input. They argued that the method presented by them had the lowest area usage.

In this study, square root calculator was performed based on Babylon method. While calculating perfect-square numbers is easy in mathematics, the calculation of the roots of non-perfect square numbers are very difficult. In the Babylon method, the square root is calculated by a numerical repeating process. The first algorithms for the square root calculation process are known to be found by Babylonians [8].

II. MATERIAL AND METHOD

In this study, the Babylonian method, called the simple repeating algorithm, was used to calculate the square root of numbers. This algorithm is based on the repetition of simple operations until the result is reached regardless of whether the number is a perfect-square number.

In the Babylonian method, it is stated that the constant number that the series of numbers generated by the iteration algorithm for any initial value approaches is the result of the

square root of the number to be rooted [8]. The square root value of a number starts with an estimate of any initial value. This randomly selected value is the initial value of the repetition rule, and each new value obtained as a result of the operation is the new initial value.

In the Babylonian method, the calculation in the repetition process is made by using Equation 1.

$$x_{n+1} = \frac{1}{2}\left(x_n + \frac{a}{x_n}\right) \qquad (1)$$

A set of numbers is obtained by applying the repetition rule with any initial value in the equation. The number approached and repeated as a result of the sequence of numbers is the square root of the desired number.

If it is wanted to calculate the square root of the number 12 as an example of calculating the square root with the Babylon method, first any number should be selected for the initial value. With this initial value, the repetition rule must be applied and the number that is repeating in the number array must be found. The result can be expressed as a repetitive number. The square root calculation of the number 12 depending on the algorithm is given in Figure 1.

$$x_0 = 2$$
$$x_1 = \frac{1}{2}\left(x_0 + \frac{a}{x_0}\right) = \frac{1}{2}\left(2 + \frac{12}{2}\right) = 4,00$$
$$x_2 = \frac{1}{2}\left(x_1 + \frac{a}{x_1}\right) = \frac{1}{2}\left(4 + \frac{12}{4}\right) = 3,50$$
$$x_3 = \frac{1}{2}\left(x_2 + \frac{a}{x_2}\right) = \frac{1}{2}\left(3,50 + \frac{12}{3,50}\right) = 3,46..$$
$$x_4 = \frac{1}{2}\left(x_3 + \frac{a}{x_3}\right) = \frac{1}{2}\left(3,46 + \frac{12}{3,46}\right) = 3,46..$$

Figure 1 – The square root calculation of 12 by the Babylon method

As shown in Figure 1, a random number is assigned for x0 and the repetition rule is calculated based on this initial value. At each step, the result was calculated using the new initial value. The result is repeated for 4 steps as shown in the number array. In this case, the repetitive number is the square root of the number given at the entry. When this process is done with the calculator, it is concluded that the square root of the number 12 is 3.46.

Compiled libraries as standard can be used in the calculation of arithmetic operations with FPGA. Floating-point and fixed-point libraries are standard libraries that allow operations with decimal numbers. Fixed-point is frequently used for simple decimal numbers, while floating-point is used for more complex decimal numbers. Due to its structure fixed-point is an easier and faster library to implement and calculate. It is frequently used in applications in which result can be predicted and which requires speed [9].

In the literature, many algorithms such as Rough estimation method, exponential identification, Taylor series, Newton Raphson method and digit-by- digit method are used in the studies. There are many applied methods of square root calculation. They can be grouped into two classes as predictive and digit-by-digit methods. The digit-by-digit calculation method is generally divided into two groups, restoring and non-

restoring. In this method, the computational speed is lower than other methods [9, 10].

The implementation of the algorithm that returns the approximate square root result by the Babylon method on FPGA is uncomplicated because that the method contains simple mathematical expressions. Therefore, the use of a fixed-point library is sufficient to implement this algorithm and to obtain results. The use of fixed-point provides the advantage of quick calculation for applications requiring a square root calculator [11].

In the fixed-point library, the definitions are made in the form of sfixed (signed) and ufixed (unsigned) numbers. In defining the decimal number by VHDL, the exact part and the decimal part of the number are expressed separately. The definition is made by specifying a positive integer of the desired length for the full part of the number and negative integers for the decimal part. The expression of a sample number with the fixed-point library is can be defined as $x = sfixed(10 \ downto - 8)$.

The definition shown in Figure 2 indicates that the full part of the x number is 11-bit and the decimal part is 8-bit. As the value defined for the full part increases, the magnitude of the number that can be expressed increases, as the value defined for the decimal part increases, the decimal precision of the number to be expressed increases. In the calculation of the numbers expressed by the fixed-point, multipliers 2^0, 2^1, 2^2.. are used for the full part and 2^{-1}, 2^{-2}, 2^{-3}.. for the decimal part. If the number is negative, the first bit indicates the sign and the calculation is made as 1's complement to the number.

In the implementation of the Babylon method with VHDL, the repetition rule is provided by a simple loop. The initial estimate value is calculated by dividing the number by the largest and smallest multiplier. In the calculator, 4 variables are used as number, initial values, temporary value and output. The square root of the value defined by the number variable is kept at the temporary value until the output value is repeated. In the repetition where the output value is equal to the temporary value, the square root of the number is found.

III. RESULTS

FPGAs are programmed with programming languages called Verilog and VHDL [7]. In this study, the square root calculation process based on the approached Babylon method is emphasized and the square root calculator software is realized.

The realized square root calculator was run on Nexys 4 DDR FPGA development board of Digilent company. As input, the 16-bit switch on the development board is used and the result calculated on the output is expressed with 16-bit led. In order to indicate the completion of the calculation process, a status changing led is assigned to the result and a change in status is provided after the calculation.

The flowchart of the calculation of the Babylon method using FPGA with VHDL programming language is given in Figure 2.
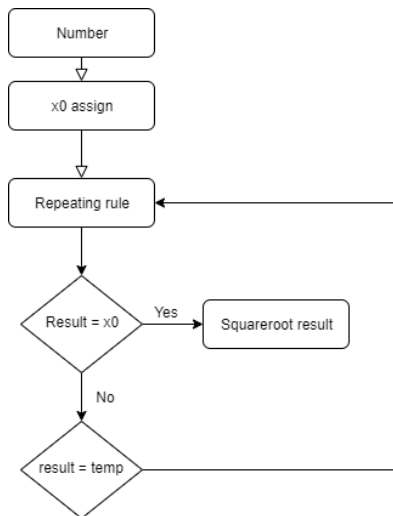
Figure 2 – Babylonian Algorithm flow chart

The process flow shown in Figure 2 starts with the assignment of the number to the input. With the assignment of the number, a random number is assigned to the initial value x_0. This assignment is performed in the random number generation block generated by the VHDL and is valued according to the multipliers of the input number. After the initial value is assigned, the repeating rule loop given in Equation 1 is executed. The value calculated during the loop is assigned to the temporary variable and held in it until the next calculation. If the temporary variable is equal to the calculated result, the square root calculator block terminates by returning the result. If the result is not equal to the transient variable, the repeating rule is reapplied, and this loop continues until it is equal.

The result obtained after the loop gives the square root of the entered number. In integer operations, the result gives the value closest to the actual value. The rounding of the number up or down varies depending on the programmer's choice during programming. In this study, square root calculator was realized using fixed-point library. Thus, even if the square root value of the entered number is a decimal number, it can be expressed.

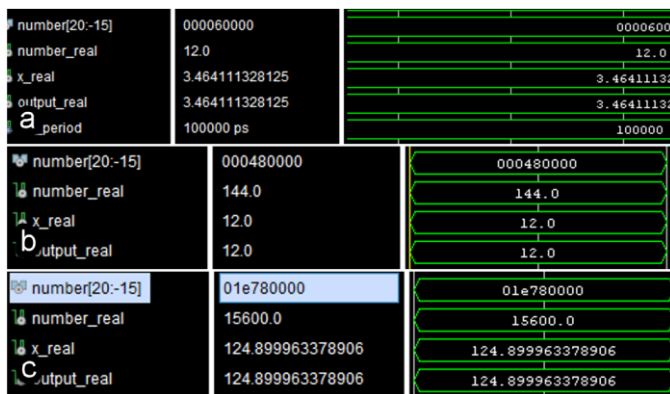Several examples of numbers calculated with the performed VHDL software are shown in Figure 3.

Figure 3 – Square root calculations of different numbers with FPGA
(a) 12 (b) 144 (c) 15600

The square root value 3.46 of the number 12 calculated in Figure 1, is the same as the algorithm result performed on FPGAs. As can be seen in Figure 4, the square root calculator with the Babylon method works on FPGA in a way that yields successful results in decimal numbers.

Calculations were tested at different clock frequencies of the processor with different values. For 10us, 1us and 10ns clock pulses, the results were checked for each rising edge. According to the results obtained, the algorithm works at a speed that can respond in a clock pulse. It was observed that the calculation time did not change by keeping the numbers to be calculated at very high values and assigning the predictive initial variable at far values. However, depending on the application that use the square root calculator and the complexity of the numbers, it is possible to obtain the calculation result at different time intervals.

As a result of this study, a square root calculator based on the Babylonian method, which can calculate with integer and decimal numbers and which the calculation result can be obtained as a decimal number has been realized by using FPGA with VHDL programming language.

REFERENCES

1. Jidin, A.Z. and T. Sutikno, *FPGA Implementation ofLow-Area Square Root Calculator*. Telkomnika, 2015. **13**(4): p. 1145.
2. Nanhe, A., et al., *Implementation of fixed and floating point square root using nonrestoring algorithm on FPGA*. International Journal of Computer and Electrical Engineering, 2013. **5**(5): p. 533.
3. Li, Y. and W. Chu. *A new non-restoring square root algorithm and its VLSI implementations*. in *Proceedings International Conference on Computer Design. VLSI in Computers and Processors*. 1996. IEEE.
4. Hasnat, A., et al. *A fast FPGA based architecture for computation of square root and inverse square root*. in *2017 Devices for Integrated Circuit (DevIC)*. 2017. IEEE.
5. Yang, B., D. Wang, and L. Liu. *Complex division and square-root using CORDIC*. in *2012 2nd International Conference on Consumer Electronics, Communications and Networks (CECNet)*. 2012. IEEE.
6. Leeser, M. and X. Wang, *Variable precision floating point division and square root*. 2005, NORTHEASTERN UNIV BOSTON MA DEPT OF ELECTRICAL AND COMPUTER ENGINEERING.
7. Kachhwal, P. and B.C. Rout. *Novel square root algorithm and its FPGA implementation*. in *2014 International Conference on Signal Propagation and Computer Technology (ICSPCT 2014)*. 2014. IEEE.
8. Flannery, D., *The square root of 2: A dialogue concerning a number and a sequence*. 2006: Springer Science & Business Media.
9. Sutikno, T., *An efficient implementation of the non restoring square root algorithm in gate level*. International journal of computer theory and engineering, 2011. **3**(1): p. 46.
10. Zhu, H., Z. Lei, and F.P. Chin, *An improved square-root algorithm for BLAST*. IEEE Signal Processing Letters, 2004. **11**(9): p. 772-775.
11. Li, Y. and M. Leeser, *HML: an innovative hardware description language and its translation to VHDL*. 1995: IEEE.

Biomedical Engineering

Computer Engineering

Electrical and Electronics Engineering

Mechanical Engineering

Mechatronic Engineering

Metallurgical and Materials Engineering

Civil Engineering

ICENTE'19

INTERNATIONAL CONFERENCE ON ENGINEERING TECHNOLOGIES

October 25-27, 2019
Konya/TURKEY

icente.selcuk.edu.tr